

ADD 443218



# Proceedings of Damping'89

8-10 February 1989  
West Palm Beach, Florida

(Pages FAA-1 through IBD-15)

November 1989

Final Report for Period Feb 86 to Feb 89

19960611 155

Approved for public release; distribution is unlimited.

DTIC QUALITY INSPECTED 3

Sponsored by:

Flight Dynamics Laboratory  
of the Air Force  
Wright Aeronautical Laboratories

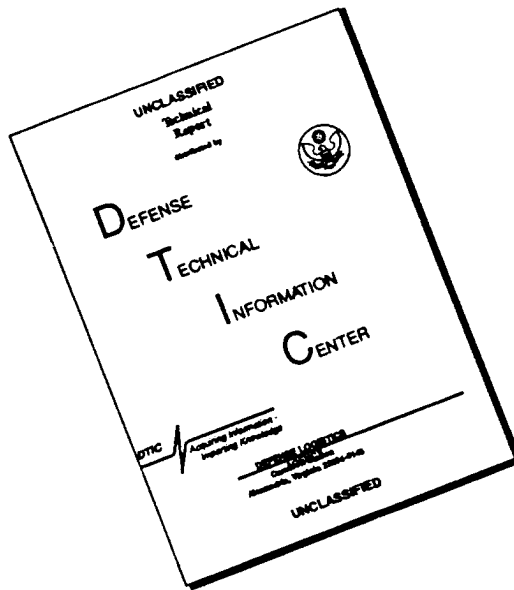
AIR FORCE SYSTEMS COMMAND  
WRIGHT-PATTERSON AIR FORCE BASE, OHIO 45433-6553

DEPARTMENT OF DEFENCE  
PLASTICS TECHNICAL EVALUATION CENTER  
ARDEC PICATINNY ARSENAL, N.J. 07806

S

PLASTEC 054102  
(PL-054103-PL-054105)

# DISCLAIMER NOTICE



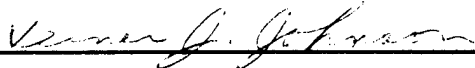
THIS DOCUMENT IS BEST QUALITY AVAILABLE. THE COPY FURNISHED TO DTIC CONTAINED A SIGNIFICANT NUMBER OF PAGES WHICH DO NOT REPRODUCE LEGIBLY.

## NOTICE

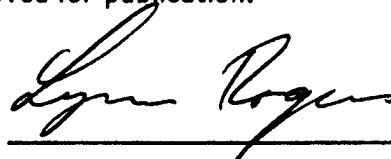
When Government drawings, specifications, or other data are used for any purpose other than in connection with a definitely Government-related procurement, the United States Government incurs no responsibility or any obligation whatsoever. The fact that the Government may have formulated or in any way supplied the said drawings, specifications, or other data, is not to be regarded by implication, or otherwise as in any manner, as licensing the holder or any other person or corporation; or as conveying any rights or permission to manufacture, use, or sell any patented invention that may in any way be related thereto.

This report has been reviewed by the Office of Public Affairs (ASD/PA) and is releasable to the National Technical Information Service (NTIS). At NTIS, it will be available to the general public, including foreign nations.

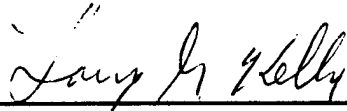
This technical report has been reviewed and is approved for publication.



VERNER J. JOHNSON, Program Manager  
Advanced Metallic Structures ADPO  
Structures ADP Branch



LYNN ROGERS, PhD  
Advanced Metallic Structures ADP



LARRY G. KELLY, Chief  
Structures ADP Branch  
Structures Division

"If your address has changed, if you wish to be removed from our mailing list, or if the addressee is no longer employed by your organization please notify WRDC/FIBAA, WPAFB, OH 45433-6553 to help us maintain a current mailing list".

Copies of this report should not be returned unless return is required by security considerations, contractual obligations, or notice on a specific document.

ADD 443218  
(ADD 443219 - ADD 443221)

Unclassified

SECURITY CLASSIFICATION OF THIS PAGE

REPORT DOCUMENTATION PAGE				Form Approved OMB No. 0704-0188	
1a. REPORT SECURITY CLASSIFICATION Unclassified			1b. RESTRICTIVE MARKINGS		
2a. SECURITY CLASSIFICATION AUTHORITY			3. DISTRIBUTION / AVAILABILITY OF REPORT		
2b. DECLASSIFICATION / DOWNGRADING SCHEDULE			Approved for public release; distribution unlimited.		
4. PERFORMING ORGANIZATION REPORT NUMBER(S) WRDC-TR-89-3116, Vol II			5. MONITORING ORGANIZATION REPORT NUMBER(S)		
6a. NAME OF PERFORMING ORGANIZATION Advanced Metallic Structures Adv Development Prog Office		6b. OFFICE SYMBOL (If applicable) WRDC/FIBAA	7a. NAME OF MONITORING ORGANIZATION		
6c. ADDRESS (City, State, and ZIP Code)  Wright-Patterson Air Force Base OH 45433-6553			7b. ADDRESS (City, State, and ZIP Code)		
8a. NAME OF FUNDING / SPONSORING ORGANIZATION Flight Dynamics Lab. Wright Research Dev. Ctr.		8b. OFFICE SYMBOL (If applicable) WRDC/FIBA	9. PROCUREMENT INSTRUMENT IDENTIFICATION NUMBER		
8c. ADDRESS (City, State, and ZIP Code)			10. SOURCE OF FUNDING NUMBERS		
			PROGRAM ELEMENT NO. 63211F	PROJECT NO. 486U	TASK NO. 11
					WORK UNIT ACCESSION NO. 02
11. TITLE (Include Security Classification)  Damping 1989 Proceedings					
12. PERSONAL AUTHOR(S)					
13a. TYPE OF REPORT Final		13b. TIME COVERED FROM Feb 86 TO Feb 89		14. DATE OF REPORT (Year, Month, Day) 1989 November	
				15. PAGE COUNT 678	
16. SUPPLEMENTARY NOTATION  Pages FAA-1 through IBD-15					
17. COSATI CODES			18. SUBJECT TERMS (Continue on reverse if necessary and identify by block number)		
FIELD	GROUP	SUB-GROUP			
			Vibration damping, controls/structure interaction.		
19. ABSTRACT (Continue on reverse if necessary and identify by block number)  Individual papers of Damping 89 held 8-10 February 1989 in West Palm Beach FL are presented. The subjects included: mechanical properties of polymers, experimental methods, damping in metal matrix composites, friction damping, design of damping structure, modal damping values, and applications of damping, etc.					
20. DISTRIBUTION / AVAILABILITY OF ABSTRACT <input checked="" type="checkbox"/> UNCLASSIFIED/UNLIMITED <input type="checkbox"/> SAME AS RPT. <input type="checkbox"/> DTIC USERS			21. ABSTRACT SECURITY CLASSIFICATION Unclassified		
22a. NAME OF RESPONSIBLE INDIVIDUAL Dr Lynn Rogers			22b. TELEPHONE (Include Area Code) (513)255-6622		22c. OFFICE SYMBOL WRDC/FIBAA



## **Workshop Administration**

### **Director**

Dr. Lynn Rogers  
Flight Dynamics Laboratory of the Air Force  
Wright Aeronautical Laboratories

### **Administrative Chairman**

Mrs. Melissa Arrajj  
Martin Marietta Astronautics Group

### **Assistant Administrative Chairman**

Ms. Jo Ellen Dunn  
CSA Engineering, Incorporated

### **Session Chairmen**

Dr. M. Aswani, Aerospace Corporation  
LTC R. L. Bagley, Air Force Institute of Technology Wright Patterson AFB  
Mr. S. D. Bigelow, Boeing Aerospace Company  
Dr. A. J. Bronowicki, TRW Space and Technology Group  
Dr. D. I. G. Jones, Materials Laboratory, AFWAL  
Dr. M. A. Cutchins, Auburn University  
Mr. M. L. Drake, University of Dayton Research Institute  
Mr. P. G. Gauthier, Naval Sea Systems  
Mr. R. N. Gehling, Martin Marietta Astronautics Group  
Dr. J. L. Gubser, McDonnell Douglas Astronautics Company  
Dr. J. P. Henderson, Materials Laboratory, AFWAL  
Mr. W. Hoskins, Lockheed Missiles & Space Company  
Dr. R. Ikegami, Boeing Aerospace Company  
Dr. C. D. Johnson, CSA Engineering, Incorporated  
Mr. L. Kelly, Flight Dynamics Laboratory, AFWAL  
Dr. E. M. Kerwin, BBN  
Dr. R. LeMaster, W. J. Schaffer, Association  
Dr. Y. P. Lu, DTNSRDC  
Mr. D. R. Morgenthaler, Martin Marietta Astronautics Group  
Mr. A. D. Nashif, Anatrol Corporation  
Dr. T. S. Nishimoto, Rockwell International - SSD  
Mr. M. L. Parin, Anatrol Corporation  
Dr. K. E. Richards, Jr., Martin Marietta Astronautics Group  
Dr. S. S. Sattinger, Westinghouse R&D Center  
Dr. T. D. Scharton, Jet Propulsion Laboratory  
Dr. J. Soovere, Lockheed - California Company  
Mr. C. V. Stahle, Jr., General Electric Company  
Mr. J. A. Staley, General Electric Company  
Mr. S. J. Starr, LTV Aerospace - Aircraft Products  
Dr. R. C. Stroud, Synergistic Technology, Incorporated  
Dr. J. Unruh, Southwest Research Institute  
Mr. H. Wolfe, Flight Dynamics Laboratory, AFWAL

## FOREWORD

This publication includes the individual papers of DAMPING '89 held 8-10 February 1989, West Palm Beach, Florida. The Workshop was sponsored by the Air Force Wright Aeronautical Laboratories through the Advanced Metallic Structures Advanced Development Program Office (AFWAL/FIBAA).

It is desired to transfer vibration damping technology in a timely manner within the aerospace community, thereby, stimulating research, development and applications.

# TABLE OF CONTENTS

## Paper No.

Damping - A Key to More, Faster, Farther, Higher (Keynote Address) Major General Thomas R. Ferguson, Jr.	AAA
Pioneering Damping in Space at General Electric Astro Space Division (Invited Speaker) C. V. Stahle, Jr.	AAB
Aircraft Modal Suppression Yaw Damper System (Invited Speaker) Dr. J. R. Fuller	AAC
SESSION BA—Complex Modulus	
Loss Modulus and Damping Behavior of Poly (Vinyl Methyl Ether)-Polystyrene Blends and IPN's J. J. Fay, Dr. C. J. Murphy, Dr. D. A. Thomas and Prof. L. H. Sperling	BAA
Time-Temperature Superposition in Multi-Component Polymer Blends Prof. R. E. Wetton	BAB*
Predicting Loss Factor Master Curves Using Stiffness Master Curves Derived From Transmissibility Data Dr. S. O. Oyadyi and Prof. G. R. Tomlinson	BAC*
SESSION BB—Aircraft Applications	
Add-on Damping for A-10 Gumbay Life Extension K. R. Wentz	BBA*
Development of a Damped A-10 Engine Air Inlet Ring D. L. Giunto and S. N. Vacca	BBB
Status of Aircraft Integral Damping Demonstration C. L. Rupert and R. Tate	BBC
SESSION BC—Composites	
Damping in Metal Matrix Composites - An Overview Dr. S. P. Rawal, Dr. J. H. Armstrong, Dr. M. S. Misra and Dr. S. G. Fishman	BCA
Highly Damped Gr/Mg Composites for Flexible Space Structures U. K. Kashalikar and J. Boyce	BCB

\*Not available for publication.

# TABLE OF CONTENTS (Continued)

	<u>Paper No.</u>
Measured Damping and Modulus of Composite Cylinders J. B. Andriulli	BCC
SESSION CA—Electro-Rheological & Hydraulic	
The Usage of Electro-Rheological Materials in Viscoelastic Layer Damping Applications J. P. Coulter, T. G. Duclos and D. N. Acker	CAA
Analysis of a Modified Passive Hydraulic Damper with Variable Damping Characteristics H. Su, Dr. S. Rakheja and Dr. T. S. Sankar	CAB
An Experimental Investigation on the Active-Damping Characteristics of a Class of Ultra-Advanced Intelligent Composite Materials Featuring Electro-Rheological Fluids S. B. Choi, Prof. B. S. Thompson and Prof. M. V. Gandhi	CAC
SESSION CB—Damping Identification	
Identification of System Parameters in a Slewing Control Experiment E. Garcia and Prof. D. J. Inman	CBA
An Alternative to FFT for Precise Damping Estimates Prof. S. M. Pandit	CBB
Coupled Modes Resolution by an Exponential Window Prof. A. Agneni, Prof. L. Balis-Crema and Prof. A. Castellani	CBC
SESSION CC—Analysis	
Passive Damping Design Methods Using NASTRAN M. J. Matla	CCA
Application of the Ritz Procedure to Damping Prediction Using a Modal Strain Energy Approach J. C. Parekh and S. G. Harris	CCB
Formulation and Inversion of Transfer Functions of Combined Elastic/Viscoelastic Structures Prof. S. B. Skaar, Dr. G. A. Nariboli and L. Tang	CCC

\*Not available for publication.

# TABLE OF CONTENTS (Continued)

## Paper No.

### SESSION DA—Fractional Derivatives

The Fractional Order Initial Value Problem and  
Its Application to State Space Control Theory  
LTC R. L. Bagley

DAA\*

The Optimal Control of Viscoelastically Damped Structures  
LTC R. L. Bagley, R. Walker and R. Calico

DAB

Solution Techniques for the Fractional Order Eigenvalue Problem  
LTC R. L. Bagley and M. Deveraux

DAC

The Rheology of Anelastic Media Studied by Means of the  
Observation of the Splitting of Its Eigenfrequencies  
Prof. M. Caputo

DAD

### SESSION DB—Space Applications

A Viscous Isolator for Shuttle Hubble Space Telescope Resupply  
L. P. Davis, F. Schmitt and C. L. See

DBA

Constrained Layer Damping for a Space-Based Optical System  
N. C. Bond and R. M. Laurenson

DBB

Hydrostatic Damper for the Space Shuttle Main Engine (SSME)  
High Pressure Oxidizer Turbopump (HPOTP)  
D. G. Goggin, J. K. Scharrer and R. F. Beatty

DBC

Optimized Designs of Viscoelastic Damping Treatments  
Dr. W. C. Gibson and Dr. C. D. Johnson

DBD

Considerations of Synthesized System Damping in  
Dynamic Analysis of Space Structures  
Dr. W. T. Tsai

DBE

### SESSION DC—Basics

Modal Damping - Please Stand Up  
R. B. Fost, M. J. Yan and J. Reed

DCA\*

On Passive Spot Damping Anomalies  
Dr. M. I. Young

DCB

Vibration Damping Performance—What We Should Know About It  
J. Chahine and P. Saha

DCC

Description of Structural Damping  
Prof. L. Gaul, Lt. Col. P. Klein and Dr.-Ing. S. Kempfle

DCD

\*Not available for publication.

# TABLE OF CONTENTS (Continued)

Paper No.

## SESSION FA—Complex Modulus Data

### Interactive Characterization and Database Storage of Complex Modulus Data

B. L. Fowler

FAA

### Comparison of Complex Modulus Data Generated by Three Different Measurement Techniques

M. L. Drake and Dr. A. Sircar

FAB

### Frequency-Temperature Dependence of Polymer Complex Modulus Properties

T. Lewis, A. D. Nashif and Dr. D. I. G. Jones

PL-054103

FAC

### Complex Modulus Measurements Over a Wide Range of Frequencies and Material Characteristics Through the Confrontation of Two Instruments

C. Chesneau, J. Y. Cavaille and J. P. Laures

FAD

## SESSION FB—Structural Applications

### Optimal Application of Damping to the Stanford Gravity Wave Experiment

F. A. McLoughlin and Prof. D. B. DeBra

FBA

### Viscoelastic Passive Dampers for Structures

Dr. P. Mahmoodi and J. M. Kelly

FBB\*

### Large Strain Viscoelastic Dampers for Structures

Dr. P. Mahmoodi, T. T. Soong and L. E. Robertson

FBC\*

### An Internal Damping Configuration for Tubes and Hollow Panels

Dr. E. M. Kerwin, Jr.

PL-054104

FBD

## SESSION FC—Control Structure Interaction

### Active Vibration Control of Flexible Structures

S. P. Sun, Dr. P. K. Raju and M. J. Crocker

FCA

### Robust Realization/Identification of Damped Structures

M. J. Roemer and Dr. D. J. Mook

FCB

### Optimum Selection of Dampers for Freely Vibrating Multidegree of Freedom Systems

Dr. J. J. Gilheany

FCC

### Optimization of Energy Dissipation Rate in Structures

Prof. V. H. Neubert

FCD

\*Not available for publication.

# TABLE OF CONTENTS (Continued)

## Paper No.

### SESSION FD—Non-Linear

#### Effect of Damping on the Predicted Fatigue Life of a Nonlinear Plate

R. N. Miles

FDA

#### The Role of Damping in the Suppression of Parametric Resonances in Nonlinear Systems

Dr. L. D. Zavodney and S. M. Shihada

FDB

#### Distributed Parameter Nonlinear Damping Models for Flight Structures

A. V. Balakrishnan and L. W. Taylor

FDC\*

#### Non-Linear Dynamic Analysis with Frequency-Dependent Damping

F. Venancio-Filho and A. M. Claret

FDD

### SESSION GA—Fluids

#### Fluid Inertia Effects in Squeeze Film Dampers

A. El-Shafei

GAA

#### A New Class of Fluid-Loop Dampers

Dr. A. M. Baz, L. Gumusel and Dr. J. Fedor

GAB

#### Tuned Liquid Damper (TLD) for Suppressing Horizontal Motion of Structures

Dr. Y. Fujino, B. M. Pacheco, L. M. Sun and P. Chaiseri

GAC

### SESSION GB—Friction

#### Contact Stresses in Cables Due to Tension and Torsion

Dr. K. Kumar, Dr. J. E. Cochran, Jr., and Dr. M. A. Cutchins

GBA

#### Effect of Inertial Forces on Damping in a Dry Friction Joint

Dr. O. Vinogradov

GBB

#### Modal Damping of Suspended Cables

Prof. H. Yamaguchi

GBC

### SESSION GC—Struts

#### Analysis, Optimization, Fabrication and Test of Composite Shells with Embedded Viscoelastic Layers

Dr. A. J. Bronowicki and H. P. Diaz

GCA

\*Not available for publication.

# TABLE OF CONTENTS (Continued)

Paper No.

## Passive Damping Concepts for Space Structures With Tubular Members

Prof. Z. Razzaq and B. S. Najjar

GCB

## Design and Analysis of Viscoelastic Struts for Large Space Structures

Y. C. Yiu

GCC

## SESSION GD—Phenomena

### Increased Graphite Fiber Damping via Intercalation

G. A. Lesieutre, A. J. Eckel and J. A. DiCarlo

PL-054105 (GDA)

### Modeling Material Damping Using Augmenting Thermodynamic Fields (ATF)

G. A. Lesieutre

GDB

### Experimental Determination of Damping Mechanisms in a Composite Beam

H. T. Banks and Prof. D. J. Inman

GDC

## SESSION HA—Viscous

### Experimental Investigation of a Passive, Adjustable, Viscous Damper

R. W. Taylor and Prof. J. M. Starkey

HAA\*

### Sliding Laminated Vibration Damper

M. Koleda

HAB\*

### Application of Viscouselastic Damping to Reducing a Light Motorcycle Drive-By Noise

L. Xiaoquian, T. Xieru, C. H. Ku and R. Mingzhang

HAC\*

## SESSION HB—Large Space Structures

### A Survey of Damping in Control of Flexible Structures

Prof. D. J. Inman and G. C. Horner

HBA

### Damping of a Large Space Platform

Dr. A. S. Bicos

HBB

### Payoff of Passive Damping in Active Control of Large Space Structures

Dr. J. Garibotti

HBC

\*Not available for publication.



# TABLE OF CONTENTS (Continued)

## Paper No.

### SESSION HC—Intrinsic

An Experimental Study of the Complex Dynamic Modulus  
G. G. Wren and Dr. V. K. Kinra

HCA

A Design for Improving the Structural Damping Properties  
of Axial Members  
D. J. Barrett

HCB

Optimization of Intrinsic Damping  
Prof. R. D. Adams

HCC\*

### SESSION HD—Joints

Damping-Like Effect of Irregularities in Nearly  
Periodic Structures  
C. Pierre and P. D. Cha

HDA\*

Study of the Damping Capacity of Structural Joints  
Made of Graphite Epoxy Composite Material  
M. D. Rao, Prof. M. J. Crocker and P. K. Raju

HDB

Damping at a Lap Joint Interface Undergoing  
Microslip Under Arbitrary Load History  
Dr. A. F. Artiles and J. Walton

HDC\*

### SESSION IA—Optimization

Simplified Analysis Approach for Optimizing  
Constrained Layer Damping  
S. Forness

IAA\*

Optimal Constrained Viscoelastic Tape Lengths  
for Maximizing Damping in Laminated Composites  
P. R. Mantena, Prof. R. F. Gibson and Dr. S. J. Hwang

IAB

Optimum Configuration of Constrained Viscoelastic Layers  
Dr. B. H. Lu and Prof. C. H. Ku

IAC\*

### SESSION IB—Aircraft Experiment

Practical Stand-Off Damping Treatment for Sheet Metal  
M. L. Parin, Dr. L. C. Rogers, M. Falugi and Dr. Y. Moon

IBA

Enhanced Damping for the Sikorsky ACAP Composite Airframe  
E. W. Jacobs, C. A. Yoerkie, Jr., and J. A. Moore

IBB

\*Not available for publication.

# TABLE OF CONTENTS (Continued)

	<u>Paper No.</u>
Damping Materials for Control of Propeller Induced Structure-Borne Noise Dr. J. F. Unruh	IBC
Application of Constrained Layer Damping to the F/A-18 Horizontal Tail Dr. R. N. Yurkovich	IBD
SESSION IC—Vibration Suppression	
Fiber Optic Vibration Sensors for Structural Control Applications W. B. Spillman, Jr., and B. R. Kline	ICA
Active Vibration Suppression Using NiTiNOL Sensors and Actuators D. G. Wilson, Dr. R. Ikegami, J. R. Anderson and G. J. Julien	ICB
Damping of Structural Vibrations with Piezoelectric Materials and Passive Electrical Networks N. W. Hagood and Prof. A. von Flotow	ICC
Passive Electromagnetic Vibration Dampers B. W. Maxfield, J. K. Hulbert and P. Smiley	ICD
SESSION ID—Free Layer	
Development of a Nomogram for Selection of a Viscoelastic Free Layer Damping Material R. J. Dominic	IDA
Coupled Modal Damping in Transient Solutions B. C. McFarland and Dr. A. J. Bronowicki	IDB
A Perturbation Method for the Analysis of Free-Layer Damping Treatments S. Shen and Dr. K. K. Stevens	IDC
SESSION JA—Laminates	
Damping and Vibration Control of Some Laminated Composite Beams Using Add-On Viscoelastic Materials V. S. Rao, Prof. C. T. Sun and B. V. Sankar	JAA

\*Not available for publication.

# TABLE OF CONTENTS (Continued)

## Paper No.

**Classification in the Frequency-Temperature Range of  
Viscoelastic Materials for Damping of Flexural Waves in  
Sandwich Structures with Various Boundary Conditions**  
Dr. M. J. Ghaleb and M. Khoury

JAB

### **SESSION JB—Launch**

**The Application of Statistical Energy Analysis in the  
Design of Viscoelastic Passive Damping**  
D. W. Johnson, Dr. R. Ikegami and K. S. Hunziker

JBA

**RELSAT Damped Satellite Equipment Panels - Dynamic Performance**  
C. V. Stahle, Jr., J. A. Staley and J. C. Strain

JBB

**RELSAT Damped Satellite Equipment Panels - Analysis  
and Experimental Verification**  
C. V. Stahle, Jr., J. A. Staley and J. C. Strain

JBC

**RELSAT Damped Equipment Panels - Fabrication**  
K. Schmidt, F. Curtis, E. Muziani and L. Amore

JBD

### **SESSION JC—Model Verification**

**Prediction and Measurement of Damping of a Laminated Beam  
With a Constrained Viscoelastic Layer**  
D. J. Segalman and Lt. P. Reamy

JCA

**A New Approach to Model Determination of Large Flexible  
Space Systems**  
Dr. F. Y. Hadaegh, D. S. Bayard, Y. Yam and E. Mettler

JCB

**Perturbations on Natural Modes Due to Nonproportionality of  
Viscous Damping**  
Dr. B. M. Pacheco and Dr. Y. Fujino

JCC

**Measured Vibration Modes of Constrained Layer Damping  
Using Time Averaged Holographic Interferometry**  
P. R. Bernier, S. T. Fryska, C. T. Griffen and  
A. M. Revello

JCD

### **SESSION JD—Metals**

**Damping Associated with Incipient Melting in  
Aluminum-Idium Alloys**  
O. Diehm, C. R. Wong and D. C. Van Aken

JDA

\*Not available for publication.

# TABLE OF CONTENTS (Continued)

	<u>Paper No.</u>
<b>Damping Capacity of Aluminum 6061-Indium Alloys</b> C. R. Wong, D. C. Van Aken and O. Diehm	JDB
<b>Interlaboratory Study of Damping Capacity in Leaded Brass and Lead-Free Brass</b> A. Wolfenden, T. G. Aldridge, Jr., E. W. Davis, Jr., Prof. V. K. Kinra, G. G. Wren and J. M. Wolla	JDC
<b>A Study of the Vibrational and Acoustical Properties of Thermoset Composites, Steel and Aluminum</b> K. M. Lombardo	JDD*
<b>SESSION KA—Sandwich</b>	
<b>Investigation of Structural Damping Combining Linear and Non-Linear Constrained Viscoelastic Mechanisms</b> J. M. Ting, C. K. Kim and Dr. E. F. Crawley	KAA
<b>Vibration Reduction via Contrained Layer Damping Techniques</b> J. F. Schultze and Dr. J. B. Kosmatka	KAB
<b>Damping Behavior of Flexible Laminates</b> Dr. V. A. Coveney, A. H. Muhr and A. G. Thomas	KAC
<b>SESSION KB—Impact</b>	
<b>Application of the Component Element Method to the Impact Damped Simple Harmonic Oscillation</b> Prof. C. M. North, Jr., and R. E. Jones	KBA
<b>Time History Study of a Classical Cantilever Beam Damped by Internal Mechanical Means</b> Prof. C. M. North, Jr., and T. A. Nale	KBB
<b>Nonobstructive Impact Damping Applications for Cryogenic Environments</b> Dr. H. V. Panossian	KBC
<b>Pendulum Impact Damper to Suppress Vibrations</b> G. S. Chua, Y. Fujino, B. M. Pacheco and M. Ito	KBD*
<b>SESSION KC—Space Applications II</b>	
<b>Damping Treatment for Jitter Reduction on a High Power Optical Bench</b> Dr. P. H. Chen and E. M. Austin	KCA

\*Not available for publication.

# TABLE OF CONTENTS (Concluded)

	<u>Paper No.</u>
<b>Analysis and Testing of a Damping Treatment for a Multi-Component Space Structure</b> E. M. Austin, Dr. C. D. Johnson and L. S. Gittleston	KCB
<b>Modal Survey of the PACOSS DTA</b> R. N. Gehling	KCC
<b>Application of Passive and Active Damping Techniques to the PACOSS Representative System</b> D. R. Morgenthaler	KCD
<b>SESSION KD—Applications</b>	
<b>A Damping Treatment for Resonant Test Fixtures</b> F. Cericola, Dr. J. D. Rogers and D. J. Segalman	KDA
<b>The Recent Advances in Viscoelastic Waveguide Absorbers for Passive Vibration Control</b> Dr. Y. S. Shin and K. S. Kim	KDB*
<b>Optimization of Dynamic Vibration Absorber - Case of Cantilever Boring Bars</b> Dr. E. I. Rivin and H. L. Kang	KDC
<b>Development of a Scaled-Down Inertia Brake Dynamometer to Evaluate the Effect of Pad Damping Liners on Brake Squeal Noise</b> Prof. R. Singh and R. Beer	KDD*

\*Not available for publication.

## **DAMPING - A KEY TO MORE, FASTER, FARTHER, HIGHER**

Major General Thomas R. Ferguson, Jr.  
Deputy Chief of Staff for Technology  
and Requirements Planning  
Headquarters Air Force Systems Command  
Andrews Air Force Base, Maryland

Vibration is everywhere. And where there is vibration, there is damping. Most often, vibration is bad and damping is good. There are exceptions, but since this conference is about damping, we will leave the undamping crowd to their own devices.

After getting my primer on this subject, I was reminded that damping is a complicated subject. In simple terms, vibratory response can lead to cracked structure, defocused optics, or other types of degraded performance. Historically, the damping in a vibratory system has been "take what you get", called intrinsic damping. Only in the last few years has damping been a design parameter. So let's begin with a scramble: start the engines...on take off, light the burner. In my flying experience with the B-52, it was be sure all eight were running and start the Hound-Dogs on the roll...there's a lot of noise coming out of these engines. During take-off roll, there are two paths from the engine exhaust noise to the aft structure: one is direct, the other is reflected from the runway. Take-off is typically the highest acoustic environment the structure is exposed to. The skin panel responds to sound pressure level as does a microphone and it vibrates. It can vibrate enough to literally crack and break. The skin panel also re-radiates the sound into the interior. That's called "thru transmission." That's also the technical term for being able to hear people thru the motel wall, at least the motels government per diem can afford in places like Boston and Washington.

That aircraft skin panel also transmits vibratory energy into the substructure--the stringers, frames, and bulkheads. So internal equipment also gets hit with structural-borne vibratory energy at points like mounting brackets and with acoustic energy on their covers. Internal equipment can fail, malfunction or degrade to lower performance levels. As our pilot retracts the gear and accelerates, the dynamic pressure increases and the turbulent boundary layer, especially behind protuberances, can create very high sound pressure levels. At about mach 0.9, the oscillating shocks have the same effect. When we maneuver, especially transonically, the aeroacoustic levels on the leading and trailing edges (and external stores) reach high levels. When we open weapons bay doors, the open cavity acts like a giant whistle and the internal structure and stores can be subjected to tones of extremely large amplitude. Since we fly to fight, we carry weapons; we fly at ever-higher dynamic pressures and maneuver at transonic speeds to survive: This makes the vibroacoustics problem more severe. Today, to do our engineering right, structures-and-vibration-and-damping-engineers must participate in the original design of these modern flying machines.

Vibration is also no longer an earthly problem. It is becoming a design factor in satellites as well. Launch vibroacoustics typically cause the highest vibration levels and can break equipment. There are also more vibratory disturbances in orbit than you might think. There are always imbalances in reaction wheels, momentum wheels, and control moment gyros used for attitude control. Coolant flow, shifting solar arrays, liquid slosh, gravity gradient, particle impact, to name just a few, are all vibratory disturbances which, just for example, can degrade performance of sensitive optics.

I shouldn't have to convince this audience--we know that vibration is everywhere. Although the obvious is obvious to us, let's also acknowledge that damping is a highly specialized subject. A damping engineer is a specialist because he must first be a vibration engineer, who was probably a structures engineer to start with. So, right off, we have a specialty within a specialty within a specialty. The successful damping engineer must know more than damping. He'd better know systems integration and be very conversant about the operational environment. A prime example of this is the highly successful "Damping Wrap" for the inlet guide vanes on the engines used in the F-111F fighter. So many cracks were forming so quickly that the inlet guide vane case had to be refurbished after T00 few hours of service. Air coming into the engine is turned slightly by the inlet guide vanes to get best performance from the rotating first stage compressor. The IGV case consists of titanium inlet guide vanes welded to inner and outer rings. Vibration was suspected as the cause of the cracks which were forming in the heat affected zones of the welds. The intrinsic damping was extremely low, and in this case, the dynamic magnification factors at resonances were high. Obviously, the stage was set for a damping engineer to really impress his boss. Adding damping to the inlet guide vane was easy; developing a satisfactory damper wrap for a complex systems operational environment was not. Sophisticated bonding technology was used so that the damper wrap would adhere while exposed to the air flow. The wrap had to be thin to minimize inlet blockage area, since reduced air flow would affect engine performance. Engine stall characteristics, anti-icing effectiveness, erosion, corrosion, and durability were all investigated and proven satisfactory. The point being...this was a complex interdisciplinary problem--solved very successfully. This project has estimated cost avoidance savings to the Air Force of \$50M. Spin-off damping applications in similar situations may well account for another \$200 million. Other very recent demonstrations of vibration-caused structural failures fixed by damping are the A-7 center section leading edge flap, A-10 gun bay floor and side wall, and F-111 spoilers. Once again the logistics improvements in terms of dollars were significant. I should also add these improvements lower the heart rate for our maintainers.

For the most part, successful damping treatments have been of the add-on variety. The hardware has been designed and a vibration problem rears its ugly head. A damping treatment is designed and "added to" existing structure. Once the hardware exists, add-on damping may be an extremely cost effective solution. But it's better to avoid the problem altogether and that can be done with integral damping. Commercial examples are laminated valve covers, oil pans, and timing gear covers used in automobile and diesel engines.

Integral damping is also the key to longer life, more durable aircraft structure. The objective is increased sortie generation rate and reduced maintenance cost. Since we often learn more from our failures, there's no shame to admit there have been many unsuccessful attempts to design damping solutions. I'm told you don't have to be in this business very long to have been bit. In fact, you don't earn your damping wings until you've been humbled more than once. I don't want to focus on this aspect, but during breaks and at social opportunities it also pays to discuss the failures as well as the successes.

DAMPING '89 is put together to detail the state of the art, but the keynote role allows me latitude to summarize. A baseline of damping materials and manufacturing processes is established. We can measure properties of materials fairly well. Data banks on damping materials are also established. You can analyze simply supported beams in closed form and can perform finite element analysis of damped structure to predict modal frequencies and damping limits. You can experimentally measure the modal frequencies and damping of structure. There are a growing number of successful add-on and integral damping applications and you have quantified these successes in terms, pay-off terms, that management understands. Damping, in fact, is a hot, new tool in the engineer's kit bag. But it's good not to believe as the song goes "Oh Lord it's hard to be humble when you're perfect in every way." What we already know is just a glimpse of the future. There is still great opportunity. Therefore, it's important to make good investment decisions as we plan the future.

As in most technical disciplines, the explosion in computational power, coupled with advancements in damping technology, can greatly accelerate our knowledge. Better dynamic test techniques are needed; a greater range of materials properties should be measured and catalogued; and extensions to analytical methods would really expand the range of applications. With these wishes met, let's peer in the not too distant future and I'll make some predictions:

- o Measurement of the dynamic mechanical properties of viscoelastic damping materials will be more accurate, more efficient, and have less scatter.
- o Existing materials will be screened for toxicity, flammability, outgassing, corrosion, long-term environmental stability and others. These are properties which are mandatory for system application.



- o A fully computerized data clearing center will exist soon.
- o Wide-temperature range and low-temperature damping materials will be developed.
- o Approximate closed form analysis methods will come into use for structures like thin plates and shells, brackets, pipes and tubing.
- o Approximate finite element analysis models will be developed as preliminary design tools for damped structures such as satellite equipment support structures.
- o Computer aided design will yield optimum solutions by interacting finite element analysis of damped structure with a data base of damping materials.
- o Most aircraft sheet metal will be laminated, ditto for automobiles and household appliances.
- o Interest in damped composite structural materials will rise.
- o Housings and circuit boards of avionics equipment will be damped.
- o Logistics imperatives--maintainability and reliability--will dictate much more use of damping.
- o And, some of you who think you'll be millionaires exploiting these opportunities will probably go bankrupt because of Murphy. So, maximize the opportunity this conference offers.
- o Learn!!
- o Go home and apply the technology: Be passionate...become zealots for your work and the opportunity it presents.
- o Share your successes and failures with as wide a technical community as possible.
- o Think of yourselves as a team: Academia and practitioners in commercial and military applications. All must play their roles to see the most intelligent and widespread use of this technology.

I want to conclude with some non-damping thoughts. My boss, the AFSC Commander, General Randolph, just gave a talk at the AF Association's Tactical Air Warfare Symposium. He ok'd my use of some of his remarks because the message is so important for all of us. That message is about total quality management.

In the book, "A Passion for Excellence," Peters and Austin recall the management style of General Electric's aircraft engine pioneer, Gerhard Neumann when he worked with Claire Chennault's World War II Flying Tigers. Neumann wanted make sure his maintenance people fixed aircraft engines right...the first time. So each day he used to ask a few of his squadron mechanics to "volunteer" to test fly in the Single-Seat fighter they'd just repaired. The pilot would sit on the crew chief's lap, and neither could sit on a parachute because the cockpit wasn't big enough.

Well, improvements in workmanship were dramatic! In his book, "Herman the German," Neumann writes that each night, "Way past dinnertime, the airfield looked as if it were invaded by glowworms; the twinkling came from flashlights mechanics used to check--once more--the tightness of pipes or connections they had made in case Neumann might suggest that they 'Volunteer' to ride in their planes the next day."--Now there's a guy who knew how to motivate quality. TQM's an overdue sign of a national quality revolution. It's a buzzword you see in commercials, hear at symposiums, and notice in bookstores. But don't just dismiss TQM as yet another acronym that will die off. As a term, TQM might well change over time. However, as a philosophy TQM will last, as more companies and managers come to understand what continuous quality improvement means and what it can do. Affordable price tags, fair profits and high product quality will prove TQM's merits long after the trendiness of the buzzword disappears. It offers opportunities for every person involved in research, development, test, production and operations.

TQM--is BETTER QUALITY AT LOWER COST. It's the prerequisite to good performance. AFSC's senior people have been through training seminars with W. Edwards Deming, one of the best-known quality leaders in the world. Deming's philosophy is that 85 percent of quality problems are caused by the system; just 15 percent are caused by people. Just to be sure we're communicating--you're likely to be part of the 85 percent! If the products of U.S. industry are not well liked, loved, by the customer, you are involved because you're that 85 percent of the system that designs-in-problems the manufacturing work force can't correct.

General Randolph was challenged about his intensity on this subject of total quality management. The person said it sounds as if quality issues are a matter of life and death. He said no, they're much more important than that. Think about these statistics:

If the U.S. had service suppliers who did their jobs right 99.9 percent of the time, there would still be:

- 20,000 wrong prescriptions filled each year;
- Unsafe drinking water almost one hour each month;
- 2 long or short airplane landings a day (That's an accident) at Los Angeles and New York;

- And 2000 lost articles of mail per hour every day.
- In the defense arena, given 1 million grenades, you would have 999 duds--and 1 will go off in "0" seconds.

Where is your quality meter set?

General Randolph closed his talk with this story President Kennedy would tell and I'll do the same. It's about a retired French General whose hobby was gardening. He was a very cultured man with a deep sense of history. On his 80th birthday he bought a small shrub and instructed his gardener to plant it in the garden.

"But, Sir," the gardener protested, "that plant won't flower for a hundred years!" "Then by all means," the General said, "plant it now."

The total quality we plant in our work today is FREEDOM FOR TOMORROW. We need to plant more flowers.

# **INTERACTIVE CHARACTERIZATION AND DATABASE STORAGE OF COMPLEX MODULUS DATA**

Bryce L. Fowler  
CSA Engineering, Inc.  
Palo Alto, California

## **ABSTRACT**

Test data for viscoelastic damping materials often do not provide thorough coverage of temperature and frequency. A methodology for processing damping material complex modulus data and presenting it in a manner that is meaningful to the damping designer is discussed. The use of a computer program for characterization of complex modulus data is described. A database program for storage and retrieval of characterized complex modulus data is also described.

# 1. Introduction

Successful design of passive damping treatments using viscoelastic materials (VEM's) such as elastomers depends upon several factors. One important factor is accurate knowledge of the sensitivity of VEM properties to variations in temperature and frequency. Since it is impossible to test a viscoelastic material at every combination of temperature and frequency, the material is tested at discrete temperatures and frequencies and a mathematical relationship is developed that characterizes the material at all other combinations of temperature and frequency. This process is referred to as characterization.

The equations used in characterization are all of a parametric nature, often easily represented on computers. The hard part of characterization is to correctly choose the equation parameters so that they accurately represent the VEM's. Interactive computer graphics have greatly improved the process of choosing and adjusting the correct parametric values.

As the body of characterized viscoelastic material data grows, the need for a centralized VEM database becomes increasingly important. Computers may again be used to allow damping designers and fabricators access to a database of VEM information based on the characterization parameters and material properties.

This paper provides a methodology for obtaining initial parameter values to represent analytically the complex modulus of VEM's and describes computer programs used for VEM characterization and for database storage and retrieval.

## 2. Complex Modulus Theory

For infinitesimal strain and rate of strain, the time-dependent stress-strain relations for a viscoelastic material can be described by linear differential equations with constant coefficients. This linear behavior requires

$$\beta \equiv \left. \frac{d \log G_M}{d \log f_R} \right|_{\text{transition}} = \left. \frac{d \log G_R}{d \log f_R} \right|_{\text{transition}} = \left. \frac{d \log G_I}{d \log f_R} \right|_{\text{transition}} \quad (1)$$

and

$$\eta_{\max} \cong \tan \frac{\pi \beta}{2} \quad (2)$$

where

- $G_M$  = magnitude of the complex modulus
- $G_R$  = real (storage) part of the complex modulus
- $G_I$  = imaginary (loss) part of the complex modulus
- $\eta = G_I/G_R$  (also known as the loss factor or  $\tan \delta$ )
- $f_R$  = reduced frequency =  $f_i \alpha_T(T_i)$

$f_i$  = experimental frequency  
 $T_i$  = experimental temperature  
 $\alpha_T$  = temperature shift function

It has been shown by Rogers that a solution to this requirement is given by the fractional complex modulus equation<sup>1</sup>

$$G^*(f_R) = \frac{G_e + G_g z^\beta}{1 + z^\beta} \quad (3)$$

where

$$z = j f_R / f_{R_0}$$

The parameters,  $G_e$ ,  $G_g$ , and  $f_{R_0}$ , as well as parameters for  $\alpha_T$  must be found such that the curve described by Eq. 3 fits the data within the error bounds of the material test. Initial values for the parameters are first determined graphically and then are iterated and regressed for the best mathematical fit.

### 3. Initial Parameters

Values for  $G_e$  and  $G_g$  may be obtained directly by drawing a plot of  $\eta$  versus  $G_M$ , as shown in Figure 1. Note, this plot is a useful indicator of data quality in that resonance and other qualitative errors such as broken fixturing will appear as data points that do not follow the overall inverted "U" shape from  $G_e$  to  $G_g$  (Figure 2). To evaluate  $\beta$ , the equation

$$\eta_{max} = \frac{\left(1 - \frac{1}{A}\right) \tan \frac{\pi\beta}{2}}{1 + \frac{1}{A} + \sqrt{\frac{2}{A}} \cos \frac{\pi\beta}{2}}, \quad \text{where } A = \frac{G_g}{G_e} \quad (4)$$

is derived from Eq. 3. A value for  $\eta_{max}$  is obtained from the plot in Figure 1.  $\beta$  is then calculated iteratively. The transition region is defined by choosing an  $\eta_{cutoff}$  value from the plot in Figure 1. The use of  $\eta_{cutoff}$  to define the transition region is shown in Figure 3.

### 4. Temperature Shift Function

Historically, the WLF equation has been used to define  $\alpha_T$ .<sup>2</sup> This has not been able to shift all viscoelastic material data correctly outside the transition, however. A new approach is to use a spline fit of the slopes of  $\alpha_T$  for a relatively small number

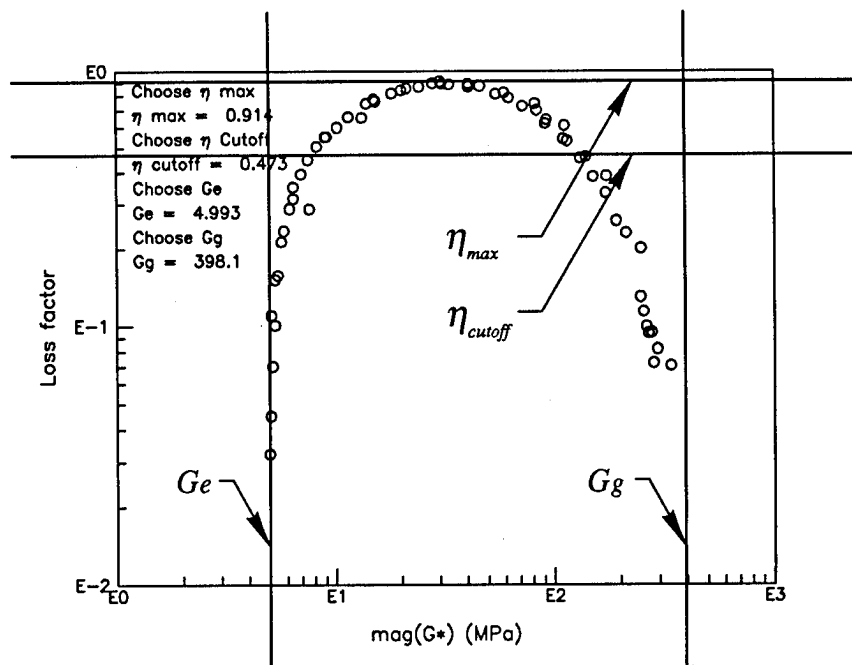


Figure 1. Obtain  $\eta_{max}$ ,  $\eta_{cutoff}$ ,  $G_e$ , and  $G_g$

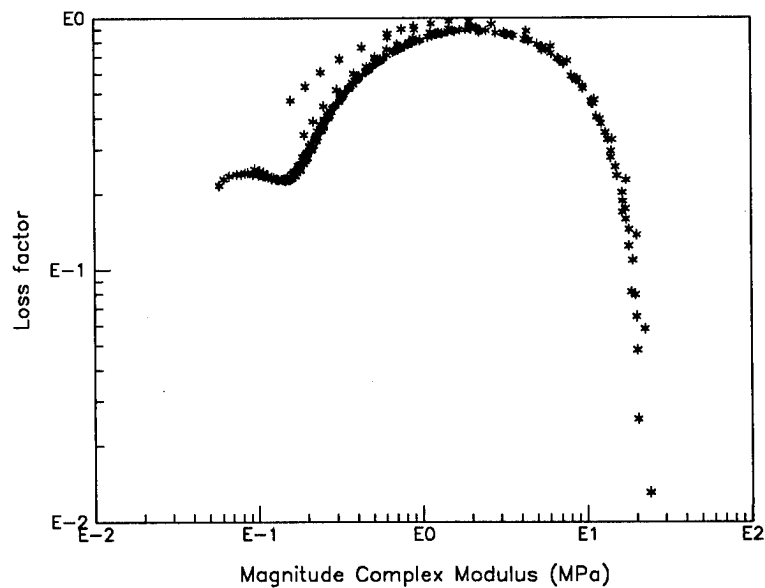


Figure 2. Qualitative error

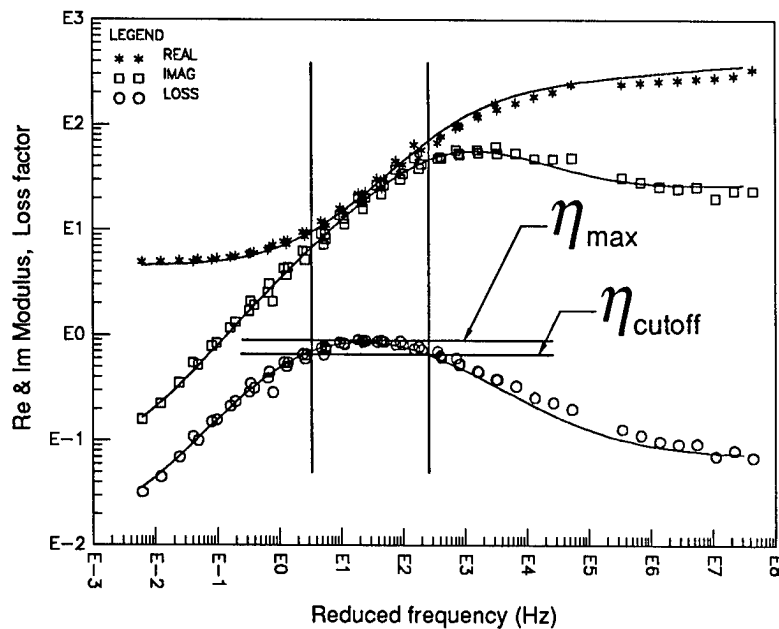


Figure 3. Transition region defined

of equally-spaced temperature points (e.g., 5 points) to define  $\alpha_T$ . The reference temperature,  $T_Z$ , is obtained by fitting a quadratic function through the data points of  $\log \eta$  versus  $T$ , solving for zero slope, and rounding to the nearest evenly-spaced temperature point.

Initial values for the reference slope,  $S_{AZ}$ , and  $f_{R_0}$  are obtained by solving Eq. 3 for  $\alpha_T/f_{R_0}$

$$\frac{\alpha_T(T_i)}{f_{R_0}} = \frac{1}{j f_i} \left[ \frac{G_i^* - G_e}{G_g - G_i^*} \right]^{\frac{1}{\beta}} \quad (5)$$

Since Eq. 5 is valid in the transition region, a quadratic is fit through the data points defined within the transition by  $\eta \geq \eta_{cutoff}$  for  $\alpha_T/f_{R_0}$  as a function of temperature. Using  $\alpha_T \equiv 1.0$  at  $T_Z$ ,  $f_{R_0}$  is obtained from the reciprocal of the quadratic at  $T_Z$ .  $S_{AZ}$  is obtained as the slope of the quadratic at  $T_Z$  multiplied by the initial  $f_{R_0}$ .

A modified version of the WLF equation is then used

$$\log \alpha_T = - \frac{S_{AZ} (T - T_Z) (T_Z - T_\infty)}{(T - T_\infty)} \quad (6)$$

with  $T_\infty$  set equal to 10.0 to generate initial values of slope at all the other temperature-slope points.

Finally,  $\alpha_T$  is calculated as the integral of the spline of the slopes where the constant of integration is given by the  $\alpha_T \equiv 1.0$  at  $T_Z$  relationship.



The accuracy of the  $\alpha_T$  parameters is checked by looking at a plot of the complex modulus data versus the reduced frequency. The parameters must be adjusted iteratively to remove any isotherm "shingles."

## 5. Complex Modulus

Improvements to Eq. 3 which add adjustment factors to account for non-linearity have been offered by Bagley, Rogers, Nashif, and others.<sup>3 4 5</sup> All equations work for some damping materials. None can adequately fit all sets of VEM data. Present methods use a piecemeal approach. An equation that has successfully fit the type of material of interest in the past or that is the most general is used and parameters are adjusted using regression and trial-and-error to get the best fit. If the best fit is not adequate, a different equation is tried. This approach has been implemented on a computer with nine different complex modulus equations available.<sup>6</sup>

Initial estimates of parameters vary for each model. For example, if the series fractional Maxwell equation, given by

$$G^* = G_e + \sum_{k=1}^n \frac{G_k}{1 + z_k^{-\beta_k} + \Delta_k z_k^{-\rho_k}}, \quad z_k = j \left( \frac{f_R}{f_{R0}} \right)_k \quad (7)$$

where

$$G_e < G_k < G_g \quad (\text{stepping logarithmically})$$

$$\beta_k = \text{slope of storage modulus corresponding to } G_k$$

$$\Delta_k = \text{pole multiplier}$$

$$\rho_k = \text{pole exponent}$$

is chosen,  $\beta_k$  is set equal to the previously calculated  $\beta$ ,  $\Delta_k$  is the slope of the glassy intercept with the abscissa on a Cole-Cole plot (i.e.  $G_I$  versus  $G_R$ ), and  $\rho_k$  is set to 0.1 for all  $k$ .<sup>7</sup>

## 6. Graphical Presentation

Jones and, more recently, Jones and Rao have developed methods to present complex modulus data graphically.<sup>8 9</sup> These are the reduced-temperature nomogram (also known as the international plot) and inverted "U" plot respectively (Figures 4 and 5).

The international plot consists of the real and imaginary moduli displayed logarithmically in megaPascals (MPa) on the left vertical axis along with the dimensionless loss factor. The horizontal scale is the reduced frequency defined in Eq. 3.

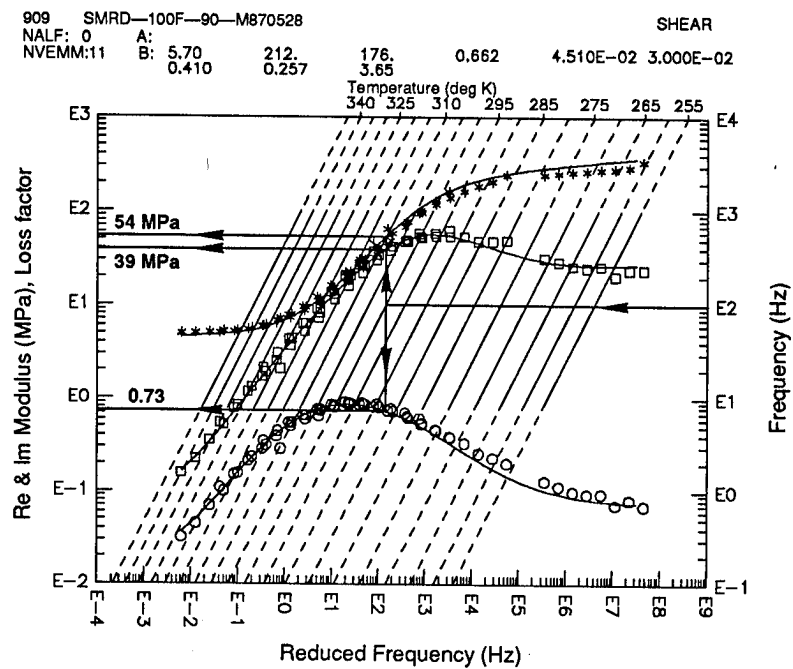


Figure 4. Reduced-temperature nomogram (international plot)

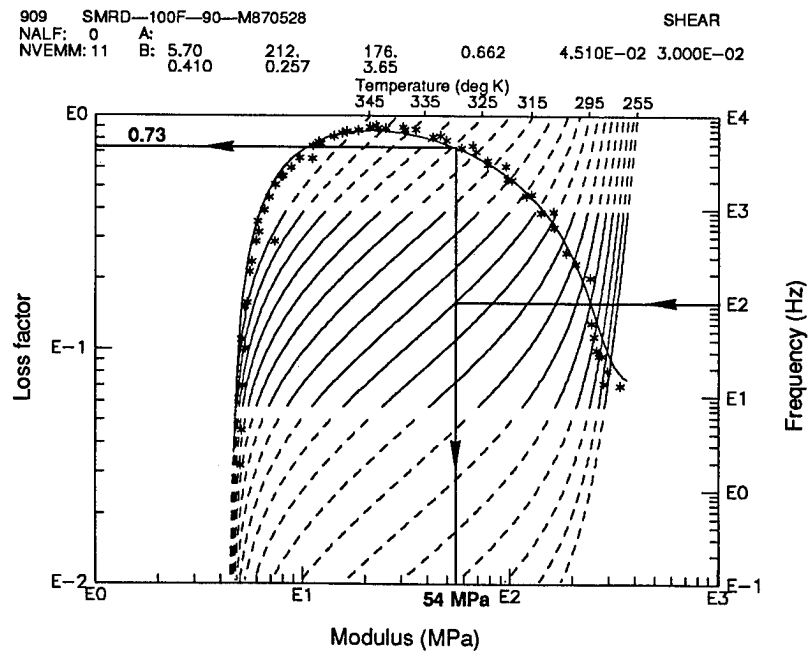


Figure 5. Inverted "U" plot

The right vertical axis is cyclic frequency displayed logarithmically in hertz (Hz). Lines of constant temperature are superimposed on the plot from the relationship

$$\log f_R = \log f_i + \log \alpha_T (T_i) \quad (8)$$

These isotherm lines are usually calculated for steps of five degrees Kelvin and range from  $T_L$  to  $T_H$  to preclude extrapolation of temperature for which viscoelastic materials are highly sensitive. The range of experimental frequency is indicated by the solid region of the isotherm lines. In the area of extrapolated frequency, the isotherms are dashed. The use of the international plot to read interpolated values of modulus and loss factor is demonstrated in Figure 4. To get modulus and loss factor values corresponding to 100 Hz and 300°K, one reads the 100 Hz frequency on the right-hand scale and proceeds horizontally to the 300°K temperature line. Then proceed vertically to intersect the curves along a line of reduced frequency. Finally, proceed horizontally from these intersections to the left-hand scale to read the values of 54 MPa for the real modulus, 39 MPa for the imaginary modulus, and 0.73 for the loss factor.

The inverted "U" plot utilizes similar methodology, but removes the reduced frequency scale and directly superimposes constant temperature lines onto a plot of loss factor versus the real part of the complex modulus. Cyclic frequency is still displayed on the right-hand axis. To follow the same example as above, start at the 100 Hz frequency value on the right-hand scale and move horizontally to the 300°K temperature line. Drop vertically downward to read 54 MPa off the horizontal axis for the real modulus, and proceed upward to the curve and then horizontally to read 0.73 off the left-hand vertical scale for the loss factor.

Other plots of interest include

1.  $\log \alpha_T$ ,  $d \log \alpha_T / dT$ , and the apparent activation energy versus temperature
2.  $\log f_i$  versus temperature
3. real and imaginary components of  $G^*$ , and  $\eta$  versus temperature

## 7. VEM Database

A VEM database program has been written to store and retrieve characterized viscoelastic material data.<sup>10</sup> It uses the characterization equations and parameters to interpolate modulus and loss factor values to match design criteria. The focus of the first page, Search Specifiers (Figure 6), is toward finding materials using frequency, temperature, modulus range, and loss factor range. Up to three different search points using these property specifiers may be used. The search temperature may be in units of Fahrenheit, Rankine, Centigrade, or Kelvin. The search modulus

Page: **Search Specifiers**

Report Name: **SEARCH\_1**  
Units: **English Fahrenheit**      Points: **1**

	Point 1		Point 2		Point 3	
Frequency:	1.0		10.		1.00E+02	
Temp (deg F):	72.		72.		72.	
	Lower	Upper	Lower	Upper	Lower	Upper
Modulus (psi):	1.0	10.	10.	50.	1.00E+02	2.00E+02
Loss factor:	0.10	0.50	0.10	0.70	0.10	1.0

Search Reports  
  
Report name: **SEARCH\_1**  
Output to: **Screen**  
Units: **English Fahrenheit**  
Report type: **Tables & Plots**  
Tables: **Brief**  
Plots: **International**      Markers: **On**  
Lower: **10.**      Upper: **1.00E+03**

**Search specifiers**

**Librarian**

**Beam specifiers**

**Setup**

Figure 6. Search Specifiers page

range values may be in units of pounds per square inch (psi) or megapascals. All units, however, must be in the same measurement system – English or SI. The program will also find materials based on their names, manufacturers, material types, and availability in the Librarian page.

Reports are generated on request when one or more materials in the database file fall within the range of at least one search point. All materials that meet that criteria are flagged for inclusion into a report. Once a report is generated, it may be sent to either the computer screen or a hardcopy device. Different fields may be set to define the form of the report. Output is in the form of text data and information, the international and inverted “U” plots, and constant temperature and constant frequency plots. Figures 7 and 8 are examples of the output from the database.

## 8. Observations

Most viscoelastic materials data are for engineering applications and justifiably do not provide scientific coverage of temperature and frequency. The challenge is to make the data useful to the damping designer and simultaneously indicate limitations.

Full directory of SEARCH-1

Material Name	Manufacturer	Type	Available
SMRD-100F-90 -M870528	MANUFACTURER	UNSPECIFIED	YES

This is the information field for SMRD-100F-90-M870528. This is where you would enter information about material handling, name and address of material suppliers, material properties such as outgassing, ease of use, etc.

SMRD-100F-90 -M870528

SHEAR

		ALPHA-T MODEL					
HALF	NA	A(1)	A(2)	A(3)	A(4)	A(5)	A(6)
0	0						

		COMPLEX MODULUS MODEL					
NUM	NB	B(1)	B(2)	B(3)	B(4)	B(5)	B(6)
11	9	827.	212.	176.	0.662	4.510E-02	3.000E-02
		B(7)	B(8)	B(9)			
		0.410	0.257	3.65			

COMPLEX MODULUS DATA AS A FUNCTION OF TEMPERATURE AND FREQUENCY

Temp (Deg F)	Freq (Hz)	MReal (psi)	Eta	MImag (psi)	Alpha-t	
-2.440	7.600	3.5389E+04	0.1300	4601.	4.3215E+04	T
-2.440	15.60	3.6549E+04	0.1140	4167.	4.3215E+04	T
-2.440	31.20	3.7710E+04	9.9700E-02	3760.	4.3215E+04	T
-2.440	62.50	3.8580E+04	9.4100E-02	3630.	4.3215E+04	T
-2.440	125.0	3.9885E+04	9.4700E-02	3777.	4.3215E+04	T
-2.440	250.0	4.0755E+04	7.2100E-02	2938.	4.3215E+04	T
-2.440	500.0	4.2351E+04	8.1600E-02	3456.	4.3215E+04	T

SMRD-100F-90 -M870528

SHEAR

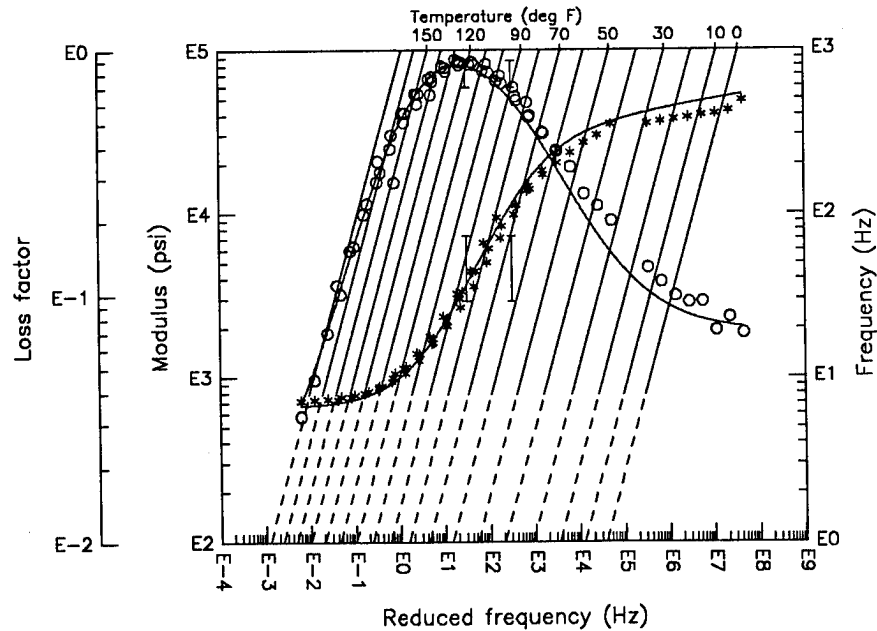


Figure 7. VEM database output  
Text data and the International plot

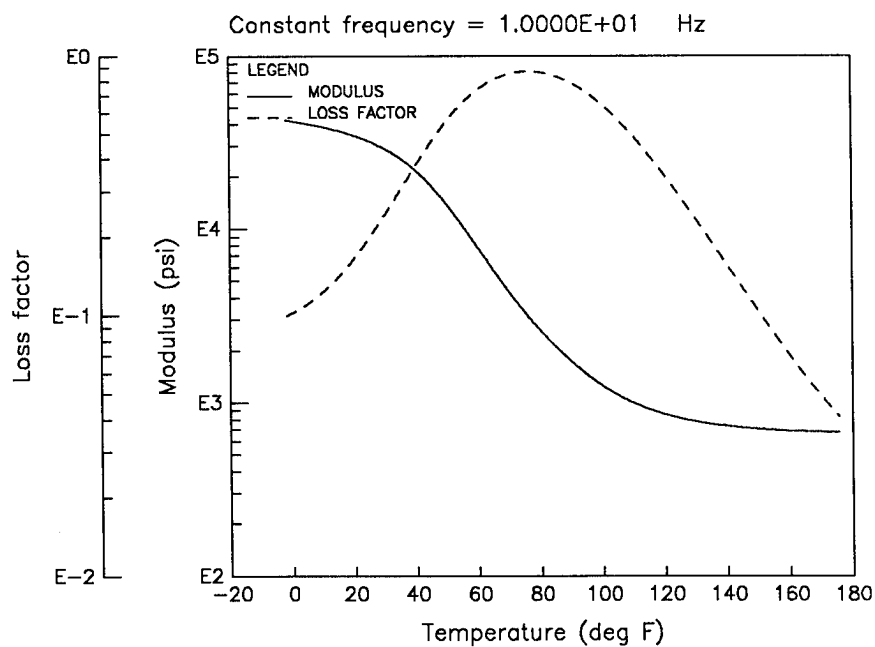
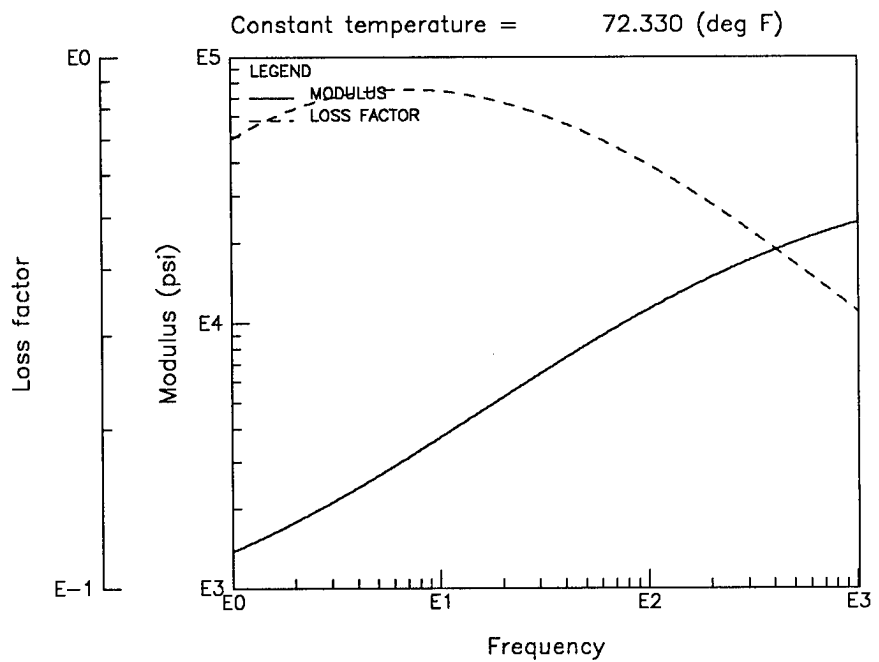


Figure 8. VEM database output (continued)  
 Constant temperature and constant frequency plots

Using the methodology and graphical presentation outlined in this paper, this challenge can be mostly met. Care must always be taken, however, when using the various accepted equations to insure that an appropriate representation of the complex modulus has been chosen. Errors of several orders of magnitude are still too easily introduced when the wrong parameters and/or the wrong equations are used.

The need for good characterization has always been present. With advances in damping design tools the need has become even more critical. As a design tool, the VEM database must have accurately characterized materials to be useful. Work must still be done to improve the equations used to characterize viscoelastic materials so that they will accurately characterize all damping materials.

## References

1. Rogers, L. C., "Operators and Fractional Derivatives for Viscoelastic Constitutive Equations," *J. Rheology*, 27(4), pp 351-372, 1983.
2. Ferry, J. D., *Viscoelastic Properties of Polymers*, John Wiley and Sons, 3rd ed., 1980.
3. Bagley, R. L., "Applications of Generalized Derivatives to Viscoelasticity," AF Materials Lab TR-79-4103, November 1979, (Available from Defense Technical Information Center as ADA 081131.)
4. Rogers, L. C., "DAMPING: On Modeling Viscoelastic Behavior," *Shock and Vibration Bulletin*, No. 51, 1981.
5. Nashif, A. D., Jones, D. I. G., Henderson, J. P., *Vibration Damping*, John Wiley and Sons, 1985.
6. Fowler, B. L., "Interactive Viscoelastic Material Properties Program," CSA Engineering Report No. 88-05-02, May 1988.
7. Cole, K. S. and Cole, R. H., *J. Chem. Phys.*, 9, 341-351, (1941).
8. Jones, D. I. G., "A Reduced-Temperature Nomogram for Characterization of Damping Material Behavior," 48th Shock and Vibration Symposium, October 1977.
9. Jones, D. I. G. and Rao, D. K., "A New Method for Representing Damping Material Properties," ASME Vibrations Conference, Boston MA, September 1987.
10. Fowler, B. L., "Viscoelastic Materials Database User's Manual," CSA Engineering Report No. 88-05-01, May 1988.

COMPARISON OF COMPLEX MODULUS DATA  
GENERATED BY THREE DIFFERENT MEASUREMENT TECHNIQUES

By

Michael L. Drake and Anil Sircar  
University of Dayton Research Institute  
Dayton, OH 45469  
(513) 229-2644

INTRODUCTION

There are many different test instruments which can determine the complex modulus properties of materials, and there are numerous ways that these complex data can be displayed on a reduced frequency nomogram (RFN). This paper will present the complex modulus properties of Dyad 609 which is a commercially available copolymer marketed by the Soundcoat Company and a highly loaded UDRI formulation of Vinac B-100. Vinac B-100 is a polyvinyl acetate material marketed by Air Products.

The three complex modulus test instruments evaluated were the ASTM E-756 BEAM Test system, the Polymer Laboratories DMTA machine, and the Rheometrics RSA II. Table 1 presents the basic temperature and frequency ranges over which each of these test instruments operate and the specimens which are typically used.

There were three different forms of the shift factor ( $\alpha_T$ ) used to develop the complex modulus data display on a RFN. The equations used were:

(1) the WLF equation [1]

$$\log \alpha_T = \frac{C_1(T-T_0)}{C_2+T-T_0}$$

where  $C_1 = 12$  and  $C_2 = 525$

(2) an Arrhenius equation [2]

$$\log \alpha_T = \frac{T_A}{T} - \frac{T_A}{T_0}$$

and

(3) a quadratic in  $\frac{1}{T}$  where [3]

$$\log \alpha_T = (a[\frac{1}{T} - \frac{1}{T_Z}] + 2.303[\frac{2a}{T_Z} - b]) \log \frac{T}{T_Z} + \frac{b}{T_Z} - \frac{a}{T_Z^2} - S_{AZ})(T-T_Z)$$

The complex modulus data obtained from each test and the effects of the various  $\alpha_T$  equations are presented in the following paragraphs.



## DYAD 609

The Dyad 609 RFN from the BEAM test is given in Figure 1. There are 51 complex data points plotted. The temperature range for the test was  $-5^{\circ}\text{F}$  to  $246^{\circ}\text{F}$  and the frequency range was 260 Hz to 3400 Hz. A free layer test specimen was used to determine the glassy modulus data and a sandwich test specimen was used to determine the transition and rubbery modulus data. The WLF form of  $\alpha_T$  was used to generate Figure 1 and the  $T_0$  value was chosen to be  $240^{\circ}\text{F}$ .

Figure 2 displays the S2-73 committee suggested inverted U plot of material loss factor versus magnitude Young's modulus. The switch from the free layer to sandwich test specimen data occurs near  $10^5$  PSI. The inverted U plot indicates that there is some scatter in the BEAM data; however, overall the data appears to be acceptable.

The Dyad 609 DMTA results are given in Figure 3 (RFN) and Figure 4 (inverted U). There are 211 complex modulus data points which cover the temperature range of  $79^{\circ}\text{F}$  to  $212^{\circ}\text{F}$  and a frequency range of 0.3 Hz to 30 Hz. A bending test specimen was used for the DMTA test. The WLF  $\alpha_T$  with a  $T_0$  of  $356^{\circ}\text{F}$  was used to generate Figure 3. Figure 4 illustrates very little scatter in the DMTA data.

The RSA II test results are given in Figure 5 (RFN) and Figure 6 (inverted U). There are 112 complex data sets plotted. These data cover the temperature from  $-20^{\circ}\text{F}$  to  $110^{\circ}\text{F}$  and a frequency from 0.1 Hz to 15 Hz. A bending specimen was used in the RSA II test. The WLF  $\alpha_T$  with  $T_0 = 356^{\circ}\text{F}$  was used to generate Figure 5. Figure 6 illustrates the value of the inverted U plot. In Figure 6 it is obvious that the data near and above a modulus of  $10^4$  PSI is inaccurate. This problem developed from the geometry of the bending specimen used. To collect accurate data into the transition region through the rubbery region, a different geometry of bending specimen and a shear specimen would be required.

The reduced frequency data for all three tests appears, if viewed individually, to be a reasonable representation of the material properties. Table 2 presents a comparison of the nomogram data presented in Figures 1, 3, and 5. This table illustrates the significant difference in the three data sets.

In the WLF  $\alpha_T$  equation, the value of the constants  $C_1$  and  $C_2$  were derived from the comparison of a large number of high frequency damping property tests. This is probably the reason that the  $T_0$  for the BEAM data is so different from the  $T_0$  of the DMTA and RSA II.

The value of the maximum material loss factor compares well for the BEAM and DMTA tests, however, the temperature at which the peak occurs is different by  $14^{\circ}\text{F}$  at 100 Hz. The temperature difference leads to the large variation in the modulus at peak damping determined by each test. Generally, at temperatures below peak damping, the BEAM data indicated a high modulus while at temperature above peak damping, the BEAM data indicated a lower modulus.

Figure 7 presents all three complex modulus data sets on the inverted U plot. The RSA II and DMTA data match quite closely up to the point where the RSA II data becomes unstable. The BEAM test data demonstrates a shift to higher modulus values across the range.

Figure 8 presents all three data sets on a RFN with  $T_0 = 240^\circ\text{F}$ . This  $T_0$  is obviously inappropriate for the DMTA and RSA II data. Figure 9 presents the same data with  $T_0 = 356^\circ\text{F}$ . The BEAM and DMTA loss factor data collapse to the same curve. However, the modulus trend illustrated in Table 2 has changed in that the BEAM data now exhibits a higher modulus value across the entire range. This change in data comparison led to the investigation of other  $\alpha_T$  equations.

Figure 10 presents the Dyad 609 data sets on a reduced frequency plot where  $\alpha_T$  is equation Number 2. The loss factor trend and the modulus trend is the same as seen with the high value of  $T_0$  in the  $\text{WLF}\alpha_T$  RFN (Figure 9).

The current S2-73 draft standard uses the  $\alpha_T$  equation Number 3. The BEAM and DMTA data were characterized using the S2-73 procedure. The BEAM data RFN in S2-73 draft standard form is presented in Figure 11; while the DMTA data RFN is presented in Figure 12. Again, both data sets when viewed independently appear to be reasonable characterizations of the damping material.

Table 3 compares the S2-73 characterization of the BEAM and DMTA data sets. The S2-73 characterization is conservative on the value of peak damping when compared to the other two methods; however, the tendency of the BEAM data to have a slightly lower temperature of peak damping at a given frequency is consistent with the previous characterization methods. The discerning thing in Table 3 is the modulus trend illustrated. In Table 3 it can be seen that the beam characterization has a lower modulus value across the board than the DMTA characterization.

Table 4 summarizes the variation in the complex modulus data at the peak loss factor between the four different  $\alpha_T$  equations evaluated. The data in Table 4 combined with the data presented earlier in Figure 7 do make definite statements.

First, from Table 4, there can be a significant variation in the complex modulus properties depending upon the characterization method used. This fact by itself is extremely concerning to the design engineer who intends to use complex modulus data to design damped systems.

Secondly, from Figure 7, different test methods can produce different complex modulus data. The plot of loss factor versus modulus, as shown in Figure 7, is independent of frequency, temperature and  $\alpha_T$ . The fact that there is variation between the test data in Figure 7 states simply that there are differences in the three sets of test results. These differences are generated by the inherent error in each test and the unaccounted for nonlinear frequency effect in a non-thermal-rheologically simple material.

## VINAC B-100

A formulation of Vinac B-100 with a high level of mica filler was also evaluated by the BEAM, RSA II, and DMTA test methods.

Figure 13 and Figure 14 present the BEAM test results in RFN form and the inverted U plot respectively. Although there is scatter on the inverted U plot, the data appear to be reasonable representation of the complex modulus data for mica loaded B-100.

The BEAM test complex modulus data set consists of 41 complex points. A sandwich test specimen was used to generate the data. The temperature range was 72 to 270°F, while the frequency range was 240 to 4660 Hz. The WLF form of  $\alpha_T$  with a  $T_0 = 200^\circ\text{F}$  was used to generate Figure 13. It should be noted that the glassy modulus is above  $10^4$  psi; therefore, since the complex modulus data was collected from a sandwich test, the upper transition and glassy modulus data are inaccurate. Without the knowledge of the type or types of test specimens used, the engineer cannot judge the true accuracy of complex modulus data. Close scrutiny of the data often will not reveal inaccuracies resulting from inappropriate test specimens as can be seen in this example. This is true regardless of the test system used.

Figures 15 and 16 present the RFN and the inverted U plot for the DMTA test results of B-100. There are 160 complex data points in Figure 15 which were collected over the temperature range from 86 to 185°F and a frequency range of 0.3 to 50 Hz. A bending specimen was used during the DMTA test. The WLF form of  $\alpha_T$  with  $T_0 = 392^\circ\text{F}$  was used to generate Figure 15.

The DMTA RFN (Figure 15) contains some scatter; however, by itself, the DMTA RFN would be judged an adequate representation of the complex modulus data for B-100 with mica added.

Table 5 compares the data characterization given in Figures 13 and 15. From Table 5 one can see that the trend of the Beam  $T_0$  being less than to DMTA  $T_0$  continues to hold. The value of peak loss factor for the DMTA is somewhat higher than the BEAM peak value. The modulus data indicates that the rubbery data compare well but the glassy data is significantly different. As was stated earlier, the BEAM data is wrong in the glassy area.

Figure 17 presents the DMTA, BEAM, and single frequency RSA II data sets on the same RFN with  $T_0 = 392^\circ\text{F}$ . In this RFN comparison, the DMTA and RSA II loss factor data agree. All three data sets agree well in the transition and rubbery modulus regions; however, each set separates in the glassy region. The BEAM data has the lowest value of glassy modulus; but, as was stated earlier, the glassy data from the BEAM test is wrong because of using a sandwich test specimen to collect modulus data above  $10^4$  psi.

## CONCLUSIONS

At the outset of this effort the intent was to discuss the limitations of and variations between three test methods for determining complex modulus properties of damping materials. However, in an effort to develop the comparison between the various test results, a variation between various  $\alpha_T$  equations was discovered. It is quite logical to expect that some

level of variation would be generated by different  $\alpha_T$  equations; but, it was totally unanticipated that three widely accepted  $\alpha_T$  equations would generate such significant differences in the data.

Figure 18 presents a compilation of information on the BEAM, DMTA, and RSA II test systems. The cross-hatches area for each test system indicates modulus values where inaccurate data is often collected. In these areas the data inaccuracies may manifest themselves in a very obvious way such as negative loss factor or modulus values; or, the inaccurate data may appear to be consistent within itself such as the glassy modulus data from a sandwich beam test where the modulus values are above  $10^4$ psi. The accuracy, or lack thereof, in the modulus areas is dependent upon the test specimen used and the geometry of the particular test specimen. For many engineeringly practical materials, it is impossible to establish accurate complex modulus data across the entire glassy to rubbery transition with a single test specimen.

The material testers and complex modulus data users must make themselves aware of these potential problems and review not only the final complex modulus data presented but also the test procedure and test specimens used to generate the data.

The question as to which  $\alpha_T$  relationship is the most accurate is a difficult one to answer. The S2-73 committee is working on a complex modulus data presentation standard which currently has several other  $\alpha_T$  relationships that can be chosen besides the one used in this paper. There are many additional  $\alpha_T$  relationships currently in use which are not considered in the S2-73 standard.

So long as engineers and scientists are also human beings, there will always be disagreement on the most appropriate test method and  $\alpha_T$  relationship to use.

#### ACKNOWLEDGEMENTS

Thanks are due to Dr. D. I. G. Jones WRDC/MLLN, Dr. L. C. Rogers WRDC/FIBAA, and Mr. B. Fowler of CSA Engineering for their support in generating RFN plots for several complex modulus data sets and general discussions concerning the results.

#### REFERENCES

1. J. E. Ferry, Viscoelastic Properties of Polymers, John Wiley and Sons, Inc., New York, 1961.
2. D. I. G. Jones, T. Lewis, A. D. Nashif, "Frequency/Temperature Dependence of Polymer Complex Modulus Properties," Damping '89, paper number FAC.
3. L. C. Rogers, "Graphical Presentation of Damping Material Complex Modulus - Proposed Standard," ANSI (ASA)/52-73; ISO/TC108/WG13.

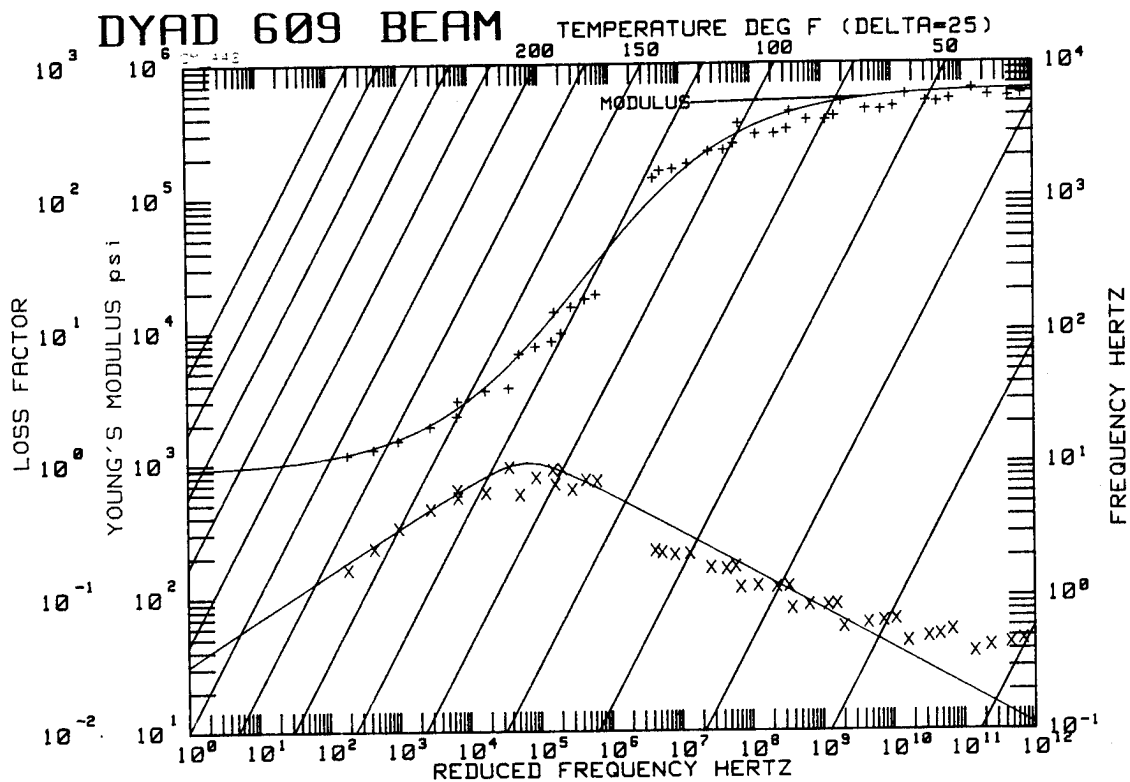


Figure 1. Dyad 609 Beam Test Results.

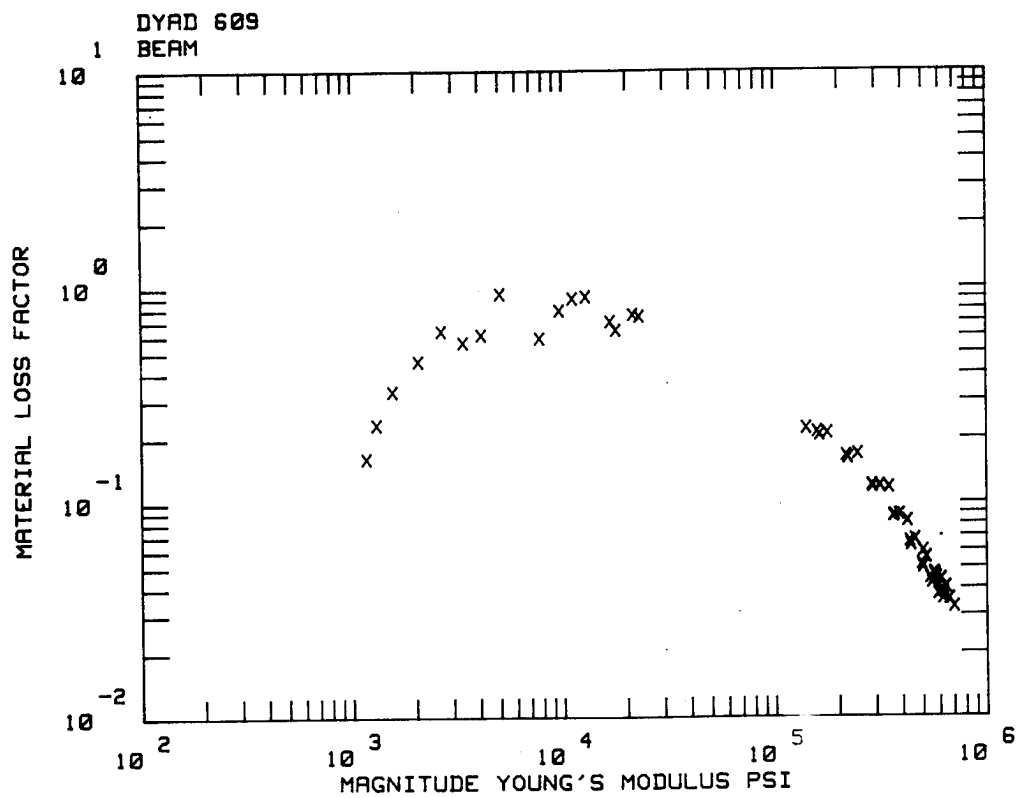


Figure 2. Dyad 609 Beam Test Complex Modulus Data.

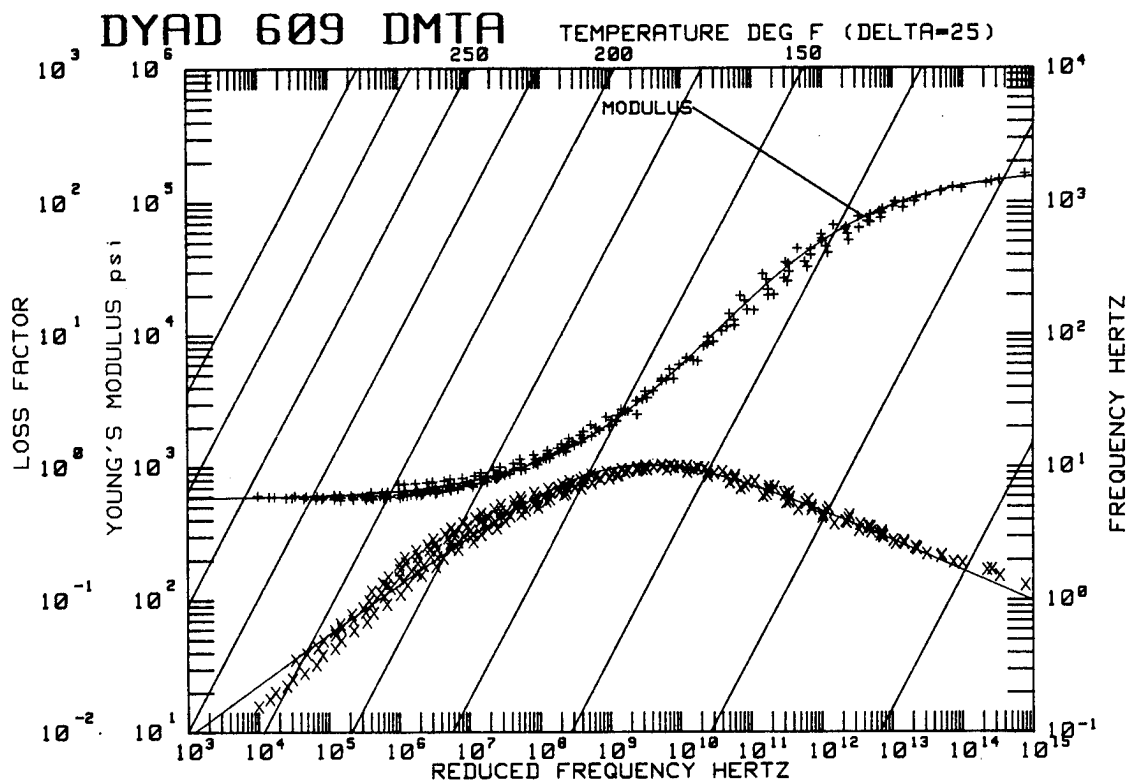


Figure 3. Dyad 609 DMTA Results.

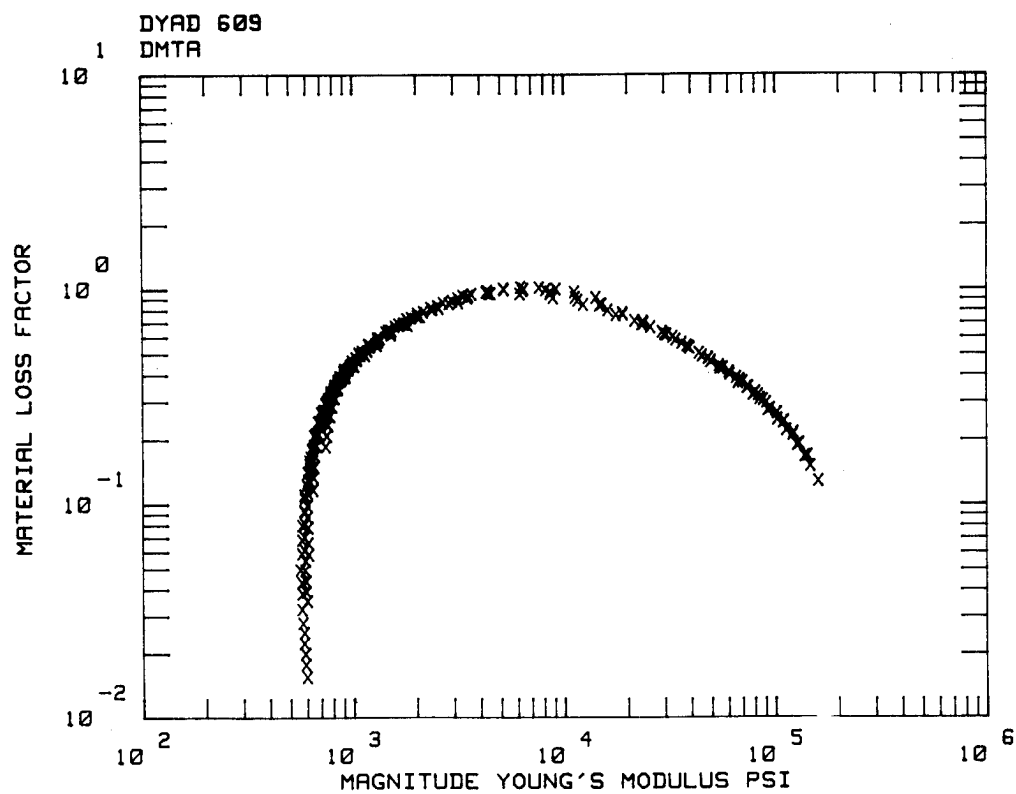


Figure 4. Dyad 609 DMTA Complex Modulus Data.

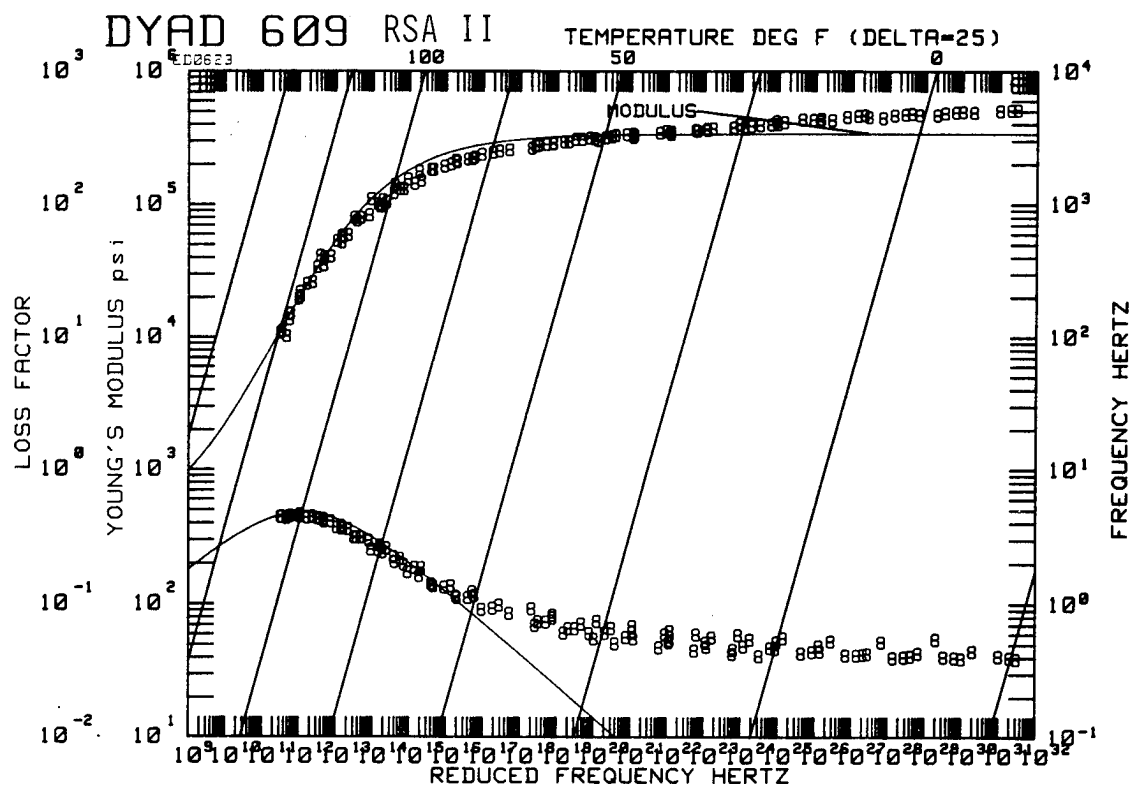


Figure 5. Dyad 609 RSA II Test Results.

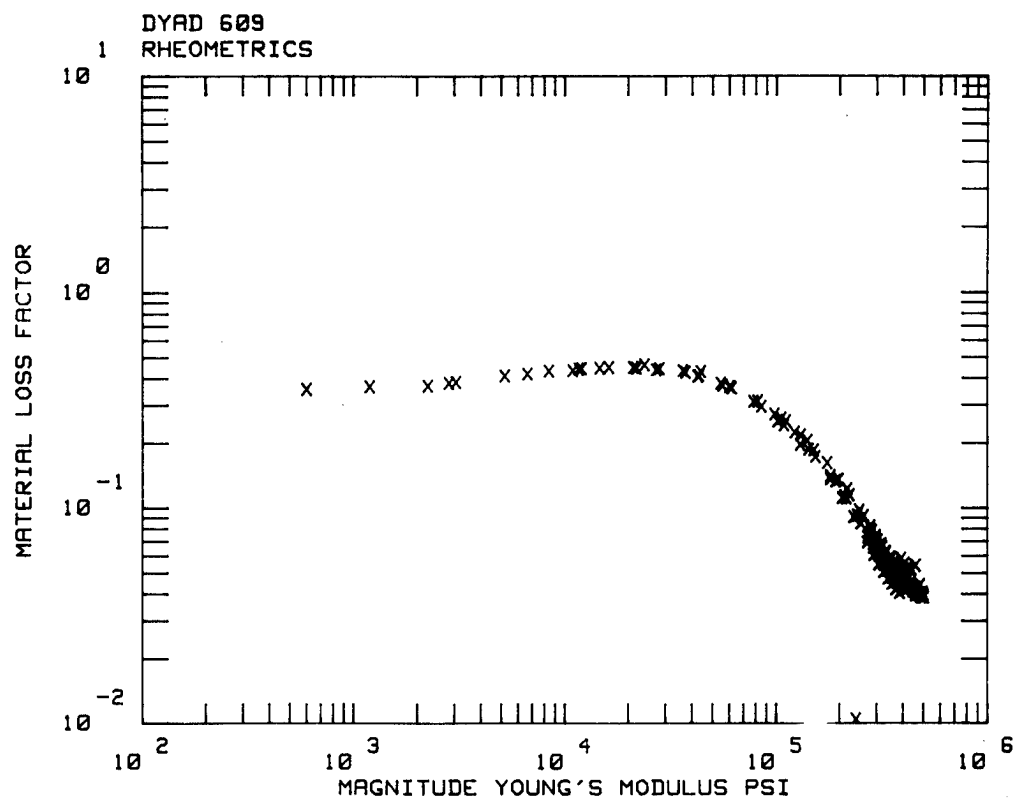


Figure 6. Dyad 609 RSA II Complex Modulus Data.

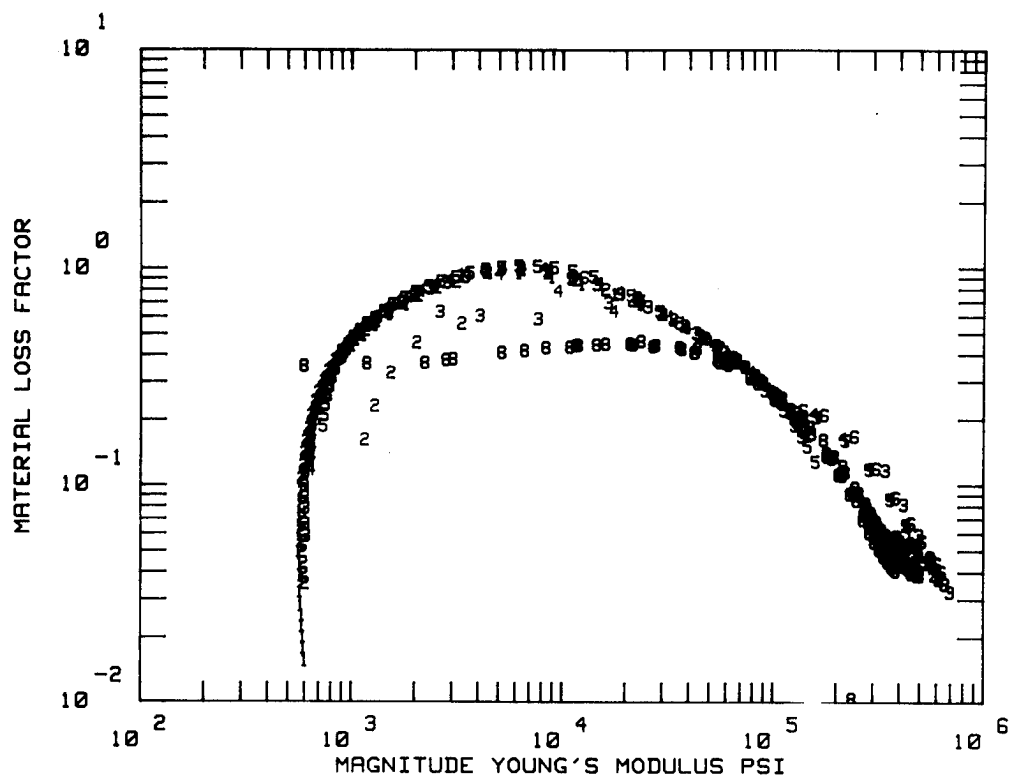


Figure 7. All 3 Complex Modulus Data Sets.

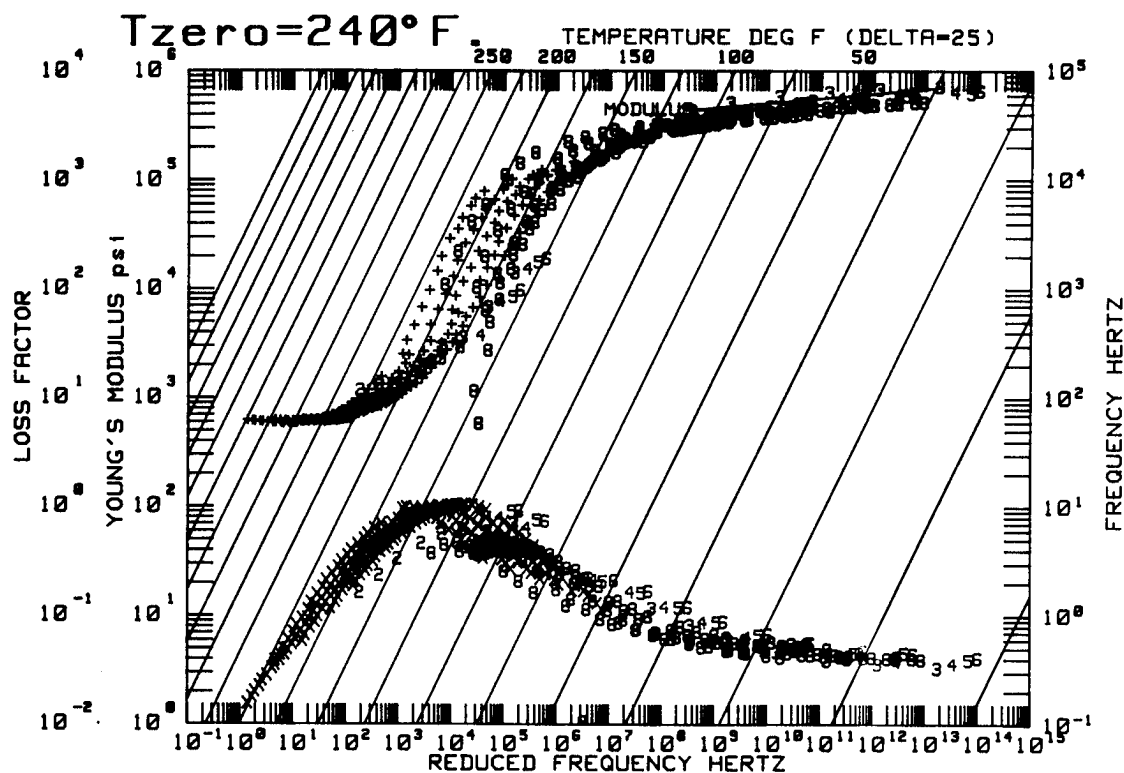


Figure 8. All 3 Complex Modulus Data Sets with  $T_0 = 240^\circ\text{F}$ .



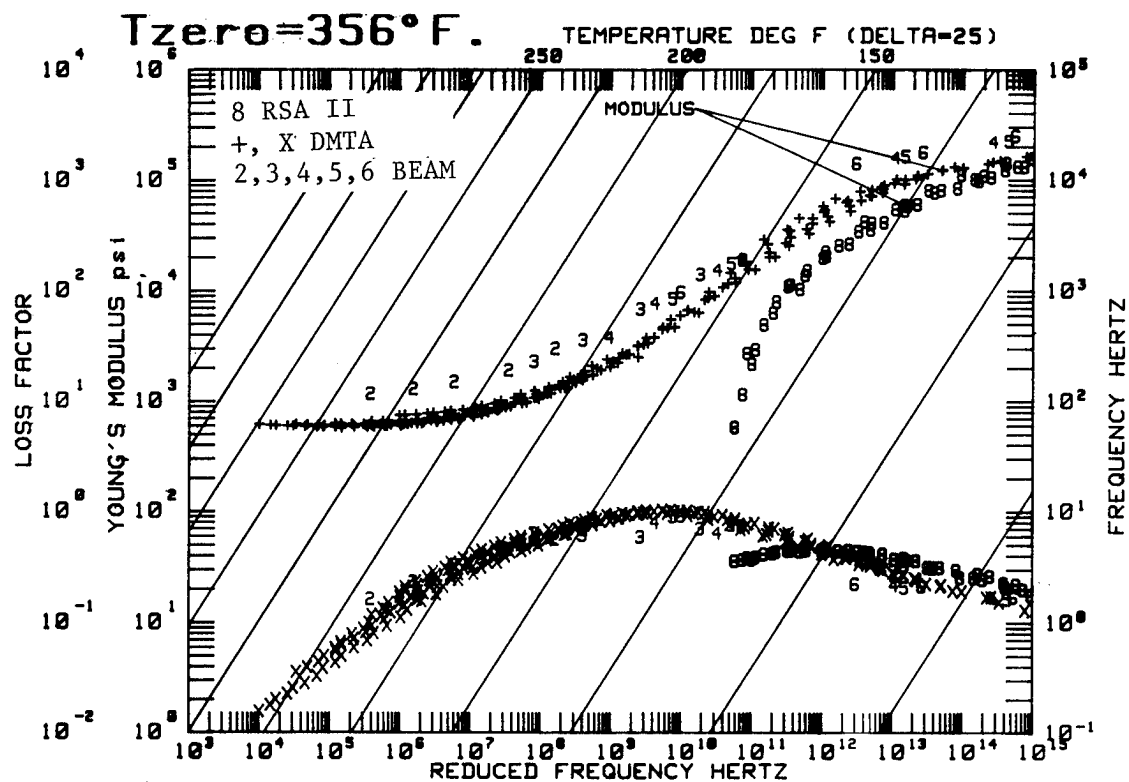


Figure 9. All 3 Complex Modulus Data Sets with  $T_0 = 356^\circ\text{F}$ .

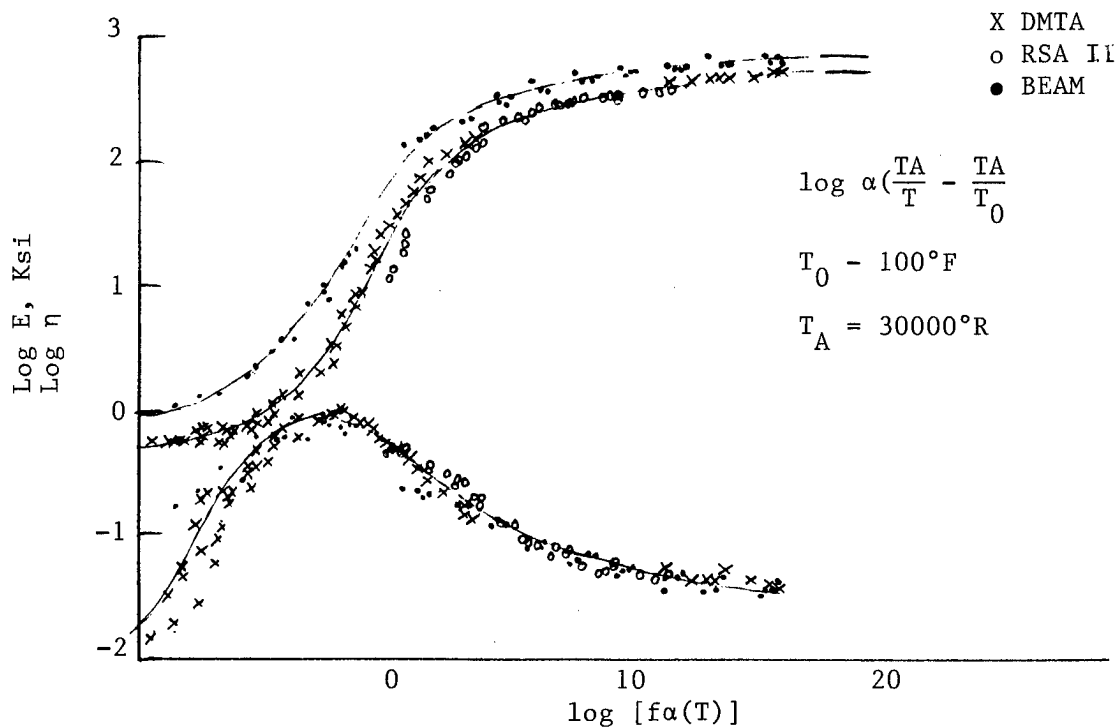


Figure 10. All 3 Data Sets Plotted with  $\alpha_T$  Proportional to  $\frac{1}{T}$ .

# BEAM

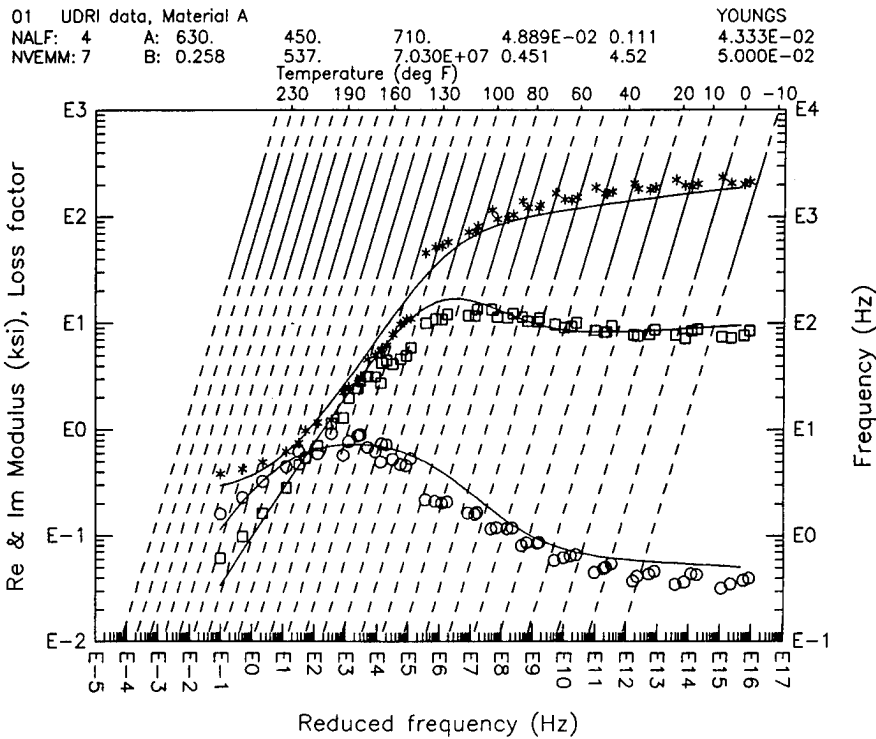


Figure 11. BEAM Data in S2-73 Draft Standard Form.

# DMTA

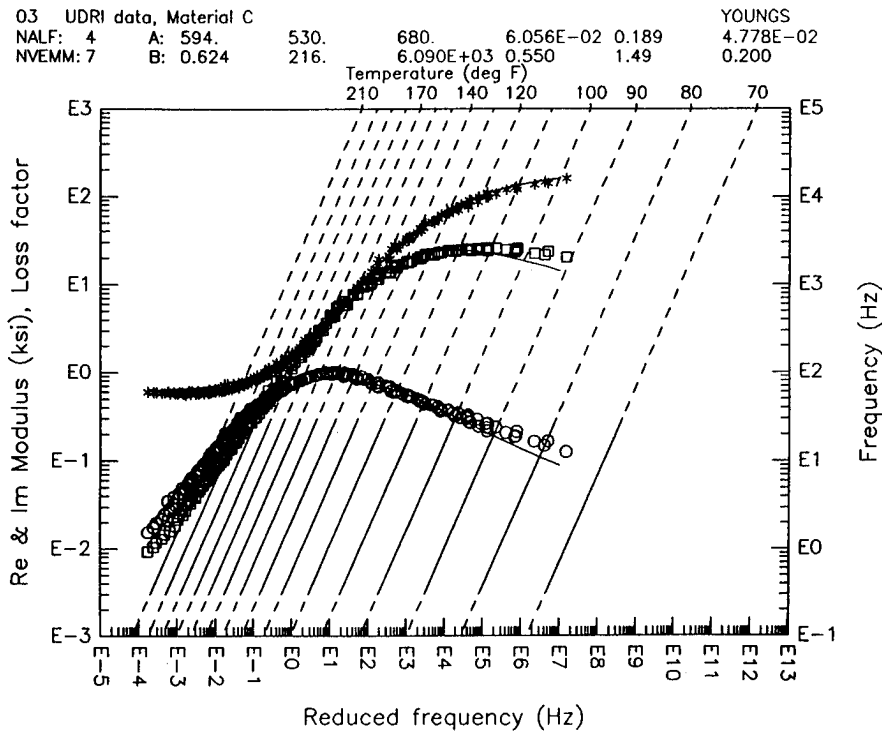


Figure 12. DMTA Data in S2-73 Draft Standard Form.

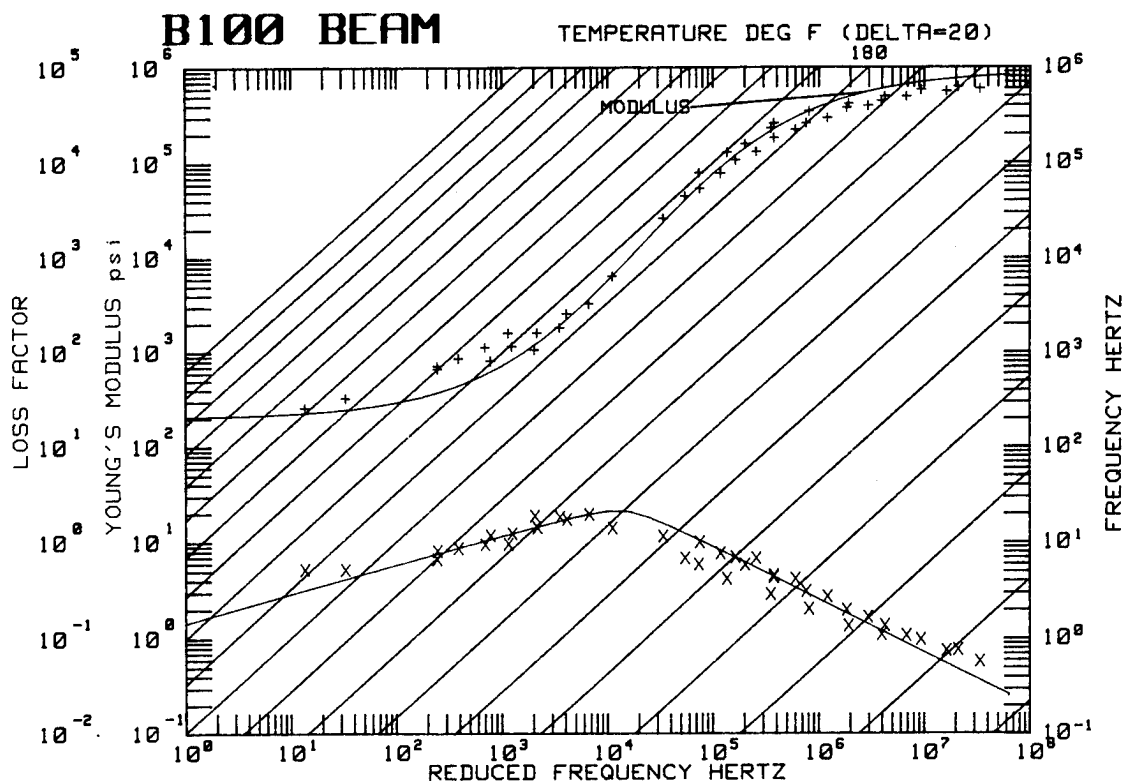


Figure 13. RFN For Vinac B-100 BEAM Test Results.

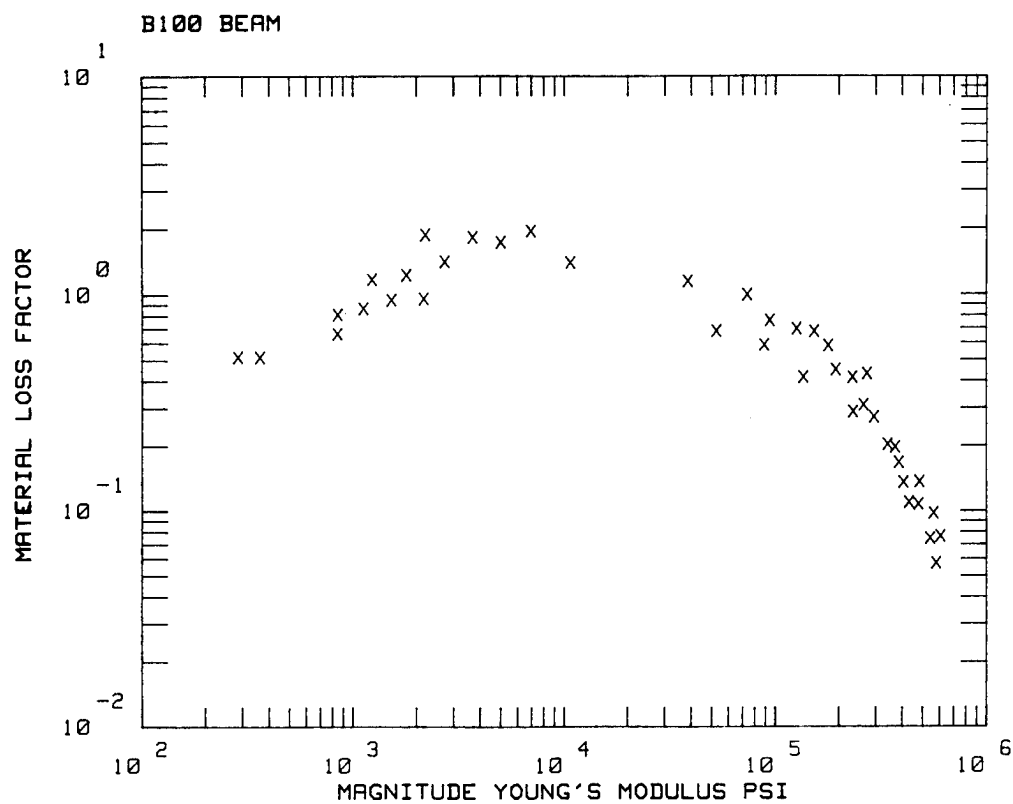


Figure 14. Complex Modulus Plot for the BEAM Test of Vinac B-100.

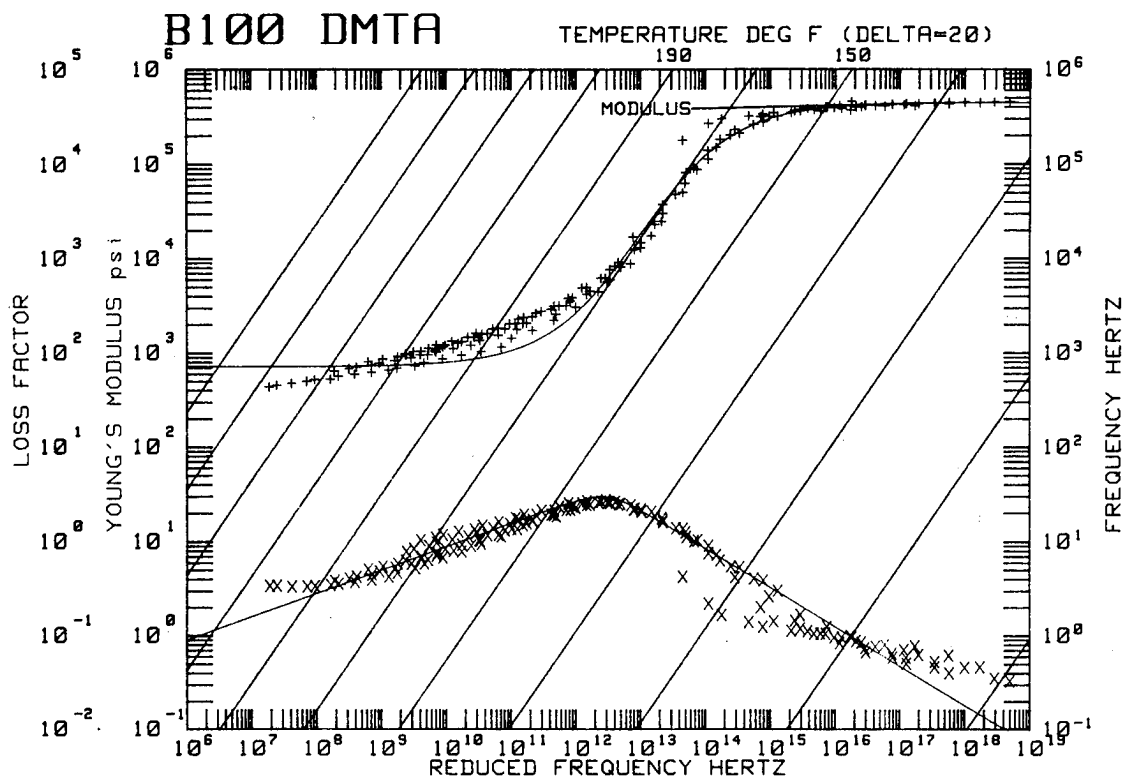


Figure 15. RFN of the DMTA Results for Vinac B-100.

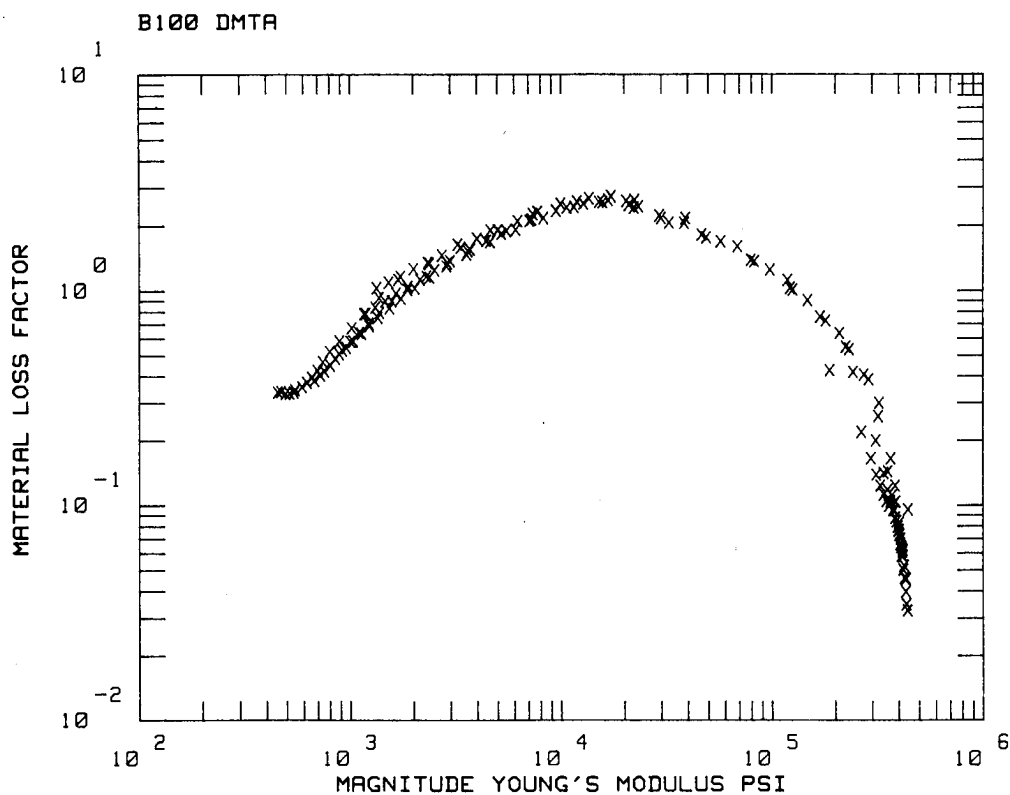


Figure 16. Complex Modulus Plot of the DMTA Results for Vinac B-100.

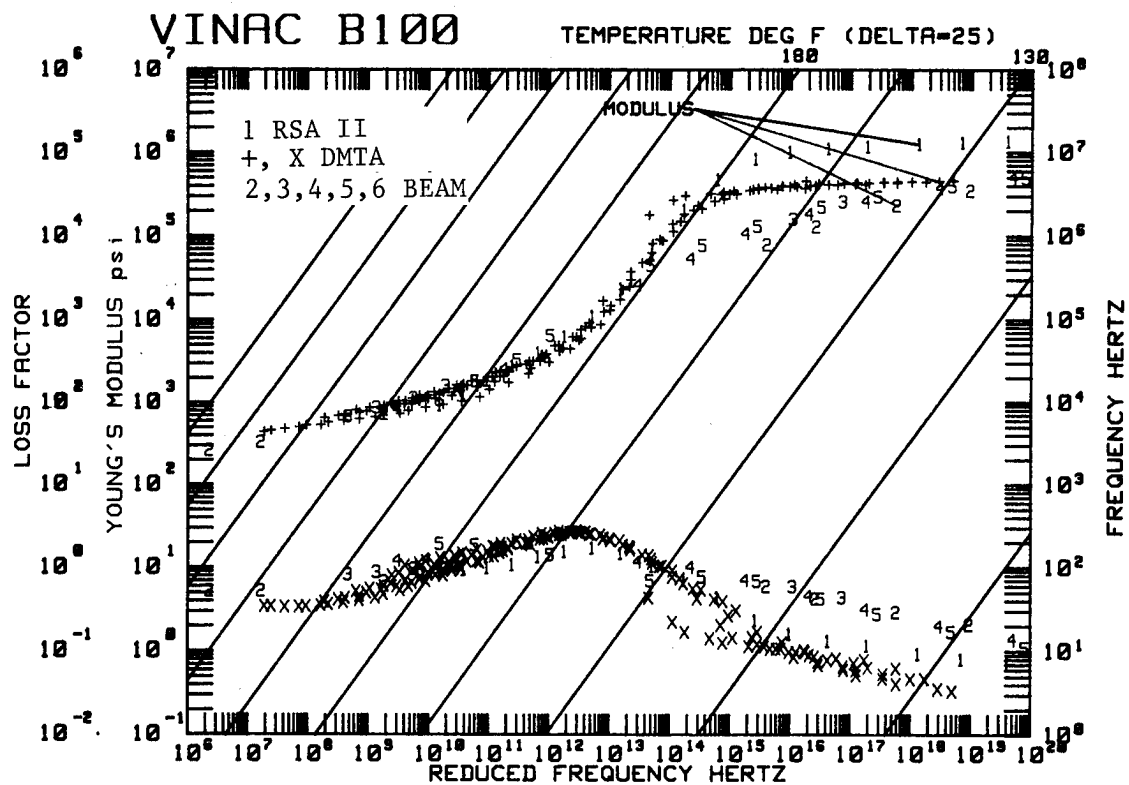


Figure 17. DMTA, BEAM, and RSA II Complex Modulus Data with  $T_0 = 392$

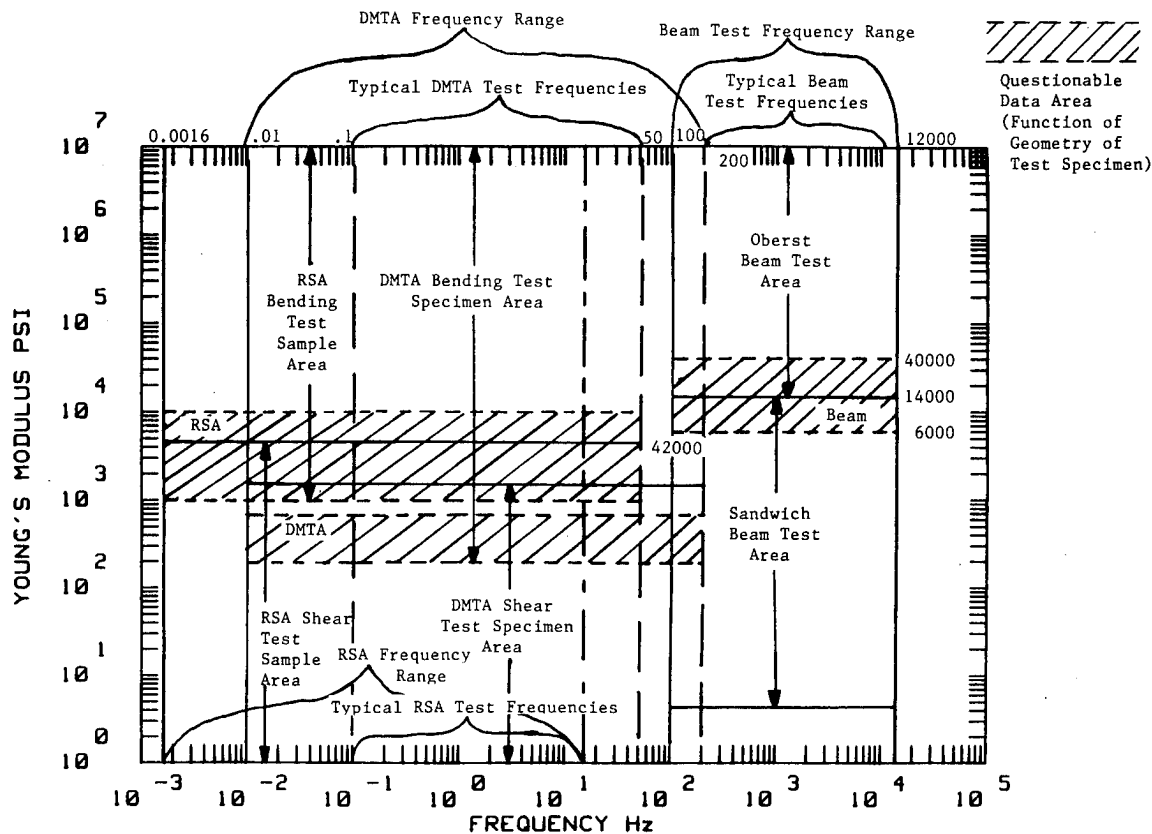


Figure 18. Frequency and Modulus Ranges Where the BEAM, DMTA, and RSA II are Usable.

TABLE 1  
THE MEASUREMENT TECHNIQUES

ASTM E-756 - BEAM Test:  
Frequency: 100 to 12000 Hz  
Temperature: -100°F to 2000°F  
Specimens: Free Layer, Sandwich, Uniform

Polymer Laboratories - DMTA:  
Frequency: 0.01 to 200 Hz  
Temperature: -233°F to 1472°F  
Specimens: Shear & Bending

Rheometrics - RSA II:  
Frequency: 0.0016 to 16 Hz  
Temperature: -233°F to 1112°F  
Specimens: Shear & Bending

TABLE 2  
COMPARISON OF DYAD 609 CHARACTERIZATION USING THE WLF  $\alpha_T$

	$T_0(^{\circ}\text{F})$	$\eta_p$	Modulus at $\eta_p$ (PSI)	Temp. of at 100 Hz ( $^{\circ}\text{F}$ )	$\Delta T$ Where $\eta \geq 0.7 \eta_p$ ( $^{\circ}\text{F}$ ) at 100 Hz	Modulus @ 117°F and 100 Hz	Modulus @ 130°F and 100 Hz	Modulus (PSI) @ 164°F and 100 Hz	Modulus (PSI) @ 176°F and 100 Hz
BEAM	240	1.02	7742.6	140	117-164	26,266	12,703	3152.0	2319.7
DMTA	356	1.03	3396.6	154	130-176	51,418	20,237	1992.9	1273.8
RSA II*	356	N/A	N/A	N/A	N/A	N/A	N/A	N/A	N/A

\* Due to the specimen used, the RSA II results did not define the peak damping level.

TABLE 3  
THE S2-73 CHARACTERIZATION COMPARISON  
DYAD 609

	$T_0(^{\circ}\text{F})$	$\eta_p$	Modulus at $\eta_p$ (PSI)	Temp. of at 100 Hz ( $^{\circ}\text{F}$ )	$\Delta T$ Where $\eta \geq 0.7 \eta_p$ ( $^{\circ}\text{F}$ ) at 100 Hz	Modulus @ 106°F and 100 Hz	Modulus @ 120°F and 100 Hz	Modulus (PSI) @ 187°F and 100 Hz	Modulus (PSI) @ 185°F and 100 Hz
BEAM	150	0.73	3569	145	106-187	27,100	11,000	656.6	700
DMTA	133	0.84	5101	154	120-185	70,000	34,406	1200.0	1350

TABLE 4  
A SUMMARY OF COMPLEX MODULUS DATA CHARACTERIZATIONS EVALUATED

	Loss Factor Peak				Modulus at Peak Loss Factor (PSI)			
	WLF		$\frac{1}{T}$	$(\frac{1}{T})^2$	WLF		$\frac{1}{T}$	$(\frac{1}{T})^2$
	High	Low			High	Low		
	$T_0$	$T_0$			$T_0$	$T_0$		
BEAM	1.02	1.02	1.0	0.73	8200	7742	14962	3569
DMTA	1.03	1.03	1.0	0.83	5000	3346	4597	5101

TABLE 5  
COMPARISON OF THE  $WLF\alpha_T$  CHARACTERIZATION OF  
BEAM AND DMTA COMPLEX MODULUS DATA FOR VINAC B-100

	$T_0(^{\circ}F)$	$\eta_p$	Modulus $\eta_p$ psi	Temp of $\eta_p$ at 100 Hz	Modulus at 130°F & 100 Hz	Modulus at 170°F & 100 Hz
BEAM	200	2.15	7.76E3	122	3.87E3	5.21E2
DMTA	392	3.0	4.57E3	149	1.1E5	9.5E2

FREQUENCY-TEMPERATURE DEPENDENCE OF POLYMER  
COMPLEX MODULUS PROPERTIES

by

Tom Lewis and Ahid D. Nashif  
Anatrol Corporation, Cincinnati, Ohio 45241

and

David I.G. Jones  
Materials Laboratory (AFWAL/MLLN)  
Wright-Patterson AFB, Ohio 45433

**ABSTRACT**

Advances in the frequency-temperature analysis of complex modulus properties of polymeric materials are described. Means are identified for minimizing the errors in data analysis for determination of parameters in an Arrhenius shift-factor relationship. The approach is illustrated for data obtained by several test methods, for a commercial polymeric viscoelastic adhesive, over wide frequency and temperature ranges.



## INTRODUCTION

It has long been recognized that the complex modulus behavior of polymeric viscoelastic materials depends on temperature and frequency through a combined variable which is the product of the frequency and a function of the temperature. The form of this function depends on the particular material being investigated, and is determined in principle by examining plots of  $\log(\text{modulus})$  and  $\log(\text{loss factor})$  versus  $\log(\text{frequency})$ , and determining the necessary shift along the  $\log(\text{frequency})$  axis required to collapse all the data points on to a unique pair of master curves. This process is considered to be applicable only to thermorheologically simple materials, but practical experience indicates very broad applicability of the approach. The current state of the art is such that most experimental data for specific materials is subject to systematic and random errors, often of significant magnitude, and the problems of determining reliable estimates of the shift factors are compounded by these errors and by the limited frequency and temperature ranges over which data is obtained. It is not usually possible to completely overcome these problems for any given data set, except by additional more carefully conducted testing, but some measure of data qualification can be achieved relatively simply.

The first step is to create a plot of  $\log(\text{loss factor})$  versus  $\log(\text{modulus})$ , using every experimental point available at all frequencies and temperatures. This process, which is becoming quite widely applied, eliminates frequency and temperature as independent variables, and the resulting graph should have all the points clustered along a unique, smooth curve. Points deviating too far from the majority may be eliminated as being in error, if for unknown reasons. Following this, detailed examination of the plots of  $\log(\text{modulus})$  and  $\log(\text{loss factor})$  versus frequency, for each temperature, will also allow one to identify points which deviate too far from the main body of data. In this way, one may be sure of having more consistent data, if not more accurate data.

The next step is to postulate a definite relationship between the shift factor required to merge all data into a set of unique master curves and the temperature. This relationship should have one or more selectable parameters. The simplest relationship, usually referred to as an Arrhenius relationship, is a linear plot of  $\log(\text{shift factor})$  versus inverse absolute temperature. The selectable parameters, the activation energy, and the reference temperature are varied until the scatter in the master curves is a minimum. The process can often be simplified even further by analyzing not the modulus and loss factor versus frequency, but rather a modulus ratio incorporating the estimated minimum and maximum modulus values and the loss factor.

## ANALYSIS

The starting point for frequency-temperature analysis of complex modulus properties is the assumed relationships:

$$E_r = (T_0/T) E(f_r) \quad (1)$$

$$\eta_r = \eta(f_r) \quad (2)$$

$$f_r = f\alpha(T) \quad (3)$$

$$\text{with } \log\alpha(T) = T_A/T - T_A/T_0 \quad (4)$$

for an Arrhenius type shift factor relationship. The "activation temperature"  $T_A$  is equal to  $Q/2.303R$ , where  $Q$  is the activation energy and  $R$  is the Universal Gas Constant.  $Q$  is a function of temperature, in general, but there is considerable evidence that it is constant over fairly wide temperature ranges when only one major mechanism of energy dissipation is dominant.  $T_0$  is the reference temperature, which may be chosen arbitrarily, although a temperature within the transition region is usually selected. Equations (3) and (4) define a temperature-compensated frequency  $f_r = f \exp(Q/RT)$ , on which the modulus ( $E$  or  $G$ ) and the loss factor ( $\eta$ ) depend. The ratio  $T_0/T$  (or more precisely  $\rho_0 T_0/\rho T$ ) allows for bulk expansion of the sample as a function of absolute temperature, and is often approximated by 1.0 for simplicity and convenience. Further simplification of the analysis is achieved by postulating a simple relationship between  $E_r$  and  $f_r$  [1] of the form:

$$E_r(f_r) = E_{r\infty} - (E_{r\infty} - E_{r0}) \frac{1}{1 + \beta(f_r)^n} \quad (5)$$

which may be re-stated in the form:

$$E_e = \frac{E_r(f_r) - E_{r0}}{E_{r\infty} - E_r(f_r)} = \beta(f_r)^n \quad (6)$$

$$\log(E_e) = n \log(f_r) + \log(\beta) \quad (7)$$

where  $E_{r0}$  is the asymptotic value of  $E_r$  at zero frequency ( $f_r$ ) and  $E_{r\infty}$  is the asymptotic value of  $E_r$  at infinite value of  $f_r$ . Equation (7) implies a linear relationship between  $\log(E_e)$  and  $\log(f_r)$ , and forms the basis for a simple linear regression analysis of the test data.

$$\text{Furthermore } n_r = \frac{K_2(f_r)^{(p-1)}}{(1+K_3(f_r)^p)^m} \quad (8)$$

A prior investigation [2] has shown that an Arrhenius model fully describes the frequency-temperature behavior of a specific polymer, and that other equations such as the WLF equation represent modest deviations from the Arrhenius model which are often not supported by the experimental data, especially in view of the scatter usually encountered. This is the basis for the foregoing, very simple analysis. The further introduction of a modulus ratio  $E_e$ , which is assumed to be a simple function of the reduced frequency  $f_r$ , allows one to utilize simple statistical methods for determining the optimum value of the activation temperature  $T_A$ . Both of these simplifications not only simplify computer-based analysis of the data, but represent also a simple physical-mathematical model which may be verified for each material on the basis of how well it fits the experimental data. So far, no data has been encountered which fails to fit this type of model. The illustration which follows, demonstrating the application of the approach to a viscoelastic adhesive, is typical.

## ILLUSTRATION

The approach just described will be applied to a data set obtained for a commercial viscoelastic adhesive, 3M-966 [3], by several test techniques. Complex modulus properties were measured by the ASTM standard vibrating beam test and by relaxation and impedance methods. The test techniques have been described adequately elsewhere [1,4,5]. The measured complex modulus data, for shear deformations, is summarized in Table 1. Figure 1 shows a plot of frequency versus temperature, which identifies the conditions pertaining to each test point and test method. It is seen that many points were obtained between  $-50^{\circ}\text{F}$  and  $250^{\circ}\text{F}$ , and between 100 Hz and 10,000 Hz, a few between  $0^{\circ}\text{F}$  and  $100^{\circ}\text{F}$  and between  $1\text{E}-4$  Hz and 0.1 Hz, but that a gap appears between 0.1 Hz and 50 Hz for all temperatures. No test technique was fully satisfactory in this region. Efforts to develop improved techniques for data acquisition in the gap area are under way, but even without such data, the data readily collapses by the reduced-variables method outlined earlier. Figure 2 shows the standard plot of  $\log(\text{loss factor})$  versus  $\log(\text{modulus})$ . Some points which deviated significantly from the main body of data were culled from the data set.

The next step in the data reduction process was to apply an Arrhenius type of shift process, in accordance with equation (4), and vary the activation temperature  $T_A$  until scatter in the plots of  $\log(\text{modulus})$  and  $\log(\text{loss factor})$  versus  $\log(\text{reduced frequency})$  is minimized. This process is illustrated in Figures 3 through 11 for values of  $T_A$  equal to 5000, 7000, 8000, 8900, 10000, 11000, 12000, 13000, and 15000°R. It is seen that the low frequency data, in particular, serves to indicate deviation from full collapse. The figures show the progressive reduction of scatter to an optimum near  $T_A = 8900^\circ\text{R}$ , with greater errors for lower and higher values of  $T_A$ . The scatter may be measured in several ways, including visual judgement, plotting of the progression of the gap between selected pairs of points, or through more elaborate statistical analysis of a larger number of selected points.

Following the first identification of an optimum value of  $T_A$ , the plots may also indicate the possibility that an Arrhenius model may not be completely satisfactory. As Figure 6 shows, however, for  $T_A = 8900$  very few points clearly indicate deviations from the "linear" shift factor relationship implied in equation (4). In fact, no material data has yet been identified for which the deviation from this type of "linearity" is sufficiently large to be visible over the general level of scatter in the data.

Further iteration of the identification process may now be exercised by examining the plots of  $\log(G_e)$  versus  $\log(\text{reduced frequency})$ , as defined by equations (5) to (7). These plots are summarized in Figures 12 to 20, for the same values of  $T_A$  and for  $G_0 = 8 \text{ Lb/in}^2$  and  $G_\infty = 1.5e5 \text{ Lb/in}^2$ . Again, the scatter reduces as  $T_A$  approaches the optimum value of about 8900°R. The iterative process now involves careful analysis of the effects of varying  $G_0$  and  $G_\infty$  as well as  $T_A$  until the plot is as linear as possible and the scatter a minimum. Simple statistical analysis may be applied.

Finally, a nomogram may be created in the usual way [1], as shown in Figure 21. This completes the data analysis for this specific material. Similar data analyses have been conducted for 3M-966 in tension-compression and for many other materials. The "linear" Arrhenius model of the shift factor behavior with respect to temperature seems to apply in every case, and no deviations have been observed within the limits of scatter. The significance of this is still not fully understood.

## CONCLUSIONS

It has been shown that a "linear" Arrhenius model for the dependence of frequency-temperature shift factors on temperature is effective for producing low scatter "master" plots of complex modulus properties versus a reduced frequency depending on frequency and temperature. The approach has been illustrated for a specific material. Other data supports the same conclusion. The simplicity of the Arrhenius relationship, along with the initial assumption of a simple relationship between modulus and

reduced frequency further allows simple linear regression analysis to be applied to the search for the optimum value of the activation temperature, which is a direct measure of the activation energy.

#### REFERENCES

1. A.D. Nashif, D.I.G. Jones and J.P. Henderson, Vibration Damping, Wiley Interscience, 1985.
2. D.I.G. Jones, A.D. Nashif and D.K. Rao, "Investigation of Shift Factors in Material Damping," ASME Paper 87-WA/AERO-7, Presented at ASME Winter Annual Meeting, Boston, MA, Dec. 1987.
3. 3M-966 Viscoelastic Damping Adhesive, 3M Company, St. Paul, MN.
4. ASTM Standard E756-80, "Standard Method for Measuring Vibration-Damping Properties of Materials," 1980.
5. M.L. Parin, A.D. Nashif and T.M. Lewis, "Relsat Damping Material Data," AFWAL-TR-86-3059, Vol. 1, pp AD-1 to AD-80, 1986.

Table 1: Complex Modulus Data - 3M Y-966

10" Sandwich Beam

Temperature	Frequency	Modulus	Loss Factor
94.33	134.18	75.83	1.313057
94.33	366.06	119.91	1.471784
94.33	706.23	155.60	1.352790
94.33	1167.19	260.90	1.297942
94.33	1739.49	311.56	1.251339
114.00	131.59	52.21	0.954046
114.00	359.55	61.30	1.256684
114.00	702.18	106.12	0.969221
114.00	1152.72	122.02	1.299971
114.00	1724.19	171.99	1.141671
134.00	129.29	30.39	0.883965
134.00	357.32	44.00	0.960007
134.00	696.54	59.73	0.913520
134.00	1147.93	87.67	0.922173
134.00	1715.25	100.85	1.008548
153.63	128.35	22.41	0.706620
153.83	355.28	28.36	0.868475
153.83	1709.91	67.98	0.866073
174.00	127.65	16.81	0.584690
174.00	354.17	21.96	0.693342
233.17	126.20	6.31	0.226837
253.00	126.10	6.63	0.169085
253.00	350.97	7.84	0.220534
55.80	169.90	460.54	1.429654
55.80	782.36	930.38	0.857959
55.80	1898.74	2060.02	1.039232
65.25	154.80	309.50	0.999700
65.25	761.69	663.70	1.491555
65.25	1833.27	1320.26	0.958539
74.40	154.28	309.31	0.892138
74.40	391.65	378.94	1.161334
74.40	1204.48	658.90	0.952200
74.40	1789.95	839.49	1.047756
85.00	139.81	132.31	1.295457
85.00	377.36	234.06	1.101109
85.00	718.61	255.44	1.129037
85.00	1176.33	350.73	1.360883
85.00	1760.87	532.12	1.123667
70.40	393.59	387.19	1.421225
70.40	753.82	615.02	0.983556
70.40	1873.74	1836.24	0.626351
43.00	201.33	1100.83	1.013737
43.00	956.47	3598.22	0.522952
29.67	237.22	2839.00	0.702139
29.67	592.87	4460.24	0.660257
29.67	1092.90	7119.03	0.381514
20.50	256.79	5230.67	0.594997
20.50	670.60	8735.28	0.630281
11.00	268.39	9120.56	0.390761
11.00	698.17	12861.83	0.390824

Table 1: Complex Modulus Data - 3M Y-966 (Con't.)

10" Sandwich Beam (Con't.)

<u>Temperature</u>	<u>Frequency</u>	<u>Modulus</u>	<u>Loss Factor</u>
2.25	276.60	14505.64	0.312686
2.25	733.90	20638.89	0.277731
2.25	1334.38	22239.30	0.244773
2.25	1977.63	20316.67	0.220431
-7.50	281.90	21619.36	0.226373
-7.50	755.38	29109.55	0.205839
-7.50	1406.68	33452.94	0.233467
-7.50	2143.24	31346.35	0.248907
-16.50	285.59	31386.20	0.175795
-16.50	772.46	40569.11	0.142938
-16.50	2269.37	46608.91	0.102699
-33.00	787.46	57987.82	0.073777
-33.00	1484.05	59747.66	0.111454
-33.00	2360.83	63172.90	0.058559
-49.00	795.07	71529.93	0.048820
-49.00	1499.56	68480.48	0.047705
-49.00	2404.18	73744.40	0.039597

5" Sandwich Beam

<u>Temperature</u>	<u>Frequency</u>	<u>Modulus</u>	<u>Loss Factor</u>
-47.00	5000.00	71601.62	0.043944
-25.00	1122.85	43884.45	0.078826
-25.00	2760.72	52564.42	0.081239
-25.00	4838.90	61488.95	0.082077
-8.00	1059.89	28380.08	0.176317
-8.00	2551.63	34920.95	0.183963
-8.00	4434.21	41254.14	0.188414
9.00	952.00	14931.14	0.344016
26.00	821.54	7202.87	0.560541
26.00	1953.31	9970.31	0.360439
26.00	3450.49	11749.96	0.485872
46.67	666.43	2631.76	0.858444
46.67	1606.08	2736.74	0.935332
46.67	3036.27	4132.80	0.777935
58.00	1519.18	1428.80	1.009958
58.00	2914.09	2243.93	0.892514
72.00	538.78	454.95	1.142293
72.00	1469.46	729.50	0.926019
72.00	2840.06	1164.90	0.829148
92.50	520.21	198.03	1.064238
92.50	1439.97	325.81	0.965631

Table 1: Complex Modulus Data - 3M Y-966 (Con't.)

Shear Relaxation

<u>Temperature</u>	<u>Frequency</u>	<u>Modulus</u>	<u>Loss Factor</u>
0.00	1.380E-004	10.29	0.307000
0.00	2.800E-004	11.58	0.394000
0.00	5.600E-004	13.43	0.484000
0.00	1.110E-003	16.02	0.585000
0.00	2.200E-003	19.53	0.699700
0.00	4.450E-003	24.61	0.816000
0.00	8.900E-003	31.56	0.971000
0.00	1.760E-002	42.81	1.094000
0.00	3.560E-002	76.90	1.122300
26.00	1.400E-004	6.79	0.117250
26.00	2.800E-004	7.12	0.153000
26.00	5.600E-004	7.56	0.202000
26.00	1.110E-003	8.13	0.265000
26.00	2.220E-003	8.98	0.358000
26.00	4.450E-003	10.24	0.447100
26.00	8.890E-003	11.68	0.565000
26.00	1.779E-002	13.82	0.756000

SDOF Resonance

<u>Temperature</u>	<u>Frequency</u>	<u>Modulus</u>	<u>Loss Factor</u>
93.00	109.40	42.77	0.968000
125.00	72.50	18.90	0.720000
150.00	69.46	17.36	0.670000
175.00	56.27	11.40	0.550000
25.00	2041.70	15006.70	0.330000
0.00	3115.60	34945.00	0.200000
50.00	725.79	1896.40	0.580000
80.00	182.08	119.40	1.000000



Table 1: Complex Modulus Data - 3M Y-966 (Con't.)

SDOF Shear Impedance

<u>Temperature</u>	<u>Frequency</u>	<u>Modulus</u>	<u>Loss Factor</u>
150.00	71.88	17.20	1.039500
150.00	90.63	20.60	0.974600
150.00	109.38	22.20	0.955300
150.00	131.25	25.20	0.914900
150.00	150.00	28.30	0.894800
150.00	171.88	32.60	0.840000
150.00	190.63	33.30	0.816500
175.00	90.63	14.30	0.725600
175.00	109.38	18.80	0.569200
175.00	131.25	21.80	0.640700
25.00	1809.38	14347.80	0.486800
25.00	1903.13	14731.60	0.471200
25.00	2003.13	14815.40	0.445800
25.00	2103.13	15032.70	0.444000
25.00	2203.13	15265.30	0.424100
25.00	2303.13	15635.00	0.409500
25.00	2403.13	15829.00	0.399200
25.00	2503.13	16241.00	0.382900
25.00	2603.13	16407.10	0.380000
25.00	2703.13	16838.20	0.357500
25.00	2803.13	17046.30	0.349800
25.00	2903.13	17406.00	0.350000
25.00	2996.88	17867.70	0.329200
0.00	2718.75	34259.40	0.236600
0.00	2806.25	34353.40	0.229100
0.00	2900.00	34340.20	0.220600
0.00	3000.00	34586.60	0.219300
0.00	3100.00	34632.60	0.213800
0.00	3200.00	34810.20	0.208900
0.00	3300.00	34982.20	0.204200
0.00	3400.00	35294.00	0.198500
0.00	3500.00	35641.30	0.194200
0.00	3600.00	35890.00	0.194500
0.00	3700.00	36038.70	0.189000
0.00	3800.00	36414.30	0.178000
0.00	3900.00	36806.90	0.178400
0.00	4000.00	37158.30	0.168500
50.00	706.25	1761.00	1.155600
50.00	900.00	2250.60	0.940100
50.00	1100.00	2556.50	0.831200
50.00	1300.00	2948.70	0.764500
50.00	1500.00	3333.30	0.696100
50.00	1700.00	3808.20	0.616900
50.00	1900.00	4221.40	0.574700
50.00	2000.00	4447.10	0.505900

Table 1: Complex Modulus Data - 3M Y-966 (Con't.)

SDOF Shear Impedance (Con't.)

<u>Temperature</u>	<u>Frequency</u>	<u>Modulus</u>	<u>Loss Factor</u>
80.00	200.00	127.30	1.630000
80.00	300.00	195.00	1.261100
80.00	400.00	254.20	1.102700
80.00	500.00	312.70	0.990900
80.00	600.00	390.60	0.893200
80.00	700.00	469.10	0.815600
93.00	150.00	60.00	1.455000
93.00	162.50	63.70	1.412400
93.00	175.00	68.20	1.371400
93.00	187.50	71.70	1.338700
93.00	200.00	77.60	1.278700
125.00	90.63	21.60	1.074300
125.00	112.50	24.70	1.041100
125.00	131.25	28.50	0.944200
125.00	150.00	32.20	0.868800
125.00	171.88	35.80	0.848900
125.00	190.63	40.40	0.823900
125.00	200.00	42.20	0.794500

Shear Creep

<u>Temperature</u>	<u>Frequency</u>	<u>Modulus</u>	<u>Loss Factor</u>
82.00	1.995E-003	6.05	0.125120
82.00	3.990E-003	6.41	0.142020
82.00	7.980E-003	6.80	0.149730
82.00	1.596E-002	7.30	0.177180
82.00	3.192E-002	7.73	0.206000
82.00	6.384E-002	8.34	0.255640
82.00	1.277E-001	9.76	0.295020

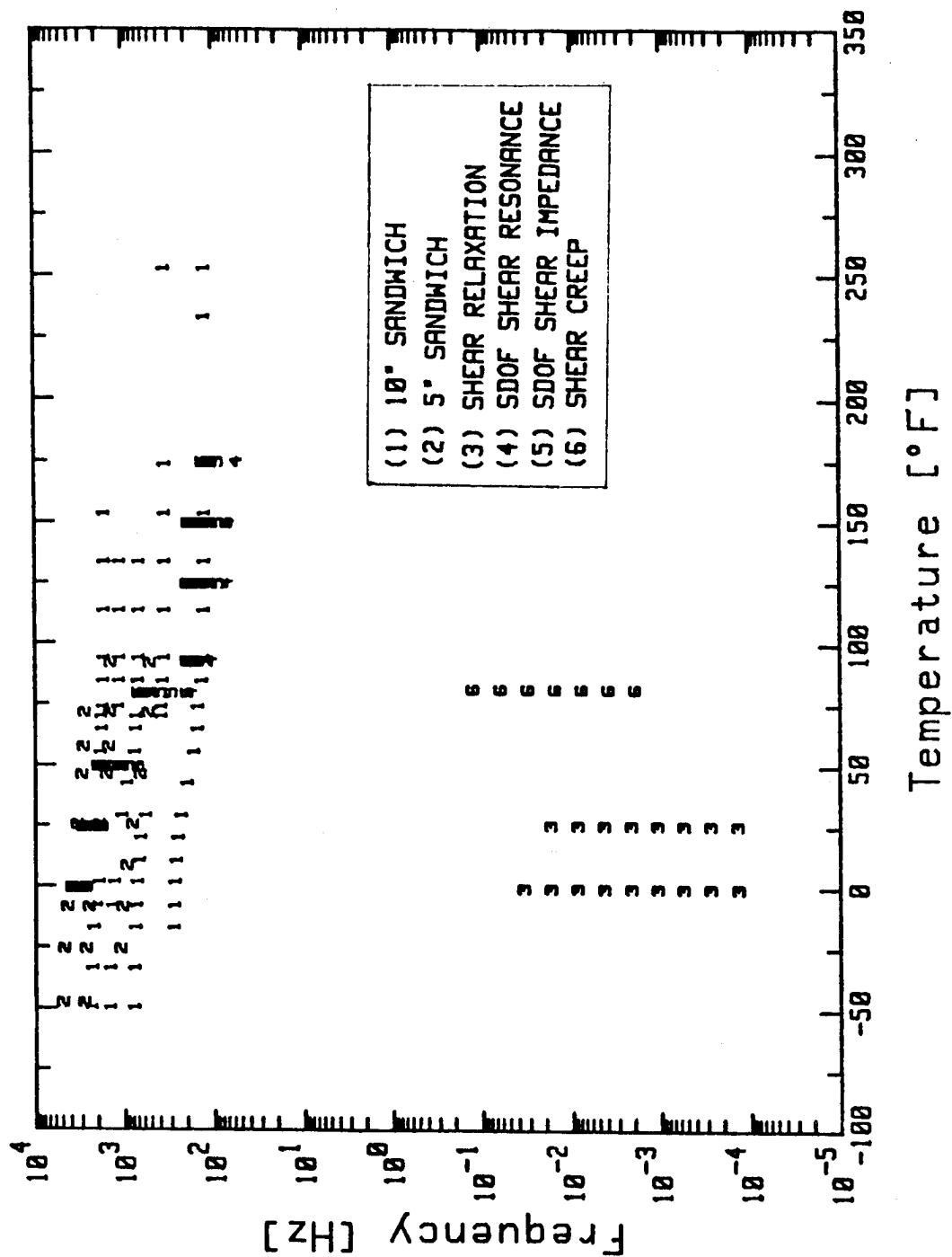


Figure 1: All Data Points Plotted Versus Temperature and Frequency, Illustrating the Areas Covered/Not Covered by the Test Techniques Used

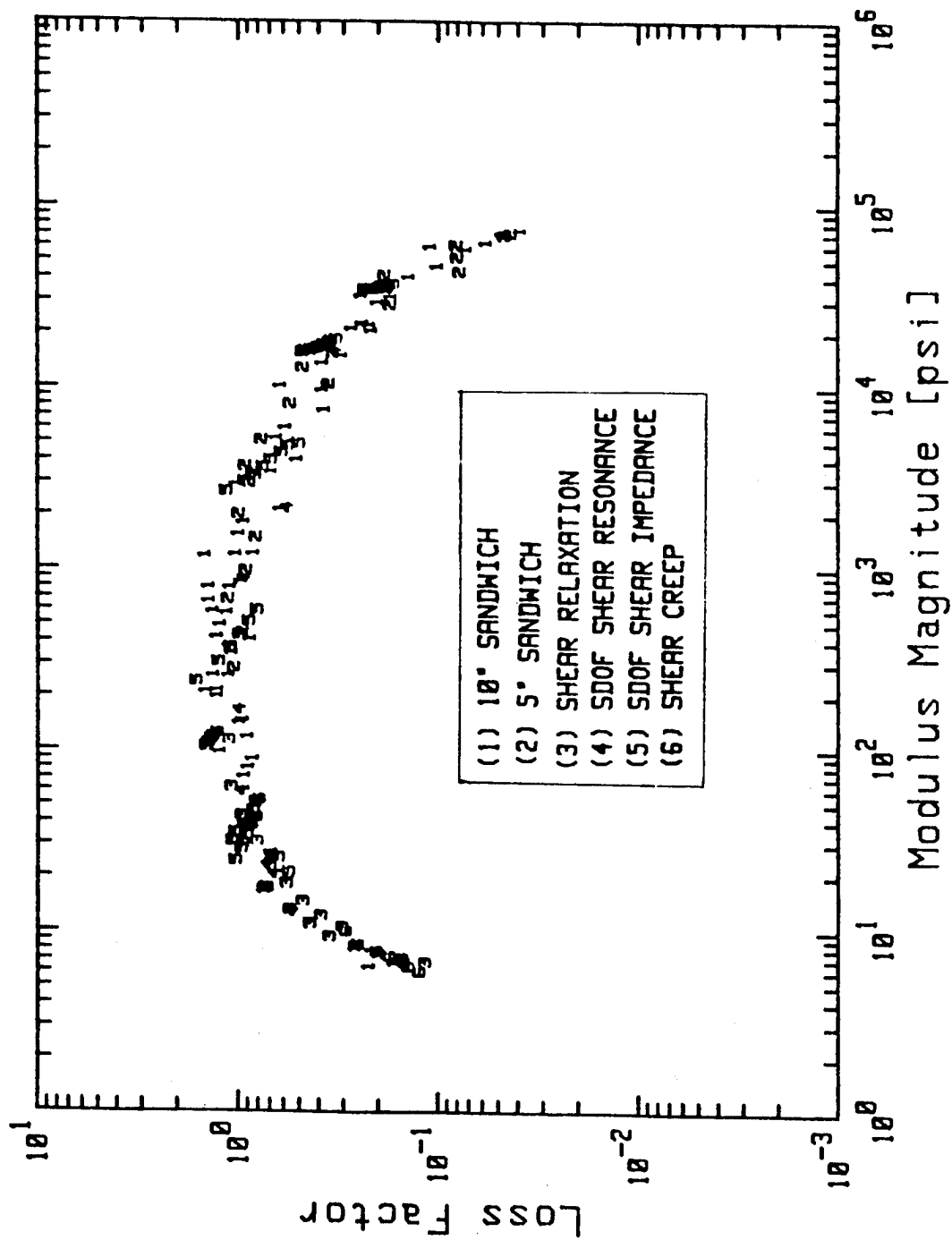


Figure 2: Plot of Loss Factor Versus Modulus, Showing Measure of Uniqueness of Relationship Between the Real and Imaginary Parts of the Complex Modulus

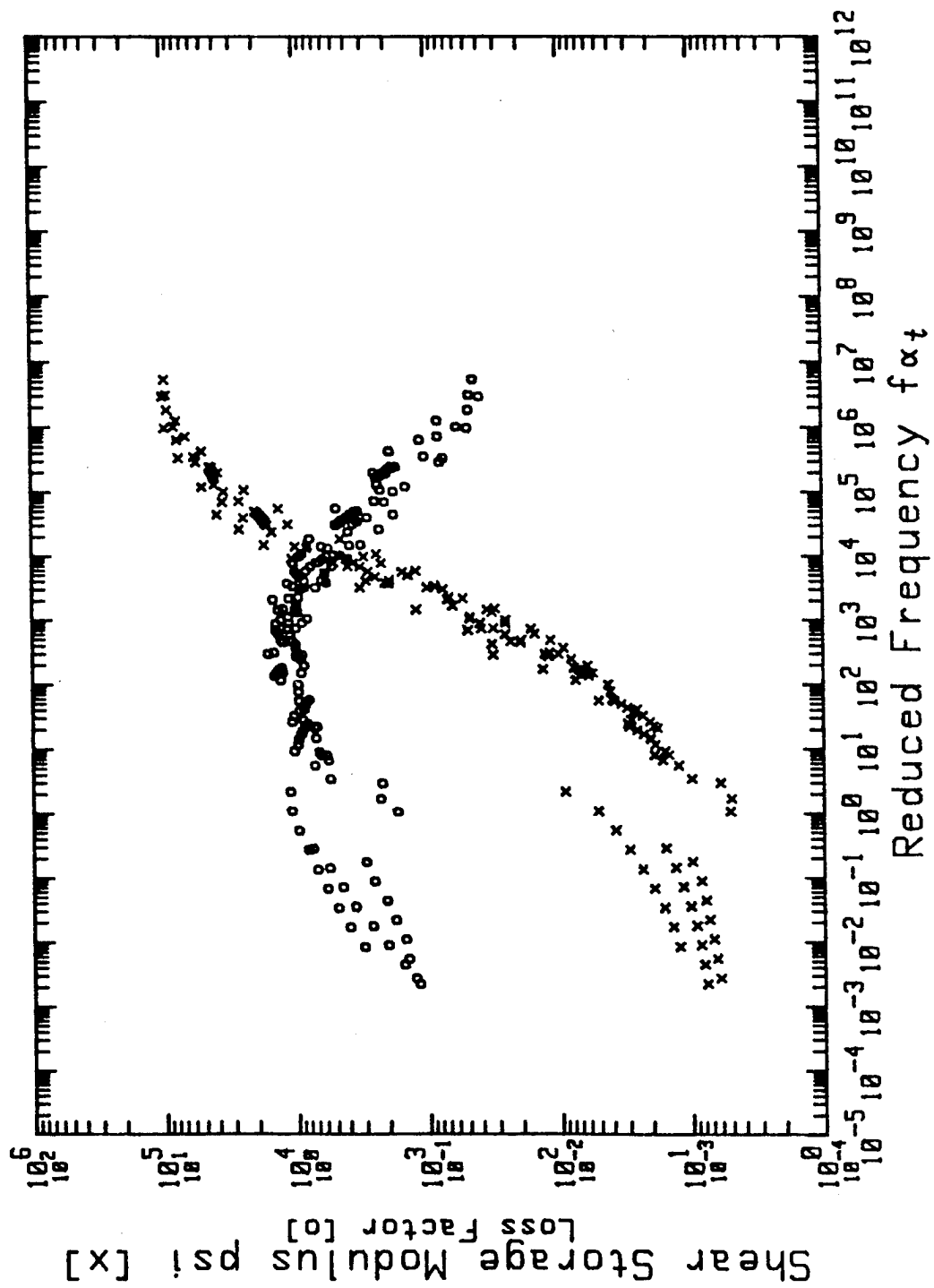


Figure 3: Plot of Shear Modulus and Loss Factor Versus Reduced Frequency  
( $T_A = 5000^\circ R$ )

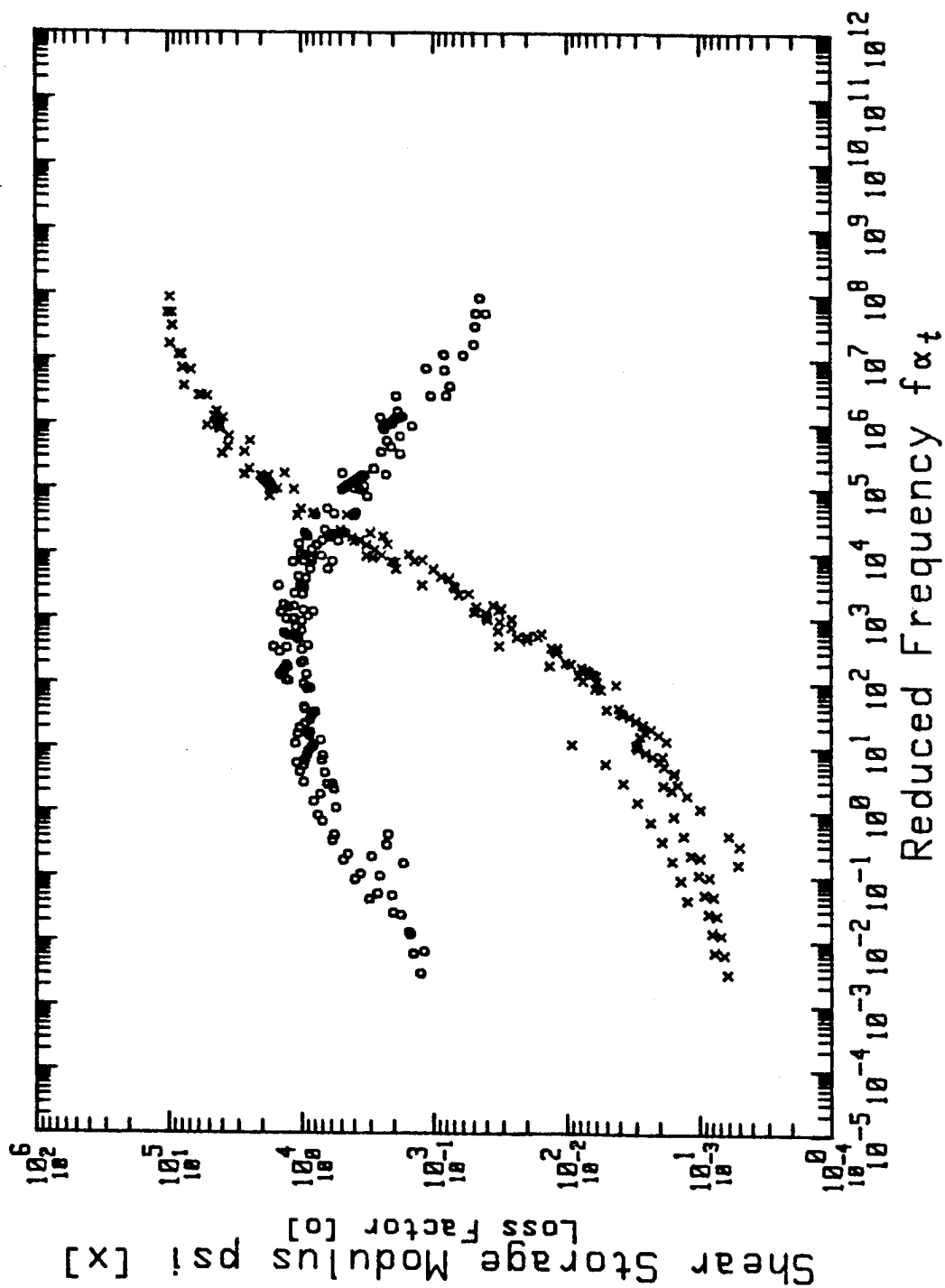


Figure 4: Plot of Shear Modulus and Loss Factor Versus Reduced Frequency  
( $T_A = 7000^\circ R$ )

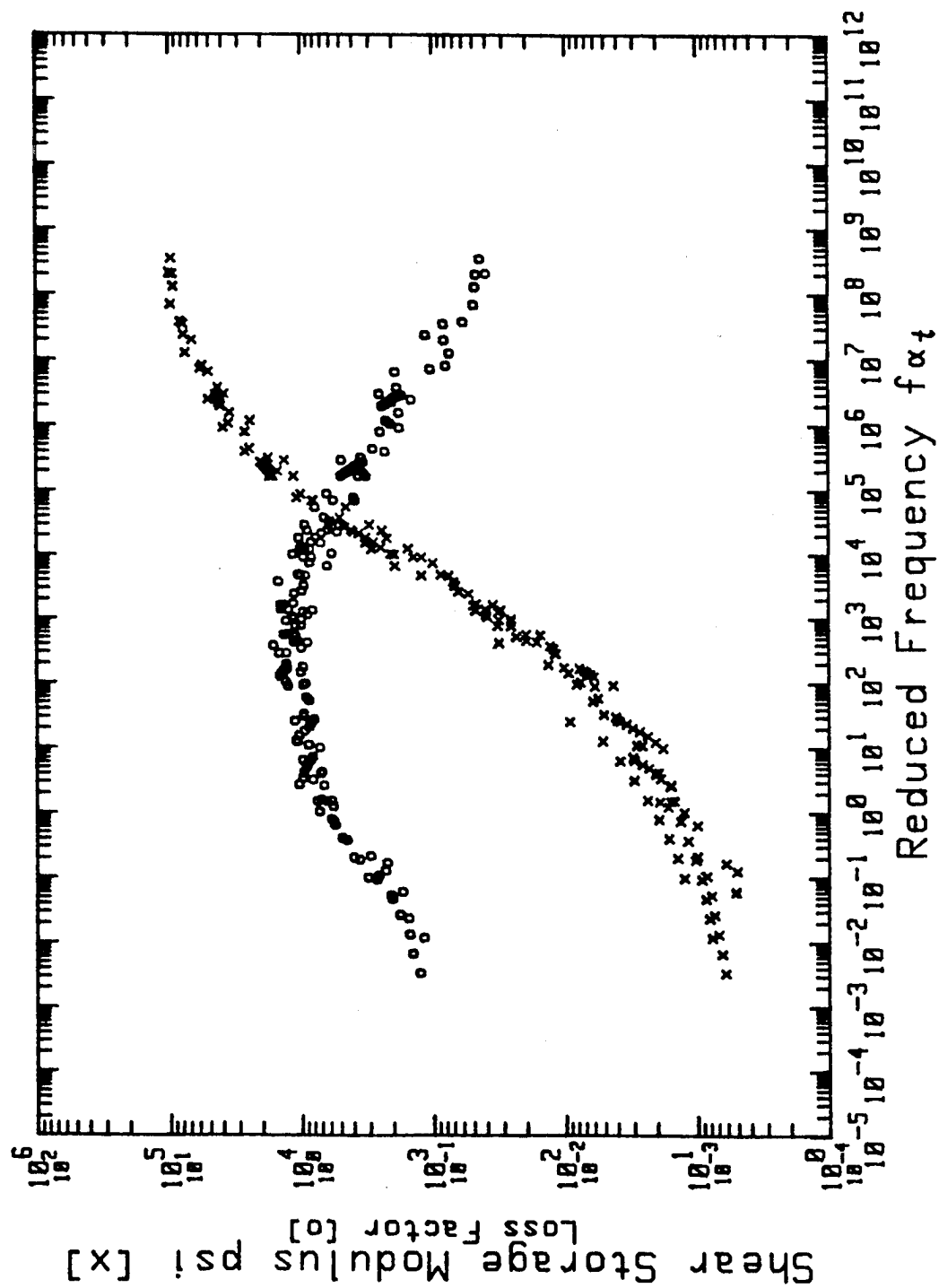


Figure 5: Plot of Shear Modulus and Loss Factor Versus Reduced Frequency  
( $T_A = 8000^\circ\text{R}$ )

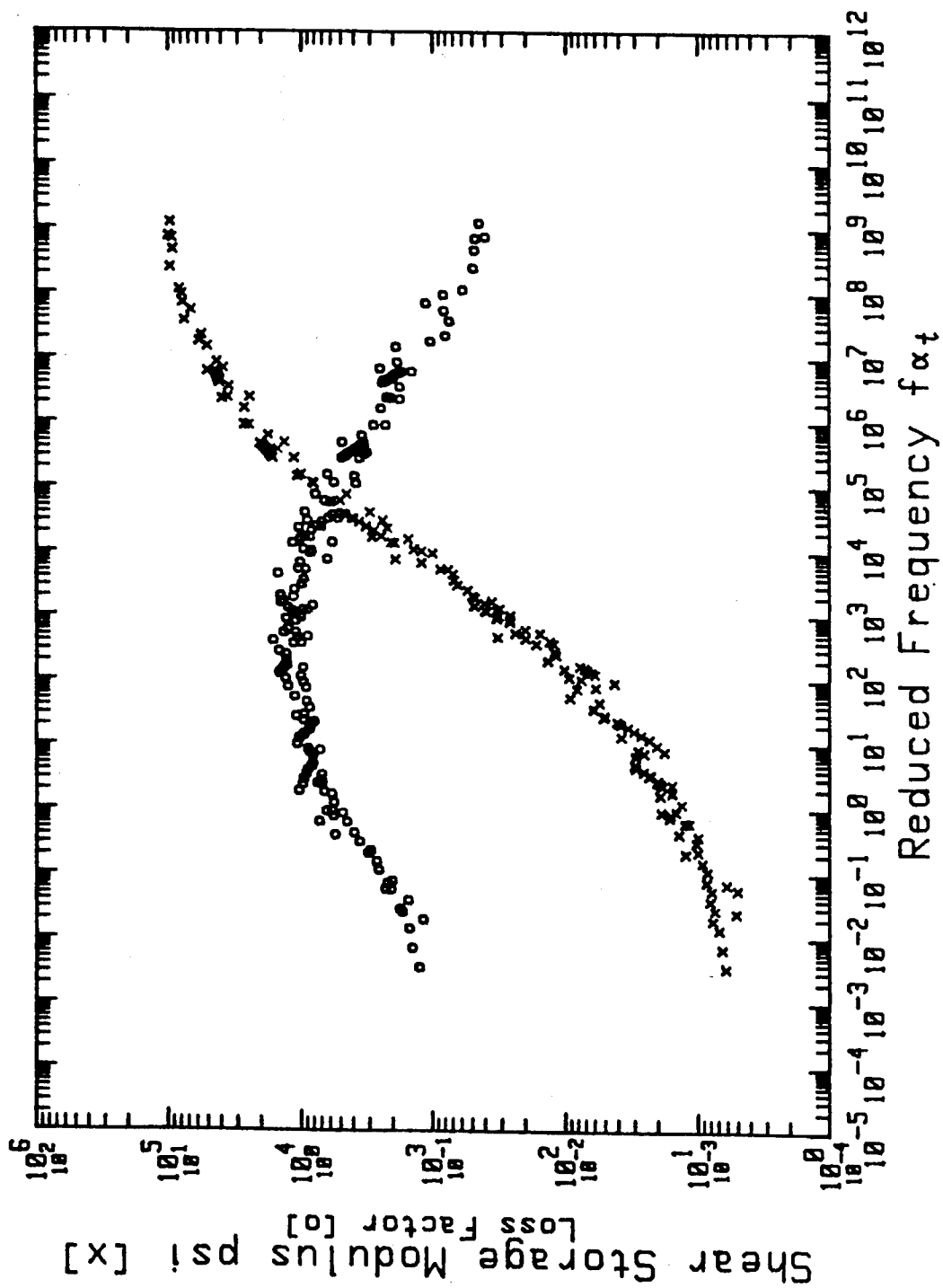


Figure 6: Plot of Shear Modulus and Loss Factor Versus Reduced Frequency  
( $T_A = 8900^\circ R$ )



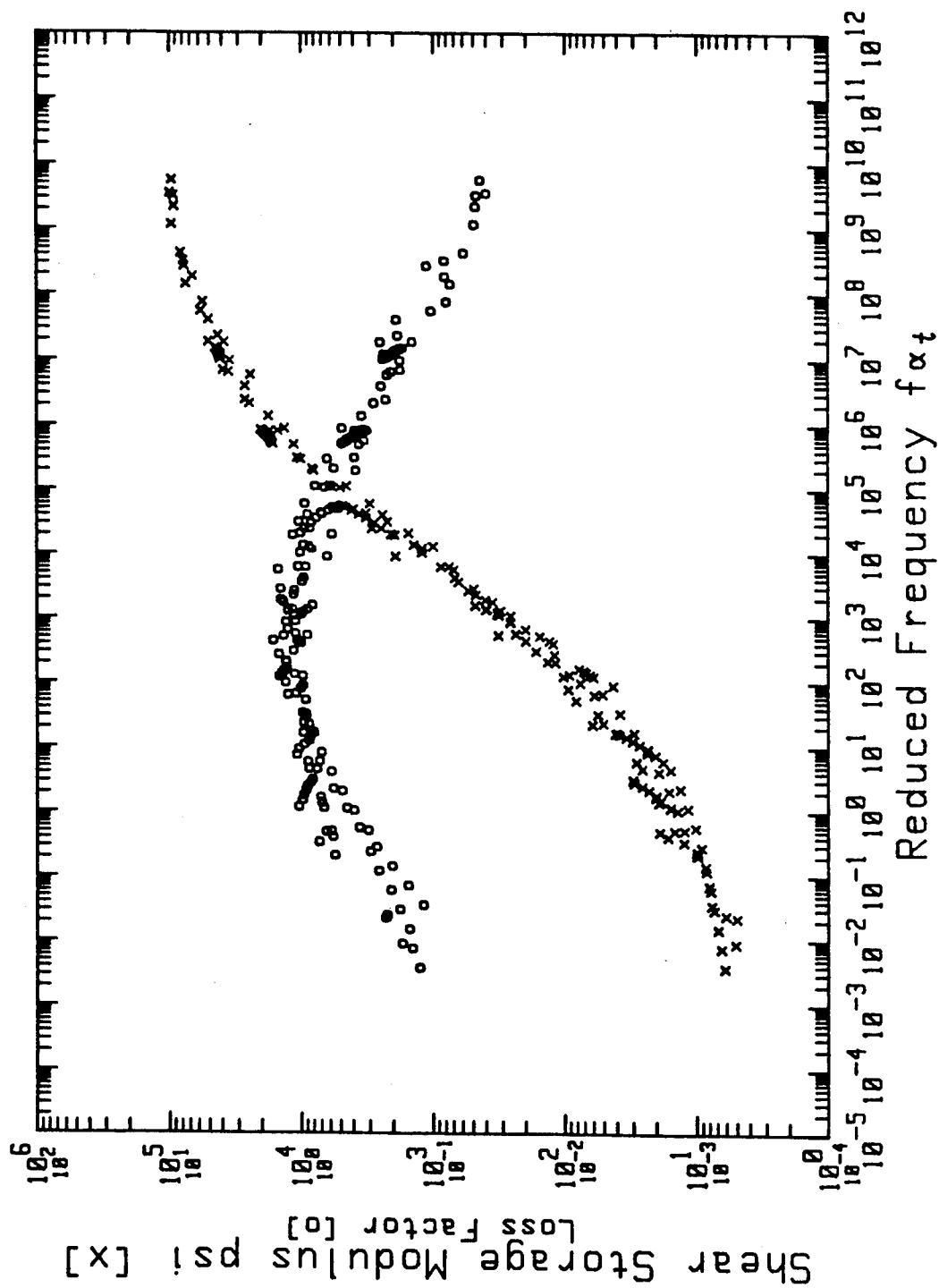


Figure 7: Plot of Shear Modulus and Loss Factor Versus Reduced Frequency  
( $T_A = 10000^\circ\text{R}$ )

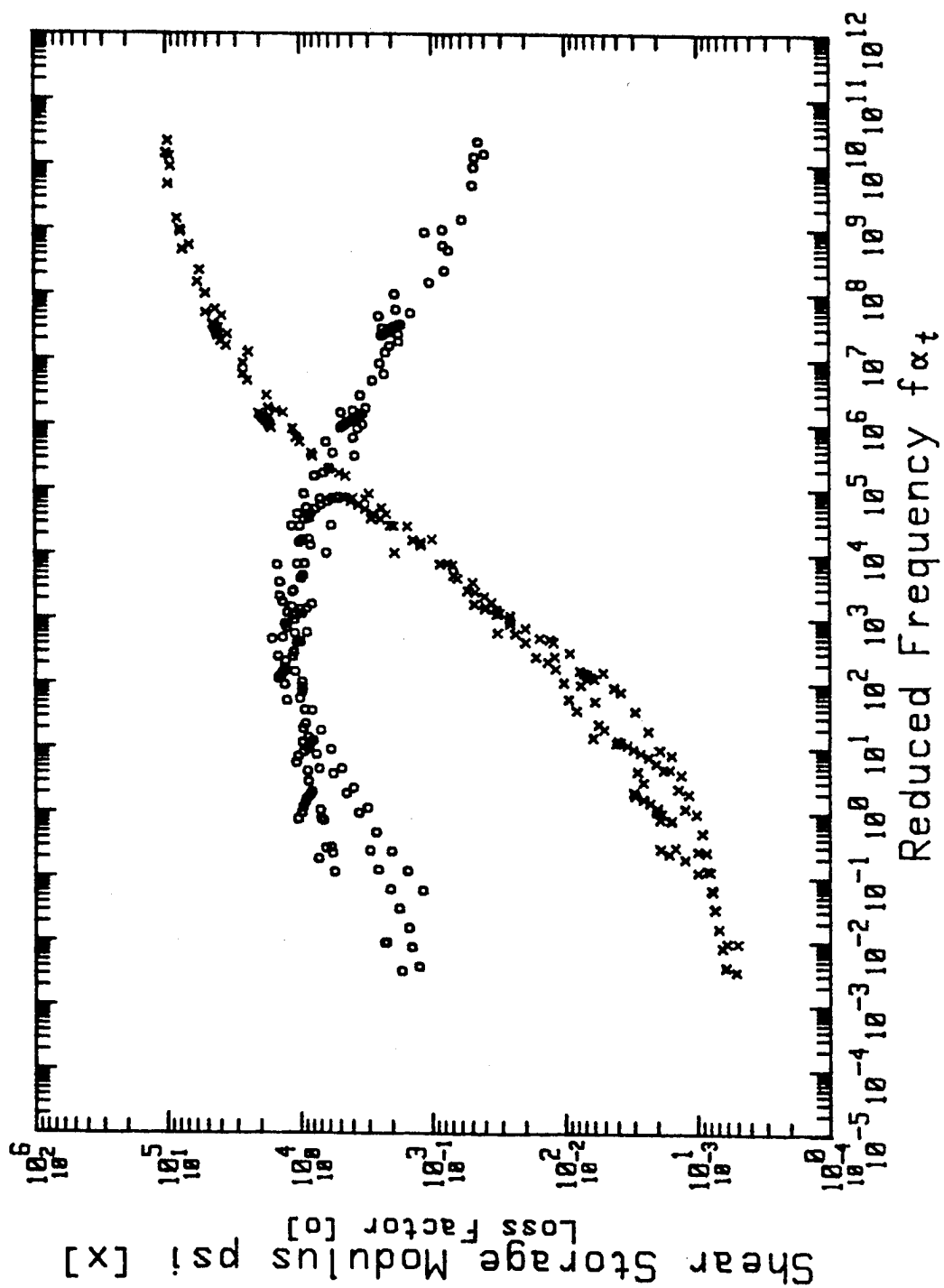


Figure 8: Plot of Shear Modulus and Loss Factor Versus Reduced Frequency  
( $T_A = 11000^\circ\text{R}$ )

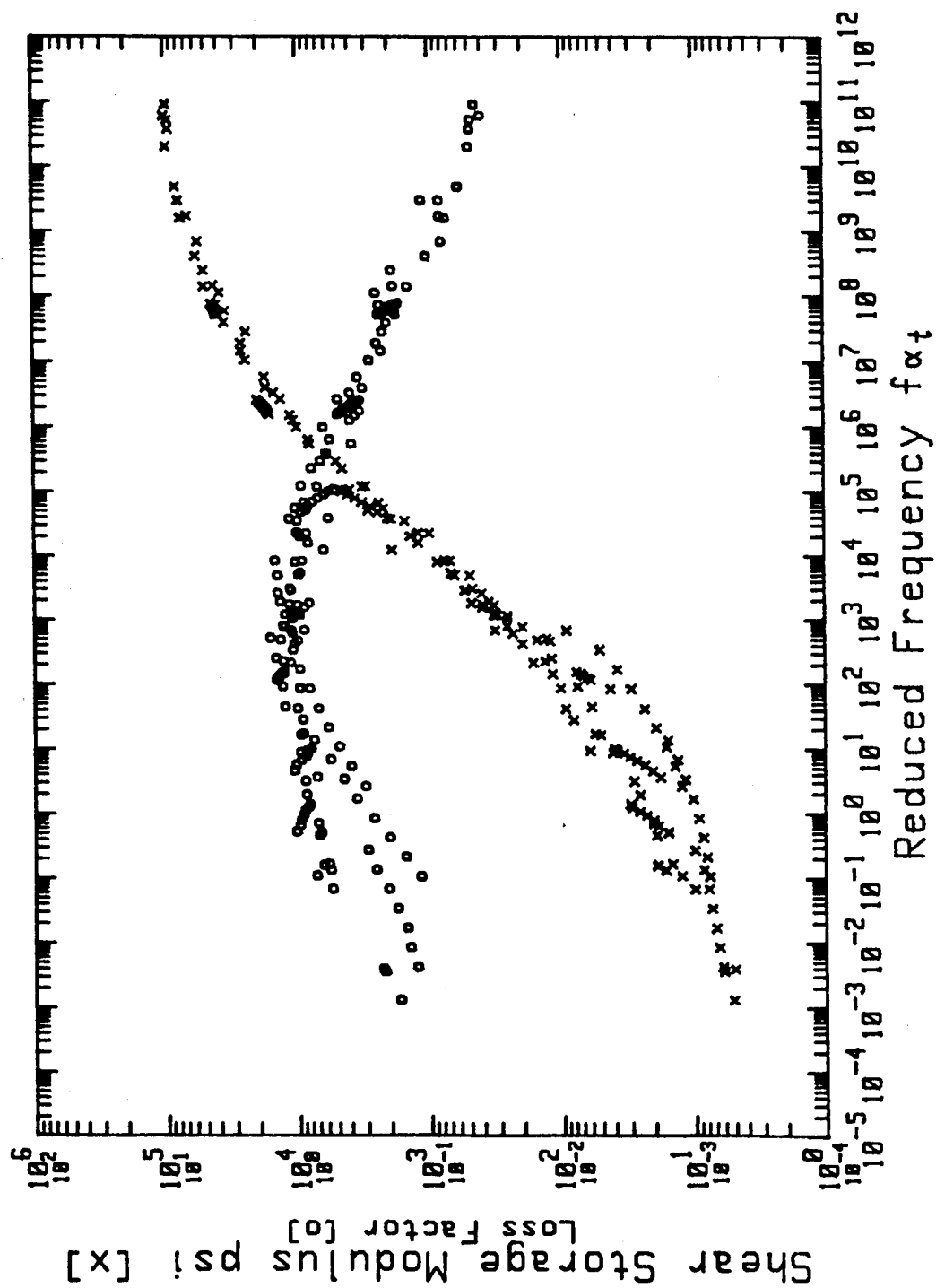


Figure 9: Plot of Shear Modulus and Loss Factor Versus Reduced Frequency  
( $T_A = 12000^\circ R$ )

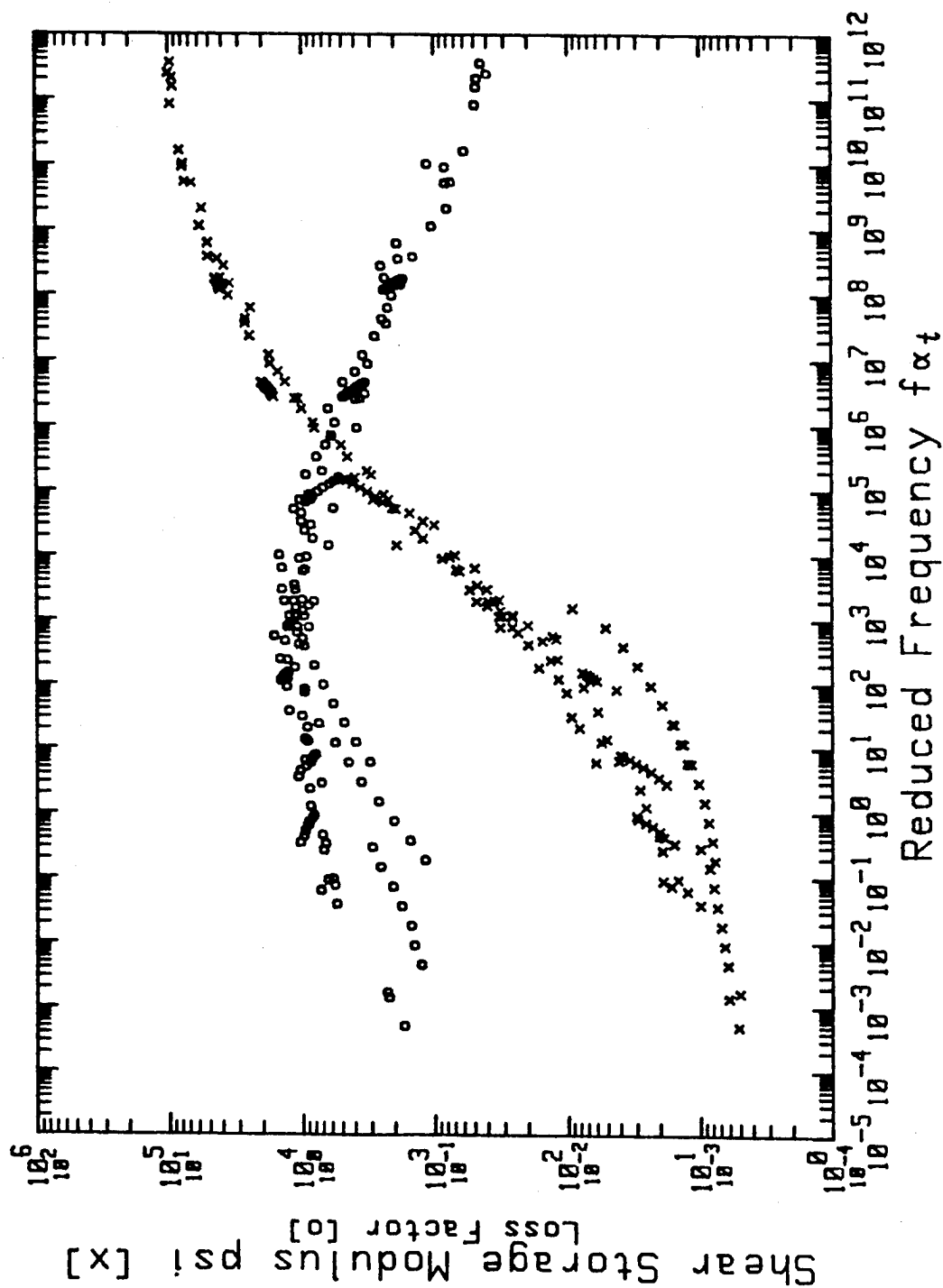


Figure 10: Plot of Shear Modulus and Loss Factor Versus Reduced Frequency  
 $(T_A = 13000^\circ R)$

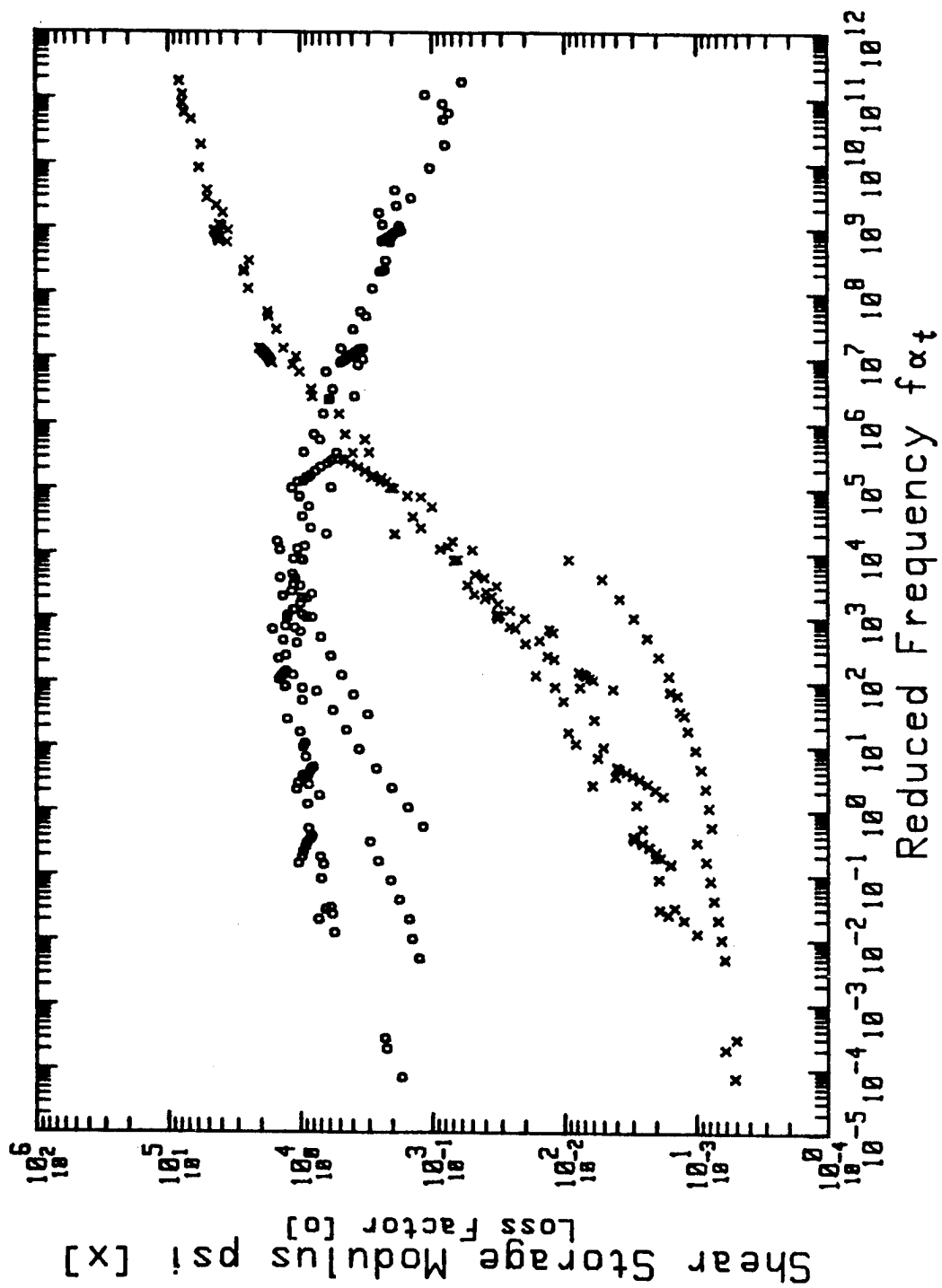


Figure 11: Plot of Shear Modulus and Loss Factor Versus Reduced Frequency  
( $T_A = 15000^\circ\text{R}$ )

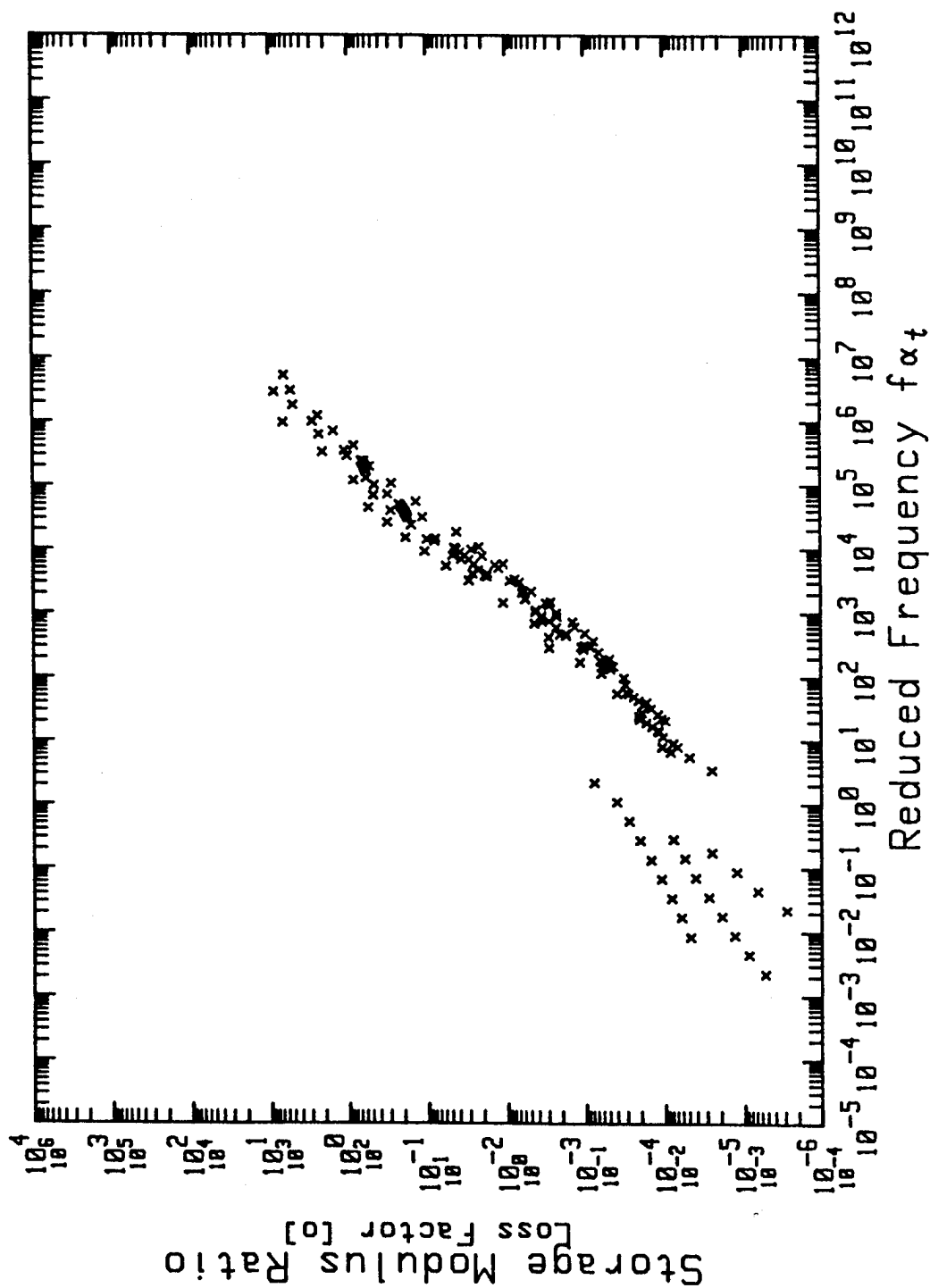


Figure 12: Plot of Modulus Ratio ( $G_e$ ) Versus Reduced Frequency  
( $T_A = 5000^\circ R$ )

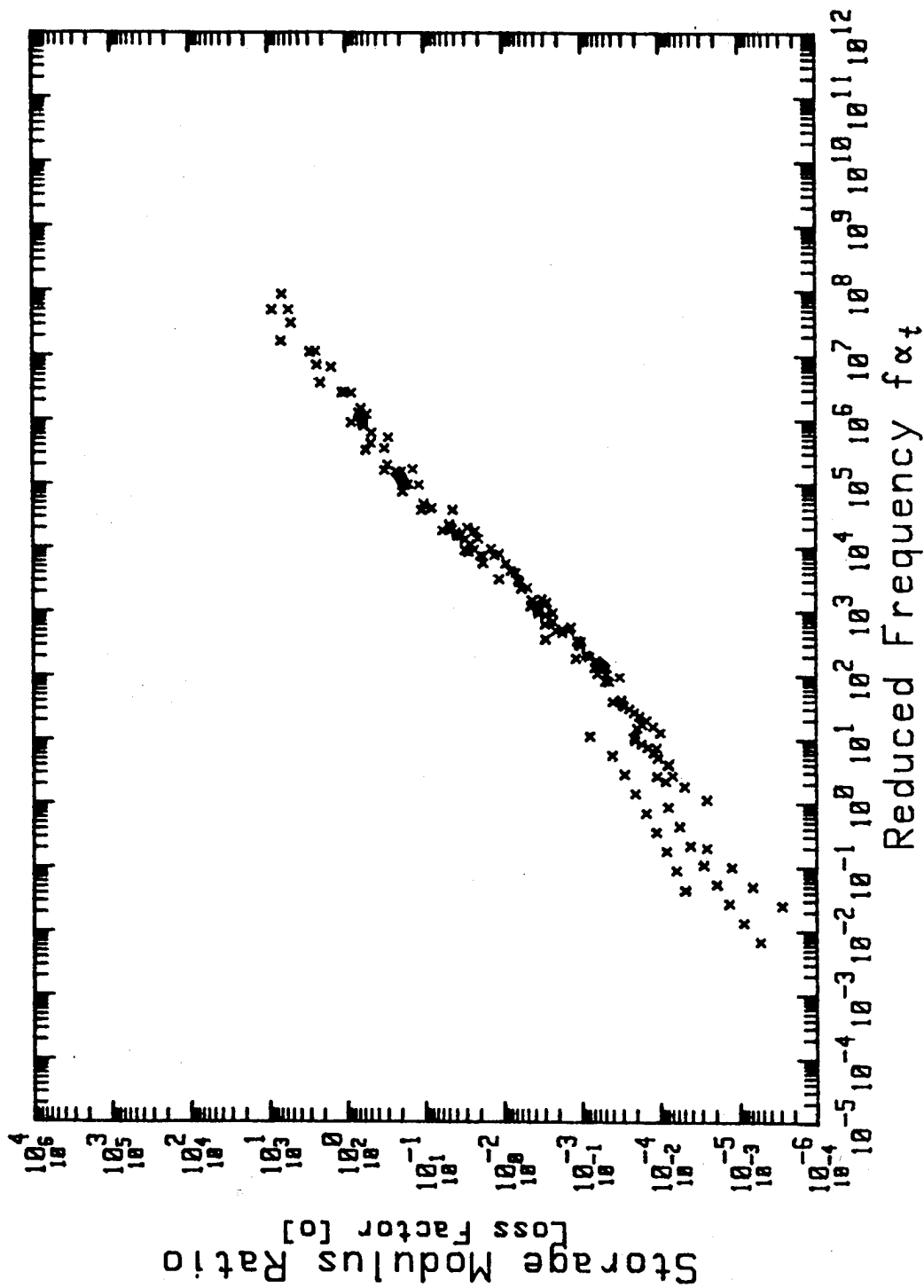


Figure 13: Plot of Modulus Ratio ( $G_e$ ) Versus Reduced Frequency  
( $T_A = 7000^\circ R$ )

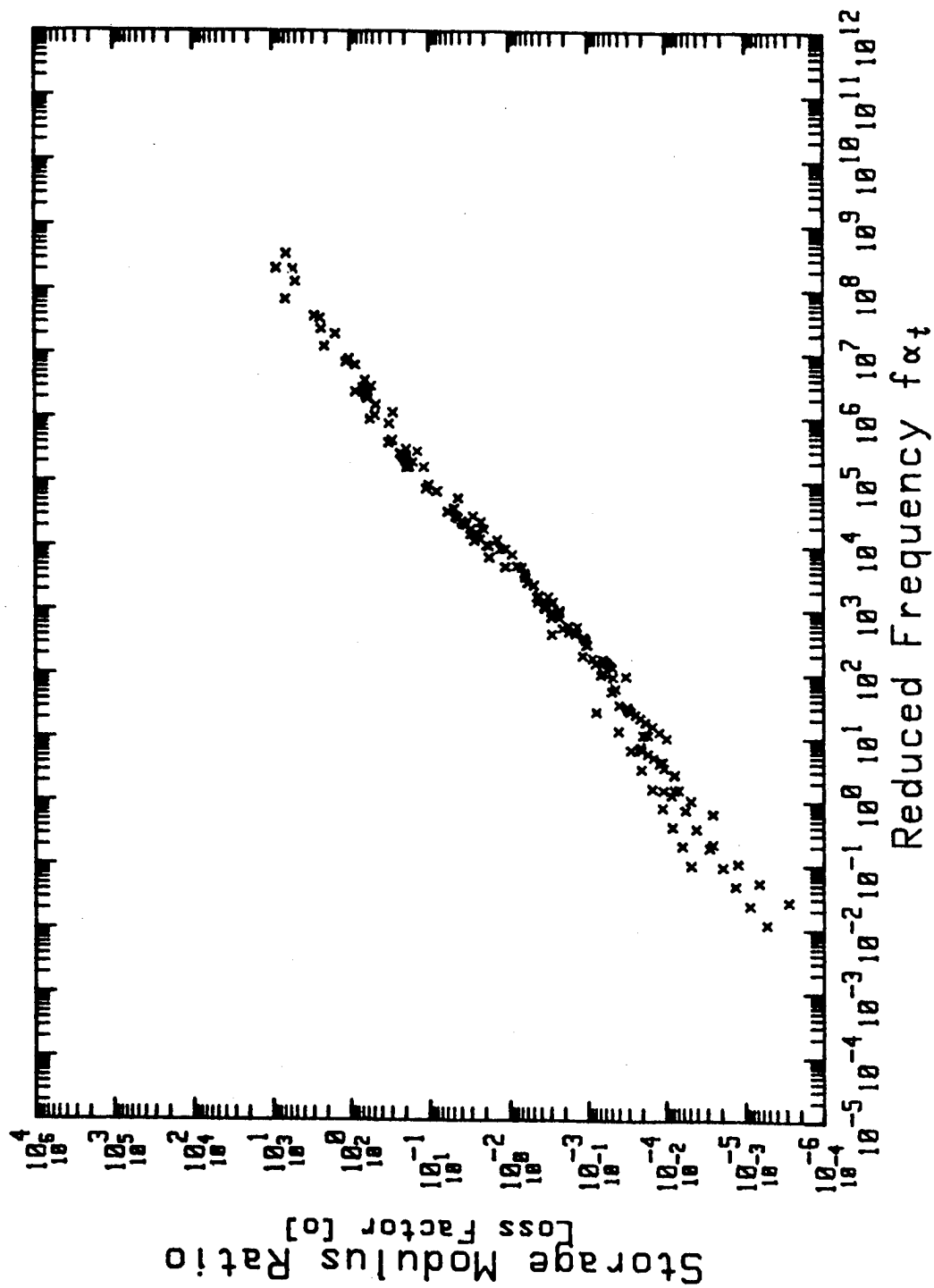


Figure 14: Plot of Modulus Ratio ( $G_e$ ) Versus Reduced Frequency  
( $T_A = 8000^\circ R$ )



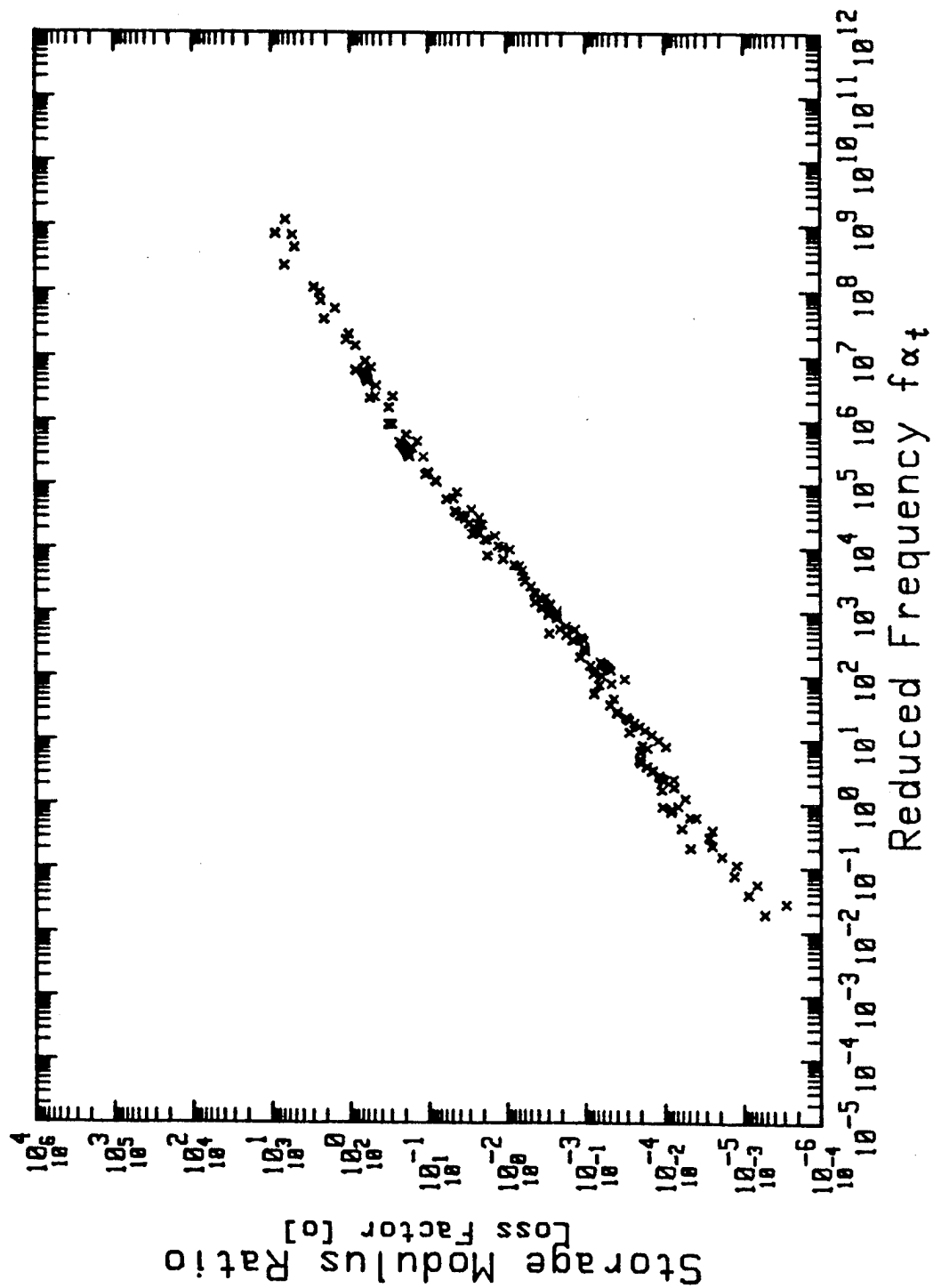


Figure 15: Plot of Modulus Ratio ( $G_e$ ) Versus Reduced Frequency  
( $T_A = 8900^\circ R$ )

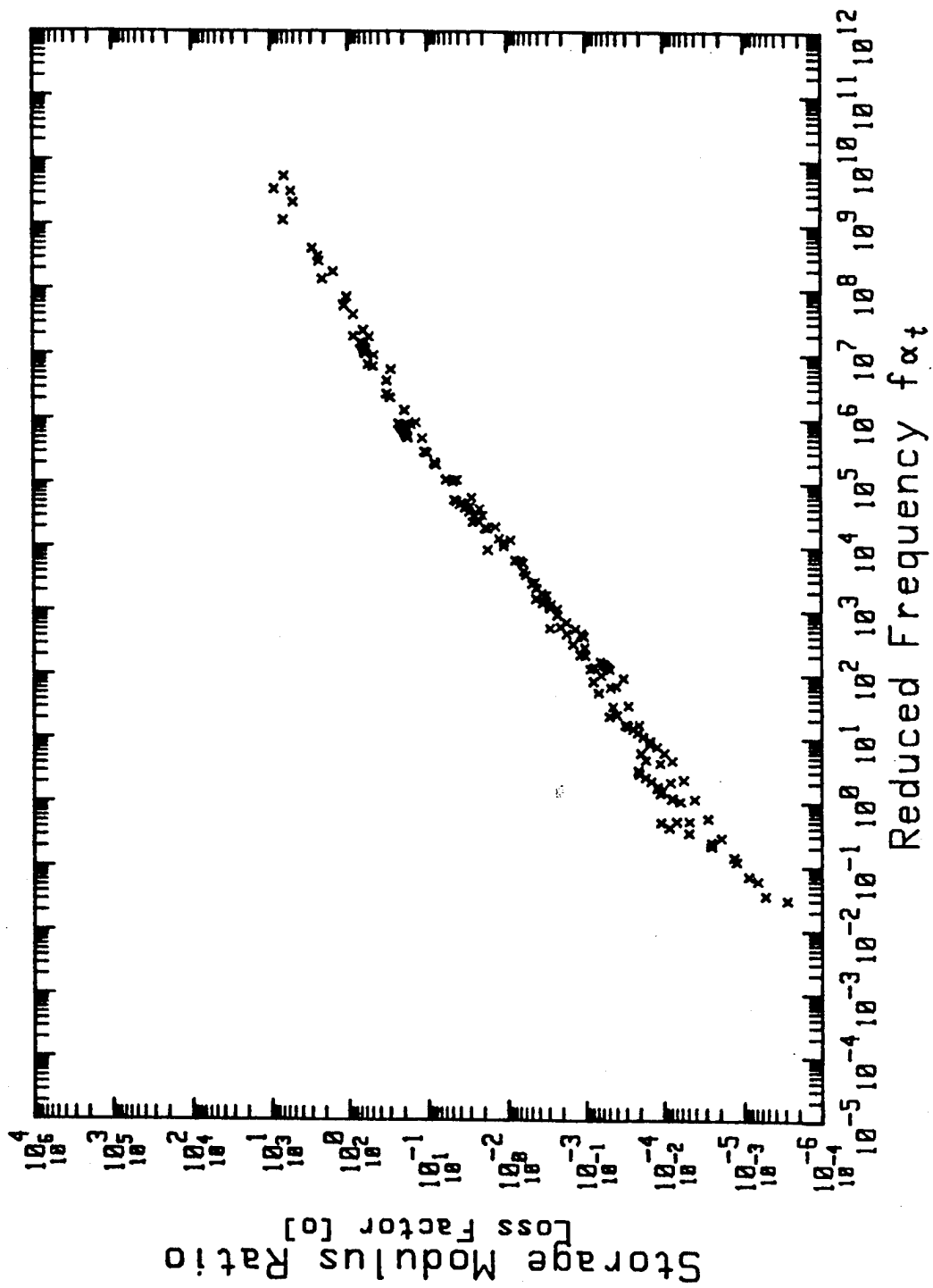


Figure 16: Plot of Modulus Ratio ( $G_e$ ) Versus Reduced Frequency  
( $T_A = 10000^\circ R$ )

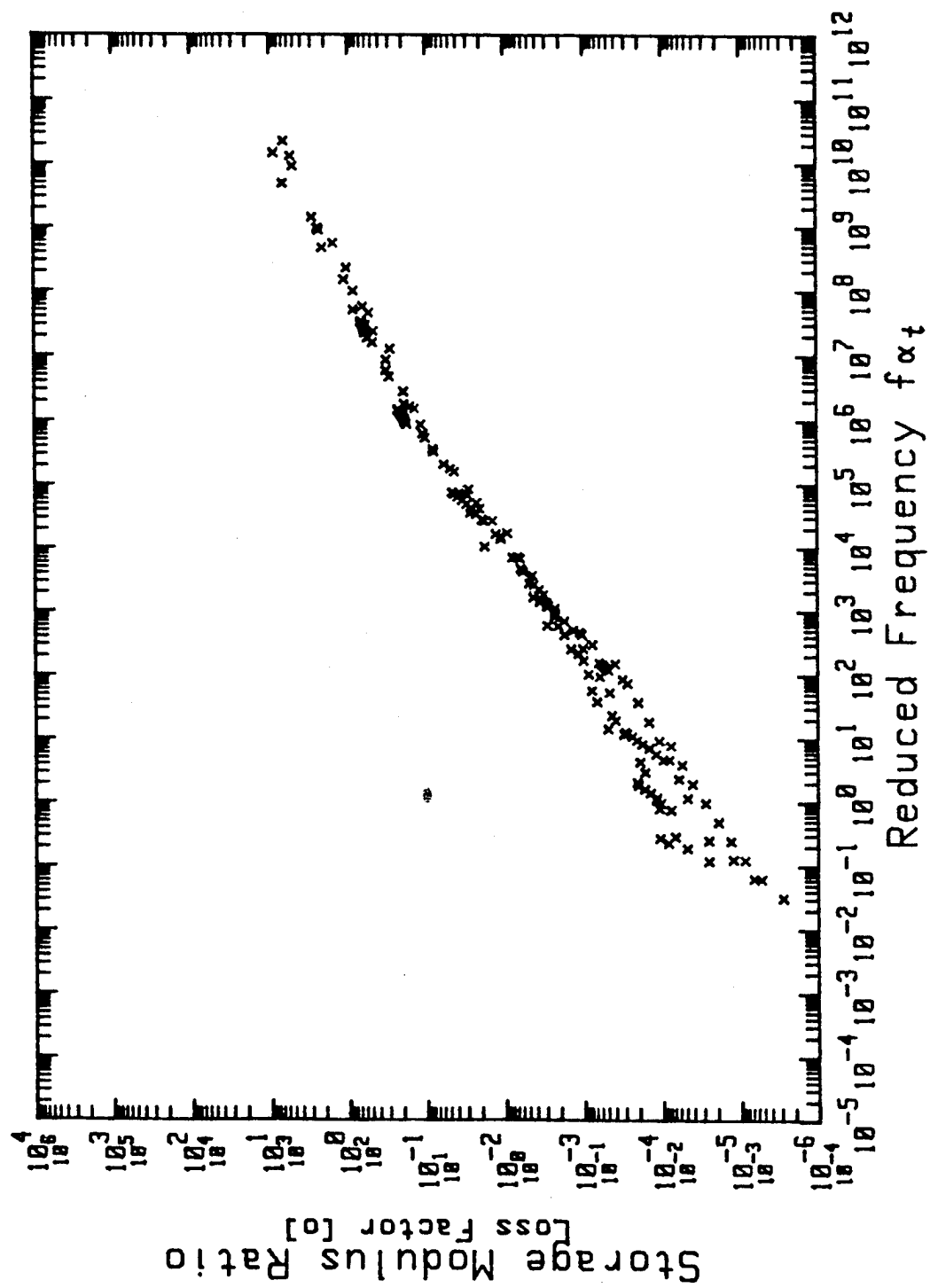


Figure 17: Plot of Modulus Ratio ( $G_e$ ) Versus Reduced Frequency  
( $T_A = 11000^\circ R$ )

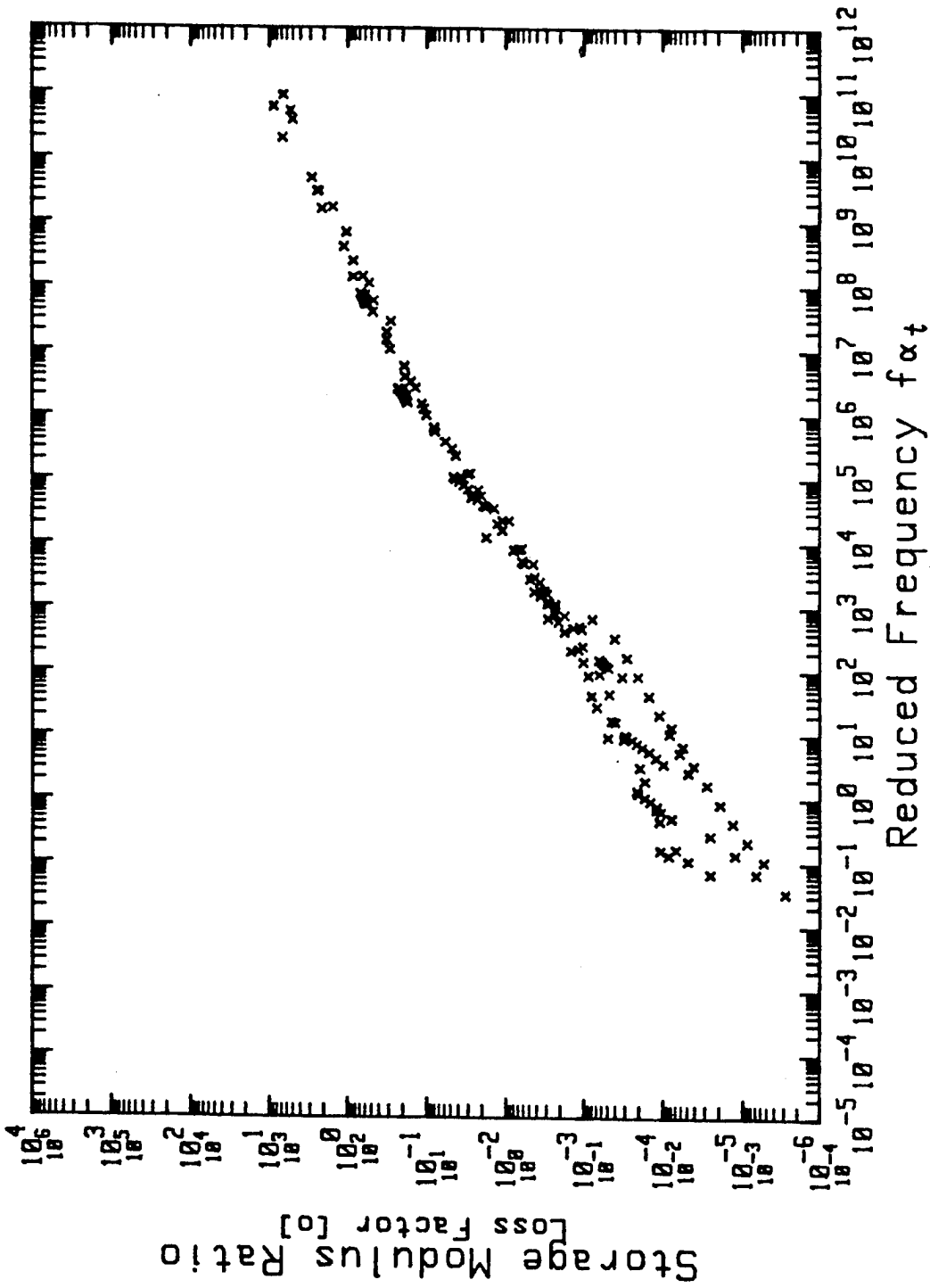


Figure 18: Plot of Modulus Ratio ( $G_e$ ) Versus Reduced Frequency  
( $T_A = 12000^\circ R$ )

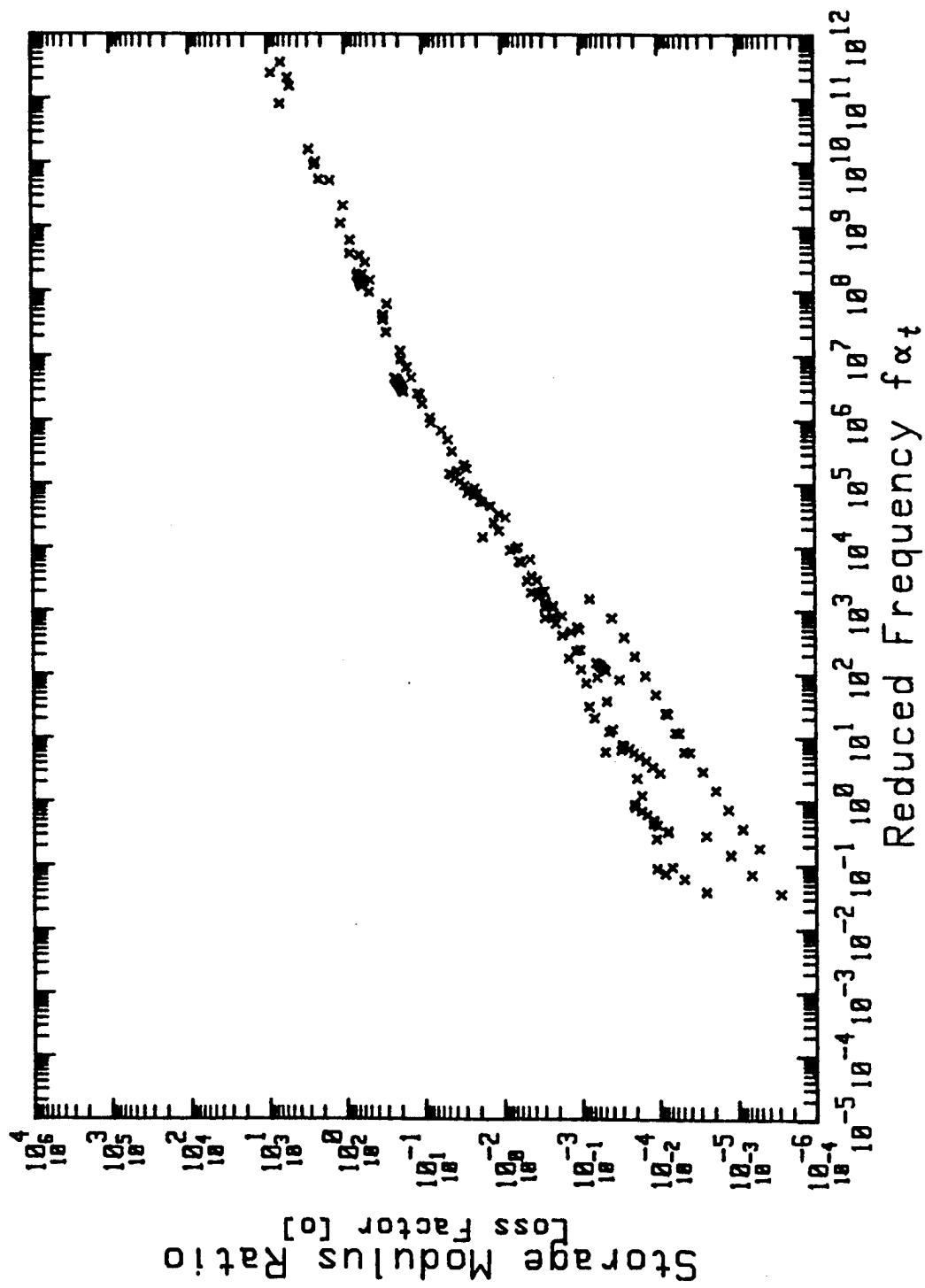


Figure 19: Plot of Modulus Ratio ( $G_e$ ) Versus Reduced Frequency  
( $T_A = 13000^\circ R$ )

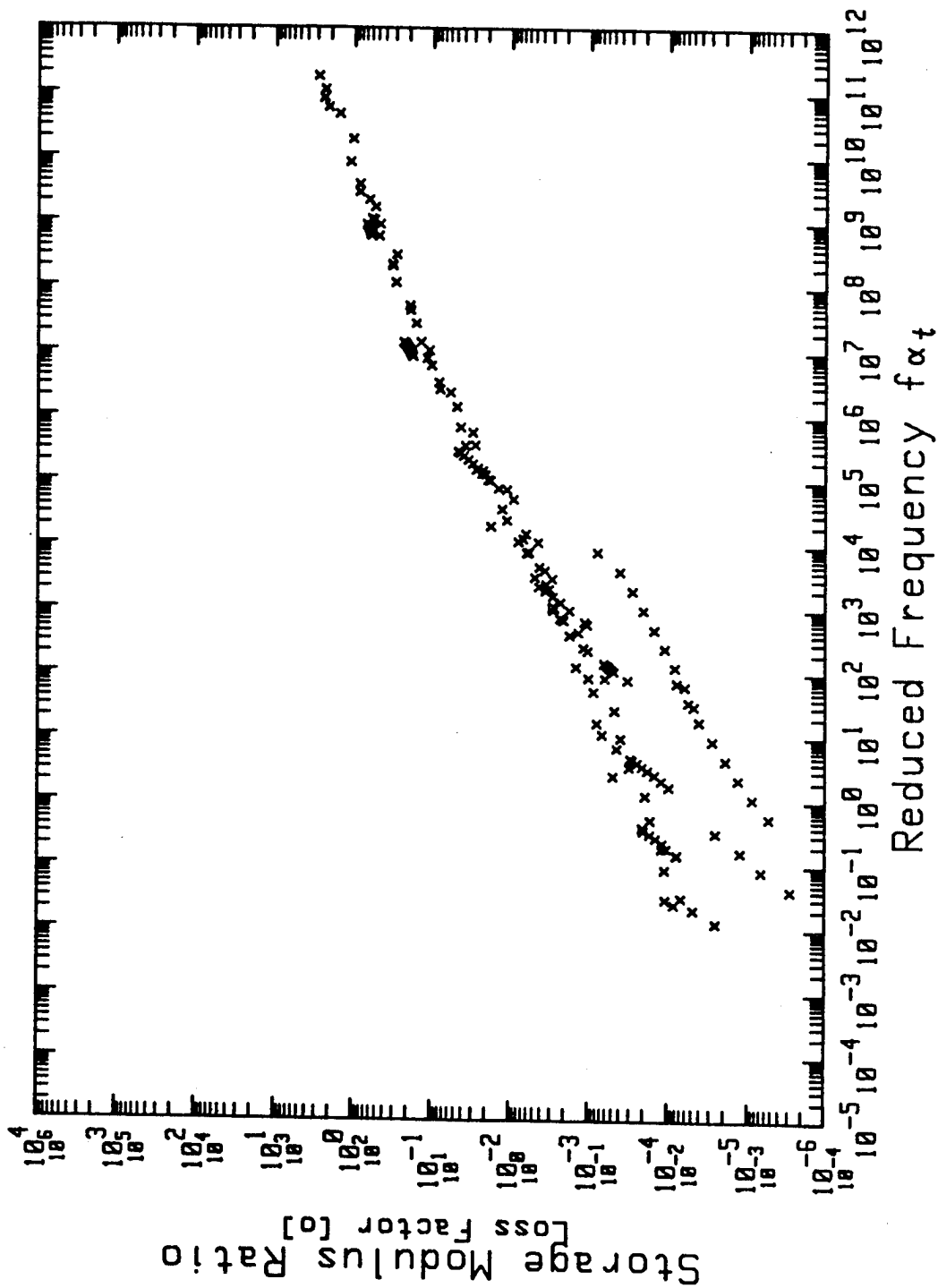


Figure 20: Plot of Modulus Ratio ( $G_e$ ) Versus Reduced Frequency  
( $T_A = 15000^\circ R$ )

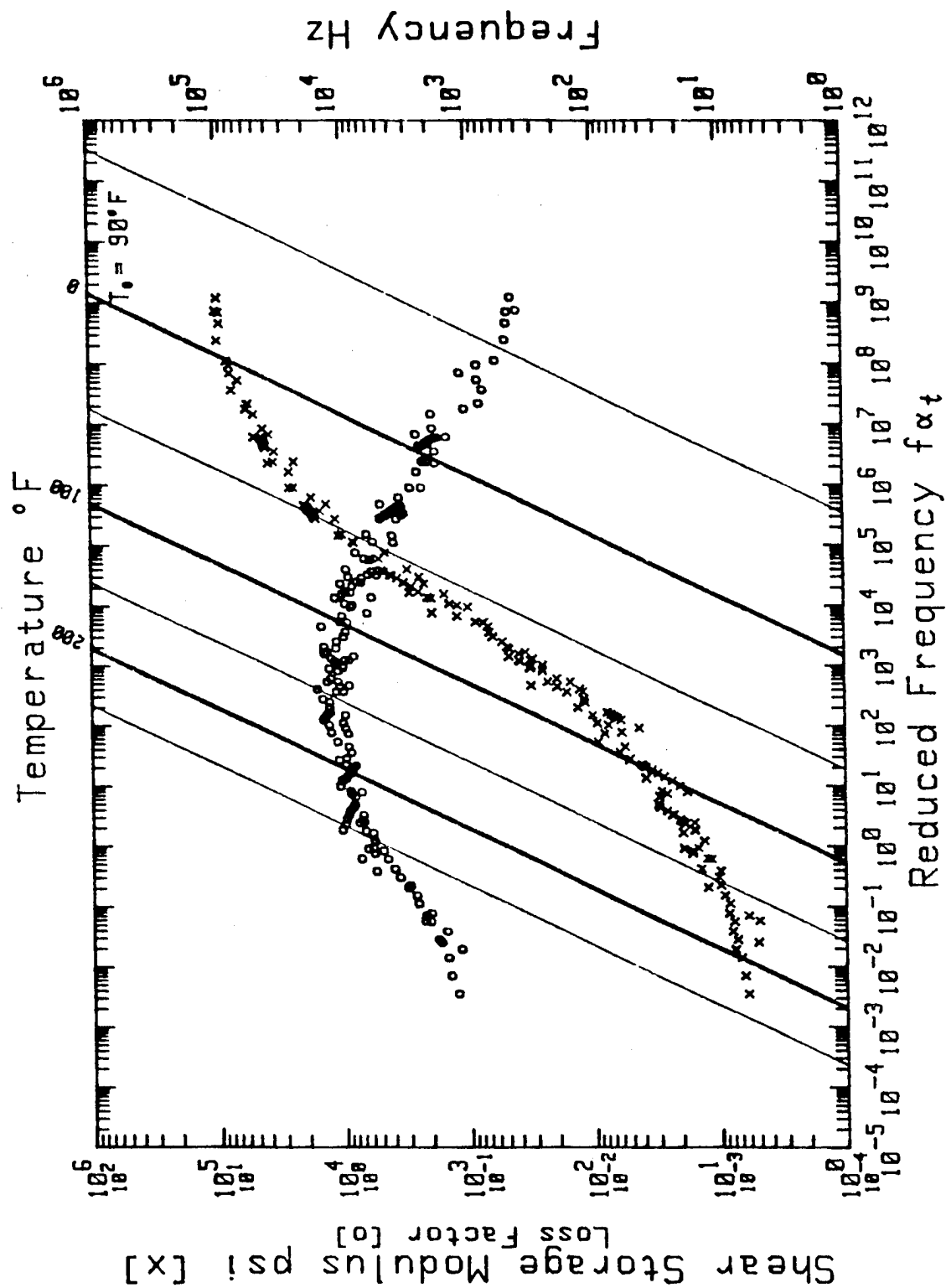


Figure 21: Reduced Frequency Nomogram for 3M Y-966 Adhesive  
( $T_A = 8900^\circ\text{R}$ )

COMPLEX MODULUS MEASUREMENTS OVER  
A WIDE RANGE OF FREQUENCIES AND  
MATERIAL CHARACTERISTICS THROUGH  
THE CONFRONTATION OF TWO INSTRUMENTS

---

Chris CHESNEAU : METRAVIB R.D.S  
64 chemin des Mouilles  
B.P. 182  
69132 ECULLY Cédex (FRANCE)

Jean Yves CAVAILLE : I.N.S.A - GEMPPM Bât 502  
20 avenue Albert Einstein  
69100 VILLEURBANNE (FRANCE)

Jean Philippe LAURES : INDIKON - METRAVIB Instruments Inc.  
26 New Street  
CAMBRIDGE MA. 02138 (U.S.A)

ABSTRACT

Two instruments are used to measure the viscoelastic properties of polymers. The instruments are presented and three different applications are shown. The measurement of the magnitude modulus and damping characteristics of a damping material is used to illustrate the compatibility of both instruments. The curing of two different materials is shown. In particular, the information contained in viscoelastic measurements proves to be quite helpful in following the evolution of the polymer structure throughout the process. Mechanical spectrometry of two homopolymers and a blend further exemplifies this concept.



COMPLEX MODULUS MEASUREMENTS OVER  
A WIDE RANGE OF FREQUENCIES AND  
MATERIAL CHARACTERISTICS THROUGH  
THE CONFRONTATION OF TWO INSTRUMENTS

-----

C. CHESNEAU - METRAVIB R.D.S - B.P. 182 - 69132 ECULLY Cédex (FRANCE)  
J.Y CAVAILLE - INSA - 20 avenue A.Einstein - 69100 VILLEURBANNE (FRANCE)  
J.P LAURES - METRAVIB Instruments Inc.-26 New Street- CAMBRIDGE MA.02138  
(USA)

INTRODUCTION

A number of techniques are commonly used to obtain viscoelastic material data. Methods such as the vibrating beam where material characteristics are deduced from the dynamics of simple systems can be referred to as indirect while methods where a force is directly applied to a material sample and the resulting displacement measured fall under the direct category. This paper will concentrate on two direct measurement instruments : the VISCOANALYSER and the MICROMECHANALYSER from METRAVIB INSTRUMENTS.

Modern design techniques for sophisticated technical products require accurate, consistant data for a variety of materials and configurations. It is also very important to manufacturers of finished products to have a data base over a given temperature and frequency range for many materials in order to compare them from one supplier to the next. In many instances, material makers themselves need good data as they have a difficult time reproducing mechanical and damping characteristics with sufficient precision form batch to batch. Variations of to 25 % are not uncommon in natural and synthetic rubbers. Furthermore, scientific research calls for precise phase angle data since it is becoming a popular tool to understand the physics and micromechanics of molecular structure.

A problem is indeed that various instruments using different operating principles usually yield slight discrepancies in measured data. This can be for several reasons.

- i) The mode of strain can differ. For example, the use of 3 point bending to measure Young's modulus can induce errors due to the variable shear component of strain which appears in such a configuration.
- ii) Different techniques for holding the sample. Various mechanical stresses due to sample holding (clamped, simply supported ...) can perturb measurements. Adhesive bonding is mechanically clean but is problematic with porous materials, extreme temperatures and certain polymers for which glueing is excessively difficult.

- iii) Inertial effects can, for certain high frequency measurements, yield polluted data (for instance 3-point bending in the case of solids and annular pumping in the case of liquids). The importance of the inertial term can easily be evaluated but it is nonetheless a limitation to be reckoned with.
- iv) Another reason comes the design of any instrument. They are almost all designed with a specific application in mind. This gives the instrument a design philosophy making it more suited to particular materials or stiffness and temperature ranges. Of course, the quality of data usually increases as the instrument's optimal domain is reached. For example, the Viscoanalyser was designed to measure the glass transition of most solid polymers while the Micromecanalyser was conceived with mechanical spectrometry in mind.

Ideally, all techniques should yield the same result, and when they do the benefit is great due to the number of applications. Damping predictions, design of load bearing structures and scientific research have been mentioned. Process control, the study of curing and data bases for computer F.E.M. codes can be added to this non exhaustive list.

The purpose of this paper is to show how, when two instruments are compatible and complementary, the domain of validity of measurements and the confidence level in the results are increased. The two instruments must show consistant data when measuring the same material under similar conditions while having distinct preferred applications.

### THE VISCOANALYSER

This instrument measures the force and the displacement acting on a sample submitted to an oscillatory regime. The schematic diagram of figure 1 illustrates the basic mechanics of the instrument. From the sample outward this diagram runs as follows. The sample is placed on a rigid column, incorporating a force transducer, which links it to a fixed, solid, metallic base. The sample is surrounded by a furnace, capable of temperatures of up to 350°C using electric heating elements, and of temperatures as low as -100°C obtained by liquid nitrogen cooling. The upper part of the sample is attached to an electrodynamic shaker via a rigid column similar to the lower one. The shaker is fastened to an upper chassis. The displacement and acceleration of the upper column are recorded by two transducers.

The height of the upper chassis can be adjusted, as well as the pre-strain on the specimen.

Many sample holders exist : tension compression, shear, 3 point bending, annular shear and annular pumping. These allow the measurement of characteristics of materials ranging from oils to rigid reinforced polymers.

The general characteristic of the instrument are the following :

- Frequency : 5 Hz - 1000 Hz
- Displacement : 0.1  $\mu\text{m}$  - 500  $\mu\text{m}$  (option 3000  $\mu\text{m}$ )
- Strain :  $10^{-4}$  -  $10^{-1}$
- Force : 0.1 N to 100 N (option 150 N)
- Temperature : 200 K - 600 K
- Loss angle :  $0.5^\circ$  -  $90^\circ$

#### THE MICROMECHANALYSER

This inverted torsion pendulum operates under forced oscillations. The oscillation are created by a sinusoidal electromagnetic force obtained by running an A.C. current through Helmholtz coils (figure 2). The angular displacement is measured using an optical sensor to detect a light beam reflected off a mirror placed on the sample holder connection rod. The sample can be placed in a sealed compartment filled with air or an inert gas.

This instrument allows creep with D.C. current through the coils. Its extreme sensitivity in phase angle makes it ideal for mechanical spectrometry. Indeed, the apparatus can measure phase angles as small as  $0.03^\circ$  and theoretically as large as  $90^\circ$ , though no solid is entirely viscous. More generally, the characteristics are :

- Frequency :  $10^{-5}$  Hz - 5 Hz
- Angular displacement :  $0^\circ$  -  $0.5^\circ$  (option  $10^\circ$  in creep)
- Strain :  $10^{-6}$  -  $10^{-3}$
- Torque :  $2 \cdot 10^{-7}$  Nm -  $1.5 \cdot 10^{-2}$  Nm
- Temperature : 100 K - 670 K
- Loss angle :  $0.03^\circ$  -  $90^\circ$

In practice, the  $10^{-5}$  Hz range is seldom used. The principal advantage of this feature is to aid in the separation of relaxation peaks in very temperature-sensitive materials. An application of this is with polymer alloys.

#### DYNAMIC STIFFNESS, MODULUS AND VISCOSITY

It is common when dealing with harmonic systems to represent physical concepts such as stiffness, modulus or viscosity in the complex plane.

A viscoelastic sample has a dynamic stiffness  $K^*$  defined by its response to sinusoidal sollicitation :

$$K^* = \frac{F^*}{U^*} \quad (1)$$

where  $F^*$  is the forcing function :

$$F^* = F_0 \exp i(\omega t + \delta) \quad (2)$$

and  $U^*$  the harmonic displacement :

$$U^* = U_0 \exp i\omega t \quad (3)$$

The phase shift,  $\delta$ , is linked to the vibration damping characteristics of the material and its tangent,  $\tan \delta$ , is often called the loss factor.

From equations (1) to (3), the stiffness  $K^*$  becomes :

$$K^* = (F_0 / U_0) \exp i\delta$$

The real and imaginary parts of  $K^*$ ,  $K'$  and  $K''$  respectively, are thus given by :

$$\begin{aligned} K' &= F_0 / U_0 \cos \delta \\ K'' &= F_0 / U_0 \sin \delta \end{aligned}$$

The Viscoanalyser yields directly  $F_0 / U_0$  and  $\delta$ .

The same equations can be written in torsion where force is replaced by torque and displacement by angular displacement.

The instrument's software then proceeds to calculate the modulus of the material, which is an intrinsic value, and ideally should not depend on the type of apparatus employed. In this respect, the general equation (4) is used :

$$M^* = K^* \frac{e}{S_e} F_s \quad (4)$$

where  $M^*$  is the complex modulus, for example  $M^* = E^*$  (Young's modulus) in tension and  $M^* = G^*$  (shear modulus) in shear,  $S_e$  is the excited surface,  $e$  is the distance between sollicitation surfaces and  $F_s$  is the shape factor.

The shape factor is the biggest source of incertainly when trying to determine the modulus of a material, especially in the case of fibrous or anisotropic materials. It is also a problem in the case of shear-rate dependent viscosity liquids. In general, however the shape factor can be chosen close to unity (tall and slender in tension-compression, short and fat in shear) to minimize error.

In the complex plane, harmonic displacement ( $U^*$ ) is proportional to harmonic velocity ( $V^*$ ) :

$$V^* = i\omega U^*$$

The complex shear modulus is therefore related to complex viscosity ( $\eta^*$ ) by:

$$G^* = i\omega \eta^* \quad (5)$$

They represent the same intrinsic quantity in the overall description of a material.

There is a difference however, in the sense that the usual terminology differs according to whether the material flows under constant stress or not.

Viscoelastic materials can of course be either clearly solid or clearly liquid, but they can also be somewhere in between. The shear modulus applies to mostly solid-like materials while the viscosity applies to mostly liquid-like materials. Materials can change in a continuous fashion from liquid to solid. This is typically a curing process.

#### MECHANICAL PROPERTIES OF USUAL MATERIALS

Figure 3 shows usual materials in relation to each other with respect to their mechanical characteristics. The vertical direction reflects intrinsic dynamic stiffness while the horizontal axis represents damping.

The numbers shown on the modulus, viscosity and loss factor scales are indicative "ball-park" figures and should not be considered otherwise.

On the figure, the domain of validity of both the Micromecanalyser and Viscoanalyser appears.

One notices that the Viscoanalyser is more suited to the softer, higher loss materials while the Micromecanalyser is best for high modulus materials.

For example :

Metals and composites are typically materials which can be measured most accurately with the Micromecanalyser while oil, tar, pastes and gels are reserved for the Viscoanalyser.

Both instruments have a wide overlapping range in which most polymers including vibration damping materials can be found.

Curing which can be studied using both instruments is, mechanically, the evolution from a viscous liquid-like substance to a complete solid.

The specific qualities required of the instrumentation here is the capacity to measure properties over a wide range without changing sample holders.

It can be noted that most materials are covered by the measurement ranges of these instruments. In fact, one is hard put to think of a material of very low modulus and very low loss factor ! As it is seen from the graph, the materials are all along a diagonal going from high loss or viscous liquids to elastic solids.

#### DAMPING MATERIAL CHARACTERIZATION

Two master curves are shown.

The material is GE. SMRD. The measurements were made at METRAVIB but the data were compiled and exploited by Dr. Lynn ROGERS.

Figure 4 was obtained with Viscoanalyser while figure 5 was derived from Micromecanalyser data.

The Viscoanalyser's measurement parameters were :

Frequency : 5 Hz → 500 Hz  
Temperature : -10°C → + 60°C

In the case of the Micromecanalyser, these were :

Frequency : 0.0078 Hz → 1 Hz  
Temperature : 0°C → + 50°C

The two graphs have different scaling factors, but overall, if one looks at the actual numbers, the two curves are consistant.

For example :

-----  
Consider the values of the real modulus and loss factor at the glass transition peaks in table 1.

	Elastic shear Modulus G' (MPa)	Loss factor
Micromecanalyser	28.80	1.01
Viscoanalyser	31.20	.866
Δ %	+ 8.3%	- 14.2%

In view of the fact these measurements were obtained using two instruments with different techniques (plane shear versus torsion), these are quite acceptable. In fact this is confirmed by the loss factor versus magnitude modulus plots of figures 6 and 7 for the Viscoanalyser and Micromecanalyser respectively. The two plots superpose quite neatly.

### POLYMER CURING

Figures 8 and 9 show the curing kinetics of two polymers.

Figure 8 shows the constant temperature (160°C) cure of a two component adhesive. The test was performed with a Viscoanalyser using an annular pumping sample holder.

The various stages are as follows :

- 1) In the first few minutes of cure, the resin - a polymeric liquid at first - fluidifies under the effect of temperature and the stiffness decreases.
- 2) As the chemical reaction progresses the molecular chains grow to form ramifications and finally a complete network. During this time, the stiffness increases while the loss factor at first decreases then increases to a maximum. This maximum defines the gelation time (here 16 mins). This peak is accompanied by a change in slope in the stiffness ( $\log(K)$ ) curve and is a result of the competition between the rates of increase of viscosity  $K''$  and elasticity  $K'$ . Indeed, a various times during the gelation process, the increase in total stiffness ( $K$ ) is at times mostly due to an increase in elasticity, and at other times mostly due to an increase in viscosity.
- 3) After about 40 minutes, the material is fully cured. The curing temperature here was above the glass transition temperature of the finished product; the chemical structure is therefore stable.

In figure 9 the curing spectrum is that of a braid impregnated with resin. The study was done with the Micromecanalyser. Here, the material was slowly heated from 100 K to 500 K.

From 100 K to 250 K, the material is literally frozen. The loss factor spectrum shows two minor relaxations associated with the uncured epoxy components.

Above 250 K thaw takes place. The resin fluidifies, the loss factor tends to infinity (loss angle = 90°) and the stiffness decreases to reveal the stiffness of the glass fiber braid. Around 400 K, gelation starts to take place followed by vitrification (around 420 K). The glassy polymer then reaches its glass transition temperature (460 K) and the classical glass transition peak and drop in modulus is observed.

## MECHANICAL SPECTROMETRY

Figures 10 and 11 show the micromechanical property-temperature spectra of BuA (Butyl Acrylate) and VAc (Vinyl Acetate) homopolymers.

Three frequencies (0.01, 0.1 and 1 Hz) are represented. Four sets of curves labeled a, b, c and d are shown.

Set a :  $\log (G'/G_0)$  (with  $G_0 = 1.5 \cdot 10^9 \text{ N/m}^2$ ) as a function of temperature for pure poly (BuA)

Set b :  $\log (\tan \delta)$  (loss factor) for pure poly (BuA) as a function of temperature

Set c :  $\log (G'/g_0)$  (with  $G_0 = 1.5 \cdot 10^9 \text{ N/m}^2$ ) as a function of temperature for pure poly (VAc)

Set d :  $\log (\tan \delta)$  (loss factor) for pure poly (VAc) as a function of temperature

What is clear here is that the two polymers have radically different spectra. The loss factor curves reveal not only that the two have different transition temperatures but that the BuA peak is much smaller than the VAc. The drop in modulus is 3.5 decades in both cases.

The micromechanical spectrum of the blend of the previous homopolymers is shown figure 12. The blend was obtained using equal masses of both BuA and VAc coalesced at room temperature.

The graph indicates that the loss factor peak of ABu (first transition) is much smaller than appeared before (10 time smaller) while the VAc peak suffers only a slight drop (25 %). The same is true of the drop in modulus. The first drop is much smaller than the second drop (VAc).

However both peaks are very clearly apparent which shows that micromechanical spectrometry holds a trace of the structure of the material, and the various polymers in the blend can be readily identified.



## CONCLUSION

Two principal uses of dynamic mechanical measurement are illustrated through two different instruments.

- 1 - Obtention of viscoelastic data
- 2 - Determination of structural properties

When used in a complementary fashion, each instrument allows the extension of the other's measurement capacity.

For example :

- 1) They combine to cover 8 decades in frequency ( $10^{-5}$  Hz to  $10^3$  Hz)
- 2) They can measure practically all materials known.

The instruments are consistent and both can be used for scientific research, quality control and design.

# BIBLIOGRAPHY

"The study of curing through dynamic testing."

C. CHESNEAU, B. DUPERRAY

S.A.C.P./S.S.P. Pittsburg conference and exposition on : "Analytical chemistry and applied Spectroscopy" - ATLANTIC CITY (New-Jersey)-9-13 march 1987

"Comparison of micromechanical properties of latex films obtained by different emulsion copolymerisation pathways."

J.Y. CAVAILLE, C. JOURDAN, X.Z. KONG, J. PEREZ, C. PICHOT

Polymer, Vol. 27, pp 693-702 (1986).

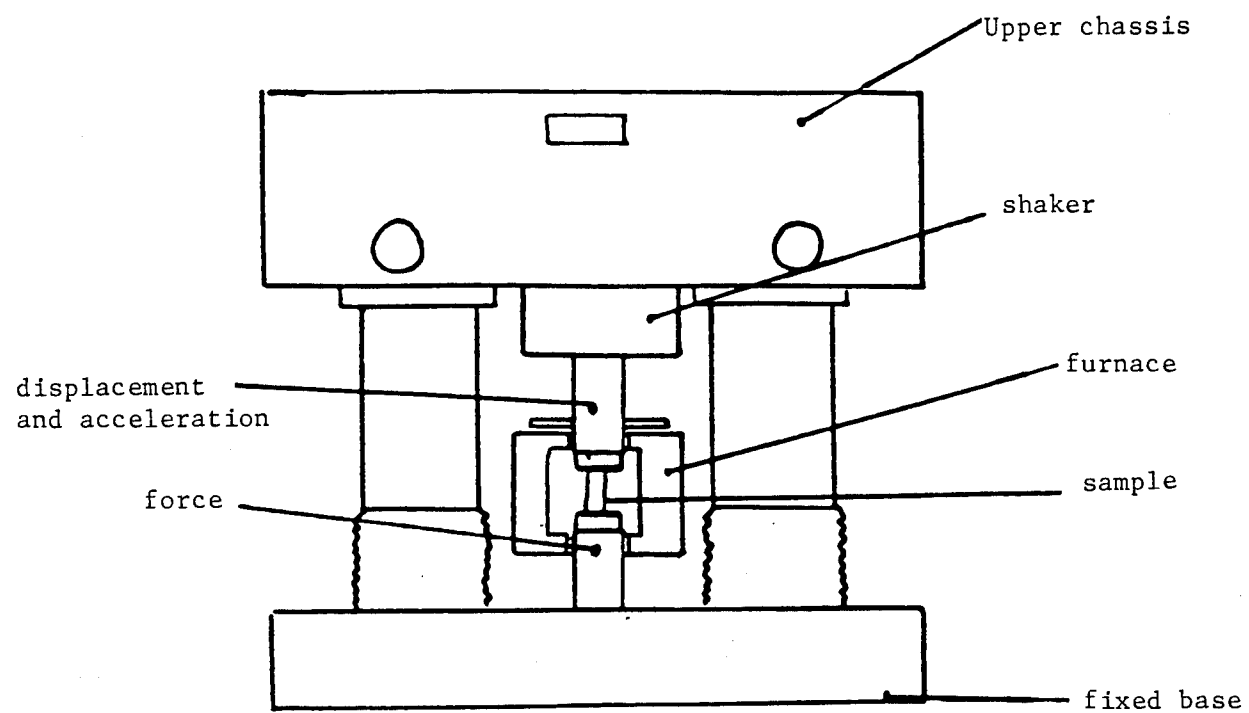


Figure 1 : VISCOANALYSER

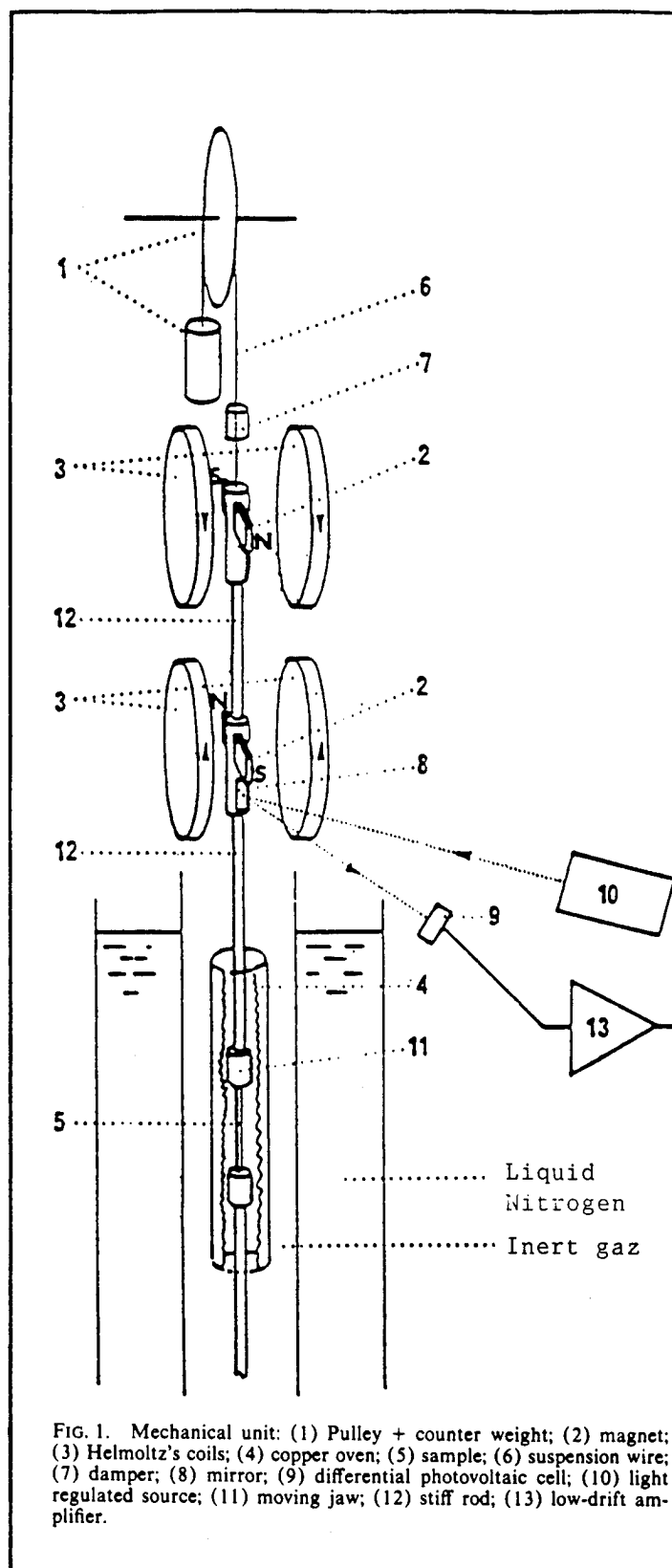


Figure 2 : MICROMECHANALYSER

# MECHANICAL PROPERTIES OF USUAL MATERIALS

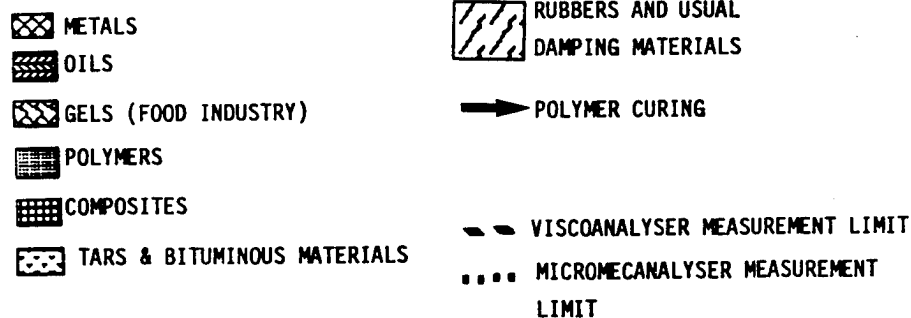
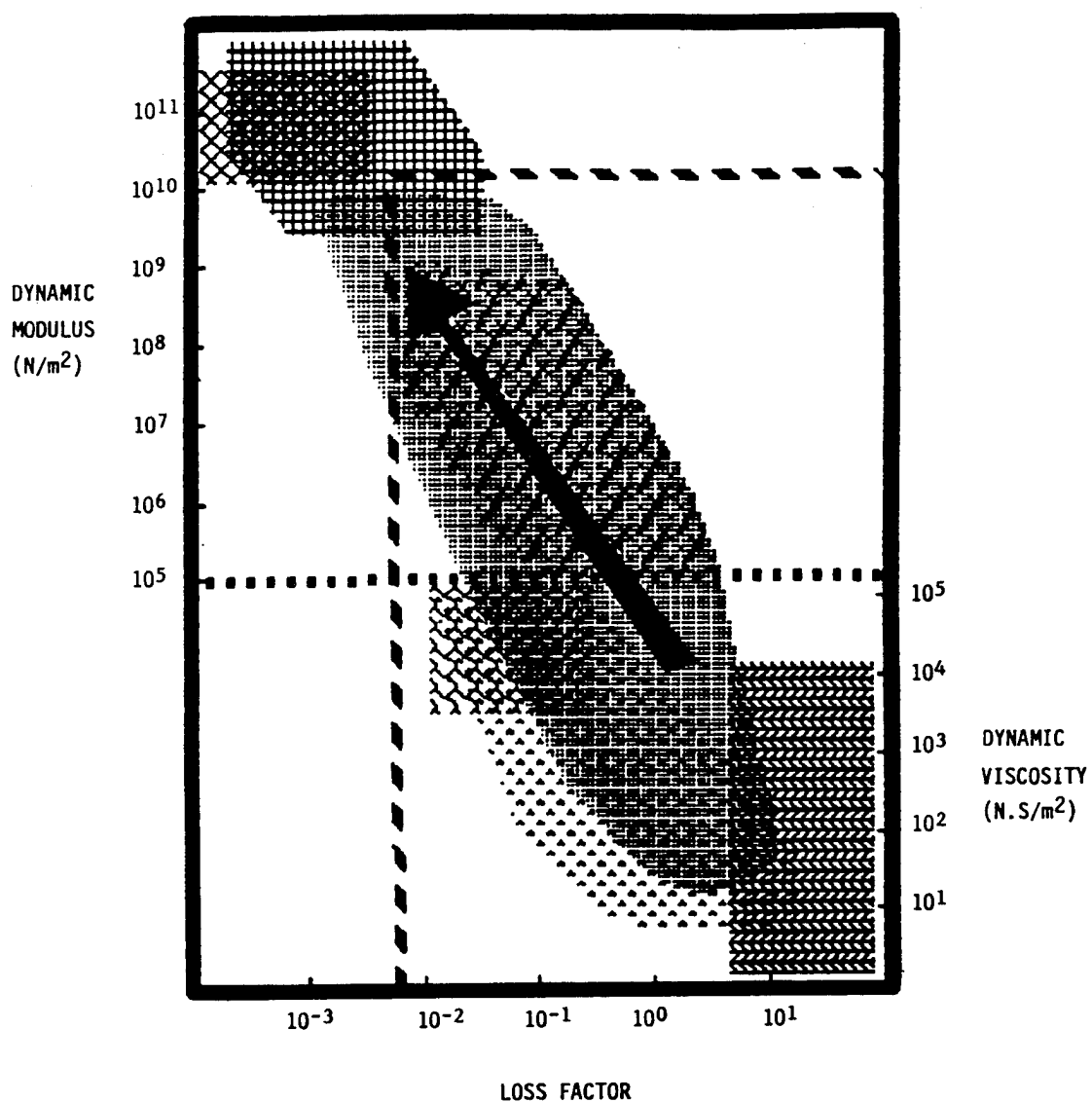


Figure 3

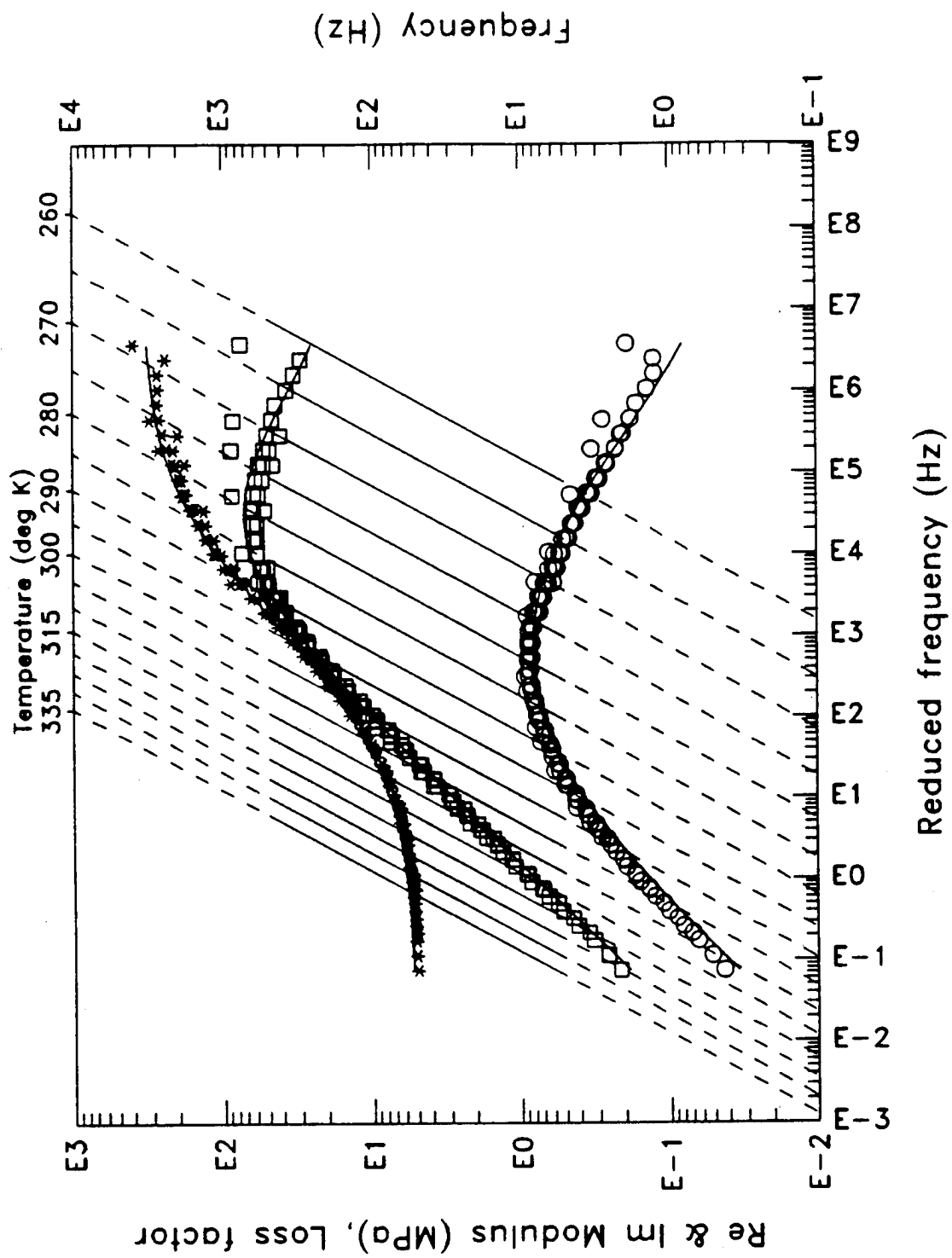


Figure 4 : GE SMRD Master curve  
obtained using the VISCOANALYSER

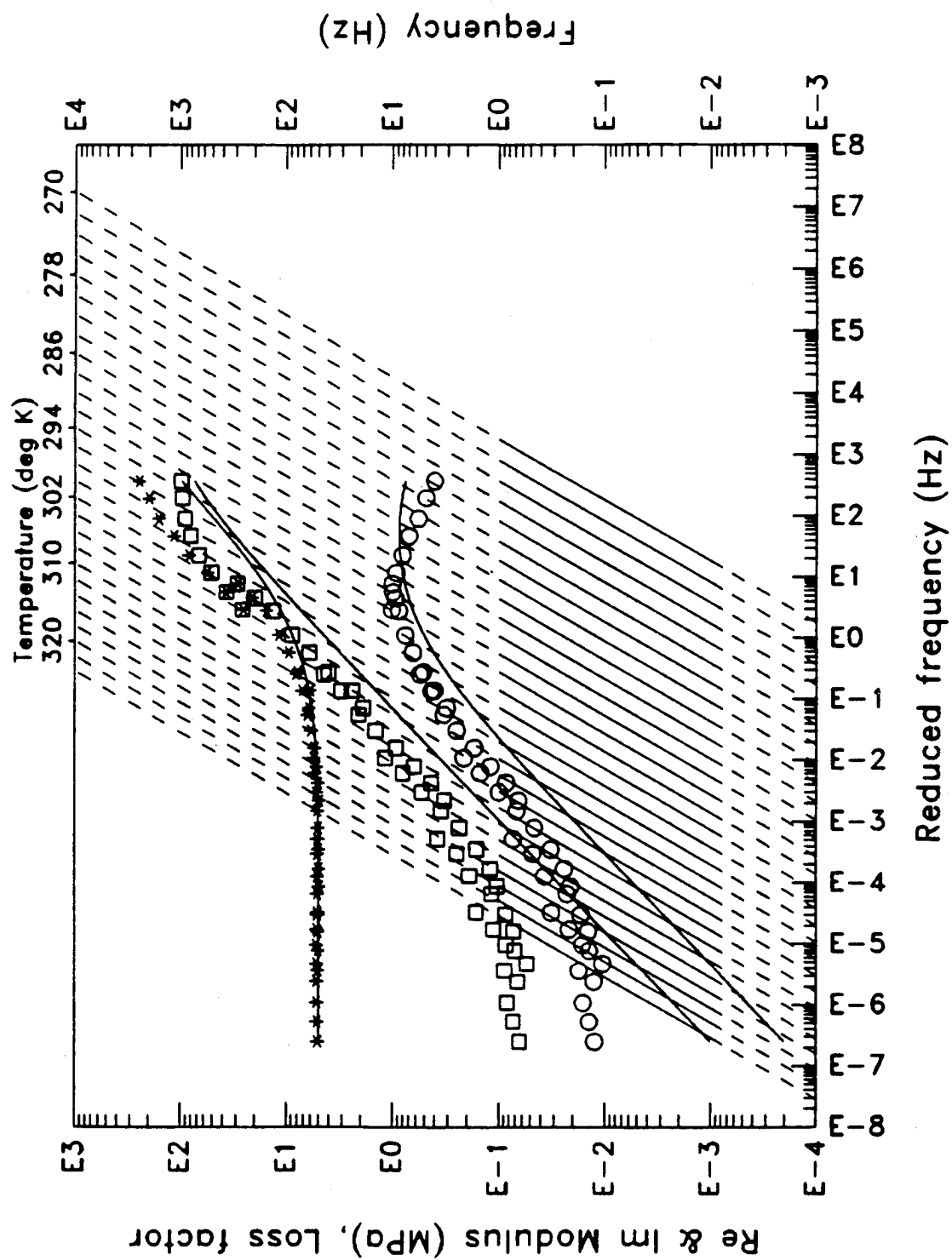


Figure 5 : GE SMRD - Master curve obtained  
using the MICROMECHANALYSER

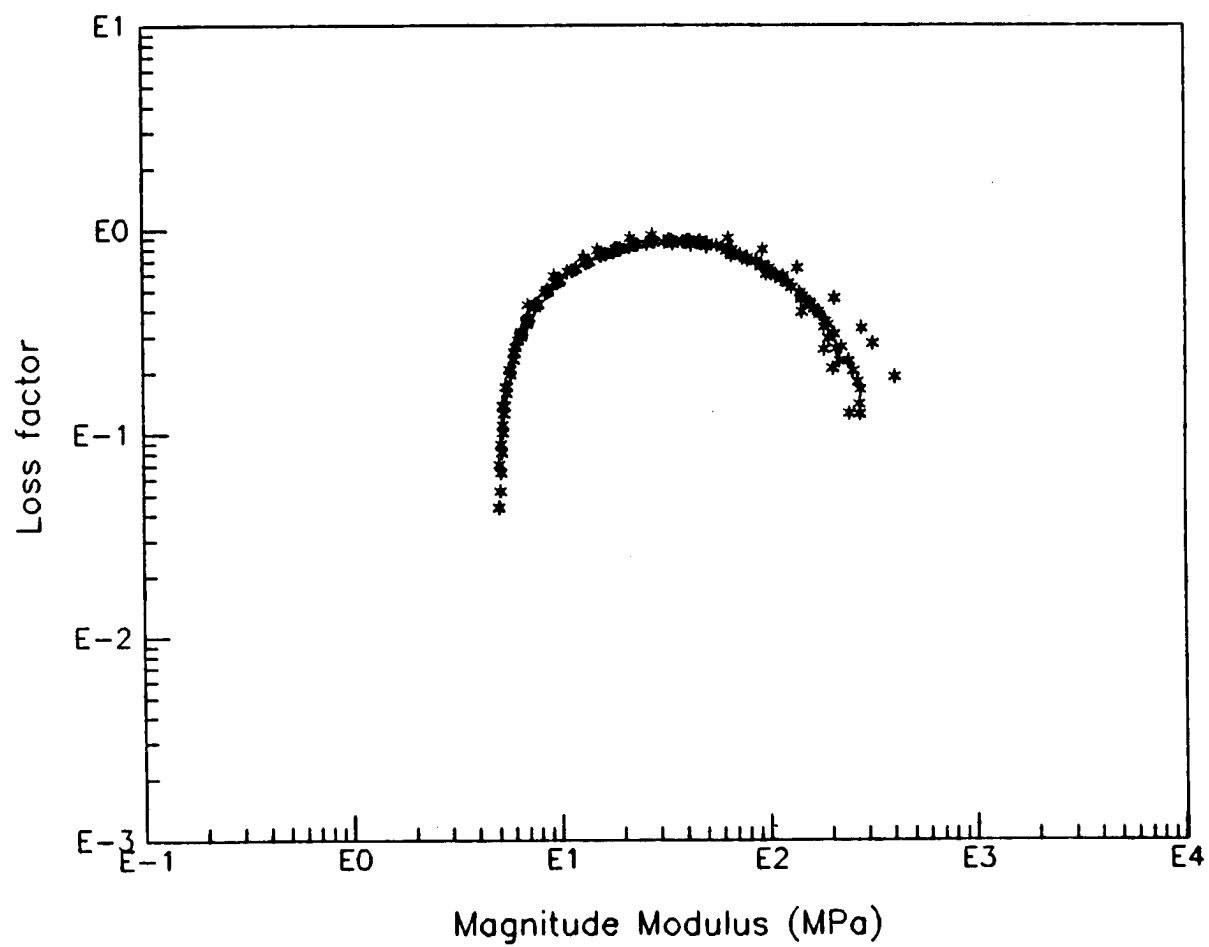


Figure 6 : Loss factor v/s modulus for GE SMRD  
obtained using the VISCOANALYSER



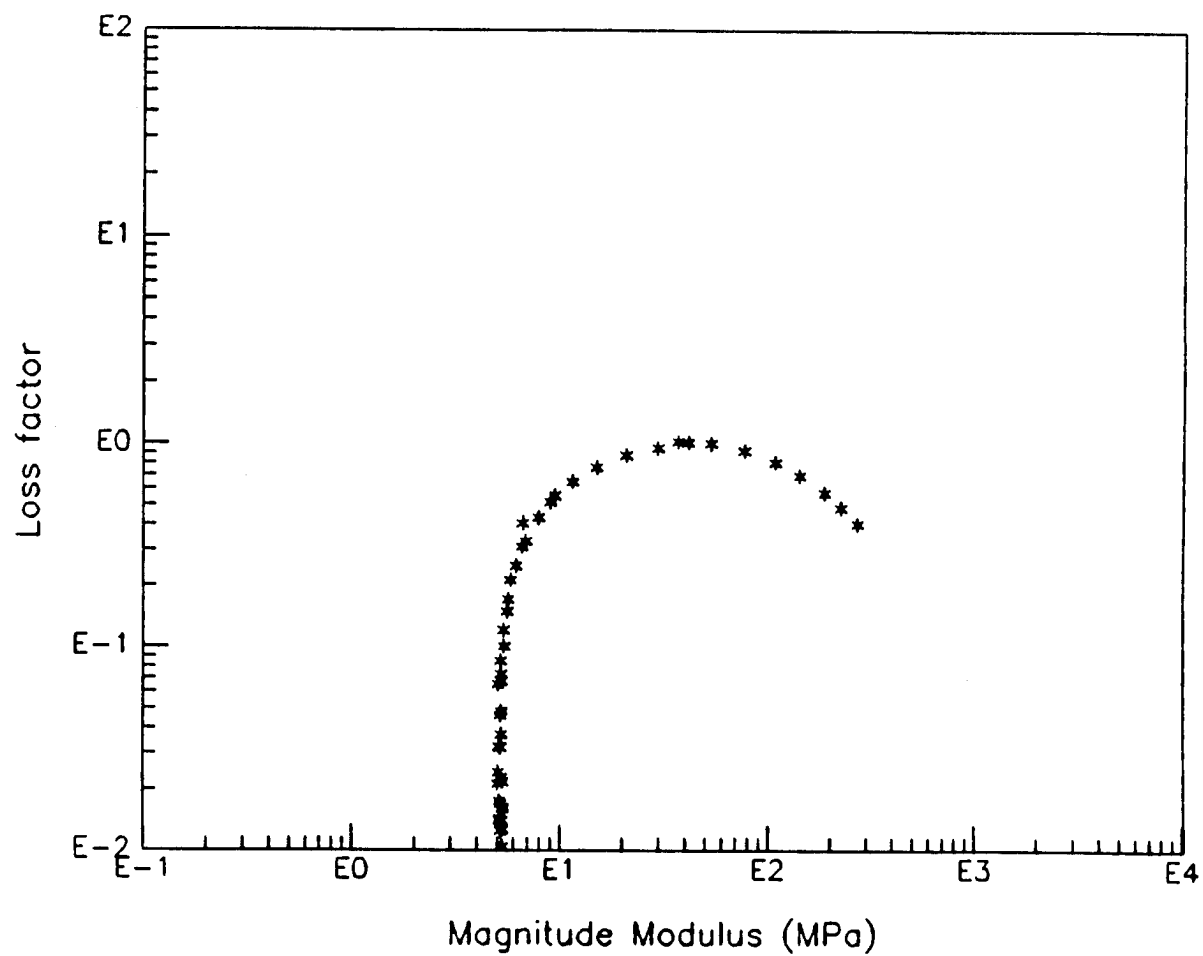


Figure 7 : Loss factor v/s modulus for GE SMRD  
obtained using the MICROMECHANALYSER

# CURING OF AN ADHESIVE

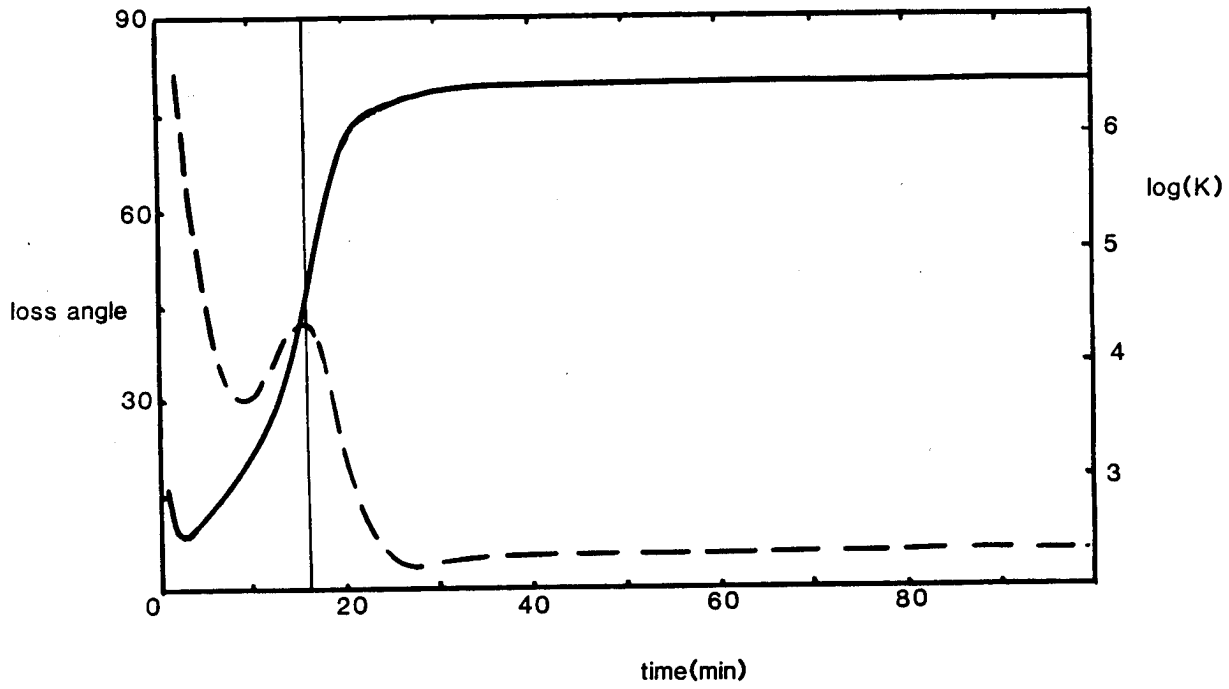


Figure 8

# TORSION HEATING SPECTRUM

GLASS FIBER IMPREGNATED WITH EPOXY RESIN

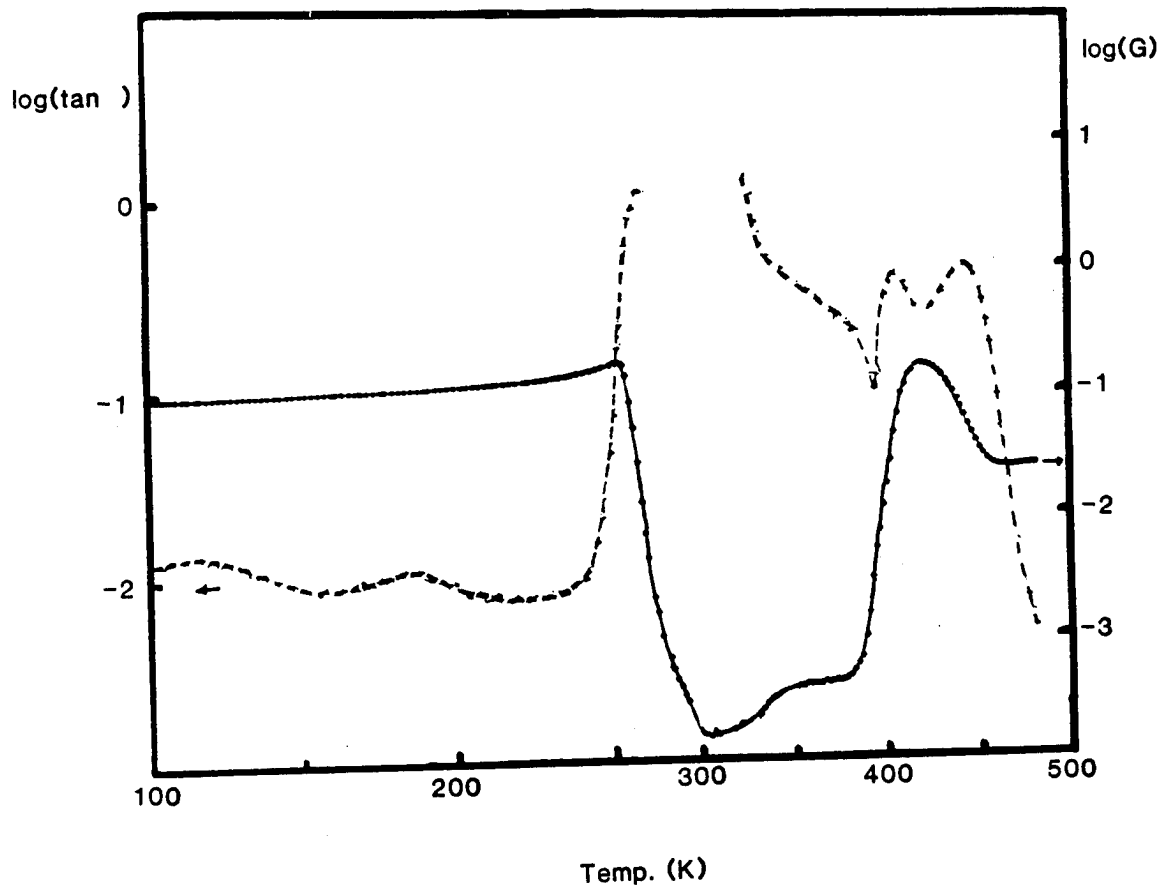


Figure 9

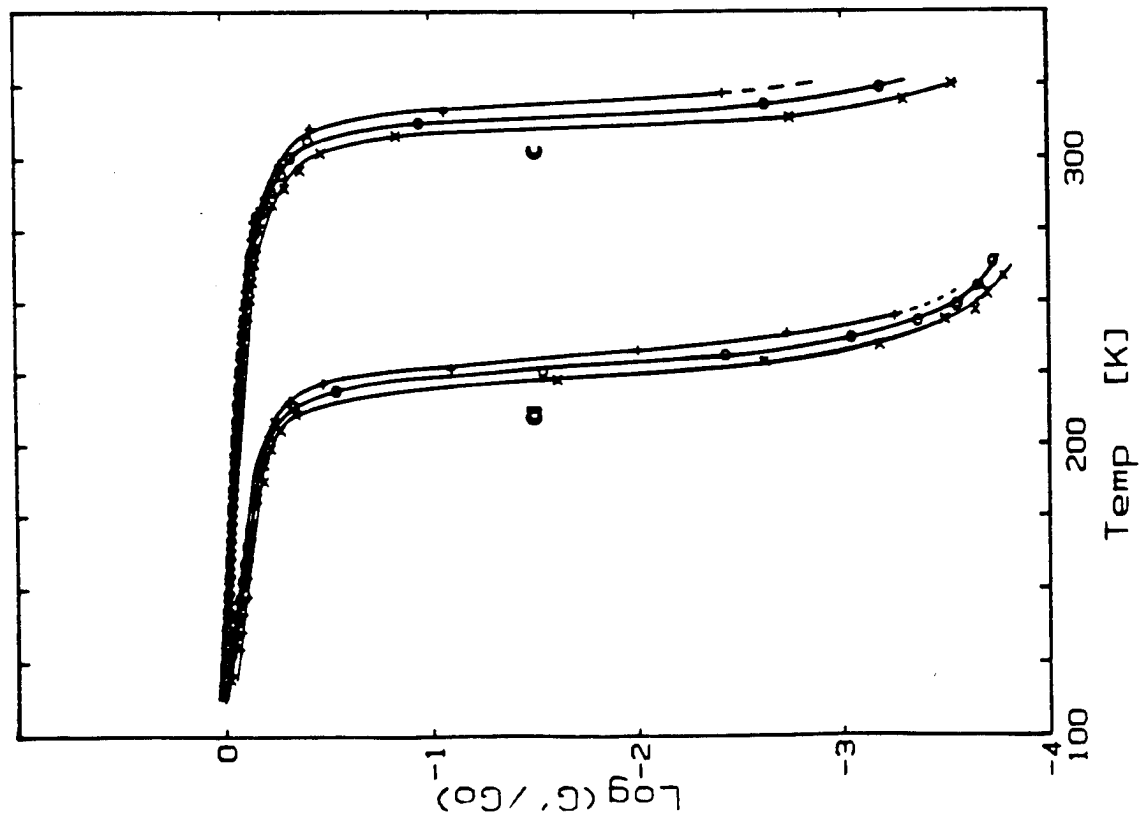


Figure 10 : Micromechanical  
G' - temperature spectra ( $G_0 = 1.5 \cdot 10^9$  Pa)  
a) poly (BuA) c) poly (VAc)

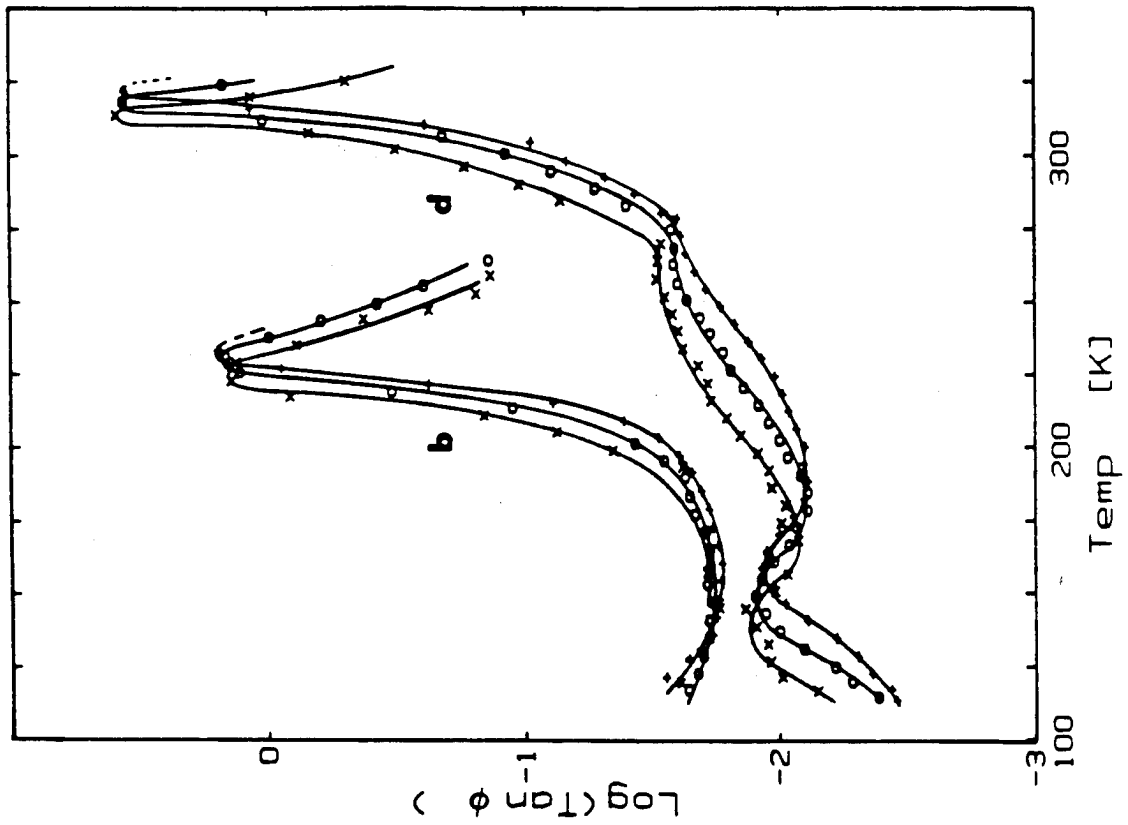


Figure 11 : Micromechanical  
tan  $\delta$  - temperature spectra  
b) poly (BuA) d) poly (VAc)

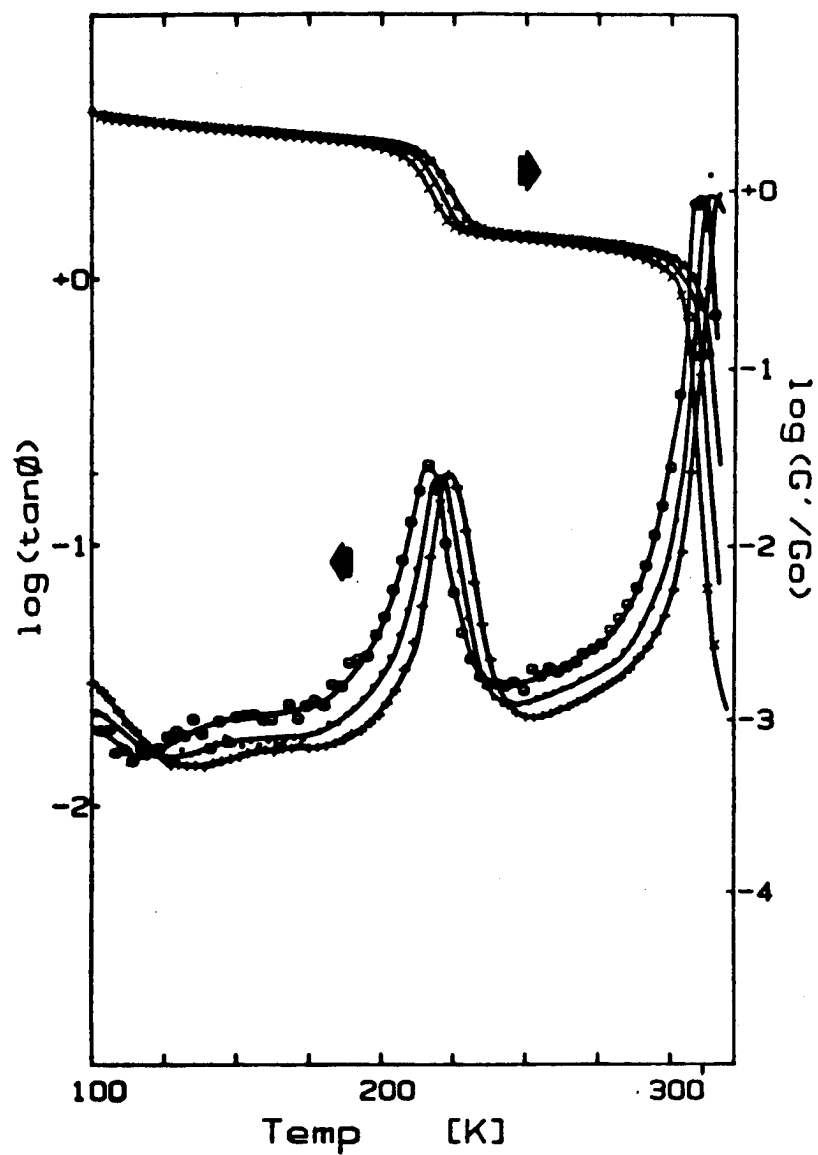


Figure 12 : Micromechanical property-temperature spectra for BuA - VAc copolymer

# Optimal Application of Damping to the Stanford Gravity Wave Experiment \*

Frank A. McLoughlin<sup>†</sup>  
013 Durand Building  
(415)-723-1260

Daniel B. DeBra<sup>‡</sup>  
028-B Durand Building  
(415)-723-3388

Department of Mechanical Engineering  
Stanford University, Stanford, California 94305

## Abstract

This paper discusses the application of passive damping to the Stanford Gravity Wave Experiment [1,2,3]. The experiment's objectives and methodology are described, and mechanical design requirements are identified for this high order, cryogenically maintained, and very flexible structure. The need for damping in the structure is motivated, and the selection of passive magnetically induced eddy-current damping in lieu of active control as a baseline is discussed. A design procedure which attempts to optimally allocate viscous damping elements in linear discrete structures is presented. Damper sizing and design considerations aimed at providing a stiffness-damping structural impedance match are also discussed.

## 1 Introduction

### 1.1 Experiment Description

The Stanford Gravity Wave Experiment apparatus shown in Figure 1 is aimed at sensing the infinitesimal momentum and energy carried by the gravity waves predicted by Einstein's general theory of relativity, and which result from the motion of objects in space. The energy content of gravity waves is extremely small. Only gravity waves associated with galactic phenomena such as stellar collapses can hoped to be distinguished at this time. The experiment consists of sensing gravity waves by making state-of-the-art measurements of their dynamical interaction with the first longitudinal vibration mode of a 4800 kg aluminum bar (see Figure 2). The bar consequently acts as a gravity wave *antenna*, and is designed to have its first longitudinal vibration mode at about 850 Hz. Sensing of

---

\*Supported by NSF under contract PHY85-05755 and by TRW Space and Technology Group

<sup>†</sup>Graduate Research Assistant

<sup>‡</sup>Professor of Aeronautics and Astronautics and Mechanical Engineering

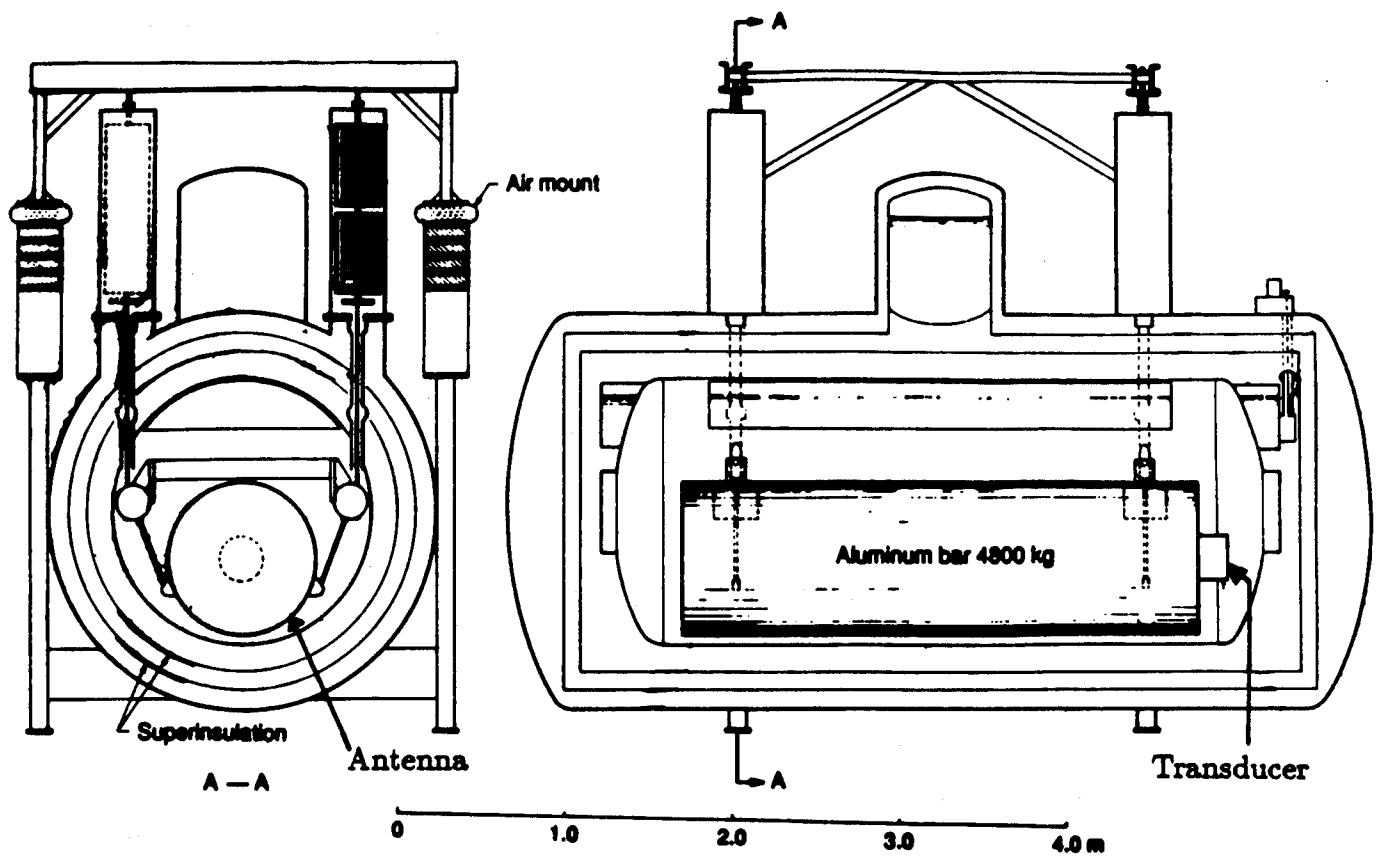


Figure 1: Schematic diagram of the 4800 kg cryogenic gravity wave detector at Stanford University

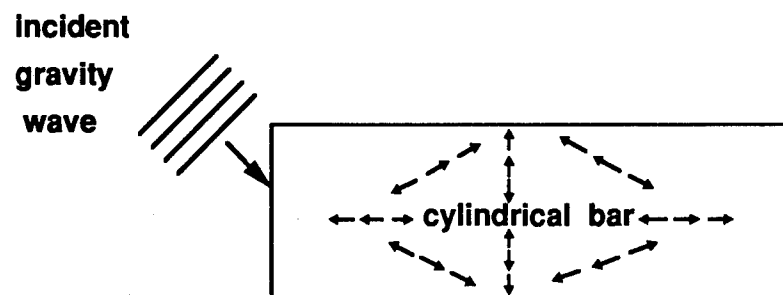


Figure 2: Incident gravity waves induce strain in cylindrical bar

the longitudinal strain in the bar is performed with a superconducting variable inductance resonant transducer and SQUID amplifier [2,3].

Because of the weakness of these signals, a great deal of effort is spent minimizing disturbances to the antenna. To reduce Brownian noise disturbances [4] sufficiently for the level of sensing required, the antenna is held at a temperature of 4 K. The antenna is also isolated from cultural and seismic ground disturbances in the laboratory by 250 dB at the frequency of its longitudinal resonance. Furthermore, the antenna is maintained in a near vacuum to minimize the possibility of acoustic disturbances propagating through air to the antenna. To amplify the dynamical interaction of interest, and to consequently make the sensing possible, the antenna is made of a high mechanical quality factor,  $Q$ , material [2]. For the existing system, the antenna is made of Aluminum and has a  $Q$  of  $\sim 4 \times 10^6$  ( $Q = 1/2\zeta$ ,  $\zeta$ =damping ratio) at 4 K in the mode of interest.

Isolation of the antenna from external disturbances is provided by an isolation system consisting of four isolation stacks each with ten spring-mass pairs for high frequency isolation, and an air bag for low frequency isolation (see Figure 1). 250 dB of mechanical isolation in 6 degrees of freedom over a 200 Hz bandwidth centered at 850 Hz is provided by this system. The isolation system is also external to, and thermally insulated from the cryogenic region housing the antenna.

The next generation gravity wave detector at Stanford University<sup>1</sup> is currently being designed (see Figure 3). A comparison between the characteristics of the existing system and the goals of the next generation system is provided in Table 1. The goal of the new system is a 1 to 2 order of magnitude increase in measurement sensitivity. To this end, the new system will maintain the antenna at 40 mK to reduce Brownian noise and to further increase the signal-to-noise ratio. In order to uncouple the thermal and isolation design problems, and to minimize interaction with internally generated and difficult to identify noise sources, the present strategy is to enclose the vibration isolation system in the low temperature region.

The springs and masses for the next generation isolation system are currently being designed. The objective is to design spring elements which will, when stacked together, be compliant enough to provide the isolation required at the antenna longitudinal resonance frequency. Concurrently, the springs must statically support the weight of the antenna with minimal stress in the spring material. The motivation for minimizing stress levels in the springs is discussed in section 1.2. The goal is to have the maximum static stress in the springs be less than 10% of the 0.2% yield stress of the material.

In addition to stiffness properties, another issue underlying material selection is the way in which the system's components can be interfaced. As is discussed in section 1.2, the system cannot tolerate nonlinear disturbance energy resulting from *sloppy* joints. All components of the isolation system must be connected with welds or brazes which have as close to a monolithic interface structure as possible. The materials currently under consideration for spring fabrication are beryllium-copper and aluminum (e. g. Al 7075).

Note that the isolation must be provided in 6 DOF (degrees of freedom). The approach taken is to design the springs and masses so that the same resonant frequencies are obtained

---

<sup>1</sup>Sponsored by NSF. Peter Michelson is principal investigator.



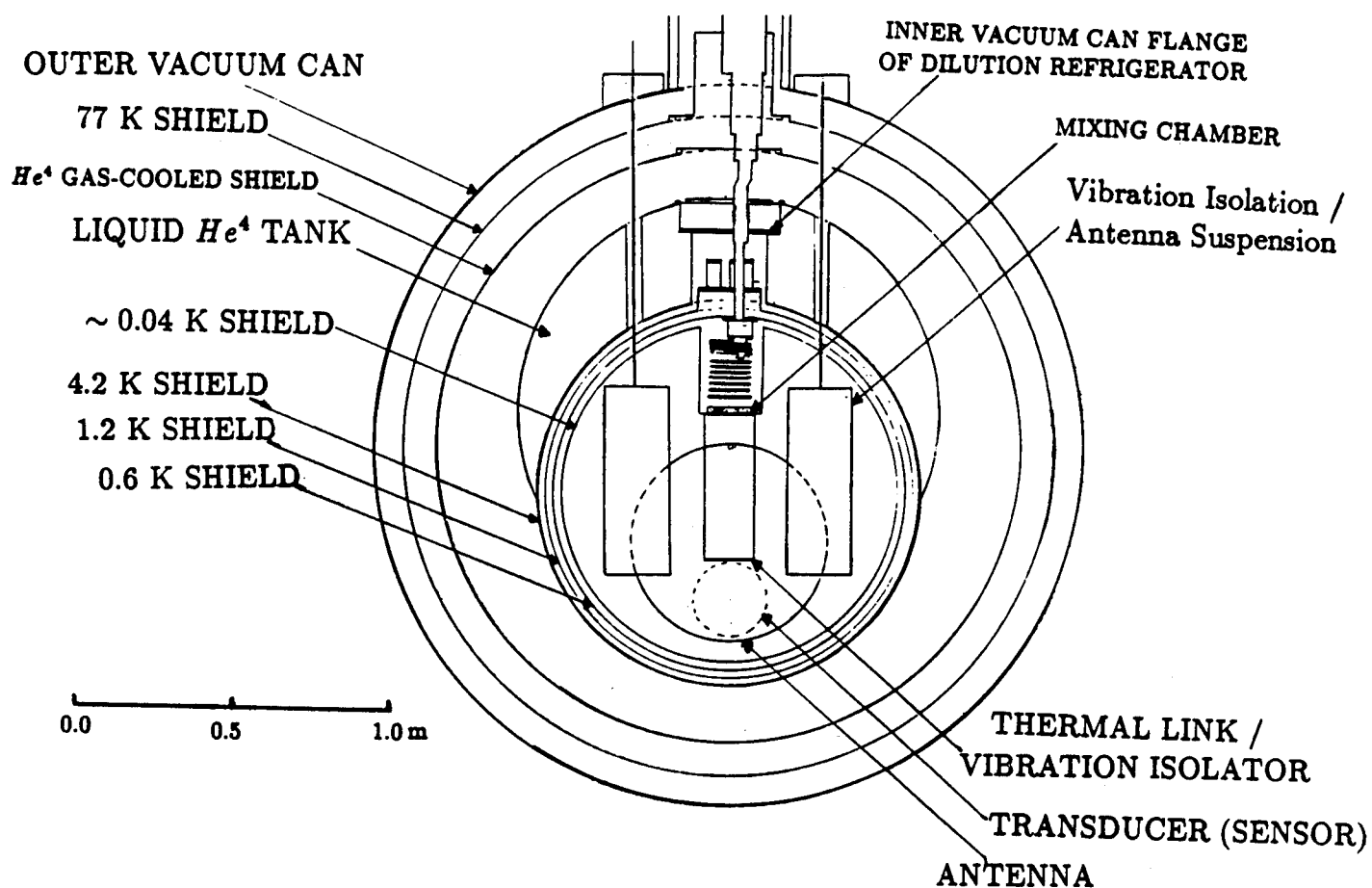


Figure 3: Next generation ultra-low temperature gravity wave detector cryostat

parameter	purpose	existing system	next generation
isolation	<ul style="list-style-type: none"> <li>- isolate antenna from ground (seismic &amp; cultural)</li> <li>- must be as purely linear as possible in dynamic range</li> </ul>	250 dB over 200 Hz BW centered at antenna resonance	300 dB over 200 Hz BW about antenna resonance
temperature	<ul style="list-style-type: none"> <li>- minimize brownian noise in antenna</li> <li>- allow operation of superconducting sensor</li> </ul>	4 K	40 mK
pressure	<ul style="list-style-type: none"> <li>- minimize disturbances on antenna due to air (e.g. acoustic)</li> </ul>	~ vacuum	~ vacuum
antenna longitudinal damping	<ul style="list-style-type: none"> <li>- High Q material reduces brownian motion noise</li> </ul>	$Q \approx 4 \times 10^6$	$Q > 10^7$ ( $\zeta < 5(10^{-8})$ )
sensing	<ul style="list-style-type: none"> <li>- inductive superconducting resonant transducer and SQUID amplifier</li> </ul>	strain ( $\Delta l / l$ ) $\approx 10^{-18}$	strain ( $\Delta l / l$ ) $\approx 10^{-20}$

Table 1: Gravity Wave Experiment characteristics

in each DOF. To this end, consider basis unit vectors  $x$ ,  $y$ , and  $z$  of a cartesian coordiante frame fixed in the laboratory. Let  $k_x$ ,  $k_y$ , and  $k_z$  be linear translational stiffnesses and let  $k_{\theta_x}$ ,  $k_{\theta_y}$ , and  $k_{\theta_z}$  be linear rotational stiffnesses of the springs for the designated axes. Similarly, let each mass element have mass  $m$  and central moments of inertia  $I_x$ ,  $I_y$ , and  $I_z$  for axes  $x$ ,  $y$ , and  $z$ , respectively. Matching resonant frequencies requires that for each spring-mass pair:

$$\omega_r = \sqrt{\frac{k_i}{m}} = \sqrt{\frac{k_{\theta i}}{I_i}}, \quad (i = x, y, \text{ and } z). \quad (1)$$

The current spring configuration is shown in the hashed portion of Figure 4(a). The springs have a *clover-leaf* like configuration. Each lobe of the *clover-leaf* springs acts between two mass elements of the isolation stack. The concept for interfacing the spring and mass elements is shown in Figure 4(b). The mass elements are shown as *H*-shaped bodies which are intended to be approximately rigid.

## 1.2 Damping Issues

The previous section described objectives and system level issues for the existing and next generation gravity wave detectors at Stanford. This section motivates the need for damping in the isolation system of the next generation experiment. There are two issues. First is the baseline decision to place the isolation system in the coldest temperature region, and

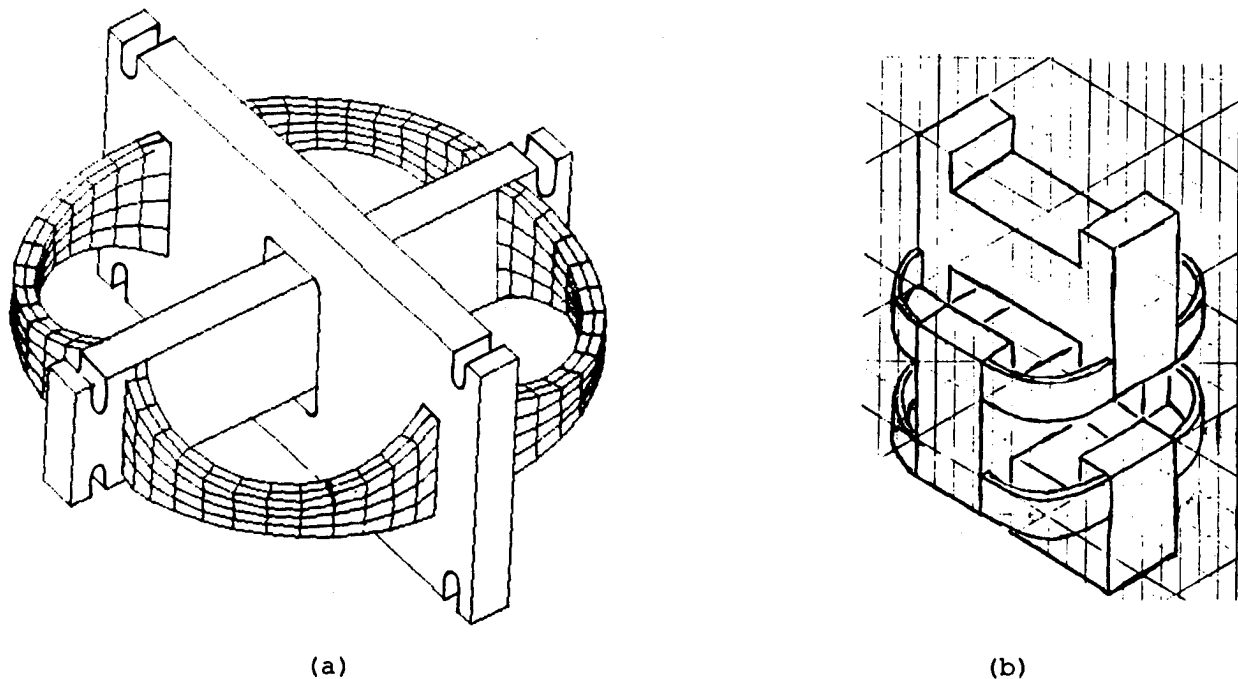


Figure 4: Isolation system concept: (a) isolation spring element, and (b) spring-mass interfacing concept.

second is increased concern associated with the sensitivity to nonlinear *creaking* in the system.

At 40 mK the isolation system itself will have mechanical  $Q$ 's on the order of  $10^7$  or higher in all of its vibrational modes (see Figure 5) [4,5]. The resulting amplification of the spectral content of the disturbances at the resonant frequencies ( $\sim 70 - 250$  Hz) of the isolation system poses a key problem. These greatly amplified inputs may cause the system to deviate from purely linear behavior. The effect is conversion of the narrow band input disturbance into a broadband disturbance. Sufficient energy at the 850 Hz antenna mode resulting from the broadband disturbance may corrupt the measurements. Although physical mechanisms for this type of nonlinear behavior have not been clearly identified for this system, hypotheses have been formulated. Among these are the hypotheses that the large amplification of low frequency disturbances causes nonlinear *creaking* at stress concentration areas of joints throughout the system. These concentrations of stress can result in local hysteretic deformations of the material which can propagate as broadband acoustic energy [2,6].

Design candidates for mitigating this problem include actively and/or passively damping the isolation system. The goal is to remove mechanical energy from the system which results from low frequency disturbance amplification. The effect of damping is to reduce the steep but narrow, and consequently relatively low energy, resonant peaks in the isolation's frequency response. In addition to reducing these peaks, added damping will reduce the RMS (root mean square) dynamic stresses in the isolation springs. This in turn will reduce the probability of localized hysteretic deformations which result in broadband disturbances.

In regard to implementing damping for this system, there are a few interesting constraints which must be considered. First, the damping must be realizable at ultra-low

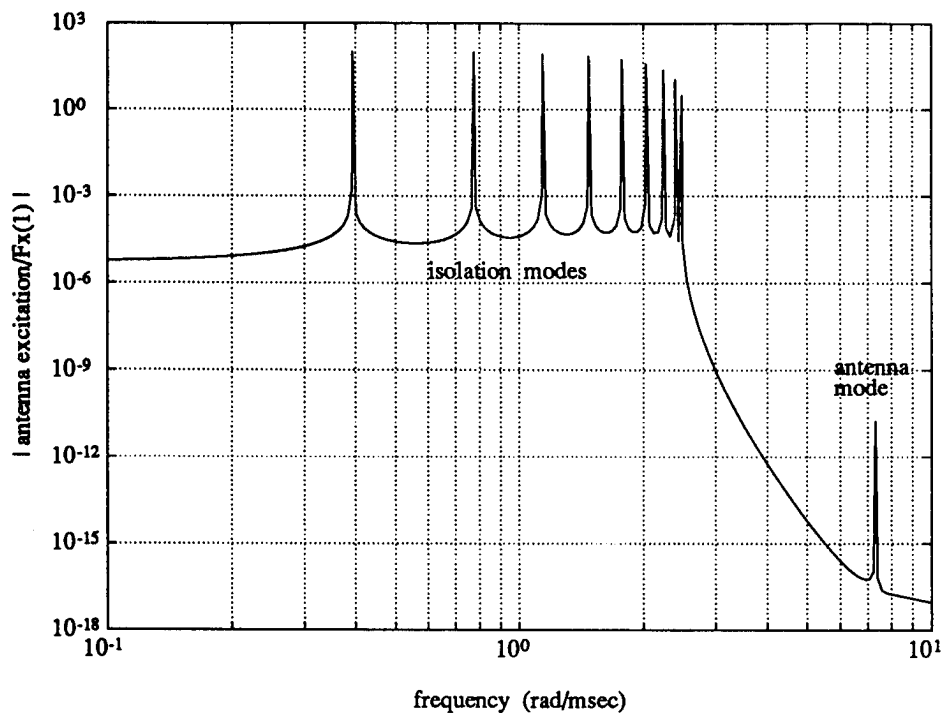


Figure 5: Undamped frequency response ( $Q = (10)^7$ ) from input at top of isolation stack in  $x$ -direction to antenna excitation

temperatures. Potential energy dissipation candidates at this point include electronic absorption of ultra-sounds, low temperature relaxation of dislocations, magnetic hysteresis, dry friction, or magnetically induced eddy-current damping [7]. Furthermore, the damping is required to be predictable/repeatable, and it is required that the damping mechanism not have substantial energy content at the antenna longitudinal resonance frequency. Consequently dry friction, for example, is inappropriate because of the broadband spectral content of this nonlinear phenomenon. Another interesting design issue which is discussed in section 6, is matching the impedance between the dampers and the stiffness elements.

The baseline approach is to use passive eddy-current damping. The negligible impact of the low temperature environment upon permanent magnets make this phenomenon realizable at low temperatures. Furthermore, eddy-current damping devices can be designed to provide nearly purely viscous damping, and can be made free of *sloppy* nonlinear joints. Finally, by using a superconducting wire, the energy absorbed by the eddy-current damper can be dissipated in an external resistor in a warmer region of the dewar. The concern regarding remotely dissipating energy, however, is that the damper then has the Brownian motion noise of the warmer region where the energy is being dumped.

Among the key design parameters are the placement and sizing of the dampers. Summarized below are design considerations which guided the definition of these parameters.

- The added damping should minimize the RMS dynamic strain in the isolation system's modes.
- The added damping should not compromise the isolation provided to the antenna.

- The 1<sup>st</sup> longitudinal resonance mode of the antenna is intentionally very lightly damped for measurement purposes. The added damping should damp the isolation system modes without damping this antenna mode.
- Energy dissipated as heat cannot be arbitrarily dissipated in the system. Because of the severe refrigeration requirements at the lowest temperature region, only about 10  $\mu$ W of power dissipation as heat can be tolerated in this region. In the warmer insulation shells, such as the 0.6 K shell (see Figure 3), as much as 1 mW of heat can be tolerated.

The sections that follow discuss how these considerations were used to establish baseline damping allocation requirements for the Gravity Wave Experiment system.

## 2 Damping Allocation Design Procedure

This section discusses a design procedure being developed which is aimed at aiding a structural designer to identify the degree to which damping can be of value, and to identify locations on a structure which are in some sense optimal for the inclusion of damping. The procedure also identifies levels of viscous damping which are also optimal in some sense. Furthermore, the procedure is automated by software written in PRO-MATLAB [8] and FORTRAN 77.

The motivation for the development of such a tool is to include damping as a parameter in the design of controlled structures. The potential payoffs are numerous. Recent studies (e. g. Passive and Active Control of Space Structures (PACOSS)) have demonstrated that passively included damping elements can reduce the number of control actuators and total control energy required in some large flexible structure control problems. Furthermore, when actively controlling a structure, a higher closed-loop bandwidth can frequently be achieved by adding damping to an otherwise lightly damped structure.

The task of identifying an optimal allocation of damping in a structure is complicated by many design issues. Certainly cost, complexity, repeatability, geometry, and environmental conditions are just a few of the many typical design considerations. These considerations can have quite varied characters, are often difficult to quantify, and can be difficult to compare on an equal footing for trade-off purposes. Furthermore, the damping which can be incorporated into a structure may be distributed or discrete, may have a wide range of thermal or frequency dependencies [7], and may vary nonlinearly with amplitude or velocity.

The design procedure described here focuses on outputs derivable from the response of a linear structure to external inputs. The goals are to determine locations on a structure where damping elements will have their greatest influence on specific outputs, and to identify the level of influence at these outputs. Typical outputs may include the response of a radio frequency antenna mounted on a spacecraft or the control energy required by actuators on a structure.

A key underlying idea in the damping allocation optimization scheme used here is that damper placement should be tailored to a system's specific input and output characteris-

tics. Consequently, specific information regarding a system's input locations, directions, and spectral content, as well as outputs of interest, must be available. The outputs must be derivable from a linear combination of the states (i.e. positions and velocities) of the system. A cost function computed as a weighted norm of the RMS or  $1\sigma$  values of the states of a discrete linear system model is used to determine an optimal damping allocation. This condition on the types of outputs allowable is not as restrictive as it may seem. As will be discussed in section 4, outputs which have been used include the resonant excitation of a large flexible bar (the Stanford Gravity Wave antenna), the average power dissipated as heat in dampers placed on a structure, and the dynamic strain induced in elements throughout a structure. Furthermore, should the peak rather than RMS value of an output be regarded as the appropriate quantity for optimization, then a reasonable approximation to the peak can be obtained by considering the  $3\sigma$  or  $4\sigma$  value of the output.

An important feature in this damping allocation procedure is the specific emphasis on the sensitivity of damper placement to specific input and output characteristics. Methods for damping allocation which are based solely on modal strain energy considerations, for example, and which attempt to identify energy concentration areas and consequently attempt to minimize the global energy in a system, may result in effort expended to remove energy that does not seriously impact outputs of interest. Furthermore, there is a possibility of a mode of vibration with relatively little energy, but for which an important output is seriously impacted. An example may be the vibration of a small antenna on a massive spacecraft. Another consideration is the possibility that inputs to a structure may have points of application, directions, or spectral content which do not significantly excite the vibration modes for which outputs of interest have large mode shape values.

## 2.1 Assumptions

Several assumptions underlie the design procedure developed. The procedure requires the existence of a nominal structural model. The dynamics of the structure must be describable by a linear, constant coefficient, matrix equation of the form:

$$[M]\{\ddot{x}\} + [C]\{\dot{x}\} + [K]\{x\} = \{f(t)\} \quad (2)$$

where  $[M]$ ,  $[C]$ , and  $[K]$  are the time-invariant mass, viscous damping, and stiffness matrices, respectively, of the structure associated with the  $n$  generalized coordinates comprising the vector  $\{x\}$ .  $\{f(t)\}$  is a time dependent vector of input forces. The mass and stiffness matrices,  $[M]$  and  $[K]$ , are assumed to be real and symmetric, and the stiffness matrix is assumed positive definite. The viscous damping matrix must be real, and need not be proportional damping (i.e. a linear combination of the mass and stiffness matrices). These assumptions consequently require a discrete linear structural model, such as is available from finite element software packages. In the case of a finite element model of the structure, the generalized coordinates are the node displacements in all active degrees of freedom.

The nominal structure is assumed asymptotically stable. Consequently some positive viscous damping must be modeled in each mode of the nominal structure, though the damping in each mode may be arbitrarily small.

There can be an arbitrary number of temporally uncorrelated external forces acting on the structure. These forces can be applied at arbitrary nodes and in any direction. The input forces must be capable of being modeled as filtered zero-mean, gaussian, ergodic, white noise. The coloring filters, which define the spectral content of the input forces, must be strictly proper continuous filters with no poles at the origin.

Damping added to the nominal structural model is assumed to be in the form of purely viscous discrete damping elements. Each element is attached to the structure at two distinct nodes. Furthermore, each damping element may provide damping in as many as six degrees of freedom, with an arbitrary viscous damping constant in each degree of freedom.

## 2.2 Candidate Damper Locations

The design procedure consists of two steps: a more synthetic step discussed in this section, and an optimization step discussed in the next section. The synthetic step is aimed at identifying *good* candidate locations for placing dampers in a structure. In the optimization step, the candidate locations are compared by determining the impact upon outputs of interest of placing dampers at these locations.

Several approaches can be taken to identify good locations for dampers. The approach taken here is motivated by an attempt to identify which locations on a structure have the greatest *influence* upon the outputs of interest. The result is the development of easily computed influence coefficients. The coefficients consider the location and spectral content of external inputs as well as the system outputs.

Consider the modal coordinates for a system described by equation (2). The modal coordinates  $\{\eta\}$  are related to the physical coordinates  $\{x\}$  by:

$$\{x\} = [U]\{\eta\} \quad (3)$$

where  $[U]$  is the system's real  $n \times n$  matrix of eigenvectors (mode shapes) normalized according to:

$$[U]^T[M][U] = [I_n], \quad (4)$$

where  $[I_n]$  is the  $n \times n$  identity matrix. Using (3) and (4), the system's dynamical equations can be expressed in modal coordinates as:

$$\{\ddot{\eta}\} + [2\zeta\Omega]\{\dot{\eta}\} + [\Omega^2]\{\eta\} = [U]^T\{f(t)\} \quad (5)$$

where  $[2\zeta\Omega]$  and  $[\Omega^2]$  are real diagonal matrices of modal damping and natural frequencies squared, respectively. Note, it has been assumed that the nominal system's inherent damping matrix,  $[C]$ , has sufficiently small damping to be at least approximately uncoupled by a coordinate transformation using  $[U]$ . Taking the Laplace transform of (5) ignoring initial conditions yields:

$$\eta(s) = ([I_n]s^2 + [2\zeta\Omega]s + [\Omega^2])^{-1}[U]^T\{F(s)\} \quad (6)$$

so that using (3):

$$x_j(s) = \sum_{i=1}^n \frac{u_{j,i}}{s^2 + 2\zeta_i\omega_i s + \omega_i^2} \{u_i\}^T F(s) \quad (7)$$

where  $x_j$  is the  $j^{th}$  element of  $\{x\}$ ,  $\{u_i\}$  is the  $i^{th}$  mode shape (column of  $[U]$ ),  $u_{j,i}$  is the  $j^{th}$  element of  $\{u_i\}$ ,  $\zeta_i$  is the damping ratio of mode  $i$ , and  $\omega_i$  is the natural frequency of mode  $i$  ( $i = 1, \dots, n$ ).

Now consider the effect of introducing to the nominal system, a discrete viscous damping element acting between generalized coordinates  $x_a$  and  $x_b$  ( $1 \leq a, b \leq n$ ). Assuming for the moment that this damper is massless, the dynamical effect on the system is identical to the effect of adding equal magnitude but oppositely directed forces at  $x_a$  and  $x_b$  which are proportional to the relative velocity between these coordinates. These damping forces can be considered by adding a force vector in equation (2) with forcing terms in the  $a^{th}$  and  $b^{th}$  elements, that is:

$$f_{damp}^T = \left[ \underbrace{0 \dots 0 \quad c(\dot{x}_b - \dot{x}_a) \quad 0 \dots 0}_{b} \quad -c(\dot{x}_b - \dot{x}_a) \quad 0 \dots 0 \right]. \quad (8)$$

Considering only the contribution of these damping forces to  $x_j(s)$ , we can write

$$x_j(s) = \sum_{i=1}^n \frac{u_{j,i}(u_{a,i} - u_{b,i})c}{s^2 + 2\zeta_i\omega_i s + \omega_i^2} s(x_b(s) - x_a(s)). \quad (9)$$

In fact, these damping forces result when relative motion between coordinates  $x_a$  and  $x_b$  is induced by external forces. With this in mind, and noting that  $x_a(s)$  and  $x_b(s)$  in equation (9) can be expressed in the same form as  $x_j(s)$  in equation (7):

$$x_j(s) = \sum_{i=1}^n \frac{u_{j,i}(u_{a,i} - u_{b,i})c}{s^2 + 2\zeta_i\omega_i s + \omega_i^2} \left[ \sum_{k=1}^n \frac{(u_{b,k} - u_{a,k})s}{s^2 + 2\zeta_k\omega_k s + \omega_k^2} \{u_k\}^T \right] F(s). \quad (10)$$

Now consider the case in which the external force consists only of a force applied at coordinate  $m$ , and also only consider the contribution to  $x_j(s)$  from mode  $r$  ( $i = r$  in equation (10)) and express this as  $(x_{j,m})_r$ :

$$(x_{j,m})_r(s) = \frac{u_{j,r}(u_{a,r} - u_{b,r})c}{s^2 + 2\zeta_r\omega_r s + \omega_r^2} \left[ \sum_{k=1}^n \frac{(u_{b,k} - u_{a,k})s}{s^2 + 2\zeta_k\omega_k s + \omega_k^2} u_{m,k} \right] F_m(s). \quad (11)$$

Recalling that the objective is to identify some measure of *influence* from an input to an output with discrete viscous damping acting between two arbitrary coordinates, it can be seen that equation (11) expresses this influence, with  $m$  as the input coordinate,  $j$  as the output coordinate, and  $a$  and  $b$  as the coordinates between which the damper acts.

Now let  $s$  vary along the  $J\omega$ -axis ( $J = \sqrt{-1}$ ), emphasizing an interest in the dependence of this influence upon the spectral content of the input, to obtain:

$$(x_{j,m})_r(J\omega) = \frac{u_{j,r}(u_{a,r} - u_{b,r})c}{\omega_r^2 - \omega^2 + J * 2\zeta_r\omega_r\omega} \left[ \sum_{k=1}^n \frac{(u_{b,k} - u_{a,k})J\omega}{\omega_k^2 - \omega^2 + J * 2\zeta_k\omega_k\omega} u_{m,k} \right] F_m(J\omega). \quad (12)$$

Evaluating at  $\omega = \omega_r$ , since it is the contribution of mode  $r$  under consideration, the following measure of the gain or influence at mode  $r$  associated with an input at coordinate



$m$ , an output at coordinate  $j$ , and a viscous damper acting between coordinates  $a$  and  $b$  is obtained:

$$\left| \frac{u_{j,r}(u_{a,r} - u_{b,r})c}{2\zeta_r\omega_r^2} \left[ \sum_{k=1}^n \frac{(u_{b,k} - u_{a,k})J\omega_r}{\omega_k^2 - \omega_r^2 + J * 2\zeta_k\omega_k\omega_r} u_{m,k} \right] \right| |F_m(J\omega_r)|. \quad (13)$$

Furthermore, for outputs of interest which are linear combinations of system states, such as:

$$\{y\} = [C]\{x\}, \text{ so that } y_j = \sum_{i=1}^n C(j,i)x(i) \quad (14)$$

where  $[C]$  is a real constant  $outputs \times n$  matrix, then the influence coefficient for output  $y_j$  is obtained by replacing  $u_{j,r}$  in equation (13) with  $\sum_{i=1}^n C(j,i)u_{i,r}$ .

A PRO-MATLAB function has been written to automate the computation and sorting of these influence coefficients. By easily specifying input locations, the spectral content at each input location, outputs, and damping coordinate pairs, this function aids a designer to generate a first cut at good candidate damper locations. Furthermore, by ranking the influence coefficients by mode, one can identify which modes are most significant for the inputs, outputs, and damper locations considered. Application of this procedure to the Stanford Gravity Wave Experiment is discussed in section 3.

## 2.3 Optimization Analysis

Section 2.2 discussed a procedure to generate a collection of *good* candidate damper locations in a structure. This section discusses an analysis tool developed to evaluate the impact of incorporating viscous damping elements in a controlled structure. The objective of this tool, which is fully automated in PRO-MATLAB software [8], is to identify which of a collection of candidate damper placement scenarios in a structure is optimal for a particular application, and furthermore what level of damping is appropriate. The hope is that damping will be allocated in an efficient way to adequately damp all important modes. Each damper allocation case considered can include an arbitrary number of arbitrarily distributed and directed damping elements, each with arbitrary viscous damping constant. Furthermore, the procedure will include the impact upon a nominal structure of damping elements with arbitrary mass and stiffness properties. Typical of candidate damper locations to consider are those generated by the algorithm of section 2.2.

Several inputs are required for this analysis. A nominal discrete linear (finite element) model must exist for the structure under consideration. The model must consist of  $n \times n$  mass, stiffness, and viscous damping matrices, where  $n$  is the number of active structural degrees of freedom. The location, direction, and spectral content of all inputs must be known. Finally, a collection of outputs of interest must be identified.

This section begins by constructing a state-space realization for a general system considered. This realization demonstrates the ability to address systems which include structural dynamics states; sensor, actuator, and estimator states as needed; and coloring filter states to model the spectral character of external inputs. The topology for the optimization, as well as the structure of the performance index used is then discussed. A procedure to sub-optimize over damping constant values for each case is also discussed.

A state space model for the nominal structure, or plant, is modeled using plant coordinates,  $\{x_p\}$ , as:

$$\{\dot{x}_p\} = [A_p]\{x_p\} + [B_{px}]\{f_x(t)\} + [B_{pc}]\{f_c(t)\} \quad (15)$$

where,

$$\{x_p\} \triangleq \begin{Bmatrix} x \\ \dot{x} \end{Bmatrix}, [A_p] \triangleq \begin{bmatrix} 0 & I_n \\ -M^{-1}K & -M^{-1}C \end{bmatrix}, \quad (16)$$

$$[B_{px}] \triangleq \begin{bmatrix} 0 \\ -M^{-1}B_x \end{bmatrix}, [B_{pc}] \triangleq \begin{bmatrix} 0 \\ -M^{-1}B_c \end{bmatrix}. \quad (17)$$

$[M]$ ,  $[C]$ ,  $[K]$ , and  $\{x\}$  are as defined in equation (2), and  $I_n$  is the  $n \times n$  identity matrix.  $\{f_x(t)\}$  is a vector of  $m_x$  external inputs and  $\{f_c(t)\}$  is a vector of  $m_c$  control inputs.  $[B_x]$  and  $[B_c]$  are input distribution matrices for external inputs and control inputs, respectively. Note that for numerical stability, care must be taken to select appropriate units for  $[M]$ ,  $[C]$ , and  $[K]$  so that  $[A_p]$  is well conditioned.

Now consider the inclusion of actuator dynamics to the nominal plant. Let  $\{f_c(t)\}$  be the vector of controls actually input to the plant, and  $\{u_a(t)\}$  be the vector of actuation commands. Furthermore, let a state space realization from the  $i^{th}$  actuator input,  $f_{c,i}$ , to the  $i^{th}$  actuator command,  $u_{a,i}$ , be given by:

$$\{\dot{x}_{a,i}\} = [\alpha_{a,i}]\{x_{a,i}\} + \{\beta_{a,i}\}u_{a,i} \quad (18)$$

$$f_{c,i} = [\gamma_{a,i}]\{x_{a,i}\} + \delta_{a,i}u_{a,i} \quad (19)$$

The combined plant-actuator system can then be realized as:

$$\{\dot{x}_{pa}\} = [A_{pa}]\{x_{pa}\} + [B_{pa}]\{u_a\} + [B_{px}]\{f_x\} \quad (20)$$

where,

$$\{x_{pa}\} \triangleq \begin{Bmatrix} x_p \\ x_a \end{Bmatrix}, [A_{pa}] \triangleq \begin{bmatrix} A_p & B_{pc}\Gamma_a \\ 0 & A_a \end{bmatrix}, [B_{pa}] \triangleq \begin{bmatrix} B_{pc}\Delta_a \\ B_a \end{bmatrix}, \quad (21)$$

$$[A_a] \triangleq \text{diag}[\alpha_{a,1} \ \alpha_{a,2} \ \dots \ \alpha_{a,m_c}], [B_a] \triangleq \text{diag}[\beta_{a,1} \ \beta_{a,2} \ \dots \ \beta_{a,m_c}], \quad (22)$$

$$[\Gamma_a] \triangleq \text{diag}[\gamma_{a,1} \ \gamma_{a,2} \ \dots \ \gamma_{a,m_c}], [\Delta_a] \triangleq \text{diag}[\delta_{a,1} \ \delta_{a,2} \ \dots \ \delta_{a,m_c}]. \quad (23)$$

The notation  $\text{diag}[\dots]$  refers to a block diagonal matrix with the arguments on the diagonal.  $[A_a]$ , for example, is a block diagonal matrix with the blocks  $\alpha_{a,i}$  ( $i = 1, \dots, m_c$ ) on the diagonal.

Now consider the inclusion of sensor dynamics to the nominal plant-actuator system. Let  $[C_m]$  be a real constant measurement matrix such that an  $m_s$ -vector of ideal measurements,  $\{y_{ideal}\}$ , is given by:

$$\{y_{ideal}\} = [C_m]\{x_{pa}\} \quad (24)$$

To accommodate sensor dynamics, let a state space realization from the  $i^{th}$  element of  $\{y_{ideal}\}$  to the  $i^{th}$  element of the actual measurement vector,  $\{y\}$ , be given by:

$$\{\dot{x}_{s,i}\} = [\alpha_{s,i}]\{x_{s,i}\} + \{\beta_{s,i}\}y_{ideal,i} \quad (25)$$

$$y_i = [\gamma_{s,i}] \{x_{s,i}\} + \delta_{s,i} y_{ideal,i} \quad (26)$$

The combined plant-actuator-sensor system can then be realized as:

$$\{\dot{x}_{pas}\} = [A_{pas}] \{x_{pas}\} + [B_{pa}] \{u_a\} + [B_{px}] \{f_x\} \quad (27)$$

where,

$$\{x_{pas}\} \triangleq \begin{Bmatrix} x_{pa} \\ x_s \end{Bmatrix}, \quad [A_{pas}] \triangleq \begin{bmatrix} A_{pa} & 0 \\ B_s C_m & A_s \end{bmatrix}, \quad (28)$$

$$[A_s] \triangleq \text{diag}[\alpha_{s,1} \ \alpha_{s,2} \ \dots \ \alpha_{s,m_s}], \quad [B_s] \triangleq \text{diag}[\beta_{s,1} \ \beta_{s,2} \ \dots \ \beta_{s,m_s}], \quad (29)$$

and note that  $\{y\}$  is given by:

$$\{y\} = [C_s] \{x_{pas}\}, \quad \text{where } [C_s] \triangleq [\Delta_s C_m \ \Gamma_s] \quad (30)$$

where,

$$[\Gamma_s] \triangleq \text{diag}[\gamma_{s,1} \ \gamma_{s,2} \ \dots \ \gamma_{s,m_s}], \quad [\Delta_s] \triangleq \text{diag}[\delta_{s,1} \ \delta_{s,2} \ \dots \ \delta_{s,m_s}]. \quad (31)$$

Now consider designing a control system for the structure being considered. To this end, assume that the control law generated is in the form of feedback of estimated plant, actuator, and sensor states. Simpler control laws, such as feedback of sensor outputs alone with no estimation, are a subset of this more general construction. Actuator commands are then given by:

$$\{u_a\} = -[K] \{\hat{x}_{pas}\} \quad (32)$$

where  $[K]$  is constant control gain matrix and  $\{\hat{x}_{pas}\}$  is a vector of estimated plant, actuator, and sensor states.  $[K]$  may, for example, be the gains resulting from a solution of the linear quadratic regulator (LQR) control optimization problem [9]. The estimator state equation is assumed to be of the following form:

$$\{\dot{\hat{x}}_{pas}\} = [A_{pas}] \{\hat{x}_{pas}\} + [B_{pa}] \{u_a\} + [L] [\{y\} - [C_s] \{\hat{x}_{pas}\}]. \quad (33)$$

$[L]$  is a constant estimator gain matrix, and may, for example, be the steady state Kalman-Bucy filter gains associated with the linear quadratic estimator (LQE) optimization problem [9].

By combining equations (27), (32), and (33), the entire system can be realized as:

$$\{\dot{x}_{pase}\} = [A_{pase}] \{x_{pase}\} + [B_{px}] \{f_x\} \quad (34)$$

where,

$$\{x_{pase}\} \triangleq \begin{Bmatrix} x_{pas} \\ \hat{x}_{pas} \end{Bmatrix}, \quad [A_{pase}] \triangleq \begin{bmatrix} A_{pas} & -B_{pa}K \\ LC_s & A_{pas} - B_{pa}K - LC_s \end{bmatrix}. \quad (35)$$

Finally, consider the inclusion of continuous filter states used to shape the spectral content of the  $m_x$ -vector of external inputs,  $\{f_x\}$ . The external forces can be the result of a directly applied force, or the result of external *ground* motion acting through linear translational or rotational springs and/or viscous dampers. It is assumed that the MSSD (mean square spectral density) also referred to as the PSD (power spectral density) of

either the applied force or ground motion is known, and can be adequately modeled as continuously filtered white noise. The Laplace transform of the coloring filters is assumed to have no purely imaginary poles. The  $i^{th}$  external input can be written as:

$$f_{x,i} = k_{x,i}\phi_{x,i} + c_{x,i}\dot{\phi}_{x,i} \quad (i = 1, \dots, m_x) \quad (36)$$

where  $\phi_{x,i}$  is the  $i^{th}$  filtered input. Let a state space realization from an external input with a white PSD,  $\omega_{x,i}$ , through the  $i^{th}$  shaping filter to  $\phi_{x,i}$  be written as:

$$\{\dot{x}_{x,i}\} = [\alpha_{x,i}]\{x_{x,i}\} + \{\beta_{x,i}\}\omega_{x,i} \quad (37)$$

$$\phi_{x,i} = [\gamma_{x,i}]\{x_{x,i}\} + \delta_{x,i}\omega_{x,i} \quad (38)$$

Now assume that the transfer function of these filters in the Laplace domain is strictly proper so that  $\delta_{x,i} = 0$  ( $i = 1, \dots, m_x$ ). Then by substituting equations (37) and (38) into equation (36):

$$f_{x,i} = [a_{kc,i}]\{x_{x,i}\} + b_{kc,i}\omega_{x,i} \quad (39)$$

where,

$$[a_{kc,i}] \triangleq k_{x,i}[\gamma_{x,i}] + c_{x,i}[\gamma_{x,i}][\alpha_{x,i}], \quad (40)$$

$$b_{kc,i} \triangleq c_{x,i}[\gamma_{x,i}]\{\beta_{x,i}\}. \quad (41)$$

The combined system with plant, actuators, sensors, estimator, and external input shaping filters can then be realized as:

$$\{\dot{x}_{sys}\} = [A_{sys}]\{x_{sys}\} + [B_{sys}]\{\omega_x\} \quad (42)$$

where,

$$\{x_{sys}\} \triangleq \begin{Bmatrix} x_{pase} \\ x_x \end{Bmatrix}, [A_{sys}] \triangleq \begin{bmatrix} A_{pase} & B_{px}A_{kc} \\ 0 & A_x \end{bmatrix}, [B_{sys}] \triangleq \begin{bmatrix} B_{px}B_{kc} \\ B_x \end{bmatrix}, \quad (43)$$

$$[A_x] \triangleq \text{diag}[\alpha_{x,1} \ \alpha_{x,2} \ \dots \ \alpha_{x,m_x}], [B_x] \triangleq \text{diag}[\beta_{x,1} \ \beta_{x,2} \ \dots \ \beta_{x,m_x}], \quad (44)$$

$$[A_{kc}] \triangleq \text{diag}[a_{kc,1} \ a_{kc,2} \ \dots \ a_{kc,m_x}], [B_{kc}] \triangleq \text{diag}[b_{kc,1} \ b_{kc,2} \ \dots \ b_{kc,m_x}]. \quad (45)$$

$\{\omega_x\}$  is a vector of external inputs,  $\omega_{x,i}$  ( $i = 1, \dots, m_x$ ), which are assumed to be ergodic uncorrelated zero mean gaussian distributed inputs with white PSD.

With a state-space realization available to model a wide class of linear system descriptions, the way this realization is used can now be discussed. To this end, the *optimization* portion of the damping allocation procedure shown in Figure 6 will now be discussed. This portion of the procedure considers each *good* candidate damper application case individually. For each case, a list of damper geometries is specified, as well as nominal viscous damping constants, and mass and stiffness properties of the dampers. The  $[M]$ ,  $[C]$ , and  $[K]$  matrices in equation (16) are modified from their nominal values to appropriately accommodate the added dampers, and are then used to construct a modified plant model. Actuator and sensor dynamics can then be added to the plant model, a control system can

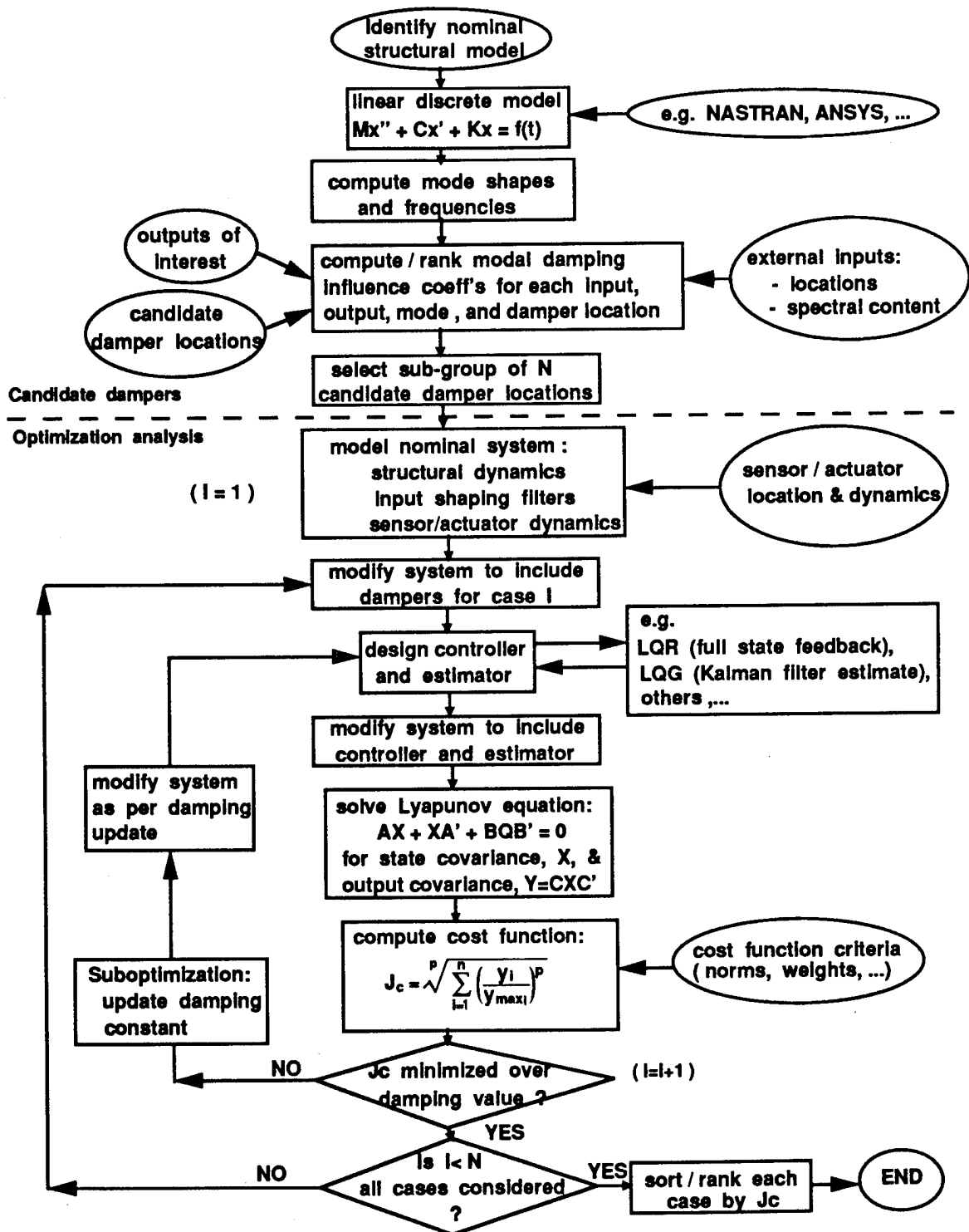


Figure 6: Damping allocation procedure flow chart

be designed as indicated in equations (32) and (33), and a system model constructed as per equation (42).

The optimal damper configuration selection is based upon minimizing a cost function constructed from RMS values of system outputs. Computing the RMS values for high order systems can be computationally intensive. For a linear system with uncorrelated inputs, one method of finding the RMS values,  $x_{RMS}$ , of a state  $x$  resulting from a random ergodic input  $f(t)$  is to perform the following integration [10]:

$$x_{RMS} = \sqrt{\frac{1}{2\pi} \int_{-\infty}^{+\infty} |G_{fx}(J\omega)|^2 S_f(\omega) d\omega} \quad (46)$$

$G_{fx}(J\omega)$  is the transfer function from  $f$  to  $x$  in the Laplace domain and evaluated at  $s = J\omega$ .  $S_f(\omega)$  is the PSD of  $f$  and is defined by:

$$S_f(\omega) \triangleq \int_{-\infty}^{+\infty} R_f(\tau) e^{-J\omega\tau} d\tau \quad (47)$$

where,  $R_f(\tau) = E[f(t)f(t - \tau)]$  for an ergodic process. The procedure for computing and integrating  $G_{fx}(J\omega)$  for all inputs and outputs is computationally intensive. A more efficient approach is to solve a continuous-time Lyapunov equation [11] of the form:

$$[A_{sys}][P] + [P][A_{sys}]^T + [B_{sys}][Q][B_{sys}]^T = 0 \quad (48)$$

for the matrix  $[P]$ . If  $[A_{sys}]$  is asymptotically stable (i.e. all eigenvalues have negative real part) and  $[Q]$  is positive semidefinite, then there is a unique solution  $[P]$  which is positive semidefinite and satisfies:

$$[P] = \int_0^{\infty} e^{A_{sys}^T t} B_{sys}^T Q B_{sys} e^{A_{sys} t} dt. \quad (49)$$

If all inputs to the system are regarded as uncorrelated purely random (white PSD) inputs with unity spectral density (input shaping filters account for gain differences), then  $[Q]$  is an identity matrix and  $[P]$  is the steady-state covariance matrix for the system's states.

Now consider an  $m_o$ -vector,  $\{y_o\}$ , consisting of outputs of interest for the system, and related to  $\{x_{sys}\}$  by:

$$\{y_o\} = [C_o]\{x_{sys}\} \quad (50)$$

The output covariance matrix,  $[Y_o]$ , is then given by:

$$[Y_o] = [C_o][P][C_o]^T \quad (51)$$

A vector  $\{y_{RMS}\}$  of RMS outputs of interest can then be computed as the square root of the diagonal elements of  $[Y_o]$ .

As a computational note, equation (48) is computed in PRO-MATLAB by transforming to schur form, solving for the upper-triangular system, and then transforming back [8]. Because  $[B_{sys}][B_{sys}]^T$  can be poorly conditioned, it is numerically more robust to compute

the SVD (singular value decomposition) [12,13] of  $[B_{sys}]$  and then solve a related Lyapunov equation [14]. To this end, let the SVD of  $[B_{sys}]$  be given by:

$$[B_{sys}] = [U][\Sigma][V^*]^2, \quad (52)$$

where  $[U]$  and  $[V]$  are unitary matrices and  $[\Sigma]$  is a diagonal matrix containing the singular values of  $[B_{sys}]$ . The following related Lyapunov equation can then be solved for  $\bar{P}$ :

$$[\bar{A}_{sys}][\bar{P}] + [\bar{P}][\bar{A}_{sys}]^T + [\Sigma][\Sigma]^T = 0 \quad (53)$$

where,

$$[\bar{A}_{sys}] \triangleq [U^*][A_{sys}][V] \quad \text{and} \quad [\bar{P}] \triangleq [V^*][P][U]. \quad (54)$$

The desired covariance matrix,  $[P]$ , is then obtained by transforming back using  $[P] = [V][\bar{P}][U^*]$ .

Having obtained RMS values, the next step is to compute a cost function,  $J_{cost}$ , which is a weighted  $p$ -norm of the elements of  $\{y_{RMS}\}$ , and is given by:

$$J_{cost} = \left[ \sum_{i=1}^{m_o} \left( \frac{y_{RMS,i}}{y_{RMS\ max,i}} \right)^p \right]^{1/p}. \quad (55)$$

The optimal damping case is that for which  $J_{cost}$  is minimized. The quantities  $y_{RMS\ max,i}$  are weightings which represent the maximum tolerable values of  $y_{RMS}(i = 1, \dots, m_o)$  as determined by system level requirements. The default value used for  $p$  is 2, but any value can be used.

For each case, there is a simple sub-optimization scheme used to identify what level of damping minimizes  $J_{cost}$ . The sub-optimization scheme used modifies the nominal damping constant in each damper by the same factor. At this point the factor is chosen simplistically using a secant direct search method [15].

After addressing each case, the cases are ranked and sorted by  $J_{cost}$ .

A drawback of the optimization procedure is that it is computationally intensive both in regard to number of operations and memory requirements. Although not yet developed, it is felt that model reduction techniques can be used to handle extremely high order systems. To date, the largest system to which this optimization phase was applied contained 292 states, and required a maximum of 16 megabytes of memory. Another drawback is the current inability to easily handle the inclusion of hysteretic damping [7] either in the nominal structure, or as appended damping.

### 3 Candidate Damper Locations for Gravity Wave Experiment

This section provides an example of the procedure discussed in section 2.2 to identify *good* candidate damper locations. The application is the simplified finite element model

---

<sup>2</sup> $[ ]^*$  denotes Hermitian transpose of  $[ ]$

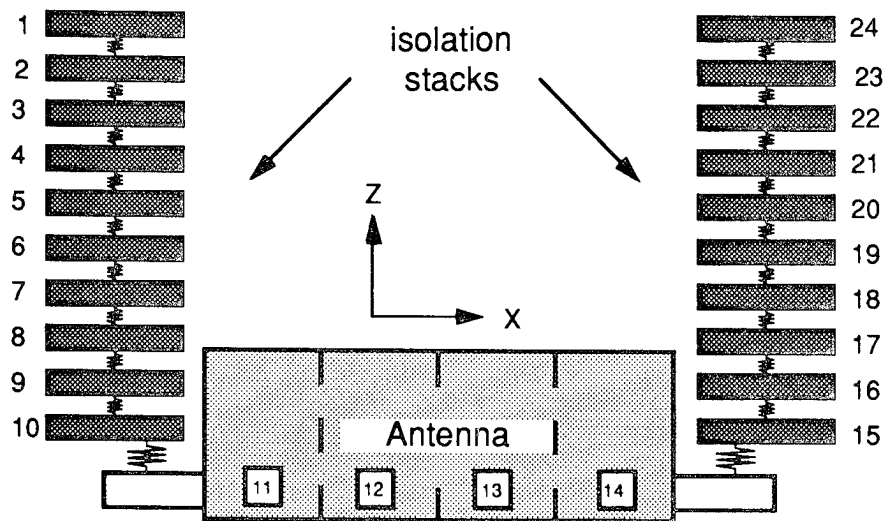


Figure 7: Simplified model of Gravity Wave Experiment structure

of the Stanford Gravity Wave experiment shown in Figure 7. The model consists of two spring-mass isolation stacks, each stack consisting of ten 6-DOF springs and masses. The isolation stacks are connected at each end of a 4 node cylindrical bar modeling the antenna. Four nodes are sufficient because primary interest is in the first longitudinal mode. The complete structure has 144 DOF.

Inputs of interest for the Gravity Wave experiment are cultural and seismic noise in the laboratory. For this example, only seismic noise is modeled, and it is assumed to be applied in three translational DOF at the top of each isolation stack. The PSD of seismic ground motion used is shown in Figure 8, and was adapted from chapter 10 of reference [16]. For the sake of this example we will regard excitation of the antenna as the sole output of interest. A measure of this excitation is the relative motion between nodes 11 and 14 in the  $x$ -direction (see Figure 7).

The objective is to place viscous dampers in the isolation stack so that they have maximal effect upon the output considered. The damper can be placed to dissipate energy due to the relative motion between any pair of masses in the isolation stack. As a result of the symmetry in this model, only one isolation stack need be considered. Using an automated PRO-MATLAB procedure, the *gain factors* of equation 13 were quickly computed for all 45 ( $n(n-1)/2$ ,  $n = 10$ ) possible damper locations, for all 144 modes of the model, and for the input and output specified. Among the outputs of the procedure is a 3-D contour plot of peak *gain factors* versus the damper connection coordinate pairs.

Figure 9 shows the contour plot for this case. The height of the contour at any intersection is the *gain factor* associated with placing a damper between coordinates  $a$  and  $b$  designated by the horizontal axes. A large peak and a smaller plateau stand out in the figure. The large peak indicates the effectiveness of placing dampers between coordinates 5 and 10, or between coordinates 6 and 10. The plateau indicates that dampers are effective



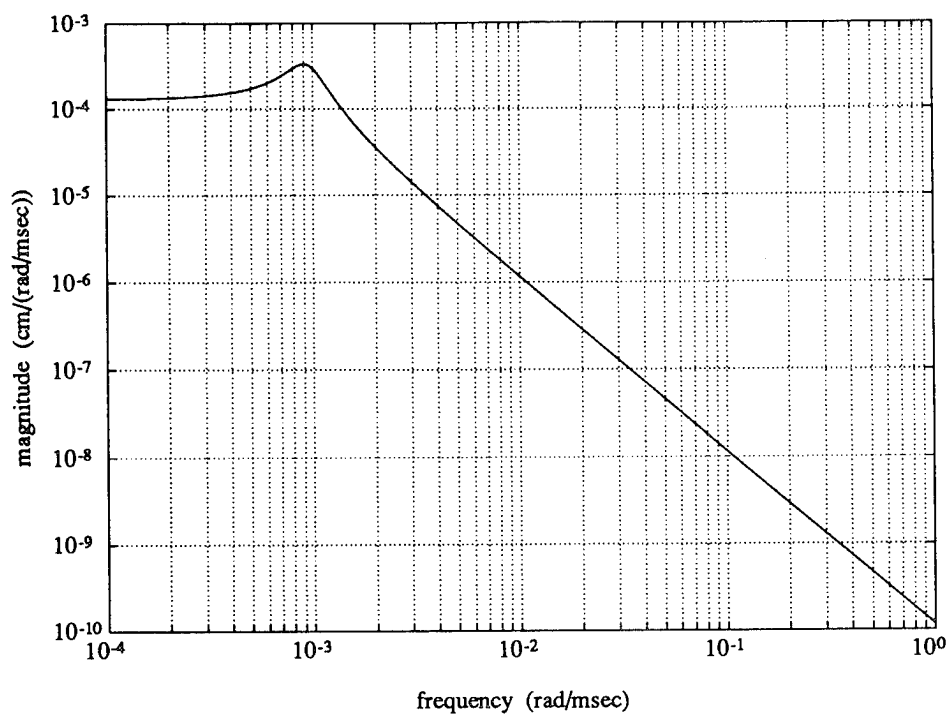


Figure 8: Position PSD coloring filter for seismic disturbances

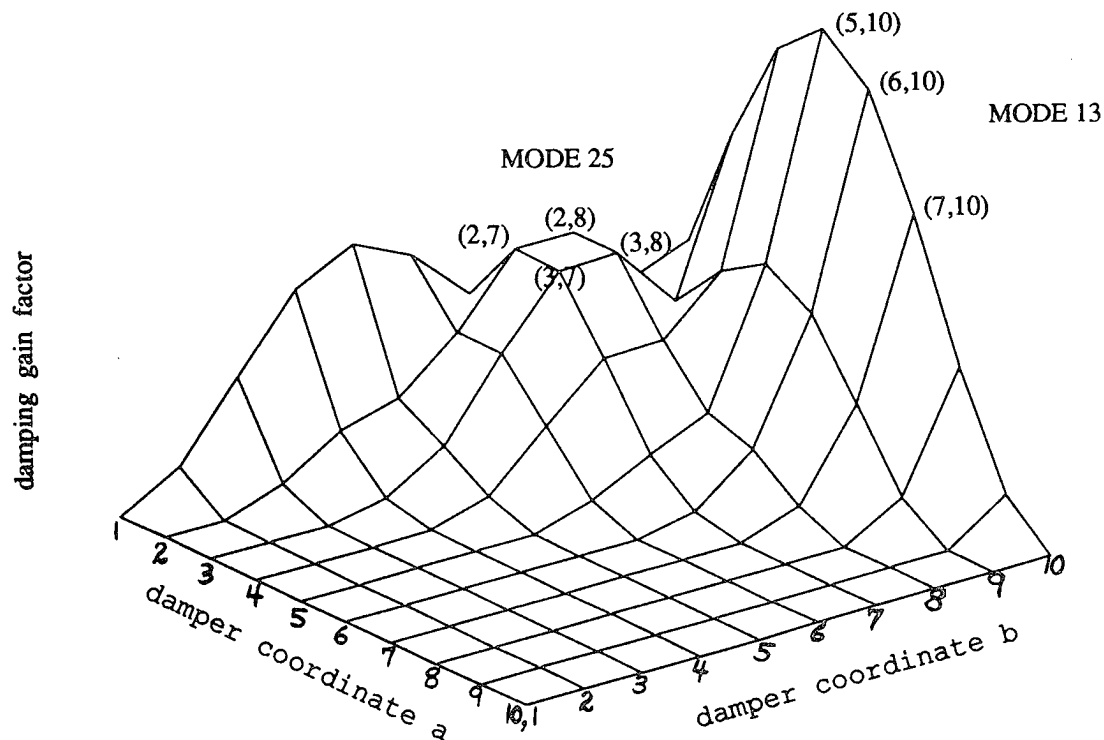


Figure 9: Contour plot of *gain factors* versus damper connection coordinate pairs for simplified Gravity Wave Experiment model

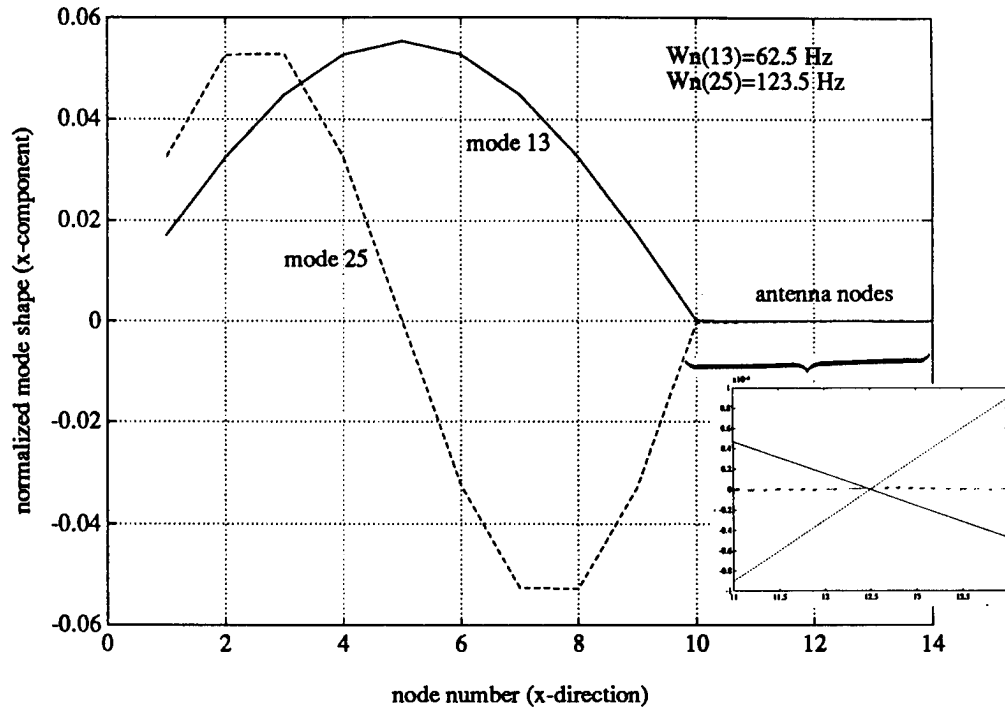


Figure 10: Normalized mode shapes for modes 13 and 25 of simplified Gravity Wave Experiment model

between coordinates coordinates 2 or 3 and coordinates 7 or 8. In addition, the program identifies the mode of vibration which produced the peak *gain factor* for a specific damper geometry. The peak in the contour is associated with the 13<sup>th</sup> mode, whereas the plateau is associated with mode 25. These results are supported by the mode shape plots shown in Figure 10. Mode 13 shows substantial relative motion between coordinates 5 and 10 and between coordinates 6 and 10. Similarly, mode 25 shows large relative motion between coordinates 2 or 3 and coordinates 7 or 8. Furthermore, for both of these modes there is large relative motion between coordinates 11 and 14 (the output of interest), as indicated by the *blow-up* of coordinates 11 through 14 in Figure 10. The *blow-up* is required because the antenna is quite massive and stiff so that its motion is small relative to motion of the isolation stack elements. Another interesting result is that although mode 25 has larger relative peak-to-peak motion than mode 13, the contour plot indicates that damping mode 13 is more effective. This apparent contradiction is clarified by looking at the spectral density of the input. Figure 8 shows that for frequencies above 0.15 Hz ( $\sim 9(10^{-4})$  rad/msec) the input PSD shaping filter is rolling off at 40 dB/decade. Because mode 25 is at 123.5 Hz and mode 13 is at 62.5 Hz, the input shaping filter has about 1/4 of the gain at mode 25 than at mode 13. Consequently, sufficiently more disturbance energy density at the frequency of mode 13 makes this mode the more desirable mode to damp.

Note that the above example was provided primarily to illustrate the procedure that generates *good* candidate damper locations. For application to the actual Gravity Wave Experiment, a more detailed finite element model of the system was used, and the outputs of interest identified in section 1.2 were considered.

## 4 Optimal Allocation for Gravity Wave Experiment

This section discusses the application of the optimization procedure described in section 2.3 to a collection of candidate damper configurations generated as discussed in section 3. Because there is no active control for this example, the nominal system need only be modified to include appended dampers and the external disturbance filter states. As in section 3, the inputs are comprised only of seismic disturbances acting in 3 DOF at the top of each isolation stack. The appended dampers were assumed to have negligible stiffness and mass, an assumption which can be abandoned in future studies as the damping hardware becomes defined better.

The outputs to be optimized for this case provide an interesting sample application of the procedure. The optimization objectives are summarized as follows:

- Minimize the RMS dynamic strain in all of the isolation springs.
- Minimize the average rate of energy dissipation as heat.
- Maximize the amount of isolation provided to the antenna at the antenna's longitudinal resonance frequency.
- Maximize the  $Q$  in the antenna longitudinal mode (i. e. do not damp the antenna mode).

RMS dynamic strains in the translation degrees of freedom of each spring are computed as the RMS dynamic stretch in each spring divided by the static vertical deflection in each spring. Average power dissipation as heat is computed for each damper as the damping constant times the covariance of the relative velocity between the damper connection coordinates. RMS motion between the antenna end faces is used as an approximate measure of the isolation of the antenna longitudinal mode. Since no appropriate measure of the  $Q$  in the antenna's longitudinal mode is available from the RMS state outputs, this figure of merit was excluded from the optimization. Verification that the inherent  $Q$  in the antenna's longitudinal mode was not significantly reduced by the added damping was performed after the optimization by studying the resulting frequency responses.

The cost function,  $J_{cost}$ , constructed for this application is given below:

$$J_{cost} = \sqrt{\left(\frac{\epsilon_{max}}{\epsilon_{max_{allow}}}\right)^2 + \left(\frac{\dot{E}_{heat}}{\dot{E}_{heat_{allow}}}\right)^2 - \left(\frac{antenna_{excite}}{antenna_{excite_{allow}}}\right)^2}. \quad (56)$$

$\epsilon_{max}$  is the maximum RMS strain in all springs of the isolation system with all degrees of freedom considered.  $\dot{E}_{heat}$  is the total rate of energy dissipation as heat in all dampers for each case considered.  $antenna_{excite}$  is the RMS relative motion between the antenna's end faces. The weighting factors designated by the notation  $( )_{allow}$  represent the maximum allowable values of the quantities in  $( )$  as determined by system level requirements. These requirements are listed in Table 2.

The structure of this optimization provides for interesting trade-offs. First of all, the allocation of damping must be such that it damps all isolation modes with a minimal

Quantity	Requirement	Current value
max. RMS dynamic stress in isolation	< 1% of 0.2% spring yield stress	~0.2% of 0.2% spring yield stress
max. average heat dissipation in dampers	< 10 $\mu$ W in 40 mK region	~0.18 $\mu$ W per damper * 8 = 1.44 $\mu$ W
antenna isolation	~ 300 dB	~250 dB
antenna resonance Q	$\approx 10^7$	$\approx 10^7$

Damping required in 6 DOF :

direction	x, y, z (N-s/m)	$\theta_x, \theta_y$ (N-s-m)	$\theta_z$ (N-s-m)
damping constant	300	0.1	0.2

Table 2: Baseline design requirements for added damping in Gravity Wave Experiment

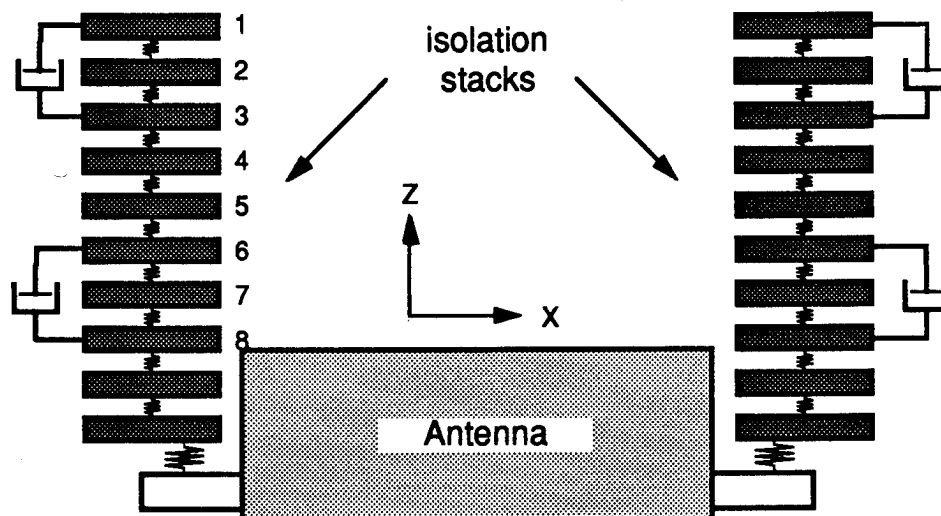


Figure 11: Baseline damping allocation for simplified model of Gravity Wave Experiment structure

number of dampers, and yet does not damp the antenna mode or compromise the isolation. Secondly, the desire to minimize RMS dynamic strains tends to demand large damping constants, whereas the requirements to minimize heat dissipation and maximize antenna isolation at the antenna resonance tend to reduce the desired damping constants.

## 5 Baseline Damping Allocation and Design Requirements

Application of the optimization procedure produced a set of baseline damping allocation requirements. The procedure was used to identify the effectiveness of using either one or two 6-DOF dampers for each isolation stack. Using two dampers per stack provided enough performance improvement, as measured by the cost function  $J_{cost}$ , to warrant the additional hardware. The baseline allocation is shown in Figure 11. Applying 6-DOF of damping between the 1<sup>st</sup> and 3<sup>rd</sup> stages, and between the 6<sup>th</sup> and 8<sup>th</sup> stages of each isolation stack was considered optimum by the procedure.

Note, that the locations identified in section 3 are quite different from the *optimum* locations obtained. One reason for this apparent discrepancy is that the criteria of antenna excitation used in section 3 was just one of three criteria used in the optimization of section 4 (see equation 56). Secondly, antenna excitation is a quantity to be *minimized* since it is used as a measure of the isolation provided to the antenna.

Table 2 compares system requirements with values obtained from the optimization procedure for the quantities specified in section 4. As discussed in section 1.2, the requirement on maximum RMS dynamic strain in the isolation springs is intended to minimize the probability of nonlinear *creaking* in the isolation system. The design value of 0.2% of

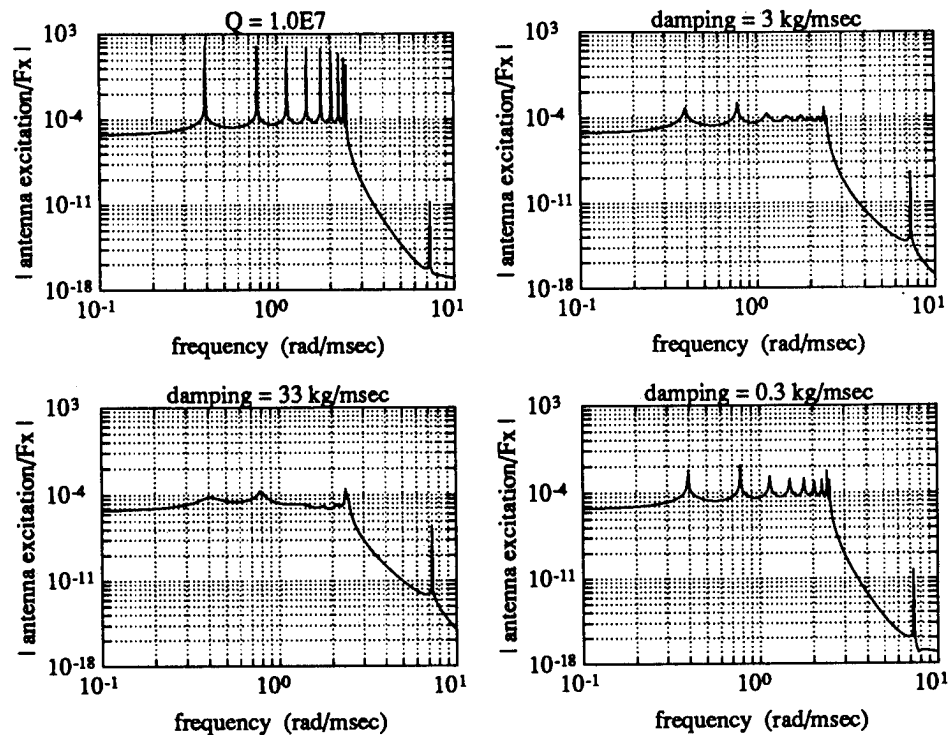


Figure 12: Frequency responses from input at top of isolation stack in  $x$ -direction to antenna excitation with added damping in baseline configuration and damping constants of: (a) 0, (b) 3 kg/msec, (c) 33 kg/msec, and (d) 0.3 kg/msec

the 0.2% yield stress is well within the 1% maximum. Assuming that the entire isolation system is enclosed in the 40 mK region, the maximum tolerable heat dissipation is  $10 \mu\text{W}$ . For the baseline design there is an energy dissipation rate as heat of about  $0.18 \mu\text{W}$  per damper, or about  $1.44 \mu\text{W}$  for all eight dampers, which is well within the requirement.

Note that the current isolation system design does not meet the isolation requirement. This condition, however, is primarily associated with the stiffness of the springs modeled. Figure 12 shows the frequency responses from a disturbance excitation at the top of the isolation stacks in the  $x$ -direction (see Figure 11) to relative motion between the antenna end faces for various damping constant values. As can be seen from Figure 12(a), even with no added damping, the isolation provided to the antenna at the antenna resonance is about 250 dB. The springs currently being designed, and which will be used for future modeling, will be made less stiff to improve the isolation. It remains to be seen to what extent the reduced stiffness impacts the ability to meet the dynamic strain requirements.

As can also be seen in Figure 12, the level of damping used at the baseline damper locations has an interesting impact upon the isolation to the antenna mode, and upon the  $Q$  of the resonant peaks in the isolation modes. Figure 12(b) shows that for a damping constant of 3 kg/msec in all translational dampers, the resonant  $Q$ 's of the isolation system are substantially reduced from  $10^7$  to about  $10^1 - 10^2$ , but the isolation to the antenna mode is reduced by 45 dB. As the damping is increased to 33 kg/msec, the isolation system's maximum resonant  $Q$ 's are reduced further to about  $10^1$ , but the isolation to the antenna is reduced by about 80 dB. Figure 12(d) shows the frequency response for the design

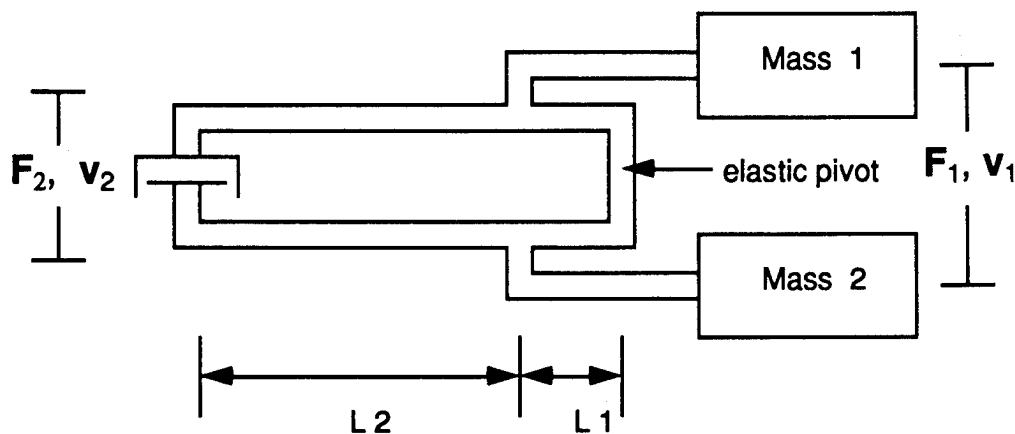


Figure 13: *Concept* for matching impedances between stiffness and damping elements

damping values given in Table 2, and indicates that the maximum isolation resonant  $Q$ 's are reduced to less than  $10^3$ , while the isolation to the antenna mode is reduced by only 24 dB. The design damping constant values provide a good compromise between resonant peak reduction in the modes of the isolation system, and the level of isolation provided to the antenna at the antenna longitudinal resonance. Note that the damping allocation is such that for all damping constant values used in Figure 12, the resonance  $Q$  of the antenna's 1<sup>st</sup> longitudinal mode deviates indistinguishably from its undamped value of  $10^7$ .

## 6 Damping–Stiffness Impedance Matching

Section 1.2 discussed issues associated with realizing damping in the Stanford Gravity Wave Experiment. This section discusses still another important damping realization issue, namely the impedance mismatch between the stiffness acting between the isolation system's masses (see section 1.1) and the damping to be used between the masses. A feature of the optimization procedure discussed in section 2.3 is the computation of RMS values for all states of the system. For the model of seismic motion used, typical RMS dynamic forces are about 0.15 – 0.5 N. Recall that these forces are associated with the stretching of the isolation springs. Typical RMS dynamic torques are about  $2(10^{-3})$  N-m. RMS relative velocities between masses of the isolation system are about  $1 \mu\text{m}/\text{sec}$ . From the standpoint of damping implementation, these quantities represent an impedance mismatch. A viscous damper which provides a comparable level of force for these velocities would require a damping constant of about  $3(10^5)$  N-sec/m. This would require the construction of a sizable damping element.

This impedance mismatch can be reduced, however. The idea, illustrated purely conceptually in Figure 13, is to use a lever mechanism to amplify the motion of interest. Consider an RMS force  $F_1$  acting between masses 1 and 2 in the figure, and an associated RMS relative velocity  $v_1$ . By using the advantage shown, the relative velocity can be am-

plified at a remote location by the leverage ratio  $L_2/L_1$ , where  $L_1$  and  $L_2$  are as shown ( $L_1 < L_2$ ). Consequently the magnified velocity is  $v_2 = \left(\frac{L_2}{L_1}\right) v_1$ . In addition, the remote force  $F_2$  which would cause the same motion between masses 1 and 2 as  $F_1$  is related to  $F_1$  by  $F_2 = \left(\frac{L_1}{L_2}\right) F_1$ . A damper sized to match the stiffness impedance at location (1) is given by  $b_1 = F_1/v_1$ , and the rate of energy dissipation resulting from this damper is given by  $\dot{E}_1 = b_1 v_1^2$ .

A damper sized to match the stiffness impedance at location (2) is given by:

$$b_2 = \frac{F_2}{v_2} = \left(\frac{L_1}{L_2}\right)^2 \frac{F_1}{v_1} = \left(\frac{L_1}{L_2}\right)^2 b_1 \quad (57)$$

and the energy dissipation rate for this damper is:

$$\dot{E}_2 = b_2 v_2^2 = \left(\frac{L_1}{L_2}\right)^2 b_1 \left(\frac{L_2}{L_1}\right)^2 v_1^2 = b_1 v_1^2 = \dot{E}_1 \quad (58)$$

Consequently, if  $L_1 \ll L_2$ , then equations (57) and (58) indicate that the same energy dissipation rate can be obtained at (2) as at (1) by using a damper with a factor of  $(L_1/L_2)^2 \ll 1$  less damping constant than used at (1).

This impedance matching concept is key to constructing reasonably sized damping elements for application to the Stanford Gravity Wave Experiment. Furthermore, because of the experiment's sensitivity to nonlinear components, it is important that the mechanism used for motion amplification have no *sloppy* joints. Hinging elements based solely upon the elastic deformation of materials, such as the concept shown in Figure 13, are consequently an important requirement.

## 7 Status / Conclusions

This paper has motivated and discussed the need for damping in the high order, cryogenically maintained, and nominally extremely lightly damped isolation system of the Stanford Gravity Wave Experiment. Issues associated with realizing damping in this system were mentioned and the selection of passive magnetically induced eddy-current damping as a baseline was discussed.

A general procedure aimed at optimally allocating and sizing viscous damping in controlled flexible structures was introduced. Characteristics of the procedure were motivated, underlying assumptions were discussed, and algorithmic details were developed. This design procedure was applied to the Stanford Gravity Wave Experiment system using a unique set of optimization criteria. The result was the specification of reasonable baseline damping allocation design requirements which provide a good compromise between the various optimization objectives.

The eddy-current dampers to be used for 6-DOF of damping in the Gravity Wave Experiment are currently being designed. The importance of a damping-stiffness structural impedance match was mentioned, and mechanisms for providing this match are being worked into the damper design process. Work is also in progress to refine the stiffness values used in modeling the system.



## References

- [1] P. F. Michelson, W. M. Fairbank, J. Henderson, K. Lane, M. S. McAshan, J. C. Price, T. Stevenson, R. C. Taber, and B. Vaughan. The Stanford Gravitational Wave Detection Program: A Plan for Observing the Next Supernova. In *International Symposium on Experimental Gravitational Physics*, August 1987.
- [2] Peter F. Michelson, John C. Price, and Robert C. Taber. Resonant-Mass Detectors of Gravitational Radiation. *Science*, 237:150-157, July 1987.
- [3] John C. Price. Optimal Design of Resonant-Mass Gravitational Wave Antennas. *Physical Review D, Particles and Fields*, 36(12):3555-3570, December 1987.
- [4] V. B. Braginsky, V. P. Mitrofanov, and V. I. Panov. *Systems with Small Dissipation*. The University of Chicago Press, 1985.
- [5] Peter Veitch. *Development and Preliminary Operation of a Cryogenic Gravitational Radiation Antenna*. PhD thesis, University of Western Australia, 1986.
- [6] F. J. Laner, editor. *Acoustic Emission*. IFI/Plenum, New York, 1979.
- [7] Ahid D. Nashif, David I. G. Jones, and John P. Henderson. *Vibration Damping*. John Wiley and Sons, 1985.
- [8] Cleve Moler, John Little, and Steve Bangert. *PRO-MATLAB<sup>TM</sup> User's Guide*. The MathWorks, Inc., 21 Eliot Street, South Natick, MA, August 1988.
- [9] Arthur E. Bryson, Jr. and Yu-Chi Ho. *Applied Optimal Control*. Hemisphere Publishing Corporation, Washington, D.C., 1975.
- [10] Leonard Meirovitch. *Analytical Methods in Vibrations*. Macmillan Publishing Co., Inc., New York, N.Y., 1967.
- [11] H. Kwakernaak and R. Sivan. *Linear Optimal Control Systems*. Wiley-Interscience, New York, 1972.
- [12] Ben Noble. *Applied Linear Algebra*. Prentice-Hall, Inc., Englewood Cliffs, New Jersey, 1969.
- [13] C. B. Moler and G. E. Forsythe. *Computer Solution of Linear Algebraic Systems*. Prentice-Hall, Inc., Englewood Cliffs, New Jersey, 1967.
- [14] A. Laub. Computation of Balancing Transformations. In *JACC*, 1980.
- [15] P. E. Gill, W. Murray, and M. H. Wright. *Practical Optimization*. Academic Press, Inc., London, England, 1981.
- [16] K. Aki and P. Richards, editors. *Quantitative Seismology : Theory and Methods*. Volume 1, Freeman and Co., 1980.

# AN INTERNAL DAMPING CONFIGURATION FOR TUBES AND HOLLOW PANELS

by

Edward M. Kerwin, Jr.  
BBN Systems and Technologies Corporation

## Abstract

The provision of an effective internal damping treatment for the bending vibrations of a hollow structure is a difficult task. This report on Work in Progress explores the possible use of a stiff-skin laminate with a thick viscoelastic core as a damping insert for a box beam. The work of Kurtze and Watters [J. Acoust. Soc. Am., 31, 739-748 (1959)] has shown that in its mid-frequency, core-shear range such a laminate has its dominant elastic energy of transverse-wave deformation in shearing of the core, with negligible extension of the stiff skins. As a result the transverse-wave loss factor of the laminate alone is the loss factor of the core, making the laminate an attractive candidate as an internal damper. Coupling to the interior of the box beam would be through normal forces driving the transverse displacement, with relative tangential displacements allowed by a "slip" layer of low shear stiffness. The analysis to date explores the wave propagation and damping properties of the composite structure (box beam plus insert). The results show that high damping could be realized if the core-shear mode of the insert laminate could be made to dominate the composite properties. Unfortunately this clear dominance would require that the coupled-skin bending stiffness of the insert greatly exceed the bending stiffness of the box beam, a result unlikely to be achieved in practice. Continuing work will explore the utility of the laminate insert under more realistic requirements. Other insert-damper configurations also await evaluation.

## 1. INTRODUCTION

The damping of bending waves of hollow structures by internal treatments has long represented a vexing problem. Standard approaches (such as simple free or constrained viscoelastic layers) are not very effective, principally because of geometric and kinematic limitations imposed by trying to work inside a structure, as well as the ever present bounds on the properties of dissipative materials. This paper is a first report on work-in-progress, and proposes a treatment concept that can in principle provide effective damping (although the required properties of the structural parts of the treatment appear to be elusive).

The particular damping treatment configuration chosen for first study is a core-shear composite adapted from the the work of Kurtze and Watters on the control of the speed of transverse waves in acoustical panels. The proposed damping treatment is unusual in that it is to be driven by the transverse displacement and normal forces (vs. interface shear forces) of the structure to be damped.

In this paper we describe the concept, illustrate its potential to provide significant elastic energy storage in the viscoelastic core, and describe the dynamic functional behavior of the components of the combined system (hollow structure plus internal damper), including the expected system loss factor. In our conclusions we note the material-properties limitations that appear to block the realization of an ideal damping treatment as first proposed. However, alternatives and further analyses are both indicated.

## 2. THE DAMPING PROBLEM CHOSEN

### 2.1 The Box Beam

The structure to be damped is the box beam of Figure 1. The walls are of equal thickness on all sides, and are thin relative to the cross dimension of the beam. We are to assume that it is important to the problem at hand that an effective level of damping be provided for the (free) bending vibrations of this beam. The objective is to be pursued aggressively, including the consideration of heroic (heavy etc.) measures.

A common first suggestion as a damping treatment for such a hollow beam is that it be filled with a dissipative material. Such an approach effectively places a simple viscoelastic beam within the structural beam. The result as is seen in Figure 2 is that the neutral planes of the two beams coincide; they undergo the same transverse displacements and rotations of cross sections. No shear is generated between the two, and the elastic energies of deformation for maximum displacement  $y_0$  at wave number  $k$  are those of individual bending as follows:

$$\begin{aligned} V_{\text{Box Beam}} &\equiv V_b = \frac{1}{4} B_b k^4 y_0^2 \\ V_{\text{VE}} &\equiv V_{\text{ins}} = \frac{1}{4} B_{\text{ins}} k^4 y_0^2 \end{aligned} \tag{1}$$

where, in each case,  $B = EI$ , the bending stiffness  
 $E$  = Young's modulus  
 $I$  = area moment of the cross section

and

$$k = \frac{2\pi}{\lambda} = \frac{2\pi f}{c},$$

the wavenumber\* of the transverse displacement, and

$\lambda$  = wave length  
 $f$  = frequency  
 $c$  = wave speed.

If we assign a loss factor  $\eta_i$  to the insert and assume the box beam is (relatively) without losses, we have for the loss factor of the composite (beam plus core damper)

$$\eta = \frac{\sum \eta_j V_j}{\sum V_j} = \frac{V_{ins}}{V_b + V_{ins}} \eta_{ins}. \quad (2)$$

For a homogeneous insert within a thin walled beam we will find

$$I_{ins} \doteq I_b \quad (3)$$

(The two are equal where the wall thickness is 0.08 times the outside dimension of the beam), and we expect that  $E_{ins} \ll E_b$ .

It then follows that  $V_{ins} \ll V_b$ ; and Eq. (2) become

$$\eta \doteq \frac{E_{ins}}{E_b} \eta_{ins}. \quad (4)$$

Thus, in this case the system loss factor is only a small fraction of that of the insert material, and such a treatment is ineffective.

An alternative suggestion that is frequently made is that one employ a structural beam as an insert, with a thin layer of viscoelastic material between it and the inside walls of the box beam. For such a treatment one argues as before that there is no relative motion generated in bending of the composite, hence no shear deformation of the viscoelastic layer, and essentially no damping.

---

\*The wavenumber  $k = 2\pi/\lambda$  is very useful in describing phenomena that are harmonic in space with spatial period  $\lambda$ . By analogy with the circular frequency  $\omega = 2\pi f = 2\pi/T$ , which describes a phenomenon that is harmonic in time with temporal period  $T=1/f$ , the wavenumber is sometimes called the spatial frequency.

## 2.2 The Shear-Core Configuration

Clearly, one needs to find a way to generate more deformation in the damping insert. The work of Kurtze and Watters<sup>1</sup> suggests such a mechanism. They were concerned about controlling the speed of bending waves in acoustical panels, because good acoustic transmission loss could be preserved if a way could be found to keep the bending wave speed below sonic speed through enough of the audible frequency range.<sup>2-4</sup> This bending-wave-speed problem had become more important with the advent of lighter, stiffer panels.

Kurtze and Watters evolved a stressed-skin panel construction (see Figure 3) in which the shear properties of the thick core placed the broad transition region between coupled-skin bending at low frequencies, and uncoupled-skin bending at high frequencies so as to keep the "bending" (i.e., transverse) wave speed subsonic, as the Figure shows. In the transition region, the panel skins appear essentially inextensible so that core shear controls the stiffness of the panel in transverse deformation. As a result, the wave speed is essentially constant at a level determined by the panel mass and the core shear stiffness. A consequence of this behavior, as Kurtze and Watters recognized, is that in the transition region the panel loss factor is essentially that of the core material. If such a "panel" could be adapted as an insert damper that could control the transverse motion of the composite (box beam plus damping insert), then high system loss factors might be realized. It is this possibility that lead us to investigate the shear-core insert.

Figure 4 sketches the desired transition-region, core-shear behavior in comparison to the simple bending insert discussed earlier and shown in Figure 2. In core-shear deformation, cross sections do not rotate but rather stay vertical and parallel. This motion is forced by the stiff skins, which must "slip" relative to the inside surface of the box beam. As a result, the core shears throughout (if it is homogenous), and the core stores an average elastic energy  $V_{CS}$  per unit length of

$$V_{CS} = \frac{1}{4}GAk^2y_o^2 \quad (5)$$

where  $G$  = shear modulus of the core  
 $A$  = cross section of the core  
 $y_o$  = maximum transverse displacement.

Comparing the elastic energies of the shear core and the viscoelastic beam inserts (See Equation 1), taking them to be made of the same material, we find

$$\frac{V_{CS}}{V_{VE}} = \frac{GA}{Bk^2} = \frac{12G}{E(kh)^2} = \frac{4}{(kh)^2} \text{ (Large)}. \quad (6)$$

Note that the ratio is large because for simple bending of the system we would find  $(kh)^2 = (2\pi h/\lambda)^2$  to be small relative to unity. Thus the shear core can store much more elastic energy than a viscoelastic beam of the same material.

As we noted earlier, the shear core laminate has three distinct free transverse wave types in different frequency ranges:

low frequency: coupled-skin bending with dominant elastic energy in stretching of the skins

$$V_{BC} = \frac{1}{4} B_c k^4 y_o^2 \quad (7)$$

transition region: core-shear transverse deformation with dominant elastic energy in core shear; skins essentially inextensible

$$V_{CS} = \frac{1}{4} G A k^2 y_o^2 \quad (8)$$

high frequency: uncoupled skin bending with dominant elastic energy in the bending of the two skins

$$V_{BU} = \frac{1}{4} \cdot 2B_{skin} k^4 y_o^2 \quad (9)$$

These regions are indicated asymptotically in Figure 5 as wavenumber vs. frequency. In each of the bending regions, coupled bending (BC) at low frequencies and uncoupled bending (BU) at high frequencies, the bending wave speed increases as  $f^{1/2}$ . In the transition region (if it is broad enough), the wavespeed is essentially constant so that wavenumber increases as  $f$ .

The "break" frequencies between these regions occur at wavenumbers  $k_I$  and  $k_{II}$ , at which the elastic energies for the two adjacent transverse wave types would be equal. That is, where

$$V_{BC} = V_{CS},$$

$$k^2 = k_I^2 = \frac{GA}{B_c},$$

and where

$$V_{CS} = V_{BU},$$

$$k^2 = k_{II}^2 = \frac{GA}{B_u} = \frac{GA}{2B_{skin}}. \quad (10)$$

It follows that the transition range of core-shear behavior in wavenumber and in frequency is

$$\frac{f_{II}}{f_I} = \frac{k_{II}}{k_I} = \frac{B_c}{2B_{skin}}^{1/2}. \quad (11)$$

Kurtze and Watters, see Figure 3, showed a panel design with a transition range of two decades. A little thought shows that a broad range should also, in principle, be achievable in a damping insert.

### 3. THE COMPOSITE BOX BEAM WITH SHEAR CORE INSERT

Figure 6 shows the composite beam that we wish to consider; a stressed-skin insert with a viscoelectric shear core placed as a damper within the box beam. The "slip" interface that is required between insert and box beam is assumed to transmit normal forces between the two, but to allow relative shear displacement with only minimal shear stresses. For the moment, let us assume that this is accomplished with a thin layer having a low shear modulus.

#### 3.1 Component Impedances for Transverse Motion

In determining the characteristics of the composite beam in bending, i.e., its wavenumber (or wavespeed) and loss factor, we require the impedances of both box beam and insert for transverse motion. In either case, the impedance is the ratio of a transverse force at wavenumber  $k$  and frequency  $f$  to the resulting transverse velocity at  $k$  and  $f$ . For a beam in simple bending one has

$$Z_p = i \frac{Bk^4}{\omega} [1 - (k_p/k)^4] = -i\omega m [1 - (k/k_p)^4] \quad (12)$$

where  $B$  = Bending stiffness (ratio of bending moment to resulting curvature)

$m$  = Mass per unit length of the beam, and

$k_p^4 = \omega^2 m / B$ , the wavenumber of free bending waves.

With the appropriate parameters  $B$  and  $m$ , this expression also describes the impedance of the insert in its bending regimes at low and high frequencies. Since our convention here is a time dependence  $e^{-i\omega t}$ , positive reactance represents stiffness, and negative reactance represents mass.

The condition for the propagation of free waves is that the impedance go to zero (in the case of losses, one sets the imaginary part equal to zero). Thus the wavenumber for free bending waves is  $k_p$ , as defined above.

The impedance expression of Equation (12) shows that at a given frequency one finds the following:

$k < k_p$  ,  $Z_b \rightarrow$  mass reactance

$k > k_p$  ,  $Z_b \rightarrow$  stiffness reactance

The physical interpretation of these results is that if we try to bend a beam dynamically at a wave length longer than its freewave length ( $k < k_p$ ), its behavior is as a mass. Correspondingly, if we try to bend the beam at a wavelength shorter than its free wavelength ( $k > k_p$ ), it appears as a stiffness that increases rapidly with increasing  $k$ .

For the insert in its core-shear region, we can show that the transverse impedance is the following:

$$\begin{aligned}
 Z_{cs} &= i \frac{GAk^2}{\omega} [1 - (k_s/k)^2] \\
 &= -i\omega m_s [1 - (k/k_s)^2]
 \end{aligned}
 \tag{13}$$

where  $k_s = \omega^2 m/GA$ , the free wavenumber.

For the insert in core-shear the wave-number dependence of the impedance at a frequency is qualitatively like that of the bending beam, that is, a massive reactance for  $k < k_s$  and stiffness reactance for  $k > k_s$ . However, the variations with  $k$  are less rapid than for the beam (see the following section).

### 3.2 Characteristics of the Composite Beam

In Figure 7 we show the wavenumber dependence of the beam and shear core impedances. Each impedance is normalized by  $\omega m$ , the mass reactance at the frequency considered, i.e., the transverse reactance found as  $k \rightarrow 0$ , simple transverse translation. Here  $m$  represents  $m_b$  or  $m_s$ . Also, each reactance is plotted as a function of the wavenumber relative to its respective free wavenumber. In each case, the reactance is massive approaching  $\omega m$  for small wavenumber, and dropping to zero at the free wave-number.

Above the free wavenumber, the reactance is stiff, and increases rapidly with  $k$ . This is especially true for the bending beam (note the right-hand scale which is compressed 100 times relative to the left-hand scale. Also note that the stiffness reactance for the shear core is plotted at 10 times its value, i.e., the reactance itself has a value of 10 where the right hand scale shows  $10 \times \text{Insert} = 100$ ).

To illustrate the desired behavior of the shear-core insert as a damper in the box beam, we show the free wavenumber characteristics of both as functions of frequency in Figure 8. The three characteristics appear for the shear core, the core-shear branch being the one of principal interest for damping. In each case, the nature of the transverse impedance is indicated qualitatively as "S" for stiffness above the free wavenumber line, and "M" for massive below. The relative frequency and wavenumber scales are each unity at the crossover "c" of the beam and core-shear characteristics.

The free-wavenumber characteristic for the composite beam will lie between the box-beam characteristic and the dominant characteristic of the insert, i.e., the one closest to the beam characteristic at the frequency of interest. (The true insert characteristic will fair smoothly from one of its branches to another. The asymptotic lines are being used here to illustrate the behavior.)

Figure 9 shows the combined wavenumber-frequency characteristic for the composite beam. In the region well below  $f_c$ , the crossover of box-beam bending and insert core shear, the composite approaches a line lying above the core-shear characteristic, by the following factor



$$\begin{aligned}
 k/k_s &\rightarrow (1 + m_b/m_s)^{1/2} \\
 \eta &\rightarrow \eta_s \qquad f \ll f_c
 \end{aligned}
 \tag{14}$$

and the expected composite loss factor approaches  $\eta_s$ , that of the shear core. This happy result depends, however, on the assumption that the insert behavior is controlled by core shear, and that the transition to coupled-skin bending lies far enough below the frequency and wavenumber range shown. (See Conclusions below.)

At frequency  $f_c$  the free wavenumber of the composite coincides with those of the box beam and the insert individually. Because only the insert has significant losses, the composite loss factor is

$$\eta = \eta_s / (1 + m_b/m_s), \quad f = f_c. \tag{15}$$

That is, the composite loss factor is reduced by the ratio of insert mass to total mass at this crossover frequency. This result is indicative of the relative vibrational energies in the two components of the composite.

Again, as shown in Figure 9, at frequencies well above  $f_c$ , the stiffness of the box beam controls, and

$$\begin{aligned}
 k/k_b &\rightarrow (1 + m_s/m_b)^{1/4} \\
 \eta/\eta_s &\rightarrow \frac{f_c/f}{[(m_b/m_s)(1 + m_b/m_s)]^{1/2}} \qquad f \gg f_c
 \end{aligned}
 \tag{16}$$

In this high-frequency region where the box-beam bending dominates progressively, the composite loss factor decreases inversely with frequency; and again the system mass parameters conveniently describe the results.

The loss factor variation over the frequency range  $0.1 f_c$  to  $10 f_c$  is shown in Figure 10 as the ratio of composite loss factor to  $\eta_s$ . The result presented is for the example  $m_s = m_b$ , i.e., the insert and box beam have equal mass. The performance shown represents a significant fraction of the core loss factor and can be realized if, as we have assumed, the core-shear properties of the insert are effective over the frequency range, especially at the lower frequencies.

#### 4. EVALUATION AND CONCLUSIONS

In this preliminary assessment of the damping potential of the shear core insert we have used asymptotic expressions to characterize the insert. Our focus has been on the interaction between the box beam and the insert in the frequency region in which core shear dominates the behavior of the insert.

Implicit in this approach are several assumptions about the insert's characteristics -- namely,

- a) that core shear dominates over a broad frequency range so that the expected high levels of damping will be realized over a sufficient bandwidth, and
- b) that the lower break frequency  $f_I$  between core shear and coupled-skin bending (at lower frequencies) lies well below  $f_c$  where the core-shear freewave characteristic intersects the box-beam free bending wave characteristic (see Figure 8).

The first of these does not of itself appear troublesome. As we saw in Figure 3, Kurtze and Watters demonstrated a core-shear region (actually a spread between break frequencies) of two decades in frequency.

On the other hand, the second assumption imposes the requirement that

$$\left(\frac{B}{m}\right)_{\text{insert coupled-skin}} \gg \left(\frac{B}{m}\right)_{\text{box beam}} .$$

This is indeed a condition that may prove difficult, if not impossible to meet. Further, the damping results of Equations 14-16 as indicated in Figure 10 show that the mass of the insert must not be too small, and probably should be comparable to the mass of the box beam. Thus, a requirement for effective damping may be

$$B_{\text{insert coupled-skin}} \gg B_{\text{box beam}} .$$

Energy arguments would support such a result.

It would be difficult to achieve a coupled-skin bending stiffness of the insert that is much larger than the bending stiffness of the box beam particularly since the insert must fit within the box beam. (We note that the coupled-skin bending stiffness varies approximately as

$$B_{\text{coupled-skin}} \sim E_{\text{skin}} h_1 h_2^2$$

so that the core thickness is a strong determinant of the bending stiffness. The box beam is assumed to be made of a material with high elastic modulus, so that  $E_{\text{skin}}$  cannot be very large in comparison.)

It appears unlikely that the idealized conditions first assumed can be realized. (i.e.,  $B_{\text{insert}} \gg B_{\text{box beam}}$ ). However, the damping achievable with less extreme requirements should be determined in the continuing work. In addition, the simple shear-core configuration is only one of several damping insert designs presently under consideration.

Incidentally, we note that since the shear-core configuration is driven by the lateral motion of the beam-to-be damped, its performance is not dependent on its being inside the beam. Thus there may be cases in which an external core-shear damping treatment (with its dimensions not restricted by the inner dimensions of a hollow beam or panel) may prove effective.

#### ACKNOWLEDGMENT

Support for this work has been provided by the Science Development Program of the BBN Systems and Technologies Corporation. The author is also grateful to his colleague, P.W. Smith, Jr., for a number of helpful discussions.

Note: The damping treatment considered here is one of several that are the subjects of a pending patent.

#### REFERENCES

1. Kurtze, G., and B.G. Watters, "New Wall Design for High Transmission Loss or High Damping", *Journal of the Acoustical Society of America* 31, 739-748 (1959).
2. Cremer, L., *Akustische Zeitschrift*, 7 p. 81 (1942).
3. See discussion in L. Beranek, Ed., *Noise Reduction*, McGraw-Hill, New York 1960 (p. 290,ff).
4. Cremer, L., M. Heckl, E.E. Ungar, *Structure-Borne Sound*, Second Edition, Springer-Verlag, New York (1988).

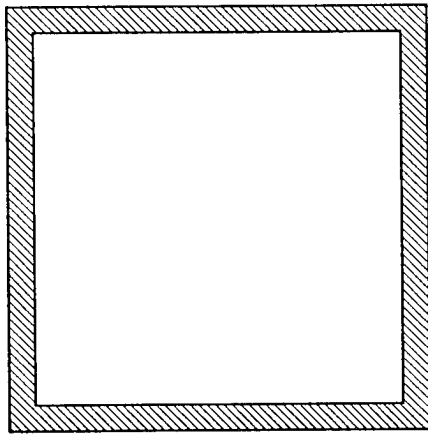


Fig. 1. Box beam.

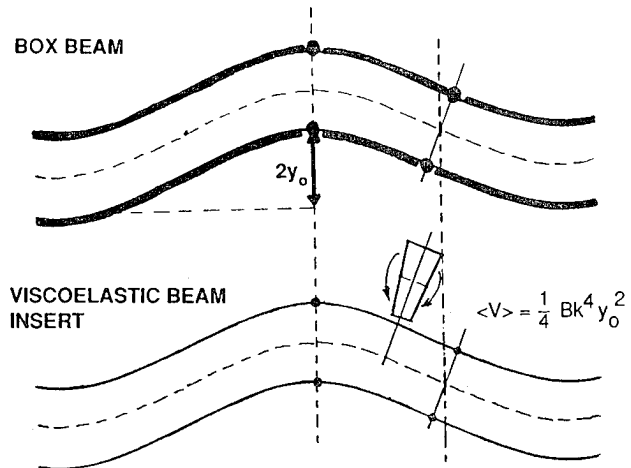


Fig. 2. Bending deformations of box beam and of viscoelastic beam insert.

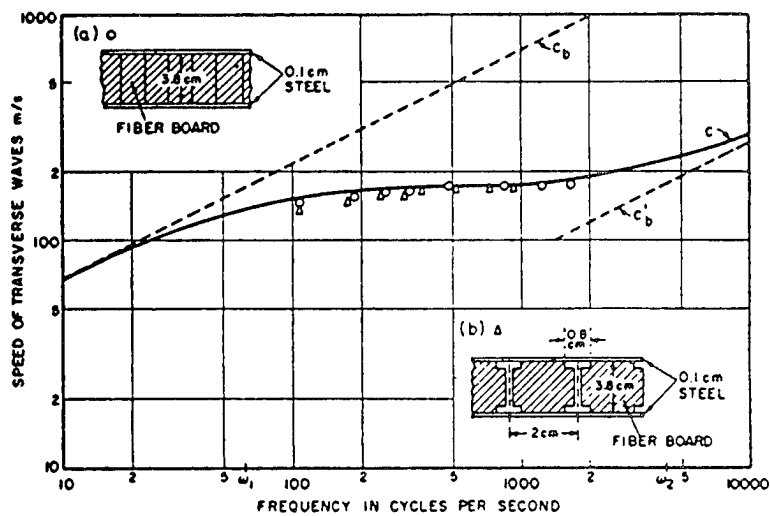


Fig. 3. Experimentally determined transverse wave speed versus frequency, for sandwich bars of wood fiber-board cores and steel skins. (a) For core material arranged with the grain perpendicular to bar (for lowest shear stiffness). (b) For grain of core layer parallel to axis of bar, shear stiffness reduced by cutouts (Kurtze and Watters, Ref. 1).

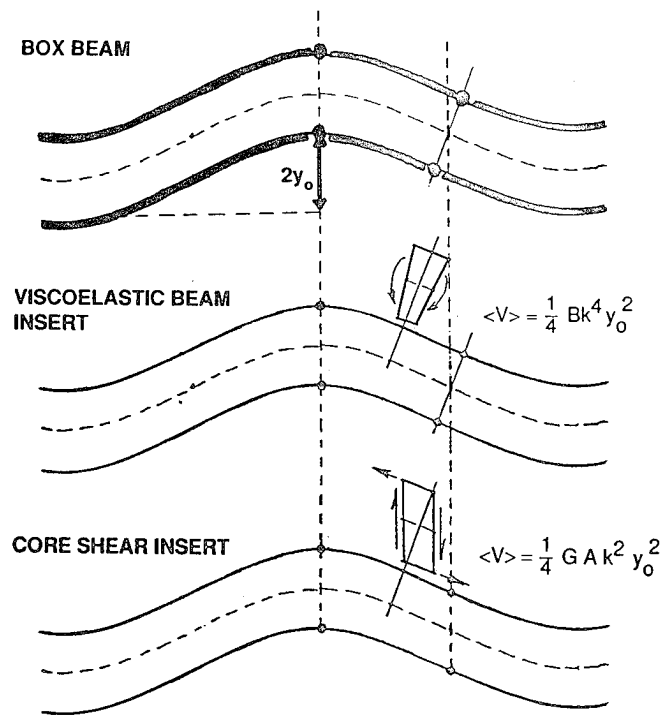


Fig. 4. Transverse deformation of box beam, viscoelastic beam, and core shear insert.

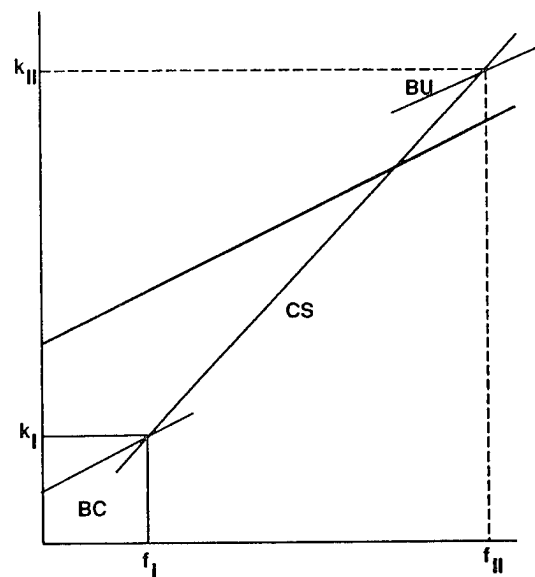


Fig. 5. Transverse wavenumber regimes for shear-core insert; BC; coupled-skin bending, CS; core shear, BU; uncoupled-skin bending.

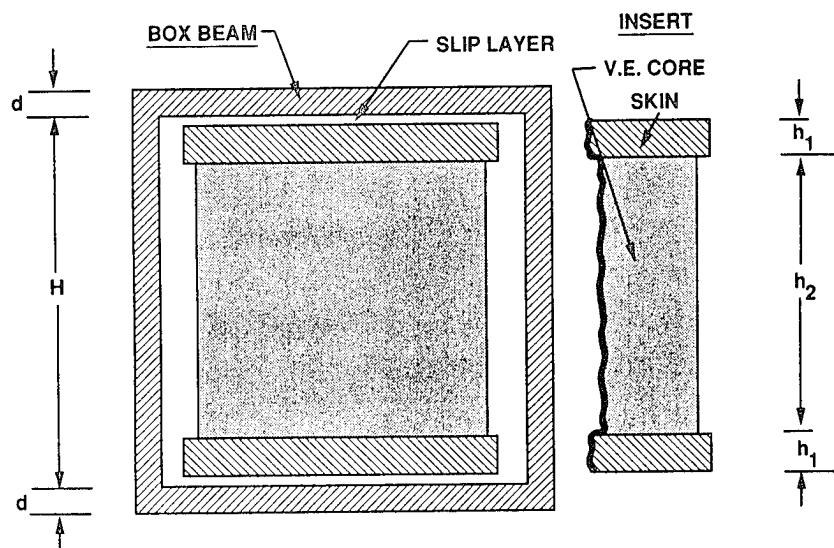
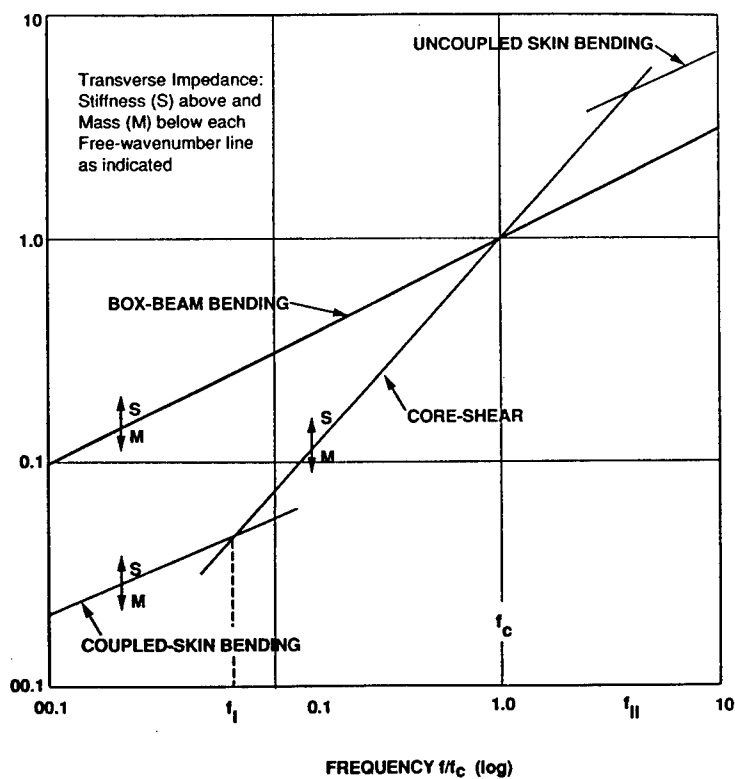
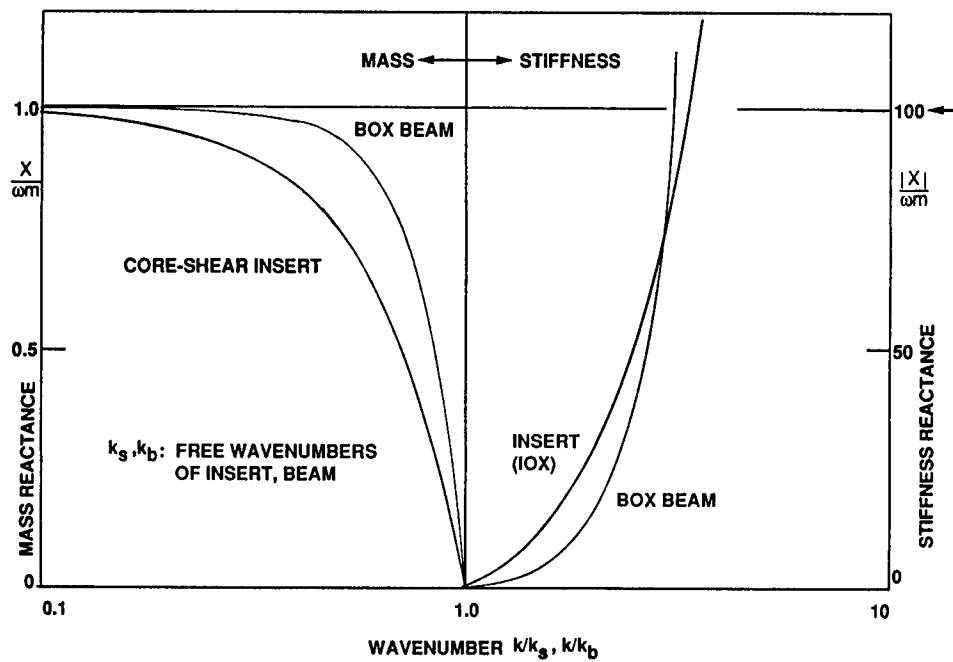


Fig. 6. Core-shear insert damper for box beam.



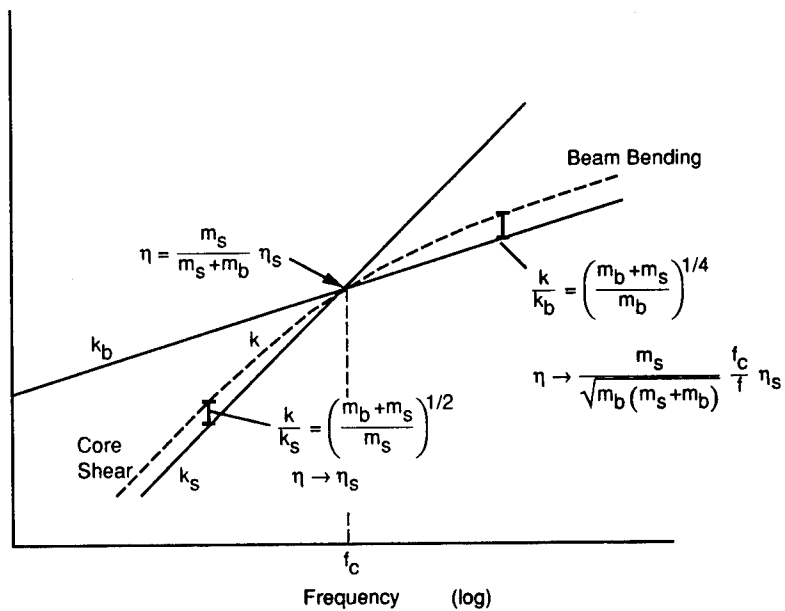


Fig. 9. Wavenumber  $k$  of the box beam with core shear insert.

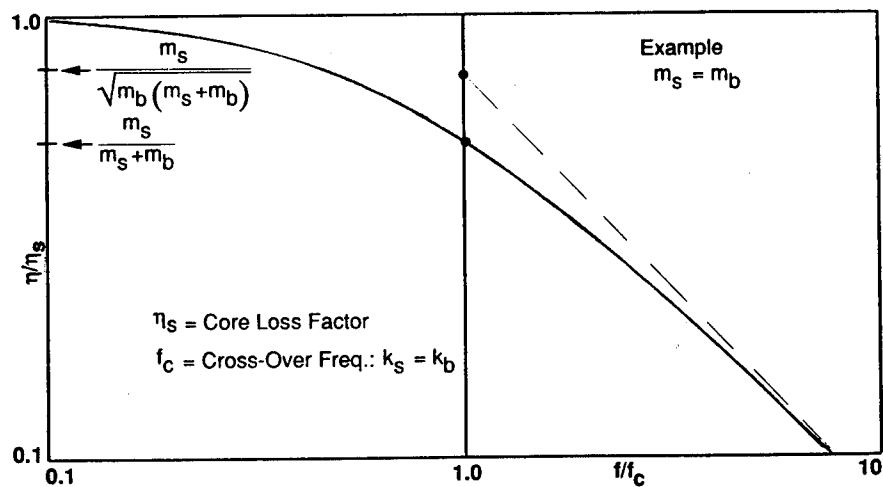


Fig. 10. Box beam with core-shear insert. Relative loss factor  $\eta/\eta_s$  vs frequency.

## ACTIVE VIBRATION CONTROL OF FLEXIBLE STRUCTURES

S. P. Sun, P. K. Raju, and Malcolm J. Crocker

Department of Mechanical Engineering  
Auburn University, Auburn, AL 36849

### ABSTRACT

There has been an increasing interest in the active vibration control of structures. This paper is concerned with the development of a computer simulation model for characterizing and controlling the elastic motion of a flexible structure. Active control techniques are used for suppressing the vibration of the structure at designated locations. The effect of control "spillover" on the performance of the vibrating system is also studied. The method is capable of performing time-domain analysis which is essential for making performance evaluations of active control systems. The generality of the model offers a powerful tool for performing simulation studies to gain more insight into the behavior of active control of structural systems.



## INTRODUCTION

There has been an increasing interest in active vibration control of structural systems. Vibration control is of importance in many areas of engineering, such as aerospace, civil and mechanical<sup>1,2,3</sup>. In space applications the structures are large, lightweight and flexible. The vibration in these structures can be caused by power plant excitations, maneuvering loads and firing loads. Unless special care is taken to minimize and damp such vibrations their functional activity like pointing and aiming accuracy will be affected. It is likely that both passive and active damping and control measures must be aggressively studied and designed<sup>4</sup>.

Several investigators<sup>5,6,7</sup> have studied the general problem of vibration suppression of structural systems wherein the concepts of active vibration control is utilized. An active control technique using mobility symmetry relations is developed in reference 8 for plate vibrations. A general approach for establishing active vibration control of flexible systems is presented in reference 9.

The dynamics of controllers based on active modal control theory are complex and difficult to solve. Balas<sup>10,11</sup> applied the linear state variable feedback control theory to solve this problem. This method is based on linearized dynamics of the elastic structure. The elastic structure is represented by linearly independent eigenfunctions. Modal expansion techniques are then used to derive a closed form solution of the differential equations of the linear structure.

The active vibration control of the structure may be simulated using the concept of single-input, single output (SISO) control which implies a single-sensor and single-actuator. A simulation model is developed for actively controlling the vibrations of a structure at a designated point. Active vibration control of the structure is obtained using optimal feedback control<sup>12</sup>. The model is capable of performing time domain analysis and is also used to study the 'spillover' effect of single actuator-sensor control for a large flexible structure.

## PROBLEM FORMULATION

The space structure is modeled as a clamp-free beam. We consider the problem of suppressing the transverse vibration of this beam. The beam dynamics is modeled using the Euler-Bernoulli partial differential equation<sup>10,11</sup>.

$$M \ddot{U}(x,t) + A U(x,t) = F(x,t). \quad (1)$$

$M$ ,  $A$  are the mass and stiffness matrices. They are symmetric, positive definite matrices.  $U(x,t)$  is transverse displacement of the beam and  $F(x,t)$  is applied force distribution. In Eq. (1) damping has been neglected. Eq. (1) can be written in the form,

$$\ddot{U}(x,t) + (A/M) U(x,t) = B f(t). \quad (2)$$

The control forces provided by  $N$  actuators with influence functions  $b_i(x)$  is given by

$$F(x,t) = B f(t) = \sum_{i=1}^N b_i(x) f_i(t). \quad (3)$$

The solution of Eq. (1) can be represented as

$$U(x,t) = \sum_{k=1}^L U_k(t) \phi_k(x), \quad (4)$$

where  $L$  is the mode shape number,  $U_k(t)$  is the mode amplitude,  $\phi_k(x)$  is the corresponding eigenvector. Then Eq (1) can be shown to be

$$\ddot{U}(t) + \Lambda U(t) = B f(t), \quad (5)$$

where  $\Lambda = (\Lambda^{1/2})^2$  and  $\Lambda^{1/2}$  is a  $L \times L$  diagonal matrix with  $\omega_1, \omega_2, \omega_3, \dots, \omega_k, \dots, \omega_L$  as diagonal entries. Where  $\omega_k$  is the natural frequency of the structure.

Now introducing the state vector as

$$V_k(t) = [U_k^T(t), \dot{U}_k^T(t)]^T, \quad (6)$$

then Eq (5) can be written as

$$\dot{\hat{V}}_k(t) = A_k V_k(t) + B_k f(t). \quad (7)$$

Where

$$A_k = \begin{bmatrix} 0 & I_k \\ -\Lambda_k & 0 \end{bmatrix}, \quad B_k = \begin{bmatrix} 0 \\ B_L \end{bmatrix}. \quad (8)$$

$B_L$  is the eigen vector for the chosen mode and  $I$  is the identity matrix. Eq. (7) represents the estimate state of dynamics of the flexible structure. The actual response of the structure is determined by the controlled modes (given by the estimate state) and the residual (uncontrolled) modes.

The residual mode state can be expressed as

$$V_R(t) = [U_R^T(t), \dot{U}_R^T(t)]^T, \quad (9)$$

and similarly

$$\dot{\hat{V}}_R(t) = A_R V_R(t) + B_R f(t). \quad (10)$$

Where

$$A_R = \begin{bmatrix} 0 & I_R \\ -\Lambda_R & 0 \end{bmatrix}, \quad (11)$$

and

$$B_R = \begin{bmatrix} 0 \\ B_R \end{bmatrix}. \quad (12)$$

The system output can then be written as

$$y(t) = C_k V_k(t) + C_R V_R(t), \quad (13)$$

where  $C_k$  and  $C_R$  are linearized output constants and are represented by diagonal matrices.

## MODAL CONTROL

The control force is developed using a well known state variable method for the system ignoring the residual modes. The active controller consists of two parts.

(1) A state estimator which accepts the measurements from the sensor and produces the estimate of the state.

(2) A linear state variable feedback law which produces the control force by using the product of the state estimate and a constant gain. The control force can be written as

$$f = -G V_k, \quad (14)$$

where  $G$  is the matrix of control gains. The control gains may be obtained by using a pole placement algorithm or can be designed using an optimum regulator to minimize a certain performance index.

## EFFECT OF RESIDUAL MODES

Most of the work on active vibration<sup>6,7,8</sup> control of structures is performed by ignoring the residual modes. However in many of the systems the residual modes are found to exist and hence it is important to study their effect. The feed back control will stabilize selected modes of the flexible system but the actuators will excite the (uncontrolled) residual modes. In structural systems, such control "spillover" can severely degrade the system performance.

The composite closed-loop system state may be written as

$$W(t) = [Z_k^T(t), V_R^T(t)]^T \quad (15)$$

where

$$Z_k(t) = [V_k^T(t), e_k^T(t)]^T \quad (16)$$

Where  $e_k$  is the reconstruction error. Following reference 12 the composite closed-loop system equations may be written as follows:

$$\dot{W}(t) = \begin{bmatrix} H_{11} & H_{12} \\ H_{21} & H_{22} \end{bmatrix} W(t) \quad (17)$$

Where

$$H_{11} = \begin{bmatrix} A_k + B_k G_k & B_k G_k \\ 0 & A_k - K_k C_k \end{bmatrix} \quad (18)$$

$$H_{12} = \begin{bmatrix} 0 \\ k_k C_R \end{bmatrix}, \quad H_{21} = [B_R G_k, B_R G_k]$$

$$H_{22} = [A_R]$$

If the observation spillover is zero, then  $H_{12} = 0$ . In this case the poles of the composite closed loop system are the poles of  $A_k + B_k G$ ,  $A_k - k_k C_k$  and  $A_R$  due to block triangularity.

Equation 17 can be written as:

$$\dot{\bar{W}}(t) = \begin{bmatrix} A_k + B_k G_k & B_k G_k & 0 & v_i \\ 0 & A_k - k_k C_k & 0 & e_k \\ B_R G_k & B_R G_k & A_R & v_R \end{bmatrix} \quad (19)$$

The response of the residual mode system is given by

$$\hat{v}_R(t) = A_R v_R + B_R G_k [v_k(t) + e_k(t)] \quad (20)$$

Since the response of the system depends on both controlled and residual modes, the excitation of the residual modes can degrade the system response but it cannot destabilize the system.

The most convenient method of eliminating observation spillover is to prefilter the sensor data using a set of narrow bandpass filters<sup>13,14</sup>. Once the observation spillover is removed the feedback controller cannot produce instabilities in the closed loop system.

A block diagram of active control of a flexible structural system is shown in Fig. 1. The effect of spillover is shown in the diagram.

#### NUMERICAL EXAMPLE

The vibrating system is modeled as a clamp-free beam. Sensors and actuators are located at certain positions on the beam. From Equations 7 and 8, the system equations for control of the first three modes of the structure may be written as follows.

$$\dot{V} = \begin{bmatrix} \dot{U}_1 \\ \dot{U}_2 \\ \dot{U}_3 \\ \ddot{U}_1 \\ \ddot{U}_2 \\ \ddot{U}_3 \end{bmatrix} = \begin{bmatrix} \begin{bmatrix} 0 \end{bmatrix}_{3 \times 3} & \begin{bmatrix} I \end{bmatrix}_{3 \times 3} \\ -\omega_1^2 & 0 & 0 & \begin{bmatrix} 0 \end{bmatrix} \\ 0 & -\omega_2^2 & 0 & \begin{bmatrix} 0 \end{bmatrix} \\ 0 & 0 & -\omega_3^2 & \begin{bmatrix} 0 \end{bmatrix}_{3 \times 3} \end{bmatrix} \begin{bmatrix} U_1 \\ U_2 \\ U_3 \\ \dot{U}_1 \\ \dot{U}_2 \\ \dot{U}_3 \end{bmatrix} + B_k f(t) \quad (21)$$

and

$$f(t) = -G_k V_k. \quad (22)$$

Where  $G_k$  is the control gain and  $V_k$  is the state vector obtained from measurement.

The natural frequencies and the material properties of the clamp-free beam are given in Table 1. This system equation can be applied for either single-sensor, actuator control or multi-sensor, multi-actuator control. Fig. 2 shows a schematic of the control system for the structure with a single sensor and a single actuator. Then for this system  $B_k$  in equation [15] may be written as,

$$B_k = [0, 0, 0, \phi_1(x), \phi_2(x), \phi_3(x)]^T \quad (23)$$

where  $\phi_i(x)$  ( $i=1,2,3,\dots$ ) is the mode shape at location  $x$ .

$$G_k = [0, 0, 0, 2\xi_1\omega_1, 2\xi_2\omega_2, 2\xi_3\omega_3], \quad (24)$$

where  $\xi$  is the damping ratio obtained by active control. Structural damping of the beam is neglected in order to highlight the effect of active control. Figures 3, 4, and 5 show the system's response for the first three modes. Fig. 6 shows the displacement measured by the sensor at a point which is at a specified distance from the fixed end [Fig. 2].

The effect of using an active controller, is also clearly presented in Fig. 3, 4, and 5. Fig. 6 shows the effect of the active controller at a point where the sensor is located on the cantilever beam. From Fig. 6 we can observe how effectively the vibrations of the beam are controlled. This result supports the fact that pointing precision of space structures can be improved and their life extended by use of active control methods.

#### EFFECT OF CONTROL SPILLOVER

The control force may excite the uncontrolled modes (residual modes) which result in an unwanted excitation. From Eq. 20, the residual mode subsystem is given as,

$$\ddot{U}_R(t) + A_{RR} \dot{U}_R(t) = B_{Rk} G_k [V_k(t) + e_k(t)] . \quad (25)$$

This is a system of oscillators, driven by  $V_n(t)$  and  $e_n(t)$ . Hence any control spillover will excite these residual modes at their resonance frequencies, since the response of the complete system depends both on the controlled and uncontrolled modes. In the actual case, the physical system would have certain natural damping which may cause the unwanted excitation at residual modes to die out. Consequently the effect of control spillover is only to extend the system response time. The spillover effect of the uncontrolled modes on the structure is shown in Fig. 7.

### CONCLUSION

A mathematical model for the study of the dynamics of a flexible system has been developed. Mathematical (IMSL) software and computer simulation techniques are employed to characterize the elastic motion of a flexible structure. Active control techniques are then used for suppressing vibrations at some designated points in the vibrating system.

The method is capable of performing time-domain analysis, which is necessary for performance evaluation of an active control system. The generality of this scheme offers a powerful tool for performing numerical studies to gain more insight into the behavior of such systems.

PARAMETER	VALUE
Young's Modulus	7.238x10 Pa
Length	36 in
Mass	6.22x10 Kg
Natural Frequency (1st mode)	1.19 rad/sec
Natural Frequency (2nd mode)	7.492 rad/sec
Natural Frequency (3rd mode)	20.97 rad/sec
Sensor Location	30 in
Force Actuator Location	20 in
Initial Condition of U1	0.5 in
Initial Condition of U2	0.5 in
Initial Condition of U3	0.5 in

Table 1 PROPERTIES OF ACTIVE CONTROL SYSTEM



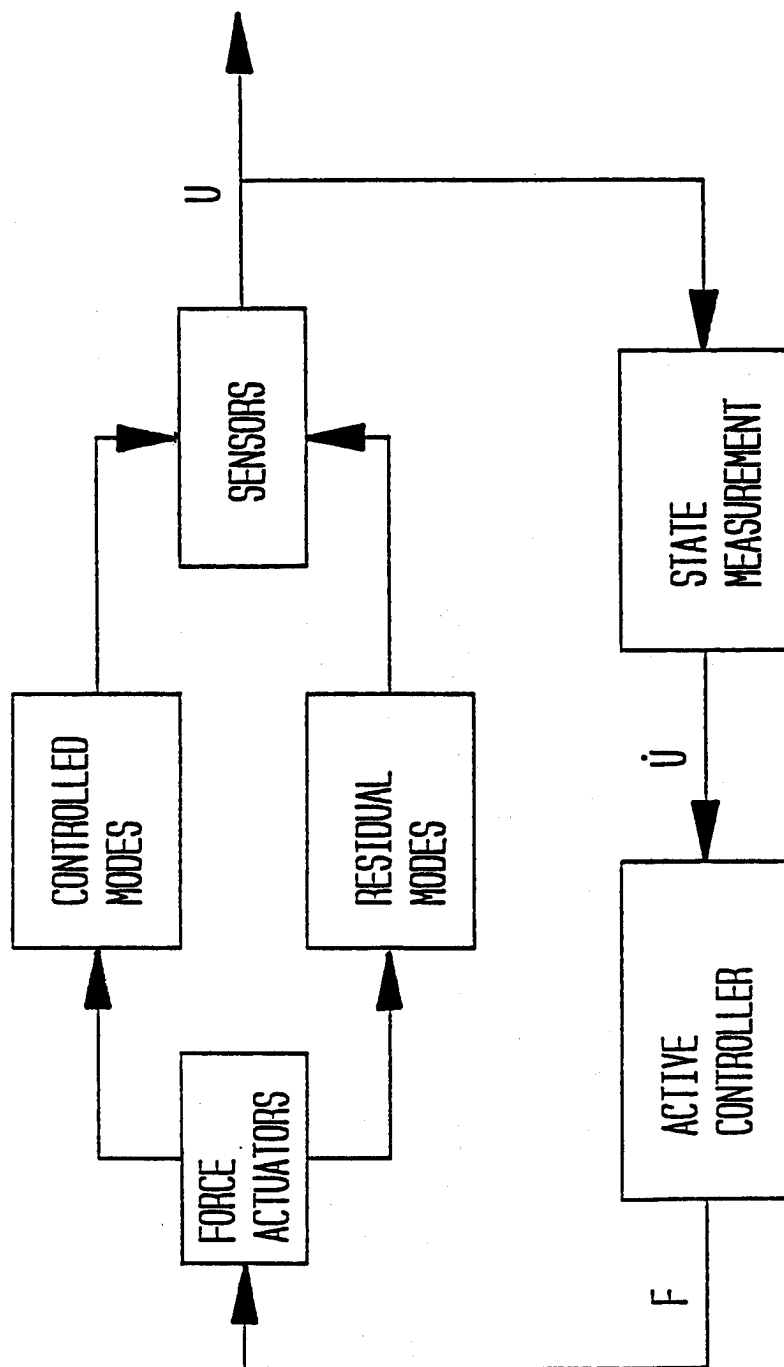


Fig. 1 BLOCK DIAGRAM OF THE ACTIVE CONTROL SYSTEM

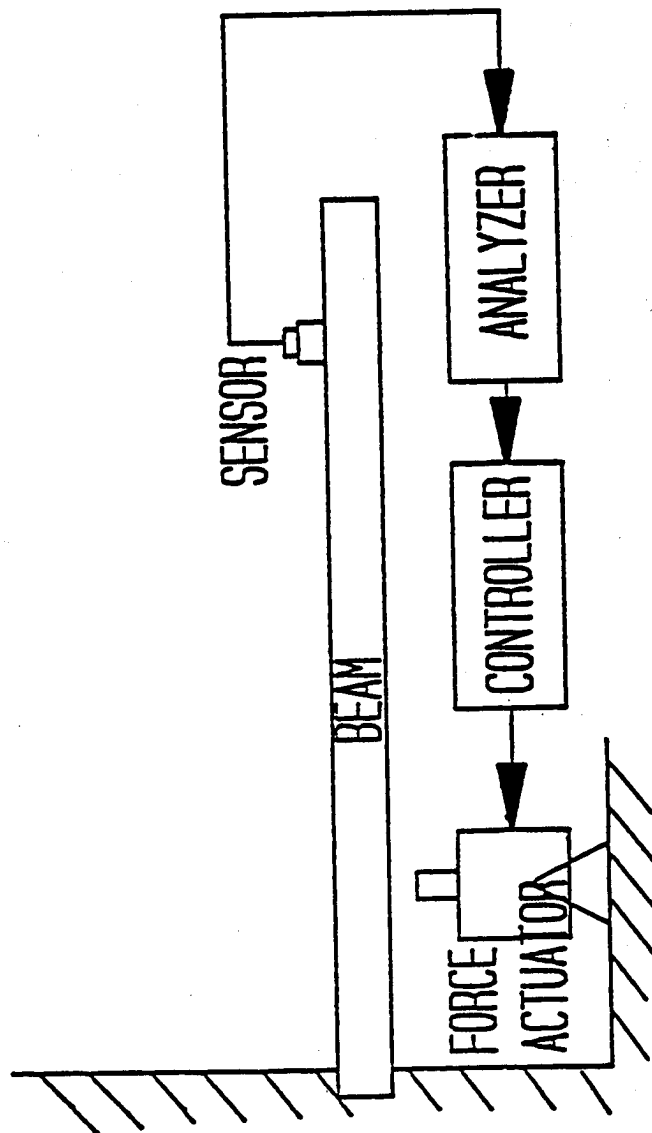


Fig. 2 SCHEMATIC DIAGRAM OF THE ACTIVE CONTROL SYSTEM

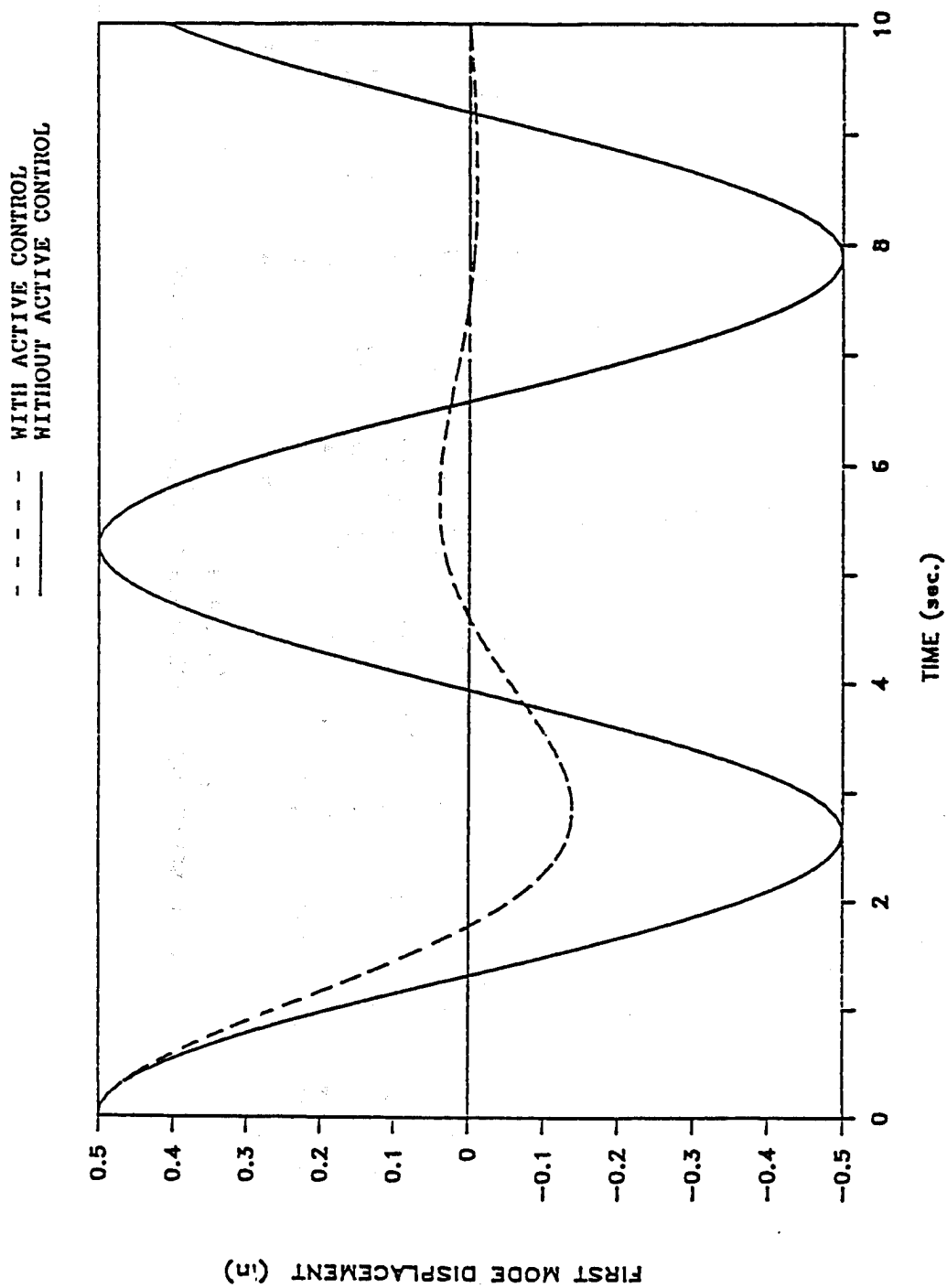


Fig. 3 EFFECT OF ACTIVE CONTROL OF THE FIRST MODE

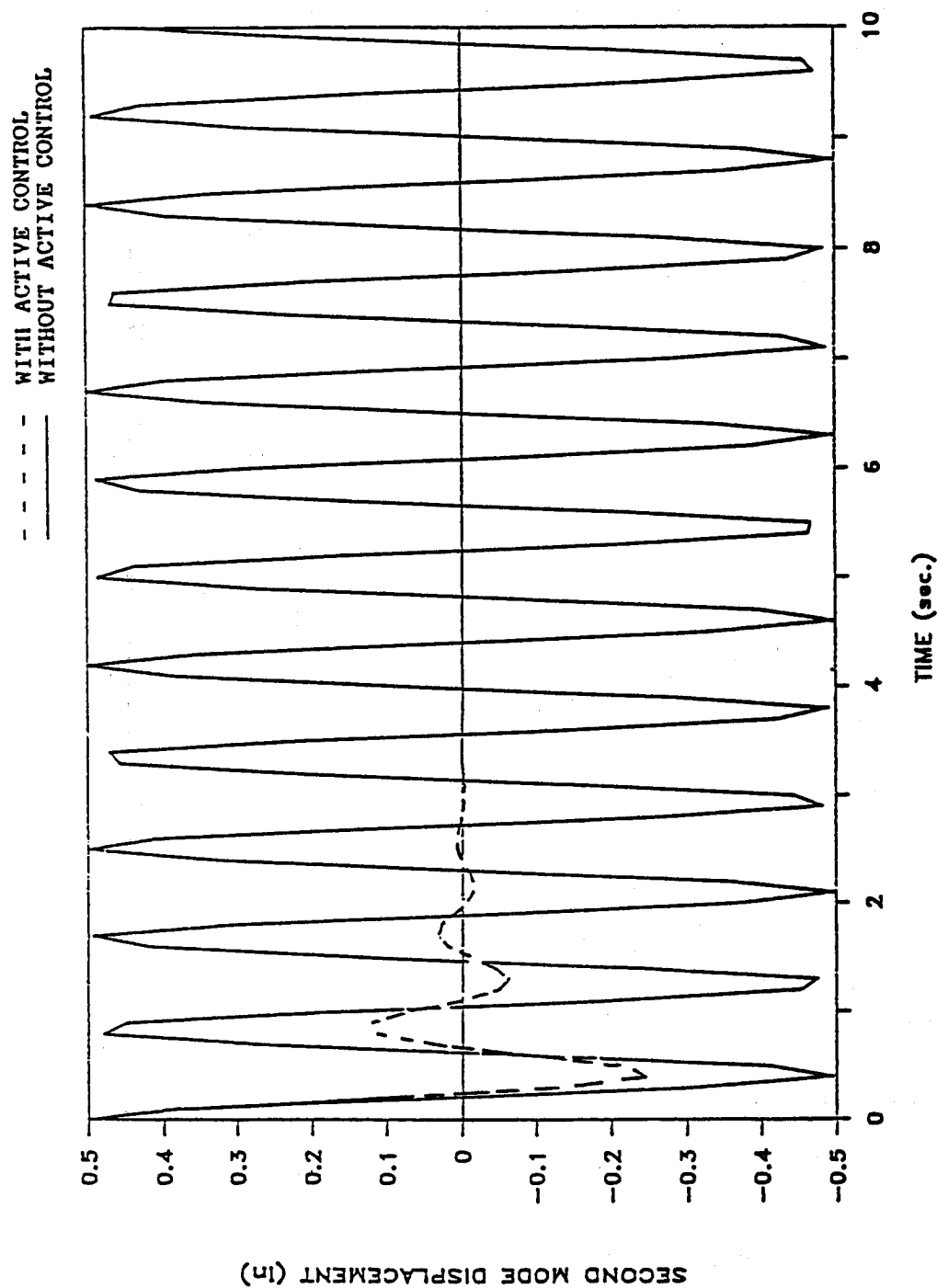


Fig. 4 EFFECT OF ACTIVE CONTROL OF THE SECOND MODE

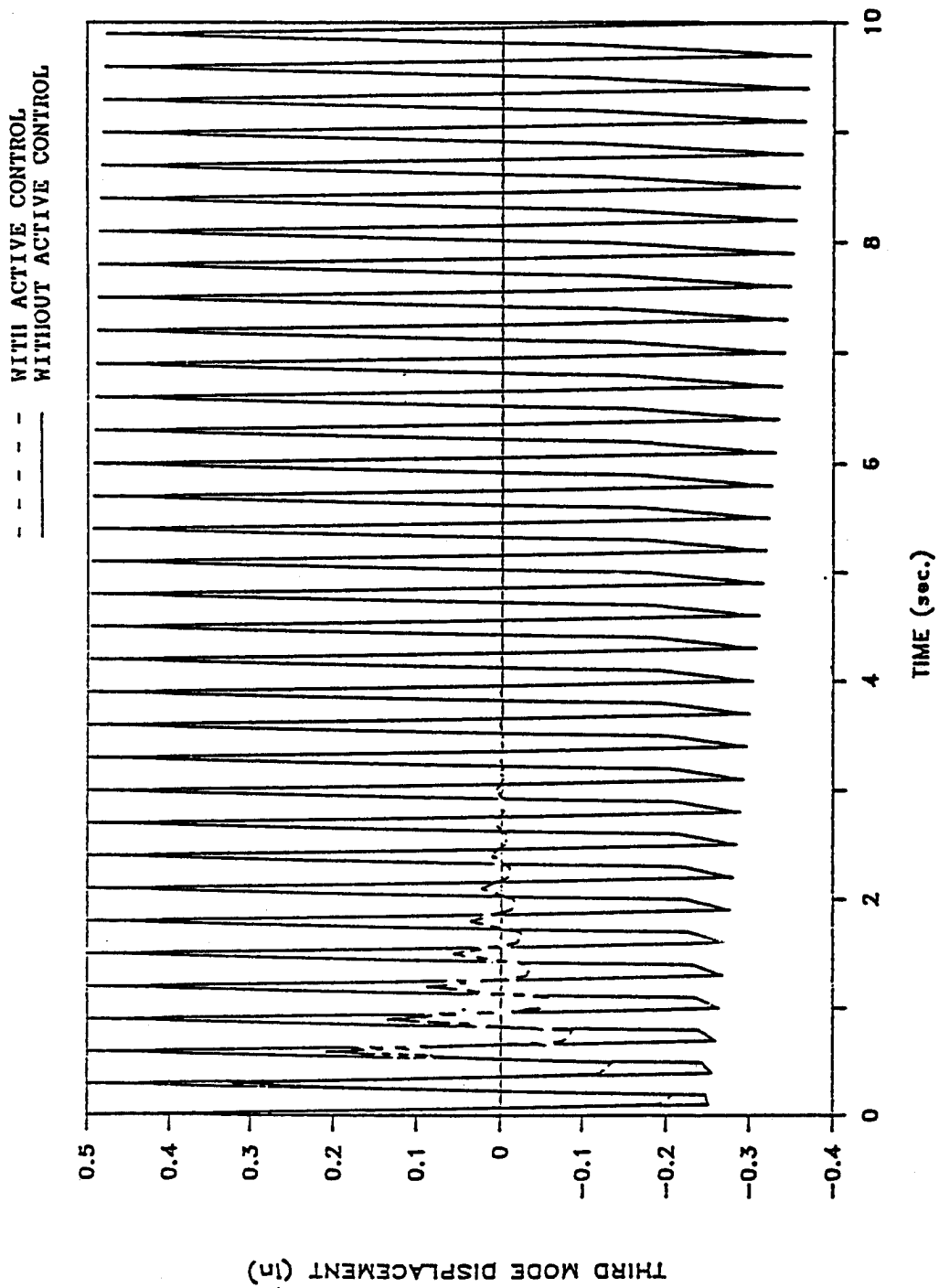


Fig. 5 EFFECT OF ACTIVE CONTROL OF THE THIRD MODE

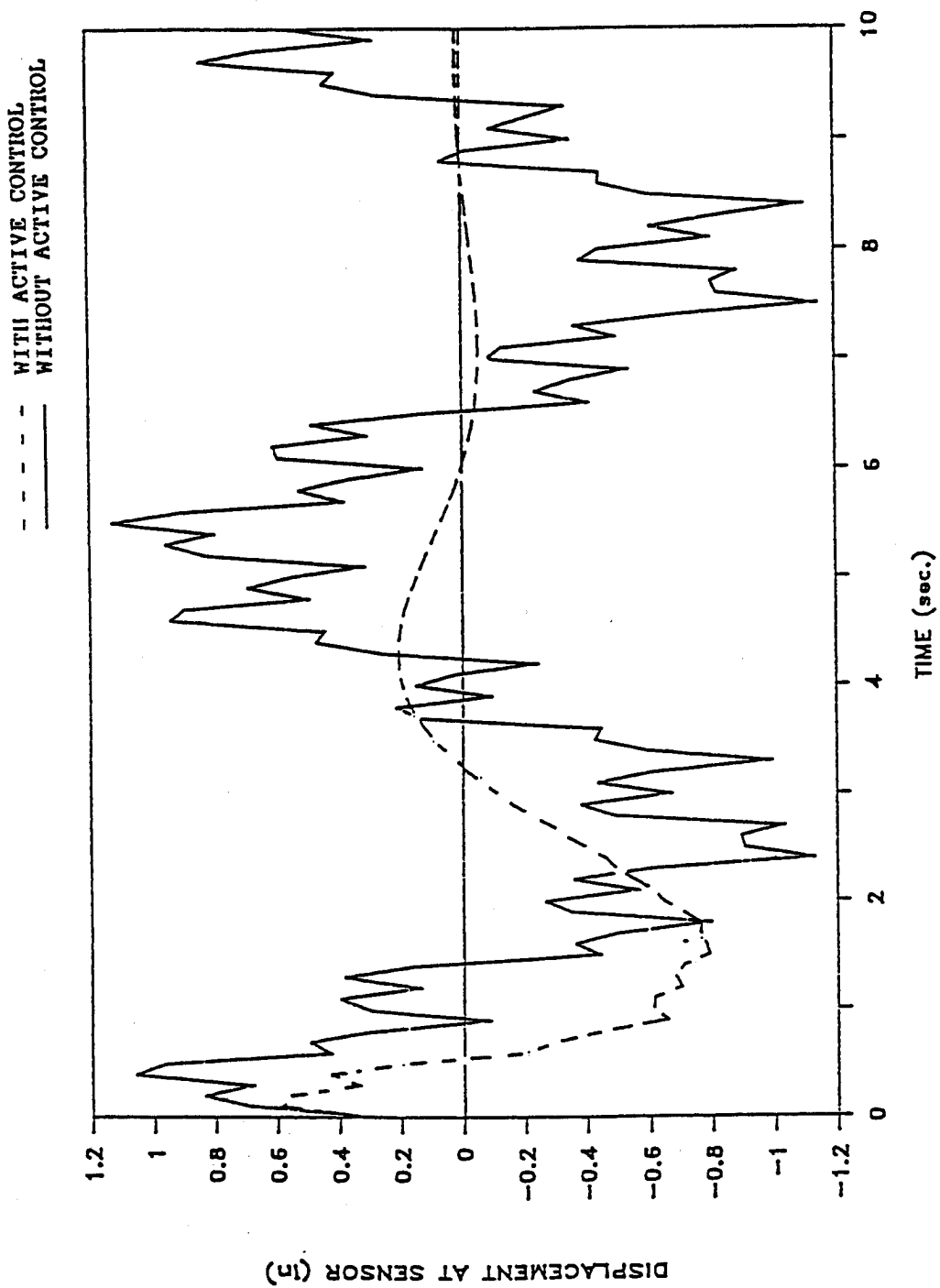


Fig. 6 EFFECT OF ACTIVE CONTROL OF THE FLEXIBLE SYSTEM

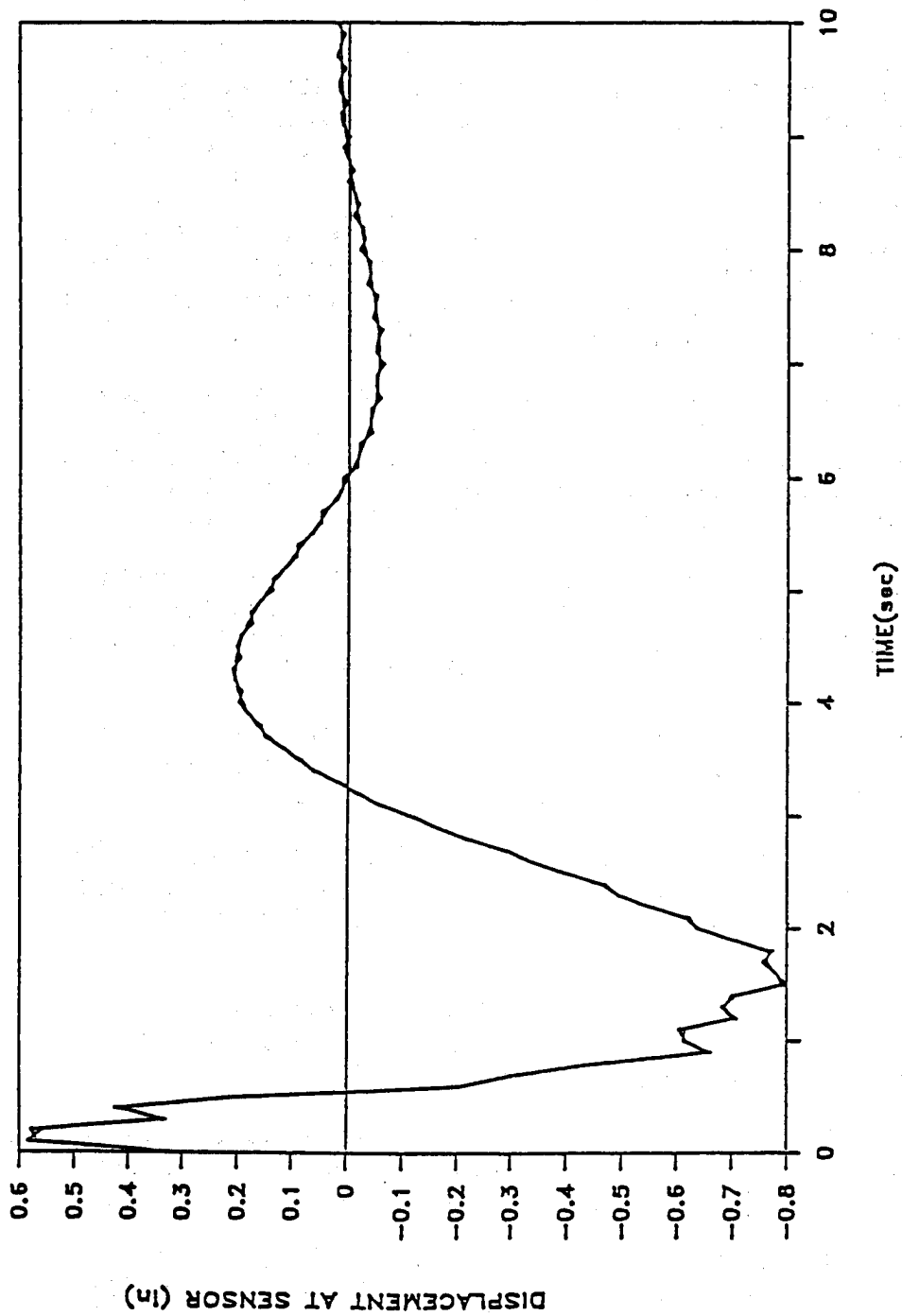


Fig. 7 SPILLOVER EFFECT OF THE CONTROL SYSTEM

## REFERENCE

1. Meirovitch, L., and Quinn, R.D., 1987. "Maneuvering and Vibration Control of Flexible Spacecraft," *Journal of the Astronautical Sciences*, Vol. 35, No. 3, pp. 301-328.
2. Meirovitch, L., and Ghosh, D., "Control of Flutter in Bridges," *Proceedings of the Second International Symposium on Structural Control*, (Ed.: H.H.E. Leipholz), M. Nijhoff Publishers, Dordrecht, The Netherlands, 1987, pp. 458-472.
3. Alberts, T.E., Hastings, G.G., Book, W.J., and Dickerson, S.L., 1987. "Experiments in Optimal Control of a Flexible Arm with Passive Damping," *Proceedings of the Fifth VPI&SU/AIAA Symposium on Dynamics and Control of Large Structures*, Blacksburg, VA, pp. 423-436.
4. Crocker, M.J., Raju, P.K., Christensen, E., Madsen, N.H., et.al., 1988. "Structural Vibration of Space Power Station Systems" *Proceedings of the O.E. LASE 88 Symposium on Innovative Science and Technology*, SPIE Vol. 871 Space Structures, Power and Power Conditioning, pp. 205-214.
5. Bennighof J.K., Meirovitch, L., 1988 "Active Vibration Control of a Distributed System with Moving Support," *Transactions of ASME Journal of Vibration, Acoustics, Stress and Reliability in Design*, Vol. 110, pp. 246-253.
6. Rockwell, T. and Lawther, J., 1984. "Theoretical and Experimental Results on Active Vibration Dampers" *J. Acoustical Society America* 36, pp. 1507-1515.
7. Knyazer, A. and Tartakovoku, B., 1965. "Application of Electronmechanical Feedback for the Damping of Flexural Vibrations in Rods", *Soviet Physics-Acoustics* 11, pp. 150-154.
8. Walker, L. and Yaneske, P., 1976. "Characteristics of an Active Feedback System for the Control of Plate Vibrations", *J. Sound and Vibration*, 46(2), pp. 157-176.
9. Sun, S.P. 1987. "Dynamic Analysis and Semi-active Control of Vibration in Long Road Vehicles", Master Thesis. University of Alabama at Birmingham, Birmingham, Alabama.
10. Balas, M.J., 1978. "Feedback Control of Flexible Systems", *IEEE 41th Automatic Control*, Vol. AC-23 No. 4, pp. 673-679.



11. Balas, M.J., 1978. "Modal Control of Certain Flexible Dynamic System", J. Control and Optimization, Vol. 16, No. 3, pp. 450-462.
12. Kwakernuk, H. and Sivan, R., 1972. "Linear Optimal Control System", Wiley-Interscience, New York.
13. Gustafson, D. and Spoyer, J., 1976. "Linear Minimum Variance Filters Applied to Carrier Tracking," IEEE Transactions on Automatic Control, Vol. AC-21, pp. 65-73.
14. Viterbi, A., 1966. "Principles of Coherent Communication," McGraw-Hill Book Company, New York.

# Robust Realization/Identification Of Damped Structures

Michael J. Roemer† and D. Joseph Mook\*

Department of Mechanical and Aerospace Engineering  
State University of New York at Buffalo  
Buffalo, New York 14260

## Abstract

Often, physical structures are sufficiently complicated to preclude constructing an accurate mathematical model of the system dynamics from simple analysis using the laws of physics. Consequently, determination of an accurate model requires utilization of (generally noisy) output measurements from dynamic tests. In this paper, we present a robust method for constructing accurate structural dynamic models from discrete time-domain measurements. The method processes the measurements in order to determine the number of modes present, the damping and frequency of each mode, and the mode shape. The structure may be highly damped. Although the mode shape identification is more sensitive to measurement noise than the order, frequency, and damping identification, the method is considerably less sensitive to noise than other leading methods. Accurate detection of the modal parameters and mode shapes is demonstrated for normal and complex mode structures whose damping ratios exceed 15 percent.

---

† Graduate Research Assistant

\* Assistant Professor

## Introduction

The enduring problem of accurately identifying the mode shapes of structures and/or systems using (noisy) output measurements is of significant importance in several aspects of mechanical and aerospace engineering. For example, the structural community has expended considerable effort attempting to correctly identify modal properties of flexible structures (Hendricks<sup>1</sup>; Ibrahim and Mikulcik<sup>2</sup>; Rajaram and Junkins<sup>3</sup>; Chen<sup>4</sup>). However, mode shape identification methods are very sensitive to measurement noise, and lose accuracy in high measurement noise circumstances. Addressing this problem, the paper develops an algorithm that aids in accurately identifying mode shapes of a structure from output measurements. The algorithm combines a recently developed identification/realization technique with a method of model error reduction to successfully identify mode shapes even with high noise levels in the measurements. Note; modal properties refers to: (1) natural frequencies and damping ratios, and (2) mode shapes.

Recently, the Eigensystem Realization Algorithm (ERA) was developed by Juang and Pappa<sup>5</sup>; Pappa and Juang<sup>6</sup>. The algorithm was developed for the realization and identification of minimum order structural dynamic models. The ERA technique is based on the singular value decomposition of a generalized Hankel matrix composed of discrete, time-domain measurements. In theory, the order of the realized model is determined from the number of nonzero singular values computed from the Hankel matrix decomposition. However, due to the "real world" presence of noise in the output measurements, the decomposition produces nonzero singular values which should (in theory) be zeros. Consequently, the user must choose a "cutoff" magnitude of singular values, below which the singular values are assumed to be due to noise and not due to extra order in the model. In a paper extending their original work, Juang and Pappa<sup>7</sup> conducted an investigation studying the effects of singular value truncation. Their results show that the choice of singular value cutoff affects the number of modes retained in the realization and the accuracy of the modal properties identified. Choosing a low cutoff produces a model which includes more modes than the true number, and results in reduced accuracy of the identified modal properties. Conversely, choosing a high cutoff results in a lower order model (some real modes are truncated), but produces better accuracy in identifying the modal properties of the retained modes. Therefore, the difficult choice of an appropriate cutoff magnitude when a high degree of noise is present is of great importance for accurate mode shape identification.

The ERA technique is capable of accurately identifying modal properties for cases involving perfect or low-noise measurements. The procedure of singular value decomposition, as opposed to transfer function analysis, has the benefit of good numerical stability (Klema and Laub<sup>8</sup>), and the ERA is simple to implement and accurate. However, difficulties may arise when high noise levels are present in the output measurements.

Reducing the noise sensitivity of the Eigensystem Realization Algorithm was first investigated by Mook and Lew<sup>9</sup>, whose results were based on the simulation of a structure with a three mode truth. Given a highly noisy measurement set (20% deviation from the truth), their combined ERA/MME algorithm demonstrated significant improvements in the identification of the structure's natural frequencies as well as model order determination. However, they did not attempt to derive any results for improving upon the identification of the physical mode shapes of the structure. Damping was also excluded from their simulated structure.

In this paper, we develop an algorithm (via noise reduction in the measurements) that is less sensitive to measurement noise and can identify mode shapes accurately. Also, the proposed algorithm demonstrates the ability to identify mode shapes of structures including significant damping. The combined results reveal that mode shape identification is much more dependent on measurement noise than identification of natural frequencies, yet may still be significantly enhanced by combining the ERA and the MME procedures.

## Eigensystem Realization Algorithm

The basic development of the state-space realization concept is attributed to Ho and Kalman<sup>10</sup>, who introduced the principle of minimum order realization. The Eigensystem Realization Algorithm (ERA) utilizes singular value decomposition to develop a method of minimum order realization. The ERA algorithm has been successfully applied to realization/identification of several structures from experimental data (e.g., Pappa and Juang<sup>6</sup>). We now give a summary of the algorithm.

Consider the discrete-time linear time-invariant dynamic equation

$$x(k+1) = Ax(k) + Bu(k) \quad (1)$$

$$y(k) = Cx(k) \quad (2)$$

where  $x$  is the  $n \times 1$  state vector,  $u$  is the  $p \times 1$  input vector,  $y$  is the  $q \times 1$  output vector; and  $A$ ,  $B$ , and  $C$  are  $n \times n$ ,  $n \times p$ , and  $q \times n$  constant matrices, respectively. Two special solutions for Eqs. (1)-(2) are given by Markov parameters as the impulse response,

$$Y(k) = CA^{k-1}B \quad (3)$$

and the initial state response,

$$Y(k) = CA^k[x_1(0) \ x_2(0) \dots x_i(0) \dots x_p(0)] \quad (4)$$

where  $x_i(0)$  represents the  $i^{th}$  set of initial conditions. The ERA begins by forming the  $r \times s$  block matrix

$$H(k-1) = \begin{pmatrix} Y(k) & Y(k+m_1) & \dots & Y(k+m_{s-1}) \\ Y(k+l_1) & Y(k+l_1+m_1) & \dots & Y(k+l_1+m_{s-1}) \\ \vdots & \vdots & \ddots & \vdots \\ Y(k+l_{r-1}) & Y(k+l_{r-1}+m_1) & \dots & Y(k+l_{r-1}+m_{s-1}) \end{pmatrix} \quad (5)$$

where  $r$  and  $s$  are arbitrary integers satisfying the inequalities  $rq \geq n$ ,  $sp \geq n$ , and  $l_i$  ( $i = 1, 2, \dots, r-1$ ) and  $m_j$  ( $j = 1, 2, \dots, s-1$ ) are arbitrary integers. For the initial state response measurements,  $H(k-1)$  is replaced by  $H(k)$ . From Eqs. (3)-(5) it can be shown that

$$H(k) = V_r A^k W_s \quad (6)$$

where

$$V_r = \begin{pmatrix} C \\ CA^{l_1} \\ \vdots \\ CA^{l_{r-1}} \end{pmatrix}$$

$$W_s = \begin{pmatrix} B \\ A^{m_1} B \\ \vdots \\ A^{m_{s-1}} B \end{pmatrix}^T$$

$V_r$  and  $W_s$  are generalized observability and controllability matrices. The ERA is derived by using singular value decomposition for  $H(0)$ , defined by

$$H(0) = PDQ^T \quad (7)$$

where  $P$  and  $Q$  are  $rq \times n$  and  $sp \times n$  isometric matrices, respectively, and  $D$  is a diagonal matrix whose diagonal elements are the positive singular values. The rank  $n$  of  $H(0)$  is determined by testing the singular values for zero, i.e., by choosing the cutoff magnitude below which the singular values are assumed to represent noise and not modes. The reduced-order realization of dimension  $n$  can be constructed by forming

$$A^k = D_n^{-\frac{1}{2}} P_n^T H(k) Q_n D_n^{-\frac{1}{2}} \quad (8)$$

$$B = D_n^{\frac{1}{2}} Q_n^T E_p \quad (9)$$

$$C = E_q^T P_n D_n^{\frac{1}{2}} \quad (10)$$

where  $P_n$  and  $Q_n$  are formed from the first  $n$  columns of  $P$  and  $Q$ ,  $D_n$  is an  $n \times n$  left upper block matrix,  $E_p^T$  is  $[I_m, 0]$ , and  $E_q^T$  is  $[I_q, 0]$ , where  $I_p$  and  $I_q$  are identity matrices of order  $p$  and  $q$ , respectively, and  $0$  is the zero matrix of appropriate dimensions.

Finally, from the eigensolution of the realized state space matrix  $A^k$ , the modal damping ratios and damped natural frequencies are calculated from the real and imaginary parts of the eigenvalues, after transformation from the  $z$  to  $s$  plane using the relationship

$$s = [\ln(z) \pm i2k\pi]/(\Delta\tau); \quad i = \sqrt{-1}$$

where

$$z = \text{eigenvalues of } A^k$$

The mode shapes are then calculated using the matrix

$$E_q^T P_n D_n^{\frac{1}{2}} \Psi$$

where

$$\Psi = \text{eigenvector matrix of } A^k$$

## Minimum Model Error Estimation

The idea of filtering noise from measurement data is certainly not unique. Various versions of Kalman filters and other similar algorithms have been extensively studied and implemented (e.g., Gelb<sup>11</sup>; Lewis<sup>12</sup>). A major problem with utilizing traditional filter algorithms is that they require good accuracy in the assumed model for the measured signal. In the case of structural realization/identification, the object of the work is to obtain this model. Therefore, while it is possible that judicious use of a filter-smoother algorithm may benefit the ERA, we have not pursued this approach because of the theoretical modeling difficulties just mentioned.

Recently, a new approach for performing optimal state estimation in the presence of significant model error has been developed by Mook and Junkins<sup>13</sup>. The new technique, called Minimum Model Error (MME) estimation, does not assume that the model error is a white noise of known covariance as do the filters. Instead, the model error is assumed to be an unknown quantity and is estimated as part of the solution. The theoretical advantages of this assumption are obvious for the present problem, since the model is unknown *a priori*. In several previous studies, the MME has been shown to produce state estimates of high accuracy for problems involving both significant model error and significant measurement error (Mook and Lin<sup>14</sup>; Mook<sup>15</sup>; Junkins and Mook<sup>16</sup>). A brief derivation of the Minimum Model Error estimation technique follows.

Given a system whose state vector dynamics is modeled by the (linear or nonlinear) system of equations,

$$\dot{\underline{x}} = \underline{f}[\underline{x}(t), \underline{u}(t), t] \quad (11)$$

where

$$\underline{x} \equiv n \times 1 \text{ state vector}$$

$$\underline{f} \equiv n \times 1 \text{ vector of model equations}$$

$$\underline{u} \equiv p \times 1 \text{ vector of forcing terms,}$$

and given a set of discrete measurements modeled by the (linear or nonlinear) system of equations,

$$\tilde{y}(t_j) = \underline{g}_j[\underline{x}(t_j), t_j] + \underline{v}_j, \quad j = 1, \dots, m \quad (12)$$

where

$$\begin{aligned}\underline{\tilde{y}}(t_j) &\equiv r \times 1 \text{ measurement set at } t_j \\ \underline{g} &\equiv r \times 1 \text{ measurement model equations} \\ m &\equiv \text{total number of measurement sets} \\ \underline{v}_j &\equiv r \times 1 \text{ measurement error vector}\end{aligned}$$

where,  $v_j$  represents a zero-mean, gaussian random sequence of known covariance  $R_j$ , determine the optimal estimate for  $\underline{x}(t)$  (denoted by  $\underline{\hat{x}}(t)$ ), during some specified time interval  $t_0 \leq t \leq t_f$ .

In the MME, the optimal state trajectory estimate is determined on the basis of the assumption that the measurement-minus-estimate error covariance matrix must match the measurement-minus-truth error covariance matrix. This condition is referred to as the "covariance constraint". The covariance constraint is defined mathematically by requiring the following approximation to be satisfied:

$$\left\{ [\underline{\tilde{y}}(t_j) - \underline{g}(\underline{\hat{x}}(t_j), t_j)] [\underline{\tilde{y}}(t_j) - \underline{g}(\underline{\hat{x}}(t_j), t_j)]^T \right\} \approx R_j \quad (13)$$

Thus, the *estimated measurements*  $\underline{g}(\underline{\hat{x}}(t_j), t_j)$  are required to fit the *actual measurements*  $\underline{\tilde{y}}(t_j)$  with approximately the same error covariance as the actual measurements fit the truth. Otherwise, the estimate cannot be correct.

The estimated measurement set at time  $t_j$  is based on the current state estimate,  $\underline{\hat{x}}(t_j)$ . The between-measurement state estimate is based on integration of the system dynamic model. Thus, if the system dynamic model contains errors, the integration does not yield the correct state estimate, and the residuals between the estimated and the actual measurements are too large. However, due to the noise in the measurements, it is not appropriate to force the model to predict the measurements exactly. Instead, the measurement-minus-estimate residuals should have the same covariance as the measurement noise. This condition is enforced by the covariance constraint.

When the covariance constraint has been satisfied, the state estimate is considered to have been optimized. If errors are present in the state dynamic equations, satisfaction of the covariance constraint generally requires that these errors be corrected when the model is integrated between measurements. The MME method may be used to produce these model error corrections.

Model error is represented by adding a *to-be-determined* unmodeled disturbance vector  $\underline{d}(t)$  to the right-hand sides of the original state model equations, Eq. (11), to produce the modified state governing equations,

$$\dot{\underline{x}} = \underline{f}[\underline{x}(t), \underline{u}(t), t] + \underline{d}(t) \quad (14)$$

Next, the following cost functional is minimized with respect to  $\underline{d}(t)$ :

$$J = \sum_{j=1}^m \left\{ [\underline{\tilde{y}}(t_j) - \underline{g}(\underline{\hat{x}}(t_j), t_j)]^T R_j^{-1} [\underline{\tilde{y}}(t_j) - \underline{g}(\underline{\hat{x}}(t_j), t_j)] \right\}$$

$$+ \int_{t_0}^{t_f} \underline{d}(\tau)^T W \underline{d}(\tau) d\tau \quad (15)$$

where

$W \equiv k \times k$  weight matrix to be determined

The functional  $J$  in Eq. (15) is the sum of two penalty terms. The first is a weighted sum of discrete terms which penalize the deviation of the predicted measurements (based upon the estimated states) from the actual measurements. Minimization of this summation term tends to drive the state estimates toward values which, when substituted into the measurement model, predict the actual measurements. The weighting  $R_j^{-1}$  on each of these penalty terms is the inverse of the associated measurement error covariance; thus, accurate measurements (small  $R_j$ ) are weighted more heavily than inaccurate measurements (large  $R_j$ ). The second term in  $J$  is an integral term which reflects the assumption that the amount of unmodeled effect to be added should be minimized. However, the unmodeled effect must be sufficient to cause the estimate to satisfy the covariance constraint. The proper balance between the two competing effects depends on the choice of  $W$ . The weight matrix,  $W$ , is determined such that the covariance constraint is satisfied.

An algorithm for the minimization of  $J$  in Eq. (15) follows directly from a modification of the so-called Pontryagin's necessary conditions. For a given  $W$ , the minimization of  $J$  in Eq. (15) with respect to  $\underline{d}(t)$  leads to the TPBVP summarized as:

$$\dot{\underline{x}} = \underline{f}[\underline{x}(t), \underline{u}(t), t] + \underline{d}(t) \quad (14)$$

$$\dot{\underline{\lambda}} = - \left( \frac{\partial \underline{f}}{\partial \underline{x}} \right)^T \underline{\lambda} \quad (16)$$

$$\underline{d} = -\frac{1}{2} W^{-1} \left[ \frac{\partial \underline{f}}{\partial \underline{u}} \right]^T \underline{\lambda} \quad (17)$$

$$\underline{x}(t_0) = \text{specified, or } \underline{\lambda}(t_0^-) = \underline{0} \quad (18)$$

$$\underline{\lambda}(t_j^+) = \underline{\lambda}(t_j^-) + 2H_j^T R_j^{-1} [\underline{y}(t_j) - \underline{g}(\underline{x}(t_j), t_j)] \quad (19)$$

$$\underline{x}(t_f) = \text{specified, or } \underline{\lambda}(t_f^+) = \underline{0} \quad (20)$$

where

$$H \equiv \left. \frac{\partial \underline{g}}{\partial \underline{x}} \right|_{\underline{x}(t_j), t_j}$$

If the assumed model in the MME algorithm is linear, then a multiple shooting technique may be used to solve the two-point boundary value problem described by Eqs. (14)-(20). This technique converts the TPBVP into a set of linear algebraic equations which may be solved using any linear equation solver (Lew and Mook<sup>17</sup>). In the present case, the model produced by the ERA and used for input to the MME is always linear, so the MME solution is obtained from linear algebraic equations.



## Realized vs. Physical Mode Shapes

Before considering some examples, it is important to become familiar with the relationships describing the physical system's mode shapes. To achieve this, a derivation devoted to the connection between the realized and physical system's mode shapes is provided.

We begin the derivation with the familiar boundary-value problem describing the free vibration of a beam. The boundary-value problem can be reduced to the differential equation

$$\frac{d^2}{dx^2} \left[ EA(x) \frac{d^2 \Phi(x)}{dx^2} \right] = \omega^2 m(x) \Phi(x), \quad 0 < x < L$$

and the boundary conditions

$$y(0, t) = y(L, t) = 0$$

where  $EA(x)$  is the flexural rigidity,  $m(x)$  is the mass per unit length at any point  $x$ ,  $\Phi(x)$  is the eigenfunction related to the mode shapes, and  $\omega$  is the natural frequency of each corresponding mode shape. Based on the separation of variables, the exact solution can be expressed in the following form:

$$y(x, t) = \sum_{i=1}^{\infty} \phi_i(x) \eta_i(t)$$

For this solution,  $\phi_i(x)$  represents the individual mode shapes of the structure depending on the spatial variable  $x$  alone, and  $\eta_i(t)$  indicates the type of motion the structure exhibits.

Although the free vibration problem for a continuous beam is different from the discretized problem, the general approach to their solutions is the same. Therefore, discretizing the continuous beam, a new system can be defined as having mass, stiffness, and damping matrices  $M$ ,  $K$ , and  $C$  respectively and the governing equation

$$M\ddot{x}(t) + C\dot{x}(t) + Kx = 0 \quad (21)$$

This discrete system representation can be transformed into its state space form given below:

$$\begin{pmatrix} \dot{\underline{x}}(t) \\ \ddot{\underline{x}}(t) \end{pmatrix} = \begin{pmatrix} 0 & \vdots & I \\ \dots & \dots & \dots \\ M^{-1}K & \vdots & M^{-1}C \end{pmatrix} \begin{pmatrix} \underline{x}(t) \\ \dot{\underline{x}}(t) \end{pmatrix} \quad (22)$$

where,

$$A = \begin{pmatrix} 0 & \vdots & I \\ \dots & \dots & \dots \\ M^{-1}K & \vdots & M^{-1}C \end{pmatrix}$$

Rewriting equation (22) into its familiar form, we obtain

$$\dot{\underline{x}}(t) = A\underline{x}(t)$$

The state space  $A$  matrix can be represented in its Jordan canonical form

$$A = P\Lambda P^{-1}$$

where  $P$  is the eigenvector matrix and  $\Lambda$  is the diagonal eigenvalue matrix. Therefore, similar to the continuous time problem, the solution to the discretized problem for one specific time takes the following form:

$$\underline{x}(t_i) = P \begin{pmatrix} e^{\lambda_1 t_i + j\Theta_1} \\ e^{\lambda_2 t_i + j\Theta_2} \\ \vdots \\ e^{\lambda_{2n} t_i + j\Theta_{2n}} \end{pmatrix} \quad (23)$$

Now, we extend this solution to include a succession of discrete time values.

$$X = \begin{pmatrix} \underline{x}(t_1) & \underline{x}(t_2) & \dots & \underline{x}(t_m) \end{pmatrix} = PE, \quad m \geq 2n$$

where,

$$E = \begin{pmatrix} e^{\lambda_1 t_1 + j\Theta_1} & e^{\lambda_1 t_2 + j\Theta_1} & \dots & e^{\lambda_1 t_m + j\Theta_1} \\ e^{\lambda_2 t_1 + j\Theta_2} & e^{\lambda_2 t_2 + j\Theta_2} & \dots & e^{\lambda_2 t_m + j\Theta_2} \\ \vdots & \vdots & \ddots & \vdots \\ e^{\lambda_{2n} t_1 + j\Theta_{2n}} & e^{\lambda_{2n} t_2 + j\Theta_{2n}} & \dots & e^{\lambda_{2n} t_m + j\Theta_{2n}} \end{pmatrix}$$

The relationship  $PE$  becomes the definition of the generalized Hankel matrix and its first derivative is defined as the shifted Hankel matrix. The generalized Hankel matrix is denoted by  $H(0)$  and its shifted version is denoted  $H(1)$ :

$$X = PE = H(0) \quad (24)$$

$$\dot{X} = P\Lambda E = H(1) \quad (25)$$

The next step is to perform the singular value decomposition on the Hankel matrix

$$X = H(0) = U\Sigma V^T$$

or

$$X = H(0) = U\Sigma^{\frac{1}{2}}\Sigma^{\frac{1}{2}}V^T \quad (26)$$

where  $U$  and  $V$  are isometric matrices and  $\Sigma$  is the diagonal matrix of singular values. The realization that is defined by the Eigensystem Realization Algorithm takes on the following form:

$$\bar{A} = (U\Sigma^{\frac{1}{2}})^{-1} H(1) (\Sigma^{\frac{1}{2}}V^T)^{-1} \quad (27)$$

or after substituting  $H(1) = P\Sigma E$ ,

$$\bar{A} = \Sigma^{-\frac{1}{2}} U^T P \Sigma E V \Sigma^{-\frac{1}{2}} \quad (28)$$

Now by setting  $U\Sigma^{\frac{1}{2}} = PS$ , where  $S$  is some unknown matrix that is responsible for this equation being satisfied, we get the following sequence of steps leading to the new definition of  $\bar{A}$ :

$$H(0) = U\Sigma V^T = U\Sigma^{\frac{1}{2}} \Sigma^{\frac{1}{2}} V^T \quad (29)$$

after substitution of  $U\Sigma^{\frac{1}{2}} = PS$ , and recalling that  $H(0) = PE$  the following relationship holds:

$$PE = PS\Sigma^{\frac{1}{2}} V^T \quad (30)$$

Rearranging to solve for  $S^{-1}E$  we obtain

$$S^{-1}E = \Sigma^{\frac{1}{2}} V^T \quad (31)$$

After substitution of Equation (31) and  $U\Sigma^{\frac{1}{2}} = PS$  into the Equation (28) we obtain

$$\bar{A} = (PS)^{-1} P \Lambda E (S^{-1}E)^{-1} \quad (32)$$

Taking the inverses,

$$\bar{A} = S^{-1} P^{-1} P \Lambda E E^{-1} S \quad (33)$$

and this reduces to the continuous time realization

$$\bar{A} = S^{-1} \Lambda S \quad (34)$$

It now becomes apparent by observing equations (22) and (34) that there is in fact a difference between the realized and physical system's eigenvector matrices. The physical system's eigenvector matrix is  $P$ , while the realized system's eigenvector matrix is  $S^{-1}$ . However, it is worth noting that the eigenvalues of both systems are identical. Therefore, if we wish to calculate the physical system's eigenvectors, we simply employ the relationship

$$P = U\Sigma^{\frac{1}{2}} S^{-1} \quad (35)$$

where  $S^{-1}$  is the realized system's eigenvector matrix.

## Enhanced Mode Shape Identification Algorithm

The enhanced (i.e. higher accuracy in the presence of noise) mode shape identification algorithm for robust system realization/identification can be summarized in the following steps.

1. Apply the ERA procedure to the measurements in the usual manner to produce a minimum-order realization model with mode shapes.

2. Input the realized model and the measurements into the MME algorithm to produce optimal state estimates.

3. Sample the MME produced state estimates at discrete-time intervals to create simulated measurements of higher accuracy than the original measurements.

4. Apply ERA to the simulated measurements in order to realize/identify the new mode shapes.

5. Examine the newly calculated mode shapes for some convergence criteria, and repeat the procedure if necessary.

## Examples

The intent of the following examples is to contrast the mode shape identification abilities of the proposed algorithm verses ERA by itself. Consider the axial vibrations of a cantilever aircraft wing illustrated below in Figure 1.

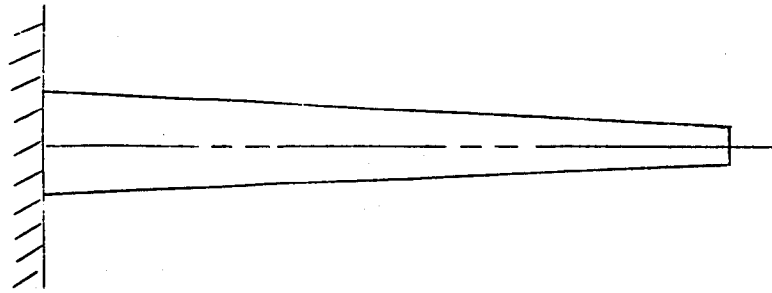


Figure 1 Cantilever Aircraft Wing

Rather than solving the continuous differential eigenvalue problem (Meirovitch<sup>18</sup>), the approach taken here is to discretize the cantilever wing into a four degree-of-freedom system consisting of four masses with idealized springs and dampers between each mass. The governing equations of the discrete system are transformed into the state space form shown below and the proper constants for each mass, spring, and damper substituted.

$$\begin{pmatrix} \dot{\underline{x}}(t) \\ \ddot{\underline{x}}(t) \end{pmatrix} = \begin{pmatrix} 0 & \vdots & I \\ \dots & \dots & \dots \\ M^{-1}K & \vdots & M^{-1}C \end{pmatrix} \begin{pmatrix} \underline{x}(t) \\ \dot{\underline{x}}(t) \end{pmatrix}$$

For the first example,  $C = 0$  with  $M$  and  $K$  equal to:

$$M = \begin{pmatrix} 1 & 0 & 0 & 0 \\ 0 & 1 & 0 & 0 \\ 0 & 0 & 1 & 0 \\ 0 & 0 & 0 & 1 \end{pmatrix}; \quad K = \begin{pmatrix} 10 & -5 & 0 & 0 \\ -5 & 10 & -5 & 0 \\ 0 & -5 & 10 & -5 \\ 0 & 0 & -5 & 10 \end{pmatrix}$$

For the second example,  $M$  and  $K$  stay the same but,

$$C = \begin{pmatrix} 0.3 & 0 & 0 & 0 \\ 0 & 0.3 & 0 & 0 \\ 0 & 0 & 0.3 & 0 \\ 0 & 0 & 0 & 0.3 \end{pmatrix}$$

Utilizing the matrix exponential, the exact time domain solution of each example is calculated. The exact mode shapes, natural frequencies, and damping ratios are then calculated by ERA using the exact time domain solution as input measurements.

For the first example, no damping was included in the system's model ( $C=0$ ). Assuming only positional measurements are available, the exact solution as given by ERA is indicated in Tables 1.1 and 1.2. The solution consists of the singular values (revealing the number of modes identified), the eigenvalues (indicating each modes natural frequency and damping ratio), and the mode shapes. It should be noted that each mode identified is normally associated with a pair of singular values. However, for simplicity each pair of singular values is averaged together so that the number of nonzero averaged singular values equals the number of modes identified.

With the exact solution known, a gaussian distributed white noise approximately 5-10% the size of the signal amplitude is added to the perfect measurements to investigate the performance of each algorithm. The results of the stand alone Eigensystem Realization Algorithm processing the noisy measurements are displayed in Tables 1.3 and 1.4. Examining the singular values of Table 1.3, one would conclude that only 3 modes were identified, and the remaining nonzero singular values represented noise in the measurements. Directly related to this, a pair of eigenvalues and its corresponding mode shape were completely unidentifiable. Therefore, due to measurement uncertainty the ERA algorithm only identified 3 of the 4 participating modes. Moreover, comparing Table 1.1 with Table 1.3 we see that the identification of the eigenvalues is very poor. Similarly, comparing Table 1.2 with Table 1.4, the mode shape identification is poor.

**TABLE 1.1**  
**Exact Solution Of Example # 1**

Singular Values	Eigenvalues
17.706	$0.000 \pm 4.253i$
10.192	$0.000 \pm 3.618i$
3.215	$0.000 \pm 2.629i$
0.269	$0.000 \pm 1.382i$
0.000	
0.000	
0.000	
0.000	

**TABLE 1.2****Exact Mode Shapes (4 discrete points)**

Mode 1	Mode 2	Mode 3	Mode 4
0.3717	-0.6015	0.6015	-0.3717
0.6015	-0.3717	-0.3717	0.6015
0.6015	0.3717	-0.3717	-0.6015
0.3717	0.6015	0.6015	0.3717

**TABLE 1.3****Stand Alone ERA Results**

Singular Values	Eigenvalues
17.692	$-0.07495 \pm 4.0421i$
10.282	$-9.53686 + 62.8312i$
3.132	$-33.8623 + 0.00000i$
0.398	$-0.02049 \pm 2.6538i$
0.306	$-0.01701 \pm 1.3841i$
0.278	
0.256	
0.240	

**TABLE 1.4****ERA Identified Mode Shapes (4 discrete points)**

Mode 1	Mode 2	Mode 3	Mode 4
0.4012	-0.5945	0.2087	-0.0751
0.5743	-0.3622	0.2532	0.4508
0.5912	0.4039	0.1717	-0.7844
0.3992	0.6069	0.3515	0.6279

Note: The final tabulated results for both algorithms given in Tables 1.3-1.6 are an average of 10 individual results provided by 10 different seeds of a random number generator. This truncated use of a Monte Carlo analysis produced convergence upon the true mode shapes, otherwise not obtained for individual cases. Therefore, in analyzing "real world" problems, taking many different sets of measurements and averaging the results should produce more reliable results.

Tables 1.5 and 1.6 give the results of the Enhanced Mode Shape Identification Algorithm proposed in this paper. For this particular example only two cycles of the procedure summarized above were needed for convergence. Examining the singular values of Table 1.5, one would conclude that 4 modes were identified by the enhanced algorithm and the remaining singular values represented noise. Notice, the mode not identified by the stand alone ERA is accurately recovered by the combined algorithm. Also, the other three mode shapes are more precisely identified. The improved accuracy of the eigenvalues is also apparent. For this example, the true mode shapes and those identified by ERA alone (measurements), and the enhanced algorithm (estimate) are illustrated in Figures 2 through 5.

**TABLE 1.5**  
**Enhanced Algorithm Results**

Singular Values	Eigenvalues
17.654	$-0.04505 \pm 4.343i$
10.159	$-0.19430 \pm 3.798i$
3.204	$-0.02898 \pm 2.634i$
0.301	$-0.01298 \pm 1.393i$
0.089	
0.080	
0.071	
0.064	

**TABLE 1.6**  
**Enhanced Algorithm Mode Shapes**

Mode 1	Mode 2	Mode 3	Mode 4
0.3705	-0.5685	0.5645	-0.3223
0.6098	-0.3810	-0.4193	0.6001
0.6005	0.3711	-0.3486	-0.7101
0.3891	0.6395	0.6312	0.4541

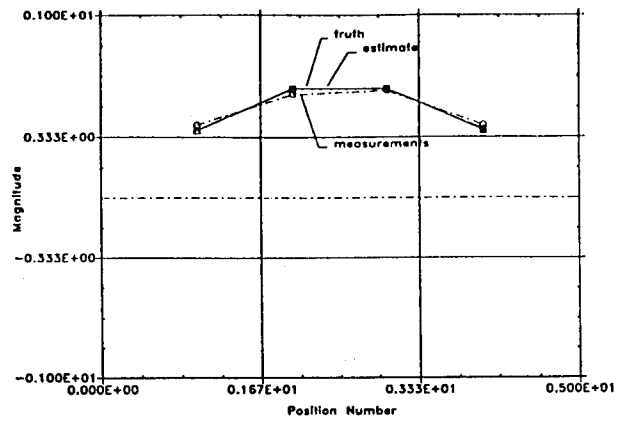


Figure 2 Mode Shape # 1 (no damping)

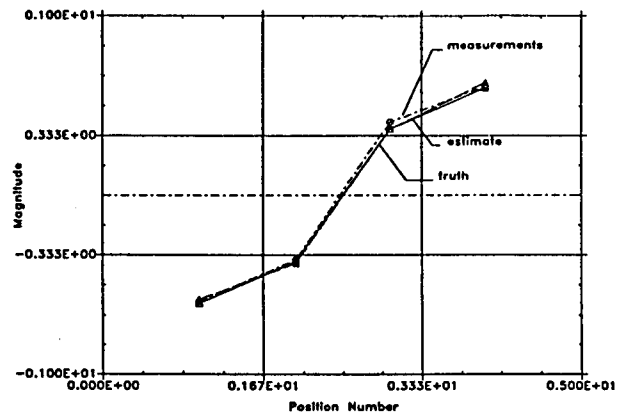


Figure 3 Mode Shape # 2 (no damping)

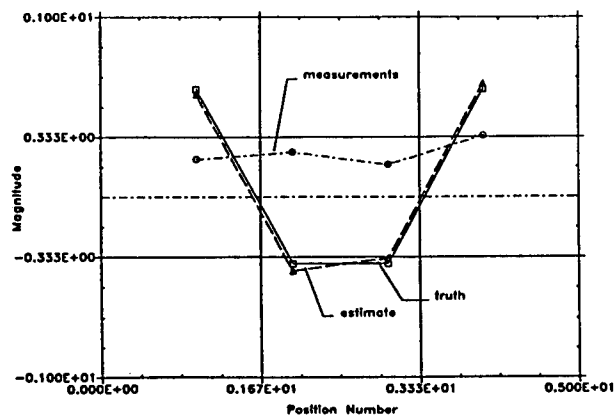


Figure 4 Mode Shape # 3 (no damping)



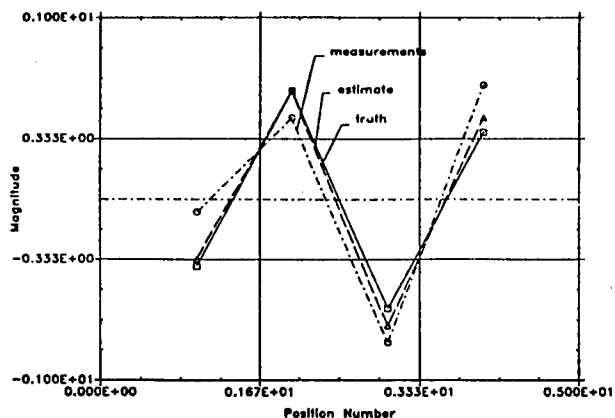


Figure 5 Mode Shape # 4 (no damping)

In the second example, the system's model includes proportional damping exceeding a 15% damping ratio. The results were calculated in the same fashion as the previous example. The results are given in Tables 2.1 through 2.6. Again, by examination of the singular values of Table 2.3, it is obvious that only 3 modes were identified by ERA and the remaining nonzero singular values represented noise in the measurements. Also, the same pair of eigenvalues and its corresponding mode shape were not identified. Therefore, due to the combination of measurement uncertainty and structural damping, the ERA algorithm only identified 3 modes.

TABLE 2.1  
Exact Solution Of Example # 2

Singular Values	Eigenvalues
13.298	$-0.1500 \pm 4.250i$
7.023	$-0.1500 \pm 3.615i$
2.374	$-0.1500 \pm 2.624i$
0.197	$-0.1500 \pm 1.374i$
0.000	
0.000	
0.000	
0.000	

**TABLE 2.2****Exact Mode Shapes (4 discrete points)**

Mode 1	Mode 2	Mode 3	Mode 4
0.3717	-0.6015	0.6015	-0.3717
0.6015	-0.3717	-0.3717	0.6015
0.6015	0.3717	-0.3717	-0.6015
0.3717	0.6015	0.6015	0.3717

**TABLE 2.3****Stand Alone ERA Results**

Singular Values	Eigenvalues
13.132	$-0.4637 \pm 4.0391i$
6.931	$-15.9319 + 0.00000i$
2.332	$-76.8623 + 62.8318i$
0.326	$-0.17097 \pm 2.6627i$
0.289	$-0.17551 \pm 1.3721i$
0.262	
0.250	
0.239	

**TABLE 2.4****ERA Identified Mode Shapes (4 discrete points)**

Mode 1	Mode 2	Mode 3	Mode 4
0.4048	-0.5982	0.5294	-0.0482
0.5613	-0.3470	0.5839	0.4502
0.5971	0.4052	0.5217	-0.7690
0.4067	0.6154	-0.1205	0.6332

Tables 2.5 and 2.6 show the results of the Enhanced Mode Shape Identification Algorithm for the second example including damping. Similar to the first example, only two cycles of the algorithm's summarized steps were necessary for convergence. The singular values listed in Table 2.5 show that 4 modes were identified by the proposed algorithm as opposed to the 3 modes identified by ERA. The mode not identified by the stand alone ERA was again accurately identified by the combined algorithm. The illustrations of the mode shapes identified by both algorithms are given in Figures 6 through 9. The presence of damping in the structure did effect the mode shape identification, however, an accurate recovery of all four mode shapes was still obtained.

**TABLE 2.5**  
**Enhanced Algorithm Results**

Singular Values	Eigenvalues
13.219	$-0.29915 \pm 4.3243i$
7.668	$-0.28050 \pm 3.7947i$
2.235	$-0.17647 \pm 2.6355i$
0.232	$-0.16090 \pm 1.3871i$
0.098	
0.090	
0.077	
0.069	

**TABLE 2.6**  
**Enhanced Algorithm Mode Shapes**

Mode 1	Mode 2	Mode 3	Mode 4
0.3901	-0.6165	0.4645	-0.3165
0.5843	-0.3767	-0.2193	0.6341
0.5943	0.3825	-0.4486	-0.5622
0.3965	0.5983	0.7312	0.4541

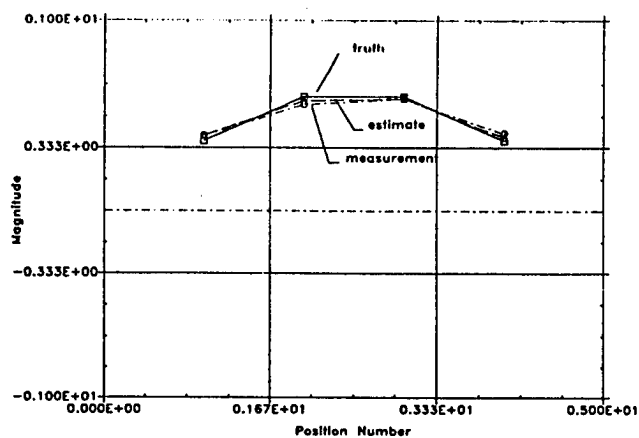


**Figure 6 Mode Shape # 1 (with damping)**

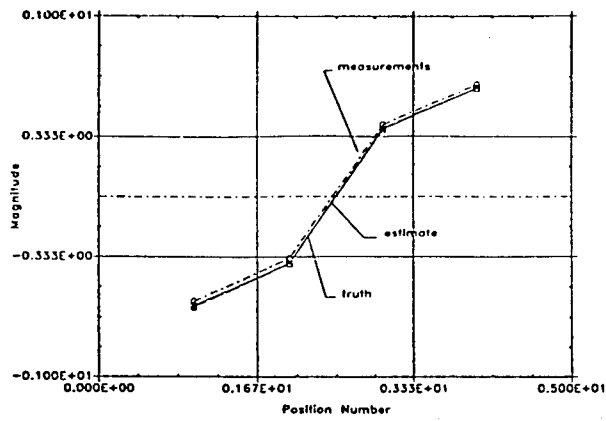


Figure 7 Mode Shape # 2 (with damping)

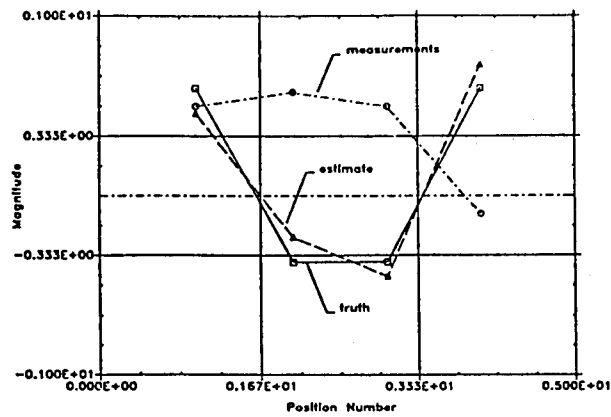


Figure 8 Mode Shape # 3 (with damping)

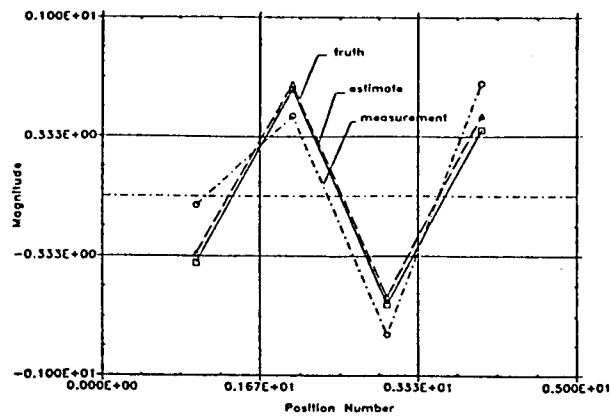


Figure 9 Mode Shape # 4 (with damping)

## Complex Mode Identification

The mode shapes identified in the previous two examples are referred to as real or normal modes. Normal modes are identified in hypothetical systems that are most commonly characterized by mathematical models that assume either no damping or proportionally distributed damping of the form

$$[C] = \alpha[M] + \beta[K]$$

The required assumptions for normal mode systems is in many cases very accurate and is therefore commonly used. For example, the off-diagonal damping terms of the  $[C]$  matrix (often producing non-proportional damping) are often regarded as very small and therefore are neglected. In addition, the physical interpretation of normal modes is easily attained. However, for structures involving the use of composite materials or possessing concentrated damping sources the structure can only be accurately modeled using complex modes.

Identification of complex modes is most commonly associated with structures exhibiting significant "non-proportional" damping distributions. In a more general sense, complex modes will be present if the coefficient matrices of a discretized lumped-mass system do not commute as shown below.

$$[C][M]^{-1}[K] \neq [K][M]^{-1}[C]$$

Recall that this is also the condition for a system that cannot be diagonalized. As one would expect, complex mode shapes are difficult to construe in a physical sense. The common description of such a phenomenon is demonstrated by drifting nodal locations in an animated mode shape display. In other words, the phase angles associated a particular complex mode are not in phase with each other.

The ERA technique and inturn the robust mode shape identification algorithm introduced in this paper are capable of identifying complex modes. The original ERA derivation was conducted in a normal mode basis. Therefore, the real modes have zero degree phase angles as compared to a complex mode formulation where the real modes possess phase angles of  $\pm 45^\circ$  or  $\pm 135^\circ$ . In either case, a real mode can easily be determined if the phase angles are equal or  $180^\circ$  out of phase. In many circumstances, the ability to identify complex modes is essential to the development of mathematical models that can accurately describe the motions of particular structures.

To demonstrate the ability of complex mode identification, an example is provided that involves this type of computation. As previously stated, complex modes are frequently produced by concentrated damping in isolated locations of a structure. To simulate this type of damping while continuing to utilize the previous example's mass and stiffness matrices the following damping matrix was employed.

$$C = \begin{pmatrix} 2.0 & 0 & 0 & 0 \\ 0 & 0 & 0 & 0 \\ 0 & 0 & 0 & 0 \\ 0 & 0 & 0 & 0 \end{pmatrix}$$

For this example, the same procedure was utilized as the previous two examples with respect to the singular values and eigenvalues. However, the complex modes can not be illustrated as in the normal mode case. Instead, the complex mode shapes are tabulated with respect to the magnitude and phase angles of each complex number contained in the respective mode shapes. Note; if the four complex numbers representing each mode shape were plotted in the complex plane and they formed a straight line, then the mode shape is a normal mode. Table 3.1 represents the true eigenvalues and calculated singular values of the simulated four degree-of-freedom structure. One can plainly see the four distinct modes. Table 3.2 contrasts the ERA algorithm's results with those of the robust mode shape identification algorithm. Examining the singular values of each algorithm one would determine that only 3 modes were identified by the ERA while all 4 modes were recognized by the enhanced algorithm. These results are in agreement with the previous two examples.

**TABLE 3.1**  
**Exact Solution Of Complex Mode Example**

Singular Values	Eigenvalues
12.852	$-0.06446 \pm 4.1785i$
6.401	$-0.34364 \pm 3.3992i$
3.721	$-0.45722 \pm 2.7047i$
0.282	$-0.13467 \pm 1.4209i$
0.000	
0.000	
0.000	
0.000	

**TABLE 3.2**  
**ERA and Enhanced I.D. Algorithm Comparison**

ERA ALONE		ENHANCED ALGORITHM	
Singular Values	Eigenvalues	Singular Values	Eigenvalues
12.362	$-0.19156 \pm 4.0624i$	12.423	$-0.06031 \pm 4.1672$
6.942	$-77.4706 + 62.831i$	6.925	$-0.30825 \pm 3.2153$
3.360	$-11.0999 + 0.0000i$	3.410	$-0.65604 \pm 2.6112$
0.324	$-0.29788 \pm 2.6670i$	0.275	$-0.13634 \pm 1.4209$
0.298	$-0.15241 \pm 1.4044i$	0.0834	
0.274		0.0756	
0.266		0.0641	
0.251		0.0556	

The last four tables, Table 3.3 through Table 3.6, are the complex mode shapes of the exact solution, those identified by ERA alone, and the enhanced identification algorithm. The results presented here are even more substantial than the previous two cases. Notice complex modes number 3 and 4, neither of these modes were identified very well by the

ERA algorithm alone. However, all four complex modes were identified accurately by the robust mode shape identification algorithm. These results are observed clearly in the following tables.

**TABLE 3.3**

**Complex Mode # 1**

Truth	ERA Alone	Robust Algorithm
$0.374 + 19.0^\circ$	$0.437 + 13.0^\circ$	$0.387 + 19.4^\circ$
$0.607 + 1.4^\circ$	$0.584 + 1.2^\circ$	$0.589 + 1.5^\circ$
$0.619 - 4.9^\circ$	$0.602 - 5.3^\circ$	$0.619 - 5.3^\circ$
$0.386 - 7.6^\circ$	$0.371 - 7.8^\circ$	$0.391 - 7.4^\circ$

**TABLE 3.4**

**Complex Mode # 2**

Truth	ERA Alone	Robust Algorithm
$0.826 + 13.1^\circ$	$0.622 + 5.1^\circ$	$0.864 + 8.7^\circ$
$0.585 - 42.9^\circ$	$0.450 - 24.2^\circ$	$0.497 - 45.0^\circ$
$0.414 - 150.2^\circ$	$0.377 - 152.3^\circ$	$0.423 - 148.6^\circ$
$0.544 + 169.3^\circ$	$0.633 + 178.8^\circ$	$0.431 + 171.4^\circ$

**TABLE 3.5**

**Complex Mode # 3**

Truth	ERA Alone	Robust Algorithm
$0.824 - 36.3^\circ$	$0.543 + 0.0^\circ$	$0.805 - 85.0^\circ$
$0.815 - 151.8^\circ$	$0.579 + 0.0^\circ$	$0.839 - 163.6^\circ$
$0.383 + 136.5^\circ$	$0.511 - 0.0^\circ$	$0.364 + 101.5^\circ$
$0.698 + 14.9^\circ$	$0.324 - 180.0^\circ$	$0.791 + 10.5^\circ$

**TABLE 3.6**

**Complex Mode # 4**

Truth	ERA Alone	Robust Algorithm
$0.268 - 52.0^\circ$	$0.114 + 171.1^\circ$	$0.183 - 79.1^\circ$
$0.584 + 173.9^\circ$	$0.328 + 177.2^\circ$	$0.523 + 169.7^\circ$
$0.696 + 4.6^\circ$	$0.713 + 0.70^\circ$	$0.705 + 4.1^\circ$
$0.465 - 171.3^\circ$	$0.609 - 179.0^\circ$	$0.515 - 174.2^\circ$

## Summary and Conclusions

The successful results of the proposed algorithm convey significant improvements when identifying mode shapes in structures with corrupted output measurements. For instance, when the example structures were subjected to a 5-10% noise level, one mode shape was completely unidentifiable using the Eigensystem Realization Algorithm alone (with and without damping). However, when the enhanced mode shape identification algorithm was tested under the same circumstances, all four mode shapes could be identified accurately (with and without damping). These results are consistent with the singular values calculated from the realized state matrix. The cutoff point (indicating the number of modes identified) for the singular values of Tables 1.3 and 2.3 (ERA) was clearly 3, while the cutoff for Tables 1.5 and 2.5 (enhanced algorithm) was clearly 4.

Examining the the complex mode example, we found significant improvements when identifying the third and forth modes. These robust results can inpart be contributed to the fact that no assumptions were made regarding the model error in the estimation procedure. This infact is especially suited for identifying modes that are not excited very much in the testing procedure. The advantages of such a technique become obvious to the modal testing community.

Also, for noise levels less than 3% of the signal amplitude both algorithms could identify all four mode shapes, while for noise levels exceeding 15% different combinations of identified modes were observed. However, in all cases the Enhanced Mode Shape Identification Algorithm gave improved results. These results confirm the robust nature of the enhanced mode shape identification algorithm and demonstrate structural realization/identification of mode shapes in the presence of high measurement noise.

## Acknowledgements

This work was partially supported by the Air Force Office of Scientific Research (Dr. Anthony Amos, contract monitor) and NASA Langley Research Center (Dr. Jer-Nan Juang, contract monitor). This support is gratefully acknowledged.



## References

1. Hendricks, S.L., et. al., "Identification of Mass, Damping, and Stiffness Matrices for Large Linear Vibratory Systems", **AIAA Journal of Guidance, Control, and Dynamics**, Vol. 7, No. 2, pp. 244-245, March-April 1984.
2. Ibrahim, S.R., and Mikulcik, E.C., "A Method for the Direct Identification of Vibration Parameters from the Free Response," **Shock and Vibration Bulletin**, No. 47, Pt. 4, pp. 183-198, Sept. 1977.
3. Rajaram, S., and Junkins, J.L., "Identification of Vibrating Flexible Structures", **AIAA Journal of Guidance, Control, and Dynamics**, Vol. 8, No. 4, pp. 463-470, July-Aug. 1985.
4. Chen, J.C., et.al., "Direct Structural Parameter Identification by Modal Test Results", 24th Structures, Structural Dynamics, and Materials Conference, Pt. 2, 1983.
5. Juang, J.-N., and Pappa, R.S., "An Eigensystem Realization Algorithm (ERA) for Modal Parameter Identification and Model Reduction", **AIAA Journal of Guidance, Control, and Dynamics**, Vol. 8, No. 5, pp. 620-627, Sept.-Oct. 1985.
6. Pappa, R.S., and Juang, J.-N., "Galileo Spacecraft Modal Identification Using an Eigensystem Realization Algorithm", **Journal of the Astronautical Sciences**, Vol. 33, pp. 15-33, Jan.-Mar. 1985.
7. Juang, J.-N., and Pappa, R.S., "Effects of Noise on Modal Parameters Identified by the Eigensystem Realization Algorithm", **AIAA Journal of Guidance, Control, and Dynamics**, Vol. 9, No. 3, pp. 294-303, May-June 1986.
8. Klema, V.C., and Laub, A.J., "The Singular Value Decomposition: Its Computation and Some Applications", **IEEE Transactions on Automatic Control**, Vol. AC-25, No. 2, pp. 164-176, April 1980.
9. Mook, D.J., and Lew, J.S., "A Combined ERA/MME Algorithm for Robust System Realization/Identification", Proceedings of the 29th Structures, Structural Dynamics, and Materials Conference, Williamsburg, Virginia, April 1988.
10. Ho, B.L., and Kalman, R.E., "Effective Construction of Linear State-Variable Models From Input/Output Data", 3<sup>rd</sup> Annual Allerton Conference on Circuit and System Theory, pp.

449-459, 1965.

11. Gelb, A., editor, **Applied Optimal Estimation**, MIT Press, Cambridge, Massachusetts, 1984.
12. Lewis, F.L., **Optimal Estimation**, Wiley-Interscience Publication, New York, 1986.
13. Mook, D.J., and Junkins, J.L., "Minimum Model Error Estimation for Poorly Modeled Dynamic Systems", **AIAA Journal of Guidance, Control, and Dynamics**, Vol. 11, No. 4, pp. 367-375, May-June. 1988.
14. Mook, D.J., and Lin, J.-C., "Minimum Model Error Estimation of Modal Truncation Errors", Proceedings of the 1987 Spring Meeting of the Society for Experimental Mechanics, Houston, TX, June 1987.
15. Mook, D.J., "Estimation and Identification of Nonlinear Dynamic Systems", Proceedings of the 29<sup>th</sup> Structures, Structural Dynamics, and Materials Conference, Williamsburg, Virginia, April 1988. Also, to appear, **AIAA Journal**.
16. Junkins, J.L., and Mook, D.J., **Enhanced Spacecraft Attitude Estimation**, Final Report, Contract No. N60921-83-G-9-A165, Naval Surface Weapons Center, Dahlgren, Virginia, 1985.
17. Lew, J.S., and Mook, D.J., "Two-Point boundary Problems Containing Jump Discontinuities", in Review.
18. Meirovitch, L., **Elements of Vibration Analysis**, McGraw-Hill, New York, 1975.

# **OPTIMUM SELECTION OF DAMPERS FOR FREELY VIBRATING MULTIDEGREE OF FREEDOM SYSTEMS**

by

**John J. Gilheany**  
Mechanical Engineering Department  
The Catholic University of America  
Washington, DC 20064

## *Abstract*

A numerical method is presented for the optimum selection of the magnitude(s) and location(s) of from 1 to  $N$  viscous dampers, out of  $(N^2 + N)/2$  possible absolute and relative dampers, for a freely vibrating discrete  $N$  degree of freedom systems consisting of masses and springs. The optimization algorithm combines iterative application of a pattern search in damper space over all possible damper configurations, along with numerical integration of the coupled equations of motion, in order to minimize an objective function. The objective function used is the integral of time multiplied by the squared error (ITSE), where the squared error is the sum of the squares of the displacements and velocities of the masses. The method does not require the solution of the eigenvalue problem. The method can accommodate constraints on the magnitudes and locations of dampers, as well as the motion of the masses, and is also applicable for optimum selection of damper in order to minimize the total response of driven systems. Results are presented for 2 and 3 degrees of freedom systems.

## 1. INTRODUCTION

The optimum design of dynamic vibration absorber(s) has received considerable attention since the publication of the analysis of the dynamic vibration absorber by Ormondroyd and Den Hartog<sup>1</sup> and the optimization of dynamic absorber design contained in Den Hartog's<sup>2</sup> classic text. Recent efforts include analytical and/or numerical techniques for the optimum design of linear and nonlinear dynamic absorber(s) for the passive damping of the steady state response of harmonically driven discrete<sup>3-5</sup> and continuous<sup>6-9</sup> mechanical systems.

The optimal design of dynamic vibration absorbers for minimizing the transient response of freely vibrating discrete mechanical systems has received considerably less attention. Nagaev and Stepanov<sup>10</sup> obtained an analytical expression for optimum damper parameters for an undamped primary system, and Rowbottom<sup>11</sup> developed an analytical method for optimum damping of electrical transmission lines. Ebrahimi<sup>12</sup> developed a numerical algorithm for optimizing dynamic absorber design for a damped primary system using two different time-domain objective functions, i.e., the logarithmic decrement of the combined system and the real part of the roots of the characteristic equation.

In this paper a numerical method is presented for the optimum selection of the magnitude(s) and location(s) of from 1 to  $N$  viscous dampers, out of  $(N^2 + N)/2$  possible absolute and relative dampers, in order to minimize the transient response of a discrete  $N$  degree of freedom system consisting of masses and linear springs. The method involves the iterative application of a pattern search in damper space over all possible configurations of dampers, along with direct numerical integration of the coupled equations of motion, in order to minimize an objective function. The method is equally applicable to minimizing the total response of harmonically driven systems and can handle constraints on damper type and magnitude, as well as constraints on the motion of one or more of the masses.

## 2. DESIGN PROBLEM FORMULATION

A three degree of freedom system containing the maximum number of nonredundant viscous dampers, i.e., three absolute and three relative dampers, is shown in Fig. 1. A double subscript notation is employed for the dampers in order to specify their location. Equal subscripts ( $d_{11}$ ,  $d_{22}$  and  $d_{33}$ ) signify absolute dampers between masses 1 through 3 and ground, respectively. Unequal subscripts signify relative dampers between the masses identified by each of the subscripts, e.g.,  $d_{23}$  is a relative damper between  $m_2$  and  $m_3$ .

Assuming that the values of the masses and the stiffness of the springs are known, the problem of optimum selection of dampers for such a system will depend on the design constraints, e.g., the number  $ND$  of absolute and/or relative dampers permitted, constraints on the magnitude of one or more of the dampers, constraints on the absolute or relative motion of the masses, etc. For example, the design problem can vary from determining the magnitudes of the three absolute dampers which will produce maximum damping, to determining the location(s) and magnitude(s) of one or two dampers which will minimize the motion of the masses. In order to keep the problem general in nature, the approach used in this paper is to iterate over all possible configurations of dampers for the number of dampers  $ND$  over the range:  $1 \leq ND \leq N$ .

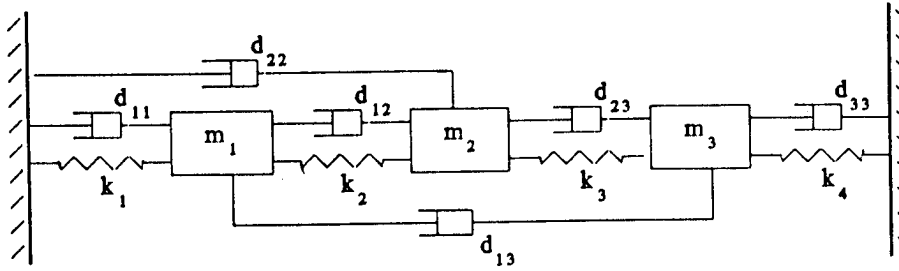


Figure 1. Three degree of freedom system with maximum number of nonredundant dampers.

The complete set of nonredundant dampers for the three degree of freedom system of Fig. 1 can be written as a  $3 \times 3$  array with zero elements below the diagonal:

$$\begin{bmatrix} d_{11} & d_{12} & d_{13} \\ 0 & d_{22} & d_{23} \\ 0 & 0 & d_{33} \end{bmatrix}$$

Generalizing to an  $N$  degree of freedom system, the complete set of nonredundant dampers is given by a  $N \times N$  array containing  $(N^2 + N)/2$  non-zero elements or nonredundant dampers. Alternately, the system damping can be described by an  $(N^2 + N)/2$  element vector, which for the system of Fig. 1 is given by:

$$\mathbf{d} = \begin{bmatrix} d_{11} \\ d_{12} \\ d_{13} \\ d_{22} \\ d_{23} \\ d_{33} \end{bmatrix} \quad (1)$$

For  $ND = 3$ , there are twenty possible configurations of the three non-zero dampers. The number of combinations  $C_r^m$  of  $r$  items from  $m$  items, where the order of selection is not important, is given by<sup>14</sup>:

$$C_r^m = m! / [(m - r)! r!]. \quad (2)$$

For  $ND = 2$  or  $ND = 1$ , there are fifteen or six possible combinations of dampers, respectively, for the 3 degree of freedom system.

The equations of motion for the system in Fig. 1. can be written in matrix notation as:

$$M \ddot{\mathbf{x}}(t) + C \dot{\mathbf{x}}(t) + K \mathbf{x}(t) = 0 \quad (3)$$

where

$$M = \begin{bmatrix} m_1 & 0 & 0 \\ 0 & m_2 & 0 \\ 0 & 0 & m_3 \end{bmatrix}, \quad K = \begin{bmatrix} (k_1 + k_2) & -k_2 & 0 \\ -k_2 & (k_2 + k_3) & -k_3 \\ 0 & -k_3 & (k_3 + k_4) \end{bmatrix},$$

and

$$C = \begin{bmatrix} (d_{11} + d_{12} + d_{13}) & -d_{12} & -d_{13} \\ -d_{12} & (d_{12} + d_{22} + d_{23}) & -d_{23} \\ -d_{13} & -d_{23} & (d_{13} + d_{23} + d_{33}) \end{bmatrix}, \quad \mathbf{x} = \begin{bmatrix} x_1 \\ x_2 \\ x_3 \end{bmatrix}.$$

The  $x_i$ 's are the displacements of the three masses relative to their equilibrium positions.

The coupled equations of motion of eqn. (3) are given by:

$$\begin{aligned} m_1 \ddot{x}_1 + (d_{11} + d_{12} + d_{13}) \dot{x}_1 - d_{12} \dot{x}_2 - d_{13} \dot{x}_3 + (k_1 + k_2)x_1 - k_2 x_2 &= 0 \\ m_2 \ddot{x}_2 - d_{12} \dot{x}_1 + (d_{12} + d_{22} + d_{23}) \dot{x}_2 - d_{23} \dot{x}_3 - k_2 x_1 + (k_2 + k_3)x_2 - \\ k_3 x_3 &= 0 \end{aligned} \quad (4)$$

$$m_3 \ddot{x}_3 - d_{13} \dot{x}_1 - d_{23} \dot{x}_2 + (d_{13} + d_{23} + d_{33}) \dot{x}_3 - k_3 x_2 + (k_3 + k_4)x_3 = 0.$$

Given the initial conditions, i.e.,  $x_1(0)$ ,  $x_2(0)$ ,  $x_3(0)$ ,  $\dot{x}_1(0)$ ,  $\dot{x}_2(0)$  and  $\dot{x}_3(0)$ , and the values of the masses, springs and dampers; the coupled equations of motion, eqn. (4), can be numerically integrated to yield the displacements, velocities and accelerations of the masses as a function of time without solving the eigenvalue problem. Application to higher order systems is straight forward. However, the values of the dampers are not know. The optimization process described in the next section is used to determine the optimum damping space vector  $\mathbf{d}$ , i.e., the magnitudes and locations of the ND dampers, which will minimize the transient motion of the system.

### 3. OPTIMIZATION

The damping optimization problem may be viewed as a determination of the damping vector  $\mathbf{d}$  which gives the coordinates of the extremum of an objective function in damper space. The objective function used to quantify the motion of the system is the integral of time multiplied by the squared error (ITSE)<sup>13</sup>, i.e.,

$$OF = \int_0^T t e^2(t) dt = \sum_{k=1}^N t_k \left[ \dot{x}_i^2(t_k) + \ddot{x}_i^2(t_k) \right] \Delta t. \quad (5)$$

The coordinates in damper space of the minimum of the ITSE objective function give the optimum damper values for the given combination of dampers, i.e., for the non-zero elements of the damping vector  $\mathbf{d}$ .

An advantage of using ITSE as the objective function is that it does not require that the eigenfrequencies of the system be determined. Also, constraints can be placed on the objective function so as to weight the motion of the individual masses, or limits can be imposed on the maximum displacement, velocity or acceleration of one or more of the masses.

The method used to determine the minimum of the objective function in damper space is the Hooke-Jeeves<sup>15</sup> pattern search. A step increment size  $\delta_i$ , a step reduction factor  $\alpha$  and a termination parameter  $\epsilon$  are defined. An initial guess is made for the non-zero elements of  $\mathbf{d}$ , the  $\mathbf{C}$  matrix of eqn. (3) is formed and the equations of motion are integrated to determine the value of OF. Next, an exploratory search is conducted by incrementing each non-zero component of  $\mathbf{d}$  by  $\pm \delta_i$  and a new OF is calculated. If the exploratory search is successful, i.e., the new value of OF is less than the previous value, then the following pattern move is made:

$$\mathbf{d}^{(k+1)} = \mathbf{d}^{(k)} + (\mathbf{d}^{(k)} - \mathbf{d}^{(k-1)}). \quad (6)$$

The procedure is continued until there is no further reduction in OF and then the step increment size is reduced by dividing it by  $\alpha$ . The process continues until the reduction in OF is less than the termination parameter  $\epsilon$ . The value of  $\mathbf{d}$  at the conclusion of the search defines the location of the minimum of OF in damper space. Numerical examples are present in the following section.

#### 4. NUMERICAL EXAMPLES

Numerical examples are presented for both two and three degree of freedom systems. In order to keep the design problem general in nature, the results of application of the optimization algorithm to all possible combinations of damper for  $1 \leq ND \leq N$  are presented. This iterative approach allows comparison of the effectiveness of optimum damping for all possible damping configurations.

For the two degree of freedom system shown in Fig. 2, the following values are assigned for the masses, springs and initial conditions:  $m_1 = 4.$ ,  $m_2 = 1.$ ,  $k_1 = 3.$ ,  $k_2 = 1.$ ,  $x_1(0) = 2.$ ,  $x_2(0) = -2.$  and  $\dot{x}_1(0) = \dot{x}_2(0) = 0.$  The undamped time history of the displacements of the masses is shown in Fig. 3.

The results of application of the optimization algorithm to all configurations of dampers for both  $ND = 2$  and  $ND = 1$  are presented in Table 1. For purposes of comparison, the value of the objective function for each configuration is normalized with respect to the minimum value of the objective function for  $ND = N$ . Review of Table 1 shows that optimum damping, i.e.,  $OF = 1.$  and  $DN = 2$ , requires two absolute dampers whose values are  $d_{11} = 6.33$  and  $d_{22} = 2.46$ . Application of the optimization algorithm to the over design case of  $ND = 3$  yields optimum damper values of  $d_{11} = 6.26$ ,  $d_{12} = 0.05$  and  $d_{22} = 2.37$  and an OF which is identical to that of the optimum  $ND = 2$  configuration previously discussed. For the configuration of an absolute damper on  $m_1$  and a relative damper between  $m_1$  and  $m_2$ , optimum damping occurs for damper values of  $d_{11} = 4.40$  and  $d_{12} = 1.37$ . This damping configuration

yields an  $OF = 1.07$ ; whereas changing the location of the absolute damper from  $m_1$  to  $m_2$  yields an  $OF = 17.08$  for optimum damper values of  $d_{12} = 1.67$  and  $d_{22} = 2.56$ . The time histories of the displacements of the masses for all three  $ND = 2$  cases are shown in Fig. 4.

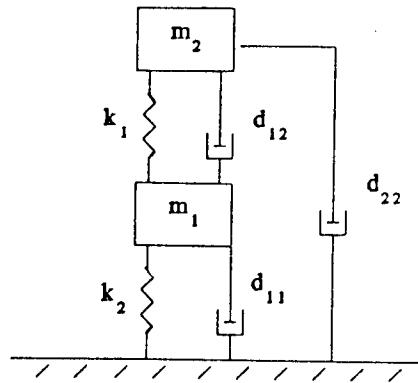


Figure 2. Two degree of freedom system with maximum number of nonredundant dampers.

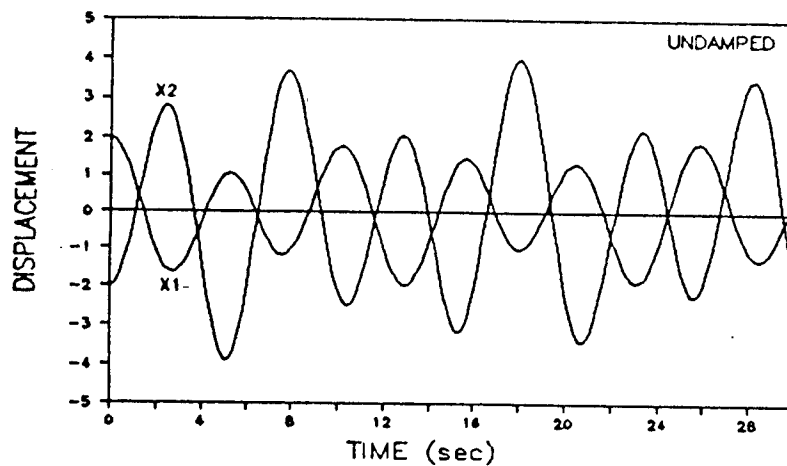


Figure 3. Time history of undamped displacements  $x_i$  of masses  $m_i$  for two degree of freedom system:  $m_1 = 4.$ ,  $m_2 = 1.$ ,  $k_1 = 3.$  and  $k_2 = 1.$

A contour plot of the objective function in damper space, i.e.,  $OF$  versus  $d_{11}$  and  $d_{22}$ , for the optimum case is shown in Fig. 5. The minimum value of  $OF$  is 7.94 with coordinates  $d_{11} = 6.33$  and  $d_{22} = 2.46$ . This minimum value of  $OF$  is used to normalize all  $OF$  values in Table 1.

The effects on the time histories of the displacements of the masses by alternately changing  $d_{11}$  and  $d_{22}$  by  $\pm 2.0$  from the optimum damping values are shown in Figs. 6 and 7, respectively. Increasing and decreasing  $d_{11}$  by 2.0 results in  $OF$  values of 1.24 and 1.34, respectively; whereas increasing and decreasing  $d_{22}$  by 2.0 results in  $OF$  values of 2.41 and 8.53, respectively.



TABLE 1

Results of optimization for two degree of freedom system with two or one dampers; system parameters:  $m_1 = 4.$ ,  $m_2 = 1.$ ,  $k_1 = 3.$ , and  $k_2 = 1.$

NUMBER OF DAMPERS	DAMPER MAGNITUDES			NORMALIZED* OBJECTIVE FUNCTION
	$d_{11}$	$d_{12}$	$d_{22}$	
2	4.40	1.37	-	1.07
2	6.33	-	2.46	1.00
2	-	1.67	2.56	17.08
1	2.78	-	-	51.19
1	-	0.44	-	91.40
1	-	-	0.88	35.65

\* Objective function divided by minimum value of objective function with number of dampers equal to the number of degrees of freedom

Using a single damper in the two degree of freedom system under consideration, optimum damping occurs with an absolute damper on  $m_2$ , i.e.,  $d_{22} = 0.88$ , with an OF = 35.65. If the location of the absolute damper is changed from  $m_2$  to  $m_1$ , the magnitude of the damper required for optimum damping is slightly more than tripled with an OF = 51.19. The least effective ND = 1 damping configuration occurs with a relative damper between  $m_1$  and  $m_2$  of magnitude  $d_{12} = 0.44$  with an OF = 91.40. The time histories of the displacements of the masses for these three ND = 1 cases are shown in Fig. 8.

For the three degree of freedom system shown in Fig. 1, the following values are assigned for the masses, springs and initial conditions:  $m_1 = 2.$ ,  $m_2 = 1.$ ,  $m_3 = 1.$ ,  $k_1 = 3.$ ,  $k_2 = 2.$ ,  $k_3 = 1.$ ,  $k_4 = 0.$ ,  $x_1(0) = 1.$ ,  $x_2(0) = 0.$ ,  $x_3(0) = -2.$  and  $\dot{x}_1(0) = \dot{x}_2(0) = \dot{x}_3(0) = 0.$  The undamped time history of the displacements of the masses is shown in Fig. 9.

The results of application of the optimization algorithm to the twenty possible configurations of dampers for ND = 3 are presented in Table 2. For ND = 3, optimum damping is achieved by an absolute damper on  $m_1$  and a pair of relative dampers between  $m_1$  and  $m_2$ , and  $m_2$  and  $m_3$ , respectively. The optimum values of the dampers are:  $d_{11} = 2.83$ ,  $d_{12} = 1.26$  and  $d_{23} = 1.76$ . The configuration of an absolute damper on each mass yields optimum damper values of:  $d_{11} = 4.44$ ,  $d_{22} = 5.37$  and  $d_{33} = 1.60$  and an OF = 1.06. Review of Table 2 indicates that there are nine other configurations of optimum dampers that will result in OF values which are less than 2.0. However, three of these configurations require unrealistically large absolute dampers on  $m_2$ . The least effective ND = 3 damper configuration is for three relative dampers, i.e.,  $d_{12} = 0.88$ ,  $d_{13} = 0.0$  and  $d_{23} = 1.29$ , with an OF value of 21.28. Unfortunately, this configuration of all relative dampers is the configuration available in many space applications. Note that the optimum value for  $d_{13}$  is zero. Time histories of the displacements for the most and least effective configurations for ND = 3 are shown in Fig. 10.

The results of application of the optimization algorithm to the fifteen configurations of dampers for ND = 2 and the six configurations for ND = 1 are presented in Table 3. Review of the ND = 2 data in Table 3 indicates five damper configurations which will result in normalized OF values which are less

than 5.0. The best ND = 2 case consists of an absolute damper on  $m_1$  and a relative damper between  $m_2$  and  $m_3$ . The optimum damper values are  $d_{11} = 1.61$  and  $d_{23} = 1.34$  with OF = 2.59. The least effective ND = 2 configuration consists of an absolute damper on  $m_3$  and a relative damper between  $m_1$  and  $m_2$ , i.e.,  $d_{33} = 1.06$  and  $d_{12} = 0.34$ , with an OF = 49.65. Time histories of the displacement of the masses for the most and least effective ND = 2 damper configurations are shown in Fig. 11.

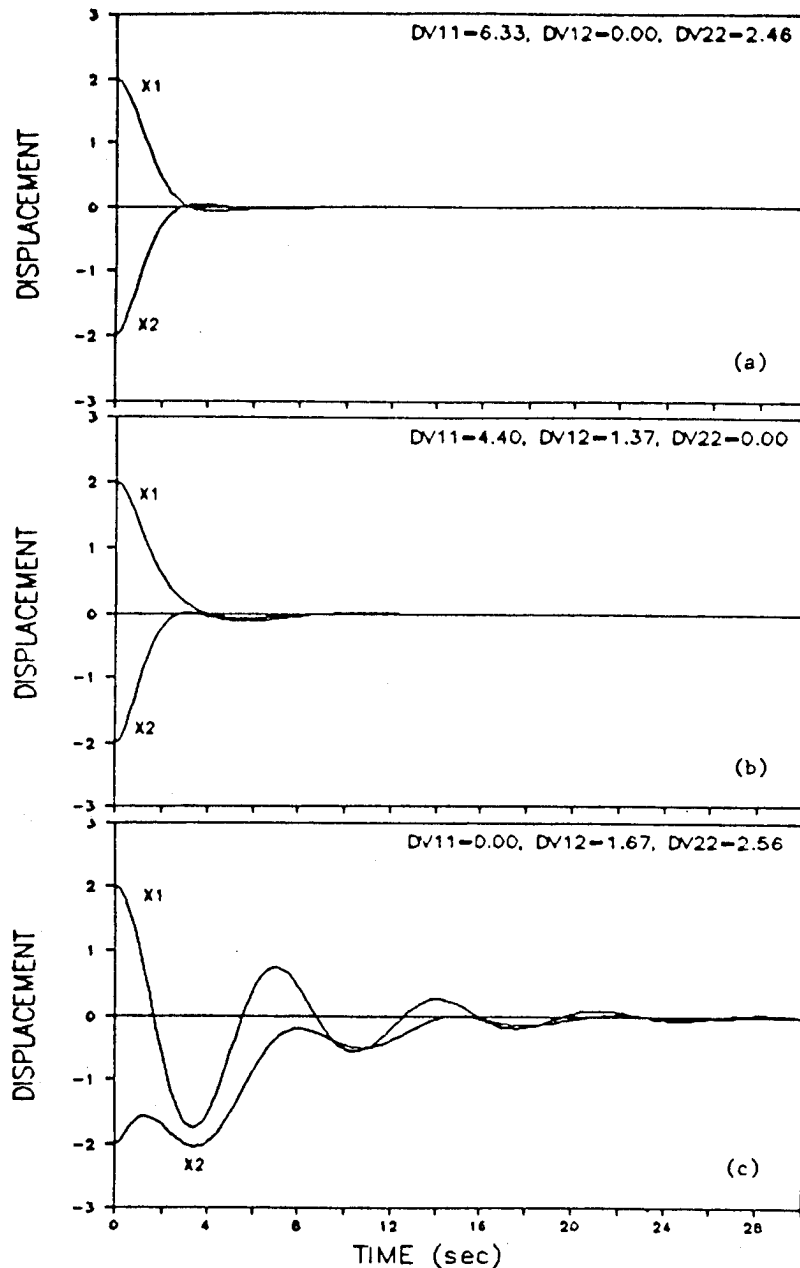


Figure 4. Time histories of the displacements  $x_i$  of masses  $m_i$  for system of Table 1 with optimum damping configurations: (a)  $d_{11} = 6.33$  and  $d_{22} = 2.46$ , (b)  $d_{11} = 4.40$  and  $d_{12} = 1.37$ , and (c)  $d_{12} = 1.67$  and  $d_{22} = 2.56$ .

If a single damper,  $ND = 1$ , is used for the three degree of freedom system under consideration, optimum damping occurs with an absolute damper on  $m_2$  of magnitude 2.29. This damping configuration results in an  $OF = 24.56$ . If only relative dampers are available, optimum damping occurs with a damper between  $m_2$  and  $m_3$  of magnitude 0.72 with an  $OF$  which is 15% higher than the previous case. The least effective single damper configuration is a relative damper between  $m_1$  and  $m_2$  of magnitude 1.98 with an  $OF$  which is over forty times greater than the most effective  $ND = 1$  configuration. The time histories of the displacement of the masses for the most and least effective  $ND = 1$  configurations are shown in Fig. 12.

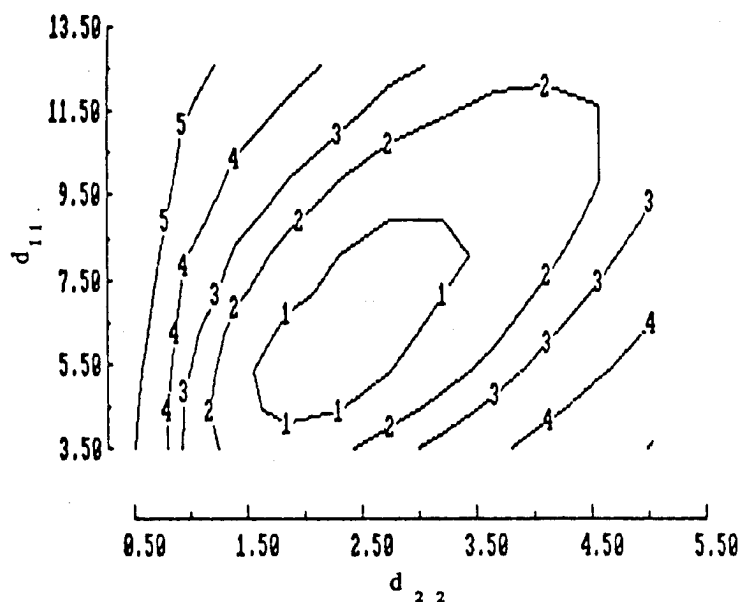


Figure 5. Contour plot of objective function (ITSE) in damper space for system of Table 1. Minimum value of  $OF = 7.94$  at coordinates  $d_{11} = 6.33$  and  $d_{22} = 2.46$ . Contour values: 1 = 10, 2 = 15, 3 = 20, 4 = 30 and 5 = 50.

## 5. CONCLUSIONS

A numerical method is presented for the optimum selection of dampers for minimizing the transient response of discrete  $N$  degree of freedom systems. Application of the algorithm in an iterative mode to all damper configurations for  $N$  dampers yields the magnitudes and locations of the  $N$  dampers, out of  $(N_2 + N)/2$  possible dampers, which will minimize the motion of the system; as well as the minimum value of the objective function. Further application of the algorithm in an iterative mode to all damper configurations for  $ND$  dampers, over the range  $1 \leq ND \leq (N-1)$ , yields the magnitudes and locations of optimum dampers for all possible damping configurations of the system. The effectiveness of each possible damping configuration of the system in minimizing motion can be compared and ranked by comparison of the respective objective functions which are normalized by the minimum objective function for the  $ND = N$  configurations.

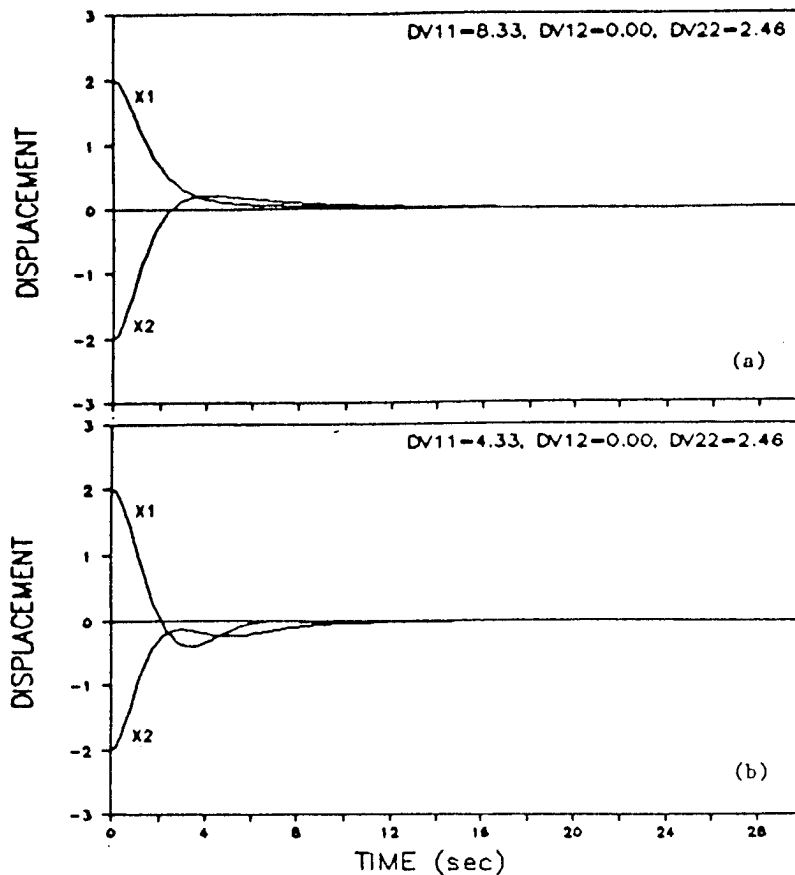


Figure 6. Effects of (a) increasing and (b) decreasing the value of  $d_{11}$  by 2.0 on system performance shown in Figure 4.(a).

Numerical examples are presented for both two and three degree of freedom systems. In the following discussion, the objective functions are normalized by the minimum value of the objective function for the  $ND = N$  configurations, and the magnitude of the optimum damper values for each configuration are not stated. In the two degree of freedom example, application of the algorithm yields the expected results that optimum damping occurs with absolute dampers on each mass. However, the configuration of an absolute damper on  $m_1$  and a relative damper between  $m_1$  and  $m_2$  results in a objective function of 1.07, whereas changing the location of the absolute damper to  $m_2$  results in an objective function 17.08. If only a single damper is used, the most effective system damping configuration is an absolute damper on  $m_2$  with an objective function of 35.65. An absolute damper on  $m_1$  results in an objective function of 51.19 and the least effective configuration is a relative damper between  $m_1$  and  $m_2$  with an objective function of 91.40. Application to the algorithm to the over design case where three dampers are used also results in an objective function of 1.00.

In the three degree of freedom example, the most effective damping configuration is an absolute damper on  $m_1$  and two relative dampers between  $m_1$  and  $m_2$  and between  $m_2$  and  $m_3$ . The configuration of an absolute damper on each mass has an objective function of 1.06. Nine other configurations of three dampers have objective functions which are less than 2.00, but three of these require unrealistically large dampers on  $m_2$ . The least effective three damper configuration is three relative dampers with an objective function of

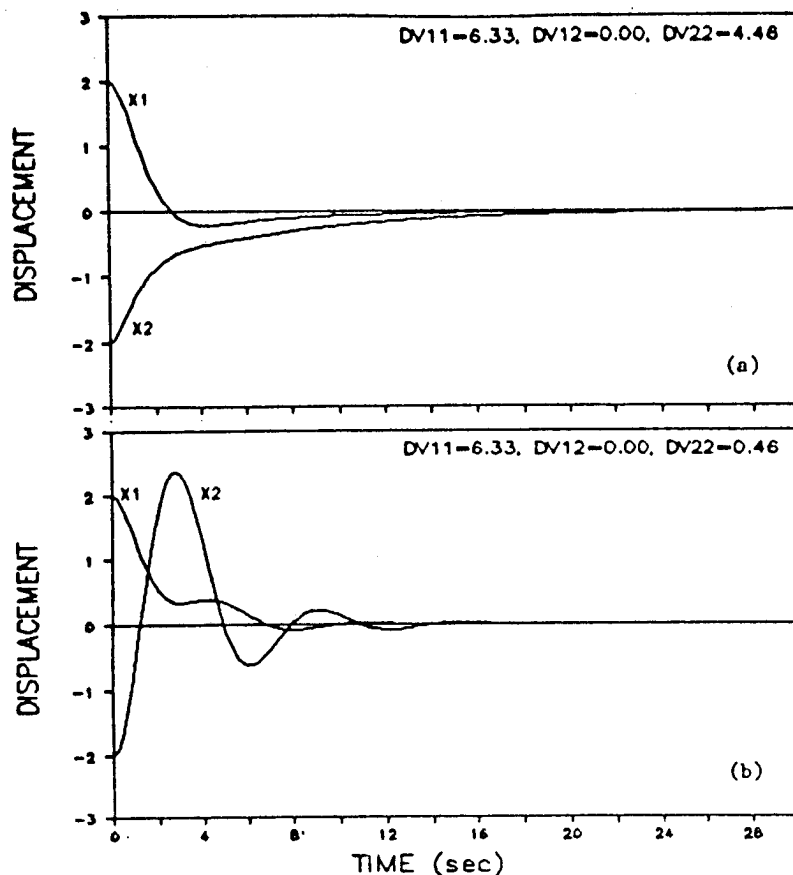


Figure 7. Effects of (a) increasing and (b) decreasing the value of  $d_{22}$  by 2.0 on system performance shown in Figure 4.(a).

21.28, however the optimum value of the relative damper between  $m_1$  and  $m_3$  is zero. If two dampers are used, the most effective configuration is an absolute damper on  $m_1$  and a relative damper between  $m_2$  and  $m_3$  with an objective function of 2.59. The least effective two damper configuration is an absolute damper on  $m_3$  and a relative damper between  $m_1$  and  $m_2$  with an objective function of 49.65. Lastly, if only a single damper is used, the most effective configuration is an absolute damper on  $m_2$  and the least effective is relative damper between  $m_1$  and  $m_2$  with objective functions of 24.56 and 1044.51, respectively.

The major advantages of the method are that both the magnitudes and locations of optimum dampers for all possible damping configurations of the system are determined, the evaluation and ranking of alternative damping configurations such as type of dampers (absolute and/or relative) and number or location of dampers is easily accomplished through comparison of the respective objective functions, and the solution of the eigenvalue problem is not required. The method is also applicable for system constraints such as limits on the motion of one or more of the masses. Also, the method can be applied to optimum damper selection for driven systems or systems involving nonlinear springs. The method is general in nature in that other objective functions which depend on the motion of the masses can be used and other optimization algorithms can be used to determine the extremum of the objective function in damper space.

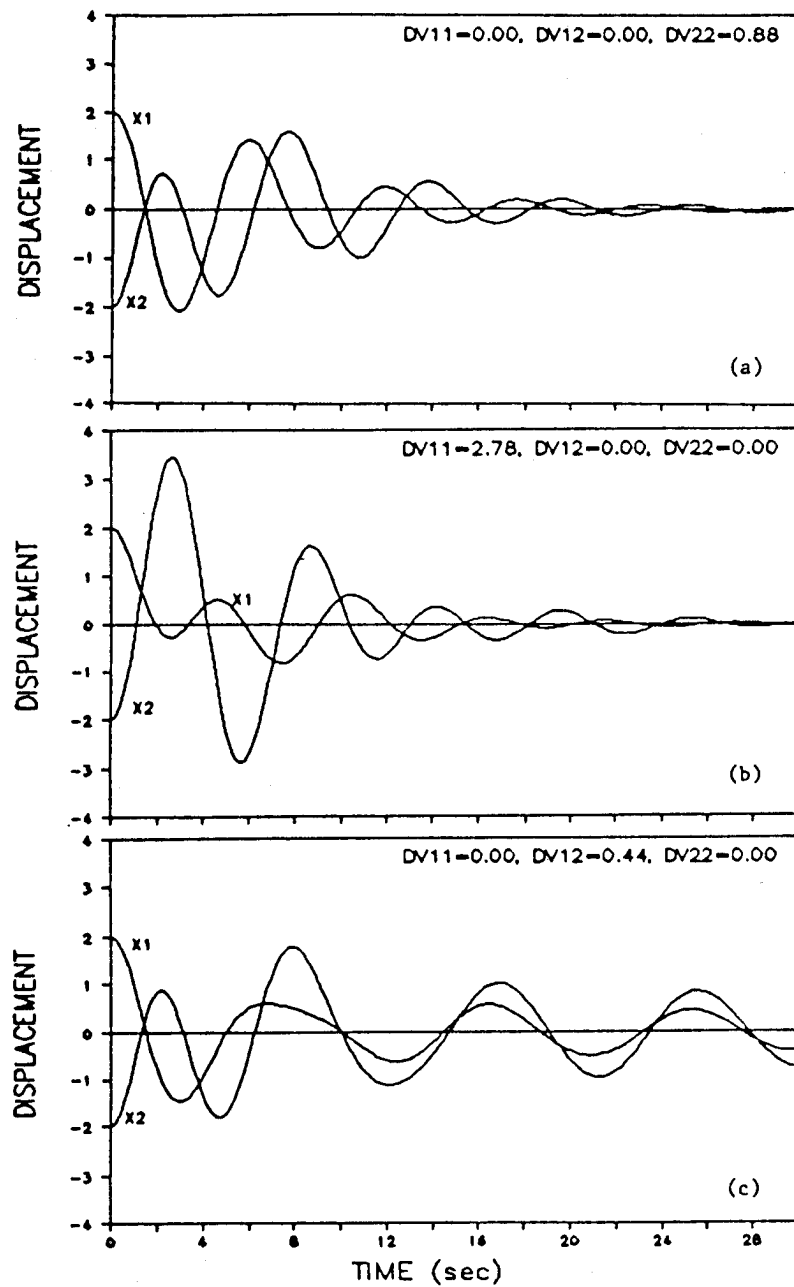


Figure 8. Time histories of the displacements  $x_i$  of masses  $m_i$  for system of Table 1 with optimum damping configurations: (a)  $d_{22} = 0.88$  (b)  $d_{11} = 2.78$  and (c)  $d_{12} = 0.44$ .

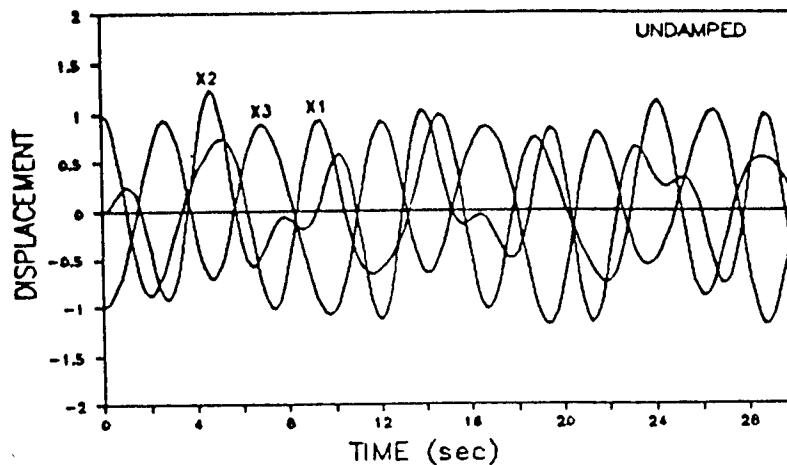


Figure 9. Time history of undamped displacements  $x_i$  of masses  $m_i$  for three degree of freedom system:  $m_1 = 2.$ ,  $m_2 = 1.$ ,  $m_3 = 1.$ ,  $k_1 = 3.$ ,  $k_2 = 2.$  and  $k_3 = 1.$

TABLE 2

Results of optimization for three degree of freedom system with three dampers; system parameters:  $m_1 = 2.$ ,  $m_2 = 1.$ ,  $m_3 = 1.$ ,  $k_1 = 3.$ ,  $k_2 = 2.$  and  $k_3 = 1.$

NUMBER OF DAMPERS	DAMPER MAGNITUDES						NORMALIZED* OBJECTIVE FUNCTION
	$d_{11}$	$d_{12}$	$d_{13}$	$d_{22}$	$d_{23}$	$d_{33}$	
3	4.16	2.11	0.58	-	-	-	1.21
3	3.31	3.16	-	0.00	-	-	4.99
3	2.83	1.26	-	-	1.76	-	1.00
3	5.13	1.28	-	-	-	1.33	1.11
3	3.30	-	0.87	2.06	-	-	1.36
3	3.07	-	0.53	-	0.83	-	1.31
3	5.48	-	0.21	-	-	1.35	2.89
3	3.03	-	-	3.14	2.37	-	1.28
3	4.44	-	-	5.37	-	1.60	1.06
3	4.26	-	-	-	0.76	1.07	1.38
3	-	5.75	0.77	4000.91	-	-	1.32
3	-	0.88	0.00	-	1.29	-	21.28
3	-	0.56	0.47	-	-	0.48	16.34
3	-	5.16	-	3284.19	1.41	-	1.05
3	-	5.16	-	3505.00	-	1.41	1.05
3	-	0.64	-	-	1.72	0.89	9.75
3	-	-	0.66	2.11	0.00	-	4.82
3	-	-	0.66	2.11	-	0.00	4.82
3	-	-	0.42	-	1.53	1.08	12.22
3	-	-	-	0.83	0.39	1.01	11.37

\* Objective function divided by minimum objective function with number of dampers equal to the number of degrees of freedom

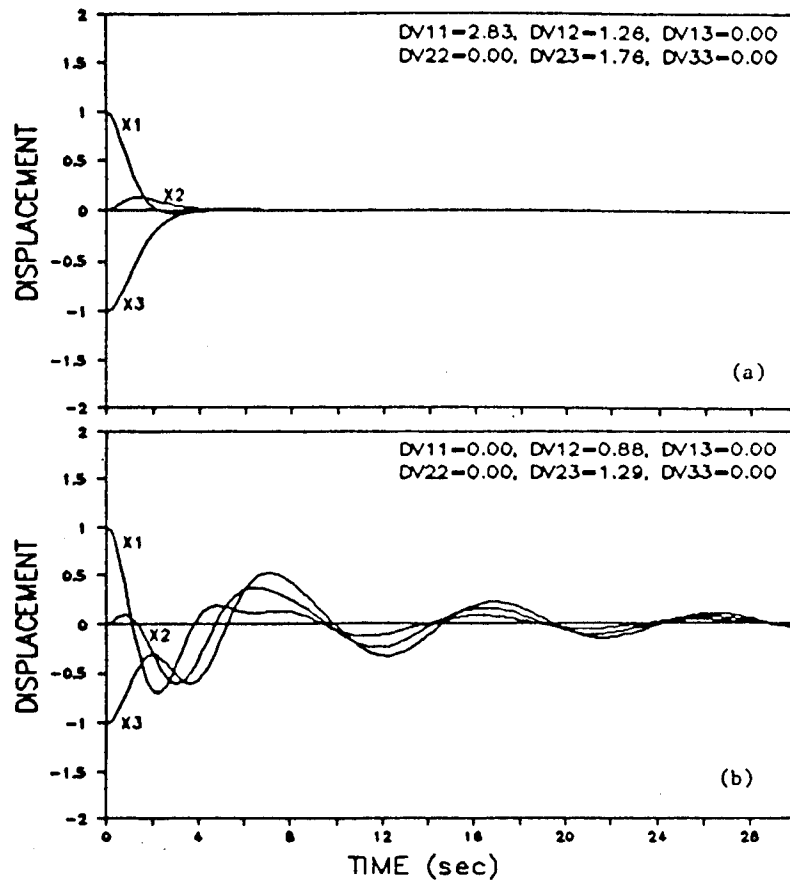


Figure 10. Time histories of the displacements  $x_i$  of masses  $m_i$  for the system of Table 2 for (a) most effective damping configuration:  $d_{11} = 2.83$ ,  $d_{12} = 1.26$  and  $d_{23} = 1.76$ ; and (b) for least effective damping configuration:  $d_{12} = 0.88$ ,  $d_{13} = 0.00$  and  $d_{23} = 1.29$ .



TABLE 3

Results of optimization for three degree of freedom system with one or two dampers; system parameters:  $m_1 = 2.$ ,  $m_2 = 1.$ ,  $m_3 = 1.$ ,  $k_1 = 3.$ ,  $k_2 = 2.$  and  $k_3 = 1.$

NUMBER OF DAMPERS	DAMPER MAGNITUDES						NORMALIZED OBJECTIVE FUNCTION*
	$d_{11}$	$d_{12}$	$d_{13}$	$d_{22}$	$d_{23}$	$d_{33}$	
2	3.31	3.16	-	-	-	-	4.99
2	6.01	-	1.28	-	-	-	3.60
2	1.31	-	-	1.51	-	-	12.87
2	1.61	-	-	-	1.34	-	2.59
2	5.53	-	-	-	-	1.62	2.91
2	-	0.69	0.54	-	-	-	24.66
2	-	2.41	-	3.14	-	-	11.45
2	-	0.88	-	-	1.29	-	21.28
2	-	0.34	-	-	-	1.06	49.65
2	-	-	0.66	2.11	-	-	4.82
2	-	-	0.28	-	0.66	-	24.19
2	-	-	1.74	-	-	2.62	39.06
2	-	-	-	0.66	0.55	-	14.20
2	-	-	-	1.37	-	1.55	12.39
2	-	-	-	-	0.62	0.54	15.82
1	2.01	-	-	-	-	-	55.87
1	-	1.98	-	-	-	-	1044.51
1	-	-	1.02	-	-	-	307.43
1	-	-	-	2.29	-	-	24.56
1	-	-	-	-	0.72	-	28.29
1	-	-	-	-	-	1.29	212.58

\* Objective function divided by minimum objective function with number of dampers equal to the number of degrees of freedom

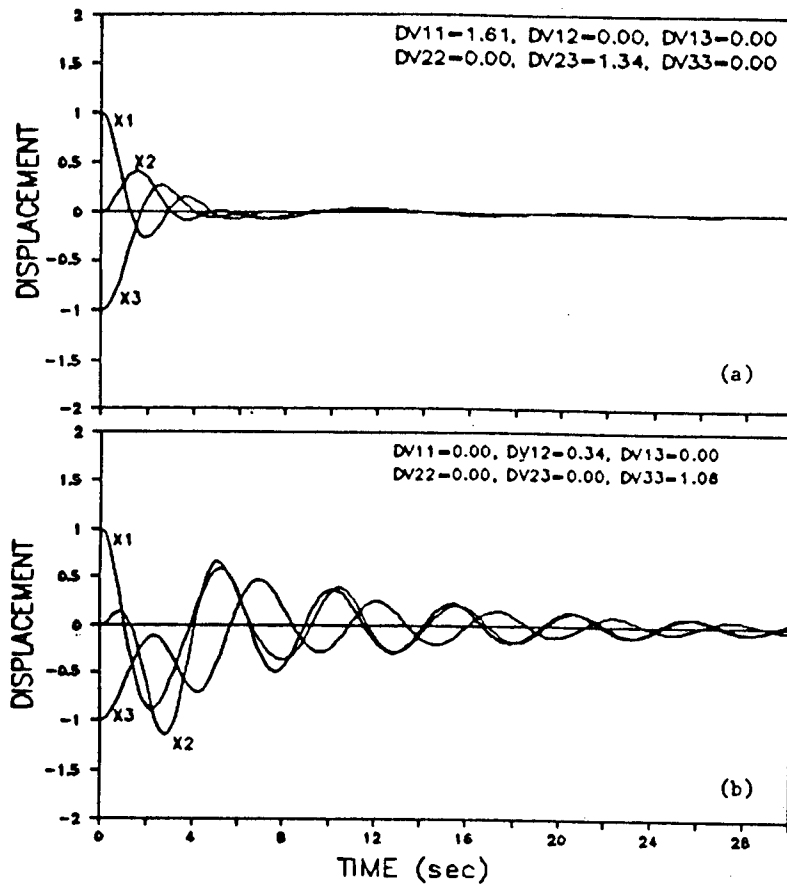


Figure 11. Time histories of the displacements  $x_i$  of masses  $m_i$  for the system of Table 3 with  $ND = 2$  for (a) most effective damping configuration:  $d_{11} = 1.61$ ,  $d_{23} = 1.34$ ; and (b) for least effective damping configuration:  $d_{12} = 0.34$  and  $d_{33} = 1.06$ .

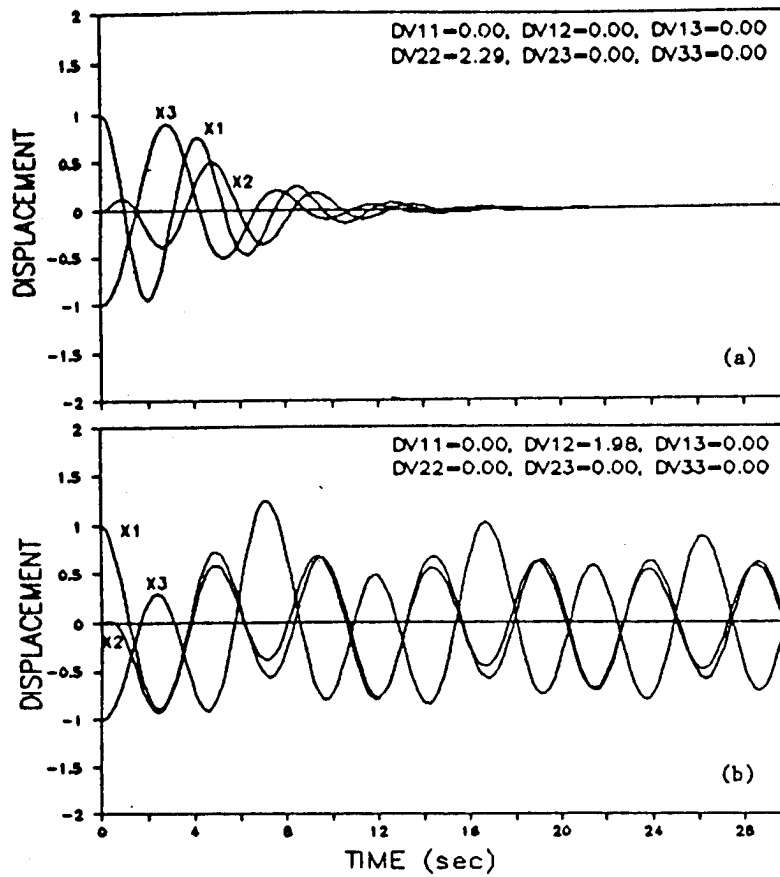


Figure 12. Time histories of the displacements  $x_i$  of masses  $m_i$  for the system of Table 3 with  $ND = 1$  for (a) most effective damping configuration:  $d_{22} = 2.29$  and (b) for least effective damping configuration:  $d_{12} = 1.98$ .

#### REFERENCES

1. J. ORMONDROYD and J. P. DEN HARTOG 1928 *Transactions of the American Society of Mechanical Engineers* 50, 9-22. Theory of the dynamic vibration absorber.
2. J. P. DEN HARTOG 1947 *Mechanical Vibrations*. New York: McGraw-Hill.
3. A. G. THOMPSON 1981 *Journal of Sound and Vibration* 77(3), 403-415. Optimum tuning and damping of a dynamic vibration absorber applied to a forced excited and damped primary system.
4. A. SOOM and MING-SAN LEE 1983 *Transactions of the American Society of Mechanical Engineers Journal of Vibration, Acoustics, Stress, and Reliability in Design* 105, 112-119. Optimal design of linear and non-linear vibration absorbers for damped systems.
5. I. N. JORDANOV and B. I. CHESHANKOV 1988 *Journal of Sound and Vibration* 123(1), 157-170. Optimal design of linear and non-linear dynamic vibration absorbers.
6. J. VAN DE VEGTE 1975 *Transactions of the American Society of Mechanical Engineers Journal of Dynamic Systems, Measurement, and Control* 97, 432-438. Optimal dynamic absorbers for plate vibration control.

7. C. W. DE SILVA 1981 *Journal of Sound and Vibration* 74(4), 495-502. An algorithm for the optimal design of passive vibration controllers for flexible systems.
8. L. KITIS, B. P. WANG and W. D. PILKEY 1983 *Journal of Sound and Vibration* 89(4), 559-569. Vibration reduction over a frequency range.
9. H. N. ÖZGÜVEN and B. ÇANDIR 1986 *Journal of Sound and Vibration* 111(3), 377-390. Suppressing the first and second resonances of beams by dynamic vibration absorbers.
10. R. F. NAGAEV and A. V. STEPANOV 1979 *Mechanics of Solids* 14, 20-24. Optimization of the damping factor of free oscillations for a two-mass system.
11. M. D. ROWBOTTOM 1981 *Journal of Sound and Vibration* 75(4), 559-576. The optimization of mechanical dampers to control self-excited galloping oscillations.
12. N. D. EBRAHIMI 1988 *Journal of Sound and Vibration* 120(3), 445-455. Optimum secondary dampers for free response of underdamped systems.
13. A. F. D'SOUZA 1988 *Design of Control Systems*. New Jersey: Prentice-Hall, Inc.
14. L. L. LAPIN 1983 *Probability and Statistics for Modern Engineers*. Massachusetts: PWS Publishers.
15. G. V. REKLAITIS, A. RAVINDRAN and K. M. RAGSDALL 1983 *Engineering Optimization: Methods and Applications*. New York: John Wiley & Sons.

# Optimization of Energy Dissipation Rate in Structures

Vernon H. Neubert

Professor of Engineering Science and Mechanics

133 Hammond Building

The Pennsylvania State University

University Park, PA, 16802

## ABSTRACT

The present paper deals with the control of free vibrations in structures by maximizing the energy dissipation rate, or minimizing the settling time of transient free vibrations. The energy dissipation rate is a generalization of the Rayleigh dissipation function for viscous damping. Both proportional and nonproportional damping are included and the eigenvalues and eigenvectors are complex in general. The dissipation rate  $D$  is a real, positive number and the integral of  $2D$  with respect to time represents the total dissipated energy for the specified time interval, which is of primary interest in designing damping treatments.

It is shown that, for free vibrations, the value of  $D$  at time  $t=0$  is sufficient information to optimize the dissipation rate, so that integration over a time period is not necessary. The dissipation rate for each mode, or a set of appropriately weighted modes, becomes the objective function. The optimum location for a limited amount of damping is determined.

Particular examples of the optimization of damping are given for a truss having ten bars. It is assumed that viscous damping is to be added to only the truss members where it will be most useful and an appropriate constraint equation is written. To carry out the optimization, the sensitivities may be determined for the eigenvalues and the eigenvectors by taking their derivatives with respect to the dashpot constants in the matrix  $C$ . The sensitivity of  $D$  may be determined by finite differences or more precisely using the eigenvalue and eigenvector derivatives. Optimization of the dissipation rate  $D$  is compared with optimization of the modal damping ratios. Results are related to settling time. Thus the problem is formulated so it can be solved by an optimization procedure, such as the Method of Feasible Directions.

A phenomenon of particular interest is demonstrated: namely, that as the damping is increased in certain areas of a structure, the modal damping of an individual mode may decrease dramatically while it increases in other modes. There is an associated change in mode shape, which would not be predicted if proportional damping had been assumed.

## Background and Related Literature

Optimal control of vibrations in structures by active or passive means is an important practical problem, as evidenced by titles of conferences<sup>1-4</sup> and published books<sup>5-8</sup>. Passive damping may be developed by the use of dashpots, piezoelectric elements, electromagnetic devices, or viscoelastic layers, to only a few methods. The present paper deals with the optimum choice of size and location of velocity- or rate-dependent linear elements. The analysis has a wide range of applications and applies to viscoelastic damping and to active control where the rate-dependent gains are constant.

Much information is available on the behavior of viscoelastic materials as a function of temperature and frequency<sup>9</sup>, but the representation of this behavior in dynamic analyses of structures is a challenging problem because of the variation of the dynamic properties with frequency and temperature. Bagley and Torvik<sup>10</sup> developed a fractional calculus approach to the representation of viscoelastic damping and have adapted it to finite element techniques. A method requiring calculation of complex stiffness matrix at each resonant frequency was outlined by Segalman<sup>11</sup> in terms of measurable viscoelastic properties. The use of fictitious, over-damped, mini-oscillators to represent frequency variation of the complex modulus is a part of the method outlined by McTavish and Hughes<sup>12</sup>. Closed-loop, constant gain, rate-dependent active control makes use of dashpots with negative parameters.

To optimize parameters, one needs the derivatives or sensitivities of the response variables in terms of the design parameters. Venkayya<sup>13</sup> presented a unified approach to optimization suitable for application to problems in many disciplines. In addition, computer programs are available, such as CONMIN, by Vanderplaats<sup>14</sup>, which will determine optimum values of design parameters using sensitivity and response variable values provided by the program user. Determination of derivatives of eigenvalues and eigenvectors is the subject of papers by Rogers<sup>15</sup>, Nelson<sup>16</sup>, and others<sup>17-20</sup>. With the assumption of proportional damping, Gibson and Johnson<sup>21</sup> optimize the size and location of viscoelastic damping on plates by optimizing modal loss factor, taken to be the ratio of the modal strain energy in the viscoelastic layer to the total modal strain energy.

# ANALYTICAL BASIS

The problem is formulated in the state vector form:

$$\begin{bmatrix} \mathbf{M} & \mathbf{0} \\ \mathbf{0} & -\mathbf{K} \end{bmatrix} \begin{Bmatrix} \ddot{\underline{z}} \\ \dot{\underline{z}} \end{Bmatrix} + \begin{bmatrix} \mathbf{C} & \mathbf{K} \\ \mathbf{K} & \mathbf{0} \end{bmatrix} \begin{Bmatrix} \dot{\underline{z}} \\ \underline{z} \end{Bmatrix} = \begin{Bmatrix} \underline{p}(t) \\ \underline{0} \end{Bmatrix}$$

or

$$\mathbf{M}^* \dot{\underline{z}} + \mathbf{K}^* \underline{z} = \underline{P}(t) \quad (2)$$

The resulting eigenvalue problem is

$$[-\lambda \mathbf{I} + \mathbf{A}] \underline{x} = 0 \quad (3)$$

where

$$\mathbf{A} = -[\mathbf{M}^*]^{-1} \mathbf{K}^*. \quad (4)$$

The matrices  $\mathbf{M}$ ,  $\mathbf{K}$  and  $\mathbf{C}$  are assumed to be symmetric.

The following modal notation is used.

$\phi_{ji}$  = the modal displacement vector,  $N \times 1$

$\psi_{ji} = \begin{Bmatrix} \lambda_i \phi_{ji} \\ \phi_{ji} \end{Bmatrix}$  = state space modal vector,  $2N \times 1$

$\underline{x}$  = displacement vector,  $n \times 1$

$T = \frac{1}{2} \dot{\underline{x}}^T \mathbf{M} \dot{\underline{x}}$  = kinetic energy

$U = \frac{1}{2} \underline{x}^T \mathbf{K} \underline{x}$  = potential energy

$D = \frac{1}{2} \dot{\underline{x}}^T \mathbf{C} \dot{\underline{x}}$  = half the rate of energy dissipation

$H = T + U$  = the Hamiltonian

Now the energies may be related to the differential equations of motion for free vibrations,

$$\mathbf{M} \ddot{\underline{x}} + \mathbf{C} \dot{\underline{x}} + \mathbf{K} \underline{x} = \underline{F}. \quad (5)$$

Pre-multiplying by  $\dot{\underline{x}}^T$ , the energies may be identified.

$$\dot{\underline{x}}^T \mathbf{M} \ddot{\underline{x}} + \dot{\underline{x}}^T \mathbf{C} \dot{\underline{x}} + \dot{\underline{x}}^T \mathbf{K} \underline{x} - \dot{\underline{x}}^T \underline{F} = 0 \quad (6)$$

$$\frac{d}{dt} \left[ \frac{1}{2} \dot{\underline{x}}^T \mathbf{M} \dot{\underline{x}} + \frac{1}{2} \underline{x}^T \mathbf{K} \underline{x} \right] + \dot{\underline{x}}^T \mathbf{C} \dot{\underline{x}} - \dot{\underline{x}}^T \underline{F} = 0 \quad (7)$$

Thus the rate of change of the Hamiltonian is equal to the rate at which external work is done on the system minus the rate of energy dissipation, or

$$\dot{T} + \dot{U} = \dot{\underline{x}}^T \underline{F} - 2D \quad (8)$$

For conservative systems, the rate of change of the Hamiltonian is zero. If Eq. (8) is integrated with respect to time, energies at time  $t$  are related

$$\text{by} \quad H(t) - H(0) = \int_0^t (\dot{\underline{x}}^T \underline{F} - 2D) dt \quad (9)$$

## Modal Energy, General Viscous Damping

Now for general viscous damping, where  $\Psi$  is  $2N \times 2N$  and  $q$  is  $2N \times 1$ , the state vector may be expanded in terms of the modal eigenvectors as

$$\begin{Bmatrix} \dot{x} \\ x \end{Bmatrix} = \Psi q \quad (10)$$

$$= \begin{bmatrix} \lambda_1 \varphi_1 & \bar{\lambda}_1 \bar{\varphi}_1 & \lambda_2 \varphi_2 & \lambda_2 \bar{\varphi}_2 & \cdot & \cdot & \lambda_n \bar{\varphi}_n \\ \varphi_1 & \bar{\varphi}_1 & \varphi_2 & \bar{\varphi}_2 & & & \varphi_n \end{bmatrix} \begin{Bmatrix} q_1 \\ \bar{q}_1 \\ q_2 \\ \bar{q}_2 \\ \cdot \\ \cdot \\ \bar{q}_n \end{Bmatrix} \quad (11)$$

The free vibration modal amplitudes  $q_i(t)$  are, as a function of time  $t$ ,

$$q_i(t) = A_i e^{-\lambda_i t} \quad (12)$$

If the mode is underdamped, then the eigenvalues  $\lambda_i$  are of the form

$$\lambda_i = -\zeta_i \omega_i + j \omega_i (1 - \zeta_i^2)^{0.5} = -\zeta_i \omega_i + j \omega_{Di} \quad (13)$$

$$\text{and} \quad \lambda_{i+1} = \bar{\lambda}_i = -\zeta_i \omega_i - j \omega_i (1 - \zeta_i^2)^{0.5} = -\zeta_i \omega_i - j \omega_{Di} \quad (14)$$

For real initial values, the response will be real, the  $q_i(t)$  occur in complex conjugate pairs, and  $q_{i+1}(t)$  will be

$$q_{i+1}(t) = \bar{q}_i(t) = \bar{A}_i e^{-\bar{\lambda}_i t}. \quad (15)$$

The kinetic energy is

$$T = \frac{1}{2} \dot{x}^T M \dot{x} = \frac{1}{2} \dot{q}^T \Phi^T M \Phi \dot{q} \quad (16)$$

and the derivative of  $T$  with respect to time is

$$\text{or} \quad \dot{T} = \dot{q}^T \Phi^T M \Phi \dot{q}. \quad (17)$$

The derivative of the potential energy with respect to time is

$$\dot{U} = \dot{q}^T \Phi^T K \Phi q \quad (18)$$

and the dissipation function  $D$  is

$$2D = \dot{q}^T \Phi^T C \Phi \dot{q} \quad (19)$$

It is helpful to see the details for a two-degree-of-freedom system.

$$2D = \begin{Bmatrix} \dot{q}_1 & \dot{q}_1 & \dot{q}_2 & \dot{q}_2 \end{Bmatrix} \begin{bmatrix} \varphi_1^T C \varphi_1 & \varphi_1^T C \bar{\varphi}_1 & \varphi_1^T C \varphi_2 & \varphi_1^T C \bar{\varphi}_2 \\ \bar{\varphi}_1^T C \varphi_1 & \bar{\varphi}_1^T C \bar{\varphi}_1 & \bar{\varphi}_1^T C \varphi_2 & \bar{\varphi}_1^T C \bar{\varphi}_2 \\ \varphi_2^T C \varphi_1 & \varphi_2^T C \bar{\varphi}_1 & \varphi_2^T C \varphi_2 & \varphi_2^T C \bar{\varphi}_2 \\ \bar{\varphi}_2^T C \varphi_1 & \bar{\varphi}_2^T C \bar{\varphi}_1 & \bar{\varphi}_2^T C \varphi_2 & \bar{\varphi}_2^T C \bar{\varphi}_2 \end{bmatrix} \begin{Bmatrix} \dot{q}_1 \\ \dot{\bar{q}}_1 \\ \dot{q}_2 \\ \dot{\bar{q}}_2 \end{Bmatrix} \quad (20)$$



It can be seen that the complex numbers in the core matrix  $\Phi^T \mathbb{C} \Phi$  matrix occur in complex conjugate pairs, since the numbers in  $\mathbb{C}$  are real.

The orthogonality relationships are, in terms of the  $2N \times 1$   $\psi$  vectors

$$\begin{aligned} \psi_s^T M^* \psi_r &= 0 & r \neq s \\ \text{and } \psi_r^T M^* \psi_r &= b_r & r = s \end{aligned} \quad (21)$$

$$\begin{aligned} \psi_s^T K^* \psi_r &= 0 & r \neq s \\ \text{and } \psi_r^T K^* \psi_r &= -\lambda_r b_r & r = s \end{aligned} \quad (22)$$

In terms of the  $N \times 1$   $\phi$  vectors, the orthogonality relationships are

$$\lambda_r \lambda_s \phi_s^T M \phi_r - \phi_s^T K \phi_r = 0 \quad r \neq s \quad (23)$$

$$\text{and } \lambda_r^2 \phi_r^T M \phi_r - \phi_r^T K \phi_r = b_r \quad r = s \quad (24)$$

$$\lambda_r \lambda_s \phi_s^T \mathbb{C} \phi_r + (\lambda_r + \lambda_s) \phi_s^T K \phi_r = 0 \quad r \neq s \quad (25)$$

$$\text{and } \lambda_r^2 \phi_r^T \mathbb{C} \phi_r + 2\lambda_r \phi_r^T K \phi_r = -\lambda_r b_r \quad r = s \quad (26)$$

The Eqs. (23)-(26) may be combined to form alternate, but not independent, orthogonality relationships as

$$\phi_s^T \mathbb{C} \phi_r + (\lambda_r + \lambda_s) \phi_s^T M \phi_r = 0 \quad r \neq s \quad (27)$$

$$\text{and } \phi_r^T \mathbb{C} \phi_r + 2\lambda_r \phi_r^T M \phi_r = \lambda_r b_r \quad r = s \quad (28)$$

From Eqs. (25) and (27) a special relationship<sup>22</sup> follows between the  $r$ th mode and its complex conjugate, due to the fact that  $\lambda_r \bar{\lambda}_r = \omega_r^2$  and  $\lambda_r + \bar{\lambda}_r = -2\zeta_r \omega_r$ ,

$$\text{namely, } \frac{\phi_r^T \mathbb{C} \bar{\phi}_r}{\phi_r^T K \bar{\phi}_r} = - \frac{2\zeta_r}{\omega_r} \quad \text{and} \quad \frac{\phi_r^T \mathbb{C} \bar{\phi}_r}{\phi_r^T M \bar{\phi}_r} = - 2\zeta_r \omega_r. \quad (29)$$

#### Choice of Objective Function for Damping Optimization

If we wish to find the optimum damping by an optimization process, it is common to specify an objective function. In modern control theory the performance index may be of the form, given for example in reference 4.

$$PI = \int_0^t (\{\psi\}^T [Q] \{\psi\} + \{f\}^T [R] \{f\}) dt \quad (30)$$

where

$\{\psi\}$  = modal vector,  $2N \times 1$

$\{f\}$  = active control vector,  $P \times 1$

$[Q]$  = state weighting matrix, positive semidefinite

$[R]$  = control weighting matrix, positive definite

If emphasis is to be placed on particular response or control points, the weighting matrices [Q] and [R] may be so adjusted. In the absence of that type of goal, then [Q] and [R] may be chosen as the unit or identity matrix. In choosing [Q] we might also consider the matrices

$$K^* = \begin{bmatrix} C & K \\ K & 0 \end{bmatrix} \quad CK^* = \begin{bmatrix} C & 0 \\ 0 & 0 \end{bmatrix} \quad KK^* = \begin{bmatrix} 0 & K \\ K & 0 \end{bmatrix} \quad M^* = \begin{bmatrix} M & 0 \\ 0 & -K \end{bmatrix} \quad (31)$$

$$\text{where } K^* = CK^* + KK^*$$

$$\text{Then } \Psi^T K^* \Psi = \Psi^T CK^* \Psi + \Psi^T KK^* \Psi \quad (32)$$

$$= \Lambda^T \Phi^T C \Phi \Lambda + \Psi^T KK^* \Psi \quad (33)$$

and  $\Phi^T C \Phi$  and  $\Phi^T KK^* \Phi$  are not diagonal, even though  $\Phi^T K^* \Phi$  is diagonal. Products  $\Psi_i^T C \Psi_j$  appear on the diagonal of  $\Phi^T C \Phi$ , but off the diagonal terms like  $\Psi_j^T C \Psi_i$  occur which are not zero, and in fact may be of the same magnitude as the diagonal terms.

The product  $\Psi^T CK^* \Psi$  is important, because it is the kernel of the Rayleigh dissipation function D, as seen in Eq. (34). Note that  $\Phi$  is  $N \times 2N$  and  $C$  is  $N \times N$ .

$$2D = \dot{q}^T \Phi^T C \Phi \dot{q} = q^T \Lambda \Phi^T C \Phi \Lambda q \quad (34)$$

#### The Rayleigh Dissipation Rate as an Objective Function

The Rayleigh Dissipation Function D is given by

$$2D = \dot{x}^T C \dot{x} \quad (35)$$

In state vector form, the velocity and displacement are expressed in terms of modal coordinates by

$$\begin{matrix} 2N \times 1 & 2N \times 2N & 2N \times 1 \\ \left\{ \begin{matrix} \dot{x} \\ x \end{matrix} \right\} & = \Psi & \left\{ \begin{matrix} q \\ \dot{q} \end{matrix} \right\} = \begin{bmatrix} \Phi & \Lambda \\ \Phi & \end{bmatrix} \left\{ \begin{matrix} q \\ \dot{q} \end{matrix} \right\} \end{matrix} \quad (36)$$

Hence the dissipation function may be gotten from the product

$$2D = \left\{ \begin{matrix} \dot{x} \\ x \end{matrix} \right\}^T \begin{bmatrix} C & 0 \\ 0 & 0 \end{bmatrix} \left\{ \begin{matrix} \dot{x} \\ x \end{matrix} \right\} = q^T \Psi^T CK^* \Psi q \quad (37)$$

The dissipation function D is a real, positive number. There are  $2N$  modal coordinates,  $q_i(t)$ , in the form of  $N$  complex conjugate pairs. The initial values  $q_i(0)$  are gotten from the initial value vectors  $\dot{x}(0)$  and  $x(0)$ . An efficient approach is to use the orthogonality relationship Eq. (21) so that

$$\Psi^T M^* \begin{Bmatrix} \dot{x}(0) \\ x(0) \end{Bmatrix} = B^D q(0). \quad (38)$$

Here  $B^D$  is a diagonal matrix of  $b_r$ 's and the eigenvectors have been normalized so that each  $B^D = I$ , the identity matrix. From Eq. (36) we see that if  $q(0)$  is real, then  $\underline{x}(0)$  is real. If we wanted to excite a pure second mode, for example, the following relationships would exist from Eq. (38)

$$\begin{Bmatrix} \underline{\psi}_1^T & \bar{\underline{\psi}}_1^T & \underline{\psi}_2^T & \bar{\underline{\psi}}_2^T & \dots \end{Bmatrix} \begin{bmatrix} M^* \end{bmatrix} \begin{Bmatrix} \underline{\psi}_2 + \bar{\underline{\psi}}_2 \end{Bmatrix} = \begin{Bmatrix} q_1(0) \\ \bar{q}_1(0) \\ q_2(0) \\ \bar{q}_2(0) \end{Bmatrix} = \begin{Bmatrix} 0 \\ 0 \\ 1 \\ 1 \\ : \end{Bmatrix} \quad (39)$$

The vector  $\underline{\psi}_2 + \bar{\underline{\psi}}_2$  is real, and Eq. (39) shows that the initial value vector is a pure 2nd modal vector when  $q_2(0) = \bar{q}_2(0) = 1$ . This idea will be used next in finding the dissipation function  $D$  when we wish to excite a pure mode or group of modes.

It may be observed that an upper bound on the dissipation rate at  $t=0$  can be determined by taking the sum of the absolute values of the real parts of the numbers in the complex matrix  $\Psi^T C K^* \Psi$ . The sum is then a candidate for an objective function, to be maximized, in a free vibration problem. It may appear that the magnitude of the dissipation rate is somewhat arbitrary, but it should be noted that because of the normalization of the eigenvectors by  $\Psi^T M^* \Psi = B^D = I$ , then the initial value of the energy  $T(0) - U(0) = 2n$ , where  $n$  is the number of modes excited. In the examples given below, the initial potential energy  $U(0)$  is very small, so the settling time depends on the time it takes the energy level given in Eq. (40) to reach zero. This equation also

$$T(0) + U(0) - \int_0^t 2D \, dt \cong 2n - \int_0^t 2D \, dt \quad (40)$$

shows that the settling time depends simply on the time for  $2D$  to reach zero.

#### Sensitivity of the Rayleigh Dissipation Function

The sensitivity of the dissipation rate  $D$  is gotten by taking the partial derivative  $\partial D / \partial C_m$ , where  $C_m$  is the value of the  $m$ th dashpot parameter, and  $D$  may be taken in the following form,

$$2D = \dot{\underline{x}}^T C \dot{\underline{x}} = \underline{\eta}^T C K^* \underline{\eta} = \underline{q}^T \Psi^T C K^* \Psi \underline{q} \quad (41)$$

with

$$\underline{\eta} = \begin{Bmatrix} \dot{\underline{x}} \\ \underline{x} \end{Bmatrix} = \Psi \underline{q} = \begin{Bmatrix} \dot{\Phi} \Lambda \\ \Phi \end{Bmatrix} \quad (42)$$

Symbolizing derivative by a comma as  $\partial D/C_m \equiv D_{,c}$  the derivative of Eq. (41) is

$$2 D_{,c} = 2 \mathbf{q}_{,c}^T \Psi^T \mathbf{C} \mathbf{K}^* \Psi \mathbf{q} + 2 \mathbf{q} \Psi_{,c}^T \mathbf{C} \mathbf{K}^* \Psi \mathbf{q} + \mathbf{q} \Psi^T \mathbf{C} \mathbf{K}^*_{,c} \Psi \mathbf{q} \quad (43)$$

Here  $\mathbf{q}_i = \mathbf{q}_i(0) e^{-\lambda_i t}$ . From Eq. (42) the derivative  $\Psi_{,c}$  involves the derivative of the eigenvalues  $\lambda_i$  and the eigenvectors  $\Phi$ , which may be found by the methods of references 16 through 21.

Next an example of a ten-bar truss is presented, where first the optimization of modal damping ratios is discussed and then the optimization of the energy dissipation rate  $D$  is considered.

#### OPTIMIZATION OF DAMPING RATIO AND DISSIPATION RATE, TEN-BAR TRUSS

The question addressed in this section is: suppose the total dashpot capability, with units of lb-s/in, is limited, then on which members of the truss may it be used most efficiently to maximize the damping ratios,  $\zeta_i$ , of selected modes? Thus, with  $\alpha_i$  appropriate weighting functions, the objective function, OBJ, is

$$\text{OBJ} = \sum_i \alpha_i \zeta_i. \quad (44)$$

If CTOT is the total dashpot capacity to be used, then a corresponding constraint equation is

$$G(1) = \sum \gamma_m C_m - \gamma_T \text{CTOT} \leq 0.0 \quad (45)$$

where  $\gamma$  are weighting factors and  $tC_m$  are the viscous dashpot constants, taken here as design parameters.

As an example, the ten-bar truss shown in Figure 1 was investigated. The connections are assumed to be frictionless pins. The bars are all made of the same material with Young's modulus  $E$ , and the cross-sectional areas  $A_m$  are as listed in Table 1. The stiffness of each bar is  $K_m = A_m E_m / L_m$ . Parallel to each bar there is a dashpot, not shown, with damping parameter  $C_m$ . Note that members 2, 5, 6, and 10 have much smaller areas than the other six bars.

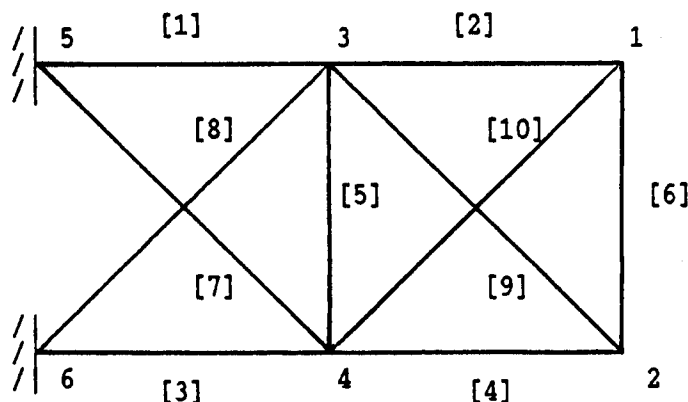


Figure 1 Ten-bar Truss, with Node and Member Numbers

Table 1 Member Areas, Lengths, Stiffnesses and Damping Parameters

El. No. $m$	Area $A_m$ in	Length $L_m$ in	Stiffness $K_m$ lb/in	Damping $C_m$ ( $\beta_m=1$ ) lb s/in
1	31.5	360.000	875 000	276.699 30
2	0.1	360.000	2 778	0.878 41
3	23.0	360.000	638 889	202.034 41
4	15.5	360.000	430 556	136.153 62
5	0.1	360.000	2 778	0.878 41
6	0.5	360.000	4 167	4.392 05
7	7.5	509.117	147 314	46.584 75
8	20.5	509.117	402 658	127.331 65
9	21.0	509.117	412 479	130.437 30
10	0.1	509.117	1 964	0.621 13

A factor  $\beta_m$  is arbitrarily introduced such that  $C_m = \frac{\beta_m K_m}{\sqrt{E}}$ . Hence if all the  $\beta_m$  are the same, the damping matrix  $C$  is proportional to the stiffness matrix  $K$ . The mass matrix  $M$  is diagonal, formed by lumping half the mass of each bar at its ends. The values of the modal damping ratios,  $\zeta_i$ , and the natural frequencies,  $\omega_i$ , are given in Table 2, for the values of  $C_m$  when  $\beta_m = 1$ , for  $m = 1$  to 10. The damping ratios for the higher modes are the largest. The  $\omega_i$  range from 131.13 to 796.21 rad/s and are well separated.

Table 2 Natural Frequencies  $\omega_i$  and Damping Ratios  $\zeta_i$  for all  $\beta_m=1.0$ 

$i$	$\zeta_i$	$\omega_i$ (rad/s)
1	0.0207 3350	131.1301
2	0.0274 1571	173.3921
3	0.0426 4408	269.7048
4	0.0515 5221	326.0448
5	0.0730 5049	462.0119
6	0.0948 6770	599.9960
7	0.1051 3561	664.9360
8	0.1258 9253	796.2143

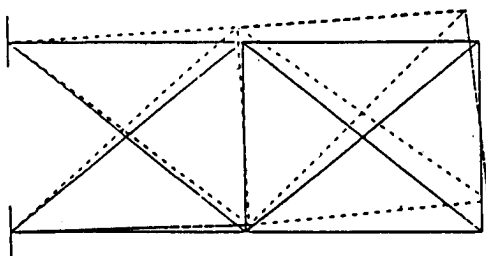
The eight mode shapes for zero damping are shown in Figure 2. Intuition tells us that, for a dashpot to be effective: (1) there must be a high relative velocity between the end-points and (2) it should be in parallel with a bar or relatively small stiffness. The first criterion is satisfied if there is a large extension of the of the bar on the mode shape. Inspection of the shape for mode 2 reveals that bars 2, 5, 7 and 10 have large deformations; for mode 4, bars 2 and 10; for mode 7, bars 6 and 10; and so on. If damping is added in a proportional manner, then the mode shapes, or vectors, remain real and the same as shown. If damping becomes nonproportional, the mode shapes do change and eigenvectors contain complex numbers. As the mode shapes change the optimum distribution of the damping to the various members may change from that which was most favorable for small or no damping. This effect is not accounted for in analyses that assume that the damping is proportional. The derivatives  $\partial \zeta_i / \partial C_m$  of the  $i$ th modal damping with respect to the  $m$ th dashpot  $C_m$  indicate how  $\zeta_i$  is changing with increased damping, and the  $\partial \phi_i / \partial C_m$  show the rate of change of the mode shape with the  $m$ th dashpot. The derivatives of  $\zeta_i$  were found and are discussed next.

#### Sensitivities of Modal Damping Ratios and Natural Frequencies

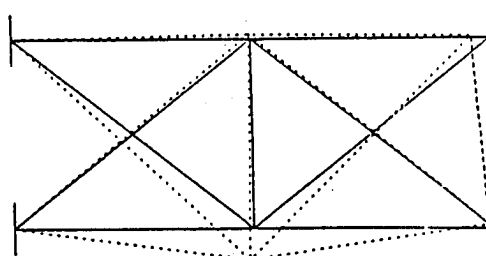
The exact derivatives  $\partial \zeta_i / \partial C_m$  were calculated and their values are listed in Table 3. There are 80 elements, corresponding to 8 modes and 10 bars. The total for each row and column is also given, and these sub-totals add to the grand total of 10.27867. By the sums at the bottoms of the columns, the list of the bars in order of the magnitudes of the sensitivities is 2,10,6,5,4,9,3,8,1,7. By stiffness, from smallest to largest, the order is 10,2,5,6,7,8,4,4,3,1. Bar 7 seems to be somewhat out of order, but notice that there are two negative values in the column for bar 7. In a ranking of potential effectiveness according to the absolute sum of the columns, the value for dashpot 7 would be 0.037637 and it would precede dashpot 3 in the sensitivity list.

The fact that negative derivatives occur for bar 7 on modes 1 and 2 shows that the modal damping ratio will decrease for these modes as the value of  $C_7$  is increased. These derivatives were calculated for the damping level where all  $\beta_m=1$  and the values of the modal damping ratios  $\zeta_i$  are the same as those given in Table 2. Thus the negative sensitivity has occurred at small levels of damping.

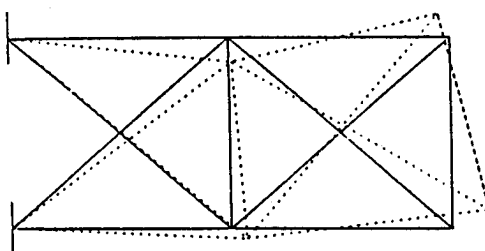
MODE 1, 131.13 RAD/S



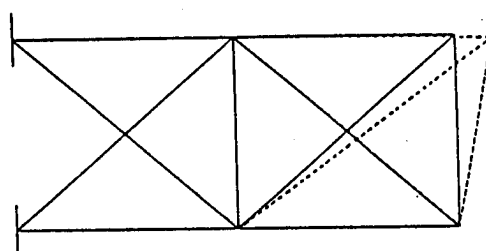
MODE 2, 173.39 RAD/S



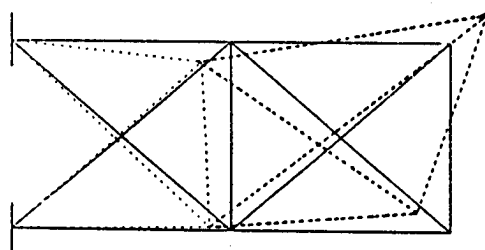
MODE 3, 269.70 RAD/S



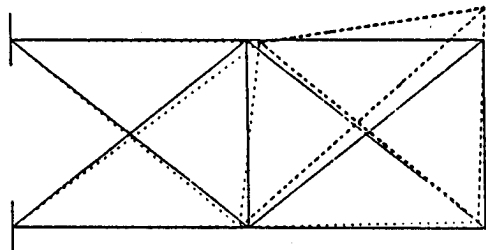
MODE 4, 326.04 RAD/S



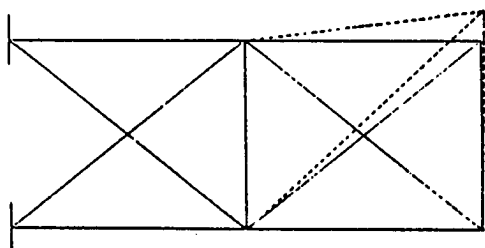
MODE 5, 462.01 RAD/S



MODE 6, 600.00 RAD/S



MODE 7, 664.94 RAD/S



MODE 8, 796.21 RAD/S

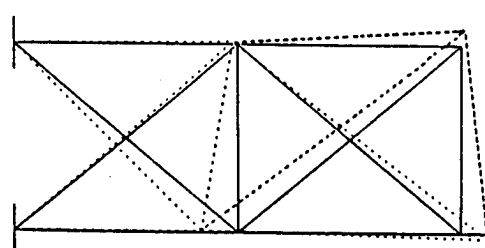


Figure 2 Mode Shapes for Zero Damping

### Variation of $\zeta_5$ , $\zeta_6$ , $\omega_5$ , and $\omega_6$ with $C_1$

As the values of the  $C_m$  are changed nonproportionally, the modal amplitudes become complex numbers and the derivatives or gradients change in an unexpected manner in some cases. The variation of  $\zeta_5$  and  $\zeta_6$  with  $C_1$  is shown in Fig. 3. The values of all other  $C_m$  were taken as zero. The plot shows that, for  $0 \leq C_1 \leq 3$ , both  $\zeta_5$  and  $\zeta_6$  increase monotonically. However, for  $C_1 > 3$ , the rate of increase of  $\zeta_6$  becomes larger while  $\zeta_5$  decreases. The slopes of these lines are plotted in Fig. 4, where it is seen that the  $\partial\zeta_5/\partial C_1$  changes sign and finally approaches zero as  $C_1$  increases.

The corresponding variation of the damped natural frequencies  $\omega_{D5}$  and  $\omega_{D6}$  with  $C_1$  is shown in Fig. 5. Here  $\omega_{Di}$  defined as in Eq. (13). Note that  $\omega_{D6}$  decreases in magnitude while  $\omega_{D5}$  is increasing. At  $\beta_1 \cong 6$ , the curves cross and thereafter  $\omega_{D5}$  approaches a constant value but remains greater than  $\omega_{D6}$ . As  $\beta_1 \cong 12.0$ ,  $\zeta_6$  approaches unity or critical damping as  $\omega_{D6}$  approaches zero. As  $\beta_1$  is further increased, the eigenvalues for mode 6 become real and negative, while the other fourteen eigenvalues are still complex conjugate pairs, for underdamped modes. Actually, if the modes are numbered initially in terms of the magnitude of  $\omega_{Di}$ , from smallest to largest, then it is clear that they will change their relative positions as the damping increases. Hence their identities must be traced carefully if changes in a mode having a particular "name" are of interest. The tracing of mode numbers is especially challenging when more than one mode is overdamped, since they no longer occur in complex conjugate pairs.

### Optimization of $\zeta_3$ with Respect to $C_3$ and $C_4$ .

Now the optimization of one modal damping ratio is undertaken, with the objective function taken as  $\zeta_3$  and the design variables  $C_3$  and  $C_4$ . Constraint function  $G(1)$  puts a limit CTOT on the total damping available.

$$OBJ = \zeta_3$$

$$G(1) = C_3 + C_4 - CTOT \leq 0.0 \quad (46)$$

By limiting the total number of design variables to two, we can show a two-dimensional plot of the interaction between  $\zeta_3$  and the two design variables. Contours for  $\zeta_3 = 0.05, 0.10, 0.15$ , and  $0.20$  are shown in Figure 6. The three



dotted, straight lines are constraint lines which were chosen to be approximately tangent to the given contour lines. They would be  $45^\circ$  lines if the vertical and horizontal scales were equal. Since the contours are convex toward the feasible region the optimum solution, which maximizes  $\zeta_3$ , will be along the constraint boundary line. The results are summarized in Table 4 for three values of CTOT, namely CTOT = 1157.3, 1838.5, and 2525.4 lb-s/in. The associated values of optimum  $\zeta_3$  are close to 0.10, 0.15 and 0.20.

Table 4 Optimum Values of  $\zeta_3$  on  $C_3$  vs.  $C_4$  Plot

$\beta_3$	$\beta_4$	$C_3$	$C_4$	$\zeta_3$	$C_3+C_4$
0.796 537	7.318	160.928	996.373	0.0994 4614	1157.301
3.560 435	8.22	719.330	1119.184	0.1470 4782	1838.514
6.142 305	9.434	1240.957	1284.475	0.2015 5902	2525.432

#### Optimization of 2D(0) for Mode 3 using parameters $C_3$ and $C_4$

Next the dissipation rate at  $t=0$ ,  $2D(0)$ , was optimized when only mode 3 is excited in free vibrations by taking  $q_3(0) = \bar{q}_3(0) = 1.0$ . The interaction curves of contours of  $2D(0)$  on a plot of  $C_3$  versus  $C_4$  are shown in Figure 6. The curved contour lines are for  $2D(0) = 50, 100, 150$ , and  $200$  in-lb/s. The solid, straight, constraint line represents the constraint  $C_3 + C_4 \leq 1040$ , and the region between this line and the coordinate axes includes feasible, or acceptable solutions, as specified by the constraint equation. Obviously the optimum solution is at the point of tangency between the constraint boundary and a contour line, which occurs approximately at  $C_3 = 860$  and  $C_4 = 860$  lb-s/in.

#### Optimization of 2D(0) for modes 4 and 7 using parameters $C_6$ and $C_{10}$

In Figures 8, 9, and 10 three more interaction curves, each of a different shape, are shown for  $2D(0)$ . They are for modes 4 and 7 excited separately and simultaneously, with the contours of  $2D(0)$  plotted against  $C_6$  versus  $C_{10}$ . In each case the contours are either nearly straight lines, as in Figure 8 and 9, or outwardly convex curves, as in Figure 10. In these situations, the optimum solution is seen to be a corner of the feasible region, with the solutions for the design parameters being  $C_6=0, C_{10}=8.3$ ;  $C_6=8.3, C_{10}=0$ ; and  $C_6=0, C_{10}=8.3$  on the respective Figures 8, 9 and 10.

Table 4 Sensitivities  $\frac{\partial \xi_i}{\partial C_m} \times 10^2$

At  $C_m$  as given in Table 1

Bar No. $m \rightarrow$	1	2	3	4	5	
Mode No.						
$i$						
1	0.002 025	0.004 389	0.000 900	0.001 138	0.007 674	
2	0.000 197	0.021 051	0.001 518	0.000 001	0.154 036	
3	0.000 180	0.004 650	0.005 255	0.010 230	0.006 373	
4	0.000 054	4.336 10	0.000 037	0.000 021	0.000 486	
5	0.008 992	0.045 043	0.004 783	0.001 471	0.007 432	
6	0.011 616	0.009 531	0.005 680	0.000 325	0.000 890	
7	0.000 203	0.018 862	0.000 531	0.000 367	0.000 079	
8	<u>0.000 314</u>	<u>0.000 946</u>	<u>0.017 544</u>	<u>0.051 749</u>	<u>0.000 016</u>	
	0.023 581	4.440 572	0.036 248	0.065 302	0.176 986	
$m \rightarrow$	6	7	8	9	10	All
$i$						
1	0.000 035	-0.001 810	0.006 954	0.001 747	0.007 211	0.030 263
2	0.000 238	-0.012 466	0.000 762	0.000 059	0.029 303	0.194 699
3	0.000 355	0.006 633	0.007 399	0.003 263	0.001 391	0.045 729
4	0.033 031	0.000 104	0.000 117	0.000 000	1.853 09	6.223 04
5	0.001 360	0.003 230	0.014 265	0.012 294	0.039 581	0.138 451
6	0.069 406	0.003 364	0.003 603	0.031 427	0.081 899	0.217 741
7	2.122 32	0.000 344	0.000 039	0.001 667	1.164 52	3.308 932
8	<u>0.007 902</u>	<u>0.009 686</u>	<u>0.000 024</u>	<u>0.010 797</u>	<u>0.020 834</u>	<u>0.119 812</u>
	2.234 647	0.009 085	0.033 163	0.061 254	3.197 829	10.278 67

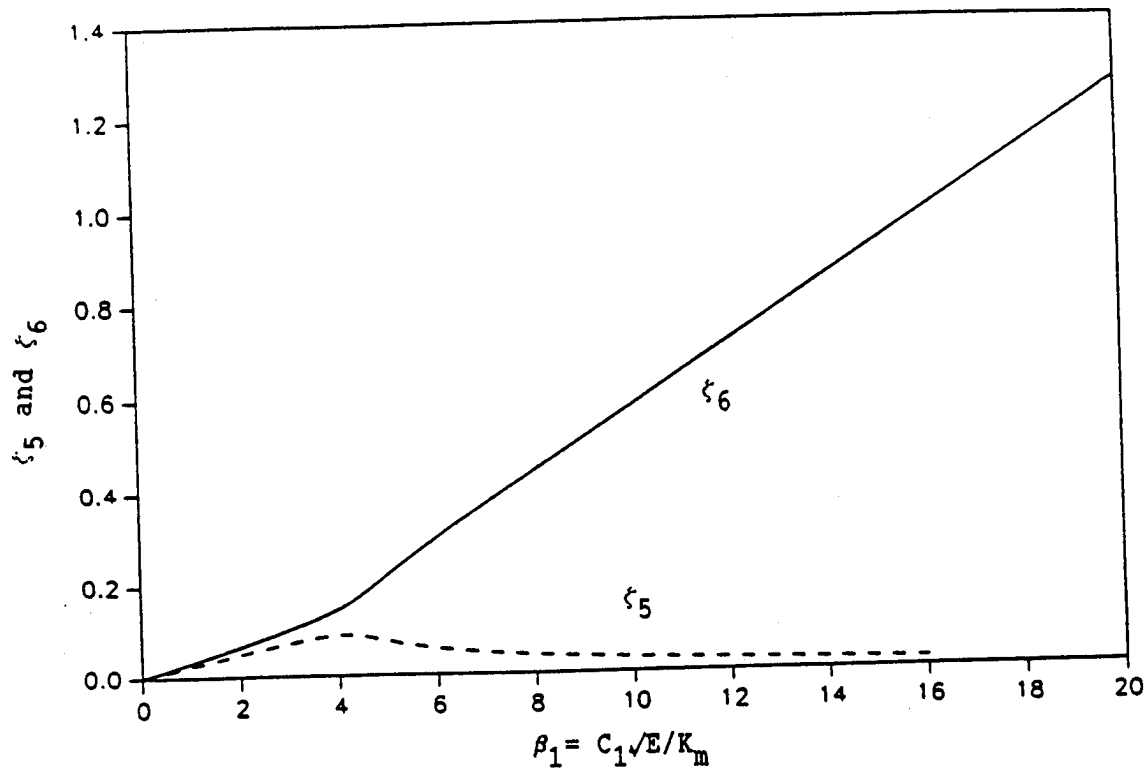


Figure 3 Modal damping ratios,  $\zeta_5$  and  $\zeta_6$  versus  $C_1$ .

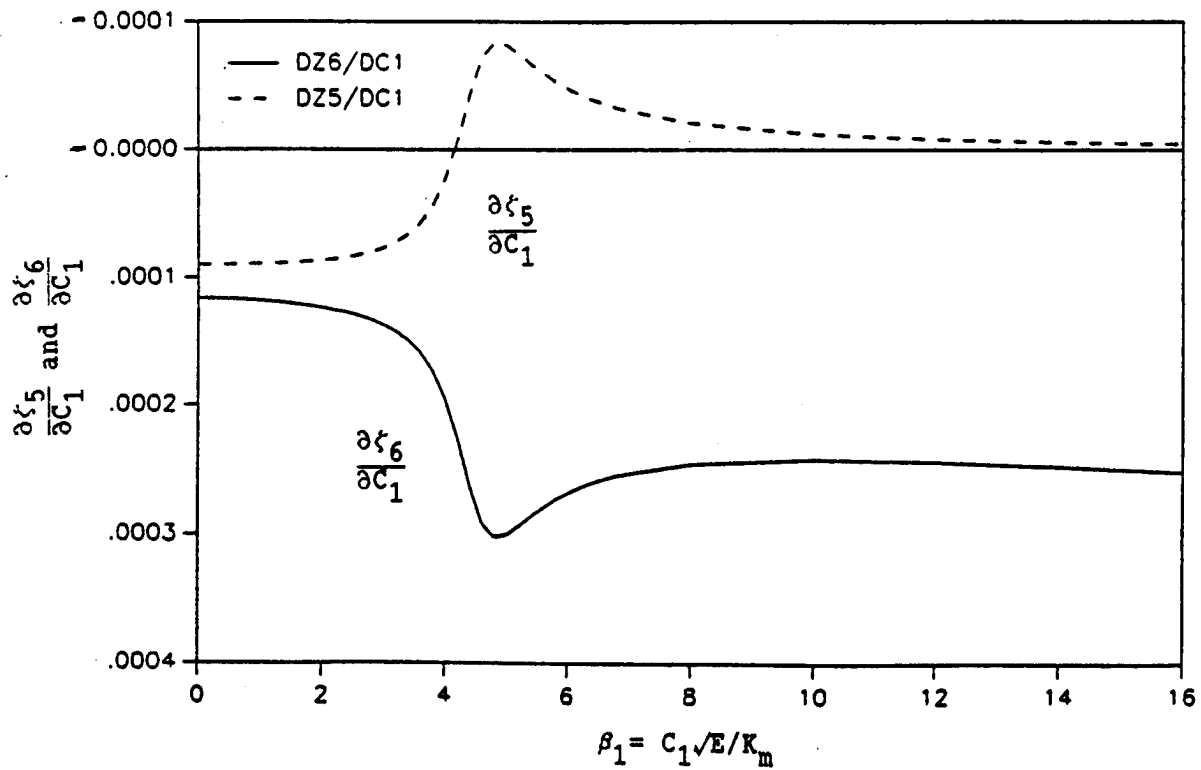


Figure 4 Sensitivities,  $\frac{\partial \zeta_5}{\partial C_1}$  and  $\frac{\partial \zeta_6}{\partial C_1}$ , versus  $\beta_1$ .

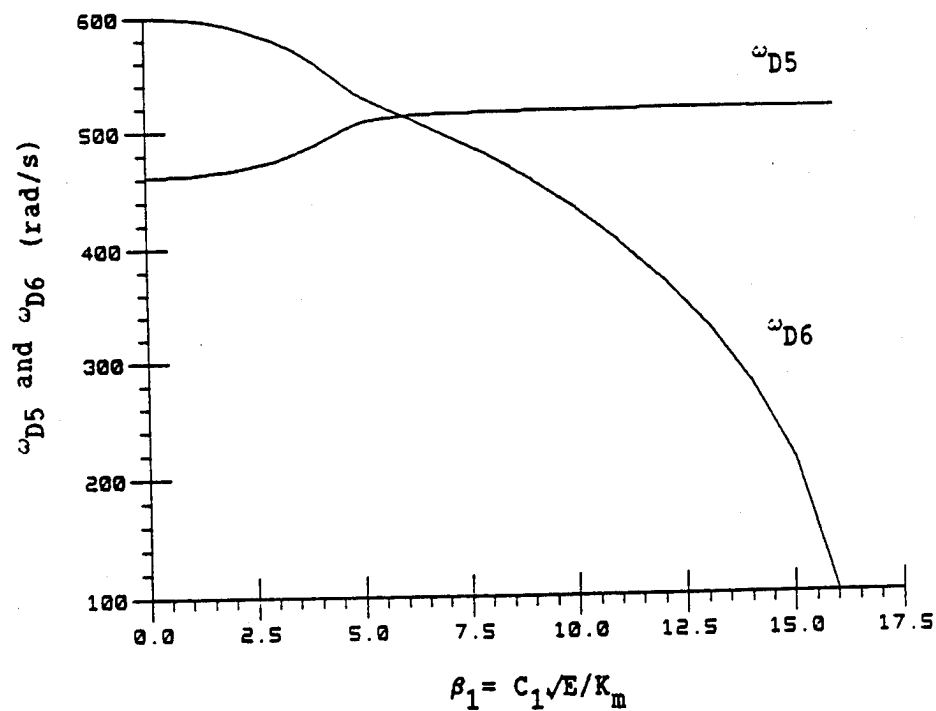


Figure 5 Damped Natural Frequencies  $\omega_{D5}$  and  $\omega_{D6}$  versus  $\beta_1$ .

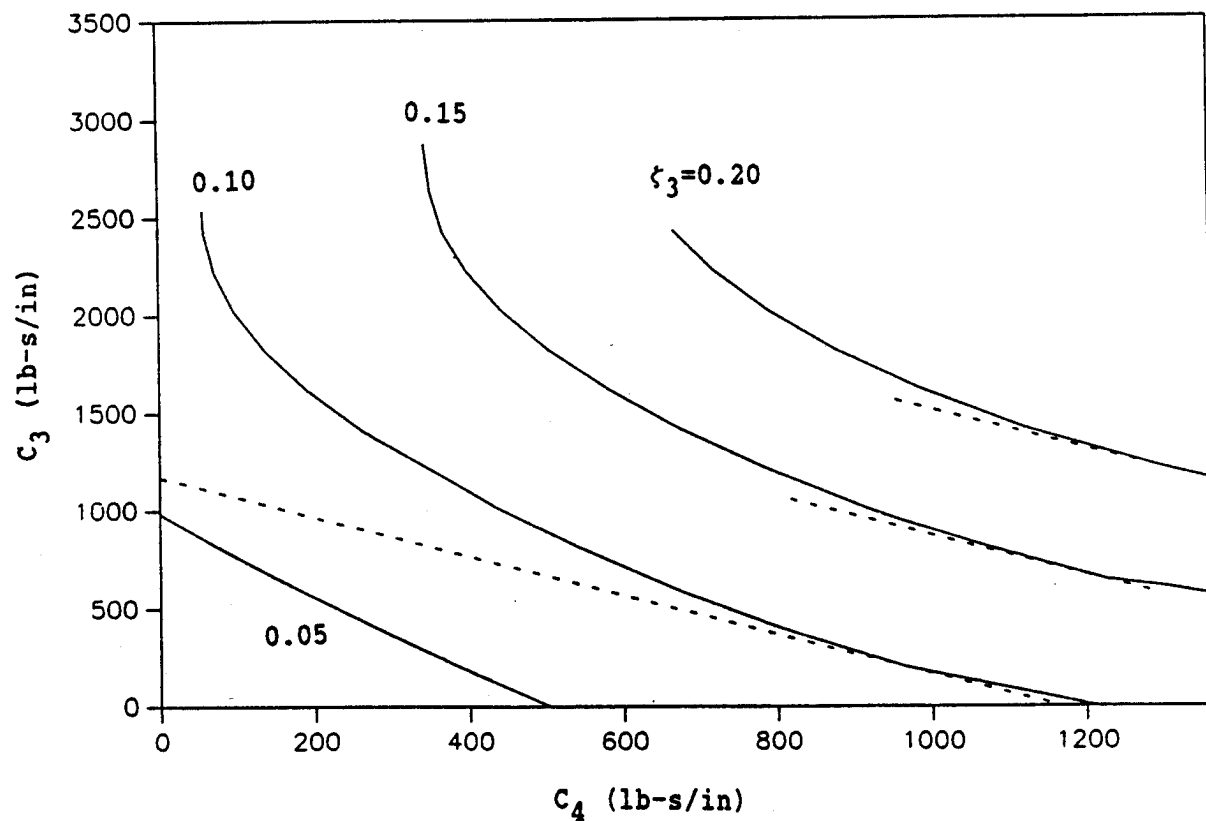


Fig. 6. Interaction of  $\zeta_3$  with  $C_3$  and  $C_4$ , with Constraint Boundaries (Dotted)

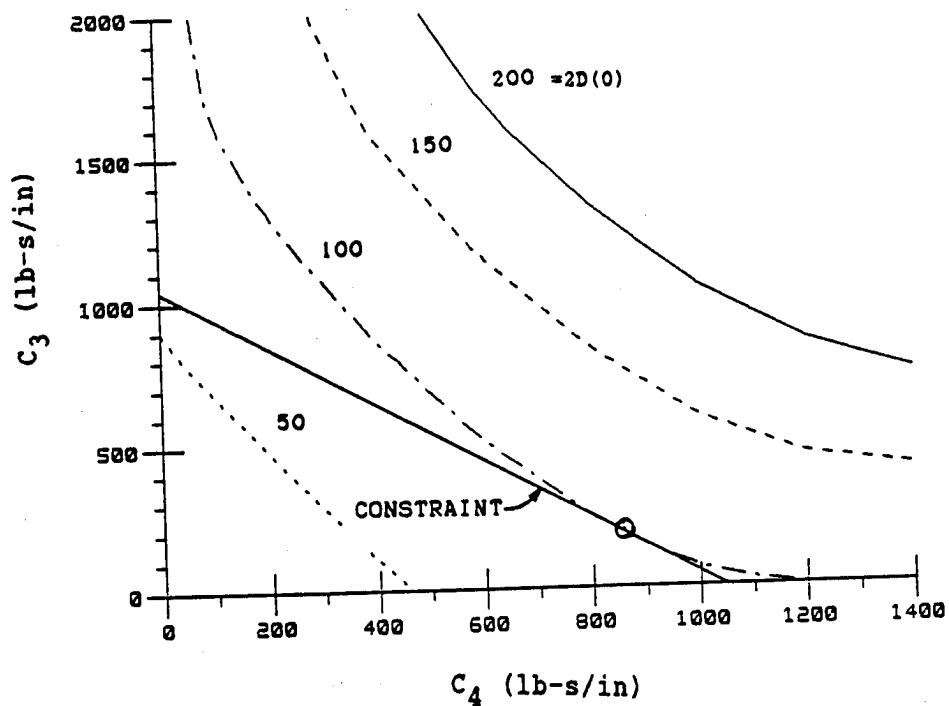


Figure 7 Interaction of  $2D(0)$  with  $C_3$  and  $C_4$ , Mode 3 Excited.

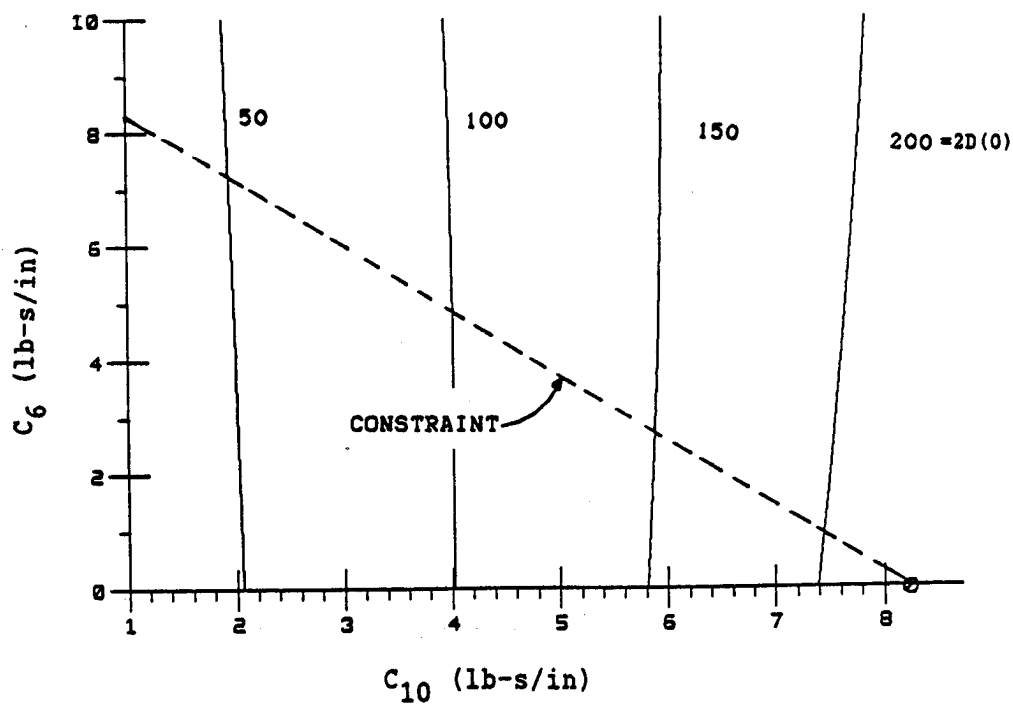


Figure 8 Interaction of  $2D(0)$  with  $C_6$  and  $C_{10}$ , Mode 4 Excited.

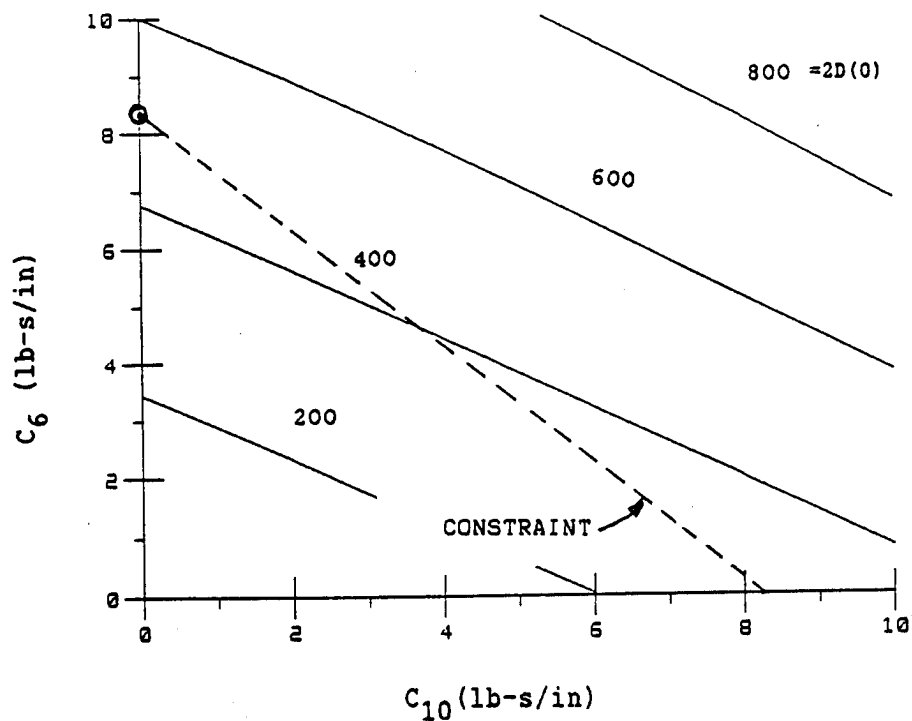


Figure 9 Interaction of  $2D(0)$  with  $C_6$  and  $C_{10}$ , Mode 7 Excited.

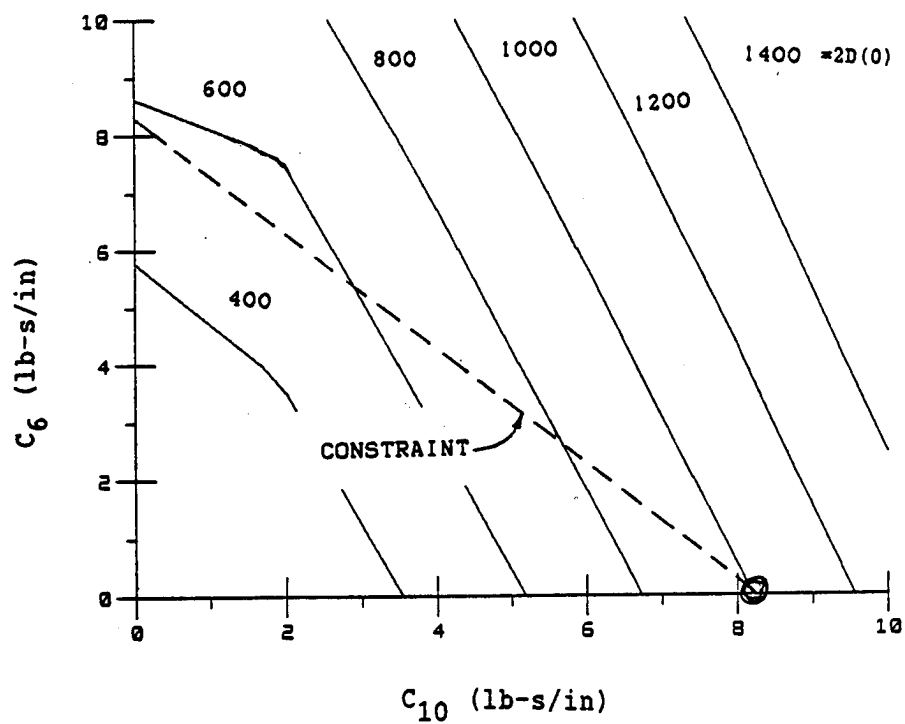


Figure 10 Interaction of  $2D(0)$  with  $C_6$  and  $C_{10}$ , Modes 4 & 7 Excited.

## Timewise Variation of the Dissipation Rate $2D(t)$ for Modes 5 and 6

The timewise variations of the energy dissipation rate for modes 5 and 6 excited separately and simultaneously are shown in Figures 11 and 12, for proportional and nonproportional damping respectively. In Figure 11 the solid curve is for modes 5 and 6 excited simultaneously and the two other lines are for modes 5 and 6 excited separately. The solid line seems to be a sum of the other two. In Figure 11, for nonproportional damping, where  $\beta_1=1.0$  and all other  $\beta_m=0$ , the case is entirely different and the dissipation rate at  $t=0$  for the simultaneous excitation of modes 5 and 6 is almost double that achieved by excitation of the modes individually. This is because, as mentioned above, the core matrix used for solving for the dissipation rate is nondiagonal, and the additional contribution is due to nondiagonal, or modal cross-product elements contributing to the dissipation rate. In Table 5, a portion of this matrix is shown for the rows and columns involving modes 5 and 6. Mode 5 would be excited by making the initial values  $q_5(0) = \bar{q}_5(0) = 1.0$ , or simply inserting ones for  $q_5$  and  $\bar{q}_5$  in the given matrices. It can be seen that the resulting value of  $2D(0)$  is equal to the sum of the complex numbers in the upper corner,  $2 \times 2$ , of this portion of the matrix. Here the notation is:  $(a,b) = (a+jb)$ . So the value of  $2D(0)$  with only mode 5 excited is the real number 46.64 in-lb/s. If only mode 6 is excited, the numbers in the lower corner  $2 \times 2$  are summed to yield 78.68 in-lb/s. If the two modes are excited simultaneously, the entire  $4 \times 4$  matrix is summed for a total of 246.49 in-lb/s, which is almost twice the total obtained by exciting the modes individually. In Table 6 the values of the kinetic and potential energies,  $T$  and  $U$ , and their timewise derivatives at  $t=0$  are also given. Note that  $\dot{T}(0) + \dot{U}(0) + 2D(0) = 0$  and  $T(0) - U(0) = 2n$ , as expected, where  $n$  is the number of modes excited. The ratio  $2D(0)/[T(0)+U(0)]$  is meaningful because it is the ratio of the dissipation rate to the total initial energy excited. From this point of view, for proportional damping, the

Table 5 Portion of core of  $\Lambda^T \Phi^T C \Phi \Lambda$  complex matrix.

$(q_5 \bar{q}_5 q_6 \bar{q}_6)$	(11.52, -2.54)	(11.80, -0.00)	(15.32, -0.02)	(14.97, -3.28)	$q_5$
	(11.80, 0.00)	(11.52, 2.54)	(14.97, 3.28)	(15.32, 0.02)	$\bar{q}_5$
	(15.32, -0.02)	(14.97, 3.28)	(19.44, 4.23)	(19.90, 0.00)	$q_6$
	(14.97, -3.28)	(15.32, 0.02)	(19.90, 0.00)	(19.44, -4.23)	$\bar{q}_6$

Table 6 Energies and Energy Rates, Prop. and Nonprop. Damping

Modes Excited	T(0)	U(0)	$\dot{T}(0)$	$\dot{U}(0)$	$\frac{2D(0)}{T(0)+U(0)}$
Proportional Damping, $\beta_m = 1.0$ , all $\beta_m$ .					
5	2.0027	0.0027	-101.34	-33.84	135.18 67.41
6	2.0045	0.0045	-171.02	-57.18	228.20 113.59
5&6	4.0072	0.0072	-272.36	-91.02	363.38 90.52
Nonproportional Damping, $\beta_1 = 1.0$ , $\beta_m = 0.0$ , $m \neq 1$ .					
5	2.0317	0.0317	-34.83	-11.82	46.64 22.60
6	2.0228	0.0228	-58.68	-20.00	78.68 38.46
5&6	4.0605	0.0605	-154.09	-92.40	246.49 59.82

ratio is largest if mode 6 is excited by itself, but for nonproportional damping the ratio is more favorable if modes 5&6 are excited simultaneously.

It should be noted with regard to Table 5 that here all the real parts of the complex numbers are positive. This is not true of the entire core matrix in general, and it may be necessary to excite the modes with varying initial phase to achieve the maximum damping rate, and the rate achieved in this manner may still be somewhat less than  $\|Core\|$ , herein defined as the sum of the absolute values of the real numbers in the core matrix.

#### Sensitivity of $\|Core\|$ to parameters $C_m$

Finally the sensitivity of  $\|Core\|$  to changes in  $C_m$  as found by the finite difference method are given in Table 7. In each case, the initial  $C_m = 1.0$  and  $\Delta C_m = 0.10$ . The largest gradients occur for the dashpots 2, 6, and 10.

Table 7 Sensitivity of  $\|Core\|$  to  $\Delta C_m$

m	$C_m$	$\ Core\ $	$\frac{\Delta\ Core\ }{\Delta C_m}$
1	1	1.74	1.74
2	1	110.77	109.56
3	1	3.86	3.86
4	1	4.26	4.26
5	1	4.67	4.67
6	1	103.89	101.88
7	1	4.69	4.69
8	1	2.11	2.11
9	1	6.01	6.01
10	1	204.91	204.47



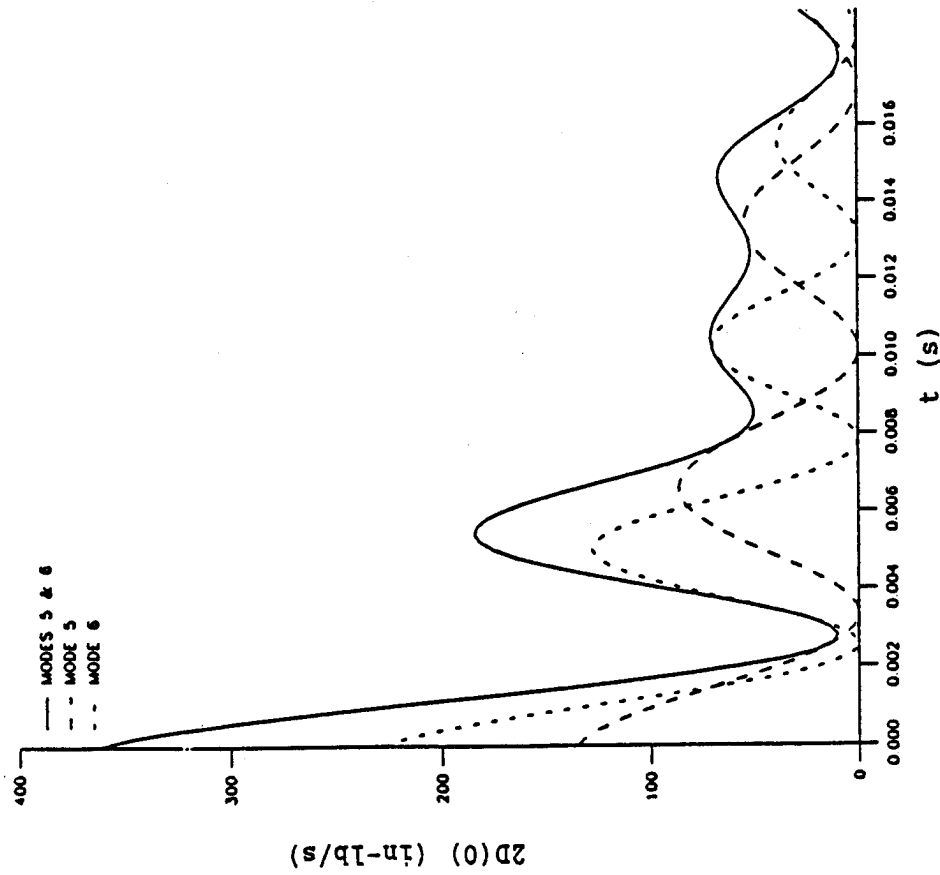


Figure 11  $2D(0)$  versus Time, All  $\beta = 1.0$ .  
Proportional Damping  
Modes 5, 6 and 5 & 6.

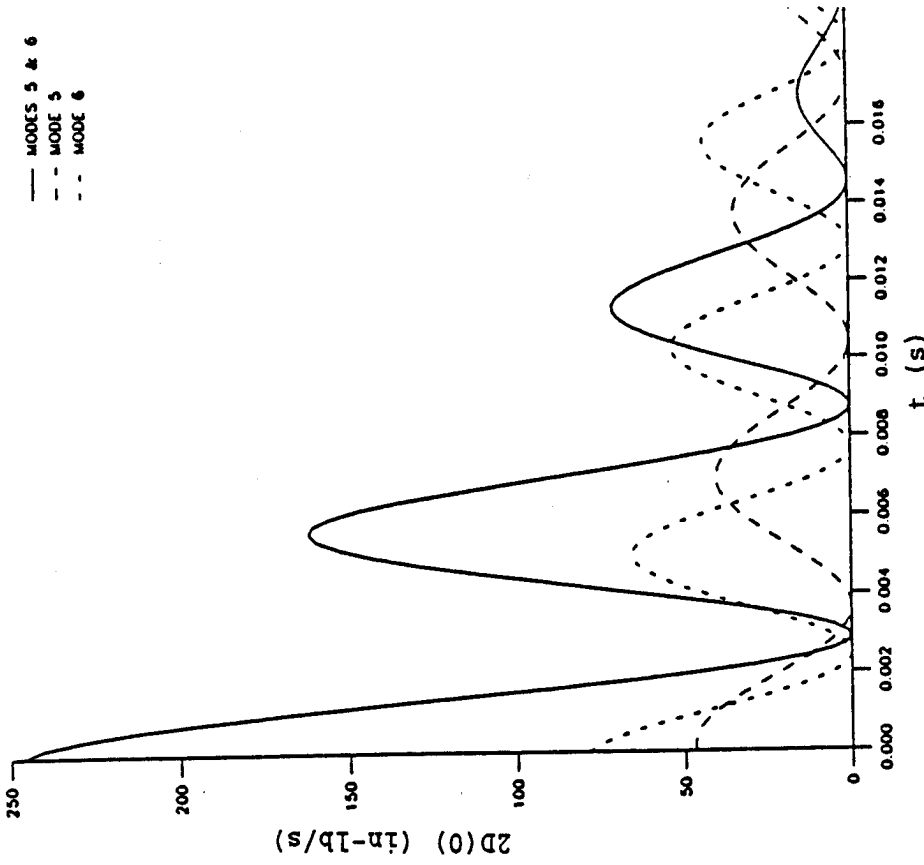


Figure 12  $2D(0)$  versus Time, Only  $\beta_1 = 1.0$ .  
Nonproportional Damping  
Modes 5, 6 and 5 & 6.

### Summary and Conclusions

1. It is demonstrated that the energy dissipation rate may be optimized simply by using its value at time  $t=0$  as the cost function. The settling time depends on the total initial energy, which is the sum of the initial kinetic and potential energies  $T(0)$  and  $U(0)$  and the dissipation rate  $2D(0)$ .

2. Because of the modal normalization procedure used in the present work, the sum  $T(0)-U(0)=2n$ , where  $n$  is the number of modes excited with unit amplitude. In the examples given, the  $U(0)$  was much smaller than  $T(0)$ , so the total initial energy equals  $T(0)$  and  $T(0) \cong 2n$ .

3. An upper bound on the maximum energy dissipation rate which may be achieved, if all the modes are excited with unit amplitude, is equal to the sum of the absolute values of real parts of the complex numbers in the CORE of the matrix from which  $2D$  is calculated, which is

$$2D = \mathbf{g}^T \mathbf{A}^T \mathbf{\Psi}^T \mathbf{C} \mathbf{K}^* \mathbf{\Psi} \mathbf{A} \mathbf{g} = \mathbf{g}^T \text{CORE } \mathbf{g}$$

If desired, the individual modes may be weighted differently when excited, to put more emphasis on modes of interest. In a practical problem, the initial values  $\mathbf{g}(0)$  could be taken as those which actually exist.

4. The derivative, or sensitivity, of the Core to the damping parameters may be calculated by taking the derivative of the given expression, which is seen to involve the derivatives of the eigenvalue and eigenvector matrices,  $\mathbf{A}$  and  $\mathbf{\Psi}$ , as well as the damping matrix  $\mathbf{C}$ .

5. The problem of deciding which truss members to damp and how much damping to use is reduced to a standard optimization problem. This problem may be solved by the Method of Steepest Descent or the Method of Feasible Directions. The solution may be obtained using a computer program such as CONMIN, which has been used by the writer to minimize the forced random response of the given truss while maintaining constraints on the modal damping ratios, so the damping is evenly distributed to the modes.

6. Study of the sensitivities of the damping ratios and damped natural frequencies of free vibration shows that as the viscous damping of a particular dashpot is increased, the damping ratio of one mode may decrease while the damping ratios of the other modes is increasing. Concurrently, the damped natural frequency of that one mode will be increasing while that of the other modes is decreasing. In the example given, one mode finally absorbed all the damping provided. Thus, in a practical situation, it appears possible that in some rare situations increasing damping could make matters worse, if damping is decreasing in the mode or modes that are being excited. The effect described is due to change in mode shape.

### Acknowledgments

The benefit of discussion with Dr. V. B. Venkayya, V. Tischler, D. Velez R. Kolonay, Capt. R Canfield, and Dr. L. Rogers of Wright-Patterson Air Force Base is gratefully acknowledged.

### References

1. NASA/DOD Control/Structures Interaction Technology, NASA CP 2447, Parts 1 and 2, 1986.
2. Carne, T. G., and Simonis, J.C., Editors, Modal Testing and Analysis, ASME DE-Vol. 3, Sept., 1987.
3. Rogers, L. and Simonis, J. C., Editors, The Role of Damping in Vibration and Noise Control, ASME DE-Vol.4, Sept., 1987.
4. Inman, D. J. and Simonis, J. C., Editors, Vibration Control and Active Vibration Suppression, ASME DE-Vol.5, Sept., 1987.
5. Leipholz, H. H. E. and Abdel-Rohman, Control of Structures, Martinus Nijhoff Publ, Boston and Lancaster, and Kluwer Acad. Publ., Hingham, MA 1986.
6. Meirovitch, L., Introduction to Dynamics and Control, Wiley, NY, 1985.
7. Neubert, V. H., Impedance: Modelling/Analysis of Structures, Jostens Publ. Co., State College, PA, 1988.
8. Nashif, A. D., Jones, D.I.G., and Henderson, R. P., Vibration Damping, Wiley, New York, 1985.
9. Soovere, J. and Drake, M.L., Aerospace Structures Technology Damping Design Guide, Vol. I-Technology Review, Vol. II-Design Guide, Vol. III- Damping Material Data, AFWAL-TR-84-3089, December 1985.
10. Bagley, D.L. and Torvik, P.J., "Fractional Calculus-A Different Approach to the Analysis of Viscoelastically Damped Structures", AIAA Journal, v.21, n.5, pp. 741-748, 1983.
11. Segalman, D.J., "Calculation of Damping Matrices for Linearly Viscoelastic Structures," Journal of Applied Mechanics, v. 54, pp.585-588, Sept, 1987.
12. McTavish, D.J. and Hughes, P.C., "Finite Element Modeling of Linear Viscoelastic Structures," in Ref. 3, pp. 9-18.
13. Venkayya, V. B., "Optimality Criteria: A Basis for Multidisciplinary Design Optimization," Computational Mechanics, 1988.
14. Vanderplaats, G. N., "CONMIN - A Fortran Program for Constrained Function Minimization, User's Manual," NASA(Ames)TMX-62,282, Aug 1973 and CONMIN User's Manual Addendum", May 1978.
15. Rogers, L. C., "Derivatives of Eigenvalues and Eigenvectors", AIAA Journal, v. 8, pp. 943-944, May 1970.
16. Nelson, R. B., "Simplified Calculation of Eigenvector Derivatives," AIAA Journal, v.14, n.9, pp. 1201-1205, Sept. 1976.

17. Sutter, T. R., Carmarda, C. J., Walsh, J. L., and Adelman, H. M., "A Comparison of Several Methods for the Calculation of Vibration Mode Shape Derivatives", Proc. AIAA/ASME/ASCE/AHS 27th Structures, Structural Dynamics and Materials Conference, San Antonio, TX, May 1986.
18. Lim, K. M., Junkins, J. L., and Wang, B. P., "Re-examination of Eigenvector Derivatives," Rev. Received AIAA Journal, Feb. 20, 1987.
19. Ojalvo, I. U., "Efficient Computation of Mode-Shape Derivatives for Large Dynamic Systems", AIAA Journal, v. 25, n. 10, 1986.
20. Fetterman, T. L. and Noor, A.K., "Computational Procedures for Evaluating the Sensitivity Derivatives of Vibration Frequencies and Eigenmodes of Framed Structures", NASA CR 4099, 1987.
21. Gibson, W. C. and Johnson, C. D. "Optimization Methods for Design of Viscoelastic Damping Treatments", In Reference 3, pp. 279-286.
22. Crandall, S. H. and McCalley, R.B., "Numerical Methods of Analysis," in Harris, C. M. and Crede, C.E., Shock and Vibration Handbook, McGraw-Hill, Inc. 1961.

Effect of Damping on the Predicted Fatigue  
Life of a Nonlinear Plate

R.N. Miles  
Department of Mechanical and  
Industrial Engineering,  
State University of New York,  
Binghamton, New York 13901  
607-777-4038

Abstract:

Numerous experimental studies have shown that when plate structures are subjected to sufficiently intense random excitations, the resonant response peaks, as observed in the response power spectral density, tend to broaden. This effect has been attributed to nonlinear damping. However, numerical simulations of the random response of nonlinear plates have shown that the broadening effect can occur in a plate with linear damping and nonlinear stiffness, which results from in-plane strain at large deflections. Contrary to what is seen in linear structures, in this situation an increase in the value of the linear damping loss factor results in a decrease in the width of the resonant peak. Since the response spectrum of the nonlinear plate is affected by damping in a non-intuitive way one may be concerned that the addition of damping could have an unexpected effect on the fatigue life.

In this paper it is shown that for a plate with linear damping and nonlinear stiffness, the addition of damping to the structure can provide a substantial improvement in fatigue life, although somewhat less than improvement observed in a linear plate. It is shown that the method of equivalent linearization gives estimates of the effect of damping on the fatigue life of a nonlinear plate which agree closely with those of more accurate numerical simulations.

## I. Introduction

In acoustic fatigue tests it is often necessary to drive structures with extremely high excitation levels in order to obtain failures within a reasonable period of time. It is not uncommon to drive structures with sufficient excitation to achieve highly nonlinear response. When a structure responds nonlinearly, one must exercise great care in interpreting response and fatigue data. The present study grew out of an observation that for a structure with nonlinear stiffness and linear damping, if one looks at the response power spectral density, an increase in the damping can result in a decrease in the width of the resonant response peaks. Conversely, decreasing the damping can broaden the resonant peaks. This is the opposite of what happens in linear structures. Since damping has a non-intuitive effect on the spectrum, and since the spectrum plays an important role in fatigue estimation, it seems appropriate to re-examine procedures for estimating the fatigue lives of nonlinear structures and review the effect of damping on fatigue life.

In the following, measured power spectral density plots will be shown for a nonlinear structure with random excitation. Predicted results obtained by both numerical simulation and an approximate method [1] are then shown to illustrate the effects of nonlinear stiffness and linear damping on the spectral response. The effect of damping on fatigue life is then examined using three different methods, a probabilistic formulation, numerical simulation, and the method of equivalent linearization. It is found that while damping has a somewhat counter-intuitive effect on the spectral response of the nonlinear system, an increase in damping increases the fatigue life in a manner that is predictable by classical methods.

## II. Measured and Predicted Spectra for Nonlinear Structures with Random Excitation

Figure 1 shows the measured power spectral density of the response of a beam with clamped ends for three levels of white noise base excitation. It is shown that as the excitation level is increased, the resonance peak associated with the fundamental mode (at about 35 Hertz) tends to increase in frequency and broaden substantially [2]. This effect has been observed in a large number of sonic fatigue tests in which the structure is driven with high noise levels to accelerate the rate of damage. While it is certainly possible that a nonlinear damping mechanism may contribute to the spectral broadening observed in this data, in the following it will be shown that the nonlinear stiffness, which is a well known characteristic of beams and plates with large deformations [3], can itself cause the spectral response to show substantial broadening of the resonant peaks.

To illustrate the effect of nonlinear stiffness on the response spectrum, consider the frequency response of a Duffing system with a deterministic, sinusoidal input as shown in figure 2 [3]. The Duffing equation is commonly used to represent the response of the fundamental mode of beams and plates. For large deformations, the stiffness becomes proportional to the cube of the displacement. The figure shows that as the amplitude of the sinusoidal input increases, the resonance response peak bends to the right. The cause of the bending of the frequency response curve is that as the deflection amplitude is increased, the stiffness of the system increases and consequently the system natural frequency increases. When the excitation is random rather than sinusoidal as in figure 2, the frequency response is quite different but there will continue to be a close coupling between the response amplitude and the resonant frequency.

The relationship between response amplitude and resonant frequency is illustrated in the time domain response of a nonlinear plate with random excitation as shown in figure 3. The figure shows the response of a plate with white acoustic excitation with levels of 130 decibels and 150 decibels. When the excitation level is 130 decibels the response is nearly linear and the time domain response shows a dominant frequency component at the frequency of the fundamental mode of the plate. When the excitation is increased to 150 decibels, the response remains fairly sinusoidal but it can be seen that as the amplitude of the random response increases, the dominant frequency component also increases.

The effect of the relationship between frequency and amplitude of a nonlinear system on the spectral response is shown in figure 4. The figure shows the power spectral density of the response of the fundamental mode of a nonlinear plate with random acoustic excitation. The jagged data is the result of numerical simulations of the response and the smooth curves are the result of an approximate solution for the response that accounts for the random fluctuations in the system resonant frequency [1]. The data shows that for this system (which has nonlinear stiffness but linear damping) as the excitation level is increased, the width of the resonant peak tends to broaden. The broadening of the peak in this case results from the fact that the resonant frequency of the nonlinear system depends on the response amplitude and since the response is random, the resonant frequency becomes random. Since the calculation of the power spectral density involves averaging the response over time, the fluctuations in the resonant frequency cause the resonant peak to broaden.

Since nonlinear stiffness can have a strong effect on the width of a resonant peak, it is important to consider what an increase in damping does in a nonlinear system. Figure 5 shows the predicted spectra for a nonlinear plate having a damping loss factor of .1 and .005. The excitation level is 140 decibels which is sufficient to result in nonlinear response. The figure shows that as the loss factor is increased to .005 the width of the resonant peak increases substantially.

The increase in the width of the peak results from the fact that decreasing the damping will increase the response amplitude and therefore cause the nonlinear stiffness effect to be more pronounced.

### III. Fatigue Life Estimation

A primary motivation for increasing the damping in a system is often to increase its useful service life. Since the spectral response is influenced by damping in a very different manner for linear and nonlinear structures, and since the response spectrum can influence the fatigue life, it is important to carefully consider the influence of damping on the fatigue life of a nonlinear structure. In the following we will review three different methods for fatigue life estimation which will then be employed to estimate the effect of damping on the fatigue life of a nonlinear plate.

For the present study we will assume that the relation between the stress amplitude,  $S$ , and the number of cycles to failure  $N$ , may be approximated by the well known relation,

$$N = \frac{c}{S^b} \quad (1)$$

where  $c$  and  $b$  are experimentally obtained constants for a given material. It will be assumed that the number of fatigue cycles experienced by the structure is equal to the number of positive stress peaks, or stress reversals, that occur over time. A sample time history is shown in Figure 6 where the positive peaks are identified by circles.

The assumption that damage occurs at each positive stress peak may be conveniently combined with the Palmgren-Miner linear damage accumulation rule [4] to produce fatigue life estimates. In this theory, the damage,  $D_i$ , caused by stress reversals at the stress level  $S_i$  is

$$D_i(S_i) = \frac{n(S_i)}{N(S_i)} \quad , \quad (2)$$

where  $n(S_i)$  is the number of stress reversals experienced by the structure at the stress level  $S_i$  and  $N(S_i)$  is the number of reversals required to cause failure at this stress level. The total damage,  $D_m$ , will be the sum of the damage at all stress levels that occur,

$$D_m = \sum_i D_i(S_i) = \sum_i \frac{n(S_i)}{N(S_i)} \quad . \quad (3)$$



From equation (1),

$$N(S_i) = \frac{c}{S_i^b}, \quad (4)$$

so that equation (3) becomes

$$D_n = \frac{1}{c} \sum_i n(S_i) S_i^b \quad (5)$$

The form of equation (1) assumes that all stress peaks occur at positive stress levels as would be the case for sinusoidal loading. When a resonant system is subjected to random loading, however, we must allow for the possibility of stress peaks at negative stresses which make positive contributions to the accumulated damage. To account for this, we will take the absolute value of the stress level,  $S_i$ , so that equation (5) becomes

$$D_n = \frac{1}{c} \sum_i n(S_i) |S_i|^b \quad (6)$$

Failure is predicted to occur when  $D_n = 1$ .

Since the response and rate of damage accumulation in the structure is assumed to be random, the fatigue life may be estimated from the expected value of the rate of damage accumulation. This may be expressed as an integration over all possible stress levels in the form

$$E[D_n] = \int_{-\infty}^{\infty} n(S) \frac{|S|^b}{c} P(S) dS, \quad (7)$$

where  $P(S)$  is the probability density for response peaks.

The assumption that the response process is stationary gives the fatigue life as

$$T = \frac{1}{E[D_n]} \quad (8)$$

In the case where the system is linear and has a single lightly damped resonant mode, the peak probability density may be approximated by a Rayleigh distribution for a narrowband process,

$$P(S) = \frac{S}{\sigma_s^2} e^{-\frac{S^2}{2\sigma_s^2}}, \quad S \geq 0, \quad (9)$$

where  $\sigma_s^2$  is the mean square stress level.

#### IV. Approximate Methods for Single Degree of Freedom Systems

For a linear single degree of freedom system, Miles [5] has replaced  $n(S)$  in equation (7) with the system resonant frequency in Hertz,  $\omega_o/2\pi$ . Equations (7) and (9) then give Miles' single degree of freedom formula [5],

$$E[D_m] = \frac{\omega_o}{2\pi c} (\sqrt{2}\sigma_s)^b \Gamma\left(\frac{b+2}{2}\right), \quad (10)$$

where,

$$\Gamma(y) = 2 \int_0^{\infty} x^{2y-1} e^{-x^2} dx, \quad y > 0. \quad (11)$$

If a single degree of freedom oscillator is nonlinear it is possible to evaluate equation (7) by replacing  $n(S)$  with the expected total number of peaks per unit time,  $E[M_t]$ . If we again assume that the response process is narrowband, it is not difficult to approximate the peak probability density,  $P(S)$ . If the displacement response,  $x(t)$  is governed by Duffing's equation,

$$\ddot{x} + \omega_o^2 (x + \epsilon x^3) + \alpha \dot{x} = f(t) \quad (12)$$

where  $\omega_o^2$  is the linear natural frequency,  $\epsilon$  and  $\alpha$  are constants, and  $f(t)$  is Gaussian white noise, then the damage rate may be approximated by [6]

$$E[D_m] = \frac{1}{c} C \omega_o^2 K^b \int_0^{\infty} x^b (x + \epsilon x^3) e^{-\frac{x^2}{2\sigma_o^2} - \frac{\epsilon x^4}{4\sigma_o^2}} dx, \quad (13)$$

where

$$\frac{1}{C} = \sqrt{2\pi\omega_o^2\sigma_o^2} \int_{-\infty}^{\infty} e^{-\frac{x^2}{2\sigma_o^2} - \frac{\epsilon x^4}{4\sigma_o^2}} dx, \quad (14)$$

and  $\sigma_o^2$  is the mean square displacement response when  $\epsilon=0$ ,  $\sigma_o^2 = G_f/(4\omega_o^2\alpha)$ , where  $G_f$  is the constant single-sided power spectral density of the excitation in units of  $f^2$ /Hertz. The constant  $K$  in equation (13) is an assumed (for the present study) linear relation between stress and displacement, i.e.

$$S = Kx \quad (15)$$

When  $\epsilon=0$  equation (13) reduces to equation (10).

An alternative approach to estimate the fatigue life is to solve equation (12) numerically and use equation (15) to determine the stress as a function of time. When a stress reversal occurs at the stress level  $S$ , one simply increments the accumulated damage according to

$$D_m = D_m + \frac{|S|^b}{c}, \quad (16)$$

where  $D_m$  is initially set to zero. If the solution is simulated for a time period equal to  $\tau$  then the damage rate is  $D_m/\tau$  and the predicted fatigue life is

$$T = \frac{\tau}{D_m} \quad (17)$$

The fatigue life of a nonlinear structure may also be estimated using the method of equivalent linearization [7]. Equivalent linearization consists of approximating the nonlinear system in equation (12) by

$$\ddot{x} + \omega_o^2 x + \alpha \dot{x} + e(x) = f(t), \quad (18)$$

where  $\omega_o$  is the equivalent linear natural frequency and  $e(x)$  is the error in the approximation.  $\omega_o$  is chosen so that the mean square of  $e(x)$  is minimized. This leads to

$$\omega_o^2 = \frac{\omega_o^2}{2} \left( 1 + \sqrt{1 + 12\epsilon\sigma_o^2} \right), \quad (19)$$

where, as before

$$\sigma_o^2 = \frac{G_f}{4\omega_o^2\alpha} \quad (20)$$

is the mean square response when  $\epsilon=0$ .

The mean square value of the response of the nonlinear system is then approximated by

$$\sigma_x^2 = \frac{G_r}{4\omega_0^2 \alpha} \quad (21)$$

To obtain an estimate of the fatigue life of a system governed by equation (12) we could simply calculate the fatigue life of an equivalent linear system such as in equation (18) with  $e(x)$  neglected. This may be accomplished by using equation (10) with  $\omega_0$  replaced by  $\omega_*$  and  $\sigma_s$  replaced by  $K \sigma_x$ ,

$$E[D^m] = \frac{\omega_*}{2\pi c} \left( \sqrt{2} K \sigma_x \right)^b \Gamma\left(\frac{b+2}{2}\right) \quad (22)$$

It is important to note that equation (22) assumes that the response is a narrowband process and that the stress peaks have a Rayleigh distribution. The nonlinear response does not appear to be narrowband, as shown in figure 4, and the peak probability density is not a Rayleigh distribution [6] but the effects of these approximations on the estimated fatigue life are not clear from the equations.

Equivalent linearization may be easily applied to estimate the spectral response. The results shown in figure 7 indicate that the method fails to depict the spectral broadening effect seen in the response of a plate with strong nonlinearity.

## V. Governing Equation for a Nonlinear Plate

To predict the fatigue life of a system using the methods of the previous section we will calculate the coefficients of Duffing's equation (12) corresponding to the response of a nonlinear plate with simply-supported boundaries. We will assume that the plate response may be described by a single resonant mode.

If the in-plane motion of the plate is constrained at the edges, the Berger hypothesis<sup>3</sup> leads to

$$\begin{aligned} D\nabla^4 w - \rho h \epsilon c_p^2 (w_{,xx} + w_{,yy}) \\ + \rho h \ddot{w} + \alpha \dot{w} = p(x, y, t) \end{aligned} \quad (23)$$

where

$$e = \frac{1}{2L_x L_y} \int_0^{L_y} \int_0^{L_x} (w_{,x}^2 + w_{,y}^2) dx dy \quad (24)$$

$w$  is the transverse displacement,  $\rho$  is density,  $h$  is the thickness,  $\alpha$  is the viscous damping coefficient, and  $p(x,y,t)$  is the applied pressure.  $L_x$  and  $L_y$  are the dimensions of the plate in the  $x$  and  $y$  directions. The constants  $D$  and  $C_p$  are the bending rigidity and wave speed,

$$D = \frac{E h^3}{12(1-\nu^2)}, \quad C_p^2 = \frac{E}{\rho(1-\nu^2)} \quad (25)$$

$E$  is Young's modulus and  $\nu$  is Poisson's ratio. Comma denotes partial differentiation. For a simply supported plate,

$$w(x,y,t) = A(t) \sin\left(\frac{\pi x}{L_x}\right) \sin\left(\frac{\pi y}{L_y}\right), \quad (26)$$

where  $A(t)$  is an unknown function of time.

By substituting equation (26) into equations (23) and (24) the governing equation takes the form of equation (12),

$$\ddot{A} + \omega_0^2 (A + \epsilon A^3) + \alpha \dot{A} = F(t), \quad (27)$$

where,

$$\omega_0^2 = \frac{D}{\rho h} \left[ \left( \frac{\pi}{L_x} \right)^2 + \left( \frac{\pi}{L_y} \right)^2 \right]^2, \quad (28)$$

$$\epsilon = \frac{3}{2h^2}, \quad (29)$$

and

$$F(t) = \frac{4}{\rho h L_x L_y} \int_0^{L_y} \int_0^{L_x} \sin\left(\frac{\pi x}{L_x}\right) \sin\left(\frac{\pi y}{L_y}\right) p(x,y,t) dx dy \quad (30)$$

Let the excitation have the form

$$p(x,y,t) = p_o(t) \sin \left( \frac{\pi x}{L_x} \right) \sin \left( \frac{\pi y}{L_y} \right) \quad (31)$$

Equations (30) and (31) give

$$F(t) = \frac{p_o(t)}{\rho h} \quad (32)$$

The damping coefficient,  $\alpha$ , in (27) is taken to be

$$\alpha = \omega_o \eta \quad (33)$$

where  $\eta$  is the loss factor.

For the present study we will obtain the stress-displacement relation, equation (15), by neglecting in-plane displacements and assuming that the maximum stress may be approximated by

$$S = E \epsilon_y \quad (34)$$

where  $\epsilon_y$  is the strain in the  $y$  direction at the surface of the plate at its mid-point ( $x=L_x/2$ ,  $y=L_y/2$ ). For a simply-supported plate this will be the location of maximum stress. It is assumed that the  $y$  component of the strain is greater than the  $x$  component which will be true if  $L_x > L_y$ . Evaluating the stress in this case gives

$$\begin{aligned} S &= E \frac{h}{2} \frac{\partial^2 w}{\partial y^2} = E \frac{h}{2} \left( \frac{\pi}{L_y} \right)^2 A \sin^2 \frac{\pi}{2} \\ &= \frac{Eh}{2} \left( \frac{\pi}{L_y} \right)^2 A \quad (35) \end{aligned}$$

The constant  $K$  in equation (15) is then

$$K = \frac{Eh}{4} \left( \frac{\pi}{L_y} \right)^2 \quad (36)$$

This is, of course, a very crude approximation but it will suffice for our present purposes.

The remaining constants to be determined for our comparisons are the material properties  $b$  and  $c$  in the damage accumulation model, equation (6). These must be obtained experimentally. For this study, we only need to use "typical" numbers for a common material. The constants used in the calculations are

$$b = 6.33 \text{ and } c = 6.56 \times 10^{30} \quad (37)$$

The results presented in the following correspond to an aluminum plate with the following properties: (English units)

$$E = 10^7 \text{ PSI}, \rho = 0.1 \text{ lbs./in}^3, \nu = 0.3, L_x = 20 \text{ in.}, L_y = 10 \text{ in.},$$

and  $h = 0.063 \text{ in.}$

The excitation is assumed to result from acoustic pressure fluctuations. The driving sound pressure level is given by

$$L_p = 20 \log \frac{P}{P_{ref}} \quad (38)$$

where  $P_{ref} = 0.0002 \mu \text{ bar}$ . A pressure of one pound per square inch corresponds to a sound level of approximately 170 dB.

## VI. Results and Conclusions

Fatigue life estimates for the nonlinear plate are shown in figure 8. The figure shows the fatigue life as a function of excitation level for a plate with a modal loss factor of .005. Predictions are shown for each method described in section IV. The results identified as "exact" correspond to the probabilistic formulation, equations (13), (14) and (8) and the numerical simulation approach of equations (16) and (17). The method of equivalent linearization, equation (22), gave only slightly lower estimates of fatigue life. The estimated fatigue life of the system when nonlinearity is neglected is also shown and is found to be significantly less than that for the nonlinear case. This effect follows from the fact that the nonlinearity increases the stiffness when the deflections are large and consequently limits the response amplitude.

The effect of damping on the estimated fatigue life was examined by performing the calculations with the excitation level set to 140 decibels and varying the loss factor from .0005 to .5. It was found, as can be seen in equations (13) and (14), that increasing the loss factor by a factor of 10 has the same effect as reducing the excitation level by 10 decibels. This is shown in the upper x-axis in figure 8.

The results shown in figure 8 indicate that while damping can have a strange effect on the spectral response as seen in figure 5, it has a beneficial and easily predicted effect on the fatigue life. The excellent agreement between the methods of estimating fatigue life indicate that it is possible to obtain reasonably accurate results without accurately accounting for the probability densities of the response and of the response peaks. The assumption that the response is a narrowband process also does not adversely affect the results.



## References

- 1) R.N. Miles, "An approximate solution for the spectral response of Duffing's oscillator with random input", to appear Journal of Sound and Vibration, 1989.
- 2) C.F. Ng and R.N. Miles unpublished results obtained at NASA Langley Research Center, 1988.
- 3) A.H. Nayfeh and D.T. Mook, Nonlinear Oscillations. John Wiley and Sons, New York, 1979.
- 4) M.A. Miner, "Cumulative damage in fatigue", Journal of Applied Mechanics, 12, pp. A 159-164, (1945).
- 5) J.W. Miles, "On structural fatigue under random loading", Journal of the Aeronautical Sciences, 21, pp. 753-762, (1954).
- 6) Y.K. Lin, Probabilistic Theory of Structural Dynamics. McGraw-Hill, Inc., New York, 1967.
- 7) T.K. Caughey, "Equivalent linearization techniques", Journal of the Acoustical Society of America, 35 (11), pp. 1706-1711, (1963).

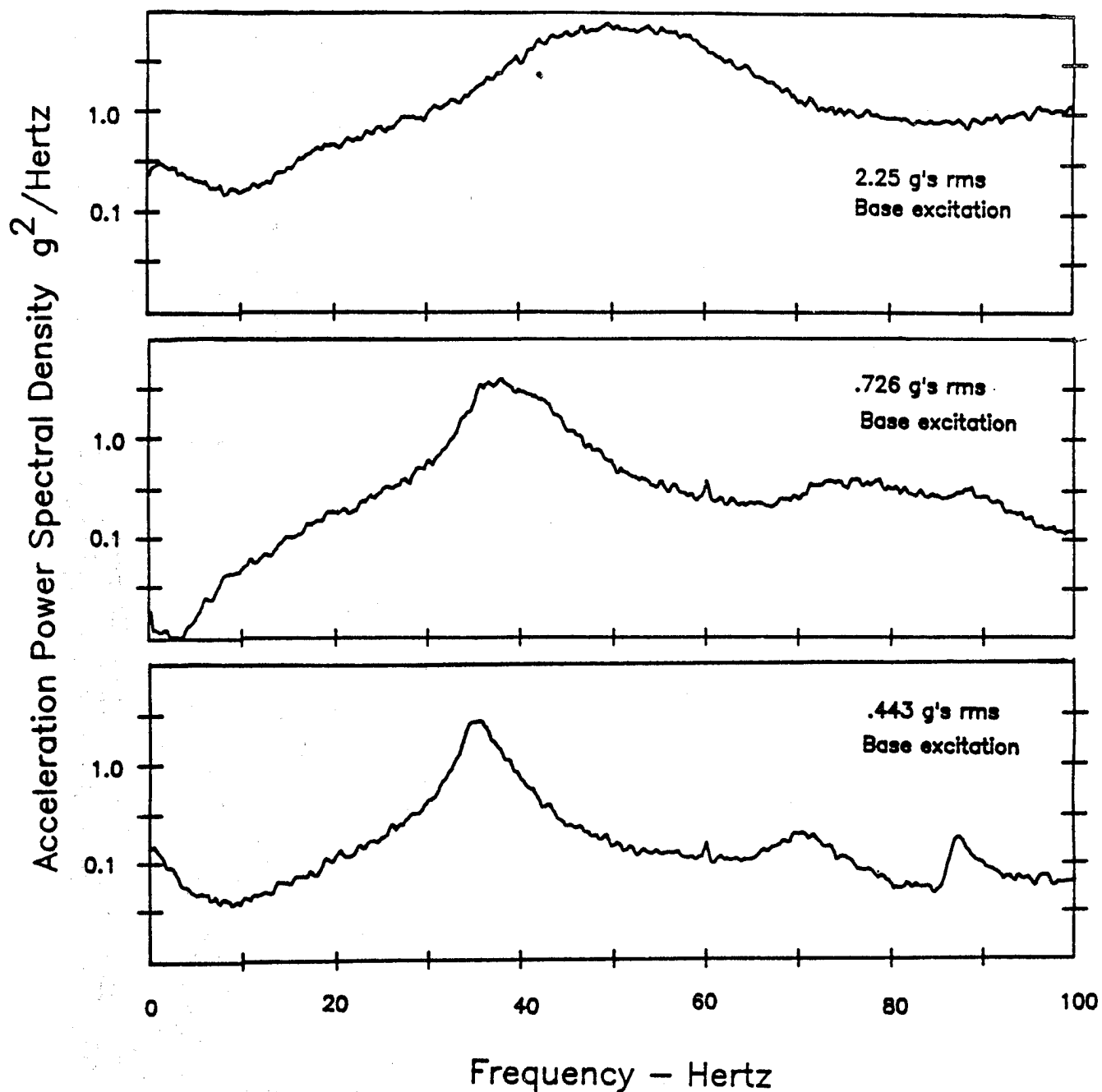


FIGURE 1 Measured acceleration spectral density  
of base excited beam

.25 Hertz bandwidth  
64 Averages  
Aluminum beam 2"X15"X.032"  
Clamped ends  
White noise base excitation  
Response measured at center of beam

FIGURE 2 Approximate Response due to Single Frequency Excitation

$$w(x,y,t) = b(t)\phi(x,y) , \quad \text{single resonant mode}$$

$$\ddot{b} + \omega_1^2 b + d\dot{b} + 8b^3 = f_0 \cos(\omega t) \quad \text{Duffing Equation}$$

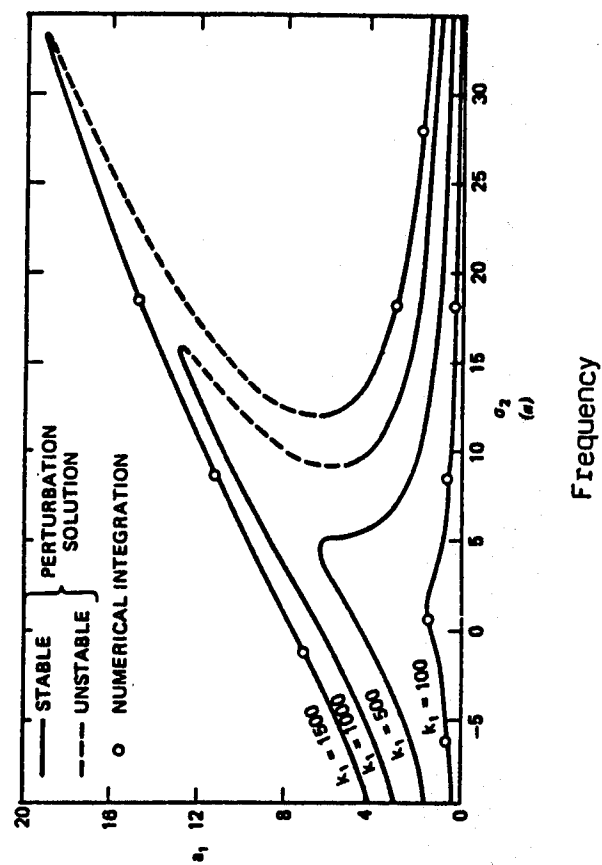
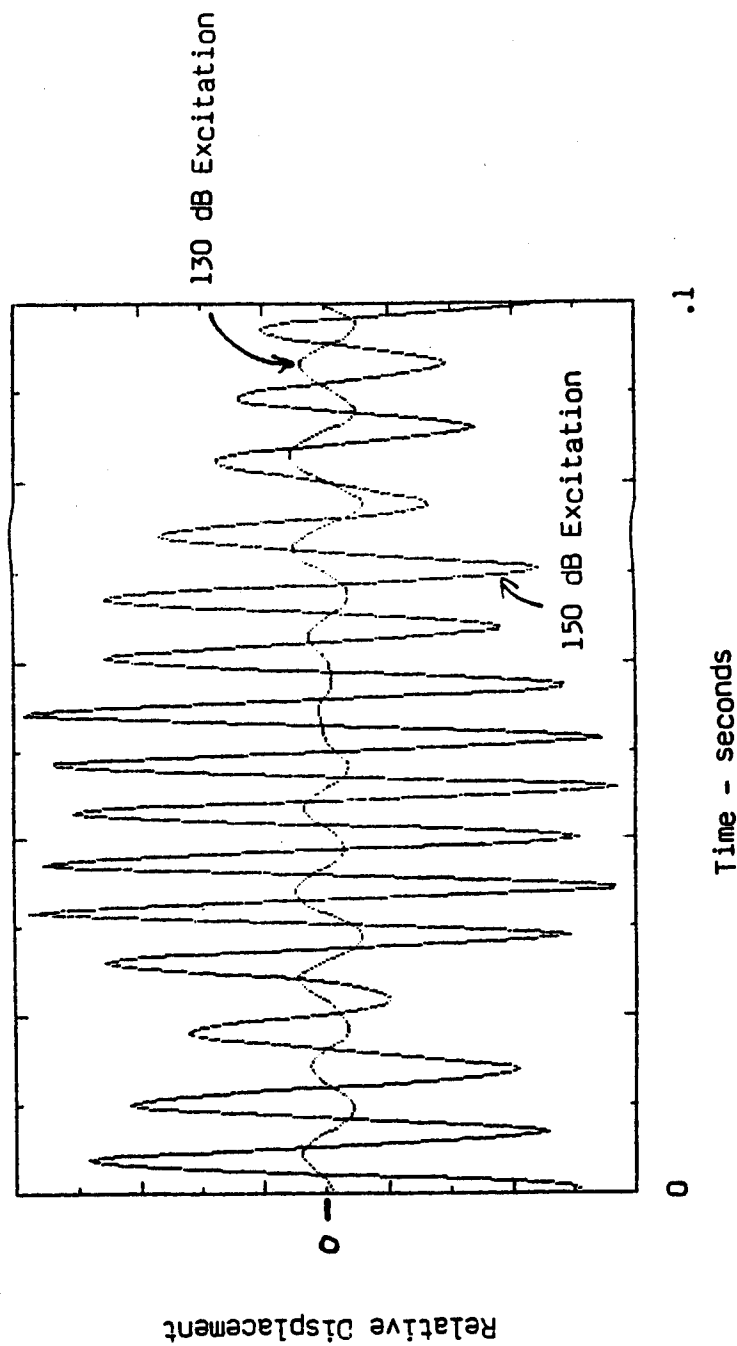


FIGURE 3

Simulated Response Time History

Duffing's Equation



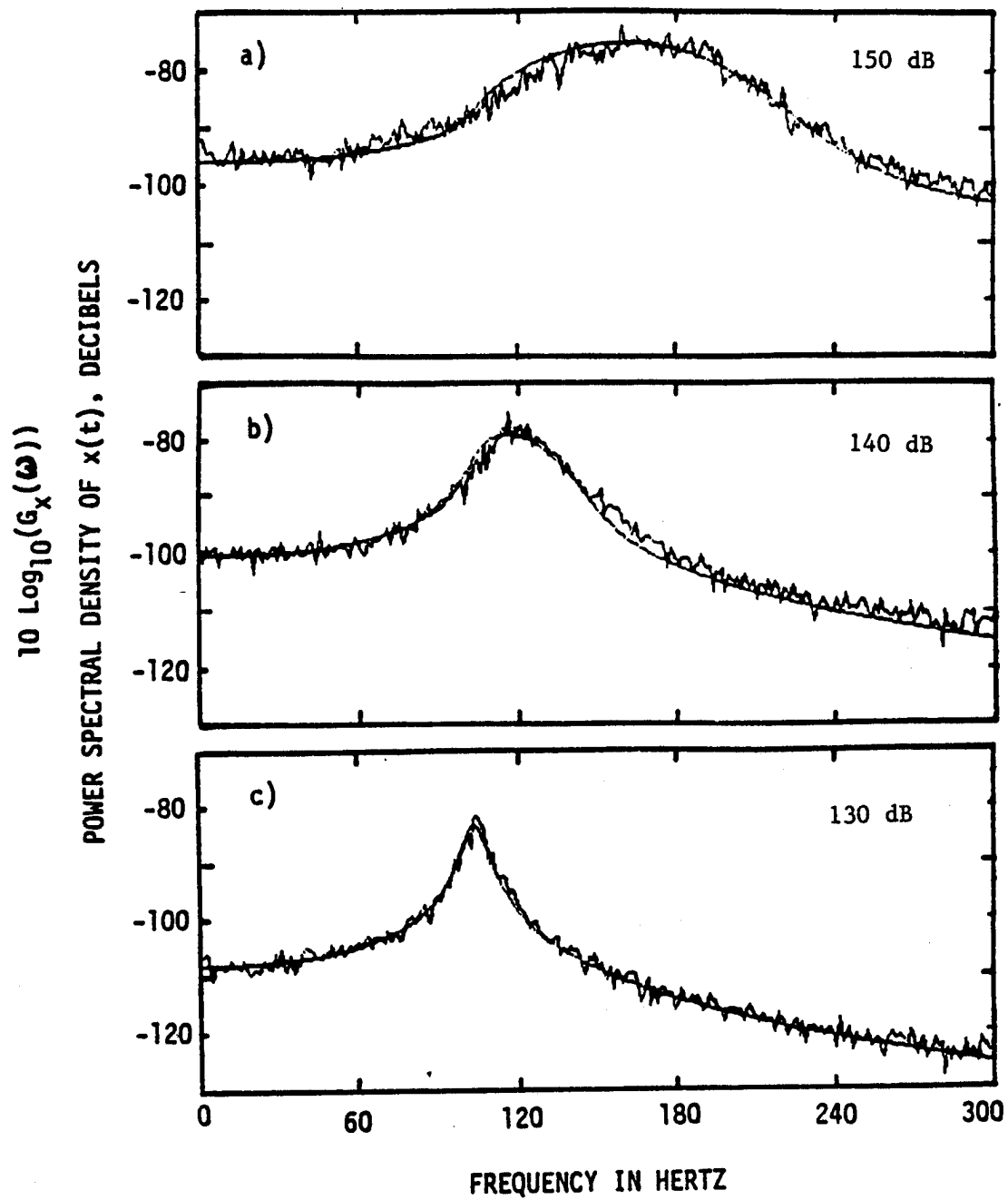
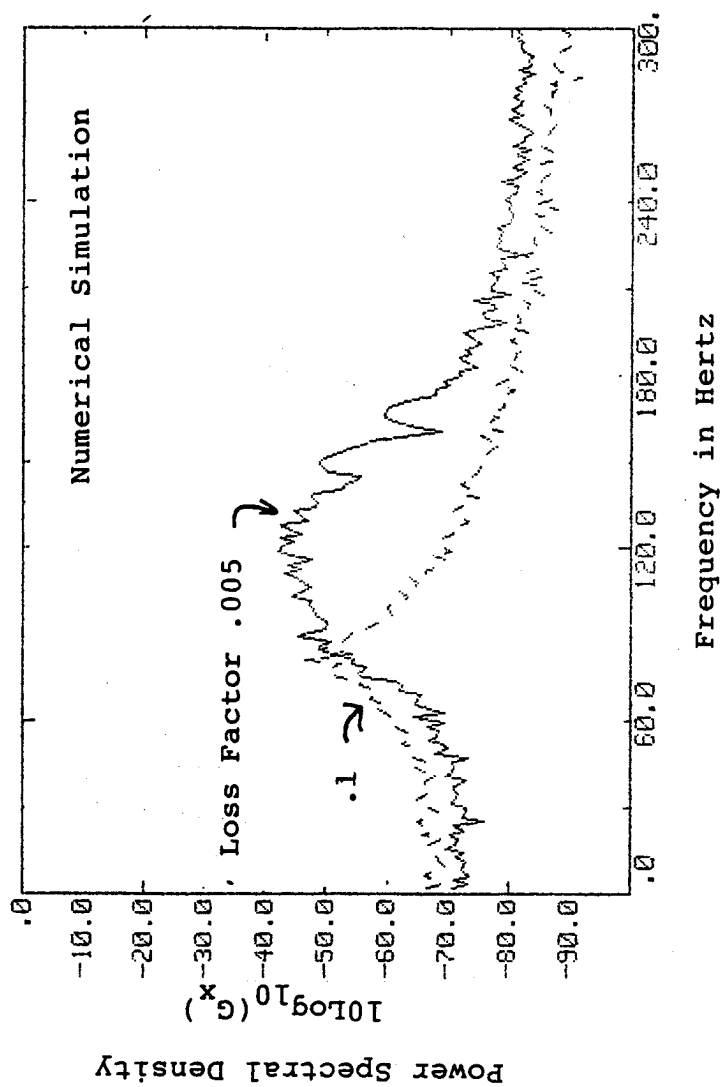


FIGURE 4 COMPARISONS OF APPROXIMATE SOLUTIONS TO DUFFING'S EQUATION  
WITH RESULTS OF NUMERICAL SIMULATIONS

FIGURE 5

Effect of Damping on Spectrum



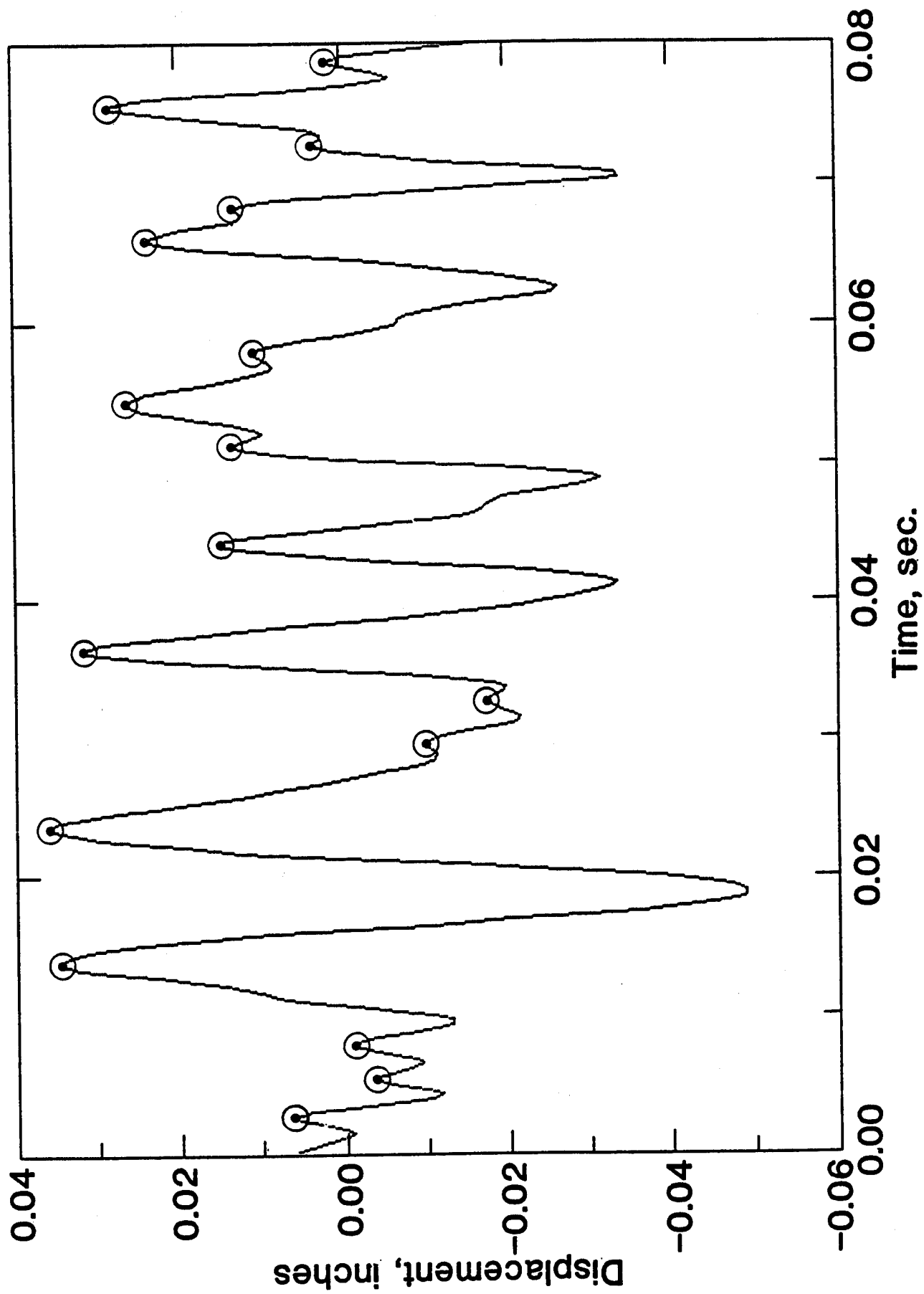


FIGURE 6 Simulated response time history.

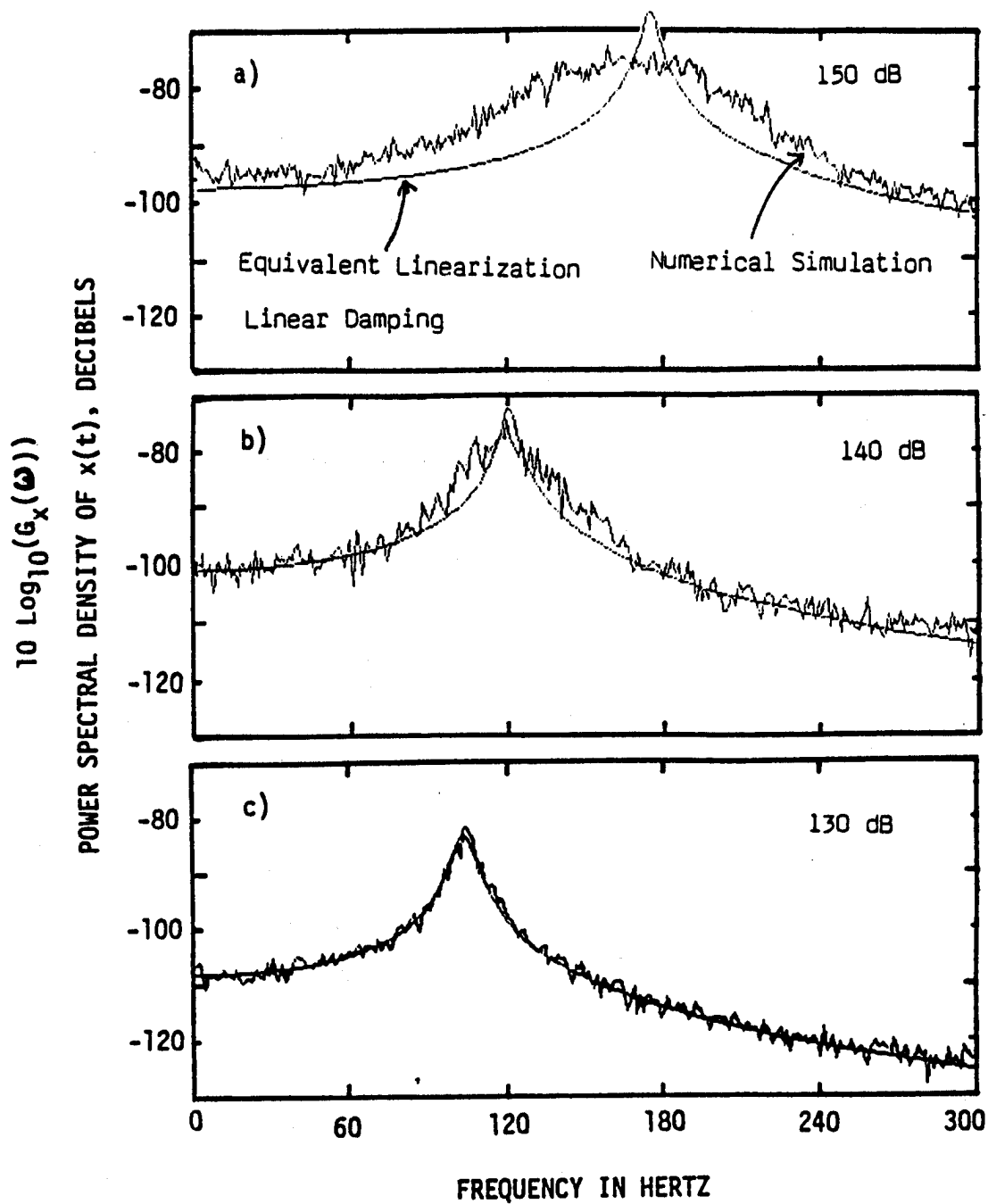


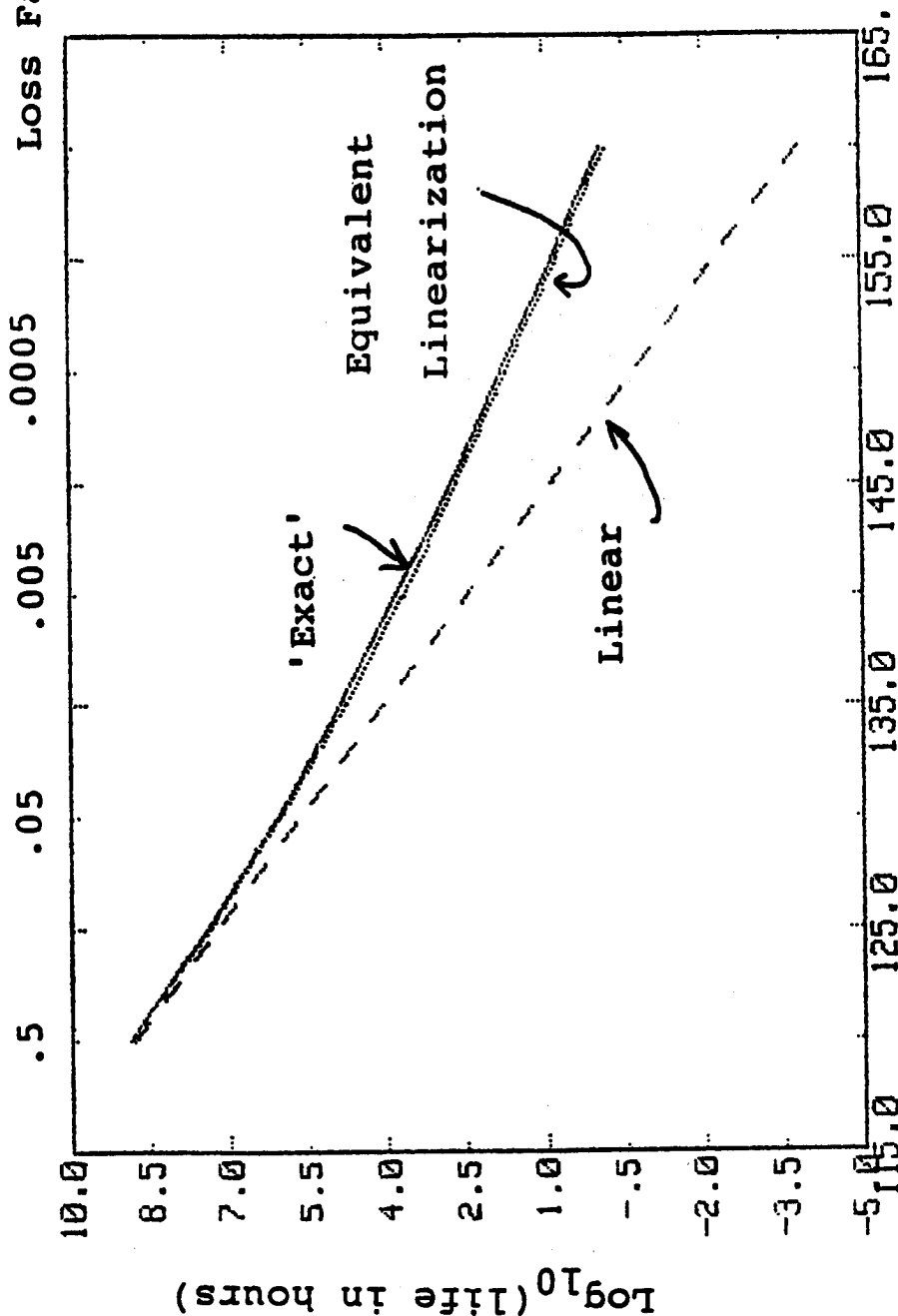
FIGURE 7      COMPARISONS OF APPROXIMATE SOLUTIONS TO DUFFING'S EQUATION  
WITH RESULTS OF    NUMERICAL SIMULATIONS



FIGURE 8

# Predicted Fatigue Life of Nonlinear Plate

Loss Factor at 140 dB



Sound Pressure Level - Decibels

at .005 loss factor

# THE ROLE OF DAMPING IN THE SUPPRESSION OF PARAMETRIC RESONANCES IN NONLINEAR SYSTEMS

Lawrence D. Zavodney and Samir M. Shihada

Department of Engineering Mechanics  
The Ohio State University  
Columbus, Ohio 43210  
(614) 292-2209

## Abstract

Parametrically excited systems are not uncommon in the many structures and systems built today. Classical analysis shows that the presence of viscous damping in a linear system does not limit the infinite amplitude of the parametric resonance. In this paper we investigate the role of damping in the suppression of both fundamental and principal parametric resonances in nonlinear systems. The results show that critical values of damping are required to suppress a parametric resonance. In some cases, the nonlinearity causes a multivalued response that allows nontrivial responses to exist at levels of damping that exceed the critical threshold of damping for stability predicted by linear theory. For small values of damping, chaotic responses were observed.

## 1. Introduction

Problems associated with structural vibrations present a major hazard and design limitation for a wide range of engineering systems. There are numerous structures, including proposed large flexible spacecraft and space stations, for which structural integrity is of paramount concern, and for which a thorough and precise knowledge of the dynamic characteristics is essential. The most important aspect of vibration is the phenomenon of resonance. Resonant oscillations are forced oscillations, except for internal resonance, occurring for some specific relationship between the frequency of excitation and the natural frequencies of the system.

In addition to conventional external excitation, structures can also be parametrically excited. Parametric excitation appears in the governing differential equations in the form of time-dependent coefficients. In parametrically excited systems, nonlinearity is seen to be quite important in the analysis of steady-state responses. Although the analysis of the linearized system provides us with some information, such as the regions of instability, it cannot predict the steady-state response. The reason for this is that as the amplitude of response grows, the nonlinearity--not the linear viscous damping--will come into play and limit the growth to some finite value. This finite-amplitude behavior is consistent with

observations in the field and laboratory. Hence, any investigation of the role of damping in parametric resonance needs to include the nonlinear stiffness terms in the governing equations. Without the nonlinear terms, the equations will admit non-convergent solutions when the system parameters dictate a presence inside the "unstable region" of parametric resonance.

The role of damping and nonlinearity in externally excited systems is fairly well understood. The same cannot be said about parametrically excited nonlinear systems. Since even the linearized differential equations with time-dependant coefficients are difficult to analyze, nonlinear parametric excitation problems have not been treated extensively. Nonlinearity plays a major role in limiting the unbounded growth of a parametric resonance in comparison to the secondary role played by linear viscous damping. This is in contrast to the external oscillator where the presence of damping does indeed significantly reduce the steady-state amplitude of the response. In a parametric resonance, viscous damping will attenuate the rate of growth of a parametric instability, but will do little to affect the steady-state amplitude of a parametric resonance.

In parametric systems, nonlinearity is seen to be quite important in the analysis of steady-state responses. Although the analysis of the linearized system provides us with some information, such as the regions of instability, it cannot predict the steady-state amplitude of response. The reason for this is that as the amplitude of response grows, the nonlinearity in the system will come into play and limit the growth to some finite value. This behavior is consistent with observations in the field and in the laboratory. Hence any investigation of the role of damping in parametric resonance needs to include the nonlinear terms in the governing equations. Without the nonlinear terms, the equations will admit non-convergent solutions when the system parameters dictate a presence inside the "unstable region" of parametric resonance. In this region, any influence of the damping on the actual amplitude of response will be lost.

There is little literature available on the role damping plays in a parametric resonance. Linear damping in single-degree-of-freedom systems is seen to simply increase the threshold value (by decreasing the size of the instability region) of the excitation, but does not attenuate the unbounded response. Chelomei [1977] briefly discusses nonlinear vibrations of a single-degree-of-freedom system with parametrically excited friction and stiffness. He found that it is possible to excite parametric instability by introducing parametric damping.

Hsieh [1980] investigated the influence of linear viscous damping on the stability of the Mathieu equation with a cubic nonlinear restoring force. He demonstrated that the presence of damping raises the threshold required for a parametric resonance. Nayfeh and Mook [1979] reported similar behavior of the parametrically excited Duffing oscillator.

Yano [1984a,b] considered parametric excitations in a self-excited (van der Pol) system with dry (Coulomb) friction and a nonlinear restoring

force of the cubic type. He found that dry friction suppressed the negative (van der Pol) damping but not the parametric resonance. Yano and his colleagues have published a series of papers dealing with parametrically excited systems, but they primarily include van der Pol damping.

Hsu [1977] summarized some major developments in parametrically excited systems, including a single-degree-of-freedom nonlinear system with quadratic damping. He also considered a string hanging in a fluid subjected to vertical support motion, appearing as a parametric excitation.

Zavodney [1987] and Zavodney and Nayfeh [1988, 1989a] investigated the influence of nonlinearity on the fundamental and principal parametric resonances of a viscously damped linear single-degree-of-freedom system. They found that the presence of nonlinearity limited the unbounded growth of parametric resonance and caused a subcritical instability. Zavodney [1987] and Zavodney and Nayfeh [1989b] also investigated the principal parametric resonance of a slender beam carrying a lumped mass; they found excellent agreement with theoretical and experimental results.

For a comprehensive review of parametric vibration during the last decade, the reader is referred to Zavodney [1989].

In this paper, we consider single-degree-of-freedom systems governed by

$$\ddot{u} + 2\epsilon\mu\dot{u} + [\omega_0^2 + \epsilon\delta u + \epsilon^2\alpha u^2 + \epsilon g \cos \Omega t]u = 0, \quad (1)$$

where the coefficients  $\epsilon$ ,  $\mu$ ,  $\omega_0$ ,  $\alpha$ , and  $g$  are constants and  $\Omega$  is the parametric excitation frequency. Equations of this type model structural elements; the quadratic term may be due to curvature or an asymmetric material nonlinearity and the cubic term may be due to mid-plane stretching or a symmetric material nonlinearity. The parametric term may be due to a harmonic axial load.

## 2. Fundamental Parametric Resonance

Fundamental parametric resonance occurs when the excitation frequency  $\Omega$  is close to one of the system natural frequencies; in our case there is only one natural frequency and fundamental parametric occurs when  $\Omega \approx \omega_0$ . This is also called secondary or second-order parametric resonance because the small-divisor term in the amplitude response equations appears at the second order. Hence, it requires a much higher amplitude of excitation to excite the fundamental resonance compared to the principal resonance discussed later.

A second-order uniform solution of (1) is sought using the method of multiple scales in the form

$$u(t; \epsilon) = u_0(T_0, T_1, T_2) + \epsilon u_1(T_0, T_1, T_2) + \epsilon^2 u_2(T_0, T_1, T_2) + \dots, \quad (2)$$

where  $T_0 = t$  is a fast scale associated with changes occurring at the frequencies  $\omega_0$  and  $\Omega$ , and  $T_1 = \epsilon t$  and  $T_2 = \epsilon^2 t$  are slow scales associated with the modulations in the amplitude and phase caused by the damping, nonlinearity, and resonances. An approximate solution can be expressed as (Zavodney [1987] and Zavodney and Nayfeh [1988])

$$\begin{aligned} u = & a \cos(\omega_0 t + \beta) + \epsilon \{ (\delta a^2 / 6\omega_0^2) \cos(2\omega_0 t + 2\beta) \\ & + [ga/2\Omega(\Omega + 2\omega_0)] \cos[(\Omega + \omega_0)t + \beta] \\ & + [ga/2\Omega(\Omega - 2\omega_0)] \cos[(\Omega - \omega_0)t - \beta] - \delta a^2 / 2\omega_0^2 \} + \dots, \end{aligned} \quad (3)$$

where the amplitude  $a$  and the phase  $\gamma$  are governed by the reduced first-order nonlinear differential equations

$$\dot{a} = -\epsilon \mu a + (5\epsilon^2 \delta g a^2 / 24\omega_0^3) \sin \gamma + (\epsilon^2 g^2 a / 8\omega_0^3) \sin 2\gamma, \quad (4)$$

$$a \dot{\gamma} = \epsilon^2 \left[ \left( \frac{\mu^2}{2\omega_0} + \frac{g^2}{12\omega_0^3} \right) a - \alpha_e a^3 \right] + \frac{5\epsilon^2 \delta g a^2}{8\omega_0^3} \cos \gamma + \frac{\epsilon^2 g^2 a}{8\omega_0^3} \cos 2\gamma + \epsilon^2 \sigma a, \quad (5)$$

where

$$\alpha_e = (3\alpha/8\omega_0) - (5\delta^2/12\omega_0^3), \quad \gamma = \epsilon^2 \sigma t - \beta. \quad (6)$$

It follows from (3) - (5) that to the second approximation, the damping has two effects: (a) it causes a linear first-order exponential decay in the amplitude which competes with the parametric terms and (b) it causes a frequency change proportional to the amplitude of the response.  $\alpha_e$  is seen to be an effective cubic nonlinearity which depends on both the relative magnitude of  $\delta$  compared to  $\alpha$  and on the sign of  $\alpha$ .

Periodic solutions of (1) correspond to the fixed points (i.e., constant solutions) of the modulation equations (4) and (5), which in turn correspond to  $\dot{a} = 0$  and  $\dot{\gamma} = 0$ . It follows from (4) and (5) that periodic solutions correspond to either  $a = 0$  or

$$\mu = (5\epsilon\delta ga/24\omega_0^3)\sin \gamma + (\epsilon g^2/8\omega_0^3) \sin 2\gamma , \quad (7)$$

$$\sigma + [(\mu^2/2\omega_0) + (g^2/12\omega_0^3) - \alpha_e a^2] = -(5\delta ga/8\omega_0^3)\cos \gamma - (g^2/8\omega_0^3) \cos 2\gamma . \quad (8)$$

In this case, for a given  $\mu$ , (7) and (8) need to be solved numerically to determine  $a$  and  $\gamma$ .

Not all of the steady-state solutions are stable and hence, physically realizable in simulation or practice. To determine the stability of the trivial fixed points, we investigate the solutions of the linearized form of the complex amplitude-response equation, and obtain unstable trivial responses when

$$(g^4/16\omega_0^4) - (2\omega_0\sigma + \mu^2 + g^2/6\omega_0^2) > 4\omega_0^2\mu^2/\epsilon^2 . \quad (9)$$

To determine the stability of the nontrivial fixed points, we perturb the steady-state amplitude and phase by letting

$$a = a_0 + a_1(t), \quad \gamma = \gamma_0 + \gamma_1(t) , \quad (10)$$

and study the behavior of the disturbance. If the disturbance decays, we say the solution is stable; if the disturbance grows, we say the solution is unstable. The equations obtained are

$$\begin{aligned} \dot{a}_1 = & [(5\epsilon^2\delta ga_0/24\omega_0^3) \sin \gamma_0]a_1 + [(5\epsilon^2\delta ga_0^2/24\omega_0^3) \cos \gamma_0 \\ & + (\epsilon^2 g^2 a_0/4\omega_0^3) \cos 2\gamma_0]\gamma_1 , \end{aligned} \quad (11)$$

$$\begin{aligned} \dot{\gamma}_1 = & -[2\epsilon^2\alpha_e a_0 - (5\epsilon^2\delta g/8\omega_0^3) \cos \gamma_0]a_1 - [(5\epsilon^2\delta ga_0/8\omega_0^3) \sin \gamma_0 \\ & + (\epsilon^2 g^2/4\omega_0^3) \sin 2\gamma_0]\gamma_1 . \end{aligned} \quad (12)$$

In general, the stability of the fixed points is a continuous function of the system parameters. As one of the parameters of the system, say damping, is varied, it may happen that the corresponding fixed point may undergo a change in stability. For positive damping the system changes stability when one real eigenvalue of (11) and (12) passes from the left to the right half of the complex plane through the origin. This corresponds,

under some nondegeneracy conditions, to a turning point in the response curves and gives rise to the jump phenomenon.

Before considering the system response to a parametric excitation, we investigate the free response. The singular (equilibrium) points of the system are calculated from (1) by setting the excitation  $g$  and all derivative terms equal to zero. The roots of the reduced equation are then given by

$$u = 0, \quad (1/2\epsilon\alpha)[- \delta \pm (\delta^2 - 4\omega_0^2\alpha)^{1/2}] . \quad (13)$$

For the cases analyzed in this paper, we chose  $\omega_0 = 1.0$ ,  $\alpha = 4.0$ , and  $\epsilon = 0.10$ . This large value of  $\epsilon$  is permitted because we are considering the fundamental parametric resonance. When we consider the principal resonance, we will require much smaller values of  $\epsilon$ . When  $\delta = 5.0$  there are two stable equilibrium positions (foci) and one unstable equilibrium (saddle) point. When  $\delta = 4.0$ , the radical vanishes and the left focus and saddle point merge to form a cusp; when  $\delta = 3.0$ , the only real root is the origin. Phase plane plots and potential energy diagrams are shown in Figure 1 for these three cases. The perturbation analysis was applied to motions about the equilibrium point at the origin.

In the presence of damping and excitation, an approximate expression for the response is given by equation (3). The steady-state response phase  $\gamma$  used to calculate  $u(t)$  is determined numerically from

$$F(\gamma) = \sigma + \frac{\mu^2}{2\omega_0} + \frac{g^2}{12\omega_0^3} - \alpha_e \left( \frac{24\mu\omega_0^3}{5\epsilon\delta g \sin \gamma} - \frac{3g \sin 2\gamma}{5\delta \sin \gamma} \right)^2 \\ + \frac{5\delta g \cos \gamma}{8\omega_0^3} \left( \frac{24\mu\omega_0^3}{5\epsilon\delta g \sin \gamma} - \frac{3g \sin 2\gamma}{5\delta \sin \gamma} \right) + \frac{g^2 \cos 2\gamma}{8\omega_0^3} = 0 , \quad (14)$$

and then the amplitude  $a$  is calculated directly from equation (7). The stability of each solution, including the trivial solution, is determined from equations (9), (12) and (13). Since we are examining the parametric resonance we will consider oscillations about the singular point at the origin. The response around the left well is combined external and parametric vibration; hence the perturbation solution here is not valid for oscillations about the left equilibrium point. Hence, to insure that we stay in the neighborhood of the origin, we will consider only the case of the single-well potential shown in Figure 1. All three cases have stable trajectories about the origin which are quite similar in nature. The differences become apparent when the amplitude of the motion becomes large enough to be affected by the homoclinic orbit; however, at these

amplitudes, the small amplitude assumption underlying the perturbation solution may not be valid.

Before investigating the effect of damping on the steady-state response, the frequency response of the system for a selected value of the damping coefficient will be investigated; a typical curve is shown in Figure 2. In this case, the nonlinear coefficients are such that the effective cubic nonlinearity given by equation (6) is negative. Hence the overall nonlinearity is of the softening type. Figure 2 displays this softening behavior by bending to the left. This is due to the quadratic nonlinearity which is always of the softening type, even though the cubic nonlinearity is positive. This figure shows that there are five bifurcation values of  $\sigma$  that divide the  $\sigma$  axis into six distinct intervals.

The effect of viscous damping on the fundamental parametric resonance is shown in Figure 3. For large positive values of  $\sigma$ , solutions do not exist. As  $\sigma$  is decreased from above, stable nonlinear solutions appear simultaneously with the stable trivial solution. Since the trivial solution is stable, we have not yet entered the region of parametric resonance. However, we see that two solutions exist. As  $\sigma$  is decreased further, the nonlinear solutions intersect the trivial branch; the intersection marks the critical damping point predicted by linear theory. Probably the most significant feature of this amplitude-response curve is that it is quite flat for small values of damping. If one wanted to suppress (by damping out) a parametric resonance, it can be accomplished only by exceeding the critical value of damping predicted by nonlinear theory. Also note that significant increases in the value of the damping coefficient produce modest attenuations of the amplitude of the response. If  $\mu = 0.5$ , Figure 3 shows that by doubling or tripling the damping, one accomplishes less than 10% reduction of the amplitude.

Note that when  $\sigma = 0$ , the perturbation solution shows four bifurcation values that divide the damping axis into five distinct regions. When  $\mu > \mu_4$ , where  $\mu_4 = 2.25$ , only the trivial solution is possible, which is stable. When  $\mu_3 < \mu < \mu_4$ , where  $\mu_3 = 2.05$ , there are three possible solutions: the trivial solution which is stable and two nontrivial solutions, the larger one being stable and the smaller one being unstable. When  $\mu_2 < \mu < \mu_3$ , where  $\mu_2 = 1.92$  and is the critical damping coefficient, there are five possible solutions: the trivial solution which is still stable and four nontrivial solutions, two of which are stable. When  $\mu_1 < \mu < \mu_2$ , where  $\mu_1 = 1.75$ , there are five possible solutions: the trivial solution which is now unstable and four nontrivial solutions, three of which are stable. When  $\mu < \mu_1$  there are three possible solutions: the trivial solution which is unstable, and two nontrivial solutions which are both stable.

This behavior shows that linear analysis is not sufficient to predict an absence of stable nontrivial solutions based upon a stability analysis of the linearized equation. As shown by this analysis, it is possible to have co-existing stable nontrivial solutions with a stable trivial attractor.



The results shown in region II of Figure 3(c) for  $\sigma = 0.0$  predict three stable solutions; these solutions (obtained by integrating the governing equation using a fifth and sixth order Runge-Kutta-Verner algorithm) are shown in the time domain in Figure 4. Since several stable solutions coexist, the initial conditions determine the final state. Note that the larger of the two smaller solutions requires much more time to achieve steady state.

### 3. Principal Parametric Resonance

Principal parametric resonance occurs when the excitation frequency  $\Omega$  is close to two times the system natural frequencies; in our case it occurs when  $\Omega \approx 2\omega_0$ . This is also called primary or first-order parametric resonance because the small divisor term in the amplitude response equations appears at the first order. Hence, this is the most common of the parametric resonances and the most easily excited. A similar analysis is performed for this case; a second-order approximate solution can be expressed as (Zavodney [1987] and Zavodney and Nayfeh [1989a])

$$u = a \cos\left(\frac{1}{2} \Omega t - \frac{1}{2} \gamma\right) + \left(\frac{1}{6} \delta a^2 \cos(\Omega t - \gamma)\right) + \frac{ga}{2\Omega(\Omega+2\omega_0)} \cos\left[\frac{3}{2} \Omega t - \frac{1}{2} \gamma\right] - \frac{1}{2} \delta a^2 + \dots \quad (15)$$

where the amplitude- and phase-modulation equations are given by

$$\dot{a} = -\epsilon \mu a - \frac{\epsilon g}{4\omega_0} \left(1 - \frac{\epsilon \sigma}{2\omega_0}\right) a \sin \gamma, \quad (16)$$

$$a\dot{\beta} = \epsilon^2 \left( \left( \frac{3g^2}{64\omega_0^3} - \frac{\mu^2}{2\omega_0} \right) a + \alpha_e a^3 \right) + \frac{\epsilon g}{4\omega_0} \left(1 - \frac{\epsilon \sigma}{2\omega_0}\right) a \cos \gamma, \quad (17)$$

and where

$$\gamma = \epsilon \sigma t - 2\beta, \quad (18)$$

$$\alpha_e = \frac{3\alpha}{8\omega_0} - \frac{5\delta^2}{12\omega_0^3}. \quad (19)$$

Steady-state solutions correspond to the constant solutions of (16) and (17); these fixed-points are given by

$$\epsilon \alpha_e a^2 = \frac{1}{2} \sigma - \frac{3\epsilon g^2}{64\omega_0^3} + \frac{\epsilon \mu^2}{2\omega_0} \pm \left[ \frac{g^2}{16\omega_0^2} \left( 1 - \frac{\epsilon \sigma}{2\omega_0} \right)^2 - \mu^2 \right]^{1/2} . \quad (20)$$

The stability of the trivial solution is given by

$$\frac{1}{4} g_c^2 \left( 1 - \frac{\epsilon \sigma}{2\omega_0} \right)^2 - 4\omega_0^2 \mu^2 + \left[ \sigma \omega_0 + \epsilon \mu^2 - \frac{3\epsilon g_c^2}{32\omega_0^2} \right]^2 , \quad (21)$$

where  $g_c$  is the critical value of excitation required to excite a parametric resonance, and the stability of the nontrivial solutions is governed by the perturbations given to the nontrivial solutions according to

$$\dot{a}_1 = - \frac{\epsilon g a_0}{4\omega_0} - \left( 1 - \frac{\epsilon \sigma}{2\omega_0} \right) \gamma_1 \cos \gamma_0 , \quad (22)$$

and

$$\dot{\gamma}_1 = - 4\epsilon^2 \alpha_e a_0 a_1 - 2\mu \gamma_1 . \quad (23)$$

Stable solutions, determined by the eigenvalues of the coefficient matrix, can be expressed in closed-form and occur when

$$\alpha_e \left[ \frac{1}{2} \sigma - \frac{3\epsilon g^2}{64\omega_0^3} + \frac{\epsilon \mu^2}{2\omega_0} - \epsilon \alpha_e a_0^2 \right] > 0 . \quad (24)$$

When  $\alpha_e > 0$ , the steady-state solution corresponding to the negative sign in equation (20) is unstable, whereas that corresponding to the positive sign is stable. On the other hand, when  $\alpha_e < 0$ , the steady-state solution corresponding to the positive sign in equation (20) is unstable, whereas that corresponding to the negative sign is stable.

For the principal parametric excitation, a resonant response is solicited at much lower levels of excitation than required for the fundamental resonance. This lower-level excitation is represented by a smaller value of  $\epsilon$ ; in this case we used  $\epsilon = 0.005$ . Later when we consider large amplitude responses about both foci, we will put  $\epsilon = 0.10$ . The potential wells and trajectories are identical to those shown in Figure 1; however since  $\epsilon$  is smaller, the location of the equilibrium points will be scaled according to (13). The amplitude response is shown in Figure 5 and

the frequency response is shown in Figure 6. Figure 5 is a cross-section of Figure 6 at the indicated values of  $\sigma$ .

The effect of viscous damping on the amplitude of response is shown in Figure 7. From this series of solutions for different values of detuning, we conclude that a principal parametric resonance can be excited only if the damping coefficient is below a critical value. In some cases this critical value is larger than that predicted by linear analysis (i.e., corresponding to the loss of stability of the trivial solution). We also note that for small values of damping ( $\mu < 2$ ), the amplitude of the response is quite insensitive to the value of the damping coefficient. For example, when  $\sigma = 0.0$ , the response amplitude for  $\mu = 0.2$  is 21.27, and when  $\mu$  is increased ten times to 2.0, the amplitude is attenuated to 20.37. Thus, an order of magnitude increase in the damping coefficient attenuated the response amplitude a mere 4.4%. Referring to equation (20), we see that once  $g$  is large relative to  $\mu$ , modest changes in  $\mu$  have negligible effects on the amplitude.

This behavior has two implications. First, in the field or laboratory, it shows that one does not need an extremely accurate estimate of the damping coefficient to predict a steady-state response amplitude if the excitation is large enough. Second, it shows that the reduction of the response amplitude to a parametric excitation is possible only if the critical damping coefficient is exceeded. Increasing the damping coefficient by an order of magnitude may achieve only slight reductions in the response amplitude. Although the damping is seen to have a modest effect on the steady-state response amplitude, it does affect the rate of growth of the instability caused by a parametric resonance. If one has a nonstationary parametric excitation, the presence of damping may prevent a large resonant response.

The amplitude response predicted by equation (20) and shown in Figure 7 was verified by numerically integrating the governing equation (1). When  $\sigma = -15.0$ , as shown in Figure 7(a), the perturbation solution shows two stable solutions for small values of  $\mu$  -- a nontrivial and a trivial. These responses are shown in the time domain in Figure 8. Since multiple attractors coexist, the initial conditions determine the response. It is also possible that disturbances to the system could knock the steady-state response to the other solution. For example, a trivial response could be disturbed such that it would grow to the nontrivial response, and vice-versa. The trivial solution is the only one predicted by the linearized equation, hence one could come to an erroneous conclusion regarding stability. The other response curves in Figure 7 show the progression for selected values of frequency detuning: the region of parametric resonance is seen in Figures (b) - (d) as the transition of unstable trivial solutions to stable trivial solutions occurs.

Interesting behavior occurs for larger values of  $\epsilon$ . By increasing  $\epsilon$  we increase the influence of the nonlinearity as well as the excitation and damping. By setting  $\delta = 5.0$  we have a double-well potential, and hence, more interesting behavior. The influence of damping for  $g = 14.5$  is shown

in Figure 9. For  $\mu > 5.0$ , only the trivial solution is stable. For  $\mu = 4.5$ , a small amplitude parametric resonance occurs, and is shown in Figure 9(a). As  $\mu$  is decreased further, the response amplitude increases; the steady-state response for  $\mu = 1.30$  is shown in Figure 9(b). As  $\mu$  is decreased to 1.21, a period-doubling bifurcation occurs, and is shown in Figure 9(c). This period-doubling cascade continues and culminates in chaos. Time histories for the large amplitude steady-states in Figure 9 are shown in Figure 10. For a more complete discussion of the chaotic response and fractal behavior, the reader is referred to Zavodney [1987] and Zavodney and Nayfeh [1989a].

#### 4. Summary

The influence of the linear viscous damping coefficient in a nonlinear parametrically excited one-degree-of-freedom system was investigated. Nonlinear terms were retained because they alone are responsible for limiting the infinite response--even in the presence of damping. The method of multiple scales was used to obtain a second-order uniform expansion for the response. Steady-state solutions were obtained for small but finite amplitude oscillations around the origin for both fundamental and principal parametric resonances, and it was shown that the results qualitatively describe the system response for the parameters chosen.

The perturbation solution predicts a threshold (critical) value at which parametric resonances can be excited. It also predicts a subcritical instability and up to two nontrivial responses which exist at values of the damping coefficient that exceed the critical damping required to suppress a parametric resonance based on linear theory. Hence, in both of these cases, the linear theory predicted stability when the nonlinear theory predicted large amplitude steady-state responses.

To summarize, the damping was seen to play a minor role in the suppression of parametric resonance unless the damping was large enough to exceed the critical value; in some cases one must exceed the nonlinear critical value in order to suppress the parametric resonance. This behavior was seen in the general flatness of the amplitude response curves for small values of damping followed by the rather fast attenuation or jump in the nontrivial response. The jump down and jump up was caused by a turning point bifurcation. When multiple solutions existed, the initial conditions and disturbances to the system determined the response.

#### 5. Acknowledgments

This work was sponsored by the Office of Research and Graduate Studies at The Ohio State University.

6. References

1. Chelomei, S.V. et al., (1977), "Nonlinear Vibrations with Parametric Excitation," Mechanics of Solids, ed. Mekhanika Tverdogo Tela, Allerton Press Inc., 12(3), 39-46.
2. Hsieh, D.Y., (1980), On Mathieu equation with damping. Journal of Mathematics and Physics, 21, 722-725.
3. Hsu, C.S., (1977), "On Nonlinear Parametric Excitation Problems" Advances in Applied Mechanics, ed. Yih, Chia-Shun, Academic Press, 17, 245-301.
4. Nayfeh, A.H. and Mook, D.T. (1979). Nonlinear Oscillations, Wiley-Interscience, New York.
5. Yano Sumio, (1984a), Parametric Excitation in the Self-excited Vibration System with Dry Friction (1st report, parametric resonance). Bulletin of the JSME, 27, 255-262.
6. Yano Sumio, (1984b), Parametric Excitation in the Self-excited Vibration System with Dry Friction (2nd report, in the neighborhood of the region of parametric resonance). Bulletin of the JSME, 27, 263-270.
7. Zavodney, L.D., (1987), "A Theoretical and Experimental Investigation of Parametrically Excited Nonlinear Mechanical Systems," Ph.D. Dissertation. Virginia Polytechnic Institute and State University.
8. Zavodney, L.D. (1989), "Parametric Harmonic Vibration: A Decade in Review," under preparation for Applied Mechanics Reviews.
9. Zavodney, L.D. and Nayfeh, A.H. (1988), "The Response of a Single-Degree-of-Freedom System with Quadratic and Cubic Nonlinearities to a Fundamental Parametric Resonance," The Journal of Sound and Vibration, 120(1), 63-93.
10. Zavodney, L.D. and Nayfeh, A.H. (1989a), "The Response of a Single-Degree-of-Freedom System with Quadratic and Cubic Nonlinearities to a Principal Parametric Resonance," J. of Sound and Vibration, in press.
11. Zavodney, L.D. and Nayfeh, A.H. (1989b), "The Nonlinear Response of a Slender Beam Carrying a Lumped Mass to a Principal Parametric Excitation: Theory and Experiment," International J. of Nonlinear Mechanics, in press.

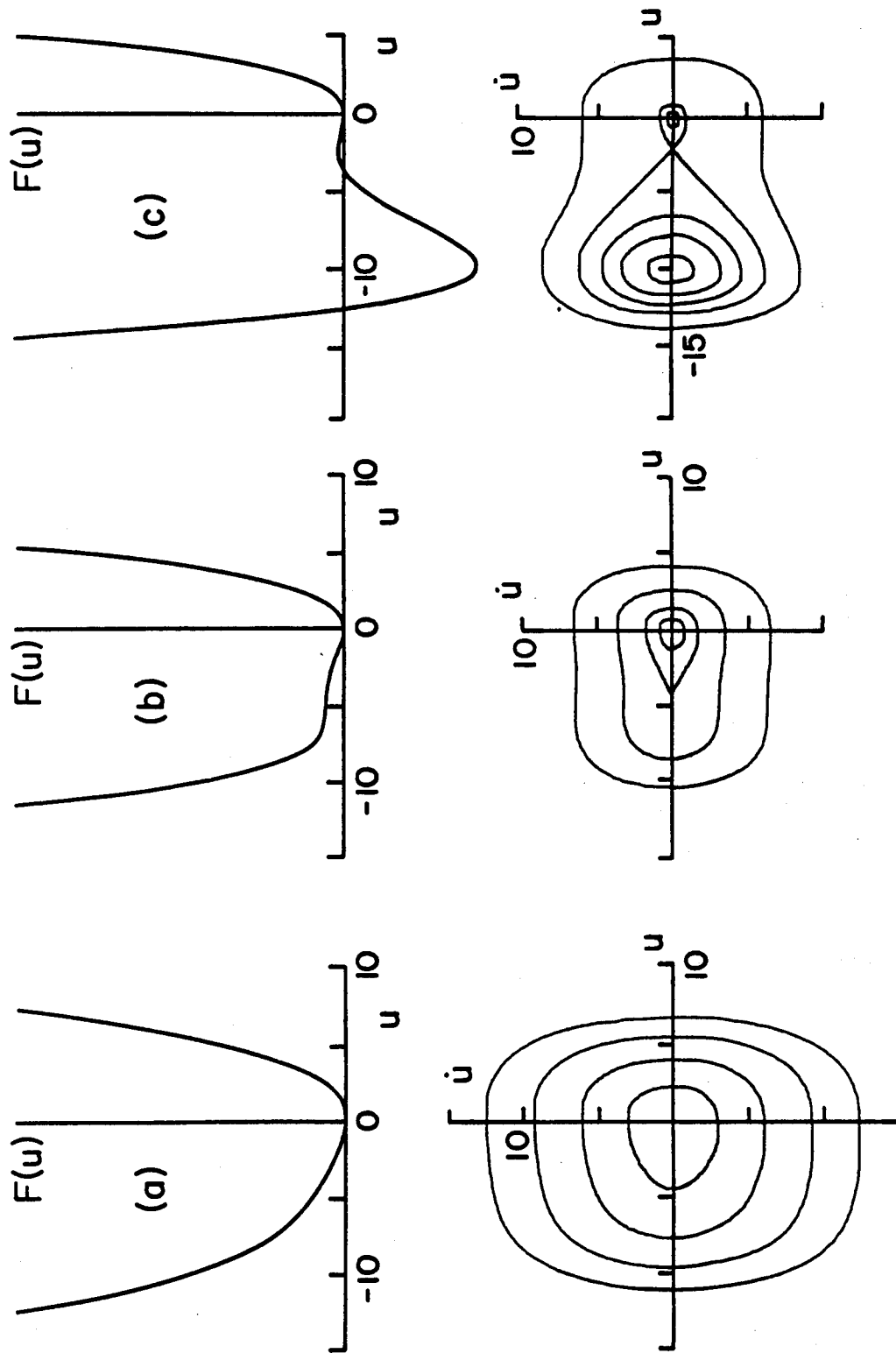


Figure 1. The potential wells and corresponding phase-plane portraits for three distinct cases: (a)  $\delta = 3.0$ , (b)  $\delta = 4.0$ , and (c)  $\delta = 5.0$ ,  $\alpha = 4.0$ ,  $\mu = 1.0$ ,  $\epsilon = 0.10$ .

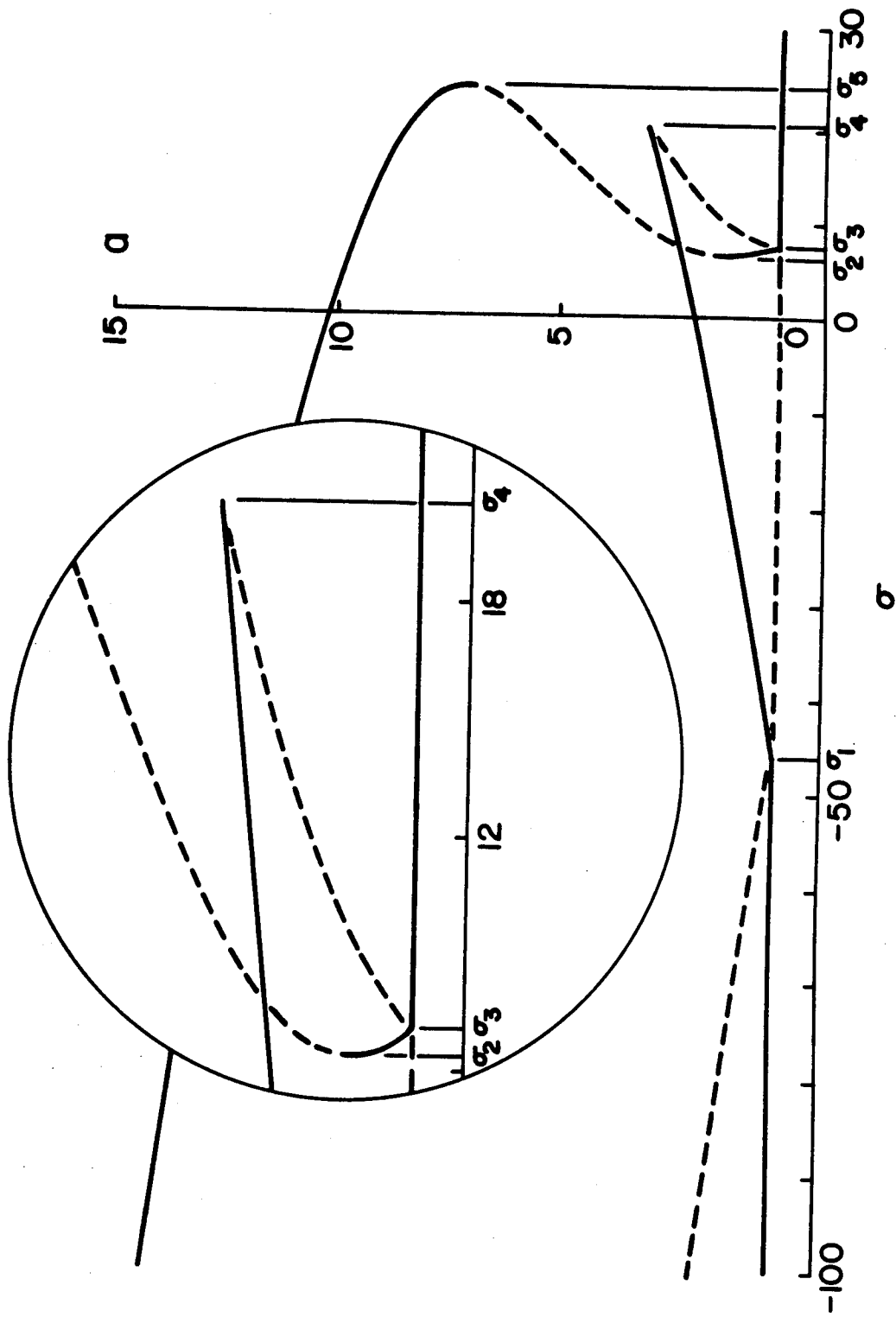


Figure 2. The variation of the steady-state response amplitude  $a$  with the excitation frequency detuning  $\sigma$ :  $\alpha = 4.0$ ,  $\delta = 3.0$ ,  $\mu = 1.0$ ,  $g = 15.0$ ,  $\epsilon = 0.10$ .

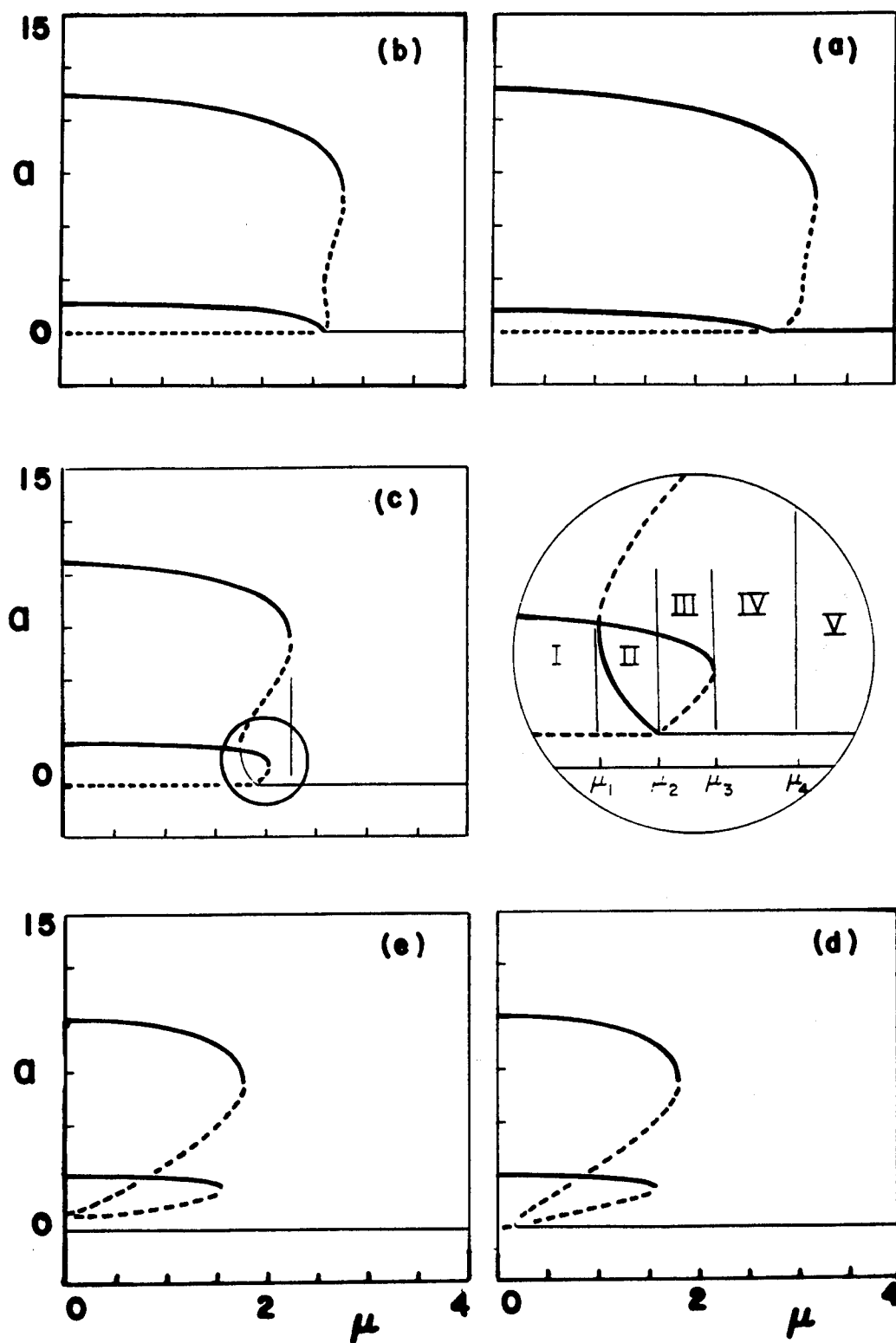


Figure 3. The variation of the amplitude with the damping coefficient  $\mu$  for selected frequencies of excitation: (—) stable, (---) unstable,  $\alpha = 4.0$ ,  $\delta = 3.0$ ,  $g = 15.0$ ,  $\epsilon = 0.10$ , (a)  $\sigma = -15.0$ , (b)  $\sigma = -12.0$ , (c)  $\sigma = 0.0$ , (d)  $\sigma = 9.0$ , (e)  $\sigma = 12.0$ .



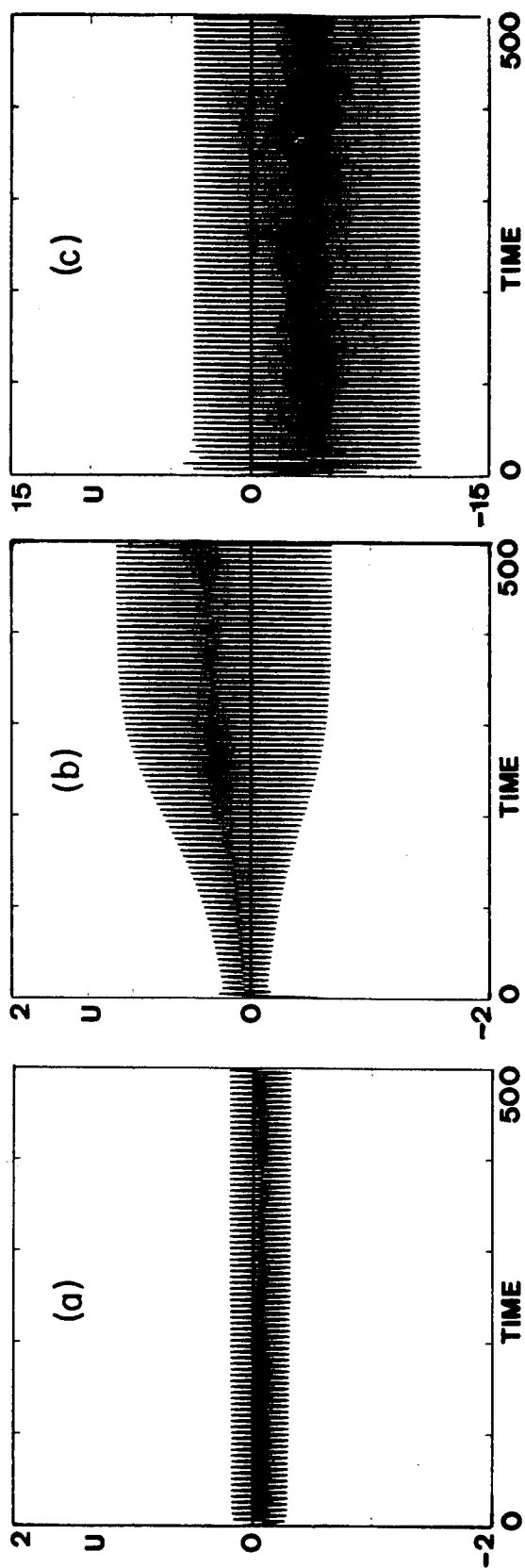


Figure 4. The time history of the three steady-state solutions shown in Figure 3 (c) for  $\sigma = 0.0$ ,  $\alpha = 4.0$ ,  $\delta = 3.0$ ,  $\mu = 1.8$ ,  $g = 15.0$ ,  $\epsilon = 0.10$ . The initial conditions  $(u(0), \dot{u}(0))$  used to obtain the three responses are: (a)  $(0.1, 0.0)$ , (b)  $(0.01, -1.0)$ , and (c)  $(1.35, 0.0)$ .

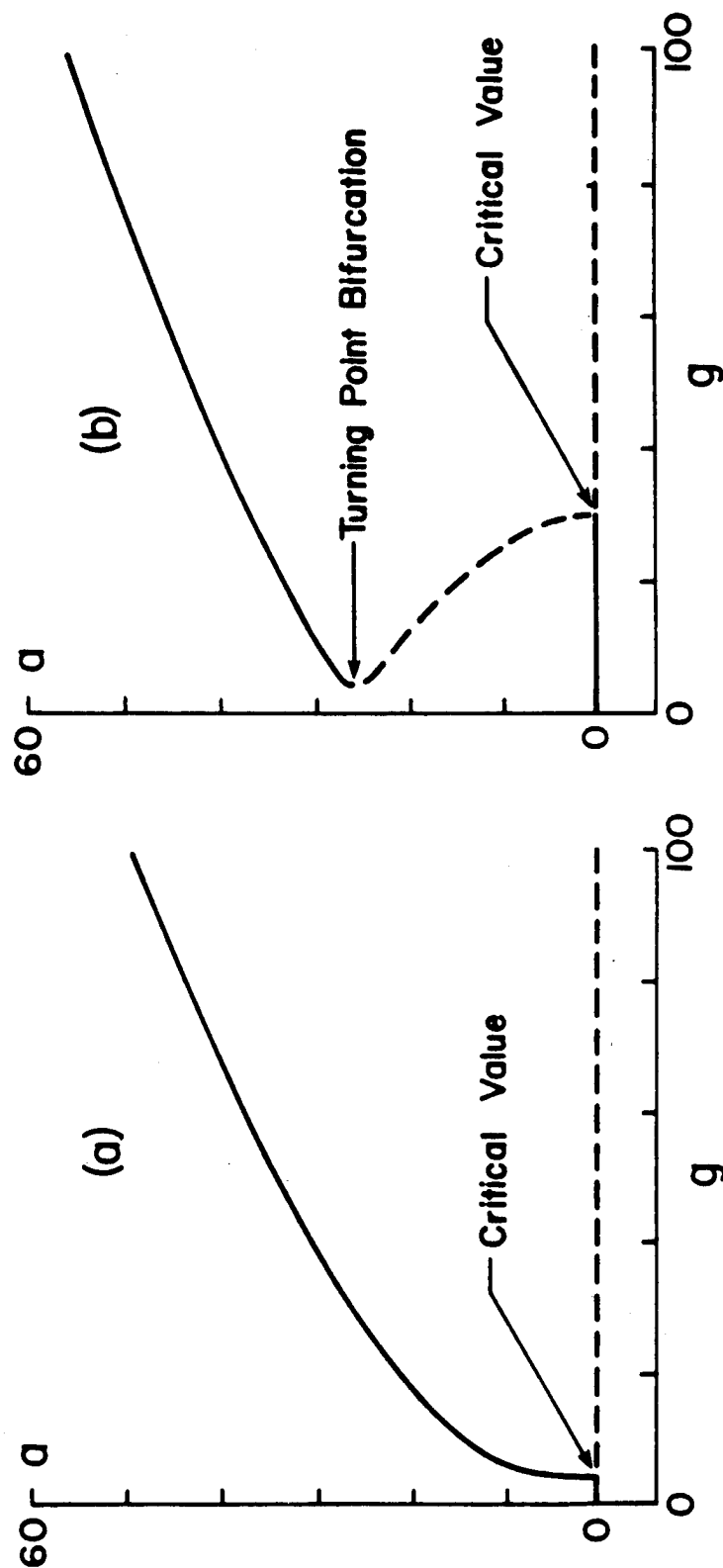


Figure 5. The variation of the steady-state response amplitude  $a$  with the excitation amplitude  $g$ : (—) stable, (---) unstable,  $\alpha = 4.0$ ,  $\delta = 3.0$ ,  $\mu = 1.0$ ,  $\epsilon = 0.005$ , (a)  $\sigma = 0.0$ , (b)  $\sigma = -15.0$ .

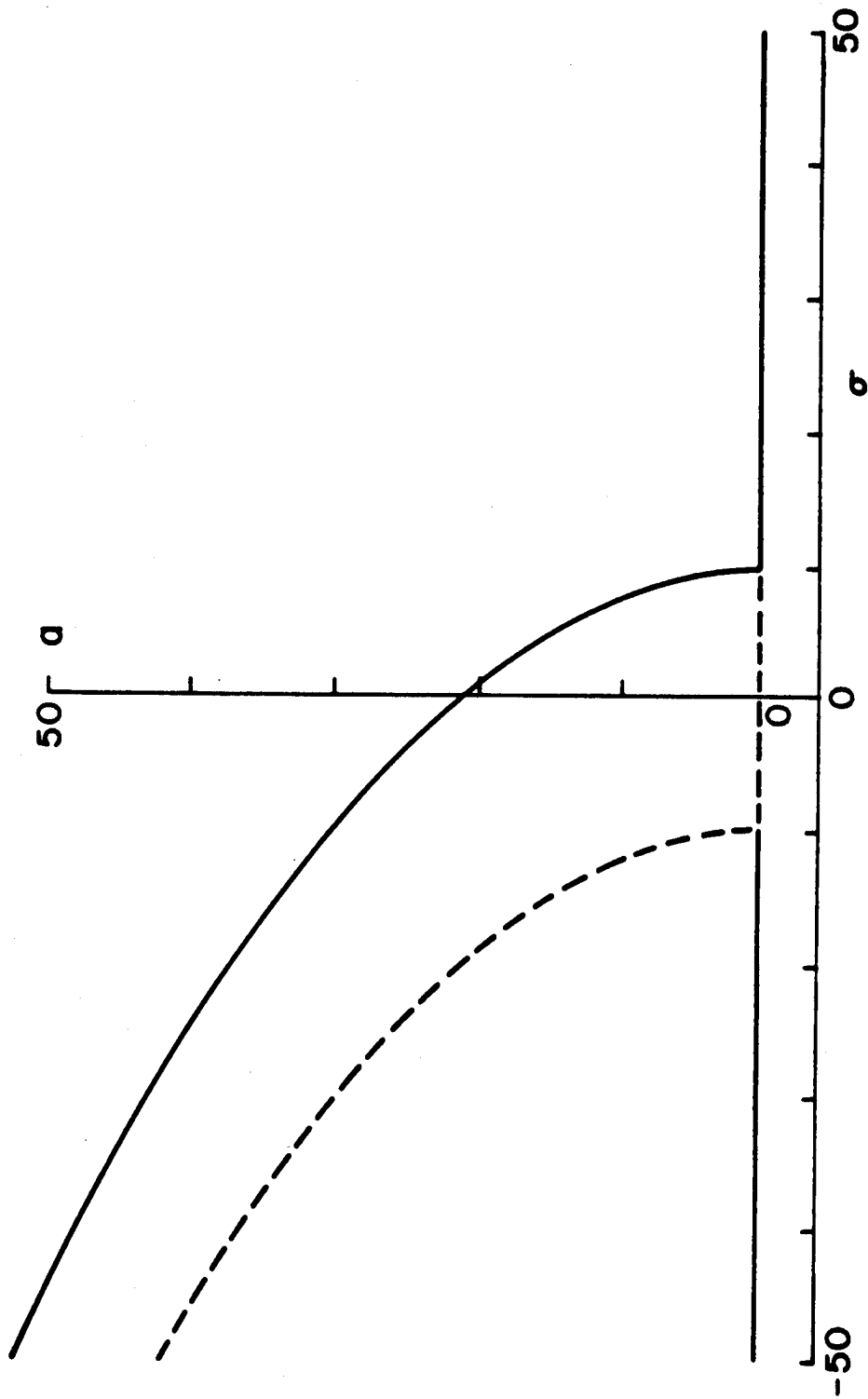


Figure 6. The variation of the steady-state response amplitude  $a$  with the excitation frequency detuning  $\sigma$ : (—) stable, (---) unstable,  $\alpha = 4.0$ ,  $\delta = 3.0$ ,  $\mu = 1.0$ ,  $g = 20.0$ ,  $\epsilon = 0.005$ .

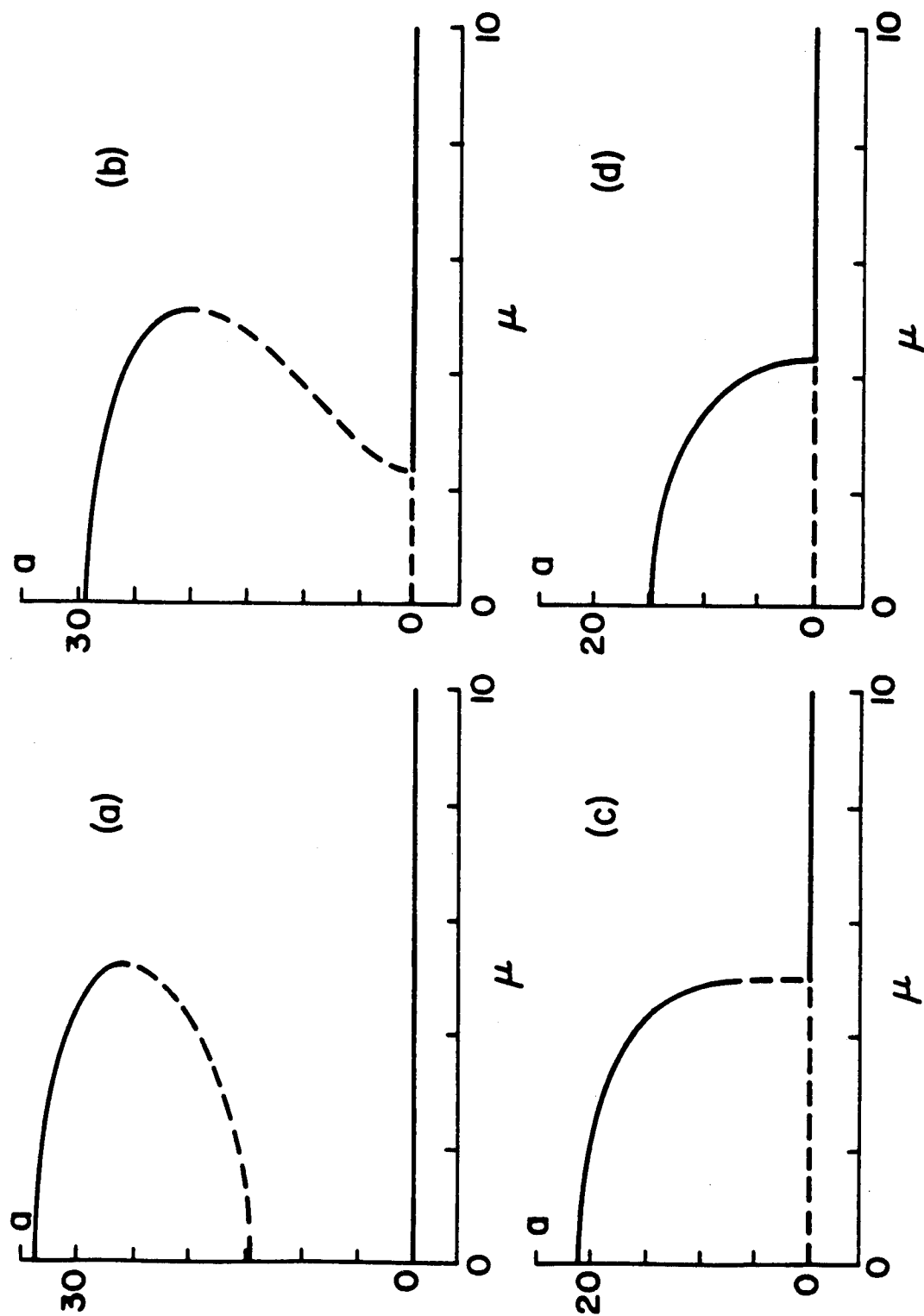


Figure 7. The variation of the steady-state response amplitude  $a$  with the damping coefficient  $\mu$ : (—) stable, (---) unstable,  $\alpha = 4.0$ ,  $\delta = 3.0$ ,  $g = 20.0$ ,  $\epsilon = 0.005$ , (a)  $\sigma = -15.0$ , (b)  $\sigma = -9.0$ , (c)  $\sigma = 0.0$ , (d)  $\sigma = 5.0$ .

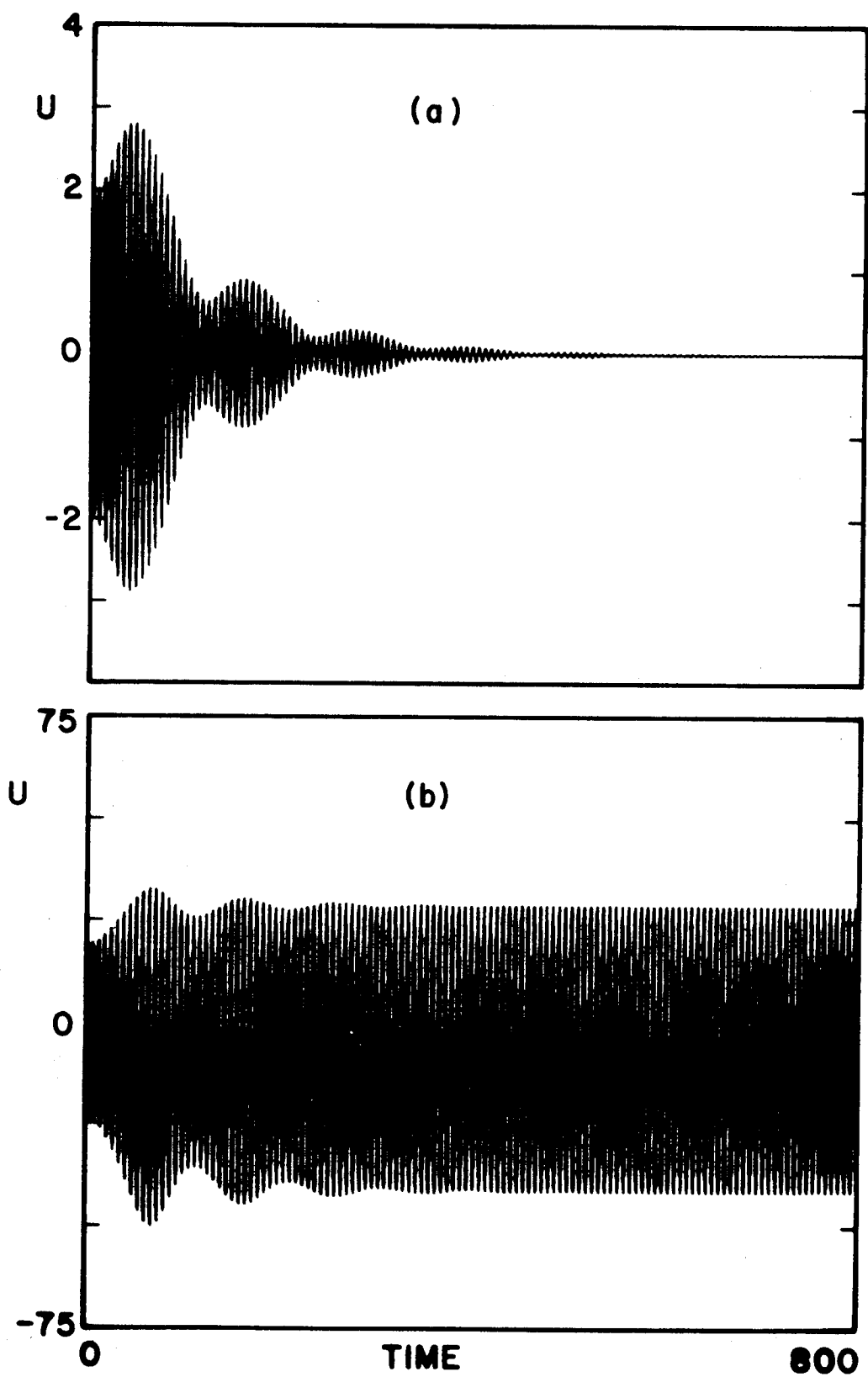


Figure 8. The time history showing the response of equation (1) for the case shown in Figure 7(a) for  $\mu = 2.0$ . The initial conditions  $(u(0), \dot{u}(0))$  used were (a)  $(2.0, 0.0)$ , (b)  $(20.0, 0.0)$ .

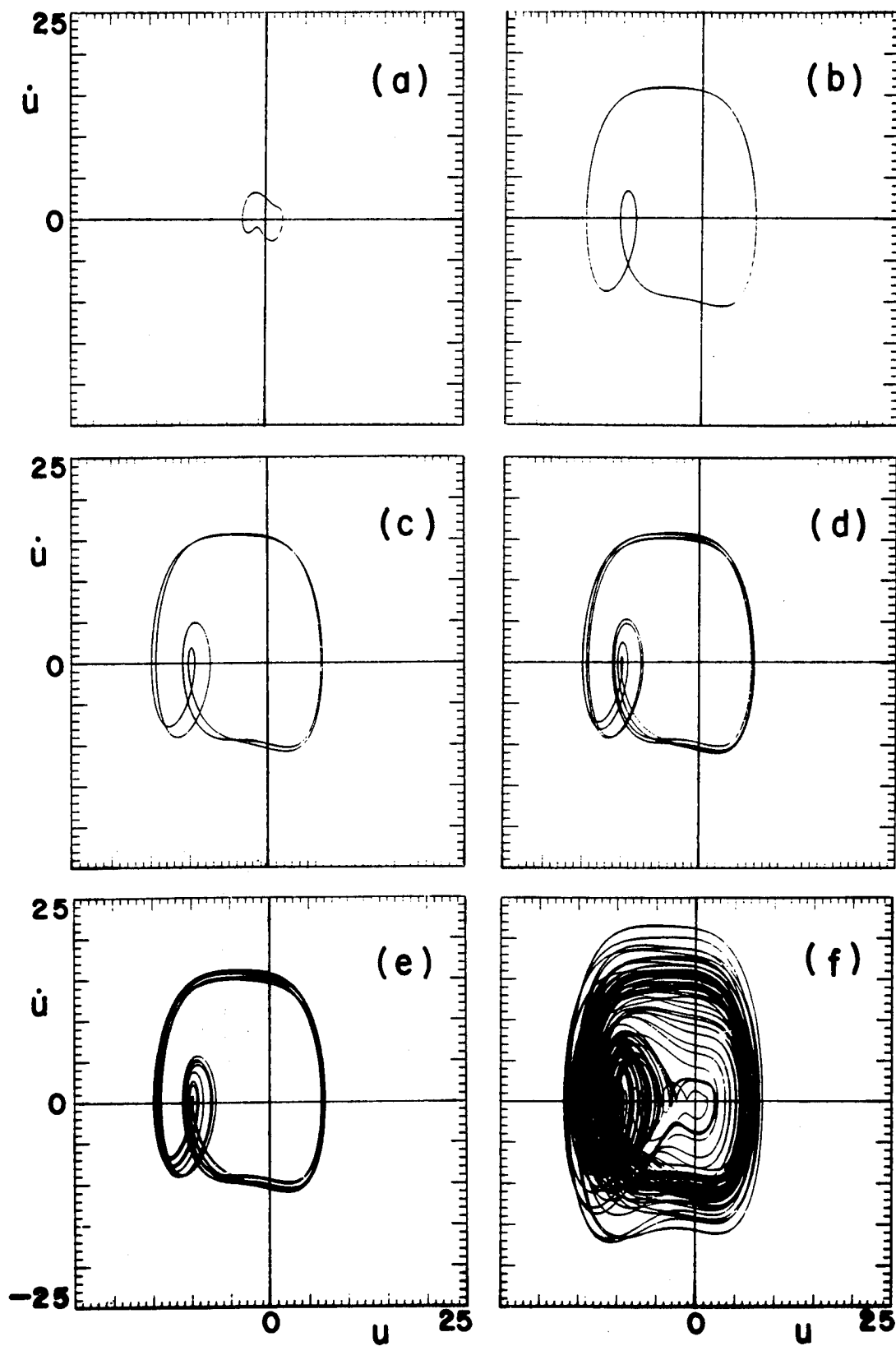


Figure 9. The response shown in the phase plane for selected values of the damping coefficient  $\mu$  for the system shown in Figure 7(c):  
 $\epsilon = 0.10$ ,  $\delta = 5.0$ ,  $\alpha = 4.0$ ,  $\sigma = 0.0$ ,  $g = 14.5$ , (a)  $\mu = 4.5$ ,  
 (b)  $\mu = 1.30$ , (c)  $\mu = 1.21$ , (d)  $\mu = 1.18$ , (e)  $\mu = 1.16$ ,  
 (f)  $\mu = 1.00$ .

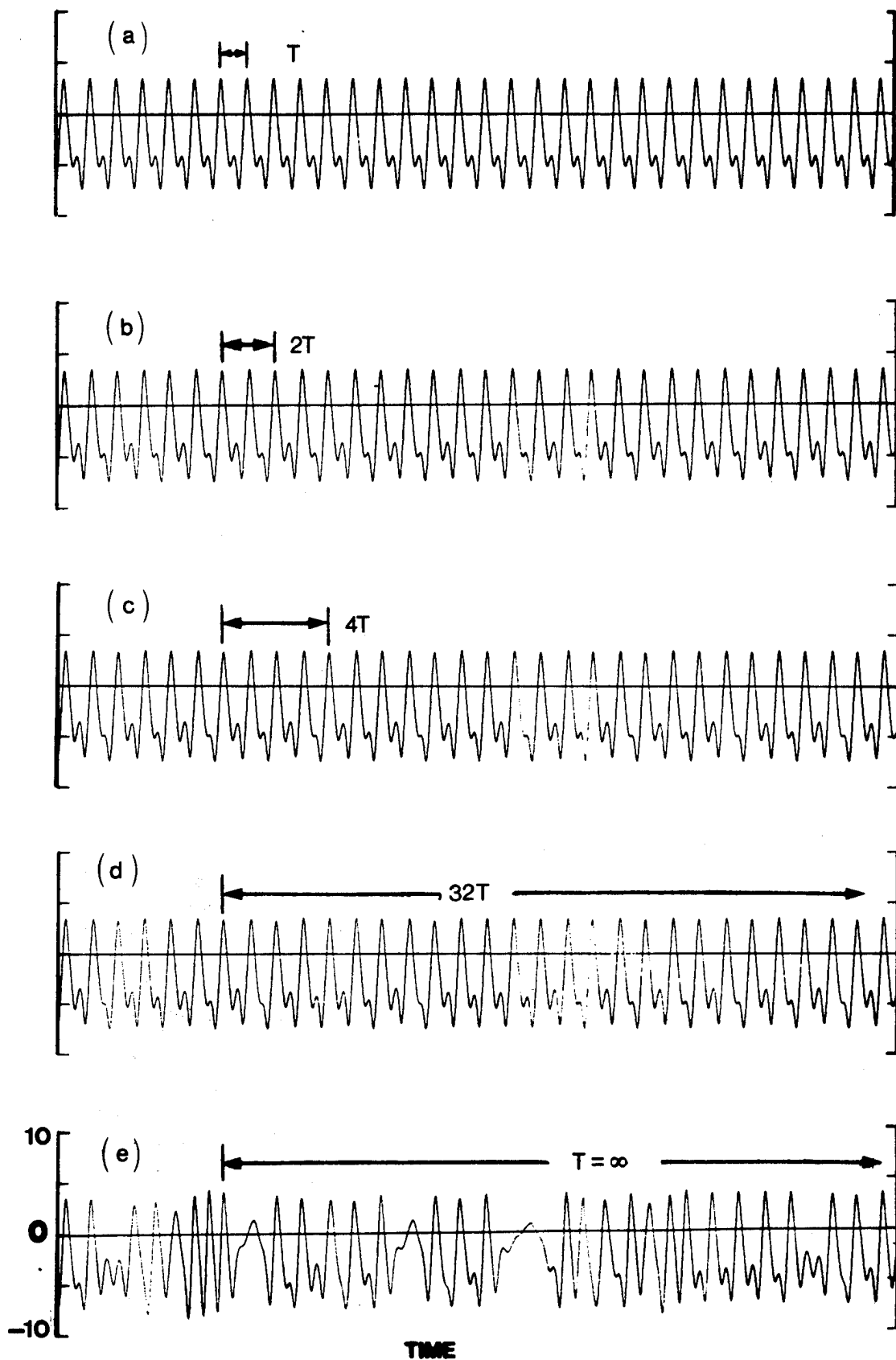


Figure 10. The time history of the system shown in Figure 9 (a)  $\mu = 1.3$ , (b)  $\mu = 1.21$ , (c)  $\mu = 1.18$ , (d)  $\mu = 1.16$ , (e)  $\mu = 1.00$ .

DISTRIBUTED PARAMETER NONLINEAR DAMPING MODELS  
FOR FLIGHT STRUCTURES

A. V. Balakrishnan\*  
6731 Boelter Hall  
UCLA #159410  
Los Angeles, CA 90024

L. W. Taylor  
Mail Stop 489  
NASA Langley Flight Research Center  
Hampton, VA 23665-2552

ABSTRACT

Experimental results on single mode free response using the SCOLE configuration at NASA Langley Flight Research Center exhibit significant nonlinear damping effects. To account for the observed behavior a class of nonlinear damping models is proposed for energy conservation systems. The Krylov-Bogoliubov technique provides a remarkably good approximation at all reasonable damping constants. It also shows that many of the known damping models such as constant friction, air-damping in flow at high Reynolds numbers among others cannot be distinguished from one generic model -- the "energy" model -- appropriately specialized, based on free response alone. This in turn raises the question whether forced response -- in particular response to random white noise -- could help resolve the ambiguity. Some exact analytical results for the non-Gaussian distributions that arise are presented based on the Fokker-Planck equations. Finally, several nonlinear damping models for distributed-parameter systems are suggested which would exhibit the observed single-mode free response.

\* Research supported in part under AFOSR grant no. 88-0252, Applied Math Division, USAF.



# SCALE DAMPING

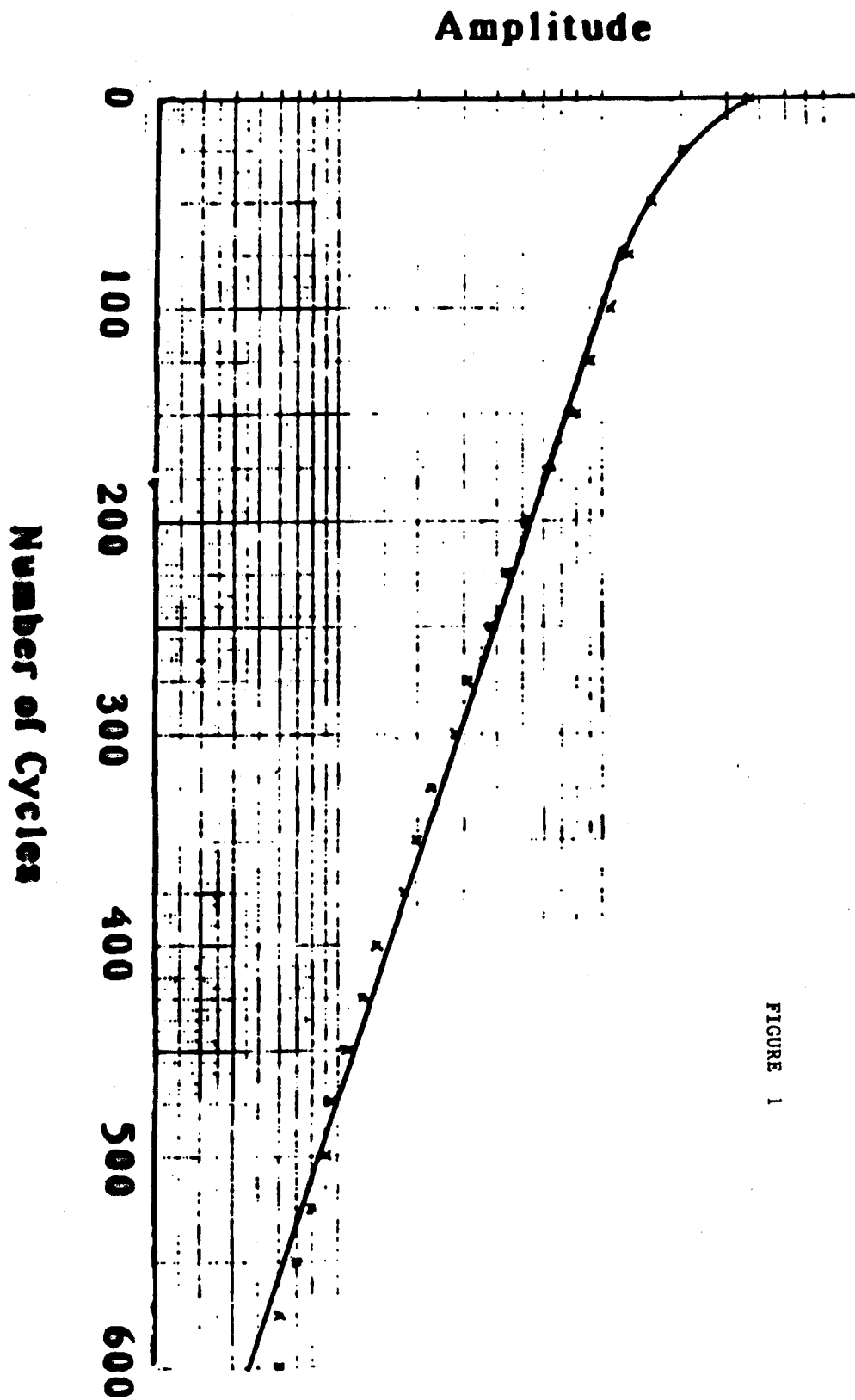


FIGURE 1

## 1. INTRODUCTION

Although the inherent damping phenomena in flight structures are still little understood, many studies of free response -- such as the recent experiments with SCOLE [1] -- would indicate nonlinear behavior especially at high amplitudes. A typical free response curve is shown in Figure 1, which shows the characteristic "convex-downward" or CUP feature. Many nonlinear models have been proposed in the literature [2]. Thus in terms of the basic second-order dynamics for the displacement variable  $x(t)$  in free response:

$$\frac{d^2x}{dt^2} + \omega^2 x(t) + \gamma D(x(t), \dot{x}(t)) = 0 \quad (1.1)$$

where  $\omega$  is the mode frequency and  $\gamma$  the (small) damping constant, we have for "Coulomb Friction" Damping:

$$D(x(t), \dot{x}(t)) = \text{sign } \dot{x}(t) . \quad (1.2)$$

For high Reynolds number flow:

$$D(x(t), \dot{x}(t)) = |\dot{x}(t)| \dot{x}(t) \quad (1.3)$$

modifications of which include "nonanalytic" functions (see [2]):

$$D(x(t), \dot{x}(t)) = |\dot{x}(t)|^\alpha \dot{x}(t) , \quad 0 < \alpha < 1 . \quad (1.4)$$

Our purpose here is to examine these models particularly from the point of view of System Identification (from orbit data, for example). We shall show that these models cannot be distinguished based on single-mode free response data. In particular we also suggest a new class of models based on the instantaneous total energy in the system. We also present some explicit results on response to random excitation using the Fokker-Planck equations, still in the single-mode case. Finally we present a variety of models for distributed parameter systems such as in vibrating strings and beams which can exhibit the kind of single-mode response discussed.

## 2. NONLINEAR DAMPING MODELS: SINGLE MODE RESPONSE

The basic dynamics are described by:

$$\frac{d^2x}{dt^2} + \omega^2 x(t) + \gamma D(x(t), \dot{x}(t)) = 0 . \quad (2.1)$$

To determine possible nonlinear damping models, we note first that the instantaneous energy  $E(t)$  is given by

$$E(t) = \frac{1}{2}(\omega^2 x(t)^2 + \dot{x}(t)^2) . \quad (2.2)$$

The rate of change is

$$\begin{aligned}\frac{d}{dt} E(t) &= (\omega^2 x(t) + \ddot{x}(t)) \dot{x}(t) \\ &= -\gamma D(x(t), \dot{x}(t)) \dot{x}(t) .\end{aligned}\quad (2.3)$$

Hence, since we are only considering energy conservative systems, we must have that

$$D(x(t), \dot{x}(t)) \dot{x}(t) \geq 0 . \quad (2.4)$$

In terms of independent variables  $x, y$ , the function  $D(\cdot, \cdot)$  must be such that

$$D(x, y)y \geq 0 \quad \text{for all } x, y .$$

Note that this condition is satisfied by the models (1.2), (1.3), (1.4) in Section 1, taken from the literature. We may generalize these to:

$$D(x, y) = x^{2m} |x|^\alpha y^{2n+1} |y|^\beta \quad (2.5)$$

where  $m$  and  $n$  are positive integers and  $0 \leq \alpha, \beta \leq 1$ , first presented in [1]. The primary question is whether we can identify the parameters involved  $m, n, \alpha, \beta$  from free response data. For this purpose since the damping is small (small  $\gamma$ ) it is convenient to use the Krylov-Bogoliubov approximation [3] to determine the solution of (2.1), which we shall now rewrite separating out the linear damping part:

$$\ddot{x}(t) + \omega^2 x(t) + 2\zeta\omega\dot{x}(t) + \gamma D(x(t), \dot{x}(t)) = 0 . \quad (2.6)$$

The Krylov-Bogoliubov approximation is the slow varying sinusoid:

$$x(t) = A(t) \sin(\omega t + \phi)$$

where, defining

$$A_n = A(nT)$$

where  $T$  is the period:

$$T = \frac{2\pi}{\omega}$$

we have:

$$\log A_{k+1} = \log A_k - 2\pi\zeta - \gamma \frac{2\pi}{\omega} \cdot \frac{K(A_k)}{\omega A_k} \quad (2.7)$$

where the function  $K(\cdot)$  is determined by:

$$K(A) = \frac{1}{2\pi} \int_0^{2\pi} D(A \sin \theta, A\omega \cos \theta) \cos \theta \, d\theta . \quad (2.8)$$

For  $D(\cdot, \cdot)$  given by (2.5) we have

$$\log A_{k+1} = \log A_k - 2\pi\zeta - 2\pi\gamma\mu\omega^{2n+\beta-1} A_k^{2n+2m+\alpha+\beta} \quad (2.9)$$

where

$$\mu = \frac{1}{2\pi} \int_0^{2\pi} D(\sin \theta, \cos \theta) d\theta = f(m, n, \alpha, \beta)$$

and is easily evaluated -- see [1]. But the exact value is not important from the identification point of view since it is multiplied in (2.9) by the unknown damping constant  $\gamma$ . Comparison between the solution given by (2.9) and that obtainable by numerical solution of (2.6) using multi-step (Runge-Kutta) techniques has been examined in [4], especially the behavior for high  $\gamma$ . It should be also noted that the exponent of  $A_k$  involves a combination of  $m, n, \alpha, \beta$  and makes apparent the difficulty in resolving them.

An unexpected consequence of the validity of the Krylov-Bogoliubov approximation is that we can now present a new class of damping models -- "energy" models -- which can yield the same Krylov-Bogoliubov approximation. Thus let

$$D(x(t), \dot{x}(t)) = \dot{x}(t) E(t)^q = \dot{x}(t) \left( \frac{(\omega^2 x(t)^2 + \dot{x}(t)^2)}{2} \right)^q \quad (2.10)$$

where  $q > 0$ . This clearly satisfies (2.4) and moreover the Krylov-Bogoliubov approximation is (see [5])

$$\log A_{k+1} = \log A_k - 2\pi\zeta - 2\pi\gamma\omega^{2(q-1)} \frac{1}{2^{q+1}} A_k^{2q} \quad (2.11)$$

Thus, as first observed in [5], we can obtain the same kind of response as in (2.7) by choosing  $q$  appropriately, viz. taking

$$2q = 2n + 2m + \alpha + \beta \quad (2.12)$$

This clearly underscores the difficulty in identifying nonlinear damping models from flight data. Hence we may want to examine the possibility of using forced response -- in particular response to random (white noise) excitation.

### 3. FORCED RESPONSE WITH RANDOM NOISE EXCITATION

Especially in the Civil Engineering oriented literature there is considerable work reported on the response to random noise excitation applied to nonlinear damping models in one dimension (single mode) [6]. One particular tool used is that of equivalent linearization because of the difficulty in obtaining exact distributions which cannot of course be Gaussian. The analytical tool for evaluating the first and/or second order

steady state distributions of the response is of course provided by (and only by!) the Fokker-Planck partial differential equations. For the energy model (2.10), exact solutions have been presented in [5] for the first order steady state density, indicating explicitly the non-Gaussian nature. In particular it can be used to test validity of the equivalent linearization technique, at least for this example. Thus the first order steady state density of the forced response:

$$\ddot{x}(t) + \omega^2 x(t) + 2\zeta \dot{x}(t) + \dot{x}(t) (\omega^2 x(t)^2 + \dot{x}(t)^2)^q = N(t) \quad (3.1)$$

where  $N(\cdot)$  is white Gaussian with spectral density  $\sigma^2$  given by:

$$y \sim \dot{x}$$

$$p_{x,\dot{x}}(x, y) = c \exp. \left\{ \frac{-2\zeta\omega}{\sigma^2} (\omega^2 x^2 + y^2) - \gamma \frac{(\omega^2 x^2 + y^2)^{q+1}}{(q+1)} \right\} \quad (3.2)$$

where  $c$  is a normalizing constant:

$$1 = \frac{\pi c}{\omega} \int_0^\infty \exp - \left( \frac{2\zeta\omega r}{\sigma^2} - \frac{\gamma r^{q+1}}{q+1} \right) dr \quad (3.3)$$

where the integrand in (3.3) is actually the density of the energy  $2E(t)$ . The second term in the exponent in (3.2) clearly indicates the non-Gaussian nature. Unlike the linear case,  $x(t)$  and  $\dot{x}(t)$  are no longer independent. We can calculate that the steady state covariance of the displacement  $x(t)$  is given by

$$E[x(t)^2] = \frac{1}{2\omega^2} \cdot \frac{\int_0^\infty r e^{-\lambda r - \gamma_1 r^{q+1}} dr}{\int_0^\infty e^{-\lambda r} e^{-\gamma_1 r^{q+1}} dr}$$

where

$$\lambda = \frac{2\zeta\omega}{\sigma^2}; \quad \gamma_1 = \frac{\gamma}{\sigma^2(q+1)}.$$

For small enough  $\gamma$  we have the approximation

$$E[x(t)^2] = \left[ 1 - \frac{\gamma}{\sigma^2(q+1)!} \lambda^{q+1} \right] \frac{\sigma^2}{4\zeta\omega^3}. \quad (3.4)$$

In particular the goodness of equivalent linearization can be assessed from (3.4). The density corresponding to the first model, (2.5), would appear to be more complicated than would be indicated by using the equivalent value for  $q$ . Thus the possibility of distinguishing between models using forced response to random excitation is yet to be explored.

#### 4. NONLINEAR DAMPING MODELS FOR DISTRIBUTED PARAMETER SYSTEMS

At the present time no nonlinear damping models for energy conservative distributed parameter systems are available. Here we propose several models for the beam torsion as well as beam bending modes for a uniform Bernoulli beam. To yield the model (2.5) for the single mode response we suggest for beam bending for a beam of length  $2\ell$ :

$$\ddot{u}(s, t) + \lambda u''''(s, t) - 2\zeta\sqrt{\lambda} \dot{u}''(s, t) - \gamma \left[ \int_{-\ell}^{\ell} u'(s, t) \dot{u}'(s, t) ds \right]^{2(n+\beta)+1} u''(s, t) = 0, \quad (4.1)$$

$$-\ell < s < \ell; \quad 0 < t$$

where  $s$  denotes the spatial variable, super-dots represent derivatives with respect to time  $t$  and the primes derivatives with respect to  $s$ , and

$$0 \leq \beta < \frac{1}{2}$$

and  $\lambda$  is the appropriate structure constant. And corresponding to the energy model (2.10), we propose:

$$\ddot{u}(t, s) - 2\zeta\sqrt{\lambda} u''(t, s) + \lambda u''''(t, s) - \gamma \left[ \int_{-\ell}^{\ell} (\lambda u''(t, \sigma)^2 + \dot{u}(t, \sigma)^2) d\sigma \right]^q \dot{u}''(t, s) = 0. \quad (4.2)$$

For a proof that the single-mode response behavior corresponding to (4.1) with clamped end conditions is given by taking

$$D(x(t), \dot{x}(t)) = x(t)^{2n} \dot{x}(t)^{2n+1} |x(t)|^\beta |\dot{x}(t)|^\beta \quad (4.3)$$

reference may be made to [7]. A similar argument suffices also for (4.2). The beam torsion mode case is more complicated because the linear model for proportional damping is no longer a differential (local) operator (see [8]). Thus the nonlinear damping model proposed is:

$$\begin{aligned}
\ddot{u}(t, s) - \lambda u''(t, s) + 2\zeta\sqrt{\lambda} \int_{-\ell}^{\ell} \frac{\cos(\pi s/2\ell)}{(\sin(\pi s/2\ell) - \sin(\pi \sigma/2\ell))} \dot{u}'(t, \sigma) d\sigma \\
+ \gamma \left[ \int_{-\ell}^{\ell} \int_{-\ell}^{\ell} u(t, s) \frac{\cos(\pi s/2\ell)}{(\sin(\pi s/2\ell) - \sin(\pi \sigma/2\ell))} \dot{u}'(t, \sigma) d\sigma ds \right]^{2(n+\beta)+1} \\
\times \int_{-\ell}^{\ell} \frac{\cos(\pi s/2\ell)}{(\sin(\pi s/2\ell) - \sin(\pi \sigma/2\ell))} u'(t, \sigma) d\sigma = 0.
\end{aligned} \tag{4.4}$$

The "energy" model is obtained by replacing the term containing  $\gamma$  in (4.4) by

$$+ \gamma \left[ \int_{-\ell}^{\ell} (\lambda u'(t, s)^2 + \dot{u}(t, s)^2) ds \right]^q \int_{-\ell}^{\ell} \frac{\cos(\pi s/2\ell)}{\sin(\pi s/2\ell) - \sin(\pi \sigma/2\ell)} \dot{u}'(t, \sigma) d\sigma. \tag{4.5}$$

It will take us too far afield to show that the corresponding single mode dynamics of (4.4) correspond to (4.3) and that of (4.5) to (2.10). It should be noted that (4.1), (4.2), (4.4), (4.5) are fairly complicated nonlinear partial differential equations requiring sophisticated mathematical techniques for analysis -- see [9] for example. Computer simulation may be an attractive alternative.

#### REFERENCES

1. A. V. Balakrishnan. "A Theory of Nonlinear Damping in Flexible Structures." In: *Proceedings of the Workshop on Stabilization of Flexible Structures, December 1987*. Edited by J. P. Zolesio and A. V. Balakrishnan. Optimization Software Publications, 1988.
2. A. H. Nayfeh and D. T. Mook. *Nonlinear Oscillations*. John Wiley & Sons, 1979.
3. N. Kyrlov and N. Bogoliubov. *Introduction to Non-Linear Mechanics*. Princeton University Press, 1949.
4. J. Cisneros. "Non-linear Damping Model: Computational Results." In: *Proceedings of the 5th Annual SCOLE Workshop, November 1988*. Edited by L. W. Taylor.
5. Weijian Zhang. "Non-linear Damping Model: Response to Random Excitation." In: *Proceedings of the 5th Annual SCOLE Workshop, November 1988*. Edited by L. W. Taylor.
6. Y. K. Wen. "Equivalent Linearization for Hysteretic Systems Under Random Excitation." *Journal of Applied Mechanics*, Vol. 47 (1980), pp. 150-154.

7. A. V. Balakrishnan. "On Modelling Nonlinear Damping in Distributed Parameter Systems." Presented at: NASA Workshop on Computational Aspects in the Control of Flexible Systems, Williamsburg, Virginia, July 1988. Proceedings to be published.
8. A. V. Balakrishnan. "Damping Operators in Continuum Models, of Flexible Structures: Explicit Models for Proportional Damping in Beam Torsion." In: *Proceedings of the Workshop on Stabilization of Flexible Structures, January 1989, Montpellier*. Edited by J. P. Zolesio. Optimization Software Publications, 1989.
9. A. Lunardi. "Local Stability Results for the Elastic Beam Equation." *SIAM Journal on Mathematical Analysis*, Vol. 18, No 5 (Sept 1987).



## NON-LINEAR DYNAMIC ANALYSIS WITH FREQUENCY-DEPENDENT DAMPING

F.Venancio-Filho  
Dept. of Civil Engineering  
COPPE/UFRJ-Federal Univ. of Rio de Janeiro  
Caixa Postal 68506  
21945 Rio de Janeiro RJ-BRAZIL  
Phone: (021)280-9993  
on leave of absence at:  
Rutgers University  
P.O. Box 909  
Piscataway, NJ 08855-0909  
Phone: (201)932-2232

A.M. Claret  
Dept. of Civil Engineering  
School of Mines  
Federal Univ. of Ouro Preto  
35400 Ouro Preto MG-BRAZIL  
Phone: (031)551-1132

### ABSTRACT

Methods of dynamic structural analysis in the frequency domain are strongly indicated when the structural and damping properties are frequency-dependent. Typical problems in which this dependency occurs are soil-structure interaction problems. Moreover physical non-linearities can be present due to high strain levels in the soil.

In the present work a method of dynamic analysis in the frequency domain is presented that performs a rigorous analysis of non-linear structural systems with physical non-linearities and frequency-dependent properties. Stiffness and damping properties can be considered as frequency-dependent and the stiffness property can also be strain-dependent. The method is a step-by-step incremental one with linearized steps. In each step the integration is performed in the frequency domain through a FFT algorithm.

Examples of the analysis of SDOF soil-structure interaction system are presented in order to assess the applicability and stress the features of the method and to show the influence of frequency-dependent damping in the structural response.

## INTRODUCTION

Methods of dynamic structural analysis in the frequency domain are strongly indicated when the structural and damping properties depend on the excitation frequency. Typical problems in which this dependency occurs are soil-structure interaction problems. On the other hand physical non-linearities can be present due to high strain levels in the soil.

Linear Structural dynamic analysis in the frequency domain is well known and had a great development with the use of the FFT algorithm. Nevertheless only recently methods of non-linear dynamic structural analysis in the frequency domain have been developed. Kawamoto [1983] presented the so called Hybrid Frequency-Time Domain(HFTD) method in which the non-linearities are treated as pseudo-forces. Darbre and Wolf [1987] demonstrated the convergence for the partial version of the HFTD method.

In the present paper a method for non-linear dynamic structural analysis in the frequency domain is presented that works for Single-Degree-Of-Freedom(SDOF) systems with frequency-dependent properties and physical non-linearities. Stiffness and damping properties can be considered as frequency-dependent and the stiffness property can also depend on the displacement. The method uses a step-by-step incremental technique with linearized steps and a secant stiffness. In each step the integration of the dynamic equilibrium equation is performed exactly in the frequency domain through a FFT algorithm taking into account the frequency-dependent properties.

Examples of the analysis of non-linear SDOF systems with frequency-dependent properties submitted to transient excitation are presented. The influence of the frequency-dependent damping upon the structural response is highlighted in these examples.

## FORMULATION OF THE PROBLEM

Consider the SDOF system of Fig. 1 submitted to an arbitrary excitation  $p(t)$ . The spring stiffness  $k$  depends on the displacement  $v$  due to the system non-linearity and the damping coefficient depends on the frequency of the excitation,  $\omega$ . The problem is then to integrate the dynamic equilibrium equation

$$m\ddot{v} + c(\omega)\dot{v} + k(v)v = p(t). \quad (1)$$

As the damping coefficient is  $\omega$  dependent a frequency-domain analysis has to be performed and, as the stiffness depends on the displacement, a linearization technique must be employed. Consequently the present method is a Step-by-Step Incremental Linearization in the Frequency Domain (SILFD) method. In each linearized step a secant stiffness is considered.

## THE SILFD METHOD

In order to calculate the response of the system governed by Eq.1 two approximations are made. The first one is the approximation of the given load by piecewise linear segments. The total time interval in which the response is to be calculated is divided in intervals  $\Delta t_t = t_j - t_{j-1}$ ;  $p_j$  and  $p_{j-1}$  are the values of  $p(t)$  in times  $t_j$  and  $t_{j-1}$ , respectively, and  $\Delta p_j = p_j - p_{j-1}$ . Fig.2a. The load variation in time interval  $\Delta t_j$  is given by, Fig. 2a ,

$$p(\tau) = p_{j-1} + \frac{\Delta p_j}{\Delta t_j} \tau . \quad (2)$$

where  $\tau$  is the current time in  $\Delta t_j$  ( $0 \leq \tau \leq \Delta t_j$ ). The second approximation refers to the spring force versus displacement curve. This curve is also approximated by piecewise linear segments as indicated in Fig. 2c. The levels of these two approximations depend on the accuracy with which the load and the stiffness variation can have a good representation.

The response of the system is calculated through the linearized steps along the time intervals  $\Delta t_j$  in which the spring is considered linear with stiffness  $k_j$ . Fig. 2b. The linearized dynamic equilibrium equation in time interval  $\Delta t_j$  is

$$m\ddot{v} + c(\omega)\dot{v} + k_j v = p(\tau) \quad (3)$$

with the initial conditions  $v_{j-1}$  and  $\dot{v}_{j-1}$ , Fig. 2a. Taking the Fourier Transform (FT),  $(F)$ , of both sides of Eq. 3 and considering that  $F$  is a linear operator one obtains

$$F[m\ddot{v}] + F[c(\omega)\dot{v}] + F[k_j v] = F[p(\tau)]. \quad (4)$$

The following equations are now considered by definition:

$$F[m\ddot{v}] = \int_0^\infty m \ddot{v} e^{-i\omega\tau} d\tau ; \quad (5a)$$

$$F[c(\omega)v] = \int_0^\infty c(\omega) v e^{-i\omega\tau} d\tau ; \quad (5b)$$

$$F[k_j v] = \int_0^\infty k_j v e^{-i\omega\tau} d\tau = k_j V(\omega) ; \quad (5c)$$

$$F[p(\tau)] = \int_0^{\infty} p(\tau) e^{-i\omega\tau} d\tau = P(\omega) , \quad (5d)$$

noting that in Eq. 5c  $k_j$  is constant. Integration by parts of the right-hand sides of Eqs. 5a and b gives respectively

$$F[m\ddot{v}] = -m\dot{v}_{j-1} - i\omega m v_{j-1} - \omega^2 m V(\omega) ; \quad (6a)$$

$$F[c(\omega)\dot{v}] = -c(\omega)v_{j-1} + i\omega c(\omega) V(\omega) . \quad (6b)$$

Introducing now Eqs. 6a, 6b, 5c, and 5d into Eq. 4, the following equation is obtained

$$[H(\omega)]^{-1} V(\omega) = \bar{P}(\omega) . \quad (7)$$

In this equation

$$\bar{P}(\omega) = P(\omega) + m\dot{v}_{j-1} + i\omega m v_{j-1} + c(\omega)v_{j-1} . \quad (8)$$

is the FT of the load with due regard of the initial conditions,  $v_{j-1}$  and  $\dot{v}_{j-1}$  , and

$$H(\omega) = [-\omega^2 m + i\omega c(\omega) + k_j]^{-1} \quad (9)$$

is the system complex frequency response function in time interval  $\Delta t_j$  . The Fourier Transform of  $v(\tau)$  is obtained, by inversion in Eq. 7, as

$$V(\omega) = H(\omega) \bar{P}(\omega) . \quad (10)$$

The response  $v(\tau)$  in time interval  $\Delta t_j$  is then the inverse FT of  $V(\omega)$  , Eq. 10. In this way

$$v(\tau) = \frac{1}{2\pi} \int_0^{\infty} V(\omega) e^{i\omega\tau} d\omega . \quad (11)$$

The FT of the velocity is

$$\bar{V}(\omega) = i\omega \bar{P}(\omega) H(\omega) . \quad (12)$$

The velocity response is the inverse FT of  $\bar{V}(\omega)$  and is given by

$$v(\tau) = \frac{1}{2\pi} \int_0^{\infty} \bar{V}(\omega) e^{i\omega\tau} d\omega . \quad (13)$$

## COMPUTATIONAL PROCEDURE

The computational procedure of the SILFD method consists of the following steps:

- i. for each time interval  $\Delta t_j$  Fig. 2a, obtain  $k_j$  from the spring force versus displacement curve, Fig. 2c.
- ii. extend the load function in time  $\Delta t_j$  with a trail of zeroes in order to total  $2^m$  points ( $m$  integer); calculate the discrete FT's  $P(\omega_k)$ , Eq. 5d, and  $\bar{P}(\omega_k)$ , Eq. 8, ( $k = 1, 2, \dots, 2^m$ ), Fig. 3
- iii. calculate  $H(\omega_k)$ , considering  $c(\omega_k)$ , for  $k = 1, 2, \dots, 2^m$ .
- iv. calculate the discrete FT's  $V(\omega_k)$ , Eq. 10, and  $\bar{V}(\omega_k)$ , Eq. 12, for  $k = 1, 2, \dots, 2^m$ .
- v. calculate the inverse discrete FT's of  $V(\omega_k)$  and  $\bar{V}(\omega_k)$  to obtain  $v(\tau)$  and  $\bar{v}(\tau)$ .
- vi. if  $v_j < \bar{v}_k$ , Fig. 2c, go to time interval  $\Delta t_{j+1}$ ; if  $v_j > \bar{v}_k$ , Fig. 2c, reduce  $\Delta t_j$  and go to ii.

## EXAMPLES

The first example is the SDOF system of Fig. 1 with mass  $m = 1.0 \times 10^6$  kg. The spring force versus displacement variation is bi-linear and is given in Fig. 4 where the initial stiffness is  $k_0 = 15 \times 10^9$  N/m. Several damping coefficient versus frequency variations are considered which are shown in Fig. 5. The maximum values of these curves correspond to damping ratios of 5%, 10%, 20%, 30%, and 40% of the critical damping of the linear system. The system is submitted to the load given in Fig. 6. The curves AOC and A10 in Fig. 7 are the system responses with a constant damping coefficient corresponding to 10% of the critical damping and with the damping coefficient given by the 10% curve in Fig. 5, respectively. The consideration of variable damping, in this case, leads to greater values for the displacements. The curves in Fig. 8 display the response with damping coefficients given by the 5%, 20%, and 40% curves in Fig. 5. The great influence of the damping variation on the pseudo-period of the response and the great difference in the obtained displacements, after the load develops, is to be noted.

The second example is a SDOF linear system with  $m = 1.0 \times 10^6 \text{ kg}$ ,  $k = 1.5 \times 10^{10} \text{ N/m}$  and an hysteretic damping coefficient  $D = 0.10$  submitted to a transient excitation. The analysis is performed considering a viscous damping ratio  $\xi = 0.10$  and an equivalent viscous damping coefficient defined by  $c_{eq} = \frac{2Dk}{\omega}$ . The variation of  $c_{eq}$  with  $\omega$  is shown in Fig.9.

As this variation has a singularity for  $\omega = 0$  the following approximations are considered: horizontal (1); tangent (2); and parabolic (3). Fig. 10 shows the responses obtained with a viscous damping coefficient corresponding to a damping ratio of 10% and with equivalent viscous damping coefficients with the horizontal (CHR), tangent (CTG), and parabolic (CPA) approximations. From Fig. 10 it can be observed that, for a transient excitation, the consideration of the frequency content of the excitation leads to greater values of the response. On the other hand, for a resonant harmonic excitation, the response can be calculated with a constant equivalent damping coefficient equal to the hysteretic damping coefficient.

### CONCLUSIONS

The method presented herein is applicable to the analysis of the dynamic response of non-linear systems in the frequency domain. The stiffness and damping properties can depend on the excitation frequency, as in soil-structure interaction systems, and the stiffness can depend on the displacement in face of non-linearities.

The use of a FFT algorithm turns out the method to be competitive with methods in time domain. On the other hand the method is mandatory for systems in which the properties depend on the frequency content of the excitations. The system non-linearities are treated by incremental linearized steps with a secant stiffness.

Great differences in the responses considering constant and frequency-dependent damping are observed in the analysed cases mainly when the transient load dies out.

### REFERENCES

1. Darbre, G.R., and J. P. Wolf [1987], "Criterion of Stability and Implementation Issues of Hybrid Frequency-Time-Domain Procedure for Nonlinear Dynamic Analysis", Transactions of the 9th International Conference on Structural Mechanics in Reactor Technology, Lausanne, August 1987.
2. Kawamoto, J.D. [1983], "Solution of Nonlinear Dynamic Structural Systems by a Hybrid Frequency-Time Domain Approach", MIT Research Report R83-5, Department of Civil Engineering, Cambridge, 1983.

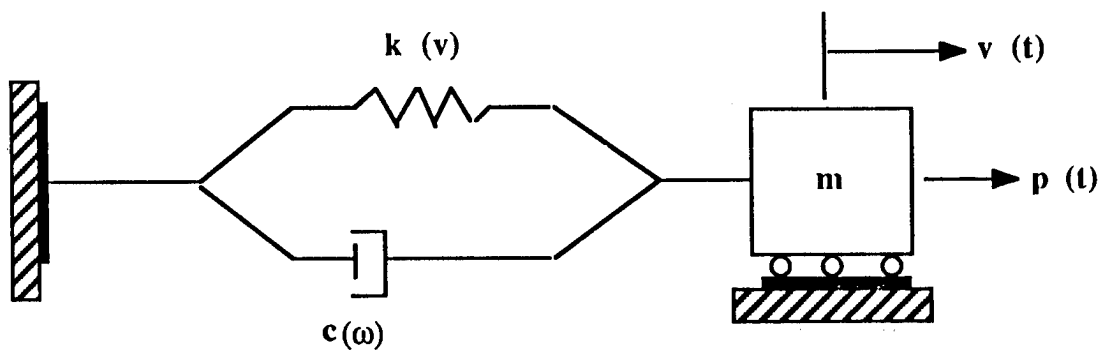


Figure 1.- SDOF System

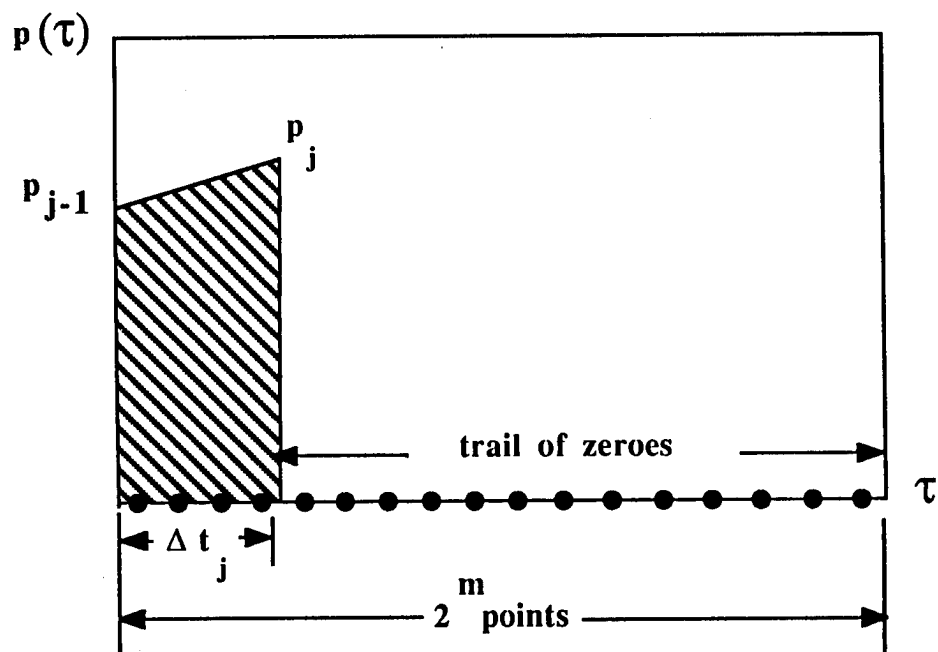


Figure 3.- Extended Load Function

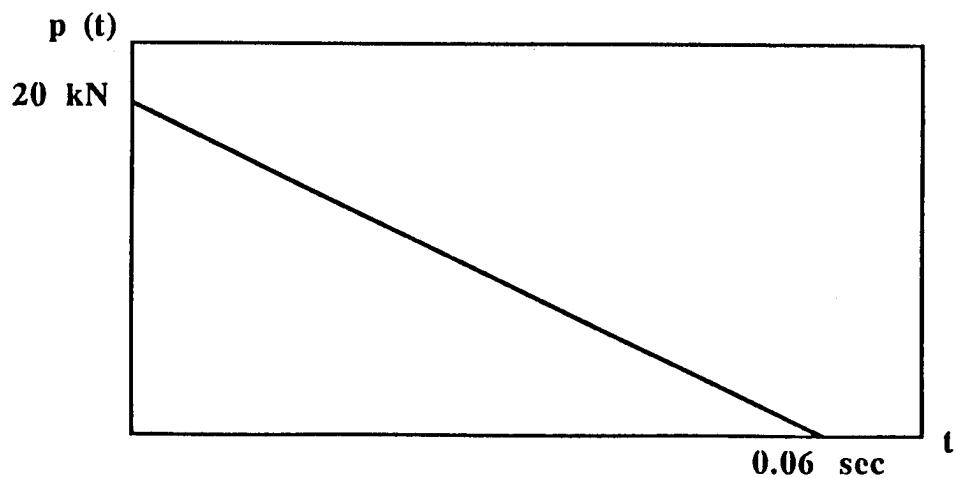


Figure 6.- Load

FDD-7

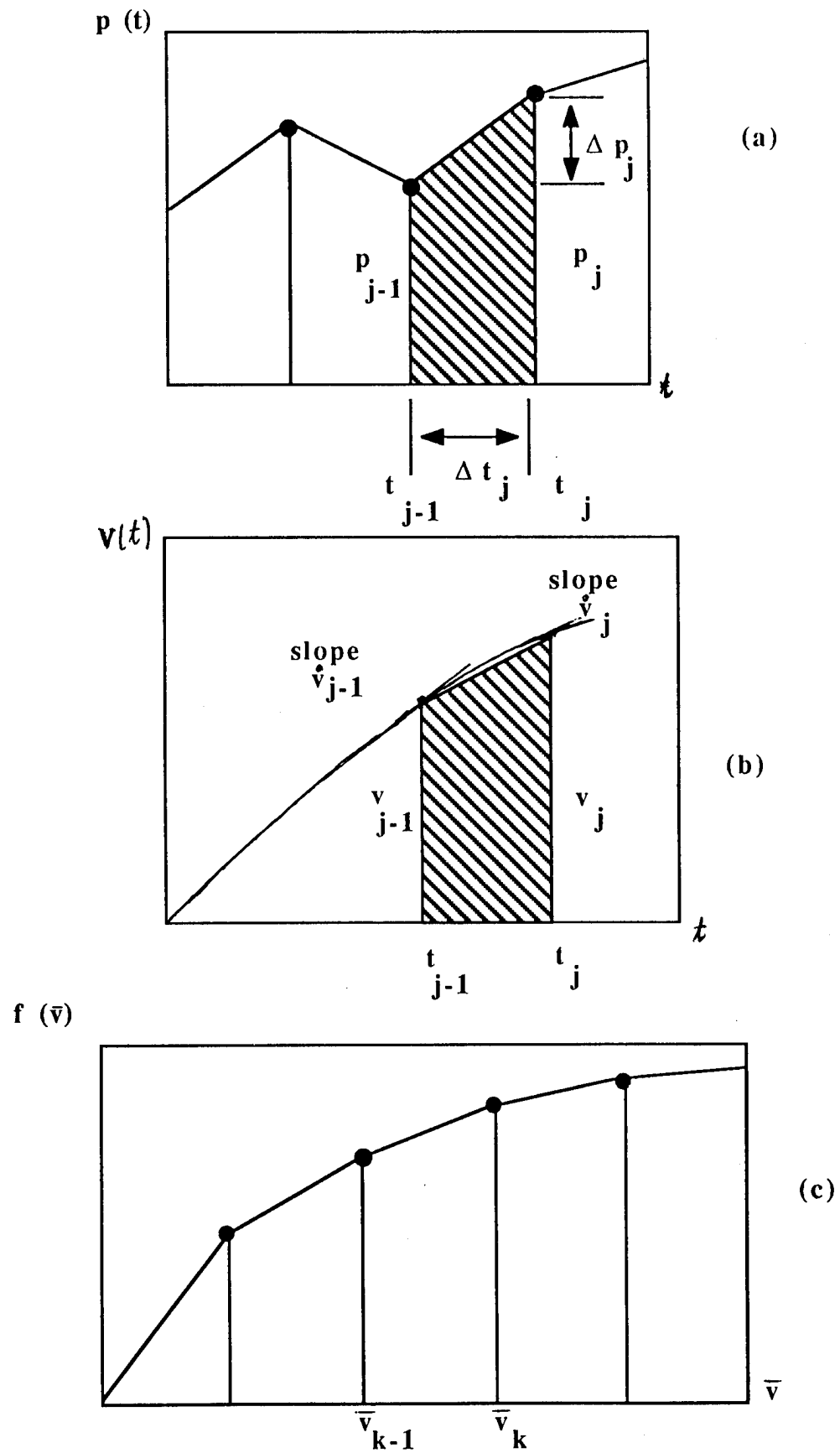


Figure 2.- a) Load; b) Displacement response; c) Spring force



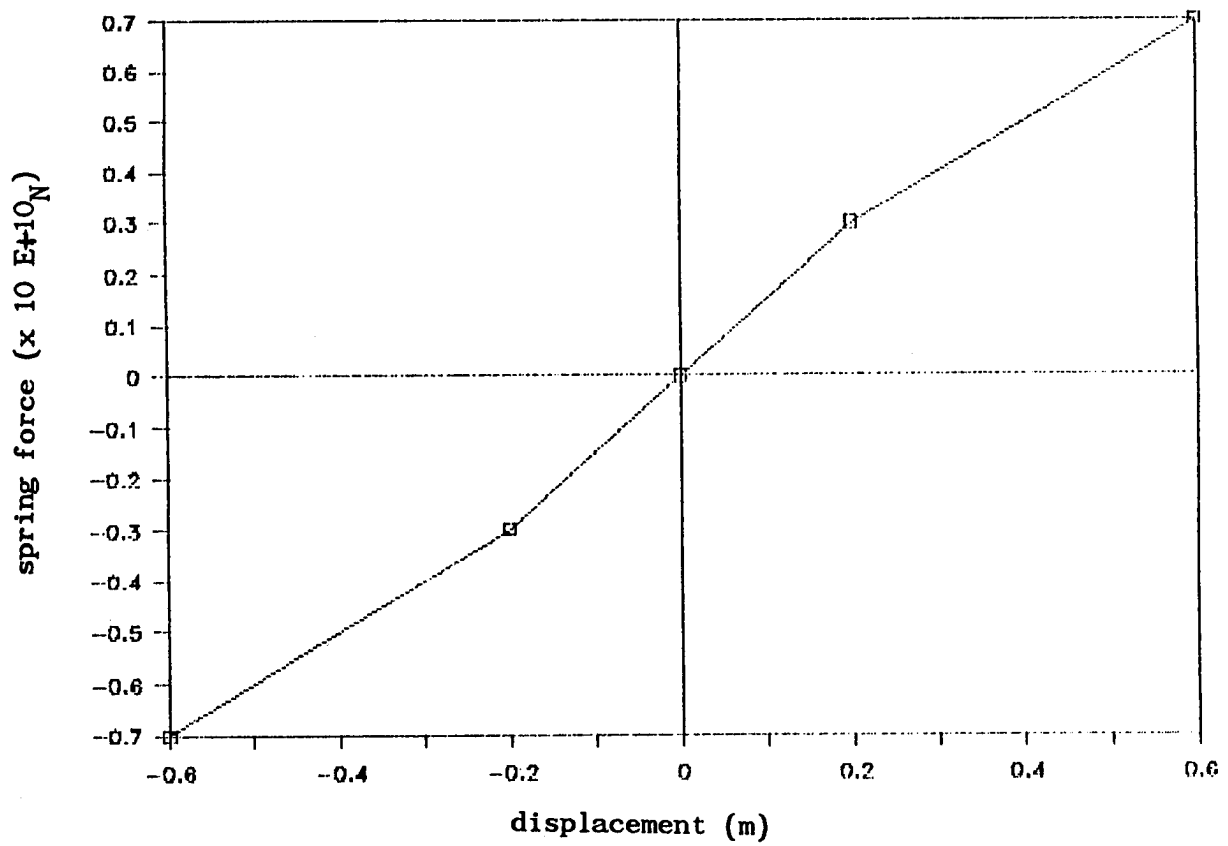


Fig. 4 - Spring force versus displacement

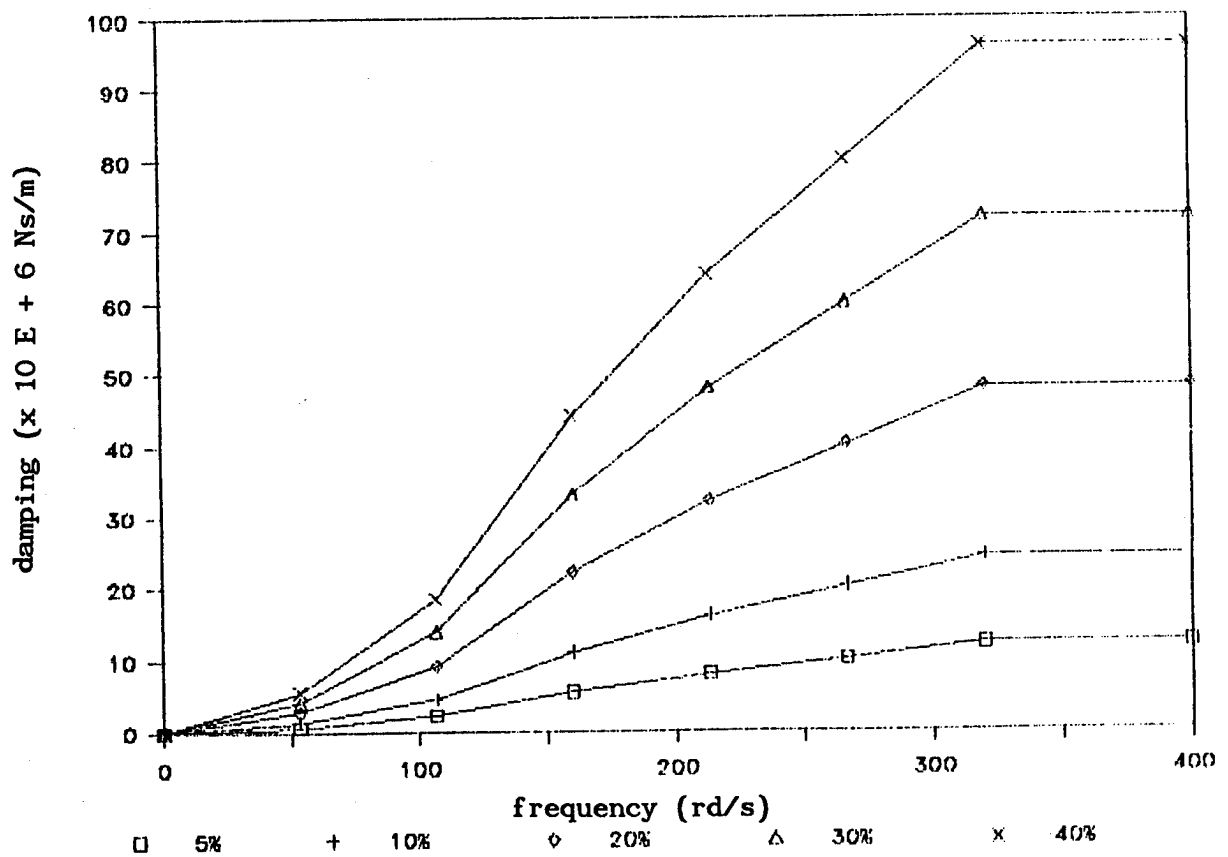


Fig. 5 - Damping coefficients versus frequency

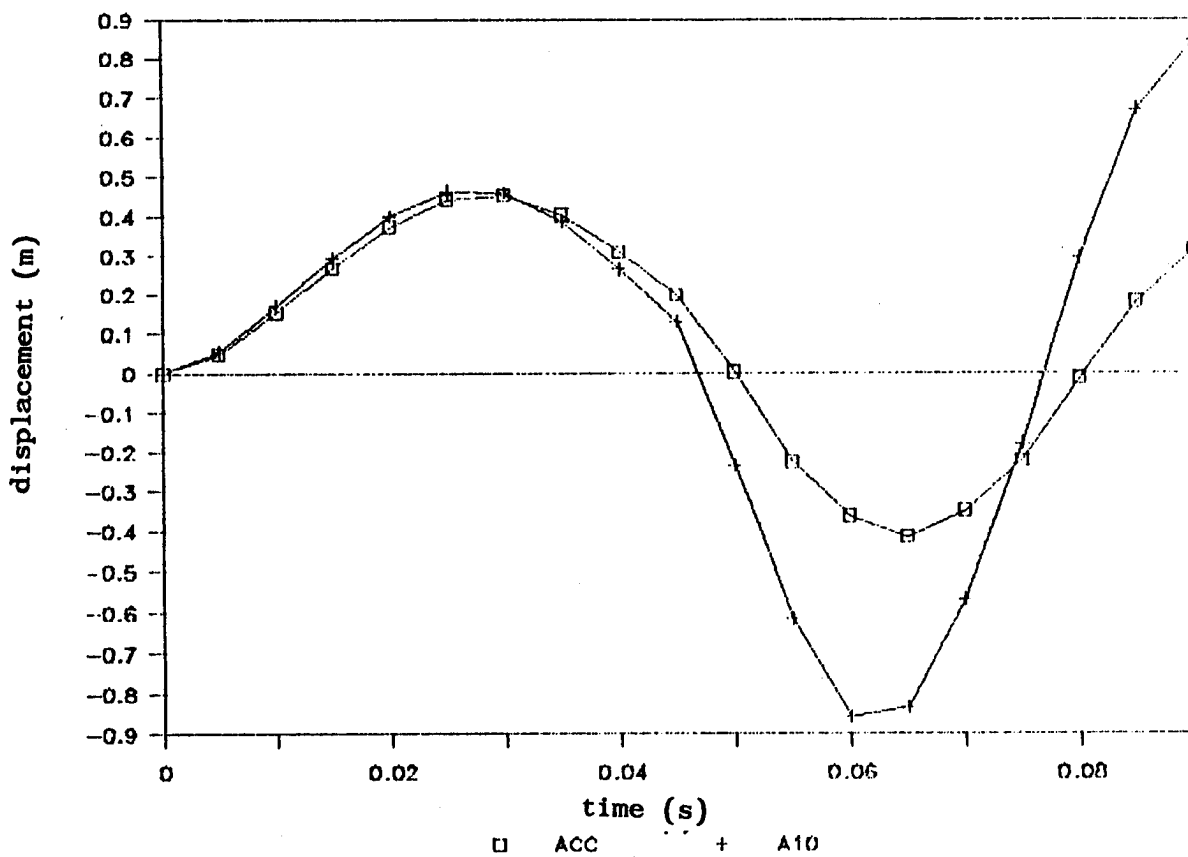


Fig. 7 - System responses

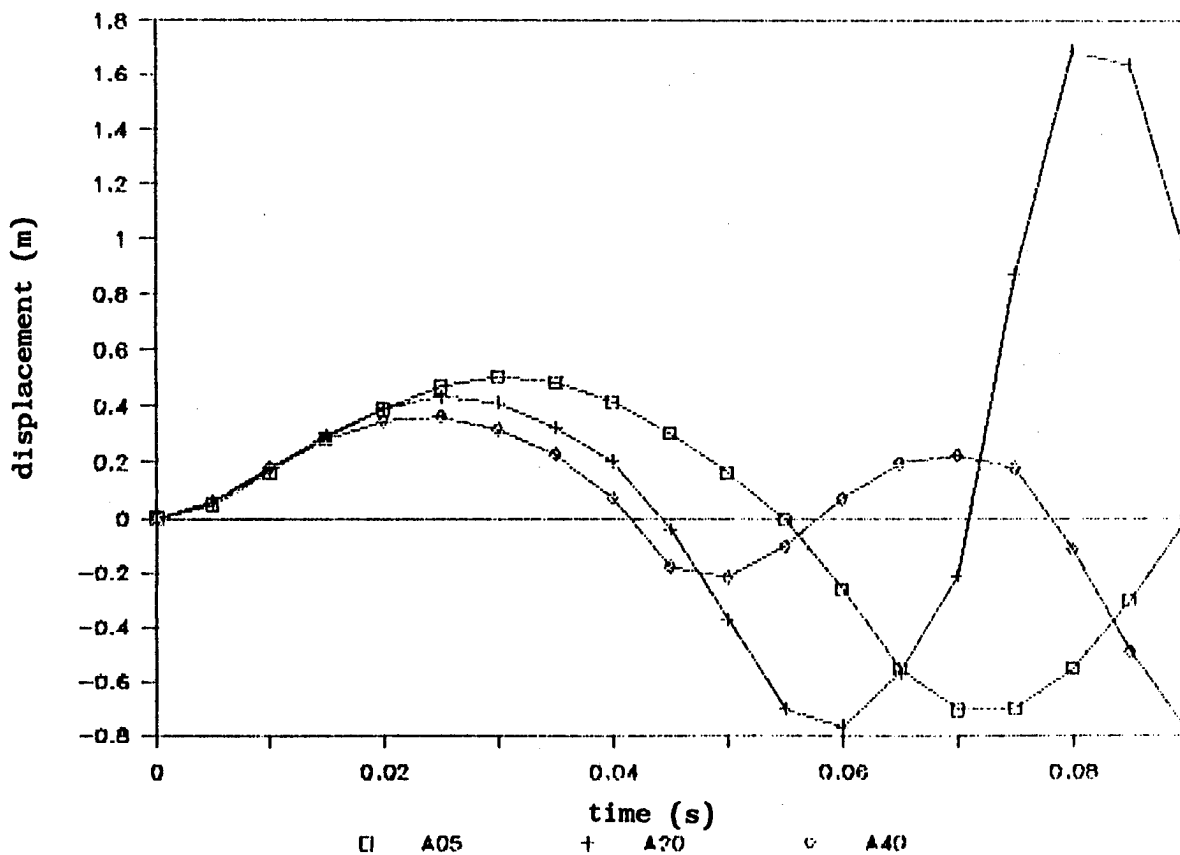


Fig. 8 - System responses

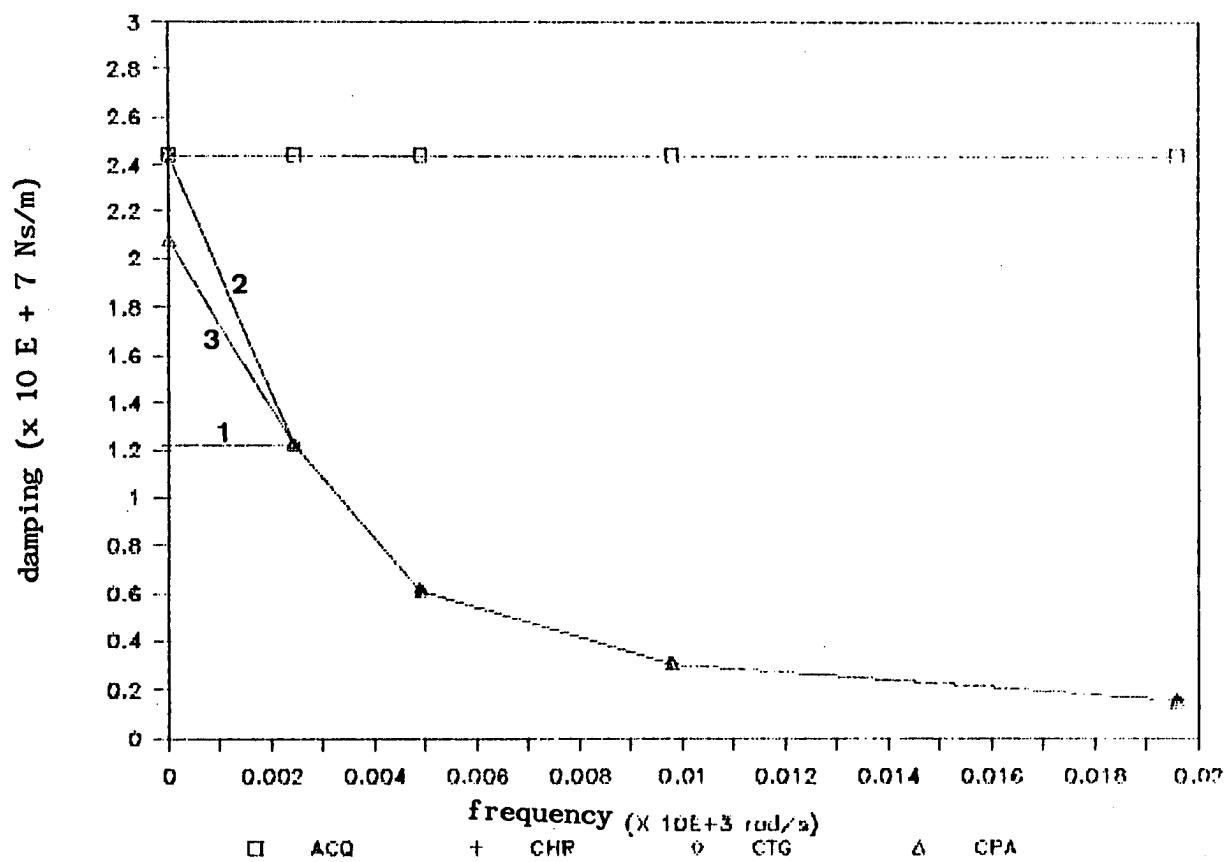


Fig. 9 - Equivalent viscous damping versus frequency

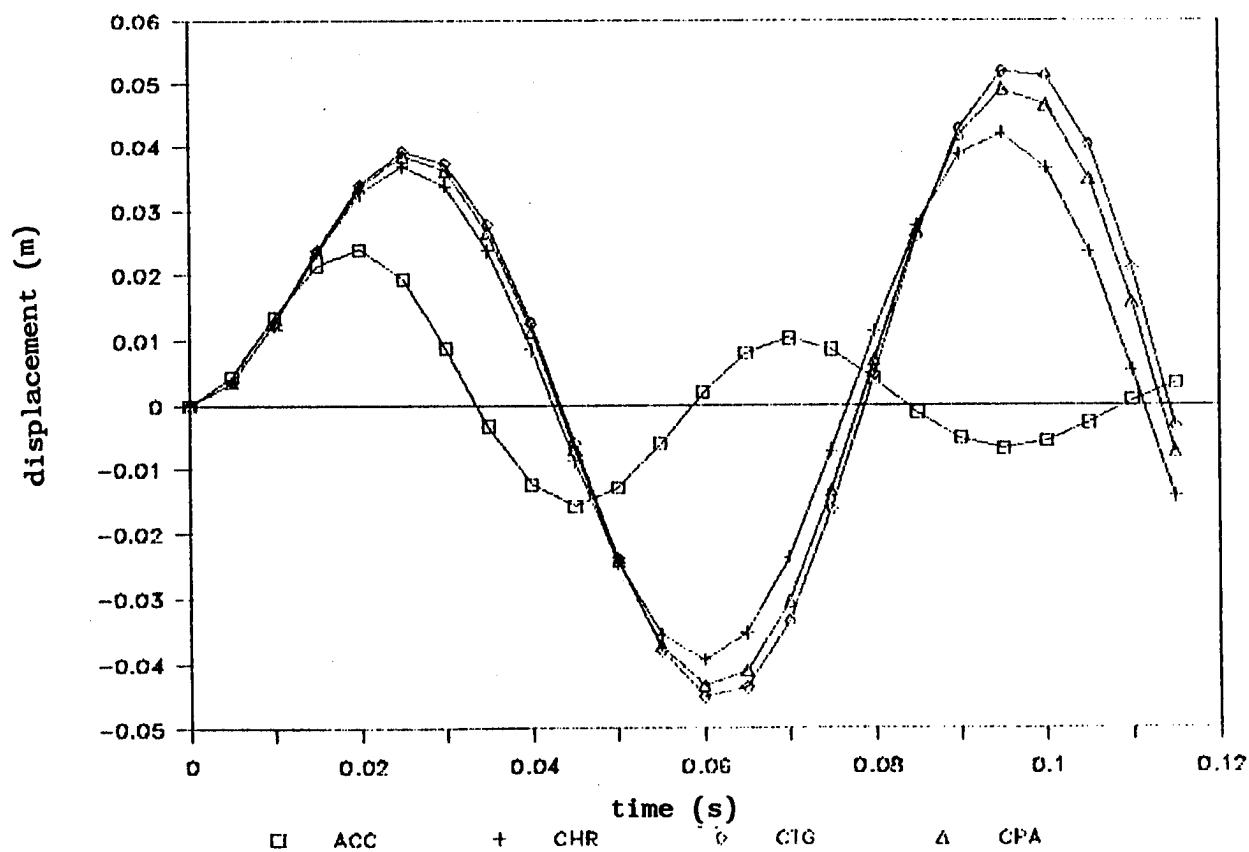


Fig. 10 - System responses

# Fluid Inertia Effects in Squeeze Film Dampers

A. El-Shafei

Assistant Professor  
Department of Mechanical Engineering  
University of South Florida  
Tampa, FL 33620

## Abstract

Fluid inertia effects in squeeze film dampers are investigated. An approximate energy method, based on the assumption that the velocity profiles of the classical lubrication theory do not change much due to fluid inertia, is used. The kinetic coenergy of the fluid is calculated and the inertia forces are obtained by Lagrange's equations in conjunction with Reynolds transport theorem. The governing equations are then solved for a small circular centered whirl. It is shown that for this case the fluid inertia forces are equal to the viscous forces in the damper at squeeze Reynolds number equal to 10, and are larger thereafter. It is also shown that the added mass due to fluid inertia can be as high as 60 times the mass of the journal and thus cannot be neglected in the dynamic analysis of rotors incorporating squeeze film dampers. Also, it is shown that the classical lubrication theory is in error with respect to the pressure field and inertia forces, but predicts the velocity field reasonably accurately, for Reynolds number within the range of usual application of squeeze film dampers.

## Introduction

Squeeze film dampers (SFDs) are damping devices used in gas turbine engines to damp the whirling vibration of rotors. Their ability to attenuate the amplitude of engine vibrations and to decrease the magnitude of the force transmitted to the engine frame makes them an attractive rotor support. Also, the energy removed in the dampers enhances the stability of the rotor-bearing system.

SFDs are usually designed based on Reynolds equation of the classical lubrication theory, which neglects the effects of fluid inertia. Recently, in their experiments on SFDs Tecza, *et. al.*<sup>9</sup> showed that fluid inertia may be a significant factor in determining the dynamic characteristics of SFDs. They encountered a critical speed in their experimental rig which they did not expect from their rotordynamic analysis. They attributed this critical to fluid inertia. This has prompted several investigations of the effects of fluid inertia in SFDs. Tichy<sup>10</sup> provided an explanation for the importance of fluid inertia in SFDs versus journal bearings. San Andrés and Vance<sup>6</sup> obtained the steady state response of a rotor incorporating SFDs, including fluid inertia effects by using an averaged momentum approximation.<sup>5</sup>

Perhaps one of the first attempts to study the effects of fluid inertia in hydrodynamic bearings, is the work of Smith.<sup>7</sup> Using a unique form of Reynolds equation, he was able to obtain inertia force coefficients for journal bearings, and his conclusion was that the effect of fluid inertia in oil film bearings is to introduce an added mass to the rotor and this may affect the dynamics of the rotor especially for short stiff rotors on wide bearings. Approximately a decade later Reinhardt and Lund<sup>4</sup> used a perturbation solution for small Reynolds number to obtain the force coefficients of journal bearings. They showed that fluid inertia introduces rather small corrections to the damping and stiffness coefficients of journal bearings and they also provided plots of inertia coefficients versus the eccentricity. They had to solve a set of differential equations numerically to arrive at these plots. Another notable paper, is the work of Szeri *et. al.*<sup>8</sup> They used a technique based on averaging the inertia forces across the film, to obtain the force coefficients in a squeeze film damper. They also had to solve the resulting differential equations numerically. A recent paper by Ramli *et. al.*<sup>3</sup> compares the results of Smith, Reinhardt and Lund, and Szeri *et. al.*; and concludes that they are in good agreement, especially for short bearings. It is pointed out, however, that Smith's approach has the advantage of computational simplicity, and leads to fairly simple asymptotic analytical expressions for very short, and very long bearings.

Here, we will show that for a SFD whose journal executes a small circular-centered whirl, the fluid inertia forces are equal to the viscous forces in the damper at squeeze Reynolds number equal to 10, and are larger thereafter. We will also show that for Reynolds number in the range of usual application of SFDs, the velocity profiles do not change much due to fluid inertia. That is, the classical lubrication theory is in error with respect to the pressure field and inertia forces, but predicts the velocity field reasonably accurately.

A recently developed model of fluid inertia in SFDs<sup>1</sup>, is based on the assumption that the velocity field predicted by the classical lubrication theory is not changed much by fluid inertia. This permits the kinetic coenergy of the fluid to be calculated, and the inertia forces to be obtained by Lagrange's equations as applied to an open system. This energy approximation has the advantage of the applicability to cavitated dampers, since it is essentially a control volume approach, and consequently can handle the free surfaces that arise due to cavitation. This model is used in this paper to predict the fluid inertia forces in SFDs whose journal execute a large amplitude orbit. The damping forces in the SFDs are obtained by Reynolds equation.

## Squeeze Film Dampers

Figure 1 shows the construction of squeeze film dampers. In a typical application, the damper consists of an oil film in an annulus surrounding a rolling element bearing whose outer race is constrained from rotating, usually by a squirrel cage. Thus the spinning of the rotor does not reach the oil, and only when the rotor whirls does the oil film act to damp the motion. The squirrel cage serves to center the journal in the sleeve as well as to keep the outer race of the rolling element bearing from spinning.

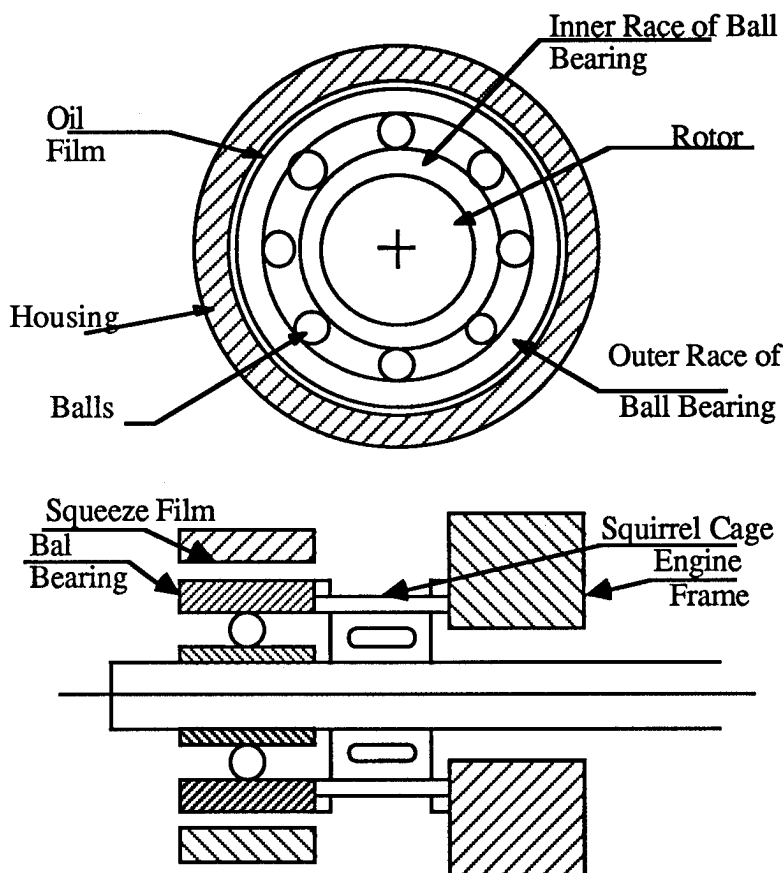


Figure 1 Construction of squeeze film dampers

Figure 2 shows a SFD, and the coordinate systems used. The film thickness  $h$  at any given location is given by

$$h = c - e \cos \theta \quad (1)$$

where  $c$  is the clearance,  $e$  is the eccentricity of the journal and  $\theta$  is measured from the positive  $r$ -axis of the whirling coordinate system ( $r, t, z$ ). The  $z$ -axis is perpendicular to the plane of the paper. Also shown in Figure 2, the stationary coordinate system ( $x, y, z$ ) and the angle  $\phi$  which is measured from the positive  $x$ -axis, and  $\theta = \phi - \psi$ . For a steady circular whirl  $\psi = \omega t$ , where  $\omega$  is the whirling frequency of the journal and  $t$  is time. The flow in the damper is described with respect to the stationary coordinate system ( $X, Y, Z$ ) shown in Figure 2.

In SFDs the ratio of the clearance  $c$  to the radius  $R$  is of the order of  $10^{-3}$ , such that the effects of curvature can be neglected, and we can use the stationary cartesian ( $X, Y, Z$ )

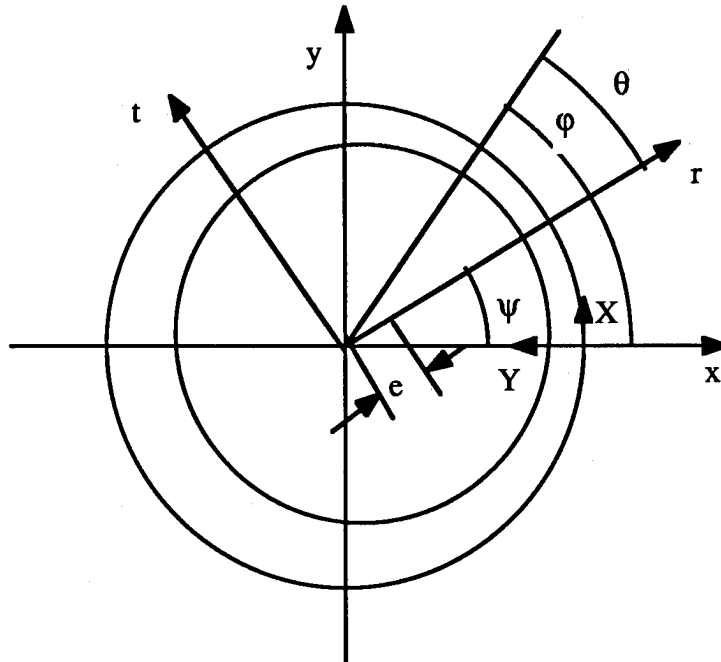


Figure 2 Coordinate frames

coordinate system shown in Figure 2, (with the Z-axis perpendicular to the plane of the paper), to describe the flow. To an observer in this coordinate system, because  $c/R$  is small, it appears as if the damper is unwrapped, as shown in Figure 3. The upper surface in Figure 3 represents the journal, while the lower surface represents the bearing. The motion of the journal, i.e. the upper surface in Figure 3, results in the motion of the fluid in the clearance between the two surfaces. Due to the motion of the journal, the upper surface in Figure 3 travels in a wave-like fashion, and also changes its shape if the journal is moving radially. It should be noted that since the flow in the damper is cyclic, i.e. the conditions at  $\phi = 0$  are the same as those at  $\phi = 2\pi$ , then the model of Figure 3 is repeated every  $2\pi R$  in the X-direction.

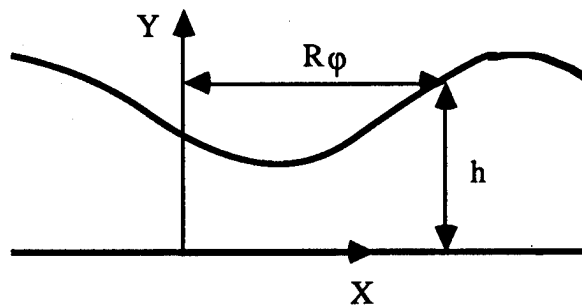


Figure 3 Unwrapped squeeze film damper

The damping forces in SFDs are obtained by the solution of Reynolds equation for fluid lubrication. There are two mathematical approximations to Reynolds equation, that have physical significance, namely the short bearing approximation and the long bearing approximation. In the short bearing approximation to Reynolds equation, which is justified if the damper is short in the axial direction, the flow in the damper is axial rather than circumferential, and thus the axial pressure gradient is much larger than the circumferential pressure gradient. On the other hand, in the long bearing approximation to Reynolds

equation, which is justified if the damper is long in the axial direction, the flow in the damper is circumferential, and thus the circumferential pressure gradient is much larger than the axial pressure gradient. In practice, if the damper is tightly sealed, then the flow is circumferential even if the dampers are physically short. In this case, the long bearing approximation would describe the conditions in the damper better than the short bearing approximation.

Integrating the pressure obtained by the solution of Reynolds equation, we obtain the damping forces in SFDs, which take the form

$$F_{rc} = -C_{rr} \dot{e} - C_{rt} e \dot{\psi} \quad (2)$$

$$F_{tc} = -C_{tr} \dot{e} - C_{tt} e \dot{\psi} \quad (3)$$

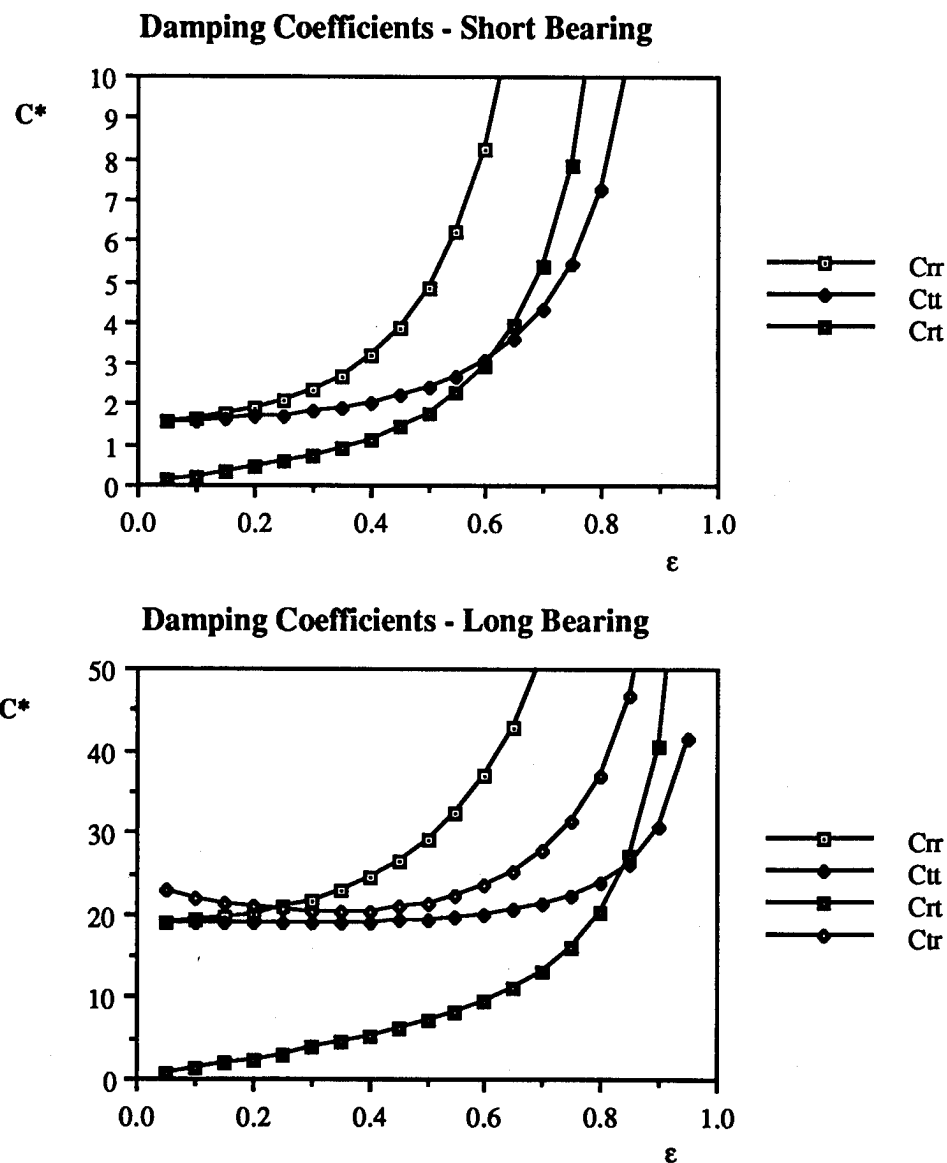


Figure 4 Damping coefficients (nondimensional) vs  $\epsilon$



where  $F_{rc}$  and  $F_{tc}$  are the radial and tangential damping forces, respectively, and  $\dot{e}$  and  $e\dot{\psi}$  are the radial and tangential velocities, respectively. The damping coefficients  $C_{rr}$ ,  $C_{tt}$ ,  $C_{tr}$  and  $C_{rt}$  are in general nonlinear functions of the position and velocity of the journal in the damper. Figure 4 shows a plot of the damping coefficients  $C_{rr}$ ,  $C_{tt}$ ,  $C_{tr}$  and  $C_{rt}$  versus the eccentricity ratio  $\epsilon$ , which is defined as the ratio  $e/c$ , for a cavitated damper using the  $\pi$ -film theory and nearly circular-centered whirl. It can be seen from Figure 4 that the damping coefficients for the short and long bearing approximations are nonlinear functions of the position of the journal in the damper. In fact, the damping coefficients increase as the eccentricity increases, and this, in one sense, is a desirable characteristic, since the damper provides more damping as the amplitude of the whirl increases which is obviously beneficial. Perhaps, this is why squeeze film dampers are such effective damping devices. On the other hand, it is precisely this nonlinear characteristic that results in the nonlinear behavior of the rotor-bearing system (jump resonance, subharmonic motion, ... etc.). Note that, in Figure 4, the damping coefficients  $C_{rt}$  and  $C_{tr}$  are equal for the short bearing.

### Fluid Inertia Forces in SFDs

To calculate the fluid inertia forces in the damper for a general orbit, it would be nearly impossible to solve the governing equations analytically, except in very special cases. Thus we have to resort to an approximate method to estimate the fluid inertia forces in the damper. We are going to use the energy method developed by El-Shafei<sup>1</sup>, which relies on the assumption that the velocity profiles in the damper can be approximated by the solution of the classical lubrication theory, which will be shown to be a valid assumption in the next section. This permits the kinetic coenergy of the fluid to be calculated, and the inertia forces to be obtained by Lagrange's equations as applied to an open system.

For a short damper, the axial velocity profile predicted by the classical lubrication theory is given by

$$w = \frac{6z}{h} \left( \frac{Y}{h} - \frac{Y^2}{h^2} \right) (e\dot{\psi} \sin \theta + \dot{e} \cos \theta) \quad (4)$$

while for a long damper the circumferential velocity profile predicted by the classical lubrication theory is given by

$$u = \frac{6R}{h} \left( \frac{Y}{h} - \frac{Y^2}{h^2} \right) \left[ \sin \theta \dot{e} - \cos \theta e\dot{\psi} + \frac{3\epsilon}{(2+\epsilon^2)} e\dot{\psi} \right] \quad (5)$$

and thus the kinetic coenergy of the fluid in the damper, which is defined by

$$T^* = \frac{1}{2} \int_{\theta_1}^{\theta_2} \int_0^h \int_{-\frac{L}{2}}^{\frac{L}{2}} \rho (u^2 + v^2 + w^2) R d\theta dY dZ \quad (6)$$

where  $\rho$  is the density of the fluid,  $R$  is the radius of the damper and  $L$  is its length. Thus the kinetic coenergy of the fluid in the damper can be calculated as

$$T^* = \frac{1}{2} m_{rr} \dot{e}^2 + \frac{1}{2} m_{tt} (e\dot{\psi})^2 + m_{rt} \dot{e} e\dot{\psi} \quad (7)$$

where  $m_{rr}$ ,  $m_{tt}$  and  $m_{rt}$  represent the inertia coefficients of the damper. For a cavitated damper we are also going to assume the  $\pi$ -film theory<sup>2</sup>, while for an uncavitated damper we will have a full film, i.e. a  $2\pi$ -film.

The inertia forces in the damper can be obtained by Lagrange's equations, but since the damper is an open system (because of the fluid being squeezed out axially), Reynolds

transport theorem<sup>1</sup> must be used in conjunction with Lagrange's equations. Thus the radial and tangential inertia forces become

$$F_{i,r} = F_{ri} + R_{ri} \quad (8)$$

$$\text{and } F_{i,t} = F_{ti} + R_{ti} \quad (9)$$

where  $F_{i,r}$  is the radial inertia force and  $F_{i,t}$  is the tangential inertia force,  $R_{ri}$  and  $R_{ti}$  are the inertia forces due to the flux of the fluid particles across the control surface, in the r- and t- directions, respectively, and  $F_{ri}$  and  $F_{ti}$  are obtained by Lagrange's equations and are given by

$$F_{ri} = - \frac{d}{dt} \left( \frac{\partial T^*}{\partial \dot{e}} \right) + \frac{\partial T^*}{\partial e} \quad (10)$$

$$\text{and } F_{ti} = - \frac{1}{e} \frac{d}{dt} \left( \frac{\partial T^*}{\partial \dot{\psi}} \right) + \frac{1}{e} \frac{\partial T^*}{\partial \psi} \quad (11)$$

The flux terms  $R_{ri}$  and  $R_{ti}$  are given by

$$R_{ri} = - \int_{cs} \frac{\partial t^*}{\partial \dot{e}} \mathbf{V} \cdot \mathbf{n} \, dS + \int_{cs} t^* \frac{\partial (\mathbf{V} \cdot \mathbf{n})}{\partial \dot{e}} \, dS$$

$$R_{ti} = - \frac{1}{e} \int_{cs} \frac{\partial t^*}{\partial \dot{\psi}} \mathbf{V} \cdot \mathbf{n} \, dS + \frac{1}{e} \int_{cs} t^* \frac{\partial (\mathbf{V} \cdot \mathbf{n})}{\partial \dot{\psi}} \, dS$$

where  $t^*$  is the kinetic coenergy per unit volume,  $\mathbf{V}$  is the velocity of the fluid with respect to the control surface  $S$ ,  $\mathbf{n}$  is the outward normal vector on the control surface. On calculating the above equations, for a  $2\pi$ -film, with the journal executing a circular centered whirl, we get for the radial and tangential forces (including the damping forces)

$$F_r = m_r e \dot{\psi}^2 - C_{rt} e \dot{\psi} \quad (12)$$

$$F_t = - m_t e \dot{\psi}^2 - C_{tt} e \dot{\psi} \quad (13)$$

where for a short damper the coefficients are given by

$$m_r = \frac{\rho R L^3}{70 c} \frac{2\pi}{\epsilon^2} \left[ 27 - \frac{(27 - 17 \epsilon^2)}{(1 - \epsilon^2)^{1/2}} \right]$$

$$C_{tt} = \frac{\mu R L^3}{c^3} \frac{\pi}{(1 - \epsilon^2)^{3/2}}$$

while for a long damper the coefficients are given by

$$m_r = \frac{12}{10} \frac{\rho R^3 L}{c} \left\{ \frac{4\pi}{(2 + \epsilon^2)^2} \left[ 6 - \frac{(10 - \epsilon^2)(1 - \epsilon^2)^{1/2}}{(2 + \epsilon^2)} \right] \right\}$$

$$C_{tt} = \frac{\mu R^3 L}{c^3} \frac{24\pi}{(2 + \epsilon^2)(1 - \epsilon^2)^{1/2}}$$

where  $\mu$  is the viscosity of the fluid. For a  $2\pi$ -film, the coefficients  $m_t$  and  $C_{rt}$  are zero for both the long and short dampers. The above inertia coefficients are plotted in Figure 5 for a  $2\pi$ -film, for the short damper and for the long damper.

This model of fluid inertia was used by El-Shafei<sup>1,2</sup> to determine the unbalance response of Jeffcott rotors incorporating squeeze film dampers. Cavitated dampers were considered and the  $\pi$ -film theory was used. The results presented in the above mentioned references indicate that, in general, the effects of fluid inertia on the dynamics of the rotor are beneficial. Fluid inertia resulted in the decrease of the possibility of the jump resonance for the short damper, and resulted in better attenuation of the amplitude response at the critical speed. However, fluid inertia introduced an additional critical speed for the Jeffcott rotor, and this resulted in the decrease of the range of good vibration isolation for the dampers. Also, it was found that in general the long dampers are better at attenuating the amplitude response of the engine, while the short dampers are better at attenuating the magnitude of the force transmitted to the engine frame.

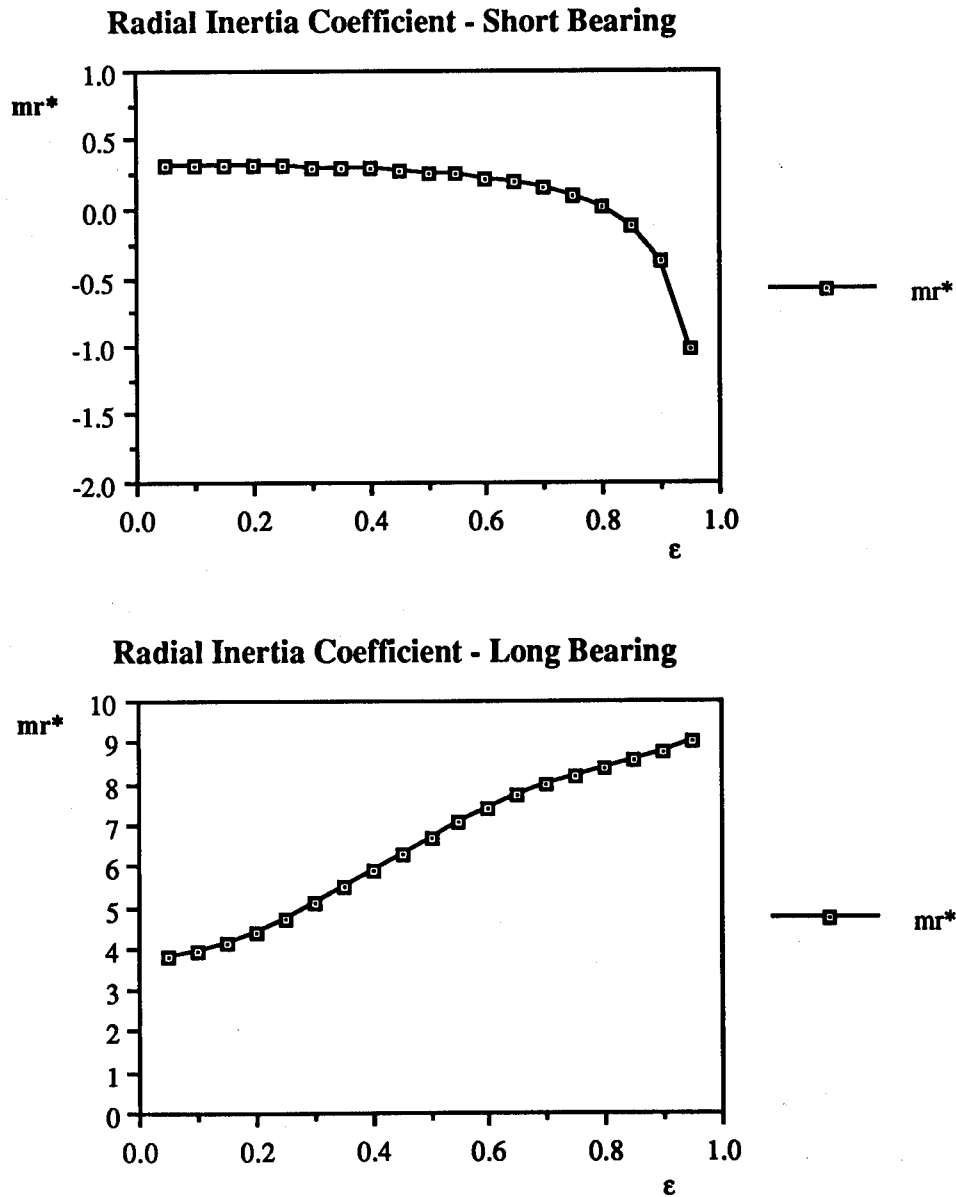


Figure 5 Inertia coefficients (nondimensional) vs  $\epsilon$

### Small Circular Centered Whirl

For a small circular centered whirl, that is with  $e \ll c$ , the convective acceleration terms in the Navier-Stokes equations can be neglected, and the governing equations for the flow in the damper become

$$\frac{\partial u}{\partial t} = -\frac{1}{\rho} \frac{\partial p}{\partial X} + \nu \frac{\partial^2 u}{\partial Y^2} \quad (14)$$

$$\frac{\partial p}{\partial Y} = 0 \quad (15)$$

$$\frac{\partial w}{\partial t} = -\frac{1}{\rho} \frac{\partial p}{\partial Z} + \nu \frac{\partial^2 w}{\partial Y^2} \quad (16)$$

and 
$$\frac{\partial u}{\partial X} + \frac{\partial v}{\partial Y} + \frac{\partial w}{\partial Z} = 0 \quad (17)$$

where  $\nu$  is the kinematic viscosity of the fluid,  $u$  is the velocity of the fluid in the X-direction,  $v$  is the velocity of the fluid in the Y-direction,  $w$  is the velocity of the fluid in the Z-direction, and  $p$  is the pressure. Furthermore, the boundary conditions on the upper surface of Figure 3, can be satisfied on the average. Thus the boundary conditions that equations (14-17) have to satisfy are

$$\text{At } y = 0 \quad u = 0 \quad v = 0 \quad w = 0 \quad (18)$$

$$\text{At } y = c \quad u = U \quad v = V \quad w = 0$$

where, for a circular whirl  $U$  and  $V$  are given by

$$U = \text{Real} \{ e \omega e^{i\theta} \}$$

$$V = \text{Real} \{ i e \omega e^{i\theta} \}$$

where  $i = (-1)^{1/2}$  and  $\omega = \dot{\psi}$  is the frequency of the whirl. In this case  $\theta = \phi - \omega t$  which suggests that the upper surface of Figure 3, travels like a wave, and thus we should seek a solution in the form

$$u = U_0 e^{i\theta} \quad v = V_0 e^{i\theta} \quad w = W_0 e^{i\theta} \quad p = P_0 e^{i\theta} \quad (19)$$

where  $U_0$ ,  $V_0$  and  $W_0$  are functions of  $Y$  and  $Z$ , while  $P_0$  is a function of  $Z$  only. Substituting (19) into (14), we get

$$\frac{d^2 U_0}{dY^2} + \frac{i \rho \omega}{\mu} U_0 = \frac{i}{\mu R} P_0$$

which can be solved for  $U_0$  using the boundary conditions (18), thus, neglecting terms of  $O(c/R)$ , we get

$$U_0 = \frac{P_0}{\rho \omega R} \left[ \frac{\sinh(s(Y-c)) - \sinh(sY) + \sinh(sc)}{\sinh(sc)} \right] \quad (20)$$

where

$$s = \frac{1}{c} \sqrt{\frac{\text{Re}}{2}} (1-i)$$

and  $\text{Re} = \rho \omega c^2 / \mu$  is the squeeze Reynolds number. Substituting (19) into (16), we get

$$\frac{d^2 W_0}{dY^2} + \frac{i \rho \omega}{\mu} W_0 = \frac{1}{\mu} \frac{dP_0}{dZ}$$

which can be solved for  $W_0$  using the boundary conditions (18), thus

$$W_0 = -\frac{i}{\rho \omega} \frac{dP_0}{dZ} \left[ \frac{\sinh(s(Y-c)) - \sinh(sY) + \sinh(sc)}{\sinh(sc)} \right] \quad (21)$$

Substituting (19), (20) and (21) into the continuity equation, equation (17), we get

$$\frac{\partial V_0}{\partial Y} = \frac{i}{\rho \omega} \left( \frac{d^2 P_0}{dZ^2} - \frac{1}{R^2} P_0 \right) \left[ \frac{\sinh(s(Y-c)) - \sinh(sY) + \sinh(sc)}{\sinh(sc)} \right]$$

The above equation can be integrated over  $Y$  and using the boundary condition  $V_0 = 0$  at  $Y=0$ , we get

$$V_0 = \frac{i}{\rho \omega} \left( \frac{d^2 P_0}{dZ^2} - \frac{1}{R^2} P_0 \right) \left[ \frac{\cosh(s(Y-c)) - \cosh(sY) + sY \sinh(sc) + 1 - \cosh(sc)}{s \sinh(sc)} \right]$$

The other boundary condition that  $V_0$  has to satisfy, namely, at  $Y=c$  the velocity  $V_0 = i e \omega$ , gives us

$$\frac{d^2 P_0}{dZ^2} - \frac{1}{R^2} P_0 = \frac{\rho e \omega^2}{c} \left[ \frac{sc \sinh(sc)}{2 - 2 \cosh(sc) + sc \sinh(sc)} \right] \quad (22)$$

which is a differential equation that the pressure  $P_0$  has to satisfy together with the boundary conditions

$P_0 = 0$  at  $Z = \pm L/2$   
and on solving (22) we get

$$P_0 = \frac{\rho e \omega^2 R^2}{c} \left[ \frac{sc \sinh(sc)}{2 - 2 \cosh(sc) + sc \sinh(sc)} \right] \left\{ \frac{\cosh\left(\frac{2Z}{D}\right)}{\cosh\left(\frac{L}{D}\right)} - 1 \right\} \quad (23)$$

where  $D = 2R$  is the diameter of the damper. Equation (23) is a finite length solution for the pressure  $P_0$  in a squeeze film damper whose journal executes a small circular-centered whirl, which is valid for all  $Re$  (in the laminar regime).

If we substitute the pressure from equation (23) into equations (20) and (21) we will get the velocity profiles in the damper. If we take the limit as  $L/D \rightarrow 0$ , i.e. the short damper case, the axial velocity profiles, for  $Z = L/4$ ,  $R = 1.25$  in.,  $c = 8$  mils and  $\theta = 1$  rad, are shown in Figure 6 for various  $Re$ . Plotted on the same figure is the velocity profile obtained by the classical lubrication theory for a short damper. SFDs usually operate at Reynolds number of the order of 20, and it can be seen from Figure 6 that the velocity profiles of short SFDs do not change much due to fluid inertia, in the range of usual application of SFDs.

If we take the limit of the velocity profiles as  $L/D \rightarrow \infty$ , i.e. the long damper case, the circumferential velocity profiles, for the same data as Figure 6, are shown in Figure 7 for various  $Re$ . Also plotted on the Figure 7 is the velocity profile obtained by the classical lubrication theory for a long damper. Although the velocity profiles of the long dampers are more sensitive to  $Re$  than those of the short damper, yet it may be concluded that also for the long dampers, in the range of usual application of SFDs, the velocity profiles do not change much due to fluid inertia.

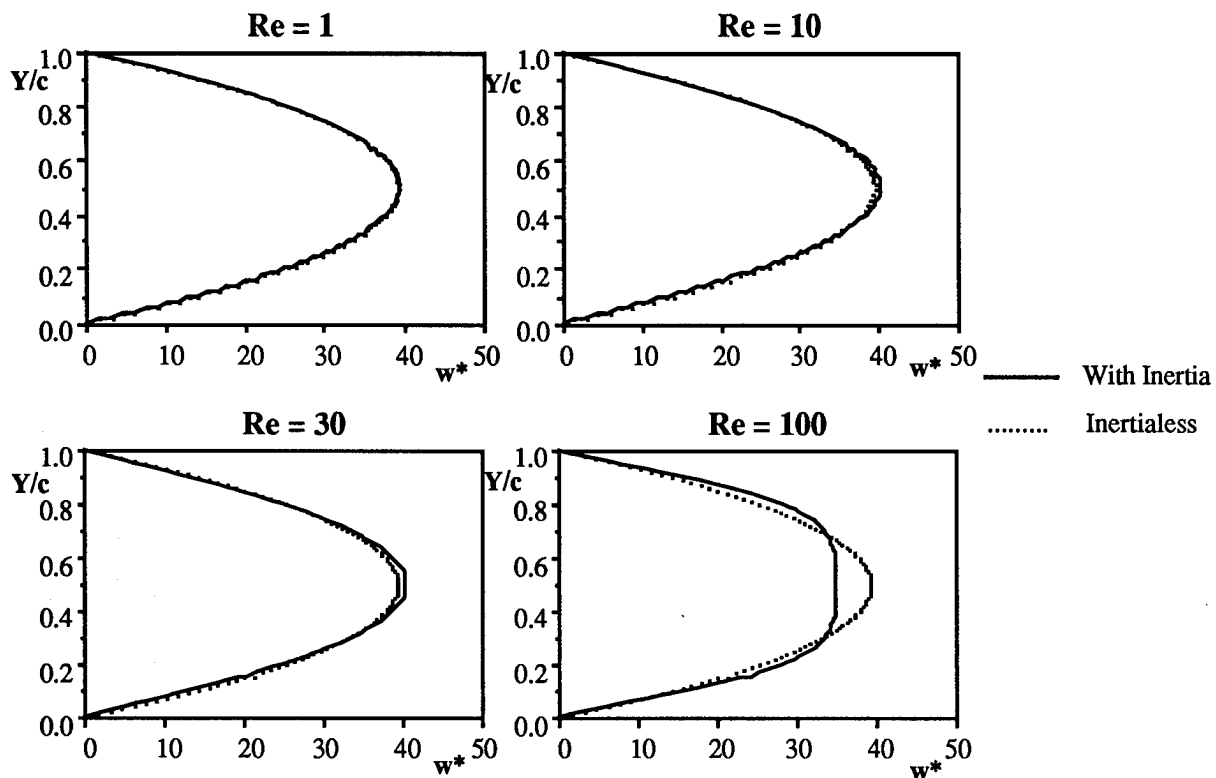


Figure 6 Velocity profiles - Short bearing (nondimensional)

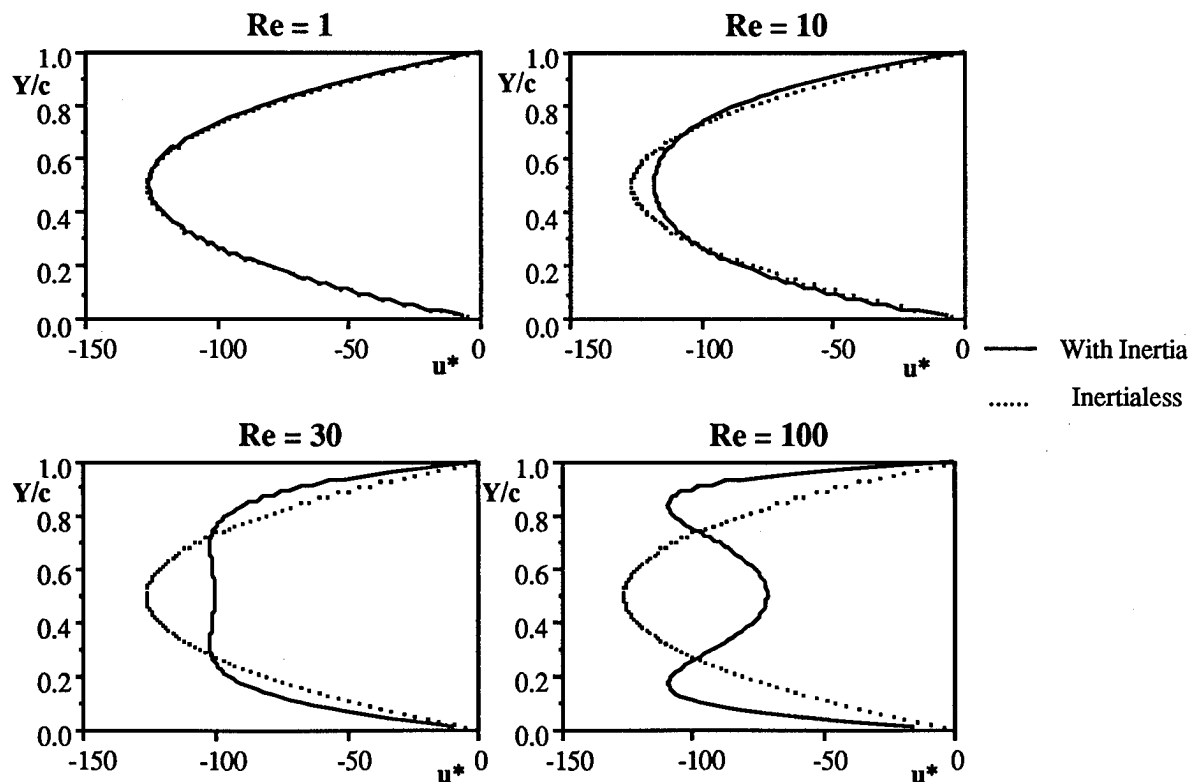


Figure 7 Velocity profiles - Long bearing (nondimensional)

The pressure in the damper is given by

$$p = \text{Real} \left\{ \left[ \frac{\rho e \omega^2 R^2}{c} \frac{s c \sinh(s c)}{2 - 2 \cosh(s c) + s c \sinh(s c)} \right] \left[ \frac{\cosh\left(\frac{2Z}{D}\right)}{\cosh\left(\frac{L}{D}\right)} - 1 \right] e^{i\theta} \right\} \quad (24)$$

The pressure in equation (24) depends on  $Re$  only through the terms inside the first square bracket, namely

$$f(Re) = \left[ \frac{\rho e \omega^2 R^2}{c} \frac{s c \sinh(s c)}{2 - 2 \cosh(s c) + s c \sinh(s c)} \right] \quad (25)$$

If we take the limit as  $Re \rightarrow 0$  of equation (25) we get

$$\lim_{Re \rightarrow 0} f(Re) = \frac{12 R^2 \mu e \omega}{c^3} \left( i + \frac{Re}{10} \right) \quad (26)$$

Figure 8 shows a plot of the real and imaginary parts of  $f(Re)$  versus  $Re$  as predicted from equation (25). Also plotted on Figure 8 are the real and imaginary parts of the limit of  $f(Re)$

### Pressure Dependence on $Re$

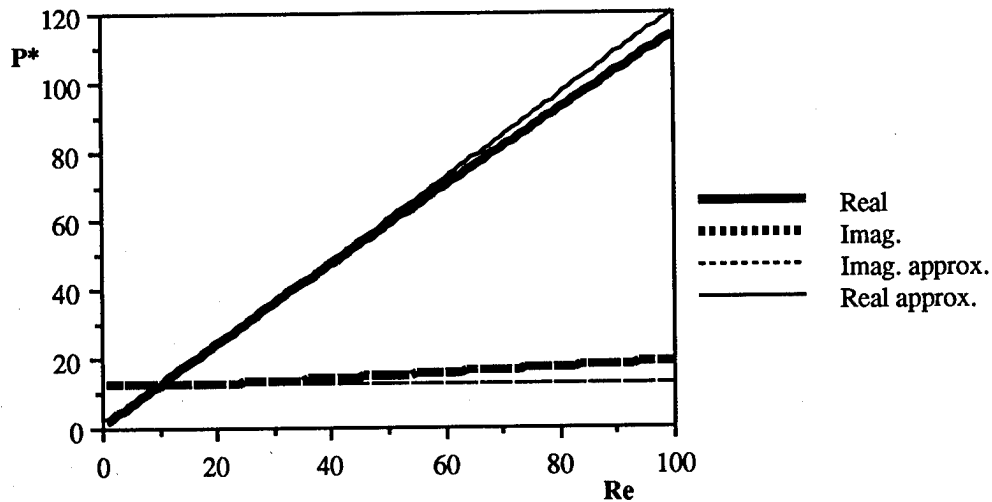


Figure 8 Nondimensional pressure vs.  $Re$

as  $Re \rightarrow 0$ , equation (26), from which it is clear that equation (26) is a good approximation of equation (25) for  $Re$  up to about 50. If we make an analogy with a mass dashpot system, it can be shown that the imaginary parts of equations (25) and (26) represent the contribution of the viscous force, while the real parts of equations (25) and (26) represent the contribution of the inertia force. In fact, the imaginary part of the approximation of equation (26) is equal to the contribution of the viscous force as predicted by the classical lubrication theory, and the real part of the approximation of equation (26) is equal to the contribution of the inertia force as predicted by the energy method described in the previous section.<sup>1</sup> Thus, it may be concluded that the energy method predicts the inertia effects reasonably accurately, in the range of application of SFDs, and this is true even for long dampers whose velocity profiles are more sensitive to  $Re$ . It is clear from Figure 8 that the inertia force is equal to the viscous force for  $Re=10$ , and is larger thereafter. In fact, the inertia force is about 4 times as large as the viscous force at  $Re = 40$ , and we can say that, at such high  $Re$ , the damper is totally dominated by the inertia forces.

The forces acting on the journal can be obtained by integrating equation (24), thus

$$F_r = - \int_{-\frac{L}{2}}^{\frac{L}{2}} \int_{\theta_1}^{\theta_2} p \cos \theta R d\theta dZ$$

$$F_t = - \int_{-\frac{L}{2}}^{\frac{L}{2}} \int_{\theta_1}^{\theta_2} p \sin \theta R d\theta dZ$$

Now using the limit of  $f(Re)$ , equation (26), in equation (24), the forces acting on the journal become

$$F_r = 12 \frac{\mu R^3 L}{c^3} e \omega \left\{ 1 - \frac{\tanh\left(\frac{L}{D}\right)}{\frac{L}{D}} \right\} \left[ - \int_{\theta_1}^{\theta_2} \sin \theta \cos \theta d\theta + \frac{Re}{10} \int_{\theta_1}^{\theta_2} \cos^2 \theta d\theta \right] \quad (27)$$

$$F_t = 12 \frac{\mu R^3 L}{c^3} e \omega \left\{ 1 - \frac{\tanh\left(\frac{L}{D}\right)}{\frac{L}{D}} \right\} \left[ - \int_{\theta_1}^{\theta_2} \sin^2 \theta d\theta + \frac{Re}{10} \int_{\theta_1}^{\theta_2} \sin \theta \cos \theta d\theta \right] \quad (28)$$

where the quantity

$$K_L = \left\{ 1 - \frac{\tanh\left(\frac{L}{D}\right)}{\frac{L}{D}} \right\}$$

has been termed a leakage factor by Warner<sup>11</sup> which accounts for the finiteness of the damper. Equations (27) and (28) represent a finite length solution to the governing equations. To be able to compare the results of the kinetic coenergy method with the above equations, we have to consider the limiting cases of long and short dampers. For a long

damper  $L/D \rightarrow \infty$  thus  $K_L \rightarrow 1$ , and for a short damper  $L/D \rightarrow 0$  thus  $K_L \rightarrow \frac{1}{3} \left( \frac{L}{D} \right)^2$

For a long damper with  $2\pi$ -film equations (27) and (28) become

$$F_r = 12 \frac{\rho R^3 L}{10 c} \pi e \omega^2 \quad (29)$$

$$F_t = - 12 \frac{\mu R^3 L}{c^3} \pi e \omega$$

The radial force is the centrifugal force and the tangential force is the damping force. These forces are the forces acting on the journal when it executes a small circular-centered orbit in a  $2\pi$ -film. These are the same forces as those predicted by equation (12) for  $F_r$  and (13) for  $F_t$ , if we take the limit as  $\epsilon$  tends to zero of the inertia and damping coefficients, which is the condition of a small orbit.

Similarly, for a short damper with  $2\pi$ -film equations (27) and (28) become

$$F_r = \frac{\rho R L^3}{10 c} \pi e \omega^2 \quad (30)$$



$$F_t = - \frac{\mu R L^3}{c^3} \pi \epsilon \omega$$

The radial force is the centrifugal force and the tangential force is the damping force. These forces are the forces acting on the journal when it executes a small circular-centered orbit in a  $2\pi$ -film. These are the same forces as those predicted by equation (12) for  $F_r$  and (13) for  $F_t$ , if we take the limit as  $\epsilon$  tends to zero of the inertia and damping coefficients, which is the condition of a small orbit. Thus it may be concluded that the forces acting on the journal when it executes a small circular-centered orbit in a squeeze film damper, obtained by taking the limit as  $Re \rightarrow 0$  of the solution of the governing partial differential equations, are the same as those predicted by the kinetic coenergy method.

Equation (29), for a long damper, indicates that the radial force is proportional to the centrifugal acceleration, thus the proportionality constant represents the added mass to the journal  $m_{ad}$

$$m_{ad} = 12 \frac{\pi \rho R^3 L}{10 c}$$

and the mass of the journal is  $m_j$

$$m_j = \rho_{st} \pi R^2 L$$

where we assumed that the journal is made of steel and  $\rho_{st}$  is the density of steel. Then the ratio of the added mass to the mass of the journal is

$$\frac{m_{ad}}{m_j} = \frac{12}{10} \frac{\rho}{\rho_{st}} \frac{R}{c}$$

For typical SFDs, the ratio  $R/c$  is 1000 and the density of oil is approximately  $800 \text{ kg/m}^3$ , and the density of steel is approximately  $7800 \text{ kg/m}^3$ , then the added mass to the journal due to the oil film is approximately 60 times the mass of the journal. This is because of the huge velocities and accelerations that the fluid undergoes in a SFD.

Similarly, for a short damper, from equation (30), the added mass to the journal is

$$m_{ad} = \frac{\pi \rho R L^3}{10 c}$$

and the ratio of the added mass to the mass of the journal is

$$\frac{m_{ad}}{m_j} = \frac{1}{10} \frac{\rho}{\rho_{st}} \frac{L^2}{R^2} \frac{R}{c}$$

If we assume  $R=L$ , and the typical values for the other parameters we used with the long dampers, then we find that the added mass to the journal due to the oil film is approximately 10 times the mass of the journal. The short dampers have a smaller added mass than the long dampers because the flow in the long dampers is the same at each section in the axial direction and thus every section is resisting the squeezing by the journal in the same manner, while for the short dampers the flow at each section in the axial direction varies linearly with the axial coordinate  $Z$ , and in fact is equal to zero at the middle of the damper. Thus the short dampers exhibit less resistance to the squeezing motion, and thus exhibit a smaller added mass.

## Conclusion

Fluid inertia can be very important in squeeze film dampers. The added mass to the journal was shown to be as high as 60 times the mass of the journal, for small circular centered whirl, which cannot be neglected in the dynamic analysis of rotors incorporating

squeeze film dampers. Also, for the case of small circular centered whirl, it was shown that the fluid inertia forces are equal to the viscous forces in the damper at squeeze Reynolds number equal to 10, and are larger thereafter.

Also it was shown that, for Reynolds number within the range of usual application of squeeze film dampers, the classical lubrication theory predicts the velocity profiles fairly accurately, which permits the kinetic coenergy of the fluid in the damper to be calculated. Finally it was shown that the fluid inertia forces predicted by the kinetic coenergy method are equal to those obtained by the solution of the governing equations for a small circular centered whirl.

## References

- [1] El-Shafei, A., "Dynamics of Rotors Incorporating Squeeze Film Dampers", Ph.D. Thesis, Department of Mechanical Engineering, Massachusetts Institute of Technology, Cambridge, MA, 1988.
- [2] El-Shafei, A., "Unbalance Response of a Jeffcott Rotor Incorporating Short Squeeze Film Dampers", ASME paper 89 - GT - 75, 1989.
- [3] Ramli, M.D., J. Ellis, and J.B. Roberts, "On the Computation of Inertial Coefficients in Squeeze-Film Bearings", Proc. I.Mech.E., Vol. 201, No. C2, 1987, pp. 125-131.
- [4] Reinhardt, E., and J.W. Lund, "The Influence of Fluid Inertia on the Dynamic Properties of Journal Bearings", Journal of Lubrication Technology, Trans. ASME, Vol. 97, No. 2, 1975, pp.159-167.
- [5] San Andrés, L.A. and J.M. Vance, "Effects of Fluid Inertia and Turbulence on the Force Coefficients for Squeeze Film Dampers", Journal of Engineering for Gas Turbine and Power, Trans. ASME, Vol. 108, No. 2, April 1986, pp. 332-339.
- [6] San Andrés, L.A. and J.M. Vance, "Effect of Fluid Inertia on Squeeze-Film Damper Forces for Small-Amplitude Circular-Centered Motions", ASLE preprint 86 - AM - 3A - 3, 1986.
- [7] Smith, D.M., "Journal Bearing Dynamic Characteristics - Effect of Inertia of Lubricant", Proc. I.Mech.E., 1964-1965, Vol. 179, pp. 37-44.
- [8] Szeri, A.Z., A.A. Raimondi, and A. Giron-Durate, "Linear Force Coefficients of Squeeze Film Dampers", Journal of Lubrication Technology, Trans. ASME, 1983, pp. 326-334.
- [9] Tecza, J.A., J.C. Giordano, E.S. Zorzi, and S.K. Drake, "Squeeze Film Damper Technology : Part 2 - Experimental Verification Using a Controlled Orbit Test Rig", ASME paper 83 - GT - 248, 1983.
- [10] Tichy, J.A., "The Effect of Fluid Inertia in Squeeze Film Damper Bearings : A Heuristic and Physical Description", ASME paper 83 - GT - 177, 1983.
- [11] Warner, P.C., "Static and Dynamic Properties of Partial Journal Bearings", Journal of Basic Engineering, Trans. ASME, June 1963, pp. 247-257.

## **A NEW CLASS OF FLUID-LOOP DAMPERS**

**A.BAZ , L.GUMUSEL**  
Mechanical Engineering Dept.  
The Catholic University  
Washington, DC 20064

and

**J.FEDOR**  
NASA- Goddard Space Flight  
Center  
Greenbelt, MD 20771

### **A B S T R A C T**

This paper presents a new class of fluid-loop dampers which is radically different from conventional nutation dampers routinely used on spinning spacecrafts. The new damper relies in its operation on the introduction of floating spheres into the fluid loops to enhance the energy dissipation mechanism . In this way the new damper can provide improved damping characteristics over a wide frequency band. It can also be lighter in weight than conventional dampers, as it requires shorter loops to achieve same damping ratio. Furthermore, the new damper eliminates the need for using the partially-filled fluid-loop approach to enhance the damping . Such an approach is found to be at the expense of altering the dynamic symmetry of the spacecraft when the liquid-gas mixture starts oscillating.

A prototype of the damper is built and tested to demonstrate the feasibility of this new class of dampers. The tests are used to study the effect of varying the concentration of the floating spheres on the dynamic characteristics of the damper.

The results obtained indicate the effectiveness of the new damper in suppressing the vibration of flexible systems as compared to the conventional fluid-loop damper. The results suggest also the potential of the proposed concept in providing a damper with multi-axes damping capability which can be used in various spacecraft applications.

## 1. INTRODUCTION

Fluid-loop dampers have been recognized for many years as simple and effective means for damping the vibration of spinning satellites. The damper consists of a loop, mounted in a plane perpendicular to the spin axis, which is filled with a moderately viscous fluid. When the satellite is subjected to excitations due to the deployment of antennas or booms, for example, it undergoes oscillatory motion that forces the fluid to flow relative to the loop walls. Such relative motion is resisted by the fluid viscous forces which results in dissipating the satellite's oscillation energy.

The fluid-loop damper was first considered, in 1965, for use on NASA's 21 Man Space Station<sup>1,2</sup> because it compares favorably with all other known dampers such as the mercury ring damper<sup>1</sup>, the mechanical pendulum damper<sup>1</sup>, the controlled damping pendulum<sup>1</sup> and the ball-in-tube pendulum<sup>3</sup>. Since then it has been extensively utilized in numerous space systems as, for example, the IMP-J<sup>4</sup> spacecraft and the Helios satellites<sup>5</sup>. Also, many future satellites, such as NASA's CRRES satellite<sup>6</sup>, are now designed to incorporate a fluid-loop damper of one type or another.

In most cases<sup>2,7,8,9</sup>, the loop dampers used are of the fully-filled type mainly because they do not alter the dynamic symmetry of the satellite. However, because of the low frequency nature of the encountered oscillations and subsequently the low flow velocities, the loops have to be long enough to render them effective. Accordingly, fully-filled loop dampers can be rather heavy if high damping characteristics are desired. For this reason, the partially-filled dampers have been introduced<sup>1,3,6,10</sup>. These dampers are found to have considerably higher damping characteristics than their fully-filled counterparts but at the expense of altering the satellite dynamic symmetry as the liquid plug starts oscillating. Furthermore, for their operation to be effective additional offset from the spin axis is needed. Also, the design intricacies of this type of dampers are rather involved because the flow is no longer single-phase and laminar as in the case of the fully-filled dampers. Proper tuning is essential to achieve effective vibration damping when relying on the partially-filled damper. This tuning is not necessary in the case of the fully-filled damper.

To avoid the limitations of the fully-filled dampers and the drawbacks of the partially-filled dampers, this study has been initiated. The study aims primarily at investigating the feasibility of a new class of fluid-loop dampers that combines the advantages of the fully and the partially-filled loop dampers. In other words, the new dampers will maintain the dynamic symmetry of the satellite and, at the same time, have high damping characteristics.

The concept of the new damper is introduced in section 2 of this paper, its experimental performance is presented in section 3 in comparison with conventional loop dampers and section 4 includes the conclusions.

## 2. CONCEPT OF THE NEW DAMPER

The idea of the new damper is conceived to avoid the above mentioned drawbacks of conventional fluid-loop dampers whether of the fully or the partially-filled types. The new damper belongs to the class of fully-filled dampers whose damping characteristics are enhanced by introducing floating spheres into its fluid loops.

The introduced spheres tend to increase the effective shear resistance of the resulting solid-liquid mixture due to several reasons. The first is attributed to the increase of the surface area of interaction between the solid and the liquid components which, in turn, increases proportionately the viscous drag resistance of the mixture. Secondly, additional form drag forces are developed by virtue of the relative motion between the spheres and the liquid layers. These forces are accompanied with flow separation on the spheres' surfaces which results in the generation of eddies and vortices. Both the viscous and the form drag components contribute considerably to the dissipation of the energy imparted to the loop. This is more and above the energy dissipated by the viscous friction resistance between the liquid and the tube walls as well as between the adjacent liquid layers as is the case in conventional fluid-loop dampers.

A third source of energy dissipation, in the new damper, results from the continuous acceleration and deceleration of the floating spheres as the fluid-loop undergoes its oscillatory motion.

All the above mentioned sources of energy dissipation account for the improved damping characteristics of the new damper.

The merits of the new damper can best be understood by considering the pressure drop-flow characteristics of solid-liquid mixtures flowing in straight tubes. Such characteristics is shown in Figure 1 along with that of pure liquid flowing in straight tubes<sup>11,12</sup>

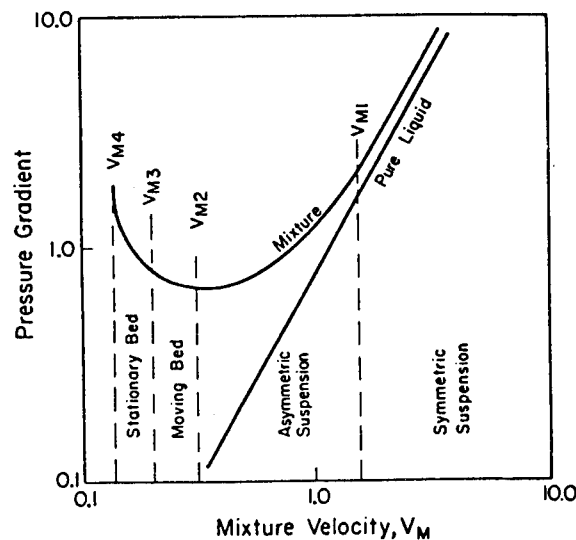


Figure 1 - Frictional resistance of solid-liquid mixtures.

From the figure, it can be seen that liquid-filled loops exhibit low but linear pressure drop-flow characteristics. Accordingly, at low nutation frequencies, the flow velocity of the fluid relative to the loop will be also low so will be the friction resistance and the energy dissipation. But, once the floating spheres are introduced, the frictional characteristics are improved particularly at low relative velocities as can be seen from Figure 1. Such an improvement is attributed to the fact that damping is not only limited to the frictional resistance at the boundaries of the loop but is enhanced by the additional energy dissipation mechanisms resulting from the relative motion between the fluid and the floating spheres.

Accordingly, it is expected that the new damper will have high damping characteristics which extend over a wide flow velocities (i.e. frequency bandwidth). Fewer number of fluid loops will be necessary to suppress the encountered vibrations. Furthermore and most importantly, the proposed damper can be effective in damping out multi-directional vibrations unlike conventional fluid-loop dampers which are only effective in resisting vibration in the plane of the loop. Such multi-directional damping capabilities result from the ability of the floating spheres to move in the vibration direction relative to the fluid.

With such features, the new damper can be very practical and simple means for damping vibrations, isolating payloads and solar panels as well as other space applications.

### **3.EXPERIMENTAL PERFORMANCE OF THE DAMPER**

#### **3.1. Experimental set-up**

A prototype of the fluid-loop damper is built from a transparent tygon tubing (A) that has an internal radius  $a = 1.1$  cm. The tube is formed into a loop that has a radius  $R = 25$  cm. The ends of the tube are joined by a plastic union which is machined to provide a smooth joint. The union is provided with a bleed valve to ensure that the loop is completely filled with liquid without any entrapped air.

The loop is mounted on a pendulum (B) which is pivoted around pivot (O) as shown in Figure 2. A weight ( $W = 1.95$  kg) is fixed to the pendulum at a distance ( $L_p$ ) from the pivot (O). The pendulum is displaced, in all the tests, an initial angle  $\vartheta_0 = 20^\circ$  from the vertical and then allowed to oscillate freely until it comes to complete stop. The instantaneous angular position of the pendulum is monitored by a position sensor (C) of the potentiometric type. The sensor signal is recorded on a chart recorder for further analysis.

#### **3.2. Experimental procedures**

The performance of the new damper is evaluated by conducting three series of tests. These tests aim at measuring the decay of the amplitude of oscillation of the pendulum alone, the pendulum with the in-active damper

and the pendulum with the active damper. The tests are repeated for different levels of concentration of the floating spheres. The results obtained are compared with those of conventional liquid-filled dampers to define the merits and the limitations of the new damper.

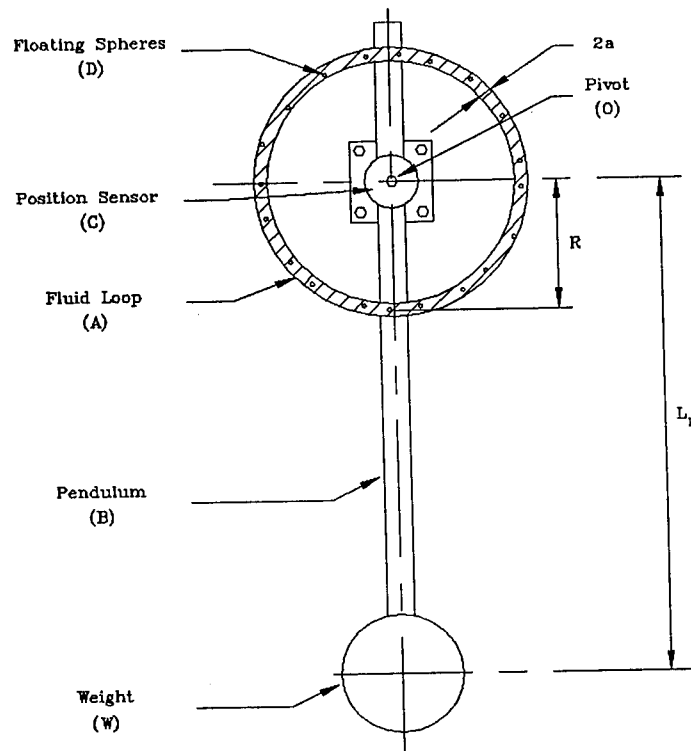


Figure 2 - Schematic drawing of the experimental set-up.

In the first series of tests, the pendulum alone is displaced from the vertical an angle  $\vartheta_0 = 20^\circ$  and left to oscillate freely until it stops. The time history of the angular position of the pendulum is recorded. The decay of the amplitude of oscillations is used to compute the inherent natural damping of the pendulum resulting from the friction in the pivot, the friction in the position sensor and the air drag on the pendulum arm.

In the second series of tests, the fluid-loop is filled with the working fluid which is a mixture of water and alcohol. The loop is plugged by placing a flat disc inside the plastic union. In this way, the liquid is prevented from flowing through the loop and the damper becomes in-active. The plugged damper is placed on the pendulum and the decay of the amplitude is measured using the logarithmic decrement  $\delta$  approach<sup>13</sup>. The obtained value of  $\delta$  serves as a datum for measuring the effectiveness of the damper when it is activated by unplugging its loop as well as when the floating spheres are introduced in it during the third group of tests.

### 3.3. Experimental results

Figure (3) shows a sample of the time history of the amplitude of oscillation of the pendulum when tested alone and with conventional liquid damper. Figure (4) shows the corresponding characteristics of the new damper for different concentrations of the floating spheres. The displayed results are obtained when the pendulum arm length ( $L_p$ ) is set at 0.55 m to give a natural frequency of oscillation ( $\omega_n$ ) of 0.66 Hz. For the case of the new damper, polyethylene spheres are used which are 1.125 cm in diameter and have specific gravity of 0.92.

Figures (3-a), (3-b) and (3-c) show the response of the pendulum alone, with plugged liquid-loop and with un-plugged liquid-loop respectively. It can be seen, in these three cases, that the amplitude of oscillation decays to half its initial magnitude after 45, 34 and 17 cycles respectively. Therefore, activating the liquid-filled damper results in doubling the damping rate as compared to the case of plugged liquid-damper.

Figures (4-a) through (4-d) display the time response of the new damper for floating sphere concentrations ranging between 2.6% to 18.6%. Reviewing the figures indicate that introducing the floating spheres into the loops has produced significant improvement in the damping of vibration as compared to the conventional liquid-filled damper. For example, the amplitude of oscillation drops to half its initial value after 10 cycles when the concentration of the spheres is 10%. Increasing the concentration to 18.6% results in halving the amplitude after 7 cycles.

It is essential here to note that the resulting improvement in the damping is obtained without any increase in the weight of the damper as the floating spheres are nearly of the same density as the liquid (liquid / sphere density = 1.01).

### 3.4. Analysis of the results

The time response characteristics of the conventional and the new dampers are analyzed to obtain the damping ratio ( $\zeta$ ) approach as well as the energy dissipated per cycle ( $\Delta E$ ). The calculation of these parameters is obtained from plotting the amplitude of oscillation of the pendulum ( $\vartheta_N$ ) as a function of the oscillation cycle ( $N$ ). Figure 5 shows such a plot with the pendulum amplitude normalized with respect to the initial amplitude  $\vartheta_0$ .

The logarithmic decrement ( $\delta$ ) can be calculated from the figure as follows

$$\delta = (1/N) \ln ( \vartheta_0 / \vartheta_N ) \quad (1)$$

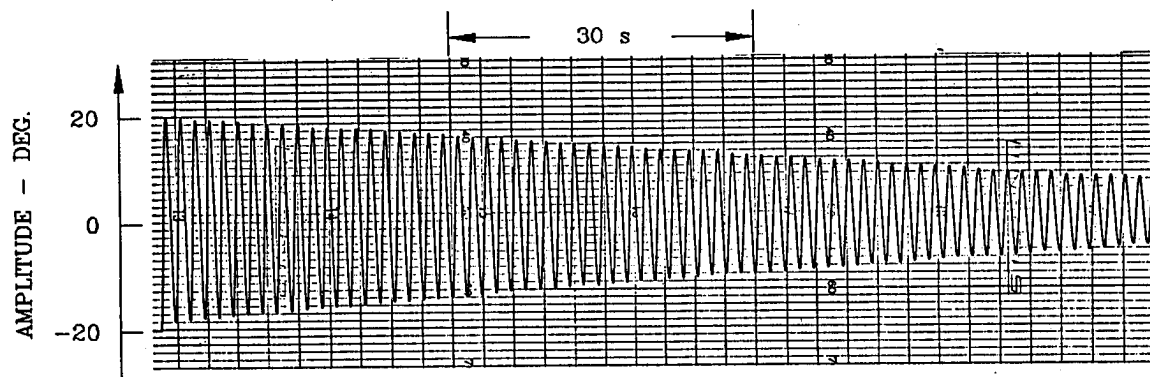
If the number of cycles to decay to half the initial amplitude is  $N_{1/2}$ , then the equation (2) reduces to

$$\delta = 0.693 / N_{1/2} \quad (2)$$

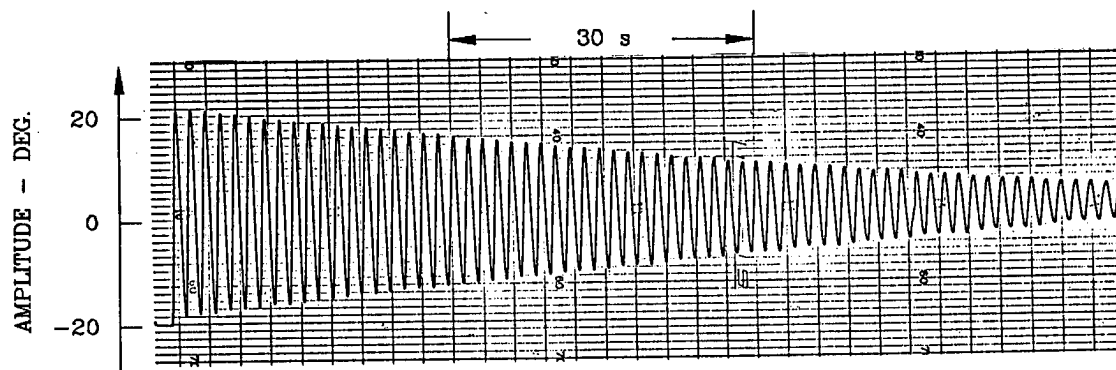
The damping ratio ( $\zeta$ ) can then be calculated from

$$\zeta = \delta / ( 2 \pi ) \quad (3)$$

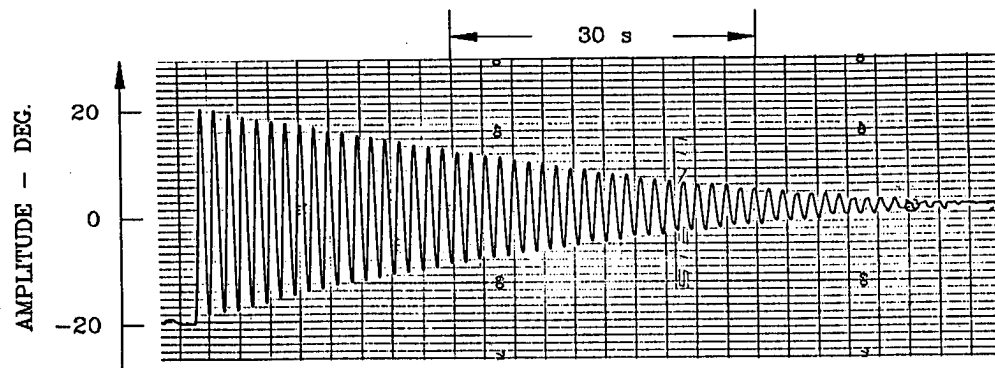




(a) PENDULUM ALONE



(b) PLUGGED FLUID-LOOP



(c) UNPLUGGED FLUID-LOOP

Figure 3 - Time response of a conventional fluid-loop damper.

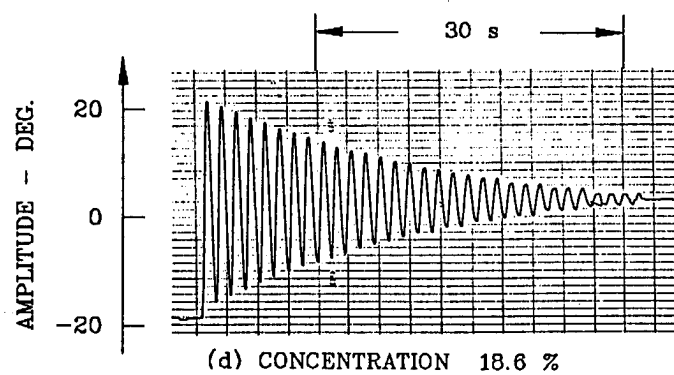
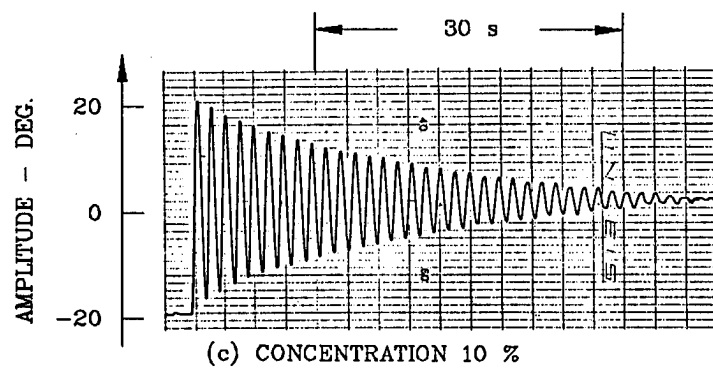
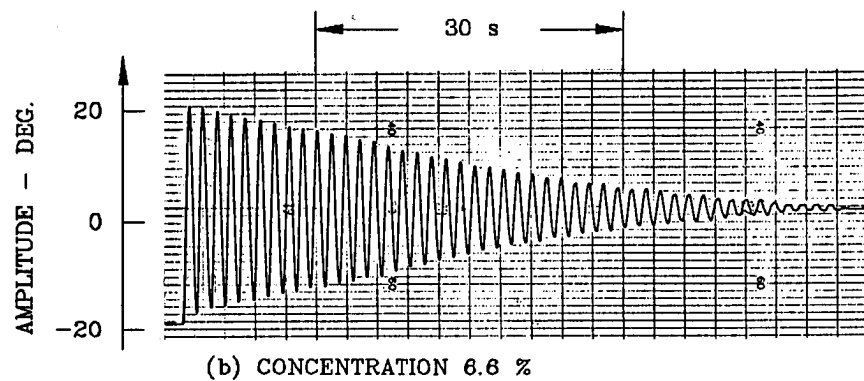
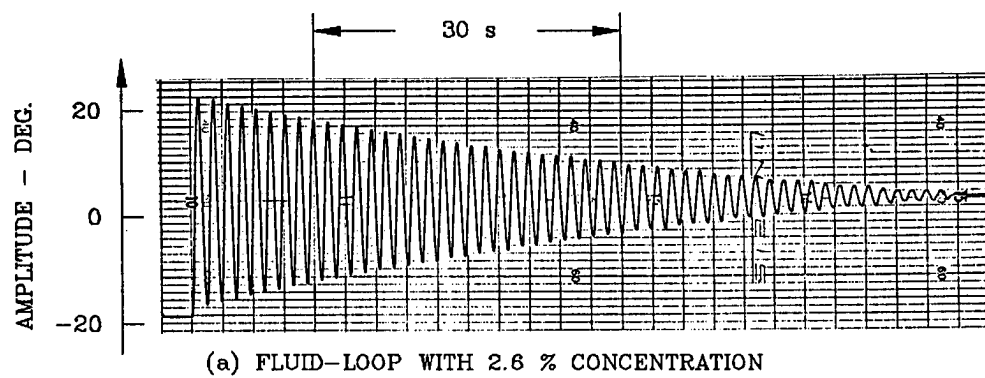


Figure 4 - Time response of the new fluid-loop damper.

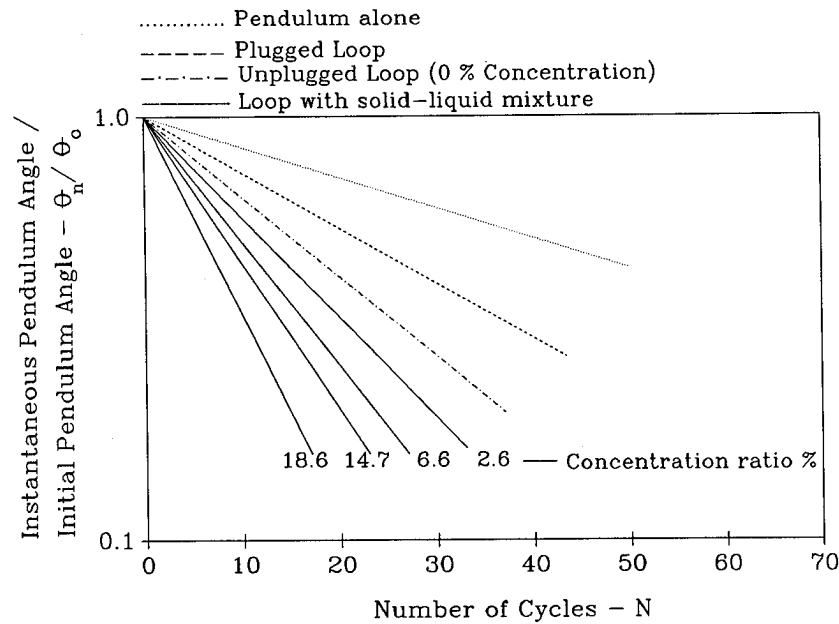


Figure 5 - Decay of amplitude as function of the number of oscillation cycles.

Figure 6 summarizes the effect of varying the volumetric concentration ratio of the spheres on the resulting damping ratio ( $\zeta$ ) of the damper for pendulum natural frequencies ranging between 0.66 to 0.33 Hz. These frequencies are obtained by varying the length of the pendulum arm ( $L_p$ ) from 0.55 m to 2.1 m respectively.

It can be seen, at oscillation frequency of 0.66 Hz, that increasing the concentration of the spheres results in significant increase in the damping ratio of the new damper as compared to the conventional damper (which has sphere concentration ratio = 0 %). Such an increase amounts to more than doubling the damping ratio of the conventional damper. However, the extent of the improvement decreases as the oscillation frequency is reduced. When the frequency drops to 0.5 the improvement becomes to 50%. Further decrease of the frequency to 0.33 Hz results in insignificant improvement.

Another parameter that is important in evaluating the performance of the new damper is the energy dissipated by the damper per cycle ( $\Delta E$ ). This parameter is calculated from the following equation

$$\Delta E = (\delta - \delta_p) [I \omega_n^2 \theta_o^2] \quad (4)$$

where

$\delta_p$  is the logarithmic decrement of the pendulum carrying the plugged loop.

and

$I$  is the inertia of the pendulum-loop system around the pivot, ( $\text{kgm}^2$ )

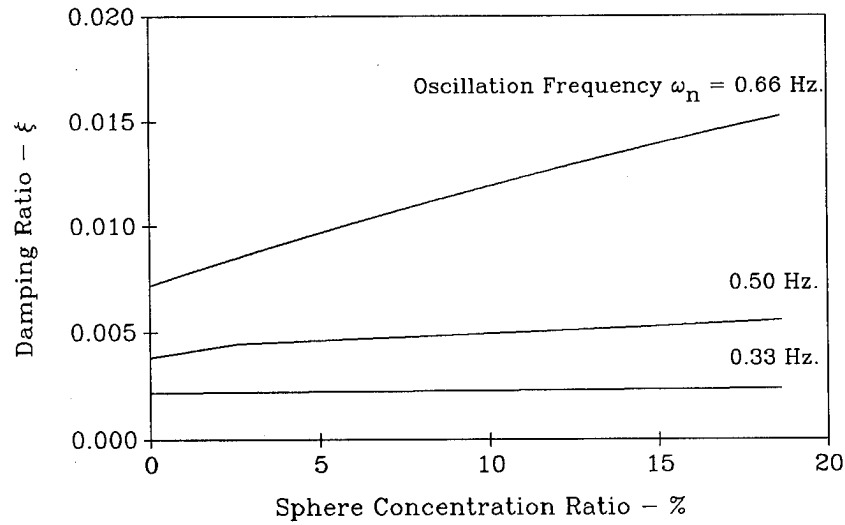


Figure 6 - Effect of volumetric concentration ratio of the floating spheres on the damping ratio for different oscillation frequencies.

In equation (4), the friction losses in the pivot and the sensor as well as the air drag on the pendulum are accounted for by the term  $\delta_p$ . These losses are subtracted from the logarithmic decrement ( $\delta$ ) of the activated damper to obtain the portion ( $\Delta E$ ) of the pendulum total energy ( $I \omega_n^2 \vartheta_o^2$ ) dissipated in the loop. In dimensionless form, the energy dissipated per cycle ( $\Delta \tilde{E}$ ) can be written as

$$\Delta \tilde{E} = \Delta E / \left[ m (R \omega_n \vartheta_o)^2 \right] \quad (5)$$

where

$m$  is the mass of the liquid filling the loop, (kg)

In equation (2), the energy dissipated is normalized with respect to the kinetic energy of the fluid inside the loop.

Combining equations (4) and (5) gives

$$\Delta \tilde{E} = (\delta - \delta_p) / (m R^2 / I) \quad (6)$$

In the above equation, the denominator represents the ratio of the inertias of the fluid loop to that of the pendulum. The parameter  $\Delta \tilde{E}$  will be used to compare the experimental results of the new damper with the optimal performance of conventional dampers as obtained by Bhuta and Koval<sup>2</sup>.

Figure 7 shows such a comparison for oscillation frequency of 0.66 Hz. It can be seen that the new damper can produce significant improvement in the amount of energy dissipated per unit inertia ( $\Delta \bar{E}$ ) as compared to the optimal conventional loop damper. Such improvement occurs when the concentration ratio of the spheres exceeds 12%. When the concentration becomes 18.6%, the measured improvement is 31.1%. In other words, the new damper can produce higher damping than an equal weight conventional damper or alternatively, it will be lighter than a conventional damper that has the same damping ratio.

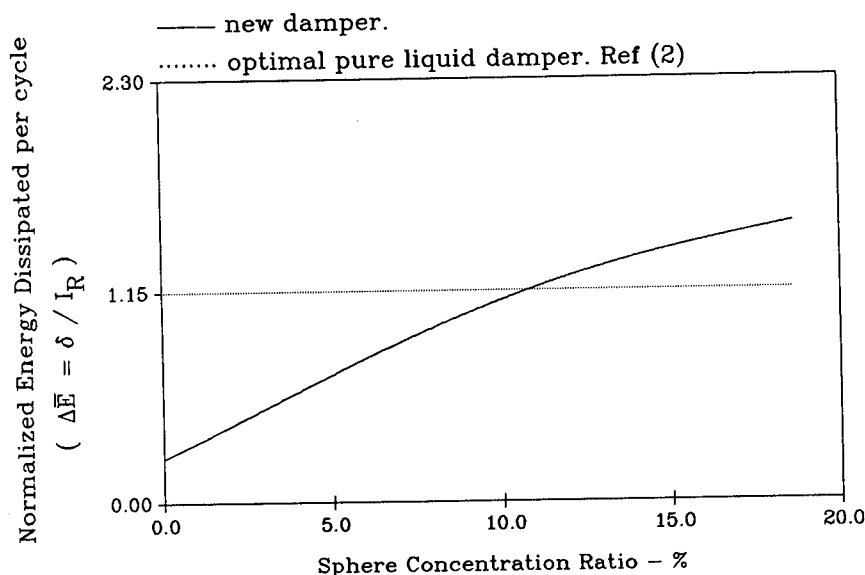


Figure 7 - Comparison between the energy dissipation capabilities of conventional and new fluid-loop dampers.

#### 4. CONCLUSIONS

This paper has presented a new fluid-loop damper which has improved damping characteristics as compared to conventional fully-filled loop dampers routinely used in spinning satellites. The improved performance is obtained by introducing floating spheres into the damper's loops.

Experimental evaluation of a prototype of the damper indicated that it can be, at 0.66 Hz, about 31.1% more effective and lighter than the optimally tuned fully-filled damper of Bhuta and Koval<sup>2</sup>.

The obtained results suggest the potential of the new damper as simple and effective means for damping the vibration of spinning satellites and

many other space applications. The damper can be equally invaluable in suppressing multi-axes vibrations . Such a capability is impossible to achieve by current fluid-loop dampers.

Experiments are planned to investigate the performance of the damper over a wide range of frequencies , different types of working fluids and floating spheres. Also mathematical models will developed to model the dynamics of the damper as influenced by its design parameters. The multi-axes damping capabilities of the damper will be tested alone and in-conjunction with flexible structures. The tests will aim at demonstrating its feasibility in isolating the vibration of the various appendages attached to these structures.

### **ACKNOWLEDGEMENTS**

This work was funded by NASA - Goddard Space Flight Center under grant number NAG 5-1037.

## REFERENCES

1. M.V.BARTON 1965 *NASA Technical Report number NASA CR-163. Feasibility study of passive dampers for manned rotating space station.*
2. P.G.BHUTA and L.R.KOVAL 1966 *Intl. J. of Mech. Sci.* 8, 383-395. A viscous ring damper for a freely precessing satellite.
3. J.E.COCHRAN and J.A.THOMPSON 1980 *J. of Guidance and Control* 3, 22-28. Nutation dampers for asymmetric spacecrafts.
4. J.V.FEDOR 1973 *NASA Technical Report number X-732-73-293. Wire Antenna motion damper for IMP-J spacecraft.*
5. K.T.ALFRIEND 1974 *J. of Spacecraft*, 11, 456-462. Partially filled viscous ring nutation damper.
6. B.G.KING and R.P.WOOLEY 1985 *Ball Aerospace Systems paper number AAS 85-054, Boulder, CO.* Modeling, tuning and effectiveness of partially-filled ring nutation dampers.
7. G.F.CARRIER and J.W.MILES 1960 *ASME Trans. J. of Applied Mechanics* 27, 237-240. On the annular damper of a freely precessing gyroscope.
8. J.W.MILES 1963 *ASME Trans. J. of Applied Mechanics*, 30, 189-192. On the annular damper for a freely precessing gyroscope II.
9. W. F. CARTWRIGHT, E. MASSINGILL AND R. TRUEBLOOD 1963 *AIAA Journal*, 1, 1375-1380. Circular constraint nutation damper.
10. K.T.ALFRIEND and T. SPENCER 1983 *J. of Astronautical Sciences*, XXXI, 189-202. Comparison of filled and partially filled nutation dampers.
11. G.W.GOVIER AND K.AZIZ 1983 *The flow of Complex mixtures in pipes.* New York : Van Nostrand Reinhold Co.
12. R.H.PERRY and C.H. CHILTON 1973 *Chemical Engineer's Handbook.* (5th Edition) . New York : McGraw-Hill Book Co.
13. J.T.BROCH 1980 *Mechanical Vibration and Shock Measurements.* Denmark : Bruel and Kjaer.

**TUNED LIQUID DAMPER (TLD)  
FOR SUPPRESSING HORIZONTAL MOTION OF STRUCTURES**

-- Investigation on Nonlinear Waves in TLD and TLD-Structure Interaction --

Yozo FUJINO  
Associate Professor

Benito M. PACHECO  
Assistant Professor

Li-Min SUN  
Graduate Student

Piyawat CHAISERI  
Graduate Student

Department of Civil Engineering, University of Tokyo  
7-3-1 Hongo, Bunkyo-ku, Tokyo 113, Japan  
Tel. 3-812-2111 ext. 7722.  
Fax. 3-813-5772

A new kind of damper named Tuned Liquid Damper (TLD) is explained that relies upon motion of shallow liquid in a rigid container for absorbing and dissipating the vibrational energy. Nonlinear equations of liquid motion inside rectangular TLD are developed based on shallow water wave theory, and a TLD-Structure Interaction model is proposed. Damping of liquid motion is evaluated semi-analytically. Liquid motion inside TLD under sinusoidal base excitation, and the effectiveness of a TLD mounted on a structural model subjected to an external force are experimentally investigated. Good agreement is found between the experiment and the theory. Among fundamental parameters of TLD, the influence of liquid viscosity is discussed in detail.

## 1. INTRODUCTION

Relatively light, flexible, and weakly damped structures are increasing in number because of growing use of high-strength materials and welded joints. Vibration of structures due to wind, earthquake and other disturbances then can create possible problems from the viewpoint of serviceability or even safety of bridges, towers, or buildings. The installation of various types of passive devices or so-called passive mechanical dampers is one way to suppress structural vibration.

This paper discusses a new type of passive mechanical damper, named Tuned Liquid Damper (TLD) (Fig. 1), which relies on motion of shallow liquid



inside a rigid container, for absorbing and dissipating structural vibration energy. Dampers using liquid motion have been in use in space satellites and marine vessels (Refs. 1-4). Recent growing interest in such a damper including TLD (for example, Refs. 5-10) is attributable to several potential advantages, including: low cost; easy installation especially in already existing structures which often have severe space constraints; adaptability to temporary use; easy trigger at small displacement amplitude; non-restriction to uni-directional excitation; and few maintenance requirements.

Studies so far on liquid dampers indicate their effectiveness. The performance of Tuned Liquid Damper (TLD) has been investigated by the authors using free-oscillation experiments (Ref. 7). It has been found that additional damping due to TLD is strongly dependent on amplitude of oscillation of liquid container. Nonlinear equations of liquid motion inside rectangular TLD were recently developed by the authors based on shallow water wave theory (Refs. 11-12), and are briefly explained in Section 2 below. It was found in Refs. 11-12 that the theory is in good agreement with the experiment in the region of relatively small vibration amplitude where no breaking of wave in TLD occurs and, hence, viscosity effect is dominant in energy absorption and dissipation.

Based on the theory of liquid motion referred to above, a TLD-Structure Interaction model is herein proposed to predict the performance of TLD. The performance of a rectangular TLD attached to a structure which is subjected to an external sinusoidal force is discussed. Experiment is carried out to confirm this model. The structural response with TLD is limited to a rather small amplitude range where no apparent wave breaking exists.

Application on a particular horizontally vibrating structure is also a goal of this study. Therefore, a commercially available, cheap and handy rectangular plastic container partially filled with water is tried as TLD, and the tested structure has horizontal natural frequency and damping similar to the object bridge girder. Prior to planned further experiments, the TLD-Structure Interaction model is used to numerically simulate structural response with attached TLD using high-viscosity liquid instead of water.

## 2. MODELLING OF LIQUID MOTION INSIDE RECTANGULAR TLD

The rigid rectangular tank (Fig. 2) has a length  $2a$ , and the mean liquid depth is  $h$ . The origin of the Cartesian coordinate system ( $o$ - $x$ - $z$ ) which is attached to the tank, is at the center of the mean liquid surface. A translational motion  $x_s$  (acceleration) is imposed on the tank in the  $x$ -direction. The following discussion is restricted to continuous surface condition (no wave breaking). The liquid particle motion is assumed to develop only in  $x$ - $z$  plane. It is also assumed that the liquid is

incompressible, irrotational fluid, and the pressure  $p$  at liquid free surface is constant.

### (1) Derivation of basic equations

The full equations governing the problem are the continuity equation

$$\frac{\partial u}{\partial x} + \frac{\partial w}{\partial z} = 0, \quad (1)$$

and the two-dimensional Navier-Stokes equations.  $u, w$  are the velocities of liquid particle (relative to the tank) in the  $x$ - and  $z$ -direction, respectively. For liquid having relatively small viscosity, the effect of internal friction in the fluid is appreciable only in the boundary layer near the solid boundary (Fig. 3). From this hypothesis, the liquid flow outside the boundary layer may be considered as potential flow, and the equations of motion become

$$\frac{\partial u}{\partial t} + u \frac{\partial u}{\partial x} + w \frac{\partial u}{\partial z} = - \frac{1}{\rho} \frac{\partial p}{\partial x} - \ddot{x}_s, \quad (-(h-h_b) \leq z \leq \eta) \quad (2)$$

$$\frac{\partial w}{\partial t} + u \frac{\partial w}{\partial x} + w \frac{\partial w}{\partial z} = - \frac{1}{\rho} \frac{\partial p}{\partial z} - g, \quad (-(h-h_b) \leq z \leq \eta) \quad (3)$$

where  $g$  is the gravity acceleration. Inside the boundary layer, the equations of motion are

$$\frac{\partial u}{\partial t} + u \frac{\partial u}{\partial x} + w \frac{\partial u}{\partial z} = - \frac{1}{\rho} \frac{\partial p}{\partial x} + \nu \frac{\partial^2 u}{\partial z^2} - \ddot{x}_s, \quad (-h \leq z \leq -(h-h_b)) \quad (4)$$

$$\frac{1}{\rho} \frac{\partial p}{\partial z} = -g, \quad (-h \leq z \leq -(h-h_b)) \quad (5)$$

where  $h_b$  is the thickness of boundary layer and is in the order of several percent of the representative length  $a$ .  $\rho$  and  $\nu$  are the density and kinematic viscosity of liquid, respectively.

The boundary conditions are

$$u = 0, \quad \text{on the wall } (x = \pm a) \quad (6)$$

$$w = 0, \quad \text{at the bottom } (z = -h) \quad (7)$$

$$w = \frac{D\eta}{Dt} = \frac{\partial \eta}{\partial t} + u \frac{\partial \eta}{\partial x}, \quad \text{at the free surface } (z = \eta) \quad (8)$$

$$p = p_0 = \text{constant} \quad \text{at the free surface } (z = \eta) \quad (9)$$

The velocity potential function  $\phi$  exists for the main flow. Based on the shallow water wave theory,  $\phi$  is assumed as (Ref. 13)

$$\phi = F(x, t) \cosh(k(h+z)). \quad (10)$$

With the aid of Eq.(10), the vertical velocity  $w$  and its differentials can be expressed in terms of the horizontal velocity  $u$ . Governing equations are integrated (Ref. 12) with respect to  $z$  from bottom to free surface and the basic equations are obtained as

$$\frac{\partial \eta}{\partial t} + h\sigma \frac{\partial(\phi u(\eta))}{\partial x} = 0, \quad (11)$$

$$\begin{aligned} \frac{\partial}{\partial t} u(\eta) + (1-T_H^2) u(\eta) \frac{\partial}{\partial x} u(\eta) + g \frac{\partial \eta}{\partial x} + gh\sigma\phi \frac{\partial^2 \eta}{\partial x^2} \frac{\partial \eta}{\partial x} \\ = -v \int_{-h}^{-(h-h_b)} \frac{\partial^2 u}{\partial z^2} dz - \ddot{x}_s, \end{aligned} \quad (12)$$

where  $\sigma = \tanh(kh)/(kh)$ ,  $\phi = \tanh(k(h+\eta))/\tanh(kh)$ ,  $T_H = \tanh(k(h+\eta))$ ,  $u(\eta)$  is the horizontal velocity of surface liquid particle, and  $k$  is wave number. Eq.(11) is the integral of the continuity equation while Eq.(12) is obtained from the equations of motion after eliminating the pressure  $p$ . The independent variables in these basic equations are  $u(\eta)$  and  $\eta$ . The first term of the right hand side of Eq.(12), which is the integral of the second term of the right hand side of the equation of motion inside the boundary layer (Eq.(4)), is referred to as the dissipation term.

## (2) Damping of liquid motion

The effect of liquid damping is significant on liquid motion near resonance. In the present formulation, assuming that the shear stress outside the boundary layer is very small, the dissipation term in Eq. (12) can be expressed as

$$v \int_{-h}^{-(h-h_b)} \frac{\partial^2 u}{\partial z^2} dz = -\frac{1}{\rho} \tau_b, \quad (13)$$

where  $\tau_b = \rho v \left( \frac{\partial u}{\partial z} \right)_{z=-h}$ , is the bottom shear stress. In the present problem, Reynolds number is in the order of 10000 and the boundary layer is considered as a somewhat turbulent one. According to Jonsson's studies (Ref. 14),  $\tau_b$  can be approximately expressed as

$$\tau_b = \frac{\rho}{2} f_b |u(\eta)| u(\eta). \quad (14)$$

The coefficient  $f_b$  in Eq. (14) is a wave friction factor associated with Reynolds number  $Re_b$ , which is defined as

$$Re = \frac{U^2(\eta)}{\omega v}, \quad (15)$$

where  $U(\eta)$  is the amplitude of  $u(\eta)$ , which is unknown, while  $\omega$  is the angular frequency of excitation.  $f_b$  can be expressed as (Ref. 14)

$$f_b = 2/\sqrt{Re} = 2\sqrt{\omega\nu} / U(\eta). \quad (16)$$

$U(\eta)$  can be eliminated from the equations by linearizing Eq. (14). Writing  $\tau_b$  in the form

$$\tau_b = \frac{\rho}{2} f_b C_e u(\eta), \quad (17)$$

then the parameter  $C_e$  is determined by equating the energy loss per cycle by Eq. 14 to that by Eq. 17. From this consideration of energy loss per cycle,

$$C_e = \frac{8}{3\pi} U(\eta). \quad (18)$$

Thus, the dissipation term can be expressed in the form

$$\frac{\nu}{(\eta+h)} \int_{-h}^{-(h-h_b)} \frac{\partial^2 u}{\partial z^2} dz = - \frac{1}{(\eta+h)} \frac{8}{3\pi} \sqrt{\omega\nu} u(\eta). \quad (19)$$

So far, only the damping effect of bottom boundary layer has been considered in the derivation of basic equations. Vandorn (Ref. 15) reported that the damping of liquid motion in a container observed from experiment is larger than that computed on account of the bottom boundary layer. Miles (Refs. 16-17) has also studied the damping of surface wave in closed basin and suggested that the dissipation term can be multiplied by  $(1+(2h/b)+S)$ , where  $b$  is the width of the tank, to account for dissipation due to side wall friction and liquid surface contamination. It is regarded that the friction of side wall boundary layer is the same as that of bottom boundary layer.  $2h/b$  is an equivalent coefficient of the damping effect per width due to the side wall boundary layer.  $S$  is a "surface contamination" factor which can vary between 0 and 2. A value of unity for  $S$  will be used in this study, which corresponds to the establishment of "fully contaminated surface". Note that Ref. 18 also used  $S=1$ .

The dissipation term with the inclusion of the effects of side wall and free surface is

$$\frac{\nu}{(\eta+h)} \int_{-h}^{-(h-h_b)} \frac{\partial^2 u}{\partial z^2} dz = - \lambda u(\eta), \quad (20)$$

$$\text{where } \lambda = \frac{1}{(\eta+h)} \frac{8}{3\pi} \sqrt{\omega\nu} (1+(2h/b)+S). \quad (21)$$

According to the linear theory of the boundary layer (Ref. 19),  $\lambda$  is evaluated as

$$\lambda = \frac{1}{(\eta+h)} \frac{1}{\sqrt{2}} \sqrt{\omega\nu} (1+(2h/b)+S). \quad (22)$$

This value is somewhat smaller than that given by Eq.21 and is also used in the numerical simulation for comparison purposes.

### (3) Numerical simulation method

The basic equations (Eqs.(11) and (12)) are discretized with respect to  $x$  into difference equations (staggered mesh) and can be solved numerically. The free surface waves originally possess a dispersion character, which is replaced by the dispersion relation produced by the discretization of the basic equations choosing a suitable division number  $n$ . The wave number  $k$  is taken as  $\pi/2$ , since the frequency around the first natural frequency is of main concern. In this paper,  $n$  is calculated using (Ref. 13):

$$n = \pi / (2 \arccos(\sqrt{(\tanh(\pi \varepsilon) / (2 \tanh(\pi \varepsilon / 2)))}). \quad (\varepsilon = h/a) \quad (23)$$

After determining the division number  $n$  and with the corresponding boundary condition

$$u(\eta) = 0, \quad (x = \pm a) \quad (24)$$

the difference basic equations are solved using Runge-Kutta-Gill method and  $u(\eta)$  and  $\eta$  can be computed.

### (4) Base shear force of the tank due to liquid motion

Considering hydrostatic pressure and vertical acceleration effect only, the pressure  $p$  can be expressed as

$$\frac{1}{\rho} (p - p_0) = g(\eta - z) - \frac{1}{k^2} \left( \frac{\partial^2 u(\eta)}{\partial x \partial t} - \frac{\partial^2 u}{\partial x \partial t} \right). \quad (25)$$

When  $\eta$  is known, integrating Eq. (25) with respect to  $z$ , the horizontal total pressure  $P$  can be calculated.

Neglecting the frictions of side wall and bottom, the base shear force of the tank due to liquid motion is

$$F = P_n - P_0. \quad (26)$$

$P_n$  and  $P_0$  are the horizontal total pressures acting on the end walls of the tank due to liquid motion. These are functions of liquid free surface elevation near the end wall (Fig. 4).

## 3. SHAKING-TABLE EXPERIMENT AND COMPARISON WITH SIMULATION

### (1) Experimental apparatus and procedure

In order to assess the validity of the model and to study the performance of liquid motion in TLD, a forced excitation experiment was carried out. A rectangular TLD tank was excited horizontally by a shaking table. A capacitance wave gage was used to measure liquid surface elevation near the end wall of the tank. For measuring base shear force of TLD tank, two load cells L1 and L2 were used to cancel the inertia force due to the TLD tank itself. Note that  $M_0$  in Fig. 5 is a mass equivalent to the mass of the tank. Output L1-L2 is the base shear force of TLD purely due to liquid motion. The evolution of liquid surface profile was photographed by a high speed camera.

A rectangular tank with length  $2a=59.0\text{cm}$  (excitation direction) and width  $b=33.5\text{cm}$ , being made of  $0.5\text{cm}$  thick acrylic plates was used (Fig. 6). The TLD tank was partially filled with plain water of  $h=3.0\text{cm}$  depth, corresponding to liquid depth ratio  $\varepsilon=h/a=0.1$ . From the linear wave theory, the natural fundamental frequency of liquid sloshing motion,  $f_w$ , was

$$f_w = \frac{1}{2\pi} \left( \frac{\pi g}{2a} \tanh\left(\frac{\pi h}{2a}\right) \right)^{1/2} = 0.458 \text{ Hz}, \quad (27)$$

i.e., the natural period was  $T_w=2.18 \text{ sec}$ . Water mass  $M_w$  was about  $5.93 \text{ kg}$ .

In the experiment, the TLD was quiescent at the start of table shaking. It was excited sinusoidally with various amplitudes. For four amplitudes of displacement of shaking table,  $A=0.1\text{cm}$ ,  $0.25\text{cm}$ ,  $0.5\text{cm}$ , and  $1.0\text{cm}$ , the excitation frequency  $f$  was varied in the range of  $0.8 < f/f_w < 1.5$ .

The quantities measured in the experiment were: 1) displacement of shaking table,  $x$ ; 2) liquid free surface elevation near the end wall,  $\eta_0$ ; and 3) base shear<sup>s</sup>force of TLD due to liquid motion,  $F$ . Data were converted from analog to digital, and were processed by a micro computer.

## (2) Results of Experiment

Figure 7 shows sample time histories of displacement of shaking table,  $x$ ; liquid free surface elevation near an end wall,  $\eta_0$ ; and base shear force,  $F$ , with liquid motion at steady state. Even under the sinusoidal excitation, the wave forms of these time histories vary as the excitation frequency varies. Unsymmetrical wave form can be observed even under the excitation of small amplitude (Fig. 7(b)). At a certain excitation frequency, two or three waves can be observed in one cycle (for example, Fig. 7(c)).

Several nondimensional parameters are defined as follows for the presentation of results.

Liquid free surface elevation,  $\eta$  equals 0 at still liquid free surface. During liquid motion,  $\eta$  has at least one maximum value  $\eta_{\max}$  (wave crest)

and one minimum value  $\eta_{\min}$  (wave trough) in one cycle (Fig. 7). The nondimensional parameters  $\eta'_{\max}$  and  $\eta'_{\min}$  are defined as

$$\eta'_{\max} = \eta_{\max}/h; \quad \eta'_{\min} = \eta_{\min}/h, \quad (28)$$

where  $h$  is liquid depth.

Under the sinusoidal excitation, base shear force  $F(t)$  has the same amplitude  $F_m$  either in positive direction or negative direction (Fig. 7).  $F_m$  is divided by the maximum inertia force of liquid as a solid mass under the sinusoidal excitation, and nondimensionalized:

$$F'_m = F_m / (M_w \omega^2 A). \quad (29)$$

The shaking table inputs energy into the TLD system, and the TLD itself dissipates energy due to liquid motion. When TLD is at steady state, it means that in each cycle the energy input into the TLD system equals the energy dissipation inside TLD. The energy input into the TLD,  $E_{\text{input}}$ , can be calculated from the base shear force  $F$  and the displacement of shaking table  $x_s$ , which are both functions of time. Thus the energy dissipation per cycle  $\Delta E$  can be calculated as

$$\Delta E = E_{\text{input}} = \int_t^{t+T} F(t) dx_s(t), \quad (30)$$

where  $T$  is the period of excitation, i.e.  $2\pi/\omega$ .

$\Delta E$  is nondimensionalized as follows,

$$\Delta E' = \Delta E / \left( \frac{1}{2} M_w (\omega A)^2 \right) \quad (31)$$

It should be noted that  $\frac{1}{2} M_w (\omega A)^2$  is just a reference value to nondimensionalize and not the energy of liquid motion.

### (3) Comparison of numerical simulation with experimental result

For numerical simulation, the motion of TLD was assumed to be quiescent at  $t=0$ . The time increment was 1/60 of the excitation period of shaking table. The computation was carried on until 80 periods where liquid motion was regarded to have reached steady state.

Figure 8 presents the transient time history responses of base shear force,  $F$  for the input base amplitude 0.25cm. Numerical simulations corresponding to this case are also shown in Fig. 8 for comparison with experimental records. The response forms vary as the excitation frequency changes. At  $f/f_w=1.001$ , two waves in one cycle can be observed. This is the second mode of liquid motion, which is excited at an excitation frequency about one half of the second natural frequency of liquid motion.

At  $f/f_w = 0.951$ , even the third mode can be observed clearly. Comparing the numerical simulation with the experimental results, good agreement can be found, i.e., the theory used here is satisfactory in accounting for the nonlinearity which induces higher modes of liquid motion.

Figure 9 shows some examples of force-displacement diagrams for the base displacement amplitude of 0.25cm. One can find in Fig. 9 that the simulation results agree well with those of the experiment.

In Fig. 10, the nondimensionalized quantities,  $\eta'_{\max}$ ,  $\eta'_{\min}$  (surface elevation),  $F'_m$  (maximum base shear force) and  $\Delta E'$  (energy loss in TLD per cycle) are plotted for the frequency-ratio range of  $0.9 < f/f_w < 1.3$ . The solid lines in Fig. 10 show the simulation results using the damping parameter  $\lambda$  by Eq. 21, and the dotted lines using Eq. 22. The difference between Eq. 21 and Eq. 22 is found to be very small. Hereafter,  $\lambda$  given by Eq. 21 was used in the simulations.

All of the cases in the experiment indicate that the liquid motions possess strong nonlinearity (Fig. 10(a) to (d)). The resonant frequency ratio is greater than 1.00 even for the smallest input amplitude case ( $A=0.1\text{cm}$ ). At a certain value of frequency ratio larger than 1.00,  $\eta'_{\max}$  jumps down suddenly, indicating that the nonlinearity of liquid motion is "hardening spring" type. As the input amplitude increases, the resonant frequency ratio becomes larger, i.e., the nonlinearity becomes stronger. The resonant frequency ratio for the base amplitude of 0.1 cm is about 1.1 and increases to about 1.25 for the base amplitude of 1.0 cm.

The local peaks of  $\eta'_{\max}$  (and also of  $F'_m$  and  $\Delta E'$ ) for the frequency less than the resonant frequency can be found in Fig. 12(a), (b) and (c) and these are due to appearance of higher modes as seen in Figs. 7-8.

For the relatively small amplitude excitation (0.1 cm, 0.25 cm, 0.5 cm), the simulation can well predict the experimental results, i.e.,  $\eta'_{\max}$ ,  $\eta'_{\min}$ ,  $F'_m$  and  $\Delta E'$ .

For the input amplitude of 1.0 cm, breaking wave already exists (Fig. 10(d)). The simulation results do not agree with those of the experiment any more. The simulation overestimates  $\eta'_{\max}$  and  $F'_m$ , although the resonant frequency ratio is well predicted. It should be noticed in Fig. 10(d) that the simulation underestimates  $\Delta E'$  at range  $1 < f/f_w < 1.25$ . It may be explained that energy dissipation for the base displacement amplitude of 1.0cm is due to not only viscosity of liquid but also wave breaking. All these results indicate that the model used here is valid as far as the continuous free surface condition is satisfied.

For large excitation amplitude (Fig. 10(d)),  $F'_m$  and  $\Delta E'$  are almost flat over a wide range of frequency.



#### 4. TLD-STRUCTURE INTERACTION

##### (1) Interaction model

A single-degree-of-freedom (SDOF) structure with attached TLD (Fig.11) is proposed as TLD-Structure Interaction model. The equation of motion of the structure, which is subjected to sinusoidal external force  $F_e = F_{e0} \sin \omega t$  and TLD base shear force  $F_{TLD}$ , can be expressed as

$$\ddot{x}_s + 2\omega_s \xi_s \dot{x}_s + \omega_s^2 x_s = \frac{1}{m_s} (F_{TLD} + F_e) \quad (32)$$

where  $\omega_s = (k_s/m_s)^{1/2}$ , is the natural frequency; and  $\xi_s = \frac{C_s}{2m_s \omega_s}$ , is the damping ratio of the structure.  $F_{TLD}$  (or  $F$  in Eq. 26) is a function of the surface elevation  $\eta$  and the surface particle velocity  $u(\eta)$  as described in Section 2, specifically in Eq. 25. The quantities  $\eta$  and  $u(\eta)$  are functions of  $x_s$  (see Eqs. 11 and 12). Accordingly, at each time step in the numerical simulation,  $x_s$ ,  $\eta$  and  $u(\eta)$  are computed simultaneously from the three coupled equations (Eqs. 11, 12 and 32, coupled through Eq. 26).

##### (2) Forced excitation experiment

The structure in the interaction experiment was a platform vibrating in a shear-type horizontal motion (Fig.12). The total structural mass  $m_s$  was 168 kg. The natural frequency  $f_s$  was 0.91 Hz (natural period  $T_s = 1.10$  Sec). The structural damping ratio was 0.32%.

Aiming for a specific practical use, a commercially available plastic container, which approximately measured 25cm x 32cm x 11cm (height), was used as TLD.

The external sinusoidal force exerted to the structure was an inertia force of the oscillating part of an exciter, which was mounted on the platform. The external force amplitude was accordingly kept constant by keeping constant the amplitude of acceleration of the oscillating part relative to the platform. Excitation frequency ( $f$ ) sweep was done with the frequency ratio  $f/f_s$  ranging from 0.85 to 1.15. The digitized data of structural displacement response  $x_s$  and liquid surface elevation at the end wall of the container  $\eta_0$ , at steady-state, were collected for the investigation.

The fixed amplitude of exciting force for that frequency range, was such as to cause the structure without TLD at resonance to vibrate at the amplitude  $A_0$  of 1.0 cm at steady-state. After attaching TLD, structural response was affected as will be discussed below. Liquid depth used in the experiments was considered shallow, i.e., liquid depth ratio  $\varepsilon = \text{liquid}$

depth/container half length  $\approx 0.2$ . No obvious wave breaking was visually observed.

### (3) Discussion of TLD effectiveness in experiment and simulation

The experimental response of the structure with TLD (mass ratio  $\mu = \text{water mass } m_w / \text{structural mass } m_s$  is about 1.0%), is shown in frequency response plots in Fig. 13 (• and ○). Note that in Fig. 13a and 13b the setting orientation of the container relative to the direction of platform motion is different, even though the mass ratio  $\mu$  is almost the same. The results of the frequency sweep test toward higher frequency and backward show no effect of initial condition on wave and structural response. It can be seen both in Fig. 13a and 13b that at the region of resonance ( $f/f_s \approx 1.0$ ), the vibration amplitude reduces drastically. Comparing Fig. 13a and 13b, however, it appears that the container with  $2a=25\text{cm}$  and  $h=2.1\text{cm}$  has a better performance than that with  $2a=32\text{cm}$  and  $h=3.6\text{cm}$ . This is caused by the difference in liquid damping  $\lambda$  of the two cases, as further discussed below.

Two clear peaks of the structural response can be seen. The first peak (at lower frequency ratio) fell below the corresponding structural response when without TLD; whereas the second peak rose a little. The results of the numerical simulation using TLD-Structure Interaction model, shown as lines in Fig. 13, agree quite well with the experiment. The few discrepancies that can be observed may be due to the irregularity in the shape of the container, which is not perfectly rectangular; e.g., the bottom is not flat. The numerical analysis is sensitive to the liquid depth  $h$  in terms of value and position of each peak in the frequency response. Further details are given in Ref. 20.

## 5. LIQUID VISCOSITY AS A TLD DESIGN PARAMETER

As in TMD (Tuned Mass Damper), the mass ratio, frequency ratio and liquid damping are controllable parameters in the design of TLDs. The first natural frequency,  $f_w$  of liquid motion in a rectangular container is a function of  $a$  and  $h$ :

$$f_w = \frac{1}{2\pi} \left( \frac{\pi g}{2a} \tanh\left(\frac{\pi h}{2a}\right) \right)^{1/2} \quad (33)$$

For the tuning, i.e.,  $f_w/f_s = 1.0$ , the smaller container (smaller  $a$ ) requires the shallower water depth  $h$  as Eq. 33 indicates.

The liquid damping is inversely proportional to the liquid depth,  $h$  as seen in Eq. 21, and consequently the smaller TLD has larger liquid damping when the same liquid is used. The results in Fig. 13 has indicated that for the more or less same mass ratio ( $\mu \approx 1\%$ ) the container with  $2a=25\text{cm}$  (and

shallower  $h$ ) was more efficient as a damper, than that with  $2a=32\text{cm}$ . This can be attributed to the differences in liquid damping.

In Fig. 13a, there remains a response peak of the structure with TLD around  $0.9\text{Hz}$ , suggesting that liquid damping is still less than the optimal value. Some smaller container ( $2a < 25\text{cm}$ ) may therefore be expected to show better performance as a damper. However, it should be noted that using smaller TLD container inherently leads to larger number of TLDs to attain the same mass ratio. This can create problems in container cost and space required for TLD installation.

Instead of changing the TLD tank size and corresponding liquid depth, the liquid damping  $\lambda$  may be also be changed by changing the liquid viscosity  $\nu$  (see Eq. 21). Figure 14 shows the simulated effect of liquid viscosity on TLD-structure interaction ( $\mu=1\%$ ,  $f_s=0.91\text{Hz}$ ,  $2a=25\text{cm}$ ,  $h=2.1\text{cm}$  and  $\xi_s=0.32\%$ ). The structural response curves for various liquid viscosities of TLD ( $\nu$  (plain water),  $5\nu$ , and  $20\nu$ ) are plotted in Fig. 14. It appears in this example case that the structural response becomes almost flat over the frequency range considered, and is suppressed effectively when the liquid viscosity is  $5\nu$ . Indeed the liquid with appropriately high viscosity significantly improves the efficiency of TLD and this allows the use of relatively large size of TLD container. It should be noted, however that the optimal viscosity would depend upon the size of container.

Figure 15 shows the frequency response curves for comparing TLD and TMD effectiveness. Note that the TLD tank in this example is slightly different from that used in the preceeding example, and it was found in Ref. 12 that  $\nu=20\nu$  is optimal in this case. Both dampers are optimized with a selected mass ratio of  $1\%$ . The optimal parameters of TMD are determined according to Ref. 21. It is found in Fig. 15 that, if optimized, the efficiency of TLD is comparable to TMD.

## 6. CONCLUDING REMARKS

The 2-dimensional basic equations of liquid motion were developed based on the "shallow water wave theory", in which the damping effects due to solid boundary friction and free surface contamination were included. No wave breaking is assumed to exist. The TLD-Structure Interaction model using a SDOF structure subjected to an external force  $F_e$  and TLD base shear force  $F_{TLD}$ , which can be calculated by using the developed basic equations, was proposed. Forced excitation experiments were conducted to investigate the performance of a TLD prototype using a commercially available rectangular plastic container in suppressing vibrations of a structure with  $0.91\text{ Hz}$  natural frequency. The experimental results showed significant reduction of structure response around resonance ( $f/f_s = 1.00$ ) region.

Good agreements between experimental and simulated results were observed, with only a few discrepancies that may be due to the irregularity in the shape of the container and to 3-dimensional effect of container width. The proposed model may be sufficient for designing real TLDs.

The theoretical simulations showed that one way to improve TLD performance would be to choose more suitable liquid viscosity. The effectiveness of TLD could be comparable to that of TMD. Development of high-viscous liquid suitable to TLD is a remaining subject of investigation, as well as the optimization of the various TLD parameters.

#### REFERENCES

- [1] Bhuta, P. G. and Koval, L. R.: A Viscous Ring Damper for a Freely Precessing Satellite, *Int. J. Mechanical Science*, Vol. 8, pp. 383-395, 1966.
- [2] Watanabe, S.: Method of Vibration Reduction, *Proc. Japan Naval Arch. Soc. Symp.*, pp. 156-179, 1969. (In Japanese).
- [3] Sayar, B. and Baumgarten J. R.: Linear and Nonlinear Analysis of Fluid Slosh Damper, *AIAA J.*, Vol. 20, No. 11, pp.1534-1538, 1982.
- [4] Matsuura, Y. et. al.: On a Mean to Reduce Excited-Vibration with the Sloshing in a Tank., *Proc Japan Naval Arch. Soc.*, No. 160, pp. 424-432, 1986. (In Japanese).
- [5] Modi, V. J. and Welt, F.: Vibration Control Using Nutation Dampers, *Proc. Int. Conf. on Flow Induced Vibrations*, England, pp. 369-376, 1987.
- [6] Welt, F.: A Study of Nutation Dampers with Application to Wind Induced Oscillations, *Ph. D. Thesis*, The University of British Columbia, 204pp, 1988.
- [7] Fujino, Y. et. al.: Parametric Studies on Tuned Liquid Damper (TLD) Using Circular Containers By Free-oscillation Experiment, *J. Struc. Eng./Earthq. Eng.*, *Proc. JSCE.*, No.398, 1988.
- [8] Tamura, Y. and Fujii. K. et. al.: Wind-Induced Vibration of Tall Towers and Practical Applications of Tuned Sloshing Damper, *Proc. Symposium/Workshop on Serviceability of Buildings*, Ottawa, pp. 228-241, 1988.
- [9] Sato, T.: Tuned Sloshing Damper. *Japan J. Wind Eng.*, Vol. 32, pp. 67-68, 1987.
- [10] Miyata, T. et. al.: Suppression of Tower-like Structures Vibration by Damping Effect of Sloshing Water Contained, *J. Struc. Eng.*, *JSCE*, Vol.34A, pp.617-625, 1988. (In Japanese).
- [11] Sun, L-M.: Simulation of nonlinear waves in rectangular Tuned Liquid Damper (TLD), *Master Thesis*, Dept. of Civil Eng., Univ. of Tokyo, Japan, 1988.
- [12] Sun, L-M, Fujino, Y., Pacheco, B. M., and Isobe, M.: Nonlinear waves and Dynamic Pressures in Rectangular TLD, *J. Struc. Eng./Earthq. Eng.*, *Proc. JSCE.* (submitted for possible publication).

- [13] Shimizu, T., and Hayama, S.: Nonlinear Response of Sloshing Based on the Shallow Water Wave Theory". JSME International Journal. Vol.30, No.263, pp806-813. (or JSME, Vol.53(486), pp357-363, 1987. (In Japanese)).
- [14] Jonsson, I. G.: Wave Boundary Layer and Friction Factors. Proc. 10th CCE, ASCE, pp.127-148, 1966.
- [15] Vandorn, W. G.: Boundary Dissipation of Oscillatory Waves, J. of Fluid Mechanics, Vol. 24, part 4, pp.769-779, 1966.
- [16] Miles, J. W.: Surface Wave Damping in Closed Basins, Proc. Royal Society of London, A 297, pp. 459-475, 1967.
- [17] Miles, J. W.: Resonantly Forced, Nonlinear Gravity Waves in a Shallow Rectangular Tank, Wave Motion, Elsevier Science Publishers, B. V. (North Holland), 7, pp.291-297, 1985.
- [18] Lepelletier, T. G. Raichlen, F.: Nonlinear Oscillations in Rectangular Tanks, J. of Engineering Mechanics, 114(1), ASCE. pp.1-23, 1988.
- [19] Lamb, H.: Hydrodynamics, Cambridge Univ. Press, pp.619-621, 1932.
- [20] Chaiser, P., Fujino, Y., Pacheco, B. M. and Sun, L-M.: Interaction of TLD and Structure, J. Struc. Eng./Earthq. Eng., Proc. JSCE., (submitted for possible publication).
- [21] Warburton G. B. and Ayorinde E. O.: Optimum Absorber Parameters for Simple Systems, Int. Jour. of Earthq. Eng. and Struct. Dynamics, Vol. 8, pp. 197-217, 1980.

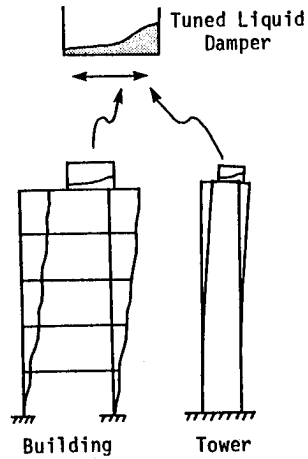


Fig. 1 Tuned Liquid Damper (TLD) installed on a building and tower

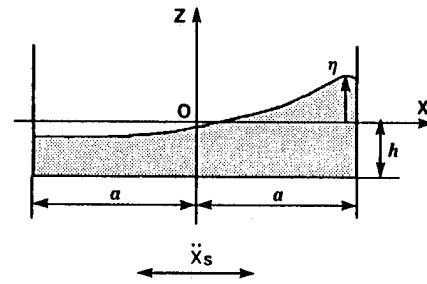


Fig. 2 Definition sketch for liquid motion in rectangular container

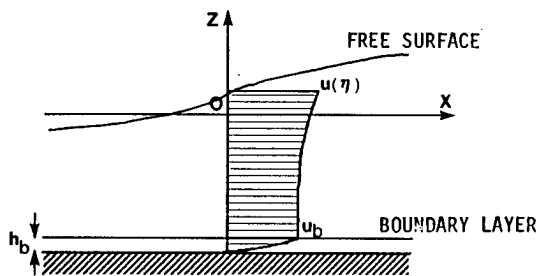


Fig. 3 The profile of liquid particle velocity in x-direction inside and outside the boundary layer

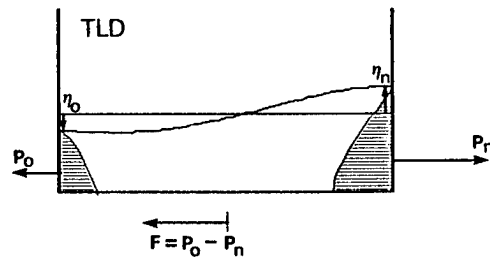


Fig. 4 Base shear force of container due to liquid motion

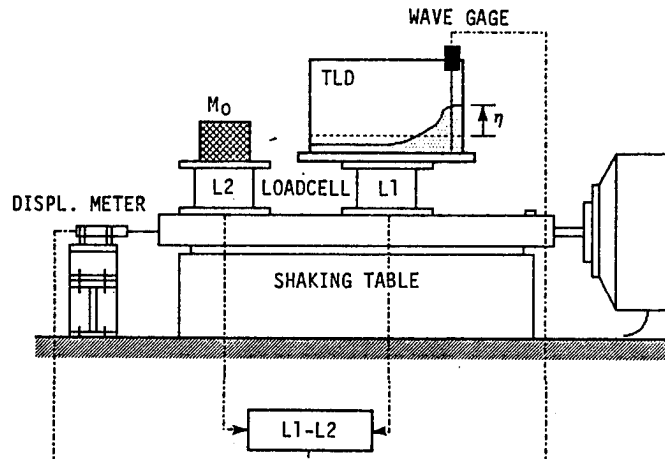


Fig. 5 The experimental apparatus

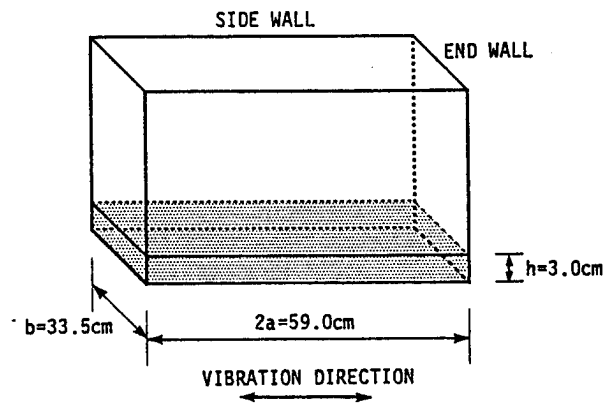


Fig. 6 TLD tank

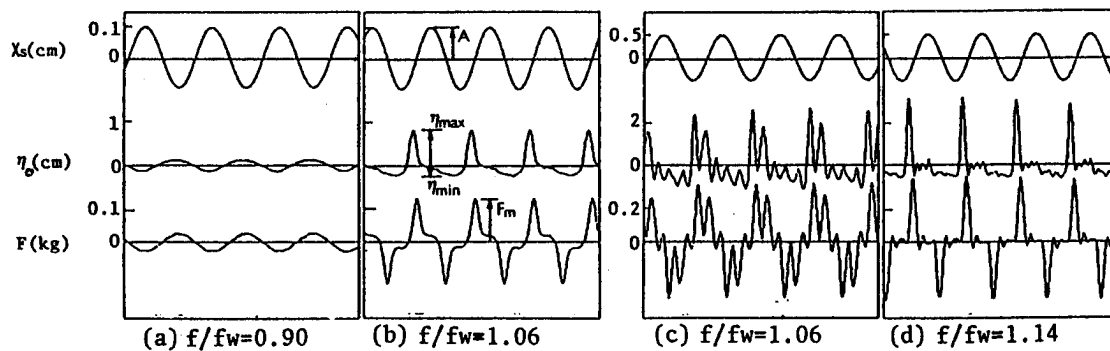


Fig. 7 Sample time histories of displacement of shaking table  $x_s$ , liquid surface elevation near the end wall  $\eta_0$  and base shear force  $F$

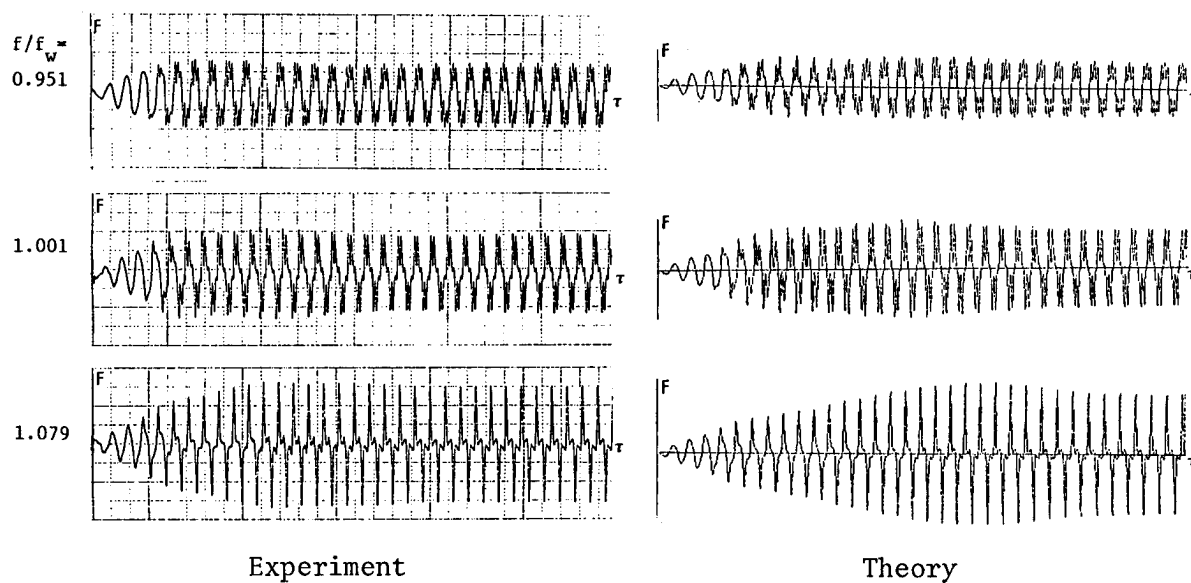


Fig. 8 The time histories of base shear force  $F$   
(base amplitude = 0.25 cm)

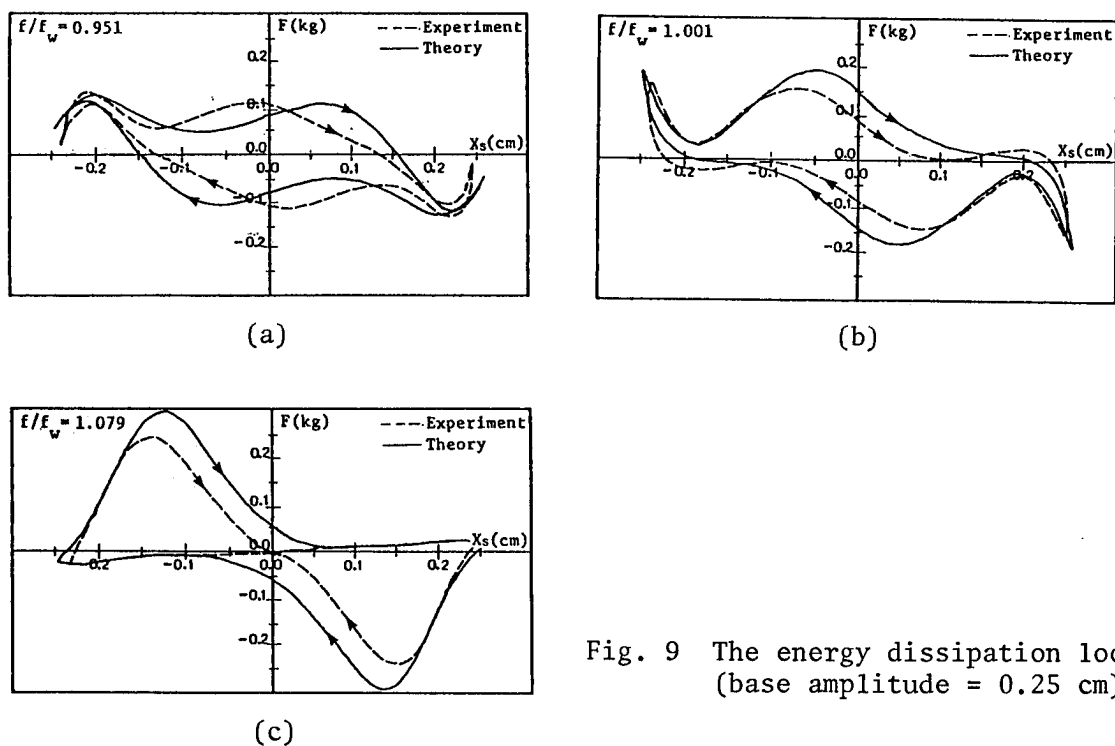
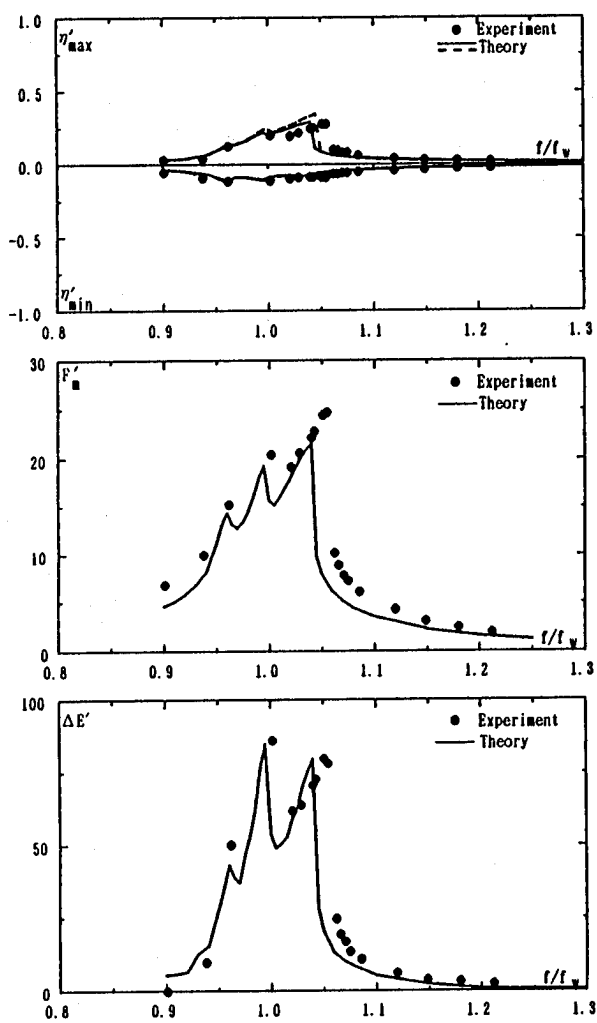
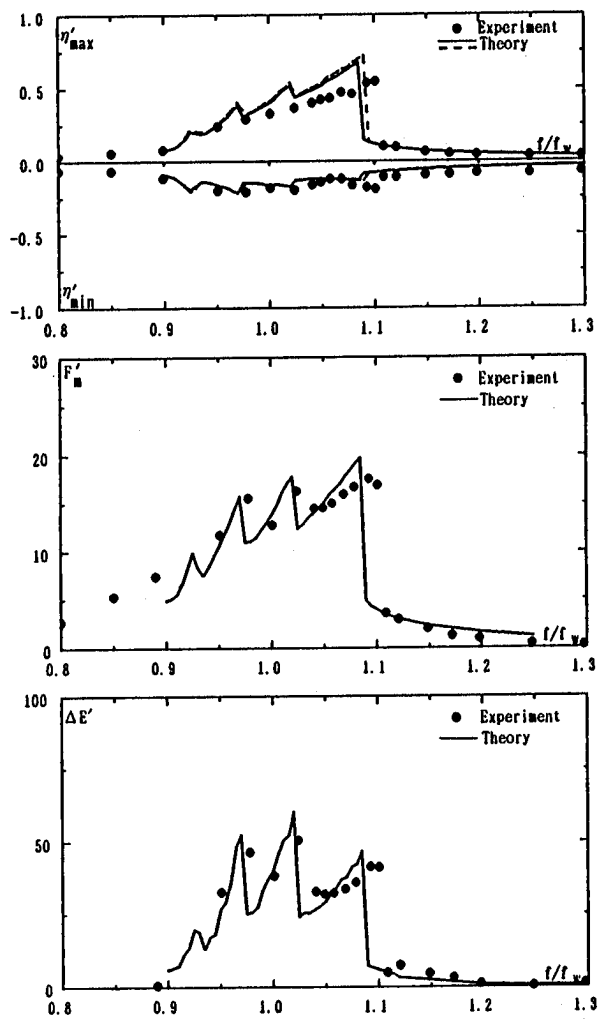


Fig. 9 The energy dissipation loops  
(base amplitude = 0.25 cm)



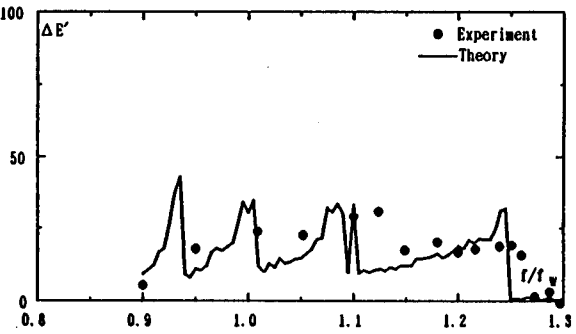
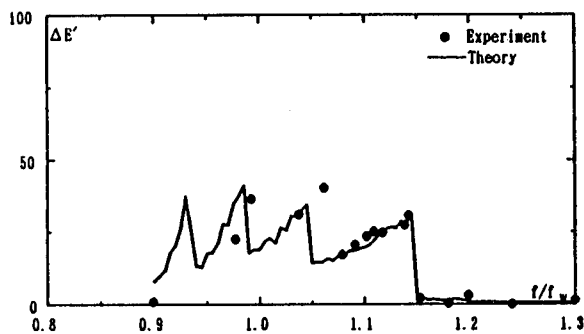
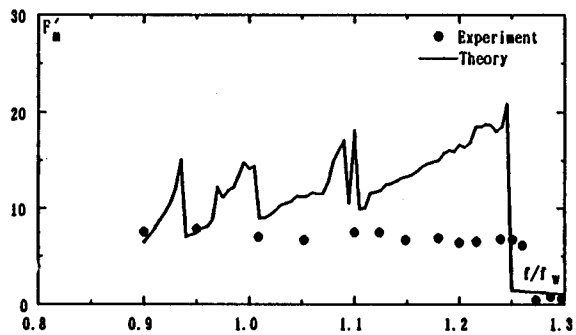
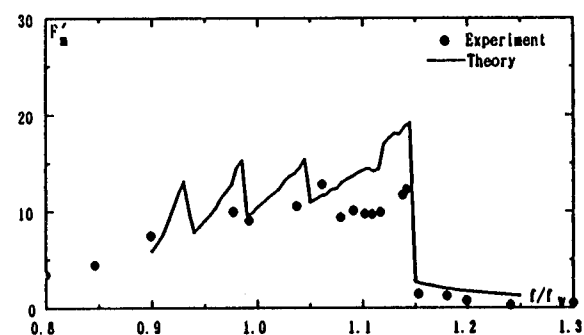
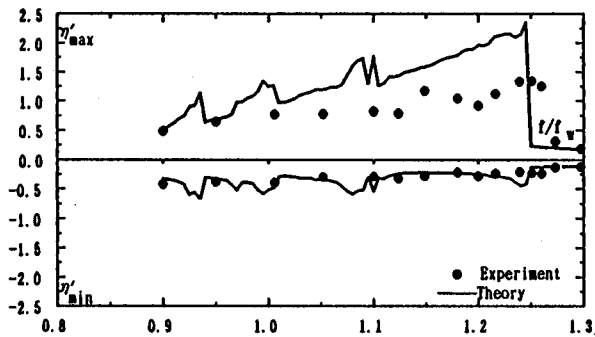
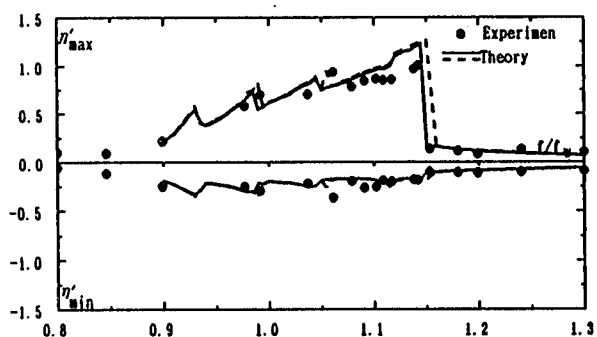


(a) base ampl.=0.1cm



(b) base ampl.=0.25cm

Fig. 10 Frequency responses of  $\eta'_{\max}$  and  $\eta'_{\min}$ ,  $F$ , and  $\Delta E'$



(c) base ampl.=0.5cm

(d) base ampl.=1.0cm

Fig. 10 (Continued)

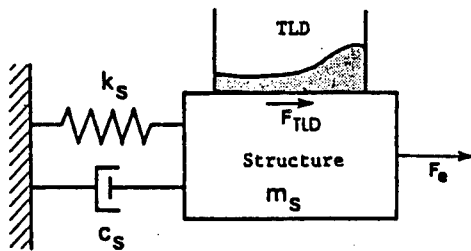


Fig. 11 TLD-Structures (SDOF) Interaction model

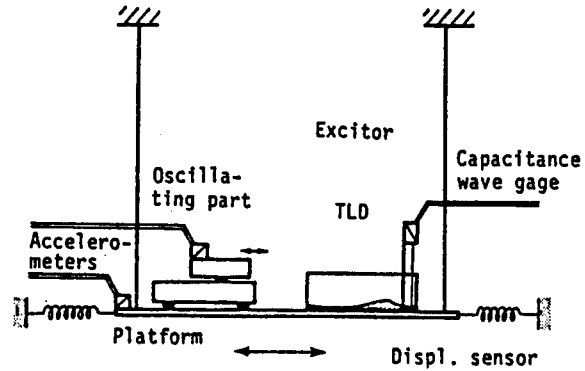


Fig. 12 Experimental set-up for TLD-structure interaction

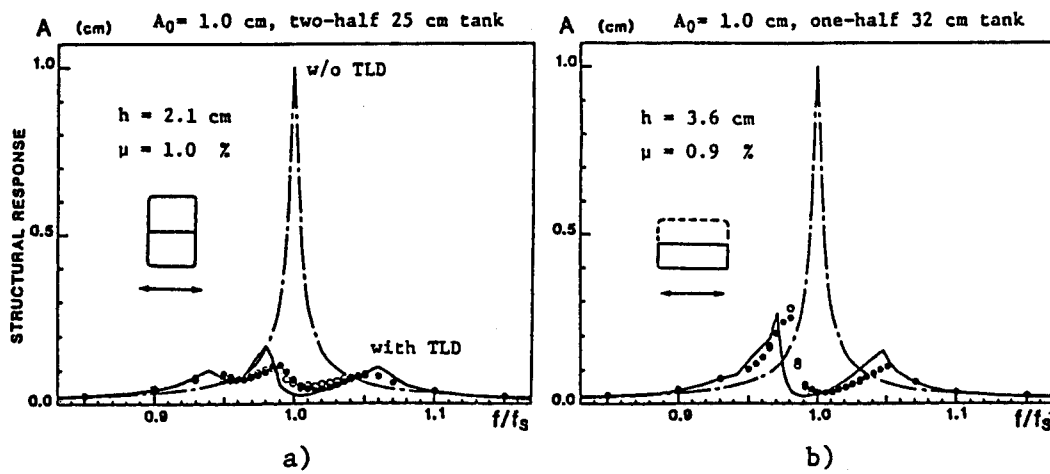


Fig. 13 Frequency response: numerical simulation and experiment (●sweep forward, ○sweep backward)

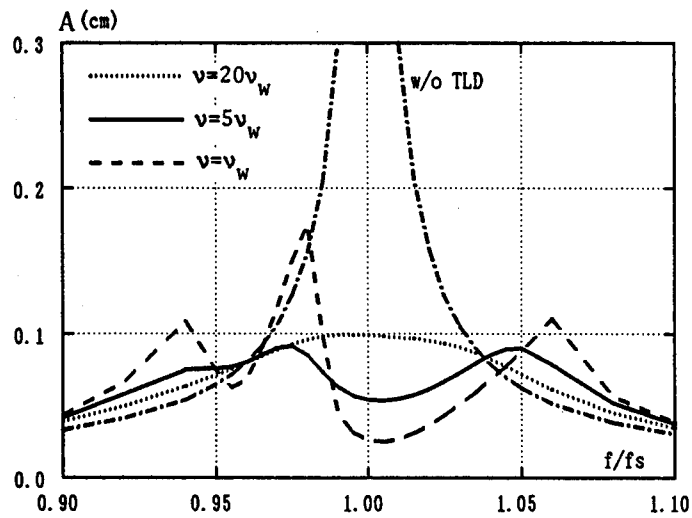


Fig. 14 Effect of liquid viscosity on TLD performance

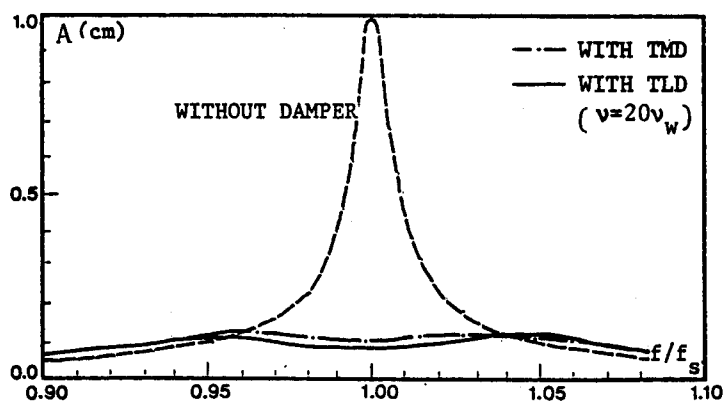


Fig. 15 Comparison of TLD and TMD

## CONTACT STRESSES IN CABLES DUE TO TENSION AND TORSION

Krishna Kumar<sup>†</sup>  
IIT, Kanpur - 208016, India

John E. Cochran, Jr.\* and Malcolm A. Cutchins\*  
Aerospace Engineering Department  
Auburn University  
Auburn University, AL 36849

### ABSTRACT

The fundamental theory of wire ropes developed by Costello and Phillips is utilized to develop closed-form expressions for contact stresses in single strand cables with fibrous cores. These should be useful for gaining insight into the influence of various cable parameters on its strength and hence design. Furthermore, since the contact stresses can be often high and approach levels on the order of the ultimate stress of the material, these expressions may facilitate the analysis of energy dissipation in vibrating cables through hysteresis due to periodic variations of stresses.

---

<sup>†</sup>Professor, Department of Aeronautical Engineering.

\*Professor, Department of Aerospace Engineering.

## INTRODUCTION

The importance of stranded cables for engineering applications is universally recognized. Yet, until recently, empirical data generated through their extensive experimentation had been the sole basis for rope-selection and design.<sup>1, 2, 3</sup> Such a conspicuous absence of earlier interests in theoretical investigations of cable deformations and stresses may be attributed to perhaps what appears to be an "overwhelming" complexity of the problem. The lack of thorough understanding of stresses in cables and the mechanisms which cause failures leads to the use of rather large factors of safety, thus leaving much to be desired for an effective usage of material in cables. Recent considerations of use of cables in large space structures (e.g., stayed columns, damping devices which utilize cables for energy dissipation or in other space applications involving tethers) require greater knowledge of cable stresses and cable-dissipative mechanisms.

A paper by Hall<sup>4</sup> together with a series of three papers by Hruska<sup>5, 6, 7</sup> on estimation of the tensile, tangential and radial forces in wire rope seemed to mark the beginning of a new era directed at theoretical studies on cable stresses and deformations. However, little attention was given to the determination of actual stresses. Leissa<sup>8</sup> was probably the first one to undertake complete stress analysis of a 6x7 wire rope under tension. Starkey and Cress<sup>9</sup> improved his analysis by incorporating the effect of wire curvature. They also considered the crossed-wire case. Bert and Stein<sup>10</sup> presented a more general treatment for computation of contact stresses in the most severe contact regions and applied it to a 6x37 Warrington IWRC rope.

In the foregoing investigations, however, several simplifying assumptions of questionable validity were made. Costello, Phillips and other associates<sup>11, 20</sup> gave a new direction to the subsequent theoretical investigations on cable stresses and deformations. They treated separately the equilibrium of each of the constituent helical wires, although the assumption of no frictional force was kept intact. Their approach, however, requires solving simultaneously the governing set of nonlinear equations using a Newton-Raphson algorithm. The use of a computer is a must to generate the results, numerically, using data specific to cables under investigation. The "Linear Theory" as used earlier by Phillips and Costello<sup>21, 22</sup> and Velinsky, et al.,<sup>23</sup> although applicable to a cross-section of arbitrary geometry, has somewhat limited utility. They exploit it for relating changes in variables/parameters of helical wires to those of strands as well as the changes in variables/parameters of strands to those of cable in the loaded configuration. However, no attempt has been made to "integrate" these linearized relations in a concise form. In the process, their linearization merely achieves some economy of computational time without altering the basic numerical character of simulation involving the simultaneous solution of a set of usually a large number of algebraic equations (depending upon the geometry of the cable cross-section). In this manner, their approach does not provide any direct design insights as to the influence of the various cable parameters on elastic deformations unless one resorts to extensive numerical simulation covering the practical range of

values for each of the system parameters. Kumar and Cochran<sup>24, 25</sup> incorporated some suitable simplifying approximations to develop closed-form solutions for elastic multilayered strand cable deformations. This latter work is now extended to develop analytical expressions for critical contact stresses in cables of the single-strand fibrous-core type. Unlike the treatment of some of the earlier theoretical investigations, the effect of torsional moment is also incorporated along with that of simple tension.

It is felt that the explicit nature of the results developed here would be particularly useful in gaining fresh insights into the influence of the various cable parameters, thus facilitating design and rope-selection. The better understanding of the contact stresses may also be crucial to modeling of the energy dissipation phenomenon in the cables likely to be exploited in some new proposed applications, e.g., for augmentation of damping in large space structures. See Cutchins, et al.,<sup>26</sup> for other wire rope related models.

#### ANALYSIS

The cable under consideration is a single strand composed of a fibrous core wrapped around helically by an arbitrary number of wires, hereafter denoted by  $m$ . The radius of the wire, its helix radius and helix angle are denoted by  $R$ ,  $r$  and  $\alpha$ , respectively. The case investigated in this paper is that of the cable subjected to an external axial pull or tensile load  $F$ , and an axial or torsional moment  $M$ . It is assumed that under this loading, the helical character of the wires is retained. The corresponding deformed variables are represented by using primes as superscripts.

From simple geometric considerations of the cable cross-section it can be shown that:

$$(R/r) = [\sin^2 \alpha / (\sin^2 \alpha + \cot^2 \pi/m)]^{1/2}$$

which, for practical situations, can be approximated, to within 1% error, as

$$R/r \approx \sin \alpha \sin \pi/m [1 + (1/2) \cos^2 \alpha \sin^2 \pi/m] \quad (1)$$

The corresponding relation for the deformed configuration can be stated as

$$R'/r' \approx \sin \alpha' \sin \pi/m [1 + (1/2) \cos^2 \alpha' \sin^2 \pi/m] \quad (2)$$

where

$$R' \approx R(1 - \nu \xi) \quad (3)$$

$\nu$  = Poisson's ratio

$\xi$  = tensile strain in the helical wires

Using these three relations, we can show

$$(r/r') = 1 + \delta \quad (4)$$

where

$$\delta = v\xi + a \cot \alpha \Delta \alpha$$

$$a = 1 - \sin^2 \alpha \sin^2 \pi/m.$$

Strain Relations: The consideration of compatibility of the cable deformations leads to the following strain relations:

$$\text{Axial strain of the cable, } \epsilon = (1+\xi) \sin \alpha' / \sin \alpha - 1 \quad (5)$$

$$\text{Rotational strain of the cable, } \beta = (r/r')(1+\epsilon) \cot \alpha' - \cot \alpha \quad (6)$$

where

$\xi$  = longitudinal strain of helical wires

Denoting the change in the wire helix angle (i.e.,  $\alpha' - \alpha$ ) by  $\Delta \alpha$ , Eqs. (5) and (6) can be written to first order in  $\Delta \alpha$  as:

$$\xi \approx \epsilon - \Delta \alpha \cot \alpha$$

$$\Delta \alpha \approx [\epsilon(1+v) \sin \alpha \cos \alpha - \beta \sin^2 \alpha] b \quad (7)$$

where

$$b \approx 1 + (\cos^2 \pi/m - v) \cos^2 \alpha + (1-2v) \cos^4 \alpha \quad (8)$$

Force and Moment Relations: We denote by  $T$  and  $G$  the resultant internal forces and moments in the helical wires, respectively. The subscripts  $n$ ,  $b$  and  $a$  are added to represent the corresponding components of  $T$  and  $G$  along the normal, binormal and axial directions, then,

$$T_a = \pi R^2 \xi E$$

$$G_n = (\pi R^4 E / 4) (\lambda'_n - \lambda_n)$$

$$G_b = (\pi R^4 E / 4) (\lambda'_b - \lambda_b)$$

$$G_a = (\pi R^4 E / 4) (\lambda'_a - \lambda_a)$$

where

$E$  = the modulus of rigidity of the material of the helical wires.



$\lambda_n, \lambda'_n = 0$ ; the initial and final components of curvature of the helical wires along the normal.

$\lambda_b, \lambda'_b = (\cos^2 \alpha / r), (\cos^2 \alpha' / r')$ , the initial and final components of curvature of the helical wires along the binormal.

$\lambda_a, \lambda'_a = (\sin \alpha \cos \alpha / r), (\sin \alpha' \cos \alpha' / r')$ ; the initial and final components of curvatures of the helical wire along the axis.

Through some suitable simplifying approximations, it can be shown that

$$T_a = \pi R^2 E [\epsilon \{1 - (1 + \nu) b \cos^2 \alpha\} + \beta b \sin \alpha \cos \alpha]$$

$$G_a = [\pi R^4 E / \{4(1 + \nu)r\}] [\nu \epsilon + \{a - \nu - \tan^2 \alpha\} \cot \alpha \Delta \alpha] \sin \alpha \cos \alpha$$

$$G_b = [\pi R^4 E / \{4r\}] [\nu \epsilon + (a - \nu - 2 \tan^2 \alpha) \cot \alpha \Delta \alpha] \cos^2 \alpha$$

$$G_n = 0$$

Now considering the equilibrium of helical wires, we obtain:<sup>13</sup>

$$T_b \approx G_a \lambda'_b - G_b \lambda'_a$$

$$q_n \approx -T_a \lambda'_b + T_b \lambda'_a$$

where  $q_n$  is the normal component of the resultant contact force per unit length. These two relations lead to:

$$T_b \approx [b \pi R^4 E / (4r^2)] [\epsilon \{(1 + 2\nu) \sin^2 \alpha - \nu^2 - \nu \cos^2 \alpha\} \cos \alpha - \beta \{\sin^2 \alpha - \nu_f \cos 2\alpha\} \sin \alpha] \sin \alpha \cos^2 \alpha \quad (9)$$

$$q_n \approx -(\pi R^2 E / r) \cos^2 \alpha [\epsilon \{1 - (1 + \nu) b \cos^2 \alpha\} + \beta b (1 + c \sin^4 \alpha) \sin \alpha \cos \alpha] \quad (10)$$

where

$$\nu_f = \nu / (1 + \nu)$$

$$c = (1/4)(1 + \nu_f)(R^2 / r^2)$$

The angle  $\gamma$  that locates the lines of action of the line contact loads of a helical wire with adjacent helical wires is given by

$$\cos \gamma = \sin \alpha \sin \pi / m [1 - \sin^2 \pi / m \cos^2 \alpha]^{1/2} \quad (11)$$

giving the following expression for the contact force per unit length denoted by  $Q$ :

$$q_n = -2Q \cos \gamma \quad (12)$$

Using the earlier expressions for  $q_n$  and  $\cos \gamma$ , we get

$$Q = [\pi R^2 E / (2r)] [\cos^2 \alpha / (\sin \alpha \sin \pi/m)] [1 + 1/2 \sin^2 \pi/m \cos^2 \alpha] \\ [\epsilon \{1 - (1+\nu)b \cos^2 \alpha\} + \beta b \{1 + c \sin^4 \alpha\} \sin \alpha \cos \alpha] \quad (13)$$

Here, the strains  $\epsilon$  and  $\beta$  are related to the tensile force ( $F$ ) and torsional moment ( $M$ ) as follows:<sup>24,25</sup>

$$\bar{F} = F_\epsilon \epsilon + F_\beta \beta \quad (14)$$

$$\bar{M} = M_\epsilon \epsilon + M_\beta \beta \quad (15)$$

where the nondimensionalized force and moment represented by  $\bar{F}$  and  $\bar{M}$  are defined as follows:

$$\bar{F} = F / (m\pi R^2 E) \quad (16)$$

$$\bar{M} = M / (m\pi R^3 E)$$

and the expressions for force and moment derivatives, ( $F_\epsilon$ ,  $F_\beta$ ,  $M_\epsilon$  and  $M_\beta$ ) developed by Kumar and Cochran<sup>24</sup> and reproduced below, are now utilized to solve Eqs. (14) and (15) for  $\epsilon$  and  $\beta$ :

$$F_\epsilon = e \sin \alpha \\ F_\beta = [b - (1+\nu)/4 \sin^2 \pi/m \sin^4 \alpha \cos^2 \alpha] \sin^2 \alpha \cos \alpha \\ M_\epsilon = (r/R) [e - (1/4)(1-\nu_f \cos^2 2\alpha) \sin^2 2\pi/m \sin^2 \alpha] \cos \alpha \\ M_\beta = (r/R) [b \cos^2 \alpha + (1/4)(1+f)] \sin \alpha \quad (17)$$

where

$$e = 1 - (1+\nu) \cos^2 \alpha - (1+\nu)(\cos^2 \pi/m - \nu) \cos^4 \alpha \\ f = \nu_f \cos 2\alpha + (1+\nu) \sin^2 \alpha \cos^2 \alpha \quad (18)$$

Substituting the resulting expressions for  $\epsilon$  and  $\beta$  into Eq. (13) followed by nondimensionalization leads to

$$\bar{Q} = Q_F \bar{F} + Q_M \bar{M} \quad (19)$$

with

$$\bar{Q} = Q/(\pi R)$$

$$Q_F = (1/2) g_1 \sin \alpha \cos^2 \alpha$$

$$Q_M = (1/v)(1+v)^2 g_2 \sin^3 \alpha \cos^3 \alpha \sin \pi/m (1 + 1/2 \sin^2 \pi/m \cos^2 \alpha)$$

$$g_1 = 1 - 2v \cos^2 \alpha + (1 + 4v + 9v^2) \cos^4 \alpha + (1 + 3v - 20v^2 - 33v^3) \cos^6 \alpha$$

$$-4 \{ \cos^8 \alpha / (\sin^4 \alpha \sin^2 \pi/m) \} \{ 1 - 3v \cos^2 \alpha + (1 + 4v + 12v^2) \cos^4 \alpha \}$$

$$g_2 = 1 - v_f^2 + 1/2 \sin^2 \pi/m \cos^2 \alpha - v(5 - 3v^2) \cos^2 \alpha - (1 - 3v - 17v^2)$$

$$\cos^4 \alpha - 3(1 - 2v + 9v^2 + 23v^3) \cos^6 \alpha + 4(1 - 2v) \{ \cos^8 \alpha / (\sin^4 \alpha \sin^2 \pi/m) \} \{ 1 - 3v \cos^2 \alpha + (1 + 4v + 12v^2) \cos^4 \alpha \}$$

#### Contact Stresses:

To compute the contact stresses, direct use can be made of the results given by Seely and Smith<sup>27</sup> in their book.

The expressions for the three principal compressive stresses due to the contact force are given below:

$$\sigma_x = 2v[\sqrt{1 + (z/p)^2} - (z/p)](p/\Delta)$$

$$\sigma_y = [(\sqrt{1 + (z/p)^2} - z/p)^2 / \{1 + (z/p)^2\}^{1/2}](p/\Delta)$$

$$\sigma_z = [1 + (z/p)^2]^{-1/2} [p/\Delta]$$

where

$\sigma_x, \sigma_y, \sigma_z$  = principal compressive stresses in the axial, tangential and radial directions, respectively.

$z$  = distance below the surface to the point under consideration.

$$p = [2 Q \Delta / \pi]^{1/2}$$

$$\Delta = [2(1-v^2)R/E]$$

Since the above compressive stresses are maximum when  $z=0$ , i.e., on the surface of the wires at the contact points, we get

$$(\sigma_x)_{\max} = 2v p / \Delta = 2v [1/(1-v^2)]^{1/2} [EQ/(\pi R)]^{1/2}$$

$$(\sigma_y)_{\max} \approx (\sigma_z)_{\max} \approx p / \Delta = [1/(1-v^2)]^{1/2} [EQ/(\pi R)]^{1/2}$$

The latter of these is the maximum normal contact stress which we denote by  $\sigma$ ; hence

$$\sigma \approx [1/(1-v^2)]^{1/2} [QE/(\pi R)]^{1/2} \quad (20)$$

Substitution of the earlier expression for  $Q$  followed by nondimensionalization leads to the maximum contact stress:

$$\bar{\sigma} \approx [(1/2) \sin \alpha]^{1/2} \cos \alpha [h_1 \bar{F} + h_2 (1+v)^2 \sin^2 \alpha \cos \alpha \sin(\pi/m) \bar{M}] \quad (21)$$

where

$$\bar{\sigma} = \sigma / E$$

$$h_1 = 1+v^2/2-2v \cos^2 \alpha + (1+4v+9v^2) \cos^4 \alpha + (1+3v-20v^2-33v^3)$$

$$\cos^6 \alpha - 4\{\cos^8 \alpha / (\sin^4 \alpha \sin^2 \pi/m)\} \{1-3v \cos^2 \alpha +$$

$$(1+4v+12v^2) \cos^4 \alpha\}$$

$$h_2 = [1+v^2/2-v_f^2 + (\sin^2 \pi/m \cos^2 \alpha)/2 - v(5-3v^2) \cos^2 \alpha$$

$$- (1-3v-17v^2) \cos^4 \alpha - 3(1-2v+9v^2+23v^3)\{\cos^6 \alpha /$$

$$(\sin^4 \alpha \sin^2 \pi/m)\} \{1-3v \cos^2 \alpha + (1+4v+12v^2) \cos^4 \alpha\}]$$

and  $\bar{F}$ ,  $\bar{M}$  are given by Eq. (16).

## RESULTS AND DISCUSSION

The expressions obtained above are of considerable significance. The results are dimensionless and explicit. These closed-form solutions provide useful information concerning the influence of the cable parameters and its properties. For a better assessment of the influence of the cable parameters and material properties, the variation of the rather involved functions,  $h_1$  and  $h_2$ , was studied over the practical range of  $\alpha$  (i.e.,  $\pi/3 \leq \alpha \leq \pi/2$ ), covering a number of cases with different values of  $m$  and  $v$ . Some typical plots are presented here (Fig. 1). It is interesting to note that for "relatively large"  $\alpha$ , the variables  $h_1$  and  $h_2$  do not show any significant variations and that both, to first order can be approximated as unity. This approximation simplifies Eq. (21) to

$$\bar{\sigma} = \{(1/2) \sin \alpha\}^{1/2} \cos \alpha [\bar{F} + (1+v)^2 \sin^2 \alpha \cos \alpha \sin(\pi/m) \bar{M}].$$

This result is of considerable importance, particularly for preliminary cable design. It clearly brings out the role of  $\alpha$  and  $m$  in affecting the contact stresses when the cable is subjected to tension and/or torsional moment. However, in view of the specified constraint on  $\alpha$  for the above expression to be valid, it would be advisable to stick to the more accurate earlier results in the final analysis. Some typical results based on this more accurate equation, Eq. (21), are presented in Fig. 2 and Fig. 3. These plots show the effect of varying the wire helix angle  $\alpha$  on the maximum

contact stress  $\bar{\sigma}$ . Three different loading conditions with pure tension, pure torsional moment and combined tension and torsion are considered. In general, in the practical range of  $\alpha$ , the dimensionless stress,  $\bar{\sigma}$ , continuously decreases with increasing  $\alpha$ , vanishing altogether at  $\alpha = \pi/2$  as expected. However, an exception to this general trend may be observed in the lower range of  $\alpha$ , particularly when  $m$  (i.e., the number of helical wires in the cable) is large. From Fig. 3, it is evident that the changes in  $v$  within practical limits for steel cables do not influence the contact stress characteristics to any perceptible extent.

## ACKNOWLEDGEMENTS

The support of NASA/MSFC under Grant NAG8-647 has been most instrumental during this work and is gratefully acknowledged.

#### REFERENCES

1. Scobble, W. A., 1920-1935, "First Report of the Wire Rope Research Committee," Proceedings of Institution of Mechanical Engineers, Vol. 115, pp. 835-868; Vol. 119, pp. 1193-1290, Third Report, Vol. 123, pp. 353-404; Fourth Report, Vol. 130, pp. 373-478.
2. Wire Rope Users Manual, 1979, Washington, D. C., American Iron and Steel Institute.
3. Code of Federal Regulations, 1980, Vol. 30, Mineral Resources, pp. 357.19-39.
4. Hall, H. M., 1951, "Stresses in Small Wire Ropes," Wire and Wire Products, Vol. 26, p. 228, pp. 257-259.
5. Hruska, F. H., 1951, "Calculations of Stresses in Wire Ropes," Wire and Wire Products, Vol. 26, pp. 766-767, pp. 799-801.
6. Hruska, F. H., 1952, "Radial Forces in Wire Ropes," Wire and Wire Products, Vol. 27, pp. 459-463.
7. Hruska, F. H., 1953, "Tangential Forces in Wire Ropes," Wire and Wire Products, Vol. 28, pp. 455-460.
8. Leissa, A. W., 1959, "Contact Stresses in Wire Ropes," Wire and Wire Products, Vol. 34, pp. 307-316, pp. 372-373.
9. Starkey, W. L., and Cress, H. A., 1959, "An Analysis of Critical Stresses and Mode of Failure of a Wire Rope," ASME Journal of Engineering for Industry, Vol. 81, pp. 307-316.
10. Bert, C. W., and Stein, R. A., 1962, "Stress Analysis of Wire Rope in Tension and Torsion," Wire and Wire Products, Vol. 37, pp. 769-770, pp. 772-816.
11. Costello, G. A., and Phillips, J. W., 1973, "Contact Stresses in Thin Twisted Rods," ASME Journal of Applied Mechanics, Vol. 40, pp. 629-630.
12. Costello, G. A., and Phillips, J. W., 1974, "A More Exact Theory for Twisted Wire Cables," ASCE Journal of the Engineering Mechanics Division, Vol. 100, pp. 1096-1099.
13. Costello, G. A., and Phillips, J. W., 1976, "Effective Modulus of Twisted Wire Cables," ASCE Journal of the Engineering Mechanics Division, Vol. 102, pp. 171-181.
14. Costello, G. A., and Sinha, S. K., 1977a, "Torsional Stiffness of Twisted Wire Cables," ASCE Journal of the Engineering Mechanics Division, Vol. 103, pp. 766-770.

15. Costello, G. A., and Sinha, S. K., 1977b, "Static Behavior of Wire Rope," ASCE Journal of the Engineering Mechanics Division, Vol. 103, pp. 1011-1022.
16. Costello, G. A., 1978, "Analytical Investigation of Wire Rope," Applied Mechanics Reviews, Vol. 31, pp. 897-900.
17. Costello, G. A., and Miller, R. E., 1979, "Lay Effect of Wire Rope," ASCE Journal of the Engineering Mechanics Division, Vol. 105, pp. 597-608.
18. Costello, G. A., and Miller, R. E., 1980, "Static Response of Reduced Rotation Rope," ASCE Journal of the Engineering Mechanics Division, Vol. 106, pp. 623-631.
19. Costello, G. A., and Buston, G. J., 1982, "Simplified Bending Theory for Wire-Rope," ASCE Journal of the Engineering Mechanics Division, Vol. 108, pp. 219-227.
20. Costello, G. A., 1983, "Stresses in Multilayered Cables," Journal of Energy Resources Technology, Vol. 105, pp. 337-340.
21. Phillips, J. W., and Costello, G. A., 1973, "Contact Stresses in Twisted Wire Cables," ASCE Journal of the Engineering Mechanics Division, Vol. 99, pp. 331-341.
22. Phillips, J. W., and Costello, G. A., 1985, "Analysis of Wire Ropes with Internal-Wire-Rope Cores," ASME Journal of Applied Mechanics, Vol. 52, pp. 510-516.
23. Velinsky, S. A., Anderson, G. L., and Costello, G. A., 1984, "Wire Rope with Complex Cross Sections," ASCE Journal of the Engineering Mechanics Division, Vol. 110, pp. 380-391.
24. Kumar, K., and Cochran, J. E., Jr., 1987, "Analytical Solutions for Static Elastic Deformations of Wire Ropes," AIAA Paper No. 87-0720, Proceedings of the 28th AIAA/ASME/ASCE/AHS Structures, Structural Dynamics and Materials Conference, Part I, April 6-8, Monterey, California, pp. 88-92.
25. Kumar, K., and Cochran, J. E., Jr., 1987, "Closed-Form Analysis for Elastic Deformations of Multilayered Strands," Journal of Applied Mechanics, Vol. 54, pp. 898-903.
26. Cutchins, M. A., Cochran, J. E., Jr., Kumar, K., Tinker, M. L., and Fitz-Coy, N. G., "Analysis of Coils of Wire Rope Arranged for Passive Damping," Proceedings of the Third International Conference on Recent Advances in Structural Dynamics, Southampton, England, July 18-22, 1988, pp. 469-479.
27. Seely and Smith, Advanced Mechanics of Materials, John Wiley & Sons, Inc., 1952, pp. 365-366.

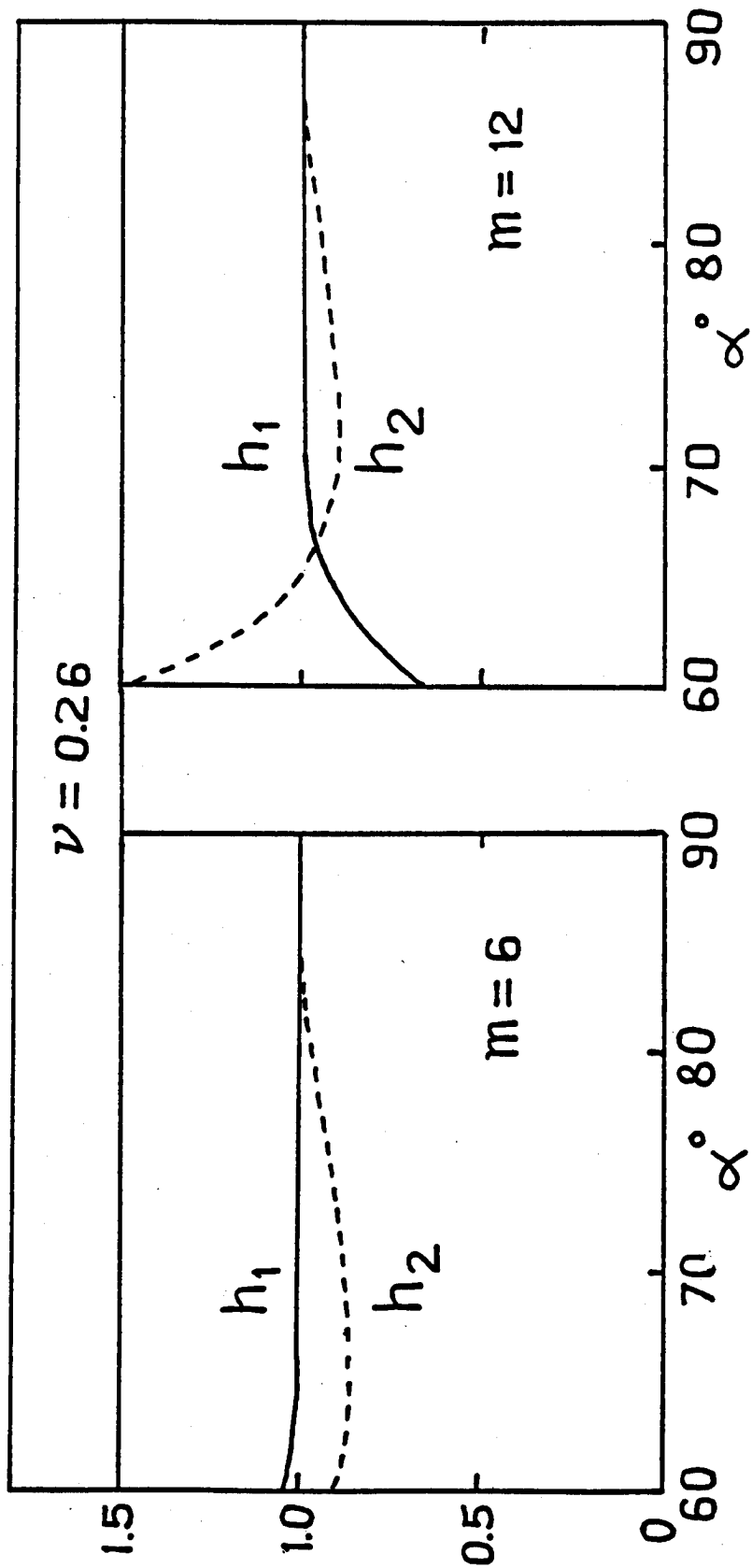


Fig. 1 Typical plots showing the effect of  $\alpha$  on  $h_1$  and  $h_2$



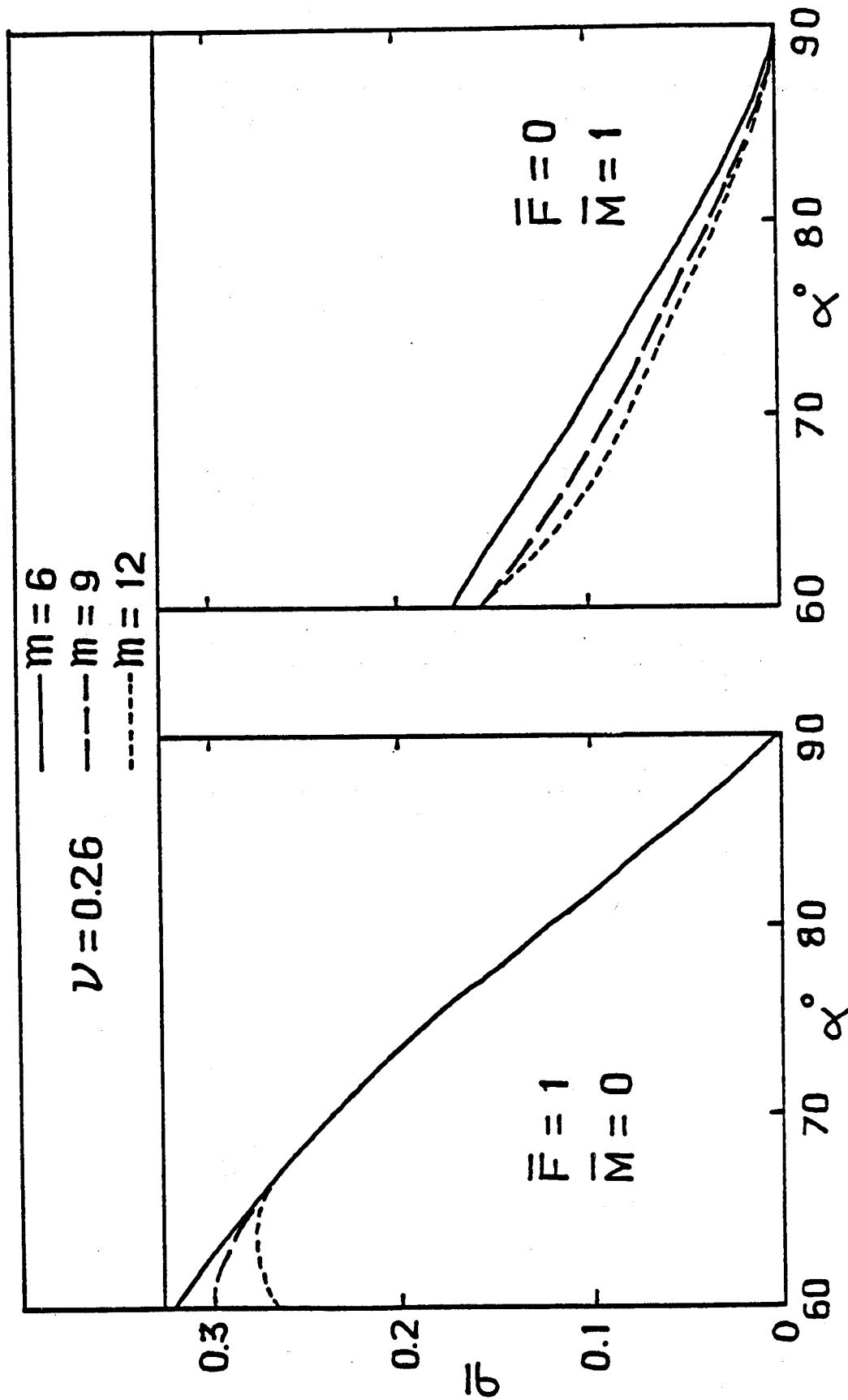


Fig. 2 System plots showing the effect of  $\alpha$  on  $\bar{\sigma}$  when the cable is subjected to pure tension or torsional moment.

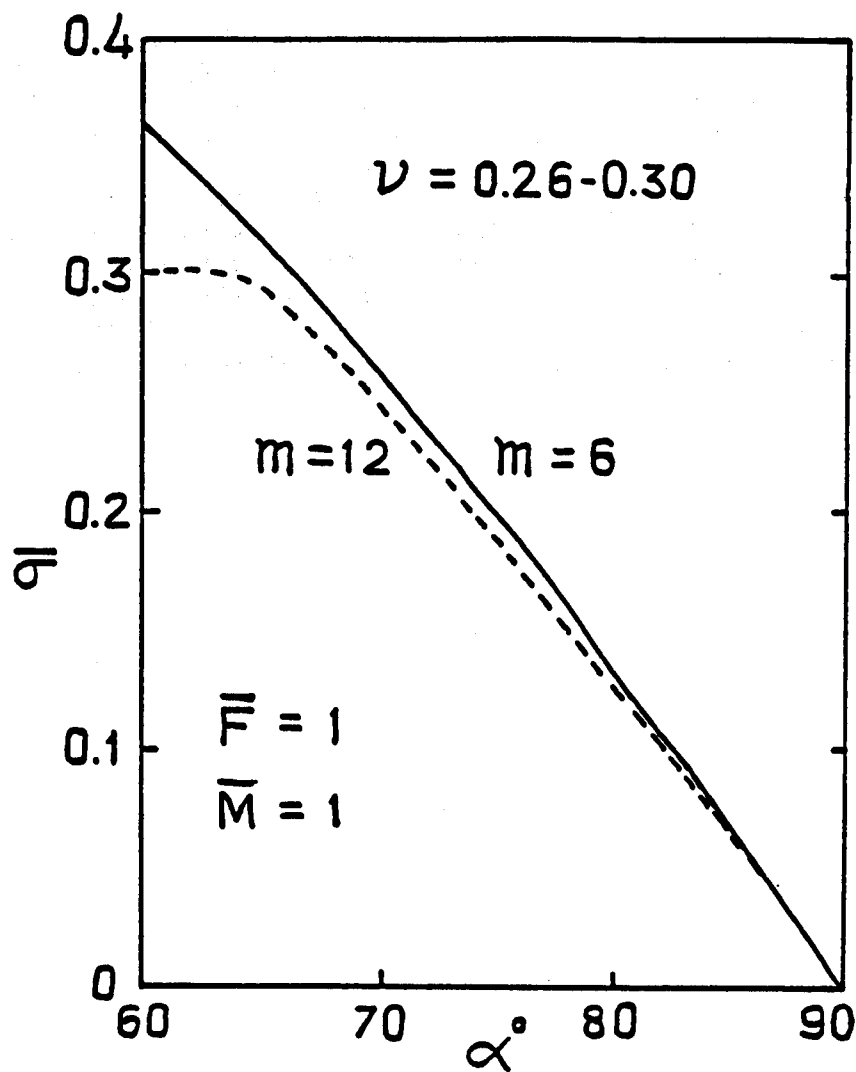


Fig. 3 System plots showing the effect of  $\alpha$  on  $\bar{\sigma}$  when the cable is subjected to tension as well as torsion.

# EFFECT OF INERTIAL FORCES ON DAMPING IN A DRY FRICTION JOINT

O. Vinogradov  
Department of Mechanical Engineering  
University of Calgary  
Calgary, Alberta, Canada T2N 1N4  
(403) 220-7187

## Abstract

In a press fit joint a rod is considered as being flexible while a bush is rigid. The rod is modelled as a discrete mass system subjected at one end to a harmonic force. Each mass is moving in the presence of dry friction forces of constant intensity. A computer simulation technique is used to investigate the effect of inertial forces on the microslip in a press fit joint and then on the frictional losses during one cycle of loading. The numerical results show that the effect of inertial forces becomes significant at ultrasound frequencies. Similarity criteria are given to extend the results of numerical simulation presented for a particular case and to show the qualitative relationship between the dynamic losses and system parameters.

## 1. Introduction

The effect of friction at the interface of structural members on the damping properties of a structure was always of interest to structural engineers. One aspect of this general problem is associated with the process which takes place in a friction joint subjected to a cyclic loading, namely, the cyclic microslip and corresponding losses. Panovko formulated and solved this problem for a press fit joint subjected to a quasi-static cyclic loading in 1958 [1].

Interest to energy dissipation in a simple joint due to friction was maintained over the past two decades [f.e. 2, 3, 4] and even became stronger in view of more rigid requirements to vibration control in space applications. In analyzing losses in a frictional joint one parameter, namely, the inertial forces, has always been ignored, while the limits of this assumption has never, to the best of author's knowledge, been studied.

The problem for a frictional joint in a dynamic formulation does not have a closed form solution analagous to that obtained by Panovko. In fact, when investigating the dynamics of a frictionally constrained rod the author preferred numerical simulation [5] to any approximate analytical approach because of the uncertainty in the dynamic behaviour which inertial forces introduce. In [5] a simulation technique was used to solve an initial value problem for a discrete system of masses subjected to a periodic load and moving in the presence of friction. However, the question of energy losses was not addressed in [5] and was only partially discussed in [6].

In this paper a more systematic numerical analysis of dynamic vs. static losses is given for a particular case. Also, the effect of such parameters as coefficient of friction and amplitude of the harmonic force is investigated. To generalize the numerical results the similarity criteria are given.

## 2. Mathematical Model and Simulation Procedure

In this paper a simple press fit joint is considered and it is assumed that the rod is flexible while the bush is rigid. The friction forces are assumed to be of constant intensity (dry friction). The rod is acted upon by a harmonic force applied at one of the ends.

A mathematical model describing the outlined problem is intrinsically non-linear due to dry friction. During each half-cycle of the loading every cross-section of the rod might be stationary over some time interval (inter-locking). These stationary cross-sections in fact make-up a stationary region (segment). At any moment in time there is a number of stationary and moving segments. The number of such segments, their length and sense of motion is not known a priori. Besides, the picture may differ from one cycle to another and it is not clear in advance whether a process would converge to a steady state one for a specific set of problem parameters. To investigate the dynamic behaviour of such a system a computer simulation technique was developed

by the author [5]. Here only a brief description of the simulation procedure is given for the sake of clarity. A rod is modelled as a discrete system of equal masses, springs and dashpots (Fig. 1). The simulation process starts during the first half-cycle of the loading when the external force becomes equal to the friction force associated with the first mass. The equation of motion of the first mass is generated and an analytical solution is obtained. This solution is valid until either the second mass starts moving or the first mass stops. At this moment it is either the one-mass system becomes a two-mass system or the whole rod becomes stationary.

In a developed process there can be masses moving in a positive direction, negative direction or remaining stationary. Motion of the entire system is represented by the motion of its subsystems. The system remains invariable if the number of sub-systems and the number of masses in each sub-system remains the same. The invariable system is governed by the linear differential equations. However, the moment in time when the status of the physical system changes cannot be determined analytically and this fact constitutes a need for simulation. A time-stepping procedure is utilized to identify the moment when the system changes its status. Between such two moments in time (events) the analytical solution is used to describe the motion.

### 3. Numerical Results

Numerical examples are given for a steel pin which is 0.025 m long and has a radius of 0.005 m. The pin is subjected to axial harmonic forces of various amplitudes and frequencies  $P = P_1 \sin(\omega t)$ . The total friction force,  $F_t$ , is used as a measure of friction. The pin is modelled as a ten-mass system, the number of discrete masses found to be sufficiently accurate for this type of a problem [6]. The material damping properties are taken in the same form as in [5].

#### 3.1 Discontinuity of Motion

Examples of the displacement of masses in time during the first few cycles of the load are shown in Figs. 2 and 3. The discontinuity of motion is clearly seen: the flat parts on the graphs indicate the length of time during which each mass remains stationary. Also it is seen that various masses start or stop moving not simultaneously. Both shift in phase and the length of the stationary period are dependent on the force frequency and amplitudes. At some frequencies and amplitudes motion becomes continuous. Note also, that it requires a few cycles before the process becomes steady.

#### 3.2 Hysteresis

Since work done by the friction forces during the cycle is equal to the work done by the external force during the same cycle the hysteretic losses were measured by considering the external force-displacement relationship during the cycle and measuring the corresponding hysteretic loop area. Two examples of hysteretic loops are shown in Figs. 4 and 5. It is seen that at  $f = 250$  Hz the system behaves as perfectly quasi-static one with the clearly identified discontinuities in stiffness,

whereas at  $f = 2\text{kHz}$  the hysteretic loop becomes more smooth which is an indication of the effect of inertial forces. However, the maximum displacement of the first mass in both cases is practically unaffected ( $U_{\max} = 2.7 \times 10^{-4} \text{ mm}$ ). It is worth mentioning that exact analytical solution according to [1] gives for given loads and pin parameters maximum displacement during the cycle as  $U_{\max} = 2.9 \times 10^{-4} \text{ mm}$ . The discrepancy is associated with the discretization [6]. A vertical part of the loop in Figs. 4 and 5 indicates a range of force over which the first mass remains stationary.

### 3.3. Cyclic Losses

The effect of frequency and nondimensional amplitude of the external force on dynamic losses is shown in Fig. 6, in which Fig. 6b provides a close-up look of curves in Fig. 6a at low frequencies. The static losses were calculated according to [1]

$$\psi = \frac{2}{3} \frac{P_1^3 L}{F_t \cdot EA} \quad (1)$$

where  $P_1$  is the amplitude of dynamic force,  $L$  is the length of the pin-hub interface,  $F_t$  is the total friction force at the interface,  $E$  is the modulus of elasticity, and  $A$  is the cross-section area of the pin.

It is seen from Fig. 6b that for practically important range of frequencies (up to 60 Hz) the effect of inertial forces on hysteretic losses is negligibly small. However, Fig. 6a indicates that at ultrasound frequencies the losses due to dry friction may grow many folds. This increase is associated with the phenomenon of macroslip of the entire pin at the interface at these frequencies [5]. The effect of inertial forces on losses at ultrasound frequencies can also be seen in Fig. 7 where the relationship between the losses and the amplitude of the dynamic force is shown for a 15 kHz frequency. A cubic parabola indicates a quasi-static relationship according to formula Eq. 1. It is seen that dynamic losses grow faster with the amplitude of the force.

### 4. Similarity Criteria

Because of a number of parameters effecting the losses in a dry friction joint it seems that computer simulation is the only tool available to investigate the phenomenon. The results of computer simulation can be extended to dynamically similar situations. The following two similarity criteria can be derived for the problem under consideration

$$\frac{S_{\omega}^2 S_{\ell}^2 S_{\rho}}{S_E} = 1 \quad (2)$$

and

$$\frac{S_F}{S_\ell^2 S_E} = 1 \quad (3)$$

where  $S_\omega$  is the ratio of frequencies,  $S_\ell$  is the ratio of geometries,  $S_\rho$  is the ratio of densities,  $S_E$  is the ratio of moduli of elasticities, and  $S_F$  is the ratio of total friction forces in two dynamically similar dry friction joints. If material properties are the same in both joints than  $S_\rho = 1$  and  $S_E = 1$  and Eqs. 2 and 3 are reduced to

$$S_\omega S_\ell = 1 \quad (4)$$

and

$$\frac{S_F}{S_\ell^2} = 1 \quad (5)$$

Equation 4 means that if, for example, the geometry of the joint increased twice,  $S_\ell = 2$ , then the frequency should decrease twice,  $S_\omega = 0.5$ , in order to ensure the similarity. At the same time, as it follows from Eq. 5, the friction forces should be four times larger. Since friction forces are proportional to the surface area, the condition Eq. 5 is satisfied if the coefficient of friction and the contact pressure are maintained the same in both joints. Note that the external force - total friction force ratio is supposed to be maintained the same. Since losses are proportional to

$$S_L \sim S_F S_\ell \quad (6)$$

for the case of identical materials Eq. 6 is reduced to

$$S_L = S_\ell^3 \quad (7)$$

where  $S_L$  is the ratio of losses in two similar systems.

## 5. Conclusions

A computer simulation approach allowed to assess the effect of inertial forces on losses in a simple press fit joint. The results of simulation show that inertial forces become significant at ultrasound frequencies for a specific example considered. The similarity criteria derived indicate that the same losses may take place at lower frequencies for a scaled-up joint. The significance of inertial forces in dry friction joints on structural losses can be assessed in each specific application using the developed methodology [5].

## Acknowledgements

The financial assistance provided by the Natural Sciences and Engineering Research Council of Canada is gratefully acknowledged.

## References

- [1] Panovko, Ya. G., Gol'fzev, D.I. and Strakhov, G.H., "Elementary Problems of Structural Hysteresis", Voprosy Dinamiki i prochnosti, Riga, Latvian Academy of Science, 1958, pp. 5-26 (in Russian).
- [2] Metherell, A.F. and Diller, S.V., "Instantaneous Energy Dissipation Rate in a Lap Joint- Uniform Clamping Pressure", J. of Applied Mechanics, 35, 1968, pp. 123-128.
- [3] Beards, C.F. and Williams, J.L., "The Damping of Structural Vibration by Rotational Slip in Joints", J. of Sound and Vibration, 53(3), 1977, pp. 333-340.
- [4] Richardson, R.S.H. and Nolle, H., "Energy Dissipation in Rotary Structural Joints", J. of Sound and Vibration, 54(4), 1977, pp. 577-588.
- [5] Vinogradov, O.G., "Dynamics of Frictionally Constrained Finite Rod", Int. J. Computers and Structures, 29(4), 1988, pp. 667-673.
- [6] Vinogradov, O.G., "Effect of Vibration on a Press Fit", Proc. 9th Symp. on Engineering Applications of Mechanics, May 29-31, 1988, University of Western Ontario, London, Canada, pp. 240-245.



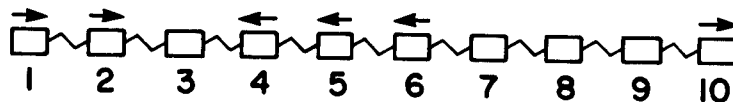


Fig. 1 Schematic representation of discrete model

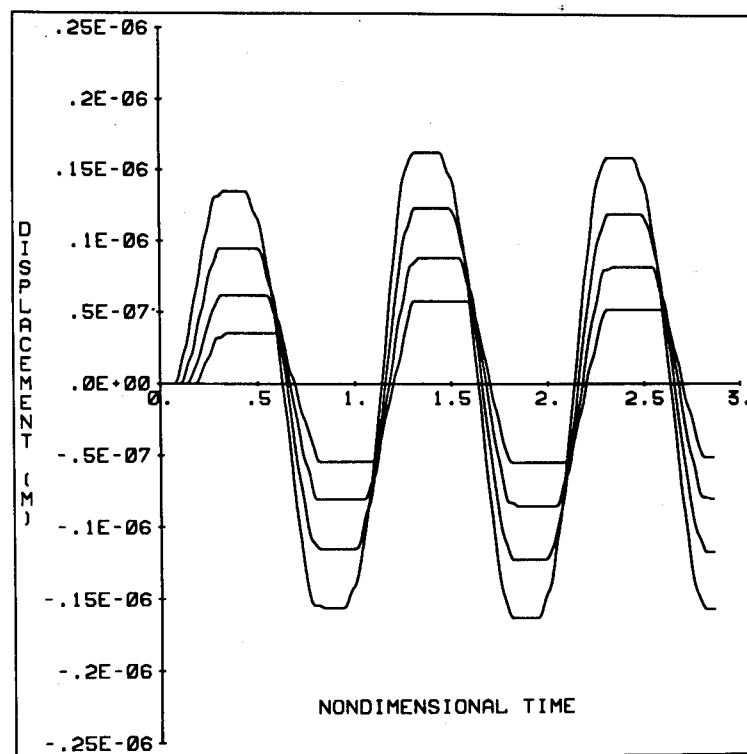


Fig. 2 Displacement of masses in a ten-mass model during first few cycles ( $F_t = 1010$  N,  $P_1 = 606$  N,  $f = 15$  kHz)

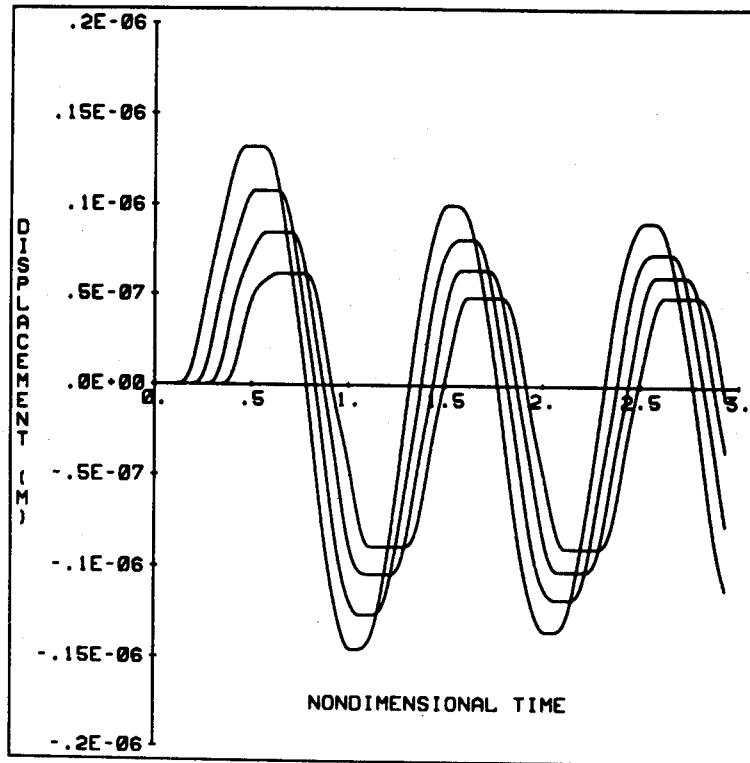


Fig. 3 Displacement of masses in a ten-mass model during first few cycles ( $F_t = 1010$  N,  $P_1 = 606$  N,  $f = 50$  kHz)

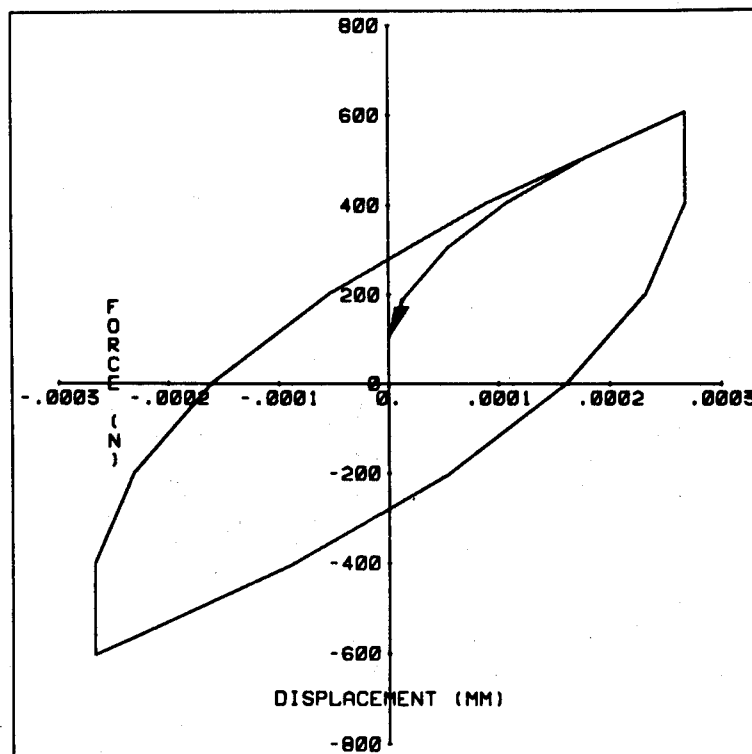


Fig. 4 Hysteretic loop ( $F_t = 1010$  N,  $P_1 = 606$  N,  $f = 0.25$  kHz)

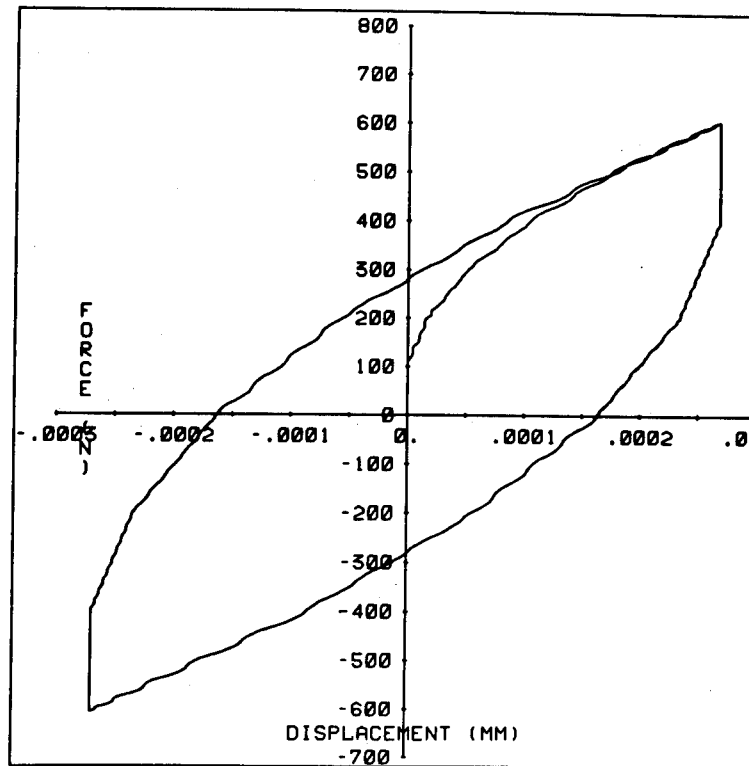


Fig. 5 Hysteretic loop ( $F_t = 1010$  N,  $P_1 = 606$  N,  $f = 2$  kHz)

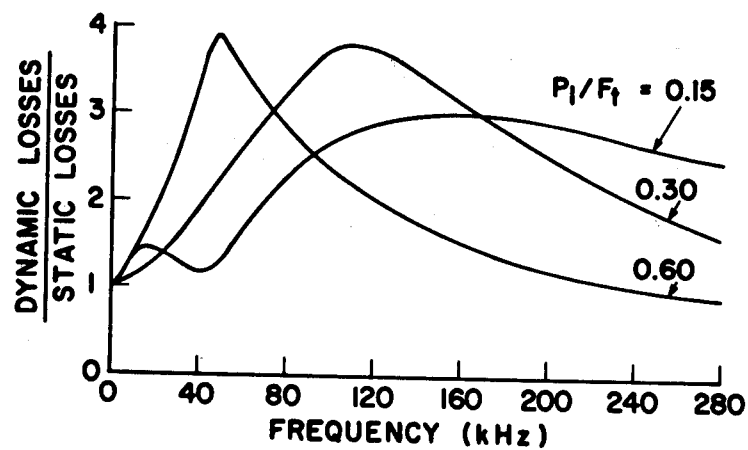


Fig. 6a Effect of frequency and amplitude of dynamic force on damping losses

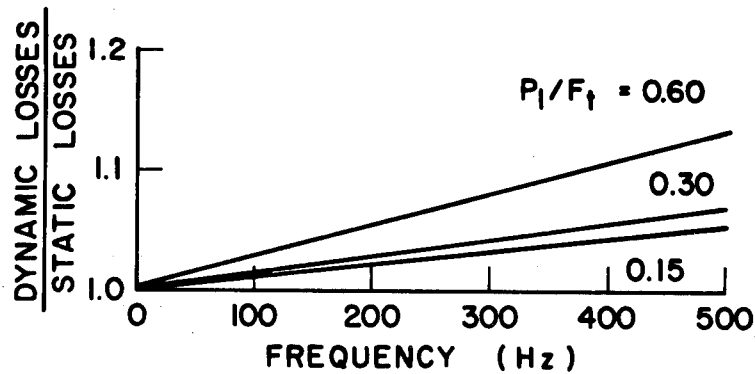


Fig. 6b Effect of frequency and amplitude of dynamic force on damping losses

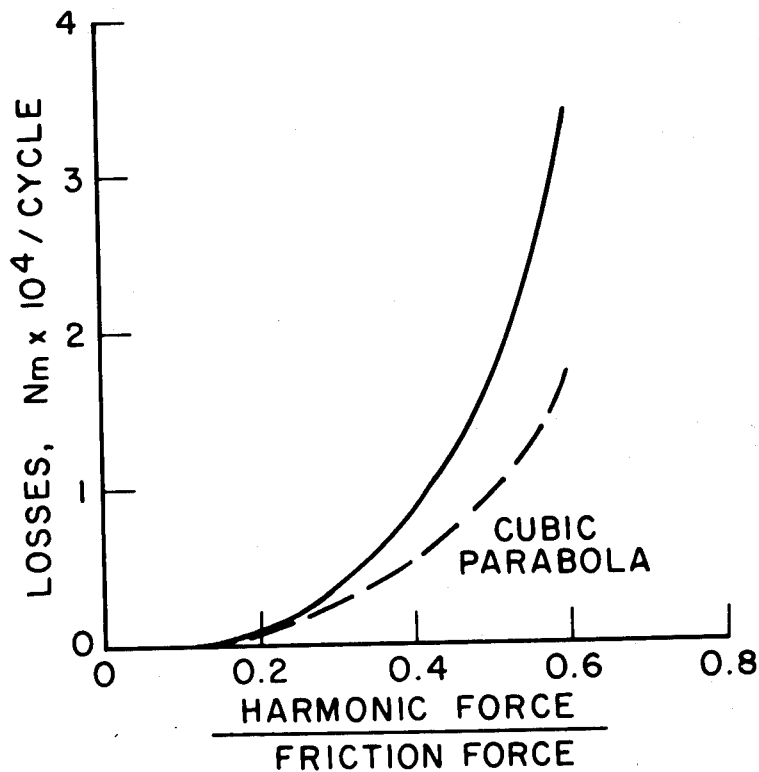


Fig. 7 Effect of the amplitude of dynamic force on damping losses (broken line indicates quasi-static cyclic losses).

## MODAL DAMPING OF SUSPENDED CABLES

**Hiroki YAMAGUCHI**

Associate Professor

Department of Foundation Engineering  
Faculty of Engineering, Saitama University  
255 Shimo-Ohkubo, Urawa, Saitama, 338 JAPAN  
JAPAN (48)852-2111 EXT2318

### ABSTRACT

Modal damping of flexural oscillation in suspended cable is investigated through free oscillation experiments with cable model and through finite element analyses. Relation between modal damping and dynamic characteristics of cable is discussed with parameters of sag-to-span ratio, span length, chord inclination, support flexibility and support damping. It is found that modal damping of cable is closely related to dynamic strain in normal mode and that internal damping of cable is a primary cause of modal damping of flexural oscillation. It is also found that damping at support contributes to modal damping directly and that the contribution of support damping is approximately proportional to square of modal support amplitude.

**KEYWORDS:** Cable, Experiment, Finite Element Analysis, Modal Damping.

### 1. INTRODUCTION

Cable has been widely used as structural member in civil engineering structures, such as suspension bridges, cable-stayed bridges, transmission lines, telecommunication lines, and so on. Especially in Japan, there is the big project; Honshu-Shikoku Bridge Project, of connecting two main islands by many over-sea bridges, most of which are cable-suspended bridges. Center span lengths of those suspension bridges are 770m, 876m, 940m, 990m, 1100m and 1990m. With the increase of span length in suspension bridge, cable becomes more and more important as structural member. As a matter of fact, it can be seen from Fig. 1 that weight proportion of cable to bridge deck increases almost linearly with span length. Fig. 1 indicates change of dead load ratio of cable to suspended structure with respect to center span length for Honshu-Shikoku Bridges and the Messina Straits Bridge in Italy. For the Akashi Straits Bridge center span of which will be 1990m, the weight of cable will be heavier and about 50% of the weight of suspended structure.

Fig. 2 is plots of maximum span length in cable-stayed bridge in Japan. As is shown in Fig. 2, many cable-stayed bridges have been constructed especially in this decade and the span length becomes longer and longer. This means cable becomes more and more important also in cable-stayed bridge.

Oscillations of cables, however, occur easily due to wind because of their light weight and high flexibility. Indeed remarkable oscillations, such as

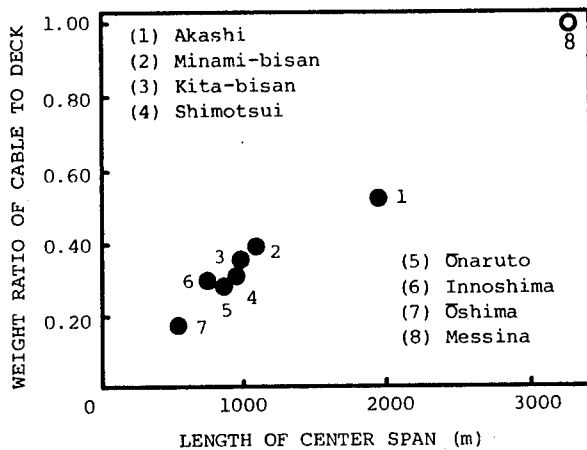


Fig. 1 Cable weight versus span length in suspension bridge

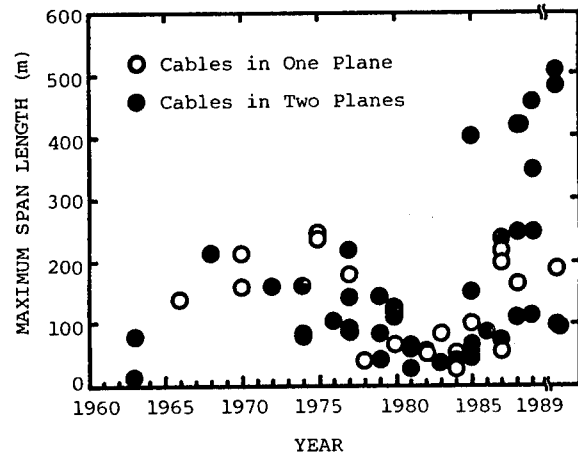


Fig. 2 Maximum span length of cable-stayed bridge in Japan

galloping and buffeting of cables in transmission lines, telecommunication lines, and cable-stayed bridges, have been reported frequently (see, for example, Rawlins [1981]; Fujino et al. [1988]; Hikami and Shiraishi [1988]) and recently the relatively new problem of rain and wind-induced vibration of cable becomes a serious engineering issue in cable-stayed bridges (Hikami and Shiraishi [1988]). Occurrence of wind-induced oscillation is much dependent on modal damping and the damping mechanism of cable is very important to consider suppression of such kind of oscillation.

Several studies have been made on damping characteristics of cables and wire ropes. Most of them deal either the first flexural modal damping of taut cable or with hysteresis damping of wire rope during axial oscillation (Hara and Ueda [1966]; Nishimura et al. [1977]; Tsuji and Kanou [1980]; Tanaka et al. [1985]; Kanou and Tsumura [1987]). This means that researches have been conducted mainly on the material damping of ropes, while there are very few investigations on the modal damping of flexural oscillation in suspended cables (Ramberg and Griffin [1977]; Yamaguchi and Fujino [1987, 1988]; Yamaguchi [1988]).

The primary objective of the present paper is to investigate modal damping characteristics of flexural oscillation in suspended cables through model experiments and finite element analyses. The sag-to-span ratio is chosen as a primary parameter in the testing and it is studied how the modal damping changes as the sag ratio changes. In addition, effects of initial tension, chord inclination, support flexibility and support damping on modal damping of cable are also discussed and the damping mechanism of cable is clarified.

## 2. OSCILLATION TEST WITH MODEL CABLE

Model cable employed in the experiment is 7-wire strand rope to which lead weights (15.0g/weight) are attached at interval of about 9.5cm distances in order to adjust weight of cable model. The tensile rigidity, tensile strength and mass per unit length of cable are  $2.40 \times 10^2$  [kN], 2.74 [kN] and 0.17 [kg/m], respectively. The details of cable model are shown in Fig. 3.

As is shown in Fig. 4, the model cable was wound with several turns around a horizontal bar steel fixed to a thick steel plate which was connected rigidly to a rigid support, and then mounted in the support through turnbuckle. Sag of cable

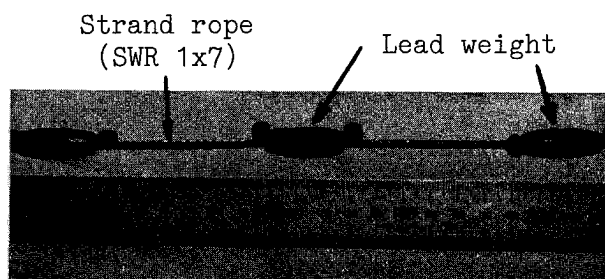


**Fig. 3** Details of model cable with lead weight

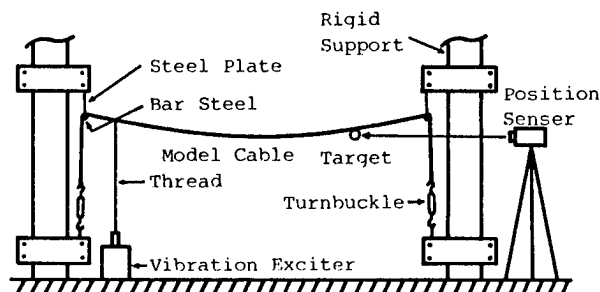


**Fig. 4** Schematic diagram of experimental set-up

was adjusted by the turnbuckle. The test cable set up with required sag-to-span ratio was forced to oscillate at each natural frequency by using vibration exciter which was connected to one point of cable through a thread. The thread was cut after stationary oscillation was attained, and the subsequent decay of free oscillation was recorded and analyzed to obtain natural frequency and modal damping. The excitation point was changed such that the mode concerned was purely excited. The dynamic displacement was measured by means of an electro-optical displacement follower (position sensor), a target of which was attached to the cable at the point of the largest amplitude of mode shape.

The span length and chord inclination were chosen as 7.3m and 0 degree, respectively. The sag-to-span ratio was changed from 0.005 to 0.1 considering sag ratios of real cable structures.

### 3. FINITE ELEMENT ANALYSIS OF CABLE OSCILLATION

Finite element analyses of free oscillation of cables were made in order to calculate natural frequencies, normal modes and additional dynamic strains. The 3 nodes quadratic element with shape function of quadratic polynomial was used and the matrices, such as mass and elastogeometric matrices, obtained by Henghold and Russell [1976] were applied. The static configuration due to dead load was analyzed first, and next eigenvalue problem was solved for small oscillation about the nonlinear equilibrium position by evaluating the tangential stiffness matrix. Using obtained mode vectors which are normalized relative to the maximum displacement value, additional dynamic strain at the internal node of each element is then calculated. Since each internal node has different value of dynamic strain, the root mean square of dynamic strains is taken as a representative value for each normal mode. Details of analyses are referred to Yamaguchi and Fujino [1987].

### 4. CHARACTERISTICS OF MODAL DAMPING

Fig. 5 shows the relation between natural frequency and sag-to-span ratio. Experimentally measured values are plotted with theoretically estimated curves for each natural mode. The distinct feature in this figure is in-plane symmetric mode. That is, there exists so-called modal transition (Yamaguchi and Ito [1979]) in certain region of sag ratio. In this modal transition region, the mode shape of symmetric mode changes into the one order higher symmetric mode with the increase of natural frequency, while natural frequencies of other modes decrease monotonically. Therefore, there exists modal crossover point at which natural

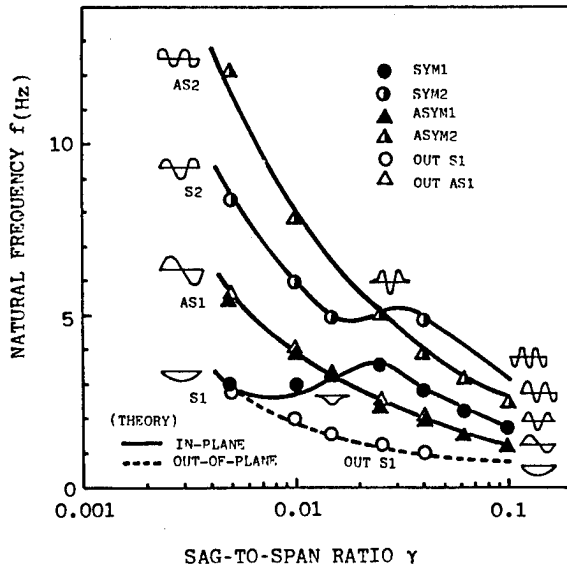


**Fig. 5** Natural frequency versus sag-to-span ratio

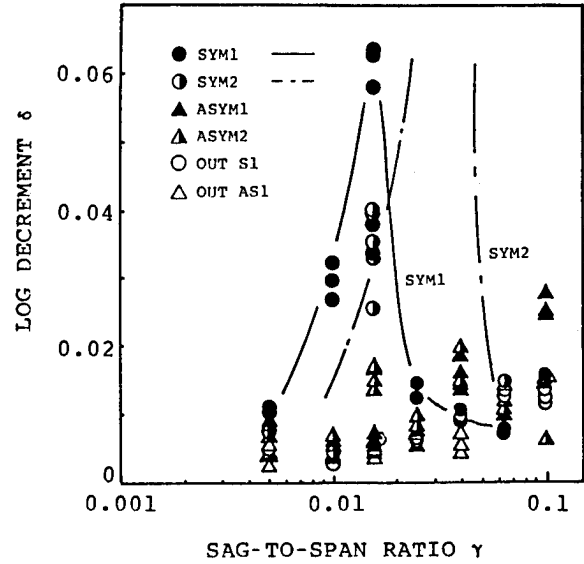


**Fig. 6** Modal damping versus sag-to-span ratio

frequency of symmetric mode coincides with that of asymmetric mode.

The experimentally measured values of corresponding modal damping represented by logarithmic decrement are shown in Fig. 6. Modal damping of cable is dependent on amplitude as has been reported by Yamaguchi and Fujino [1987], so that the damping was measured at the peak amplitude of mode shape nearly equal to 0.24% of span length. The logarithmic decrements shown in Fig. 6 were evaluated at the reference amplitude. It can be seen in Fig. 6 that the damping of in-plane symmetric mode is larger than other modal damping in the modal transition region,

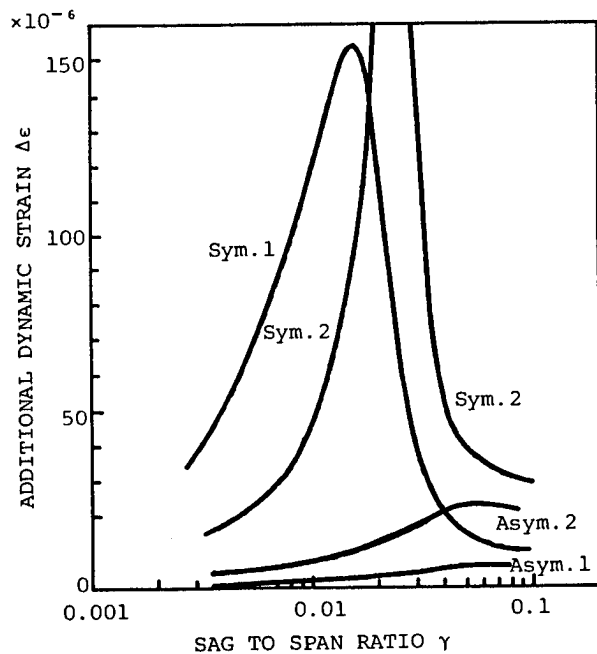


**Fig. 7** Additional dynamic strain versus sag-to-span ratio

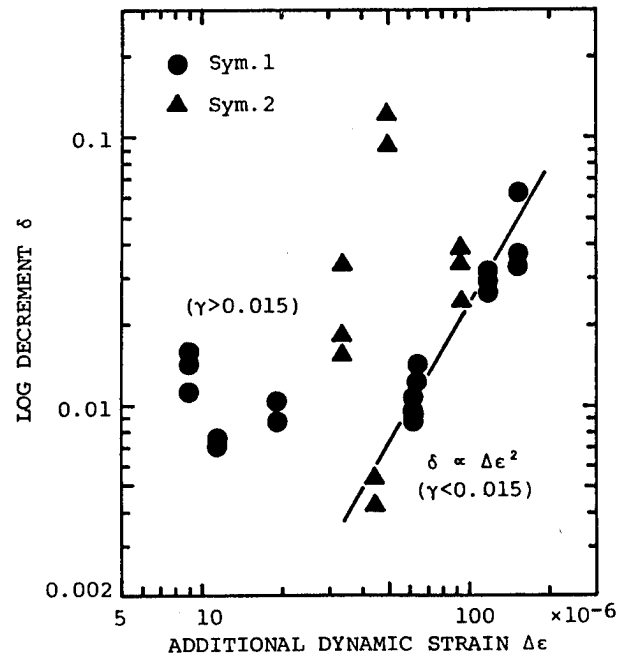


**Fig. 8** Modal damping versus additional dynamic strain



especially for the sag-to-span ratio around the modal crossover point. On the other hand, the damping for in-plane asymmetric modes and for out-of-plane modes is small and slightly increasing value over a wide range of sag-to-span ratio. It is concluded here that modal damping of cable for in-plane symmetric mode can be larger than modal damping for in-plane asymmetric and out-of-plane modes depending on sag ratio of cable.

The dynamic strain of cable during free oscillation was calculated for each normal mode in order to investigate the relation between modal damping and hysteresis energy, because the internal damping due to hysteresis energy is expected to be one primary source of cable damping. Fig. 7 is a plot of calculated dynamic strain versus sag ratio. As can be seen from Fig. 7, the change of dynamic strain with respect to sag ratio is quite similar to that of modal damping in Fig. 6. That is, the additional dynamic strain of symmetric mode takes large value in the modal transition region and has a maximum at the modal crossover point, while the dynamic strain of in-plane asymmetric mode is smaller in comparison with the symmetric mode and the dynamic strain of out-of-plane mode equals to zero in the linear theory.

The relation between modal damping and dynamic strain is shown more directly for in-plane symmetric mode in Fig. 8 where the abscissa is the calculated dynamic strain and the ordinate is the measured log decrement both in log scales. The data points plotted lie almost in a straight line of slope 2 in case of sag ratios less than the modal crossover point ( $\gamma < 0.015$ ). This means that the modal damping is in proportion to the square of dynamic strain, and that internal damping is primary cause of modal damping of cable.

Correspondence of modal damping to square of dynamic strain is poor for large sag ratios in Fig. 8 but this may be partly due to accuracy in the evaluation of dynamic strain. If geometrical nonlinear theory (Yamaguchi and Fujino [1987]) is applied, the dynamic strain for large sag ratio is calculated larger than that of linear theory (Fig. 9), and the correspondence of modal damping to square of dynamic strain for large sag ratio is improved as is shown in Fig. 10. The analysis based on the nonlinear evaluation of dynamic strain,

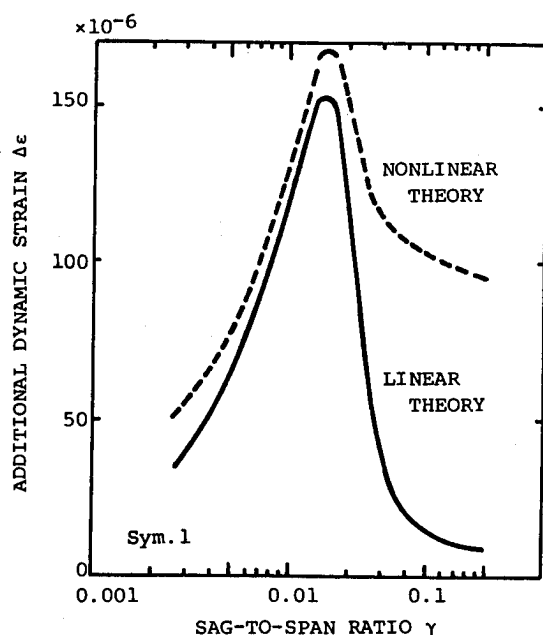


Fig. 9 Dynamic strain estimated by nonlinear theory

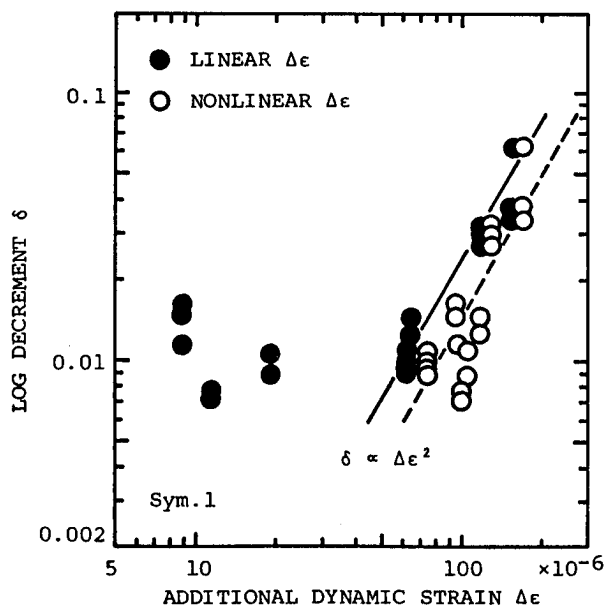


Fig. 10 Modal damping versus nonlinear dynamic strain

however, is difficult to check its accuracy and is not so reliable because nonlinear equation was used only for the evaluation of dynamic strain with linear solution of normal mode vector. The additional dynamic strain calculated by linear theory, therefore, will be only discussed in the following sections.

## 5. EFFECTS OF SPAN LENGTH ON DAMPING

Modal damping of shorter spanned cable was also measured and the effect of span length on modal damping is considered. Fig. 11 is again the relation between modal damping and dynamic strain with the new data of short cable of 2.05m span. Only data of the in-plane first symmetric mode are shown in comparison. It can be seen from Fig. 11 that the data points of short cable also lie in a straight line of slope 2. The straight line, however, is different for different span length in spite of same cable. This is supposed to be caused by the effect of initial tension of cable on internal damping.

The effect of initial tension on the first modal damping of taut cable has been reported by Hara and Ueda [1966], Nishimura et al. [1977] and Tanaka et al. [1985]. Those experimental data are arranged in Fig. 12 with the abscissa of initial tension nondimensionalized by tensile strength. In Fig. 12, the log decrement is greatly changed up to the order of 10% initial tension ratio and is larger for lower initial tension, while the log decrement takes almost constant value when the initial tension is introduced to a certain degree. This means that the friction between each wire of cable is changed by the initial tension. It should be mentioned that this characteristics of initial-tension effect is independent on what the cable is; strand wire rope, or parallel wire strand, or locked coil rope, or parallel wire cable.

Fig. 13 shows same plots of the present experimental results but on a log-log graph paper for the asymmetric and out-of-plane modes. Since modal damping of asymmetric and out-of-plane modes is not affected very much by the dynamic

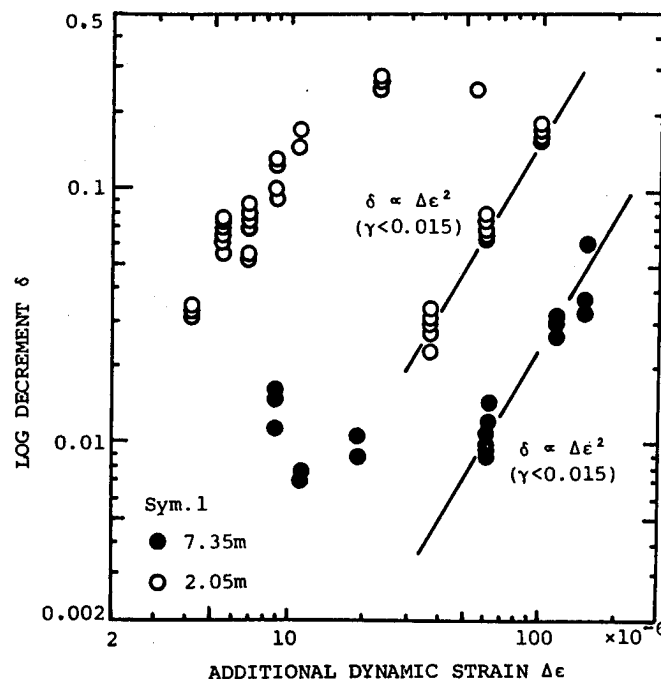


Fig. 11 Effect of span length on damping-strain relation

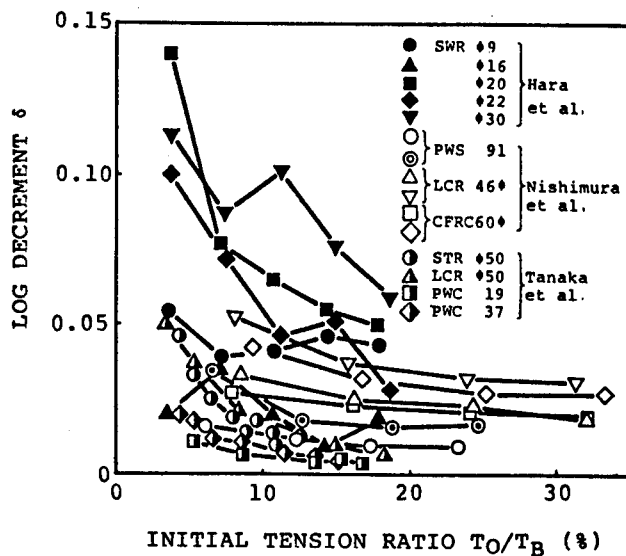


Fig. 12 Log decrement versus initial tension for taut cable

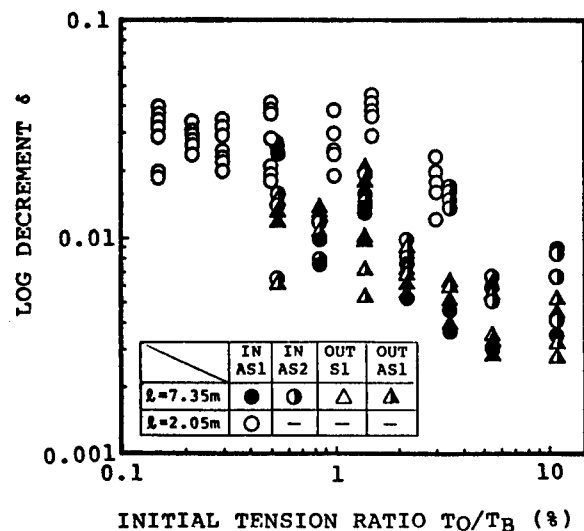


Fig. 13 Modal damping versus initial tension

strain, effects of initial tension can be investigated directly from Fig. 13. As can be seen from Fig. 13, the modal damping becomes larger for shorter cable because of low initial tension. Consequently, the difference in the first symmetric modal damping for different span length, shown in Fig. 11, can be due to this fact.

## 6. MODAL DAMPING OF INCLINED CABLE

Since cable in real structure such as cable-stayed bridge is sometimes supported at different level, the damping of inclined cable is also investigated. Fig. 14 is the plots of natural frequency versus sag ratio for 30 degrees inclined cable. It can be seen from Fig. 14 that the modal transition is different from that of horizontally supported cable in Fig. 5. That is, in case of inclined cable, the in-plane symmetric mode changes into the higher asymmetric mode and the asymmetric mode into the higher symmetric mode when the sag ratio

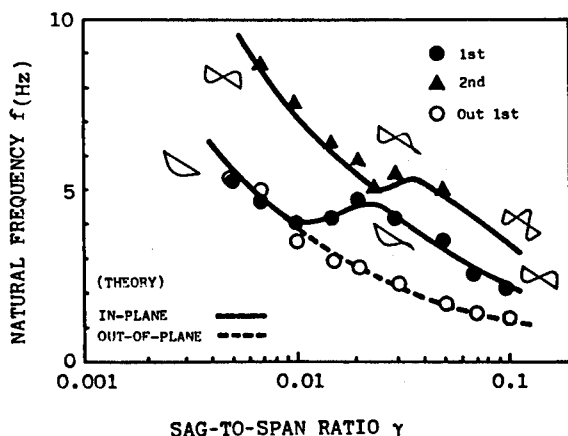


Fig. 14 Natural frequency versus sag ratio in inclined cable

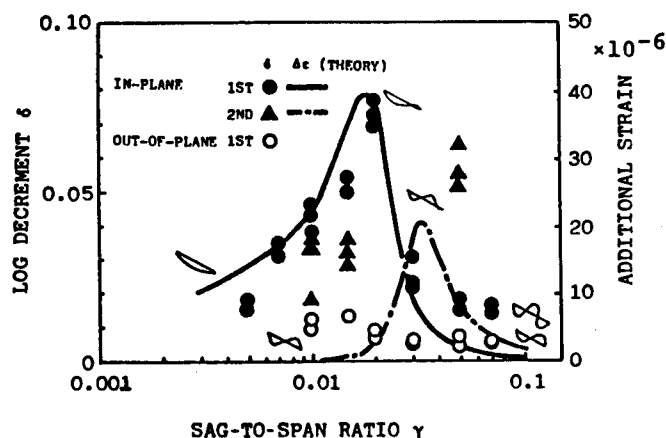


Fig. 15 Comparison of modal damping with dynamic strain in inclined cable

becomes larger (Yamaguchi and Ito [1979]). The comparison between corresponding modal damping and dynamic strain is presented in Fig. 15. The modal damping is again large in the modal transition region but the tendency is somewhat different from that for the horizontally supported cable. Even in the modal transition region, the modal damping decreases rapidly when the normal mode approaches the asymmetric mode, while the damping for pseudo-symmetric mode are still large. Changes of modal damping and dynamic strain with respect to sag ratio, however, correspond to each other very well also for the inclined cable, and the modal damping of cable can be again explained by internal damping of cable.

## 7. EFFECTS OF SUPPORT FLEXIBILITY ON MODAL DAMPING

Modal damping of rigidly supported cable was investigated in the previous sections and effects of support flexibility on modal damping are discussed next. Cable is always supported elastically in a sense in real structures and the condition of support seems to be very important in estimating wind-induced oscillation. An example can be seen in the wind tunnel study by Fujino et al. [1984] on galloping of telecommunication cable that the mode during galloping was different when the different flexibility of end support was used.

The thin steel plate of 2.5mm thickness was used at support in the experimental set-up, shown in Fig. 4, in order to realize the elastic support condition. The dynamic characteristics of support were measured directly by performing static and dynamic tests before suspending cable model. The equivalent spring constant in horizontal direction at support is 6.0kN/m and the first modal mass of cantilever plate is 0.55kg.

Fig. 16 shows theoretically estimated natural frequencies for elastic support and fixed support. There exists modal transition regardless of support condition but the transition region shifts to larger sag ratio as the support becomes flexible. The natural frequency of symmetric mode for flexible support, therefore, decreases for sag ratios in the modal transition region. As for cable

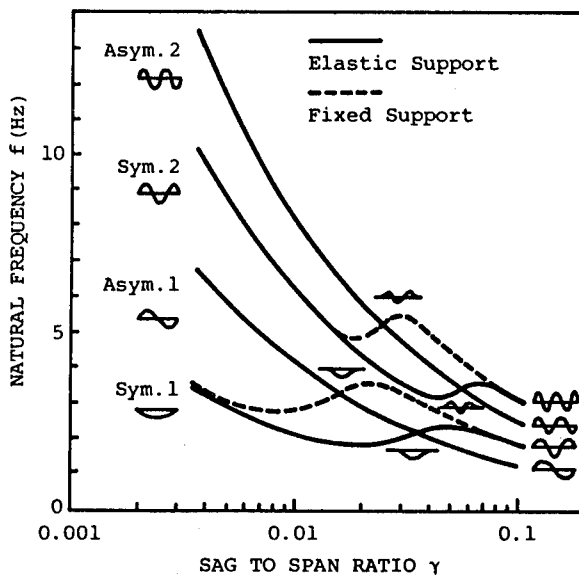


Fig. 16 Natural frequencies of elastically supported cable

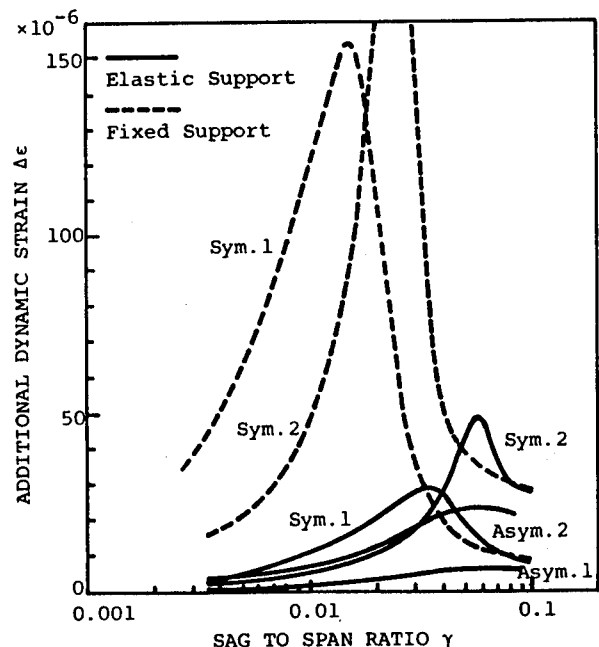


Fig. 17 Dynamic strains of elastically supported cable

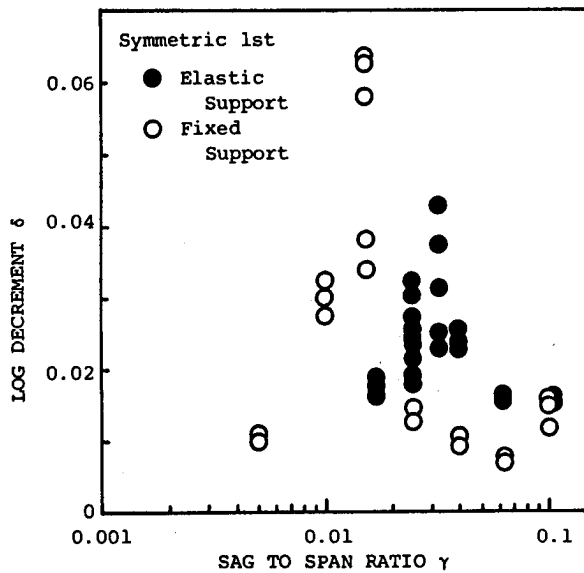


Fig. 18 Comparison of the first symmetric modal damping

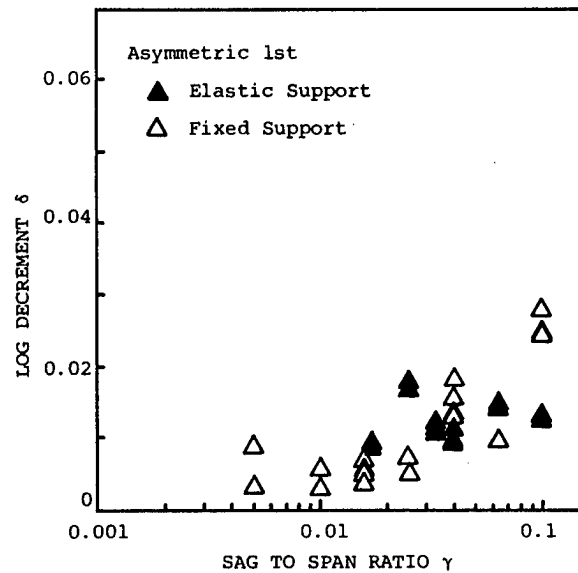


Fig. 19 Comparison of the first asymmetric modal damping

with sag ratio outside of the modal transition region, there is not so much difference in the natural frequency of symmetric mode. It should be mentioned that the natural frequency of asymmetric mode is not influenced by the support condition.

The corresponding dynamic strain of symmetric mode takes large value in the modal transition region even for elastic support as is shown in Fig. 17. The maximum dynamic strain of flexibly supported cable, however, becomes much smaller than that of rigidly supported cable, while dynamic strains of asymmetric modes for two support conditions lie on the same curve.

Corresponding to this tendency in dynamic strain, modal damping of the first symmetric mode is much affected by support flexibility. Fig. 18 shows the comparison of the first symmetric modal damping versus sag ratio for two support conditions. As can be seen from Fig. 18, the mutual relation of modal damping in magnitude for different support condition depends on the sag ratio. That is, the damping of flexibly supported cable is smaller for small sag ratio but is larger for large sag ratio, and maximum damping value becomes smaller for flexible support. On the contrary, modal damping of asymmetric mode is not significantly influenced by support flexibility (Fig. 19). This is because the asymmetric mode of elastically supported cable does not include support movement (Yamaguchi and Fujino [1988]).

Fig. 20 is again the relation between experimentally measured modal damping and theoretically calculated dynamic strain. In Fig. 20, the data points of symmetric mode plotted for elastic support also lie roughly in a straight line of slope 2. This means that the modal damping is in proportion to square of dynamic strain and that the internal damping is one of the primary causes of modal damping even for flexibly supported cable. The straight line of slope 2 for each support condition, however, differs from each other, nevertheless the same cable was used in all the cases in the experiment; the straight line shifts to the left for flexible support. This result suggests existence of another cause of modal damping which could be the result of energy loss at support. That is, the damping at support might have direct effects upon the total damping of cable. This effect of energy dissipation from flexible support will be discussed next.

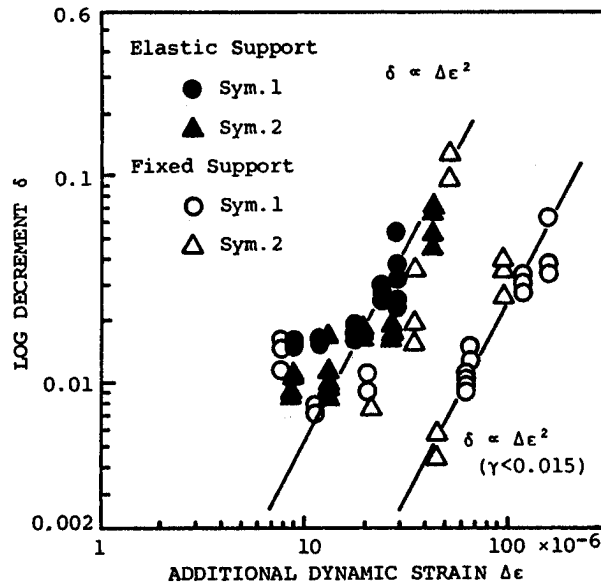


Fig. 20 Effect of support flexibility on damping-strain relation

## 8. EFFECTS OF SUPPORT DAMPING ON MODAL DAMPING

A damper was set at elastic support and modal damping of cable with support damping was measured in the same experimental procedure as previous sections. Details of damper are shown in Fig. 21. Damping value at support can be changed by changing the depth of water in the tank. Two values of water depth, 9cm and 18cm, were chosen in the experiment and damping of support itself was measured experimentally. The support damping represented by log decrement is shown in Fig. 22. Damping value of support is about 0.05 for low support-damping (9cm) and 0.15 for high support-damping (18cm) in case of small amplitude of 0.5mm.

Fig. 23 shows natural frequencies of the first symmetric mode with those of asymmetric mode which are plotted to indicate the modal crossover point. There is no significant difference in natural frequency between each support-damping

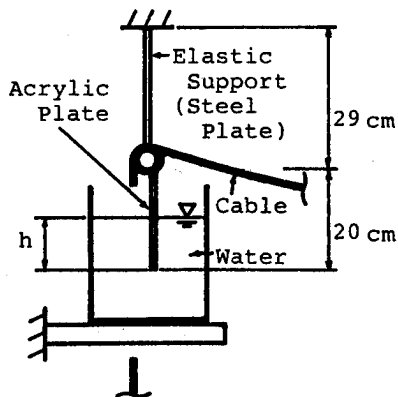


Fig. 21 Details of damper at support

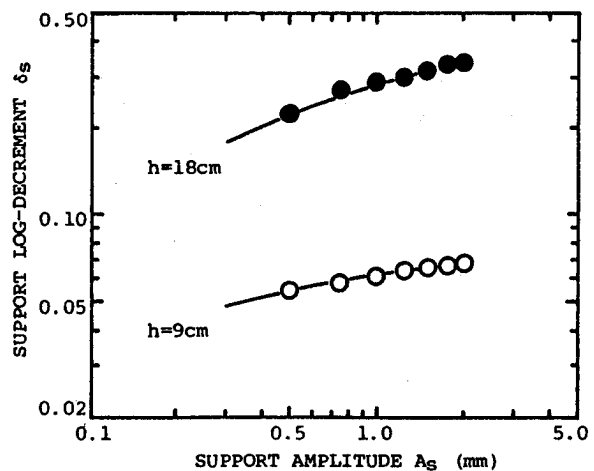


Fig. 22 Support damping versus support amplitude

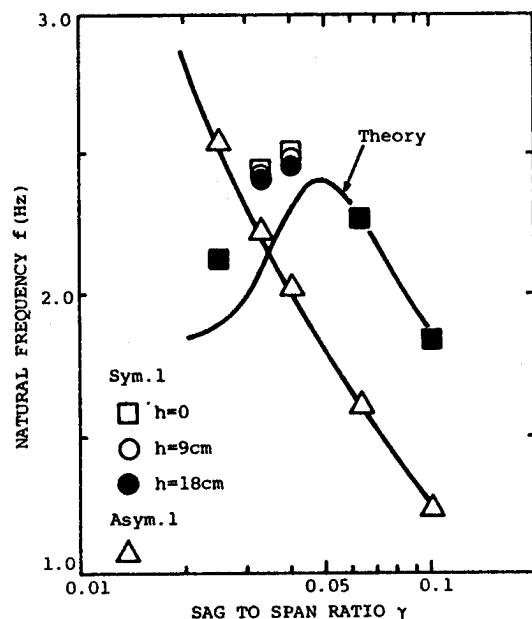


Fig. 23 Natural frequencies of cable with support damping

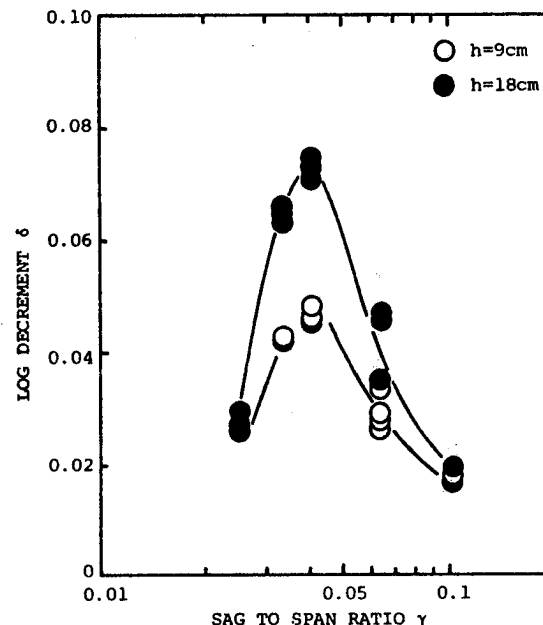


Fig. 24 Modal damping versus sag ratio for cable with support damping

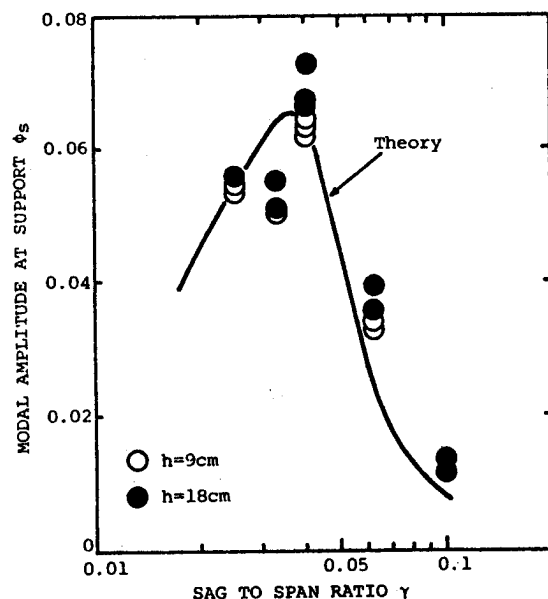


Fig. 25 Modal amplitude at support versus sag-to-span ratio

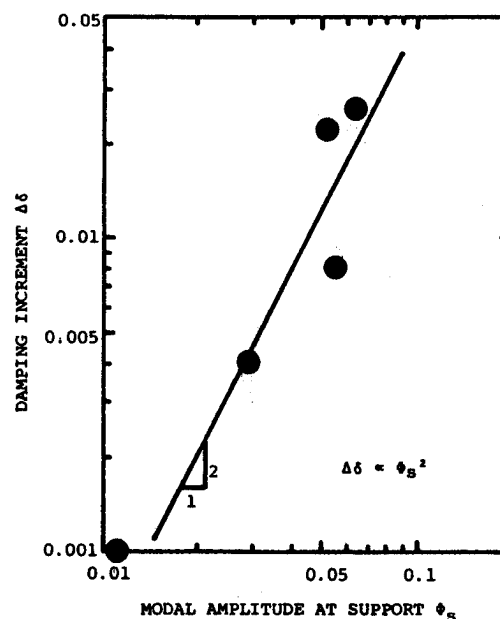


Fig. 26 Modal damping increment versus modal support amplitude

condition. This means that the damping at support is sufficiently low.

The corresponding modal damping of the first symmetric mode is large in modal transition region as is shown in Fig. 24. Modal damping of cable with high support-damping (18cm) is larger than that with low support-damping, but the increment of modal damping depends on sag ratio. That is, the modal damping increases significantly at the modal crossover point where the modal damping

takes maximum value, while there is small difference for sag ratio outside of modal transition region.

This may be due to different amount of support movement for each sag ratio. The support amplitude was, therefore, checked experimentally and theoretically. Fig. 25 is the result. The change of support amplitude with respect to sag ratio is quite similar to the change of damping increment caused by high damping at support. Fig. 26 shows the relation between damping increment and support amplitude in log-log graph paper. The damping increment was defined as difference between modal damping for  $h=18\text{cm}$  and  $h=9\text{cm}$ , and was calculated with experimental values shown in Fig. 24. As can be seen in Fig. 26, the data points plotted lie roughly in a straight line of slope 2. From this experimental fact, it can be estimated that the contribution of support damping is approximately proportional to square of modal support-amplitude and this has been estimated theoretically by Yamaguchi [1988].

## 9. CONCLUSIONS

Modal damping of flexural oscillation in suspended cable was discussed in relation to dynamic characteristics of cable. Major conclusions obtained through the present investigation are summarized as follows.

(1) Modal damping of in-plane symmetric mode is larger than other modal damping in the modal transition region.

(2) Modal damping is closely related to additional dynamic strain and one of primary causes of damping is internal damping of cable.

(3) Modal damping is larger for lower initial tension but almost independent on initial tension when the initial tension exceeds a certain level.

(4) For inclined cable, characteristics of damping are somewhat different from those for horizontally supported cable.

(5) Flexibility of support has significant effects only upon modal damping of symmetric mode in the region of modal transition.

(6) Contribution of support damping to modal damping of suspended cable is approximately proportional to square of modal support-amplitude.

## ACKNOWLEDGMENTS

The author would like to acknowledge the collaboration of K. Shimogiku, S. Sakai, T. Mizumura, T. Nagasako, H. Goto and Y. Ichikawa, formerly undergraduate students of Saitama University, K. Ishikawa and T. Yokobayashi, technicians of Saitama University, during the course of the present investigation. Financial support by Japanese Ministry of Education, Science and Culture under Grant-in-Aid for Scientific Research is also gratefully acknowledged.

## REFERENCES

- Fujino, Y., H. Yamaguchi and M. Ito 1984, "Galloping Oscillations of Figure-8 Overhead Telecommunication Cables", Proc. 8th National Symp. Wind Eng., pp. 221-226 (in Japanese).
- Fujino, Y., M. Ito and H. Yamaguchi 1988, "Three-Dimensional Behavior of Galloping in Telecommunication Cables of Figure-8 Section", J. Wind Eng. and Industrial Aerodynamics, 30, pp. 17-26.



- Hara, M. and Ueda, K. 1966, "Study on Damping of Wire Ropes", Proc. 21st Annual Conf., JSCE, I-37, pp. 37-1-2 (in Japanese).
- Henghold, W.M. and J.J. Russell 1976, "Equilibrium and Natural Frequencies of Cable Structures (a Nonlinear Finite Element Approach)", Computers and Structures, Vol. 6, pp. 267-271.
- Hikami, Y and N. Shiraishi 1988, "Rain-Wind Induced Vibration of Cables in Cable Stayed Bridges", J. Wind Eng. and Industrial Aerodynamics, 29, pp. 409-418.
- Kanou, I. and N. Tsumura 1987, "Damping of Axial Oscillation of Suspended Wire Ropes", Proc. 42nd Annual Conf., JSCE, I-347, pp. 728-729 (in Japanese).
- Nishimura, H., K. Hironaka and T. Shinke 1977, "Experimental Study on Characteristics of Rope Oscillation", Proc. 32nd Annual Conf., JSCE, I-177, pp. 334-335 (in Japanese).
- Ramberg, S.E. and O.M. Griffin 1977, "Free Vibration of Taut and Slack Marine Cables", Proc. ASCE, Vol. 103, No. ST11, pp. 2079-2092.
- Rawlins, C.B. 1981, "Analysis of Conductor Galloping Field Observations - Single Conductors", Trans. Power Apparatus and System, IEEE, Vol. PAS-100, No. 8, pp. 3744-3753.
- Tanaka, Y., K. Tamai and T. Haraguchi 1985, "On Damping of Inclined Cables", Proc. 40th Annual Conf., JSCE, I-263, pp. 525-526 (in Japanese).
- Tsuji, M. and I. Kanou 1980, "Damping of Wire Ropes", Proc. 13th Annual Conf., Japan Construction Consultant Association, pp. 73-86 (in Japanese).
- Yamaguchi, H. and M. Ito 1979, "Linear Theory of Free Vibrations of an Inclined Cable in Three Dimensions", Proc. JSCE, No. 286, pp. 29-36 (in Japanese).
- Yamaguchi, H. and Y. Fujino 1987, "Modal Damping of Flexural Oscillation in Suspended Cable", Structural Eng./Earthquake Eng., JSCE, Vol. 4, No. 2, pp. 413s-421s.
- Yamaguchi, H. and Y. Fujino 1988, "Effects of Support Flexibility on Modal Damping of Cables", Structural Eng./Earthquake Eng., JSCE, Vol. 5, No. 2, pp. 303s-311s.
- Yamaguchi, H. 1988, "Modal Damping of Cable with Support Damping", Research Report of Dept. Foundation Eng. and Construction Eng., Saitama Univ., 18, pp. 31-42 (in Japanese).

# Analysis, Optimization, Fabrication and Test of Composite Shells with Embedded Viscoelastic Layers

Allen J. Bronowicki<sup>1</sup>  
Henry P. Diaz<sup>2</sup>

TRW Space & Technology Group  
Redondo Beach CA 90278

March 10, 1989

## Abstract

Large space structures for the 90's and beyond require a combination of high stiffness, light weight and vibration attenuation not heretofore available. Advanced composites offer high stiffness while viscoelastic materials offer vibration attenuation. Both are light in weight. This paper describes finite analysis tools, and design and fabrication concepts which makes a marriage of these two material technologies feasible.

A special purpose finite element based on closed form solutions in membrane cylindrical shells is derived. Two concentric composite shells with an embedded viscoelastic layer can be analyzed with one element. Complex ply arrangements such as the Alternating Ply Concept (patent pending) can be analyzed with as few as five elements.

The analysis code was tied to an optimization package. A material figure of merit based on specific modulus weighted by a power of loss factor is optimized. A tube employing the Alternating Ply Concept, was designed using the code and fabricated. Greater than 5.5% damping was achieved across a 50° F temperature range using a relatively low loss factor silicone damping material.

<sup>1</sup>Head, Analytic Methods Section

<sup>2</sup>Member of the Technical Staff, Dynamics Department

## 1 INTRODUCTION

### 1 Introduction

Currently planned large space structures must be agile and precise. Agility involves the ability to maneuver rapidly and regain shape and pointing stability in minimum time. Precision involves the ability to maintain shape and pointing stability in the presence of dynamic and thermal disturbances. Both agility and precision can be enhanced by the use of structural concepts and materials which maximize stiffness and damping within constraints on total system mass.

Advanced composite materials can offer very high stiffness to weight ratios. This was verified in recent tests at TRW on Pitch-130 graphite epoxy in a unidirectional layup [1]. A tensile modulus of 80.6 million psi was achieved in a 60% fiber volume laminate. At a density of 0.065 lb/in<sup>3</sup>, this gives a specific modulus of  $1.24 \times 10^9$  inches. Near zero coefficient of thermal expansion (CTE) in a single direction can be achieved in graphite epoxy laminates through tailoring of ply angles, although this degrades specific modulus in the loading direction. Metal matrix composites (MMC) employing the same fiber material as an organic matrix composite will achieve somewhat lower specific stiffness since only a 50% fiber volume can be achieved in practice. MMC's can claim a distinct advantage over organic matrices in applications where near zero CTE in a single direction is desired, since no off angle plies will be required.

Viscoelastic materials (VEM) offer high energy absorption capability, again with low weight. For instance, an organic polymer such as the 3M ISD-110 material at room temperature can provide a loss factor,  $\eta$ , above 1.0 across several decades of frequency [2]. The density of this material is only 0.03 lb/in<sup>3</sup>.

The blending of advanced composites with viscoelastic damping materials offers the most likely means of meeting the dynamics requirements on precision and agility. If applied on truss structures, it will be necessary to devise a means of damping extensional motions in a member. The common practice in damping technology is to apply a continuous constraining layer to a base structure. This succeeds in damping flexural motions but not extensional motions. By segmenting the constraining layer periodically in the direction of loading, both extensional and flexural motions can be damped [3]. A segmentation length which maximizes loss factor can be derived in closed form [4]. This optimum length is 3.278 times the shear lag decay length commonly employed in the design of bonded joints. Graphite epoxy tubes with a viscoelastic damping layer and a unidirectional (all 0° plies) segmented constraining layer cocured on top have been fabricated at TRW [5]. The advantage of cocuring the VEM and constraining layer is the void free bond one can create. Application of a precured 0° constraining layer to a cylindrical surface is very difficult. Application of precured angle plies would not be possible at all. Even though it is difficult to cocure a viscoelastic material with a transition temperature below the epoxy cure temperature, the performance and fabrication advantages make the effort worthwhile.

The practical limit to damping using the segmented constraining layer approach is  $\eta = 0.1-0.12$ , or  $\zeta = 5-6\%$ . One can increase damping using constraining layers much stiffer

## 2 CONCENTRIC SHELL FINITE ELEMENT DERIVATION

than the base tube, but a figure of merit normalized by weight will begin to diminish. This practical limit on damping motivated the research described in this paper. It was apparent that more complex ply layups would be necessary to increase the strain energy induced in the VEM. This necessitated the development of new analysis and design tools as described in the ensuing sections.

## 2 Derivation of Finite Element for Concentric Shells Enclosing a Viscoelastic Medium

The analysis of constrained layer viscoelastic treatments for cylindrical tubes can become exceedingly complex when the properties of the tube, the constraining layer and the viscoelastic medium vary along the length of the tube. In many design concepts, such as TRW's proprietary Alternating Ply Concept, it is difficult to decide which is the base structure and which is the constraining layer. Material properties and thickness can vary considerably both along the length of the tube and on either side of the viscoelastic layer. Closed form solutions become inappropriate in this case.

Standard finite element analysis using plate and solid elements is also difficult in complex situations on curved surfaces with thin viscoelastic layers. Up to thousands of elements can be required to analyze one structural component in a larger structure.

The path taken here has been to develop a semi-analytical finite element based on closed form solutions for a pair of concentric cylindrical membrane shells surrounding a uniform elastic medium in a state of axisymmetric deformation. The viscoelastic nature of the problem is handled quite simply by assuming that motions are harmonic in time at a given frequency. This allows a complex modulus valid for that operating frequency to be employed. The resultant calculations are performed in complex arithmetic. The magnitude of the displacements for a given force input indicates overall tube stiffness. Tube damping or loss factor can be derived from the tangent of the displacement, which is indicative of phase of the displacement with respect to the force.

The semi-analytic solution allows a very coarse grid to be employed along the length of the tube. All the shear lag effects are modeled exactly. Only a few elements are required, typically between one and six. This makes computation time extremely short, allowing optimization algorithms to be employed inexpensively.

By analogy to the Bernoulli-Euler hypothesis, the results of the axial analysis can be applied to beam bending performance in many cases. This has been found to work quite well in test and in comparison to ordinary FEM analysis in most cases, particularly when constraining layer shear stiffness is low, or if constraining layer segments are short.

### 2.1 Membrane Cylinder Constitutive Equations

## 2 CONCENTRIC SHELL FINITE ELEMENT DERIVATION

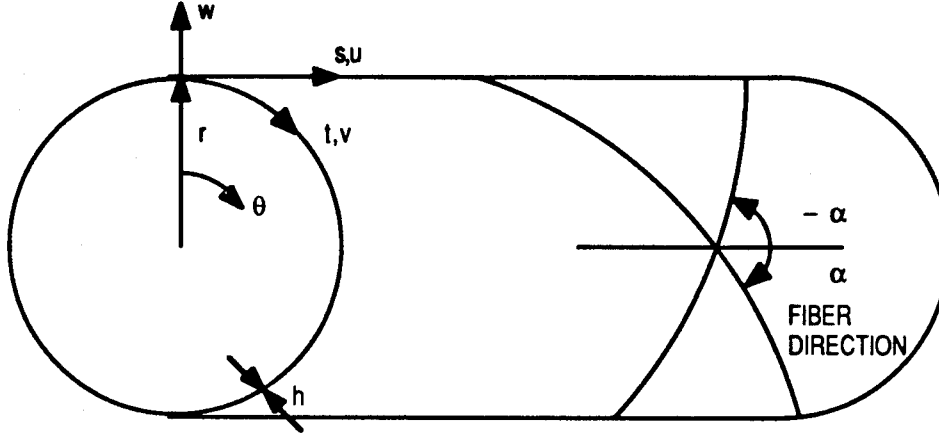


Figure 1: Membrane Cylinder Coordinates,  $r$ ,  $s$  and  $t$ , and Displacements,  $u$ ,  $v$  and  $w$ .

The equations of equilibrium in a membrane cylindrical shell [6] are defined in the meridional, circumferential and radial directions,  $s$ ,  $\theta$  and  $r$ , respectively. These coordinates are indicated on Figure 1. The tangential coordinate  $t$  is the same direction as the circumferential in that  $dt = r d\theta$ . Partial differentiation in the surface of the shell is indicated by the subscripted comma notation. The membrane shell or line force,  $N$ , is a force per unit length of shell, and the surface traction,  $q$ , is a force per unit area. Employing this nomenclature, the equilibrium equations are as follows:

$$N_{s,s} + N_{s\theta,t} + q_s = 0 \quad (1a)$$

$$N_{s\theta,s} + N_{\theta,t} + q_\theta = 0 \quad (1b)$$

$$\frac{1}{r} N_\theta = q_r \quad (1c)$$

The relations between shell force and mid-surface strain in a membrane orthotropic shell are given below.  $E$ ,  $G$  and  $\nu$  are axial modulus, shear modulus and Poisson's ratio, respectively, and  $h$  is the shell thickness.

$$\epsilon_s = \frac{1}{E_s h} (N_s - \nu_{s\theta} N_\theta) \quad (2a)$$

$$\epsilon_\theta = \frac{1}{E_\theta h} (N_\theta - \nu_{\theta s} N_s) \quad (2b)$$

$$\gamma_{s\theta} = \frac{1}{G_{s\theta} h} N_{s\theta} \quad (2c)$$

One may define membrane shell stiffness terms as follows:

$$C_{ss} \equiv \frac{E_s h}{1 - \nu_{s\theta} \nu_{\theta s}} \quad (3a)$$

## 2 CONCENTRIC SHELL FINITE ELEMENT DERIVATION

$$C_{\theta\theta} \equiv \frac{E_{\theta}h}{1 - \nu_{s\theta}\nu_{\theta s}} \quad (3b)$$

$$C_{s\theta} \equiv G_{s\theta}h \quad (3c)$$

$$C_{ss\theta\theta} \equiv \nu_{s\theta}C_{\theta\theta} = \nu_{\theta s}C_{ss} \quad (3d)$$

Equation 3d takes advantage of the reciprocity property of orthotropic materials,  $\nu_{s\theta}E_{\theta} = \nu_{\theta s}E_s$ . The relations between mid-surface strain and shell force are then found by inverting Equations 2a- 2c, giving:

$$N_s = C_{ss}\epsilon_s + \nu_{s\theta}C_{\theta\theta}\epsilon_{\theta} \quad (4a)$$

$$N_{\theta} = C_{\theta\theta}\epsilon_{\theta} + \nu_{\theta s}C_{ss}\epsilon_s \quad (4b)$$

$$N_{s\theta} = C_{s\theta}\gamma_{s\theta} \quad (4c)$$

The relations between shell mid-surface displacements and membrane strains are as follows:

$$\epsilon_s = u_{,s} \quad (5a)$$

$$\epsilon_{\theta} = v_{,t} + \frac{w}{r} \quad (5b)$$

$$\gamma_{s\theta} = u_{,t} + v_{,s} \quad (5c)$$

By substituting the strain-displacement relations, 5a-5c, into the force-strain relations, 4a-4c, one can obtain the following force displacement relations:

$$N_s = C_{ss}u_{,s} + \nu_{s\theta}C_{\theta\theta}\left(v_{,t} + \frac{w}{r}\right) \quad (6a)$$

$$N_{\theta} = C_{\theta\theta}\left(v_{,t} + \frac{w}{r}\right) + \nu_{\theta s}C_{ss}u_{,s} \quad (6b)$$

$$N_{s\theta} = C_{s\theta}(u_{,t} + v_{,s}) \quad (6c)$$

The membrane cylinder constitutive equations defined above are the basis for the elastically coupled concentric shell derivation. The stiffness properties have been derived assuming homogeneous, orthotropic materials. For a composite shell the moduli would represent equivalent through-the-thickness properties. The derivation of these equivalent properties based on composite shell theory is provided in the following section.

### 2.2 Orthotropic Shell Stiffness Properties

The membrane stiffness properties of a composite shell in an orthotropic layup are derived here. The overall properties of the shell are obtained by summing the properties of a sequence of individual plies [7]. In the following discussions an  $\alpha = 0^\circ$  ply is assumed to align with the meridional direction of the shell,  $s$ . Off-axis plies are assumed to be layed up symmetrically so that there is no axial-shear coupling. Thus for every ply at a non-zero angle  $\alpha$ , there is an identical ply at an angle  $-\alpha$ .

## 2 CONCENTRIC SHELL FINITE ELEMENT DERIVATION

### 2.2.1 Lamina Properties

Strain-stress relations for an individual lamina are given below in terms of the lamina stiffness coefficients  $Q$ . When the ply is aligned with the meridian of a cylindrical shell, the 1 and 2 directions will correspond to the  $s$  and  $t$  directions, respectively. The stiffness properties reflect a state of plane stress in the lamina.

$$\begin{Bmatrix} \sigma_1 \\ \sigma_2 \\ \tau_{12} \end{Bmatrix} = \begin{bmatrix} Q_{11} & Q_{12} & 0 \\ Q_{12} & Q_{22} & 0 \\ 0 & 0 & Q_{66} \end{bmatrix} \begin{Bmatrix} \epsilon_1 \\ \epsilon_2 \\ \gamma_{12} \end{Bmatrix} \quad (7)$$

$$Q_{11} = \frac{E_1}{1 - \nu_{12}\nu_{21}} \quad (8a)$$

$$Q_{22} = \frac{E_2}{1 - \nu_{12}\nu_{21}} \quad (8b)$$

$$Q_{12} = \frac{\nu_{12}E_2}{1 - \nu_{12}\nu_{21}} = \frac{\nu_{21}E_1}{1 - \nu_{12}\nu_{21}} \quad (8c)$$

$$Q_{66} = G_{12} \quad (8d)$$

To be physically realizable, the lamina properties must obey:  $|\nu_{12}| < \sqrt{E_1/E_2}$ , and  $\nu_{12}E_2 = \nu_{21}E_1$ .

### 2.2.2 Laminate Properties for a Symmetric Layup

For a pair of plies laid at angles  $\pm\alpha$  to the meridian, the strain-stress relations are:

$$\begin{Bmatrix} \sigma_s \\ \sigma_\theta \\ \sigma_{s\theta} \end{Bmatrix} = \begin{bmatrix} \bar{Q}_{ss} & \bar{Q}_{ss\theta\theta} & 0 \\ \bar{Q}_{ss\theta\theta} & \bar{Q}_{\theta\theta} & 0 \\ 0 & 0 & \bar{Q}_{s\theta} \end{bmatrix} \begin{Bmatrix} \epsilon_s \\ \epsilon_\theta \\ \gamma_{s\theta} \end{Bmatrix} \quad (9)$$

Note that coupling terms between extensional and shear deformations are zero due to the symmetric layup assumption<sup>1</sup>. The lamina stiffness properties are defined as follows, where the shorthand notation  $c = \cos \alpha$  and  $s = \sin \alpha$  has been employed.

$$\bar{Q}_{ss} = Q_{11}c^4 + Q_{22}s^4 + 2(Q_{12} + 2Q_{66})s^2c^2 \quad (10a)$$

$$\bar{Q}_{\theta\theta} = Q_{11}s^4 + Q_{22}c^4 + 2(Q_{12} + 2Q_{66})s^2c^2 \quad (10b)$$

$$\bar{Q}_{ss\theta\theta} = Q_{12}(s^4 + c^4) + (Q_{11} + Q_{22} - 4Q_{66})s^2c^2 \quad (10c)$$

$$\bar{Q}_{s\theta} = Q_{66}(s^4 + c^4) + (Q_{11} + Q_{22} - 2Q_{12} - 2Q_{66})s^2c^2 \quad (10d)$$

<sup>1</sup>A possible means of damping a tube we have not investigated would be to fabricate concentric tubes, the inner one having all positive ply layup angles and the outer tube having negative angle plies. Axial loads on the tube would generate opposite torsion in the two tubes, and hence shear in the enclosed VEM layer. The ends of the concentric tubes would likely need to be free to rotate independently about the tube axis to obtain maximum damping.

## 2 CONCENTRIC SHELL FINITE ELEMENT DERIVATION

The total shell thickness is the sum of the lamina thicknesses,  $h = \sum h_j$ . The total stiffness properties of the laminate  $C$  can be obtained by summing the individual lamina properties weighted by their thicknesses. Average moduli,  $E_s$ ,  $E_\theta$  and  $G_{s\theta}$ , and average Poisson's ratio,  $\nu_{s\theta}$ , may then be derived using the definitions for laminate stiffnesses given in Equations 3a-3d.

$$C_{ss} = \sum \bar{Q}_{ss}, h_j \quad (11a)$$

$$C_{\theta\theta} = \sum \bar{Q}_{\theta\theta}, h_j \quad (11b)$$

$$C_{ss\theta\theta} = \sum \bar{Q}_{ss\theta\theta}, h_j \quad (11c)$$

$$C_{s\theta} = \sum \bar{Q}_{s\theta}, h_j \quad (11d)$$

### 2.3 Mechanics of the Viscoelastic Layer

Constitutive equations are derived here for the viscoelastic layer constrained between the two concentric elastic shells, which together make up the damped tube finite element. The sandwiching arrangement is shown in Figure 2.

The viscoelastic material (VEM) is assumed to be at a single operating frequency, which allows the elastic and shear moduli,  $E_V$  and  $G_V$ , to be defined as complex numbers representing magnitude and phase of stiffness. The analysis can be repeated for different operating frequencies and temperatures. It should be emphasized that the analysis presented here is for one temperature and frequency.

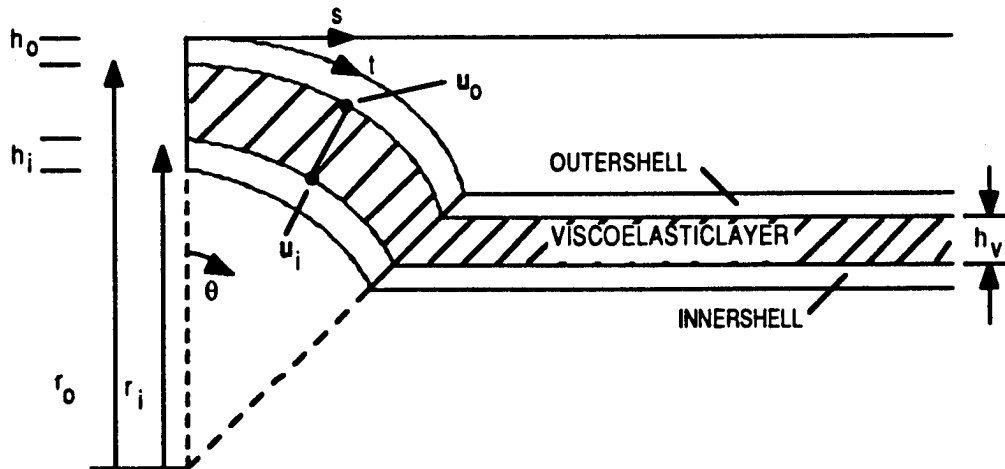


Figure 2: Representation of VEM Sandwiched Between Two Concentric Shells

The derivation is performed first for arbitrary motions in a cylindrical coordinate system, and then specialized to the case of radially symmetric motions.



## 2 CONCENTRIC SHELL FINITE ELEMENT DERIVATION

### 2.3.1 Viscoelastic Medium Constitutive Relations

The relations between displacement and strain in the VEM are given below [8]. The components of the displacement vector  $u_V$  are in the radial, meridional and tangential directions,  $r$ ,  $s$  and  $t$ , respectively.

$$\epsilon_r = u_{r,r} \quad (12a)$$

$$\epsilon_s = u_{s,s} \quad (12b)$$

$$\epsilon_\theta = u_{\theta,t} + \frac{u_r}{r} \quad (12c)$$

$$\gamma_{\theta s} = u_{\theta,s} + u_{s,t} \quad (12d)$$

$$\gamma_{sr} = u_{r,s} + u_{s,r} \quad (12e)$$

$$\gamma_{\theta r} = u_{\theta,r} + u_{r,t} - \frac{u_\theta}{r} \quad (12f)$$

Relations between strains and stresses in the VEM sandwich layer are:

$$\begin{Bmatrix} \sigma_r \\ \sigma_s \\ \sigma_\theta \end{Bmatrix} = \frac{E_V}{(1+\nu)(1-2\nu)} \begin{bmatrix} 1-\nu & \nu & \nu \\ \nu & 1-\nu & \nu \\ \nu & \nu & 1-\nu \end{bmatrix} \begin{Bmatrix} \epsilon_r \\ \epsilon_s \\ \epsilon_\theta \end{Bmatrix} \quad (13)$$

A modified VEM elasticity term has been defined to simplify subsequent notation:  $\tilde{E}_V \equiv \frac{E_V}{(1+\nu)(1-2\nu)}$ . The shear stress strain relations are simply:

$$\sigma_{ij} = G_V \gamma_{ij} \quad ; \quad i \neq j \quad (14)$$

### 2.3.2 Strains Given Shell Displacements

The displacements within the VEM are assumed to vary linearly in the radial direction between the inner and outer shells. This is felt to be a very good assumption when the VEM layer is thin. In that case, one can largely ignore the change in circumference of the medium in the radial direction. Thus stresses, and hence strains, will be almost uniform through the thickness of the VEM layer,  $h_V$ . The VEM displacement vector  $u_V$  is assumed to be related to the displacement vectors of the inner and outer shells,  $u_i$  and  $u_o$  as follows:

$$\begin{aligned} u_V(s, \theta, r) &= u_i(s, \theta) \frac{r_o - r}{h_V} + u_o(s, \theta) \frac{r - r_i}{h_V} \\ &\equiv u_i(s, \theta) R_i(r) + u_o(s, \theta) R_o(r) \end{aligned} \quad (15)$$

The shells have been assumed to be thin enough that the mid-surface displacements are identical to the displacements at the surface in contact with the VEM. In other words, the inner and outer shells have their stiffness properties defined at their outer and inner

## 2 CONCENTRIC SHELL FINITE ELEMENT DERIVATION

surfaces, respectively. For simplicity, the shape functions  $R_i(r)$  and  $R_o(r)$  have been defined representing radial dependence due to unit displacements of the inner and outer shells, respectively.

Strains in the VEM due to individual components of inner and outer shell displacements are obtained by inserting the displacements defined in Equation 15 into the strain-displacement Equations 12a- 12f.

$$\epsilon_r = \frac{w_o - w_i}{h_V} \quad (16a)$$

$$\epsilon_s = u_{i,s}R_i + u_{o,s}R_o \quad (16b)$$

$$\epsilon_\theta = v_{i,t}R_i + v_{o,t}R_o + \frac{1}{r}[w_iR_i + w_oR_o] \quad (16c)$$

$$\gamma_{rs} = w_{i,s}R_i + w_{o,s}R_o + \frac{u_o - u_i}{h_V} \quad (16d)$$

$$\gamma_{r\theta} = \frac{v_o - v_i}{h_V} + (w_{i,t}R_i + w_{o,t}R_o) - \frac{1}{r}(v_iR_i + v_oR_o) \quad (16e)$$

$$\gamma_{s\theta} = (v_{i,s}R_i + v_{o,s}R_o) + (u_{i,t}R_i + u_{o,t}R_o) \quad (16f)$$

Since the VEM layer is assumed to be very thin, one may assume that strains at the middle of the layer are representative of strains throughout. A correction to the average stresses to allow balance of load transfer between inner and outer shells is derived in the next section. Average extensional and shear strains,  $\bar{\epsilon}$  and  $\bar{\gamma}$ , are evaluated at the average radius,  $\bar{r} = \frac{r_i + r_o}{2}$ . The radial shape functions,  $R_i(\bar{r})$  and  $R_o(\bar{r})$ , both equal  $\frac{1}{2}$  under this assumption. The VEM strains given shell displacements then simplify to:

$$\bar{\epsilon}_r = \frac{w_o - w_i}{h_V} \quad (17a)$$

$$\bar{\epsilon}_s = \frac{1}{2}(u_{i,s} + u_{o,s}) \quad (17b)$$

$$\bar{\epsilon}_\theta = \frac{1}{2}(v_{i,t} + v_{o,t}) + \frac{1}{2\bar{r}}(w_i + w_o) \quad (17c)$$

$$\bar{\gamma}_{rs} = \frac{1}{2}(w_{i,s} + w_{o,s}) + \frac{u_o - u_i}{h_V} \quad (17d)$$

$$\bar{\gamma}_{r\theta} = \frac{v_o - v_i}{h_V} + \frac{1}{2}(w_{i,t} + w_{o,t}) - \frac{1}{2\bar{r}}(v_i + v_o) \quad (17e)$$

$$\bar{\gamma}_{s\theta} = \frac{1}{2}(v_{i,s} + v_{o,s}) + \frac{1}{2}(u_{i,t} + u_{o,t}) \quad (17f)$$

### 2.4 Coupling Shells to the Viscoelastic Medium

Through surface tractions, the thin viscoelastic layer couples the motion of the inner and outer shells which together compose the damped tube. Given some reasonable assumptions

## 2 CONCENTRIC SHELL FINITE ELEMENT DERIVATION

on the compliance of the VEM its deformations can be made wholly dependent on the shell motions, simplifying analysis considerably. The coupling procedure is explained in this section. It is developed first for arbitrary motions, and then specialized to the case of radial symmetry. Radially symmetric motions include both axial and breathing motions. The axial solution is applicable to bending motions through an analogy similar to that employed in the Bernoulli-Euler hypothesis of beam bending. Solutions for the case of radial antisymmetry (torsion) may be derived along similar lines to the radially symmetric case.

### 2.4.1 Simplifying Assumptions

The following set of assumptions allow the problem to be simplified considerably. The motion of the viscoelastic material can be made dependent entirely on shell motions, leaving these as the only independent variables.

- A. The load carrying capability of the VEM layer in its plane ( $s$ - $\theta$ ) is ignored, i.e.  $\sigma_\theta$ ,  $\sigma_s$ , and  $\sigma_{s\theta}$  are assumed to be zero. If the VEM is considerably softer than the shells this will be valid. Essentially one requires the following:

$$(E_V h_V) \epsilon_\theta \ll C_{\theta\theta}^{i+o} \epsilon_\theta \quad (18a)$$

$$(E_V h_V) \epsilon_s \ll C_{ss}^{i+o} \epsilon_s \quad (18b)$$

$$(G_V h_V) \gamma_{s\theta} \ll C_{s\theta}^{i+o} \gamma_{s\theta} \quad (18c)$$

where the superscript  $i + o$  simply means that the stiffness properties of the inner and outer elastic cylinders has been added together.

- B. The VEM will act to transfer loads between the two tubes; i.e.  $\sigma_r$ ,  $\sigma_{r\theta}$  and  $\sigma_{rs}$  are non-zero and significant. This will generally be true if the VEM layer is thin.
- C. No external surface tractions are applied to the inner or outer shells other than those due to stresses in the VEM layer. Loads are applied only through meridional and shear forces at the ends of an element, and through reactions due to boundary conditions.
- D. The loads transferred between inner tube and outer tube due to the VEM tractions must balance. Specifically this requires that

$$|q_i| r_i d\theta ds = |q_o| r_o d\theta ds = (\bar{\sigma}_V \cdot \hat{r}) \bar{r} d\theta ds \quad (19)$$

where  $\hat{r}$  is the unit vector in the radial direction,  $\bar{\sigma}_V$  is the stress tensor in the VEM evaluated at its average radius, and  $q$  is a traction vector on an inner or outer shell due to the VEM stress. The tractions applied to the shells will thus be:

$$(q_r, q_s, q_\theta)_i = +(\bar{\sigma}_{rr}^V, \bar{\sigma}_{rs}^V, \bar{\sigma}_{r\theta}^V) \frac{\bar{r}}{r_i} \quad (20a)$$

$$(q_r, q_s, q_\theta)_o = -(\bar{\sigma}_{rr}^V, \bar{\sigma}_{rs}^V, \bar{\sigma}_{r\theta}^V) \frac{\bar{r}}{r_o} \quad (20b)$$

## 2 CONCENTRIC SHELL FINITE ELEMENT DERIVATION

### 2.4.2 Specialization to Radial Symmetry

The case of radial symmetry allows many terms to be discarded. This enables the derivation of a semi-analytical finite element based on closed form solutions within the domain between circumferential nodes on the shell. Specifically, one may ignore: all partial derivatives in the circumferential direction, i.e.  $\frac{\partial}{\partial \theta}$ ; the shell quantities  $v$ ,  $q_\theta$ ,  $\gamma_{s\theta}$ , and  $N_{s\theta}$ ; and the VEM quantities  $\sigma_{r\theta}$ ,  $\sigma_{s\theta}$  (which is assumed zero in any case).

The VEM tractions on the inner and outer shells defined in Equations 20a and 20b may be inserted into the shell equilibrium equations. The meridional equilibrium Equation 1a becomes:

$$N_{s,s}^o = +\bar{\sigma}_{rs}^V \left( \frac{\bar{r}}{r_o} \right) \quad (21a)$$

$$N_{s,s}^i = -\bar{\sigma}_{rs}^V \left( \frac{\bar{r}}{r_i} \right) \quad (21b)$$

After multiplying both sides by inner or outer radius, as applicable, the radial equilibrium Equation 1c simplifies to:

$$N_\theta^o = -\bar{r} \bar{\sigma}_{rr}^V \quad (22a)$$

$$N_\theta^i = -\bar{r} \bar{\sigma}_{rr}^V \quad (22b)$$

### 2.4.3 Elimination of Radial Displacements

These equilibrium equations can be expressed entirely in terms of shell displacements. One must substitute the shell force-displacement Equations 6a and 6b, the VEM average strain-displacement Equations 17a-17e, and the VEM stress-strain Equations 13 and 14. The meridional equilibrium equations on the outer and inner shells become:

$$C_s^o u_{,ss}^o + (\nu_{s\theta} C_\theta)^o \frac{1}{r_o} w_{,s}^o = +G_V \left[ \frac{u^o - u^i}{h_V} + \frac{1}{2} (w_{,s}^o + w_{,s}^i) \right] \left( \frac{\bar{r}}{r_o} \right) \quad (23a)$$

$$C_s^i u_{,ss}^i + (\nu_{s\theta} C_\theta)^i \frac{1}{r_i} w_{,s}^i = -G_V \left[ \frac{u^o - u^i}{h_V} + \frac{1}{2} (w_{,s}^o + w_{,s}^i) \right] \left( \frac{\bar{r}}{r_i} \right) \quad (23b)$$

The radial equilibrium equations become:

$$C_\theta^o \frac{w^o}{r_o} + (\nu_{\theta s} C_s)^o u_{,s}^o = -\tilde{E}_V \bar{r} \left[ \frac{1-\nu}{h_V} (w^o - w^i) + \frac{\nu}{2} \left( \frac{w^o + w^i}{\bar{r}} + u_{,s}^o + u_{,s}^i \right) \right] \quad (24a)$$

$$C_\theta^i \frac{w^i}{r_i} + (\nu_{\theta s} C_s)^i u_{,s}^i = +\tilde{E}_V \bar{r} \left[ \frac{1-\nu}{h_V} (w^o - w^i) + \frac{\nu}{2} \left( \frac{w^o + w^i}{\bar{r}} + u_{,s}^o + u_{,s}^i \right) \right] \quad (24b)$$

Due to assumption C above, i.e. that no shell tractions exist other than those due to the VEM, the radial equilibrium equations can simply be solved for the radial displacements.

## 2 CONCENTRIC SHELL FINITE ELEMENT DERIVATION

The displacements  $w$  are thus wholly dependent on the meridional strains  $u_{,s}$  in the inner and outer tubes, and may be expressed as follows:

$$w^o = a_{oo}u_{,s}^o + a_{oi}u_{,s}^i \quad (25a)$$

$$w^i = a_{io}u_{,s}^o + a_{ii}u_{,s}^i \quad (25b)$$

The meridional equilibrium Equations 23a and 23b may now be expressed wholly in terms of the meridional displacements. Substituting 25a and 25b and collecting terms produces:

$$\left[ C_s^o + \left( \frac{\nu_{s\theta} C_\theta}{r} \right)^o a_{oo} - G_{V_o} \left( \frac{a_{oo} + a_{io}}{2} \right) \right] u_{,ss}^o + \left[ \left( \frac{\nu_{s\theta} C_\theta}{r} \right)^o a_{oi} - G_{V_o} \left( \frac{a_{oi} + a_{ii}}{2} \right) \right] u_{,ss}^i - \frac{G_{V_o}}{h_V} u^o + \frac{G_{V_o}}{h_V} u_{,ss}^i = 0 \quad (26a)$$

$$\left[ \left( \frac{\nu_{s\theta} C_\theta}{r} \right)^i a_{io} - G_{V_i} \left( \frac{a_{oo} + a_{io}}{2} \right) \right] u_{,ss}^o + \left[ C_s^i + \left( \frac{\nu_{s\theta} C_\theta}{r} \right)^i a_{ii} + G_{V_i} \left( \frac{a_{oi} + a_{ii}}{2} \right) \right] u_{,ss}^i + \frac{G_{V_i}}{h_V} u^o - \frac{G_{V_i}}{h_V} u_{,ss}^i = 0 \quad (26b)$$

This expression has been compacted by defining weighted VEM shear moduli at the outer and inner shell surfaces:  $G_{V_o} \equiv G_V \left( \frac{r}{r_o} \right)$  and  $G_{V_i} \equiv G_V \left( \frac{r}{r_i} \right)$ .

To simplify further derivations the meridional equilibrium equations are expressed in the following form:

$$\begin{bmatrix} m_{oo} & m_{oi} \\ m_{io} & m_{ii} \end{bmatrix} \begin{Bmatrix} u_{,ss}^o \\ u_{,ss}^i \end{Bmatrix} + k_V \begin{bmatrix} -\frac{r}{r_o} & \frac{r}{r_o} \\ \frac{r}{r_i} & -\frac{r}{r_i} \end{bmatrix} \begin{Bmatrix} u^o \\ u^i \end{Bmatrix} = \begin{Bmatrix} 0 \\ 0 \end{Bmatrix} \quad (27)$$

Again, for simplicity, a VEM shear stiffness per unit area,  $k_V \equiv G_V/h_V$ , has been defined.

Equation 27 is a pair of coupled second order differential equations in the meridional coordinate  $s$ . One can assume solutions of the form:

$$\begin{Bmatrix} u^o \\ u^i \end{Bmatrix} = \{\varphi\} e^{\alpha s} \quad (28)$$

Insertion into the governing differential equation and solution of the resultant eigenproblem leads to the following eigenvalues:

$$\alpha^2 = 0, \quad \frac{k_V \left[ \frac{r}{r_o} (m_{ii} + m_{io}) + \frac{r}{r_i} (m_{oo} + m_{oi}) \right]}{m_{oo}m_{ii} - m_{oi}m_{io}} \quad (29)$$

The zero eigenvalue leads to eigenvectors such that  $u^o = u^i$ . Both rigid body meridional translations and constant meridional strains are allowable solutions. Thus for the zero

## 2 CONCENTRIC SHELL FINITE ELEMENT DERIVATION

eigenvalues one obtains the following shape functions in the shell:

$$\begin{Bmatrix} u^o(s) \\ u^i(s) \end{Bmatrix} = \begin{Bmatrix} 1 \\ 1 \end{Bmatrix} (q_1 + q_2 s) \quad (30)$$

The non-zero eigenvalues lead to eigenvectors such that

$$u^o = \frac{1 + m_{oi} \frac{\alpha^2}{k_v^o}}{1 - m_{oo} \frac{\alpha^2}{k_v^o}} \cdot u^i \equiv \beta u^i \quad (31)$$

Defining the decay length  $\lambda \equiv \sqrt{1/\alpha}$  one obtains the following allowable shape functions in the shell:

$$\begin{Bmatrix} u^i(s) \\ u^o(s) \end{Bmatrix} = \begin{Bmatrix} 1 \\ \beta \end{Bmatrix} \left( q_3 \cosh \frac{s}{\lambda} + q_4 \sinh \frac{s}{\lambda} \right) \quad (32)$$

The amplitude of the shape functions,  $q_1 - q_4$ , remain to be determined. Once they are defined, the entire displacement and stress state can be found. One can assemble the displacements due to the zero and non-zero eigenvalues as follows:

$$\begin{Bmatrix} u^i(s) \\ u^o(s) \end{Bmatrix} = \begin{bmatrix} 1 & 1 & 1 & 1 \\ 1 & 1 & \beta & \beta \end{bmatrix} \begin{Bmatrix} q_1 \\ q_2 s \\ q_3 \cosh \left( \frac{s}{\lambda} \right) \\ q_4 \sinh \left( \frac{s}{\lambda} \right) \end{Bmatrix} \quad (33)$$

### 2.5 Element Definition

The preceding derivation has allowed us to solve for the internal displacements and stresses in the concentric shell and VEM layers in closed form. The displacements and stresses are dependent on a set of undetermined shape parameters  $q$ . These must be determined through application of boundary conditions to the shells. Figure 3 shows the partition of a shell into one discrete segment of length  $s_o$ . The meridional displacements of the inner and outer shells at the left and right ends, A and B, are the degrees of freedom of the element. These displacement degrees of freedom can be found by evaluating Equation 33 at  $s = 0$  and  $s = s_o$  for ends A and B, respectively. The elemental displacements are thus:

$$\{u_e\} \equiv \begin{Bmatrix} u_A^i \\ u_A^o \\ u_B^i \\ u_B^o \end{Bmatrix} = \begin{bmatrix} 1 & 0 & 1 & 0 \\ 1 & 0 & \beta & 0 \\ 1 & s_o & \cosh \frac{s_o}{\lambda} & \sinh \frac{s_o}{\lambda} \\ 1 & s_o & \beta \cosh \frac{s_o}{\lambda} & \beta \sinh \frac{s_o}{\lambda} \end{bmatrix} \begin{Bmatrix} q_1 \\ q_2 \\ q_3 \\ q_4 \end{Bmatrix} \quad (34)$$

## 2 CONCENTRIC SHELL FINITE ELEMENT DERIVATION

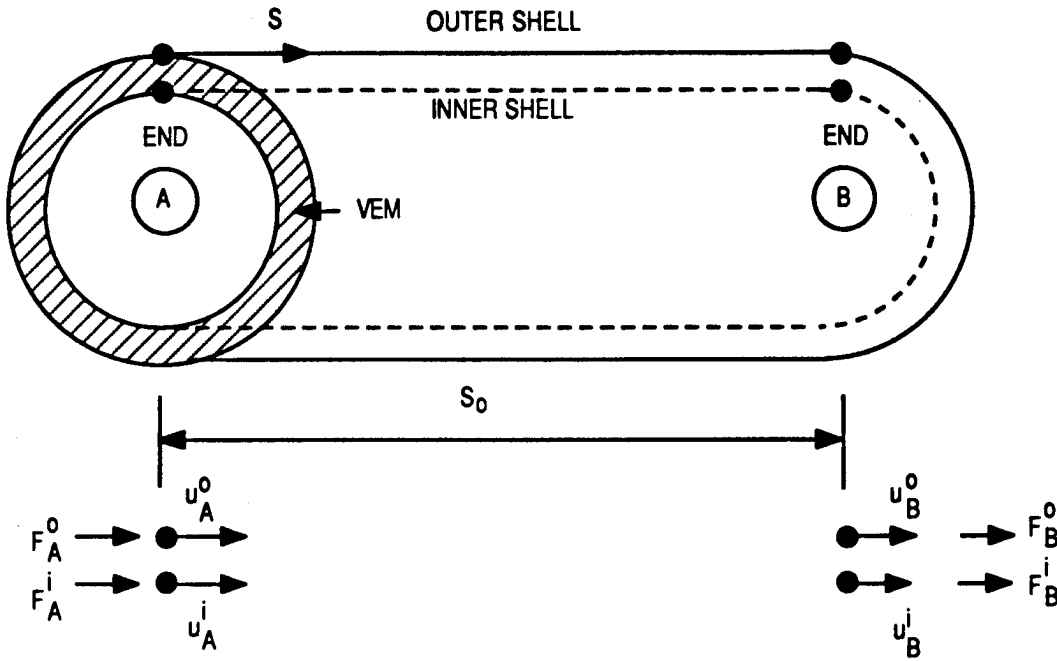


Figure 3: Axial Forces and Displacements on Radially Symmetric Shell Element

With some effort, this expression can be inverted in closed form to give the shape functions  $q$  in terms of the element end displacements  $\{u_e\}$ :

$$\begin{Bmatrix} q_1 \\ q_2 \\ q_3 \\ q_4 \end{Bmatrix} = \frac{1}{1-\beta} \begin{bmatrix} -\beta & 1 & 0 & 0 \\ \frac{\beta}{s_o} & \frac{-1}{s_o} & \frac{-\beta}{s_o} & \frac{-1}{s_o} \\ 1 & -1 & 0 & 0 \\ \frac{-1}{\tanh \frac{s_o}{\lambda}} & \frac{1}{\tanh \frac{s_o}{\lambda}} & \frac{1}{\sinh \frac{s_o}{\lambda}} & \frac{-1}{\sinh \frac{s_o}{\lambda}} \end{bmatrix} \begin{Bmatrix} u_A^i \\ u_A^o \\ u_B^i \\ u_B^o \end{Bmatrix} \quad (35)$$

To obtain a stiffness matrix for the finite element, it is necessary to compute the external forces in terms of the nodal displacements. Starting with Equation 35, one can apply unit displacements to each of the meridional degrees of freedom of the element  $\{u_e\}$  and work backwards through most of the equations of the preceding sections to obtain meridional shell forces  $N_s$  at each end of the shell element. For the case of radial symmetry the only external forces are axial. Radial forces are not allowable due to the membrane shell assumption. The external axial forces are computed from the internal meridional shell forces by integrating around the circumference to give:

## 2 CONCENTRIC SHELL FINITE ELEMENT DERIVATION

$$\{F_e\} \equiv \begin{Bmatrix} F_A^i \\ F_A^o \\ F_B^i \\ F_B^o \end{Bmatrix} = 2\pi \begin{Bmatrix} r_i N_s^i(0) \\ r_o N_s^o(0) \\ r_i N_s^i(s_o) \\ r_o N_s^o(s_o) \end{Bmatrix} \quad (33c)$$

The element forces thus computed as a function of element displacement allow one to construct an elemental stiffness matrix such that

$$\{F_e\} = [K_e] \{u_e\} \quad (34)$$

### 2.5.1 Element Assembly

Having an element stiffness matrix, one can construct larger models by mapping a series of elements together end to end. Since this is a one-dimensional element the connectivity is quite simple. Starting at one end of a tube, the axial displacements at the B node of element  $j$  are made equal to the displacements at the A end of element  $j + 1$ . A very narrow bandwidth will result, since at most two elements will be connected at any one node. In contrast, the practice of modelling a tube with quadrilateral plates will result in a very large number of elements and a poor bandwidth.

Since the radial displacements  $w$  are wholly dependent on the meridional strains in a membrane shell, and since the stiffness properties can vary from element to element, it is likely that the radial displacements predicted by two adjoining elements will differ. We are enforcing neither radial compatibility nor equilibrium between shell elements. The implications of this are not thought to be major for thin shells, since the behavior we are seeking to model is loading in the stiff in-plane directions. Loads out of plane will generally be orders of magnitude lower. In addition, the bending loads due to radial displacements on a cylindrical shell are known to decay rapidly as one moves away from the point of application in the meridional direction.

### 2.5.2 Load Transformation Matrix

In order to simplify stress and load recovery after solution of a load case at a given forcing frequency, internal element response is stored in a load transformation matrix (LTM). This matrix is computed for each element as the elemental stiffness matrix is generated. The matrix gives internal element response  $\{L_e\}$  in terms of nodal displacements in the manner:

$$\{L_e\} = [LTM] \{u_e\} \quad (35)$$

The quantities stored in the LTM are: the amplitudes of the element shape functions  $q$ ; meridional strains,  $u_{,s}$ , radial displacements,  $w$ , and axial forces,  $F$ , at ends A and B of the inner and outer shells; and VEM shear stresses,  $\sigma_{rs}$ , and radial stresses,  $\sigma_r$  at ends A and B. These quantities are generally sufficient to evaluate strength and any other constraints one



### 3 EXAMPLE PROBLEM

might impose during an optimization of the tube properties. The LTM enables one to avoid having to recover internal stresses after problem solution, greatly reducing computation time and programming complexity.

### 3 Example Problem

A simple example of the use of the code is the uniform segmented constraint. A 324 element Nastran quadrilateral plate model using eight-fold symmetry to reduce complexity, and a one element TUBES model predicted axial stiffness within 1% and loss factor within 4%. The Nastran analysis used the modal strain energy approximation, which accounts for the slightly greater discrepancy in damping predictions.

A difficult problem which can take advantage of the analysis and optimization capabilities of the TUBES program is TRW's Alternating Ply Concept damped tube. A patent application on this approach to integrating passive viscoelastic damping into fiber composite structures was submitted in 1988. The application was filed as "Viscoelastic Damping Structure and Related Manufacturing Method." A tube using this unique ply layup was designed, built and tested at TRW in 1987.

Figure 4 shows cross-sections of damped tubes employing both the uniform segmented constraining layer, which was the best available prior art, and the Alternating Ply Concept, which offers much greater damping levels.

The Alternating Ply Concept tube is essentially two concentric elastic tubes with a VEM layer in between. A large amount of energy can be forced into the VEM through the arrangement of stiff plies laid primarily in a  $0^\circ$  orientation on alternating sides of the VEM layer. These axial plies are short, with some overlap between inner and outer tubes so that load transfer can occur in shear through the VEM. The axial plies are held together by angle plies running continuously along both sides of the VEM layer. The angle plies serve to seal in the VEM. They also prevent the formation of peel stresses since they are in continuous contact with the VEM along the whole length of tube. Lacking fibers in the axial direction, the angle plies are very soft in axial deformation. They thus act as a flexure between the stiff axial plies. The flexing takes place in the gaps between the axial plies. Conversely, the angle plies are stiff in shear and torsion, and so those deformations do not get effectively damped. Axial and bending deformations of the tube can be heavily damped due to the fact that almost all the axial load is forced through the VEM layer.

The Alternating Ply Concept is a blend of series and parallel damper ideas. Design parameters can be shifted to either end of the spectrum between series and parallel. Damping is distributed along the whole length of the tube as in constrained layer damping. High damping levels can be obtained as in joint dampers. The twin parallel elastic load paths through the angle plies provide for static stiffness and strength, and dimensional stability.

### 3 EXAMPLE PROBLEM

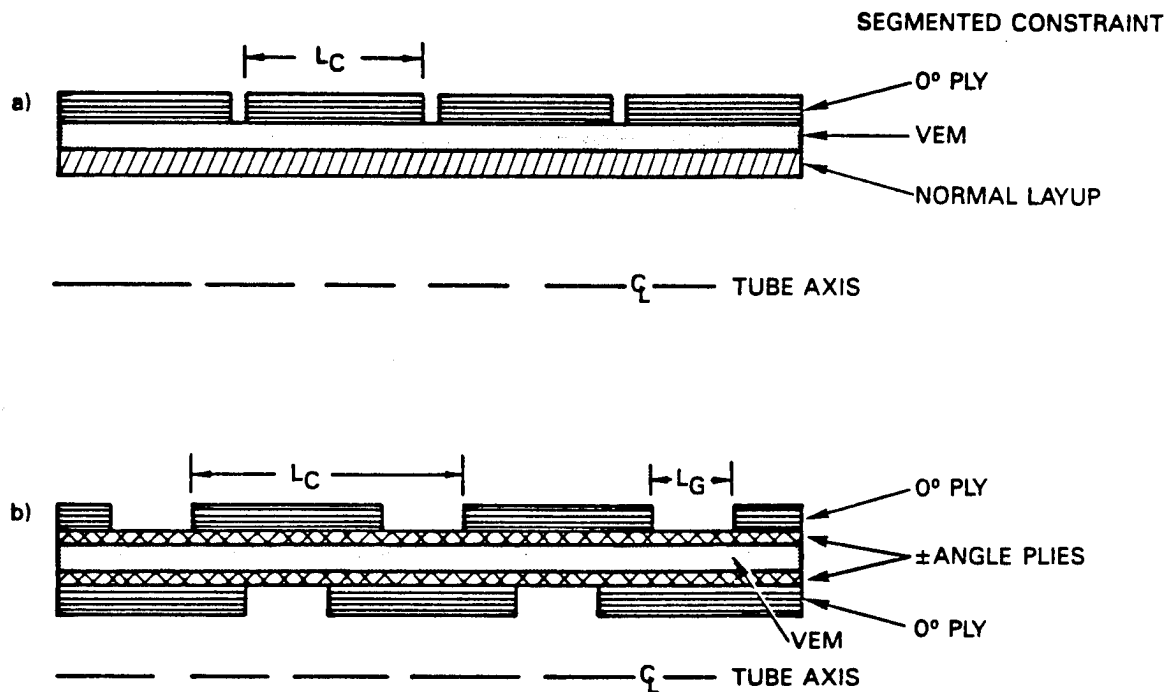


Figure 4: Layup Details and Geometric Design Variables for: a) Uniform Segmented Constraining Layer and b) Alternating Ply Concept.

#### 3.1 TUBES Model

Rather than model a whole tube, the smallest repeatable section, called the unit cell is modeled. This unit cell is shown in Figure 5, along with the element divisions and meridional displacement degrees of freedom. Note that the model consists of five elements and twelve axial displacement degrees of freedom. The displacements at the left end,  $u_1$  and  $u_2$ , are typically constrained to be zero, and the displacements at the right end,  $u_{11}$  and  $u_{12}$ , are constrained to move together. A unit force is then applied to the right end to determine the complex value of stiffness, from which dynamic stiffness and damping are determined. When inner and outer shell properties are assumed to be the same, the design variables are:  $t_0$ , the thickness of the axial plies;  $t_{45}$ , the thickness of the angle plies;  $t_v$ , the VEM thickness;  $L_c$ , the length of the unit cell; and  $L_g$ , the length of the gaps between the axial plies. Additionally, one could choose the angle of the angle plies as a design variable, rather than fixing it as we have at  $45^\circ$ .

The properties assumed for the GY-70 angle plies are:

$E_s = 43e6$  psi,  $E_\theta = .975e6$  psi,  $\nu_{s\theta} = .19$ ,  $\rho = 0.06$  lb/in<sup>3</sup>, and  $\eta = .002$  (0.1% damping). The properties assumed for the P-100 axial plies are the same as those for the angle plies except the moduli are scaled up by the ratio 74/43. The VEM properties are those for the SQDM-I material for the given operating temperature and frequency. A nomogram for this material, showing shear modulus and loss factor versus reduced frequency, is given in Figure 6. The

### 3 EXAMPLE PROBLEM

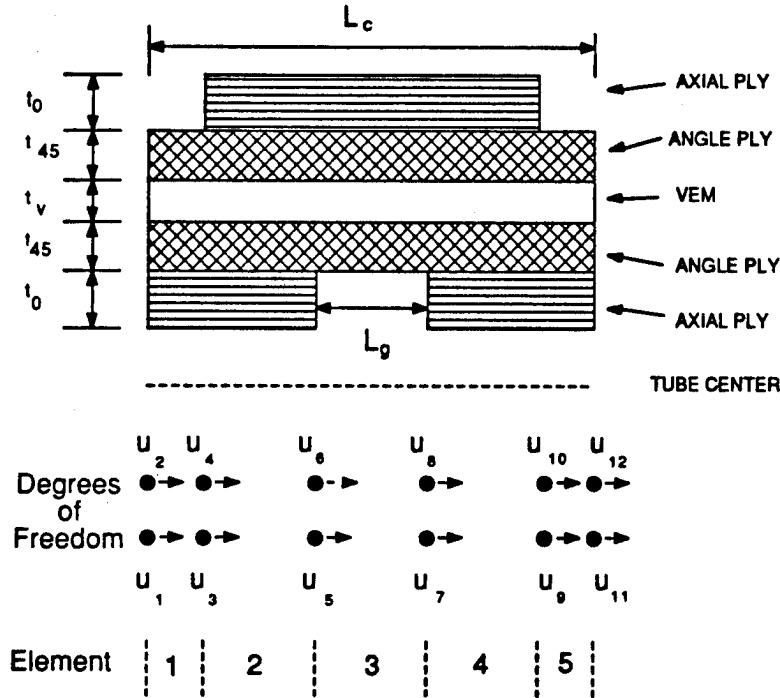


Figure 5: TUBES Model of Unit Cell of Alternating Ply Concept Tube.

VEM thickness was dictated by the available material, and is  $t_v = .024$  inches.

A design was optimized to maximize the resonant vibration figure of merit,  $FOM^{res} \equiv \frac{E}{\rho} \eta$ , which weights loss factor equally with specific modulus. A material concept which maximizes this figure of merit will minimize response at resonance if a structure were fabricated uniformly from the material. A material figure of merit can be defined for a random environment. If one assumed a flat power spectral density and well separated modal frequencies,  $\omega_n$ , mean square response [9] would be inversely proportional to  $\zeta_n \omega_n^3$ . A random vibration figure of merit would thus be  $FOM_0^{ran} \equiv \frac{E}{\rho} \eta^{2/3}$ . In realistic situations the PSD will roll off with frequency. Assuming, as in Reference 10, a  $1/\Omega$  roll-off the resultant figure of merit would be  $FOM_1^{ran} \equiv \frac{E}{\rho} \sqrt{\eta}$ . It turns out that designs optimized for these various figures of merit do not differ greatly. The resonant figure of merit emphasizes damping somewhat more, while the random figures of merit emphasize stiffness somewhat more.

The optimization was performed for VEM properties at room temperature and a frequency of 10 Hertz. The optimized design, after rounding off lengths to the nearest half inch and thicknesses to the nearest available ply thickness, is:

$L_c = 5$ ,  $L_g = 1.5$ ,  $t_{45} = .005$ , and  $t_0 = .015$ , all units in inches.

### 3 EXAMPLE PROBLEM

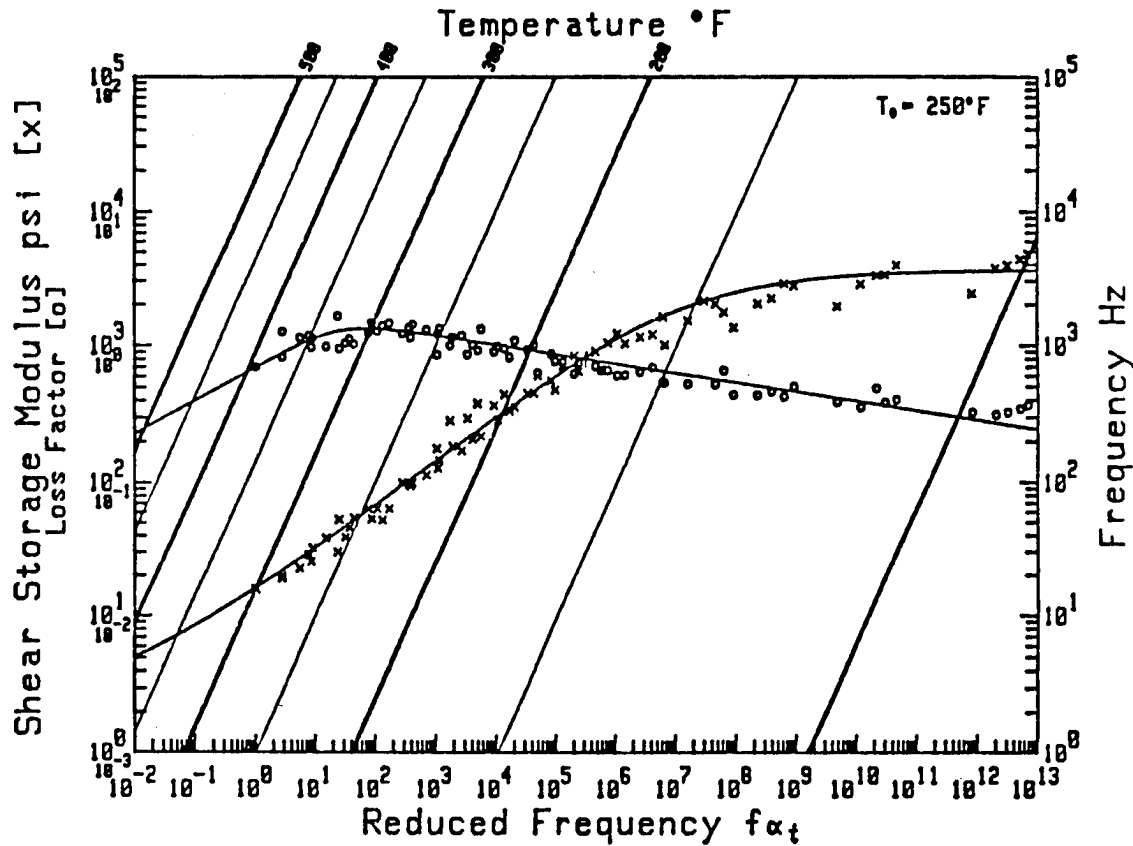


Figure 6: Frequency Nomogram for SQDM-I

### 3.2 Test Results

Process development tests were first performed to see if the VEM could be cocured into graphite epoxy. A three foot tube, 1.5 inches in diameter was then constructed using the above properties. Free decay vibration tests were performed in cantilever bending. Tip weights were varied to modify frequencies. A blow dryer was used to vary tube temperature. The temperature estimates are thus rather approximate. Six cases were run. The A cases were at room temperature and the B cases were at elevated temperature. Subscripts indicate the number of 4.2 pound tip weights added to the cantilevered tube. Test results are summarized in Table 1, along with analytic results from the TUBES model and VEM properties estimated from the frequency nomogram. Room temperature VEM properties are extrapolations since the curve does not go down low enough in frequency.

Shell stiffness was derived from the bending frequency using the following formulae:

$$EI = Eh\pi R^3$$

### 3 EXAMPLE PROBLEM

$$f = \frac{1}{2\pi} \sqrt{\frac{3EI}{ML^3}}$$

Given knowledge of the radius, natural frequency and mass, one can back out  $Eh$ , which is the effective shell stiffness of the whole layup integrated through the thickness and along one unit cell.

Two sets of damping measurements are given to indicate the difficulty in measuring this parameter when damping is high. Both curve fit and log decrement estimates are given. Natural frequencies are from the curve fit. Correlation of room temperature tests with analysis is not too bad. At elevated temperature, test data indicates that VEM stiffness breaks down more rapidly than the curve fit in the nomogram would indicate. This results in lower shell stiffness. It also is a possible explanation for the lower than predicted damping, since less strain energy will get into the VEM if it is very soft.

Table 1: Damped Tube Test Summary.

			CASE					
			$A_0$	$B_0$	$A_1$	$B_1$	$A_2$	$B_2$
Tip Weight	W	lb	1.07	=	5.27	=	9.47	=
Temperature	T	°F	71	135	71	115	71	120
Natural Frequency	$f$	Hz	23.4	19.03	9.65	8.50	7.00	5.70
Curve Fit	$\zeta$	%	4.0	8.6	4.8	7.2	6.0	6.4
Log Decrement	$\zeta$	%	3.8	9.0	4.5	6.9	5.3	9.0
Shell Stiffness	$Eh$	$10^5$ lb/in	5.4	3.54	4.8	3.7	4.64	3.1
Material Data Estimated from Nomogram								
Reduced Frequency	$f\alpha_t$		?	7E6	1E13	3E8	2E12	4E7
Shear Modulus	$G$	psi	3800	2000	3500	2600	3400	2200
Loss Factor	$\eta$		.2	.6	.25	.49	.28	.55
Analytic Results Using Material Data								
Damping	$\zeta$	%	4.3	12.	5.0	10.	6.0	11.
Shell Stiffness	$Eh$	$10^5$ lb/in	5.30	4.00	5.12	4.50	5.05	4.18

### 3.3 Conclusions

In one of the cases tested,  $A_1$ , 43% of the strain energy was absorbed by the VEM. This is phenomenal, and indicates that the use of a VEM with a loss factor of 1 or more would give 43% damping or higher. These high levels of damping can be attained with a structure having a considerable degree of static stiffness. The high damping was sacrificed in our design in order to explore the use of a VEM with reduced temperature dependence. The VEM

### 3 EXAMPLE PROBLEM

was providing a loss factor lower than .3 at room temperature, yet damping between 4 and 6% was obtained.

It is also important to note that the tube was designed in a state of axisymmetric extension, but tested in a state of asymmetric bending. The analysis and test still correlate well. This is because the fibers behave locally like they are in extension even though the tube overall is in bending. Thus the Bernoulli-Euler hypothesis we assumed which allowed axial and bending properties to be equated was verified.

### References:

1. J. S. Archer, "Application of New Structural Materials for Spacecraft Design," TRW IR&D project #89330339, January 1987-present.
2. 3M Product Information, Scotchdamp SJ-2015X Type 110, Structural Products Department, St. Paul MN.
3. Plunkett, R. and Lee, C. T., "Length Optimization for Constrained Layer Damping," *Journal of the Acoustical Society of America*, Vol. 48, No. 1, 1970, pp 150-161.
4. Kress, G., "Improving Single-Constrained-Layer Damping Treatment by Sectioning the Constraining Layer," *The Role of Damping in Vibration and Noise Control*, ASME Publication DE-Vol. 5, L. Rogers and J.C. Simonis editors, pp 41-48, presented at ASME 11<sup>th</sup> Biennial Conference on Vibration, Boston MA, September, 1987.
5. Kuritz, S.P., and Bronowicki, A.J., "Concepts in Integrally Damped Structural Members," presented at ASME 11<sup>th</sup> Biennial Conference on Vibration.
6. Kraus, H., *Thin Elastic Shells*, Wiley, N. Y., 1967.
7. Jones, R. J., *Mechanics of Composite Materials*, McGraw-Hill, N. Y., 1975.
8. Sechler, E. E., *Elasticity in Engineering*, Dover, N. Y., 1952.
9. Clough, R. W. and Penzien, J., *Dynamics of Structures*, McGraw-Hill, N. Y., 1975.
10. Bronowicki, A. J., "Structural Modification to Minimize Response of Electro-Optical Systems to Random Excitation," in Vol. 748 of the Proceedings of SPIE, *Structural Mechanics of Optical Systems II*, A. E. Hathaway Editor, 1987.

## **PASSIVE DAMPING CONCEPTS FOR SPACE STRUCTURES WITH TUBULAR MEMBERS**

**Zia Razzaq<sup>1</sup> and Bassam S. Najjar<sup>2</sup>**

**ABSTRACT:** The performance of potential passive damping concepts is investigated for a long tubular aluminum alloy member, and a two-bar grillage structure. The members are restrained partially at the ends and are of the type being considered for possible use in the construction of future outer space stations. Four different passive damping concepts are studied under free and forced vibration and include nylon brush, wool swab, copper brush, and "silly putty" dampers. It is found that the silly putty, and the wool swab dampers provide good passive damping.

### **Introduction**

Aluminum tubular members may be used in the future to construct outer space structures. These members may be subjected to vibration induced by external disturbances. One practical problem is to identify a damping concept that will reduce the vibration of these members substantially. Recent investigations (References 1-5) have been conducted to study passive damping concepts on very slender tubular steel members with various end conditions. For example, members with 0.5 in. outer diameter, a wall thickness of 0.065 in., and a length of up to 12 ft. have been tested. In these experiments, the following passive damping concepts were investigated in the presence of natural flexural vibration: mass-string dampers; external viscoelastic tape; inner metal tube core (copper, aluminum; steel, brass); polyethylene tubing; chambers with oil, oil and discs, or sand; bright zinc chain; brushes for electrostatic and frictional damping; mass-string-whiskers assembly. Except for the viscoelastic tape, these dampers were provided in the hollow space inside the members. The details are given in References 1-5. The natural vibration tests with these concepts indicated a wide range of damping efficiencies. The prime candidates for further study appeared to be the brushes for electrostatic and frictional damping as well as the mass-string-whiskers assembly.

The present paper summarizes the outcome of natural and forced flexural vibration studies conducted on a 20.86 ft. long tubular aluminum alloy member, and a two-bar grillage structure constructed from tubular members 14.75 ft. and 20.86 ft. long, with various passive damping concepts. A grillage structure is one which is subjected to loads or vibration at right angles to its own plane. The grillage structure used in the present study is obtained by retaining a typical side and a diagonal member of a cubical subassembly taken from a proposed space

---

<sup>1</sup> Professor, Department of Civil Engineering, Old Dominion University, Norfolk, Virginia 23529, Ph. (804) 683-3753.

<sup>2</sup> Graduate Student, Department of Civil Engineering, Old Dominion University, Norfolk, Virginia 23529.

station prototype model. The two bar assembly studied is in the horizontal plane while the vibration is induced vertically. The resulting subassembly represents a basic space structure and provides a convenient means of testing passive damping concepts beyond the single-member level. The members possess moderate slenderness and are provided with semi-rigid connections.

### Domain of Investigation

Figure 1 shows schematically a hollow tubular aluminum member of length 20.86 ft. with an outer diameter  $D_o = 2.0$  in. and a wall thickness of  $t_o = 0.125$  in. Both ends of the members are partially restrained in the rotational sense. The partial rotational restraint is provided by semi-rigid connections. The rotational stiffness provided by the connection is  $k$ . The member has an initial deflection  $w_o$ , and is subjected to natural or forced flexural vibration at its midspan. Also, Figure 2 shows schematically a two-member grillage structure. The member lengths are 14.75 ft. and 20.86 ft. and possess the same cross-sectional dimensions  $D_o$  and  $t_o$ . Members AC and CE are partially restrained at the ends with rotational end stiffnesses of magnitude  $k_1 = 53.1$  kip-in/rad., and  $k_2 = 48.5$  kip-in/rad., respectively. At C, the junction of the two members is supported by a pair of vertical springs CF and CG of equal stiffness  $K = 19.85$  lb/in. Natural or forced flexural vibration is introduced at midspan B of member AC. The specific problem considered herein is to first identify an efficient passive damping concept for the member shown in Figure 1, and then study its effectiveness in damping member CE of the grillage shown in Figure 2. At the member-level, the following four passive damping concepts were investigated:

- a. Nylon Brush Dampers
- b. Wool Swab Dampers
- c. Copper Brush Dampers
- d. Silly Putty in Chamber Dampers

The first three types of dampers were selected for testing since the results given in Reference 1 showed that brush or whisker dampers were quite effective in reducing natural flexural vibration. The fourth type of damper was selected owing to the plastic deformation behavior of the silly putty when subjected to external forces. In addition to the experimental study, a theoretical analysis of the member in Figure 1 was conducted using the procedures given in References 1 and 4 for the case of natural vibration.

### Passive Dampers

Figure 3 shows the four types of passive dampers studied. From one to several dampers were provided inside the hollow space of the tubular member. Figure 4 shows a typical arrangement consisting of several parts. First, a helical spring, with a stiffness of 0.44 lb/in., is attached to the inside of the connection. To the other end of the spring is attached a nylon chord which in turn is attached to the first damper. The nylon chord used in this investigation had a 40 lb capacity. Thereafter, a series of nylon chords and dampers are attached along the member length until the other end of the member is reached. The end of the nylon chord at the other end is then passed through a hole and stretched from the outside by an amount of 2.0 inches in the longitudinal direction of the member to induce a slight tension in the helical spring, and subsequently tied to the connection externally. The resulting passive damping assembly is, therefore, aligned with the longitudinal axis of the tubular member. Since the nylon chord is fairly flexible, a significant portion of the 2.0 inches of stretching is due to the elongation of the chord itself, with the remaining portion of the stretching taking place in the helical spring. The dampers are installed equidistantly between the



member ends. Tests are conducted with one or more dampers. A brief description of each of the dampers follows.

Figure 3(a) shows a nylon brush damper. It has a diameter of 1.75 in., a total length of 6.25 in., weighs 14.0 gms, and is manufactured by H. Hertzberg and Son, Inc., Middletown, N.Y. 10940. It has a plastic handle and twisted wires with which the nylon bristles are intertwined, and is commonly used for cleaning vegetables. The brush shown in Figure 3(a) is obtained by cutting the twisted wires about 1.5 in. away from where the brush starts. The twisted wires do not extend beyond the brush end.

Figure 3(b) shows a wool swab damper with a 1.0 in. diameter, a total length of 3.0 in., and a total weight of 7.1 gms. The wool swab is manufactured by Omark Industries, Onalaska, Wisconsin 54650. It has a threaded aluminum piece at one end with a twisted wire attached to it to which the wool swab is attached. The aluminum piece is 0.75 in. long, while the swab itself has a length of 2.125 in. It is commonly used in cleaning 12 in. gauge shotguns.

Figure 3(c) shows a copper brush damper with a 0.8125 in. diameter, a total length of 3.125 in., and a total weight of 13.0 gms. The brush is manufactured by Omark Industries, Onalaska, Wisconsin 54650. It has a partly threaded aluminum piece at one end with a twisted wire attached to it to which the copper bristles are attached. The aluminum piece is 1.0 in. long, while the brush itself has a length of 2.125 in. This brush is also used in cleaning 12 in. gauge shotguns.

Figure 3(d) shows a "Silly Putty in Chamber" damper. It consists of a silly putty ball of about 0.75 in. diameter placed inside a perforated hollow cylindrical chamber. The silly putty is manufactured by Binney and Smith Inc., Easton, Pennsylvania 18042. The chamber is made from a "Bristole Pipe" (PVC-1120, Schedule 40, ASTM-D-1785) having an original outer diameter of 1.28 in., and a wall thickness of 0.14 in. The chamber is made by reducing the outer diameter to 1.0625 in. through machining thus reducing its wall thickness. Since the primary purpose of the chamber is to house a ball of silly putty, its weight is reduced by drilling a total of seven, 0.25 in. diameter holes around its periphery halfway from its ends. The putty is kept inside the chamber by means of a plastic wrap taped around it with scotch tape. The putty is free to bounce around inside the chamber. The total weight of one damper including the silly putty, the chamber, and the taped wrap, is 7.4 gms.

### Test Procedure

The main instrumentation used in conducting the tests consists of a proximity probe, vibration instrumentation, and a deflection-time plotter. For natural member vibration tests, a weight  $W = 6.1$  lb. is first attached at the midspan by means of a cotton chord. To induce natural vibration, the chord is then cut by a pair of scissors to release the member. The time-dependant deflection at member midspan is recorded by means of a proximity probe which is connected to a deflection-time recorder. To induce forced flexural vibration, a vibrator (Model 203-25-DC) is used with an oscillator (Model TPO-25). The vibrator applies a forcing function of the type:

$$F(t) = F_o \sin \Omega t \quad (1)$$

in which  $F_o = 4$  lb.,  $t$  = time, and  $\Omega$  = frequency of the forcing function.

Figure 2 shows a schematic of the grillage vibration test setup. To induce natural vibration, a weight  $W = 7.9$  lb. attached at point B of the member AC is

released suddenly. The deflection-time response of the member CE is recorded at its midspan D. For the forced vibration tests, the function  $F(t)$  is applied at B and the deflection-time response is recorded at midspan D of the member CE up to a certain time whereafter the vibrator at B is disengaged to record the response for  $F(t) = 0$ .

The vibrator employed for the forced vibration tests allowed only a limited amount of travel. This meant that the deflection of the member at the location where the vibrator was attached was limited to what the vibrator could allow. Nevertheless, forced vibration tests were conducted on the individual member since it was not known initially as to whether or not the dynamic deflections would exceed the vibrator capacity. Some of the results indicated that the vibrator "constrained" the member deflection for a certain range of the forcing function frequencies including that which would otherwise have constituted a resonance condition. This limitation of the vibrator made the evaluation of the performance of the dampers difficult under forced vibration conditions through tests on the individual member. However, the only way to evaluate the performance of the dampers under forced vibration was by allowing the member to develop dynamic deflections without direct restrictions imposed by the vibrator. The grillage test procedure provided this freedom. Thus, while one member was being vibrated under the influence of a forcing function, the deflections of the other member were being recorded without any constraint at its midspan. The forced vibration tests on the member and the grillage also included the study of the wool swab and the silly putty in chamber dampers in the time domain past the discontinuation of the applied forcing function. Each test was repeated three times to obtain proper averages.

## Results

Under member natural vibration, the silly putty in chamber damper concept provides considerably greater passive damping as compared to that of the nylon brush, wool swab, and copper brush damping concepts. Figure 5 shows the dimensionless envelope of the midspan deflection versus time ( $\Delta_E - T$ ) relationships when 5 wool swab or 5 silly putty in chamber dampers were used. Figure 6 presents the damping ratio versus the number of dampers relationships for the various damping concepts. Figure 7 shows the passive damping efficiency index curves for these concepts. The index is defined as follows:

$$\eta = \frac{\zeta - \zeta_0}{M_d} \quad (2)$$

in which  $\zeta_0$  is the damping ratio in the absence of any passive damping device,  $M_d$  is the mass of the passive damping device, and  $\zeta$  is the damping ratio when dampers are provided. Also, as described earlier, due to the constrained motion imposed by the vibrator, the effectiveness of the passive dampers could not be adequately evaluated under forced conditions for the individual members. Furthermore, the theoretical results based on the procedures in References 1 and 4 for member natural vibration were in excellent agreement with the tests and are documented in Reference 6.

For the grillage under natural vibration, the 5 wool swab damper configuration provided greater damping than that of the 5 silly putty in chamber damper configuration. Under the forced vibration, the 5 silly putty in chamber damper configuration provided very effective passive damping at and around the resonant frequency. At resonance, these dampers resulted in a 52% reduction of the dynamic magnification factor, as indicated by the results plotted in Figure 8.

## Conclusion

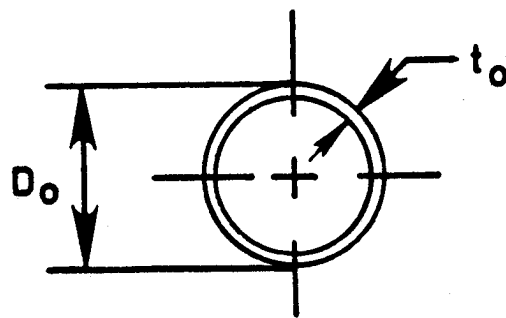
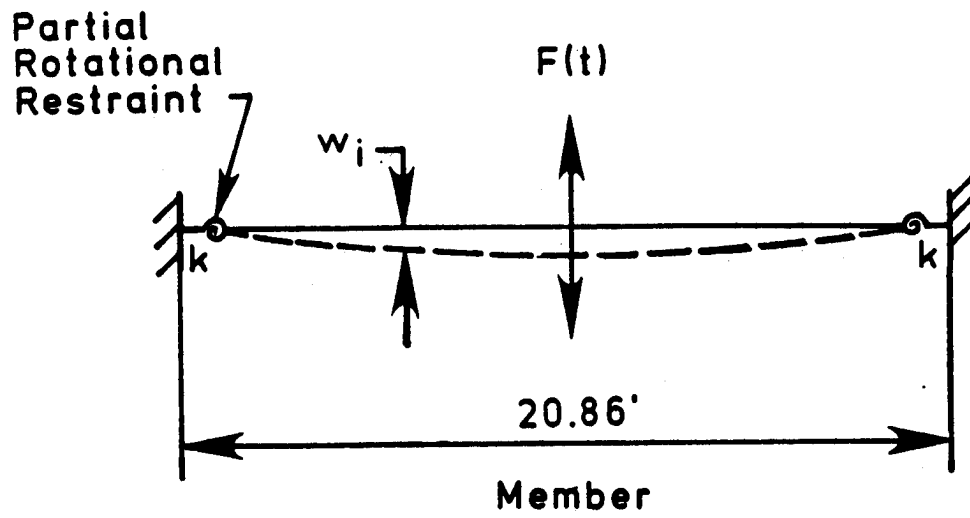
Four passive damping concepts studied show that the member and grillage vibration amplitudes can be reduced to various degrees. It appears that the silly putty in chamber dampers are generally more effective than the other three types of potential damping concepts studied.

## Acknowledgements

The motivation and help for this research have been provided by Harold G. Bush and Martin M. Mikulas, Jr. of the Structural Concepts Branch at NASA Langley Research Center. Also, Robert Miserentino and his staff helped in the calibration of the probes used in the tests. The work was supported partly by NASA Grant NAG-1-336.

## References

1. Razzaq, Z., Volland, R.T., Bush, H.G., and Mikulas Jr., M.M., "Stability, Vibration and Passive Damping of Partially Restrained Imperfect Columns," *NASA Technical Memorandum 85697*, October, 1983.
2. Razzaq, Z., "Passive Damping Concepts for Slender Columns in Space Structures," *Progress Report*, Submitted to NASA Langley Research Center Under Research Grant NAG-1-336, August, 1984.
3. Razzaq, Z., "Passive Damping Concepts for Slender Columns in Space Structures," *Progress Report*, Submitted to NASA Langley Research Center Under Research Grant NAG-1-336, February, 1985.
4. Razzaq, Z., and Ekhelikar, R.K., "Passive Damping Concepts for Slender Columns in Space Structures," *Progress Report*, Submitted to NASA Langley Research Center Under Research Grant NAG-1-336, May, 1985.
5. Razzaq, Z., and El-Aridi, N.F., "Passive Damping Concepts for Low Frequency Tubular Members," *Progress Report*, Submitted to NASA Langley Research Center Under Research Grant NAG-1-336, August, 1986.
6. Razzaq, Z., and Najjar, B.S., "Passive Damping Concepts for Free and Forced Member and Grillage Vibration," *Progress Report*, Submitted to NASA Langley Research Center Under Research Grant NAG-1-336, July, 1988.



**Cross Section**

**Figure 1. Schematic of tubular member**

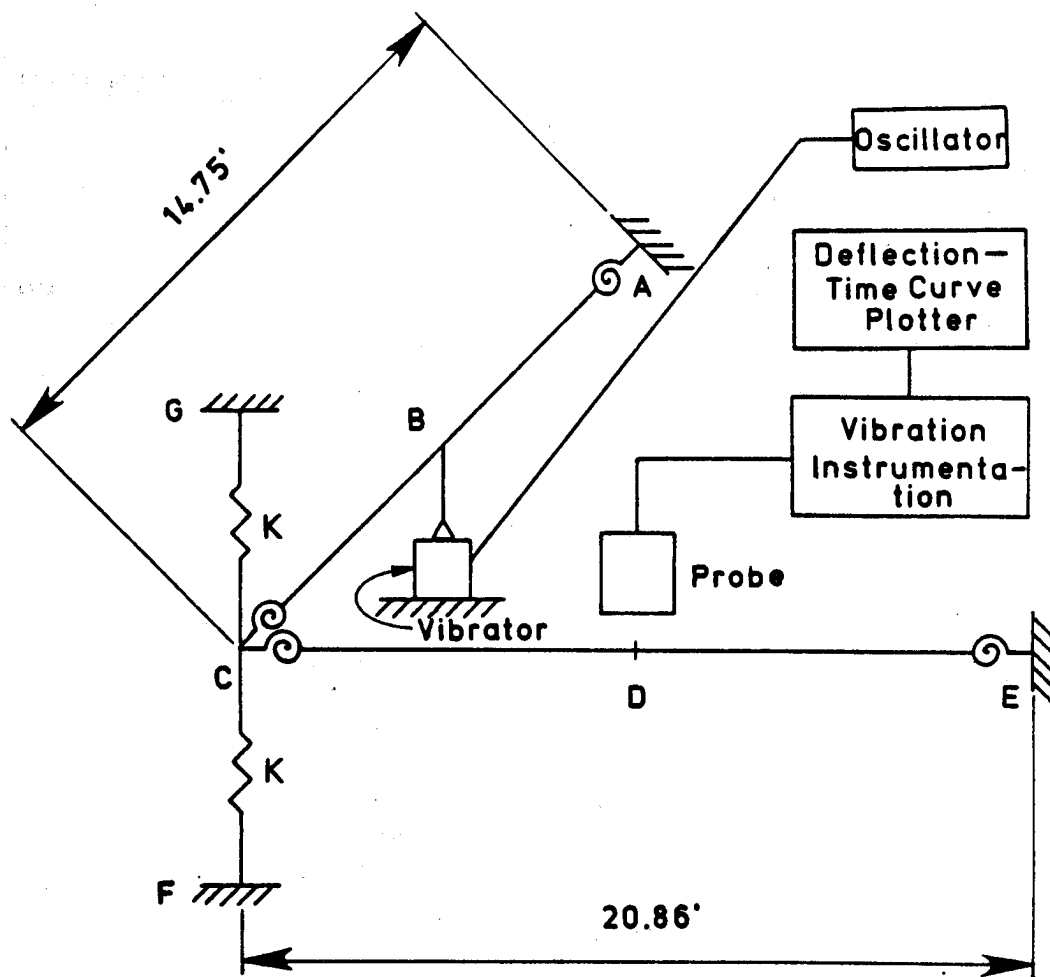


**Figure 2. Schematic of grillage test setup**



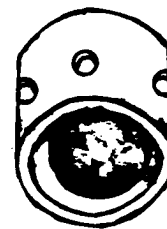
**(a) Nylon brush damper**



**(b) Wool Swab damper**



**(c) Copper brush damper**



**(d) Silly putty in chamber damper**

**Figure 3. Passive dampers**

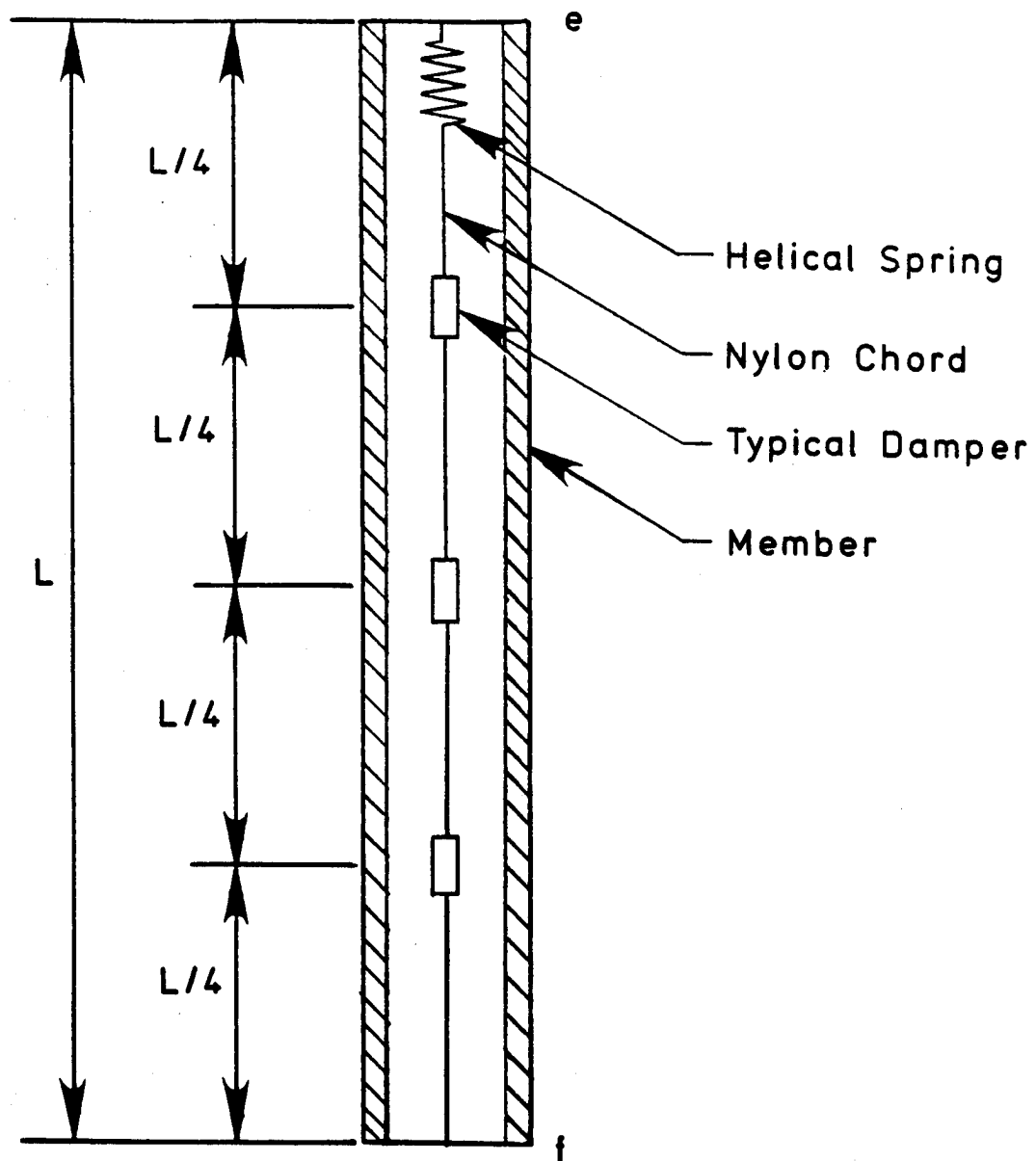


**Figure 4. Schematic for typical spacing of passive dampers**

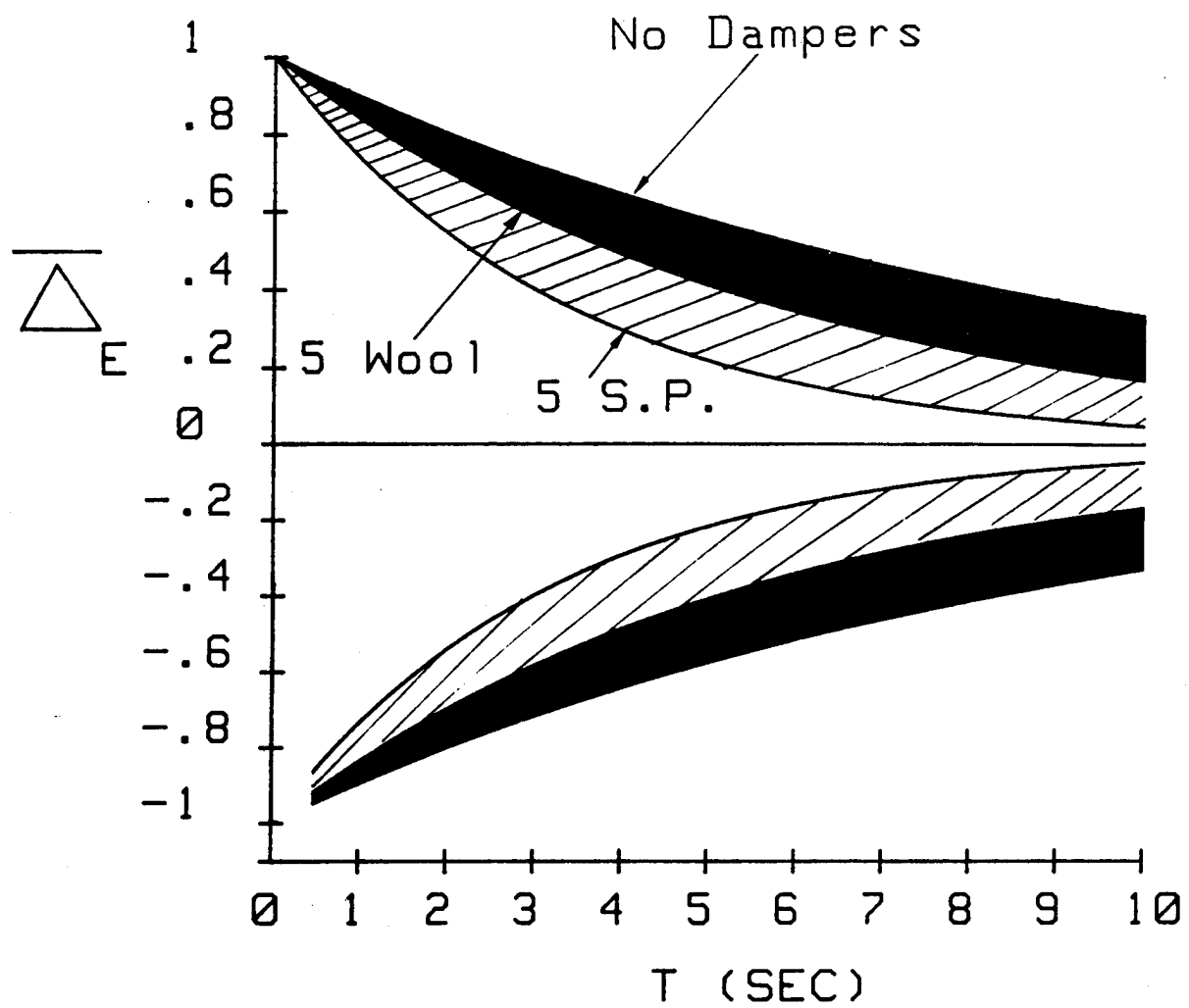


**Figure 5. Member dimensionless deflection-time envelopes**



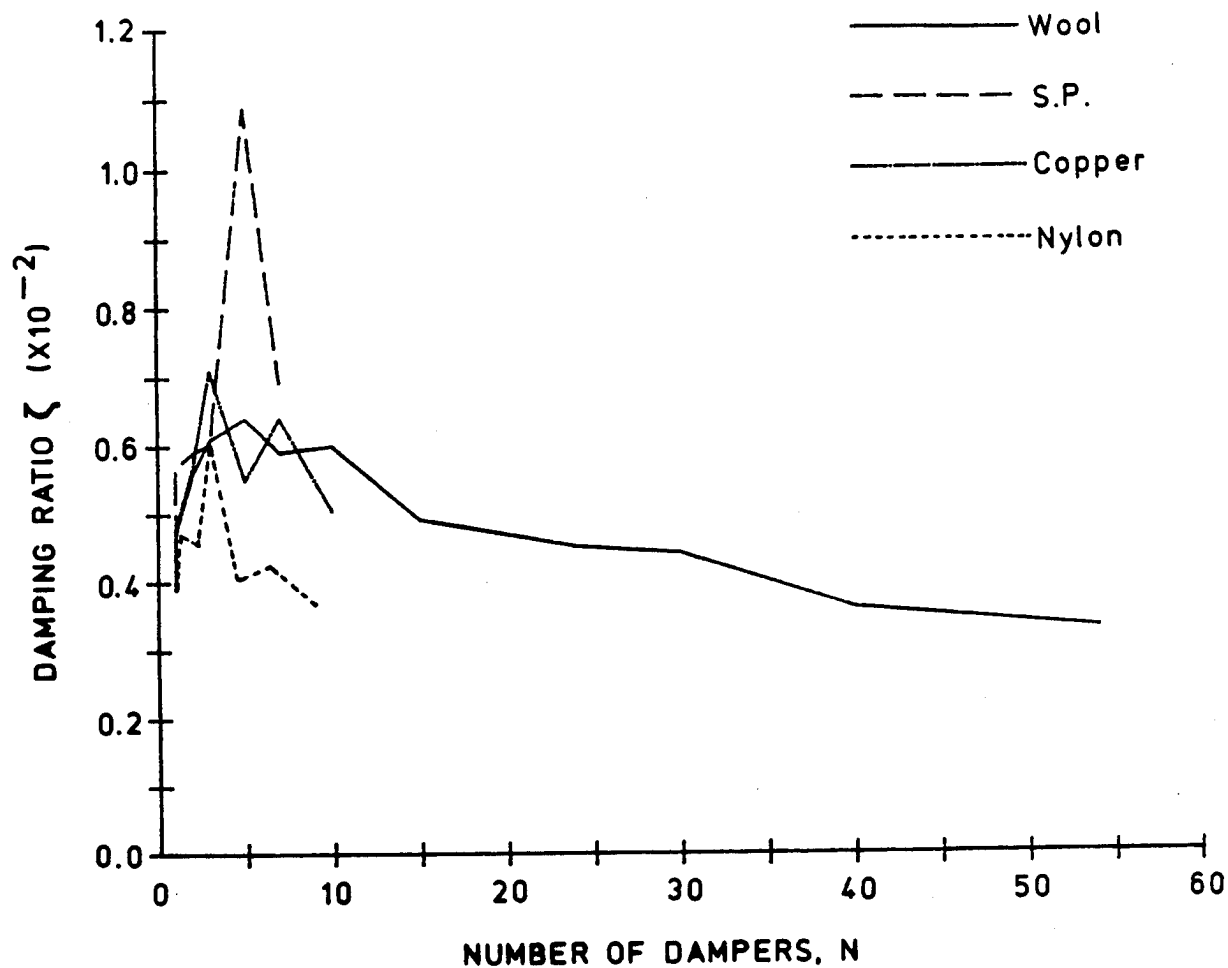


**Figure 6. Damping ratio versus number of dampers for member natural vibration**

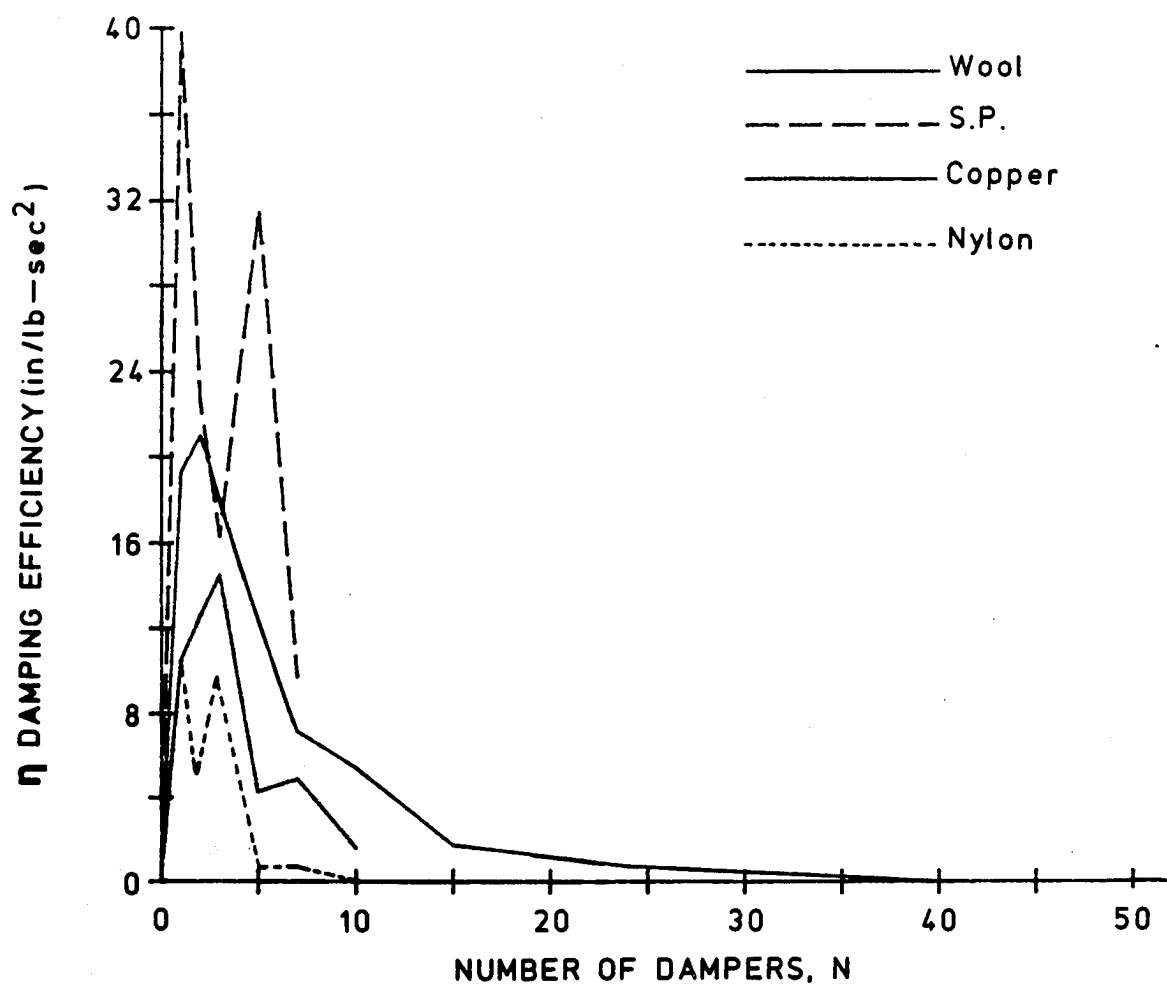


**Figure 7. Damping efficiency versus member of dampers for member natural vibration**

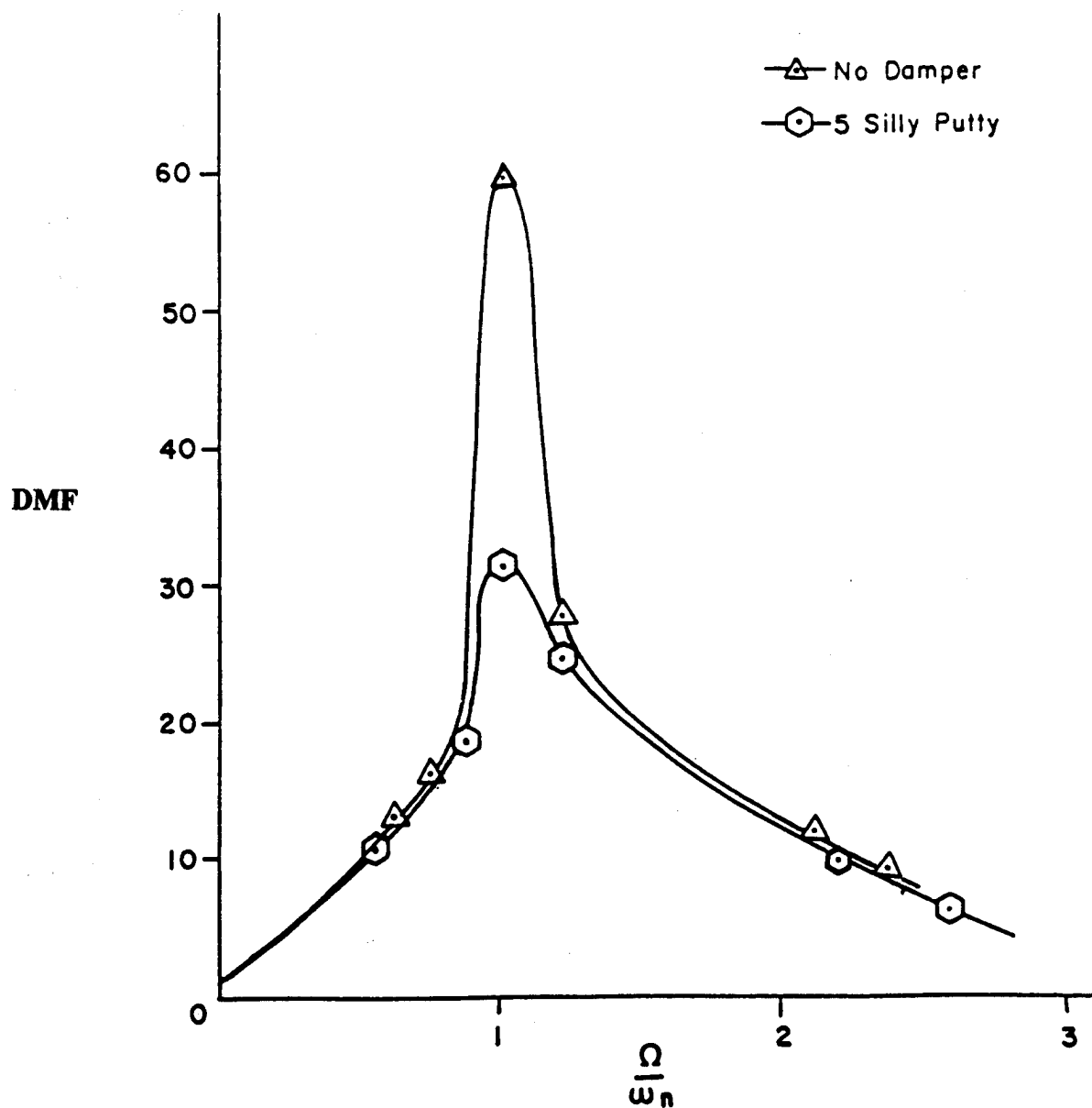


**Figure 8. Dynamic magnification factor versus frequency ratio for grillage vibration**

# **DESIGN AND ANALYSIS OF VISCOELASTIC STRUTS FOR LARGE SPACE STRUCTURES**

**Y. C. Yiu**

Structural Dynamics, Astronautics Division, Dept. 59-22, B/586E  
Lockheed Missiles & Space Company, 1111 Lockheed Way, Sunnyvale, CA 94089  
Telephone : 408-742-4048

## **ABSTRACT**

Use of the Modal Strain Energy Method for the optimization of viscoelastic structures requires extensive modal extraction and modal strain energy distribution analyses. For large structural systems, this iterative procedure becomes very inefficient and expensive. Based on the Rayleigh-Ritz principle and engineering assumptions, a method is developed for the optimization a class of viscoelastic struts. Dimensionless ratios of the system parameters of the modified design and the baseline design are derived, in closed form algebraic equations, to enable design optimization to be performed without iterative computer analyses. A finite element substructure analysis method is also derived for the efficient analysis of complex stiffness matrices due to the presence of viscoelastic materials in the detailed stress model. The results from simple design predictions and the dynamic substructuring finite element analysis show excellent correlation.

## INTRODUCTION

Large space structures require efficient structural design with high strength and light weight materials to reduce the launch weight. Truss type structures are prevalent. High stiffness and damping are required for on-orbit performance to minimize the dynamic response due to operational disturbances. However, materials with high strength and stiffness do not normally process high damping characteristics. Therefore, a combination of different materials must be used to provide the desired system response. The design of high performance structure must balance the stiffness and damping characteristics to minimize the weight of the structure.

The Modal Strain Energy (MSE) Method<sup>1</sup> has been used extensively in the design of passively damped structures using viscoelastic materials (VEM). Tests on a demonstration article<sup>2</sup> showed excellent correlation between predicted results using MSE and measured results. Therefore, within the limits of its applicability, the MSE method can be used to achieve a design with the desired damping characteristics.

When designing a large precision structure, large finite element models with high fidelity to capture the structural behavior is often required. Furthermore, for passive damping design with VEM, the MSE Method requires a detailed structural model so that the modal strain energy distribution in the VEM can be computed accurately. The procedure for designing structures with passive damping is basically an iterative modal extraction and strain energy distribution analysis. However, this type of iterative computer analysis on a large finite element model to optimize the design parameters is prohibitively expensive and inefficient. Therefore, improved efficiency of the analysis is vital to the optimal design of large damped structures.

This paper presents a method, based on the Rayleigh-Ritz principle, such that a class of viscoelastic struts can be designed and optimized efficiently for large space trusses. This method provides a desired viscoelastic strut design using the initial baseline design and simple algebraic equations. A dynamic substructuring procedure is also presented for large finite element models with complex stiffness matrices due to the presence of viscoelastic materials. This combination of design procedure and analytical technique enables better design of large space structures with viscoelastic struts with less effort and better understanding. This method is also applicable to other large structural systems.

## VIBRATION ATTENUATION

For a linear elastic single degree of freedom system, the governing differential equation for dynamic loading is :

$$m \ddot{x} + c \dot{x} + k x = p(t) \quad (1)$$

If the structure is modified to enhance its damping characteristic, the system parameters are changed to :

$$\tilde{m} = r_m m \quad (2)$$

$$\tilde{k} = r_k k \quad (3)$$

$$\tilde{f}_n = \sqrt{\frac{r_k}{r_m}} f_n \quad (4)$$

$$\tilde{\xi} = r_{\xi} \xi \quad (5)$$

where  $r_m$ ,  $r_k$  and  $r_{\xi}$  represent the ratios of the modified values to the respective baseline values. The effect of such changes on dynamic response is different for different types of vibration environments. The mass, stiffness and damping of the system must be balanced for an optimum design.

### Random Vibration

If  $p(t)$  is described by the power spectral density function  $S(f)$  and it is relatively constant around the natural frequency,  $f_n$ , the response for a lightly damped system ( $\xi < 0.3$ ) can be expressed as :

$$x_{rms} \approx \frac{S(f_n)^{0.5}}{2\sqrt{2} m^{0.25} k^{0.75} \xi^{0.5}} \quad (6)$$

Therefore, the response of the modified structure can be expressed as :

$$\tilde{x}_{rms} \approx \frac{S(\tilde{f}_n)^{0.5}}{2\sqrt{2} \tilde{m}^{0.25} \tilde{k}^{0.75} \tilde{\xi}^{0.5}} \quad (7)$$

If  $S(f)$  is relatively constant over  $f_n$  and  $\tilde{f}_n$ , then the response attenuation factor,  $\alpha$ , can be defined as :

$$\begin{aligned} \alpha &= \frac{\tilde{x}_{rms}}{x_{rms}} \\ &= \frac{1}{r_m^{0.25} r_k^{0.75} r_{\xi}^{0.5}} \end{aligned} \quad (8)$$

Therefore the attenuation factor of the modified structure can be expressed in terms of the dimensionless ratios of mass, stiffness and damping. The attenuation factor is least sensitive to mass change and most sensitive to stiffness change. However, the change in stiffness of the modified structure is normally not very large while the change in damping ratio can be significant.

For a multiple degree of freedom system with negligible modal coupling, the modal attenuation factors can also be determined in a similar way. The modal attenuation factor can be defined as :

$$\alpha_i = \frac{1}{r_{mi}^{0.25} r_{ki}^{0.75} r_{\xi i}^{0.5}} \quad (9)$$

Very often, passive damping mechanisms increase mass and damping but reduce the stiffness. An optimum design balances the contribution from these three ratios to minimize the attenuation factor. The objective function for optimization is therefore  $\alpha_i$ .

The key to optimization of structural response to a random vibration environment is therefore the ability to estimate the modal mass, stiffness and damping ratios accurately. The following design procedure fully exploits these modal ratios to achieve an optimized design.

### Other Types of Vibration

A similar approach can be used for other type of dynamic loading. For sinusoidal input, the attenuation factor can shown to be :

$$\alpha_i = \frac{1}{r_{ki} r_{\xi i}} \quad (10)$$

If  $f(t)$  is transient in nature, it is best to characterize it by shock spectrum curves. The maximum modal response is related by the ratios of the shock spectrum values at the system frequency and damping values.

## APPROACH

In order to successfully design passive damping into a large structure to control vibration response, the behavior of the structural system and disturbance characteristics must be thoroughly investigated. A finite element model of the baseline elastic structure is analyzed for its frequency characteristics, modal strain energy characteristics and dynamic response characteristics. The type and extent of the damping treatment must be identified using the baseline model. In order to accomplish an optimum viscoelastic strut design to control the system level response, the relationship between the viscoelastic materials, component design parameters and system level behavior must be understood. To implement any practical design concept, the number of design parameters must be reduced to a manageable size. Engineering assumptions must be made to simplify the analytical design process and develop a direct algebraic relationship between the design parameters and system level response. Optimization can then proceed expeditiously and a preliminary design can be developed.

### Design Optimization Assumptions

To illustrate the design procedure described herein, the following design and analysis assumptions are made :

1. Analysis Tool - The Modal Strain Energy Method is used as an analysis tool to identify candidate locations where VEM can be most effectively placed. Uncoupled modal analysis is used to analyze the performance of the design.
2. Design Parameters - Two assumptions are made to reduce the total number of design parameters. Firstly, it is desirable to use only one VEM. For a given operating environment and dominant natural frequency, only two material parameters,  $G$  and  $\eta$ , are required to be optimized. Secondly, only one viscoelastic strut design is used throughout the structure. This limits the geometric parameters to only the length and thickness of the VEM.
3. Component/System Behavior Assumption - For the modes of interest, the stiffness of the system is governed by the axial deformation of truss members. This identifies the most important behavior of the strut member and allows simplified equations to be developed to predict the stiffness and strain energy distribution of the struts and the overall system.

4. System Analysis Assumption - It is assumed that the structural system has already been optimized for mass and stiffness, and the overall system performance would be acceptable if higher damping is provided. The purpose of the viscoelastic struts is only to enhance the damping characteristic of the system. It is therefore further assumed that the modes shapes of the viscoelastically damped structure are not substantially different from the baseline structure and the mode shapes of the baseline structure are a good set of generalized coordinates for the modified structure.
5. Dynamic Loading Assumptions - It is assumed that the dynamic response of the structure is governed by a random disturbance. Reduction of the modal root mean square response is used as the objective function for optimization. The same technique can be used for other types of dynamic loading conditions.

## DESIGN AND ANALYSIS PROCEDURE

The procedure to design and analyze the structure with viscoelastic struts, as outlined in Table 1, is comprised of three basic parts. The first part involves the analysis of the baseline model. The steps are outlined in steps 1 through 4 of Table 1. The modal contributions to the system responses are identified. A modal strain energy distribution analysis of these modes is performed. Struts are then ranked according to modal strain energy level. The second part, outlined in steps 5 through 9 of Table 1, involves the use of simplified equations to optimize a viscoelastic strut design and predict the overall system performance. This bypasses the iterative analysis using the finite element models. The third part involves finite element verification of the analysis. A detailed finite element model of the viscoelastic strut is constructed. A reduced mass matrix and complex stiffness matrix of the strut are computed. These matrices are assembled into the global matrices in place of the baseline strut members. Modal extraction is performed and equivalent viscous damping is extracted. Response analysis is performed to verify the system performance. This is outlined in steps 10 through 16 of Table 1.

## ANALYSIS OF BASELINE STRUCTURE

The baseline elastic structure system satisfies the following matrix differential equation in the frequency domain :

$$[-\omega^2 \mathbf{M} + i \omega \mathbf{C} + \mathbf{K}] \mathbf{u}(\omega) = \mathbf{F}(\omega) \quad (11)$$

The structural system has an undamped eigensolution,  $\Lambda$  and  $\Phi$ . The orthogonality conditions for the system are :

$$\Phi^T \mathbf{M} \Phi = \mathbf{I} \quad (12)$$

$$\Phi^T \mathbf{K} \Phi = \Lambda \quad (13)$$

The modal differential equation of motion is :

$$[-\omega^2 \mathbf{I} + i \omega \Phi^T \mathbf{C} \Phi + \Lambda] \mathbf{Q}(\omega) = \Phi^T \mathbf{F}(\omega) \quad (14)$$

The uncoupled modal damping ratio,  $\zeta_i$ , is often assumed in the computation of dynamic responses. The uncoupled modal differential equation is :



Table 1. Summary of Design and Analysis Procedures

<p><b>Baseline Model Analysis</b></p> <ol style="list-style-type: none"> <li>1. Construct baseline structural finite element model. Perform a real eigenvalue analysis.</li> <li>2. Perform dynamic response analysis. Identify modes contributing significantly to the responses.</li> <li>3. For the modes of interest, perform strain energy distribution analysis of the elements in the baseline model.</li> <li>4. Select a group of highly strained elements to be replaced by viscoelastic struts. Compute the modal strain energy ratio, <math>\epsilon_i</math>, and modal mass ratio, <math>\mu_i</math>, of the group. Eq. (17), (22)</li> </ol>
<p><b>Design Procedure</b></p> <ol style="list-style-type: none"> <li>5. Analyze the viscoelastic strut using strength of materials and structural analysis methods. Express the strut stiffness ratio, <math>r_a</math>, and strain energy ratio in the viscoelastic material, <math>r_w</math>, in terms of design parameters, <math>G_v</math>, <math>t_v</math> and <math>l_v</math>. Eq. (26), (29)</li> <li>6. Express the modal parameters, <math>\tilde{k}_i</math>, <math>\tilde{m}_i</math>, <math>\tilde{\gamma}_i</math> and <math>\tilde{\xi}_i</math>, of the modified structure in terms of the design variables. Eq. (34), (36), (37), (42) Express modal attenuation factor, <math>\alpha_i</math>, in term of <math>r_{mi}</math>, <math>r_{ki}</math>, <math>r_{\xi i}</math>. Eq. (9)</li> <li>7. Select a viscoelastic material - <math>\eta^v(\omega)</math> and <math>G^v(\omega)</math>.</li> <li>8. Compute modal attenuation factors for the range of feasible design parameters and obtain the optimum values of design parameters.</li> <li>9. Update dynamic responses based on design parameters from steps 7 and 8. Iterate steps 4, 7 and 8, if necessary, to obtain the desired response level.</li> </ol>
<p><b>Finite Element Substructuring Analysis</b></p> <ol style="list-style-type: none"> <li>10. Construct a finite element model of the viscoelastic strut .</li> <li>11. Using the substructuring method, form the mass matrix and the real part and imaginary part of the condensed component stiffness matrix of the viscoelastic strut. Eq. (47), (48)</li> <li>12. Assemble the complex global stiffness matrix and mass matrix. Perform a real eigenvalue analysis of the modified structure.</li> <li>13. Repeat steps 10 to 12 for as many frequency dependent stiffness matrices as necessary.</li> <li>14. Extract modal damping ratios from the imaginary part of the stiffness matrix. Eq. (53),(54)</li> <li>15. Compute dynamic response based on modal parameters from finite element results.</li> <li>16. If results are not satisfactory, use the model of step 12 as the baseline model and iterate.</li> </ol>

$$[-\omega^2 + i 2 \zeta_i \omega_i \omega + \omega_i^2] q_i(\omega) = \phi_i^T F(\omega) \quad (15)$$

A dynamic response analysis is performed to identify the modes contributing significantly to the response. A modal strain energy analysis of the baseline structural model is performed to compute the strain energy,  $(w_i)_i$ , of each element of the  $i$ -th mode. The locations with the highest strain energy density are identified as a group to be replaced by viscoelastic struts. The ratio of the modal strain energy of the selected group to the strain energy of the entire structure is the modal strain energy ratio,  $\epsilon_i$ . If the strain energy ratio of the viscoelastic material to the viscoelastic strut is known, the system level modal loss factor can be estimated readily by Equations (40) and (A8). The level of damping can be increased by including more viscoelastic struts, higher strain energy ratio in the VEM and higher material loss factor. A practical level of passive damping can therefore be estimated once the modal strain energy distribution is known.

In order to analyze and fully understand the effect of viscoelastic struts on the structural stiffness, strain energy distribution and mass, it is best to separate the structure into two groups, the unmodified group and the to-be-modified group. Therefore, the global elastic stiffness matrix can be visualized as being contributed to by two matrices,  $K_1$  and  $K_2$ .

$$K = K_1 + K_2 \quad (16)$$

$K_1$  represents the stiffness matrix of the unmodified elastic elements and  $K_2$  represents the stiffness matrix of the to-be-modified elastic elements. Although the modal strain energy ratio of the to-be-modified members,  $\epsilon_i$ , is computed by the summation of individual elements, it can also be expressed as :

$$\epsilon_i = \frac{\frac{1}{2} \phi_i^T K_2 \phi_i}{\frac{1}{2} \phi_i^T K \phi_i} \quad (17)$$

Using the orthogonality condition,  $\phi_i^T K \phi_i = \omega_i^2$ , Equation (17) can be expressed as :

$$\phi_i^T K_2 \phi_i = \epsilon_i \omega_i^2 \quad (18)$$

and therefore

$$\phi_i^T K_1 \phi_i = (1 - \epsilon_i) \omega_i^2 \quad (19)$$

Similarly, an analysis of the effect of viscoelastic struts on the modal mass can be performed if the mass change is significant. The mass matrix is also separated into two parts.

$$M = M_1 + M_2 \quad (20)$$

$M_1$  is the mass matrix of the unmodified elastic elements and  $M_2$  is the mass matrix of the to-be-modified elastic elements. The modal mass ratio,  $\mu_i$ , can also be defined as :

$$\mu_i = \frac{\phi_i^T M_2 \phi_i}{\phi_i^T M \phi_i} \quad (21)$$

Since  $\phi_i$  is mass normalized, then

$$\phi_i^T M_2 \phi_i = \mu_i \quad (22)$$

and

$$\phi_i^T M_1 \phi_i = (1 - \mu_i) \quad (23)$$

## DERIVATION OF DESIGN EQUATIONS

Based on the stated engineering assumptions, the viscoelastic strut has only four design parameters. It is necessary to derive approximate closed form equations relating the material constants to the strut component parameters and then to the system performance parameters. Consequently, trade studies and optimization of the viscoelastic strut can be performed expeditiously by using simple tools such as a spreadsheet. This allows a comprehensive design optimization to be performed in a very short time and without substantial computer cost. It also offers a better physical insight into the effect of each parameter on the component and system behavior.

### Analysis of Viscoelastic Strut

It is assumed that the stiffness of the truss, for the modes of interest, is governed by the axial deformation of the truss members. The axial stiffness and strain energy distribution of the damped strut can be derived based on a strength of materials approach. The ratio of the stiffness of the damped strut to the baseline strut,  $r_a$ , and the strain energy ratio of the VEM to the strut,  $r_w$ , are two dimensionless ratios at the strut component level which are important to the optimization process. The component stiffness ratio,  $r_a$ , affects the system stiffness and natural frequencies while the component strain energy ratio,  $r_w$ , controls the amount of damping introduced by the VEM into the system. In addition, the mass ratio,  $r_m$ , of the strut can also be computed if necessary.

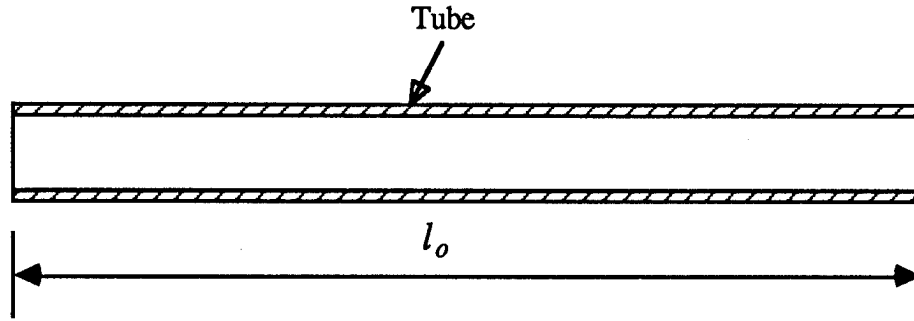
Different viscoelastic strut design concepts have been proposed<sup>3</sup> and some were built and tested<sup>2</sup>. A simple strut design concept, as show in Figure 1, is used to illustrate the design and analysis procedure. When the strut is deformed axially, the VEM carries the force in shear. Consequently, it provides the strain energy necessary for damping. It is further assumed, for the sake of simplicity, that the material constants and cross sectional areas of the inner and outer tubes are the same.

The axial stiffness of the original strut without viscoelastic material is :

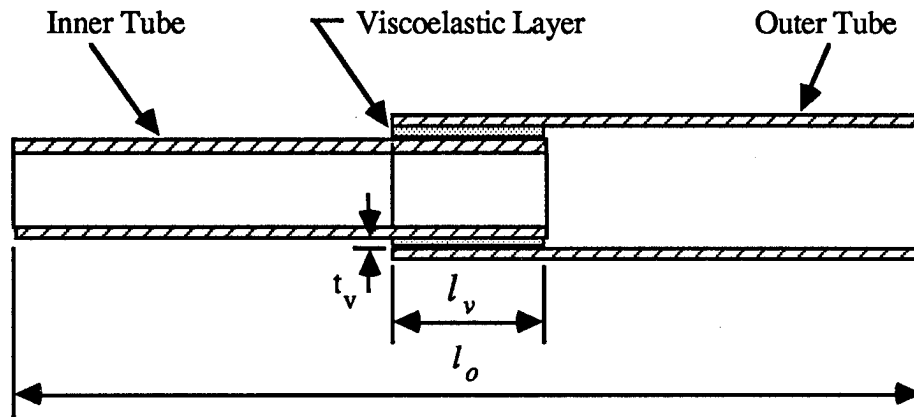
$$k_o = \frac{EA}{l_o} \quad (24)$$

The axial stiffness of the strut with viscoelastic material is :

$$k_v = \frac{1}{\frac{l_o}{EA} - \frac{l_v}{3EA} + \frac{t_v}{2\pi l_v G_v}} \quad (25)$$



a. Baseline Strut



b. Conceptual Viscoelastic Strut

Figure 1. Conceptual Strut Design

The ratio of the damped strut stiffness to the original strut stiffness is :

$$r_a = \frac{1}{1 - \frac{l_v}{3 l_o} + \frac{E A t_v}{2\pi \bar{r} l_v G_v l_o}} \quad (26)$$

The strain energy in the viscoelastic material is :

$$W_v = \frac{t_v}{4\pi \bar{r} l_v G_v} \quad (27)$$

The total strain energy in the damped strut is :

$$W_t = \frac{1}{2k_v} \quad (28)$$

The ratio of the viscoelastic material strain energy to the total strain energy in the damped strut is :

$$r_w = \frac{t_v k_v}{2\bar{r} l_v G_v} \quad (29)$$

This procedure for component analysis is applicable to one class of viscoelastic strut design. When a different viscoelastic strut design is used, different expressions for  $k_v$  and  $W_v$  are obtained. However, the design and analysis procedure is the same.

### Analysis of Viscoelastic Structures

In order to predict the system level response due to the introduction of viscoelastic struts, the three important modal ratios of the modified structure must be expressed in terms of the design parameters. The modified structural system satisfies the following matrix differential equation :

$$[-\omega^2 \tilde{M} + i \omega \tilde{C} + \tilde{K}] U(\omega) = F(\omega) \quad (30)$$

However, using this equation for design purposes in conjunction with large finite element models is impractical. Simple algebraic equations must be derived for optimization purposes.

The Modal Strain Energy Method uses mode shapes from the real eigenvalue solution and assumes that the modal equations are uncoupled. In addition, the mode shapes of the modified structure are assumed to be insignificantly affected by the modification of a small group of truss members. By the Rayleigh-Ritz principle, using the mode shapes of the baseline structure as the generalized coordinates, the approximate modal equation of the modified structure can be written as :

$$[-\omega^2 \phi_i^T \tilde{M} \phi_i + i \omega \phi_i^T \tilde{C} \phi_i + \phi_i^T \tilde{K} \phi_i] Q_i(\omega) = \phi_i^T F(\omega) \quad (31)$$

Assuming  $\tilde{C}$  can be diagonalized to  $\tilde{c}_i$ , then

$$[-\omega^2 \tilde{m}_i + i \omega \tilde{c}_i + \phi_i^T \tilde{K}^R \phi_i + i \phi_i^T \tilde{K}^I \phi_i] Q_i(\omega) = \phi_i^T F(\omega) \quad (32)$$

If the behavior of the structural system is governed by the axial deformation of the truss members, the modified global stiffness matrix can be approximated by :

$$\tilde{K}^R \approx K_1 + r_a K_2 \quad (33)$$

and the generalized modal stiffness can be written as :

$$\begin{aligned} \tilde{k}_i &= \phi_i^T K_1 \phi_i + r_a \phi_i^T K_2 \phi_i \\ \tilde{k}_i &= (1 - \epsilon_i + r_a \epsilon_i) \omega_i^2 \end{aligned} \quad (34)$$

Therefore, the ratio of the generalized stiffness of the modified structure to the baseline structure is:

$$r_{ki} = \frac{\tilde{k}_i}{\omega_i^2} = (1 - \epsilon_i + r_a \epsilon_i) \quad (35)$$

The corresponding generalized modal mass and the ratio of generalized mass can be written as :

$$\tilde{m}_i = r_{mi} = 1 - \mu_i + r_m \mu_i \quad (36)$$

The (Rayleigh-Ritz) frequency of the modified structure can therefore be expressed as :

$$\tilde{f}_i = \frac{1}{2\pi} \sqrt{\frac{\tilde{k}_i}{\tilde{m}_i}} \quad (37)$$

The modal strain energy ratio in the viscoelastic struts is :

$$\begin{aligned} \epsilon_i &= \frac{\frac{1}{2} r_a \phi_i^T K_2 \phi_i}{\frac{1}{2} r_a \phi_i^T \tilde{K}^R \phi_i} \\ &= \frac{r_a \epsilon_i \omega_i^2}{\tilde{k}} \end{aligned} \quad (38)$$

The modal strain energy ratio in the VEM of the viscoelastic struts is therefore,

$$\epsilon_i^v = \frac{r_w r_a \epsilon_i}{r_{ki}} \quad (39)$$

The modal loss factor can be expressed as :

$$\begin{aligned} \eta_i &= \eta^v \epsilon_i^v \\ &= \frac{\eta^v r_w r_a \epsilon_i}{r_{ki}} \end{aligned} \quad (40)$$

The equivalent viscous damping introduced into the i-th mode based on the modal strain energy method is :

$$\tilde{\zeta}_i = \frac{\eta^v r_a r_w \epsilon_i}{2 r_{ki}} \quad (41)$$

If the inherit damping in the i-th mode is  $\zeta_i$ , then the modal damping of the modified structure is :

$$\xi_i = \tilde{\zeta}_i + \zeta_i \quad (42)$$

The ratio of the modal damping of the modified structure to the baseline structure is :

$$r_{\xi_i} = \frac{\xi_i}{\zeta_i} \quad (43)$$

Therefore, the modal ratios,  $r_{mi}$ ,  $r_{ki}$  and  $r_{\xi_i}$ , are all expressed in terms of the four design parameters,  $\eta$ ,  $G$ ,  $t_v$  and  $l_v$ , in simple algebraic form as shown in Equations (35), (36) and (43). The minimization of the modal attenuation factor,  $\alpha_i$ , is therefore quite simple as shown in the example.

## SUBSTRUCTURING ANALYSIS OF VISCOELASTIC STRUCTURES

Once a set of optimum design parameters is obtained, a finite element analysis should be performed to verify the performance of the system. The use of a substructuring method is ideal in this case since only one strut design is used. Since the model has to contain enough refinement to compute the stress distribution, substructuring allows a detailed damped strut model to be added to the large FEM without increasing the size of the model, and in this case without major modification of the existing model.

### Finite Element Analysis Assumptions

1. Modal Strain Energy Method - Since the viscoelastic material is characterized by a complex modulus, the element stiffness matrix and global stiffness matrix are also complex. Real eigenvectors of the real part of the stiffness matrix are used to span the solution space. The eigenvectors are used to extract equivalent modal damping from the complex part of the global stiffness matrix. Uncoupled modal analysis is then performed.
2. Dynamic Substructuring Method - Dynamic substructuring is used to reduce the total number of degrees of freedom of the problem. Boundary node static vectors and constrained normal modes are used to condense the matrices of the substructure. Consistent with the global analysis, the set of real vectors is used to span the solution space of the complex part of the substructure stiffness matrix.

### Dynamic Substructuring Method for Complex Stiffness Matrix

A detailed finite element model of the optimized viscoelastic strut is used to represent an elastic strut element. Plate elements are used to model the elastic tube. Solid elements are used to model the VEM so that the shear energy can be computed. Rigid offset transformations in the computer code, if available, should be used to model connections between plate elements and solid elements to reduce the number of degrees of freedom and improve the numerical performance. Stiff spoke systems are used at both ends of the strut model to allow for boundary connectivity to the beam elements. The material modulus is chosen at the dominant structural response frequency and operating temperature but iteration may be necessary. The strut component stiffness matrix,  $k$ , is composed of the real part,  $k^R$ , and the imaginary part,  $k^I$ .

$$k(\omega) = k^R(\omega) + i k^I(\omega) \quad (44)$$

The real part of the component stiffness matrix,  $k^R$ , has stiffness contribution from two types of elements -  $k_e^R$  from the elastic elements and  $k_v^R$  from the viscoelastic elements.

$$k^R = k_e^R + k_v^R \quad (45)$$

By the definition of the material loss factor,  $\eta^v$ , the imaginary part,  $k^I$ , can be expressed as:

$$k^I(\omega) = \eta^v(\omega) k_v^R(\omega) \quad (46)$$

Since the strut substructure is a structure by itself, consistent with the system level assumptions, a set of real vectors is used to span the solution. This set of real vectors,  $v$ , is comprised of the static boundary vectors and the constrained normal mode vectors of the mass and real stiffness matrix. The condensed stiffness matrix,  $\kappa$ , also consists of two parts, the real part,

$\kappa^R$ , and the imaginary part,  $\kappa^I$ . The real part of the condensed element stiffness matrix,  $\kappa^R$  can be computed in a straightforward way :

$$\kappa^R(\omega) = v(\omega)^T k^R(\omega) v(\omega) \quad (47)$$

The imaginary part,  $\kappa^I$ , can be computed in a similar fashion :

$$\begin{aligned} \kappa^I(\omega) &= v(\omega)^T k^I(\omega) v(\omega) \\ \kappa^I(\omega) &= \eta^v(\omega) v(\omega)^T k_v^R(\omega) v(\omega) \end{aligned} \quad (48)$$

If only boundary vectors are used, this becomes an extension of the static condensation (Guyan Reduction) procedure applied to the complex stiffness matrix problem. For the strut model, a reduced twelve by twelve matrix can be used as the element stiffness matrix in lieu of the beam stiffness matrix. The global matrix therefore has the same size and connectivities.

For practical implementation,  $\kappa^R$  may be computed using the static condensation method to calculate the condensed stiffness matrix of the finite element model. In order to construct  $\eta^v k_v^R$ , the same model with zero material stiffness for the elastic elements is used. However,  $v$  from the model with both elastic and viscoelastic elements must be used to extract a consistent  $\kappa^I$  by matrix triple product or other computational procedure. Then  $\kappa^R$  and  $\kappa^I$  are used as element stiffness matrices to assemble the global  $\tilde{K}^R$  and  $\tilde{K}^I$  matrices.

$$\tilde{K} = \tilde{K}^R + i \tilde{K}^I \quad (49)$$

$\tilde{K}^I$  is quite sparse with nonzero entries only at those degrees of freedom connected to viscoelastic struts.

The element mass matrix can be assembled using consistent formulation but normally a lumped mass procedure will suffice and hence it is not elaborated upon here.

$$[-\omega^2 \tilde{M} + i \omega \tilde{C} + \tilde{K}^R + i \tilde{K}^I] u(\omega) = F(\omega) \quad (50)$$

By the Modal Strain Energy Method,  $\tilde{M}$  and  $\tilde{K}^R$  matrices are used to extract the real eigenvectors. However,  $\tilde{K}^R$  is not a constant coefficient matrix. This makes the solution of the exact eigenvalue problem extremely difficult. Different methods<sup>4</sup> can be used to compute an approximate solution to this frequency dependent problem. For dynamic response determined by a single mode or a limited number of modes with no modal interference, this is not a major difficulty.

If  $\tilde{\phi}_i$  is the  $i$ -th mode shape vector of the viscoelastic structure, the modal equation is therefore:

$$[-\omega^2 \tilde{\phi}_i^T \tilde{M} \tilde{\phi}_i + \tilde{\phi}_i^T \tilde{K}^R \tilde{\phi}_i + i \omega \tilde{\phi}_i^T \tilde{C} \tilde{\phi}_i + i \tilde{\phi}_i^T \tilde{K}^I \tilde{\phi}_i] q_i(\omega) = \tilde{\phi}_i^T F(\omega) \quad (51)$$

$$[-\omega^2 + \tilde{\omega}_i^2 + i \omega \tilde{c}_i + i \tilde{\phi}_i^T \tilde{K}^I \tilde{\phi}_i] q_i(\omega) = \tilde{\phi}_i^T F(\omega) \quad (52)$$



From Equation (A12), the modal loss factor contributed by the VEM can be approximated by :

$$\tilde{\eta}_i = \frac{\tilde{\phi}_i^T \tilde{K}^I \tilde{\phi}_i}{\tilde{\omega}_i^2} \quad (53)$$

So, the equivalent modal viscous damping ratio contributed by the VEM is :

$$\tilde{\zeta}_i = \frac{\tilde{\eta}_i}{2} \quad (54)$$

and the total equivalent modal viscous damping of the structural system is :

$$\tilde{\xi}_i = \zeta_i + \tilde{\zeta}_i \quad (55)$$

Modal dynamic response analysis can then be performed using  $(\tilde{\omega}_i, \tilde{\xi}_i, \tilde{\phi}_i)$  as the system modal quantities.

## EXAMPLE

### Analysis of Baseline Structure

The structure used as an illustrative example is a large truss type structure shown in Figure 2. The model consists of 2052 nodes and the EAL<sup>5</sup> finite element code was used. To reduce the computation required, a selective modal extraction<sup>6</sup> was performed for the large finite element model.

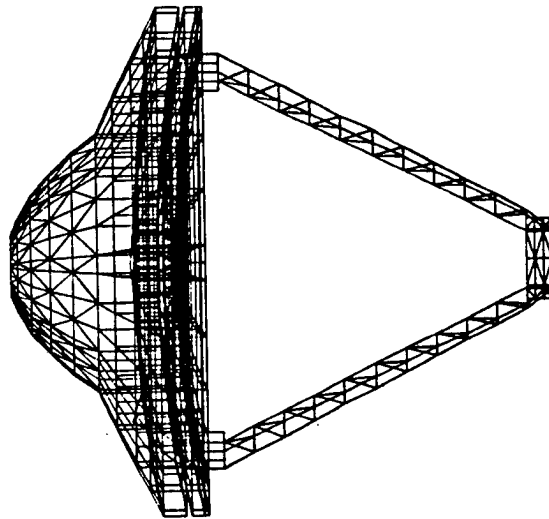
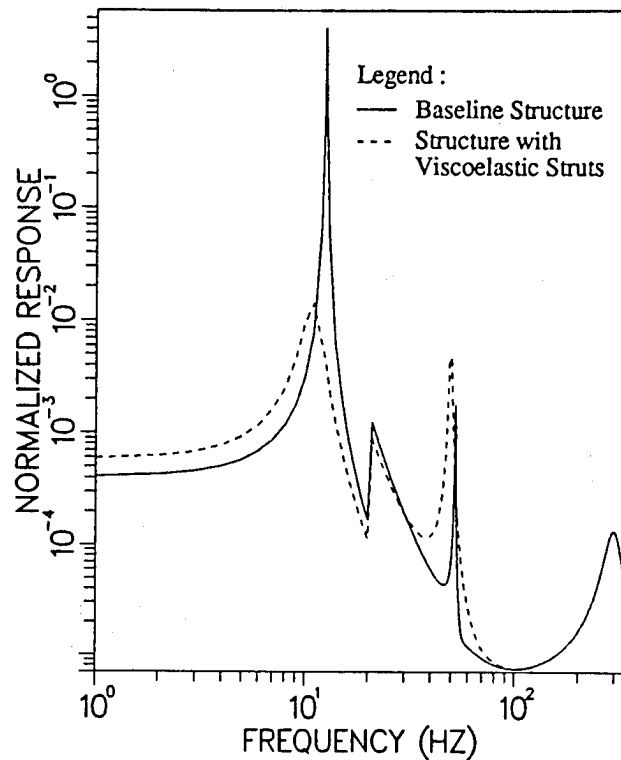


Figure 2  
Finite Element Model of the Baseline Structure



**Figure 3**  
**Response Power Spectral Density**

The Line of Sight jitter response to a power spectral density input was used to evaluate the performance of the system. The response power spectral density curve in Figure 3 shows that the jitter response is dominated by the first truss bending mode of the structure.

Modal strain energy distribution analysis was performed to identify a group of members with high strain energy. These elements with high modal strain energy are the most efficient locations for application of VEM for passive damping. In this example, the longerons were found to contain the largest percentage, 26.9%, of strain energy in the dominant mode. Within this group of members, the 28 struts selected for replacement contain 54.0% of the strain energy in all of the longeron struts.

### **Design and Analysis of Viscoelastic Struts and Structure**

The viscoelastic material reduces the stiffness of the strut while increasing the damping. It is desirable to concentrate most of the strain energy in the VEM to increase the damping which demands that the rest of the strut act as rigid links. However, this degrades the strut stiffness significantly. With these two opposing trends, optimization of the strut design can only be determined in the system response level and not at the component level.

The derived equations were coded in a spreadsheet. The VEM material with the best modulus and loss factor at the reference temperature of 25° F and frequency of 10 Hz was chosen. The effect of the VEM parameters on the component ratios is shown in Figure 4. The effect of the VEM on the system attenuation factor is shown in Figure 5. These two figures show that the use of more VEM in some design regions actually degrades the overall system performance. Therefore an optimization of the design at the system level is absolutely necessary. The predicted system parameters and attenuation factor for the optimized design are summarized in Table 2.

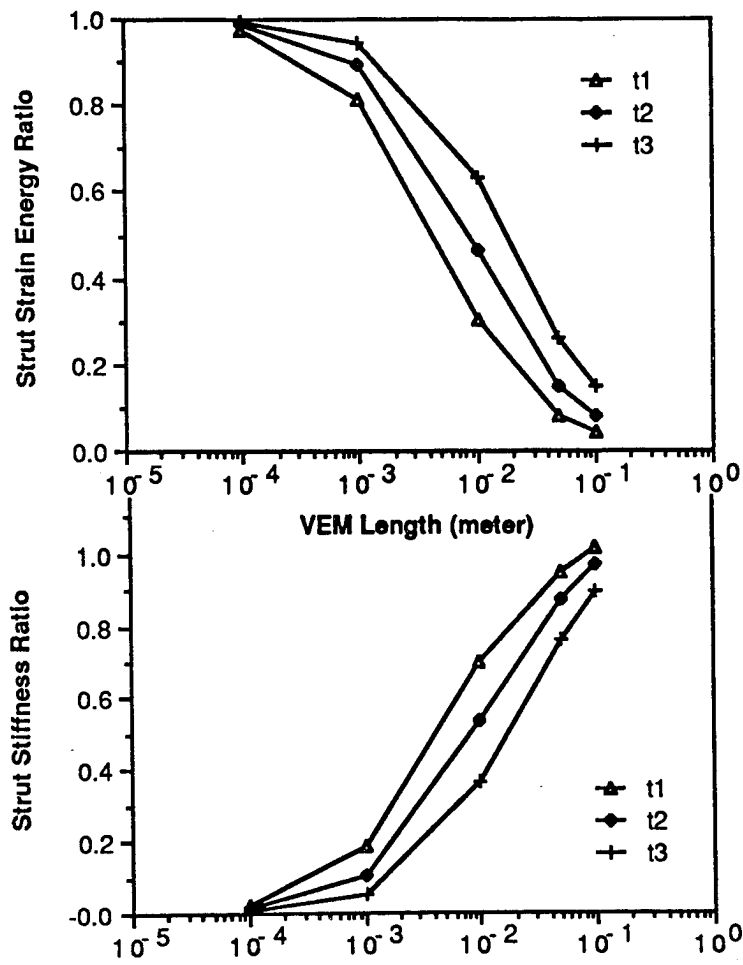


Figure 4  
Strain Energy and Stiffness Ratios of Viscoelastic Strut

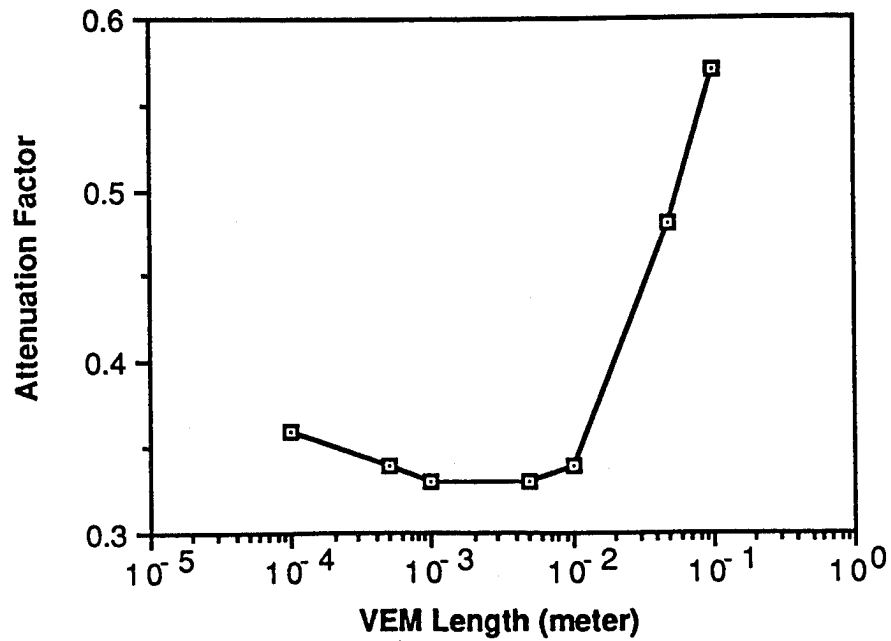


Figure 5  
System Attenuation Factor due to Viscoelastic Struts

Table 2  
Results of Derived Equations and Finite Element Method  
for Viscoelastic Structure

Structural Parameters	Derived Equations	Finite Element Model
Dominant Modes Frequency (Hz)	11.7	10.9
Modal Viscous Damping Ratio	0.100	0.097
Modal Attenuation Factor	0.24	0.27

### Substructuring Analysis of Viscoelastic Structure

A detailed finite element model of the viscoelastic strut is shown in Figure 6. The condensed matrices of the optimized strut design were assembled into the baseline model as a directly specified spring matrix. This substructure method reduces the 210 node model of the strut into a two node element which can replace the existing element in the large finite element model. This includes the stiffness information in the model without requiring any modification of the geometry or connectivity of the existing baseline model. The new mode shapes were compared with the original shapes to verify that there were no significant changes in the mode shapes. The results of the finite element analysis are summarized in Table 2. The comparison with the design predictions is extremely favorable.

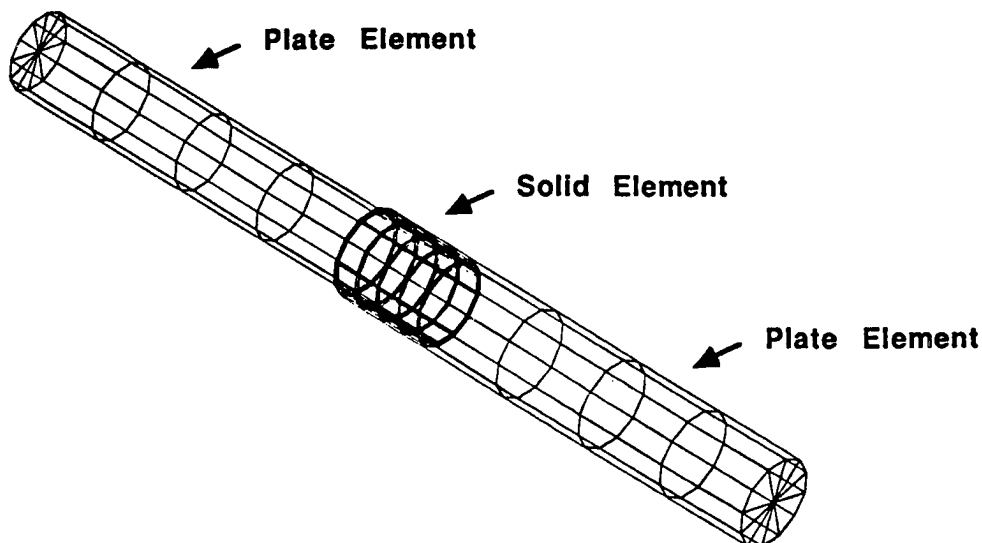


Figure 6  
Finite Element Model of the Viscoelastic Strut

## CONCLUSION

The design procedure presented enables the structural analysts/designers to develop viscoelastic struts which optimize the global response of very complex structures with a minimum amount of computer analysis. Information from the baseline design can be used to the maximum extent. The knowledge of the system overall behavior enables accurate assumptions to be made to optimize the design. The design optimization is based a set of closed form algebraic equations derived from Rayleigh-Ritz principle. A substructuring method for the viscoelastic materials with complex stiffness matrices was derived and proven to be very efficient. The excellent comparison of the results from these two methods reinforces the soundness of the basic approach in both the design and analysis procedures. This method can easily be extended to the design and analysis of similar components and structures under different dynamic environments.

## ACKNOWLEDGEMENTS

This study was funded by an Independent Development Program of the Astronautics Division, Lockheed Missiles and Space Company. The model used in the example was constructed by L.A. Strugala. M.L. Andrepont performed the optimization and the substructuring analysis used in the example. E. Weston provided a detailed review of the paper. Contributions of these colleagues are gratefully acknowledged.

## NOMENCLATURE

### Symbols

$c$	=	viscous damping coefficient
$f_n$	=	natural frequency
$i$	=	imaginary unit, $\sqrt{-1}$
$I$	=	identity matrix
$K, k$	=	stiffness
$M, m$	=	mass
$r$	=	ratio
$v(\omega)$	=	unit boundary displacement vectors
$W, w$	=	strain energy
$\alpha$	=	attenuation factor
$\epsilon_i$	=	strain energy ratio of selected group, i-th mode
$\Phi$	=	matrix of eigenvectors
$\eta$	=	loss factor
$\kappa$	=	condensed stiffness
$\mu_i$	=	mass ratio, i-th mode
$\xi$	=	damping ratio
$\Lambda$	=	matrix of eigenvalues
$\zeta$	=	viscous modal damping
$\omega$	=	frequency, radian/second
$\sim$	=	denoting modified elements

### Subscripts

$a$	=	strut axial stiffness
$e$	=	elastic
$i$	=	for the i-th mode
$j$	=	the group selected for modification
$k$	=	stiffness
$m$	=	mass
$o$	=	baseline design
$v$	=	viscoelastic
$\xi$	=	damping ratio

### Superscripts

$I$	=	Imaginary
$R$	=	Real
$T$	=	matrix transpose
$v$	=	viscoelastic material constant

## REFERENCES

1. Johnson, C.D., and Kienholz, D.A., 'Finite Element Prediction of Damping in Structures with Constrained Viscoelastic Layers', *AIAA Journal* Vol 20, No. 9 (Sept. 1982).
2. Johnson, C.D., and Kienholz, D.A., 'Design and Testing of a Sixty-Foot Damped Generic Space Truss', *Damping 1986*, AFWAL-TR-86-3059, Flight Dynamics Laboratory, Air Force Wight Aeronautical Laboratories (1986).
3. White, C.W., 'Viscoelastic Component Damper Design Problems', *Damping 1986*, AFWAL-TR-86-3059, Flight Dynamics Laboratory, Air Force Wight Aeronautical Laboratories (1986).
4. R.K. Frater, 'Implementation of Modal Strain Energy Method Using MSC/NASTRAN and Post-processing Utility Programs', *Damping 1986*, AFWAL-TR-86-3059, Flight Dynamics Laboratory, Air Force Wight Aeronautical Laboratories (1986).
5. Engineering Information Systems, Incorporated, EAL, *Engineering Analysis Language Reference Manual* (1983).
6. Y.C. Yiu, 'Selective Modal Extraction for Dynamic Analysis of Space Structures', *AIAA/ASME/ASCE/AHS/ASC 30TH Structures, Structural Dynamics and Materials Conference* (1989).
7. J. Schafer, *DALPRO User's Manual*, Lockheed Missiles and Space Co. (1986).
8. Nashif, A.D., D.I.G. Jones, and J.P. Henderson, *Vibration Damping*, John Wiley & Sons (New York, 1985).

## APPENDIX

### 1. VEM Characteristics

The VEMs are strongly frequency and temperature dependent. Most often the energy dissipation is through the shear energy in the VEM. The energy dissipation property of the VEMs is conveniently modelled by the complex modulus of the material. The shear stress and shear strain constitutive relationship is often measured and expressed as :

$$\tau(\omega) = G^*(T, \omega) \gamma(\omega) \quad (A1)$$

$$G^*(T, \omega) = G(T, \omega) [1 + i \eta(T, \omega)] \quad (A2)$$

This relationship is generalized to the general stress and strain constitutive relationship by :

$$\sigma_{ij} = C^*_{ijkl} \epsilon_{kl} \quad (A3)$$

$$C^*_{ijkl} = C_{ijkl} [1 + i \eta(T, \omega)] \quad (A4)$$

### 2. Finite Element of Viscoelastic Material

Based on the complex modulus material characterization of the viscoelastic material, the element stiffness matrix at a constant temperature is therefore also complex with both real and imaginary parts.

$$k(\omega) = k^R(\omega) + i k^I(\omega) \quad (A5)$$

$$k(\omega) = k^R(\omega) + i \eta(\omega) k^R(\omega) \quad (A6)$$

Consequently, the global structural stiffness matrix is also complex :

$$K(\omega) = K^R(\omega) + i K^I(\omega) \quad (A7)$$

### 3. Modal Strain Energy Method

The Modal Strain Energy Method provides an efficient alternative to direct frequency response methods. The MSE method is the first tool which enables the analyst to design high modal damping into a structure by using viscoelastic materials. This allows deliberate design of passive damping into the structure. By using real normal modes of the undamped structure and assuming that modal coupling is negligible, the viscoelastic system can be characterized by modal equations of motion with modal hysteretic (structural) damping. Modal loss factors are used to approximate the damping contribution from the imaginary part of the complex stiffness. The modal loss factor for the  $i$ -th mode,  $\eta_i$ , can be approximated by:



$$\eta_i = \frac{\sum_j \eta_j^v (w_j)_i}{\sum_k (w_k)_i} \quad (\text{A8})$$

- $\eta_i$  = modal loss factor  
 $\eta_j^v$  = material loss factor of the j-th viscoelastic element  
 $\omega_j$  = strain energy in the j-th viscoelastic element  
 $\omega_k$  = strain energy in the k-th element of the structure

If  $\epsilon_{ji}^v$  is defined as the strain energy ratio of the j-th element of the i-th mode, then

$$\epsilon_{ji}^v = \frac{(w_j)_i}{\sum_k (w_k)_i} \quad (\text{A9})$$

and if the sum of the the viscoelastic elements is  $\epsilon_i$ , then

$$\epsilon_i^v = \sum_j \epsilon_{ji}^v \quad (\text{A10})$$

If only one material is used, then

$$\eta_i = \eta^v \epsilon_i^v \quad (\text{A11})$$

In matrix form,

$$\eta_i = \frac{\frac{1}{2} \phi_i^T \mathbf{K}^I \phi_i}{\frac{1}{2} \phi_i^T \mathbf{K}^R \phi_i} \quad (\text{A12})$$

## ***INCREASED GRAPHITE FIBER DAMPING VIA INTERCALATION***

George A. Lesieutre  
SPARTA, Inc.  
Laguna Hills, CA

Andrew J. Eckel  
Sverdrup Technology, Inc.  
Cleveland, OH

James A. DiCarlo  
NASA Lewis Research Center  
Cleveland, OH

### ***ABSTRACT***

The damping of several commercial graphite fibers was experimentally characterized over a temperature range from -200°C to +400°C, for frequencies from about 50 to 2000 hz. A unique flexural test apparatus was used with *single* 10-micron diameter fibers. The baseline fibers exhibited peak damping ratios in the vicinity of  $2 \times 10^{-4}$ . Damping in some copper chloride- and bromine-intercalated P100 fibers was also measured over similar ranges of temperature and frequency—peak damping values were observed to increase by more than an order of magnitude. Results from the literature indicate that intercalation does not deleteriously affect other fiber engineering properties.

## INTRODUCTION

In order to better observe and influence our world, the U.S. commercial and military presence in space will continue to expand. The future capabilities of the U.S. in strategic defense will rely on space assets with very demanding performance requirements. Many of these spacecraft will require precise payload pointing, rapid slewing, and extreme dimensional stability in severe mechanical and thermal environments, including enemy-induced hostile environments. Damping will be essential to the attainment of performance goals in these precision spacecraft. Arising, however, as the result of a multitude of complex unrelated physical mechanisms acting in concert, passive damping remains the least understood aspect of structural dynamic behavior.

In common built-up structures which operate in the atmosphere, air damping and joint damping typically dominate system damping. However, material damping will be an important contributor to damping in "monolithic" structures and to on-orbit damping in precision spacecraft. Air damping is clearly eliminated in space, and the effects of joint damping will be reduced because of requirements for precision ("tight" joints) and low vibration levels (friction "lockup").

Some effort has gone into the integration of high-damping *non-structural* materials with a control/structure design, but associated weight penalties, potential outgassing problems, and temperature sensitivity may limit their use. The development of high damping *structural* materials therefore represents a high-payoff research direction.

Graphite-reinforced composite materials are ideal for use in these structures because of their superior mechanical and thermal properties—high modulus, high thermal conductivity, low density, and low coefficient of thermal expansion are especially important. Constituent contributions to damping in a mechanically-perfect composite material are weighted by their contribution to strain energy.

When such composite materials are deformed, the high modulus of the carbon fibers relative to that of typical reinforcing matrix materials causes most of the strain energy (typically 80–90%) to be found in the fiber. Efforts to increase composite material damping are therefore best focused on the highly-leveraged carbon fibers [1].

A large number of graphite fibers are currently commercially available, and little is known in general about their damping properties. Much of what is known has been inferred from tests of built-up composite materials, although a few researchers have directly investigated the damping of single fibers. The authors have previously reported the results of an investigation of the damping of some commercial graphite fibers [2], as well as known related work [*c.f.*, 3, 4]. Some of the findings are repeated herein to provide context for new data on the damping of intercalated fibers.

## EXPERIMENTAL PROCEDURE

The damping of baseline commercial and experimental intercalated graphite fibers was measured over a temperature range from -200°C to +400°C, for frequencies from about 50 to 2000 hz. High modulus fibers were emphasized because of their promise for use in advanced spacecraft. The baseline fibers included three mesophase pitch-based fibers of different modulus (P55, P100, P120), and one polyacrylonitrile (PAN)-based fiber having a modulus close to that of one of the pitch fibers (T50). Damping in some copper chloride- and bromine-intercalated P100 fibers was also measured over similar ranges of temperature and frequency.

All testing was performed at the NASA Lewis Research Center in Cleveland, Ohio. The test technique consisted basically of the forced flexural vibration and free decay of cantilevered fibers in a high-vacuum cryostat furnace. Figure 1 shows a schematic of the equipment configuration, and Figure 2 illustrates in more detail the means used to control the specimen

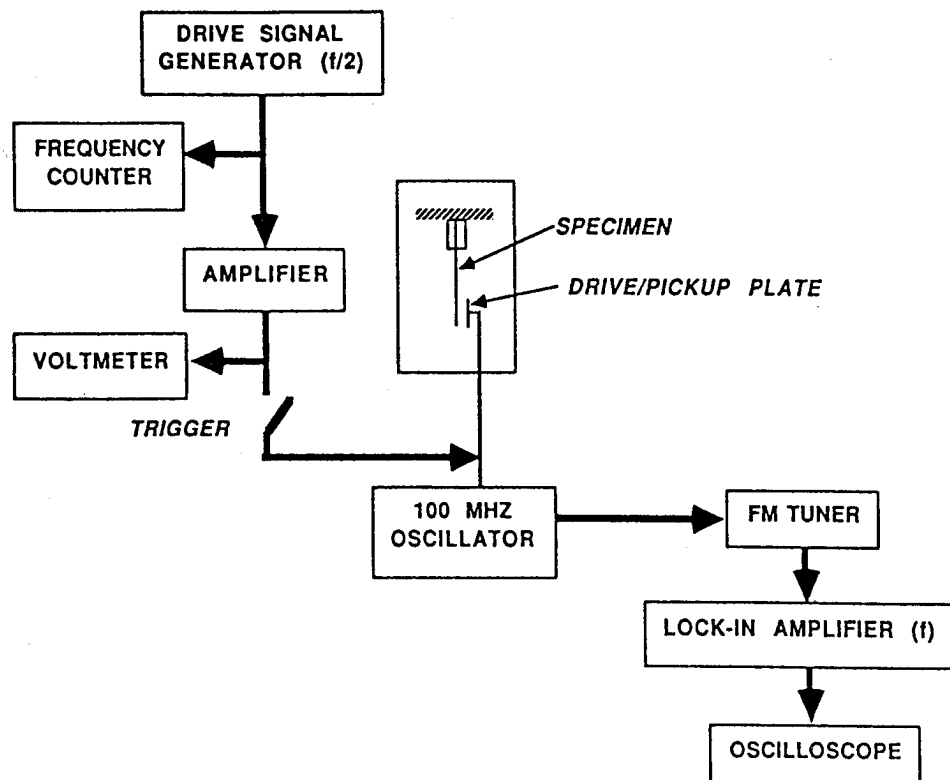


Figure 1: Schematic of the Test Apparatus

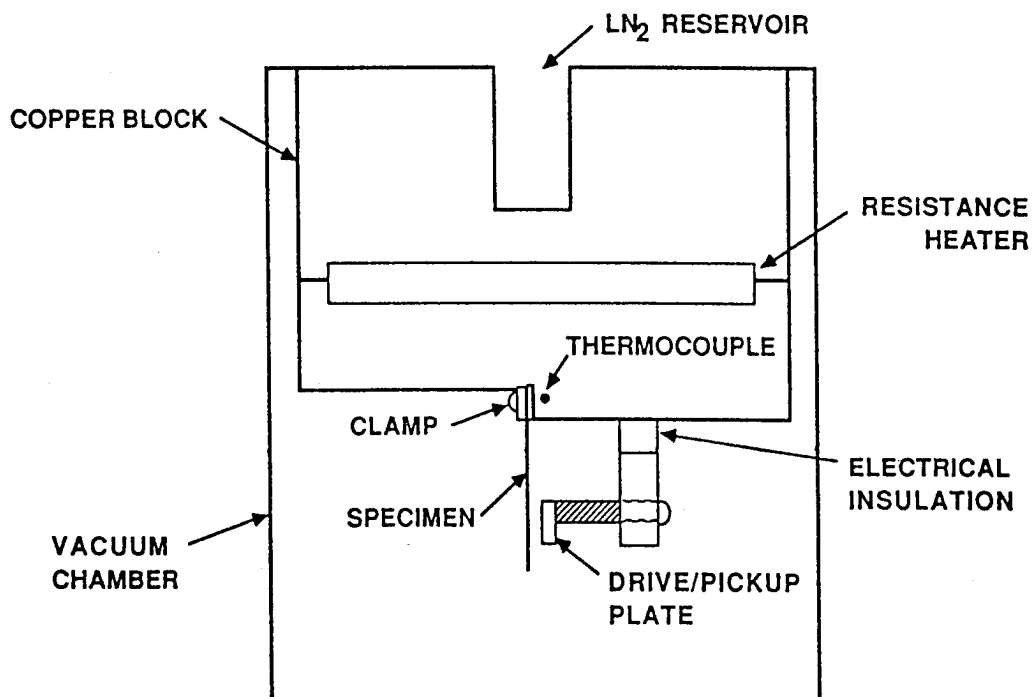


Figure 2: Detail of the Specimen Mount, Drive/Pickup, Vacuum, and Thermal Control

environment. The test procedure and some of the significant challenges posed by testing single graphite fibers are discussed in [2].

Observed material damping depends on the type of deformation experienced under load. An extensional or a flexural test method was required to generate data relevant to the deformation experienced by single fibers as part of a composite spacecraft structure. The flexural vibration test method was selected, because it had been successfully used at the NASA Lewis Research Center to characterize other small-diameter fibers and therefore represented less development risk [5]. The authors are unaware of any previous measurements of the damping of single graphite fibers in such an appropriate mode of deformation.

The tests were performed in a diffusion-pump vacuum ( $10^{-6}$  torr), as vibration response amplitudes were typically 200 times smaller in vacuum than at one atmosphere. Strain amplitudes at the fiber root surface were on the order of  $10^{-6}$ , and no significant amplitude-dependence of damping was observed for amplitudes near this level.

## DATA REDUCTION

### MEASURES OF DAMPING

As a consequence of the second law of thermodynamics, no real structure can sustain unforced vibratory motion indefinitely. Many different approaches to quantifying this damping ability have been devised, *e.g.*, the time required for the displacement response amplitude to settle to some fixed fraction of its initial amplitude. The most useful of these damping measures, however, are dimensionless, and generally quantify the fractional displacement or energy loss per cycle or radian of vibration. A few of these dimensionless measures are shown below:

$\Psi$	Damping capacity
$\delta$	Log decrement
$Q$	Quality factor
$\eta$	Loss factor
$\zeta$	Damping ratio

Damping ratio is the most common measure of damping used by satellite designers and structural dynamicists. Because one of the purposes of this work is to make damping more accessible as a design property of advanced materials and structures, damping ratio is the unit in which all damping results are presented. For small damping, these results can be converted to other units with the use of the following scale factors.

$$\zeta = \eta/2 = 1/2Q = \delta/2\pi = \Psi/4\pi$$

### LOG DECREMENT METHOD

As discussed in [2], a variation of the conventional log decrement method was used to determine damping ratios from fiber free decay data. In practice, the amplitude of vibration was read off photographs of decay traces at a number of equally-spaced time increments, instead of just two as in the conventional log decrement method, and a line was fit to the data. A computer program was written to automate this calculation, to determine the quality of the fit to the data, and to plot the data. In all, some 650 damping ratios were calculated for various fibers under various conditions, from 6000 measured data points. The great majority of data did fit a line well.

## RESULTS

As reported in [2], the three baseline pitch fibers exhibited similar damping, with a peak damping ratio of just over  $2 \times 10^{-4}$  observed at a temperature of about  $-40^{\circ}\text{C}$ , dropping off slowly at lower temperatures and more rapidly at higher temperatures. At  $400^{\circ}\text{C}$ , a typical damping ratio was found to be about  $0.35 \times 10^{-4}$ . The PAN fiber exhibited damping similar to the pitch fibers at high temperatures, but had only about a third the damping at lower temperatures. Figure 3 summarizes the damping and frequency results for the baseline fibers. Reference [6] contains complete data for each fiber and each test run.

Damping in the intercalated P100 fibers was measured over a similar range of temperatures and frequencies. Peak damping values increased by more than an order of magnitude, as shown in Figure 4. The P100/ $\text{CuCl}_2$  fiber exhibited a peak damping ratio of nearly  $3 \times 10^{-3}$ , at a temperature of about  $200^{\circ}\text{C}$ . Irreversible processes at high temperatures resulted in a permanent loss of peak damping in this fiber (note the arrow on the data trace); this finding is consistent with environmental stability results published in the literature [7]. Brominated P100 fibers exhibited a peak damping ratio of about  $2.3 \times 10^{-3}$ , in the vicinity of  $-50^{\circ}\text{C}$ . This behavior was relatively stable over the temperatures considered.

A second brominated fiber was tested to verify the results, and similar damping was observed. Because the results appeared to be characteristic of a point defect damping mechanism, the damping was measured in detail at two separate frequencies, over a range of temperatures. Figure 5 shows this damping data. A curve fit of the data yielded estimates of the temperatures at which peak damping is observed. Some key values are summarized below:

<u>Mode</u>	<u>Frequency</u>	<u>Temperature(<math>\zeta_{\text{peak}}</math>)</u>
A	76.7 hz	210.46 °K
B	465.4 hz	222.16 °K

By noting the temperature shift between the data taken at two frequencies, some characteristics of the physical mechanism underlying the observed damping were established. Based on the assumption of a point defect mechanism, an activation energy of 0.47 eV was estimated. The following equation was used to determine this [8]:

$$Q = k ((T_1 T_2) / (T_2 - T_1)) \ln(f_2 / f_1)$$

Where:       $Q$       is the activation energy  
                   $k$       is Boltzmann's constant  
                   $T_i$       is the temperature at which peak damping is observed at frequency  $f_i$

In addition, a characteristic jump frequency ( $\nu_0 = 1/\tau_0$ ) of about  $1.1 \times 10^{14} \text{ s}^{-1}$  was determined. The assumption of a constant activation energy and jump frequency was found to be good, but not perfect. This information can be used to estimate fiber damping at any frequency and temperature via the following equations:

$$\zeta = \zeta_0 (2\omega\tau) / (1 + (\omega\tau)^2)$$

with     $\tau = \tau_0 e^{Q/kT}$

Where:       $\zeta_0$       is the peak damping ratio for the defect  
                   $\omega$       is the radian frequency of vibration  
                   $\tau_0$       is the jump time constant for zero activation energy

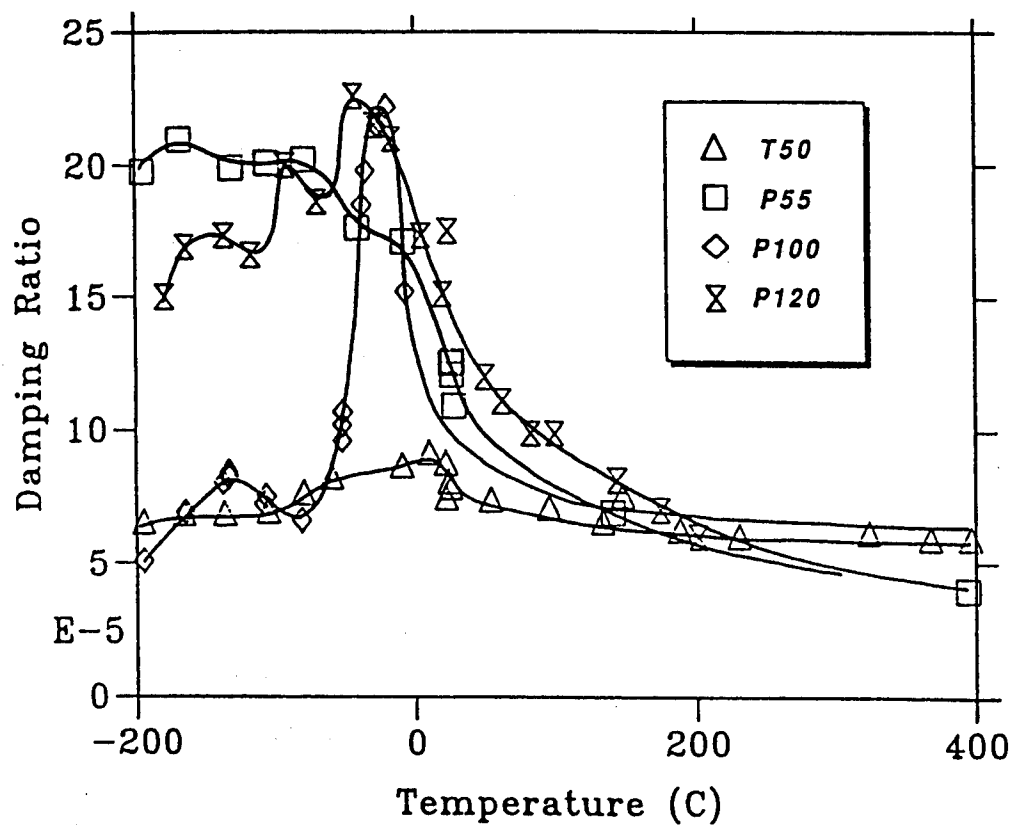


Figure 3(a): Baseline Fiber Damping versus Temperature

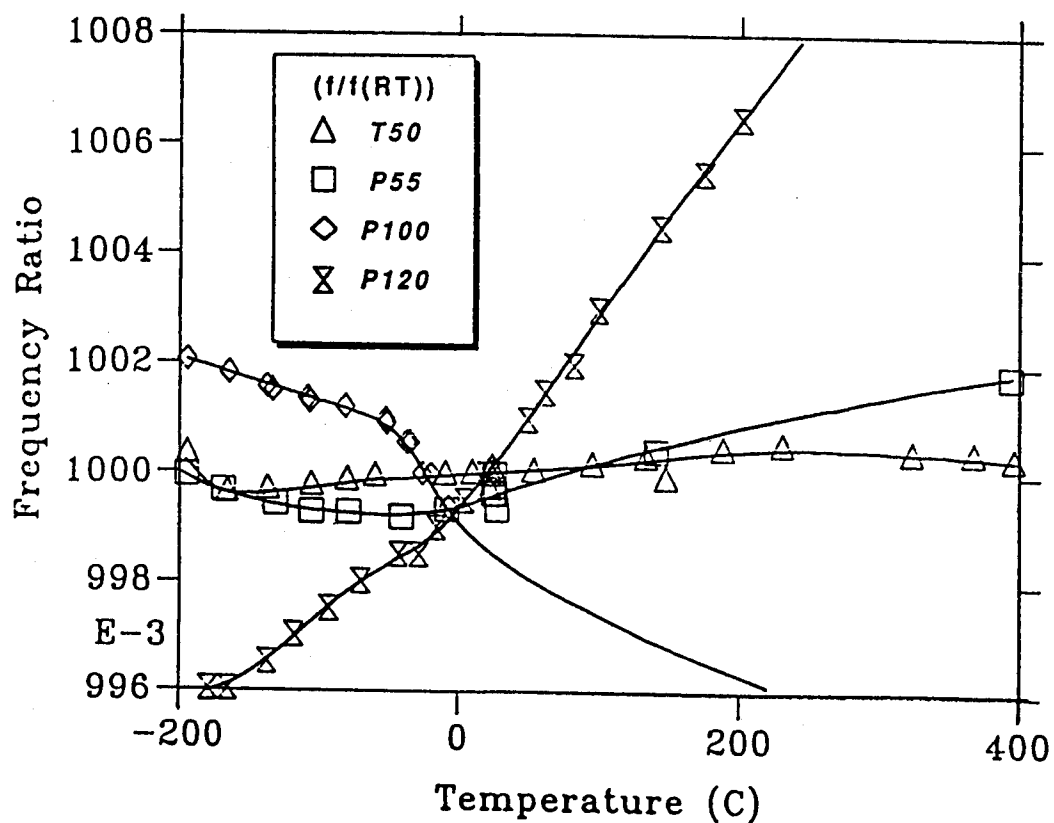


Figure 3(b): Baseline Fiber Frequency versus Temperature

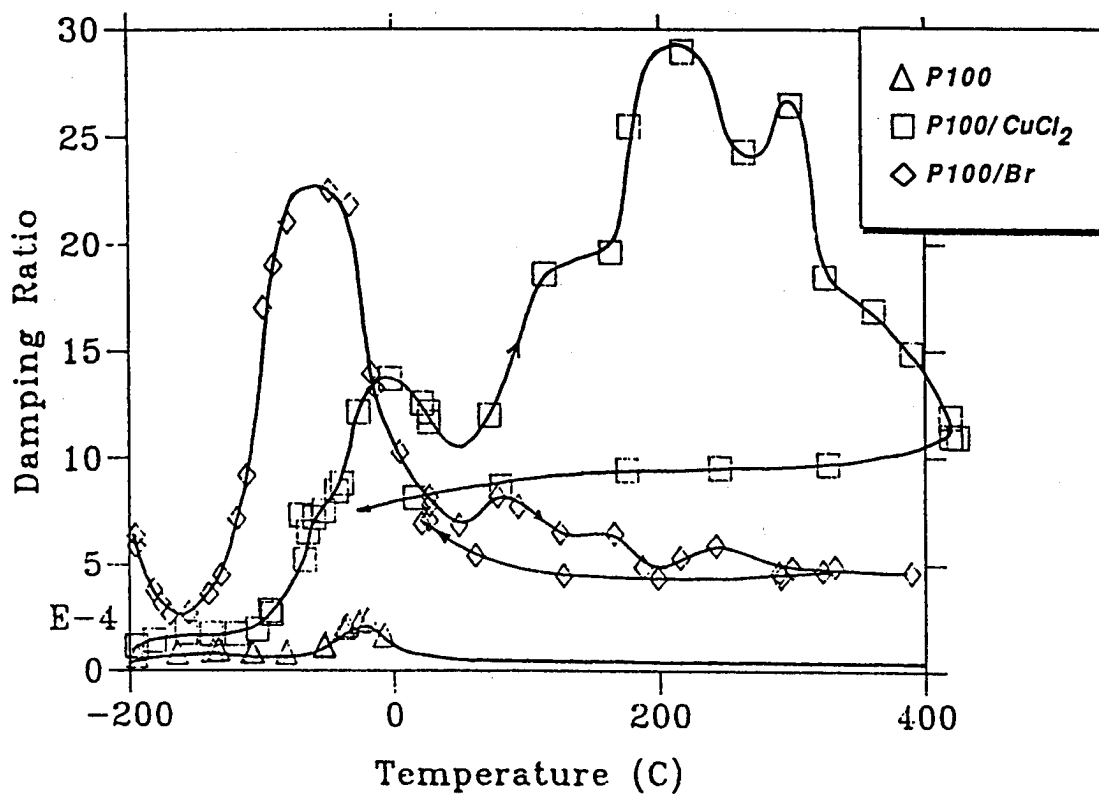


Figure 4: Damping of Intercalated Fibers and Baseline P100 Fiber versus Temperature

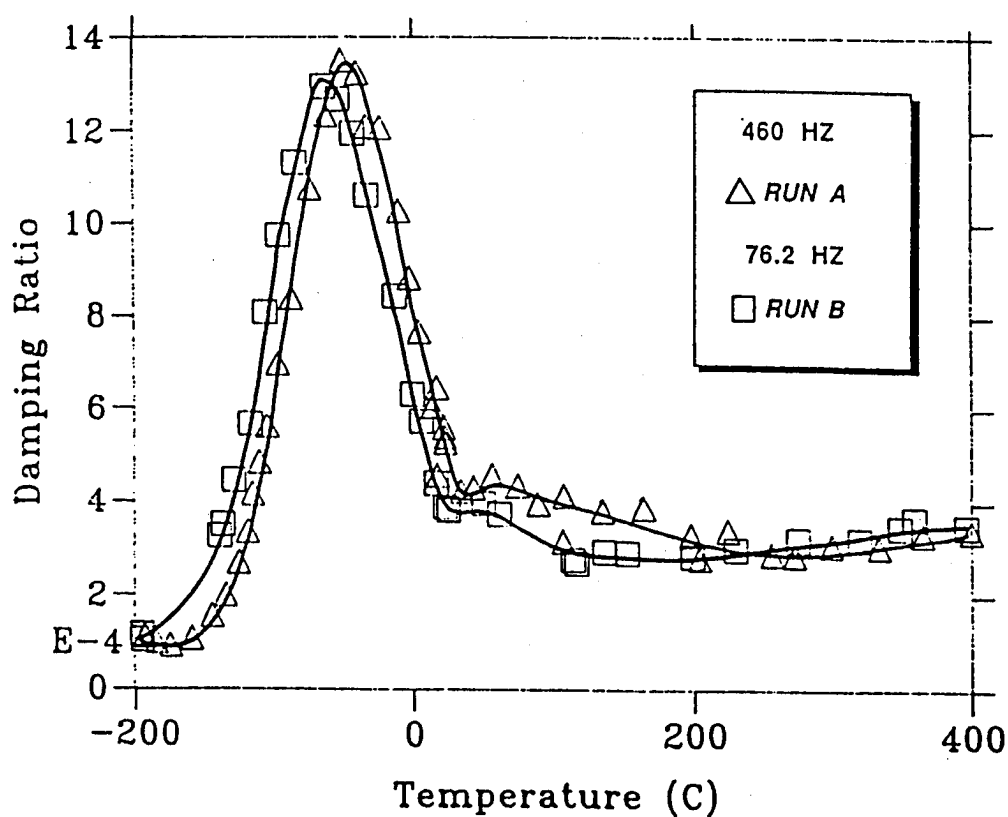


Figure 5: Damping of Bromine-Intercalated Fibers versus Temperature at Two Frequencies



In order for spacecraft designers to select and define specific materials for specific applications, they must have data on all relevant design properties. Advantages and drawbacks of various materials designs can then be weighed in making a final decision. Of interest for demonstrated increased electrical conductivity, intercalated graphite fibers have been studied by other researchers in the past. Data from those studies was collected to supplement that measured in this work. Although damping changes significantly from its baseline values in brominated fibers, other design properties such as modulus, strength, and thermal conductivity change only slightly [9], as shown in Table 1.

### ACKNOWLEDGMENTS

This work reported herein was the result of an informal collaborative effort between SPARTA, Inc. and the NASA Lewis Research Center. SPARTA's efforts were supported by the Strategic Defense Initiative Organization, the Office of Naval Research, and the Naval Surface Warfare Center under a Small Business Innovation Research (SBIR) program (Contract N60921-87-C-0257). Mr. A.P. (Dave) Divecha of NSWC and Dr. Steven Fishman of ONR monitored the work.

SPARTA has a patent pending in this new technology area.

### REFERENCES

1. Lesieutre, G.A., "Damping in Unidirectional Graphite/Metal Composites and Material Design Potential," Proceedings of the ASME 11th Biennial Conference on Mechanical Vibration and Noise, September, 1987, Boston, MA.
2. Lesieutre, G.A., Eckel, A.J., and DiCarlo, J.A., "Temperature-Dependent Damping of Some Commercial Graphite Fibers," at the 12th NASA/DoD Conference on Composites Materials and Structures, Cocoa Beach, Florida, January, 1988.
3. Adams, R. D., "Dynamic Longitudinal Shear Modulus and Damping of Carbon Fibers," *J. Phys. D*, 8(7), 1975, pp. 738-48.
4. Henrichsen, R.E., "Dynamic Torsional Response of Individual Carbon Fibers," Ph.D. dissertation, University of Washington, November, 1975.
5. DiCarlo, J.A., and Williams, W., Dynamic Modulus and Damping of Boron, Silicon Carbide, and Alumina Fibers," NASA TM 81422, 1980.
6. Lesieutre, G.A., "High Damping Graphite Fiber," Contract N60921-87-C-0257, SPARTA Report NSW41-Final, March, 1988.
7. Gaier, J.R., Slabe, M.E., and Shaffer, N., "Stability of Bromine, Iodine Monochloride, Copper (II) Chloride, and Nickel (II) Chloride Intercalated Pitch-Based Graphite Fibers," NASA Technical Memorandum 89904, 1987.
8. Nowick, A.S., and Berry, B.S., *Anelastic Relaxation in Crystalline Solids*, Academic Press, 1972.
9. Jaworske, D.A., Vannucci, R.D., and Zinolabedini, R., "Mechanical and Electrical Properties of Graphite Fiber-Epoxy Composites Made from Pristine and Bromine Intercalated Fibers," *J. Composite Materials*, vol. 21, June, 1987, pp. 580-592.

Table 1: Property Tradeoffs for Bromine-Intercalated Graphite Fibers

PROPERTY	P100	P100/BR	COMMENTS
$\zeta$ ( $10^{-4}$ )	2	20	ORDER OF MAGNITUDE INCREASE
R ( $\mu\Omega$ - cm)	250	50	DECREASE BY 5
E (GPa)	690	735	SLIGHT INCREASE
$\sigma_U$ (GPa)	2.2	?	LITTLE CHANGE
$\rho$ (g/cm <sup>3</sup> )	2.18	2.30	SLIGHT INCREASE
$k_L$ (W/mC)	350	315	SLIGHT DECREASE
$\alpha_L$ (ppm/C)	-1.6	?	LITTLE CHANGE

- FIBER DIAMETER INCREASES BY ABOUT 5%
- HIGHER CONCENTRATION OF BR IN FIBER CENTER

***MODELING MATERIAL DAMPING  
USING AUGMENTING THERMODYNAMIC FIELDS (ATF)***

George A. Lesieutre  
SPARTA, Inc.  
Laguna Hills, CA

***ABSTRACT***

A method of modeling frequency-dependent material damping (and moduli) in engineering structural dynamics analysis is reported. Motivated by results from materials science, augmenting thermodynamic fields (ATF) are introduced to interact with the usual mechanical displacement field. The methods of irreversible thermodynamics are used to develop consistent coupled material constitutive relations and partial differential equations of evolution (PDE). The resulting PDE are implemented for numerical solution within the computational framework of the finite element method and the results are compatible with conventional structural analysis techniques. This ATF damping modeling method is illustrated for the case of longitudinal vibration of a rod.

## INTRODUCTION

### SUMMARY

Vibration damping is an important aspect of many engineering systems. Knowledge of damping characteristics is especially critical when the dynamic response of a flexible structure is to be controlled by a high performance control system. Current analytical treatments of damping in engineering structural dynamics are inaccurate and inadequate, often founded on mathematical convenience rather than on an understanding of the underlying fundamental physical processes.

A new, physically-motivated method of modeling material damping in structural dynamics analysis is presented. The method combines elements of the microscopic approach of materials science and the macroscopic approach of continuum structural dynamics using irreversible thermodynamics.

### BACKGROUND

Material damping is likely to be an important, perhaps dominant, contributor to damping in "monolithic" structures and to on-orbit damping in precision spacecraft. In common built-up structures which operate in the atmosphere, air damping and joint damping typically dominate system damping. However, air damping is clearly eliminated in space, and the effects of joint damping will be reduced because of requirements for precision ("tight" joints) and typically low vibration levels (friction "lockup").

Material damping is generally a complex function of frequency, temperature, type of deformation, amplitude, and structural geometry. Figure 1, adapted from Elasticity and Anelasticity of Metals [Zener, 1948] illustrates the typical frequency-dependence of material damping. Current popular treatments of damping in structural dynamics are not physically-motivated and are unable to reproduce this fundamental behavior.

Several methods for incorporating material damping into structural models have been used, and continue to be used within the engineering community. These methods include viscous damping, frequency-dependent viscous damping, hysteretic damping, complex modulus, structural damping, viscoelasticity, hereditary integrals (memory functions), and modal damping [Bert, 1973]. Each has some utility, but each suffers from one flaw or another. Although some potentially accurate models exist (e.g., viscoelasticity), they are not widely used in the engineering community—perhaps because of the lack of physical motivation for, or the difficulty of use of, such models.

### RELATED RESEARCH

Several results in the recent engineering literature are related to this work and are briefly discussed below.

Golla, Hughes, and McTavish (GHM) of the University of Toronto have recently developed a time-domain finite element formulation of viscoelastic material damping [Golla and Hughes, 1985; McTavish and Hughes, 1987]. Their work was motivated by the same general perceived need as this work, but was guided by the observation that experimental results, often recorded in the frequency domain, are of little direct use in time-domain models. The results reported here resemble theirs in some ways, for example, in the introduction of additional "dissipation coordinates." However, the results differ in important ways: no attempt is made to provide a physical interpretation of the GHM dissipation coordinates as thermodynamic field variables; the GHM model is restricted to consideration of what is termed here "microstructural

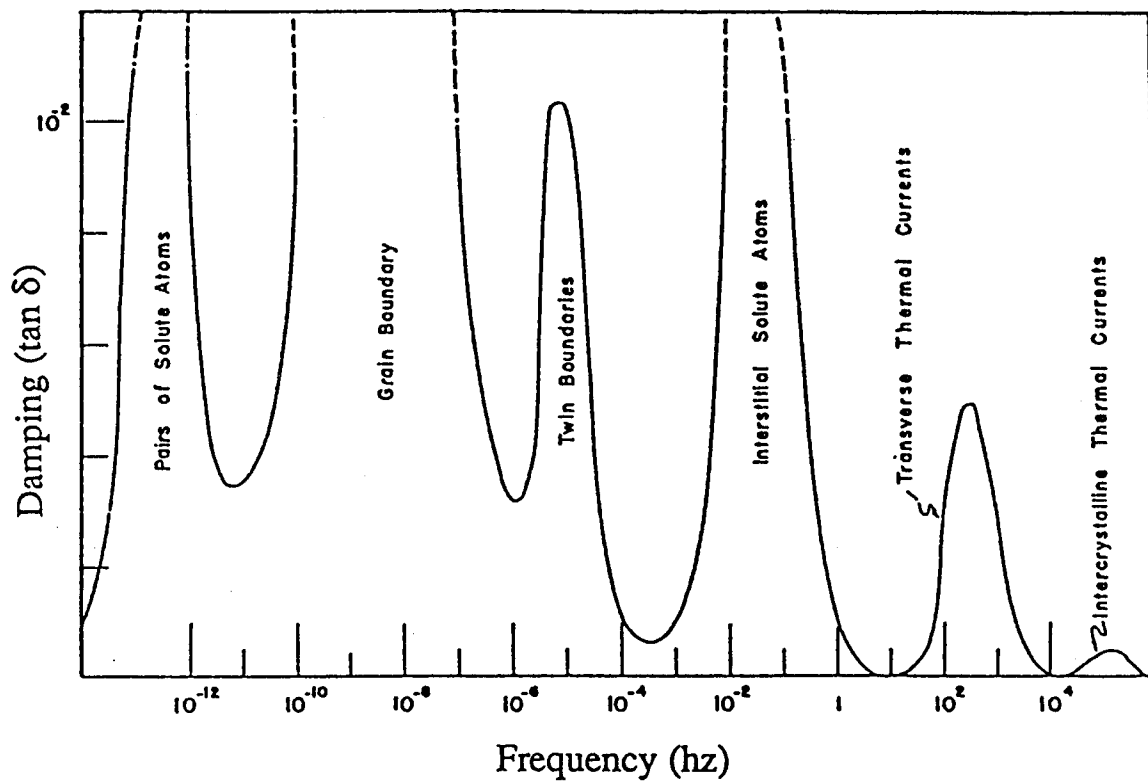


Figure 1: Typical Frequency-Dependence of Material Damping (from [Zener, 1948])

damping," in which the governing thermodynamic relaxation is essentially a scalar process; the "dissipation coordinates" of GHM are internal to individual elements, while the augmenting thermodynamic fields of ATF are continuous from element to element; and the mathematical form of the GHM augmenting equations is restricted to be second order, the same as that of the fundamental equations of mechanical vibration. As shown in their examples, however, the GHM technique can be successfully used to fit a portion of an experimentally-determined curve of damping versus frequency, and standard structural analysis tools can be used to solve the resulting equations.

Both ATF and GHM have advantages over the more conventional modal strain energy (MSE) modeling method in that they are time-domain models, modal damping is calculated concurrently with modal frequency (no look-up tables or iterative procedures are required to converge on both), and the resulting complex modes more accurately reflect the relative phase of vibration at various points on a structure. The ATF method is primarily distinguished from the GHM approach in that it is a *direct* time-domain formulation, amenable to numerical treatment using conventional finite element methods.

D.J. Segalman of Sandia National Laboratories has recently addressed the calculation of stiffness and damping matrices for structures made from linearly viscoelastic materials [Segalman, 1987]. His is essentially a perturbation technique: the perturbation solution for a "slightly viscoelastic" structure is required to match the corresponding solution for a "slightly damped" structure. He works exclusively in the time domain and avoids introducing additional coordinates, although the resulting stiffness and damping matrices are generally unsymmetric. How the assumption of "small viscoelasticity" limits the utility of the approach is currently under investigation.

Torvik and Bagley of the Air Force Institute of Technology have also developed a relevant model of material damping [Torvik and Bagley, 1987]. The core of their approach is the use of fractional time derivatives in material constitutive equations. Their development was motivated by the observation that the frequency dependence observed in real materials is often weaker than the dependence predicted by first-order viscoelastic models. With four and five parameter models, they have been able to accurately represent the elastic and dissipative behavior of over 100 materials over frequency ranges as broad as 8 decades. For most viscoelastic polymeric materials they have examined, the parameter representing the order of differentiation is in the range  $1/2$  to  $2/3$ . The application of the general fractional derivative approach to time-domain analysis, however, is cumbersome and is an area of continuing research.

Other relevant, current work in the engineering aspects of material damping focuses primarily on the development of experimental techniques and measurement of damping in various materials [*c.f.*, Lesieutre, 1988; Crawley, 1983]. In addition, the use of the MSE method for estimating the damping of built-up structures and composite materials from the measured damping of constituents continues to grow.

## BACKGROUND AND APPROACH

Material damping is a subject familiar to many scientists, who have used "internal friction" as an investigative tool with which to explore the basic structure of materials; their work is largely unknown in the engineering community. By measuring damping as a function of frequency, temperature, load type, and amplitude, they are able to determine the mobility and activation energies of various microstructural features of materials. They have shown material damping to be the result of the mutual coupling of stress and strain to other material state variables, variables which can change to new values only through kinetic processes such as diffusion. A multitude of internal variables and relaxation mechanisms which range in geometrical scale from crystal lattice dimensions on up to structural dimensions have been identified [Nowick and Berry, 1972].

While it is an oversimplification to state that dynamics is the study of the evolution of momentum, it provides useful contrast to the statement that thermodynamics is the study of the evolution of energy. Material damping, involving the transfer of energy from structural vibration to other forms of energy, is fundamentally a thermodynamic phenomenon. The field of non-equilibrium thermodynamics provides a general framework for the macroscopic description of irreversible processes [deGroot and Mazur, 1962]. Thermodynamic considerations constrain the form of coupled material constitutive equations and guide the development of coupled field equations of evolution.

Given field equations of evolution, the finite element method is arguably the most powerful and popular method for solving them. Piecewise-continuous trial displacement functions are assumed over a local region of the system being analyzed, individual element matrices are computed using the method of weighted residuals (MWR) or variational principles, then assembled into global system matrices. The output of this procedure is a set of discretized equations of motion that are readily solved using standard computational techniques on digital computers.

### APPROACH

The physically-significant "internal state variables" of materials science play a central role in this work, motivating the introduction of augmenting thermodynamic fields (ATF) to interact with the usual mechanical displacement field of continuum structural dynamics. The techniques of nonequilibrium, irreversible thermodynamics are used to develop coupled material constitutive equations and coupled partial differential equations of evolution. Constitutive equations of damped materials describe the coupling of all dependent fields (*e.g.*, as the coefficient of thermal expansion couples the displacement and temperature fields in thermoelasticity).

To illustrate the ATF modeling method, general field equations are specialized to the simplest continuum case, *viz.*, that of one-dimensional vibration of an isotropic rod; an alternate form of the governing equations is also investigated. For simplicity, a single augmenting field is employed. In practice, however, additional fields could be used as needed to better approximate experimental data over a frequency range of interest (*e.g.*, by curve-fitting as in the GHM method).

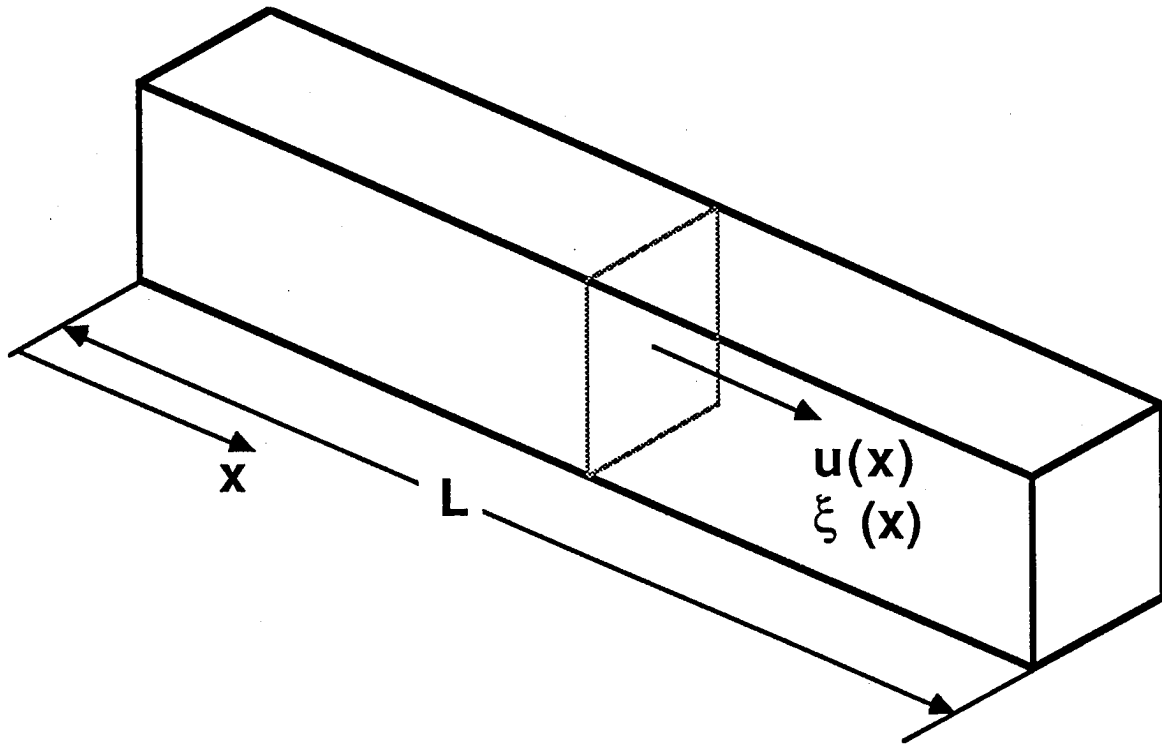
The solution of the coupled partial differential equations are addressed in several ways. Analytical Fourier analysis yields an approximate relationship between damping and frequency, while numerical finite element analysis results in a set of coupled discrete differential equations of evolution. A free vibration eigenvalue problem for these discrete equations can then be solved to yield complex modes.

The method of weighted residuals (MWR) is used to develop damped finite element matrices. Because it can reduce the order and continuity required of assumed approximate displacement fields, integration by parts is an important part of the process of developing element matrices in MWR. However, its use can also present an analyst with a choice between alternate matrices, with no *a priori* rules for choosing between them. A series of numerical experiments was performed for the damped rod elements to identify those matrices superior in terms of convergence to the solution obtained via Fourier analysis. The ATF method readily accommodates the use of multiple materials and ATF-damped elements can be used concurrently with undamped elastic elements.

## LONGITUDINAL VIBRATION OF A ROD

### GOVERNING EQUATIONS

Consider the case of one-dimensional motion, corresponding to longitudinal vibration of a thin rod, as shown in Figure 2. The mechanical displacement along the rod is denoted by  $u(x)$



Coupled Fields:      Mechanical displacement,  $u(x)$   
                                 Augmenting thermodynamic,  $\xi(x)$

Figure 2: Example Application—Longitudinal Vibration of a Thin Rod



(strain  $\epsilon(x)=u'(x)$ ), and the rod has uniform mass density  $\rho$  and (unrelaxed) modulus of elasticity  $E$ . A single augmenting thermodynamic field,  $\xi(x)$ , is introduced. The fields which are thermodynamically conjugate to  $\epsilon$  and  $\xi$  are the stress,  $\sigma$ , and the affinity,  $A$ . The affinity can be interpreted as a thermodynamic "force" driving  $\xi$  towards equilibrium. The material property  $\delta$  describes the strength of the coupling of the two dependent fields,  $u$  and  $\xi$ . In the absence of coupling of the two fields, increments of stress and strain are proportional, with  $E$  the relating factor. Analogously,  $\alpha$  is the material property that relates changes in  $A$  to those in  $\xi$ . The material constitutive equations may be found as:

$$\sigma = \frac{\partial f}{\partial \epsilon} = E\epsilon - \delta\xi$$

$$A = - \frac{\partial f}{\partial \xi} = \delta\epsilon - \alpha\xi$$

The usual stress-strain constitutive relations are seen to be augmented by an additional term in  $\xi$ , similar to the way in which temperature changes couple to stress and strain. The equation of evolution for the mechanical displacement field is developed from consideration of momentum balance (zero body forces are assumed). The equation of evolution for the augmenting thermodynamic field,  $\xi$ , is found through the use of a basic assumption of irreversible thermodynamics, namely that the rate of change of  $\xi$  is proportional to  $A$  or, in other words, that the rate of change of  $\xi$  is proportional to its deviation from an equilibrium value. The result is a set of two coupled partial differential equations in  $u$  and  $\xi$ :

$$\rho \ddot{u} - Eu'' = -\delta \dot{\xi}$$

$$\dot{\xi} + B\xi = \left(\frac{B\delta}{\alpha}\right) u'$$

With appropriate boundary conditions, this set of equations can be shown to be dissipative and well-posed, guaranteeing a solution which depends continuously on the initial conditions. Fourier analysis reveals that the damping and effective modulus are frequency dependent; an approximate equation for the damping ratio (for small damping) is:

$$\zeta = \frac{1}{4} \left( \frac{\delta^2}{E\alpha} \right) \frac{2(\frac{\omega}{B})}{\left(1 + (\frac{\omega}{B})^2\right)}$$

This result is in accord with experimental results obtained by materials scientists for many microstructural damping mechanisms although, as noted by Torvik and Bagley, many materials exhibit weaker frequency-dependence. Note that peak damping is observed at  $\omega=B$ , and that the magnitude of the peak depends on strength of the coupling of the two equations. Also note that, in accord with the principles of irreversible thermodynamics, the entropy generation rate may be expressed as:

$$\sigma' = \frac{1}{T} \left( \frac{\alpha}{\rho} \right) \dot{\xi}^2$$

An alternative formulation of this one-dimensional case may also be considered. For example, the preceding equations can be expressed in terms of  $\gamma$ , the gradient of the  $\xi$ -field, as

follows:

$$\rho \ddot{u} - E u'' = -\delta \gamma$$

$$\dot{\gamma} + B\gamma = \left(\frac{B\delta}{\alpha}\right) u''$$

This formulation contains only even spatial derivatives, and leads to some benefits in numerical solution, such as symmetric element submatrices.

### FINITE ELEMENT TREATMENT

The method of weighted residuals (MWR) is used to develop element matrices. The  $u$ - $\gamma$  formulation of the equations has been shown to be better than the  $u$ - $\xi$  formulation, and is employed here. Integration by parts is employed, changing the continuity required of the approximating and weighting functions. This approach can yield alternate element matrices and matrix equations, with no *a priori* rules for selection among them. The same functions used to approximate the behavior of the dependent fields in the spatial region bounded by the element are used here as weighting functions—when there is only one dependent field, this is known as Galerkin's method. Let  $u(x)$  and its weighting function be approximated by:

$$u(x) = \Phi^T(x) Cq$$

where  $q$  is the vector of nodal mechanical displacements. Employ a similar approximation for  $\gamma(x)$  and its weighting function:

$$\gamma(x) = \Theta^T(x) Dp$$

where  $p$  is the vector of nodal ATF displacements. Substituting the preceding into the appropriate PDE and integrating over the length of the element, one finds:

$$\int_0^L \left\{ \rho C^T \Phi \Phi^T C \dot{q} + E C^T \Phi' \Phi'^T C q \right\} dx = \int_0^L \left\{ -\delta C^T \Phi \Theta^T D p \right\} dx$$

$$\int_0^L \left\{ D^T \Theta \Theta^T D \dot{p} + B D^T \Theta \Theta^T D p \right\} dx = \int_0^L \left\{ -\left(\frac{B\delta}{\alpha}\right) D^T \Theta' \Phi'^T C q \right\} dx$$

These sets of equations may be written in first-order form as:

$$\begin{bmatrix} M & 0 & 0 \\ 0 & I & 0 \\ 0 & 0 & C \end{bmatrix} \begin{Bmatrix} \ddot{q} \\ \dot{q} \\ \dot{p} \end{Bmatrix} + \begin{bmatrix} 0 & K & B \\ -I & 0 & 0 \\ 0 & F & H \end{bmatrix} \begin{Bmatrix} q \\ q \\ p \end{Bmatrix} = \begin{Bmatrix} 0 \\ 0 \\ 0 \end{Bmatrix}$$

In this treatment, both fields are approximated with linear interpolation functions using:

$$\Phi^T = [1 \ x]$$

Figure 3 illustrates the element and the nodal values for the two dependent fields,  $u$  and  $\gamma$ . If the elemental degrees of freedom are ordered to facilitate assembly as:

$$\mathbf{x} = [\dot{q}_1, q_1, \dot{p}_1, \dot{q}_2, q_2, \dot{p}_2]^T$$

the elemental equations may be expressed as:

$$\mathbf{A}\dot{\mathbf{x}} + \mathbf{B}\mathbf{x} = 0$$

and the ATF-damped rod elements are:

$$\mathbf{A} = \begin{bmatrix} \left(\frac{\rho AL}{3}\right) & 0 & 0 & \left(\frac{\rho AL}{6}\right) & 0 & 0 \\ 0 & 1 & 0 & 0 & 0 & 0 \\ 0 & 0 & \left(\frac{AL}{3}\right) & 0 & 0 & \left(\frac{AL}{6}\right) \\ \left(\frac{\rho AL}{6}\right) & 0 & 0 & \left(\frac{\rho AL}{3}\right) & 0 & 0 \\ 0 & 0 & 0 & 0 & 1 & 0 \\ 0 & 0 & \left(\frac{AL}{6}\right) & 0 & 0 & \left(\frac{AL}{3}\right) \end{bmatrix}$$

$$\mathbf{B} = \begin{bmatrix} 0 & \left(\frac{EA}{L}\right) & \left(\frac{\delta AL}{3}\right) & 0 & \left(-\frac{EA}{L}\right) & \left(\frac{\delta AL}{6}\right) \\ -1 & 0 & 0 & 0 & 0 & 0 \\ 0 & \left(\frac{B\delta A}{\alpha L}\right) & \left(\frac{BAL}{3}\right) & 0 & \left(-\frac{B\delta A}{\alpha L}\right) & \left(\frac{BAL}{6}\right) \\ 0 & \left(-\frac{EA}{L}\right) & \left(\frac{\delta AL}{6}\right) & 0 & \left(\frac{EA}{L}\right) & \left(\frac{\delta AL}{3}\right) \\ 0 & 0 & 0 & -1 & 0 & 0 \\ 0 & \left(-\frac{B\delta A}{\alpha L}\right) & \left(\frac{BAL}{6}\right) & 0 & \left(\frac{B\delta A}{\alpha L}\right) & \left(\frac{BAL}{3}\right) \end{bmatrix}$$

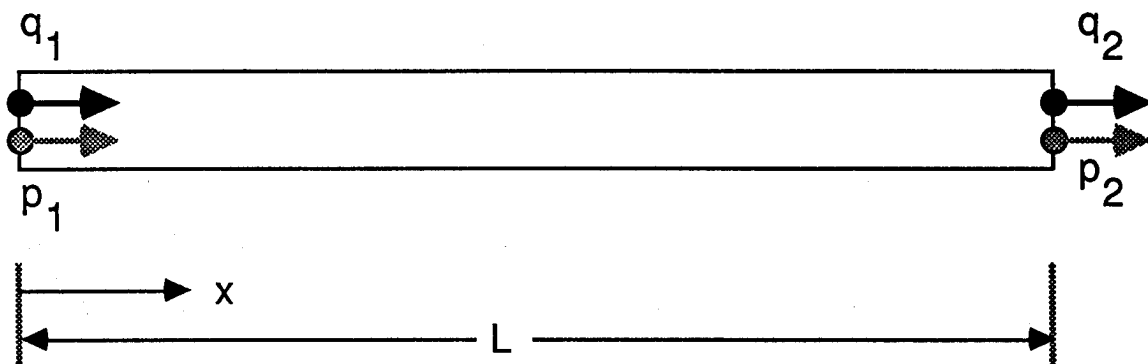
#### NUMERICAL RESULTS FOR FREE VIBRATION EIGENVALUE PROBLEM

In order to evaluate the performance of this formulation of an ATF-damped rod element, a specific problem is addressed, viz., the determination of the natural modes of vibration of a free-free rod. The results are compared to those obtained using approximate Fourier analysis.

Assuming a solution for  $\mathbf{x}(t)$  in the form  $e^{\lambda t}$ , the following eigenvalue problem is defined:

$$[\lambda \mathbf{A} + \mathbf{B}]\mathbf{x} = 0$$

The matrix equations of motion are formulated and this problem is solved to yield complex eigenvalues,  $\lambda$ , and mode shapes,  $\mathbf{x}$ . Element matrices may be assembled into global system matrices in the usual manner of structural finite element analysis. The damping ratio for each mode is calculated as the ratio of the negative of the real part of the eigenvalue to the total magnitude. The damping ratio,  $\zeta$ , is then plotted against the magnitude of the eigenvalue. Note that the



Mechanical displacement field

$$u(x) = \left[ \left( 1 - \frac{x}{L} \right) \left( \frac{x}{L} \right) \right] \begin{Bmatrix} q_1 \\ q_2 \end{Bmatrix}$$

Augmenting thermodynamic field

$$\gamma(x) = \left[ \left( 1 - \frac{x}{L} \right) \left( \frac{x}{L} \right) \right] \begin{Bmatrix} p_1 \\ p_2 \end{Bmatrix}$$

Figure 3: The ATF-Damped Linear-u, Linear- $\gamma$  Rod Element

spectrum of eigenvalues will contain "vibration modes," "relaxation modes," and "rigid-body modes." In the complex plane, the damped vibration modes lay near the imaginary axis, slightly in the LHP with negative real parts; the relaxation modes lie on the negative real axis. These relaxation modes are characteristic of the response of the  $\gamma$  field.

The numerical parameter values used are:

$$\begin{aligned} E &= 7.13e10 \\ \rho &= 2750 \\ L &= 10 \\ B &= 8000 \\ \alpha &= B \\ \delta &= 4.7766e6 \end{aligned}$$

The elastic properties correspond roughly to those of aluminum in SI units. Using the results of the Fourier analysis, values for the "dissipative" properties were chosen to yield a peak damping ratio of 1% at the frequency of the 5<sup>th</sup> mode; in practice, these would be obtained from experimental data.

Figure 4 shows typical numerical results yielded by this approach, using 20 damped rod elements. The characteristic variation of material damping with frequency is apparent and, as previously noted, conventional damping modeling techniques are incapable of producing such results.

### *SUMMARY AND CONCLUSIONS*

A physically-motivated material damping model compatible with current computational structural analysis methods has been developed. Referred to as the ATF method, its key feature is the introduction of augmenting thermodynamic fields to interact with the usual displacement field of continuum structural dynamics. Note that an increase in the accuracy of a structural dynamic model comes with a cost of dimensionality—additional coordinates are required to represent additional aspects of material behavior, viz., damping.

Coupled material constitutive equations and partial differential equations of evolution have been developed for microstructurally-damped rods, and ATF-damped finite elements developed and used to solve a free vibration eigenvalue problem. Numerical finite element results compared favorably with results obtained using Fourier analysis.

Although a single augmenting field was generally discussed, the results are readily extended to multiple fields. In addition, although all the elements of the example structures were assumed to be damped, the method is compatible with conventional structural analysis techniques and readily accommodates both damped and undamped elements. With the continued development of better analytical tools such as this ATF method, damping will be modelled more accurately in the design of engineering systems and may ultimately become more accessible to design specification.

### *ACKNOWLEDGMENTS*

This work is based on the author's dissertation research [Lesieutre, 1989]. He wishes to thank Professor D.L. Mingori of UCLA for his participatory guidance, and R. Quartararo and H. Rediess for their encouragement. The financial support of SPARTA, Inc. through a tuition reimbursement program and free computer time is noted. A more detailed presentation of this work will be made at the 1989 Structures, Structural Dynamics, and Materials Conference in Mobile, Alabama.

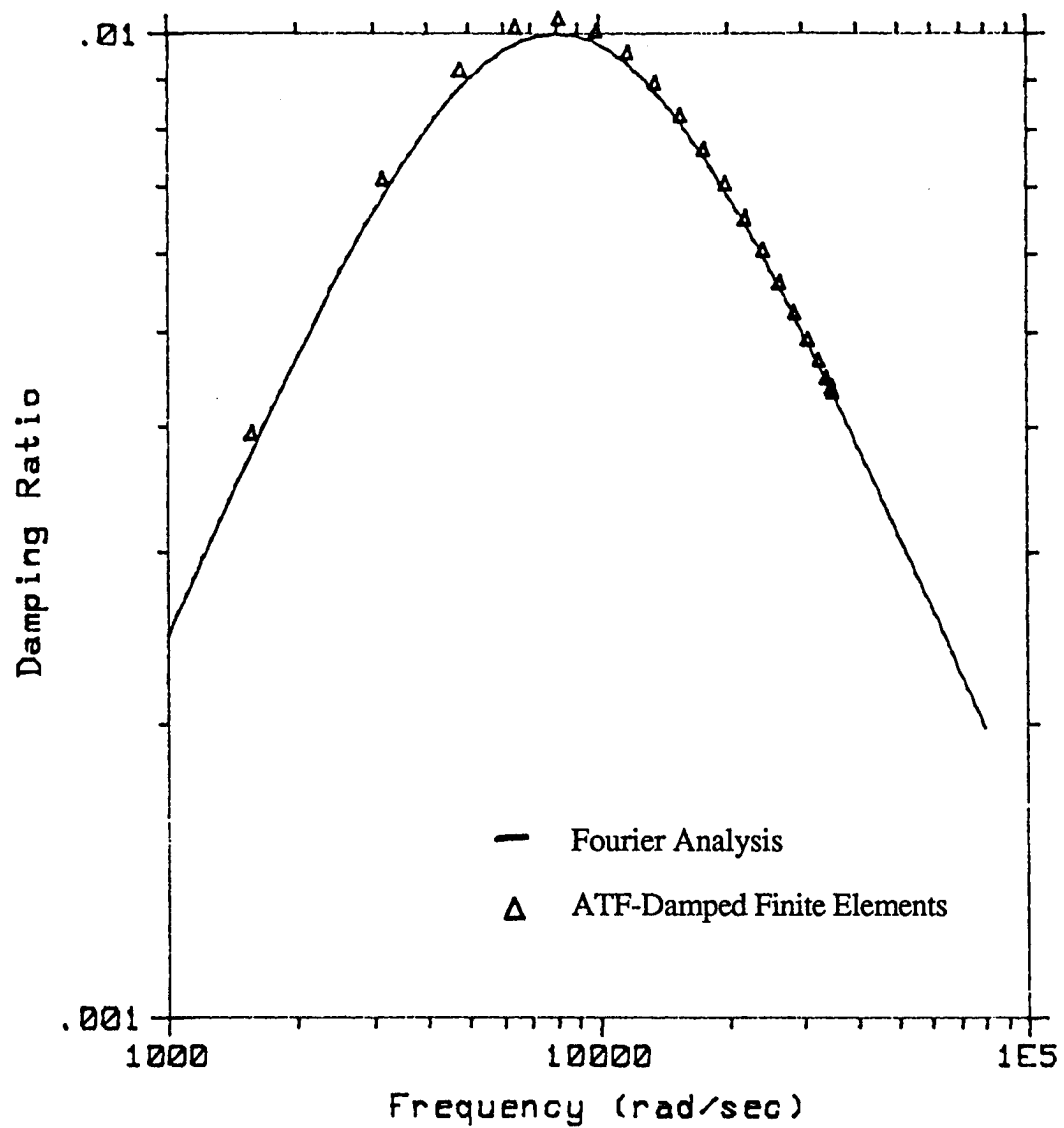


Figure 4: Damping versus Frequency for 20 ATF-Damped Rod Finite Elements and Fourier Analysis

## REFERENCES

- Bert, C.W., "Material Damping: An Introductory Review of Mathematical Models, Measures, and Experimental Techniques," *J Sound and Vibration*, Vol. 29, No. 2, 1973, pp. 129-153.
- Crawley, E.F., and Mohr, D.G., "Experimental Measurements of Material Damping in Free-Fall With Tuneable Excitation," AIAA Paper 83-0858, May 1983.
- deGroot, S.R., and Mazur, P., *Non-Equilibrium Thermodynamics*, North-Holland (Interscience), 1962.
- Golla, D.F., and Hughes, P.C., "Dynamics of Viscoelastic Structures - A Time-Domain, Finite Element Formulation," *J Appl Mech*, Vol. 52, December, 1985, pp. 897-906.
- Lesieutre, George A., Eckel, Andrew J., and DiCarlo, James A., "Temperature-Dependent Damping of Some Commercial Graphite Fibers," *Proceedings of the NASA/DoD Composites Materials and Structures Conference*, January, 1988, Cocoa Beach, FL.
- Lesieutre, G.A., "Finite Element Modeling of Frequency-Dependent Material Damping using Augmenting Thermodynamic Fields," Ph.D. Dissertation, Aerospace Engineering, University of California, Los Angeles, 1989 (expected).
- McTavish, D.J., and Hughes, P.C., "Finite Element Modeling of Linear Viscoelastic Structures," *Proceedings of the 11<sup>th</sup> ASME Biennial Conference on Mechanical Vibration and Noise*, September, 1987, Boston, MA.
- Nowick, A.S., and Berry, B.S., *Anelastic Relaxation in Crystalline Solids*, Academic Press, 1972.
- Segalman, D.J., "Calculation of Damping Matrices for Linearly Viscoelastic Structures," *Proceedings of the 11<sup>th</sup> ASME Biennial Conference on Mechanical Vibration and Noise*, September, 1987, Boston, MA.
- Torvik, P.J., and Bagley, D.L., "Fractional Derivatives in the Description of Damping Materials and Phenomena," *Proceedings of the 11<sup>th</sup> ASME Biennial Conference on Mechanical Vibration and Noise*, Boston, Massachusetts, September, 1987.
- Zener, C.M., *Elasticity and Anelasticity of Metals*, University of Chicago Press, 1948.

Experimental Determination of Damping  
Mechanisms in a Composite Beam

H.T. Banks  
Center for Control Sciences  
Division of Applied Mathematics  
Brown University  
Providence, Rhode Island 02912

D.J. Inman  
Department of Mechanical and Aerospace Engineering  
State University of New York at Buffalo  
Buffalo, New York 14260

**Abstract**

A partial differential equation model of a cantilevered beam with a tip mass at its free end is used to study damping in a composite. Four separate damping mechanisms consisting of air damping, strain rate damping, spatial hysteresis and time hysteresis are considered experimentally. Dynamic tests were performed to produce time histories. The time history data is then used along with an approximate model to form a sequence of least squares problems. The solution of the least squares problem yields the estimated damping coefficients. The resulting experimentally determined analytical model is compared with the time histories via numerical simulation of the dynamic response. The procedure suggested here is compared with a standard modal damping ratio model commonly used in experimental modal analysis.



## I. Introduction

This paper examines a variety of damping mechanisms of a quasi-isotropic pultruded composite beam. The approach taken here is a physical one. The beam is modeled by a partial differential equation describing the transverse vibration of a beam with tip mass. The damping mechanisms considered are all physically based rather than the usual modal models. In total, four possible damping mechanisms are considered, one external and three internal. They are:

- viscous damping (air damping)
- strain rate damping
- spatial hysteresis
- time hysteresis

In addition, various combinations of these mechanisms are considered. These physical damping models are incorporated into the Euler-Bernoulli beam equation, taking care to adjust the boundary conditions for the various damping forces. The resulting partial differential equation is approximated using cubic splines. The time histories of the measured experimental responses are then used to form a least squares fit-to-data parameter estimation problem. The mathematical details for this procedure are complete and imply convergence of a sequence of parameter estimates obtained from finite dimensional models to a set of best fit coefficients of the partial differential equation model. The least square estimates of the various different damping parameters are then used in the partial differential/integral equation to numerically predict the response of the system. This numerically generated time response of the estimated system is then compared with the actual experimental time histories. These comparisons allow several conclusions to be drawn regarding the physical damping mechanisms present in the composite beam.

In particular it is shown that the spatial hysteresis model combined with a viscous air damping model results in the best reproduction of experimental time histories. The results agree well with the physically intuitive notion that air damping should play a more significant role in lower modes while internal damping plays a more significant role for higher modes. It is also shown explicitly that the proposed damping models listed above cannot be modeled with any degree of success or consistency by using standard modal damping ratios, as the traditional modal analysis approach completely masks the physics of damping mechanisms.

## II. Basic Beam Model

The beam considered here is a pultruded quasi-isotropic composite beam constructed for use in the proposed space station.<sup>1</sup> As such, the configuration of interest is a cantilevered beam with a mass attached to the free end. The beam is constructed of a biaxial (0°/90°) fiberglass roving held in place with knitted polyester yarn with an equal volume of fibre in both orientations. An isophthalic polyester resin system was used as the matrix. This material provides an alternative to aluminum which is lower in cost, has higher specific strength but is dynamically similar. As is illustrated here, this material also has interesting damping properties - dissimilar to those of aluminum.

The equation of motion for the flexural vibration of a beam is easily calculated from considering the equilibrium of forces acting on a differential segment of beam (see for instance Reference 2). In this formulation, damping can easily be included by adding the appropriate force or moment to the equations of equilibrium. A general partial differential equation model of the beam with general damping is of the form

$$u_{tt}(x,t) + L_1 u_t(x,t) + L_2 u(x,t) \frac{\partial^2}{\partial x^2} + \left[ \frac{EI(x)}{\rho A} u_{xx}(x,t) \right] = f(x,t) \quad (1)$$

for  $x \in (0, l)$ ,  $t > 0$ , subject to the appropriate boundary and initial conditions (taken to be  $u = u_t = 0$  at  $t = 0$ ). Here  $\rho$  is the mass density (mass per unit length) of the beam,  $A$  is the cross sectional area of the beam,  $EI(x)$  is the spatial varying flexural stiffness of the beam, the subscript indicates partial differentiation with respect to the indicated variable and  $u(x, t)$  is the beam displacement in the transverse direction. The function  $u(x, t)$  is assumed to be smooth enough so that all the appropriate derivatives exist. The term  $L_1 u_t(x, t) + L_2 u(x, t)$  forms the subject of this paper. The nature of the operator  $L_1$  is determined by the external damping mechanisms while the nature of the term  $L_2 u(x, t)$  is determined by internal damping mechanisms.

The boundary conditions of interest here are those for a beam clamped at the end  $x = 0$  and with a free end at  $x = l$ . Also at  $x = l$ , a mass of mass  $m_T$  and rotational inertia  $J$ , resides. The fixed end requires that the displacement and the slope of the displacement both be zero. This yields:

$$u(0, t) = 0 \quad (2)$$

$$u_x(0, t) = 0 \quad (3)$$

The free end requires that the sum of the moments at  $x = l$  and the sum of the forces acting at  $x = l$  must both be zero. For the case of a tip mass at the free end, these boundary conditions become

$$EI(l)u_{xx}(l, t) = -J u_{tt}(l, t) \quad (4)$$

$$[EI(l)u_{xx}(l, t)]_x = m_T u_{tt}(l, t) \quad (5)$$

as long as only external damping is present.

Equations (1) - (5) describe the transverse vibration of a beam satisfying the Bernoulli-Euler assumption that the bending wave length is several times larger than the cross sectional dimensions of the beam, and that only lower frequency excitations are applied to the beam. It is also assumed that rotary inertia of the beam, shear displacement of the beam and axial displacements are negligible.

If the tip mass is not present, the boundary conditions of equations (4) and (5) change accordingly. In addition, the nature of the damping operator  $L_2$  will effect the boundary conditions. For the case of  $L_1 = L_2 = 0$ , the vibration analysis problem is very simple as is the inverse problem addressed here. The nature of the damping mechanisms drastically changes the nature of the solution to the vibration problem and hence controls the response of the beam. The following section discusses several possible choices for modeling the operator  $L_2$  in equation (1) and hence the damping mechanisms.

### III. Damping Models

As mentioned in the introduction four models of the damping mechanism are examined. Two of these are time independent proportional models lending themselves to modal expansions, the other two are nonproportional hysteretic models. Various combinations of these models are also considered.

*Viscous Air Damping* The most straight forward method of modeling the damping of a beam (or other object) vibrating in air is to use a viscous model proportional to velocity. In this case the operator  $L_1$  becomes

$$L_1 = \gamma I_0 \quad (6)$$

where  $I_0$  is the identity operator and  $\gamma$  is the viscous damping constant of proportionality. The physical basis of this approach is a sample model of air resistance. As the beam vibrates it must displace air causing the force  $\gamma u_t(x, t)$  to be applied to the beam. Mathematically, this form of damping is used because it is proportional and easily treated using the same methods of analysis used for undamped systems (see Reference 3 for instance). Both experimental modal analysis and

theoretical modal analysis depend on the validity of these models. This form of damping is often called external damping.

**Kelvin-Voight Damping** Kelvin-Voight damping, or strain rate damping as it is sometimes called, is damping of the form

$$L_2 = c_d I \frac{\partial^5}{\partial x^4 \partial t} \quad (7)$$

where  $I$  is the moment of inertia and  $c_d$  is the strain rate damping coefficient or strain velocity. This model also satisfies a proportional damping criteria and hence is mathematically convenient. This model is compatible with theoretical modal analysis and is also widely used in finite element modeling along with viscous damping. Physically, this form of damping is referred to as internal damping and represents energy dissipated by friction internal to the beam.

Unlike viscous external damping, inclusion of this form of damping affects the free end boundary conditions because it is strain dependent. The strain rate dependance results in a damping moment  $M_D$  of the form

$$M_D = c_d I(x) \frac{\partial^3 u}{\partial x^2 \partial t} \quad (8)$$

which is included in the derivation of the equation of motion<sup>2</sup> and hence must also be included in any boundary conditions (such as a free end condition) depending on the moment.

The full equation of motion and boundary conditions for the linear viscously damping case becomes

$$\begin{aligned} \rho u_{tt} + \frac{\partial^2}{\partial x^2} [E I u_{xx}] + c_d I u_{xxxxt} + \gamma u_t &= f(x, t) \quad x \in (0, l), \quad t > 0 \\ u(0, t) = u_x(0, t) &= 0, \quad t > 0 \\ E I u_{xx}(l, t) + c_d I \frac{\partial^3}{\partial x^2 \partial t} u(l, t) &= -J u_{xtt}(l, t), \quad t > 0 \\ \frac{\partial}{\partial x} [E I u_{xx}(l, t)] + \frac{\partial}{\partial x} [c_d I u_{xxt}(l, t)] &= m_T u_{tt}(l, t), \quad t > 0 \end{aligned} \quad (9)$$

Here, note that the tip mass is present in the boundary conditions as well as the damping moment. The total damping mechanism used in (9) is the analog to proportional damping i.e., a linear combination of mass ( $I$ ) and stiffness.

**Time Hysteresis** Hysteretic damping terms are most commonly associated with sinusoidal loadings. The generic idea of including a mechanism in the beam vibration constitutive equation indicating that stress is proportional to strain plus the past history of the strain can be accomplished by introducing an integral term of the form

$$\int_0^\gamma g(s) u_{xx}(x, t+s) ds \quad (10)$$

where the history kernel  $g(s)$  is defined by

$$g(s) = \frac{\alpha e^{\beta s}}{\sqrt{-s}} \quad (11)$$

where  $\alpha$  and  $\beta$  are constants. Since the introduction of the heredity integral occurs in the stress strain relationship, the boundary conditions must also be modified. In this case the boundary value problem of interest becomes

$$\rho u_{tt}(x,t) + \frac{\partial^2}{\partial x^2} \left[ EI u_{xx} - \int_{-\gamma}^0 g(s) u_{xx}(x,t+s) ds \right] = f(t,x), \quad x \in (0,1), \quad t > 0$$

$$u(0,t) = u_x(0,t) = 0 \quad t > 0 \quad (12)$$

$$EI u_{xx}(l,t) - \int_{-\gamma}^0 g(s) u_{xx}(l,t+s) ds = J u_{xtt}(l,t), \quad t > 0$$

$$\frac{\partial}{\partial x} \left[ EI u_{xx}(l,t) - \int_{-\gamma}^0 g(s) u_{xx}(l,t+s) ds \right] = m_T u_{tt} \quad t > 0$$

Note again that the inclusion of a damping mechanism in the equation of motion also effects the boundary condition.

*Spatial Hysteresis* Another type of damping proposed by Russell<sup>4</sup> is based on interpreting the energy lost in the transverse vibration of a beam as resulting from differential rates of neighboring beam sections causing internal friction. This is modeled by the expression

$$\frac{\partial}{\partial x} \left[ \int_0^l h(x,\xi) \{ u_{xt}(t,x) - u_{xt}(t,\xi) \} d\xi \right] \quad (13)$$

where the kernel  $h(x,\xi)$  is defined by

$$h(x,\xi) = \frac{a}{b\sqrt{2\pi}} e^{-(x-\xi)^2/2b^2} \quad (14)$$

Under these circumstances the equation of the beam vibration becomes

$$\rho u_{tt} + \frac{\partial^2}{\partial x^2} [EI u_{xx}] + \gamma u_t$$

$$- \frac{\partial}{\partial x} \left[ \int_0^l h(x,\xi) \{ u_{xt}(x,t) - u_{xt}(\xi,t) \} d\xi \right] = f(x,t), \quad x \in (0,l), \quad t > 0 \quad (15)$$

$$u(0,t) = u_x(0,t) = 0, \quad t > 0$$

$$EI u_{xx} = -J u_{xtt} \quad t > 0, \quad x = l$$

$$\frac{\partial}{\partial x} [EI u_{xx}] - \left[ \int_0^l h(x,\xi) \{ u_{xt}(x,t) - u_{xt}(\xi,t) \} dx \right] = m_T u_{tt} \quad t > 0, \quad x = l$$

where again the damping mechanism changes the boundary conditions.

In total the various models represented by equations (9), (12) and (15) represent four possible sources of damping presented in various combinations. The approach taken here is to attempt to fit each of the combinations of damping models listed above to experimentally measured data. By examining each model's ability to numerically reproduce measured data, a best model is chosen from these as being most representative of the cantilever quasi-isotropic beam. As is discussed in section V, these models all admit reasonable mathematical formulations.

#### IV. Problem Statement

The various damping coefficients introduced in the preceding discussion cannot be measured by static experiments. Thus, the damping constants  $\gamma$ ,  $c_d$ ,  $\alpha$ ,  $\beta$ ,  $a$ , and  $b$  must all be estimated based on measurements taken from dynamic experiments. The procedure suggested here is to estimate various groups of damping parameters such as indicated in the three models of equations (9), (12) and (15). Once these coefficients are estimated they are used in the model to produce a numerical simulation of the response of the structure under consideration subjected to identical experimental inputs. The analytical time response (with the estimated coefficients) is then compared with the experimentally measured time response. The model with the damping mechanism that best agrees with (predicts) the experimental response is then considered to be a valid physical model.

In particular, several vectors of parameters,  $\mathbf{q}$ , are defined one for each model of interest. For the three cases discussed here they are:

$$\mathbf{q}_1 = [EI \quad c_d I \quad \gamma] \quad (16)$$

which delineates the first damping model as defined by equation (9). Here  $c_d$  is the internal strain rate damping coefficient and  $\gamma$  is the linear air damping coefficient. The second model considered, as defined by equation (12), is characterized by the parameter vector

$$\mathbf{q}_2 = [EI \quad \alpha \quad \beta] \quad (17)$$

where  $\alpha$  and  $\beta$  characterize the time historetic damping term. The last model considered contains a combination of linear air damping, defined by the coefficient  $\gamma$ , and spatial hysteresis defined by the constants  $a$  and  $b$ . The parameter vector for the third system defined by equation (15) is

$$\mathbf{q}_3 = [EI \quad \gamma \quad a \quad b] \quad (18)$$

Other combinations of the four damping mechanism are possible but were dismissed as discussed in the later section on results.

Note that in each case the parameter vector contains the flexural stiffness constant  $EI$ . For most common materials  $EI$  is tested, tabulated and well known. However in this case the material is a prototype composite with unknown material properties. Thus  $EI$  is also estimated. Because of the relative size of the air damping coefficient  $c_d$ , the term  $c_d I$  is estimated.

#### V. Results

First the problem  $\mathbf{q}_1$  is addressed by experimental modal analysis methods. In this case the coefficients of  $\mathbf{q}_1$  are estimated by fitting the parameters of  $\mathbf{q}_1$  to the measured damping ratios,  $\zeta_n$  and natural frequencies  $\omega_n^2$  using least squares. The results given by Cudney and Inman<sup>5</sup>

illustrate clearly that the air damping dominates the dissipation in the lower modes while strain rate damping dominates the response in higher modes. The modal model, which depends on knowing the analytical expression for the systems eigenvalues (of a cantilevered beam in this case) give consistent results in a frequency range of up to 750 Hz.

The modal equations for the problem  $\mathbf{q}_1$  are given by

$$\ddot{a}_n(t) + \left( \frac{\gamma}{\rho A} + \frac{c_d I}{\rho A} \beta_n^4 \right) \dot{a}_n(t) + \frac{EI}{\rho A} \beta_n^4 a_n(t) = f_n(t) \quad (19)$$

where  $\beta_n^4$  are the eigenvalues of the stiffness operator with respect to the appropriate boundary conditions and must be known analytically for the modal approach to work. The coefficients of

$a_n(t)$  and  $\dot{a}_n(t)$  are compared with the measured modal damping ratios  $\hat{\zeta}_n$ , and natural frequencies,  $\hat{\omega}_n^2$ . A least squares fit is then made between the measured modal data and the analytical coefficients using

$$\beta_n^4 \frac{EI}{\rho A} = \hat{\omega}_n^2 \quad \text{and} \quad \frac{\gamma}{\rho A} + \frac{c_d I}{\rho A} \beta_n^4 = 2 \hat{\zeta}_n \hat{\omega}_n \quad (20)$$

The results for a number of impact tests are given in figures 1 and 2.

Table 1 lists the analytical expressions used for the eigenvalues  $\beta_i$  for the first 9 modes as tabulated by Gorman for the beam parameters given in table 2. Figure 1 illustrates the modal estimate of the elastic modulus which is basically constant at  $E = 2.68 \times 10^{10} \text{ N/m}^2$  with a variance of  $6 \text{ N/m}^2$ . Figure 2 illustrates the consistency of the damping estimates over the mode number for a weighted least squares fit to equation (20). Reference 5 contains the details. The dashed line indicates the analytically determined damping coefficient  $2\zeta_n \omega_n$ , based on the estimate of  $\gamma (= 1.75 \text{ N-sec/m}^2)$  and  $c_d (= 20,500 \text{ N-sec/m}^2)$ , versus mode number (1-9). The solid line

corresponds to the measured values  $2 \hat{\zeta}_n \hat{\omega}_n$  versus mode number. The results are fairly consistent, however not in exact agreement. The disagreement motivates the search for a more exotic damping mechanism such as the hysteresis term considered next.

Note that solving the second of equations (20) for the damping ratio  $\zeta_n$  yields

$$\zeta_n = \frac{\gamma}{2\omega_n} + \frac{c_d}{2E^2 I} \omega_n \quad (21)$$

This states explicitly that the viscous air damping (external) is most dominate at the lowest modes,  $n = 1, 2$ , and that the strain rate (internal) damping mechanism dominates the decay rate at the higher modes. This agrees with physically intuitive notion that the low frequency modes are pushing more air than the higher frequency, lower amplitude modes. In fact, for a free-free configuration it is claimed by Vinson<sup>6</sup> that this effect can be subtracted.

The modal approach is not capable of examining hysteresis effects. Hence, spline inverse procedures are used. These time domain procedures are not limited to modal damping ratios or assumptions of time invariance and allow for spatially varying coefficients. Hence, they are used to estimate and compare the three models suggested in section IV. This procedure, described in Reference 7, uses cubic spline approximations to each set of differential equations and forms a sequence of least squares problems minimizing the difference between the analytical and experimental accelerations (for velocities, if so desired). The sequence converges to the best value of  $\mathbf{q}$  for a given set of data. The functionals minimized are of the form

$$J^N(\mathbf{q}) = \sum |u_{it}^N(t_i, x_j, \mathbf{q}) - \hat{u}_{it}(t_i, x_j)|^2 \quad (22)$$

where  $\hat{u}$  denotes measurements at time  $t_i$  and point  $x_j$  (at the tip in many cases), and where the summation is over the number of discrete time measurement,  $i$ . The superscript  $N$  denotes the order of each term of the sequence of approximations as discussed in Reference 7.

Problem  $q_1$  was solved again using a slightly more complicated cantilevered beam with a tip mass. The stiffness parameter (elastic modulus)  $E$  was estimated to be  $2.71 \times 10^{10} \text{N/m}^2$ , in good agreement with the modal estimation results above. Estimates of air damping by itself or strain rate by itself proved to be inadequate in reproducing time histories matching those of the experimental data, indicating a poor model. The difference between the numerical solution for the time history of the acceleration  $u_{tt}(x_i, t)$  for the analytical model with the estimated parameter  $q_1$  and the experimentally measured accelerations define the residual which is generally small.<sup>8</sup> The analytical time response is plotted along with the measured time response versus time in figure 3. While the agreement is fair, the residual is larger for some time intervals, warranting further modeling.

Next, the temporal hysteresis model  $q_2$  is considered as a possible candidate for modeling the damping in the composite. In this case, the estimation procedure produces (i.e., consistent with our previous methods for estimating  $q_1$ ) a good value for  $E$  but drives the air damping coefficient to zero. The residual, however, is better than that for model  $q_1$ . Figure 4 illustrates a plot of the measured acceleration versus time as well as the acceleration predicted by the estimate. The difference between the measured and predicted value of the time interval of interest is almost negligible. Because this model drives the air damping coefficient to zero violating physical intuition, a third model ( $q_3$ ) was considered.

The last model considered is based on a concept of spatial hysteresis as defined by problem  $q_3$ . Again the resulting estimate of the elastic modulus  $E$  is consistent with those estimated previously. The values estimated for the spatial hysteresis ( $a = 1.040394$ ,  $b = 0.064362$ ) and air damping coefficient ( $\gamma = .090189$ ) produce an excellent match between predicted and measured response as indicated<sup>9</sup> in figure 4. However, the external damping coefficient  $\gamma$ , differs from that estimate by the  $q_1$  model ( $\gamma = .0315$ ).

## VI. Conclusion and Discussion

Three different models of damping have been presented to account for the experimentally description observed dissipation in a composite beam. A spline based inverse procedure (SIP) which relies on the distributed parameter nature of the damping mass and stiffness parameters was used to estimate the form of the proposed damping mechanism. External air damping, strain rate damping, spatial hysteresis and time hysteresis models were considered. The spline based method was also compared to a standing experimental modal analysis (EMA) approach. The EMA approach is not applicable to the various hysteresis models, nor is it applicable to systems with spatially varying parameters in general. Both the SIP and EMA approaches yield consistent values for the elastic modulus ( $E$ ) for all three estimations models. This is consistent with the fact that frequencies are much more robust to estimate than damping quantities are. Both hysteresis models produce better results than the strain rate damping mode. However, the spatial hysteresis model allows for the air damping term which time hysteresis does not. Since air damping is obviously present the time hysteresis result is less satisfying. A comparison of the hysteresis models is given in reference 9. However, the physical explanation of spatial hysteresis is equally unsatisfying. Hence, further analysis and modeling is required before a critical decision can be made among the various models.

## VII. Acknowledgements

This research was supported in part under the following grants and contracts: NASA: MSM-8351807 (DJI) and several DOD equipment grants: AFOSR: 85-0119,87-0099 (DJI). The author also wishes to acknowledge H.H. Cudney, R.H. Fabiano, H. Ito, I.G. Rosen, D.L. Russell and Y. Wang for their comments, suggestions and data.

### VIII. References

1. Wilson, M.L. and Miserentino, R, "Pultrusion Processes Development for Long Space Boom Models," Proceedings of the 41st Annual Conference of the Reinforced Plastics/Composites Industry, Paper #6-D, 1986.
2. Clough, R.W. and Penzion, J, *Dynamics of Structures*, John Wiley and Sons, New York, NY, 1975.
3. Inman, D.J., *Vibration with Control, Measurement and Stability*, Prentice Hall, Englewood Cliffs, NJ, 1989.
4. Russell, D.L., "On Mathematical Models for the Elastic Beam with Frequency Proportional Damping," *Control and Estimation in Distributed Parameter Systems*, SIAM, to appear.
5. Cudney, H.H. and Inman, D.J., "Experimental Verification of Damping Mechanisms in a Composite Beam," Proceedings of the 7th International Modal Analysis Conference, pp. 1989.
6. Spirnak, G.T. and Vinson, J.R., "The Effect of Temperature on the Material Damping of Graphite/Epoxy Composites in a Simulated Space Environment," *Recent Advances in the Macro-Micro-Mechanics of Composite Materials and Structures*, AD- Vol. 4, ASME, pp. 189-192, 1988.
7. Banks, H.T., Crowley, J.M. and Rosen, I.G., "Methods for the Identification of Material Parameters in Distributed Models for Flexible Structures," *Mathematical Applications and Computations*, Vol. 5, pp. 139-168, 1986.
8. Banks, H.T., Wang, Y., Inman, D.J. and Cudney, H.H., "Parameter Identification Techniques for the Estimation of Damping in Flexible Structures Experiments," Proceedings of the 26th IEEE Conference on Decision and Control, Vol. 2, 1987, pp. 1392-1395.
9. Banks, H.T., Fabiano, R.H., Wang, Y., Inman, D.J. and Cudney, H.H., "Spatial Versus Time Hysteresis in Damping Mechanisms," Proceedings of the 27th IEEE Conference on Decision and Control, pp. 1674-1677, 1988.

Table 1. Theoretical eigenvalues of a clamped-free beam.

Mode Number	Eigenvalue ( $\beta_i$ )
1	1.875
2	4.694
3	7.855
4	10.996
5	14.137
6	17.279
7	20.420
8	23.562
9	26.704

Table 2. Beam parameters.

Length (meters) ( $l$ )	1.0
Moment of Inertia (meter <sup>4</sup> ) ( $I$ )	$1.64 \times 10^{-9}$
Density (kilograms/meter <sup>3</sup> ) ( $\rho$ )	1710
Area, cross section (meter <sup>2</sup> ) ( $A$ )	$0.597 \times 10^{-3}$



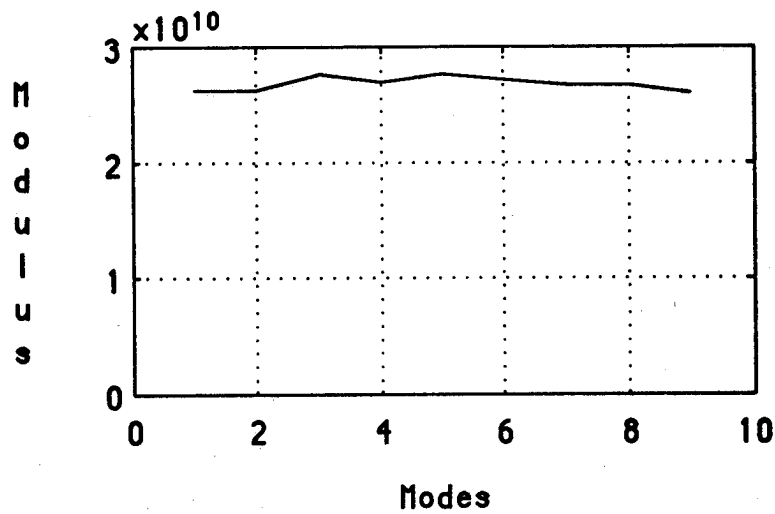


Figure 1. Estimated Youngs' modulus (N/m²) for each mode.

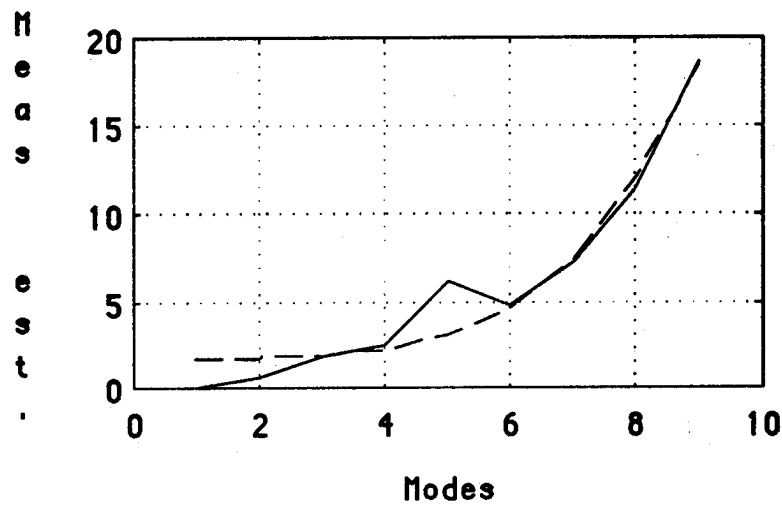


Figure 2. Measured modal parameters,  $2\zeta_n\omega_n$  (solid line) and  $\frac{1}{\rho A}\gamma + \frac{\beta_i I}{\rho A}c_d$  (dashed line) for each mode (N-sec/m²).

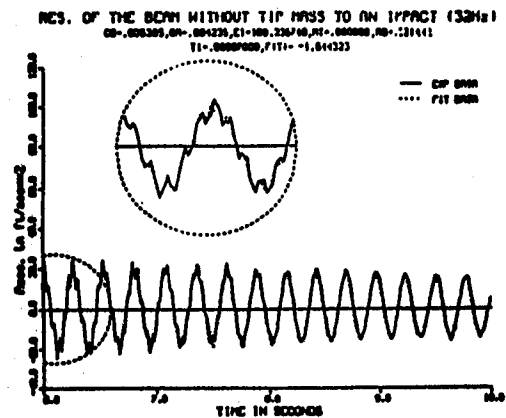


Figure 3. A comparison of the experimentally measured time response and model  $q_1$ .

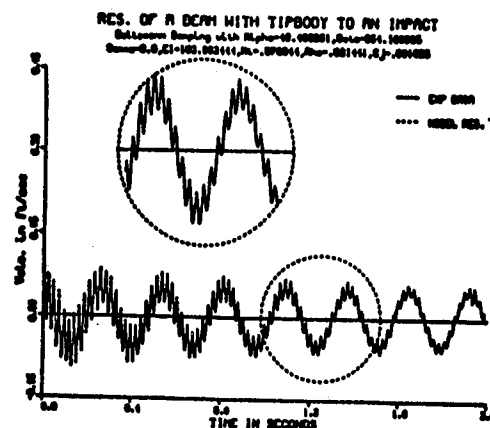


Figure 4. A comparison of the experimentally measured time response and model  $q_2$ .

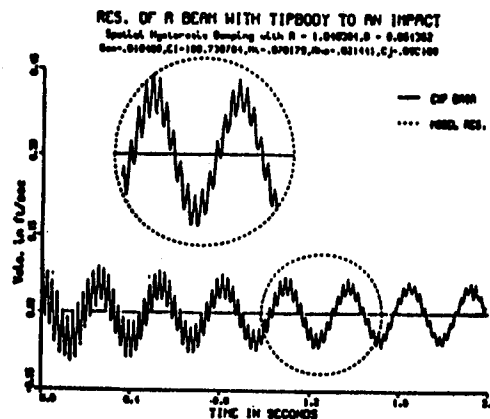


Figure 5. A comparison of the experimentally measured time response and model  $q_3$ .

# A Survey of Damping in Control of Flexible Structures

D.J. Inman

Department of Mechanical and Aerospace Engineering  
State University of New York at Buffalo  
Buffalo, NY 14260

Garnett C. Horner

Configurations and Concepts Manager  
NASA Langley Research Center  
Hampton, VA 23665

## Abstract

This paper surveys the use of active damping in suppressing vibrations of flexible structures, in the sense that various uses of active damping are summarized. In addition, a comparison is made between active and passive damping in a simple configuration. Specifically, the loss factor of a layered damping treatment is compared to that of a piezoelectric sensor/actuator pair. Next, the use of active damping in several slewing control experiments is surveyed and examined. The nature of the interplay between active and passive damping is illustrated in both linear actuators (proof-mass actuator) and rotational actuators (electric motors). Several experiments as well as numerical simulations are used to illustrate the nature of active damping.

## I. Introduction

The objective of this work is to encourage those vibration engineers expert in passive damping applications to consider active damping capabilities and limitations and to encourage those experts in active damping methodology to consider the use of passive damping as well. This is accomplished by making a theoretical comparison of the loss factor of a passively damped aluminum beam treated with a layered damping material and that of the same aluminum beam treated with an active piezoelectric feedback control system. This provides an example of an improvement in response performance provided by active damping.

One valid argument against the use of active control is the increased cost and loss of reliability involved in adding actuator and sensor hardware to the structure. In the case of slewing maneuvers however, the control hardware is already present so that active damping is available for "free." Section III of this paper discusses how damping is introduced by the slewing actuator and summarizes the amount of damping available from several reported slewing experiments. Section IV defines the interaction between a linear actuator and damping in the controlled structure and provides a case for the enhancement of active damping by use of passive damping.

## II. Active Versus Passive Damping

It is difficult to make comparisons between two approaches in an attempt to decide that one method is better than another. Rather the attempt here is to make a comparison that illustrates that active control can under some circumstances provide larger damping rates than passive damping treatments for relatively the same increase in mass and geometric size. The comparison is made using the well accepted Ross-Kerwin-Unger equations<sup>1</sup> for the loss factor of an unconstrained-layer damping treatment. Let the untreated beam be a 1.22 meter x .028 mm x 3.18 mm piece of aluminum ( $E_A = 10.3 \times 10^6$  psi,  $\eta = .001$ ). The expression for the loss factor obtained by adding a layer of LD400 (Lord Corporation) damping material ( $E_L = 1.5 \times 10^5$  psi) is computed from

$$\eta_c = \frac{e_2 h_2 (3 + 6 h_2 + 4 h_2^2 + 2 e_2 h_2^3 + e_2^2 h_2^4)}{(1 + e_2 h_2)(1 + 4 e_2 h_2 + 6 e_2^2 h_2^2 + 4 e_2^3 h_2^3 + e_2^4 h_2^4)} \quad (.001) \quad (1)$$

where  $h_2 = H_2/(0.028)$  the ratio of the thickness of the added damping treatment to the thickness of the structure (beam) and  $e_2 = E_2/E_A$  the ratio of elastic modulus of the damping treatment to that of the aluminum beam. The composite loss factor  $\eta_c$  is used as the measure of how effective the added damping, either passive or active, is.

The result of adding this passive damping treatment is compared to that of using active control. For the active control system a piezoelectric polymer (PVF<sub>2</sub>) is used along with an accelerometer as described by Hubbard<sup>2</sup>. The PVF<sub>2</sub> material is layered on the aluminum beam in the same fashion as the LD400. In addition an accelerometer is placed at the top of the beam to close the feedback loop. Using equation (1) applied to the PVF<sub>2</sub> under velocity feedback control yields higher loss factors for the active system. If the passive and active system are required to have the same thickness, the active loss factor is five times that of the passive case. If the two systems are required to have the same weight then the active system produces a loss factor three times larger than that of the passive system.

This comparison shows a substantial advantage in using active control over using passive control. However, active control still requires a voltage source and computational device. If these are not already available as they are in many spacecraft, then passive damping may be the only available

solution. The following two papers (HBB and HBC) present logical mixtures of using passive and active damping. The following sections present some uses of active damping.

### III. Damping in Slewing Maneuvers

An example of a situation where active damping can be applied without the need for additional components is in the slewing control of a flexible structure. Such systems usually consist of an electric motor with a beam attached to its shaft (see HBB for an alternative example) as depicted in figure 1. Here a control system actuator (i.e., an electric motor) is already present to provide the pointing motion of the beam. The sensors and motor can also be used to feedback the velocity of the beam at some point and hence, provide increased damping.

The damping added to the structures by the actuator depends upon the motor's torque and generator constants, the motor's electrical resistance, the gear ratio and the structures frequency. The motor back emf is used by the feedback control to provide increased damping.

Many slewing control experiments have been performed. Juang<sup>3</sup> et al illustrates an increase in damping from 2% to 17.5% in the first mode of a steel beam and to 15.57% in the first mode of a slewing solar panel. This increased damping allows the slewing maneuver to be performed faster than without active damping.

A variation of the slewing maneuver is sketched in figure 2. In this case the motor is used as a hinge to connect two beam segments, one of which is cantilevered the other free to rotate. Figure 3 shows the step response of the second mode of the combined beam and motor system. Note that the second mode damping is increased from .04 to .18 as reported by Cudney<sup>4</sup>, et al. Unfortunately, the first mode damping ratio increases very little. The reason for this is that the hinge is close to a node of the first mode of the combined structure and hence has difficulty adding damping to that mode. Hence, it seems plausible that a passive damping material could be used in combination with the active system to enhance the closed loop systems behavior.

Another example of active damping is provided by a proof-mass actuator.<sup>5</sup> This solenoid like device is a self contained space realizable actuator capable of providing velocity feedback at its mounting point. As shown by Zimmerman<sup>5</sup> et al, this actuator increases the damping in a meter long beam from 1% to 9.4% as illustrated in figure 4.

Again, as in the case of the slewing control experiments, situations often arise with feedback control systems that can benefit by the combined use of both active and passive damping. This has been recently discussed by Miller and Crawley<sup>6</sup> for inertial mass or proof-mass actuators.

### IV. Conclusions

It is shown that active damping is capable of yielding larger loss factors per same geometric shape and mass than passive damping treatments in some cases. Often both passive and active added damping are needed to provide the best response. The results of several active damping experiments were summarized. There exists a need for more comparisons between active and passive damping as well as for design criteria to be established. Combined design of active and passive damping is encouraged.

### V. References

1. Nashif, A.D., Jones, D.I.G. and Henderson, J.P., *Vibration Damping*, John Wiley and Sons, 1985.
2. Bailey and Hubbard, J., "Distributed Piezoelectric-Polymer Active Vibration Control of a Cantilever Beam," *AIAA Journal of Guidance, Control and Dynamics*, Oct. 1985, pp. 605-611.

3. Juang, J-N., Horta, L.G. and Robertshaw, H.H., "A Slewing Control Experiment for Flexible Structures," *AIAA Journal of Guidance, Control and Dynamics*, Vol. 9, No. 5, Sept.-Oct. 1986, pp. 599-607.
4. Cudney, H.H., Inman, D.J. and Horner, G.C., "Vibration Control of Flexible Beams Using an Active Hinge," *Proceedings of the 5th VPI and SU Symposium on Dynamics and Control of Large Structures*, July 1985, pp. 19-26.
5. Zimmerman, D.C., Horner, G.C. and Inman, D.J., "Microprocessor Controlled Force Actuator," *AIAA Journal of Guidance, Control and Dynamics*, Vol. 11, No. 3, May-June 1988, pp. 230-236.
6. Miller, D.W. and Crawley, E.F., "Theoretical and Experimental Investigation of Space-Realizable Inertial Actuation for Passive and Active Structural Control," *AIAA Journal of Guidance, Control and Dynamics*, Vol. 11, No. 5, Sept.-Oct., 1988, pp. 449-458.

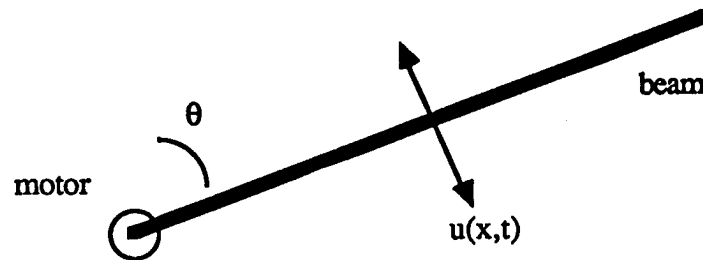


Figure 1. Schematic of a slewing maneuver.

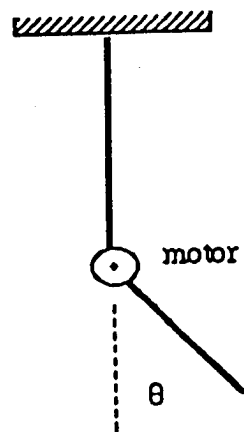
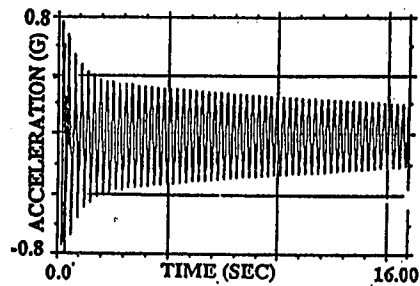


Figure 2. A two beam, or hinged beam slewing control.

o Uncontrolled Structure



o Controlled Structure

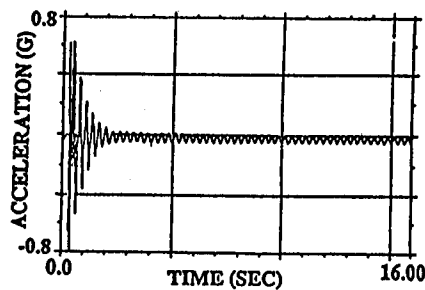


FIGURE 4

Figure 3. Comparison of active damping obtained with proof-mass actuator.

#### TRANSIENT RESULTS

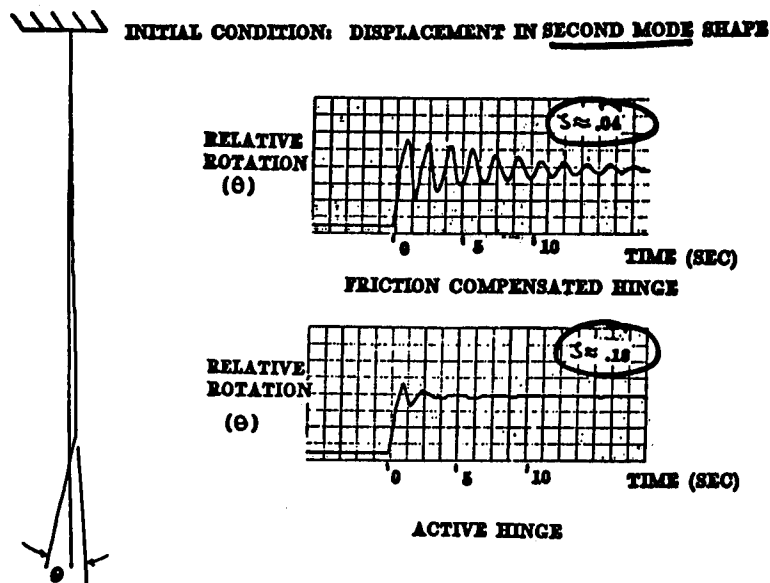


Figure 4. Damping for controlled (bottom) and uncontrolled (top) hinge.

## **DAMPING OF A LARGE SPACE PLATFORM**

**Andrew S. Bicos  
McDonnell Douglas Space Systems Company  
Huntington Beach, California 92647  
(714) 896-1534**

### **ABSTRACT**

An investigation of the damping needed to satisfy stringent settling time requirements typical of several classes of large space platforms was conducted. The method investigated for decreasing the settling time was to use composite materials for the structure and to then increase the damping of certain critical members. In general, composites are more stiff and have higher material damping than aluminum; therefore, a composite structure will have decreased settling time compared to an aluminum structure. This investigation showed that by using composite materials the platform settling time can be reduced by a factor of more than two. This reduced settling time does not satisfy the more stringent settling time requirements of some spacecraft; therefore, more damping can be added to further reduce the settling time. The damping in each critical member has to be increased beyond what is usually available from passive or active means alone. Therefore, both passive and active damping will be required. The degree to which each will be utilized is being determined in an ongoing controls-structure interaction (CSI) program at McDonnell Douglas Space Systems Company.

### **INTRODUCTION**

Space truss structures suitable for large space platforms, such as required by the space station, large deployable reflectors, and space-based weapon systems, can have strict performance requirements, which include (1) minimum structural weight to minimize launch costs, (2) survivability in the natural and hostile space environment, and (3) very short settling times for structural vibrations caused by rapid maneuvers of the platform to maximize observation and/or firing time. The settling time was chosen as the primary performance requirement in this investigation. Designs and methods for achieving the required performance in the more stringent cases have not yet been demonstrated. The high specific stiffness and damping of composite materials make them ideal candidates for applications that require increased performance. The increase in performance due to the composite material alone, however, only will satisfy some less stringent requirements, such as those of the initial phase of the space station; for more stringent requirements, such as those of a tactical neutral particle beam (NPB) platform, a larger increase is needed.

An investigation of how much damping is needed to satisfy these requirements was conducted. The role of passive damping in the satisfying of the requirements was also studied. The primary method investigated



for increasing the damping of the platform, and thereby increasing its performance, was to increase the damping of certain critical members. This approach showed that by increasing the damping of only a few critical members, which were determined by looking at the amount of strain energy in the members, the damping of the whole platform could be significantly increased. The damping in each critical member had to be increased beyond what is probably available from passive or active methods alone. Therefore, both passive and active damping will be required. The degree to which each will be utilized is being determined in an ongoing controls-structures interaction (CSI) effort. The first part of that study looked at the interaction of passive damping and active damping on the space station.

## DAMPING REQUIREMENTS

The existing preliminary design of the Neutral Particle Beam Integrated Space Experiment (NPB-ISE) truss structure was used as a baseline in the investigation. A detailed NASTRAN model of the NPB platform was developed before the NPB program was cancelled, therefore, in order to save time and money this model was used as the baseline space platform model. The material used in the baseline platform was aluminum. The physical properties of the baseline platform are on Figure 1. The settling time was selected for determining the damping needed to satisfy space platform mission requirements. The settling time is defined in the present context as the time between the end of the slew maneuver of the platform and the residual vibration amplitudes becoming less than the allowable deformations. The settling time is a function of the inverse of the product of specific stiffness and damping of the structure. The time required for the reduction of dynamic structural deflections to an acceptable level is shortened as the specific stiffness and damping increase. Compared with aluminum, advanced composite materials have up to 7 times the specific stiffness and up to 10 times the damping [1,2]. Plotted in Figure 2 is the bending vibration

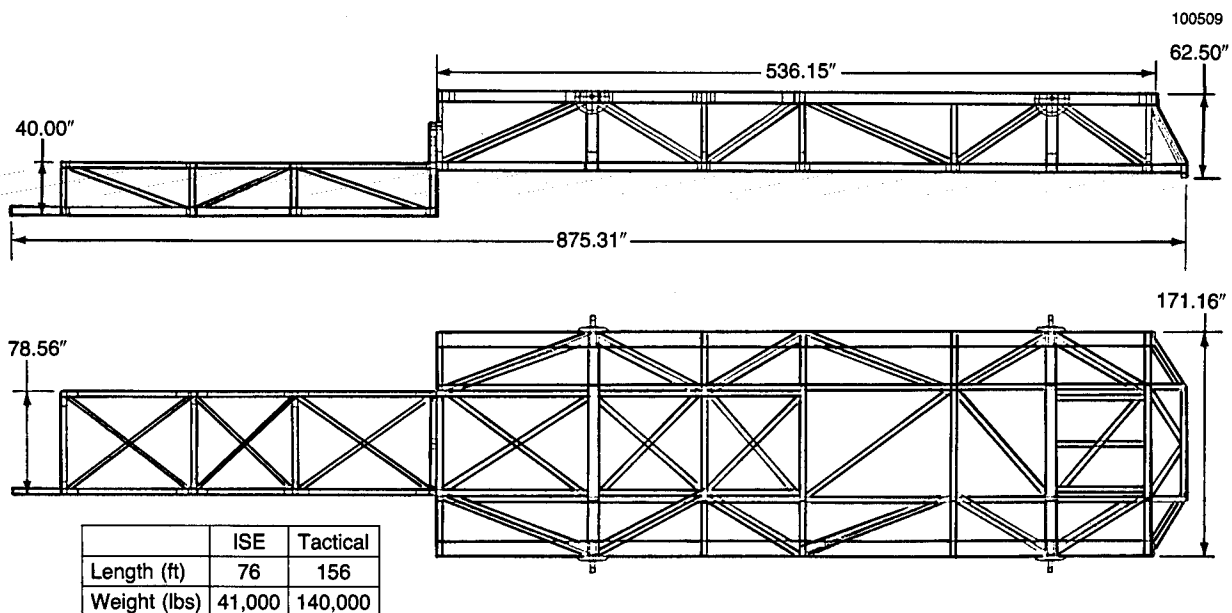
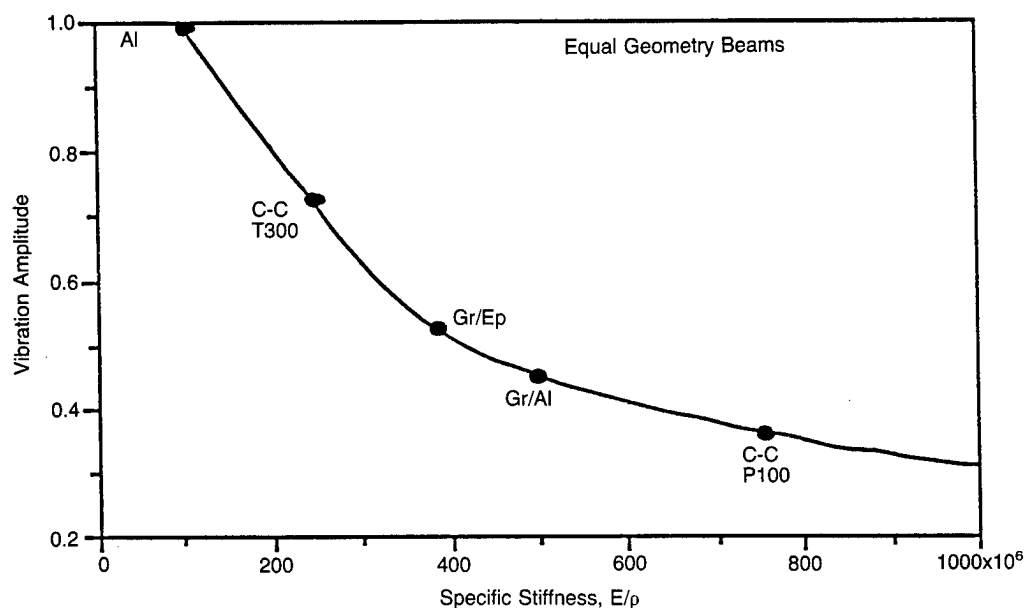


Figure 1. NPB Physical Properties



**Figure 2. Amplitude of Vibration Versus Specific Stiffness. Amplitudes Normalized with Respect to Aluminum**

amplitude as a function of material specific stiffness for equal geometry beams subjected to the same excitation. Plotted on top of this curve are several points representing typical composite materials and the curve is normalized with respect to the amplitude of an aluminum beam. Figure 2 shows that by using a composite material the amplitude of the response can be significantly reduced without even considering damping. The use of materials with higher specific stiffness to reduce the amplitude of the structural response to acceptable levels may be good enough for some applications but is still far from good enough for the more stringent requirements of a space-based weapon system, which is the technology driver in this case.

The baseline NPB model structural members were redesigned for several composite materials. The members were resized such that the total platform weight remains constant for each design. Then the performance of each is evaluated based on settling time. There are two displacements that settling time depends on, one is the initial displacement due to the residual vibration and the other is the displacement requirement at the point of interest. The initial displacement depends on the external excitation, in this case the slow maneuver forcing function. Therefore, to obtain an initial displacement typical of a tactical NPB space platform during operation a slow maneuver and corresponding thruster forces had to be selected. The typical slow maneuver selected was 10 degrees pitch in less than one second. The thrusters were chosen to be located at the four corners of the main part of the platform, as shown in Figure 3. The thruster forces and firing profile had to be chosen such that the required slow maneuver produced typical initial displacements. The thruster firing profile selected was a bang-bang type tuned to the fundamental frequency of the platform, as shown in Figure 3b. The tuning of the thruster firing profile gives reasonable initial displacements and is a first cut at optimizing the thruster firing profile. If the tuning is not done,

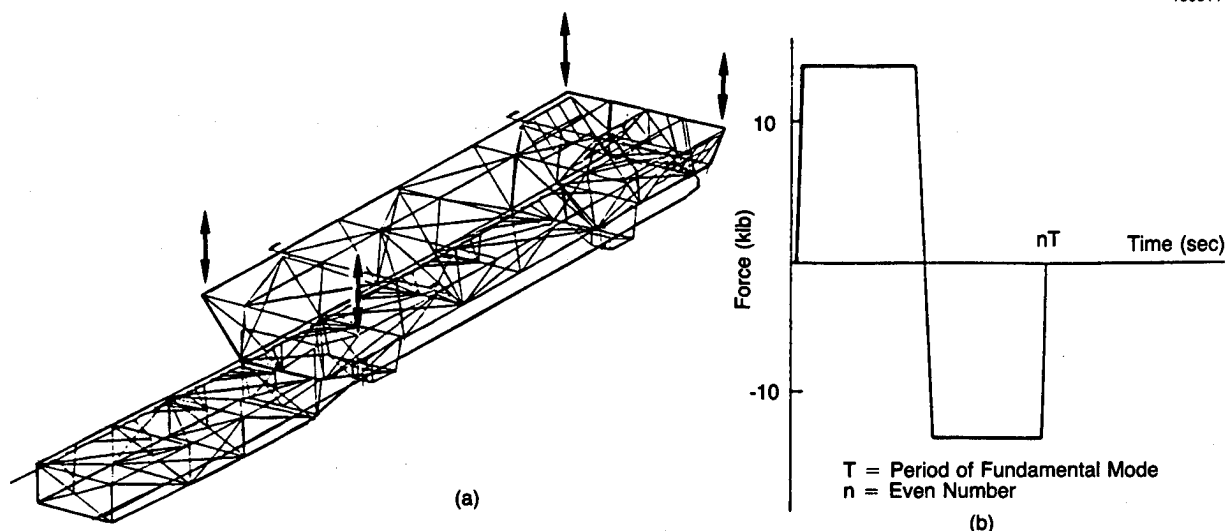


Figure 3. (a) Thruster Locations and Directions, (b) Force Profile for Each Thruster

then unusually large displacements result from the residual vibration, as shown in Figure 4. The resulting magnitude of the thruster forces is about 13,000 pounds at each of the four thruster locations. These are large forces and they induce large stresses in the structure.

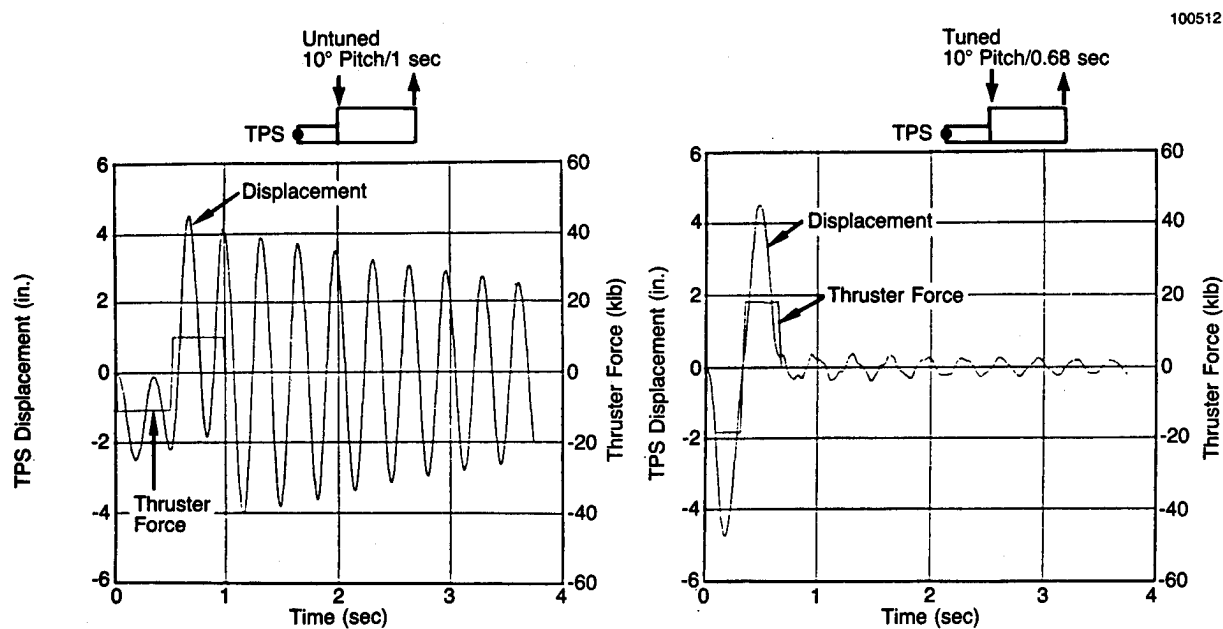


Figure 4. Thruster Tuning Effects on Structural Residual Vibration Amplitude at the Tracking and Pointing System (TPS) Location

The performance of the baseline truss, i.e., the NPB-ISE platform, was determined using the slew maneuver described above. The fundamental frequencies, slew maneuver, thruster force, damping, and settling times are given in Table 1. The settling time for the aluminum baseline platform vibration amplitudes to decrease to below the 0.001 inch requirement at the tracking and pointing system (TPS) location is about 250 seconds, which is about 600 times greater than required.

Two advanced composite materials were selected so that a comparison with the performance of the baseline platform could be made. The materials selected were graphite-epoxy (Gr/Ep) and graphite-aluminum (P100-Gr/Al). These materials were chosen because their properties are typical of advanced materials. The baseline truss members were redesigned for each of these materials so that the weight of the structure would remain constant for comparison purposes.

The results for the performance evaluation are given in Table 1, along with the results of the aluminum baseline platform. The settling time is a function of the inverse of the product of the frequency of vibration and the damping at the frequency. Therefore, the larger the frequency and damping, the shorter the settling time. Considering the frequency data alone the most promising candidate material seems to be the graphite-aluminum. Because of its high specific stiffness, it has the highest fundamental frequencies and thus the shortest settling time if the damping of the materials considered was the same. The damping of the materials, however, is not the same. The aluminum and the graphite-aluminum have approximately equal damping factors[1], while the graphite-epoxy can have many times the damping of aluminum depending on the layup of the composite[2]. Therefore, both the graphite fiber composites are good candidate materials. Assuming typical damping ratios for the materials gives settling times on the order of hundreds of seconds, which is much larger than the required settling times. Therefore, assuming that

**Table 1. Performance Evaluation Based on NPB-ISE NASTRAN Model**

100516

Primary Structural Material		Al	Gr/Al	Gr/Ep
Fundamental Frequencies (Hz)	Longitudinal Bending	2.96	6.15	4.96
	Torsion	4.75	10.04	8.02
	Transverse Bending	5.63	11.78	9.50
Tuned 10° Pitch Slew Maneuvering Time, $T_M$ (sec)		0.676	0.650	0.812
Required Thruster Force (klbs)		13.0	13.5	10.8
Material Damping, $\zeta$ (%)		0.1	0.1	0.35
Total Time: Slew Initiation to Weapon Firing, $T_T$ (sec)		1.1	1.1	1.1
Calculated Settling Time, $T_S$ (sec)		247	119	43
Required Settling Time, $T_R$ (sec) ( $T_M + T_R \leq T_T$ )		0.424	0.450	0.288
Ratio of Calculated to Required Settling Time, $T_S/T_R$		583	264	149

h5068: 516 03/06/89

these are the materials that will be used on SDI-type platform structures, one way to decrease the settling time is to increase the damping in the structure.

If damping is to be added to the structure to decrease the settling time, the question is how much damping is needed in the structure? Using the data in Table 1, the total damping needed by the NPB platform structure is plotted as a function of the required settling time for the candidate materials in Figure 5. For the graphite-aluminum platform the total damping needed is about 20 to 30 percent. The mechanisms from which the damping is coming have not been specified at this point. This 20 to 30 percent represents the energy dissipation rate that is required to meet the settling time specification for the NPB platform. The damping mechanisms can be passive, active, or a mix of the two depending on the application and design of the structure.

One way of increasing the damping of the structure is to introduce high damping into certain critical members. These members are selected based on the magnitude of the strain energy in them in response to the slew maneuver; those selected as most critical are the ones with the most strain energy and the least critical are those with the least. In the model a certain number of critical members, which originally have a nominal damping ratio of one percent, are replaced with members having much higher damping ratios. Plotted in Figure 6 is the damping ratio of the overall structure as measured by the response decay at the TPS position as a function of the number of replaced members. The members are replaced with other members having 10, 20 and 40 percent damping ratios. As can be seen from Figure 6, it only requires relatively few members to be replaced with higher damping members to make a significant difference in the damping of the total structure. For example, looking at Figure 6, if there exist members that have a

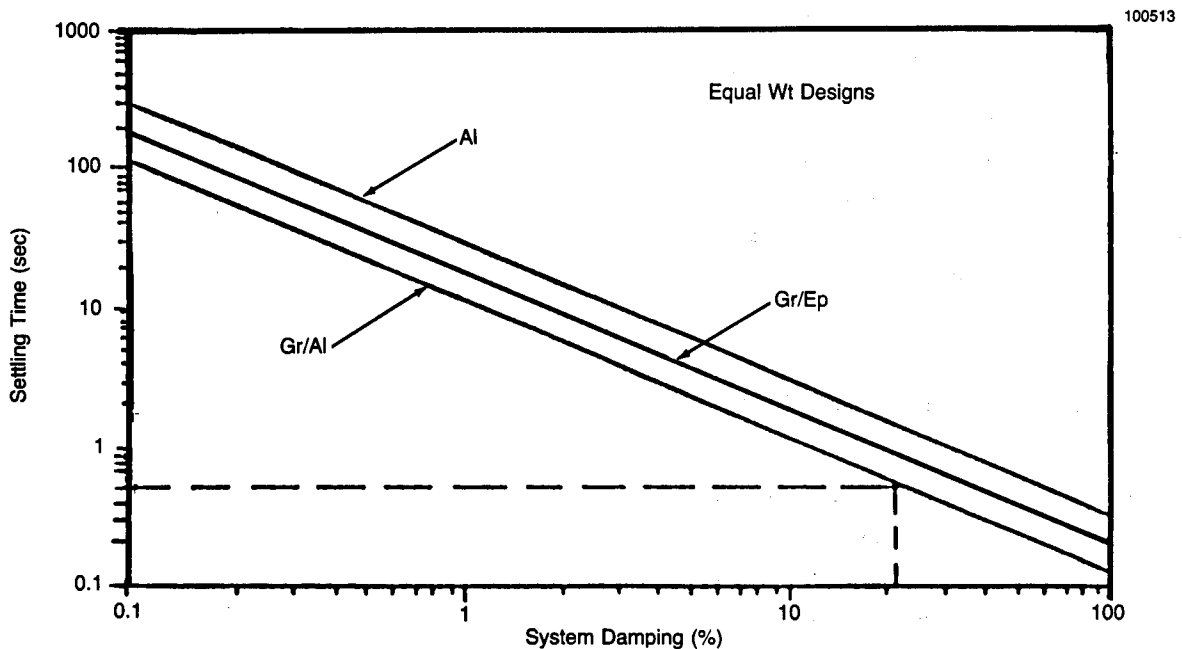
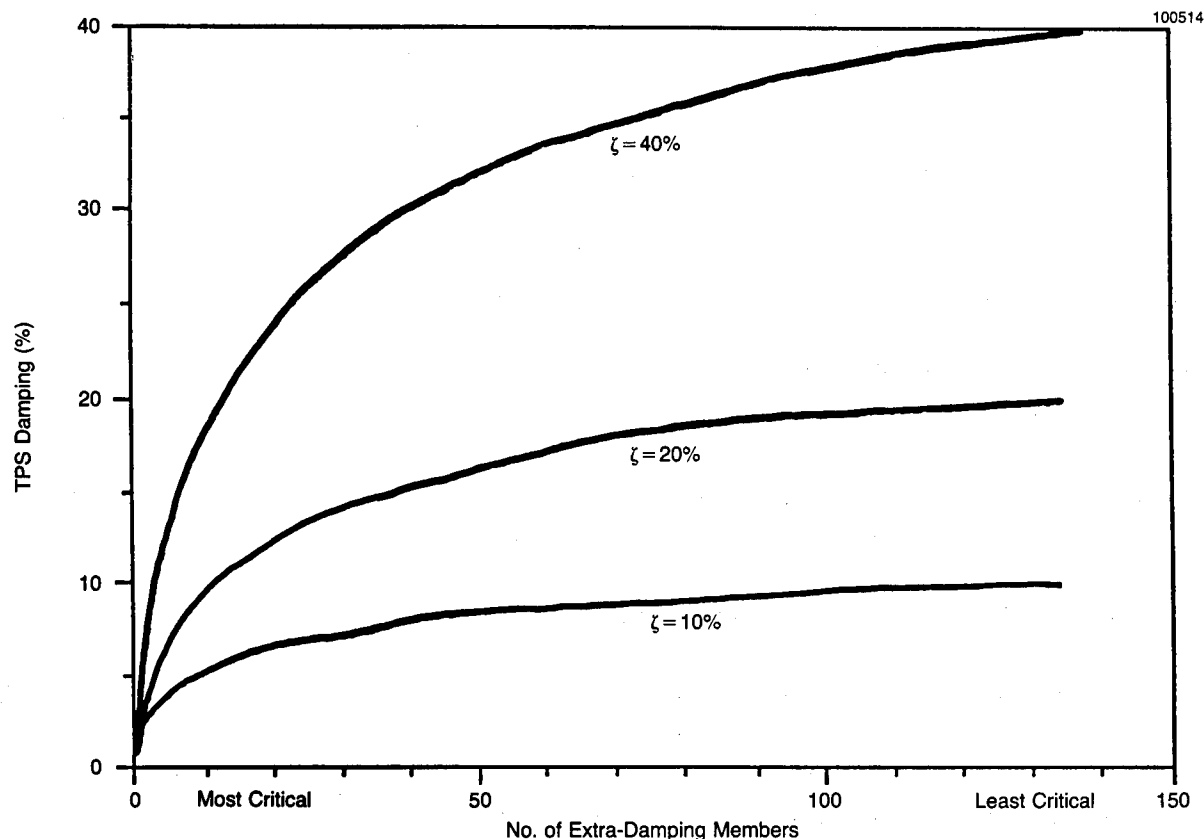


Figure 5. NPB Settling Time Versus Overall System Damping for Various Materials

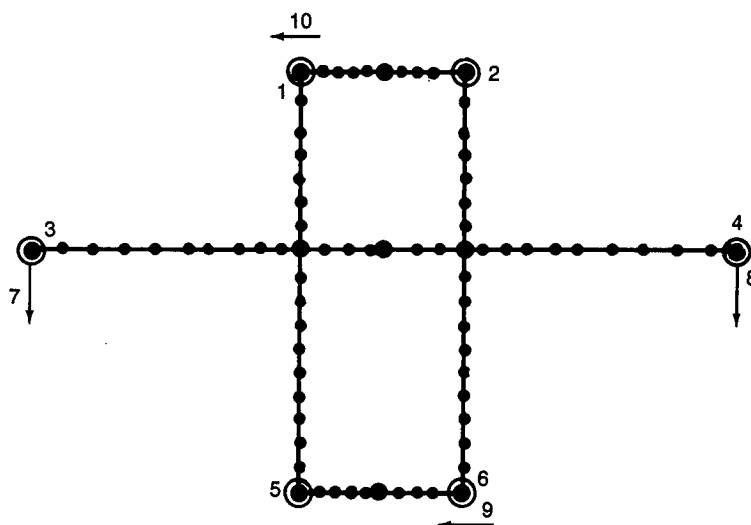


**Figure 6. TPS Damping Versus Number of Extra-Damping Members That Replaced Nominal Damping Members**

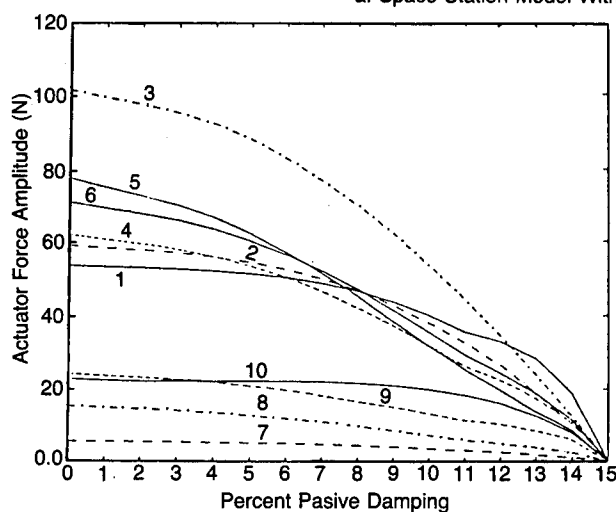
damping ratio of 40 percent then we need only replace 12 of the most critical members out of a total of 134 members to reach an overall structure damping ratio of 20 percent. What the mechanisms are for obtaining members with high damping ratios has not been considered in this study to date. How to obtain these levels of damping (passively, actively, and a mix of the two) in the critical members without significantly degrading the stiffness and increasing the weight of the structure is currently being investigated. The optimum mix of passive and active damping is highly dependent on the spacecraft and mission requirements.

### **PASSIVE AND ACTIVE DAMPING ROLES**

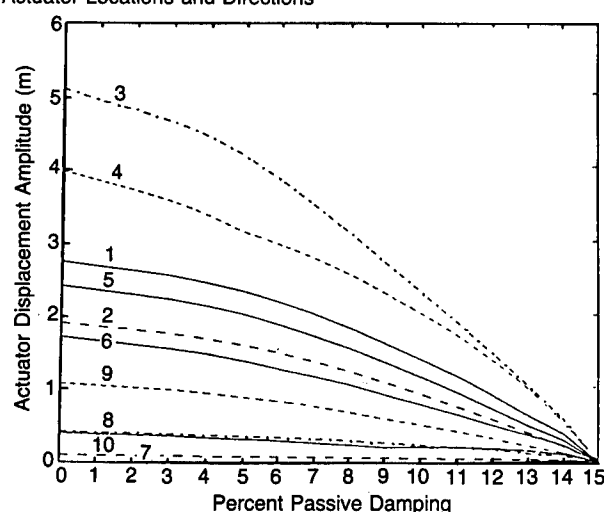
To determine what the roles of passive and active damping should be in the vibration suppression and control of large space platforms a model of the space station was used. This model is shown in Figure 7. The excitation to the structure is representative of a space shuttle hard-docking maneuver at the center of the station. It was desired to investigate how a variation in the passive damping affects the required active control system in terms of actuator forces and displacements and structural displacement at the actuator positions.



a. Space Station Model With Actuator Locations and Directions



b. Actuator Force Amplitudes Versus Passive Damping



c. Actuator Displacement Amplitudes Versus Passive Damping

**Figure 7. Effects of Increased Passive Damping on the Actuator Forces and Displacements for the Space Station**

The actuators selected for this study were proof-mass actuators with the proof-mass component of the actuator weighing 150 pounds. As shown in Figure 7a, there are 81 candidate actuator locations with 3 directions per location giving a total of 243 candidate actuator positions. A low authority controller (LAC) and 10 actuator-sensor pairs were selected. The requirement of 15 percent damping was set. Based on an optimization routine, 10 actuator positions were chosen so as to give at least 15 percent active damping to the 10 most critical modes when the passive damping is negligible. The critical modes were chosen based on the amplitude of the rotation at certain payload positions due to the given excitation. The results of the simulation are presented in Figures 7b and 7c. The actuator force amplitudes are plotted in Figure 7b versus the amount of passive damping. The sum of passive and active damping is always about 15 percent, which is the requirement set above. As can be seen the actuator force required drops off with increasing passive

damping. In Figure 7c the maximum displacement amplitudes of the actuator masses are plotted versus the passive damping. The maximum proof-mass displacement decreases with increasing passive damping. The envisioned design for the space station proof-mass actuators is a 150 pound proof mass running along a truss member. The space station truss longitudinals and battons are 5 meters in length; therefore, if the actuator proof mass is centered before activation, then the maximum it can displace during a control operation is less than 2.5 meters. It can be seen from Figure 7c that if the space station must have at least 15 percent damping ratio and uses proof-mass actuators then either the proof mass of the actuators must increase, the number of sensor-actuator pairs must increase, or the passive damping ratio can be increased to about 11 percent, which would give a proof-mass displacement of about 2 meters.

## CONCLUSION

Beginning with the construction and operation of the space station, the large space platforms that are going to be orbited in the next decade will require varying degrees of damping to perform their missions. In some applications little or modest levels of damping will be required that can probably be handled with either passive or active methods of energy dissipation. There will be some applications like NPB, however, where much more damping is required, say more than 10 percent and up to as high as 40 to 50 percent. To achieve these levels of damping performance will require the use of both passive and active damping methods. As was shown above, the two methods can complement each other, the degree to which this occurs depends on the damping required and the system constraints and characteristics.

## REFERENCES

1. Crawley, E.F. and Van Schoor, M.C., "Material Damping in Aluminum and Metal-Matrix Composites," *Journal of Composite Materials*, Vol. 21, No.6, 1987, pp. 553-568.
2. Bicos, A.S., "Free Damped Vibration of Composite Plates and Shells," Ph.D. Thesis, Stanford University, 1987.



# **ROLE OF PASSIVE DAMPING IN ACTIVE STRUCTURAL CONTROL**

**FEBRUARY 1, 1989**

**JOSEPH GARIBOTTI  
KETEMA, INC.  
CM DIVISION  
3611 SOUTH HARBOR BLVD.  
SANTA ANA, CA 92704  
(714) 545-8825**

**THE RESULTS CONTAINED IN THIS BRIEFING WERE GENERATED  
BY THE FOLLOWING INDIVIDUALS**

<b>DR. JOSEPH F. GARIBOTTI</b>	<b>KETEMA INC. / CMD</b>
<b>DAN M. NGUYEN</b>	<b>KETEMA INC. / CMD</b>
<b>P. J. LAD</b>	<b>KETEMA INC. / CMD</b>
<b>DR. ARUN NAYAK</b>	<b>CONSULTANT</b>
<b>DR. D. L. MINGORI</b>	<b>PROFESSOR OF MECHANICAL ENGINEERING, UCLA, CONSULTANT TO KETEMA INC. / CMD</b>
<b>JONG YI LIN</b>	<b>PHD STUDENT, UCLA, CONSULTANT TO KETEMA INC. / CMD</b>

**OBJECTIVE:**

Large space structures are vulnerable to vibration problems due to rapid maneuvering disturbances. To obtain stability and pointing accuracy, a vibration control method (i.e. the integration of passive damping with an active structural control system) has been used to study structural responses.

# **OBJECTIVE**

---

## **TO INVESTIGATE:**

- **THE ROLE OF PASSIVE DAMPING ON DYNAMIC RESPONSE OF ACTIVELY CONTROLLED LARGE SPACE STRUCTURES, e.g. SBL**
- **EFFECT OF PASSIVE DAMPING ON THE COMPLEXITY OF ACTIVE STRUCTURAL CONTROL SYSTEM DESIGNS**

#### ADVANCED MATERIALS FOR SPACE STRUCTURES - VIBRATION SUPP.

The structural response of a large SBL spacecraft can be studied by establishing a simple finite element model. A control system using 21 collocated sensors and actuators were mounted on the structure and parametric studies were performed wherein control forces and control effort were calculated versus passive system damping (modal damping). The LOS requirement was assumed to be 50 nanoradians within 3.0 seconds of end of slew.

**ADVANCED MATERIALS FOR  
SPACE STRUCTURES  
VIBRATION SUPPRESSION**

---

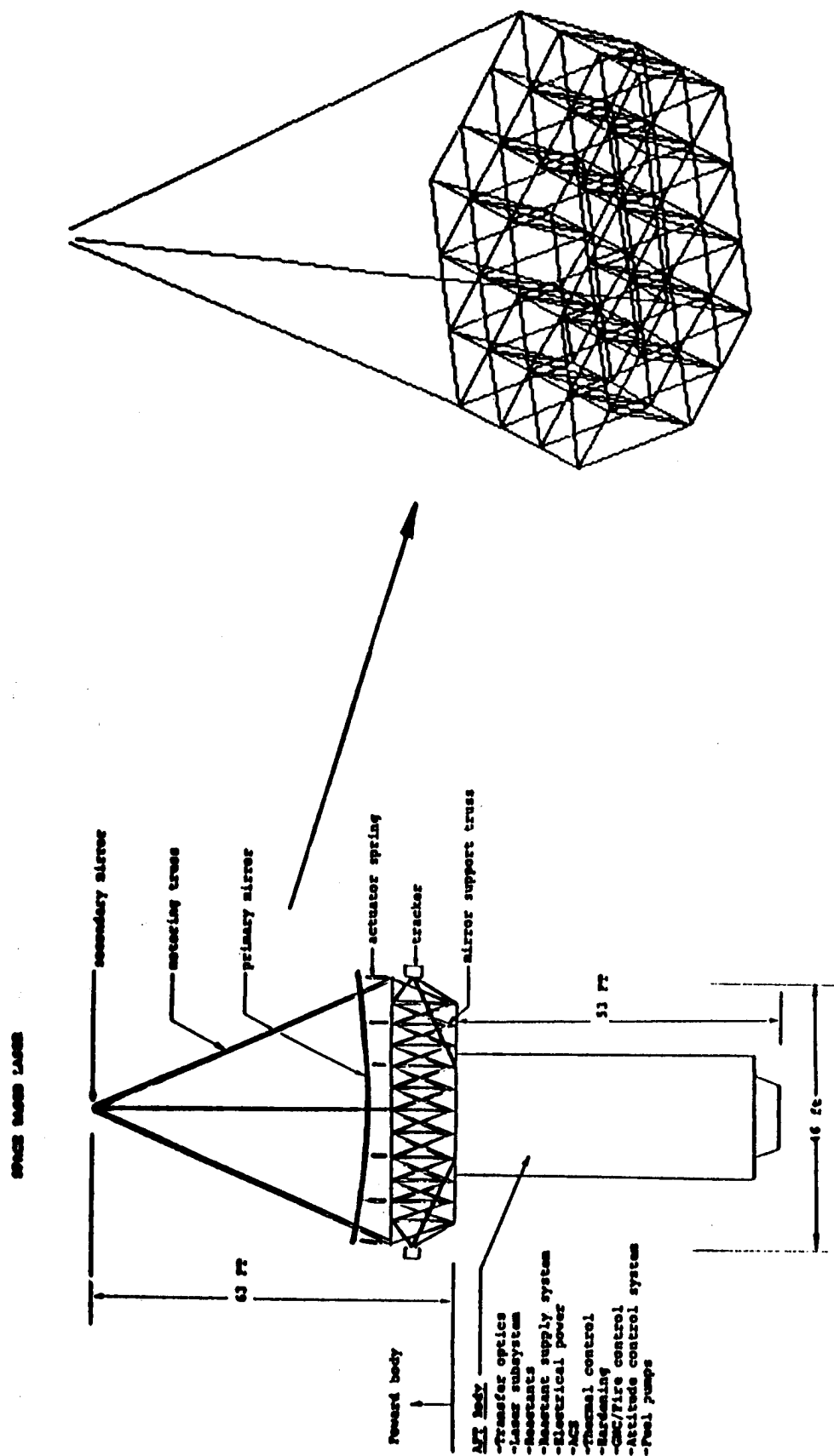
**ACTIVE CONTROL / PASSIVE DAMPING SYNERGISM STUDY**

- **VERY PRELIMINARY RESULTS**
- **GENERIC SBL RETARGET**
- **24 FLEXIBLE MODES**
- **21 COLLOCATED SENSOR/ACTUATORS**
- **1 SEC. BANG-BANG TORQUE PROFILE**
- **AT 1.1 SEC. ACTIVE CONTROL TURNED ON**
- **REQUIREMENT AT 3.0 SEC. IS 50 NANORADIANS**

#### **FINITE ELEMENT MODEL - SBL**

The design of this SBL system is based on a generic design that was generated by the AFWL. The SBL structure is 116 feet long; it consists of two parts: a forward body and an AFT body. The forward body section consists of a secondary mirror, metering truss, and primary mirror. The metering structure is a tripod structure that provides accurate alignment/separation of the primary and secondary mirrors.

# FINITE ELEMENT MODEL SBL



FEM MODEL

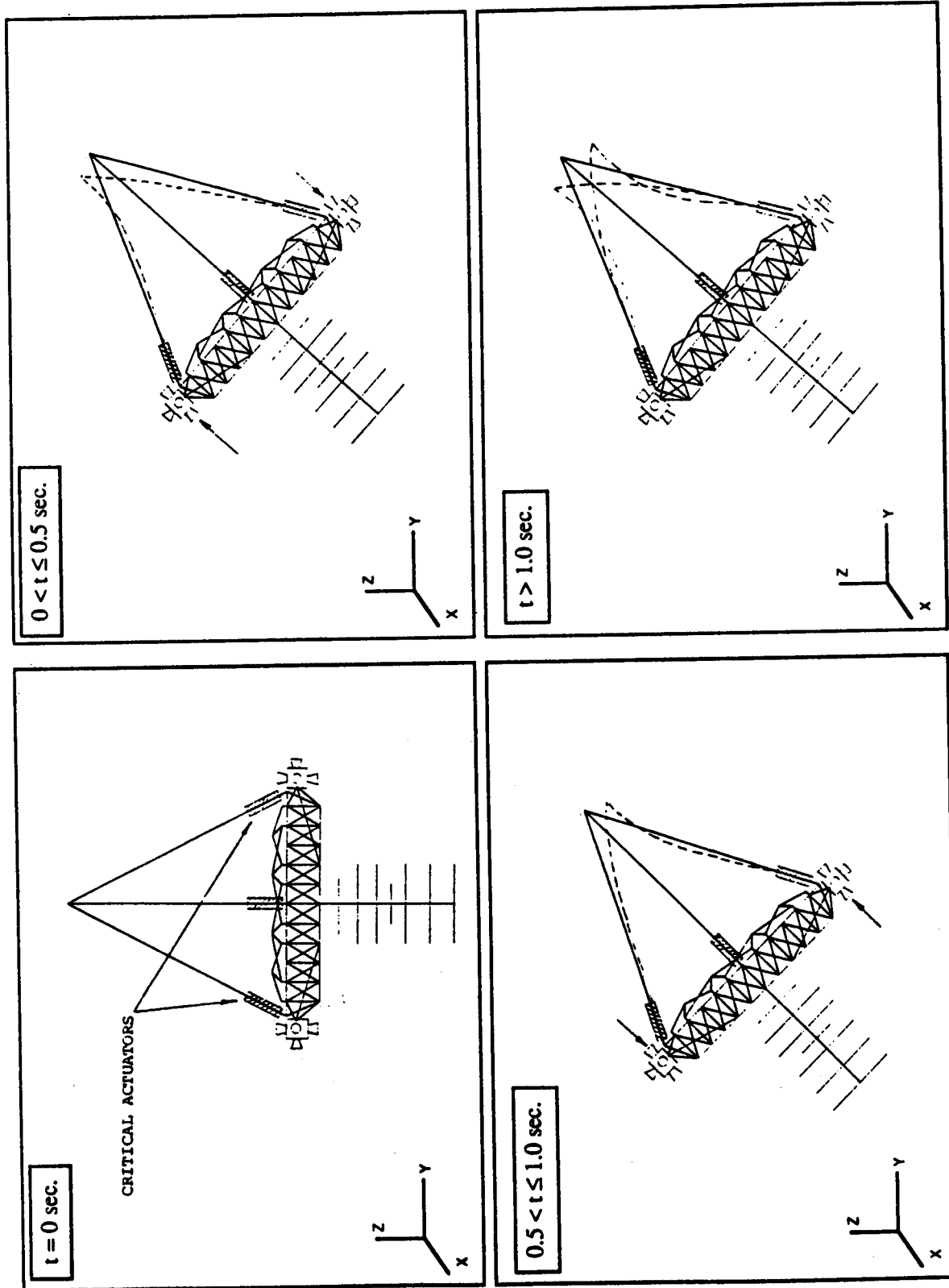
SBL DESIGN



#### **ADVANCED MATERIALS FOR SPACE STRUCTURES - VIBRATION SUPP.**

The slewing and retargeting is mathematically generated by firing the jets in equal and opposite directions to create enough thrust to turn the beam expander 10 degrees from the original position. The time interval for forward firing and reverse firing is a total of 1 second.

# ADVANCED MATERIALS FOR SPACE STRUCTURES VIBRATION SUPPRESSION



### SPACE BASED LASER - MODAL ANALYSIS DESCRIPTION

The modal analysis was performed on this SBL structural model with three different specific stiffness values. The eigenvectors are calculated by the unit mass normalized method (  $\phi^T M \phi = I$  ) where  $\phi$  = eigenvector matrix and  $M$  = mass matrix and they are subsequently used for generating the state variables.

# **SPACE BASED LASER MODAL ANALYSIS DESCRIPTION**

---

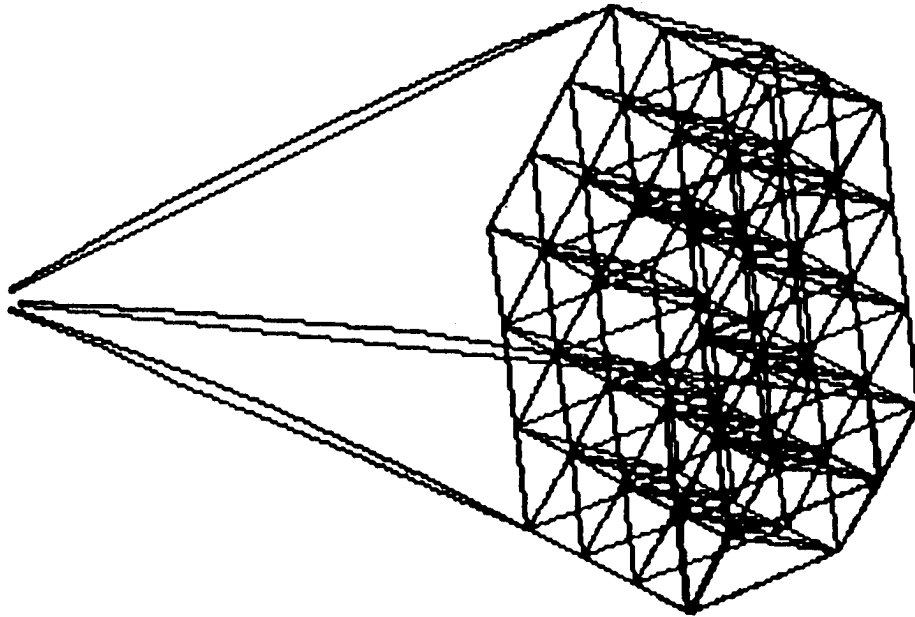
- **SET UP FINITE ELEMENT MODEL**
  - 164 NODES
  - 253 BAR ELEMENTS
  - 21 ELASTIC SPRING ELEMENTS
  - 51 CONCENTRATED MASS ELEMENTS
  - 22 RIGID BODY ELEMENTS
- **CALCULATE NATURAL FREQUENCIES AND  
MODE SHAPES**
  - MASS NORMALIZED MODE SHAPE CALCULATION
  - SIGNIFICANT MODES ARE PLOTTED FOR CONTROL  
SYSTEM DESIGN

### **TYPICAL MODE SHAPE**

The mode shape plot reveals the natural responses of all structural members. The deflected shape of the structure is used for determining critical vibration locations, so that the control system designer knows where to install the collocated sensors and actuators in order to obtain optimal damping, thereby achieving the LOS requirement effectively.

# **TYPICAL MODE SHAPE**

(THIRD FLEXIBLE MODE - FREQUENCY = 12.856 Hz.)



#### PREPARATION FOR CONTROL DESIGN AND ANALYSIS

MATLAB was used in the control system design procedure. Prior to using MATLAB, the control system designer must generate the eigenvector matrix, eigenvalue matrix, system damping matrix, directional cosine matrix (nodal connectivity of linear actuators and sensors), and control distribution matrix.

# **PREPARATION FOR CONTROL DESIGN AND ANALYSIS**

---

- **ANALYTICAL TOOLS**
  - **MATLAB**
- **PRE-PROCESSING PROCEDURE**
  - **CONVERT FINITE ELEMENT ANALYSIS RESULTS INTO MATLAB FORMAT**
  - **LOCATE ACTUATORS AND SENSORS AT THE CRITICAL (MAXIMUM DEFLECTION) LOCATIONS**
  - **COMPUTE DIRECTION COSINES AT EACH ACTUATOR LOCATION; GENERATE CONTROL DISTRIBUTION MATRIX**



### CONTROL SYSTEM DESIGN & ANALYSIS PROCEDURE

In this parametric study, 30 modes are used for the control design and analysis. There are 6 rigid body modes and 24 flexible modes. The 6 rigid body modes are considered as slew motion (i.e. the entire SBL structure moves from one reference position to another). The time interval for slewing the SBL structure 10 degrees was assumed to be 1.0 second. At 1.1 seconds the vibration control system is activated to damp out the vibration due to the 24 flexible modes. The actuators/sensors control system continue to function until the LOS requirement is achieved (e.g., LOS error is less than or equal to 50 nanoradians within 2.0 seconds).

# **CONTROL SYSTEM DESIGN AND ANALYSIS PROCEDURE**

---

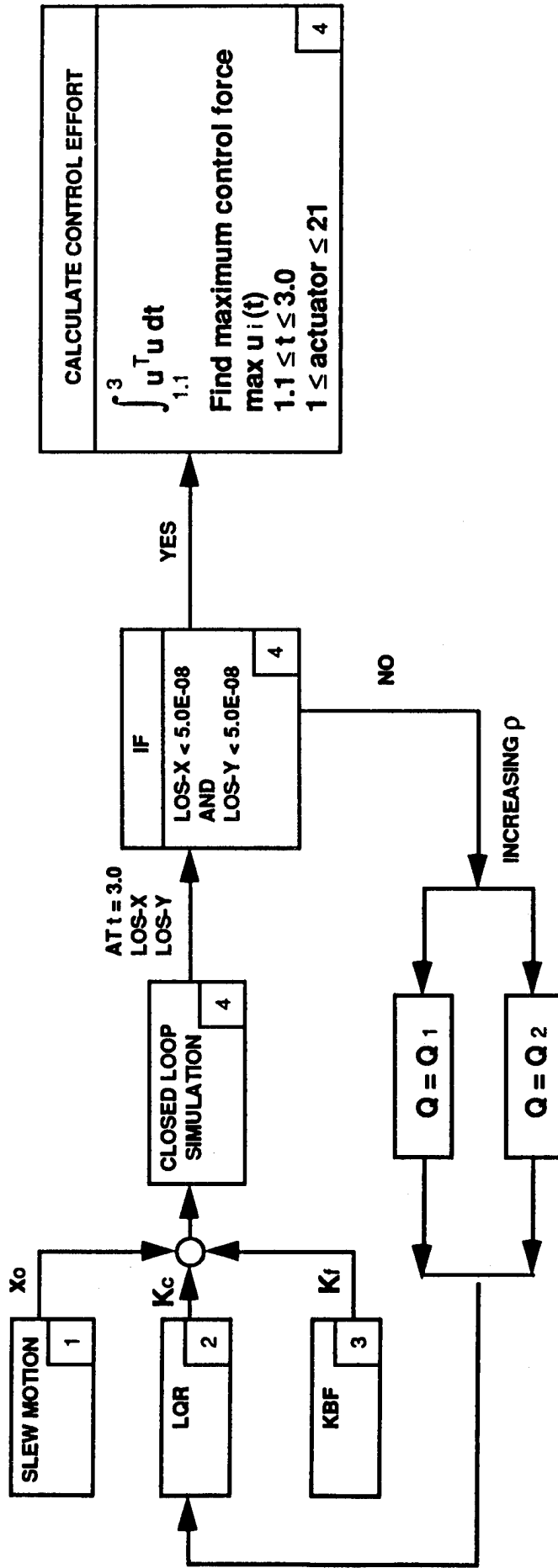
---

- **SLEW MOTION (RIGID BODY MODES)**
  - SLEW TO A DESIRED POSITION ( $10^\circ$ ) USING JET FORCES (IN 1 SECOND)
  - CONSIDER 6 RIGID BODY MODES AND 24 FLEXIBLE MODES
  - LET THE RIGID BODY MOTION STOP AT THE END OF THE SLEW
  - FIND THE STATE AT 0.1 SECOND AFTER THE SLEW
- **ACTIVE CONTROL DESIGN (FLEXIBLE MODES)**
  - SUPPRESS THE VIBRATION DUE TO THE SLEW BELOW 50  
NANORADIANS AFTER  $t = 3$  SECONDS
  - CONSIDER ONLY 24 FLEXIBLE MODES
  - USE THE STATE OF THE FLEXIBLE MODES AT  $t = 1.1$  SEC. AS THE  
INITIAL STATE OF THE ACTIVE CONTROL DESIGN

### **CLOSED LOOP SIMULATION**

**This chart shows the control system design/analysis procedure. Two different expressions were used for representing performance in the objective function, leading to slightly different results as shown in the following charts.**

# CLOSED LOOP SIMULATION



HBC-20

## CODES:

- 1 SIMJET.M
- 2 LORGEN.M
- 3 LOEGEN.M
- 4 ENR.M

(1)

$$(\text{LOS } \dot{x})^2 + (\text{LOS } \dot{y})^2 + (\text{LOS } \ddot{x})^2 + (\text{LOS } \ddot{y})^2 = x \dot{Q}_1 x$$

$$Q_1 \triangleq \text{diag.} (\bar{Q}_1)$$

(2)

$$(\text{LOS } x)^2 + (\text{LOS } y)^2 = x^T \bar{Q}_2 x$$

$$Q_2 \triangleq \bar{Q}_2 + \varepsilon I$$

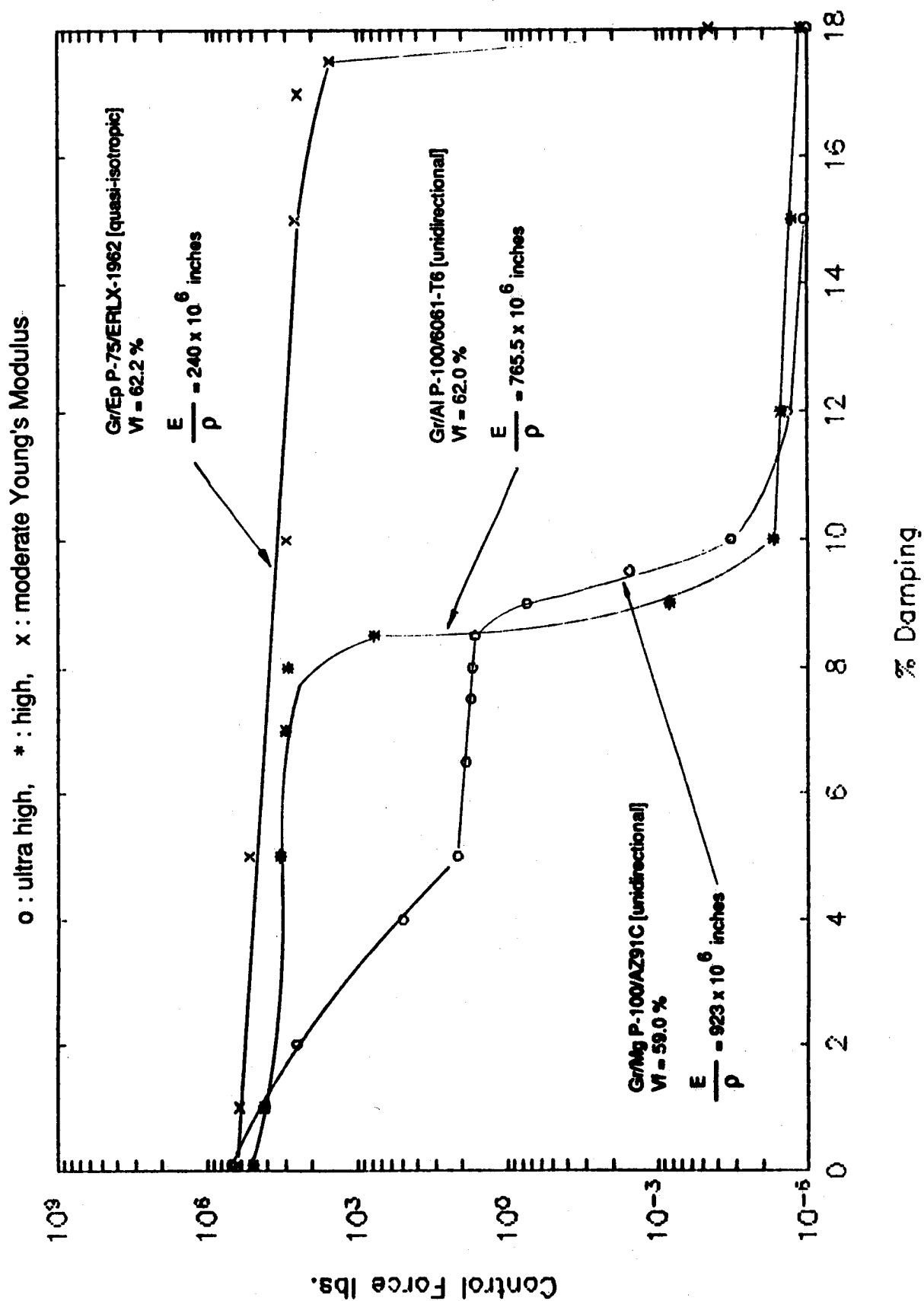
$$\text{where } \varepsilon = 1.0 \times 10^{-18}$$

## **CONTROL FORCE VS.% DAMPING**

### **Case $Q = Q1$**

**In this case the control force provided by the actuators decreases as the system damping increases. For the case of high specific modulus, the control force tends to go near zero at 8.5 % system damping.**

# CONTROL FORCE VS. % DAMPING

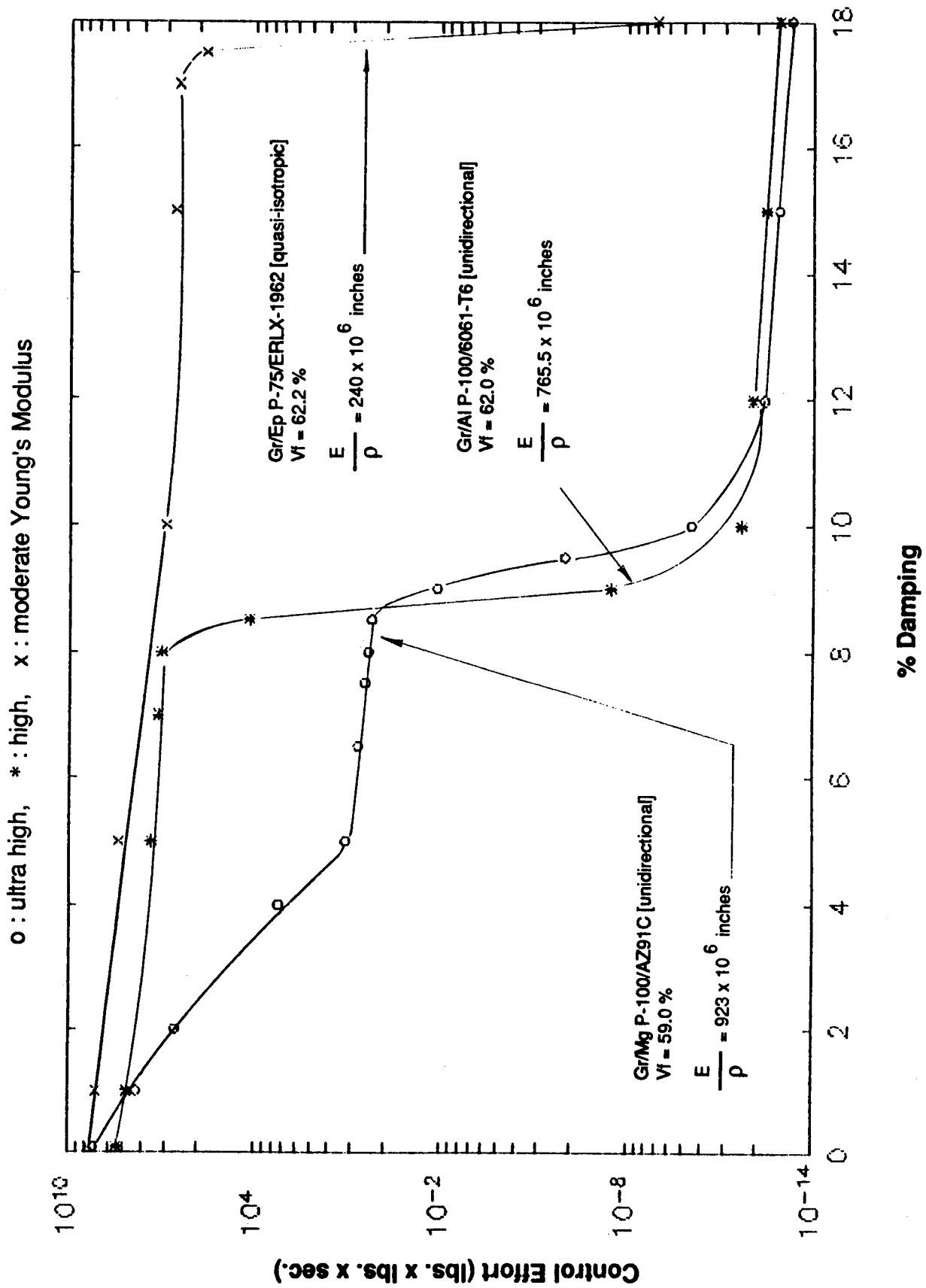


### CONTROL EFFORT VS. % DAMPING

#### Case $Q = Q_1$

For the case  $Q=Q_1$ , the control effort required to control the vibration within the 50 nanoradian limit is plotted against the percent system damping.

# CONTROL EFFORT VS. % DAMPING



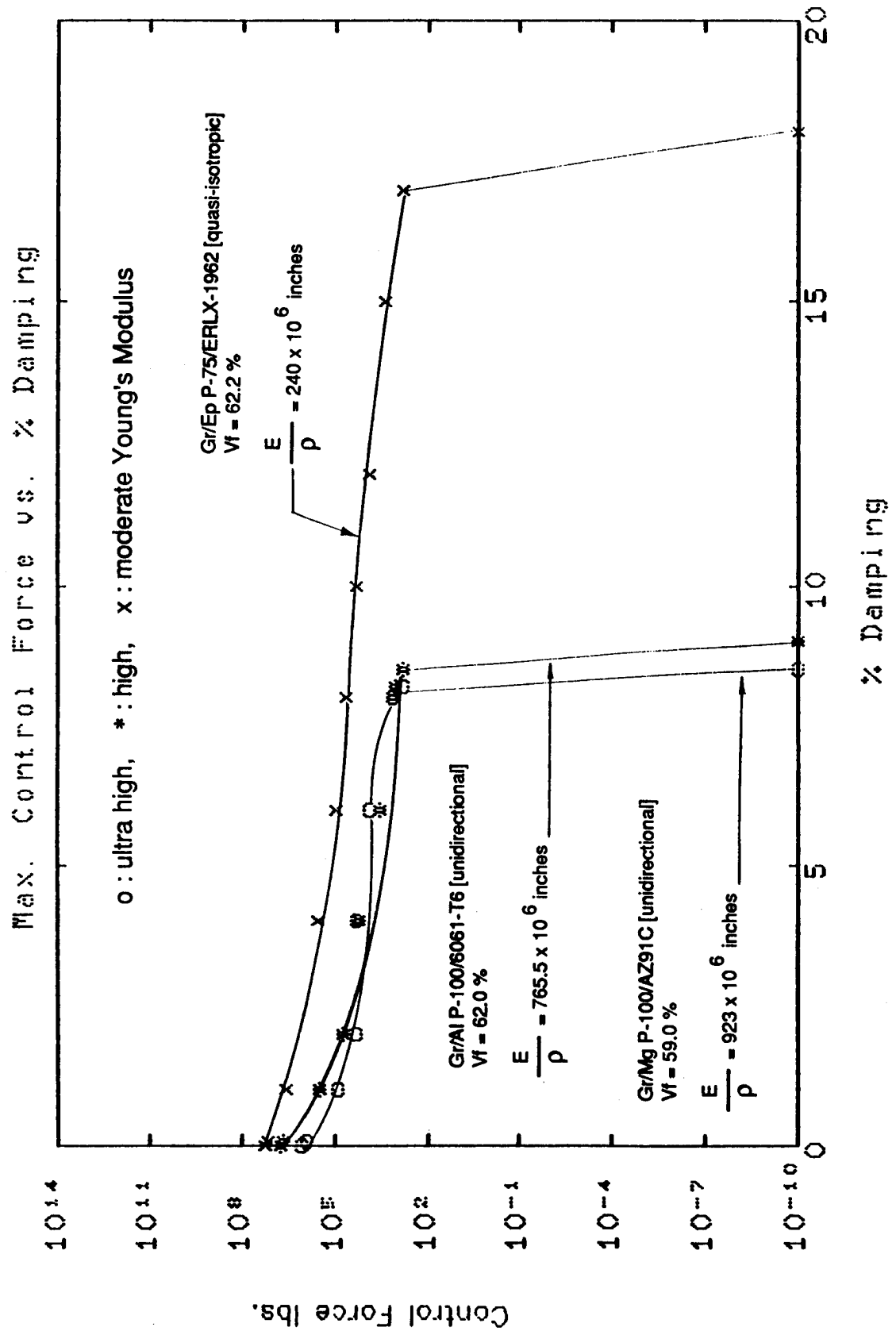


## CONTROL FORCE VS. % DAMPING

### Case $Q = Q_2$

The control force provided by the actuators decreases as the system damping increases. For the case of high specific modulus, the control force tends to go near zero at 8.5% system damping.

# CONTROL FORCE VS. % DAMPING

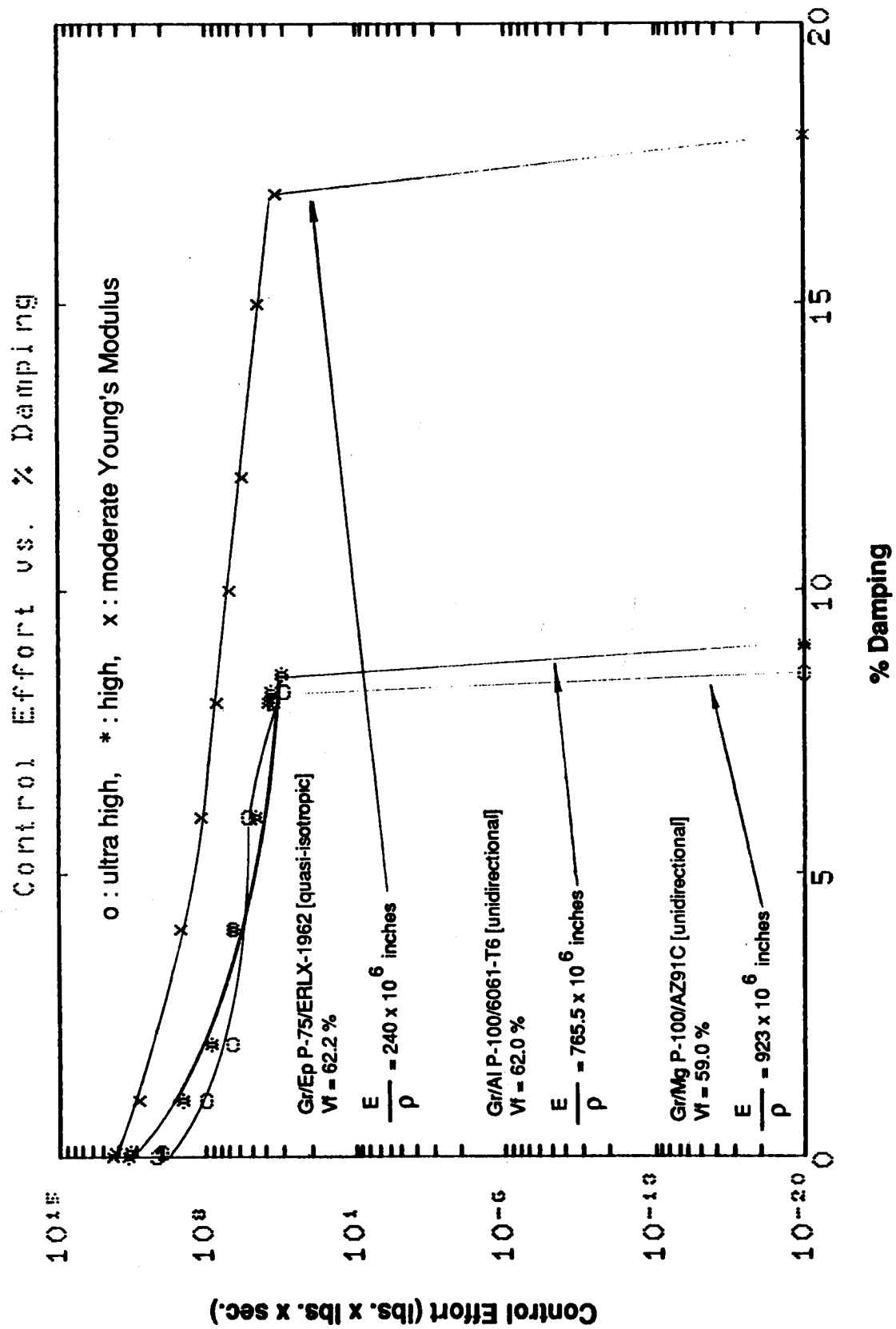


## **CONTROL EFFORT VS. % DAMPING**

### **Case $Q = Q_2$**

**For the case  $Q=Q_2$  the control effort required to control the vibration within the 50 nanoradian limit is plotted against the percent system damping.**

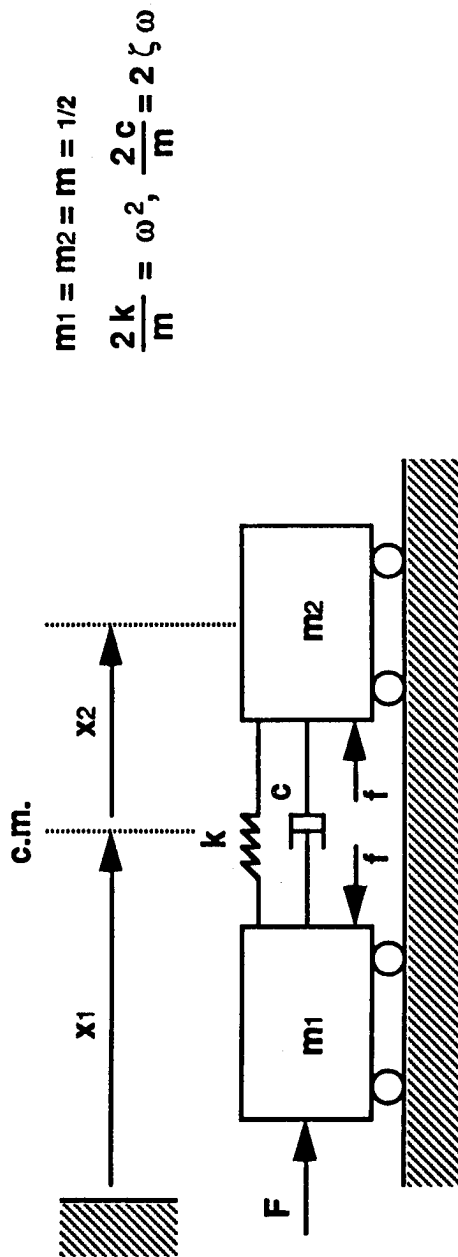
# CONTROL EFFORT VS. % DAMPING



## **TWO MASS SYSTEM**

The role of passive damping together with an active control system on dynamic structural response was also investigated by using a two degree of freedom spring mass system. This two mass system provides insight into the role passive techniques can play in vibration suppression. The provided actuator force for this two mass system is denoted as "f".

# TWO - MASS SYSTEM



## • TWO MODES IN THIS SYSTEM

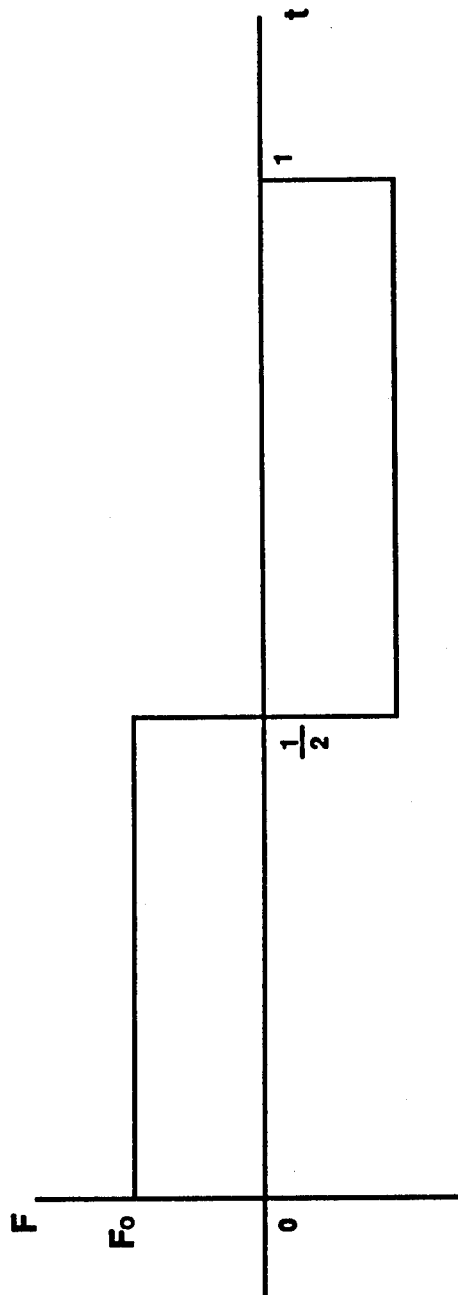
- RIGID BODY MODE :  $\ddot{X}_1 = F$
- FLEXIBLE MODE :  $\ddot{X}_2 + 2\zeta\omega\dot{X}_2 + \omega^2 X_2 = f - F$

## CONTROL SYSTEM DESIGN AND ANALYSIS

The "slew" motion of a two degree of freedom system is mathematically generated by using a step function of magnitude  $F_0$ , and the system is assumed to move 1 unit away from its reference point. The center of mass of the system stops at time equal to 1 second.

# CONTROL SYSTEM DESIGN AND ANALYSIS

- SLEW MOTION ( $f = 0$ )



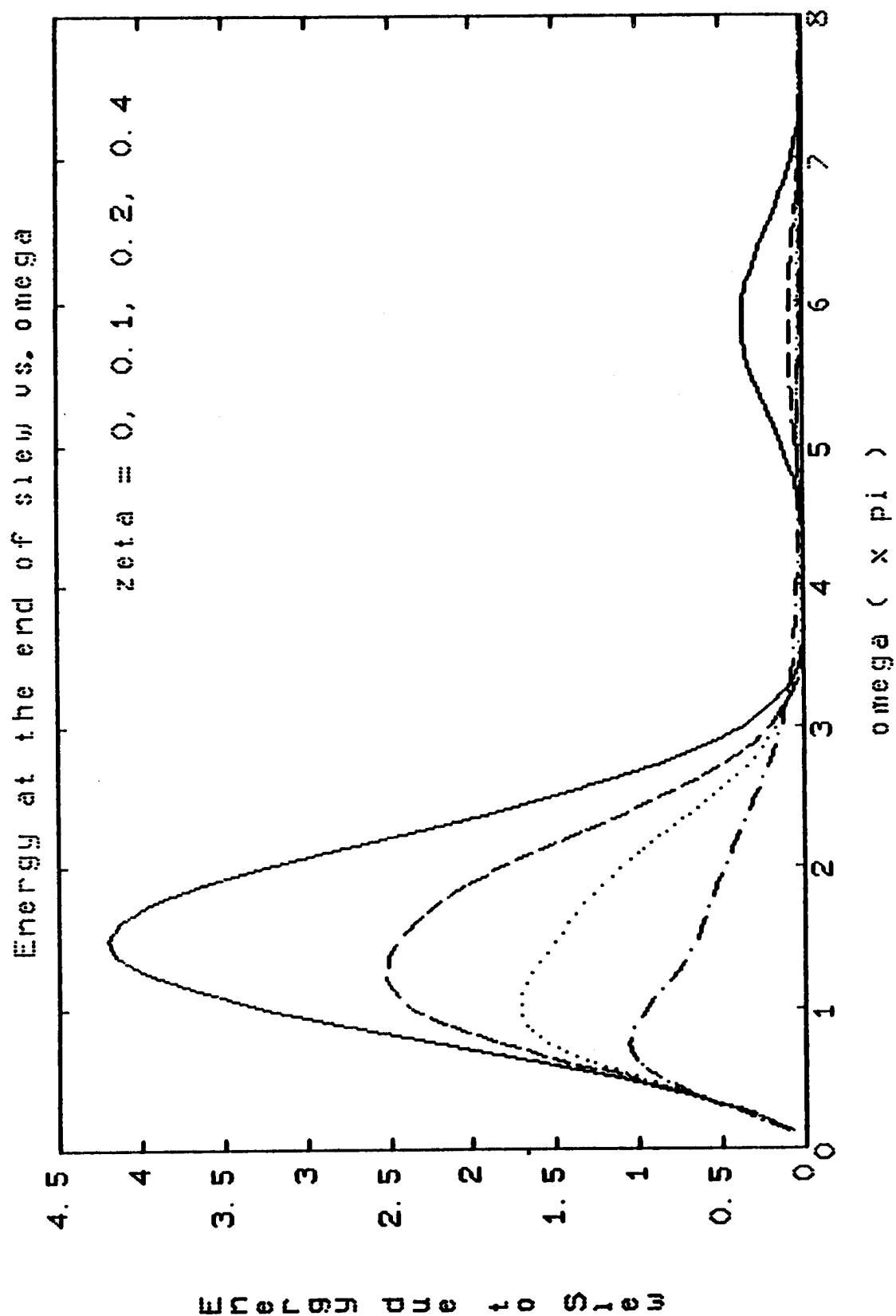
- MOVE THE C.M. (CENTER OF MASS) 1 UNIT TO THE RIGHT IN  $t = 1$  sec. ( $F_0 = 4$ )
- $X_1(1) = 1$  and  $\dot{X}_1(1) = 0$
- $\ddot{X}_1(t) = 0$  ,  $t \geq 1$
- COMPUTE THE ENERGY STORED IN THE SYSTEM RIGHT AFTER THE SLEW MOTION



### ENERGY AT THE END OF SLEW VS. OMEGA

This chart shows the energy in the system at the end of the 1 second slew versus the system frequency for various values of damping. Note that at  $\omega = 4\pi$  the energy is near zero for all values of damping.

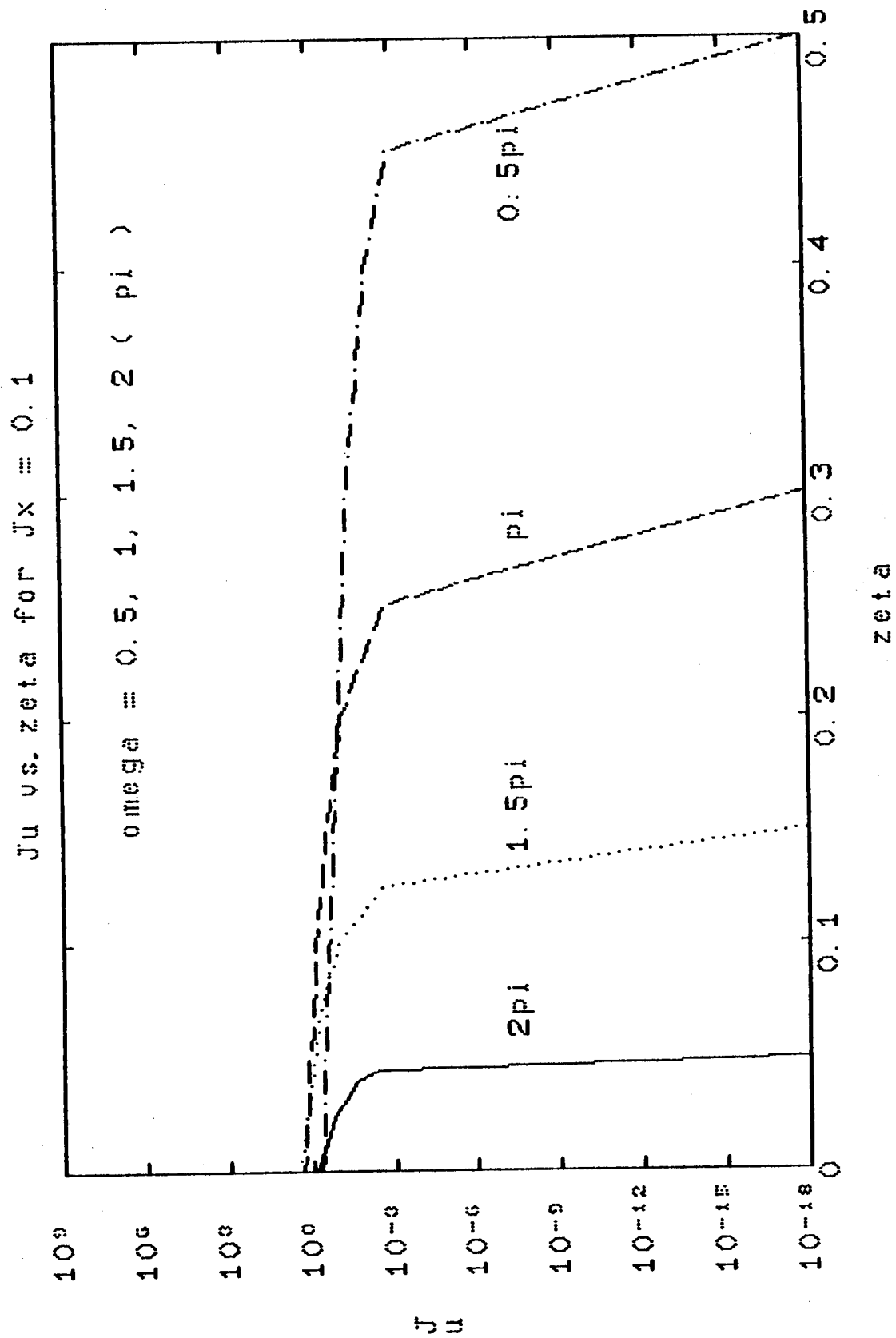
# ENERGY AT THE END OF SLEW VS. OMEGA



#### **Ju VS. ZETA FOR $Jx = 0.1$**

This chart shows the control effort required to minimize the relative displacement of the two masses versus system damping for various values of system natural frequency. This shows a similar behavior to the results obtained from the SBL study.

# Ju vs. ZETA FOR Jx = 0.1



# OBSERVATIONS

---

---

## FOR THE CASES CONSIDERED :

- SUFFICIENT PASSIVE MODAL DAMPING TOGETHER WITH HIGH SPECIFIC STIFFNESS STRUCTURAL MATERIALS IS AN EFFECTIVE WAY TO ACHIEVE PERFORMANCE WHILE MINIMIZING CONTROL SYSTEM COMPLEXITY
- E.G., THE CONTROL EFFORT AND CONTROL FORCE REQUIRED TO ACHIEVE SBL PERFORMANCE DROPS CONSIDERABLY WITH DAMPING; FOR  $E/\rho = 760e+06$  in. AT  $\zeta \geq 9\%$  AND FOR  $E/\rho = 235e+06$  in. AT  $\zeta \geq 18\%$
- TRENDS FROM THE SBL CASES AND THE TWO DEGREE-OF-FREEDOM SYSTEM ARE SIMILAR

## AN EXPERIMENTAL STUDY OF THE COMPLEX DYNAMIC MODULUS

Flight Lieutenant Graeme G. Wren  
(Royal Australian Air Force)  
and

Dr Vikram K. Kinra  
Aerospace Engineering Department  
Texas A&M University  
College Station, Texas, 77843  
(409) 845-1667

### ABSTRACT

An overview of an experimental program for determining the dynamic flexural constitution of materials is presented. This program entails the development of a fully-automated flexural apparatus, its calibration, and studies of structural damping and dynamic flexural modulus of a variety of materials. Furthermore, Graphite/Aluminum laminates,  $[\pm\theta]_s$ , with  $\theta$  ranging from zero to ninety in fifteen degree increments, were tested. Classical laminate theory and the work of Ni and Adams was found to adequately predict both the modulus and the damping. It is demonstrated that the attachment of an end-mass (to vary the resonant frequency) does not contribute to the measured damping.

**KEYWORDS:** Damping, modulus, composite material, flexural, structural, dynamic, experimental, logarithmic decrement, vacuum.

## SYMBOLS USED

A = cross sectional area of beam, amplitude  
 $C_p$  = specific heat per unit mass at constant pressure  
 $D_{ij}$  = components of the flexural modulus matrix for a laminate  
E = Young's modulus  
f = frequency (cycles/second)  
h = beam thickness  
I = second moment of area of beam  
 $k_t$  = transverse thermal conductivity (in thickness direction)  
L = beam length  
m = end-mass, cosine of ply (fiber) orientation  
n = sine of ply (fiber) orientation  
T = absolute temperature  
t = time  
w = beam width  
W = maximum elastic energy stored during a cycle  
 $\Delta W$  = mechanical energy dissipated per cycle  
x = coordinate along the length of the beam  
y = amplitude of transverse vibration  
 $\alpha$  = linear coefficient of thermal expansion, eigenvalue  
 $\beta$  = eigenvalue  
 $\delta$  = logarithmic decrement  
 $\epsilon_\psi$  = accuracy of experimental damping measurement  
 $\zeta = \xi$  = damping ratio  
 $\eta$  = loss factor  
 $\lambda$  = eigenvalue  
 $\rho$  = density per unit volume of beam material  
 $\tau$  = relaxation time  
 $\phi$  = phase angle by which the applied stress leads the resulting strain  
 $\omega$  = frequency (radians/second),  $2\pi f$   
 $\omega_0$  = resonant frequency of beam without an end-mass  
 $\psi$  = damping =  $\Delta W/W$   
( $\cdot$ )' = real part of a complex quantity ( $\cdot$ )  
( $\cdot$ )" = imaginary part of a complex quantity ( $\cdot$ )

## 1.0 INTRODUCTION

The design of any structure requires the quantitative knowledge of many parameters pertaining to the material of which the structure is built. Two parameters of importance in the analysis of structures subject to dynamic loads are the dynamic modulus and damping capacity. The measure of these entities, particularly damping, depends on the type of dynamic loading applied. Intrinsic, or material damping, is defined herein as the dissipation of energy within a material through the excitation of internal defect phenomena by the application of a homogeneous strain

field. Structural damping on the other hand, is composed of both intrinsic (material) and extrinsic (structural) components, and is defined to be the dissipation of energy produced by the application of a non-homogeneous strain field which is determined by specimen shape and structural application. Hence, a specimen subject to uniaxial tensile or compressive loading deforms and dissipates energy under a homogeneous strain field and therefore yields a measurement of intrinsic material damping. However, the strain field in a beam of the same material subject to flexural oscillations varies in the thickness direction and with position along the beam; this variation depending on boundary conditions. Therefore, energy dissipation within the beam will also be a function of thickness and position along the length of the beam, and will give a measure of structural damping. An example of such damping is the transport of thermal currents across the thickness dimension of a beam (Zener or thermoelastic relaxation).

Many experimental techniques have been proposed and developed to measure the dynamic constitution of materials. The technique described herein determines the dynamic properties in flexure with speed, automation, and measures of accuracy and precision. The experimental apparatus consists of a beam specimen mounted under cantilevered boundary conditions and vibrated in first-mode flexural resonance. Data acquisition and reduction techniques entail accurate determination of the resonant frequency, and a measure of the rate of decay in free-vibrational amplitude using a logarithmic decrement method for ascertaining the dynamic flexural modulus and structural damping, respectively<sup>1</sup>.

Results pertaining to the flexural modulus and structural damping of 6061 aluminum and a symmetric four-ply metal-matrix composite composed of pitch-55 graphite fibers in a 6061 aluminum matrix are presented. These results are compared with those predicted by Euler-Bernoulli, Zener (thermoelastic), and laminate theories and show good agreement. End-masses were used to vary the resonant frequency of the test specimens<sup>2</sup>. A brief overview of the end-massed beam analysis and experimental results is presented to show that the addition of an end-mass only alters the resonant frequency of the specimen and does not contribute to the measure of damping. Damping results are presented in the form  $\psi = \Delta W / W$ , where  $\Delta W$  is the energy dissipated during each loading cycle and  $W$  is the maximum energy stored. Calibration of the cantilevered configuration for apparatus losses was carried out in two steps. First, the damping of fused quartz, a material possessing negligible damping, was measured in a free-free apparatus<sup>1</sup>. This yielded a determination of the free-free apparatus losses. Second, flexural damping data for annealed 6061 aluminum obtained from both free-free and cantilevered configurations were compared. Results showed that, within the range of experimental



scatter, both configurations provided the same measure of damping. This agreement of the data justified equating the cantilevered apparatus losses to those of the free-free configuration. Accuracy of the experimental dynamic flexural modulus values was dependent upon the measurement of the resonant frequency and specimen parameters. An estimate of accuracy was obtained by comparing the results of the present study with those of an experimental study using ultrasonic wave propagation<sup>3</sup>. These procedures determined accuracy of the modulus and damping values to be 0.1 percent and  $\epsilon_p = 3.0 \times 10^{-4}$ , respectively. It is noted that  $\epsilon_p$  is a systematic error and  $\epsilon_p > 0$ . Statistical analysis of all experimental data ascertained the precision to be 0.1 percent and  $5 \times 10^{-4}$  (one standard deviation), for modulus and damping, respectively.

## 2.0 SPECIMENS

A variety of specimens were tested including annealed 6061 and 6061T6 aluminum alloys, magnesium-0.6% zirconium alloy, magnesium-1% manganese alloy, leaded and lead-free brass, fused quartz, and three metal-matrix composite laminates, one comprising continuous pitch-55 graphite fibers (P55Gr) in a matrix of 6061 aluminum (P55Gr/6061Al), the second P55Gr fibers in a matrix of magnesium with 0.6 percent zirconium (P55Gr/Mg-0.6%Zr), and the third was constructed of P55Gr fibers in a matrix of magnesium with one percent manganese (P55Gr/Mg-1%Mn). The P55Gr/6061Al specimens were cut from a four-ply, balanced, symmetric, laminated plate at angles ranging from zero to ninety degrees in fifteen degree increments; in a zero degree specimen, the fibers are aligned along the length dimension of the beam. The P55Gr/Mg-0.6%Zr and P55Gr/Mg-1%Mn specimens were cut from a zero-degree, eight-ply laminate.

The P55Gr/6061Al diffusion bonded laminated composite beam specimens were constructed of four orthotropic, unidirectional lamina oriented at specific angles to the longitudinal beam axis and symmetrically disposed to the midplane of the laminate. During the fabrication process Gr/Al precursor tows each containing 2000, 10  $\mu$ m diameter fibers were consolidated between 0.089 mm thick 6061 aluminum face sheets at the angles appropriate to the particular laminate layout. The laminate was processed at 588°C and 24.1 MPa for 20 minutes, yielding a composite plate of 50% fibre volume. Two specimens of each laminate orientation were tested. Specimen dimensions for the 6061 aluminum and metal-matrix laminate specimens are given in Table 1.

### 3.0 EXPERIMENTAL APPARATUS

A schematic diagram of the experimental apparatus utilized in this research is presented in Figure 1. This equipment determines the dynamic properties in flexure with speed, automation and measures of accuracy and precision. The apparatus consists of a beam specimen supported under cantilevered boundary conditions and vibrated in first-mode flexural resonance, a Wavetek Model 164 frequency generator, a Bruel and Kjaer electromagnetic transducer, a power amplifier for increasing the signal received by the transducer, a Micro-Measurements BAM-1 strain bridge, a Data Precision Model 6000/611 waveform analyzer, and a Hewlett Packard 9000/217 computer connected to the Data 6000 by an IEEE 488 interface. To isolate the system from the effects of air damping, the specimen was mounted in a vacuum chamber connected to a Cenco Hypervac 25 vacuum pump capable of drawing a hard vacuum of 0.013 Pa.

### 4.0 THEORETICAL BACKGROUND

To preserve the succinct nature of the paper only the final results of the Euler-Bernoulli, logarithmic decrement, thermo-elastic, and laminate theories entailed in these studies will be given here.

#### 4.1 Dynamic Flexural Modulus

Let  $\omega'$  be the frequency of a cantilevered beam made of an isotropic anelastic material, and  $E'$  be the real part of the Young's modulus. By the use of the Correspondence Principle of linear viscoelasticity<sup>4</sup>, and the Euler-Bernoulli theory of flexure, the relationship between  $E'$  and  $\omega'$  is given by:

$$\omega' = \frac{\alpha^2}{L^2} \sqrt{\frac{E'I}{\rho A}} \quad (1)$$

where  $(\ )'$  denotes the real part of a complex quantity,  $\alpha$  is the eigenvalue, which for the fundamental mode of a cantilevered beam has a value of 1.875,  $E$  is the Young's modulus,  $I$  is the second moment of area,  $\rho$  is the density per unit volume, and  $A$  is the cross-sectional area. This analysis assumes that the free vibrations of low-loss viscoelastic materials are approximately harmonic<sup>5</sup>.

#### 4.2 Logarithmic Decrement

The logarithmic decrement technique entails measuring the rate at which the free-vibration amplitude decays with time. An

expression for the damping is given by:

$$\psi = \frac{\Delta W}{W} = \frac{4\pi \ln[A(t_1)/A(t_2)]}{\omega_r [t_2 - t_1]} \quad (2)$$

where  $\omega_r$  is the resonant frequency, and  $A(t_1)$  and  $A(t_2)$  are the peak displacements at times  $t_1$  and  $t_2$ , respectively. In accordance with equation (2),  $\ln[A(t_1)/A(t_2)]$  was plotted against  $(t_2 - t_1)$ , the least squares method was used to fit a straight line, and from the slope,  $m$ , of the straight line, the damping was calculated from:

$$\psi = 4\pi m / \omega_r \quad (3)$$

Several other definitions of damping currently appear in the literature. For the convenience of the reader, their inter-relationship is documented here:

$$\psi = 2\pi \tan \phi = 2\pi \eta = 4\pi \zeta = 4\pi \xi = 2\pi Q^{-1} = 2\pi E''/E' = 4\pi \omega''/\omega' = 2\delta$$

#### 4.3 Thermoelastic (Zener) Damping

The variation of damping with frequency due to the transport of thermal currents as determined from Zener theory<sup>6</sup> is given by:

$$\psi = \psi_0 \left( \frac{\omega \tau}{1 + \omega^2 \tau^2} \right) \quad (4)$$

where  $\psi_0 = \frac{2\pi \alpha^2 E T}{\rho C_p}$  and  $\tau = \frac{h^2 \rho C_p}{\pi^2 k_t}$

Equation (4) describes the damping in a beam produced from the transport of thermal currents across the thickness dimension. This form of energy dissipation is dependent on the structural configuration and is produced by a non-homogeneous strain field. It is therefore a form of structural damping. This equation has been used in calculating the curves in Figures 4, 6 and 7.

#### 4.4 Laminate Theory

The following expressions for flexural modulus and damping for a balanced, symmetric, laminated composite beam were derived using general plate theory of laminated composites<sup>7</sup> and the studies of Ni and Adams<sup>8</sup>, respectively. It is noted that this laminate theory is based on the theory of linear elasticity and does not include thermoelastic effects. The coordinate system of the lamina (on-axis, principal, [1,2,3]) and laminate (off-axis, [x,y,z]), and the laminate ply counting sequence are shown in

Figures 2 and 3, respectively. The effective flexural modulus in free-flexure, where bending-twisting coupling is not constrained, is given by:

$$E_f = \frac{12}{h^3 D'_{11}} \quad (5)$$

Although it is obvious that the boundary conditions used do not constrain bending-twisting coupling (except at the clamped-end), this constraint was investigated for confirmation and completeness. The constrained flexural modulus, termed pure-flexure, is given by:

$$E_p = \frac{12 D'_{66}}{h^3 [D'_{11} D'_{66} - (D'_{16})^2]} \quad (6)$$

where  $D'_{ij}$  are components of the laminate flexural modulus matrix.

The total flexural damping is given by:

$$\psi = \psi_1 + \psi_2 + \psi_{12} \quad (7)$$

where  $\psi_1 = \frac{\Delta W_1}{W}$      $\psi_2 = \frac{\Delta W_2}{W}$      $\psi_{12} = \frac{\Delta W_{12}}{W}$

$$\psi_1 = \frac{\psi_L}{3 D'_{11}} \sum_{k=1}^n m^2 (\bar{Q}_{11} D'_{11} + \bar{Q}_{12} D'_{12} + \bar{Q}_{16} D'_{16}) \frac{(m^2 D'_{11} + mn D'_{16}) (h_k^3 - h_{k-1}^3)}{(m^2 D'_{11} + mn D'_{16}) (h_k^3 - h_{k-1}^3)}$$

$$\psi_2 = \frac{\psi_T}{3 D'_{11}} \sum_{k=1}^n n^2 (\bar{Q}_{11} D'_{11} + \bar{Q}_{12} D'_{12} + \bar{Q}_{16} D'_{16}) \frac{(n^2 D'_{11} - mn D'_{16}) (h_k^3 - h_{k-1}^3)}{(n^2 D'_{11} - mn D'_{16}) (h_k^3 - h_{k-1}^3)}$$

$$\psi_{12} = \frac{\psi_{LT}}{3 D'_{11}} \sum_{k=1}^n mn (\bar{Q}_{11} D'_{11} + \bar{Q}_{12} D'_{12} + \bar{Q}_{16} D'_{16}) \frac{(2mn D'_{11} - [m^2 - n^2] D'_{16}) (h_k^3 - h_{k-1}^3)}{(2mn D'_{11} - [m^2 - n^2] D'_{16}) (h_k^3 - h_{k-1}^3)}$$

and  $m = \cos \theta_k$  and  $n = \sin \theta_k$ . The above relations were derived assuming negligible shear deformation and rotary inertia (Euler-Bernoulli beam theory) which holds for length-to-thickness ratios greater than approximately 30<sup>9</sup>. The length-to-thickness ratio for the composite specimens tested was of the order of 100.

## 5.0 EXPERIMENTAL PROCEDURE

Vibrational motion of the beam specimen was induced using an electromagnetic transducer driven at the resonant frequency of the specimen. As the specimens were non-magnetic, a small, high permeability disc was attached to the end of the specimens to provide coupling with the transducer. The cyclic signal representing the motion of the specimen was obtained via a strain gage attached near the root. This gage was connected to the direct-current strain bridge, whose analog voltage output was passed to the Data 6000 acquisition device. When the specimen reached steady-state, forced vibrational motion, the resonant frequency was recorded by the computer. The current to the excitation transducer was then interrupted and the specimen went into free vibrational decay. The steady-state and the free-decay motion were recorded in digital form by the Data 6000 where the voltage of each positive peak of the waveform was determined and passed via the IEEE 488 bus to the computer.

In order to study the variation of dynamic flexural modulus and structural damping with frequency, an end-mass was attached to the end of the specimen to facilitate the variation of its resonant frequency<sup>2</sup>. The dynamic flexural modulus was calculated using equation (1) and the experimental values of resonant frequency and specimen parameters. Structural damping was determined using equations (2) and (3).

## 6.0 EXPERIMENTAL ERROR

Calibration of the cantilevered configuration for apparatus losses was carried out in two steps. First, the damping of fused quartz, a material possessing negligible damping, was measured in a free-free apparatus<sup>1</sup>. A reported damping value for fused quartz is  $1.2 \times 10^{-6}$ <sup>10</sup>. The value measured using the free-free vibrational apparatus was  $3 \times 10^{-4}$ . As the cited value is negligibly small,  $3 \times 10^{-4}$  is determined to represent apparatus losses, and is denoted  $\epsilon_\psi$ . Therefore, the measured value of damping of any material using this apparatus can be decomposed into the thermo-elastic (Zener) and intrinsic damping of the material plus apparatus losses:

$$\psi_{\text{measured}}^{\text{free-free}} = \psi_{\text{Zener}}^{\text{free-free}} + \psi_{\text{intrinsic}} + \epsilon_\psi^{\text{free-free}} \quad (8)$$

Because it is impractical to measure the damping of fused quartz using a cantilevered apparatus due to the required clamping pressures and the fragile nature of the material, a comparison between measured damping values for annealed 6061 aluminum in

both free-free and cantilevered configurations was carried out. As shown in Figure 4, results displayed a negligible difference in the mean damping values obtained from the two techniques. The standard error for the least squares curve fit of all the data was  $5 \times 10^{-4}$ . In an analogous manner to that used for the free-free apparatus, the measured damping value of a material can again be decomposed according to equation (8):

$$\psi_{\text{measured}}^{\text{cantilever}} = \psi_{\text{Zener}}^{\text{cantilever}} + \psi_{\text{intrinsic}} + \epsilon_{\psi}^{\text{cantilever}} \quad (9)$$

As the intrinsic damping of a material is a constitutional property, and the thermoelastic (Zener) damping is the same for both configurations, as comparison was made at the same frequency using specimens of the same dimensions, therefore:

$$\psi_{\text{Zener}}^{\text{free-free}} = \psi_{\text{Zener}}^{\text{cantilever}} \quad (10)$$

Since the measured values of damping obtained from two different techniques agree over the range of frequencies and strain amplitudes studied, it follows from equations (8), (9) and (10) that

$$\epsilon_{\psi}^{\text{free-free}} = \epsilon_{\psi}^{\text{cantilever}} \quad (11)$$

Therefore, from equation (11) and the agreement between the experimental results shown in Figure 4, the apparatus losses of the cantilevered configuration can be equated to the measured value of extraneous losses in the free-free apparatus; that is, for both configurations, the accuracy in the measurement of damping, defined by  $\epsilon_{\psi}$ , is  $3.0 \times 10^{-4}$ . An additional point of interest obtained from Figure 4 is that the value of Zener damping, which is strain amplitude independent, lies within the range of intercept of the least squares best-fit straight line and the lines specifying the standard error. This adds credence to the measured data, and also demonstrates that, for the particular material tested where intrinsic damping is very low, an accurate measure of the intrinsic damping cannot be determined from the flexural damping as it lies within the range of experimental scatter. However, one may put bounds on its magnitude; that is  $0 < \psi_{\text{intrinsic}} < 5 \times 10^{-4}$ .

Accuracy of the experimental dynamic flexural modulus values is dependent upon the measurement of the resonant frequency and specimen parameters. A measure of the accuracy and precision of the modulus data was determined by calculating the modulus from thirty independent tests in which the resonant frequency was disturbed by attaching different end-masses to the end of a speci-

men<sup>2</sup>; this will be discussed further in the next section. Evaluation of the dynamic flexural modulus from the thirty different experimental values of frequency, and the corresponding eigenvalues determined from the end-mass used, resulted in a mean value of 69.376 GPa  $\pm$  0.1% (one standard deviation). This agrees within 0.1% with the value of 69.439 GPa  $\pm$  0.1% obtained from an independent study using ultrasonic wave propagation<sup>3</sup>.

Thus, the accuracy of the measured modulus and damping values presented herein are 0.1 percent and  $3.0 \times 10^{-4}$ , respectively. Precision of the experimental data was ascertained to be 0.1 percent and  $5 \times 10^{-4}$  (one standard deviation), for modulus and damping, respectively.

## 7.0 RESULTS AND DISCUSSION

For continuity the essential results pertaining to the attachment of an end-mass to a beam specimen to facilitate the variation of resonant frequency are reproduced from<sup>2</sup>. This technique was used to determine the frequency dependence of dynamic flexural modulus and structural damping for the specimens tested. The data, covering almost two decades of frequency, were obtained using five different beam lengths and six different end-masses. The length, mass and frequency matrix is shown in Table 2.

The relationship between the frequency and end-mass is given by equation (1)<sup>2</sup> where now the eigenvalues,  $\alpha$ , are the solutions of the transcendental equation:

$$\frac{1 + \cos \alpha \cosh \alpha}{\alpha (\sin \alpha \cosh \alpha - \cos \alpha \sinh \alpha)} = \frac{m}{\rho A L} \quad (12)$$

Figure 5 shows the normalized frequency as a function of normalized mass for annealed 6061 aluminum and justifies the applicability of Euler-Bernoulli beam theory in the analysis. Further, each experimental data point is an independent measure of the dynamic flexural modulus since the eigenvalues are specified by equation (12) and vibrational frequencies are experimentally determined. Thus, the modulus can be calculated via a rearrangement of equation (1). It is emphasized that each data point provides an independent determination of the modulus as all parameters in equation (1), except the eigenvalues, are experimentally measured. Evaluation of the dynamic flexural modulus from the thirty experimental data points resulted in a mean value of 69.376 GPa  $\pm$  0.1% (one standard deviation). This agrees very well with the value of 69.439 GPa  $\pm$  0.1% obtained from an independent study<sup>3</sup>.

Figure 6 shows the normalized damping as a function of normalized frequency for 6061 aluminum. The vertical arrow points to the frequency common to five of the reference beam length/end-mass combinations (11.19 Hz). These five measurements lie in the range  $\psi = 0.81 \times 10^{-2} \pm 0.02 \times 10^{-2}$  ( $\pm 2.5\%$ ). It is important to note that this observation of precision agrees well with the value of  $5 \times 10^{-4}$  obtained from the independent study of comparative damping values for the free-free and cantilevered configurations. The experimental program was designed to cover a broad range of frequency values on either side of the Zener relaxation frequency  $\omega\tau=1$  and, as shown, experimental results follow the Zener curve very well. Figure 7 displays the normalized damping as a function of normalized mass for four nominal frequencies, namely, 8, 11.19, 16, and 20 Hz. Clearly, within the bounds of experimental error, the damping is insensitive to the end-mass.

The dependence of flexural modulus and damping with ply-angle for the P55Gr/6061Al metal-matrix composite laminate specimens was investigated at fixed values of frequency (35 Hz) and strain amplitude ( $55\mu\epsilon$ ). Two specimens of each ply-angle were tested. The experimental flexural modulus results and the curves defined by equations (5) and (6) are shown in Figure 8. Locations where only one symbol is shown indicate that agreement of the experimental data was within the size of the graphing symbol. The variation of the unconstrained (free) dynamic flexural modulus with ply-angle, as defined by equation (5), is illustrated as the solid line in Figure 8. This semi-empirical curve was generated using experimental values of the longitudinal and transverse moduli, Poisson's ratio, and the resultant element value of the laminate flexural modulus matrix,  $D'_{11}$ , calculated from a laminate code. As the shear modulus was unavailable, this parameter was varied in the laminate code to give the least-squares best-fit curve through the experimental flexural modulus data. From this routine a longitudinal shear modulus value of 16.5 GPa was obtained. The curve for the constrained (pure) flexural modulus, as defined by equation (6), is shown as the dashed line in Figure 8. Comparison of the two curves indicate that flexure is best modelled by considering twisting due to the bending-twisting coupling terms to be unconstrained, as expected.

Prediction of laminate structural damping, as given by equation (7), was calculated from the laminate code using the experimentally determined value for  $G_{LT}$  (from the flexural modulus curve-fit), measured values of  $\psi_L$ ,  $\psi_T$ , obtained from flexural damping experiments on zero and 90 degree specimens, and curve-fitting for  $\psi_{LT}$ . The theoretical curve and experimental data are shown in Figure 9. The curve shown was generated using an analogous least-squares best-fit routine as that used to determine  $G_{LT}$ . This resulted in a value of  $\psi_{LT}=0.039$ . Experimental results



indicate that within experimental scatter, laminate theory predicts the flexural modulus and damping in graphite-aluminum metal-matrix laminates reasonably well. Tables 3, 4 and 5 provide a summary of the experimentally determined mechanical properties of annealed 6061 aluminum, continuous Pitch 55 graphite fibers, and the P55Gr/6061Al metal-matrix composite specimens tested, respectively.

## 8.0 CONCLUSIONS

The cantilevered flexural resonance apparatus discussed herein facilitates the measurement of the dynamic flexural modulus and structural damping capacity of a material. The attachment of an end-mass does not contribute to measured values of flexural modulus or damping. Experimental values obtained for the flexural modulus and structural damping of annealed 6061 aluminum display good agreement with Euler-Bernoulli and Zener (thermoelastic) theories. Experimental results obtained from specimens cut from a four-ply, balanced, symmetric, P55Gr/6061Al metal-matrix composite laminate at angles ranging from zero to ninety degrees in increments of fifteen degrees indicated that the flexural modulus and structural damping varied with ply angle. The classical laminate theory of Ni and Adams<sup>8</sup> adequately predicts this variation. Accuracy of the modulus and damping values were determined to be 0.1 percent and  $\epsilon_p = 3.0 \times 10^{-4}$ , respectively. Statistical analysis of all experimental data ascertained the precision to be 0.1 percent and  $5 \times 10^{-4}$  (one standard deviation), for modulus and damping, respectively.

## ACKNOWLEDGMENT

The specimens and a small financial contribution of the research were provided by the Martin Marietta Aerospace Corporation, Denver, Colorado (Program Managers: Dr M.S. Misra and Dr S.P. Rawal).

## 9.0 REFERENCES

1. Wren, G.G., and Kinra, V.K., "An Experimental Technique for Determining a Measure of Structural Damping," Journal of Testing and Evaluation, Vol. 16, No. 1, January 1988, pp 77-85.
2. Wren, G.G., and Kinra, V.K., "On The Effect of End-Mass on Damping," to appear in Experimental Mechanics.
3. Kinra, V.K., Petraitis, M.S., and Datta, S.K., "Ultrasonic Wave Propagation in a Random Particulate Composite," Interna-

- tional Journal of Solids and Structures, Vol. 16, pp 301-312, 1980.
4. Schapery, R.A., "Viscoelastic Behavior and Analysis of Composite Materials," Composite Materials, 2, edited by Sen-deckjy, Academic Press, New York (1974).
  5. Read, B.E., and Dean, G.D., The Determination of Dynamic Properties of Polymers and Composites, Adam Hilger, Bristol, England, 1978.
  6. Zener, C.M., Elasticity and Anelasticity of Metals, University of Chicago Press, Chicago, 1948.
  7. Halpin, J.C., Primer on Composite Materials, Technomic Publishing Co., Lancaster, 1984.
  8. Ni, R.G., and Adams, R.D., "The Damping and Dynamic Moduli of Symmetric Laminated Composite Beams - Theoretical and Experimental Results," Journal of Composite Materials, Vol. 18, March 1984, pp 104-121.
  9. Whitney, J.M., Structural Analysis of Laminated Anisotropic Plates, Technomic Publishing Co., Lancaster, 1987.
  10. Kimball, A.L., and Schenectady, N.Y., "Vibration Problems -Part V -Friction and Damping in Vibrations," Journal of Applied Mechanics, September 1941, pp A-135 to A-137.

TABLE 1 - SPECIMEN PARAMETERS

Specimen ID	L m $\times 10^2$	w m $\times 10^2$	h m $\times 10^2$	$\rho$ kg/m <sup>3</sup> $\times 10^3$	E <sub>L</sub> GPa	$\Psi$ $\Delta W/W$ $\times 10^2$
0-1	13.10	1.214	0.211	2.41	156.10	0.35
0-2	13.08	1.212	0.208	2.41	160.65	0.4
15-1	13.18	1.089	0.208	2.43	124.38	1.03
15-2	13.23	1.146	0.203	2.41	125.48	0.9
30-1	13.03	0.955	0.208	2.43	74.39	2.0
30-2	13.20	1.143	0.211	2.41	72.81	1.8
45-1	15.21	1.217	0.208	2.41	47.09	2.35
45-2	15.24	1.212	0.208	2.38	45.78	2.1
60-1	13.13	0.957	0.211	2.41	36.13	2.6
60-2	13.51	0.955	0.211	2.41	35.51	2.7
75-1	15.47	1.212	0.203	2.43	37.37	2.25
75-2	13.59	1.214	0.203	2.43	36.82	2.35
90-1	13.18	1.146	0.203	2.43	36.68	1.6
90-2	13.30	1.140	0.203	2.43	36.47	1.5

TABLE 2 -THEORETICAL VALUES OF RESONANT FREQUENCIES  
FOR DIFFERENT LENGTH/END-MASS COMBINATIONS

beam length (cm)	end-mass (g)					
	m <sub>6</sub> 91.17	m <sub>5</sub> 40.09	m <sub>4</sub> 19.96	m <sub>3</sub> 10.34	m <sub>2</sub> 4.99	m <sub>1</sub> 0.17
L <sub>1</sub> 12.70	11.19	16.68	23.15	31.10	41.70	78.46
L <sub>2</sub> 16.51	7.52	11.19	15.44	20.55	27.11	46.90
L <sub>3</sub> 20.32	5.49	8.15	11.19	14.76	19.20	31.15
L <sub>4</sub> 24.13	4.24	6.25	8.55	11.19	14.90	22.19
L <sub>5</sub> 27.94	3.39	4.99	6.79	8.82	11.19	16.96
width=1.27 cm, thickness=0.162 cm						

TABLE 3 - MECHANICAL PROPERTIES OF ANNEALED 6061 ALUMINUM

E GPa	G GPa	$\nu$	$\rho$ kg/m <sup>3</sup> x10 <sup>3</sup>	$\alpha$ $\mu\text{m}/\text{m}^\circ\text{K}$	k J/m <sup>2</sup> Ks	C <sub>p</sub> J/kg <sup>2</sup> K
68.9	25.9	0.33	2.70	23.0	180.2	895.8

TABLE 4 - MECHANICAL PROPERTIES OF CONTINUOUS PITCH 55  
CONTINUOUS GRAPHITE FIBERS

E <sub>L</sub> GPa	E <sub>T</sub> GPa	G <sub>LT</sub> GPa	$\nu_{LT}$	$\rho$ kg/m <sup>3</sup> x10 <sup>3</sup>	$\alpha$ $\mu\text{m}/\text{m}^\circ\text{K}$	k J/m <sup>2</sup> Ks
379.2	3.4	17.2	0.41	1.99	-1.25	120.9

TABLE 5 - EXPERIMENTALLY DETERMINED MECHANICAL PROPERTIES  
OF P55Gr/6061Al METAL MATRIX COMPOSITE

E <sub>L</sub> GPa	E <sub>T</sub> GPa	G <sub>LT</sub> GPa	$\nu_{LT}$	$\rho$ kg/m <sup>3</sup> x10 <sup>3</sup>	V <sub>f</sub>	$\psi_L$	$\psi_T$	$\psi_{LT}$
157.9	36.7	16.5	0.33	2.43	0.5	0.004	0.0155	0.039

V<sub>f</sub>: volume fraction $\psi$ :  $\Delta W/W$ Note: G<sub>LT</sub> and  $\psi_{LT}$  were deduced from experimental results of flexural modulus and damping, respectively.

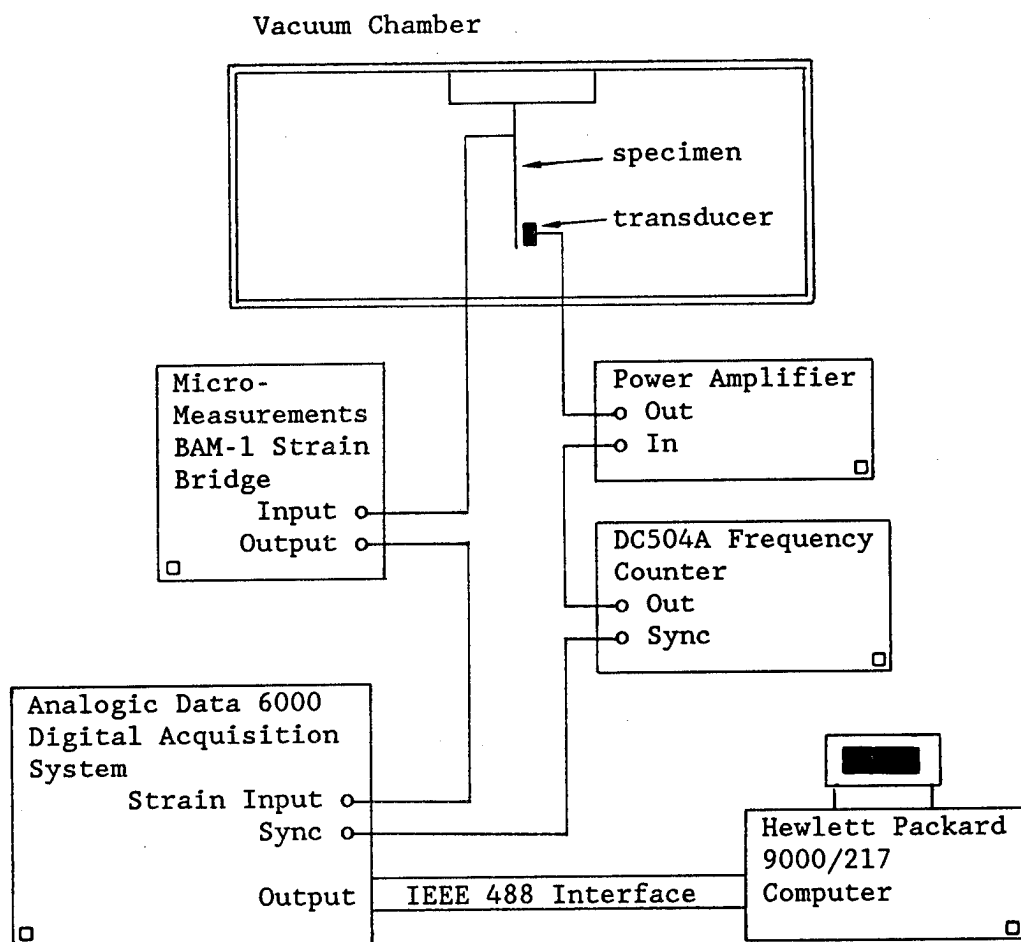


Figure 1 - Experimental Configuration

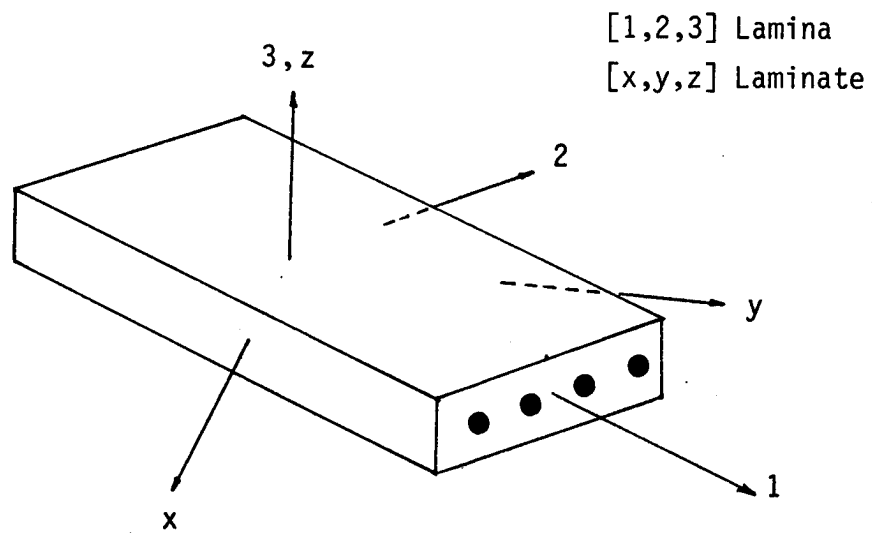


Figure 2 - Laminate Coordinate System

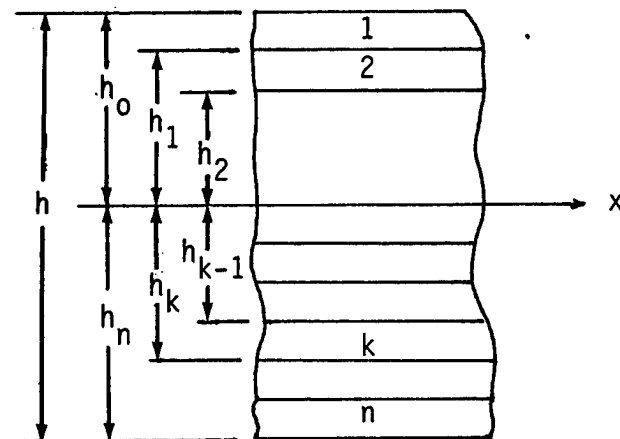


Figure 3 - Ply Counting Sequence

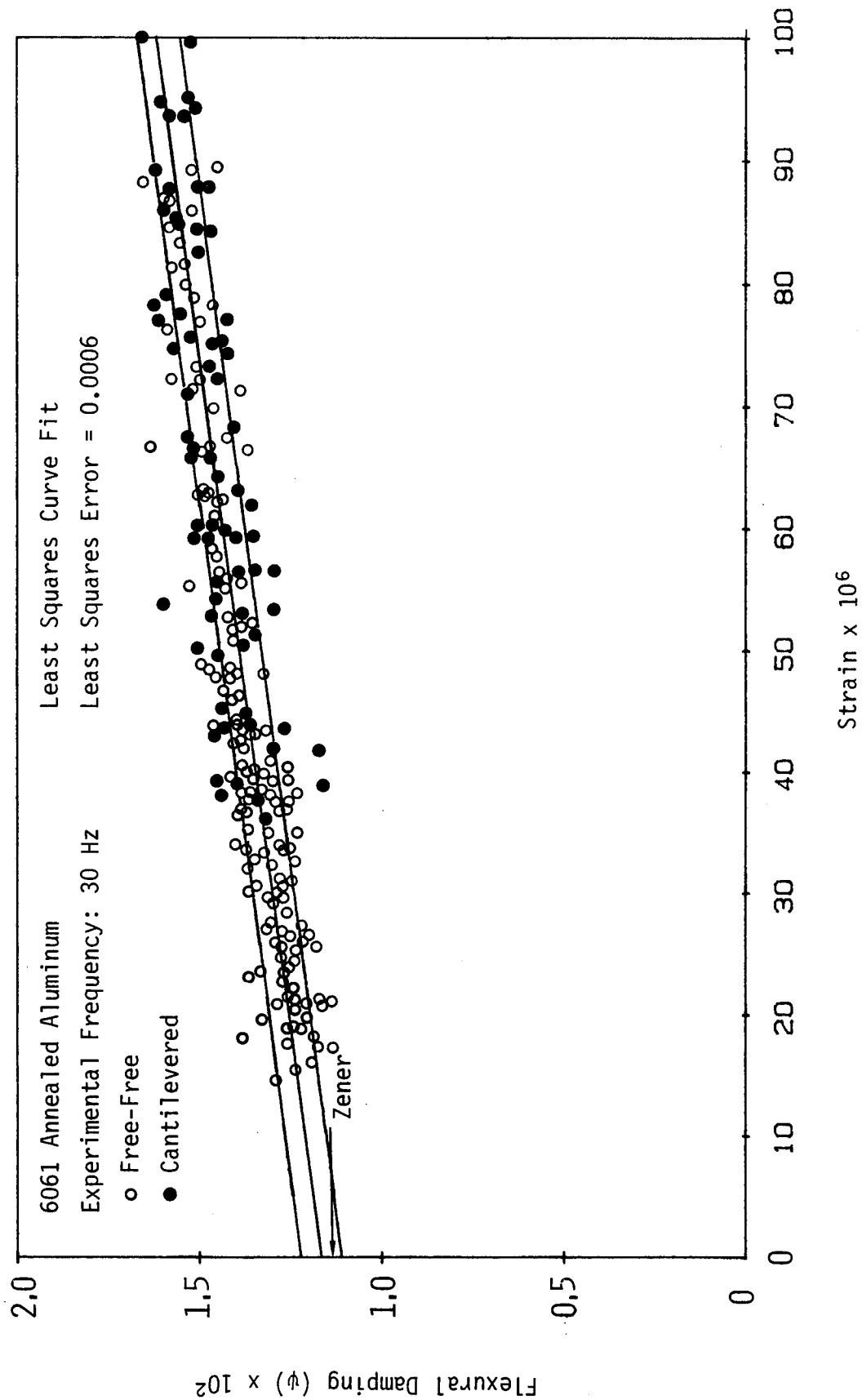


Figure 4 - Comparison of Flexural Damping Data from Free-Free and Cantilevered Configurations



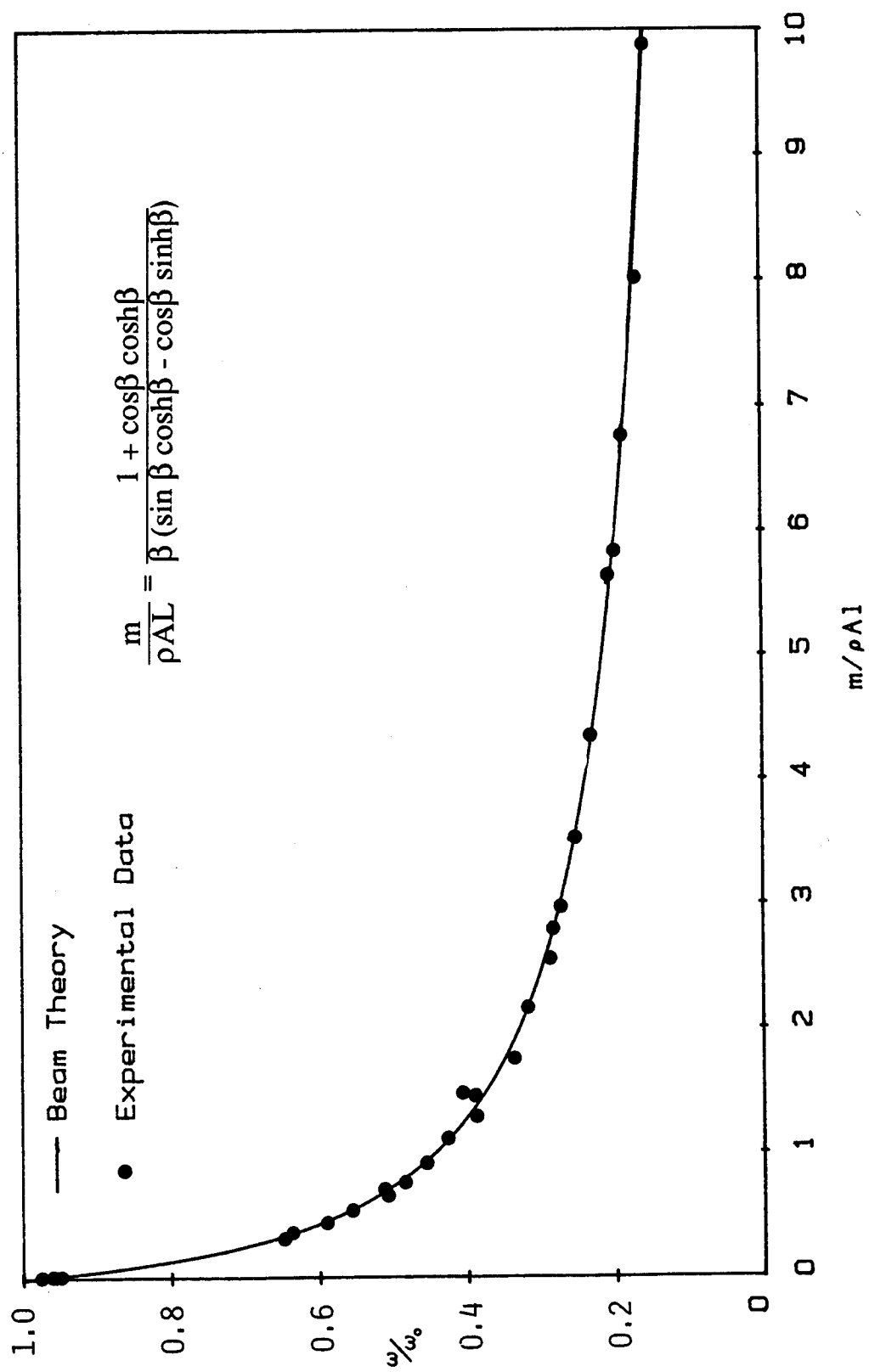


Figure 5 - The Effect of an End-mass on the Resonant Frequency of a Cantilevered Beam

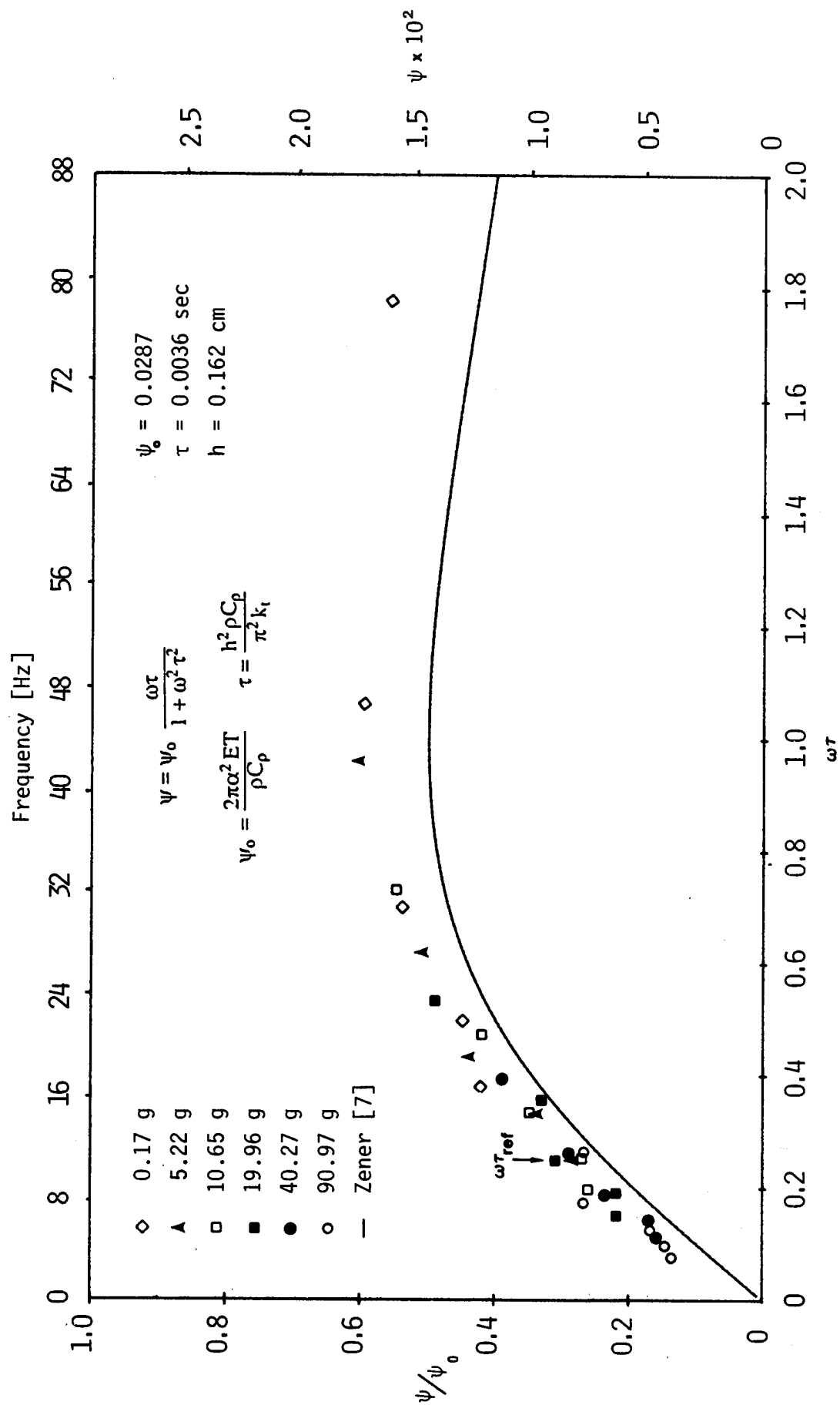


Figure 6 - Normalized Damping vs Normalized Frequency for 6061 Aluminum

Five beam lengths and six end-masses were chosen to produce the same resonant frequency (marked by arrow). Within the errors of measurement the measured damping does not depend on end-mass.

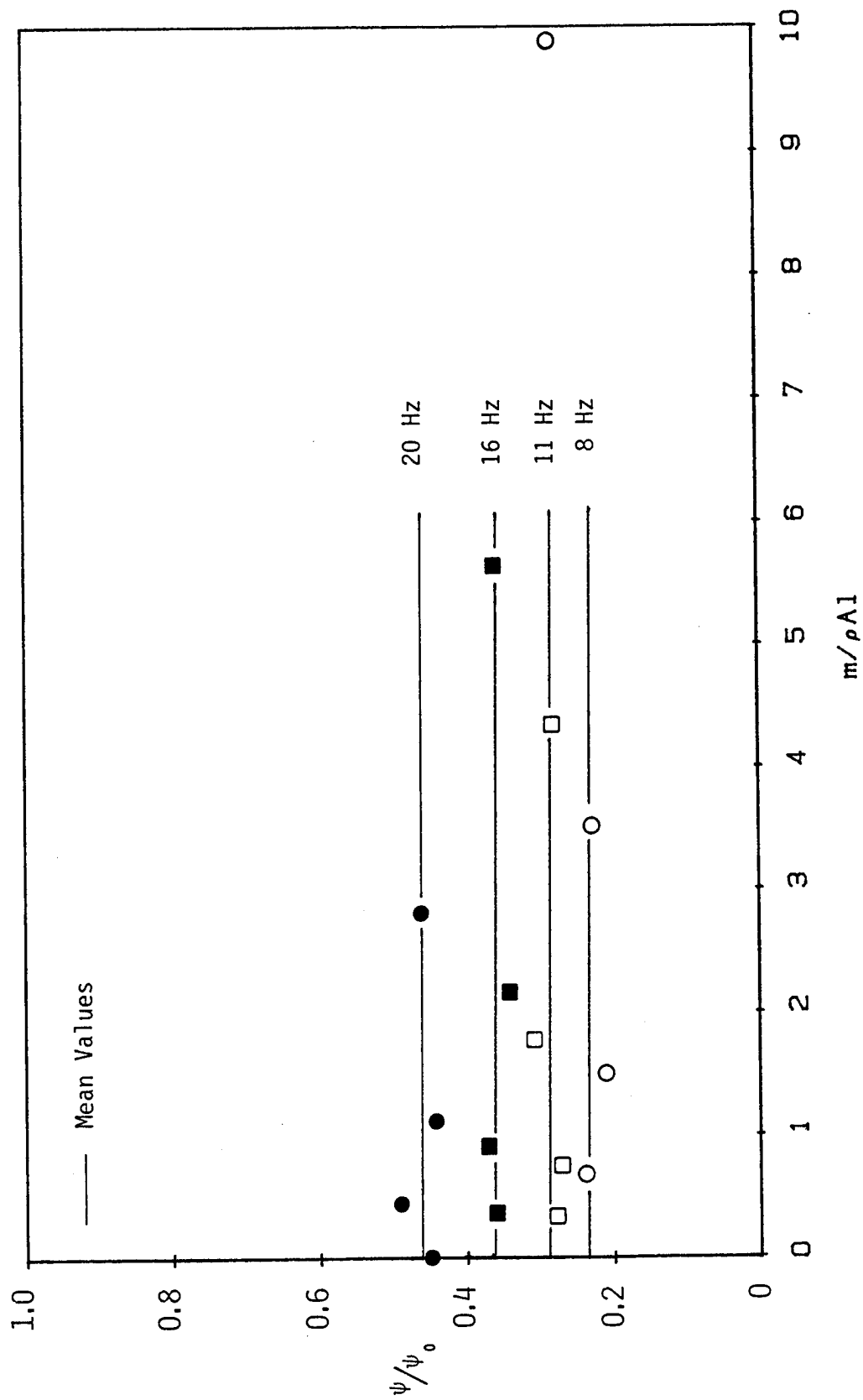


Figure 7 - Damping as a Function of End-mass for Four Nominal Frequencies

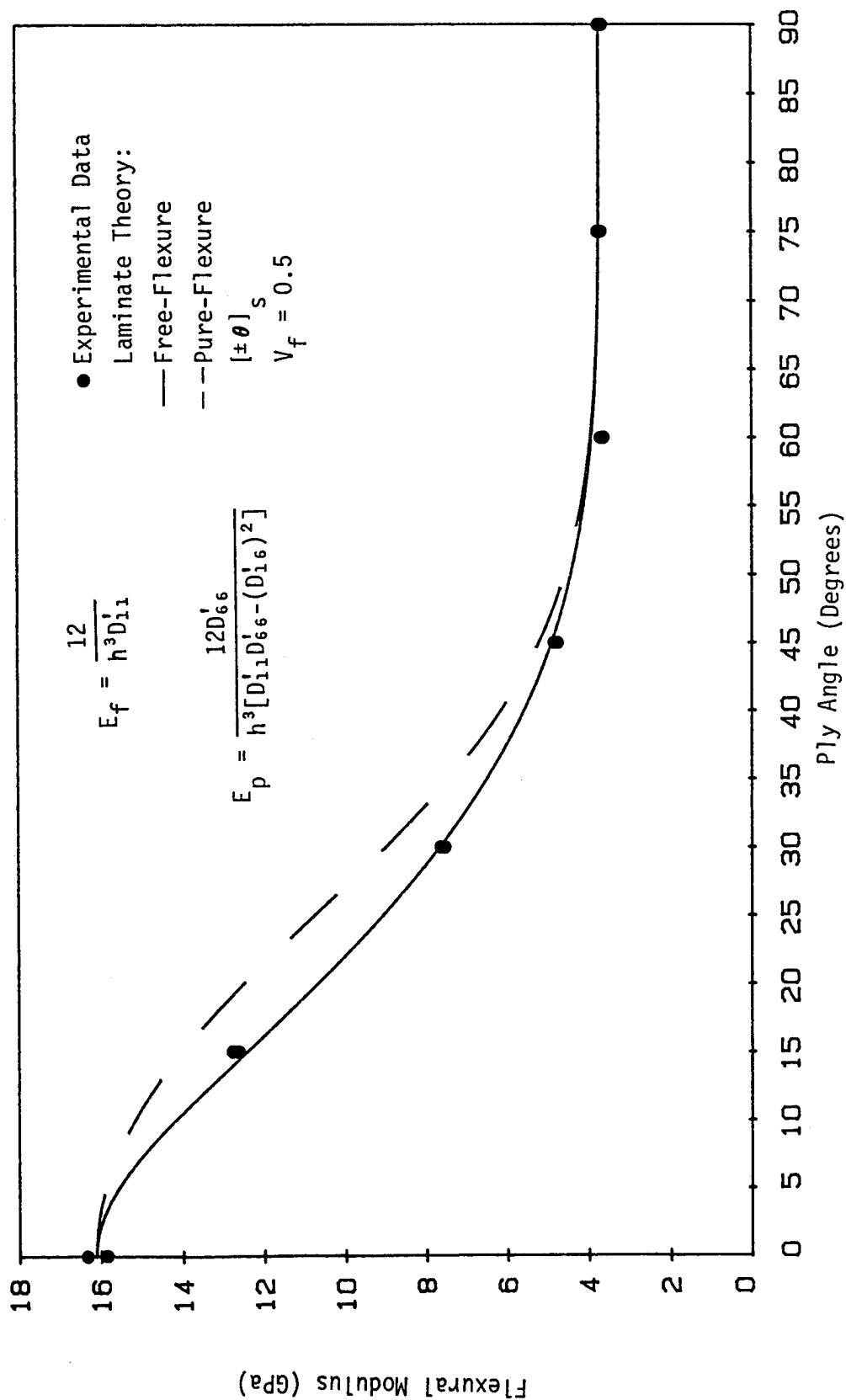


Figure 8 - Flexural Modulus vs Ply-Angle for Symmetric 4-Ply P55Gr/6061Al Composite

Two specimens of each ply angle were tested - the experimental data overlap

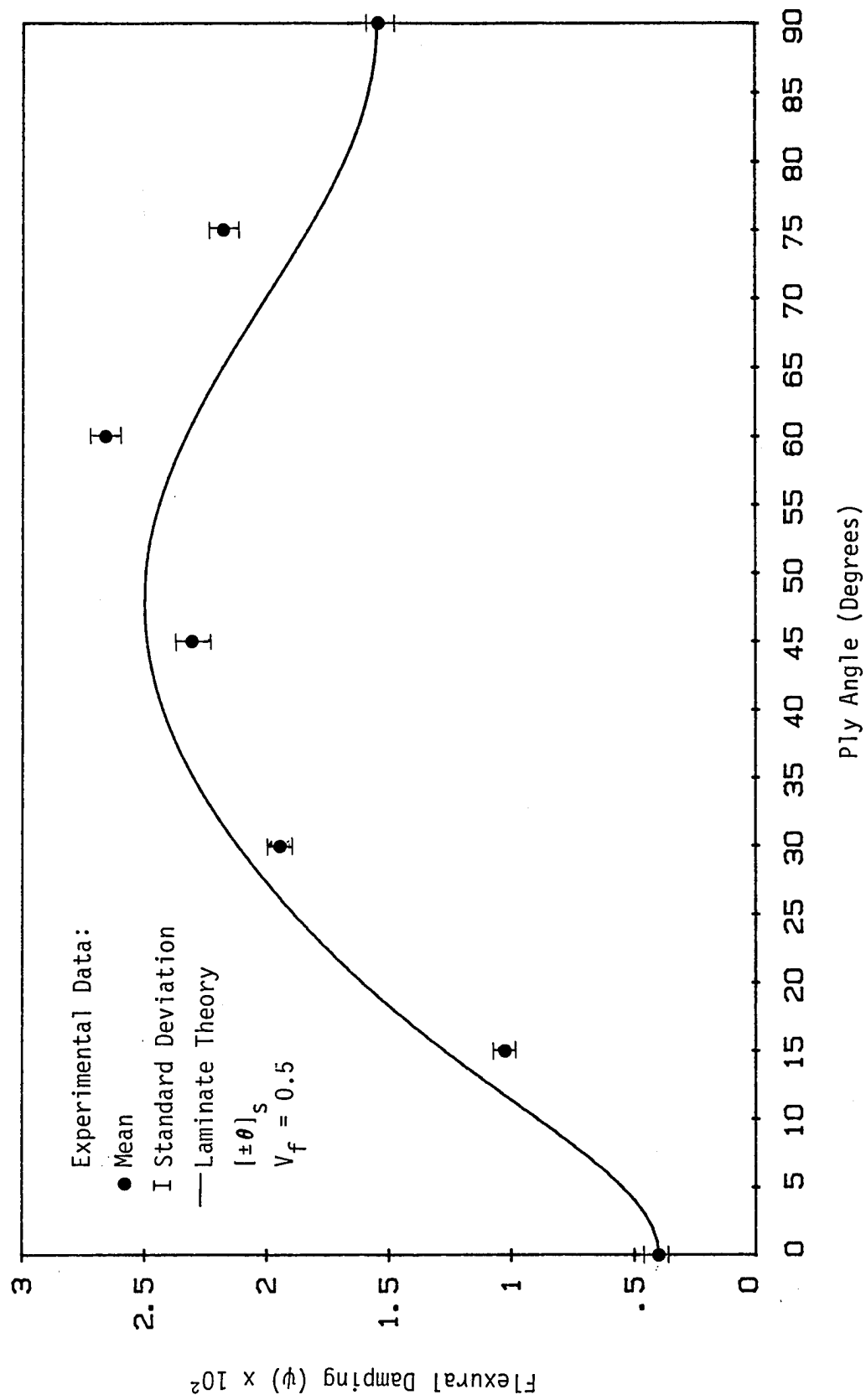


Figure 9 - Flexural Damping vs Ply Angle for Symmetric P55Gr/6061Al Composite

A DESIGN FOR IMPROVING THE STRUCTURAL DAMPING PROPERTIES  
OF AXIAL MEMBERS

David John Barrett  
Advanced Structures Technology Branch  
Naval Air Development Center  
Warminster, PA 18974-5000  
(215) 441-3770

ABSTRACT

In this work a laminated composite construction is studied for the purposes of improving the damping properties of axially loaded structural members. The lamination consists of an anisotropic arrangement of stiffness and damping materials. Under vibratory loading the anisotropy produces stress coupling effects that shear the damping materials, thus leading to a high dissipation of vibrational energies. A structural theory is formulated for examining this construction and is applied to the analysis of a three layered member. Parametric studies are performed for a specific design case. The results demonstrate the effectiveness of the new design for controlling the resonant response of simple harmonic oscillators.

## 1.0 INTRODUCTION

Although traditionally treated as a secondary design variable, damping is being increasingly relied upon to improve the performance of sophisticated structures. A popular design method for increasing structural damping is the combination of viscoelastic materials and stiffness materials into composite constructions. Structural components based on this approach possess stiffness, strength and a high damping capacity [1-2].

A well-established composite construction is the constrained layer treatment which consists of laminations of stiffness and damping layers. The study of this design is now new; such designs have a technological history approximately as old as that of modern composite materials. Over this period, theories and practice methods have arisen to address beam and plate components [3-9]. Constrained layer treatments are now the preferred method of construction in many designs that require high structural damping in order to control bending modes of vibration.

In spite of their success, damping methods have an inherent limitation. Damping materials typically have a high shear viscosity but a low bulk viscosity. Thus, vibrational energies are not dissipated unless high frequency shear modes are excited. For some structural components, such as axially loaded members, relying on such a driving mechanism can render a damping design virtually ineffective.

To rectify this shortcoming, a new design for axial members is proposed. This design makes use of the stress coupling of anisotropic constructions which can be used to generate local and global shear deformations. In a composite construction these deformations can be employed to shear layers of damping materials.

The pioneering work in the use of stress coupling to assist the control of dynamic responses examined the performance of sandwich plates [10]. The results of this study were limited since the analytical model was based on displacement fields that were too elementary to fully characterize the deformational response of composite constructions. This shortcoming was rectified in a later work [11] which examined laminated sandwich constructions.

In the present work a structural theory is devised which characterizes the behavior of an axially loaded composite construction. The axial member consists of concentric cylindrical layers of stiffness and damping materials. Stress coupling can be introduced into this design through the use of off-axis orthotropic materials and/or orthotropic constructions (surface waffling, spiral stiffeners, surface scoring, etc.). The equations of the theory are solved for the steady state damped response of a simple harmonic oscillator.

## 2.0 THEORY OF LAMINATED ANISOTROPIC AXIAL COMPOSITE CONSTRUCTION

### 2.1 Analytical Model

The axial composite construction is a cylinder of successive concentric layers whose central axis is oriented along the axial coordinate line of a right handed cylindrical coordinate system (Figure 1). Although other constructions are possible, this work assumes that each damping cylinder is bounded by stiffness cylinders. The thickness of an individual layer is designated  $h_n$  while the radial location of the layer's midsurface

is  $R_n$ . The symbol  $n$ , used as a subscript and a superscript in this text, refers to the layer of interest (the numbering proceeds from inside to outside). The overall length of the cylinder is  $l$ .

The mechanical response of the axial composite construction is examined through it's role as a support for a lumped mass single degree of freedom oscillator subjected to a steady state harmonic axial excitation. The equation of motion for such a system can be derived directly from elementary equilibrium considerations. It remains then to characterize the viscoelastic spring stiffness of the support. In doing so the elastic spring stiffness is initially computed with the viscosity introduced later through the use of the Correspondence Principle.

In determining the elastic stiffness, the following assumptions are made:

1. The stiffness cylinders can be treated with thin wall theory.
2. The moduli of the damping cylinders are negligible in comparison to the moduli of the stiffness cylinders.
3. The cylinders are perfectly bonded together.

Assumption 1 implies that in each stiffness cylinder the membrane stresses are independent of the radial coordinate and that the non-membrane stresses are negligible. From Assumption 2, and the purely axial loading,, it is seen that all of the stresses in the damping cylinders are negligible except for the radial-tangential shear stress. Assumption 3 implies that the displacements are continuous across the interfaces. From the geometry of the construction and the type of applied loading, it follows that all of the field variables are independent of the circumferential coordinate.

The method of solution will be to develop the equilibrium equations for the individual cylinders in terms of the local displacements and tractions. By applying interfacial equilibrium the tractions are eliminated from these equations yielding a set of linear simultaneous differential equations. The solution to these displacement equilibrium equations can be used to compute the stiffness characteristics of the composite construction.



## 2.2 Stiffness Cylinders

From the assumptions it is seen that the midsurface displacements in the stiffness cylinders reduce to

$$U_z^n(Z, \theta, R) \longrightarrow U_z^n(Z) \quad (1)$$

$$U_\theta^n(Z, \theta, R) \longrightarrow U_\theta^n(Z) \quad (2)$$

$$U_R^n(Z, \theta, R) \longrightarrow U_R^n(Z) \quad (3)$$

Then using the stress-strain relations of an orthotropic system, the stress-displacement equations become:

$$\sigma_{zz}^n = C_{11}^n U_{z,z}^n + C_{12}^n R_n^{-1} U_R^n + C_{16}^n U_{\theta,z}^n \quad (4)$$

$$\sigma_{\theta\theta}^n = C_{12}^n U_{z,z}^n + C_{22}^n R_n^{-1} U_R^n + C_{26}^n U_{\theta,z}^n \quad (5)$$

$$\sigma_{z\theta}^n = C_{16}^n U_{z,z}^n + C_{26}^n R_n^{-1} U_R^n + C_{66}^n U_{\theta,z}^n \quad (6)$$

where the  $C_{ij}^n$  are the elastic stiffnesses and a comma denotes

differentiation with respect to the listed variable. Imposing equilibrium and eliminating the radial displacement yields the following equations:

$$\left( C_{11}^n - \frac{C_{12}^n C_{12}^n}{C_{22}^n} \right) U_{z,zz}^n + \left( C_{16}^n - \frac{C_{12}^n C_{26}^n}{C_{22}^n} \right) U_{\theta,zz}^n = 0 \quad (7)$$

$$\left( C_{16}^n - \frac{C_{26}^n C_{12}^n}{C_{22}^n} \right) U_{z,zz}^n + \left( C_{66}^n - \frac{C_{26}^n C_{26}^n}{C_{22}^n} \right) U_{\theta,zz}^n = - \frac{(\dot{T}_\theta^n b_n b_n + \dot{T}_\theta^{n+1} b_{n+1} b_{n+1})}{R_n R_n h_n} \quad (8)$$

where the  $b_n$  are the radial location of the cylinders lateral faces and

$s_{T_\theta}^n$  (innermost surface) and  $s_{T_\theta}^{n+1}$  (outermost surface) are the

circumferential tractions acting on these lateral faces.

## 2.3 Damping Cylinders

For the damping cylinders the stress-displacement relation for the radial-tangential shear stress is:

$$\sigma_{R\theta}^n(R, Z) = G^n (U_{\theta,R}^n - R^{-1} U_\theta^n) \quad (9)$$

where  $G^n$  is the shear modulus. By imposing circumferential equilibrium the circumferential displacements can be determined in terms of the displacements on the lateral boundaries which can be directly related to the displacements of the adjacent stiffness cylinders. The shear stress then becomes:

$$\sigma_{R\theta}^n(Z) = -2G^n h_2^n R^{-2} \quad (10)$$

where

$$h_2^n = \frac{b_n^2 b_{n+1}^2 (R_{n+1} U_0^{n-1} - R_{n-1} U_0^{n+1})}{R_{n-1} R_{n+1} (b_n^2 - b_{n+1}^2)} \quad (11)$$

From equation (10) the tractions on the inner  $T_{\bullet}^n$  and the outer  $T_{\circ}^{n+1}$  boundaries can be computed.

## 2.4 Interfacial Equilibrium

From interfacial equilibrium the tractions between adjacent damping and stiffness cylinders are related as

$$\dot{T}_{\bullet}^{n+1} = -\dot{T}_{\circ}^{n+1} \quad (12)$$

$$\dot{T}_{\bullet}^n = -\dot{T}_{\circ}^n \quad (13)$$

## 3.0 APPLICATION TO THREE LAYERED AXIAL MEMBER

As an application of the theory consider a composite construction of three cylinders. The outer and inner cylinders are stiffness layers while the middle cylinder is a damping layer. Solving the governing equations yields the following displacements in the stiffness cylinders.

$$U_0^1(Z) = d_1 + d_2 Z + d_3 e^{m_3 Z} + d_4 e^{m_4 Z} \quad (14)$$

$$U_0^3(Z) = d_5 + d_6 Z + d_7 e^{m_3 Z} + d_8 e^{m_4 Z} \quad (15)$$

$$U_2^1(Z) = \frac{-A_{12}^1 (d_3 e^{m_3 Z} + d_4 e^{m_4 Z}) + d_9 Z + d_{10}}{A_{11}^1} \quad (16)$$

$$U_2^3(Z) = \frac{-A_{12}^3 B_4 (d_3 e^{m_3 Z} + d_4 e^{m_4 Z}) + d_{11} Z + d_{12}}{A_{11}^1 B_2} \quad (17)$$

where the  $B_i$  and  $m_i$  are constants [12] and the  $d_i$  are constants of integration (only eight of which are independent). The stresses are then computed as:

$$\sigma_{zz}^1(Z) = V_1 d_2 + V_3 d_9 \quad (18)$$

$$\sigma_{zz}^3(Z) = V_4 d_2 + V_6 d_{11} \quad (19)$$

$$\sigma_{z\theta}^1(Z) = W_1 d_2 + W_2 (d_3 e^{m_3 Z} - d_4 e^{m_4 Z}) + W_3 d_9 \quad (20)$$

$$\sigma_{z\theta}^3(Z) = W_4 d_2 + W_5 (d_3 e^{m_3 Z} - d_4 e^{m_4 Z}) + W_6 d_{11} \quad (21)$$

where the  $V_i$  and  $W_i$  are constants [12].

The solutions for the displacement fields contain rigid body, constant strain and exponential terms. These last terms embody the effects of stress-coupling on the composite construction. Since these terms are exponential it is concluded that the contribution of the middle layer to component damping is primarily based on end effects. This observation has implications for an optimum design configuration (i.e., designs based on segmented constrained layer treatments or on variable stiffness cylinders.) The present work will not seek to treat optimum designs, which involve greater analytical difficulties, but will concentrate on examining the basic structural theory.

#### 4.0 DESIGN STUDY

##### 4.1 Description

The displacement solutions contain eight unknown constants which are determined from the displacement and traction boundary conditions acting on the ends of the stiffness cylinders. Various sets of boundary conditions have practical interest. For the purposes of this study the following boundary conditions are imposed:

$$U_z^1(0) = 0 \quad (\text{Fixed}) \quad (22)$$

$$U_z^3(0) = 0 \quad (\text{Fixed}) \quad (23)$$

$$U_z^1(l) = U_z^3(l) \quad (\text{Rigid Link}) \quad (24)$$

$$\sigma_{zz}^1(l) A_1 + \sigma_{zz}^3(l) A_3 = P \quad (25)$$

$$U_\theta^1(0) = 0 \quad (\text{Fixed}) \quad (26)$$

$$U_\theta^3(0) = 0 \quad (\text{Fixed}) \quad (27)$$

$$\sigma_{z\theta}^1(l) = 0 \quad (\text{Free}) \quad (28)$$

$$\sigma_{z\theta}^3(l) = 0 \quad (\text{Free}) \quad (29)$$

where the  $A_i$  are the cross sectional areas of the stiffness cylinders and  $P$  is the applied axial load.

Applying the boundary conditions to the general solution leads to a set of linear simultaneous algebraic equations the solution of which are the constants of integration. Once these constants are determined the solution to any field variable can be found. By applying a unit load to the column and solving for the field variables, influence coefficients and hence stiffness can be determined for any point of interest. The viscosity of the support is introduced by invoking the Correspondence Principle.

In the following example a composite construction is examined that combines a fiber reinforced material with a centrally positioned damping material (Table 1). The anisotropy of the construction is varied via a  $-\theta^0/\theta^0$  (inside cylinder/outside cylinder) off-axis fiber orientation. In addition the response of a conventional cylindrical design is also computed and used as a baseline from which to judge the performance of the new design. The baseline design [13] contains no damping layers in its section and is constructed from the same stiffness material as the composite construction. The principal material direction of the baseline design is always oriented parallel to the central axis of the cylinder (maximum static stiffness). The structural damping of the baseline design is equal to the material damping of the stiffness materials. In the design study the cross sectional area of the baseline and composite constructions are equal so that the analysis examines the effect of replacing stiffness material with damping material.

The shear modulus (.024 GPa) and the loss factor (1.0) of the damping material are taken as constants thus ignoring the frequency and temperature dependency of these properties. Since the purpose of the design study is to make structural comparisons this simplification is not critical. However for actual designs the effects of the operational environment must be considered in more detail.

The axial member to be examined here has a length of 25.4 cm and a supported mass of 232 Kg. The mass of the support, which can be treated in the analysis through a lumped mass approach, is much less than the supported mass. Therefore in this problem the frequency response is practically independent of the structural mass. Nevertheless it should be noted that viscoelastic materials are less massive than reinforced epoxies so that composite construction produces lighter structure.

#### 4.2 Results

The results of the analyses are presented as the amplitudes of the frequency response and are normalized with respect to the response of the baseline design (indicated by the superscript B on the plots).

The dynamic response of the composite construction is shown in Figure 2 where it is seen that for small offset angles the response actually increases. However moving to greater offset angles results in a dramatic decrease in resonant response. Figure 3 shows that this trend continues until further increases in structural damping (Figure 4) can no longer counter the effects of lost stiffness (Figure 5) so that it is seen that there is an optimum balance of these properties for minimizing the displacement response. Figure 3 also shows the effect of off-axis orientations on the circumferential displacements. These displacements, which drive the shearing of the damping layer, must be managed in order to produce a feasible design. Figure 6 shows that the resonant axial stresses continue to decrease even after the axial displacement begins to rebuild. This drop in stress can be directly related to the increasing loss factor. Figure 6 also shows the maximum shear and interfacial stresses which are generated in the new design. Finally, Figure 7 plots the shift in resonant frequency as the structural stiffness is lowered.

## 5.0 DISCUSSION AND CONCLUSION

The design studies explored the use of stress coupling and lamination in an axial composite construction, a new structural component, that is intended for use in vibration sensitive structure. Incorporating these components into structures will affect the structural response through several ways including: energy dissipation, the reduction of stiffness, the reduction of mass and the introduction of anisotropic effects.

Energy dissipation is the prime motivation for using the new design approach and the design study shows that by combining diverse materials (stiffness and damping) into a composite construction, components can be produced with superior structural properties. The reduction of resonant stress and displacements is directly attributable to the increase in damping in these components. That there is a trade-off in these components between static stiffness and damping simply introduces a new variable to the design process. Since in the anticipated applications the overriding design goal will be to reduce resonant responses the sacrifice of stiffness for energy dissipation presents design opportunities.

The introduction of anisotropic effects leads to the most formidable difficulties for application. Anisotropy results in shear stresses and circumferential displacements in the axial composite construction, mechanical responses that do not exist in an axially loaded baseline design. The presence of shear stresses do not necessarily represent a design penalty, especially since the axial stresses are significantly reduced. However, depending on the material of construction, shear stresses may cause new modes of failure which must be considered in the design process. The occurrence of shear stresses may also require a redesign of the structural connections. Such redesigns will be even more difficult when allowing for the circumferential displacements that occur at the ends of members. Some critical applications may justify the effort of accommodating these displacements but for the design to achieve widespread use a way of eliminating these displacements altogether must be found. If the construction had a variable axial stiffness (stepped thicknesses, variable angled filament winding, etc.) components could be produced for which the circumferential displacements vanish at the element ends. In such designs the circumferential displacements, which are necessary for shearing the damping layers, can be confined to the central portions of the component so that fixed circumferential boundary conditions can be applied while still achieving a drive for damping.

An additional advantage of the axial composite construction is its resistance to all modes of vibration. For flexural modes the component acts similar to damped sandwich constructions since the damping layers will be sheared by the displacements that occur in beam bending. Torsional modes are resisted by the same stress coupling effects that occur under axial vibrations with the difference being that the damping layers are now sheared by differential axial displacements.

The design studies were based on viscoelastic properties that assumed a peak value for the loss factor. However, both the stiffness and loss factor of these materials are frequency and temperature dependent with peak values occurring over limited ranges. In order to extend the capability of

the axial composite construction, dissimilar viscoelastic materials, each with a distinct range of peak effectiveness, could be incorporated in the component. Design approaches that may be taken include a four layer cylinder with adjacent interior damping layers or a five layer cylinder with interior stiffness and damping layers.

The work presented here demonstrates that stress coupling and lamination can be used to great advantage in increasing the damping of axial structural components. Further research in this area will investigate generalizing the basic approach to other types of structural components.

## REFERENCES

1. Nashif, A.D., Jones, D.I.G. and Henderson, J.P., "Vibration Damping," John Wiley and Sons, New York, 1985.
2. Soovere, J., and Drake, M.L., "Aerospace Structures Technology Damping Design Guide," AFWAL-TR-84-3089, December 1985.
3. DiTaranto, R.A. and Blasingame, W., "Composite Damping of Vibrating Sandwich Beams," ASME J. of Eng. for Industry, Vol. 89, 1967.
4. Yan, M.J. and Dowell, E.H., "Governing Equations for Vibrating Constrained-Layer Damping Sandwich Plates and Beams," ASME J. of Applied Mechanics, December 1972.
5. Torvik, P.J. "The Analysis and Design of Constrained Layer Damping Treatments," in Damping Applications for Vibration Control, ASME Publication AMD-Vol 38, 1980.
6. Lu, Y.P., et al., "Vibration of Three Layered Damped Sandwich Plate Composites," J. of Sound and Vibration, Vol. 64 (1), 1979.
7. Ioannides, E., and Grootenhuis, P., "A Finite Element Analysis of the Harmonic Response of Damped Three-Layer Plates," J. of Sound and Vibration, Vol. 67 (2), 1979.
8. Holman, R.E. and Tanner, J.M. "Finite Element Modeling Techniques for Constrained Layer Damping," AIAA Journal, Vol. 21 (5), May 1983.
9. Soni, M.J. and Bogner, F.K., "Finite Element Vibration Analysis of Damped Structures," AIAA Journal, Vol. 20 (5), May 1982.
10. Mukhopadhyay, A.K. and Kingsbury, H.B., "On the Dynamic Response of Rectangular Sandwich Plate with Viscoelastic Core and Generally Orthotropic Facings," J. Sound and Vibration, Vol. 47 (3), 1976.
11. Barrett, D.J., "Optimization of Damping Properties of Structural Components," Final report to NSF, Grant No. ISI-8560810, July 1986.
12. Barrett, D.J., "A Design for Improving the Structural Damping Properties of Axial Members," Report No. NADC-88056-60, April 1988.
13. Mikulas, M.M., et al, "Space Station Truss Structures and Construction Considerations," NASA TM 86338, 1985.

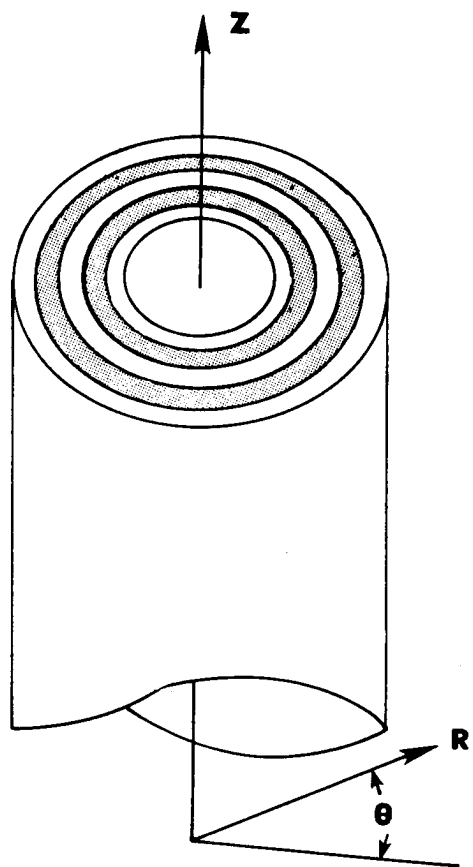


**FIGURE 1 AXIAL COMPOSITE CONSTRUCTION**



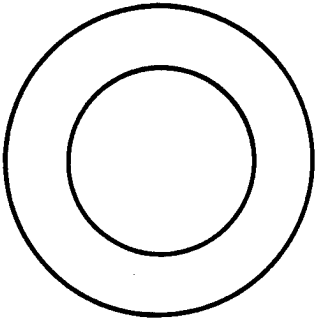
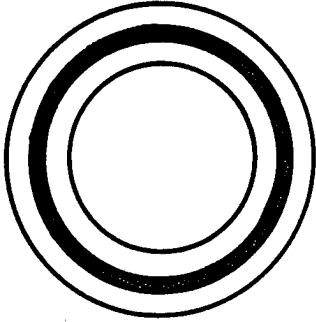
DESIGN CASE	BASELINE		COMPOSITE CONSTRUCTION	
				
	CONSTRUCTION	MONOLITHIC	THREE CONCENTRIC CYLINDERS	
	DIAMETER	2.54 cm	2.54 cm	
	WALL THICKNESS	.152 cm	.152 cm (.0699 / .0127 / .0699 cm)	
	MATERIALS	HMF GRAPHITE/EPOXY	HMF GRAPHITE/EPOXY PLUS DAMPING MATERIAL	
FIBER ORIENTATION		0°	VARIABLE	

TABLE 1 Design Description

N1808-GA-89-000000

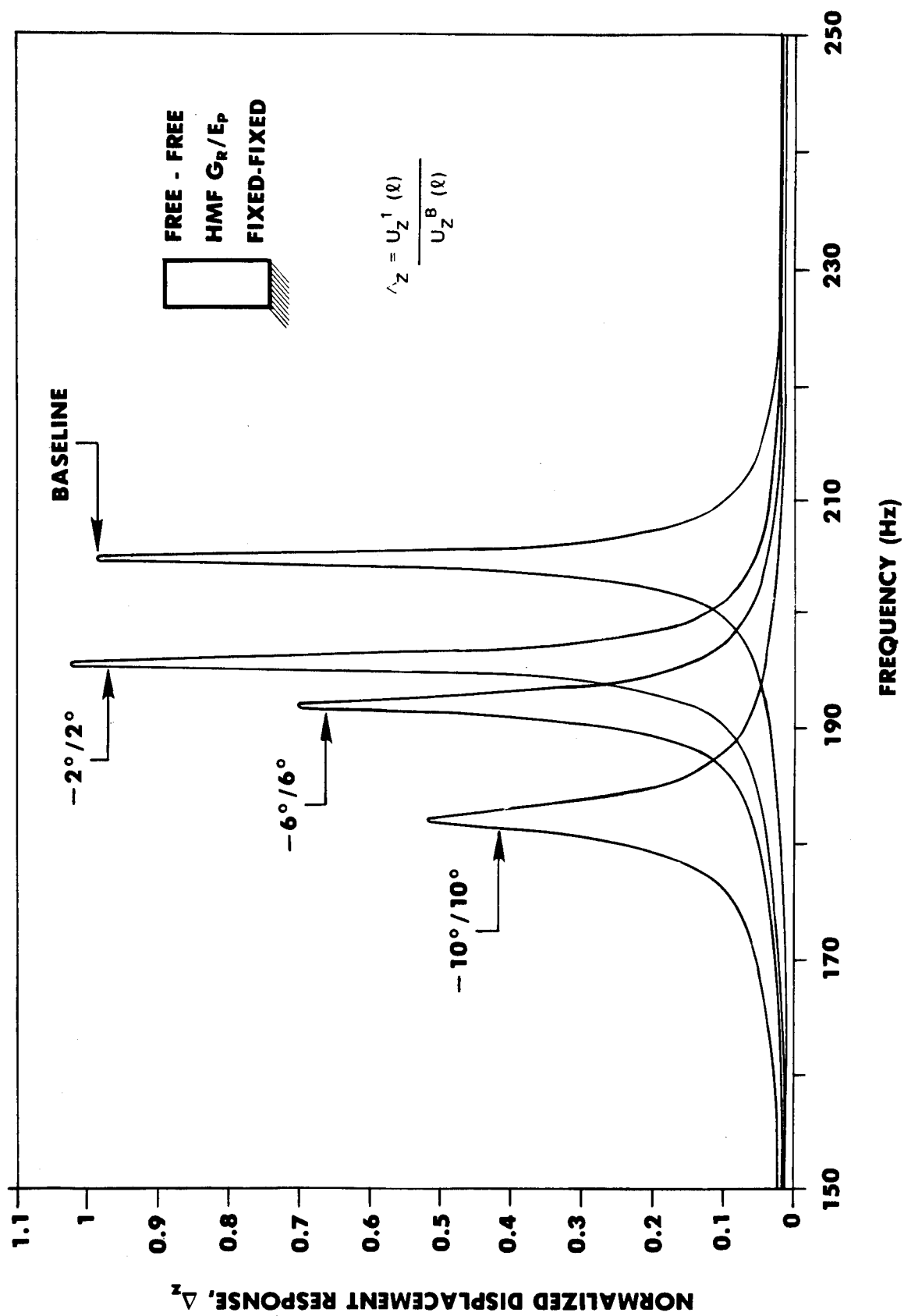
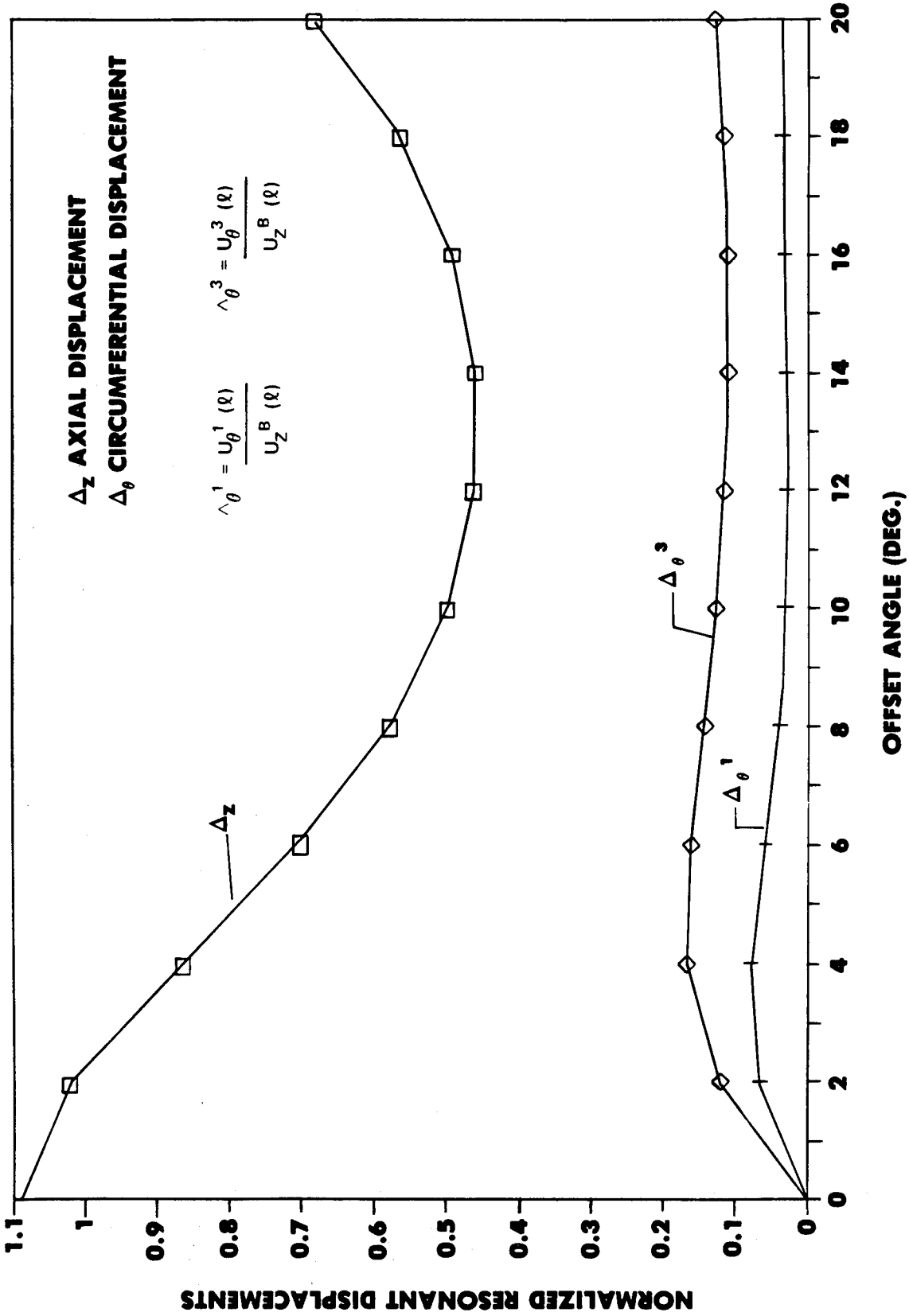


FIGURE 2 NORMALIZED DIPLACEMENT RESPONSE SPECTRUM, COMPOSITE CONSTRUCTION #1



**FIGURE 3 NORMALIZED RESONANT DISPLACEMENT VS OFFSET ANGLE, COMPOSITE CONSTRUCTION #1**

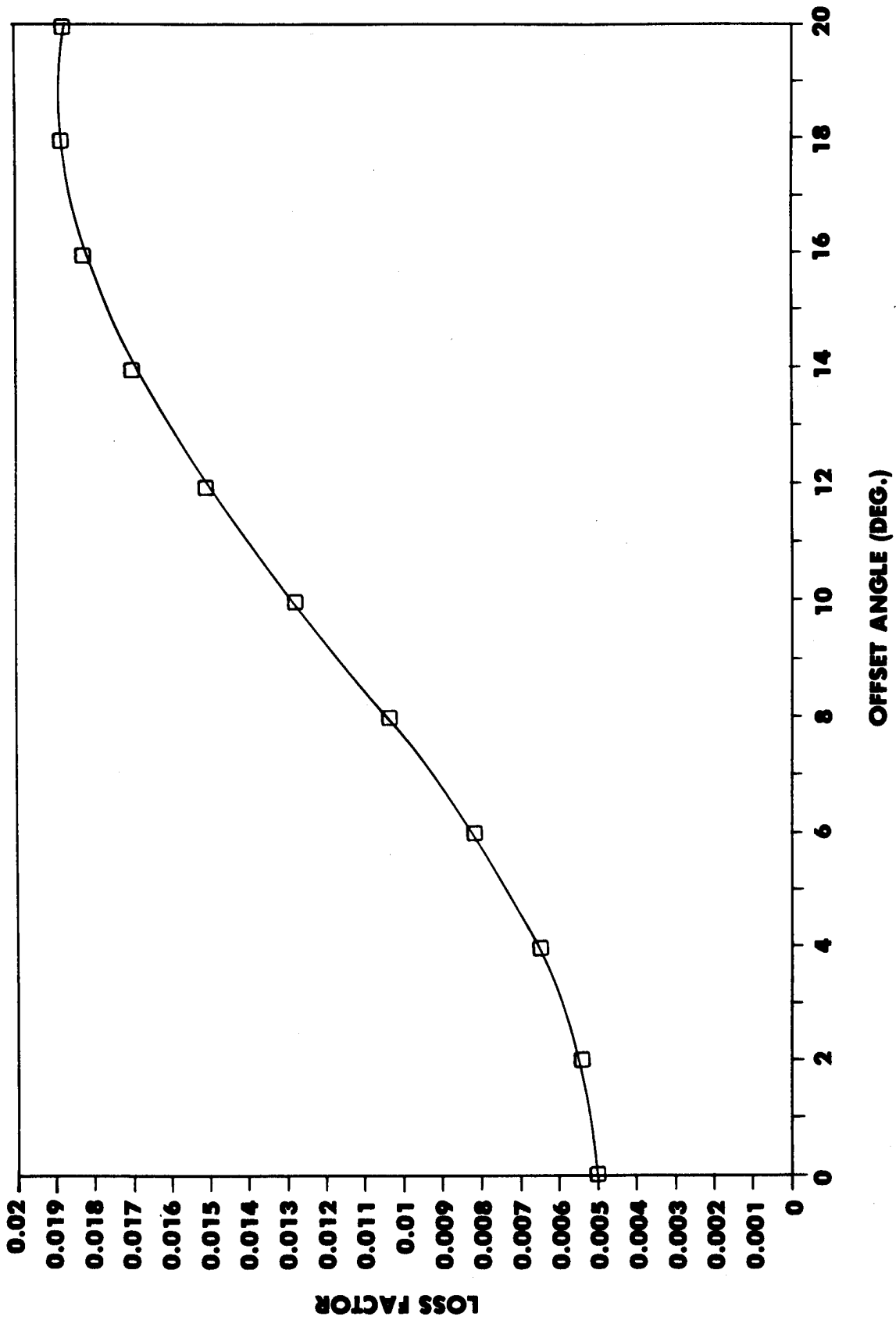
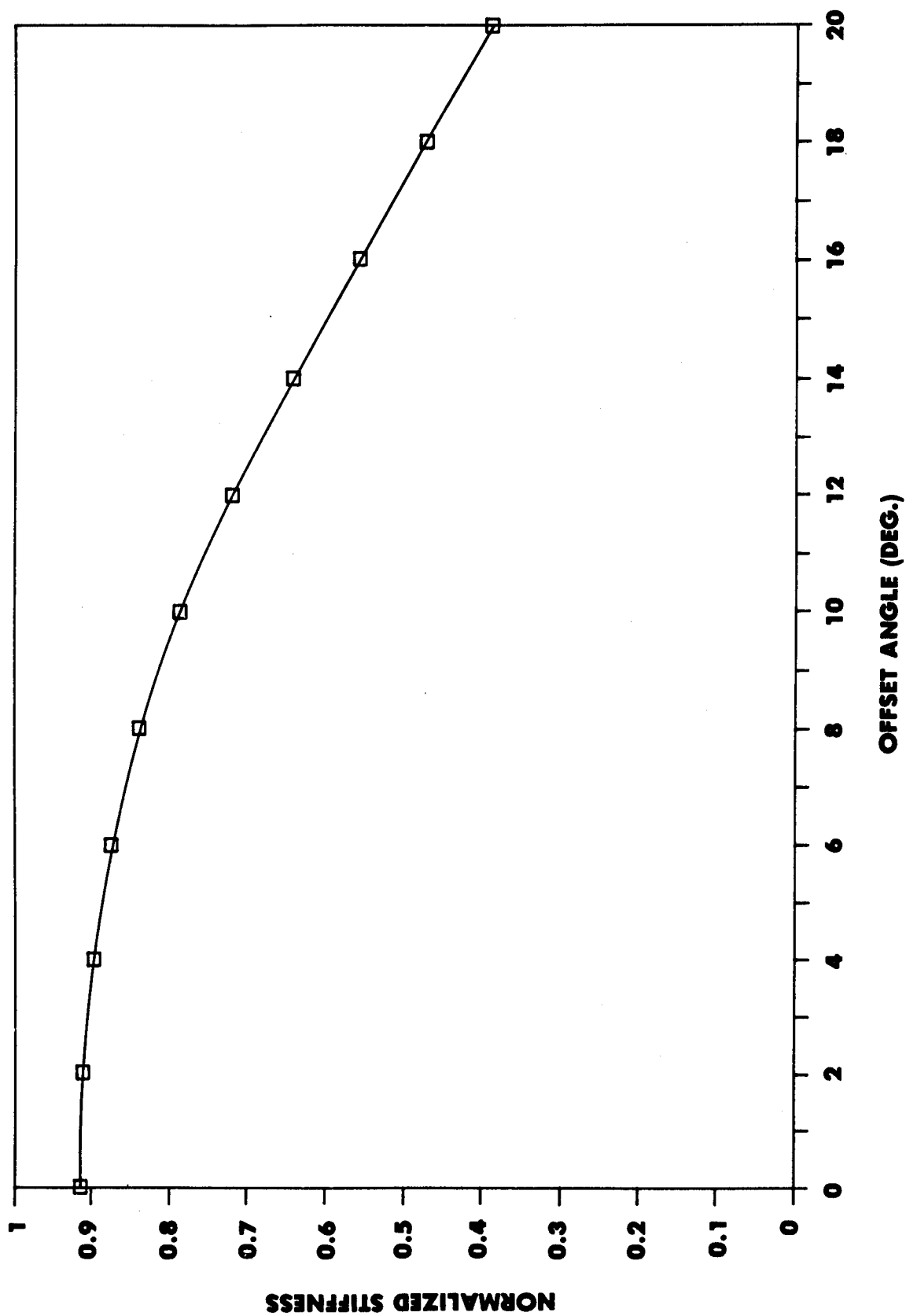
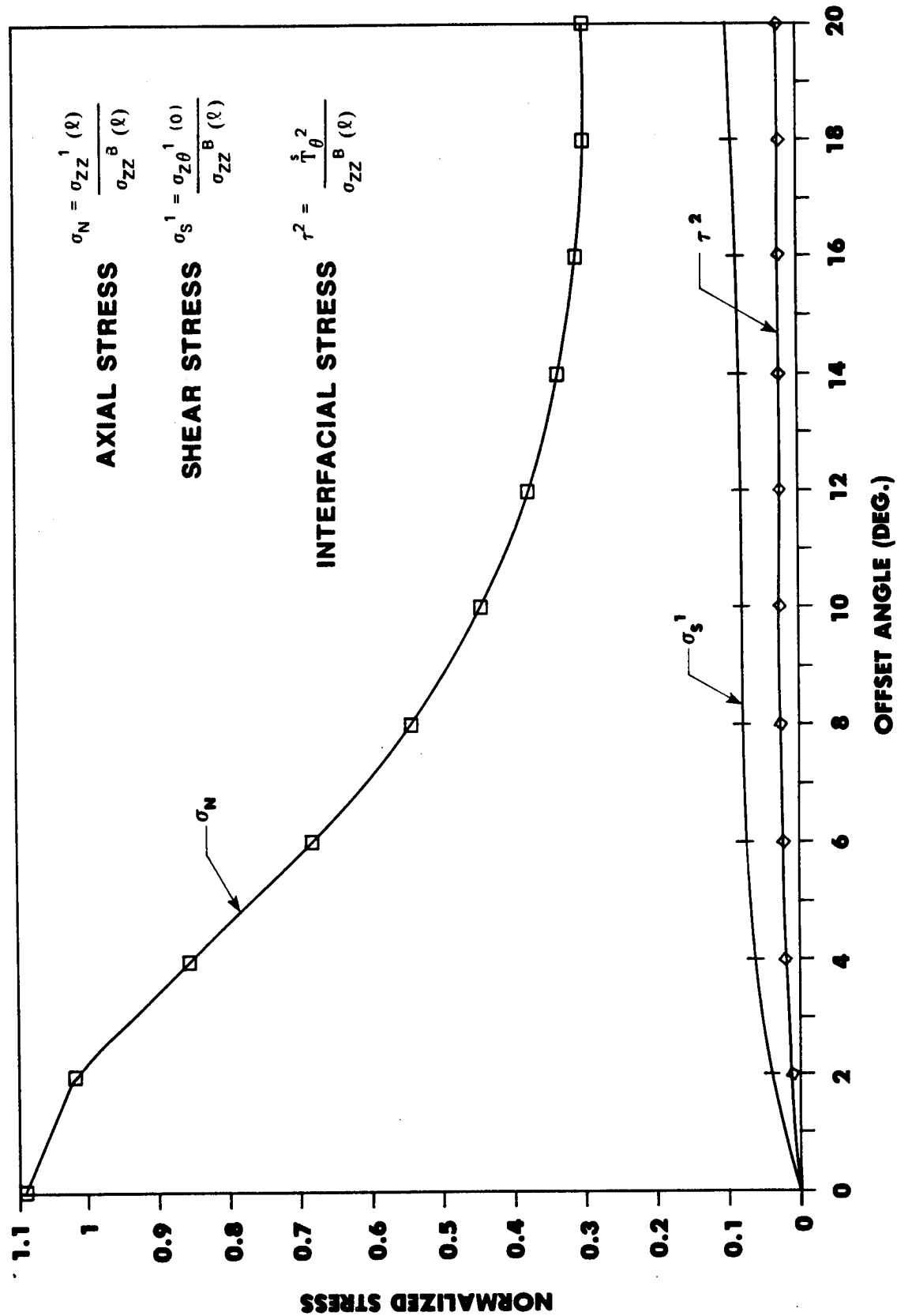


FIGURE 4 LOSS FACTOR VS. OFFSET ANGLE, COMPOSITE CONSTRUCTION #1



**FIGURE 5 NORMALIZED STIFFNESS VS. OFFSET ANGLE, COMPOSITE CONSTRUCTION #1**



**FIGURE 6 NORMALIZED RESONANT STRESSES VS. OFFSET ANGLE, COMPOSITE CONSTRUCTION #1**

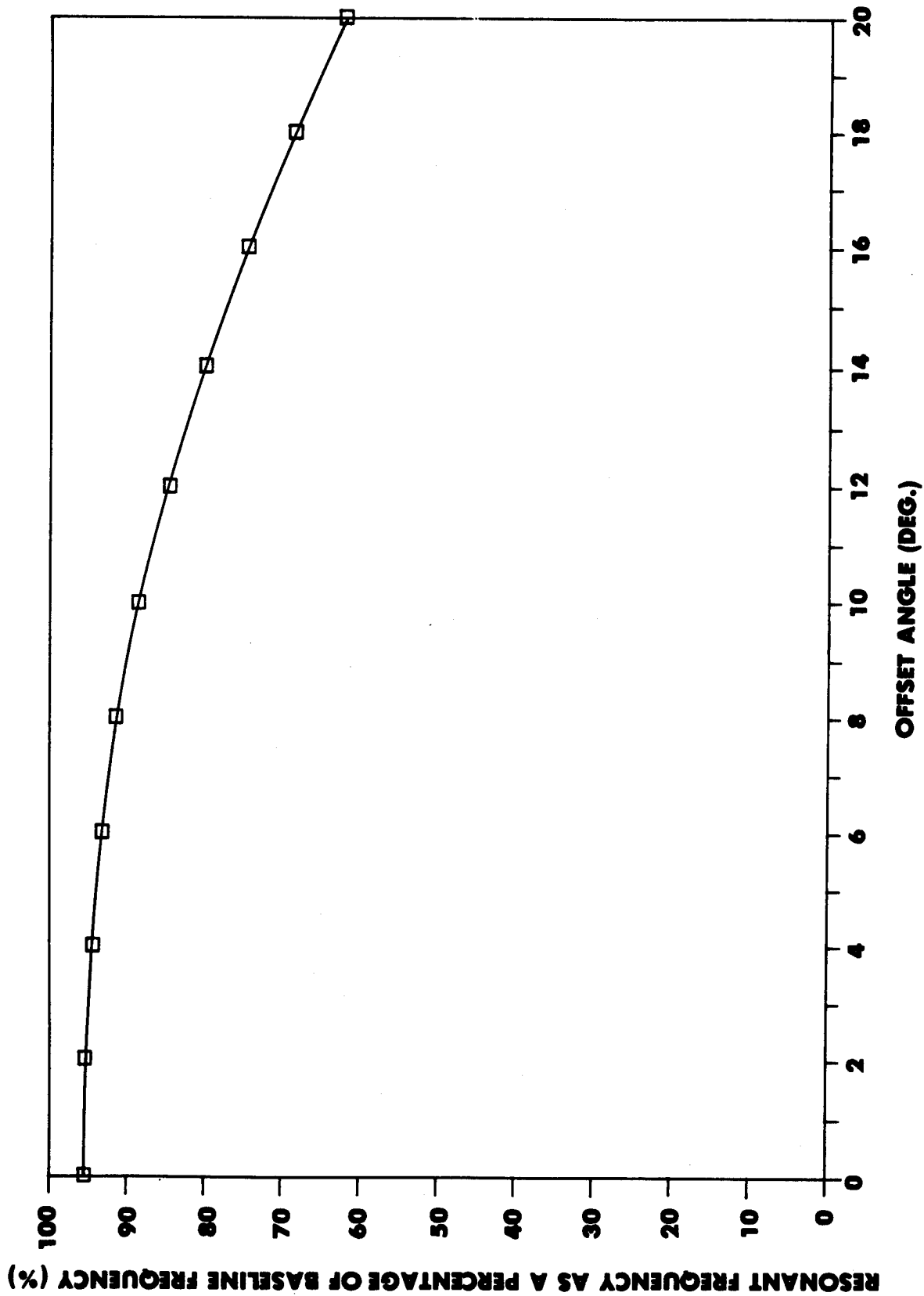


**FIGURE 7 RESONANT FREQUENCY VS. OFFSET ANGLE, COMPOSITE CONSTRUCTION #1**

# **Study of the Damping Capacity of Structural Joints Made of Graphite Epoxy Composite Material**

**Mohan D. Rao**

**Department of Mechanical Engineering-Engineering Mechanics  
Michigan Technological University  
Houghton, MI 49931**

**and**

**Malcolm J. Crocker, and P.K. Raju  
Department of Mechanical Engineering  
Auburn University  
Auburn, AL 36849**

## **ABSTRACT**

Owing to their high strength and low weight, composite materials have found applications in commercial, military, and spacecraft structures. The truss system of the Hubble Space Telescope, for example, is made of graphite epoxy beams, tubes and joints that have very low damping capacity. Vibration of the Space Telescope is undesirable since it would cause blurring of the optical system images. A specific knowledge of the damping capacity of the composite material and structural joints and the factors that influence the damping is very useful in the design of appropriate vibration isolation systems for the telescope.

Joints form an important aspect of any space structural system. Unlike metals, fiber composites cannot be welded together. The alternatives include the use of mechanical fasteners, such as bolts and rivets or adhesive bonding.

These techniques produce joints with vastly different properties. It is believed that bonded (and bolted) joints act to enhance the damping capacity of structural systems. Hence in this paper the results of analytical and experimental investigations carried out on two different types of joint composite specimens to study their damping capacity are reported.

First, a theoretical model to study the Vibration of a bonded lap joint system was developed and is described. The model can be used to predict the natural frequencies, modal damping ratios and mode shapes of the system for free flexural vibration. Good agreement between numerical and experimental results was obtained for a system of graphite epoxy beams lap-jointed by an epoxy adhesive.

The second type of bonded joint considered for the study was a double-butt joint. Experimental work conducted on these joints in a vacuum chamber is described. The damping ratio was computed by using an improved half-power points method. The increase in the values of the damping ratio due to the presence of bonded joints in the system does not appear to be very significant.



## INTRODUCTION

Structural adhesive bonding of composites to composites, as well as composites to metallic components, has developed rapidly due to advances in composite materials and adhesive bonding techniques. Structural composite bonded joints are primarily of the overlap type (single or double overlap). Scarf joints are structurally efficient, but are difficult or costly to manufacture. Butt joints, although simple to process, are not considered for primary structural joints. This is because of their limited load carrying capacity due to the presence of cleavage stresses when the loading is not a true tensile load. Tube joints are difficult and costly to manufacture.

The paper by Goland and Reissner [1] is regarded as a classic work in the area of static analysis of a simple lap joint. Goland and Reissner studied the stresses in bonded single lap joints for two different cases. In the first case, the bond layer was very thin, in the second case, the bond layer was so thick that it was the primary contributor to joint flexibility. In both cases, they derived equations to evaluate the shearing and normal stresses in the bond layer as well as those in the jointed plates. In the Goland and Reissner analysis, the peel and shear stresses were assumed to be constants across the adhesive thickness. In later works by Ojalvo and Eidinoff [2], Carpenter [3], and Kline [4], attempts are made to incorporate a linear variation of these stresses across the thickness of the adhesive. Delale and Erdogan [5] have carried out the stress analysis of a bonded lap joint system assuming that the adherents are elastic and the adhesive is linearly viscoelastic. Renton and Vinson [6], and Delale, Erdogan, and Aydinoglu [7] have attempted to include anisotropic adherents in the mathematical model.

Hart-Smith [8-11] was the first investigator to extensively use continuum mechanics approach in the analysis of bonded joints. He has analyzed double-lap, single-lap, scarf, stepped-lap and tapered-lap configurations. Tensile, compressive and in-plane shear stresses in the system were considered based on an elastic-plastic analysis of the configuration. In that work, the author has also discussed joint efficiency and potential failure modes for each of the above configurations. The above review indicates that much of the work done in this area has been confined to the static analysis of bonded joints.

### I. ANALYTICAL MODELING OF FLEXURAL VIBRATION OF A BONDED LAP-JOINT SYSTEM

The system chosen for study is shown in Figure 1. The objective is to arrive at a suitable mathematical model to evaluate the damping ratios and resonance frequencies of the system undergoing free flexural vibration. The system consists of a pair of rectangular beams lap-jointed over a certain length. The bond between the two beams is achieved by means of an adhesive whose thickness is small compared with those of the beams. The unjointed ends of the beams may have any physically realizable boundary conditions, but, in this case are assumed to be simply-supported. Equations of motion are first derived using the complex modulus approach, assuming the beams to be made of composite materials. The adhesive is assumed to be linearly viscoelastic and the widely used Kelvin-Voight model is used to represent the viscoelastic behavior of the adhesive.

The starting point for the development of this model is the consideration of the dynamic equilibrium equations of the overlap (joint) region. The equations of motion in the joint region are derived using a differential element approach. The transverse displacements of the upper and the lower beam are considered to be different. The normal force between each beam and

the adhesive layer is obtained from the Kelvin-Voight viscoelastic model of the adhesive. The shear force at the interface between the adhesive and the beam is obtained from the simple bending motion equations of the two beams. The resulting equations of motion are combined with the equations of transverse vibration of the beams in the unjointed regions. These are later solved as a boundary value problem by knowledge of the boundary conditions at the unjointed ends and the motion continuity equations at the ends of the overlap. The eigenvalues and the eigenvectors of the system are obtained numerically by an iterative technique on a computer.

The beam system is hypothetically divided into three parts as shown in Figure 2. The coordinate system chosen for each part is also shown in the same figure.

### Analysis of Part 1 of Beam System

The following assumptions are made in the analysis: a) the analysis is carried out only for the free flexural vibration of the system; the longitudinal and rotary inertia effects are neglected, b) there is no slip at the bond interfaces, c) all points on a plane normal to the longitudinal axis of the beam have the same transverse displacement, d) the longitudinal force in the adhesive layer may be neglected relative to those in the beams, and e) since the thickness of the adhesive layer is small relative to the thickness of the beam, the mass (inertia) of the adhesive may be neglected, and the normal and shear forces in the adhesive are assumed to be constant.

A free-body diagram of a differential element of length  $dx$  of the composite three-layer part of the beam system is shown in Figure 3.  $N$  is the axial force in the beam,  $V$  represents the shear force in the beams,  $M$  is the bending moment in the beam,  $s$  is the shear force per unit length at the bond interfaces, and  $p$  is the transverse force per unit length between the beam and the adhesive. The above quantities with subscript 1 refer to the upper beam and with subscript 2 refer to the lower beam. Furthermore,  $y_1 = y_1(x,t)$  is the transverse displacement of the upper beam, and  $y_2 = y_2(x,t)$  is that of the lower beam.

Equating the sum of the forces in the  $y$ -direction to the corresponding inertia forces, we get for beam 1,

$$-V_1 + \left[ V_1 + \frac{\partial V_1}{\partial x} dx \right] + p dx = \rho_1 A_1 dx \frac{\partial^2 y_1}{\partial t^2}, \quad (1)$$

and for beam 2

$$-V_2 + \left[ V_2 + \frac{\partial V_2}{\partial x} dx \right] + p dx = \rho_2 A_2 dx \frac{\partial^2 y_2}{\partial t^2}. \quad (2)$$

The term  $\rho A$  in Equations (1) and (2) is the mass per unit length, in which  $\rho$  represents the density and  $A$  represents the cross sectional area of the beam. Summing the moments about the center of the right edge, for beam 1,

$$M_1 - \left( M_1 + \frac{\partial M_1}{\partial x} dx \right) - s dx \frac{h_1}{2} + V_1 dx = 0. \quad (3)$$

for beam 2,

$$M_2 - \left( M_2 + \frac{\partial M_2}{\partial x} dx \right) - s dx \frac{h_2}{2} + V_2 dx = 0. \quad (4)$$

From Equation (1) through (4), we have,

$$\frac{\partial^2 M_1}{\partial x^2} + \frac{h_1}{2} \frac{\partial s}{\partial x} + p = \rho_1 A_1 \frac{\partial^2 y_1}{\partial t^2}, \text{ and} \quad (5)$$

$$\frac{\partial^2 M_2}{\partial x^2} + \frac{h_2}{2} \frac{\partial s}{\partial x} - p = \rho_2 A_2 \frac{\partial^2 y_2}{\partial t^2}. \quad (6)$$

Equations (5) and (6) represent the equations of motion for the upper and lower beam respectively. From the classical theory of pure bending of beams, the bending moments  $M_1$  and  $M_2$  may be related to the corresponding transverse displacements,  $y_1$  and  $y_2$  through the flexural rigidity term  $EI$ , where  $E$  is the Young's modulus of the material of the beam, and  $I$  is the second moment of the cross-sectional area with respect to the centroidal axis. Noting that the  $y$ -axis is positive downwards, from beam theory,

$$M_1 = -E_1 I_1 \frac{\partial^2 y_1}{\partial x^2} \text{ and } M_2 = -E_2 I_2 \frac{\partial^2 y_2}{\partial x^2}. \quad (7)$$

It should be noted that Equation (7) is valid for an elastic, homogeneous beam having a constant cross-sectional area. It turns out, however, that an equation similar to the above can be written for the composite beams of the present problem, by simply replacing the real modulus by its complex counterpart. This analysis is valid only for simple harmonic time dependence. With this in mind, we can write,

$$M_1 = -E_1^* I_1 \frac{d^2 y_1}{dx^2} \text{ and } M_2 = -E_2^* I_2 \frac{d^2 y_2}{dx^2}. \quad (8)$$

where  $E_1^* = E_1(1 + i\alpha\omega)$ , and  $E_2^* = E_2(1 + i\beta\omega)$ . (9)

$\alpha$  and  $\beta$  are some constants whose values depend on the material,  $\omega$  is the angular frequency, and  $i = \sqrt{-1}$ . The next objective is to find suitable expressions for  $p$  and  $s$  in terms of  $y_1$  and  $y_2$ , so that Equations (5) and (6) can be solved.

As mentioned before, the adhesive layer is modeled as a Kelvin-Voigt viscoelastic solid, because of the mathematical simplicity. A detailed derivation of a standard-linear model for a viscoelastic material and its reduction to a Kelvin-Voigt model can be found in Reference [12]. Accordingly, we can write,

$$p = K(y_1 - y_2) + c \left( \frac{\partial y_1}{\partial t} - \frac{\partial y_2}{\partial t} \right). \quad (10)$$

$K$  refers to the transverse stiffness per unit length, and  $c$  is the viscous damping coefficient.  $K$  may be related to the storage modulus  $E_c$ , the width  $b$ , and the thickness  $h_c$  of the adhesive by,  $K = E_c b / h_c$ .

The interfacial shear force  $s$  may be found by considering a small element of the viscoelastic layer as shown in Figure 4. The element is deformed due

to the axial displacements,  $u_1$  and  $u_2$  of the bonded surfaces of beams 1 and 2 respectively, caused by their bending moments. For small displacements, the shear stress  $\tau$ , is related to shear strain in the adhesive by:

$$\tau = G_c \left\{ \frac{u_1 - u_2}{h_c} \right\} + \gamma \frac{\partial}{\partial t} \left\{ \frac{u_1 - u_2}{h_c} \right\}. \quad (11)$$

The expression on the right hand side excluding  $G_c$  is the shear strain.  $G_c$  is the real part of the shear modulus of the adhesive material. As before,  $\gamma$  is another constant which is included here to take care of the viscoelastic nature of the adhesive.

Assume that the axial deformations,  $u_1$  and  $u_2$  are caused only by the bending of the beams and that there are no external axial forces in the beams. Then, from the classical theory of pure bending of beams, it can be shown that

$$u_1 = \frac{h_1}{2} \frac{\partial y_1}{\partial x}, \text{ and } u_2 = -\frac{h_2}{2} \frac{\partial y_2}{\partial x}. \quad (12)$$

In deriving the above expressions, it is also assumed that the neutral axis of the upper beam always remains above that of the lower beam. Then,

$$u_1 - u_2 = \frac{h_1}{2} \frac{\partial y_1}{\partial x} + \frac{h_2}{2} \frac{\partial y_2}{\partial x}. \quad (13)$$

From Equations (11) and (13), the interfacial shear force per unit length  $s$  is given by

$$s = \frac{G_c b}{2h_c} \left[ (h_1 \frac{\partial y_1}{\partial x} + h_2 \frac{\partial y_2}{\partial x}) + \gamma \frac{\partial}{\partial t} (h_1 \frac{\partial y_1}{\partial x} + h_2 \frac{\partial y_2}{\partial x}) \right]. \quad (14)$$

It is interesting to note here that for a simple harmonic time dependence of the form,  $e^{i\omega t}$  for  $y_1$  and  $y_2$ , Equations (10) and (14) can be written in a more familiar form as

$$p = K_c^* [y_1 - y_2], \quad (15)$$

and

$$s = \frac{G_c^* b}{2h_c} [h_1 \frac{dy_1}{dx} + h_2 \frac{dy_2}{dx}], \quad (16)$$

where

$$K_c^* = K(1 + i \frac{c\omega}{K}), \text{ and } G_c^* = G_c (1 + i\gamma\omega). \quad (17)$$

$K_c^*$  and  $G_c^*$  may be considered as the complex stiffness and complex shear modulus of the adhesive material respectively.

The next step is to obtain the final form of the equations of the motion (5) and (6) by making use of the relations developed so far for  $M_1$ ,  $M_2$ ,  $p$  and  $s$ . This is easily done by noting that  $y_1 = Y_1 e^{i\omega t}$ , and  $y_2 = Y_2 e^{i\omega t}$ , where  $Y_1$  and  $Y_2$  are now functions of  $x$  only.  $\omega$  is the complex natural frequency, the real part  $\omega_R$  represents the damped natural frequency and the ratio of the imaginary part  $\omega_I$  to  $\omega_R$  represents the modal loss factor  $\eta$ . The modal damping ratio  $\zeta$  is simply equal to  $\eta/2$ . Now, from Equations (5), (8), (15)

and (16), we obtain for the upper beam:

$$E_1 I_1 \frac{d^4 Y_1}{dx^4} - \frac{G_c^* b h_1}{4 h_c} \left[ h_1 \frac{d^2 Y_1}{dx^2} + h_2 \frac{d^2 Y_2}{dx^2} \right] + K_c^* (Y_1 - Y_2) - \rho_1 A_1 \omega^2 Y_1 = 0, \quad (18)$$

and, similarly from Equations (6), (9), (15), and (16), we get for the lower beam:

$$E_2 I_2 \frac{d^4 Y_2}{dx^4} - \frac{G_c^* b h_2}{4 h_c} \left[ h_1 \frac{d^2 Y_1}{dx^2} + h_2 \frac{d^2 Y_2}{dx^2} \right] - K_c^* (Y_1 - Y_2) - \rho_2 A_2 \omega^2 Y_2 = 0. \quad (19)$$

Here,  $Y_1 = Y_1(x)$ ,  $Y_2 = Y_2(x)$ .

Equations (18) and (19) are coupled equations of motion of the system, the solution of which can be obtained by assuming a solution of the form  $Y_1 = A e^{\lambda x}$ , and  $Y_2 = B e^{\lambda x}$ .

### Non-dimensionalization

The above equations of motion (18) and (19), should be expressed in a non-dimensional form so as to avoid overflow problems on the computer during the solution scheme. This is done in this section for the special case in which the two beams are assumed to be identical.

Let  $E_1 = E_2 = E$ , and  $h_1 = h_2 = h$ . The following non-dimensional parameters are used:

$$\bar{Y}_1 = \frac{Y_1}{h}, \quad \bar{Y}_2 = \frac{Y_2}{h}, \quad \bar{x} = \frac{x}{L}, \quad \bar{\ell} = \frac{\ell}{L},$$

where

$$L = \ell + \ell_c.$$

Also, let

$$\bar{G}_c = \frac{G_c}{E}, \quad \bar{E}_c = \frac{E_c}{E}, \quad \bar{h} = \frac{h}{L}, \quad \bar{\ell}_c = \frac{\ell_c}{L}.$$

The non-dimensional natural frequency is expressed as

$$\bar{\omega} = \frac{\omega}{\omega_0}, \quad \text{where } \omega_0^2 = \frac{EI}{\rho AL^4}. \quad (20)$$

Equations (4.24) and (4.25), written in non-dimensional form, are:

$$\frac{d^4 \bar{Y}_1}{d\bar{x}^4} - \frac{3\bar{G}_c^*}{\bar{h} \bar{h}_c} \left[ \frac{d^2 \bar{Y}_1}{d\bar{x}^2} + \frac{d^2 \bar{Y}_2}{d\bar{x}^2} \right] + \frac{12\bar{E}_c}{\bar{h} \bar{h}_c^3} (\bar{Y}_1 - \bar{Y}_2) - \bar{\omega}^2 \bar{Y}_1 = 0, \quad (21)$$

and

$$\frac{d^4 \bar{Y}_1}{d\bar{x}^4} - \frac{3\bar{G}_c^*}{\bar{h} \bar{h}_c} \left[ \frac{d^2 \bar{Y}_1}{d\bar{x}^2} + \frac{d^2 \bar{Y}_2}{d\bar{x}^2} \right] + \frac{12\bar{E}_c}{\bar{h}_c \bar{h}^3} (\bar{Y}_1 - \bar{Y}_2) - \bar{\omega}^2 \bar{Y}_2 = 0. \quad (22)$$

Here,

$$\bar{E}_c^* = \frac{E_c(1+i\eta_2)}{E(1+i\eta_1)}, \text{ and } \bar{G}_c^* = \frac{G_c(1+i\eta_2)}{E(1+i\eta_1)}. \quad (23)$$

$\eta_1$  may be considered as the modal loss factors of the beam material, and  $\eta_2$  and  $\eta_3$  as the modal loss factors of the viscoelastic material in bending and shearing motions respectively.  $\eta_1$ ,  $\eta_2$  and  $\eta_3$  may be assumed to have suitable values which depend on the material, when computing the eigenvalues and eigenvectors for each mode.

As mentioned before, Equations (21) and (22) can be decoupled by a series solution of the form

$$\bar{Y}_1 = A_n e^{\lambda_n \bar{x}}, \text{ and } \bar{Y}_2 = B_n e^{\lambda_n \bar{x}}, \quad (24)$$

where  $A_n$  and  $B_n$  are constants to be determined from the boundary conditions. Substituting Equation (24) in (21) and (22), we obtain, a matrix of the form:

$$\begin{bmatrix} (\lambda_n^4 - C_1 \lambda_n^2 + C_2 - \bar{\omega}^2) & -(C_1 + C_2) \\ -(C_1 + C_2) & (\lambda_n^2 - C_1 \lambda_n^2 + C_2 - \bar{\omega}^2) \end{bmatrix} \begin{bmatrix} A_n \\ B_n \end{bmatrix} = 0 \quad (25)$$

with

$$C_1 = \frac{3 \bar{G}_c^*}{\bar{h}_c \bar{h}}, \quad C_2 = \frac{12 \bar{E}_c^*}{\bar{h}_c \bar{h}^3}. \quad (26)$$

For a non-trivial solution, the determinant of the above matrix set equal to zero yields eight roots of  $\lambda$ . Equation (25) yields eight unique roots for  $\lambda$ . Furthermore, from the above matrix, the constants A and B are related by:

$$B_n = \phi_n A_n,$$

where

$$\phi_n = \left[ \frac{\lambda_n^4 - C_1 \lambda_n^2 + C_2 - \bar{\omega}^2}{C_1 + C_2} \right]. \quad (27)$$

Finally, we have

$$\bar{Y}_1 = \sum_{n=1}^8 A_n e^{\lambda_n \bar{x}}, \quad (28)$$

and

$$\bar{Y}_2 = \sum_{n=1}^8 \phi_n A_n e^{\lambda_n \bar{x}} \quad (29)$$

Equations (28) and (29) now have only eight constants to be determined by applying the boundary and continuity conditions.

### Analysis of Parts 2 and 3 of Beam System

The differential equations of motion for the transverse vibration of the beam portions of the system as shown in Figure 2 are:

$$D_j \frac{\partial^4 y_{bj}}{\partial x_j^4} + \rho_j A_j \frac{\partial^2 y_{bj}}{\partial t^2} = 0, \quad j = 1, 2. \quad (30)$$

For the special case of identical beams,

$$D_1 = D_2 = E^* I, \text{ and } \rho_1 A_1 = \rho_2 A_2 = \rho A.$$

Assuming  $y_{bj} = Y_{bj}(x) e^{i\omega t}$ ,  $j = 1, 2$ , Equation (30) becomes

$$\frac{d^4 Y_{bj}}{dx_j^4} - \left( \frac{\rho A}{E^* I} \right) \omega^2 Y_{bj} = 0, \quad j = 1, 2. \quad (31)$$

In non-dimensional form,

$$\frac{d^4 \bar{Y}_{bj}}{d\bar{x}_j^4} - \omega^2 \bar{Y}_{bj} = 0, \quad j = 1, 2. \quad (32)$$

The solutions of the above equations are obtained, as before by assuming a series solution of the form:

$$\bar{Y}_{b1} = \sum_{n=1}^4 C_n e^{\beta_n \bar{x}}, \text{ and } \bar{Y}_{b2} = \sum_{n=1}^4 D_n e^{\beta_n \bar{x}}, \quad (33)$$

where  $\beta_n^4 = \omega^2$ , and  $C_n$  and  $D_n$  are constants to be found from the boundary conditions.

Equations (28), (29), and (33) have 16 unknown constants. The following boundary and continuity conditions are applied to determine those constants and to obtain the frequency equation.

## II. BOUNDARY CONDITIONS

Considering simply-supported boundaries at the un-jointed ends of the two beams, at points 1 and 2 (see Figure 5), the transverse displacement and slope are zero. i.e.

$$\text{a) at } \bar{x}_1 = 0, \bar{Y}_{b1} = 0, \text{ and } \frac{d\bar{Y}_{b1}}{d\bar{x}_1} = 0, \quad (34)$$

and

$$\text{b) at } \bar{x}_2 = \bar{l}, \bar{Y}_{b2} = 0, \text{ and } \frac{d\bar{Y}_{b2}}{d\bar{x}_2} = 0. \quad (35)$$

Next, points 3 and 4 are free ends. Hence, the bending moments there are zero. Furthermore, the shear force at these points can be obtained from Equation (16). Hence, we obtain,

c) at  $\bar{x} = 0$  (point 3),

$$\frac{d^2 \bar{Y}_2}{d\bar{x}^2} = 0, \text{ and } \frac{d^3 \bar{Y}_2}{d\bar{x}^3} = \frac{6\bar{G}_c^*}{\bar{h}^2} \left[ \frac{d\bar{Y}_1}{d\bar{x}} + \frac{d\bar{Y}_2}{d\bar{x}} \right], \quad (36)$$

d) at  $\bar{x} = \bar{l}$  (point 4),

$$\frac{d^2 \bar{Y}_1}{d\bar{x}^2} = 0, \text{ and } \frac{d^3 \bar{Y}_1}{d\bar{x}^3} = \frac{6\bar{G}_c^*}{\bar{h}^2} \left[ \frac{d\bar{Y}_1}{d\bar{x}} + \frac{d\bar{Y}_2}{d\bar{x}} \right]. \quad (37)$$

Referring to Figure 5, at points A and B, we equate the displacements, slopes, bending moments, and shear forces for the two hypothetical sections of the beams. These will yield eight more equations. Hence we have a matrix equation from the above 16 conditions containing 16 constants. The determinant of the above matrix D, set equal to zero gives the frequency equation, i.e., for a non-trivial solution

$$\text{Det } [D]_{16 \times 16} = 0. \quad (38)$$

The roots of Equation (38) yield the complex natural frequencies ( $\omega_n$ ) of the system.

$$\bar{\omega}_{nj} = \bar{\omega}_{Rj} + i \bar{\omega}_{Ij},$$

where  $j = 1, 2, \dots$  represents the mode number.

$\omega_{Rj}$  = modal damped natural frequency, and

$$\eta_j = \frac{\omega_{Ij}}{\omega_{Rj}} = \text{modal loss factor.}$$

Once the eigenvalues are evaluated, the corresponding eigenvectors needed to plot the mode shapes can be found by using any 15 of the 16 equations with one arbitrary constant.



### III. NUMERICAL RESULTS AND DISCUSSION

The length and thickness of the graphite epoxy beams chosen here for study are:  $l = 12.25$  cm, and  $h = 0.25$  cm. The storage modulus of the beam material as supplied by the manufacturer is 124 GPa. The material loss factor of the beam is taken as  $\eta_1 = 0.004$ , which is taken as a constant for all the modes. This corresponds to a damping ratio of 0.2% and is believed to represent closely the material damping of the graphite epoxy material as found from various previous experiments [13, 14]. The thickness of the adhesive layer is taken as 0.05 cm. The complex modulus of the adhesive material, which is epoxy resin in the present case is taken as  $4(1 + i0.04)$  GPa which has a real part of 4 GPa as supplied by the manufacturer. The complex shear modulus of the adhesive is assumed to be  $1.4(1 + i0.04)$  GPa. Here  $\eta_2 = \eta_3 = 0.04$ , which corresponds to a constant damping ratio of 2% for the epoxy material.

The above quantities expressed in non-dimensional form are used in the numerical computation of the eigenvalues and eigenvectors. The ratio of the length of overlap to the beam length is called the overlap ratio. Numerical results are obtained for overlap ratios of 0.2, 0.4, 0.6, and 0.8. Figure 6 shows the variation of natural frequency with overlap ratio for the first three modes of vibration. From this plot, it is clear that the natural frequency of the system increases with an increase in the overlap ratio for all modes. Figure 7 is a similar plot showing the variation of the system damping (total loss factor of the system) with overlap ratio. For the case of overlap ratio = 0.2, the non-dimensional frequencies  $\bar{\omega}$  are: 2.86, 13.12 and 27.24 for the first three modes. The corresponding system damping ratios are  $\zeta_1 = 0.534\%$ ,  $\zeta_2 = 0.120\%$ , and  $\zeta_3 = 0.054\%$ . It should be noted that the above values were obtained by assuming constant values of  $\zeta = 0.02\%$  and  $\zeta = 2.0\%$  for the material damping ratio of the beam and the adhesive respectively. It is seen that, for this case, the system damping is higher than the material damping of the beam only for the first mode. For the other two modes, the system damping ratio appears to be lower than the material damping ratio of the beam. This observation, however, is true only for the above case and cannot be generalized. To substantiate this point, let us consider a different case in which the damping ratio of the adhesive was assumed to be 5%, and the material damping of the beam was kept the same. The system damping ratios computed for this case are:  $\zeta_1 = 1.66\%$ ,  $\zeta_2 = 0.33\%$ ,  $\zeta_3 = 0.16\%$ . There were no significant changes in the natural frequencies of the system. As can be seen, the system damping ratios in this case are completely different from the previous case considered. Hence, in order to predict the system damping ratios, using the present model, accurate knowledge about the material damping ratios (of the beam and adhesive) and their dependence on natural frequency is mandatory. Figures 8 shows the predicted mode shapes of the first mode for different overlap ratios.

### IV. COMPARISON WITH EXPERIMENTAL RESULTS.

Table 1 shows both theoretical and experimental results of two graphite epoxy lap joint systems with overlap ratios of 0.2 and 0.4. All of the theoretical results were generated by considering simply-supported boundary conditions at the edges.

The specimens were prepared by bonding two similar graphite epoxy beams over the desired length of overlap using an epoxy adhesive. The epoxy resin was procured from CIBA-GEIGY Corporation. Much care was taken to obtain a good bond by properly curing the joint system in an oven. The dimensions of

the unbonded beams are: length = 12.25 cm, width = 2.8 cm, and thickness = 0.25 cm. These dimensions and the material constants (Young's Modulus and Shear Modulus) were input to the computer program to predict the theoretical natural frequencies, modal damping ratios and mode shapes.

The supports to simulate simple-supported boundaries at the ends were specially fabricated in the form of two separate triangular blocks with a knife edge on each, to support the beam, one from top, and the other from bottom. The two blocks were then clamped to a rigid base. In order to evaluate the experimental simulation of these supports, a trial test was first conducted on an aluminum beam. Excellent agreement was obtained between theoretical natural frequencies (computed using simply-supported boundary conditions) and measured values. In fact, the percentage difference between the two results never exceeded 2% for the first four natural frequencies. Having established the validity of the above test fixtures, experiments were later conducted on graphite epoxy lap-jointed beams. An impact hammer with an attached force transducer was used to excite the specimen and the response was measured by a mini-accelerometer (Bruel & Kjaer 4375). The frequency response (ratio of acceleration to force signals) was immediately computed and recorded on a FFT analyzer (Bruel & Kjaer 2032). The modal parameters were then computed using the Structural Measurement Systems (SMS) modal analysis software.

Referring to Table 1 it is seen that there is good agreement between the predicted values of natural frequencies and experimental data. The percentage difference between the two results is in the range of 3 to 9%. The small discrepancies in the two results can be attributed to several assumptions made in the theoretical analysis. The major assumption is the use of a constant value, with frequency of vibration, for the modulus of the material. The measured damping ratio values in column 7 (Table 1) are higher than the predicted values. This is presumably due to additional damping contributions at the end supports in the experimental data. In order to substantiate this, damping measurements were made on the same samples without the end fixtures. Column 8 of Table 1 shows these results. In this case, testing was done by simply mounting the sample directly on a shaker using a thin layer of wax. The resonance frequencies in this case were, of course, somewhat different from those obtained previously using the simply-supported boundary conditions. But, it is interesting to notice that the predicted damping values in column 6 and the measured data in column 8 are of the same order. Next, theoretical mode shape is compared with experimental mode shape in Figure 9 for mode 1. There is excellent agreement between the two mode shapes for the first mode as seen in Figure 9.

## **V. EXPERIMENTAL STUDY OF DAMPING OF BONDED DOUBLE-BUTT JOINT SPECIMENS**

This section contains the results of experiments conducted on beam and double-butt-joint specimens in a vacuum chamber. Damping measurements were made on the following ten graphite epoxy samples which were procured from Sikorski Aircraft Company:

- i) Five identical graphite epoxy beam specimens with a double-butt joint in the middle as shown in Figure 10 and ii) Five identical graphite epoxy beam specimens of dimensions as in i but with no joints.

In each of the above experiments, the specimen was mounted at its center directly on the shaker using a thin layer of wax. This closely simulated free-free boundary conditions at the edges. Only odd numbered modes were excited, since the specimen was mounted at the center, which happens to be a node point for all even numbered modes for free-free boundary conditions. All the damping measurements were made using the usual improved half-power points method as described in [13, 14].

Much care was taken to maintain identical environmental conditions in all of the above experiments. The damping measurements were made precisely by zooming in on each mode thus increasing the frequency resolution of the analyzer and minimizing the influence of external noise.

First, measurements were made on the double-butt-jointed (DBJ) specimens. In each case, the specimen with the shaker was kept inside the vacuum chamber and damping ratios and resonance frequencies were measured for the first and third mode of vibration, before the air was pumped out. Then the measurements were repeated in a vacuum when the pressure inside the chamber was about 0.1 mm of hg. The test temperature remained ambient in both cases. Table 2 shows a summary of results for the five DBJ specimens tested under vacuum conditions. No significant change in the values of the damping ratio was noticed between the experiments conducted under normal atmospheric pressure and in a vacuum. This difference in the values of the damping ratio was in fact in the range of 0.01-0.02% during most of the trials.

From Table 2, it is seen that the average value of the damping ratio of the DBJ specimen for the first mode is 0.114% and that for the third mode is 0.155%. The small discrepancies in the values of the resonance frequencies in the five samples could be attributed to a) slight differences in their dimension and/or b) slight differences in the exact location of the excitation point during mounting.

The next set of experiments was conducted on the five beam specimens with no joints (having the same dimensions as the DBJ samples) under identical environmental conditions as maintained with the DBJ specimens. The results are tabulated in Table 3. Here, it is seen that the beam has an average value of the damping ratio of 0.107% for the first mode and 0.138% for the third mode.

By comparing the results of Table 2 and 3, it is clear that, although the damping ratio values for the jointed specimens appear somewhat higher than those of the beam specimens, this difference is almost unnoticeable. This observation is also true from the previous damping results of lap-jointed specimens with free-free boundary conditions.

## VI. CONCLUSIONS

The analytical model described in this paper can be used to predict the natural frequencies and the modes shapes of a bonded lap joint system for free vibration. The model can also be used to predict the system modal damping values by properly choosing the material damping values of the beam and the adhesive. Good agreement between numerical and experimental results for the natural frequencies of the lap-jointed beam system was obtained. From the numerical and experimental results obtained on lap-jointed beams, it is clear that the natural frequencies of the system increase with an increase in the length of overlap. From the experimental results of bonded lap-joint and bonded butt-joint specimens, the increase in the value of the damping ratio due to the presence of bonded joints in the system does not appear to be very significant. More work is, however, needed in this area to determine if the bonded joints can be relied upon to increase the system damping capacity.

## ACKNOWLEDGEMENT

The research work described in this article was conducted at the Sound & Vibration Laboratory of the Mechanical Engineering Department at Auburn University. The research was supported by NASA-MSFC, Huntsville, AL under research contract NAS8-36146. Financial support by NASA is gratefully acknowledged.

## REFERENCES

1. Goland, M., and Reissner, E., "The Stresses in Cemented Joints", *Journal of Applied Mechanics*, Vol. 11, March 1944, pp. A17-A27.
2. Ojalvo, I.U., and Eidinoff, H.L., "Bond Thickness Effects upon Stresses in Single-Lap Adhesive Joints", *AIAA Journal*, Vol. 16, No. 3, 1978, pp. 204-211.
3. Carpenter, W.C., "A Comment on Two Current Adhesive Lap Joint Theories", *AIAA Journal*, Vol. 18, No. 3, 1980, 350-352.
4. Kline, R.A., "Stress Analysis of Adhesively Bonded Joints," *Adhesive Joints*, ed. by Mittal, K.L., proc. of the International Symp. on Adhesive Joints, Sept. 1982, Kansas City, Missouri, pp. 587-609.
5. Delale, F., and Erdogan, F., "Viscoelastic Analysis of Adhesively Bonded Joints", *Journal of Applied Mechanics*, Vol. 48, June 1981, pp. 331-336.
6. Renton, W.J., and Vinson, J.R., "Analysis of Adhesively Bonded Joints Between Panels of Composite Materials," *Journal of Applied Mechanics*, March 1977, pp. 101-106.
7. Delale, F., Erdogan, F., and Aydinoglu, M.N., "Stresses in Adhesively Bonded Joints - A closed form solution," *J. Composite Materials*, Vol. 15, May 1981, pp. 249-271.
8. Hart-Smith, L.J., "Analysis and Design of Advanced Composite Bonded Joints," *NASA CR-2218*, April 1974.
9. Hart-Smith, L.J., "Adhesive-Bonded Double-Lap Joints", *NASA CR-112235*, January 1973.
10. Hart-Smith, L.J., "Adhesive-Bonded Single Lap Joints", *NASA CR-112236*, January 1973.
11. Hart-Smith, L.J., "Adhesive-Bonded Scarf and Stepped-Lap Joints", *NASA CR-112237*, January 1973.
12. Morgan, M.R., and Sinha, S.C., "Influence of a Viscoelastic Foundation on the Stability of Beck's column: An Exact Analysis", *Journal Sound and Vibration*, 91(1), 1983, pp. 85-101.
13. Rao, M.D., Crocker, M.J., Zhu, G.H. and Raju, P.K., "A Study of the Damping Capacity of Graphite Epoxy Composites in a Vacuum," *Proc. of Inter-Noise 86*, M.I.T., Cambridge, July 1986, pp. 687-692.
14. Rao, M.D., Crocker, M.J. and Guest, S.H., "Experimental Study of Damping of Graphite Epoxy Composite Material of the Space Telescope Truss System," paper presented at the 1987 Design Technology Conferences, Boston, ASME publication DE-Vol 5. (ASME, New York; 1987), pp. 271-277.

SYSTEM— TWO PARALLEL BEAMS WITH A  
LAP JOINT

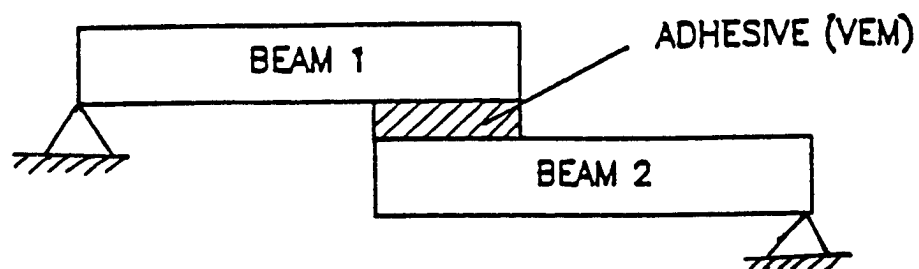


Figure 1. Two Parallel Beams with a Lap Joint

# ANALYSIS

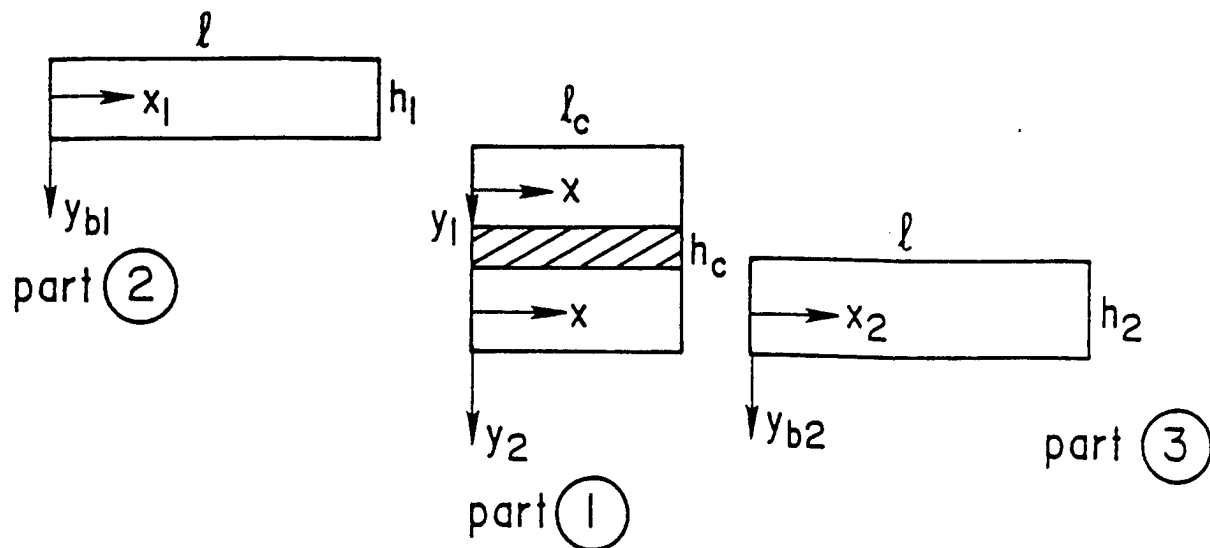


Figure 2. Hypothetical Division of the System Showing the Coordinates for Analysis

## part 1. FBD

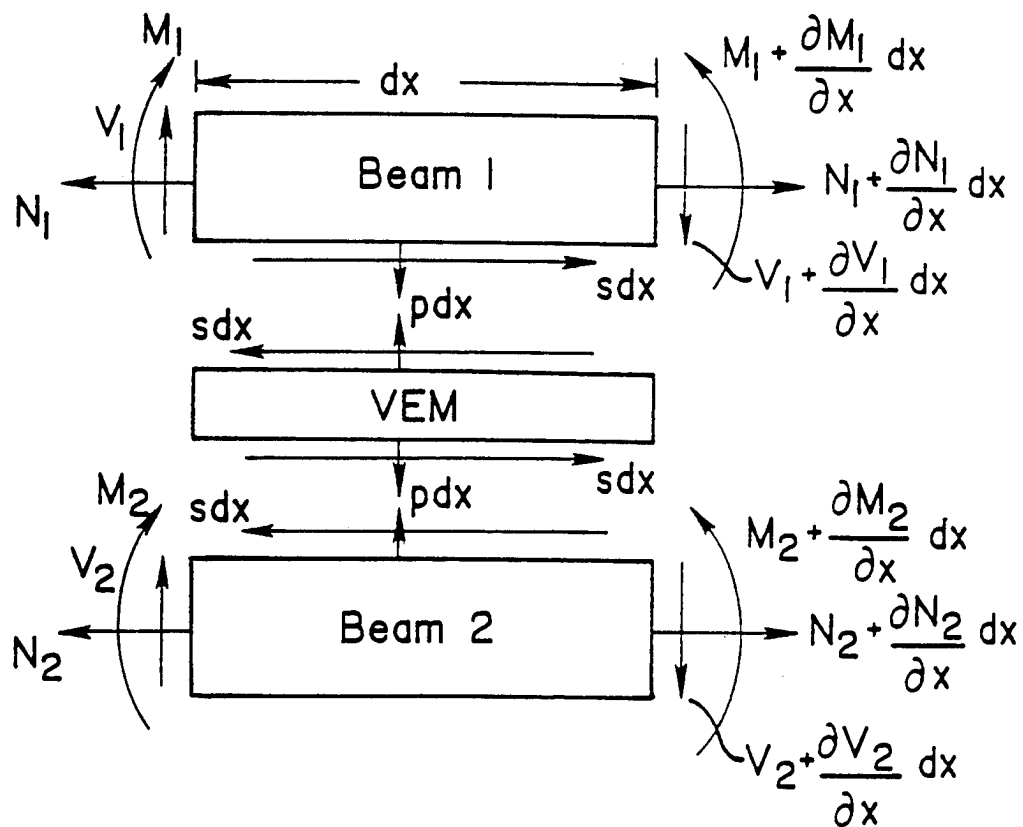


Figure 3. Free Body Diagram of a Differential Element in the Overlap Region



Figure 4. A Small Element of the Viscoelastic Layer



## Natural Frequency vs Overlap Ratio

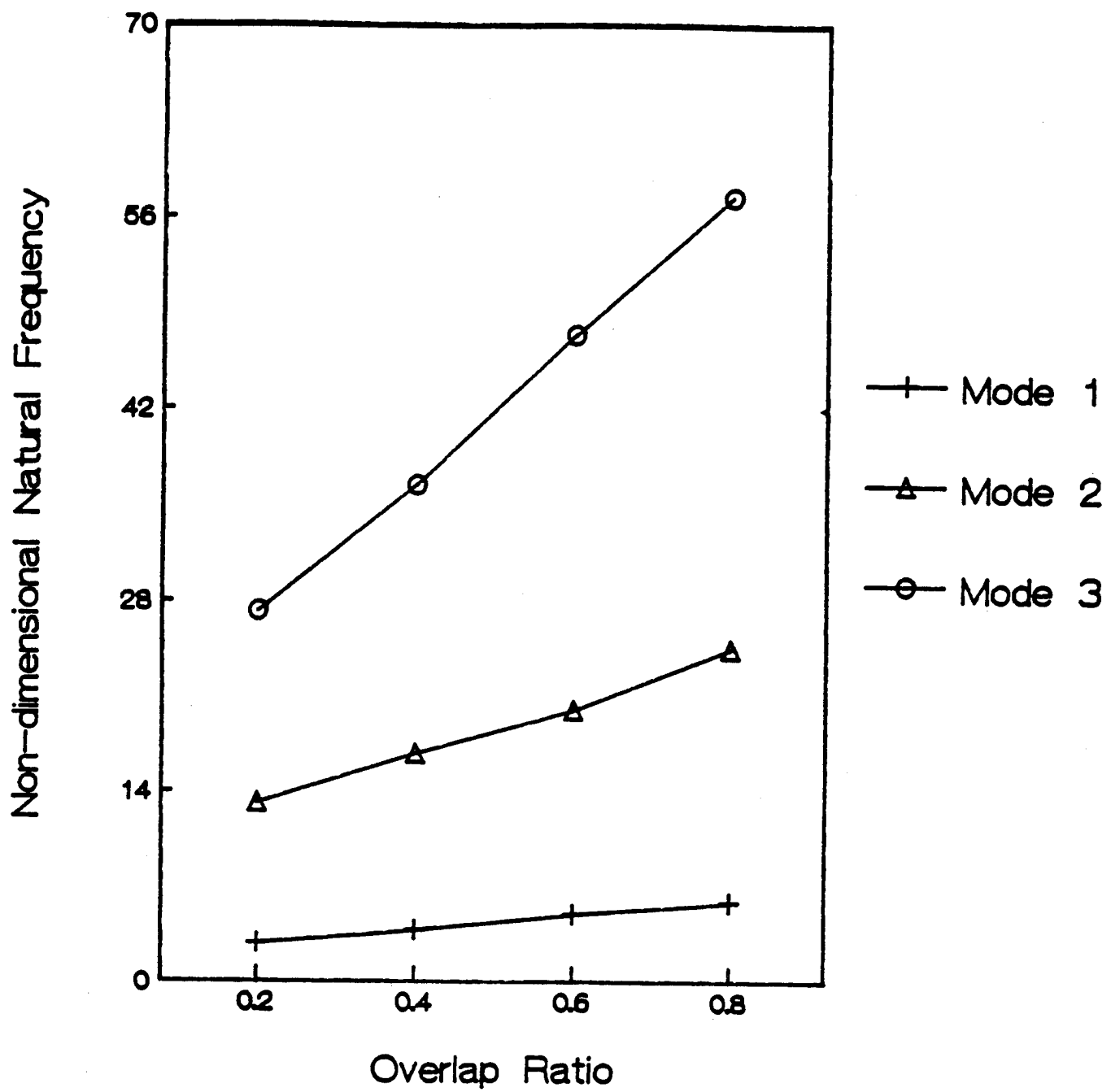


Figure 6. Plot of Natural Frequency vs. Overlap Ratio



## Damping Vs Overlap Ratio

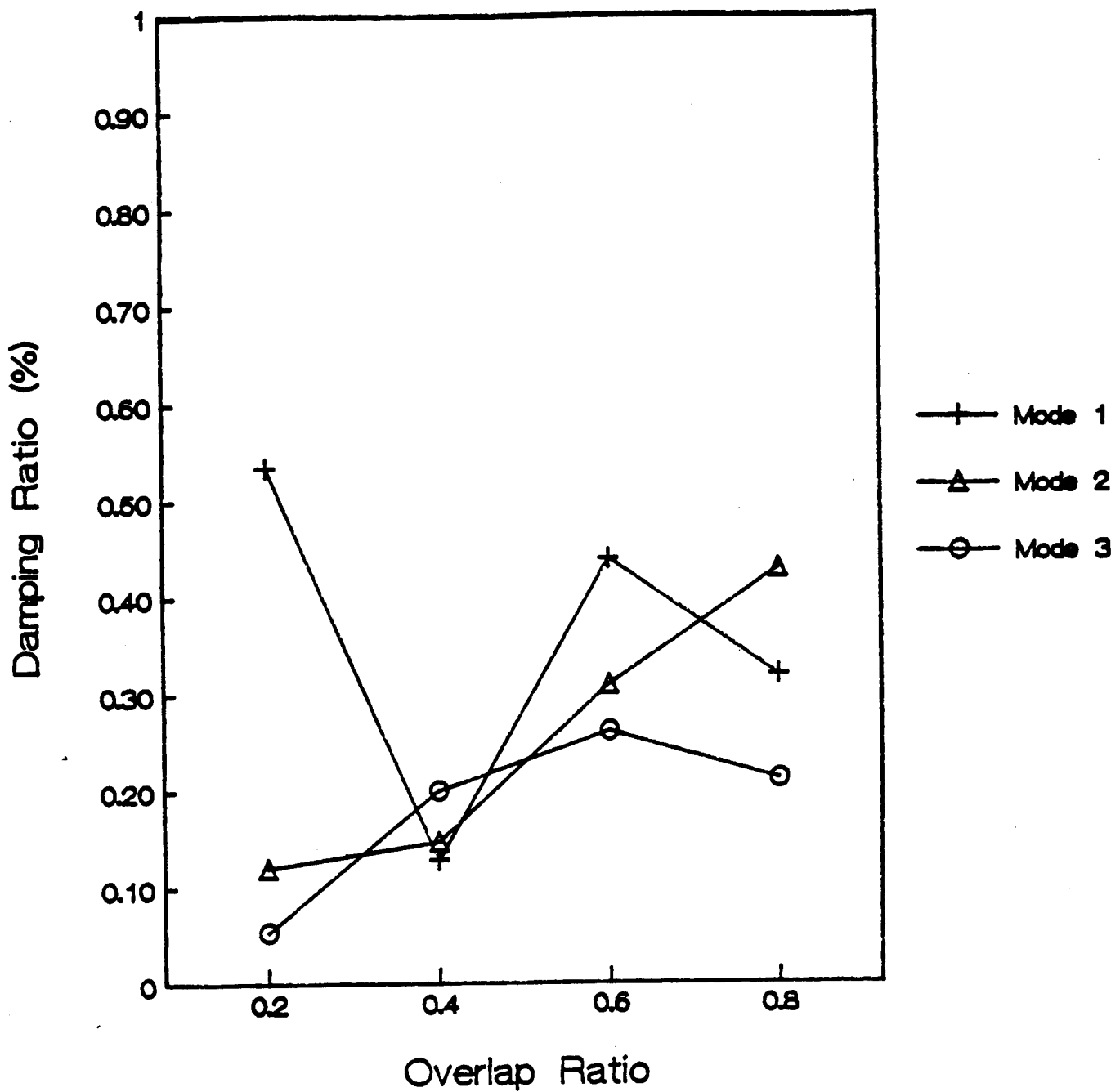


Figure 7. Plot of Damping Ratio vs. Overlap Ratio

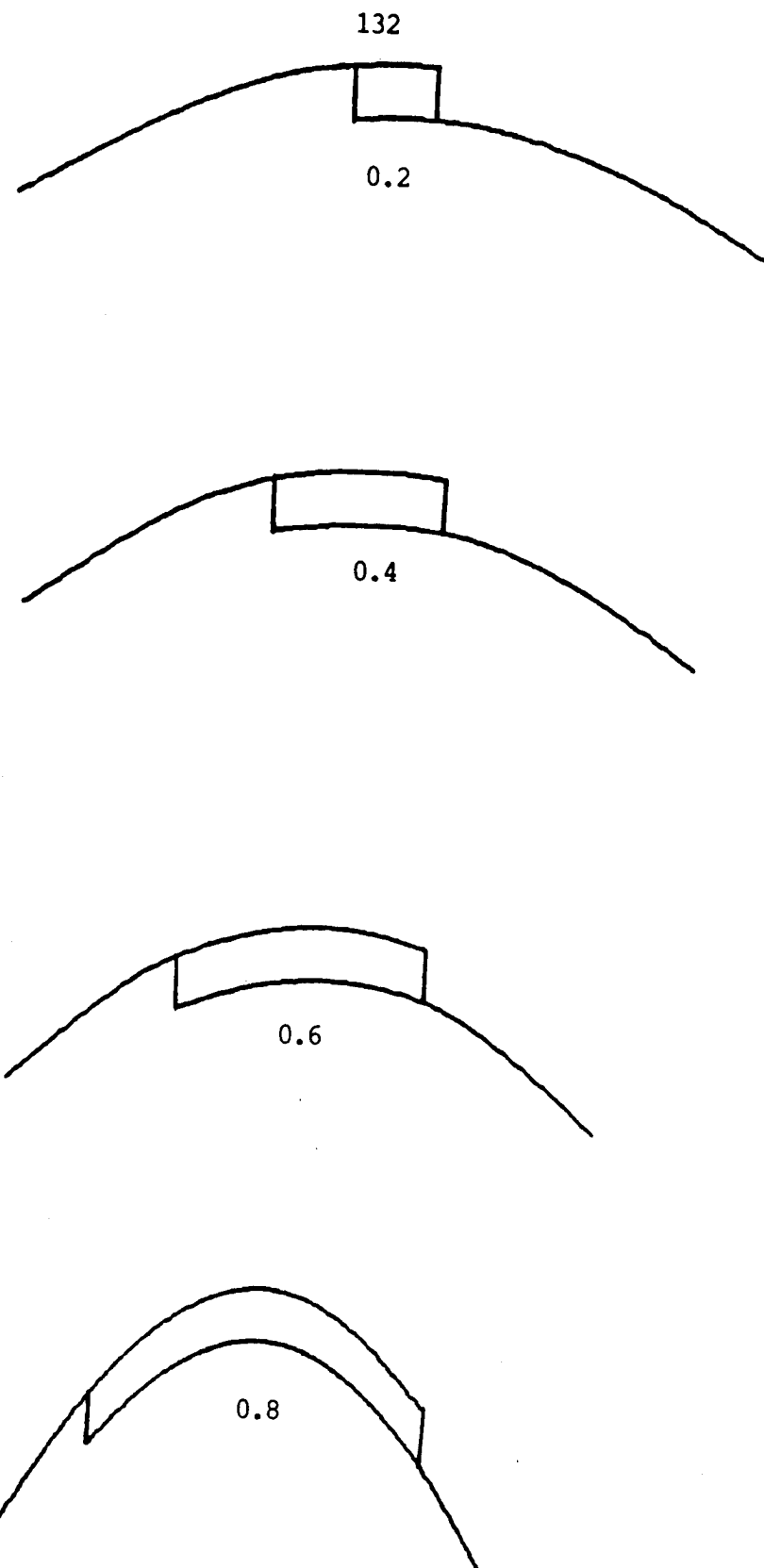


Figure 8. Theoretical Mode Shapes for Mode 1

Overlap Ratio	Mode No.	Natural Frequency(Hz)			Damping Ratio(%)		
		Theory <sup>1</sup>	Expt. <sup>1</sup>	%Error	Theory <sup>1</sup>	Expt. <sup>1</sup>	Expt. <sup>2</sup>
0.2	1	195.90	207.07	5	0.534	1.51	0.20
	2	898.46	986.22	9	0.120	1.63	0.16
	3	1864.49	1984.00	6	0.054	2.29	0.10
0.4	1	263.46	270.60	3	0.128	0.68	0.43
	2	1148.41	1075.49	-6	0.147	1.43	0.12
	3	2492.74	2684.37	7	0.200	0.83	0.15

<sup>1</sup>Using Simply-Supported boundary conditions

<sup>2</sup>Using Free Free boundary conditions.

**Table 1. Comparison of Theoretical and Experimental Results of the Graphite Epoxy Lap Joint Systems**

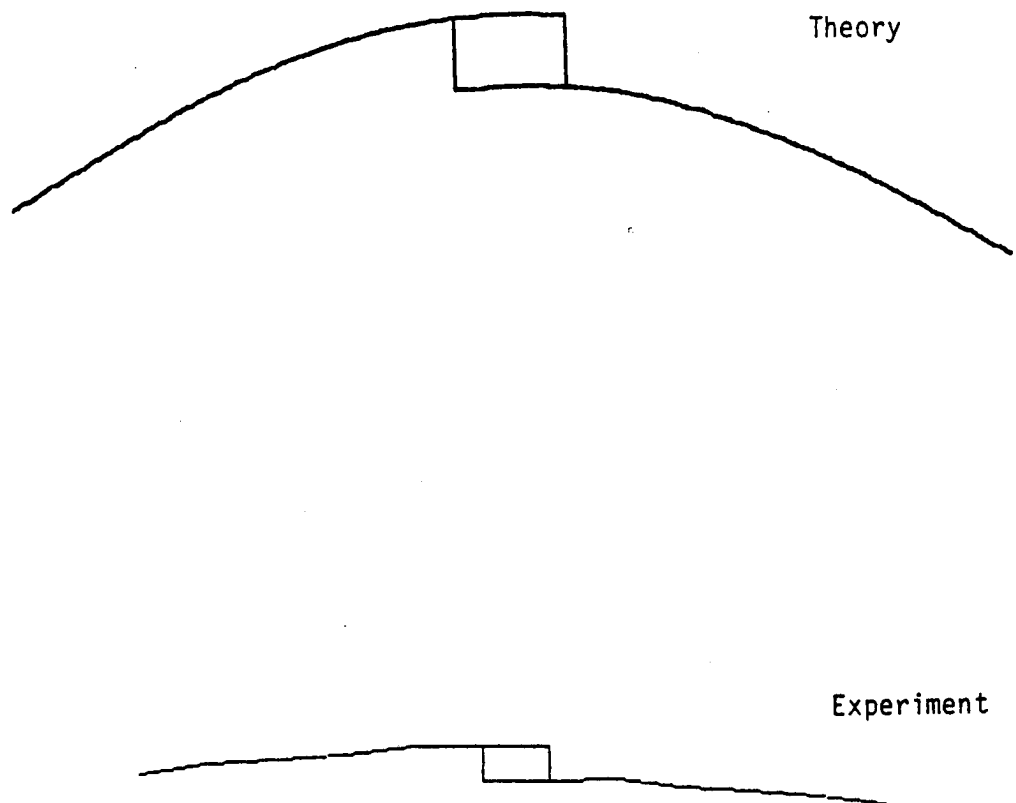
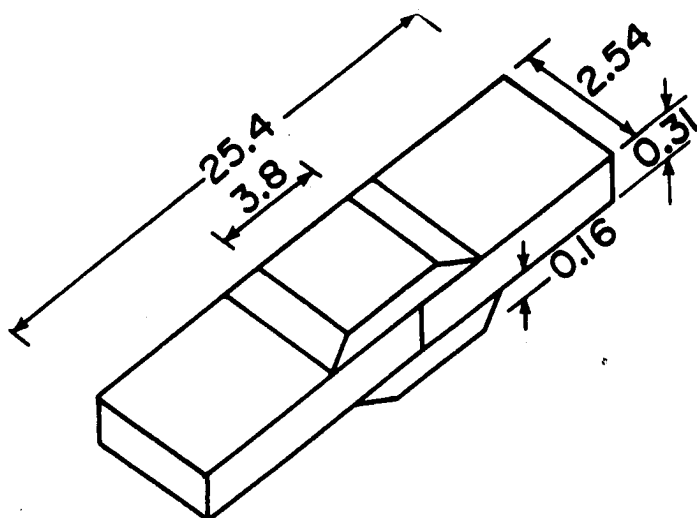


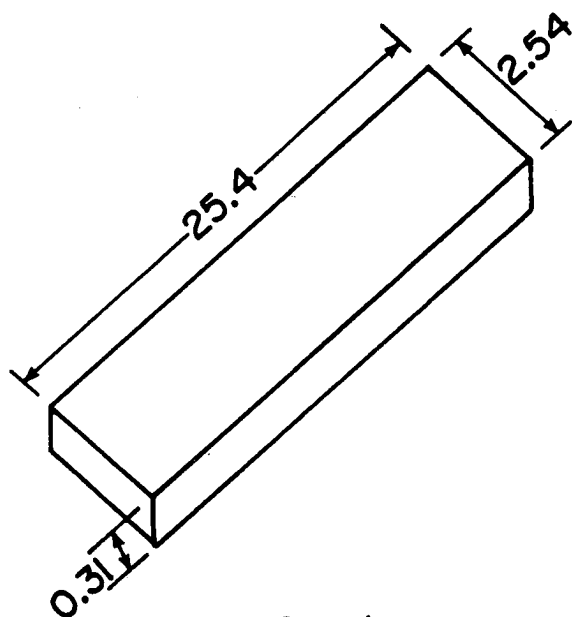
**Figure 9. Comparison of Theoretical and Experimental Mode Shapes for Overlap Ratio = 0.2, Mode 1**



Double-Butt-Jointed Specimen

Table 2.

Sample No.	Damping Ratio	
	Mode 1 (259 Hz)	Mode 3 (1376 Hz)
1	0.113%	0.144%
2	0.102%	0.126%
3	0.127%	0.169%
4	0.105%	0.174%
5	0.122%	0.162%
Average	0.114%	0.155%



Beam Specimen

All dimensions in cm.

Table 3.

Sample No.	Damping Ratio	
	Mode 1 (337 Hz)	Mode 3 (1779 Hz)
1	0.108%	0.148%
2	0.126%	0.149%
3	0.106%	0.123%
4	0.108%	0.122%
5	0.091%	0.149%
Average	0.107%	0.138%

Figure 10. Experimental Results of Double-Butt Jointed and Beam Specimens

OPTIMAL CONSTRAINED VISCOELASTIC TAPE LENGTHS FOR  
MAXIMIZING DAMPING IN LAMINATED COMPOSITES

P. RAJU MANTENA, RONALD F. GIBSON and SHWILONG J. HWANG  
Department of Mechanical Engineering,  
University of Idaho,  
Moscow, Idaho 83843.

ABSTRACT

In this paper, the results of experimental investigations conducted on glass/epoxy and graphite/epoxy composite laminated beams with constrained layer surface damping treatments, are reported. The Fast Fourier Transform based impulse technique is used for identifying an optimal length of damping tape to be applied for maximizing the structural loss factor. This requirement stems from a need (as in helicopter rotor blade applications) for a trade-off between the added weight of the viscoelastic layer and the resultant changes in the dynamic characteristics of the structure.

The experimental data is compared with analytical results obtained by a modal strain energy/three dimensional finite element method. This study has shown that, for a given composite structure and boundary conditions there exists an optimum length of the constraining layer which produces maximum shear deformation of the intermediate viscoelastic damping layer, thus providing effective vibration control in severe dynamic environments.

## INTRODUCTION

Surface damping treatments have been in vogue for quite some time for solving a variety of resonant noise and vibration problems - especially those associated with sheet metal structure vibration. Such treatments, which capitalize on the inherent damping of a highly dissipative material, can easily be applied as a single layer (as with auto undercoatings) to one or both sides of existing structures and provide high damping capability over a wide temperature and frequency range. In case of the free-layer (also referred to as extensional or unconstrained) damping treatment, when the base plate bends the amount of energy absorbed per oscillation depends on the mean longitudinal strain induced in the coating. Degree of damping is therefore limited by thickness and weight restrictions.

On the other hand, for a given weight, the shear type of damping treatment, which can be obtained by the application of commercially available damping tapes to the base structure, is found to be more efficient than the unconstrained-layer damping treatment. This efficiency is balanced, however, by greater complications in analysis and application. The treatment is similar to the unconstrained-layer type except that the viscoelastic material is constrained by a metal layer. Therefore, whenever the structure is subjected to cyclic bending, the thin and extensionally stiff metal foil placed on top of a thin layer of dissipative material (an adhesive, for example), constrains the viscoelastic layer, thus forcing it to deform in shear. Since shear deformation is considered to be one of the major mechanisms by which energy is dissipated in polymeric adhesives, the large shear strains so produced provide considerable damping. This is the basic principle that is exploited in constrained layer damping treatments.

For facilitating the desired performance, parameters other than temperature and frequency, namely geometry, stiffness, mass and resonance mode shape of the structure to which the control system is applied will also equally effect the performance. The methods of analysis for such free-layer and constrained layer damping systems were developed by Ross-Kerwin-Ungar (referred to as the RKU analysis) in the sixties<sup>1</sup> and have been most widely used for predicting the structural response under both extensional and shear deformations. Application of this RKU method with improvements and/or modifications thereof for noise reduction in helicopter cabins, in diesel engines, for vibration control in a jet engine inlet guide-vanes and in aircraft weapons dispensers<sup>2,3</sup> are reported by Jones<sup>2,3</sup>, Rogers and Nashif<sup>4</sup>, Nashif, Jones and Parin<sup>5</sup> and Nashif and Nicholas<sup>6</sup>, respectively. Ely reports of advanced designs<sup>7,8</sup> for an A-7 center section and the F-111 outboard spoiler using constrained layer damping treatment which extended their service life by a factor of at least fifty. About one-half of that improvement was attributed to constrained layers of AF-32 adhesive, the remainder of the improvement was due to changes in materials, shapes, forming and fastening.

Almost all the reported applications were designed, however, to improve the dynamic response of metallic structural elements. To the authors' knowledge, there have been a very limited number of previous applications<sup>9</sup> of constrained layer damping treatments for vibration control of composite structural elements. In the recent past, an exhaustive study of the optimization of the internal material damping of various types of advanced composites has been undertaken, both at the University of Idaho and at other research institutions. These analytical and experimental investigations included aligned short fiber composites<sup>10,11</sup>; aligned short

fiber off-axis composites<sup>12-14</sup>; randomly oriented short fiber composites<sup>15</sup>; and two and three dimensional modeling of laminated composites<sup>16-20</sup>. Parameters such as loading angle, fiber aspect ratio, fiber tip spacing, ply thickness, and damping ratio between the fiber and matrix materials were adjusted to improve the performance of composite materials in a dynamic environment.

## OBJECTIVE AND SCOPE OF RESEARCH

Designs generated by parametric studies of the type described above are, however, at best locally optimal with improvements of internal material damping being restricted by the properties of the fiber and matrix materials, along with an inherent trade-off between damping and stiffness. Many of the composite structures used in military and space applications, however, are subjected to severe dynamic loading environments where such a trade-off may not be desirable. With enhancement of internal material damping having already been exploited to its peak level by the methods described above, further vibration control by the use of surface damping treatments to reduce resonant displacements and noise level provides the scope for exploratory studies of the type reported in this paper.

As such, the objective of this research was to demonstrate the potential for improvement and optimization of damping in laminated anisotropic composite structures with constrained viscoelastic layer damping tapes. The influence of damping tape distribution and boundary conditions on damping of different modes, in unidirectional and off axis glass/epoxy and graphite/epoxy composite beams were investigated. Experimental data generated by a Fast Fourier Transform based impulse technique was compared with analytical predictions obtained by a modal strain energy / three dimensional finite element method.

## EXPERIMENTAL PROCEDURES

A 12 inches (304.8 mm) x 12 inches (304.8 mm), 16 ply unidirectional aligned continuous E-glass/epoxy (3M Scotchply 1003) composite plate with a thickness of 0.13 inches (3.3 mm) was fabricated as per manufacturer's specifications, using an autoclave-style process<sup>21</sup>. Cantilever beam specimens 5 inches long (127 mm) x 1 inch wide (25.4 mm) were machined from this plate. Similarly, unidirectional and 20° off-axis graphite/epoxy specimens having dimensions of 8 inches (203.2 mm) long x 0.75 inches (19.05 mm) wide x 0.057 inches (1.45 mm) thick were machined from a laminated plate fabricated with 12 plies of Fiberite Hy-E1034C (T300 graphite fibers / 934 epoxy resin) prepreg tape. Base line loss factor data was obtained for these bare specimens (comprising the base structure, i.e without damping tape) by testing them as cantilever beams for different span lengths (to get the frequency dependency) using the impulse-frequency response vibration technique.

In the impulse-frequency response technique, the specimen is excited by using an impulse hammer with a piezo-electric force transducer in its tip. The specimen response is measured by a non-contacting eddy current proximity transducer, located away from the nodal points. By curve fitting the resonant peak of the Fourier Transformed frequency response function displayed on the screen of the spectrum analyzer, the loss factor (a measure of damping) of the composite specimens is obtained with the half-power bandwidth relationship :



$$\eta = \frac{\Delta f}{f_n} \quad (1)$$

where  $\Delta f$  = half-power bandwidth of resonant peak frequency response curve at resonant frequency  $f_n$ .

For further details of the impulse-frequency response technique the reader is referred to Reference 22.

Damping tape (3M type SJ-2052X) having a 0.005 inches (0.127 mm) thick ISD 112 acrylic polymer viscoelastic adhesive and a 0.01 inches (0.254 mm) thick dead soft aluminum backing as the constraining layer was then applied on one side of the glass/epoxy and graphite/epoxy specimens comprising the base structure for different ratios of tape length to cantilever beam length. Loss factor data was again obtained for different boundary conditions such as tape fixed at root (i.e. at clamped end), tape free at root and for tape applied about 0.5 inches (12.7 mm) from the clamped end, as shown in Figure 1. Both first and second mode loss factor data was obtained, with three specimens tested in each category.

#### MODAL STRAIN ENERGY / FINITE ELEMENT METHOD

The resulting experimental data was compared with the analytical predictions obtained by a modal strain energy / three dimensional finite element method. The strain energy method has been proven to be an accurate and flexible technique for determining damping of structures. The concept of damping in terms of strain energy quantities was apparently first introduced by Ungar and Kerwin<sup>23</sup> and was later implemented in finite element analysis<sup>18,24,25</sup>. In the current research, this method was used in a three-dimensional finite element formulation for determining the loss factor of the composite beam specimens with variations of cross-section (due to application of damping tape for different ratios of tape to beam length) and boundary conditions. The finite element code used in this work is the SAP IV finite element program<sup>26</sup> which was modified for the calculation of the loss factor by the strain energy method<sup>19,20</sup>. For more details of this three dimensional modal strain energy / finite element technique, the reader is referred to References 19,20.

By this approach, an eigenvalue/eigenvector problem for free undamped vibration is performed with the finite element method. The structural loss factor for each mode of vibration is calculated by using the mode shape and the material loss factor for each material. That is, strain energies are calculated based on the resulting eigenvector (mode shape) without concerning the real amplitude of the mode shape. The loss factor of the overall structure (with the applied damping treatment) may therefore be formulated as the weighted average of the loss factors of the constituents (i.e. base structure, damping layer and constraining layer) along with their respective strain energies as weighting constants. Thus the structural loss factor at a macro-mechanical level may be expressed as :

$$\eta_s = \frac{\eta_a W_a + \eta_b W_b + \eta_c W_c}{W_a + W_b + W_c} \quad (2)$$

where  $\eta$  is the loss factor,  $W$  is the strain energy and subscripts s,a,b, and c refer to the total structure, adhesive layer, base (composite) structure and constraining layers, respectively. Due to the anisotropic nature of the composite base structure, further decomposition of the strain energy terms into terms associated with different stress components is also required<sup>19,20</sup>.

Based on some initial strain energy convergence studies, optimum aspect ratios (length/thickness) of the three-dimensional eight-node thick shell elements used for modeling the different layers that constitute the composite structure were selected. Figure 2 shows a typical gridwork for a composite specimen with a damping tape-to-beam length ratio of 0.6 and with a free boundary condition at the clamped end. Solution times for such a configuration and related models ranged from 250 to 500 seconds (CPU) on an IBM 4341 main frame system. Constituent material properties used in the analytical models are shown in Table 1. Because of the frequency and temperature sensitivity of both the shear modulus and loss factor of the ISD 112 viscoelastic adhesive in the damping tape, appropriate data based on nomographs supplied by the manufacturer<sup>27</sup> and Reference 28 was used to account for the differences in mode 1 and mode 2 frequencies. Also the Poisson's ratio for the nearly incompressible viscoelastic adhesive was taken as 0.49 (instead of 0.5), to avoid numerical difficulties<sup>29</sup>.

## RESULTS AND DISCUSSION

As can be observed in Figure 3, for the first mode of vibration, an optimized length of the viscoelastic material at which the system damping (glass/epoxy base structure with tape) is maximum is clearly evident for both the boundary conditions of tape fixed and tape free at root (i.e at the clamped end with  $N/L = 0$ ). Of particular interest is that for an optimum tape-to-beam length ratio of 0.5, the system damping is significantly higher for the case where the tape is fixed at the root (by about 15 times) than for the case where the tape is free at root. The existence of an optimized length of viscoelastic material for which the structural damping is maximum was also observed by Plunkett and Lee<sup>30</sup>. Their investigations were limited, however, to applications for metallic materials and the effects of tape boundary conditions were not taken into account.

For the condition where the tape was applied at a distance of 0.5 inches (12.7 mm) from the clamped end ( $N/L = 0.1$ ), Figure 5 shows that the damping effectiveness, although improved, is not as significant as for the above two cases. This is not surprising since, in the first mode of vibration, the most highly stressed region is at the clamped end. With no tape in this region to provide the additional damping mechanism (by shear deformation of the viscoelastic adhesive) the overall improvement is minimal. The experimental results (with scatter) obtained with the impulse hammer technique show fair agreement with finite element analytical predictions. Better agreement is expected if the data on complex shear modulus of the damping layer is available in the form of accurate regression equations. The results shown here are based on estimates from Nomographs.

Loss factor data for the second mode (Figures 4 and 6) beyond  $T/L = 0.6$  for all the three boundary conditions could not be experimentally obtained with the impulse hammer technique because the peaks were almost

flat (damped out) in this region. The high damping ratios predicted by the analytical model for these conditions (beyond  $T/L = 0.6$ ) also confirm this effect. As such, specimens with a longer cantilever span (instead of the five inches used here) were expected to give more distinguishable resonant peaks for the second mode of vibration. Accordingly, the unidirectional and off-axis graphite/epoxy specimens were tested with an eight inch cantilever span to facilitate complete frequency dependence of the experimental validation of the analytical predictions.

Figures 7 and 8 once again show a comparable improvement in damping for both fixed and free boundary conditions of the damping tape as applied to the unidirectional graphite/epoxy base structure. The damping ratio is not so significant, however, for the off-axis graphite/epoxy specimens (Figures 9 and 10). This is because, with the  $20^\circ$  off-axis case the base structure itself exhibited a high intrinsic loss factor (about 0.0134 for mode 1 and 0.0252 for mode 2).

The critical observation that by fixing the constrained layer tape at the clamped end, significantly higher overall damping could be obtained, was further investigated. This has important ramifications by way of added weight trade-offs when such surface damping treatments are planned, for example, in helicopter rotor blade applications. To simulate better the finite element model of the tape being fixed at root, some experiments were repeated by fixing the tape at the root with a clamp along the face of the vise instead of having the tape inside the vise (Figure 1). As shown in Table 2 the damping effectiveness is once again comparably higher than for the free at root boundary condition. (The marginal variations in the loss factor data presented here with the data in Figure 3 is attributed to a different batch of damping tape that was used for these tests). The increased through-the-thickness shear strain in the adhesive as a result of fixing the tape at the root is responsible for the increase in the system damping. This is easily verified by observing the shear strain energy ratio obtained by the 3-D finite element method for the fixed vs free boundary conditions at root, as shown in Figures 11 and 12 for both the first and second modes of vibration.

Similar conclusions on the effects of boundary conditions were reported by Mead and Markus<sup>31</sup>, who developed a closed form analytical solution for sandwich beams with fixed, free and simply supported boundary conditions. Their results suggest that the effect of boundary conditions depends on the frequency range, however, and that the maximum system loss factor is not very sensitive to boundary conditions. A direct comparison of the present results with those of Mead and Markus is not possible because the present work is concerned with discontinuous damping layers whose complex shear modulus varies with frequency, whereas Mead and Markus analyzed continuous damping layers whose complex shear modulus is assumed to be constant.

Finally, Figure 13 shows polaroid pictures of the first mode peaks in the frequency response spectrum taken from the screen of the HP3582A spectrum analyzer, for the case where the tape was fixed at the root in conjunction with different lengths of the tape applied to the base structure. The shortening and widening of the peak indicates how the tape is effective in damping resonant vibrations.

## CONCLUSIONS

Measurement and predictions show that, for a given composite cantilever beam vibrating in a given mode, there is an optimum damping tape distribution for maximum damping. Significant improvements in damping were predicted and measured when the constraining layer was clamped at the fixed end of the beam. The amount of damping tape (and its added weight) required to produce a given improvement in damping can be significantly reduced by clamping the tape at the fixed end of the beam. The three-dimensional finite element implementation of the modal strain energy method proved to be a powerful analytical tool for predicting damping of such complex systems. Finally, the impulse-frequency response technique is a fast and accurate method for measuring damping in such structures.

## ACKNOWLEDGEMENTS

The support of the Army Research Office grant No. DAAL03-88-K-0013 (Program Manager - Dr. Gary Anderson) through a subcontract from the University of Florida is gratefully acknowledged. The authors are also indebted to Dr. Dwayne Nelson of the 3M Company, St. Paul, Minnesota for the time spent in fruitful discussions and for supplying the damping tapes.

## REFERENCES

- [1] Ross, D., Ungar, E.E., and Kerwin, E.M. Jr., "Damping of Plate Flexural Vibrations by means of Viscoelastic Laminate", Structural Damping, ASME, New York, p. 49-88, 1959.
- [2] Jones, D.I.G., "Effect of Free Layer damping on Response of Stiffened Plate Structure", Shock and Vibration Bulletin, Vol. 42, Part II, p. 105, December 1970.
- [3] Jones, D.I.G., "Design of Constrained Layer Treatments for Broad Temperature Damping", Shock and Vibration Bulletin, Vol. 44, Part V, p. 1, 1974.
- [4] Rogers, L.C., and Nashif, A.D., "Computerized Processing and Empirical representation of Viscoelastic Material Property Data and Preliminary Constrained Layer Damping Treatment Design", Shock and Vibration Bulletin, Vol. 48, Part II, p. 23, 1978.
- [5] Jones, D.I.G., Nashif, A.D. and Parin, M.L., "Parametric Study of Multiple-Layer Damping Treatments on Beams", Journal of Sound and Vibration, Vol. 29, No.4, p. 423, 1973.
- [6] Nashif, A.D. and Nicholas, T., "Vibration Control by a Multiple-layered Damping Treatment", Shock and Vibration Bulletin, Vol. 41, Part II, p. 121, 1970.
- [7] Ely, R.A., and Sangha, K.B., "Prediction and Measurement of Damping of Vibrations of structures by Adhesives", Proceedings of Advancing Technology in Materials and Processes, 30th National SAMPE Symposium and Exhibition, Vol. 30, Anaheim, California, March 19-21, 1985.

- [8] Ely, R.A., "Laminated Damped Aircraft Structures", Presented at the ASME Winter Annual Meeting, New Orleans, Louisiana, December 3, 1984.
- [9] Sun, C.T., Sankar, B.V. and Rao, V.S., "Damping and Vibration Control of Unidirectional Composite Beams Using Add-On Viscoelastic Materials", 59th Shock and Vibration Symposium, Albuquerque, New Mexico, October 18-20, 1988.
- [10] Gibson R.F., Chaturvedi, S.K. and Sun, C.T., "Complex Moduli of Aligned Discontinuous Fiber-Reinforced Polymer Composites", Journal of Materials Science, Vol. 17, p. 3499, 1982.
- [11] Gibson, R.F., Sun, C.T. and Chaturvedi, S.K., "Damping and Stiffness of Aligned Discontinuous Fiber Reinforced Polymer Composites", Proceedings of the 23rd AIAA/ASME/ASCE/AHS Structures, Structural Dynamics and Materials Conference, New Orleans, Louisiana, May 10-12, 1982.
- [12] Sun, C.T., Chaturvedi, S.K. and Gibson, R.F., "Internal Damping of Short Fiber Polymer Matrix Composites" presented at the symposium on advances and Trends in Structures and Dynamics (sponsored by NASA Langley Research Center), Washington D.C., October 22-25, 1984, also published in Computers and Structures, Vol. 20, No. 1-3, pp. 391-400, 1985.
- [13] Sun, C.T., Gibson, R.F. and Chaturvedi, S.K., "Internal Damping of polymer Matrix Composites Under Off-axis loading", Journal of Materials Science, Vol. 20, p. 2575, 1985.
- [14] Suarez, S.A., Gibson, R.F., Sun, C.T. and Chaturvedi, S.K., "The influence of Fiber Length and Fiber Orientation on Damping and Stiffness of Polymer Composite Materials", Experimental Mechanics , 26 (2), pp. 175-184, June 1986.
- [15] Sun, C.T., Wu, J.K. and Gibson, R.F., "Prediction of Material Damping in Randomly Oriented Short Fiber Polymer Matrix Composites", Journal of Reinforced Plastics and Composites, Vol. 4, pp. 262-272, July 1985.
- [16] Sun, C.T., Wu, J.K. and Gibson, R.F., "Prediction of Material Damping of Laminated Polymer Matrix Composites", proceedings of Vibration Damping Workshop II, Las Vegas, Nevada March 5-7, 1986.
- [17] Wu, J.K., "Optimization Of Material Damping and Stiffness of Laminated Fiber-reinforced Composite Structural Elements", Ph.D. Dissertation, Department of Engineering Sciences, University of Florida, Gainesville, Florida, December 1985.
- [18] Hwang, S.J. and Gibson, R.F., "Micromechanical Modeling of Damping in Discontinuous Fiber Composites Using a Strain Energy / Finite Element Approach", Journal of Engineering Materials and Technology, 109, pp. 47-52, January 1987.

- [19] Hwang, S.J., "Characterization of the Effects of Three Dimensional States of Stress on Damping of Laminated Composites" Ph.D. Dissertation, Mechanical Engineering Department, University of Idaho, May 1988.
- [20] Hwang, S.J. and Gibson, R.F., "The Effects of Three Dimensional States of Stress on Damping of Laminated Composites", 34th International SAMPE Symposium, Reno, Nevada, May 8-11, 1989.
- [21] Gibson, R.F., Deobald, L.R. and Suarez, S.A., "Laboratory Production Of Discontinuous Aligned Composite Plates Using the Autoclave-style Press Cure", Journal of Composites Technology Research, ASTM, Vol. 7, No. 2, pp. 49-54, 1985.
- [22] Suarez, S.A. and Gibson, R.F., "Improved Impulse-Frequency Response Technique for Measurement of Dynamic Mechanical Properties of Composite Materials", Journal of Testing and Evaluation, 15 (2), pp. 114-121, March 1987.
- [23] Ungar, E.E. and Kerwin Jr., E.M., "Loss Factors of Viscoelastic Systems in Terms of Strain Energy Concepts", Journal of Acoustical Society of America, 34 (2), pp. 954-958, July 1962.
- [24] Johnson, C.D. and Kienholz, D.A., "Finite Element Prediction of Damping in Structures With Constrained Viscoelastic Layers", AIAA Journal, 20 (9), pp. 17-24, September 1982.
- [25] Bogner, F.K. and Soni, M.L., "Finite Element Vibration Analysis of Damped Structures", Proceedings of the 22nd Structures, Structural Dynamics and materials Conference, Atlanta, Georgia, Paper No. 81-0489, April 1981.
- [26] Bathe, K.J. et al, SAP IV a Structural Analysis Program for Static and Dynamic Response of Linear Systems, College of Engineering, University of California, Berkeley, California, April 1974.
- [27] Product Information, "Scotchdamp" Vibration Damping Tapes SJ-2052X Nomograph, Structural Products Department, 3M Center, St. Paul, Minnesota.
- [28] Nashif, A.D., Jones, D.I.G. and Henderson, J.P., Vibration Damping, John-Wiley, Interscience, 1985.
- [29] Lu, Y.P. and Everstine, G.C., "More on Finite Element Modeling of Damped Composite Systems", Journal of Sound and Vibration, 69 (2), pp. 199-205, 1980.
- [30] Plunkett, R. and Lee, C.T., "Length Optimization for Constrained Viscoelastic Layer Damping", Journal of Acoustical Society of America, Vol. 48, pp. 150-161, 1970.
- [31] Mead, D.J. and Markus, S., "Loss Factors and Resonant Frequencies of Encastre' Damped Sandwich Beams", Journal of Sound and Vibration, 12 (1), pp. 99-112, 1970.

TABLE 1. Composite structure constituent material properties.

	Density $\rho$	Longitudinal Modulus $E_1$	Transverse Modulus $E_2$	Shear Modulus $G_{12}$	Poisson's Ratio $\nu_{12}$	Fiber Volume Fraction $V_f$	Loss Factor (@ 70°F) MODE 1    MODE 2
<b>BASE STRUCTURE</b>							
E-Glass Epoxy [16 ply/0°/0.13" thick]	1.90 g/cm <sup>3</sup> (0.07 lb/in <sup>3</sup> )	36GPa (5.25MPsi)	11GPa (1.58MPsi)	3GPa (0.44MPsi)	0.28	0.50	0.0040 (a 140Hz)    0.0035 (a 880Hz)
Graphite Epoxy [12 ply/0°/0.06" thick]	1.58 g/cm <sup>3</sup> (0.06 lb/in <sup>3</sup> )	127.9GPa (18.55MPsi)	10.27GPa (1.49MPsi)	7.31GPa (1.06MPsi)	0.22	0.67	0.0029 (a 55Hz)    0.0037 (a 330Hz)
<b>CONSTRAINING LAYER</b>							
Dead Soft Aluminum Foil [Type 1100/0.01" thick]	2.76 g/cm <sup>3</sup> (0.1 lb/in <sup>3</sup> )	69GPa (10MPsi)	69GPa (10MPsi)	26GPa (3.79MPsi)	0.32	--	0.033    --
<b>DAMPING LAYER</b>							
3Ms SJ-2052X [1SD-112/0.005" thick]	0.98 g/cm <sup>3</sup> (0.04 lb/in <sup>3</sup> )	1.76MPa (255Psi)	1.76MPa (255Psi)	0.59MPa (85Psi)	0.49	--	0.87 (a 55Hz)    --
"	"	3.72MPa (540Psi)	3.72MPa (540Psi)	1.24MPa (180Psi)	"	--	--    0.90 (a 330Hz)

TABLE 2. Typical experimental data on the influence of tape boundary conditions (at the clamped end of the beam) on system damping for the first and second modes of vibration.

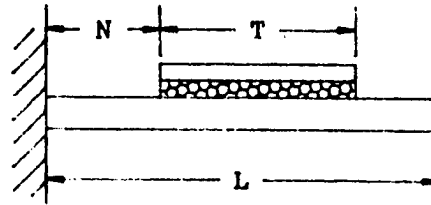
DAMPING WITH DIFFERENT TAPE BOUNDARY CONDITIONS							
Loss Factor (Untaped) Glass Epoxy Specimens*	FREE AT ROOT		FIXED (along face of vise)		FIXED (inside vise)		
	Loss Factor (Taped)	Loss Factor Ratio	Loss Factor (Taped)	Loss Factor Ratio	Loss Factor (Taped)	Loss Factor Ratio	
MODE 1	0.0040	0.049	12.2	0.070	17.5	0.080	20.3
MODE 2	0.0035	0.029	8.3	0.047	13.3	0.043	12.3

\*NOTE: Average of three specimens with  $N/L = 0.0$ ,  $T/L = 0.5$

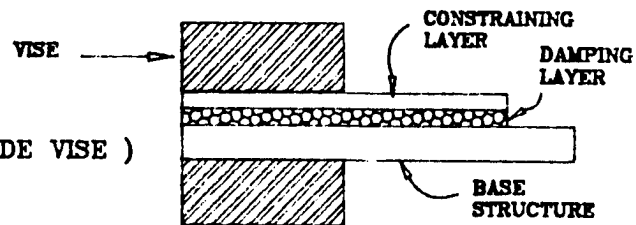


# DAMPING TAPE - DISTRIBUTION AND BOUNDARY CONDITIONS

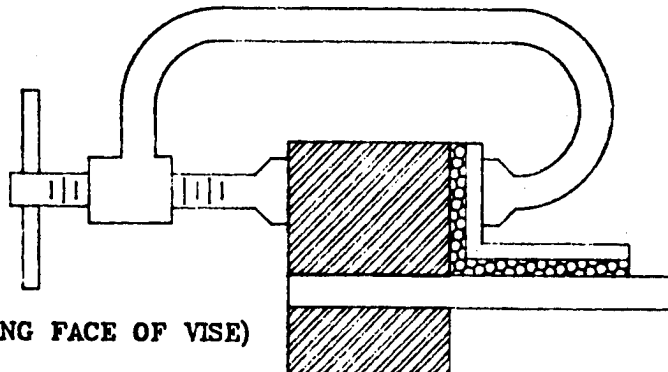
T = TAPE LENGTH  
 L = BEAM LENGTH  
 N = NO TAPE LENGTH ( AT ROOT )



FIXED AT ROOT ( TAPE INSIDE VISE )



FIXED AT ROOT  
 (TAPE CLAMPED ALONG FACE OF VISE)



FREE AT ROOT

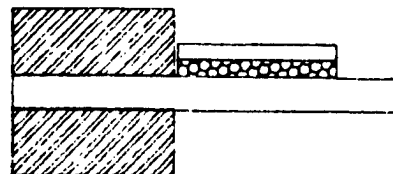


Figure 1. Distribution and boundary conditions of the damping tape applied on one side of the composite base structure.

I.D.	Element	Aspect Ratio (length/thickness)
A	Adhesive Layer	7.144:1
B	Base Structure	0.275:1
C	Constraining Layer	3.572:1

$N/L = 0$        $T/L = 0.6$   
 Number of Elements = 308  
 Number of Nodes = 904  
 Number of Degrees of Freedom = 2700  
 Total Solution Time = 334.79 sec.  
 (IBM 4341 Main Frame System OS/VS1)

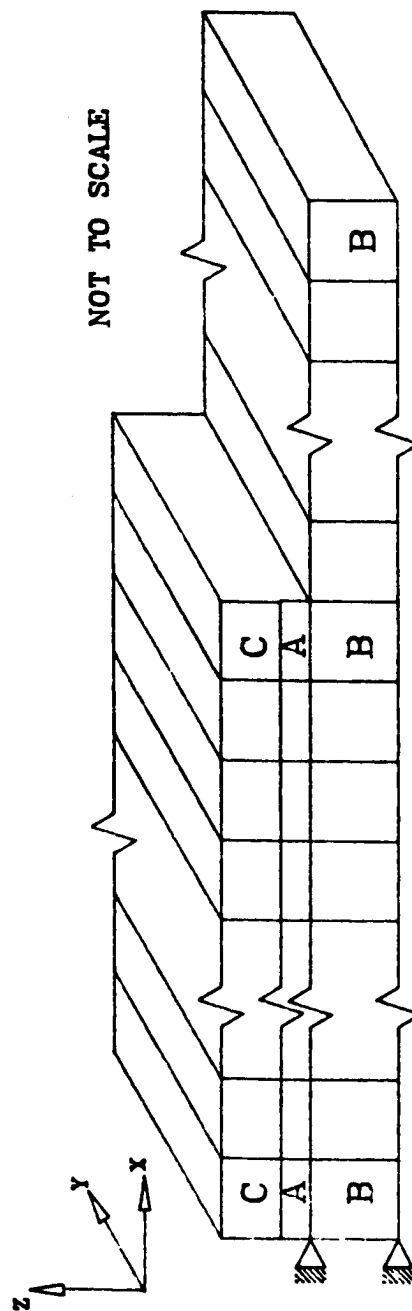


Figure 2. Typical 3-D finite element model of constrained layer damping treatment on a composite base structure (with tape free at clamped end).

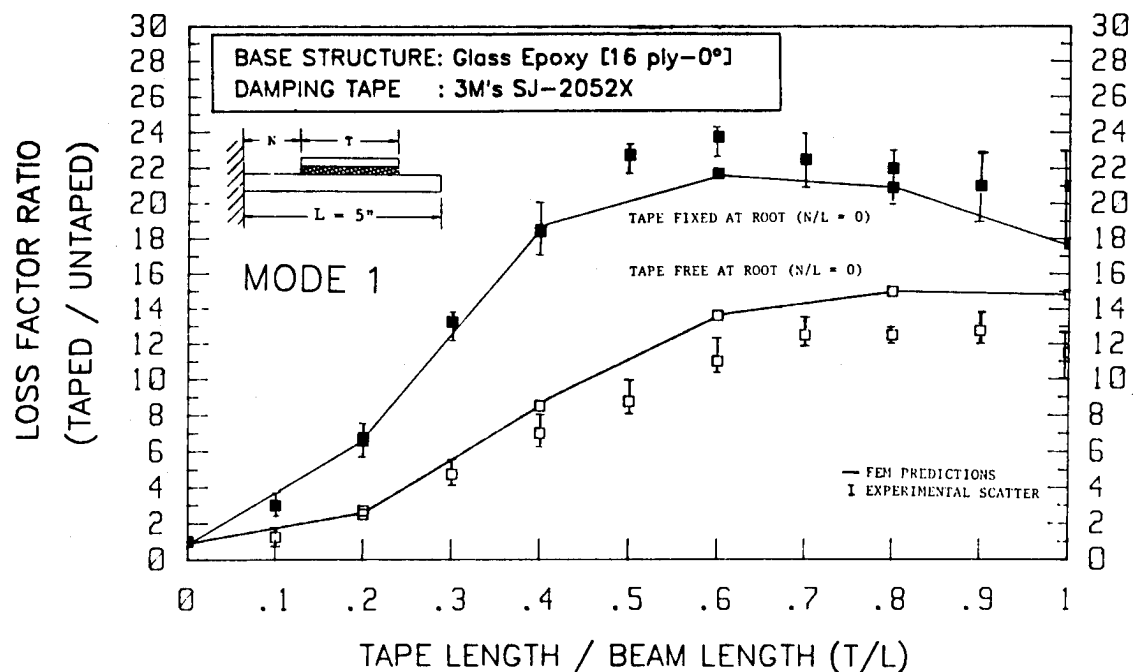


Figure 3. Variation of loss factor with tape length in mode 1 vibration for fixed and free boundary conditions at root, with a unidirectional glass/epoxy composite base structure.

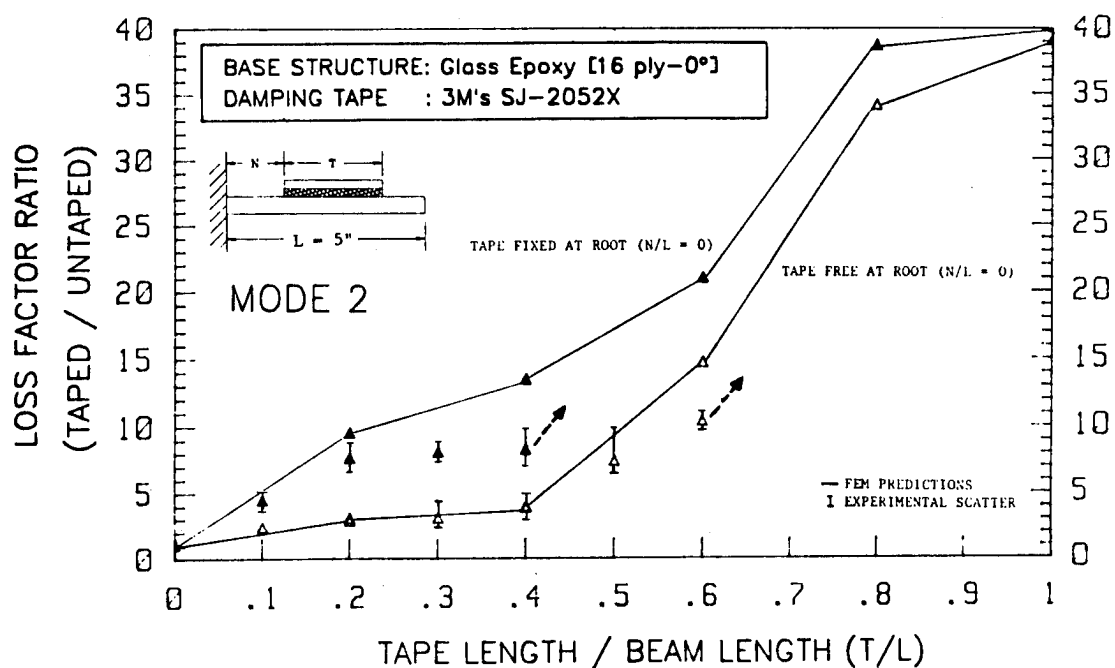


Figure 4. Variation of loss factor with tape length in mode 2 vibration for fixed and free boundary conditions at root, with a unidirectional glass/epoxy composite base structure.

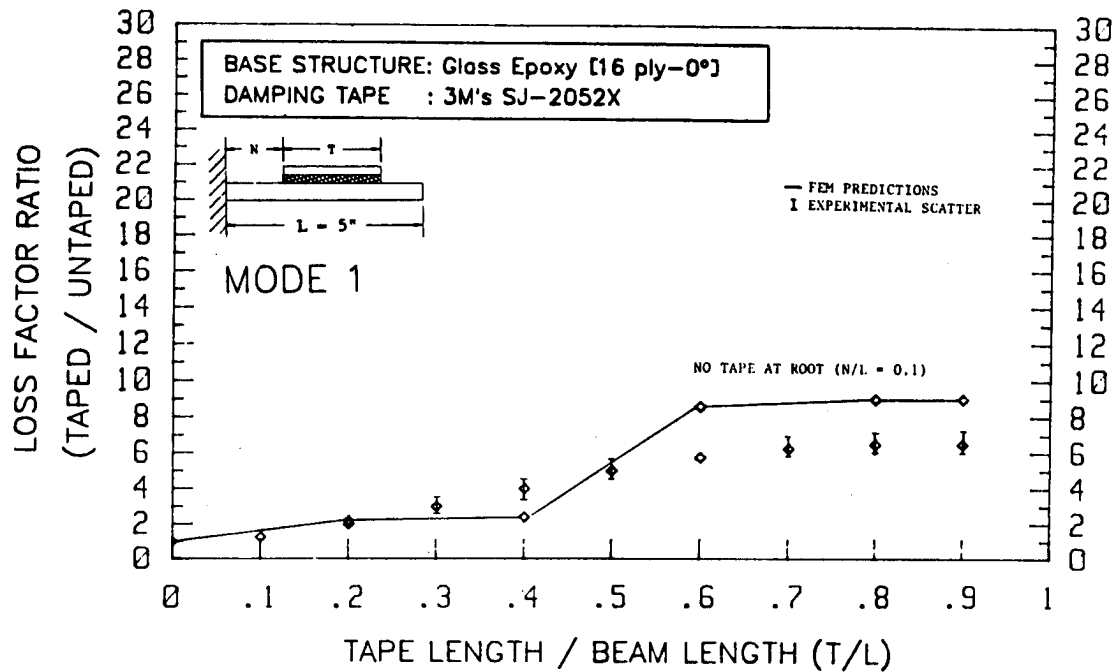


Figure 5. Variation of loss factor with tape length in mode 1 vibration for no tape at root boundary condition, with a unidirectional glass/epoxy composite base structure.

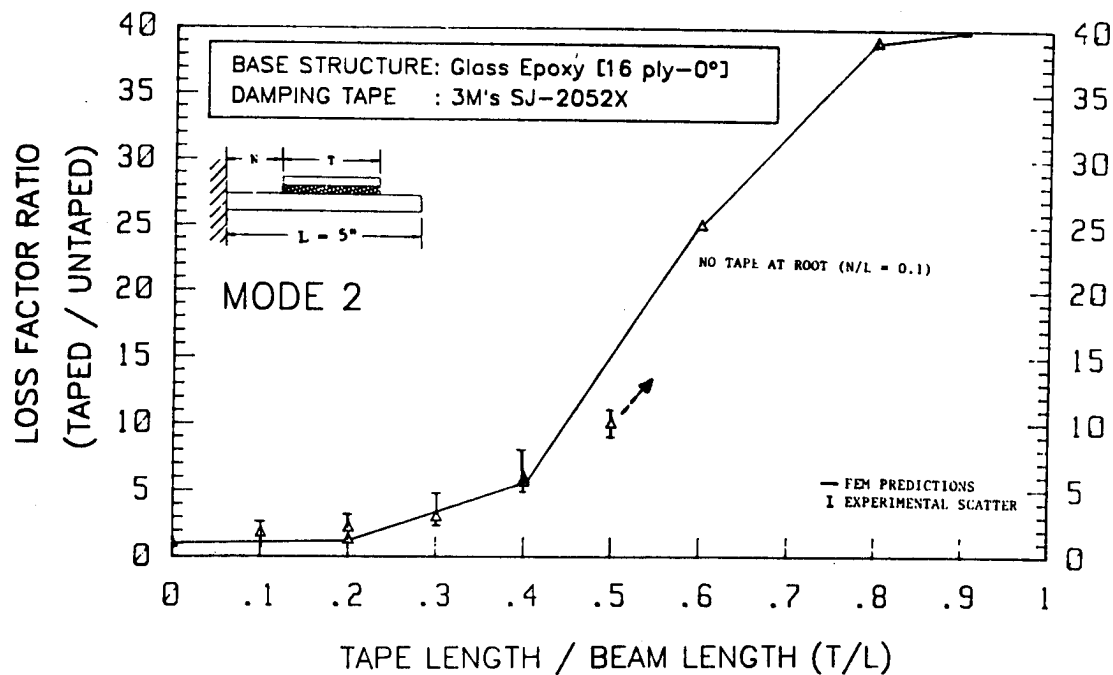


Figure 6. Variation of loss factor with tape length in mode 2 vibration for no tape at root boundary condition, with a unidirectional glass/epoxy composite base structure.

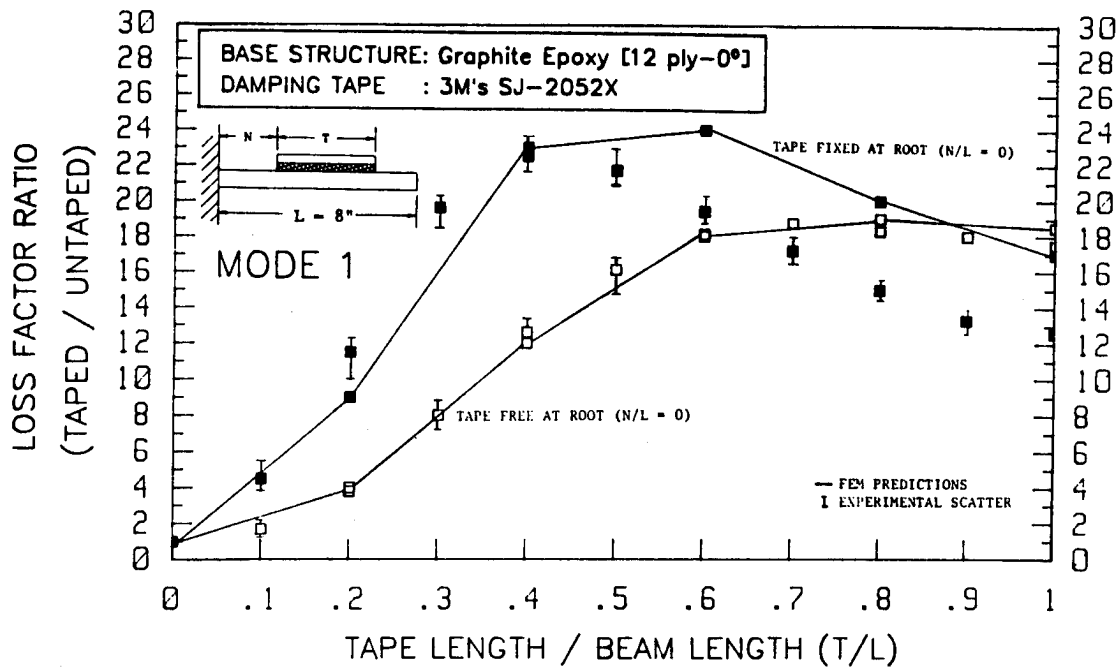


Figure 7. Variation of loss factor with tape length in mode 1 vibration for fixed and free boundary conditions at root, with a unidirectional graphite/epoxy composite base structure.

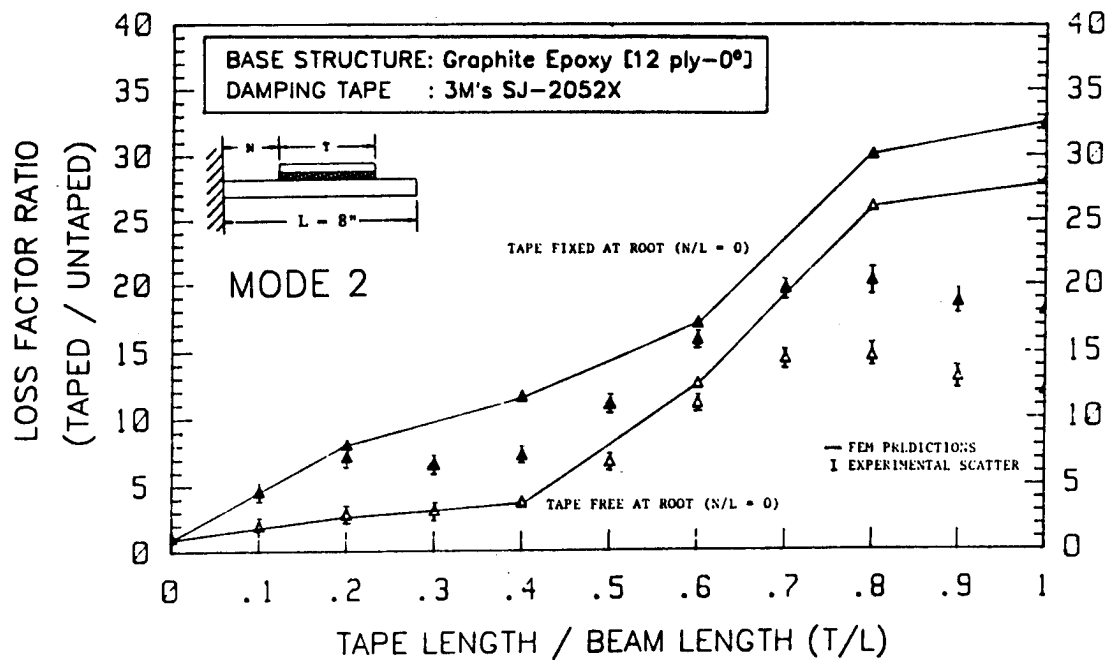


Figure 8. Variation of loss factor with tape length in mode 2 vibration for fixed and free boundary conditions at root, with a unidirectional graphite/epoxy composite base structure.

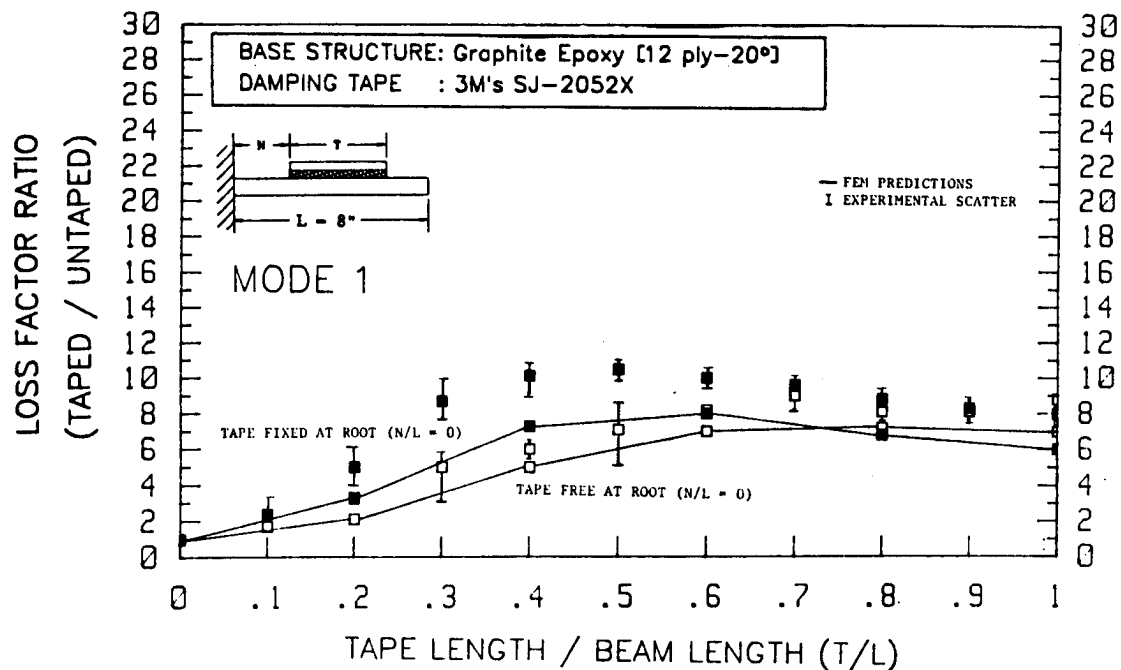


Figure 9. Variation of loss factor with tape length in mode 1 vibration for fixed and free boundary conditions at root, with a  $20^\circ$  off-axis graphite/epoxy composite base structure.

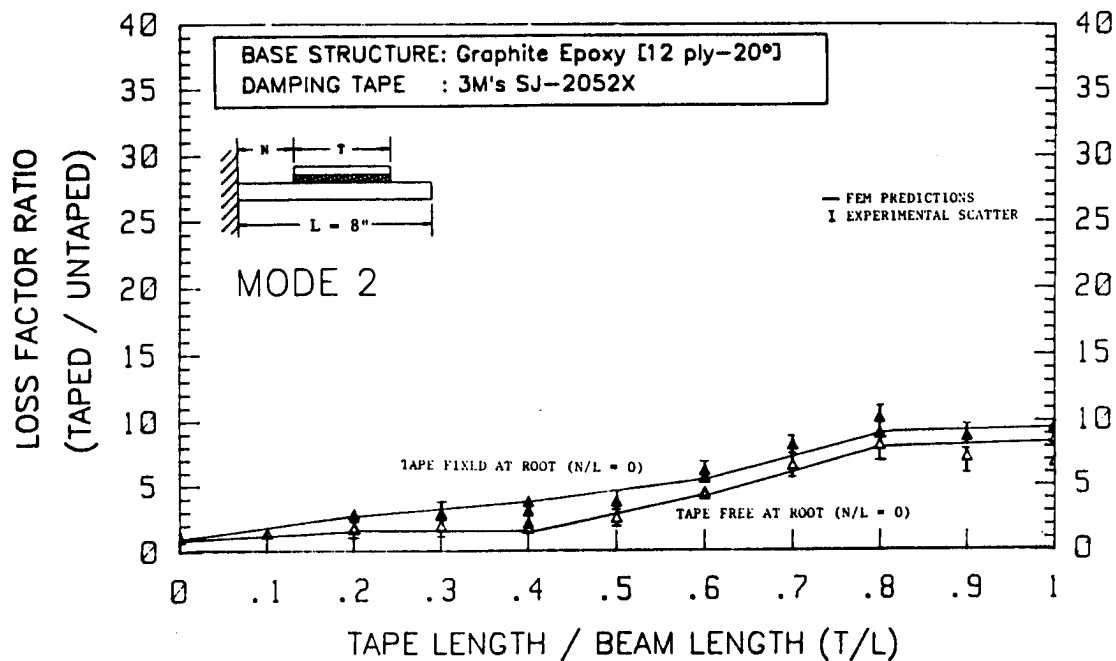


Figure 10. Variation of loss factor with tape length in mode 2 vibration for fixed and free boundary conditions at root, with a  $20^\circ$  off-axis graphite/epoxy composite base structure.

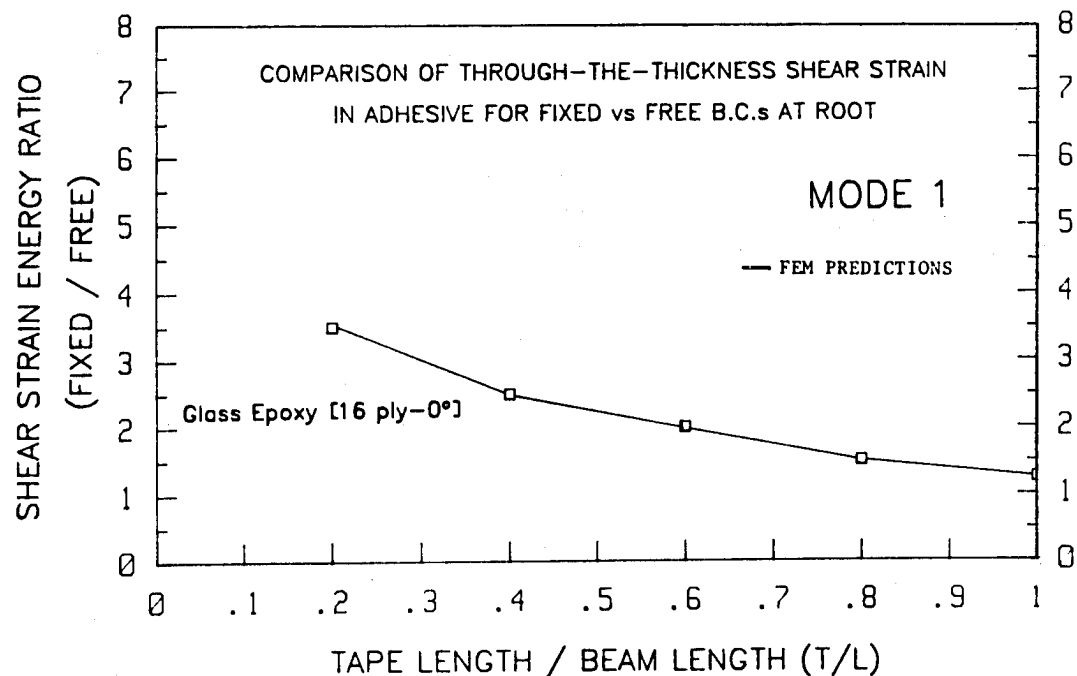


Figure 11. Analytical predictions of through-the-thickness shear strain in adhesive for fixed vs free boundary conditions at root, in mode 1 vibration.

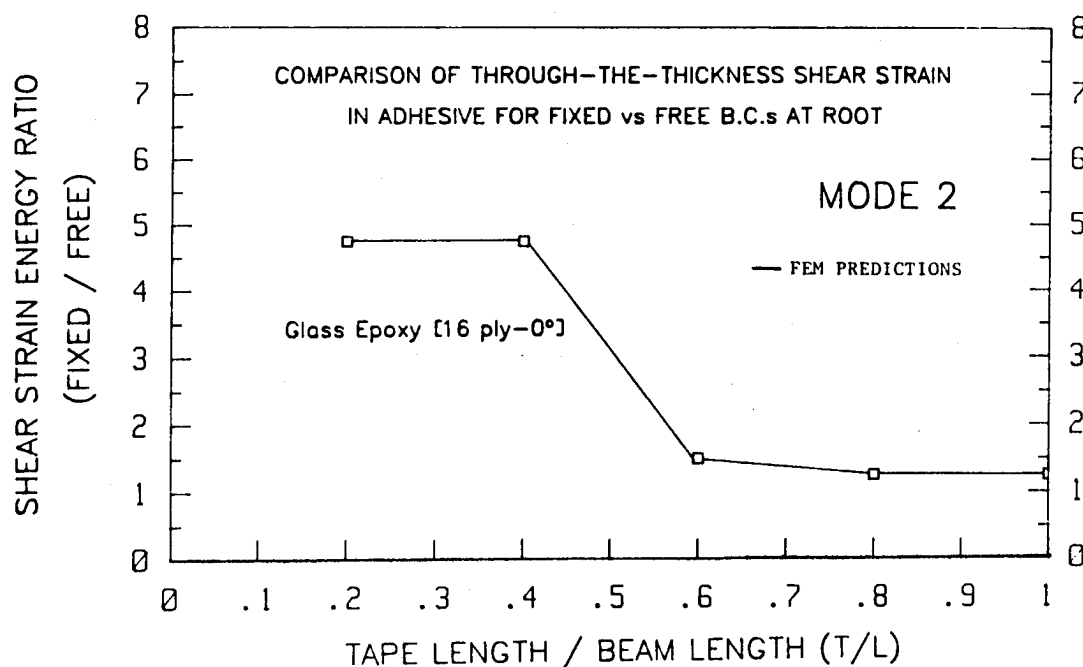
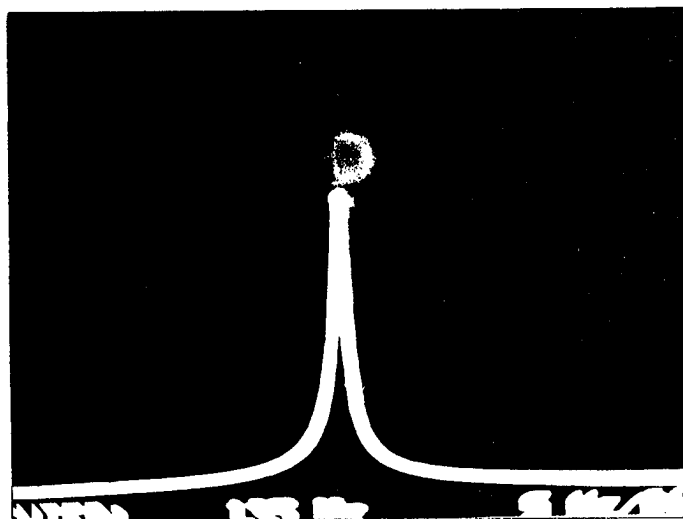
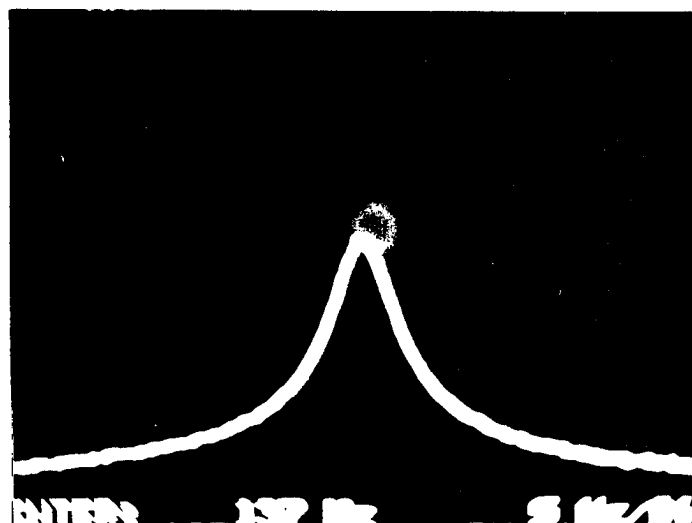


Figure 12. Analytical predictions of through-the-thickness shear strain in adhesive for fixed vs free boundary conditions at root, in mode 2 vibration.

(a) Tape/Beam Length - 0.0  
 1st Mode Frequency - 135 Hz  
 Loss factor - 0.004



(b) Tape/Beam Length - 0.2  
 1st Mode Frequency - 137 Hz  
 Loss Factor - 0.027



(c) Tape/Beam Length - 1.0  
 1st Mode Frequency - 147 Hz  
 Loss Factor - 0.083

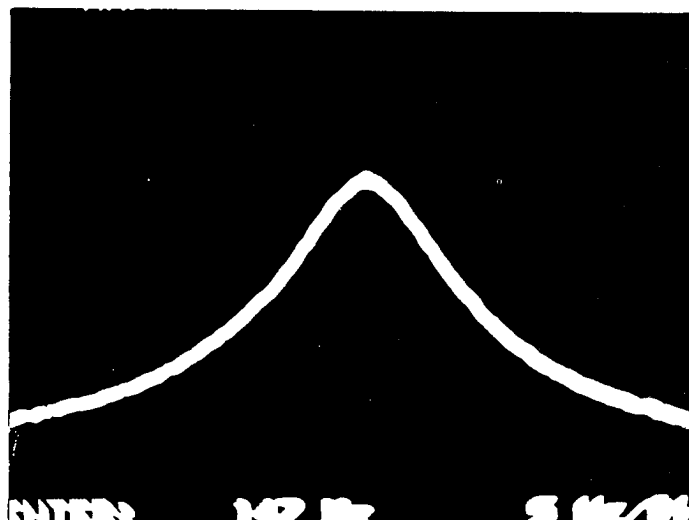


Figure 13 (a,b, and c). Shortening and widening of the 1st mode peak (as observed on the screen of the spectrum analyzer) for different tape/beam length ratios indicating how the tape is effective in damping resonant vibrations of the glass/epoxy composite specimens.



**PRACTICAL STAND OFF DAMPING  
TREATMENT FOR SHEET METAL**

**Mr. Michael L. Parin  
Visiting Scientist  
WRDC/FIBA  
Wright-Patterson AFB, OH 45433  
(513) 255-5664  
Formerly of Anatrol Corporation  
Cincinnati, Oh 45241**

**Dr. Lynn Rogers  
WRDC/FIBA  
Wright-Patterson AFB, OH 45433  
(513) 255-5664**

**Dr. Young In Moon  
Anamet Laboratories, Inc.  
P. O. Box 31041  
Overlook Branch  
Dayton, OH 45431  
(513) 252-1630**

**Mr. Michael Falugi  
Anamet Laboratories, Inc.  
P. O. Box 31041  
Overlook Branch  
Dayton, OH 45431  
(513) 252-1630**

**FOR DAMPING '89, FEB 8-10, 1989  
THE PALM HOTEL, WEST PALM BEACH, FLORIDA**

## ABSTRACT

The impressive potential of Stand-Off-Damping (SOD) systems (historically referred to as "spaced" damping treatments) to control structural resonant response levels has long been recognized. However, the inability to identify materials that store virtually no bending energy while transferring significant shear loads has essentially rendered this concept an academic novelty.

This paper presents analytical and experimental results of a study conducted to investigate a practical SOD system. The analysis for a simply supported four layer beam system, consisting of: 1) a base structure; 2) a stand-off layer; 3) a dissipative viscoelastic layer; and 4) a constraining layer are presented. The numerical results of a limited parametric study to investigate the relationship between the Stand-Off layer, damping layer, and constraining layer geometries and modulus values are presented. Computer generated plots of modal loss factor, RMS response ratio, peak response ratios, and frequency ratios as a function of temperature for a damped and undamped test case are reviewed. Finally, experimental test results of modal loss factor for a conventional three layer damping system and a SOD system are compared to the predicted values for a generic test article.

## 1.0 INTRODUCTION

Of the many critical design criteria by which modern military and civilian aircraft are designed and manufactured, those related to the dynamic behaviors of the structure are the most difficult to quantify prior to actual use of the aircraft. Specifically, fatigue failure from high-frequency vibration and acoustic noise can occur at many locations in the secondary structure; yet the determination of location and magnitude of structural response is usually obtained from component or full-scale tests. The usual consequence of finding undesirable dynamic behavior is either to redesign the structure, which is expensive, or modify it with additional structural stiffeners.

Another acceptable remedy to reduce the damaging effects of high-frequency vibration is to provide a local damping treatment of suitable density and distribution to reduce the overall amplitude. Because damping materials add weight they must, of necessity, be properly designed to achieve the required level of damping at a minimum increase in vehicle weight.

The use of viscoelastic damping materials (VEM) in constrained layers is an established technique for reducing resonant structural vibration [1,2,7,8]. However, the proper design of viscoelastic damped structures requires proven methods and techniques that have application to both new and existing aircraft structures. Some of these methods have been developed by the Wright Research and Development Center (WRDC), the Aerospace Structures Information and Analysis Center (ASIAC), and Anatrol Corporation.

The objective of any constrained-layer damping treatment is to dissipate vibration energy by deforming viscoelastic materials. In the deformation process, the temperatures of the damping materials increase because they remove kinetic energy from the total system. For structural systems which experience relatively large bending strains

without large deflections, the use of constrained layers which dissipate energy through the shearing of the viscoelastic layer is an accepted design approach.

Although there are two types of distributed damping systems, namely free layer and constrained layer, this paper is limited to an analysis of a variation on the conventional three (3) layer system illustrated in Figure 1a. The particular system considered is shown in Figure 1b and consists of a base structure, a Stand-Off layer, a dissipative viscoelastic layer, and a stiff constraining layer.

The advantage of a four layer system that employs a Stand-Off layer is illustrated in Figure 2. The Stand-Off layer provides a greater separation between the neutral axis of the base structure and that of the overall system. This Stand-Off configuration increases the shear deformation introduced into the viscoelastic layer via a kinematic amplifier technique which significantly increases the damping efficiency of the treatment. By selecting a lightweight/shear stiff material for the Stand-Off layer and then configuring it to minimize its bending stiffness and overall weight, an effective and practical Stand-Off layer was conceived.

## 2.0 DERIVATION OF GOVERNING EQUATIONS FOR FOUR-LAYER CONSTRAINED LAYER DAMPING SYSTEM

The four-layer simply supported beam model is depicted in Figure 3 with appropriate notations to be used in the derivation of the governing equations. The principal assumptions to be used are as follows:

1. Only bending and shear deformations are considered— in-plane extensional strains are assumed small and negligible.
2. Bending deformations, strains, and stresses are governed by classical Euler-Bernoulli beam theory [3].
3. Shear deformations ( $\phi$ ) of the base structure and constraining layer ( $k=1,4$  in Figure 3) are the same. The principal shearing-energy dissipation mechanism occurs in the viscoelastic damping layer ( $k=3$ ), since the shear stiffness of this layer is much less when compared to the other components' shear moduli.

Note, it is implicitly assumed that the structural and constraining layers are made of metallic materials, whereas the spacing and damping layers are made of polymeric compounds.

Additional assumptions required to complete the development will be presented as required.

The simple, one-dimensional analysis described below requires the determination of typical section properties; namely, centroid location,  $Z$ , and equivalent section stiffness,  $\overline{EI}$ . From Figure 3,

$$Z_c = \frac{H_1}{2} + Z_d \quad (1)$$

where  $Z_d$  is the distance from the mid-plane of the structural layer to the section centroid. The strains in each layer are found from:

$$\epsilon_1 = Z_d \phi' \quad (2)$$

$$\epsilon_2 = Z_2\phi' - \frac{t_2}{2}\psi_1' \quad (3)$$

$$\epsilon_3 = Z_3\phi' - (t_2 + \frac{t_3}{2})\psi_1' - \frac{t_3}{2}\psi_2' \quad (4)$$

$$\epsilon_4 = Z_4\phi' - (t_2 + t_3)\psi_1' - t_3\psi_2' \quad (5)$$

where the prime represents differentiation with respect to  $x$ . The corresponding forces in each layer are:

$$F_1 = E_1\epsilon_1t_1 = X_1Z_d\phi' \quad (6)$$

$$F_2 = E_2\epsilon_2t_2 = X_2(Z_2\phi' - \frac{t_2}{2}\psi_1') \quad (7)$$

$$F_3 = X_3(Z_3\phi' - (t_2 + \frac{t_3}{2})\psi_1' - \frac{t_3}{2}\psi_2') \quad (8)$$

$$F_4 = X_4(Z_4\phi' - (t_2 + t_3)\psi_1' - t_3\psi_2') \quad (9)$$

where

$$X_k = E_k t_k \quad k = 1, 4 \quad (10)$$

and the strains  $\epsilon_k$  are found from Equations (2)-(5). Applying the requirement for equilibrium of in-plane forces (and noting that the structural layer force,  $F_1$ , is compressive, whereas the other layers are in tension), i.e.,

$$\sum_{k=1}^4 F_k = 0 \quad (11)$$

then

$$\begin{aligned} & - (X_1 + X_2 + X_3 + X_4)Z_d\phi' \\ & + (X_2(Z_2 + Z_d) + X_3(Z_3 + Z_d) + X_4(Z_4 + Z_d))\phi' \\ & - (t_2(\frac{X_2}{2} + X_3 + X_4) + t_3(\frac{X_3}{2} + X_4))\psi_1' \\ & - t_3(\frac{X_3}{2} + X_4)\psi_2' = 0 \end{aligned} \quad (12)$$

From classical theory the centroidal location  $Z_c$  would normally be computed from Equation (12); however, the presence of  $\psi_1'$  and  $\psi_2'$  precludes this. In other words,

the section centroidal location depends on the shear that occurs in the spacing and damping layers.

To compute  $\psi'_1$  and  $\psi'_2$  the classical approach for computing shear stress is used [4], namely, based on equilibrium of the X-direction force and shear

$$F'_4 = -G_3\psi_2 \quad (13)$$

and

$$F'_3 + F'_4 = -G_2\psi_1 \quad (14)$$

The quantities  $F'_3$  and  $F'_4$  are easily found from Equations (8) and (9).

At this point it is necessary to assume a sinusoidal mode shape in order to determine  $\psi_1$  and  $\psi_2$  consistent with the definition of loss factor presented in [5]. Assuming

$$w = \sin Kx \quad (15)$$

for simplicity, then

$$\phi = w' = K \cos Kx \quad (16)$$

$$\phi' = w'' = -K^2 \sin Kx \quad (17)$$

and

$$\phi'' = w''' = -K^3 \cos Kx \quad (18)$$

Assuming that  $\psi_1$  and  $\psi_2$  have the same distribution as  $w$ , then  $\psi_1$  and  $\psi_2$  are related to  $\phi$ ; that is

$$\psi_1 = \alpha_1 \phi \quad (19)$$

and

$$\psi_2 = \alpha_2 \phi \quad (20)$$

Through subsequent differentiations of Equations (19) and (20)

$$\alpha_1 = \frac{\psi'_1}{\phi'} = \frac{\psi''_1}{\phi''} \quad (21)$$

and

$$\alpha_2 = \frac{\psi'_2}{\phi'} = \frac{\psi''_2}{\phi''} \quad (22)$$

Returning to equations (13) and (14) and using the relations in Equations (16)-(22), Equation (13) can be written

$$S_{B1}\psi''_1 + S_{B2}\psi''_2 = S_{B3}\phi'' \quad (23)$$

$$S_{B1} = X_4(t_2 + t_3) \quad (24)$$

$$S_{B2} = \left(\frac{G_3}{K^2} + X_4 t_3\right) \quad (25)$$

and

$$S_{B3} = X_4 Z_4 \quad (26)$$

Similarly, Equation (14) is written

$$S_{A1}\psi''_1 + S_{A2}\psi''_2 = S_{A3}\phi'' \quad (27)$$

$$S_{A1} = X_3\left(t_2 + \frac{t_3}{2}\right) + X_4(t_2 + t_3) + \frac{G_2}{K^2} \quad (28)$$

where

$$S_{A2} = \frac{X_3 t_3}{2} + X_4 t_3 \quad (29)$$

and

$$S_{A3} = X_3 Z_3 + X_4 Z_4 \quad (30)$$

Equations (23) and (27) can be solved to provide

$$\psi''_1 = \left[ \frac{S_{B3}S_{A2} - S_{B2}S_{A3}}{S_{B1}S_{A2} - S_{B2}S_{A1}} \right] \phi'' \quad (31)$$

and

$$\psi''_2 = \left[ \frac{S_{B1}S_{A3} - S_{A1}S_{B3}}{S_{B1}S_{A2} - S_{A1}S_{B2}} \right] \phi'' \quad (32)$$

Observing Equations (21) and (22) and returning to Equation (12),

$$-P_A Z_d + P_B - P_C \alpha_1 - P_D \alpha_2 = 0 \quad (33)$$

where

$$P_A = X_1 + X_2 + X_3 + X_4 \quad (34)$$

$$P_B = X_2(Z_2 + Z_d) + X_3(Z_3 + Z_d) + X_4(Z_4 + Z_d) \quad (35)$$

$$P_C = t_2\left(\frac{X_2}{2} + X_3 + X_4\right) + t_3\left(\frac{X_3}{2} + X_4\right) \quad (36)$$

$$P_D = \frac{X_3}{2} + X_4 \quad (37)$$

Also, from Equations (31) and (32), with (21) and (22)

$$\alpha_1 = \frac{\psi'_1}{\phi'} = Y_A - Z_d Y_B \quad (38)$$

and

$$\alpha_2 = \frac{\psi'_2}{\phi'} = Y_C - Z_d Y_D \quad (39)$$

where

$$Y_A = \frac{S_{A2}X_4(Z_4 + Z_d) - S_{B2}(X_3(Z_3 + Z_d) + X_4(Z_4 + Z_d))}{\bar{S}} \quad (40)$$

$$Y_B = \frac{S_{A2}X_4 - S_{B2}(X_3 + X_4)}{\bar{S}} \quad (41)$$

$$Y_C = \frac{S_{B1}(X_3(Z_3 + Z_d) + X_4(Z_4 + Z_d)) - S_{A1}(X_4(Z_4 + Z_d))}{\bar{S}} \quad (42)$$

$$Y_D = \frac{S_{B1}(X_3 + X_4) - S_{A1}X_4}{\bar{S}} \quad (43)$$

and

$$\bar{S} = S_{B1}S_{A2} - S_{A1}S_{B2} \quad (44)$$

noting that

$$Z_2 + Z_d = \frac{1}{2}(t_1 + t_2) \quad (45)$$

and

$$Z_3 + Z_d = t_2 + \frac{1}{2}(t_1 + t_3) \quad (46)$$

$$Z_4 + Z_d = t_2 + t_3 + \frac{1}{2}(t_1 + t_4) \quad (47)$$

then  $Z_d$  can be found from Equations (33)-(47) as

$$Z_d = \frac{P_C Y_A + P_D Y_C - P_B}{P_C Y_B + P_D Y_D - P_A} \quad (48)$$

If the section deformed with constant angle then the equation for the deflection curve can be represented in the following form:

$$\overline{EI}\phi' = M \quad (49)$$

where  $\overline{EI}$  is the flexural rigidity and  $M$  is the bending moment of the beam. The total bending moment can be expressed as follows:

$$M = \sum_{k=1}^4 M_{kk} + \sum_{k=1}^4 F_k Z_k \quad (50)$$

where  $M_{kk}$  is the bending moment of the  $k^{th}$  layer

$$M_{kk} = \phi' E_k I_k \quad (51)$$

Equations (49) and (50) define the flexural rigidity as follows,

$$\begin{aligned} \overline{EI} = & E_1 I_1 + E_2 I_2 + E_3 I_3 + E_4 I_4 \\ & + X_1 Z_d^2 + X_2 Z_2^2 + X_3 Z_3^2 + X_4 Z_4^2 \\ & - \left[ E_2 I_2 + E_3 I_3 + \frac{X_2 t_2 Z_2}{2} + X_3 \left( t_2 + \frac{t_3}{2} \right) Z_3 + X_4 (t_2 + t_3) Z_4 \right] \frac{\psi'_1}{\phi'} \\ & - \left[ E_3 I_3 + \frac{X_3 t_3 Z_3}{2} + X_4 t_3 Z_4 \right] \frac{\psi'_2}{\phi'} \end{aligned} \quad (52)$$

To compute the loss factor for the four-layer system it is necessary to consider material properties to consist of real and imaginary parts. Thus,

$$E_3 = E_3(1 + i\eta_3) \quad (53)$$



and

$$G_3 = G_3(1 + i\eta_3) \quad (54)$$

where

$$i = \sqrt{-1}$$

Using Equations (53) and (54) in Equation (52) results in

$$\overline{EI} = EI_{real} + EI_{imag}, \quad (55)$$

The intermediate manipulations required to determine  $EI_{real}$  and  $EI_{imag}$  are straightforward but very lengthy; consequently, they are not included. The system modal loss factor,  $\eta_m$ , is found from

$$\eta_m = \frac{EI_{imag}}{EI_{real}} \quad (56)$$

The modal frequency for Nth mode of vibration, is calculated by:

$$f_N = \frac{1}{2\pi} \times K_N^2 \sqrt{\frac{EI_{real}g}{\sum_{k=1}^4 H_k \rho_k}} \quad (57)$$

where:

$K^2$  = wave number;  $= K_N^2 = \frac{(N\pi)^2}{L^2}$

$H_k$  =  $k^{th}$  layer thickness;

$\rho_k$  =  $k^{th}$  layer density, mass/limit volume;

N = mode number; and

g = acceleration of gravity.

In practice the complex modulus is evaluated for the given temperature and an estimated modal frequency,  $f_e$ . The modal frequency is calculated from  $f_N$  and compared to the convergence criteria.

$$\left| 1 - \frac{f_e}{f_N} \right| \leq \epsilon_{FREQ} = 0.01 \quad (58)$$

If this condition is not met, the new estimated frequency is taken as the old calculated frequency and the process repeated.

### 3.0 Comparison of Response

The peak amplitude response for a one degree of freedom system undergoing sinusoidal excitation of amplitude  $f_0$  is

$$X_{peak} = \frac{f_0}{k\eta} = \frac{f_0}{m(2\pi f)^2\eta} \quad (59)$$

and the ratio

$$\frac{X_{peakundamp}}{X_{peakdamp}} = \frac{m_d}{m_u} \times \left(\frac{f_d}{f_u}\right)^2 \times \frac{\eta_d}{\eta_u} \quad (60)$$

The root-mean-square amplitude response  $W_{rms}$ , (equivalently, of a SS beam where the force is spatially sinusoidal and temporally random) is obtained by using the equation derived in [6]; that is

$$W_{rms} = \frac{\pi \bar{F}(w)}{2\sqrt{2}m^{1/4}K^{3/4}\eta^{1/2}} \times \left[ \frac{1 + \sqrt{1 + \eta^2}}{\sqrt{1 + \eta^2}} \right] \quad (61)$$

Noting that

$$m(w)^2 = k = m(2\pi f)^2 \quad (62)$$

Then the ratio between the responses of the damped and undamped (with and without the damping treatment) is found from

$$RMS = \frac{(W_{rms}/\bar{F}(w))_u}{(W_{rms}/\bar{F}(w))_d} = \frac{m_d}{m_u} \times \frac{\sqrt{1 + \eta_d^2}}{\sqrt{1 + \eta_u^2}} \times \frac{\left[ \frac{1 + \sqrt{1 + \eta_u^2}}{\sqrt{1 + \eta_u^2}} \right]}{\left[ \frac{1 + \sqrt{1 + \eta_d^2}}{\sqrt{1 + \eta_d^2}} \right]} \times \sqrt{\frac{\eta_d}{\eta_u}} \times \left(\frac{f_d}{f_u}\right)^{\frac{3}{2}} \quad (63)$$

where the subscript "u" refers to the base structure by itself and "d" represents the response with the damping treatment.

#### 4.0 CALCULATIONS

Figure 4 presents the flow of the computations. The characteristics of the undamped baseline beam and the characteristics of the candidate damping treatment, including parameters used to described the viscoelastic damping material, are input. The frequency of the baseline beam is calculated. For a specified temperature, the value of temperature shift function is calculated. The reduced frequency is calculated using an estimated frequency; then, the shear modulus of the viscoelastic layer is calculated. The equations derived above are used to calculate modal damping and frequency; if the calculated frequency is identical to the one used to calculate the VEM shear modulus, the results are consistent. If the convergence criteria is not met, the calculation is

iterated for a an improved value of estimated frequency. Once convergence is achieved for a temperature, the RMS and PEAK values are calculated.

To obtain a better understanding of the important parameters for an SOD system, sensitivity studies were run in which the base beam was held constant while the thickness of the Stand-Off layer, viscoelastic layer, and constraining layer were varied by 20 percent. In addition, the modulus of the constraining layer was also varied by 20 percent. Each variation was made independent of the other three. The initial model used for this study is shown in Figure 5 and consists of a .080 inch thick stand-off layer, a .005 inch layer of 3M Co. Y- 966 viscoelastic, and a .010 inch thick aluminum constraining layer. The results of the sensitivity study are presented in Table 1 and indicate that the most important parameter for increased performance is the spacer thickness. To a lesser extent, the thickness and modulus of the constraining layer also provide an increase in performance. The least sensitive parameter in this study is the thickness of the damping layer. In addition, the temperature for optimum performance is only slightly influenced by these parameters.

A second analytical study was conducted to determine the performance sensitivity of the SOD system to variations of the shear modulus of the Stand- Off layer. This was carried out using the configuration shown in Figure 5 and the results are presented in Table 2 and Figure 6. This study indicates that the SOD system investigated is relatively insensitive to large changes in the shear modulus of the Stand-Off layers. In addition, the temperature for optimum performance is shifted up as the shear modulus of the stand-off layer is decreased (Table 2).

## **5.0 HARDWARE DEMONSTRATION**

To verify the Stand-Off damping treatment analysis and concept, a practical demonstration was undertaken. The single span generic aircraft skin-stringer- frame panel, illustrated in Figure 7, was selected as the test article.

A dynamic survey was performed on the undamped test article to characterize the important modal parameters required to design a damping system. This was done by applying a known excitation load to the panel and measuring its response. For this case, an impact load was used to excite the panel at specific locations and its response was measured using a accelerometer located at a second point. These signals were input to a two channel digital signal analyzer in order to generate the inertance frequency response function between the test points. Figure 8 illustrates a typical driving point frequency response function for the undamped test article. It can be seen from the FRF that a number of resonant modes with low damping values are present in the 200 Hz to 800 Hz frequency range.

In order to effectively design a damping treatment for the test article, it was necessary to determine the deformation patterns for those modes of interest. This was accomplished by comparing the FRF between 336 different points on the panel. The relative magnitude and phase angle between all points for each resonant mode was then used to determine the deformation patterns for specific resonant models, as illustrated in Figure 9.

Based on the modal study, the fundamental panel bending model (236 Hz) was selected as the target model for correlation. An equivalent beam model compatible with the input requirements of the program was developed. The model maintained the thickness and mass distribution of the skin component but altered the Young's modulus to account for Poisson's stiffening. An equivalent simply supported beam length of five (5) inches was determined using fourth order beam and plate theory.

Two damping configurations, shown in Figure 10, were analyzed, fabricated, applied to the test panel, and tested. The first treatment was a conventional constrained layer viscoelastic material system consisting of a .005 inch damping layer and a 0.010 inch aluminum constraining layer applied to the base. The second treatment was a partial coverage SOD system with a .080 inch spacer introduced between the base structure and the viscoelastic damping layer. The predicted performance for these treatments is shown in Figures 11 and 12.

Figures 13 and 14 compare the measured driving point FRF for the test article with and without the indicated configuration at 74 degrees F. These graphs illustrate the overall vibratory reduction obtained for each of the damping designs. The same measurements were made at different temperatures and the loss factor for the target mode was determined using the half power band width technique. The measured modal loss factors at each test temperature are included in Figures 11 and 12 for the respective treatments.

These test results show excellent correlation between the predicted and measured modal loss factor over the test temperature range. Further, the experimental results confirm that modal loss factors in excess of 0.10 are achieved from approximately 60 degrees F. up to the maximum test temperature.

## 6.0 CONCLUSIONS

The analytical and experimental results presented clearly demonstrate the impressive vibratory suppression benefits a properly configured Stand-Off-Damping system can provide when compared to a conventional distributed damping systems. This performance is achieved with an add-on system that imposes only modest space and weight requirements to the overall system.

The analytical model provides a good first approximation for predicting the modal loss factor for the fundamental mode over a wide temperature range. Additional development to expand the analytical model to accommodate different boundary conditions and multiple damping/constraining layers would greatly increase its utility.

## 7.0 REFERENCES

1. Ross, D., Ungar, E. E., and Kerwin, E. M., "Structural Damping", J. E. Ruzicka, Ed., American Society of Mechanical Engineers, 1959.
2. Snowdon, J. C., "Vibration and Shock in Damped Mechanical Systems", John Wiley & Sons, 1968.
3. Fung, Y. C., "A First Course In Continuum Mechanics", Second Edition, Prentice-

- Hall, Inc., Englewood Cliffs, New Jersey, 1977.
4. Byars, E. F., and Snyder, R. D., "Engineering Mechanics of Deformable Bodies", Second Edition, International Textbook Company, Scranton, Pennsylvania, 1969.
  5. Ungar, E. E., and Kerwin, Jr., E. M., "Loss Factors of Viscoelastic Systems in Terms of Energy Concepts," The Journal of the Acoustical Society of America, Vol. 34, No. 7, pp. 954-957, July 1962.
  6. Nashif, A., and Jones, D., Henderson, J. P., "Vibration Damping", John Wiley & Sons, 1985.
  7. Rogers, L., Notes from Vibration Damping Short Course, University of Dayton Research Institute, Sections 6 and 7, November 1987.
  8. Miles, R. N., "The Prediction of the Damping Effectiveness of Multiple Constrained Layer Damping Treatments", Presented at Acoustical Society of America, Massachusetts Institute of Technology, June 11-15, 1979.

# SENSITIVITY

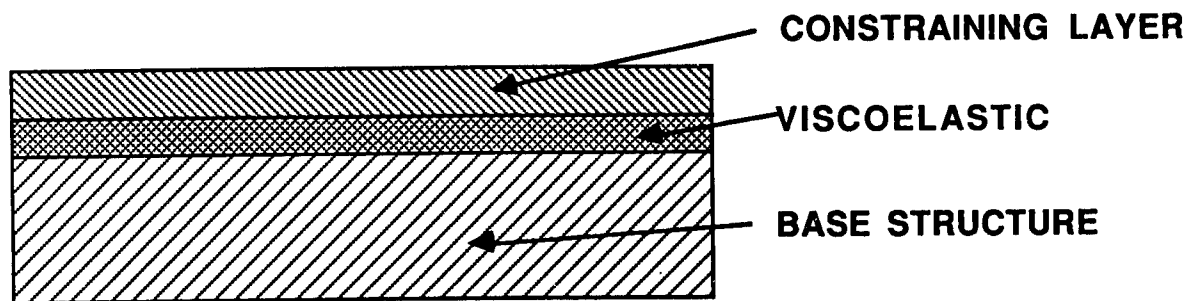
H2 (in.)	H3 (in.)	H4 (in.)	E4 (psi)	XRMSU/XRMSD (MAX)	TEMP (°F)	% CHANGE
0.080	0.005	0.010	10E6	21.68	100	BASE
0.096	0.005	0.010	10E6	25.92	100	19.56
0.080	0.006	0.010	10E6	21.96	95	1.29
0.080	0.005	0.012	10E6	24.61	95	13.51
0.080	0.005	0.010	12E6	24.16	95	11.44

TABLE 1

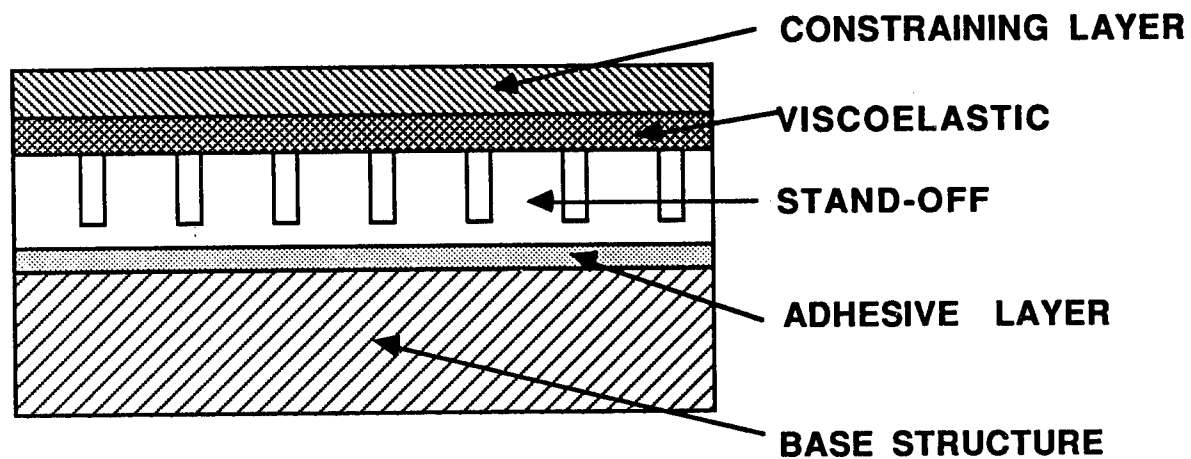
# SENSITIVITY

G <sub>2</sub> (psi)	XRMSU/XRMSD (MAX)	TEMP (°F)
200,000	21.68	100
160,000	21.64	100
83,000	21.45	100
64,000	21.34	100
32,000	20.85	100
16,000	19.95	100
8,000	18.41	100
4,000	16.08	105
2,000	13.06	110
1,000	9.88	120

TABLE 2



1a



1b

Figure 1 - Conventional and Stand-Off Constrained Layer Damping Systems

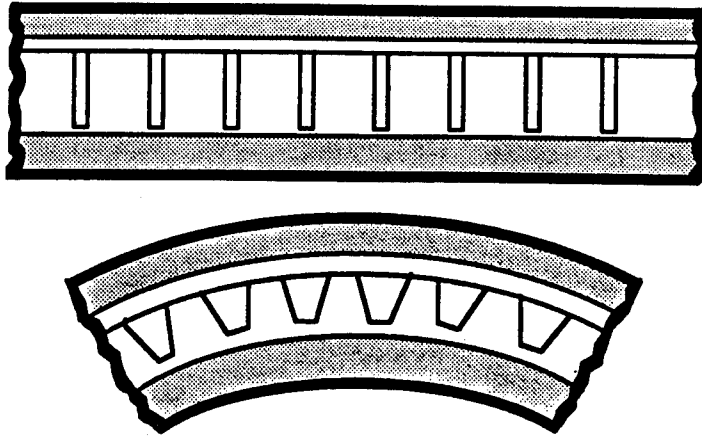


Figure 2 - Deformed Stand-Off System

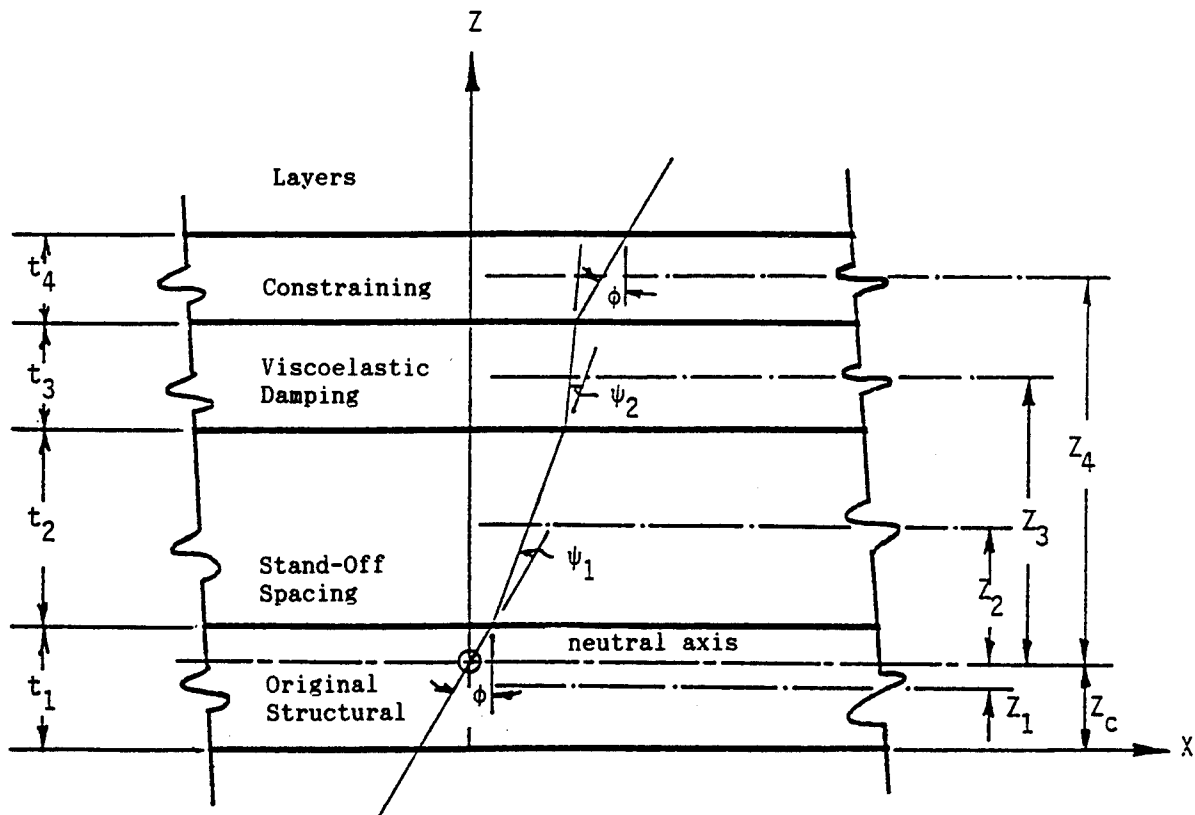


Figure 3 - Schematic of Four-Layer Viscoelastic Constrained Layer Damping System



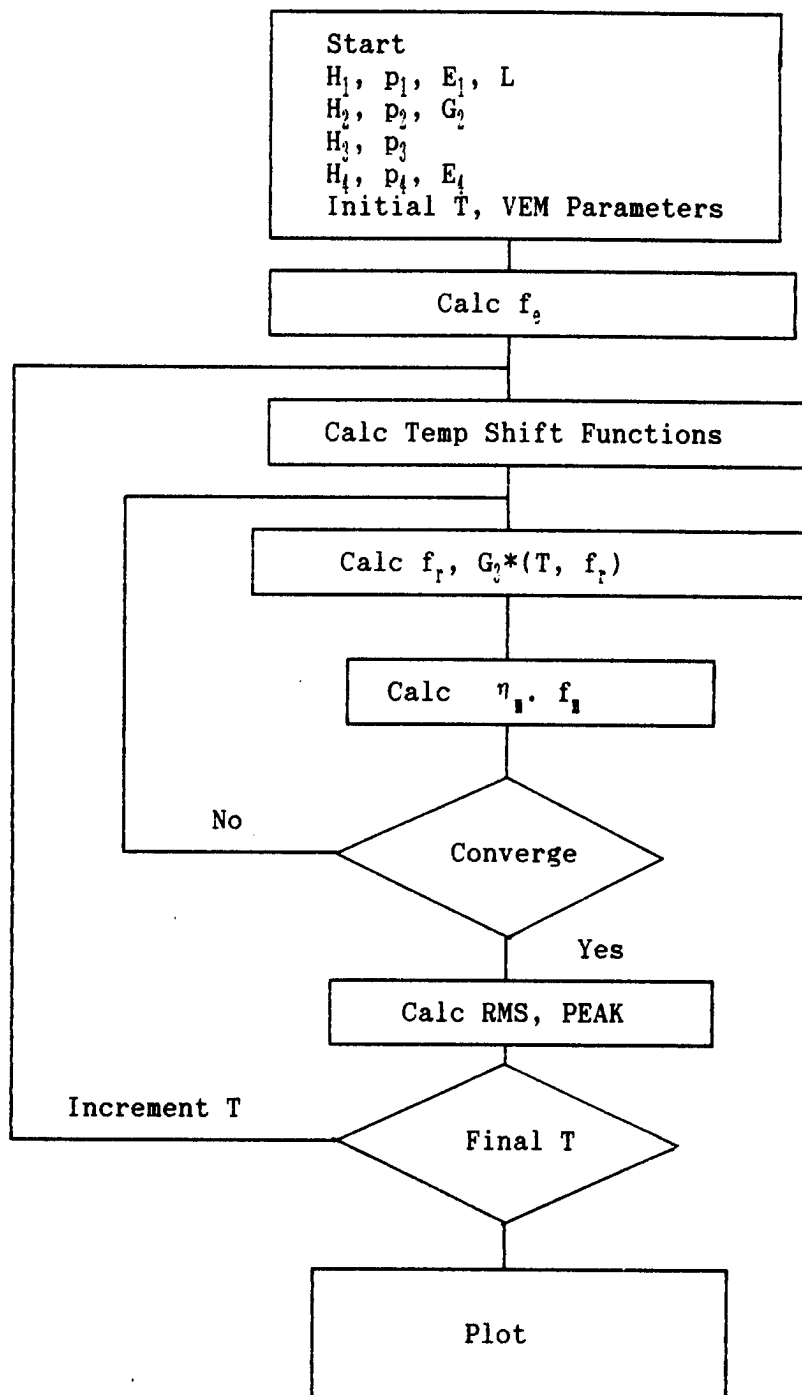


Figure 4

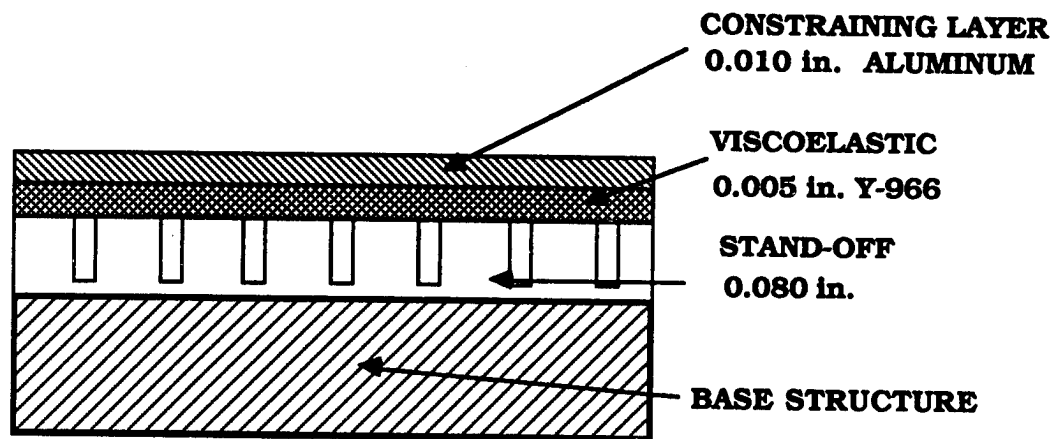


Figure 5

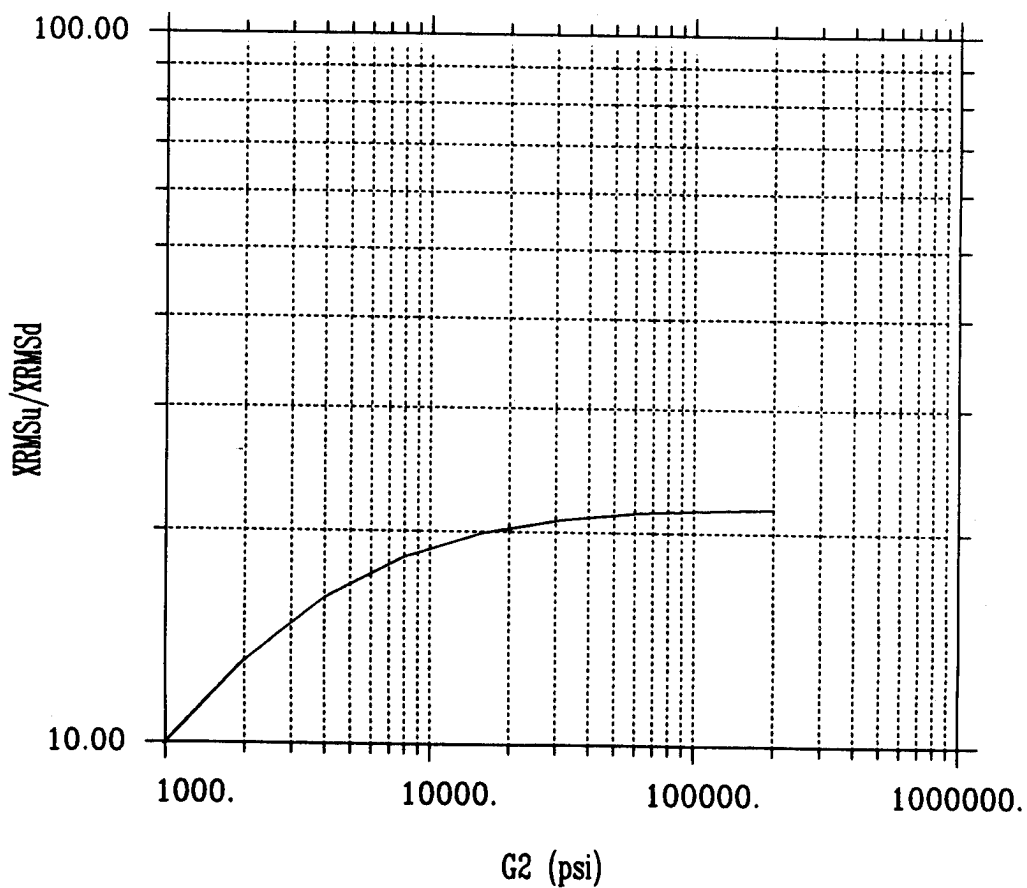
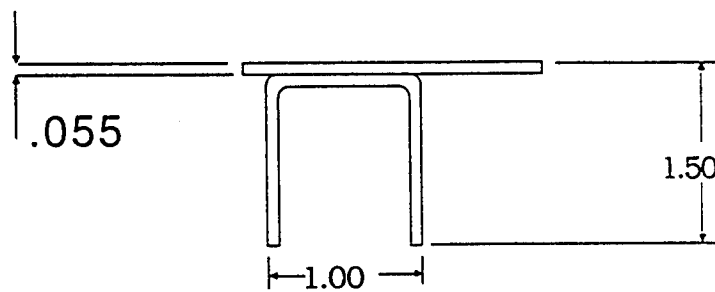
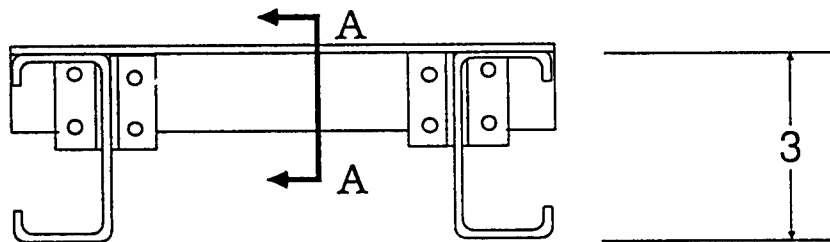
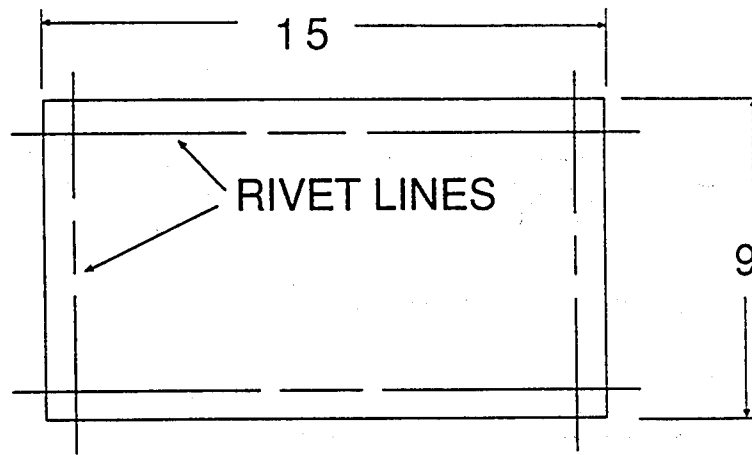


Figure 6 - Influence of Stand-Off Modulus on RMS Response Ratio



SECTION  
A-A

Figure 7

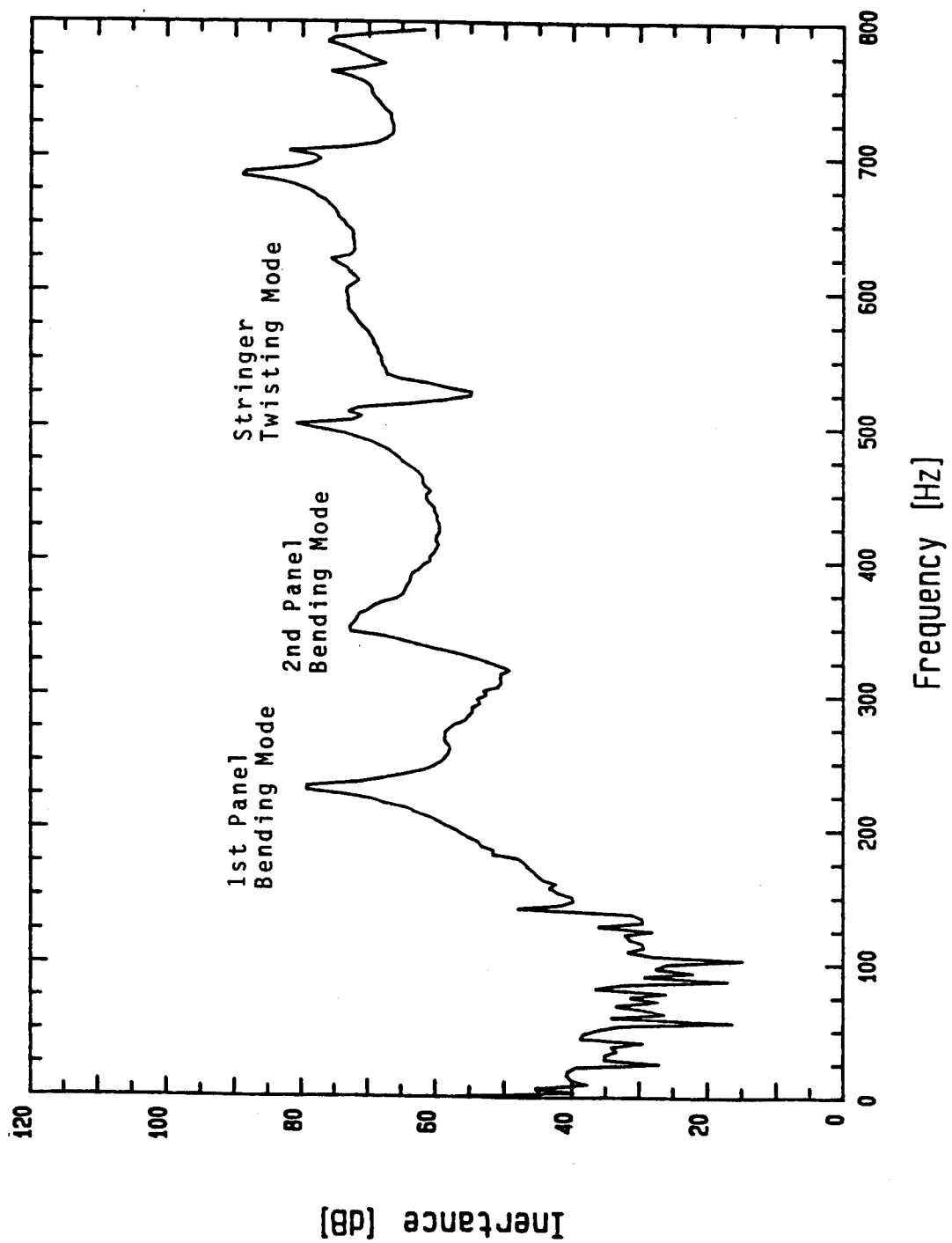
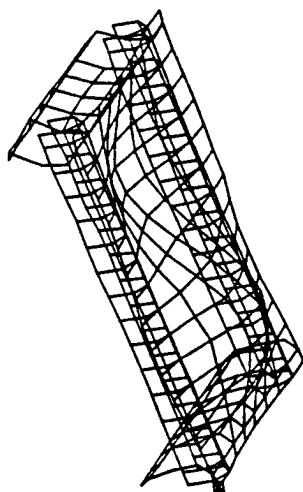
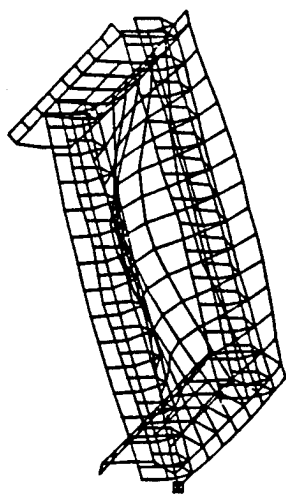


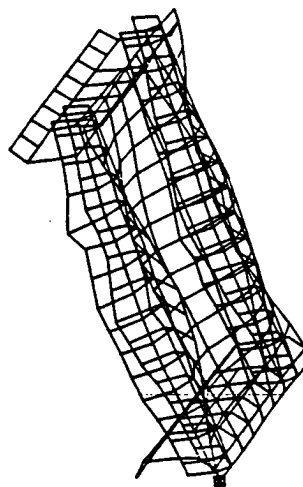
Figure 8 - Frequency Response for Bare Test Panel



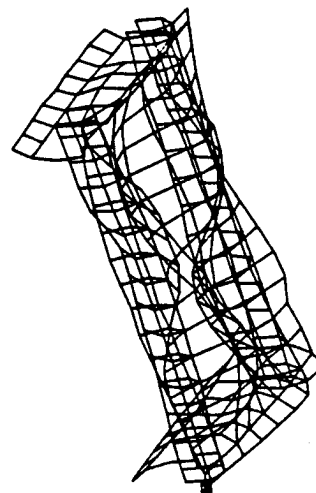
Undeformed Test Article



1st Bending Mode 236 Hz

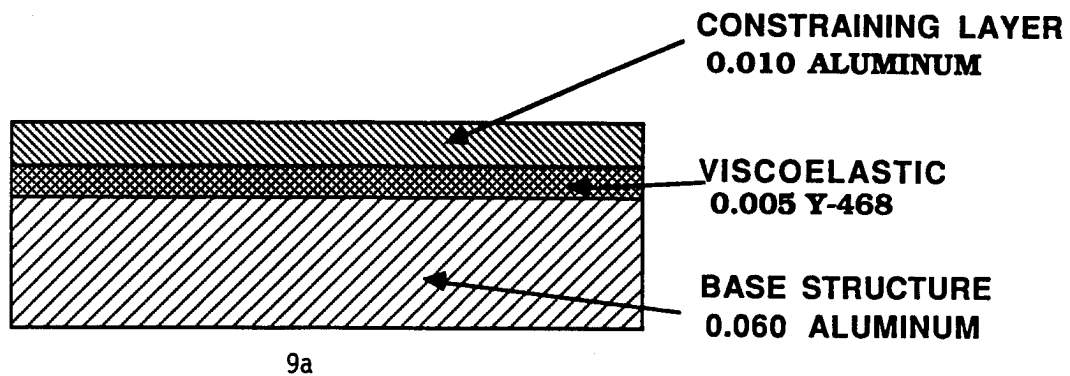


2nd Bending Mode 331 Hz

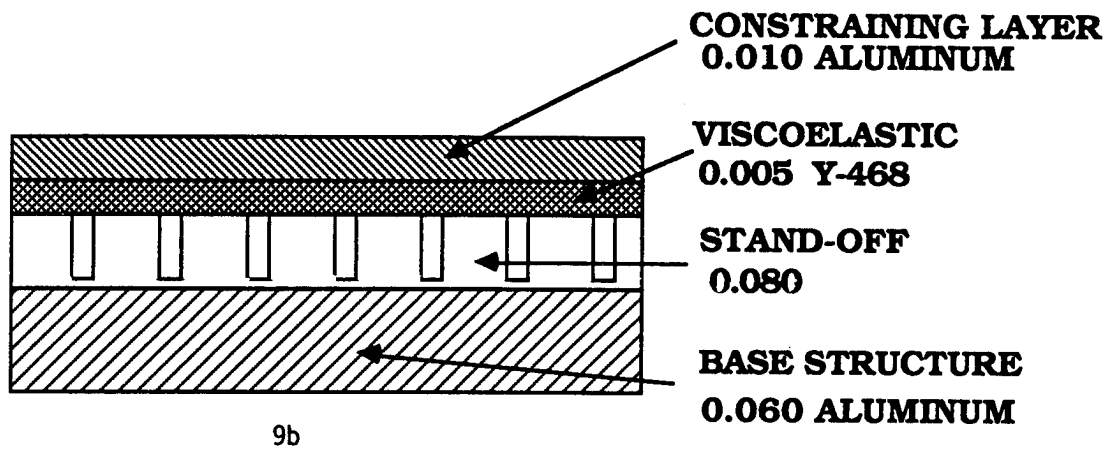


Stringer Twisting Mode 510 Hz

Stringer Twisting Mode 726 Hz



Conventional Constrained Layer System



Stand-Off Constrained Layer System

Figure 10

### THREE-LAYER BEAM, MODE 1

(MODAL LOSS FACTOR)MAX= 0.10, AT T= 95. Deg F

(XRMSu/XRMSd)MAX= 4.43, AT T= 85. Deg F

(XPEAKu/XPEAKd)MAX= 15.14, AT T= 90. Deg F

(MASSd/MASSu)= 1.20

(1) BASE BEAM H1=0.060 in, R01=.098 lb/in<sup>3</sup>, E=0.119E+08 psi

L=5.00 in, Freq= 236. hz

(2) VEM H2=0.005 in, R02=.035 lb/in<sup>3</sup>, 3M-468

(3) CONST. LAYER H3=0.010 in, R03=.098 lb/in<sup>3</sup>, E=0.960E+07 psi

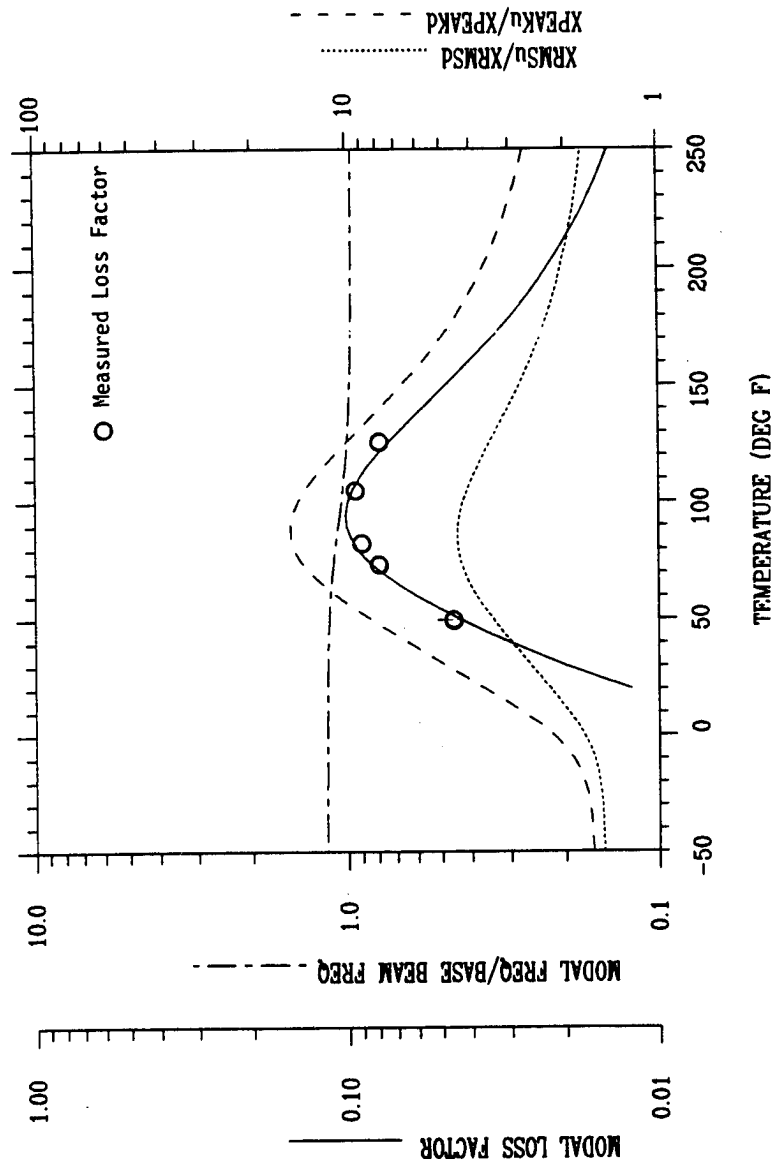


Figure 11- Comparison of Predicted and Measured Loss Factor for 1st Bending Mode with Conventional Constrained Layer

# FOUR-LAYER BEAM, MODE 1

(MODAL LOSS FACTOR)MAX= 0.41, AT T=125. Deg F

(XRMSu/XRMSd)MAX= 19.21, AT T=100. Deg F

(XPEAKu/XPEAKd)MAX= 149.29, AT T=105. Deg F

(MASSd/MASSu)= 1.26

(1) BASE BEAM H1=0.060 in, R01=0.98 lb/in<sup>3</sup>, E=0.119E+08 psi

L=5.00 in, Freq= 236. Hz

(2) SPACER H2=0.080 in, R02=0.05 lb/in<sup>3</sup>, G=0.200E+06 psi

(3) VEM H3=0.005 in, R03=0.35 lb/in<sup>3</sup>, 3M-468

(4) CONST. LAYER H4=0.010 in, R04=0.98 lb/in<sup>3</sup>, E=0.960E+07 psi

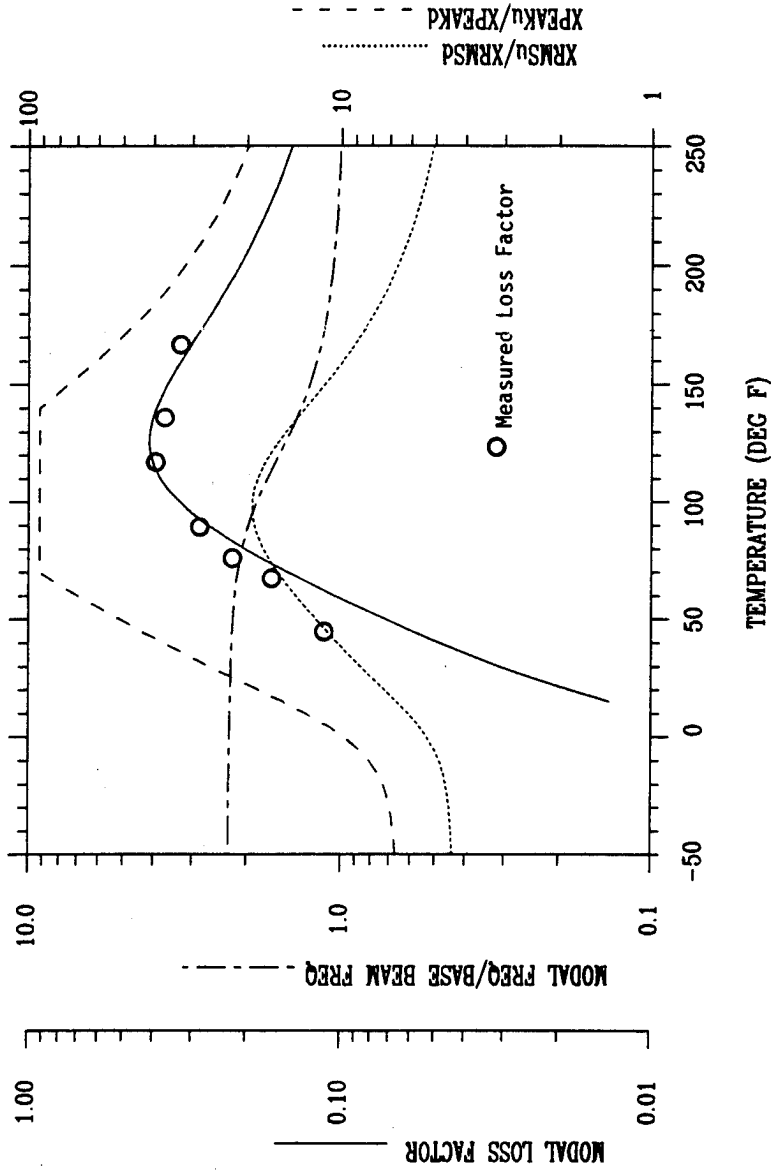


Figure '12 - Comparison of Predicted and Measured Loss Factor for 1st Bending Mode of Test Panel with SOD System



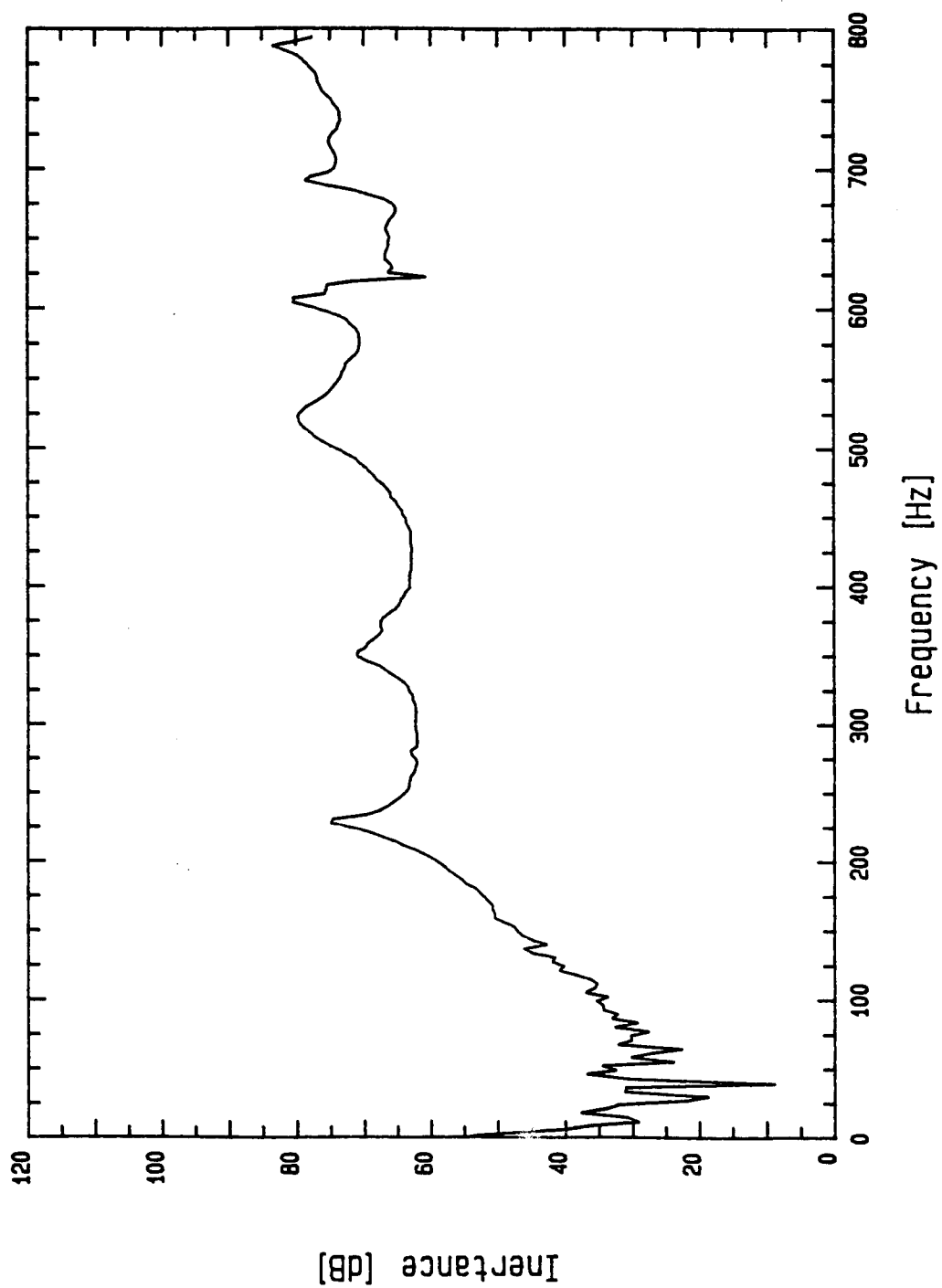


Figure 13- Driving Point Frequency Response for Test Article With Conventional  
Constrained Layer Treatment at 74 Degrees F.

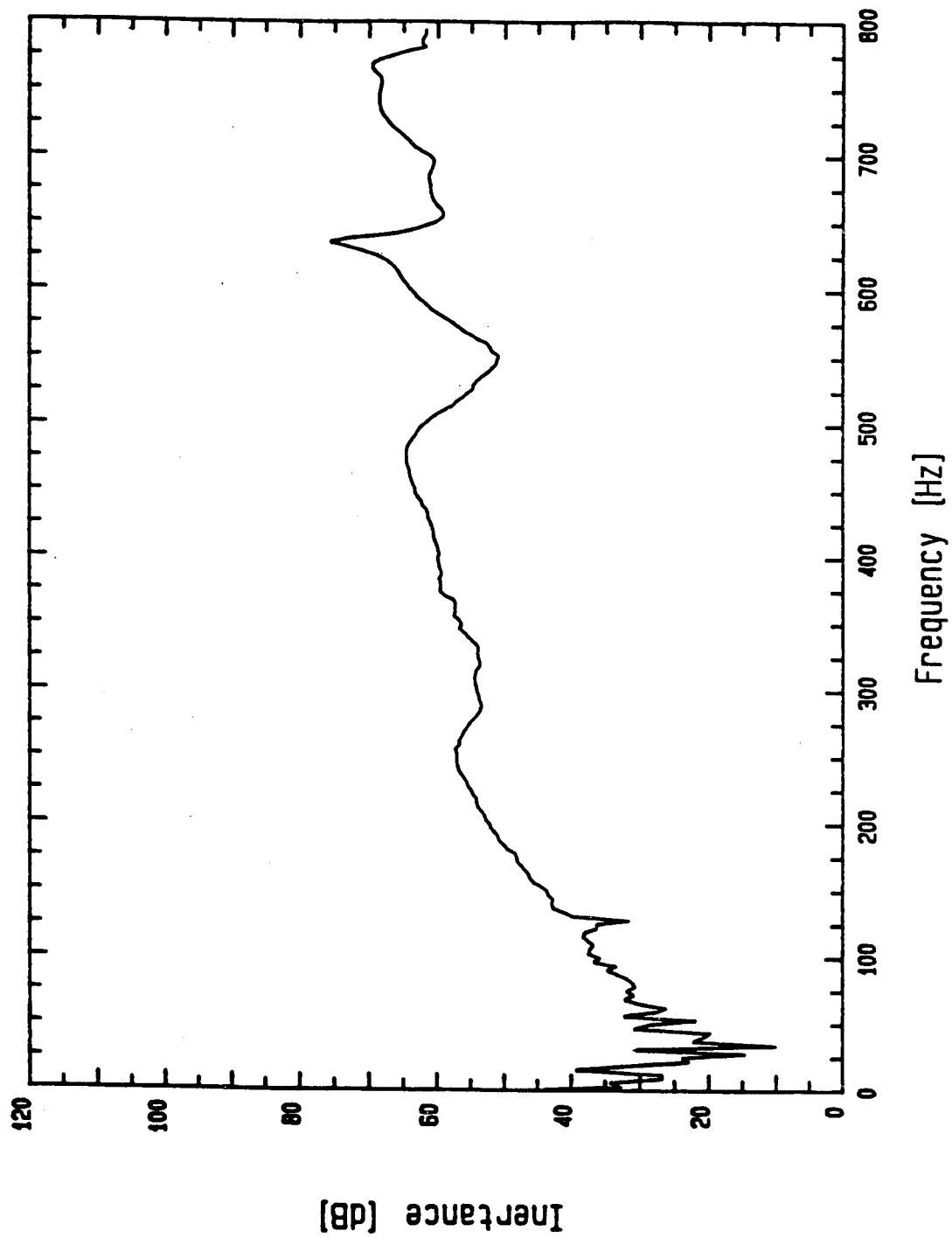


Figure 14 - Frequency Response For Test Panel With Stand-Off Damping System at 74 Degrees F.

## ENHANCED DAMPING FOR THE SIKORSKY ACAP COMPOSITE AIRFRAME

Eric W. Jacobs  
and  
Charles A. Yoerkie Jr.

United Technologies Corporation  
Sikorsky Aircraft Division  
6900 Main Street  
Stratford, CT 06601  
(203) 386-6015

and

James A. Moore  
  
Cambridge Collaborative, Inc.  
689 Concord Avenue  
Cambridge, MA 02138  
(617) 876-5777

### ABSTRACT

As part of a noise evaluation of the Sikorsky Advanced Composite Airframe Program (ACAP) helicopter, enhanced composite damping to reduce interior noise has been investigated. The present paper summarizes the effort to identify, test, and predict the potential noise reduction benefits of unconstrained woven Kevlar and off-axis unidirectional Kevlar damping laminates selectively applied to lightly damped graphite epoxy frame components to attenuate structureborne noise. Test data provided preliminary indications that woven and unidirectional damping laminates could potentially increase airframe damping levels, and Statistical Energy Analysis model predictions indicated that increased airframe damping could potentially reduce ACAP interior noise by up to 4 dB.

### INTRODUCTION

Recent development efforts in helicopter technology have increasingly incorporated composite airframe construction to reduce weight and cost. One example is the Advanced Composite Airframe Program (ACAP), a joint program of the Army Aviation Applied Technology Directorate (AATD) and Sikorsky Aircraft to design, fabricate, and evaluate a predominately composite airframe. Figure 1 shows a photograph of the Sikorsky ACAP helicopter and a breakdown of the composite materials used in the external/skin components of the ACAP is shown in Figure 2.

The suppression of interior acoustic noise is always a challenge in rotorcraft and the Sikorsky ACAP helicopter is no exception. Weight limitations and requirements for large gearing reductions and rigid drivetrain to airframe attachments can exacerbate interior noise to discomforting or fatiguing levels and necessitate interior acoustic treatments with substantial cost and weight penalties. The use of composites may further increase cabin and cockpit noise levels as the bonded joints desirable for composite fabrication eliminate major loss mechanisms for structureborne noise (e.g. fretting and air pumping effects) inherent to a riveted metallic structure. As shown in Figure 3, the subassembly damping loss factors measured on the ACAP flight

flight test article during fabrication were approximately 50% lower than those measured on the Sikorsky S-76A, a comparable metallic airframe construction.

To improve the understanding of composite airframe noise characteristics, Sikorsky Aircraft investigated the ACAP helicopter [1,2] under Phase III: Internal Acoustic Noise Evaluation of the ACAP Militarization Test & Evaluation (MT & E) program, sponsored by the AATD under contract DAAJ02-85-C-0036. The major objectives of the noise evaluation effort were to: (1) develop a Statistical Energy Analysis (SEA) model of the Sikorsky ACAP airframe; (2) refine and validate the ACAP SEA model with ground and flight test data; (3) test and evaluate, using ACAP subcomponents, two noise reduction options applicable to the ACAP composite airframe; and (4) use the ACAP SEA model to predict the potential noise reduction benefits of the tested noise reduction options. The current paper summarizes the effort to identify, test, and predict the benefits of two noise reduction design options for the ACAP composite airframe.

Because composite airframe design has and will continue to trend from mechanical to bonded joints, the investigation of potential noise reduction design options was concentrated on improving structural damping through increased composite material damping. Larger damping levels would dissipate vibratory energy before it could be acoustically radiated into the cabin and cockpit. The current study evaluated unconstrained composite damping laminates suitable for bonding to the lower end caps of the longitudinal frames (beams) and cross frames in the cabin and cockpit ceiling structure. These beams and frames, fabricated of relatively lightly damped graphite-epoxy composites, were identified through modelling and testing as the primary structureborne noise transmission paths of the ACAP airframe. Although only a secondarily bonded configuration was investigated, integral hybrid designs would be potentially feasible and advantageous.

## SEA MODELLING OF THE ACAP AIRFRAME

To permit analyses of the potential benefits of the noise reduction design options investigated for the ACAP, the first two tasks of the ACAP noise evaluation program included the development, refinement, and validation of a Statistical Energy Analysis (SEA) model of the Sikorsky ACAP composite airframe in conjunction with Cambridge Collaborative, Inc. The subsectioning of the ACAP ceiling structure for the SEA model is shown in Figure 4. The frame subsections were designated as, for example, Longitudinal Frame 7 Aft Left or LF7AL and Cross Frame 5 Middle or CF5M, and the outer skin panels were designated as, for example, Overhead Panel 57 Right or OP57R. The basic theory of SEA is given in Reference [3] and details of the SEA modelling effort can be found in References [1] and [2]. Comparisons of the ACAP SEA model estimates with ACAP flight test data for cabin and cockpit noise levels are shown in Figures 5 and 6, respectively. These comparisons show good agreement for a damping loss factor of 0.01 to 0.02 and indicate, in conjunction with similar comparisons of airframe vibration transfer functions, that the ACAP SEA model is sufficiently representative of the ACAP to permit evaluations of airframe design changes on interior noise levels.

## ACAP INTERIOR NOISE REDUCTION

The most weight effective method to helicopter interior noise control is generally source noise control to reduce vibration excitation at the primary source, i.e. the main transmission gear meshes. However, unless incorporated during the design process, gearbox noise control often requires a costly redesign of the main transmission and thus is often an impractical solution for reducing helicopter interior noise.

Noise control in current military and commercial helicopters is primarily achieved by add-on treatments such as sound absorbing backing on the interior trim panels. The trim panels then block acoustic radiation from vibrating skin panels and frame surfaces from reaching the cabin.

In addition, sound absorbing materials are often used in the cavities between the trim and skin panels to prevent excessive noise buildup from lessening the effectiveness of the trim panels. For some noise control treatments, add-on damping treatments are also applied to the frame surfaces and, in particular, the panel skins. However, all of these conventional noise treatment designs have significant weight trade-offs which inherently limit the achievable noise reduction.

Another potentially effective method of noise control in lightweight helicopter airframes focuses on the design of the airframe structure to reduce vibratory energy transmission from the main gearbox into the frames and skin panels which subsequently radiate into the cabin and cockpit. Two methods for attenuating main gearbox noise within the airframe structure were investigated for the ACAP composite airframe. One is briefly presented for comparison and involved the beneficial effects of a structural modification which introduced an impedance mismatch at the controls enclosure or "broom closet" frame junctions in the aft cockpit ceiling structure. The primary approach, and the major concentration of the ACAP noise reduction investigation, considered increased structural damping through the application of composite materials with higher damping characteristics.

#### Airframe Impedance Mismatching

Comparisons of the measured ACAP vibration transfer functions along the longitudinal transmission support beams with initial SEA model predictions revealed a significant discrepancy forward of the controls enclosure or "broom closet". The initial model predictions indicated little vibration reduction throughout the transmission support beam while the measured data showed a large reduction forward of the broom closet as can be seen for frame subsection LF7W in Figure 7. As the transmission support beam is a one-piece, single lay-up construction, the measured reduction in vibration levels was unexpected. However, the reduced vibration levels were attributable to plate stiffeners originally added to the aft broom closet frame junctions to prevent fatigue cracking. The plate stiffeners, indicated by the arrows in Figure 8, effectively created a high vibration impedance which acted to reflect the vibratory energy being transmitted along the transmission support beams. This effect is partially responsible for the build-up in vibration levels between frame subsections LF45 and LF7A evident in Figure 7. In addition, the bolt-on design of the plate stiffeners may have also provided fretting and air pumping damping benefits similar to riveted joints. The coupling loss factors in the ACAP SEA model were subsequently modified to reflect the effects of the plate stiffeners and are incorporated in the SEA predictions shown in Figure 7.

#### Increased ACAP Airframe Damping

As a result of the SEA modelling effort, several of the overhead longitudinal beams and cross/side frames were identified as the primary transmission paths for the main gearbox noise reaching the cabin and cockpit [1]. Much of the overhead ACAP airframe structure can be seen in the photographs of the forward and aft cabin ceiling structures shown in Figures 9 and 10. These airframe components are fabricated of lightly damped [4,5], unidirectional, continuous fiber graphite-epoxies, and thus were identified as the primary candidates for increased damping. Although conventional constrained layer damping treatments could be employed to increase structural damping in the ACAP airframe, the current investigation was directed at incorporating composite materials with inherently higher damping to achieve a potentially more weight effective noise control option. Only secondarily bonded composite damping options were evaluated, but integral designs would be potentially feasible and could further enhance the weight effectiveness.

Three higher damping composite materials were considered for the investigation of increased airframe damping. The candidate materials were aligned short fiber, woven Kevlar, and unidirectional Kevlar composites. Unidirectional fiber composites under off-axis loading and

woven Kevlar composites have been shown to have significantly higher damping characteristics than axially loaded, graphite reinforced composites [4,5]. Although aligned short fiber composites have demonstrated a significant potential for high damping characteristics [4,6,7,8] with acceptable strength characteristics for integral design configurations, adequate supplies of aligned short fiber composite materials were not available for the current test effort. Hence, only woven and off-axis, unidirectional Kevlar 49 composites applicable to the overhead beams and frames of the ACAP airframe were investigated.

## ACAP TRANSMISSION SUPPORT BEAM DAMPING TESTS

One objective of the ACAP MT&E evaluation of increased airframe damping was to perform testing of the higher damping composites on a test beam fully representative of the ACAP airframe. The intent was to provide damping information directly applicable to the ACAP airframe. In addition, utilizing an ACAP airframe subcomponent permitted the use of existing production tooling for test specimen fabrication. However, the deep cross-section and asymmetric design characteristics of ACAP frame components presented difficulties in choosing a test beam suitable for increased airframe damping tests. The ACAP airframe subcomponent providing the highest aspect ratio while minimizing asymmetries in all three axes was found to be the 1.37 m (54 in) cabin section of the left or port transmission support beam. The cabin section of the left transmission support beam consists of subsections LF7AL and LF5FL shown in Figures 9 and 10, respectively. The transmission support beam section was chosen to maximize the test beam aspect ratio while minimizing longitudinal asymmetry. Schematics of the ACAP test beam top and cross-sectional views are shown in Figure 11. Details of the woven Kevlar and unidirectional Kevlar damping laminates are shown in Figure 12. The damping laminates were sequentially bonded to the test beam in 0.1 in thick increments to permit evaluation of treatment thickness on beam damping levels. The orientation of the unidirectional and woven Kevlar plies in the damping laminates was based on results provided in References 4 and 5, respectively.

### Test Specimen Fabrication

To meet schedule and cost constraints, a single ACAP transmission support beam section was fabricated for sequential testing of the baseline and damped configurations. The 0.1 in thick woven Kevlar and off-axis unidirectional Kevlar damping laminates were fabricated in sheets sufficiently large to permit the cutting of three laminates each with the required dimensions for bonding to the lower end cap of the test beam. Fiberite HY-E17714AA Kevlar 49 tape was used to fabricate the unidirectional Kevlar damping laminates while the woven Kevlar damping laminates were fabricated of American Cyanamid 5143-285 Kevlar fabric. Dexter Hysol EA9309.3NA was used to bond the damping laminates to the test beam section. After testing of the ACAP beam with the 0.1 and 0.3 in woven Kevlar damping laminates, the damping laminates were debonded to permit reuse of the test beam with the off-axis unidirectional damping laminates. To debond the woven Kevlar laminates, the damping treatment bond was heated to 200-225<sup>o</sup> F, a thin scraper was used to peel the two adherents apart, and the lower end cap surface was cleaned for rebonding. The majority of the peeling action was applied to the adhesive and damping laminates to minimize effects on the test beam section.

### Test Equipment, Procedures, and Conditions

A schematic of the ACAP transmission support beam damping test setup is shown in Figure 13. The equipment necessary to acquire and reduce the damping test data included:

1. Bruel & Kjaer (B&K) 4375 accelerometers with B&K 2635 charge amplifiers.
2. a Wilcoxon F4/Z820W electromagnetic shaker and associated signal conditioning equipment.

### 3. a Hewlett Packard 3562 two-channel FFT analyzer.

The B&K 4375 accelerometers supplied the necessary frequency response characteristics with sufficiently low inertia to minimize effects on the damping measurements. The electromagnetic shaker provided white noise excitation and a source force/acceleration measurement internal to the impedance head.

Photographs giving side and end views of the test setup are shown in Figures 14 and 15. The test beam was supported in a free-free configuration. The freely supported electromagnetic shaker was stinger mounted to the upper end cap at locations sufficiently removed from nodes of the first few transverse bending modes of the test beam. The response accelerometer was mounted in several locations during testing to avoid modal nodes and permit characterization of the modal shapes and damping. Note that the C-channel design of the ACAP transmission support beam necessitated shaker mounting on the upper end cap offset from the web plane. To limit torsional contamination of the measured vibration transfer data, the offset from the web plane was minimized.

To acquire the frequency response data, a random vibratory signal was input by the electromagnetic shaker to the test beam. The white noise input signal was shaped and amplified to produce an acceleration spectrum approximately uniform in level within the required frequency range of 350 Hz to 5700 Hz. The input force and response acceleration signals were conditioned and input into the two-channel FFT analyzer. The ensuing frequency response functions (response acceleration/input force) were stored on disc for later analysis.

After testing in the baseline configuration, the ACAP transmission support beam was tested with 0.1 in and 0.3 in thick woven Kevlar damping laminates and 0.1 in, 0.2 in, and 0.3 in thick off-axis unidirectional Kevlar laminates. A complete modal survey of both the upper and lower end caps for one shaker attachment location was conducted for each test configuration.

#### Data Analysis Procedures

The measured frequency response functions for each test configuration were analyzed with Structural Measurement Systems, Inc. Modal 6.0 modal analysis software. Modal 6.0 provides global curve fitting to determine frequency and damping estimates.

#### ACAP TRANSMISSION SUPPORT BEAM DAMPING TEST RESULTS

Summaries of the transmission support beam damping test results for the second and third out-of-plane or transverse bending modes are shown in Figures 16 and 17, respectively. These results indicate that application of the damping laminates did effect up to an 80% damping increase for the test beam. However, the test results are inconsistent from the second to third mode, and thus do not provide adequate characterization of the increased beam damping levels for design evaluations.

The inconsistencies and limitations of the beam damping data were largely due to problems inherent to the test specimen. In particular, the data acquisition and analysis was severely complicated by the low aspect ratio, C-channel design of the test beam. The usable test section of 1.37 m (54 in) limited the beam aspect ratio to 6.75 and the C-channel design was asymmetric in all three principal axes. Hence, the test beam insufficiently approximated a slender beam with the transverse bending modal frequencies being much lower than pretest predictions, and the asymmetric design did not provide pure bending modes for analysis, i.e. the exhibited bending modes were contaminated by both torsional and local flange bending effects. The latter problem effectively prohibited analyses of the fourth and higher bending modes, while the location of the first bending mode at 350 - 375 Hz resulted in insufficient frequency resolution to generate reliable damping estimates.

## SEA EVALUATION OF INCREASED AIRFRAME DAMPING

The ACAP SEA model was used to analyze the potential benefits of frame (beam) damping for reducing ACAP internal noise levels. As noted previously, the overhead longitudinal beams and cross frames constitute the primary transmission paths for the gearbox vibrations in the ACAP airframe. In addition, these airframe components are fabricated of unidirectional graphite-epoxies which previous studies have identified as relatively lightly damped [4].

Based on the results of the SEA modelling of the ACAP and previously published composite material damping values [4,5], the baseline ACAP SEA model for the increased airframe damping analysis employed damping loss factors of 0.01 for the graphite-epoxy beams and frames and 0.02 for the Kevlar outer skin panels in the overhead cabin/cockpit airframe structure. The damping loss factors for the frames given in Table 1 were then increased to 0.02 and 0.03 to simulate the effects of increased airframe damping on ACAP interior noise levels. Although ACAP test results do not yet support the increase to 0.02, the previously published results for woven and unidirectional Kevlar composites [4,5] indicate that damping loss factors of 0.02 to 0.03 are potentially achievable. Also note that the subsection selection for the increased damping evaluation is only a first cut and does not represent an acoustic benefit versus weight penalty optimization.

### Longitudinal Frames (Beams)

LF45L  
LF45R  
LF5FL  
LF5FR  
LF7AL  
LF7AR  
OLF45L  
OLF45R  
OLF57L  
OLF57R

### Cross and Side Frames

CF4L  
CF4M  
CF4R  
CF5L  
CF5M  
CF5R  
CF7L  
CF7M  
CF7R  
CF45L  
CF45R  
SF4L  
SF4R

Table 1. ACAP Subsections Selected for Application of Increased Damping

The results of the SEA evaluation of increased airframe damping on ACAP interior noise levels are summarized in Figure 18 and indicate that 1 to 4 dB noise reductions may be achievable. The frequency dependency of the noise reductions shown in Figure 18 reflect the increasing importance with frequency of the damping loss factors relative to the coupling loss factors employed in the ACAP model [1,2]. Although the estimated noise reductions are relatively small, the SEA results indicate that the addition of woven or unidirectional Kevlar damping laminates to the ACAP frame components may represent a partial but weight effective noise control option.

## CONCLUSIONS AND RECOMMENDATIONS

The execution of the ACAP transmission support beam damping test was determined by contractual, schedule, and budgetary constraints. Because of the difficulties encountered in the acquisition and analysis of the beam damping data, the results do not represent a definitive characterization



of the damping potential of woven and unidirectional Kevlar in the tested applications. To achieve more reliable results, testing with a high aspect ratio, symmetrical beam design would be required. In addition, more extensive testing of the effects of laminate orientation, thickness, and composition (i.e. fabric type, epoxy/resin type, etc.) would be needed to provide quantitative guidelines for using the woven or unidirectional Kevlar laminates to increase airframe damping and decrease interior noise levels in composite rotorcraft. However, the damping data did give preliminary indications that increased damping would be feasible for the ACAP or comparable composite helicopter airframes.

The SEA model of the ACAP indicated that interior noise reductions of 1 to 4 dB are achievable with full realization of the woven and unidirectional damping characteristics demonstrated in previously published results. Although these noise reductions would only be barely significant acoustically, the application of woven or unidirectional Kevlar damping laminates to the lightly damped graphite epoxy airframe components could represent a weight effective noise control option relative to interior trim panel acoustic treatments and warrants further investigation to better characterize potential damping benefits.

#### ACKNOWLEDGMENT

The authors would like to express their appreciation in general for the financial and technical support provided by the Army AATD for the ACAP MT&E Noise Evaluation Program and in particular for the input and guidance provided by Ned Chase at AATD - Ft. Eustis. The authors also have appreciated the support provided by Ken Furnes and George Tatten at Sikorsky Aircraft, Jerome Manning, Alan Aubert, and Robert Powell at Cambridge Collaborative, and Bill Mayes at NASA-LaRC.

#### REFERENCES

1. Jacobs, E.W., Yoerkie, C.A., Gintoli, P.J., Manning, J.E., and Moore, J.A., "ACAP MT & E Program: Volume 3 - Internal Acoustic Noise Evaluation," Army Applied Aviation Technology Directorate Contractor Report, to be published.
2. Jacobs, E.W., Yoerkie, C.A., Gintoli, P.J., and Manning, J.E., "Statistical Energy Analysis of the Sikorsky ACAP Helicopter," to be presented at the 1989 ASME Winter Annual Meeting, San Francisco, CA, 10-15 December 1989.
3. Lyon, R.H., Statistical Energy Analysis of Dynamical Systems: Theory and Applications, The MIT Press, Cambridge, MA, 1975.
4. Suarez, S.A., Gibson, R.F., Sun, C.T., and Chaturvedi, S.K., "The Influence of Fiber Length and Fiber Orientation on Damping and Stiffness of Polymer Composites," Experimental Mechanics, June 1986, pp. 175-184.
5. "Vibration Damping of Kevlar Aramid, Graphite, and Fiberglass Fibers and of Composites Reinforced with These Fibers," DuPont Preliminary Information Memo No. 428, November 1981.
6. McLean, D. and Read, B.E., "Storage and Loss Moduli in Discontinuous Composites," Journal of Materials Science, Vol. 10, 1975, pp. 481-492.
7. Sun, C.T., Chaturvedi, S.K., and Gibson, R.F., "Internal Damping of Short-Fiber Reinforced Polymer Matrix Composites," Computers & Structures, Vol. 20, No. 1-3, 1985, pp. 391-400.
8. White, R.G. and Abdin, E.M.Y., "Dynamic Properties of Aligned Short Carbon Fibre-Reinforced Plastics in Flexure and Torsion," Composites, Vol. 16, No. 4, October 1985, pp. 293-306.



Figure 1. Photograph of the Sikorsky ACAP Helicopter

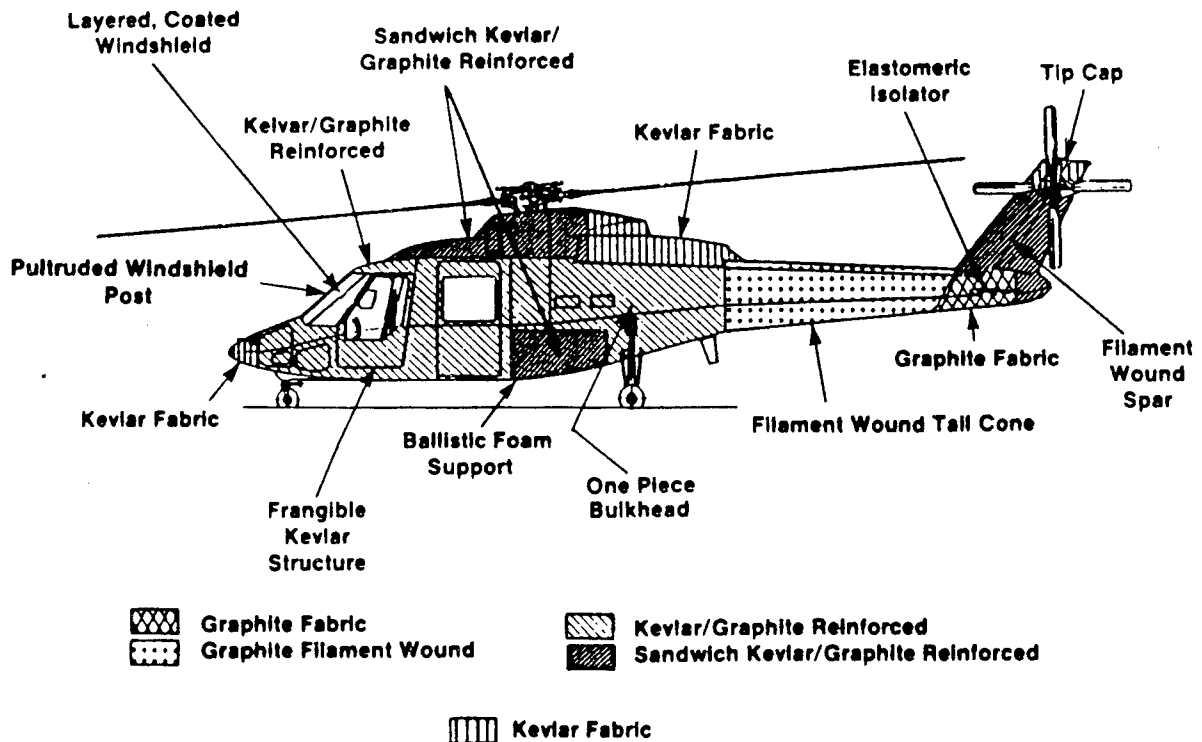


Figure 2. ACAP Airframe Materials



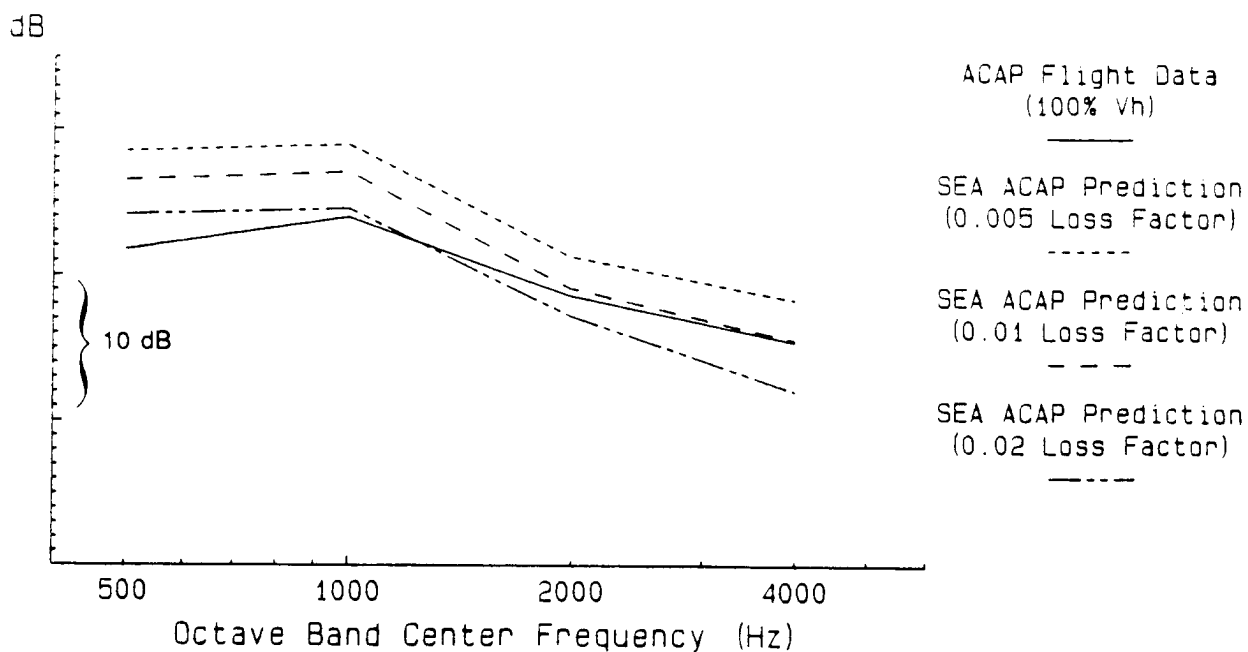


Figure 5. Measured Acoustic Levels vs. SEA Model Estimates - ACAP Cabin

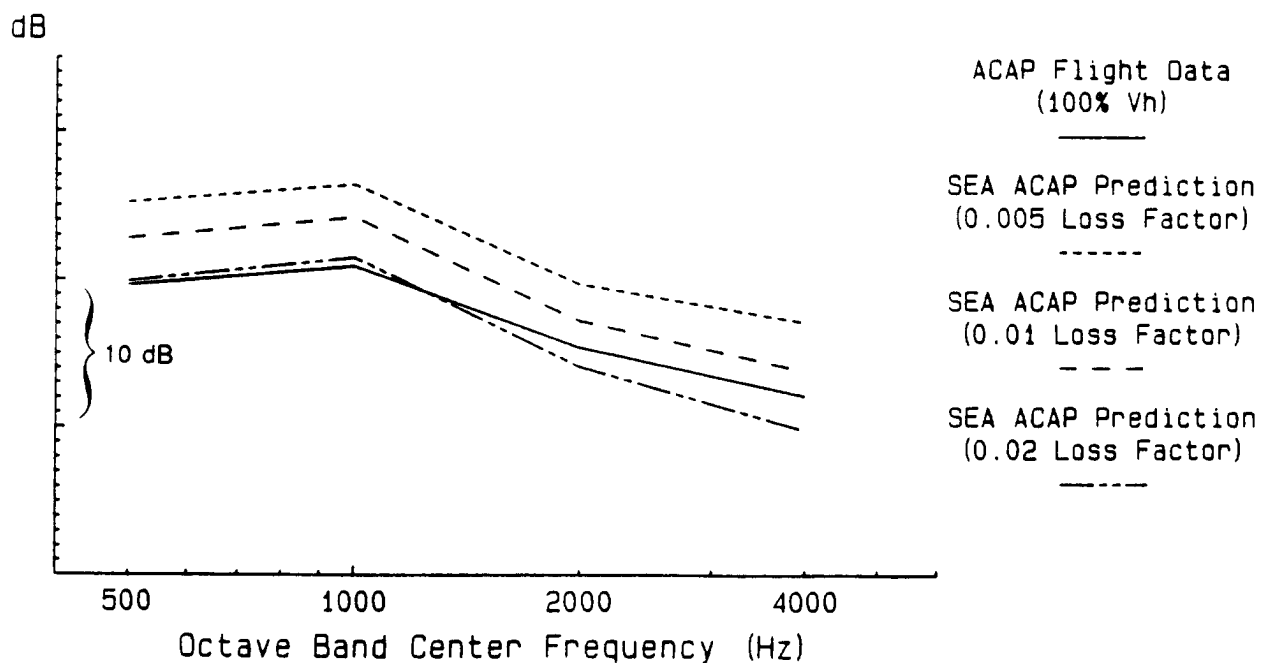


Figure 6. Measured Acoustic Levels vs. Sea Model Estimates - ACAP Cockpit

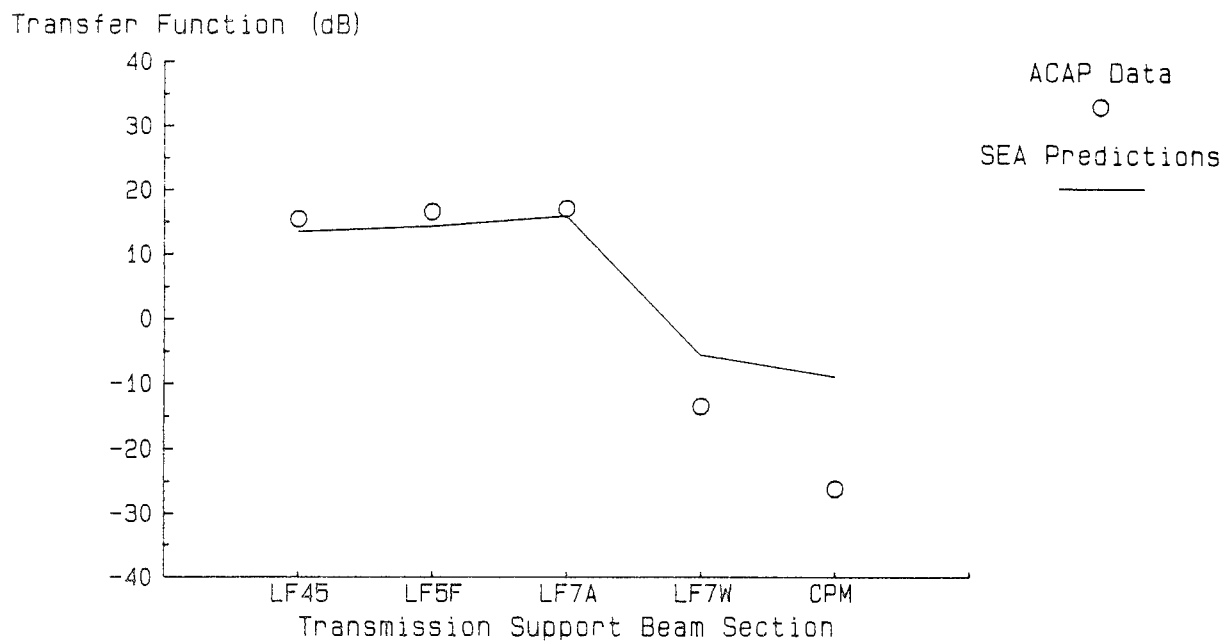


Figure 7. Measured and Predicted Vibration Transfer Functions - ACAP Transmission Support Beam (1000 Hz Octave Band)

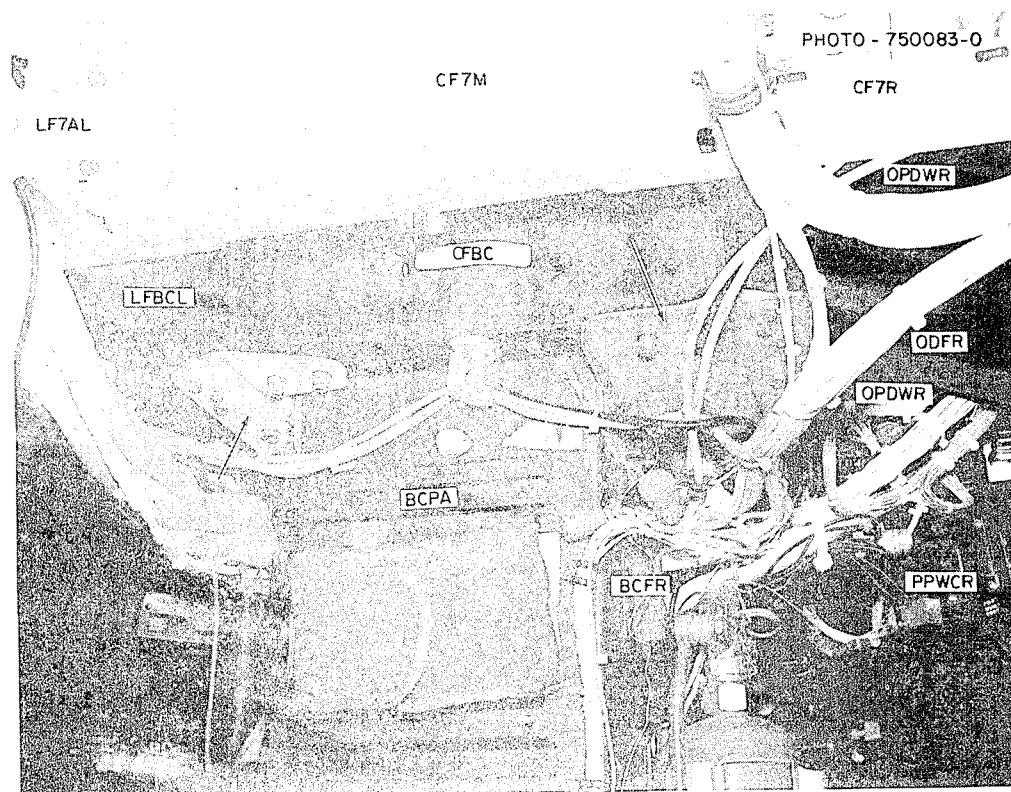


Figure 8. Photograph of ACAP Broom Closet Structure with Plate Stiffeners

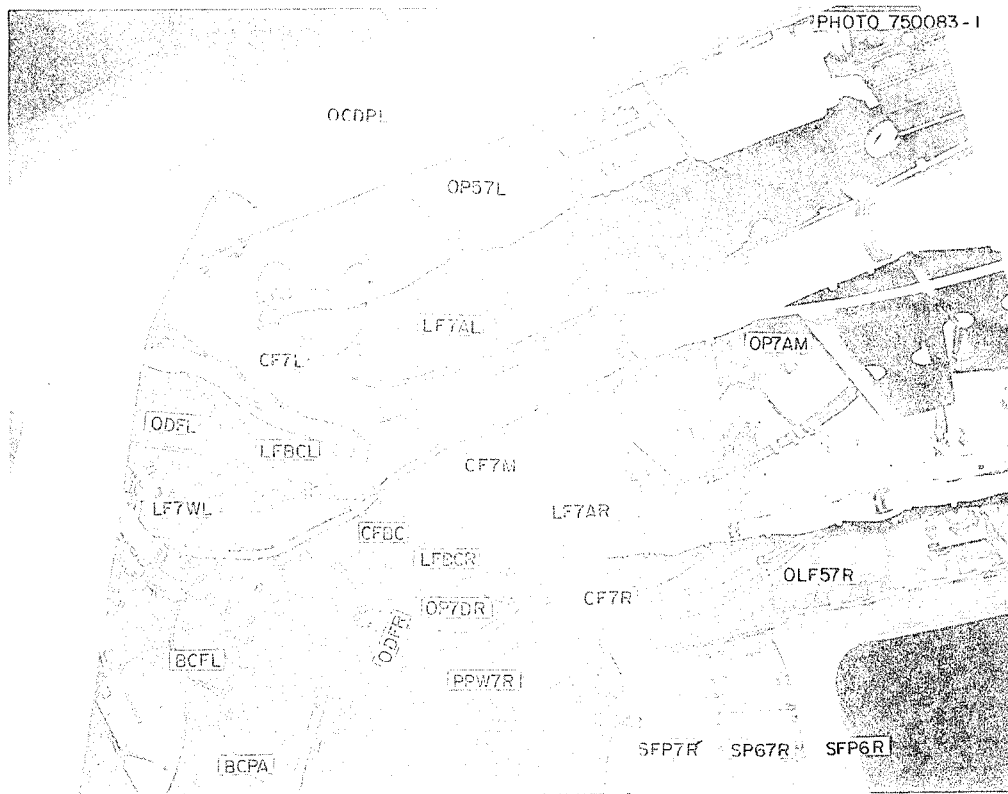


Figure 9. Photograph of ACAP Ceiling Structure - Forward Cabin



Figure 10. Photograph of ACAP Ceiling Structure - Aft Cabin



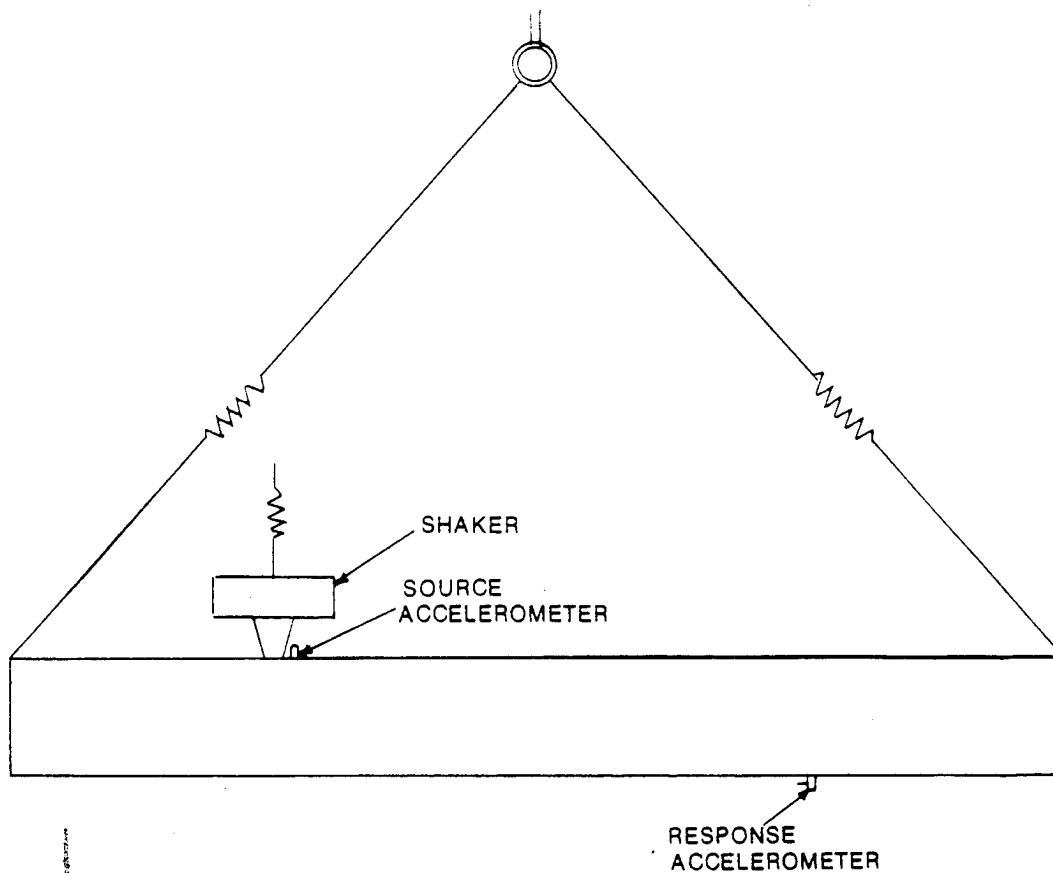


Figure 13. Schematic of Free-Free Test Configuration for the ACAP Beam Damping Test

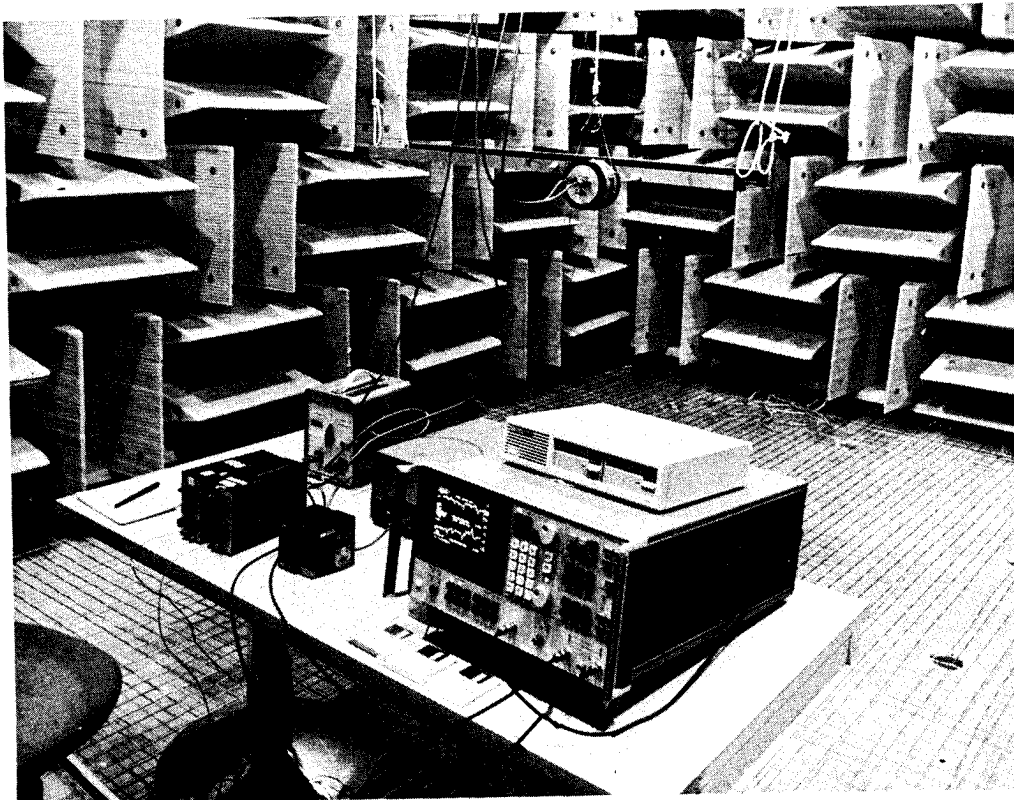


Figure 14. Photograph Showing Side View of the ACAP Beam Damping Test Setup



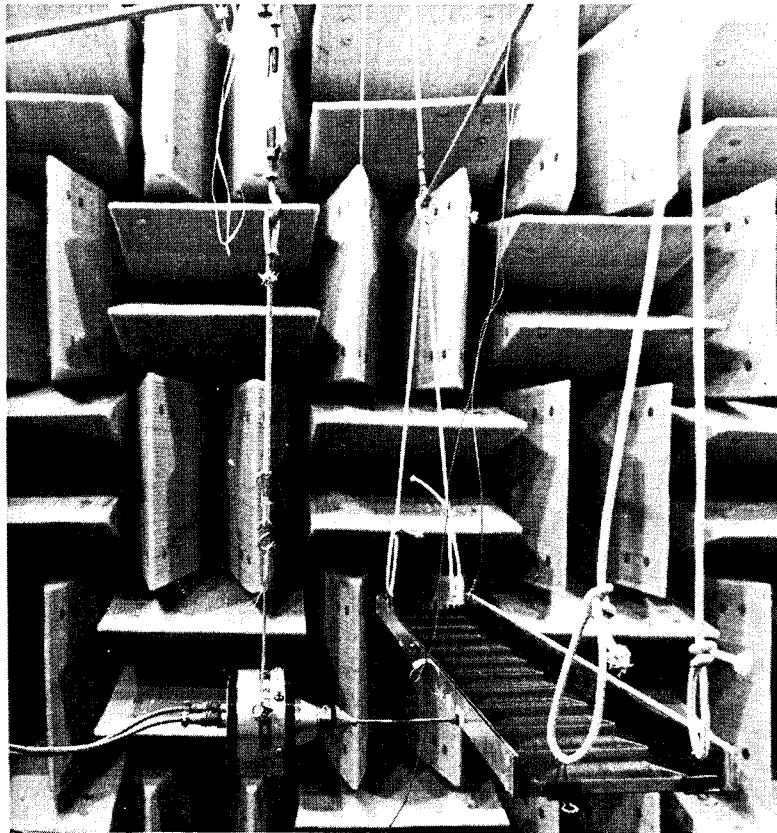


Figure 15. Photograph Showing End View of the ACAP Beam Damping Test Setup

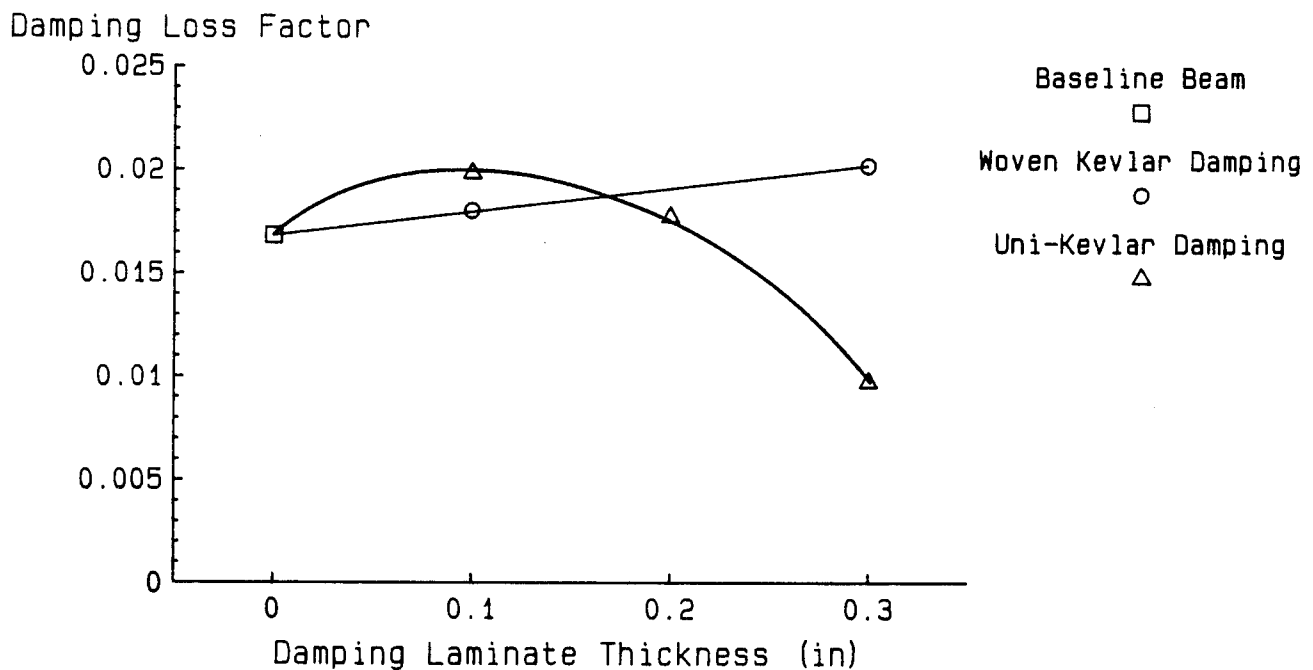


Figure 16. ACAP Transmission Support Beam Damping - 2nd Bending Mode (580 - 600 Hz)

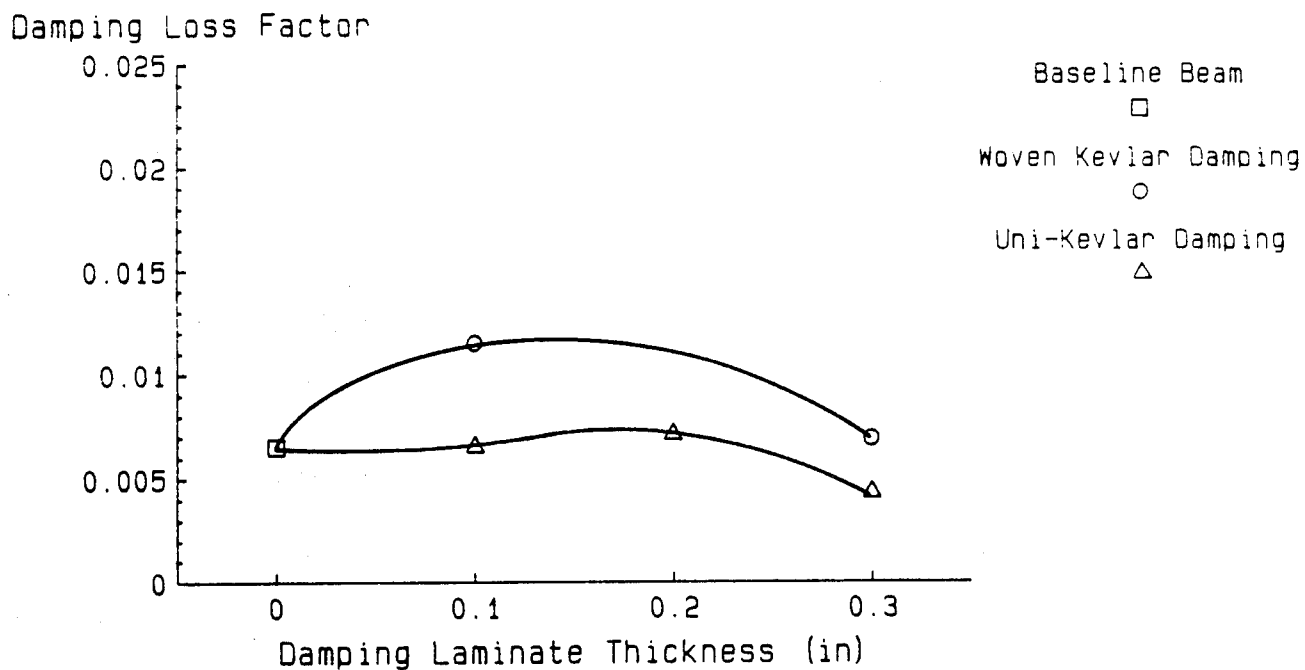


Figure 17. ACAP Transmission Support Beam Damping - 3rd Bending Mode (750 - 790 Hz)

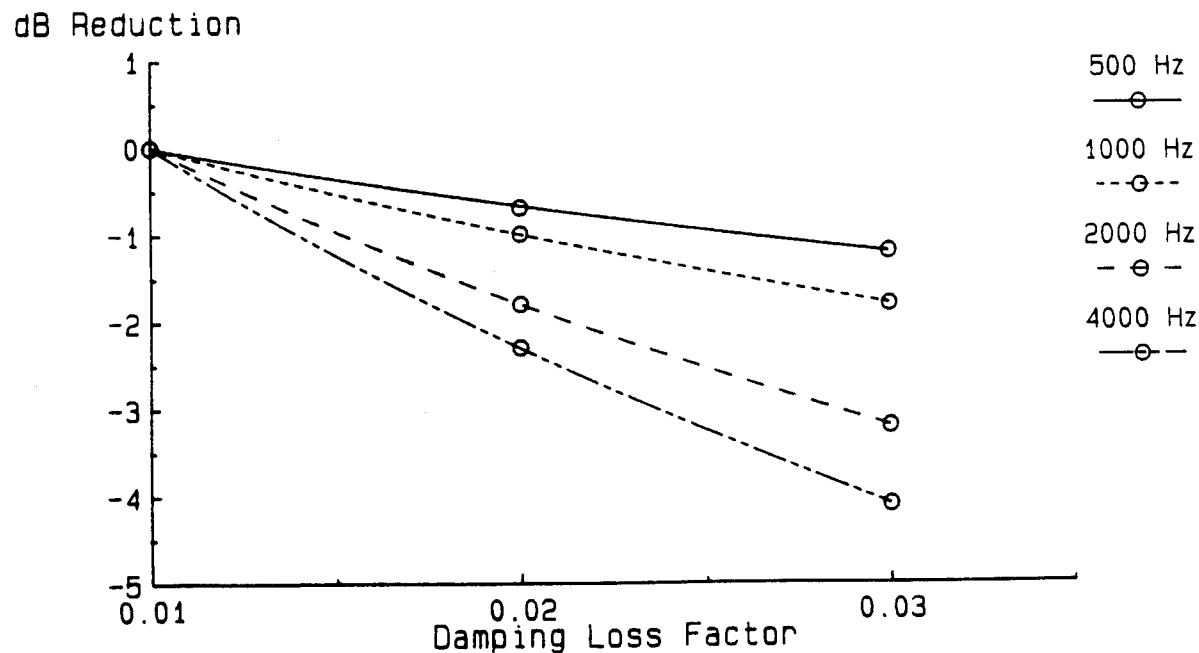


Figure 18. Estimated Effects of Increased Airframe Damping on ACAP Cabin and Cockpit Acoustic Levels

# **DAMPING MATERIALS FOR CONTROL OF PROPELLER INDUCED STRUCTURE-BORNE NOISE**

**James F. Unruh**

**Southwest Research Institute  
6220 Culebra Road  
San Antonio, Texas 78284  
(512) 522-2344**

## **ABSTRACT**

Full scale aircraft and laboratory test evaluation has shown that structure-borne interior noise transmission in propeller driven aircraft can be equal to or greater than propeller direct airborne noise transmission. Evaluations of structure-borne noise control measures were carried out in a laboratory test environment which included several promising applications of elastomeric damping materials. Increased engine/propeller vibration isolation, reduced propeller wake excited wing vibrations via tuned mechanical dampers, and selected wing panel damping treatments are discussed.

## INTRODUCTION

Interior noise levels in propeller-driven aircraft are characteristically higher than those considered marginally acceptable in other forms of transportation [1]. Reduction of the interior noise levels is highly desirable for improved safety through improved intra-cabin and air-to-ground communications, reduced pilot fatigue, and for improved comfort of crew and passengers [2,3]. The interior noise spectra of propeller-driven aircraft are generally dominated by low frequency tones, at either multiples of the engine firing frequency, multiples of the propeller fundamental, or both. The noise path may be direct airborne, structure-borne, or combination thereof.

A major focus of interior noise control for twin-engine propeller aircraft has been the reduction of the propeller direct airborne component via improved sidewall treatments [4,5]. A majority of the research effort in this area has been aimed at the advance high-speed turboprop aircraft wherein the direct airborne propeller generated noise is quite intense and appears to be most critical for the success of this new generation aircraft [6]. With continued efforts to develop lightweight sidewall treatments coupled with efforts to develop improved high-speed, low-noise propeller designs, the direct airborne sidewall transmission problem may well be resolved in the near future.

However, the potential for other sources and transmission paths governing the interior noise levels is quite high based on recent discoveries and historical data. Historically speaking, interior noise levels of propeller-driven aircraft are much higher than the acceptable levels of present-day turbofan aircraft, even after apparently ample application of noise control measures. It was believed that the structure-borne path for noise/vibration transmission provided a high level of interior noise transmission through paths unaffected by airborne sidewall noise transmission treatments. It was also felt the conventional vibration control measures, such as an appropriate application of damping material, could then be used to reduce this structure-borne noise path. An initial program of structure-borne noise transmission research in single-engine general aviation aircraft was undertaken in 1977 funded by NASA Langley Research Center [7-9] and a second program was initiated in 1985 which evaluated structure-borne noise transmission in wing mounted propeller driven aircraft [10-12]. This paper summarizes the various applications of damping materials employed as structure-borne control measures during these programs.

## ENGINE VIBRATION ISOLATORS

Engine/propeller induced structure-borne interior noise transmission has been shown to be equal to or greater than the direct airborne noise transmission levels in a single-engine aircraft, as shown in Figure 1. The single engine light aircraft test facility used to obtain the data in Figure 1 is shown in Figure 2. The stantion supports shown in Figure 2 supported the engine and cowling during engine detached data acquisition. Cabin noise and fuselage vibration levels were recorded during ground tests for engine-attached, engine-detached, interior-installed, and interior-removed configurations. By comparisons of the data, engine induced structure-borne noise was shown to be a primary source of cabin noise. Corresponding fuselage vibration levels were quite high with energy concentrated mainly in the lower frequencies. A measure of the noise control effectiveness of the interior trim, consisting of vinyl covered fiberglass, was also obtained.

Improved engine vibration isolation was proposed to be the most weight and cost efficient retrofit structure-borne noise control measure for the single engine general aviation aircraft. A study was carried out with the objectives: 1) to develop an engine isolator design specification for reduced interior noise transmission, 2) to select/design candidate isolators to meet a 15 dB noise reduction design goal, and 3) to carry out a proof of concept evaluation test. Since there was a measurable propeller airborne noise component it was felt the a laboratory based proof of concept evaluation test be carried out to eliminate the airborne component. To this end the laboratory set

up shown in Figure 3 was employed for the study. A dummy mass engine driven by a 1600 lb electrodynamic shaker provided the structure-borne noise source simulation of the engine/propeller vibrations. Force levels in the shaker were adjusted to produce equivalent interior noise levels to those measured during engine- detached engine-running tests.

A coupled analytical and empirical structure-borne noise transmission model was developed to select engine isolator dynamic properties. Description of the transmission model is given in Reference 8 and detailed design specification curves for the test aircraft are given in Reference 9. Accuracy of the analytical isolator design model is given in Figure 4 wherein predicted peak interior sound pressure level response versus 1/3 octave excitation frequency is given for a set of rigid isolators. When the rigid isolators were replaced with a set of soft (series 22002) isolators, see Figure 5, the prediction accuracy remained good out to 250 Hz. The increase in measured interior noise beyond 250 Hz is attributed to a noise floor of the laboratory setup due to direct shaker airborne noise radiation. Nevertheless, the decreased structure-borne noise (SBN) transmission using the soft rubber isolators is apparent. The correlation of design model predictions to measured A-weighted overall interior noise levels for various sets of isolators considered in the evaluation is shown in Figure 6. The original manufacture engine isolators (3006H) were for the most part rigid with an axial stiffness on the order of 30,000 lb/in at a 100 Hz while the soft rubber isolator (22002-1) showed a stiffness of approximately 300 lb/in at 100 Hz. A comparison of physical size of the isolators is given in Figure 7.

While accelerometer measurements of the vibration levels of the structure indicated multiple mode panel response no attempts were made at treating the panels with add on damping treatments. It was determined that a decrease of 10-15 dB in SBN transmission could be realized with proper design of the engine mounts and therefor further treatment would not be necessary until the propeller direct airborne component could be efficiently dealt with.

## WING VIBRATION REDUCTION

The potential for engine/propeller vibration as a manhor source of strcture-borne interior noise in wing mounted propeller aircraft has not been thoroughly investigated; nevertheless, adequate procedures for engine/propeller vibration isolation appear to be in hand. A potentially more important source of SBN transmission is provided by the interaction of the propeller wake and aircraft wing structure. The wing surface downstream of the propeller may experience significant aerodynamically-induced, fluctuating pressures due to the propeller wake, especially from the tip vortex [13]. Extensive ground tests of a Twin Otter Aircraft revealed that the propeller wake and tip vortex interaction with the wing surface was the major source of interior noise for the aircraft at 50 percent or greater engine torque [14]. The interior noise spectra were dominated by contributions at the propeller blade passage frequency and its harmonics.

Reference 10 describes a test apparatus built to study propeller wake/vortex-induced SBN transmission under controlled laboratory conditions. The principal approach to the test apparatus design was to provide a physical means of separating the airborne and structure-borne noise components so that the structure-borne noise transmission response could be studied directly without airborne noise contamination. The major components of the test apparatus, as shown in Figure 8, are the 28 inch diameter propeller source (maximum 5700 rpm) with 33 in diameter blower providing 70 ft/sec inlet flow, the 80 in span 31 in chord NACA 0012 wing providing the structural transmission path and the 40 in diameter 72 in long ring frame and stringer constructed fuselage with integral floor structure and interior trim providing the receiving acoustic volume. The 5-1/2 in thick, 54 in inside diameter, 7-ft. long concrete structure provides an acoustic shield for the fuselage from direct

airborne noise radiation from the propeller. A non-contacting acoustic seal at the wing penetration into the acoustic shield provides adequate airborne noise isolation for the fuselage structure as is shown by the test apparatus dynamic range data given in Table 1.

**TABLE 1. TEST APPARATUS DYNAMIC RANGE**

Configuration	Spatial average noise level, dB			
	3450 rpm	4260 rpm	4980 rpm	5700 rpm
1st Propeller tone				
Wing attached	54.3	62.9	82.1	91.7
Wing detached	41.9	55.8	65.6	63.5
$\Delta$ dB	12.4	7.1	16.5	28.2
2nd Propeller tone				
Wing attached	57.9	45.4	59.4	69.9
Wing detached	49.1	44.0	40.8	48.5
$\Delta$ dB	8.8	1.4	18.6	21.4

### **Blocking Mass/Fuel**

To study the potential benefits of using wing carried fuel as a blocking mass for structure-borne noise transmission from the propeller excitation the two most inboard wing cavities were fitted with a liquid retaining plastic bladder. A schematic of the test configuration with wing cell and panel nomenclature is given in Figure 9. Cell #1 in the wing leading edge area forward of the front spar and contained 7.4 lb of simulated fuel and Cell #2 occupied the volume between the front and rear spars with a 17.3 lb simulated fuel capacity. The wing overall empty weight is 29.55 lb. Baseline, no fuel, runs were made and sound pressure level responses were recorded at several interior microphone locations. When simulated fuel was added to Cell #1, negligible reduction in interior noise levels resulted. However, when simulated fuel was then added to Cell #2, a measurable noise reduction was achieved above 4800 rpm (160 Hz for the first propeller tone), as is shown in Figure 10a. Upon removal of the simulated fuel in Cell #1, leaving Cell #2 full, the noise reduction persisted as is shown in Figure 10b.

In an attempt to discover the mechanism responsible for the reduced levels of vibration transmission into the fuselage, solid masses with a total weight and center-of-gravity simulating the liquid in Cell #2 were attached to the wing front and rear spars in the Panel #2 area and the noise transmission data acquisition was then repeated. As can be seen by the data in Figure 11, the solid masses were quite effective in reducing SBN transmission.

### **Panel Damping Treatments**

A commercially available self-adhesive, low-weight, 0.16 lb/ft squared constrained layer damping material of thickness 0.016 inch was applied to wing Panel #2. The 0.040 inch thick aluminum wing skin exhibited an increase in structural loss factor from 0.018 to 0.080 upon application of a single layer of the damping material. The damping measurements were made using a single degree-of-freedom circle fit technique utilizing hammer impact frequency response function data in the frequency range from 155 to 169 Hz at a nominal test temperature of 70 degrees F. The fundamental panel frequency increased upon application of the damping material, reflecting a

constrained layer configuration. However, a negligible level of SBN transmission reduction resulted (see Figure 12) as compared to the blocking mass. Of course, the weight expenditure for the damping material is considerably less than that of the fuel in Cell #2.

Damping material was also systematically applied to various panels and panel combinations along the entire wing span on both upper and lower surfaces. The use of surface damping treatment was, for the most part, ineffective, except on the center panel areas of wing Panels #3 and #4, which are the panels directly in the wake of the propeller. The most effective use of panel damping occurred when it was used in conjunction with the blocking masses, as is seen in Figure 13. Here, we can see the damping treatment improve the SBN transmission losses of the system below 5100 rpm and somewhat degrade the reduction at the higher speeds. This should be expected since the wing center panel first mode frequency occurred around 169 Hz which corresponds to a propeller speed of 5070 rpm. One might view the propeller-induced wing vibrations as traveling waves being reflected by the blocking masses on the wing spar, then dissipated by the damping material as they are regenerated and re-reflected.

Treatment of the wing leading edge in an attempt to reduce the impact forces of the propeller wake was also evaluated using wing leading-edge damping/isolation material. Several types of damping material and/or foam products were used to shield the wing leading edge, up to 5 inches aft, along the span of the propeller. No measurable reduction in SBN transmission occurred at any of the monitored microphone locations. This was the first experimental indication that the propeller source was not highly confined to the wing leading edge which was confirmed with analytical predictions [15].

### **Tuned Mechanical Absorber**

In the frequency range from 133 Hz to 190 Hz, which contains the dominant first propeller harmonic, the design and implementation of low-damped, high-Q, tuned dampers were found to be quite difficult. Bench-proven damper design fell considerably short of expectation when mounted on the compliant wing spar and when excited by the propeller source. However, the use of an elastomerically damped tuned resonator appears to be a viable SBN transmission control measure. The Highly damped design with increased system half-power bandwidth (out to 16 Hz) provides adequate tuning design margin and propeller speed variation compensation. Such a system exhibited 10 to 15 dB interior noise reduction.

Figure 14 shows a photograph of the highly damped (5% critical) elastomeric damper design evaluated for SBN transmission control. The damper configuration consists of a base elastomeric (natural rubber) "sandwich mount," 1.5 inch diameter by 1.0 inch tall, rated as 350 lb/in in shear at 50 lb load, and 2800 lb/in in compression at 420 lb load. The sandwich mount weighing 0.11 lb supports a 2.15 lb weight with a mass center approximately 3.5 inch above the base of the mount. The high mass center allows damper response to various base input excitation. Base and support mass mounted accelerometers were used to obtain a measure of the frequency response characteristics of the damper. As shown in Figure 15 identical dampers were mounted on the upper and lower flanges of the wing from spar (at wing station 41.0). The external mounting of the damper facilitated mounting and monitoring of the damper's response. The propeller airstream did not impinge on the damper.

An electrodynamic shaker attached to the wing front spar at wing station 48.0 was used to obtain damper design installation effects and primarily provide for quick-look screening of candidate damper designs. The mechanical damper of Figure 14 shows a mass-to-base vertical resonant response of around 160 Hz when excited by the shaker. The damper resonant response decreased to around 150 Hz under propeller excitation. A resonant response in the frequency range of 150 to

160 Hz would not normally be expected for an oscillatory spring rate of 2800 lb/in and supported mass of 2.15 lb. However, the elastomer was not under preload and recall that elastomeric materials are preload sensitive and, under dynamic loading, an increase in stiffness by a factor of 2 or so is not unreasonable [16]. Typical SBN transmission reduction obtained with the mechanical damper is shown in Figure 16.

To verify that energy extraction was the principal mechanism of the tuned damper, a dummy sandwich mount was constructed from a cylindrical section of aluminum, duplicating the outside diameter, height, and weight of the elastomeric mount. The rigid damper was also tested, and the results are given in Figure 17. As can be seen, the damper provided only a small amount of blocking mass transmission loss and, thus, dissipation is the primary mechanism for the reduced SBN transmission.

It is of interest to note that for a base wing weight of 29.55 lb, an added total damper weight of 4.52 lb (15 % of wing weight) produced 10 to 15 dB of interior noise reduction in a broad range of propeller speeds, while 17.3 lb (59 % of wing weight) of liquid fuel in the same wing area produced approximately 6 dB noise reduction over a more limited propeller speed range.

## INSTALLATION EFFECTS

While subject of aircraft installation effects, such as rigid wing-to fuselage attachment and effects of an installed engine/nacelle mass [17], is beyond the scope of this paper, it is important to point out that the only SBN control measure which remained mainly unaffected by such installation effects was the tuned mechanical absorber.

## CONCLUSIONS

From full scale and laboratory evaluations of both fuselage mounted single engine and wing mounted multi-engine propeller aircraft it was found that structure-borne interior noise can be equal to or greater than direct airborne noise transmission. It was further determined that proper application of elastomeric damping materials can provide control of structure-borne noise transmission via:

- a) Increased engine/propeller vibration isolation.
- b) Reduced propeller wake excited wing vibrations via tuned mechanical dampers inboard of the propeller wake.
- c) Selected panel damping treatments when used with inboard blocking masses.

## REFERENCES

1. J. J. Catherines and W. H. Mayes, "Interior Noise Levels of Two Propeller-Driven Light Aircraft," NASA TMX-72716, July 1975.
2. J. A. Rupf, "Noise Effects on Passenger Communication in Light Aircraft." Paper No. 770446, SAE Business Aircraft Meeting, Wichita, Kansas, April 1977.
3. N. Broner, "The Effects of Low Frequency Noise on People - A Review," Journal of Sound Vibration, 58 (4), 1978.
4. J. S. Mixson and C. K. Barton, "Investigation of Interior Noise in a Twin-Engine Light Aircraft," Journal of Aircraft, Vol. 15, No. 4, April 1978, pp. 227-233.



5. J. D. Revell, F. J. Balens, and L. R. Koval, "Analytical Study of Interior Noise Control by Fuselage Design Techniques on High-Speed, Propeller-Driven Aircraft," NASA CR-159222, Lockheed-California Company, July 1978.
6. J. F. Dugan, B. A. Miller, E. J. Graber, and D. A. Sagersen, "The NASA High-Speed Turboprop Program," NASA TM 81561, October 1980.
7. J. F. Unruh and D. C. Scheidt, "Engine Induced Structural-Borne Noise in a General Aviation Aircraft", SAE Paper 790626, Business Aircraft Meeting and Exposition, Wichita, Kansas, April 3-6, 1979.
8. J. F. Unruh, "Procedure for Evaluation of Engine Isolators for Reduced Structure-Borne Noise Transmission", Journal of Aircraft, Vol. 20, No. 1, January 1983, pp. 76-82.
9. J. F. Unruh, "Specification, Design, and Test of Aircraft Engine Isolators for Reduced Interior Noise", Journal of Aircraft, Vol. 21, No. 6, June 1984, pp. 389- 397.
10. J. F. Unruh, "Propeller-Induced Structure-Borne Noise: Laboratory-Based Test Apparatus", AIAA Paper 86-1938, AIAA 10th Aeroacoustics Conference, Seattle, Washington, July 9-11.
11. J. F. Unruh, "Detection of In-Flight Propeller-Induced Structure-Borne Noise," Journal of Aircraft, Vol. 24, No. 7, July 1987, pp. 441-446.
12. J. F. Unruh, "Structure-Borne Noise Control for Propeller Aircraft", Journal of Aircraft, Vol. 25, No. 8, August 1988, pp. 752-757.
13. B. A. Miller, J. H. Dittman, and R. J. Jerachi, "The Propeller Tip Vortex -- A Possible Contributor to Aircraft Cabin Noise," NASA TM 81768, April 1981.
14. V. L. Metcalf and W. H. Mayes, "Structure-borne Contribution to Interior Noise of Propeller Aircraft," SAE Paper 830735, Business Aircraft Meeting & Exposition, Wichita, Kansas, April 12-15, 1983.
15. J. F. Unruh, "Prediction of Aircraft Propeller-Induced, Structure-Borne Interior Noise," AIAA Journal of Aircraft, Vol. 25, No. 8, August 1988, pp. 758-764.
16. J. C. Snowdon, Handbook of Vibration and Noise Control, Applied Research Laboratory, The Pennsylvania State University, Report AD/A-071485, April 1979.

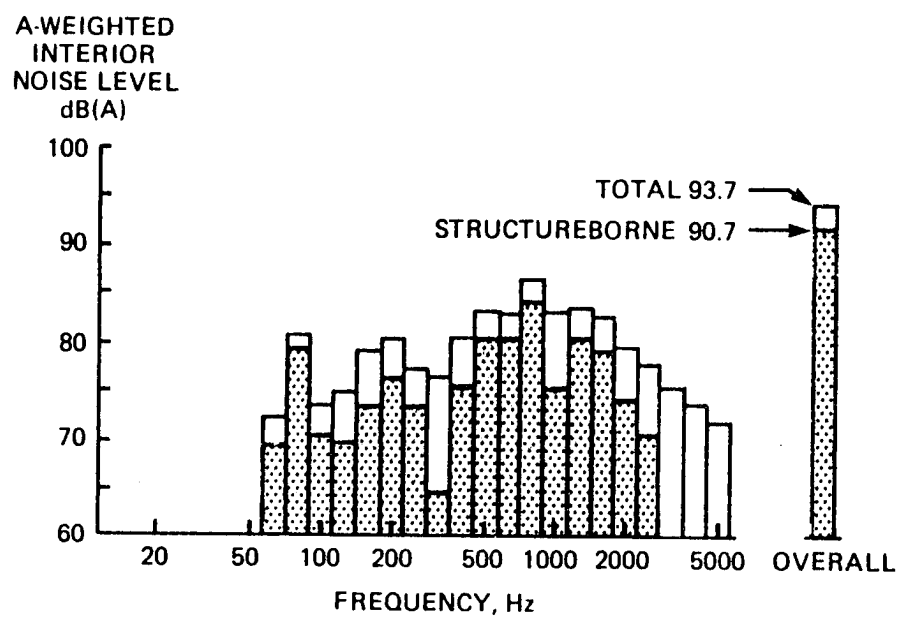


Figure 1. Structure-Borne Noise Equals Airborne Noise



Figure 2. Single Engine Light Aircraft Test Facility

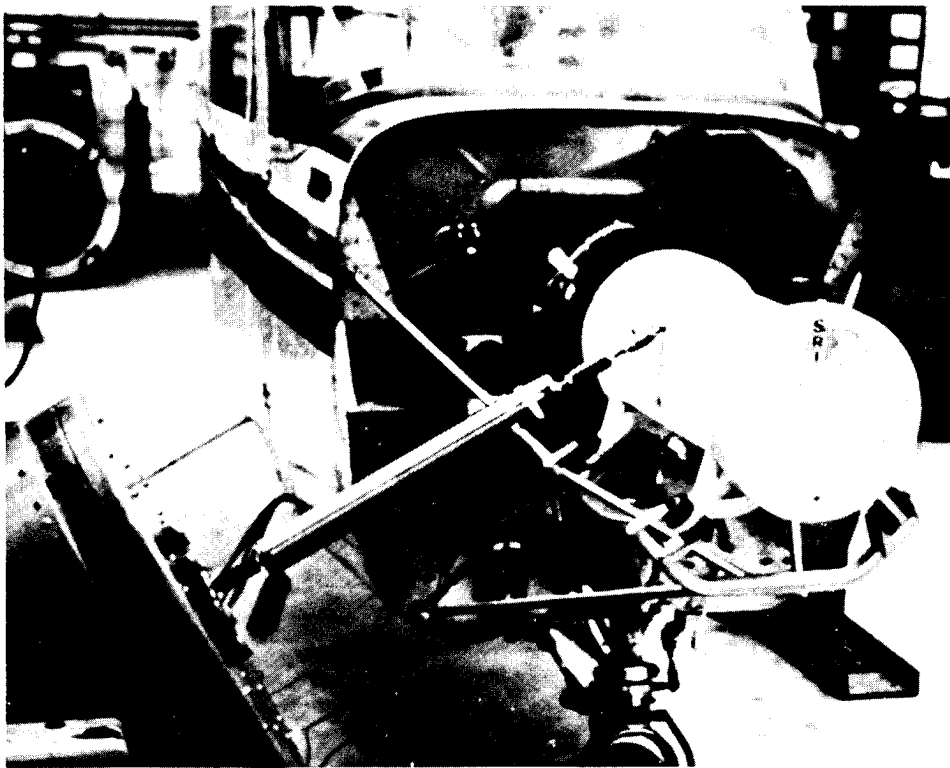


Figure 3. Dummy Engine and Test Setup

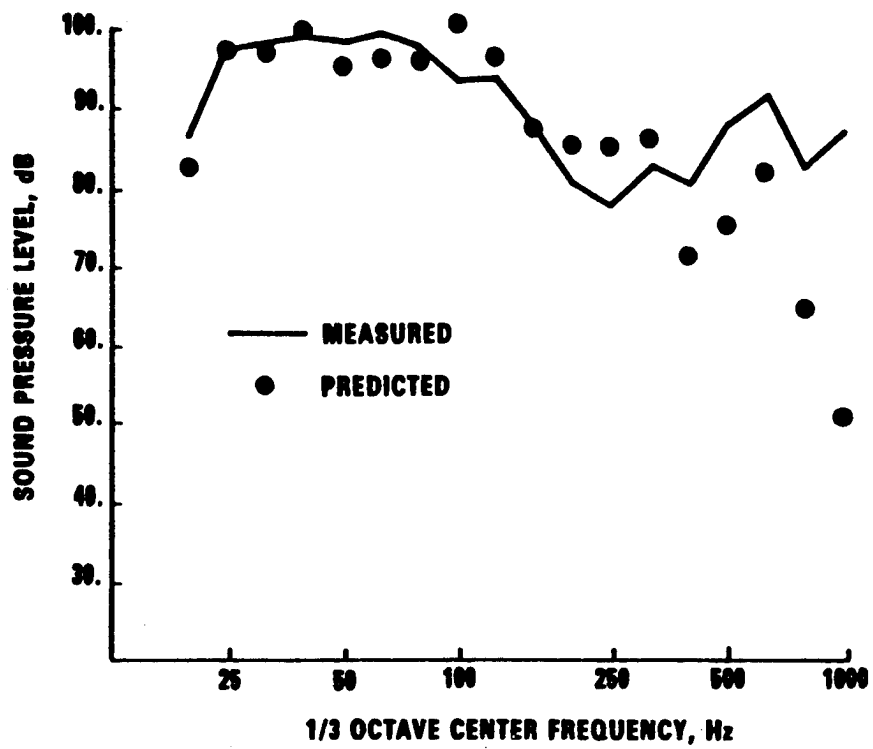


Figure 4. Peak SPL Response Rigid Isolators

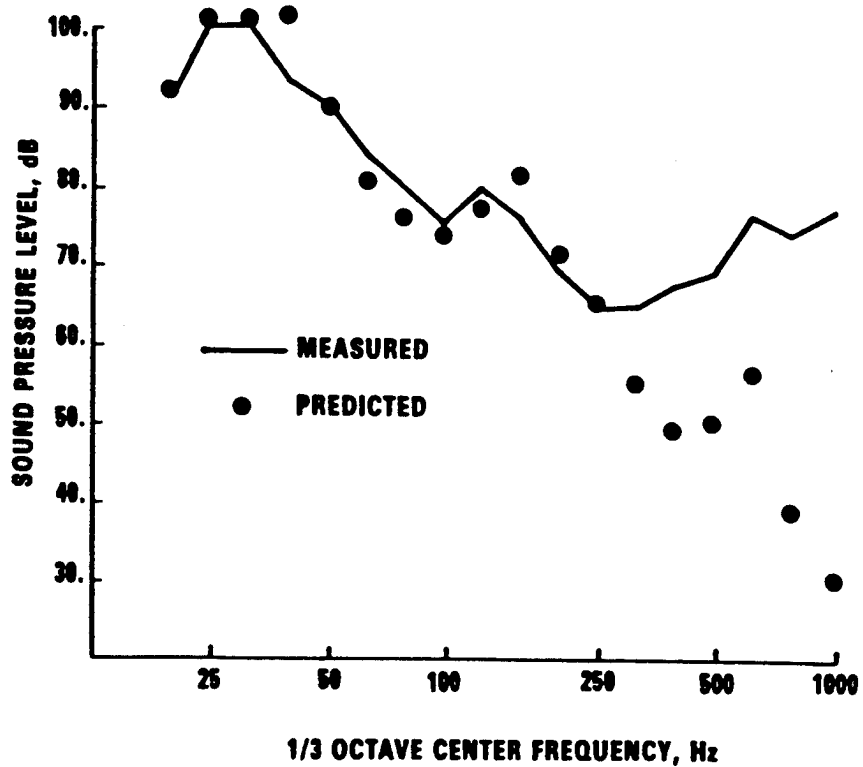


Figure 5. Peak SPL Response Soft Rubber Isolators

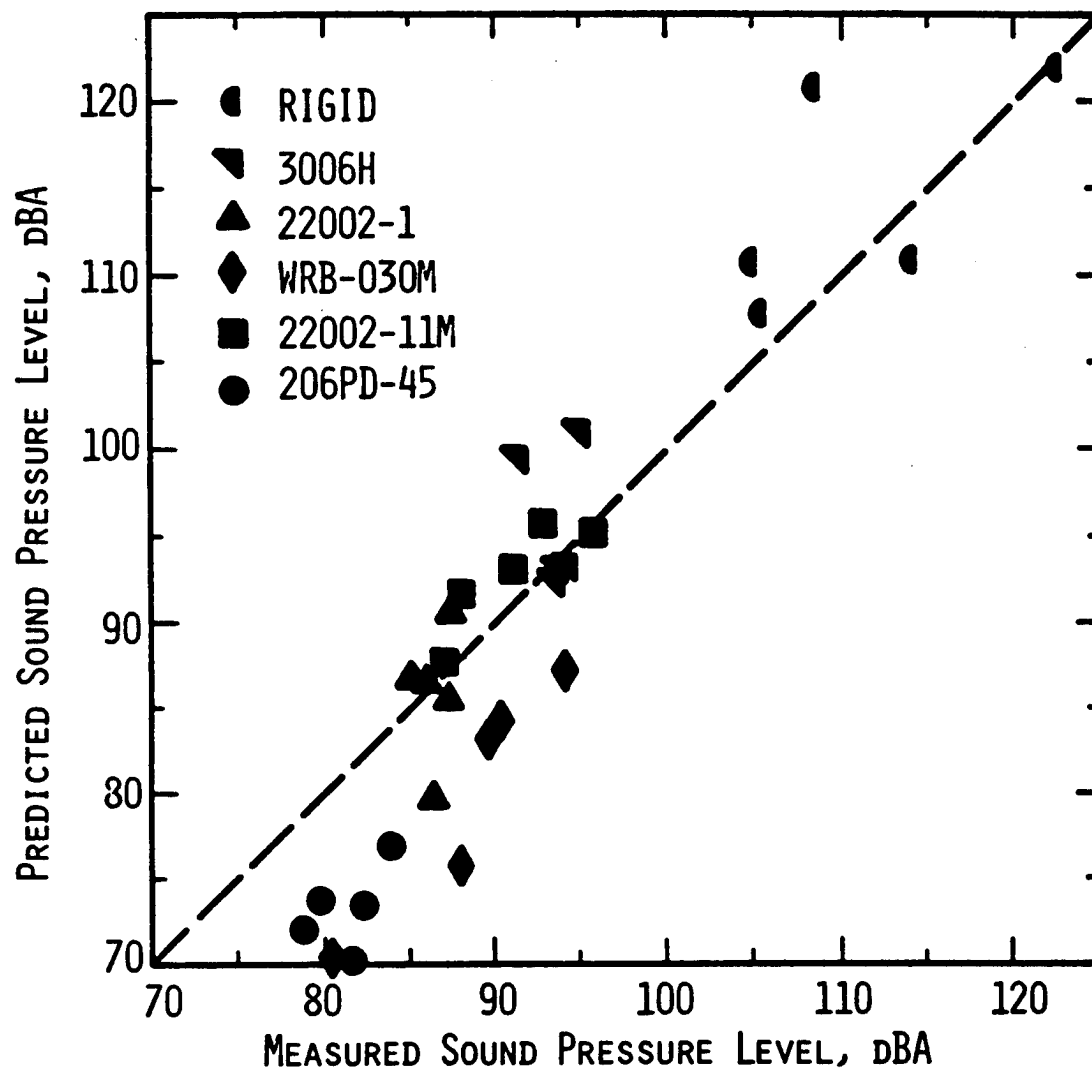


Figure 6. Correlation of Design Model Predictions to Measured A-Weighted OASPL

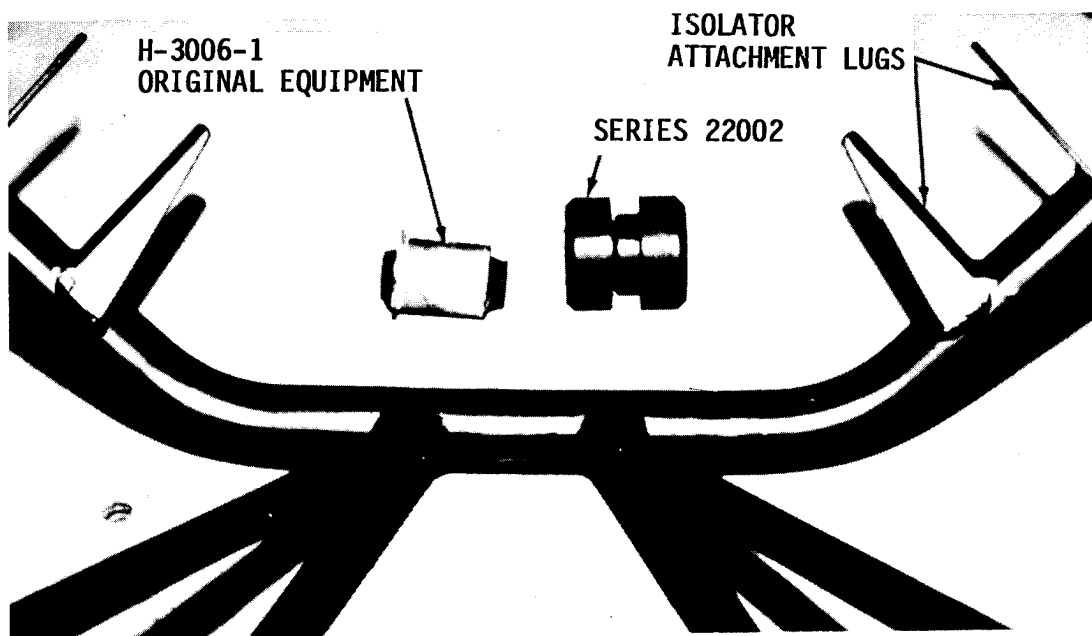


Figure 7. Engine Mount and Vibration Isolators

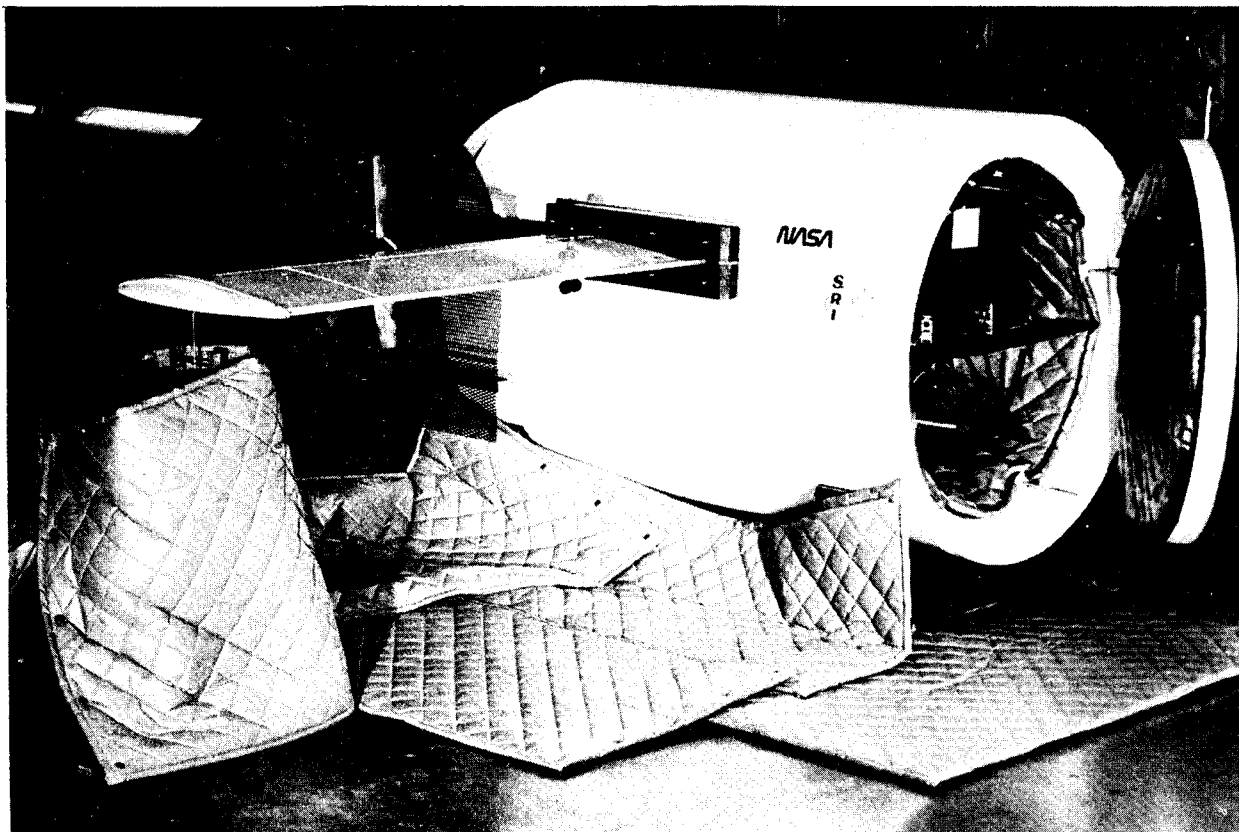


Figure 8. Structure-Borne Noise Test Facility

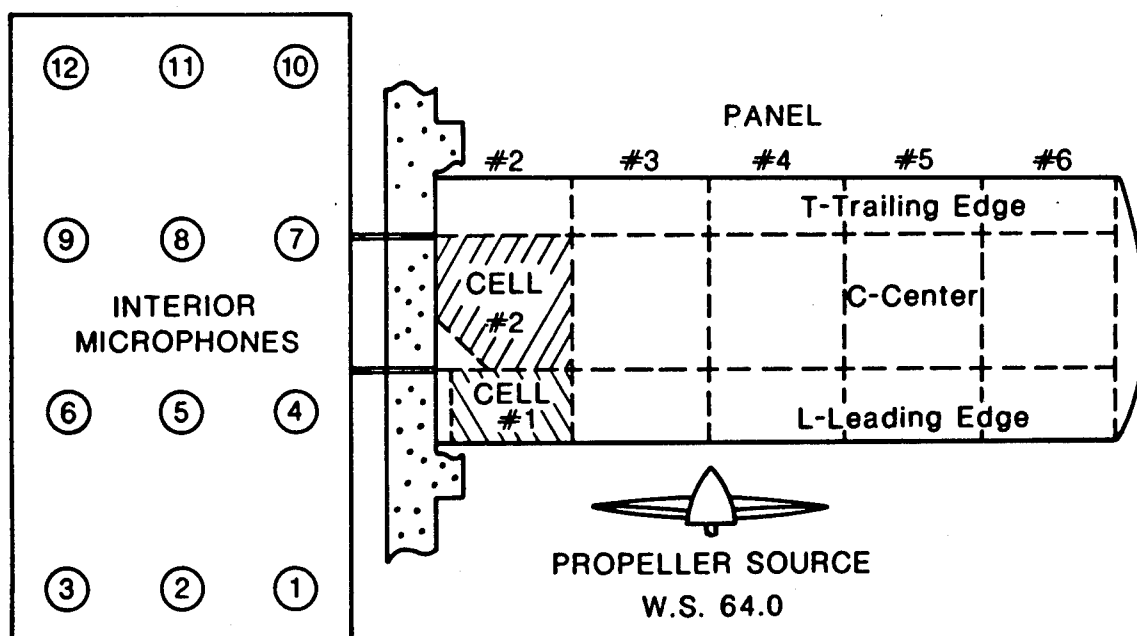
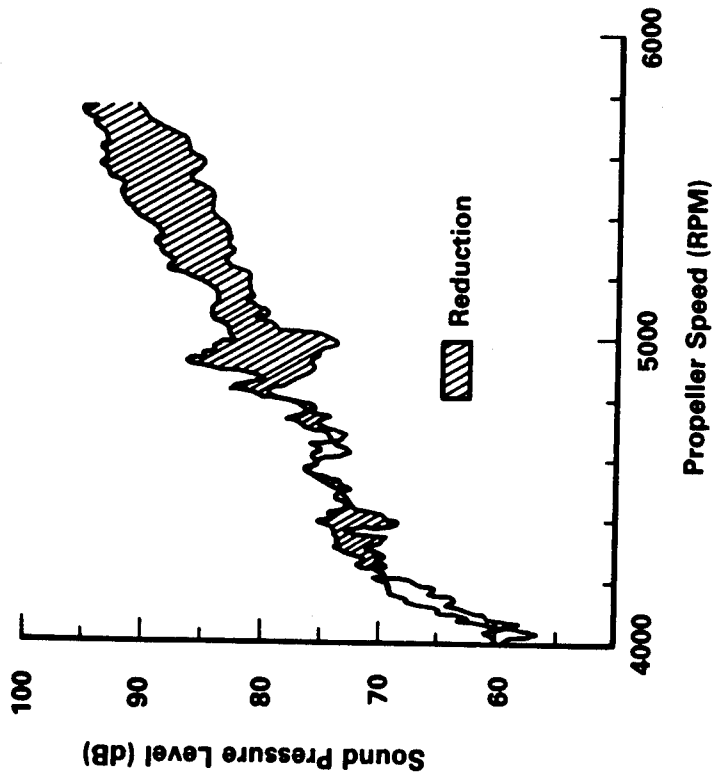
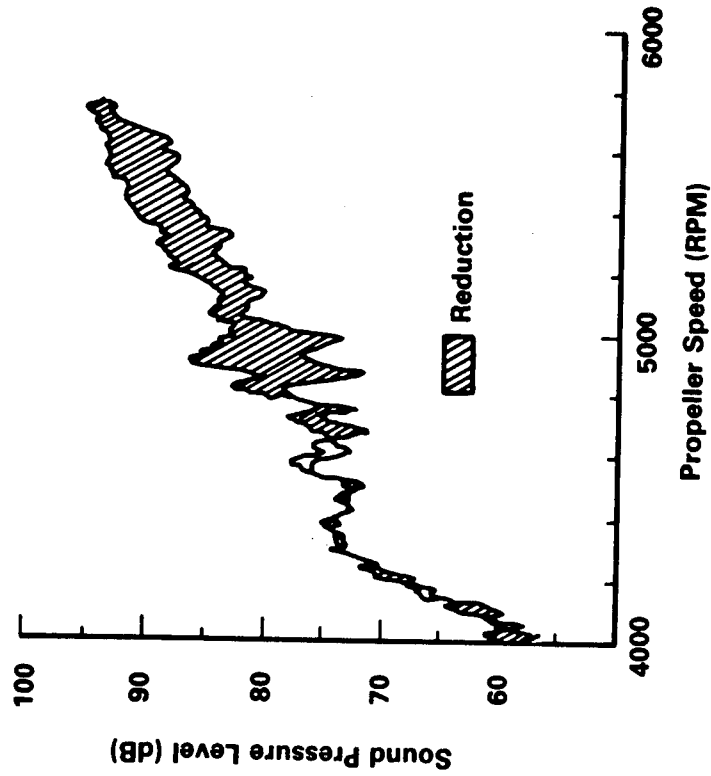


Figure 9. Schematic of Test Apparatus



a) Liquid in Cell 1 and 2



b) Liquid in Cell 2 Only

Figure 10. Effect of Simulated Wing Fuel on SBN Transmission



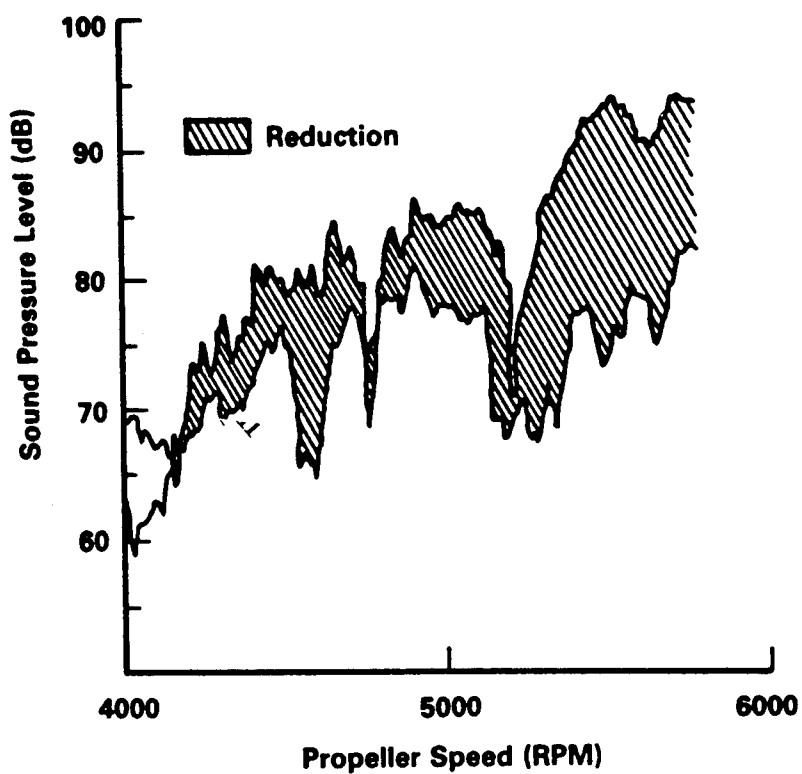


Figure 11. Typical Effect of Blocking Masses on SBN Transmission

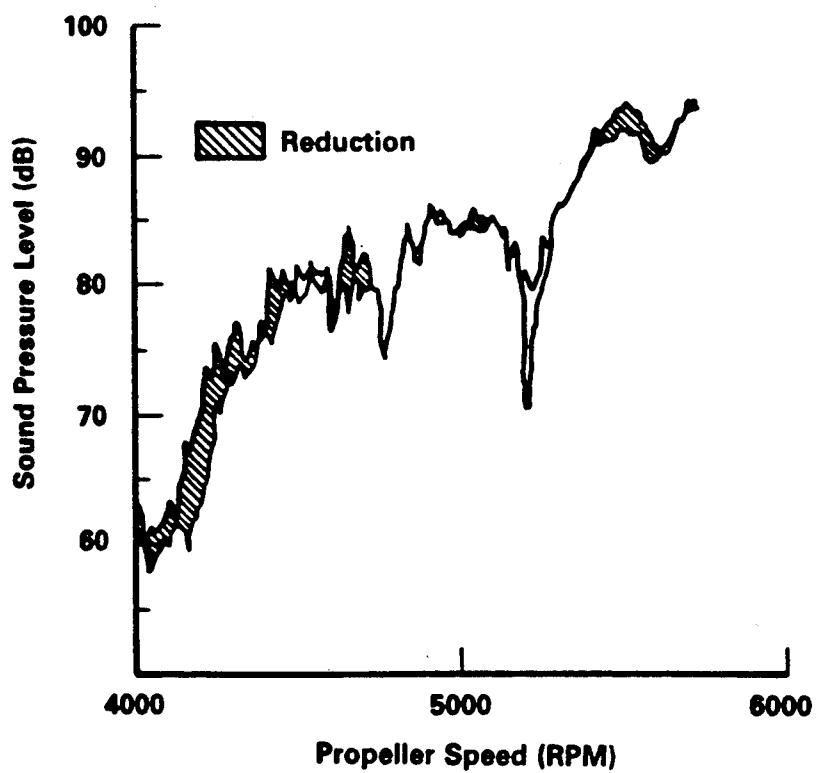


Figure 12. Typical Effect of Damping Material on SBN Transmission

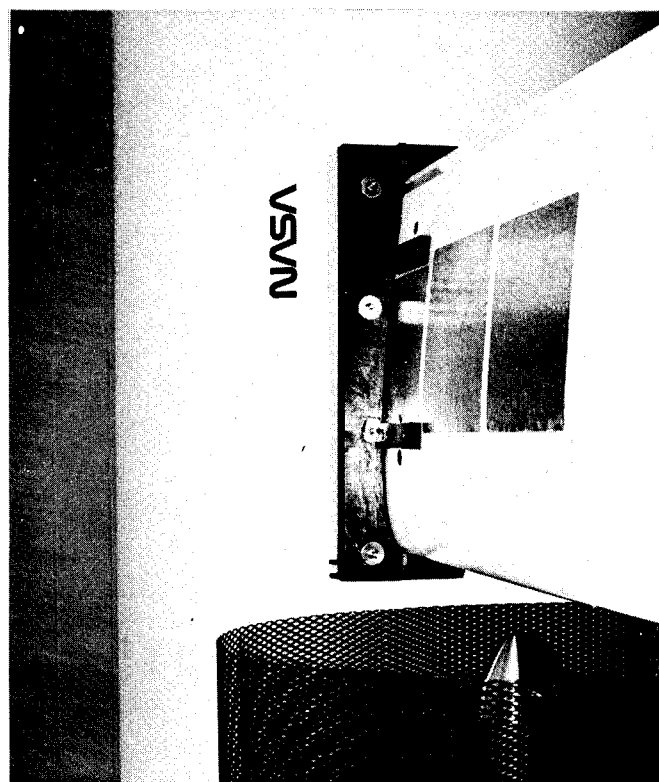
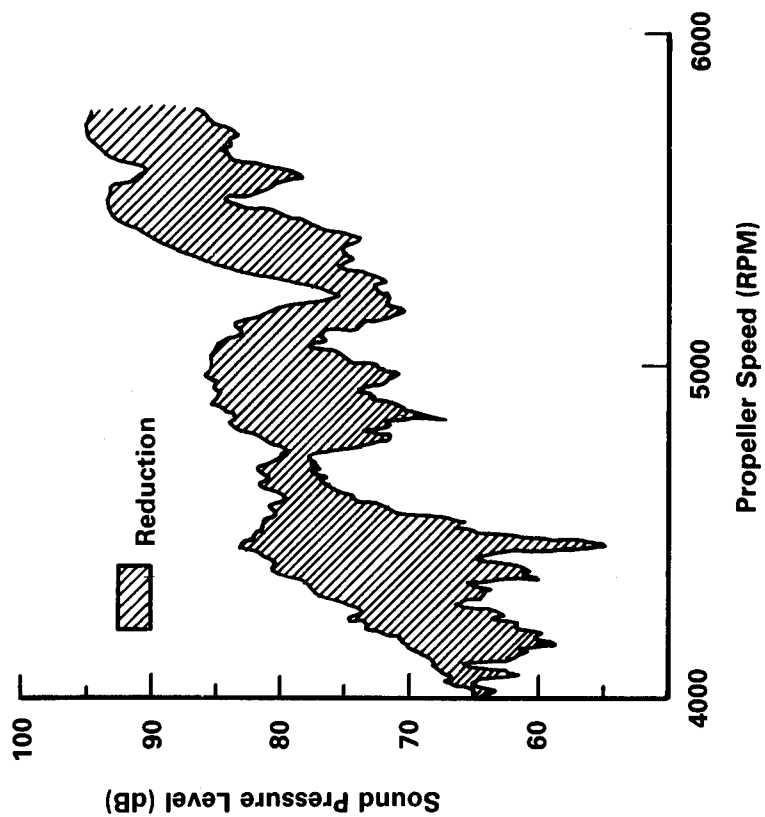


Figure 13. Combined Effect of Blocking Mass and Panel Damping Treatment on SBN TTransmission, Microphone #9

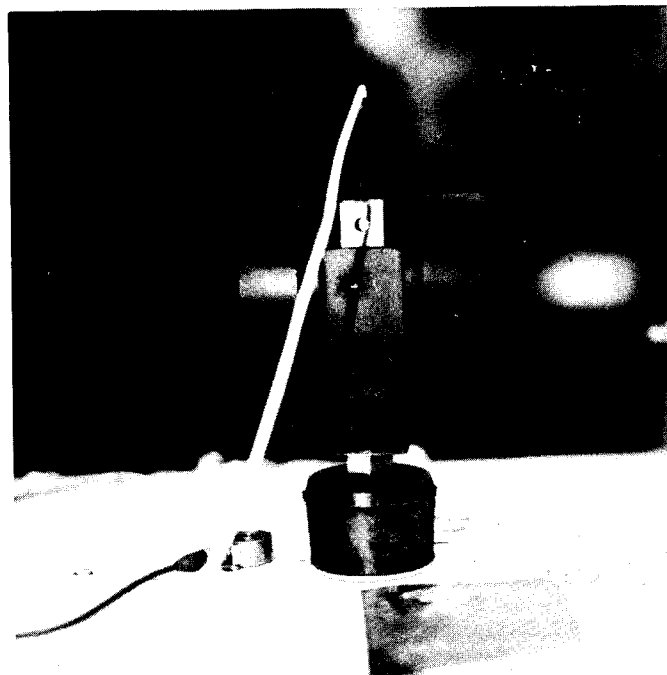


Figure 14. Tuned Mechanical Damper

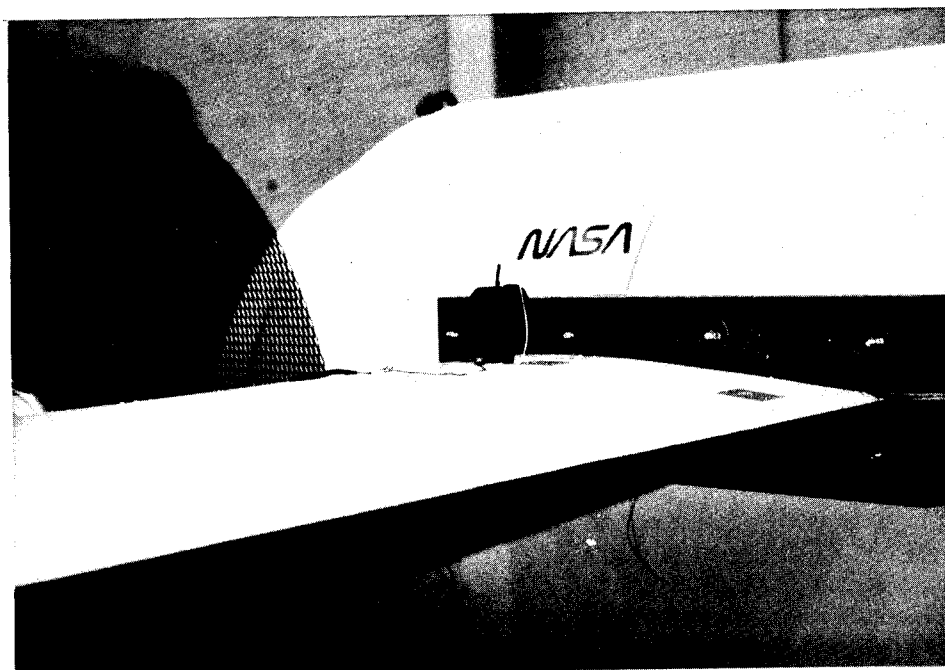


Figure 15. Tuned Damper Installation

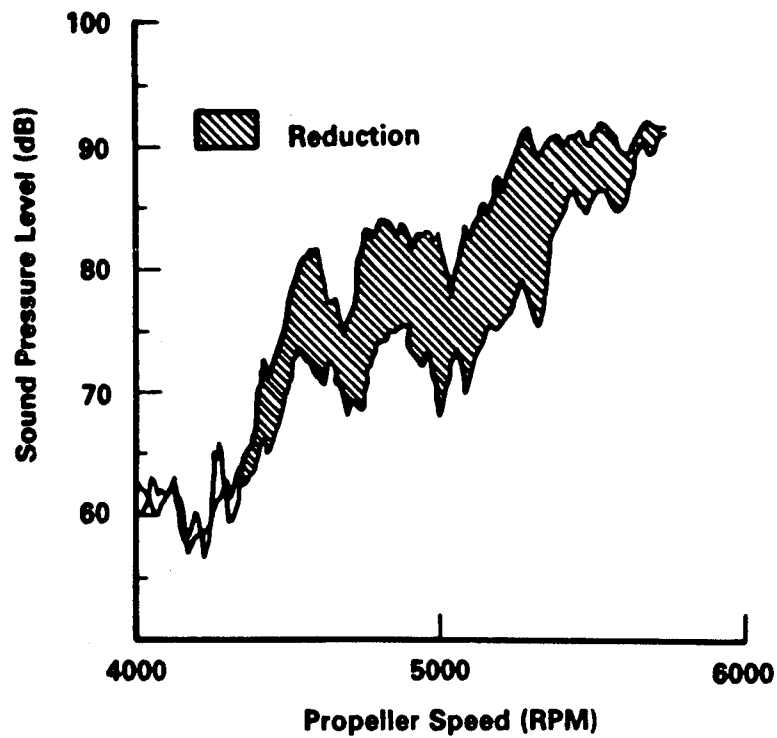


Figure 16. Effectt of Tuned Damper on SBN Transmission, Microphone #7

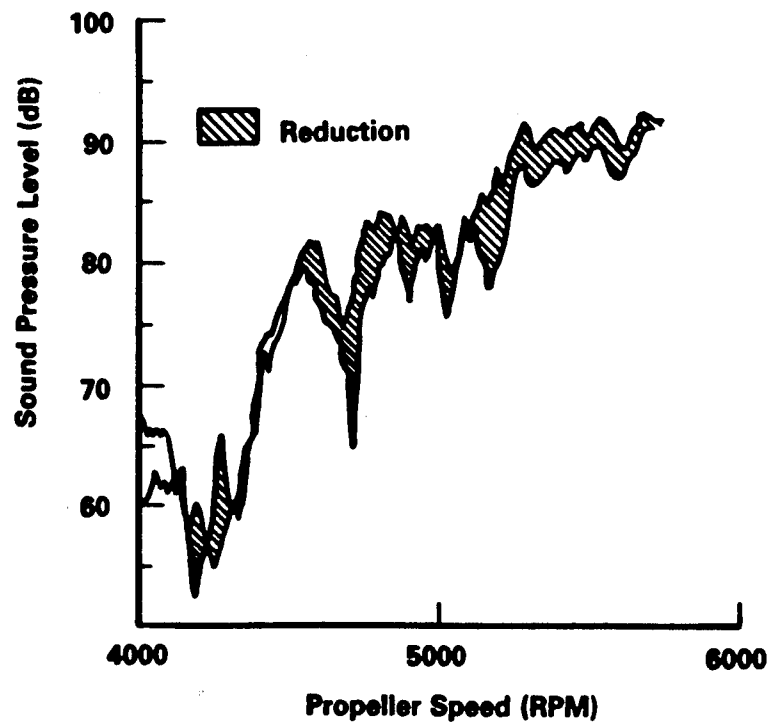


Figure 17. Effect of Rigid Damper on SBN Transmission, Microphone #7

Application of Constrained Layer  
Damping to  
the F/A-18 Horizontal Tail

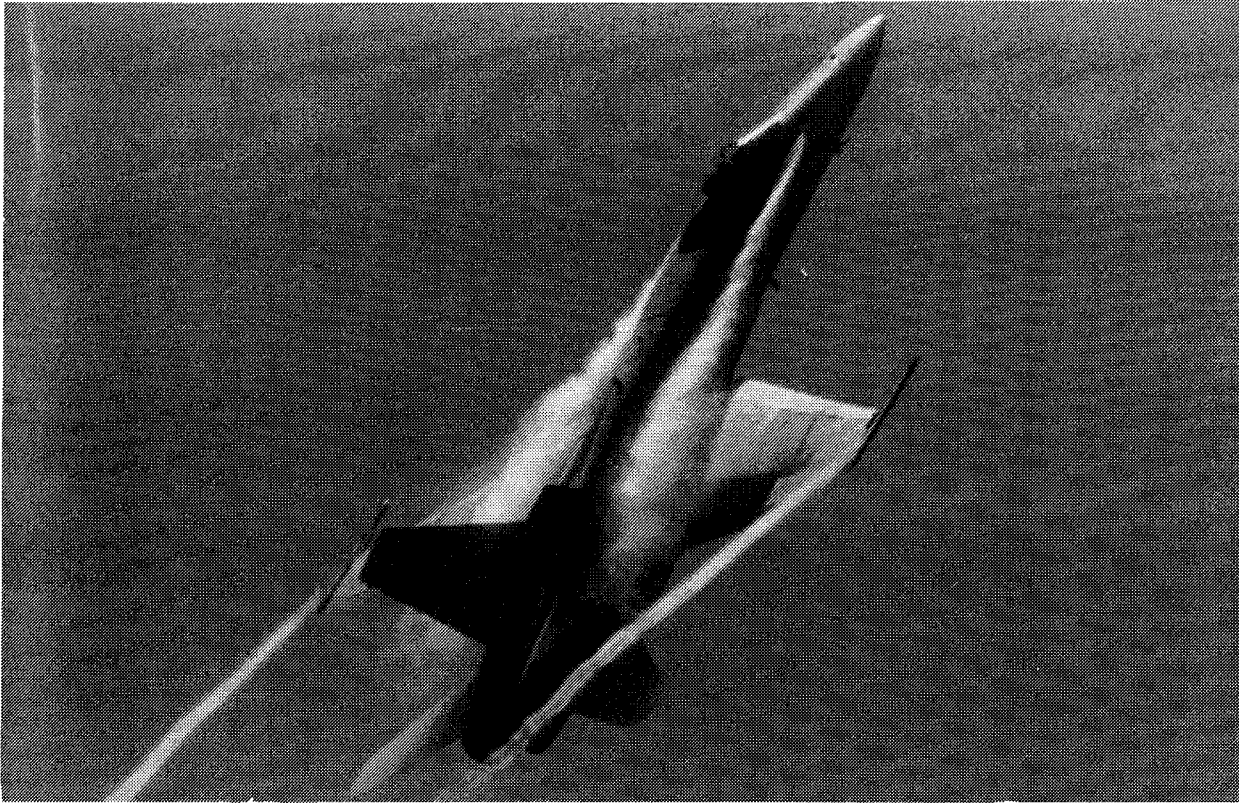
Rudy Yurkovich  
McDonnell Aircraft Co.  
McDonnell Douglas Corp.  
P. O. Box 516  
St. Louis, MO. 63166  
Internal Mail Code 0341180  
Phone (314) 233-2563

**Abstract** - At high angle of attack the F/A-18 empennage is subjected to intense dynamic loads caused by buffeting flow generated by the wing leading edge extension (LEX). At angles of attack of approximately 20 degrees the stabilator and the engine mounts both exhibit high dynamic response. Flight test data show that the engine mounts have a very strong response at approximately 45 Hz, while ground tests show that the stabilator has two resonant frequencies in this frequency range. Also, the stabilator response and the engine mount response have a very high degree of correlation as measured during flight test. Therefore, it was postulated that (a) the stabilator resonant modes drive the engine mounts and, (b) if the stabilator response could be reduced, the engine mount response could also be reduced.

A combined analytical and experimental study was under taken to determine if the stabilator response could be reduced by using constrained layer viscoelastic treatment. The goal was to cut the stabilator response in half, and, in order to do this, the level of damping in the system would have to be doubled. Since damping measured in flight for the modes of interest was about ten percent, the goal was to obtain ten percent damping in these modes on the ground. If the results of the analytical study and experiment proved positive, a flight test program to determine the effect of stabilator damping on engine mount loads under buffet flight conditions was to be carried out.

**Explanation of the Problem** - Modern high performance fighter aircraft are required to have a high degree of maneuverability as well as high speed. On the F/A-18 aircraft the ability to fly to high angles of attack is achieved by the added lift created by the leading edge extension (LEX) which acts like a low aspect ratio delta wing at high angles of attack. Under this condition, lift is generated by a vortex that forms off the LEX. In order to maintain stability at high angles of attack, the vortex flow is used to entrain air over the empennage surfaces, thus maintaining their effectiveness and hence aircraft stability. The F/A-18 at a high angle of attack flight condition is shown in Figure 1. Under conditions of high humidity, the vortex from the LEX and from the wing tip can be seen. Associated with the LEX vortex is high energy turbulent flow. When this flow impinges on an empennage surface, a high dynamic response condition results; a condition which has led to structural damage to the aerodynamic surface and to other parts of the aircraft.

Export Authority 22 CFR 125.4(b)(13) Applicable



GP93-0075-7

**Figure 1. F/A-18 Aircraft at High Angle-of-Attack Showing Vortex  
From the Leading Edge Extension and Wing Tips**

For the case of interest here, the engine mounts were being damaged. From flight test data it was determined that the engine mounts experience high dynamic loads at the same time as the stabilator is being excited by the buffeting flow. It was theorized that the loads from the stabilator were being transmitted from the stabilator into the fuselage and then into the engine mounts. This premise was supported by the fact that both the stabilator and the engine mounts have resonances in the 45 Hz range, and it is at these resonant frequencies that most of the engine mount response is observed. In addition, flight test data showed a very high correlation between engine mount response and stabilator response. Thus, based on these assumptions, it was postulated that a reduction of stabilator response would reduce engine mount response.

**Analytical Studies** - Since this is a dynamic response problem, damping is one of the factors that control the amplitude and thus, if it can be introduced, can be a solution. Constrained layer viscoelastic material will introduce damping. A procedure that can be used to compute the modal damping from the properties of the viscoelastic materials is the modal strain energy method (Reference 1). This method was used for all of the damping calculations. It requires the calculation of the ratio of the strain energy in the viscoelastic material to the total strain energy in the structure on a mode by mode basis. This ratio is an approximation to the modal damping assuming a material loss factor of 1.0 for the viscoelastic material. This calculation is shown in the following equation.

$$\eta = \frac{1/2 \phi^T K_v \phi}{1/2 \phi^T K \phi} = \frac{S_v}{S}$$

where:  $\phi$  = eigenvector

$K$  = stiffness matrix

$K_v$  = stiffness matrix for viscoelastic only

$S$  = strain energy

$S_v$  = strain energy for viscoelastic

In order to carry out this computation, a vibration model of the structure to be treated with viscoelastic material is required. A NASTRAN beam-rod vibration model of the stabilator had been developed for use in flutter studies and that model was modified for the present studies. These modifications included the addition of RBAR elements from the beam that defined the elastic axis to the surface where the viscoelastic elements were to be attached. The viscoelastic material was modeled using NASTRAN HEXA elements and the constraining layer was modeled using NASTRAN CQUAD elements. For the initial studies, the shear modulus of the viscoelastic material was assumed to be 1000 psi and the damping treatment was assumed to be applied in six sections of equal width. The stabilator with the viscoelastic material and constraining layer is shown in schematic form in Figure 2. The material properties of the damping treatment are indicated as well.

Vibration studies with this model were run to determine the strain energy in the viscoelastic elements. The damping levels determined from the strain energy ratio, as well as the modal frequencies, are shown in Figure 3. Data for the first four modes are shown. The two modes of interest here are the pitch/torsion mode and the second bending mode which have frequencies of 41.7 Hz and 47.8 Hz respectively. The engine mounts show maximum response at approximately 45 Hz. The other modal frequencies fall outside of the range of interest. The predicted level of damping in the pitch/torsion mode is relatively low. This is because there is very little strain energy in the structure, rather most of the energy is in the actuator since the motion is largely pitch about the spindle. This mode is not a candidate for viscoelastic damping applied to the surface. The second bending mode, however, has a very high level of predicted damping. Thus, if excitation from this mode were the source of the high engine mount loads, damping could be very effective in reducing them.

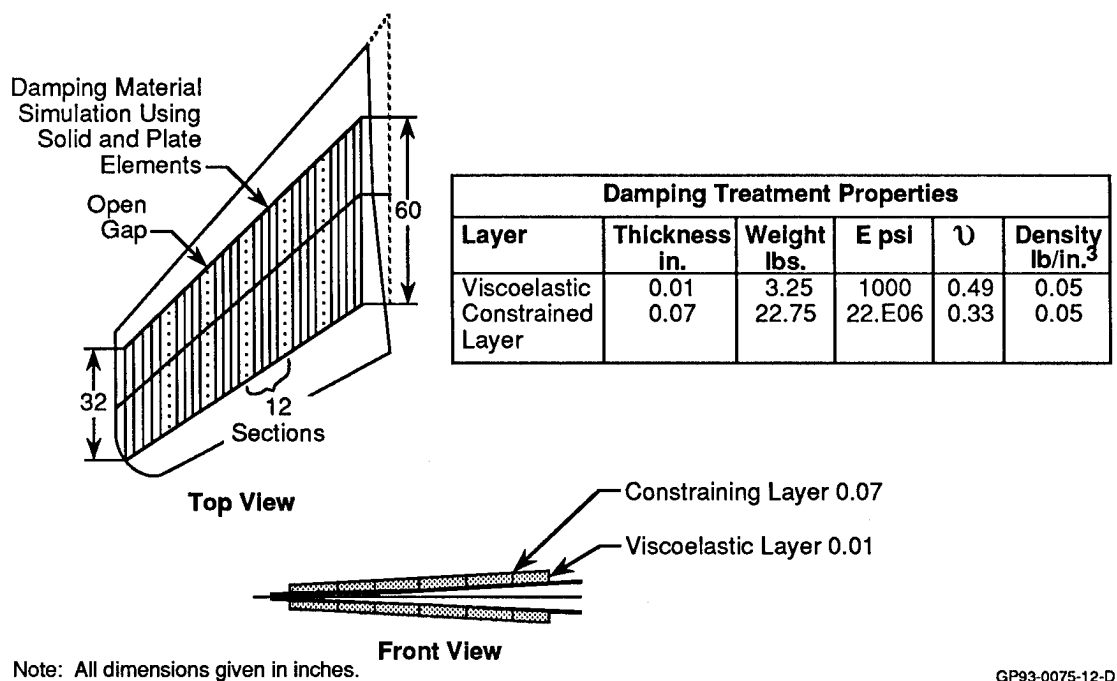


**Figure 2. F/A-18 Horizontal Tail Constrained Layer Damping Treatment**

Mode Number	Loss Factor, $\eta$	Frequency (Hz)
1 (1st Bending)	0.072	12.68
2 (Pitch/Torsion)	0.041	41.74
3 (2nd Bending)	0.191	47.78
4 (2nd Torsion)	0.102	87.53

GP93-0075-4-T

**Figure 3. F-18 Horizontal Tail Constrained Layer Damping Treatment**



In order to investigate the effectiveness of damping to control the stabilator response during buffeting flow conditions, additional analytical studies were run. Using the predicted levels of damping as calculated above, buffet response calculations were made. Unsteady pressures during buffet conditions were measured during a wind tunnel program described in Reference 2. These pressures were scaled to aircraft size and were used as the forcing function in the response calculation. The method to accomplish the scaling and for carrying out the calculation itself is also described in Reference 2. The results of these calculations are shown in Figure 4. The data are presented in the form of bending and torsion moment PSD's for a root station and a 70 percent span station. Data for the base line stabilator with only aerodynamic damping present is compared to that computed with the damping from the viscoelastic treatment included (damping levels from Figure 3). For the root, where the loads would be directly transferred into the fuselage, the response in the critical 45 Hz range is reduced by a factor of two. Thus, even though only one mode is effectively being controlled, the reduction in response is still significant.

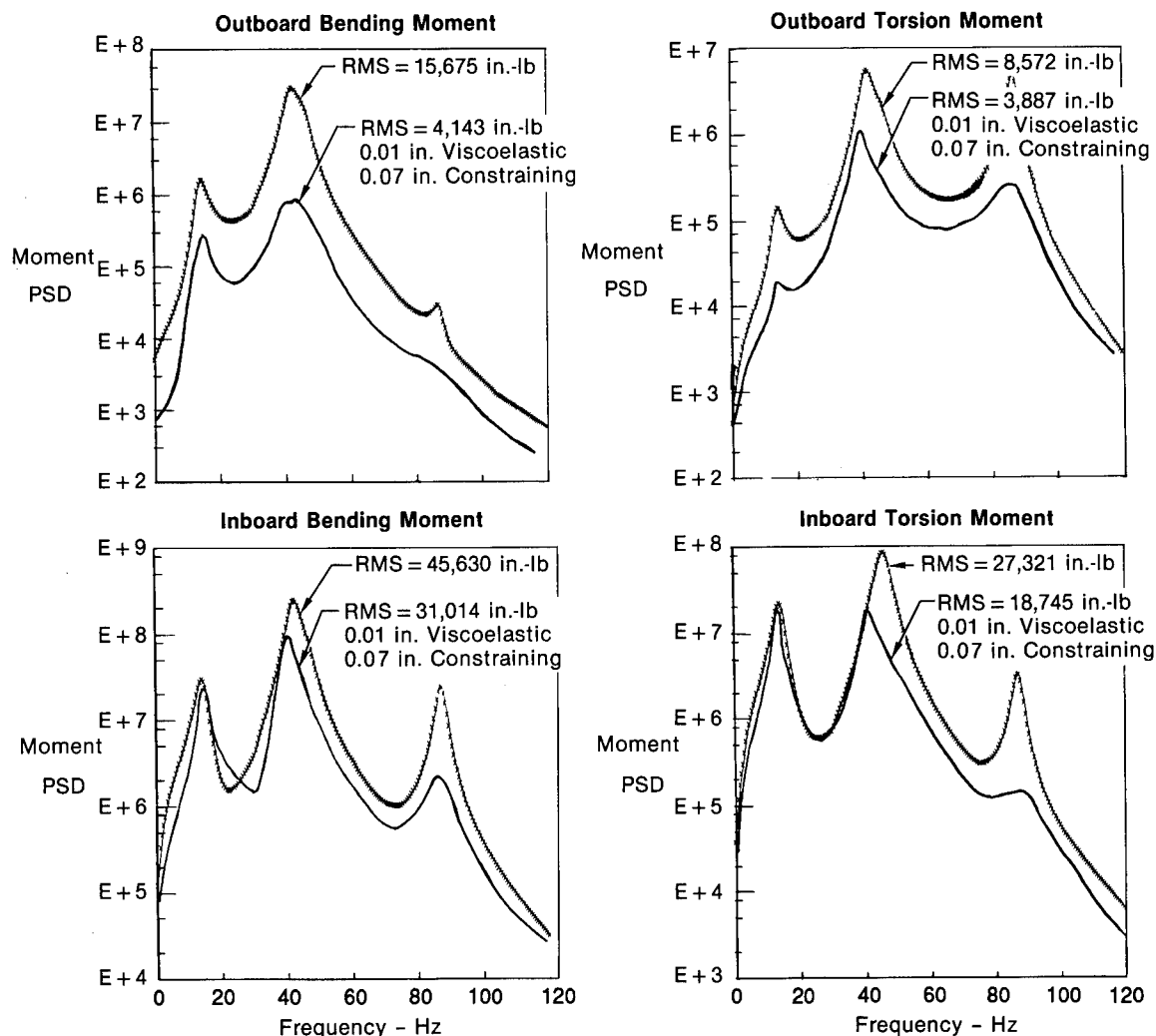
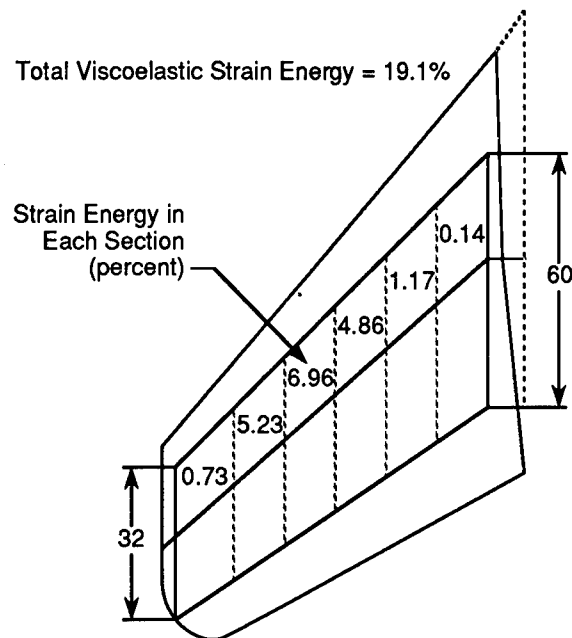


**Figure 4. F/A-18 Stabilator Buffet Response Predictions  
With/Without Viscoelastic Damping Treatment**

The distribution of modal strain energy in the second bending mode is shown in Figure 5. This figure shows that most of the strain energy is concentrated in three sections inboard of the tip. If only the second bending mode needs to be controlled, then it is necessary to install damping treatment only in this area. This is what was done since the other mode in the frequency range of interest, the pitch/rotation mode, could not be controlled by constrained layer viscoelastic treatment. The remaining modes have frequencies that fall outside the frequency range of interest.

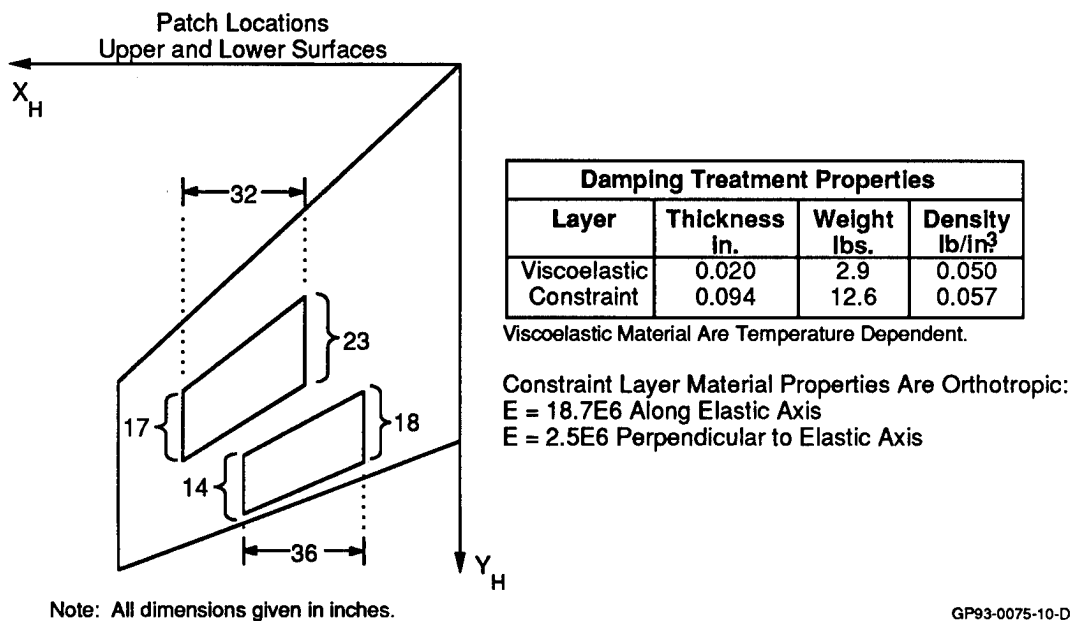


Note: All dimensions given in inches.

GP93-0075-13-D

**Figure 5. F/A-18 Horizontal Tail Constrained Layer Damping Treatment**  
Modal Strain Energy Distribution Mode 3  
(2nd Bending)

For geometric reasons the treatment configuration shown in Figure 6 was selected as best. The treatment was broken into two pieces because in the area where the treatment is required, the composite skin has several ply drop-offs. This makes the surface very irregular and, since the constraining layers are very stiff, they would be difficult to manufacture if they had to run across the ply drop-offs. The material properties for the viscoelastic and constraint material are also shown in Figure 6. The ISD-113 viscoelastic material was selected primarily because it was available at the time the test had to be run. The constraint material was carbon epoxy. A composite constraining layer was selected to maximize the stiffness to weight ratio and an orthotropic ply lay-up was selected to maximize the stiffness in the direction of maximum bending. In general, the stiffer the constraining layer is, the higher the damping.



For the viscoelastic treatment geometry shown in Figure 6, analytical studies were conducted to determine the sensitivity of damping to various geometric parameters. For example, shown in Figure 7 is a plot of modal damping as a function of shear modulus of the viscoelastic material for three different thicknesses of the viscoelastic material. It is interesting that while the peak damping changes by a small amount as the thickness changes, it also tunes to a different shear modulus. This data can be used, along with the material data shown in Figure 8 for ISD-113, to plot damping as a function of temperature. This conversion was carried out and the result is shown in Figure 9. This data is interesting in that the thickness parameter shows the ability to tune the peak damping to a given temperature in the same way that it was able to tune peak damping to a given shear modulus. Also, for the range of thicknesses studied here, the thickest material does show the highest damping. Since both the material loss factor and the shear modulus of the viscoelastic material are temperature dependent, both must be considered. However, the shear modulus accounts for most of the trend shown in Figure 9.

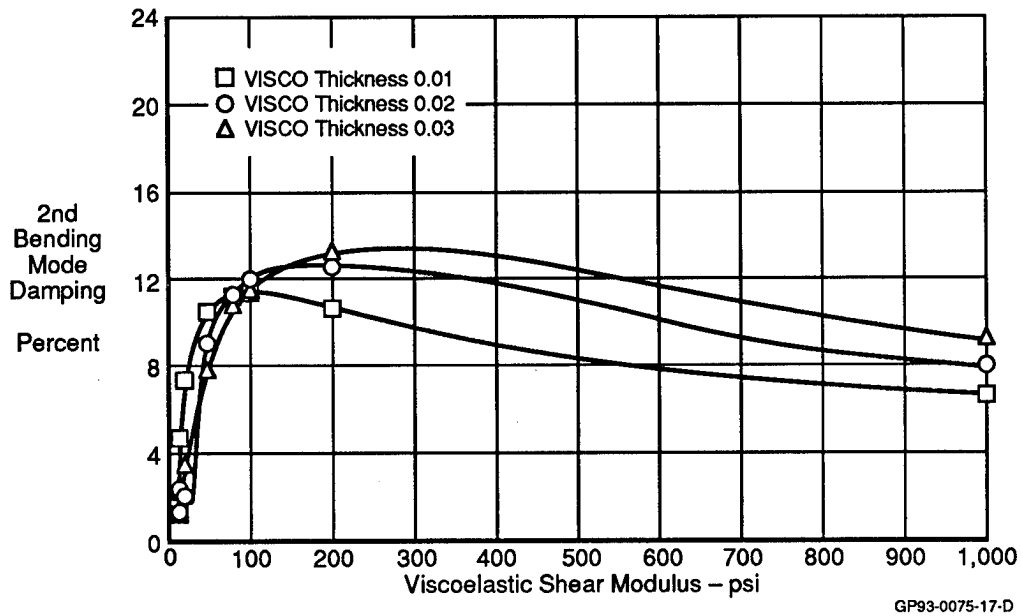


**Figure 7. F/A-18 Horizontal Tail Constrained Layer Damping Treatment**  
Damping Sensitivity to Viscoelastic Thickness Patch Length 32 In.

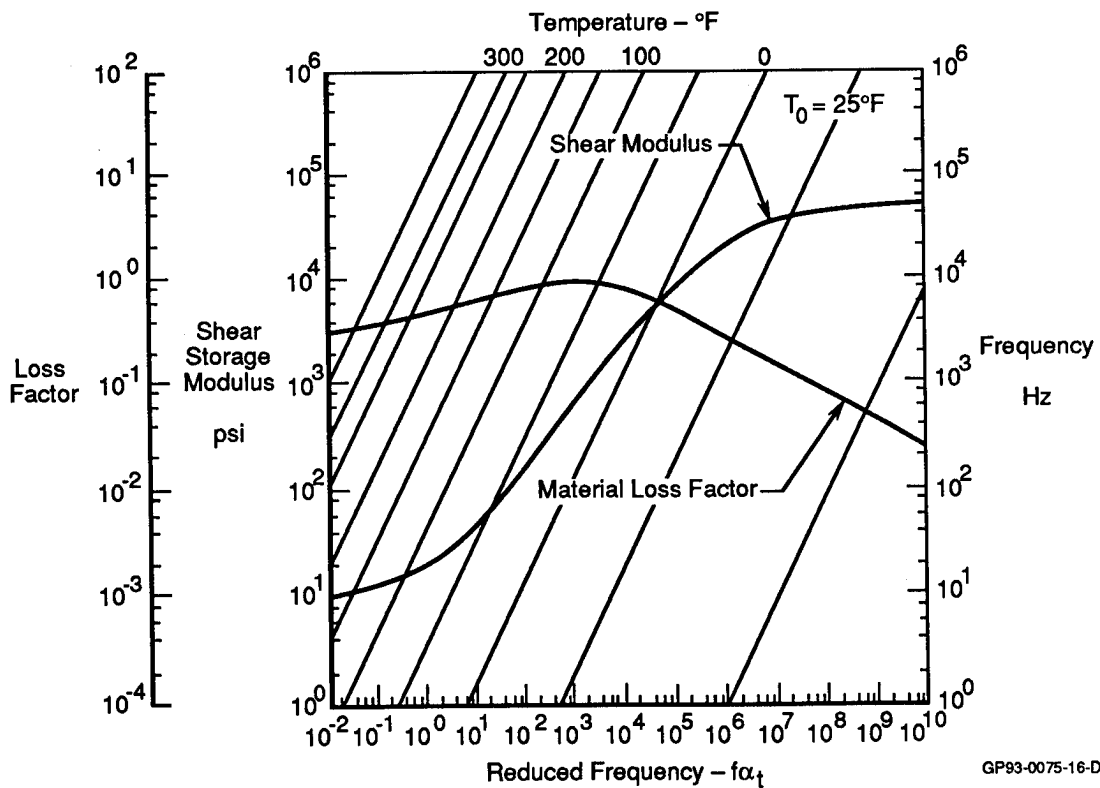


**Figure 8. Viscoelastic Material Properties ISD - 113**

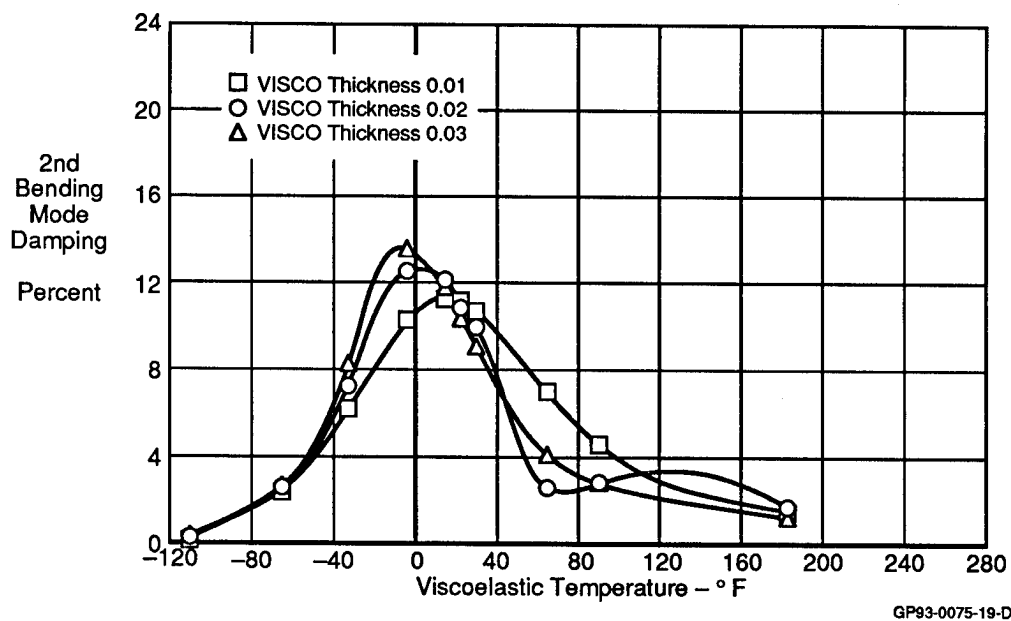


**Figure 9. F/A-18 Horizontal Tail Constrained Layer Damping Treatment**  
Damping Sensitivity to Viscoelastic Thickness Patch Length 32 In.

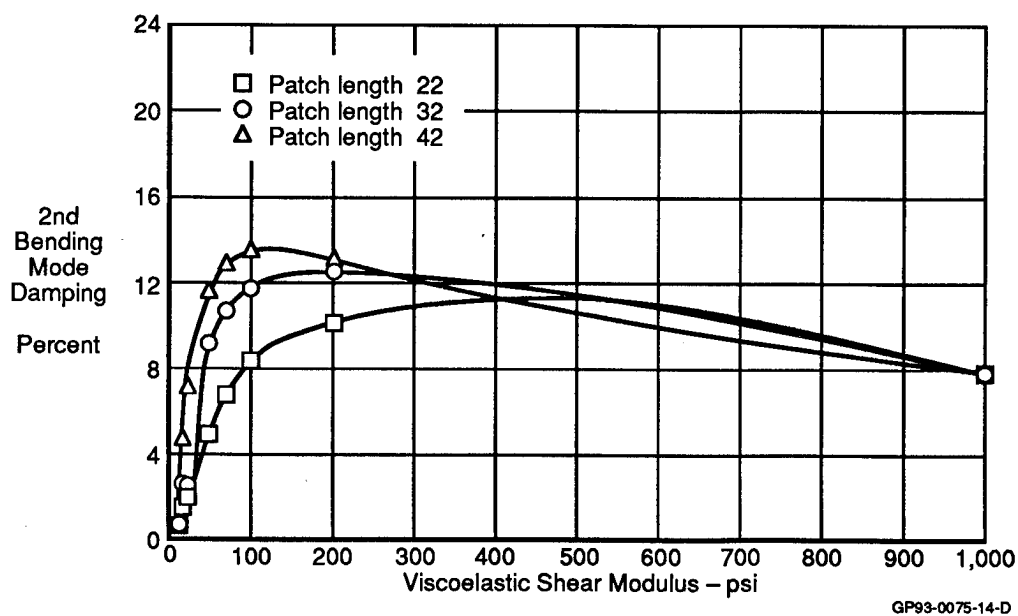
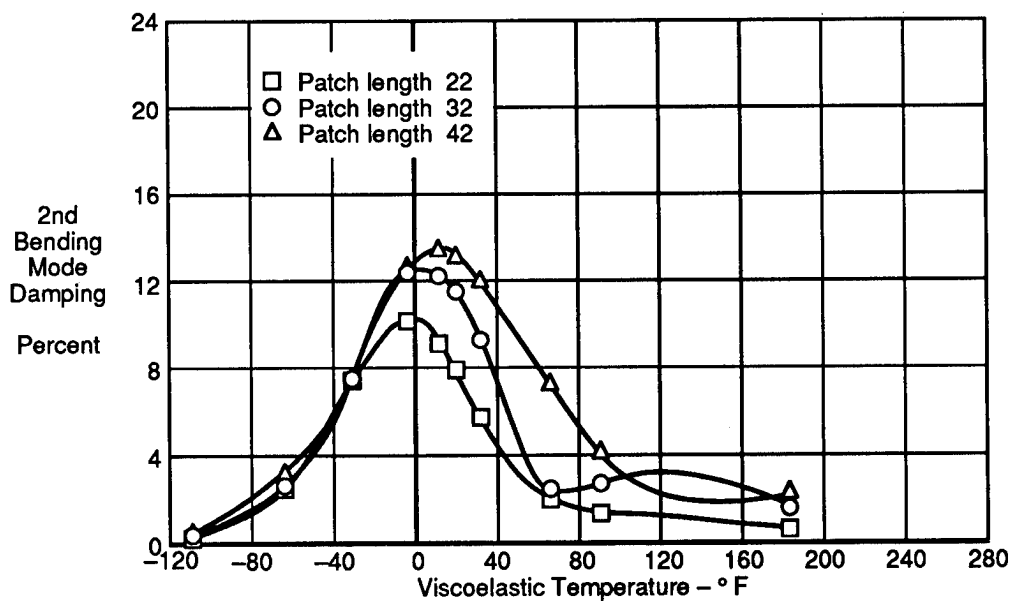


**Figure 10. F/A-18 Horizontal Tail Constrained Layer Damping Treatment**  
Damping Sensitivity to Patch Length Visco Thickness 0.02 In.

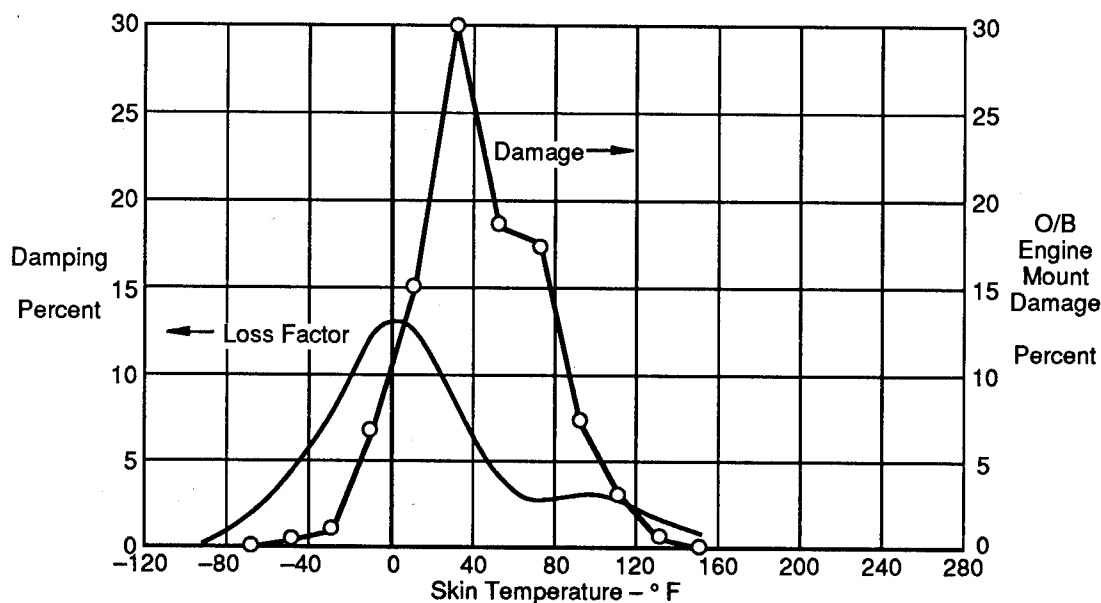


GP93-0075-18-D

**Figure 11. F/A-18 Horizontal Tail Constrained Layer Damping Treatment**  
Damping Sensitivity to Patch Length Visco Thickness 0.02 In.

Thus, both treatment length and thickness of the viscoelastic material can be used to tune peak damping to a given temperature. Because of this, the geometric properties of the damping treatment, as well as the viscoelastic material, must be selected such that peak damping occurs at a temperature that matches the temperature where structural response is a maximum. For the case at hand a length of 32 inches was fixed by the geometric considerations already mentioned. It will be shown that a longer length would have been a better choice. The thickness of the viscoelastic material was selected as 0.02 inches. This selection was based on material availability and the thought that a thicker material would help to fill local voids. A viscoelastic material thickness of 0.01 inches would have been a better choice as will be shown next.

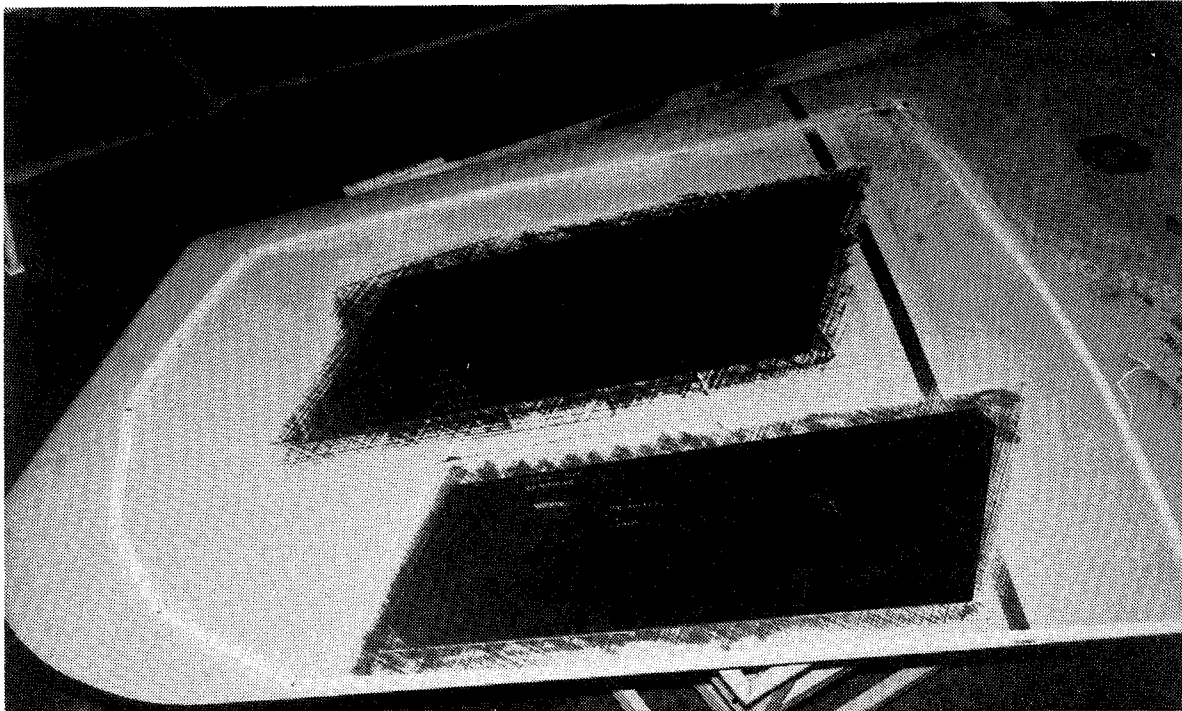
The modal damping from the analytical study for the material and geometric properties that were selected, and also a non-dimensional damage curve for the engine mounts are plotted in Figure 12 as a function of temperature. The non-dimensional damage curve was determined from aircraft usage data. Initially, the maneuver data was compiled as a function of altitude and Mach number. This data was then converted to temperature based on statistical data for aircraft usage for standard day, hot day, and cold day conditions. Each data point represents a delta temperature range of 20 degrees. Thus, for the peak damage temperature, 30 percent of the damage occurs between 20 and 40 degrees. Failure occurs when the total damage reaches 100 percent. The predicted loss factor has a peak at about zero degrees F whereas the damage curve has its peak at about 30 degrees F. Thus, the viscoelastic treatment is not optimum for the problem that it was intended to control. The temperature where peak loss factor occurs could have been tuned by reducing the thickness of the viscoelastic material or by increasing the length of the treatment. Unfortunately, the constraints mentioned previously, rendered this impossible.



GP93-0075-9-D

**Figure 12. F/A-18 Horizontal Tail Constrained Layer Damping Treatment**  
Comparison of Mode 3 Damping and Analytical Damage Versus Skin Temperature

**Experimental Investigation** - The damping treatment described in the previous section was fabricated and installed on a pair of F/A-18 horizontal tails. The treatment installation is shown in Figure 13. The constraint layer was constructed from a high modulus composite material that was laid up such that most of the fibers were orientated in the span-wise direction. Very little strain occurs in the chordwise direction and therefore no stiffness is required in that direction. The viscoelastic material was attached to the constraint layers and any air bubbles were eliminated. As a safety of flight item, a thin line of sealer was added to the leading edge and to the trailing edge of the constraint layers. This was done to ensure that the constraint layers would not peel off in flight. The backing paper was next removed from the viscoelastic material and the constraint layer/viscoelastic material combination was attached to the stabilator. The procedure used was to stick one end of the constraint layer to the stabilator using the viscoelastic material as the adhesive, and then to push down the constraining layer in order to work the bond toward the other end. This procedure was intended to remove trapped air. Once the damping treatment was attached, the stabilator was put in a vacuum bag and then into an autoclave at 150 degrees F. This was intended to ensure that the viscoelastic material was completely attached to the stabilator and to speed curing.

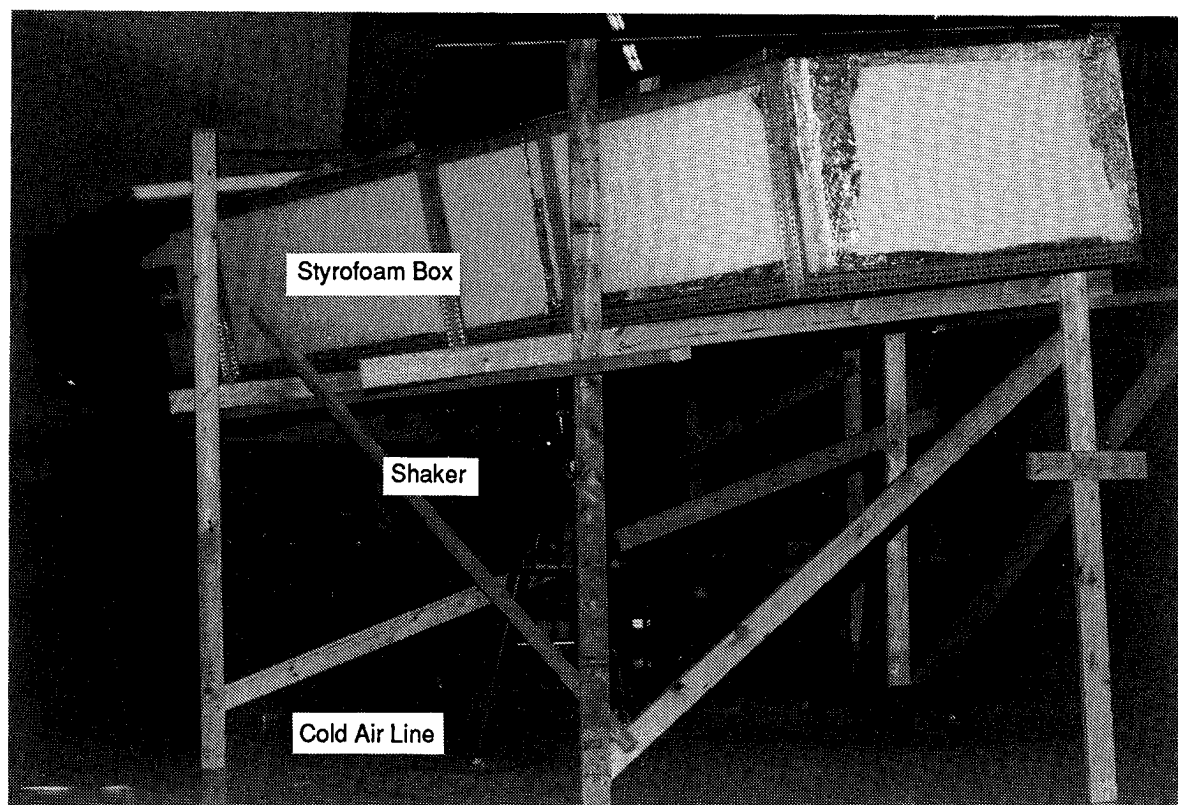


GP93-0075-5

**Figure 13. Viscoelastic Damping Treatment Installed  
on F/A-18 Stabilator**

These tails were installed on an F/A-18 aircraft and a ground vibration test to measure modal frequencies and damping was conducted. A complete modal survey of the stabilators was conducted at room temperature. This was done to verify that the mode shapes and frequencies were being correctly predicted by the analysis. The change in the mode shapes due to the damping treatment was predicted to be small and this is basically what was found in the test. Since it was well known that the damping generated by the viscoelastic material is temperature dependent, the modal frequencies and damping were measured over a temperature range from 0 degrees F to 80 degrees F. This was done by constructing styrofoam boxes around the horizontal tails and blowing air, cooled by liquid nitrogen heat exchangers, into them. The temperature of the viscoelastic material was monitored by thermocouples that were attached to the constraint layers. The procedure used to obtain data was to start cooling the stabilators and monitor the temperature of the thermocouples. As a temperature data point was being approached, the shakers were turned on and the resonant frequency for the second bending mode was tuned. This frequency and the transmissibility were recorded. Damping was measured by the decay method. A picture of the test set-up is shown in Figure 14. This system worked well and damping measurements over the temperature range of interest were obtained.





GP93-0075-6

**Figure 14. Vibration Test Setup  
Stabilator Inside Styrofoam Box**

Modal loss factors as a function of temperature, as predicted by analysis and as measured by the experiment, are shown in Figure 15. As can be seen from the figure, the measured damping is considerably less than predicted from the analysis. In addition, the temperature at which the peak damping occurred was about 30 degrees higher than what was predicted. The reasons for this are not fully understood. However, it was found from ultra-sonic inspection that the bond between the viscoelastic material and the primary structure was between 40 to 80 percent complete. This incomplete bonding was believed to have been caused by air bubbles trapped during the installation procedure. A second possible source for the discrepancy is that the sealant that was used on the leading edge and trailing edge of the constraining layer may have acted as an adhesive and prevented the constraining layer from forcing the viscoelastic material into shear. This possibility was checked by comparing the viscoelastic properties of the sealant to those of the ISD-113 and it was determined that this effect should have been small. A third possibility for error is in the modal strain energy calculation itself. The vibration model that was used for the stabilator was connected by root springs to ground. Thus, any strain energy in the fuselage would not be accounted for. During the vibration test a small but significant amount of fuselage motion was detected. Thus, some modal strain energy must be contained in that part of the structure. If this were true, then the denominator in the modal strain energy calculation would increase and reduce the predicted modal damping. Unfortunately, a finite element model of the fuselage and stabilator that could be used to evaluate this hypothesis was not available. Finally, it is possible that all of these factors could have contributed to the reduction in damping that was observed in the experiment.

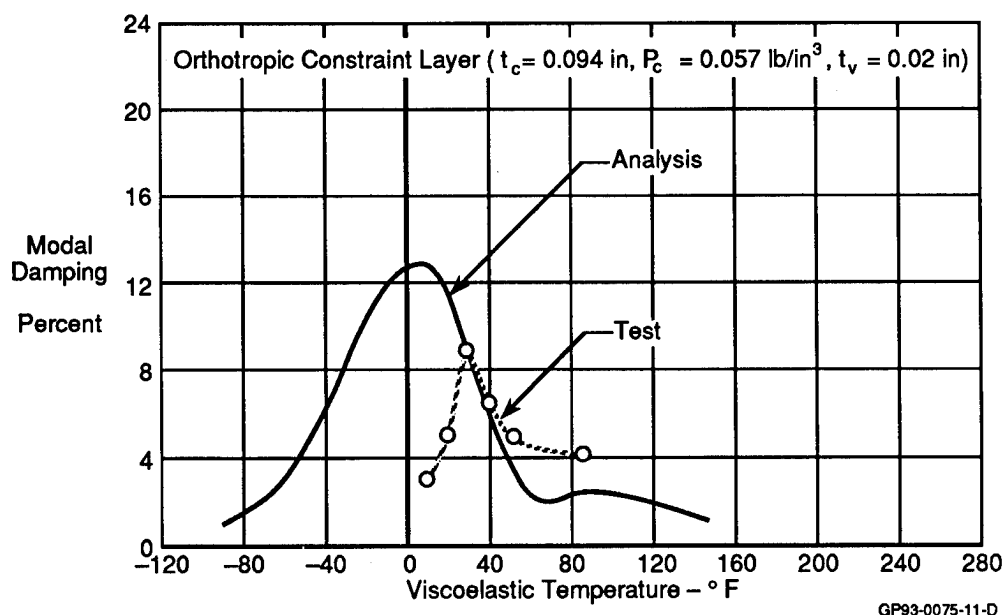


**Figure 15. F/A-18 Horizontal Tail Constrained Layer Damping Treatment  
Second Bending Mode**

Besides measuring modal damping as a function of temperature, modal frequency was also measured. This data is shown in Figure 16 for both the analysis and the test. What is interesting is that the delta frequency change over the temperature range of the test was predicted to be about 6 Hz and the measured result was about 4 Hz. This would suggest that the stiffness effects being introduced by the viscoelastic treatment are being modeled more accurately than are the damping effects. In fact, it would imply that 77 percent of the predicted stiffness increase is actually present.

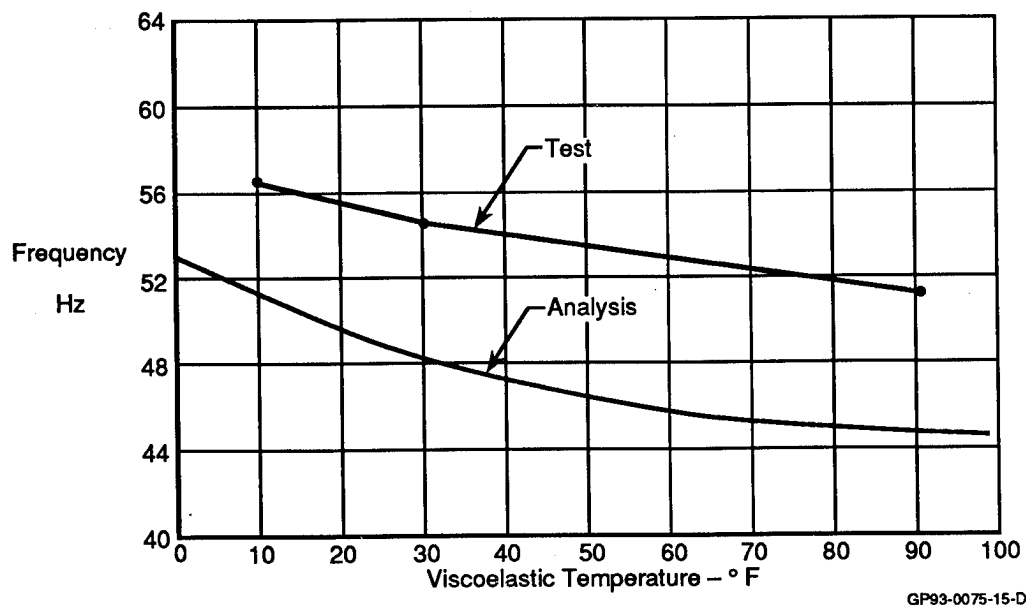


**Figure 16. F/A-18 Horizontal Tail Constrained Layer Damping Treatment  
Shift in 2nd Bending Mode Frequency With Temperature Change**

**Conclusions** - Because the predicted levels of damping were not attained during the ground vibration test, the flight test to measure engine mount loads was canceled. Thus, the assumption that stabilator response was a factor in engine mount loads was not proved or disproved by this investigation. However, the investigation showed that additional work in both the experimental and analysis areas is required if the high level of damping required by primary aircraft surfaces is to be achieved. This is especially true with composite materials as were used in these tests.

For fundamental modes of primary aircraft structure, high levels of damping are required in order to control buffet type response because, with these surfaces, high levels of aerodynamic damping are present. In general doubling the damping will cut the response in half at the resonant frequency. Thus, levels of damping must be introduced that at least match those obtained in flight if the damping treatment is to be effective.

The vibration model that was used for these studies was entirely adequate for the purpose for which it was initially constructed, modal analysis and flutter analysis where the assumption of a root fixed to the fuselage through clock springs can be used. For the modal strain energy calculation, however, a full aircraft vibration model may be required if aircraft primary vibration modes are being investigated.

Geometric properties of the damping treatment can be used to tune peak damping as a function of temperature. However, the viscoelastic material itself is the main source for controlling damping as a function of temperature.

Even though this study was not completely successful, it should not serve as a deterrent to future work in this area. What is required is a better way to install the damping treatment. If this can be found, the promise of increased structural life and reduced weight can be achieved.

**Acknowledgment** - The analytical studies reported in this paper were obtained under the McDonnell Aircraft Company's Independent Research and Development Program. The experiment conducted on the F/A-18 aircraft was conducted by the F/A-18 Project under contract number N00019-83-C-0272.

#### **References:**

1. Johnson, C. D., and Kienholz, D. A., "Finite Element Prediction of Damping in Structures with Constrained Viscoelastic Layers," Proc. 22nd Structures, Structural dynamics and Materials Conference, Atlanta, GA., Part 2, April 1981, pp. 17-24.
2. Zimmerman, N. H., and Ferman, M. A., "Prediction of Tail Buffet Loads for Design Application," NADC-880434-60, July 1987.